Miron Amusia · Larissa Chernysheva
Victor Yarzhemsky

Handbook of Theoretical Atomic Physics

Data for Photon Absorption, Electron Scattering, and Vacancies Decay

Springer

Handbook of Theoretical Atomic Physics

Miron Amusia • Larissa Chernysheva
Victor Yarzhemsky

Handbook of Theoretical Atomic Physics

Data for Photon Absorption, Electron Scattering, and Vacancies Decay

Springer

Miron Amusia
The Hebrew University
Racah Institute of Physics
Jerusalem
Israel
and
Ioffe Physica-Technical Institute
St. Petersburg
Russia

Victor Yarzhemsky
Kurnakov Institute of General
and Inorganic Chemistry
Moscow
Russia

Larissa Chernysheva
Ioffe Physica-Technical Institute
St. Petersburg
Russia

ISBN 978-3-642-24751-4 ISBN 978-3-642-24752-1(eBook)
DOI 10.1007/978-3-642-24752-1
Springer Heidelberg New York Dordrecht London

Library of Congress Control Number: 2012940247

© Springer-Verlag Berlin Heidelberg 2012
This work is subject to copyright. All rights are reserved by the Publisher, whether the whole or part of the material is concerned, specifically the rights of translation, reprinting, reuse of illustrations, recitation, broadcasting, reproduction on microfilms or in any other physical way, and transmission or information storage and retrieval, electronic adaptation, computer software, or by similar or dissimilar methodology now known or hereafter developed. Exempted from this legal reservation are brief excerpts in connection with reviews or scholarly analysis or material supplied specifically for the purpose of being entered and executed on a computer system, for exclusive use by the purchaser of the work. Duplication of this publication or parts thereof is permitted only under the provisions of the Copyright Law of the Publisher's location, in its current version, and permission for use must always be obtained from Springer. Permissions for use may be obtained through RightsLink at the Copyright Clearance Center. Violations are liable to prosecution under the respective Copyright Law.
The use of general descriptive names, registered names, trademarks, service marks, etc. in this publication does not imply, even in the absence of a specific statement, that such names are exempt from the relevant protective laws and regulations and therefore free for general use.
While the advice and information in this book are believed to be true and accurate at the date of publication, neither the authors nor the editors nor the publisher can accept any legal responsibility for any errors or omissions that may be made. The publisher makes no warranty, express or implied, with respect to the material contained herein.

Printed on acid-free paper

Springer is part of Springer Science+Business Media (www.springer.com)

Preface

The aim of this book is to present the results of calculations of cross-sections and probabilities of a large variety of atomic processes with participation of photons and electrons, namely on photoabsorption, electron scattering, and accompanying effects. Thus, we intend to produce and present newly obtained and previously collected Atomic Data.

Atomic Data are required in a number of scientific domains connected to investigation of electronic structure and physical processes in solids and liquids, molecules and clusters, astronomical objects, solar and planet atmospheres, atomic nucleus, and so on. Deep understanding of chemical reactions and processes is impossible without clear, deep, and accurate knowledge of atomic structure and processes with participation of atoms.

One should not forget also that all atoms except hydrogen and, perhaps, helium, are relatively complex systems by themselves. They are still objects of intensive theoretical and experimental studies, in which sophisticated methods are applied. For planning corresponding experiments and for estimating the value of very sophisticated new theoretical approaches, one needs data that are reasonably accurate, sufficiently general, and relatively easy to obtain. Our book serves this aim.

The role, played by atoms in macrophysics, chemistry, biology, some domains of engineering, and the entire macroworld, is similar to the role played by elementary particles in microworld. Indeed, atoms are the bricks, the main building elements from which the macroscopic world is constructed. The "glue" that keeps together the macroscopic bodies is the interatomic interaction that is modified to some extend, in many cases considerably, when many atoms are bound together.

In spite of obvious demand, there is no such a book available. Usually, if it is a book on experiment, the main focus is on the results of measurements, which are compared with available theoretical results. If a book is on theory, it concentrates on details of the presented theoretical approaches, illustrating their achievements by comparing with experimental data. In both types of books, the main interest is information on considered physical process. Our aim is to concentrate on the calculation data itself. To obtain the data, we will use theoretical methods, which open the possibility of extensive calculations and at the same time are as accurate

as possible. Of course, it would be best of all to have simple analytic formulas to calculate all necessary atomic characteristics and probabilities. Alas, the atomic structure is complicated enough. So, the analytical formulae are too crude. On the other hand, rapid development of computing facilities, PC in particular, permits to perform relatively accurate calculations, using rather complicated theoretical approaches. The result of such an approach is the subject of our book. Main attention will be given to presenting the results of calculations. As to the theoretical methods employed, they will be described briefly in order to clarify how the presented results are obtained.

We will present in this book results obtained in the best one-electron Hartree–Fock (HF) approximation and with account of multielectron correlations in the frame of so-called random phase approximation with exchange-RPAE. The corrections due to the latter proved to be very important in a broad variety of atomic characteristics and processes. There are cases when corrections determined by the multielectron nature of an atom are not too strong but still important. In these cases, we will use also so-called many-body perturbation theory—MBPT.

To explain theoretical consideration and make them as transparent as possible, we will use the diagrammatical technique, or Feynman diagram language of the many-body theory, which will make the consideration of different processes and effects transparent enough. Proper references will advice the potential reader where he or she can find all required details of the theoretical approaches used in this book.

There exist several review papers and books where table of atomic data are presented. But attention was given only to the characteristics of atomic structure, such as total energy of atoms, mean radiuses, and energy of occupied levels. To large extent the level and scope of these calculations were determined not only by the demand of the corresponding data, but also by the technical ability to perform corresponding calculations. Perhaps the first in this direction was the book written by Herman and Skillman [1]. Then several other publications appeared [2–4] where atomic data are tabulated with step by step increasing quality of the data.

In [5] and [6], the data on photoionization cross-sections and dipole angular anisotropy parameter for many atoms are presented. But the calculation results were obtained in the frame of a one-electron approach that is much simpler than HF. It is known, however, that even HF as a rule is very far from being sufficient in describing the experimental photoionization cross-sections for outer and intermediate subshells, as well as near threshold regions of the inner shells. There the role of many-electron correlations is very big. This shortcoming of [5] and [6] is eliminated in this book.

We will not limit our consideration to atoms but investigate also some negative and positive ions. Recently great attention has been given to such atom-like objects as fullerenes and endohedrals—atoms “caged” inside a fullerene shell. As a fullerene we will consider C_{60} and take into account two of its action. The first is the scattering of electrons—incoming and originating from the caged atom. The second is the modification of the incoming photon beam due to C_{60} polarization. Corresponding data will be presented for a number of endohedral atoms and ions.

As it is seen from the title, we will concentrate on the processes of electron and photon interaction with atoms. An essential reason for this is that these processes can be treated theoretically with very high accuracy and reliability. Theoretical description of each considered process will be limited by mentioning the main physical ideas essential for understanding this particular process and some key formulas that are used in our calculations. Only main points of the calculation procedure will be presented.

Such a book, as we do believe, will be important for many specialists and students, both graduate and undergraduate, who have an intention to specialize in atomic physics and related areas. This book will be useful for theorists, performing research in different domains of contemporary physics, chemistry, and biology, for technologists working on production of new materials, and for experimentalists performing research in the field of photon and electron interaction with atoms, molecules, solid bodies, and liquids. On the whole, we strongly believe that there exists a broad audience of potential readers for such a book. This is confirmed by multitude of references to our predecessors [1.1–1.6].

We will show that the data collected and the method used in obtaining these data can be useful in the theoretical description of the experiments, which are already performed. Moreover, the data can be very effective in suggesting new experiments, creating a number of desirable imaginable experiments, for which theoretical estimations or even calculations can be performed beforehand. All this could help experimentalists to plan their activity more effectively by performing preliminary rather simple investigation and research that is meaningful to call theoretical experiment.

On the whole, we will consider in this book many different physical processes, almost everything connected to the interaction of atoms and ions with photons, electrons, and positrons. For each of these processes, we will present results in one-electron Hartree–Fock approximation and with account of multielectron correlations in the frame of either the random phase approximation with exchange (RPAE) or many-body perturbation theory (MBPT).

As reference books on Quantum Mechanics and Electrodynamics in their description of atomic structure and processes, we will use the following two: Landau LD, Lifshitz EM (1977) Quantum mechanics: non-relativistic theory, 3rd edn. Pergamon Press and Berestetskii VB, Lifshitz EM, Pitaevskii LP (1982) Quantum electrodynamics, 2nd edn. Butterworth-Heinemann, Oxford. In calculating atomic characteristics and scattering cross–sections, usually radial, angular, and spin variables are separated and the integration over the angular variables and summation over spin projections are performed analytically. As a reference guide for these operations we use the book of Sobelman II (1972) Introduction to the theory of atomic spectra. Elsevier. The references to all these sources will be given as [LL], [BLP], and [IS].

Considerable overlap, particularly noticeable in notations, diagrams, which represent the physical processes, and the presentation of mathematical formulas used in this book, exists with previous publications: Amusia MYa, Atomic photoeffect. Plenum Press, New York and Amusia MYa, Chernysheva LV (1997) Computation

of atomic processes. Institute of Physics Publishing, Bristol. The references to them will be given as [AM] and [AC]. Theoretical formalism, essential for the topic of this book, can be found also in a recent book: Amusia MYa, Ivanov VK, Cherepkov NA, Chernysheva LV (2006) Processes in many-electron atoms. Nauka, Saint Petersburg, pp 1–325 (in Russian). The reference to it will be given as [AICC].

Throughout this book, we will use the atomic system of units, setting Planck's constant $\hbar$, electron charge e, and its mass m equal to 1, since otherwise formulae, calculations, and expressions will be overloaded by powers of $\hbar$, m, and e. If another system of units, with $e = 1.6 \times 10^{-19}$ C and $m = 9{,}108 \times 10^{-31}$ kg is used, the following are the atomic units: length $a_0 = \hbar^2/me^2 = 0.529 \times 10^{-10}$ $m = 5.29 \times 10^{-1}$ nm; energy $\varepsilon_0 = 2\,\mathrm{Ry} = me^4/\hbar^2 \approx 27.21$ eV $= 43.59 \times 10^{-10}$ nJ; cross-section $a_0^2 \approx 27.98 \times 10^{-18}$ cm$^2 = 27.98 \times 10^{-4}(nm)^2 = 27.98$ Mb (1 Mb being equal to 10^{-18} cm^2); velocity $v_0 = (e_0/m)^{1/2} = e^2/\hbar \approx 2.188 \times 10^6$ m/s; and time $t_0 = a_0/v_0 = \hbar^3/me^4 \approx 0.242 \times 10^{-16}$ s. Units of angular momentum are $\hbar$ and $\hbar/a_0 = me^2/\hbar$. The fine structure constant is $\alpha = e^2/\hbar c \approx 1/137.04$. In the atomic system $\alpha = 1/\mathrm{c}$ and the speed of light is $c \approx 137.04$.

We are grateful to Prof. V.A. Kilin, who contributed to the book by presenting some data in Chaps. 6 and 7.

Jerusalem Miron Amusia
St. Petersburg Larissa Chernysheva
Moscow Victor Yarzhemsky

General References

[LL] Landau LD, Lifshitz EM (1977) Quantum mechanics: non-relativistic theory, 3rd edn. Pergamon Press, Oxford
[BLP] Berestetskii VB, Lifshitz EM, Pitaevskii LP (1982) Quantum electrodynamics, 2nd edn. Butterworth-Heinemann, Oxford
[IS] Sobelman II (1972) Introduction to the theory of atomic spectra. Elsevier, New York
[AM] Amusia MYa (1990) Atomic photoeffect. Plenum Press, New York
[AC] Amusia MYa, Chernysheva LV (1997) Computation of atomic processes. Institute of Physics Publishing, Bristol
[AICC] Amusia MYa, Ivanov VK, Cherepkov NA, Chernysheva LV (2006) Processes in many-electron atoms. Nauka, Saint Petersburg, (in Russian)

References

1. Herman F, Skillman S (1963) Atomic structure calculations, Prentice-Hall Inc., Englewood Cliffs
2. Froese Ch (1968) Some Hartree–Fock results for the atomic helium to radon. University of British Columbia Report, Vancouver, BC
3. Nestor CW, Tucker TC, Carlson TA, Roberts LD, Malik FB, Froese Ch (1966) Relativistic and non-relativistic self consistent field wave functions for atoms and ions from Z = 2 to 80, together with calculations of binding energies, mean radii, screening constants, charge

distributions and electron shake-off probabilities. Oak Ridge National Laboratory Report ORNL-4027
4. Lu CC, Carlson TA, Malik FB, Tucker TC, Nestor CW (1971) Relativistic Hartree–Fock–Slater eigenvalues, radial expectation values, and potentials for atoms, $2 \leq Z \leq 126$. At Data 3:1–131
5. Yeh JJ, Lindau I (1985) Subshell photoionization cross sections and asymmetry parameters: $1 < Z < 103$. At Data Nucl Data Tab 32:1–155
6. Yeh JJ (1993) Atomic calculation of photoionization cross-sections and asymmetry parameters. Gordon and Breach Science, Langhorne

Contents

Part I Photon Absorption

1 Main Points of the Theory of Photoabsorption 3
1.1 Most Important on Photoionization 3
1.2 Single Electron Hartree–Fock (HF) Approximation 5
1.3 Diagrammatical Technique 7
1.4 Many-Body Perturbation Theory 11
1.5 Random Phase Approximation with Exchange 13
1.6 Generalizations of RPAE 18
1.7 Calculation Procedures 19
1.8 Angular Anisotropy Parameter 22
1.9 Other Characteristics of Photoionization 28
1.10 Semiclosed Subshells Atoms 29
1.11 Open Shell Atoms 32
1.12 Negative and Positive Ions 34
1.13 Endohedral Atoms: The Effect of Electron Reflections 35
1.14 Endohedral Atoms: The Effect of Fullerene Polarization 39
1.15 Two-Shell Endohedrals 43
1.16 Current Induced by Photon Momentum 46
1.17 Inelastic Photoelectron Scattering 47
1.18 Satellite Excitation 49
1.19 Two-Electron Photoionization and Recombination 51
1.20 Photoionization of the Excited Atoms 54
1.21 Electron Correlations in RPAE at High Photon Energy 54
1.22 Electron Correlations at High Photon Energy Out of RPAE Frame 58
References 59

2 Results of Calculations 65
2.1 Data Representation and Used Formulas 65
2.2 Atoms and Ions of Noble Gases 70

2.3 Atoms and Ions of Group I Elements of the Periodic Table 123
2.4 Atoms and Ions of Group II Elements of the Periodic Table 166
2.5 Ions and Atoms of Group III Elements of the Periodic Table 188
2.6 Ions and Atoms of Group IV Elements of the Periodic Table 218
2.7 Atoms and Ions of Group V Elements of the Periodic Table 232
2.8 Atoms and Ions of VI Group Elements 248
2.9 Atoms and Ions of VII and VIII Group Elements 265
2.10 Endohedral A@C_{60} Atoms and Ions 306
2.11 Onion-Type Endohedral Atoms A@C_{60}@C_{240} 390
References 414

Part II Electron Scattering

3 Main Points of the Electron Scattering Theory 421
3.1 Most Important on Electron–Atom Scattering 421
3.2 Elastic Scattering in One-Electron Approximation 427
3.3 Polarization Interaction 428
3.4 Dyson Equation 431
3.5 Inelastic Scattering of Slow and Medium Energy Electrons 432
3.6 Inelastic Scattering of Fast Particles 433
3.7 Angular Distribution of Knocked-out Electrons 438
3.8 The Compton Effect 444
3.9 GOS for Semi-filled Shells 448
3.10 Inelastic Scattering of Fast Particles upon Endohedrals 450
3.11 Bremsstrahlung of Fast Particles 456
3.12 Positron Scattering with Account of Polarization Interaction 459
References 462

4 Electron Scattering: Results of Calculations 465
4.1 Data Representation and Used Formulas 465
4.2 Atoms of Noble Gases 467
4.3 Atoms and Some Ions of Group I Elements of the Periodic Table 574
4.4 Atoms of Group II Elements of the Periodic Table 605
4.5 Atoms and Ions of Groups IV and V Elements of the Periodic Table 639
4.6 Ions of Group VII Elements of the Periodic Table 644
4.7 Endohedral A@C_{60} Atoms 648
4.8 Brief Discussion of Results 669
References 676

Part III Vacancies Decay

5 Main Points on Vacancies Decay Theory 681
5.1 Most Important About Vacancies and Their Decay 681
5.2 The Energies of Atomic Levels 684

5.3 Polarization Interaction for Vacancies 685
5.4 Self-energy Part of Green's Function and Spectroscopic Parameters 686
5.5 Satellite Lines Shapes in Photoelectron Spectra 696
5.6 Effects in Interaction Between Satellite States 699
5.7 Radiative Decay 701
5.8 Nonradiative or Auger Decay 705
5.9 Line Shapes of Low-Energy Auger Spectra 710
5.10 Two-Electron and Radiative Auger Decay 711
5.11 Single Photon Decay of Two-Hole States 714
5.12 Auger and Radiative Decay of Excited States 715
5.13 Angular Anisotropy and Spin Polarization of Auger Electrons 717
5.14 Decay of Vacancies in Endohedral Atoms 722
References 724

6 Vacancies Decay: Results of Calculations 729
6.1 Data Presentation and Used Formulas 729
6.2 Description of Figures 730
6.3 Description of Tables 740
References 758

7 Off-shell Photoionization Cross-sections: Results of Calculations 761
7.1 Data Presentation 761
7.2 Description of Figures 762
References 789

8 Conclusion and Perspectives 791
References 794

Index 795

Part I
Photon Absorption

Chapter 1
Main Points of the Theory of Photoabsorption

1.1 Most Important on Photoionization

As photoabsorption or photoionization in this book we consider a process, in which a photon of energy ω and momentum κ, $\kappa = \omega/c$ (c is the speed of light) is absorbed by a target—an atom or an ion. As a result, the target object can be either *excited* or *ionized*. Excitation means a transition of an atom or ion to one or several discrete energy levels.

Ionization is a process in which as a result of photon absorption one or several electrons can leave the target atom or ion while the residual ion is left in its lowest possible energy state. The absorption of a photon can result also in *ionization with excitation*. This is a process in which one or several electrons are eliminated from the target object and the latter is left in an excited state, on one of the discrete excited levels of the residual ion.

If the atom is treated in the frame of a one-electron picture, i.e., all electrons are considered as noninteracting and moving independently in common potential field, atom or ion can be either ionized or excited, because a single photon can interact only with a single electron. In spite of limited accuracy of the one-electron approximation, we will perform and present results of calculations in its frame. In many cases they can serve as a good initial step and serve mainly for orientation. As one-electron the Hartree–Fock approximation (HF) will be used, which is the best method compatible with the idea of independent motion of all atomic electrons in a common, so-called *self-consistent* field. We will describe the main features of HF in the next section.

However, in almost all processes considered in this book, the role of interelectron interaction is essential, and in many instances is decisively important. The account of interelectron interaction that leads to *correlations* in the atomic electron motion essentially modifies the atomic (or ionic) response to the incoming photon. Considerably altered become the photon absorption probabilities and even probabilities of eliminating of one electron. Apart from it, a whole variety of atomic processes became possible that cannot take place in the frame of one-electron approximation.

M. Amusia et al., *Handbook of Theoretical Atomic Physics*,
DOI 10.1007/978-3-642-24752-1_1, © Springer-Verlag Berlin Heidelberg 2012

Among them are the following: ionization of two and even more electrons by a single photon, ionization with excitation, and multielectron excitation.

To take into account the interelectron interaction, or as it is often called, the *multielectron correlations*, we will use in this book the random phase approximation with exchange (RPAE) or the many-body perturbation theory (MBPT). In essence, RPAE takes into account nonperturbatively, as a large correction, the dynamical variation of the self-consistent field acting upon each electron, which is caused by the incoming photon absorption [AM]. In a number of cases, however, MBPT can be used to consider atomic processes, because the interelectron interaction some times can be treated as a relatively small perturbation.

In this book, when considering photo processes we will limit ourselves by the so-called *dipole* approximation, which is valid, roughly speaking, if the wave length corresponding to the incoming photon, $\lambda = 2\pi/\kappa = 2\pi c/\omega$ is much bigger than the atomic or ionic characteristic radius r_{A}, $\omega \ll 2\pi c/r_{\mathrm{A}}$.

The operator describing the interaction between a photon and an electron can be presented in the following form [BLP]:

$$\hat{M}(\vec{\kappa}) = \sum_{i=1}^{N} \hat{\mu}_i(\vec{\kappa}) \equiv \sum_{i=1}^{N} \exp(i\vec{\kappa}\vec{r}_i)(\vec{e}\vec{\nabla}_i), \tag{1.1}$$

where $\vec{e}$ is the polarization vector of the photon, r_i is the coordinate of the electron, $\vec{\nabla}_i \equiv -i\,\partial/\partial\vec{r}_i$, and N is the total number of atomic (ionic) electrons. In the dipole approximation, the photon momentum k can be neglected, so that instead of (1.1) the interaction of an atom with a photon reduces to

$$\hat{M}_d^V = \sum_{i=1}^{N} \hat{d}^V \equiv \sum_{i=1}^{N} (\vec{e}\vec{\nabla}_i). \tag{1.2}$$

The upper index V in M^V denotes that the interaction operator is in the so-called *velocity form*. Along with this form another one, so-called *length form* exists:

$$\hat{M}^R(\omega) = \sum_{i=1}^{N} \hat{d}^R(\omega) \equiv \sum_{i=1}^{N} \omega(\vec{e}\vec{r}_i). \tag{1.3}$$

The amplitude of the process, or the matrix element $M_{i\to f}^{V,R}(\omega)$, which is determined by the following integral, describes the interaction of an atom with a photon:

$$M_{i\to f}^{V,R}(\omega) = \int \Psi_i^*(x_1,\ldots,x_N)\hat{M}^{V,R}(\omega)\Psi_f(x_1,\ldots,x_N)\prod_{i=1}^{N} \mathrm{d}x_i, \tag{1.4}$$

where $\Psi_i(x_1,\ldots,x_N)$ and $\Psi_f(x_1,\ldots,x_N)$ are the wave functions of the atom (ion) interacting with the photon, in the initial and final states, respectively. In case of

ionization, $\Psi_f(x_1, \ldots, x_N)$ includes states of continuous spectrum of one or several electrons. In (1.4) the variable $x_i \equiv r_i, s_i$, where $\boldsymbol{r}_i$ is the coordinate and s_i is the spin projection of an atomic electron. The integration over $\mathrm{d}x_i$ in (1.4) includes integration over all the infinite space $\boldsymbol{r}$ and also summation over spin projection s.

The photoionization process is characterized by the *total* $\sigma(\omega)$, *partial* $\sigma_q(\omega)$, and *differential in angle* $\mathrm{d}\sigma_q(\omega)/\mathrm{d}\Omega$ photoionization cross-sections, with Ω being the solid angle of the outgoing electron. The total cross-section $\sigma^{V,R}(\omega)$ is given by expression:

$$\sigma^{V,R}(\omega) = \frac{4\pi^2}{\omega c} \sum_f \int \left| M_{if}^{V,R}(\omega) \right|^2 \delta(E_f - E_i + \omega) \mathrm{d}E_f, \tag{1.5}$$

here E_i is the energy of the atom in its initial state, while E_f is the final state energy of the system formed by target atom after photon absorption. The summation over f goes over all state s that have the same energy E_f.

If the state f belongs to discrete spectrum of atomic excitations, the photon–atom interaction is characterized by the so-called *oscillator strength*:

$$f_{if}^{V,R} = \frac{2}{\omega_{if}} \left| M_{if} \right|^2, \tag{1.6}$$

where $\omega_{if} \equiv E_f - E_i$. Note that for precise atomic wave function the cross-sections and oscillator strengths in the length R and velocity V forms coincide, but for approximate wave functions they may be different.

The total cross-section and oscillator strength, calculated with precise initial and final state wave functions obey the so-called *golden sum rule*:

$$\sum_f f_{if}^{V,R} + \frac{c}{2\pi^2} \int_I^\infty \sigma^{V,R}(\omega) \mathrm{d}\omega = N, \tag{1.7}$$

where I is the ionization potential of an atom or the minimal energy that is necessary to remove an electron off the atom.

The partial cross-section $\sigma_q^{V,R}(\omega)$ characterizes removal of an atomic electron from a given state or energy level. The differential in angle cross-section $\mathrm{d}\sigma_q^{V,R}(\omega)/\mathrm{d}\Omega$ characterizes a process of photoionization, in which the outgoing electron, called *photoelectron*, leaves the atom at a given direction relative to that of incoming photon momentum or photon beam in the element of solid angle $\mathrm{d}\Omega$.

1.2 Single Electron Hartree–Fock (HF) Approximation

In HF approximation, the initial and final atomic wave functions are presented as antisymmetrized product of one-electron wave functions $\varphi_t(\vec{r}, s)$. In this approach, it is assumed that all electrons are moving in a self-consistent potential $\hat{U}_{\mathrm{HF}}(r)$,

so that the following equation should be solved to obtain the atomic wave function:

$$\hat{H}^{\mathrm{HF}}\Psi_E(x_1,\ldots,x_N) = \sum_{j=1}^{N}\left[-\frac{\Delta_i}{2} - \frac{Z}{r_j} + \hat{U}_{\mathrm{HF}}(r_j)\right]\Psi_E(x_1,\ldots,x_N)$$
$$= E\Psi_E(x_1,\ldots,x_N). \tag{1.8}$$

In HF approximation, the solution of (1.8) is presented as

$$\Psi_E(x_1,\ldots,x_N) \equiv \Psi_E^{\mathrm{HF}} = \frac{1}{\sqrt{N!}}\hat{A}\prod_{j=1}^{N}\varphi_j(x_j), \tag{1.9}$$

where $\hat{A}$ is the operator of permutation of coordinates and spins, which is equal to $+1$ in the case of even number of permutations and -1 in the case of the odd number of permutations. Determining the one-electron wave functions $\varphi_t(\vec{r}, s)$ and the self-consistent potential $\hat{U}_{\mathrm{HF}}(r)$ from the requirement of minimal total energy of an atom on the bases of functions (1.9), the following equation is obtained:

$$-\frac{\Delta}{2}\varphi_j(x) - \frac{Z}{r}\varphi_j(x) + \sum_{k=1}^{N}\int \mathrm{d}x'\varphi_k^*(x')\frac{1}{|\vec{r'}-\vec{r}|}$$
$$\times\left[\varphi_k(x')\varphi_j(x) - \varphi_j(x')\varphi_k(x)\right] = \varepsilon_j\varphi_j(x), \tag{1.10}$$

here ε_j stands for the individual electron energy. In the ground state of the atom, all lowest levels are successively filled. Let us introduce the *Fermi level* F as a filled level with the highest possible energy. Then the limitation in the sum over k may be denoted as $k \le F$.

The electron energy ε_j is determined by the *principal quantum number* n_j and angular momentum l_j, which determines the radial part of the wave function. The electron levels of the same energy form a *subshell*, while all levels with the same principal quantum number form a *shell*. The one-electron wave functions are orthogonal and normalized:

$$\int \varphi_j^*(x)\varphi_k(x)\mathrm{d}x = \delta_{ik}, \tag{1.11}$$

where $\delta_{ii} = 1$ and $\delta_{j\neq k} = 0$.

The solutions of (1.10) for $j > F$ are the wave functions of an additional, i.e., $(N+1)^{\mathrm{th}}$ electron. They can correspond to the *discrete* ($\varepsilon_j < 0$) and *continuous* ($\varepsilon_j > 0$) spectrum. At $\varepsilon_j > 0$ the solutions of (1.10) exist for any value of ε. At large distance from the atom these solutions oscillate and they are normalized by the following condition:

$$\int \varphi_{\varepsilon}^{*}(x)\varphi_{\varepsilon'}(x)\mathrm{d}x = \delta(\varepsilon - \varepsilon')\delta_{ll'}\delta_{mm'}\delta_{ss'}, \tag{1.12}$$

where $\delta(\varepsilon - \varepsilon')$ is the Dirac delta function, $l(l')$ is an electron angular momentum, $m(m')$ is its projection on an arbitrary chosen axis, and $s(s')$ is its spin.

In HF approximation (1.10), the dipole amplitude of photoabsorption is determined as matrix elements of the operators

$$\hat{d}^{V} = (\vec{e}\vec{\nabla}) \text{ or } \hat{d}^{R} = \omega(\vec{e}\vec{r}) \tag{1.13}$$

[see (1.2) and (1.3)]:

$$d_{if}^{V,R}(\omega) = \int \mathrm{d}x\varphi_{i}^{*}(x)\hat{d}^{V,R}\varphi_{f}(x). \tag{1.14}$$

The HF photoionization cross-section is determined by the equation similar to (1.5), with $\hat{M}^{V,R}(\omega)$ substituted by $\hat{d}^{V,R}$. The same is the situation for oscillator strengths.

1.3 Diagrammatical Technique

An important element of the theoretical description of the processes that are considered in this book is their schematic sketch: a diagram, in which the notations and method of construction presented below are used. These diagrams were introduced half a century ago in quantum electrodynamics and then successfully applied to solid state, condensed matter, and nuclear physics.

The following notations on diagrams are used:

(a) A dashed line stands for the nonstationary external field, namely a photon.

(1.15)

(b) A line with an arrow to the right denotes an electron in ν_1 state described by the HF wave function $\varphi_{\nu_1}(\vec{r}, s)$, which is determined by (1.10).

(1.16)

(c) A line with a double arrow represents an electron in discrete excited state ν_1 described by the HF wave function given by (1.10).

(1.17)

(d) A line with an arrow to the left denotes a vacancy (hole) in the state ν_2 described by the HF wave function determined by (1.10).

(1.18)

(e) A wavy line represents the Coulomb interaction between atomic electrons or that between atomic electrons and the incoming electron or positron in the process of scattering.

(1.19)

(f) A full circle–dot stands for an event of interaction between a field and an electron.

(1.20)

Using these notations, just as "words" of a very simple "vocabulary," we can build up the elementary diagrams describing the interaction between atomic electrons or between atomic electrons and the field. The following diagram accounts for the interaction of a photon with atomic electrons, which leads to creation of an electron–hole pair $\nu_1\nu_2$ and absorption of a photon with energy ω:

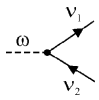

(1.21)

Annihilation (disappearance) of an electron–hole pair $\nu_1\nu_2$ with emission of a photon ω is presented like that:

(1.22)

The following elementary processes can be only virtual (temporary): "creation" of an electron–hole pair $\nu_1\nu_2$ and a photon ω from vacuum:

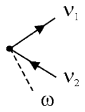

(1.23)

and annihilation of an electron–hole pair and a photon ω into vacuum.

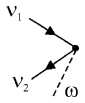

(1.24)

The interaction between two electrons ν_1 and ν_3 is depicted as an electron ν_1 scattered by another electron ν_3 leading to electrons ν_2 and ν_4:

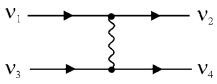

(1.25)

or as a hole ν_1 scattered by another hole ν_3:

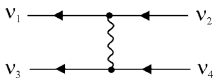

(1.26)

and a hole ν_4 scattered by an electron ν_1 or vice versa.

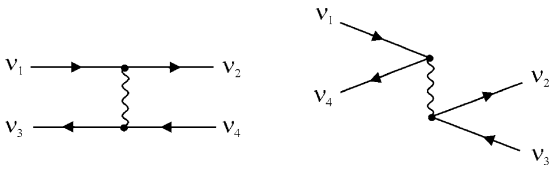

(1.27)

The second diagram in (1.27) represents the annihilation of a pair $\nu_1\nu_4$ followed by creation of the pair in different state $\nu_2\nu_3$.

The propagation of an electron ν_1 (or a hole ν_2) may be accompanied by its transition to $\nu_2(\nu_1)$ and creation of the pair $\nu_3\nu_4$. This is described as follows:

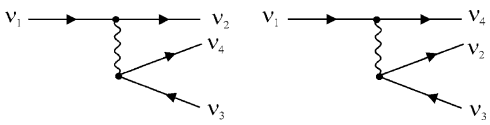

(1.28)

The propagation of an electron ν_1 or a hole ν_2 may be accompanied as well by pair annihilation, which is represented by the diagrams that are mirror reflections of (1.28) relative to the Coulomb interelectron interaction wavy line.

There are two following virtual elementary processes: creation of two electron–hole pairs $\nu_2\nu_1$ and $\nu_3\nu_4$ from vacuum and annihilation of them:

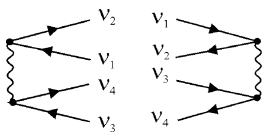

(1.29)

One or a combination of these elementary diagrams will present any physical process that will be considered in this and the following chapters of this book.

To build up a diagram of an atomic process, first of all the initial and the final states should be presented by means of elementary diagrams. For example, for photoionization with elimination of a single electron off the target atom, a photon (1.15) and an electron–hole pair account for the initial and final states, respectively. For the elastic scattering of an electron, both initial and final states are represented

by lines with right arrows (1.16). For vacancy "decay," when the state of a vacancy changes, the transition energy being released as the creation of an electron–hole pair, the initial state is a vacancy (1.18), while the final state is a vacancy and an electron–hole pair.

Building up a diagram starts from the lowest possible order in interelectron interaction. The goal is to present the process under investigation as developing from its initial to the final state as the shortest possible series of interparticle interaction elements. For instance, the simplest diagram of photoionization is (1.21), while (1.28, *left*) is the simplest diagram of the inelastic scattering of an electron with creation of an electron–hole pair.

The initial and the final states may be as well joined together with a bigger series of elementary events. For example, the following diagram presents the contribution to the amplitude of one-electron photoionization with creation of an electron ν_4 and a vacancy ν_3 that involves interaction with electron–hole pair $\nu_1\nu_2$:

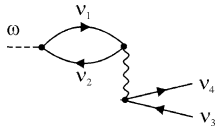

(1.30)

The diagrams present the process evolving in time. The normal course of time runs from left to the right. The following so-called correspondence rules allow us to relate an analytical expression to the diagram:

- Assign $\nu_1, \nu_2, \ldots, \nu_n$ to all electron and hole states.
- Introduce the "sections" of diagrams, i.e., draw in reality or imagination vertical lines separating each event of interaction between atomic electrons, or that of an atomic electron and a photon.
- To relate to every section the energy denominator:

$$\left(\sum \varepsilon_h - \sum \varepsilon_p + E_{in} + i\eta\right)^{-1}, \tag{1.31}$$

where $\sum \varepsilon_h$ and $\sum \varepsilon_p$ are, respectively, the total energies of all holes and electrons involved in the section, while E_{in} is the incoming energy, $\eta \to 0$.

- To each event of the interaction of a photon with an electron or a hole (1.21)–(1.24), with $\mu(\vec{k})$ given by (1.1) the following matrix element is related:

$$\left\langle \nu_1 \left| \hat{\mu}(\vec{k}) \right| \nu_2 \right\rangle \equiv \int \mathrm{d}x \varphi^*_{\nu_1}(x) \hat{\mu}(\vec{k}) \varphi_{\nu_2}(x). \tag{1.32}$$

- To interelectron interaction V the following matrix element appearing in diagrams (1.25)–(1.29) is related:

$$\langle \nu_1 \nu_3 \,|V|\, \nu_2 \nu_4 \rangle \equiv \int \mathrm{d}x \mathrm{d}x' \varphi^*_{\nu_1}(x) \varphi^*_{\nu_3} \frac{1}{\left|\vec{r} - \vec{r}'\right|} \varphi_{\nu_2}(x) \varphi_{\nu_4}(x'). \tag{1.33}$$

– To sum (and integrate) over all internal electron and hole states ν, while $\eta \to 0$ in (1.31) shows the direction of tracing the singularities.
– Multiply the obtained expression by $(-1)^Q$, where Q is the number of hole lines in the diagram added to the number of closed electron–hole loops.

The result is the contribution of the diagram to the amplitude of the process under investigation.

For instance, the contribution of diagram (1.30) is equal to

$$\Delta\mu_{\nu_3\nu_4}(\omega) = \sum_{\nu_1 > F, \nu_2 < F} \frac{\left\langle \nu_1 \left| \hat{\mu}(\vec{k}) \right| \nu_2 \right\rangle \langle \nu_2 \nu_3 \,|V|\, \nu_1 \nu_4 \rangle}{\varepsilon_{\nu_2} - \varepsilon_{\nu_1} + \omega + i\eta} \times (-1)^3, \tag{1.34}$$

here $Q = 3$ since there is an electron–hole loop and two hole lines (ν_2 and ν_3) in the diagram. More complex diagrams can be built up similarly, and analytical expressions are related to them in the same way.

In principle, infinite variety of diagrams corresponds to any physical process with given initial and final states. Having restricted the consideration to some selected diagrams, one can relate them to respective analytical expressions and thus obtain the amplitude of the investigated process, whose probability is proportional to the square of the amplitude's modulus. The total probability of the process per unit time is the sum of amplitudes' modulus squares over all possible final states averaged over the initial states with the account taken of energy conservation. Total energies of the system in its initial and final states must be equal in accordance with the energy conservation law.

1.4 Many-Body Perturbation Theory

Till now, in spite of rapid development of the computation technique, it is impossible to describe an N-electron atom, with $N > 2$, precisely, by solving the Schrödinger equation of N electrons interacting with each other via the Coulomb potential and moving in the field of a nucleus. Thus, one has to use simplifying models to study and describe atoms.

Essential simplifications become possible and justified when the interaction is weak. Then it can be considered using *perturbation theory*. In this book, we will investigate the interaction of atoms with only low intensity photon field. Therefore, the photon–electron interaction is sufficient to take into account only in the lowest order of the perturbation theory. For photoabsorption, it means that the corresponding amplitudes will be calculated in first order in $\hat{\mu}(\vec{k})$ [see (1.1)].

The situation with electron–electron and electron–nucleus interaction is much more complicated. Indeed, these interactions can be treated as perturbation in general only when the relative velocity of the interacting particles is big. Inside an atom this is not the case. Without any doubt, the HF field differs from pure nucleus field strong enough. Therefore, as one-electron or one-hole states those calculated in HF approximation (1.10) will be used.

The interaction between fast incident particle and target electrons will be limited to the first order in V. However, there exist a number of processes, e.g., vacancy decay with emission of fast electrons or high-energy photons where perturbation theory in interelectron interaction can be also applied. Perturbation theory, even in its lowest order, can be used in any case while studying a complicated process, which otherwise is too difficult or impossible to consider. In the latter case, the data obtained can be used with reasonable precaution admitting that it cannot be accurate enough.

The advantage of the perturbative approach is that the rough approximation is relatively easy to obtain, and the mechanism under consideration becomes clear and obvious. As an example of the latter situation, let us consider two-electron photoionization, i.e., a process in which two electrons are eliminated from an atom after absorbing a single photon. The simplest diagrams describing creation of two electron–vacancy pairs by one photon look as follows:

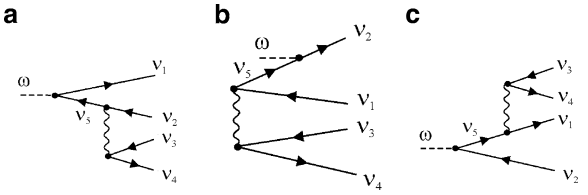

(1.35)

where diagrams (1.35a) and (1.35c) are describing the knockout of an electron and the creation of the state $\nu_3\nu_4$ due to the scattering of an electron (or a hole) ν_5 followed by the transition of the latter into the state ν_2 or ν_1. Note that in the first order along with diagram (1.35b) a similar one exists, in which the incoming photon interacts not with an electron but a hole. This diagram together with (1.35b) corresponds to the interaction between the electrons in the ground state. As a result of action of the mechanisms presented by (1.35), two electrons are removed from the atom or occupy an excited state.

To obtain accurate enough results for the two-electron photoionization at not very high ω, one should take into account nonperturbatively at least the interaction between two atomic electrons $\nu_1\nu_4$. In the initial state, the interaction between two ionizing electrons must be taken into account nonperturbatively even for high ω. However, calculations using the amplitude depicted in (1.35) give a very good first approximation to the reality.

It is rather difficult to take into account next orders corrections in V to (1.35). In fact, already inclusion of all third-order terms is a very complicated task. Therefore, calculations in MBPT are limited to not more than all third-order diagrams. Of course, some even infinite order terms are taken into account by the choice of HF functions as the one electron. But in general, with the number of interelectron interactions exceeding three, even to draw all diagrams became a rather time-consuming task. As to the calculations of corresponding matrix elements, they simply became almost impossible. Indeed, with a number of interaction events N_{int}, the number of diagrams amounts to $N_{\text{int}}!$ As to the calculation of a contribution of a given diagram, they became more and more complicated with increasing N_{int} since the number of intermediate state increases, and so the number of required integrations and summations.

However, another approach is often used. Terms of all powers of V are accounted for, but in each order q (with the product of q matrix elements of V) only a limited number of terms of the expansion are retained. Evidently, even the part of the terms of all powers in V cannot be summed up sequentially, one order after the other. However, in some cases such summation may be performed by means of establishing and solving an equation (or a set of the equations) called the closed equation wherein all functions to be found are expressed in terms of the functions already known. A version of this approach is called the random-phase approximation with exchange (RPAE).

1.5 Random Phase Approximation with Exchange

The RPAE is a generalization of HF approximation for the atom in a weak electromagnetic external field or in an excited state populated, for instance, in the collision of the atom with an electron, etc. The method is based on the assumption that both in the presence and absence of the nonstationary applied field the wave function of an atom at every moment is a Slater determinant composed from one-electron wave functions $\varphi_\nu(x,t)$. It is assumed in RPAE that the variation of the one-electron wave functions under the action of external electromagnetic field is small.

The RPAE equations account not only for the action of the external field with particular atomic electron, but also for the interaction of the external field with all other electrons. The virtual transitions induced by this interaction change the mean atomic field and therefore lead to removal or excitation of the atomic electron. In terms of the diagrams, RPAE corresponds to the account of an event of interaction between a hole and an electron. Diagrammatically, the RPAE equation is presented in the following way:

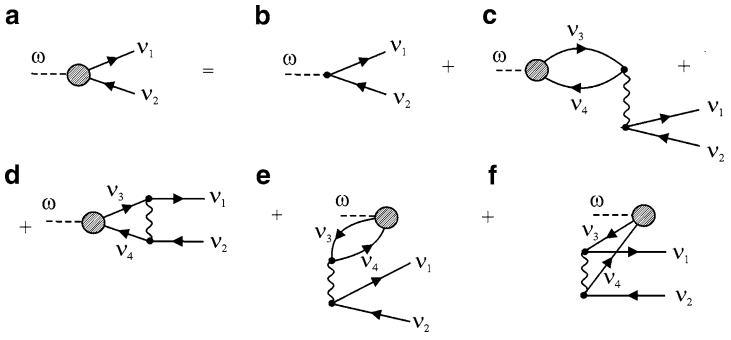

(1.36)

Here the shaded circle denotes the electron–photon interaction operator in RPAE. The diagram equation (1.36) can be iterated. The first step of this iteration is to substitute the shaded circle by a dot. Then the diagram (1.36c) transforms into (1.30).

The diagrams (1.36) present photo ionization process as developing in time, from left to right, starting with a photon and ending up with an electron–hole pair. This is why diagrams (1.36b)–(1.36d) are called "time-forward," whereas (1.36e) and (1.36f) are called "time-reverse" diagrams.

The diagram equation (1.36) may be analytically presented as an integral equation. In dipole approximation, which will be used in all but one section of this book, one has (see [AC]):

$$\langle \nu_1 \,|D(\omega)|\, \nu_2\rangle = \left\langle \nu_1 \left|\hat{d}\right| \nu_2 \right\rangle + \sum_{\nu_3,\nu_4} \frac{\langle \nu_3 \,|D(\omega)|\, \nu_4\rangle \,(n_{\nu_4} - n_{\nu_3})\, \langle \nu_4\nu_1 \,|U|\, \nu_3\nu_2\rangle}{\varepsilon_{\nu_4} - \varepsilon_{\nu_3} + \omega + i\eta(1 - 2n_{\nu_3})},$$

$$\langle \nu_4\nu_1 \,|U|\, \nu_3\nu_2\rangle \equiv \langle \nu_4\nu_1 \,|V|\, \nu_3\nu_2\rangle - \langle \nu_4\nu_1 \,|V|\, \nu_2\nu_3\rangle \tag{1.37}$$

here $\left\langle \nu_1 \left|\hat{d}\right| \nu_2 \right\rangle$ is determined as (1.32) with $\mu(\vec{k})$ substituted by $\hat{d}^{V,R}$ from (1.13) and n_ν is the so-called *Fermi step function*:

$$n_\nu = \begin{cases} 1 & \nu \le F \\ 0 & \nu > F \end{cases}. \tag{1.38}$$

Summation over continuous states in (1.37) includes also integration over their energies and therefore (1.37) is an integral equation. Important features of RPAE are that the results of "length" and "velocity" forms have to coincide and the sum rule (1.6) must be fulfilled, contrary to the HF and, in general, MBPT, approximation cases. These features will be used to check the numerical accuracy of our calculations. The RPAE photoionization cross-section is determined by equation similar to (1.4), with $\hat{M}^{V,R}(\omega)$ substituted by $\hat{D}(\omega)$. The same is the situation for oscillator strengths.

An important element of RPAE is the *effective interaction* $\Gamma(\omega)$. It differs from the pure Coulomb interaction V by the corrections caused by the virtual excitation of other atomic electrons in the course of interaction of the pair of electrons under investigation. We can express in terms of effective interaction $\Gamma(\omega)$ the RPAE corrections to the physical features of atoms and atomic processes obtained in HF approximation. Those are called *correlation corrections*.

The following considerations enable us to write an RPAE equation for $\Gamma(\omega)$. The effect of one atomic electron upon the other may be regarded as the external field:

$$B_{\nu_3\nu_4}(\vec{r}) = \int \mathrm{d}x \varphi_{\nu_3}(x) \frac{1}{|\vec{r} - \vec{r}'|} \varphi^*_{\nu_4}(x). \tag{1.39}$$

Substituting (1.39) for $\hat{d}$ in (1.37) we obtain the expression for the effective interelectron interaction in RPAE:

$$\langle \nu_1\nu_3 \,|\Gamma(\omega)|\, \nu_2\nu_4\rangle = \langle \nu_1\nu_3 \,|U|\, \nu_2\nu_4\rangle + \sum_{\nu_5,\nu_6} \frac{\langle \nu_3\nu_5 \,|\Gamma(\omega)|\, \nu_4\nu_6\rangle \,(n_{\nu_6} - n_{\nu_5}) \,\langle \nu_6\nu_1 \,|U|\, \nu_5\nu_2\rangle}{\varepsilon_{\nu_6} - \varepsilon_{\nu_5} + \omega + i\eta(1 - 2n_{\nu_5})}. \tag{1.40}$$

In terms of diagrams, the effective interaction $\Gamma(\omega)$ is presented by an equation constructed similarly to (1.36) where the first term in the right-hand side is (1.27) instead of (1.21).

It is essential to note that some uncertainty exists in the definition of HF approximation for the excited states. It was shown (see [AM]) that as a result of this some parts of RPAE diagrams contributions can be taken into account by a corresponding choice of one-electron wave functions in HF approximation. This technique will be widely used in the following parts of this book.

The HF and RPAE equations will be solved, just as MBPT calculations will be performed numerically. But to foresee what are the qualitative features that could be expected as a result of taking into account the many-electron correlations, the following approach can be used. Let us present (1.37) and (1.40) in a symbolic operator form:

$$\hat{D}(\omega) = \hat{d} + \hat{D}(\omega) \times \hat{\chi}(\omega) \times \hat{U} \tag{1.41a}$$

and

$$\hat{\Gamma}(\omega) = \hat{U} + \hat{\Gamma}(\omega) \times \hat{\chi}(\omega) \times \hat{U}, \tag{1.41b}$$

respectively. Notations are evident from comparison with (1.37) and (1.40). Using (1.41b), (1.41a) can be presented in the following form:

$$\hat{D}(\omega) = \hat{d} + \hat{d}(\omega) \times \hat{\chi}(\omega) \times \hat{\Gamma}(\omega). \tag{1.42}$$

Equations (1.41a) and (1.41b) can be easily solved in the operator form, which leads to

$$\hat{D}(\omega) = \frac{\hat{d}}{[1 - \hat{\chi}(\omega) \times \hat{U}]} \tag{1.43a}$$

and

$$\hat{\Gamma}(\omega) = \frac{\hat{U}}{[1 - \hat{\chi}(\omega) \times \hat{U}]}. \tag{1.43b}$$

Equation (1.41b) has an important feature that is of importance in solving it. Let us present $\chi(\omega)$ as a sum of two terms $\chi(\omega) = \chi_1(\omega) + \chi_2(\omega)$. Then, defining $\Gamma_1(\omega)$ by:

$$\hat{\Gamma}_1(\omega) = \hat{U} + \hat{\Gamma}_1(\omega) \times \hat{\chi}_1 \times (\omega)\hat{U}, \tag{1.44}$$

one has from (1.41b) an expression for $\Gamma(\omega)$:

$$\hat{\Gamma}(\omega) = \hat{\Gamma}_1(\omega) + \hat{\Gamma}(\omega) \times \hat{\chi}_2(\omega) \times \hat{\Gamma}_1(\omega). \tag{1.45}$$

Expressions (1.43a) and (1.43b) permit to perform qualitative analysis of the RPAE solutions. Indeed, the amplitude $\hat{D}(\omega)$ is strongly enhanced in the ω region where the denominator in (1.43) is small. If the interelectron interaction U is strong enough, the denominator at some $\omega = \Omega_{\mathrm{GR}}$, can reach zero value:

$$1 - \chi(\Omega_{\mathrm{GR}}) \times \hat{U} = 0. \tag{1.46}$$

The corresponding frequency Ω_{GR} is complex, $\Omega_{\mathrm{GR}} = \mathrm{Re}\Omega_{\mathrm{GR}} + i\,\mathrm{Im}\Omega_{\mathrm{GR}}$, where $\mathrm{Re}\Omega_{\mathrm{GR}}$ and $\Gamma_{\mathrm{GR}} = \mathrm{Im}\Omega_{\mathrm{GR}}$ are the energy and width, respectively, of the so-called *Giant resonance* (GR). They manifest themselves as powerful, broad and high, maxima in the photoionization cross-sections.

Another kind of maxima, named *Interference Resonances* (IR) and corresponding *Interference Minima* (IM) appear under the action of a subshell b, with big photoionization cross-section, upon any other, a, if the inter-subshell interaction U_{ab} is strong enough. Indeed, according to (1.41a), the amplitude of the a-subshell photo ionization is given by the following equation:

$$\begin{aligned} \hat{D}_a(\omega_{\mathrm{IR}}) &= d_a + \hat{D}_b(\omega_{\mathrm{IR}}) \times \hat{\chi}_b(\omega_{\mathrm{IR}}) \times \hat{U}_{ba} \\ &\approx \hat{D}_b(\omega_{\mathrm{IR}}) \times \hat{\chi}_b(\omega_{\mathrm{IR}}) \times \hat{U}_{ba} \gg d_a. \end{aligned} \tag{1.47}$$

The photoionization cross-section of an outer subshell, i.e., that with smaller ionization potential I_{o} is strongly modified in the vicinity of discrete excitation of the inner subshell, i.e., that with bigger ionization potential I_{i}, $I_{\mathrm{i}} > I_{\mathrm{o}}$. In this case, in the vicinity of the discrete level with energy ω_d the continuous spectrum photoionization amplitude $D_c(\omega)$ can be presented, in accordance to (1.41a) in a rather simple form.

Indeed, approximating $\chi(\omega)$ as $\chi(\omega) \approx (\omega - \omega_d)^{-1}$, it is easy to obtain an expression for the continuous spectrum amplitude having in mind that close to the singularity in $\chi(\omega)$ it is represented as $\chi(\omega) \approx \tilde{\chi}_1(\omega_d) + (\omega - \omega_d + i\delta)^{-1} = \tilde{\chi}_1(\omega_d) + (\omega - \omega_d)^{-1} - i\pi\delta(\omega - \omega_d)$. Discarding for simplicity the term $\tilde{\chi}_1(\omega_d)$,

one obtains

$$\hat{D}_c(\omega) \approx \frac{d_c}{(\omega - \omega_d - U_{dc} - i\Gamma_d)}, \tag{1.48}$$

here the *width* Γ_d is a result of the decay of the discrete level d due to its interaction with the continuous spectrum c. The symbolic relation determines Γ_d

$$\Gamma_d = 2\pi |U_{cd}|^2. \tag{1.49}$$

In principle, if there are several continuous spectra interacting with the isolated discrete level d, the relation (1.49) must be modified by adding summation over all d. Using (1.48) and (1.49), the following expression for the photoionization cross-section near discrete excitation–resonance, $\sigma_R(\omega)$ can be obtained

$$\sigma_R(\omega) = \sigma_0 \left[(1 - \rho^2) + \rho^2 \frac{(q + \zeta)^2}{1 + \zeta^2} \right]. \tag{1.50}$$

Fano derived this formula for the first time in 1961 [1.1].[1] We present here simplified expressions and explanations for the parameters in (1.50). Detailed expressions can be found in [AM]. In (1.50) ρ describes the contribution due to admixture of several continuous spectra interacting with the same discrete level d. If only one continuous spectrum interacts with the level d, then $\rho = 1$. The parameter ζ in (1.50) is defined as $\zeta = (\omega - \omega_d - U_{cd})/\Gamma_d$, σ_0 is the cross-section *without* resonance and q is the *asymmetry* parameter, determined by the relation $q = U_{cd}/\Gamma_d$.

If there are two instead of one discrete interacting level, the formulas for the cross-sections become more complicated because in this case (1.41a) reduces instead of one to a system of two coupled algebraic equations.

Oscillator strengths are also affected by the RPAE correlations. As a result they are presented by an expression that differs from (1.5) by a factor F_d:

$$f_d = \frac{2}{\tilde{\omega}_d} F_d \left| \breve{D}_d(\tilde{\omega}_d) \right|^2, \tag{1.51}$$

here the discrete level d and excitation energy ω_d, modified due to RPAE corrections is given by the equation $\tilde{\omega}_d = \omega_d + \breve{\Gamma}_{dd}(\tilde{\omega}_d)$. The amplitude $\breve{D}_d(\tilde{\omega}_d)$ and the matrix element $\breve{\Gamma}_{dd}(\tilde{\omega}_d)$ are solutions of corresponding RPAE equations, but where the terms with denominator $1/(\omega - \omega_d)$ in (1.41a) and (1.41b) are eliminated from $\chi(\omega)$. The factor F_d is connected to the derivative of $\breve{\Gamma}_{dd}(\omega)$ in ω:

$$F_d = \left[1 - \frac{\partial \breve{\Gamma}_{dd}(\omega)}{\partial \omega} |_{\omega = \tilde{\omega}_d} \right]^{-1}. \tag{1.52}$$

[1] In other chapters, this and the subsequent references will be given mentioning also its number. For example, [1.1] will be presented in other chapters as [1.1].

Again, details of the derivation of (1.51) can be found in [AM]. The factor F_d determines the admixture of other electron–hole excitations to the discrete excitation d. Quite naturally, $F_d < 1$. Most transparently the meaning of F_d is seen when the quantity $\partial \breve{\Gamma}_{dd}(\omega)/\partial\omega$ is small and only second-order correction is enough to include in $\breve{\Gamma}_{dd}(\omega)$. Considering only the important "time-forward" contribution into $\breve{\Gamma}_{dd}(\omega)$, one has:

$$F_d \approx 1 + \left.\frac{\partial \breve{\Gamma}_{dd}(\omega)}{\partial\omega}\right|_{\omega=\tilde{\omega}_d} \approx 1 - \sum_c \frac{|U_{dc}|^2}{(\omega_d - \omega_c)^2} < 1. \tag{1.53}$$

The sum over c in (1.53) presents the usual quantum-mechanical probability for the lowest order interaction between d and c to mix d with other states c.

1.6 Generalizations of RPAE

In the RPAE frame, the wave functions of all vacancies are considered as solutions of (1.10) where summation is performed over all i, from 1 to N where N is the total number of electrons in a considered atom. As it was mentioned in Sect. 1.2, for an excited electron or that in continuous spectrum the solutions of (1.10) are the wave functions of an additional, $(N+1)^{\text{th}}$ electron. However, even pure intuitively it is natural to take into account the presence of the vacancy i created after photon absorption. At first, the creation of this vacancy modifies the equation that determines the wave function of the entire excited or outgoing ionized electron. Instead of (1.10), it had to be determined by an equation, in which from the sum over all atomic electrons one term representing the ionized electron is eliminated. As a result, one has for $\varphi_k(x)$ $(k > F)$ instead of (1.10)

$$-\frac{\Delta}{2}\varphi_k(x) - \frac{Z}{r}\varphi_k(x) + \sum_{j\neq i=1}^{N} \int \mathrm{d}x' \varphi_j^*(x') \frac{1}{|\vec{r}' - \vec{r}|} \times \left[\varphi_j(x')\varphi_k(x) - \varphi_k(x')\varphi_j(x)\right] = \varepsilon_k \varphi_k(x). \tag{1.54}$$

Similarly, the equation for the wave functions of other occupied states i' can be modified by eliminating in the sum over j the term with $j = i$.

Then, correspondingly, the RPAE equations can be altered: instead of (1.37), one has the following:

$$\langle i\,|D(\omega)|\,\nu_2\rangle = \left\langle i\left|\hat{d}\right|\nu_2\right\rangle + \sum_{\nu_3,\nu_4\neq i} \frac{\langle \nu_3\,|D(\omega)|\,\nu_4\rangle\,(n_{\nu_4} - n_{\nu_3})\,\langle \nu_4 i\,|U|\,\nu_3\nu_2\rangle}{\varepsilon_{\nu_4} - \varepsilon_{\nu_3} + \omega + i\eta(1-2n_{\nu_3})}. \tag{1.55}$$

This equation represents the *generalized* version of RPAE or GRPAE. It goes beyond the theoretically consistent approach of RPAE by taking into account that while the outgoing or photoelectron leaves the atom, all states of atomic electrons are modified due to creation of this vacancy. As a result of this rearrangement or relaxation, the field of the ion acting upon the photoelectron became modified. This affects the photoionization cross-section. The alteration increases with decrease of the photoelectron energy.

The relaxation of atomic electron states due to creation of a hole leads to modification of the electron ionization potentials as compared to their HF values. Therefore, in GRPAE calculations as vacancy energies instead of HF values, the experimental ionization potentials are used.

For inner vacancies, it is essential to take into account that while the photoelectron leaves the atom, the vacancy can decay via the Auger process. As a result of this, the photoelectron moves in the field of at least double instead of a single charged ion

$$-\frac{\Delta}{2}\varphi_k(x) - \frac{Z}{r}\varphi_k(x) + \sum_{j\neq p,q=1}^{N} \int \mathrm{d}x' \varphi_j^*(x') \frac{1}{|\vec{r}' - \vec{r}|} \times \left[\varphi_j(x')\varphi_k(x) - \varphi_k(x')\varphi_j(x)\right] = \varepsilon_k \varphi_k(x), \tag{1.56}$$

here $i \to p,\ q,\ \varepsilon_\mathrm{A}$ is the dominating channel of the Auger decay of the hole i. Correspondingly, the system of equations (1.55) has to be modified by eliminating two terms from the sum ν in the right-hand side: $\nu_3, \nu_4 \neq p, q$. This approximation is called GRPAEII.

1.7 Calculation Procedures

To obtain cross-sections, oscillator strength, and other characteristics of atomic processes, calculations, both numeric and analytic, must be performed.

As a first step, the one-electron wave functions $\varphi_k(x) \equiv \varphi_{\varepsilon(n)lm\sigma}(\vec{r}, s)$—solutions of HF equations (1.10)—must be presented as a product of radial $R_{\varepsilon(n)l}(r) \equiv r^{-1} P_{\varepsilon(n)l}(r)$, angular $Y_{lm}(\vartheta, \varphi)$, and spin functions χ_σ:

$$\varphi_{\varepsilon(n)lm\sigma}(\vec{r}, s) = r^{-1} P_{\varepsilon(n)l}(r)\, Y_{lm}(\vartheta, \varphi)\chi_\sigma, \tag{1.57}$$

here $Y_{lm}(\vartheta, \varphi)$ is the spherical function, χ_σ is the spin function, $\varepsilon(n)$ is the one-electron energy (principal quantum number), l is the angular momentum quantum number, m is its projection upon a selected axis, σ is the electron spin projection, ϑ and φ are polar and azimuthal angles of the electron coordinate $\boldsymbol{r}$. Using expression (1.57), one can perform analytically the integration over angular variables and summation over spin variables, since the analytic expressions for $Y_{lm}(\vartheta, \varphi)$ and χ_σ are well known.

The technique of integrating different products of $Y_{lm}(\vartheta,\varphi)$ over ϑ, φ and summation of products χ_σ over σ is well developed and discussed at length in a number of books, e.g., in [LL, IS]. Applying this technique, at first the system of HF equations (1.10) is reduced to that for radial wave functions $R_{\varepsilon(n)l}(r) \equiv r^{-1}P_{\varepsilon(n)l}(r)$. This system is solved numerically.

After performing integration over ϑ and φ, one can present the dipole matrix elements (1.14) in the following form:

$$d^{V,R}_{i\to f} = (-1)^{l_i-m_i}\begin{pmatrix} l_i & 1 & l_f \\ -m_i & \mu & m_f \end{pmatrix}\left\langle n_i l_i \left\| d^{V,R} \right\| \varepsilon_f(n_f), l_f \right\rangle, \tag{1.58}$$

here $\begin{pmatrix} l_i & 1 & l_f \\ -m_i & \mu & m_f \end{pmatrix}$ is a $3j$-symbol (see [IS]), $l_f = l_i \pm 1$, $\left\langle n_i l_i \left\| d^{V,R} \right\| \varepsilon_f(n_f), l_f \right\rangle$ is the dipole reduced matrix element. The latter are determined by the expressions [AC] that become particularly simple for closed shell atoms:

$$d^R_{nl,n'l'} \equiv \left\langle nl \left\| d^R \right\| n'l' \right\rangle = (-1)^{(l+l'+1)/2} \times \sqrt{\frac{(l+l'+1)}{2}}\omega \int_0^\infty P_{nl}(r) r P_{n'l'}(r)\mathrm{d}r, \quad l' = l \pm 1, \tag{1.59a}$$

$$d^V_{nl,n'l'} \equiv \left\langle nl \left\| d^V \right\| n'l' \right\rangle = (-1)^{(l+l'+1)/2}\sqrt{\frac{(l+l'+1)}{2}} \times \int_0^\infty P_{nl}(r)\left(\frac{\mathrm{d}}{\mathrm{d}r} \pm \frac{l+l'+1}{2r}\right) P_{n'l'}(r)\mathrm{d}r, \tag{1.59b}$$

here sign + corresponds to $l' = l+1$ and − to $l' = l-1$.

The following notations are used for the radial integrals in (1.59):

$$d^R_l \equiv \int_0^\infty P_{nl}(r) r P_{n'l'}(r)\mathrm{d}r \quad \text{and}$$
$$d^V_{l'} \equiv \int_0^\infty P_{nl}(r)\left(\frac{\mathrm{d}}{\mathrm{d}r} \pm \frac{l+l'+1}{2r}\right) P_{n'l'}(r)\mathrm{d}r. \tag{1.60}$$

Similarly to (1.58), in Coulomb matrix elements (1.33) integration over angular parts of one-electron wave functions lead to the following expression:

$$\langle \alpha\,|V|\,\beta\rangle = \sum_{\lambda=0}^{\infty}\sum_{m=-\lambda}^{\lambda}(-1)^{m_1+m_3+m}\begin{pmatrix} l_1 & \lambda & l_2 \\ -m_1 & m & m_2 \end{pmatrix}\begin{pmatrix} l_3 & \lambda & l_4 \\ -m_3 & m & m_4 \end{pmatrix} V^\lambda_{\alpha\beta}, \tag{1.61}$$

here the matrix element $V^\lambda_{\alpha\beta}$ is determined as:

$$V^{\lambda}_{\alpha\beta} \equiv \langle \nu_1 \nu_4 \| V_\lambda \| \nu_2 \nu_3 \rangle$$
$$= \sqrt{(2l_1+1)(2l_2+1)(2l_3+1)(2l_4+1)} \begin{pmatrix} l_1 & \lambda & l_2 \\ 0 & 0 & 0 \end{pmatrix} \begin{pmatrix} l_3 & \lambda & l_4 \\ 0 & 0 & 0 \end{pmatrix}$$
$$\times R_\lambda (\nu_1 \nu_2 \nu_3 \nu_4), \tag{1.62}$$

with $\nu \equiv nl (\nu \leq F)$ or $\nu \equiv n(\varepsilon) l (\nu > F)$, i.e., the state labels ν_j include two quantum numbers instead of four in (1.33). In (1.61), $R_\lambda (\nu_1 \nu_2 \nu_3 \nu_4)$ is a pure radial matrix element given by the following two-dimensional integral:

$$R_\lambda (\nu_1 \nu_2 \nu_3 \nu_4) = \int_0^\infty P_{\nu_1}(r) P_{\nu_2}(r) \mathrm{d}r \int_0^r \frac{r_<^\lambda}{r_>^{\lambda+1}} P_{\nu_3}(r') P_{\nu_4}(r') \mathrm{d}r'. \tag{1.63}$$

The radial integrals in (1.59) and (1.63) are calculated numerically, substituting integrals with infinite upper limits by finite sums which cover distances up to $r \leq R$. In concrete calculations, we chose R as big as $R \approx 50$ atomic units, i.e., considerably bigger than the atomic size $r \approx 1$. This is possible because usually the integrands are decreasing faster than $1/r^2$. If this is not the case, the contribution of r region, $r > R$, is found analytically because far from the atom all electron wave functions and expressions that include Coulomb interelectron interaction simplify considerably.

The specific of atomic problem, i.e., the presence of the nuclear Coulomb field, dictates that it is desirable to have more points of integration in the vicinity of the nucleus, i.e., at small r. This is achieved by introducing a new variable, $\rho = \alpha r + \beta \ln r$, which permits to place integration points in ρ equidistantly. The number of integration points in ρ is about 1,000.

After the radial integrals are calculated, the contribution of isolated diagrams or the solution of RPAE (or in principle any other similar equations) may be obtained. This requires integration over one-electron energy variables ε and summation over discrete excitations n. Usually the integrals in ε are substituted by a finite sum with points located equidistantly in $k = \sqrt{2\varepsilon}$. As a result, more points are placed at small ε where the integrands as functions of ε are rapidly changing while fewer points are in the high ε area.

Usually the integrands are decreasing fast enough and it is sufficient to have about 50 points in p with the upper limit of about 5–6 ionization potentials of the considered subshell which is excited or ionized. By increasing the number of points in ρ, we can go to higher energies ε. Using modern PC, one can reach in consideration of photo ionization energies of outgoing electrons as big values as 150–200 Ry. To study higher ε considerably large computer memory is required.

An essential difficulty in numerical calculations in the frames of MBPT or RPAE originates from the fact that they include energy denominators that as it is seen from (1.31), (1.34), (1.37), and (1.40), can become equal to zero, thus leading to poles in the integrands. To calculate these singular expressions, the following idea is used: to separate the singular part and to calculate it analytically, while to calculate the

rest numerically. Indeed, let us present the integral in the vicinity of singularity as

$$\int_{\varepsilon_n}^{\varepsilon_{n+1}} \mathrm{d}\varepsilon \frac{Q(\varepsilon)}{(\omega + \varepsilon_v - \varepsilon + i\eta)} \approx -Q(\omega + \varepsilon_v) \ln \left| \frac{\omega + \varepsilon_v - \varepsilon_n}{\omega + \varepsilon_v - \varepsilon_{n+1}} \right| - i\pi Q(\omega + \varepsilon_v), \tag{1.64}$$

here $\varepsilon_n \to \varepsilon_{n+1}$ is the energy interval that includes the singularity of the integrand in (1.64). Outside this interval calculations are performed pure numerically, while the right-hand side of (1.64) presents the contribution of this interval. The accuracy of (1.64) is increasing with decrease of the interval $\varepsilon_n \to \varepsilon_{n+1}$.

It is essential to note that considerable part of RPAE diagrams may be taken into account by a proper choice of excited states one-electron HF wave functions. The more many-body diagrams are taken by the choice of the one-electron wave function, the less is left for the many-body corrections. In our calculations, we choose those wave functions that, together with respective vacancy wave functions form a given term, i.e., a state with given total angular momentum L and spin S. Angular momentum and spin projections of the excited electron and vacancy states separately are not defined in this approach. The following "time-forward" diagrams are included by this choice of wave functions:

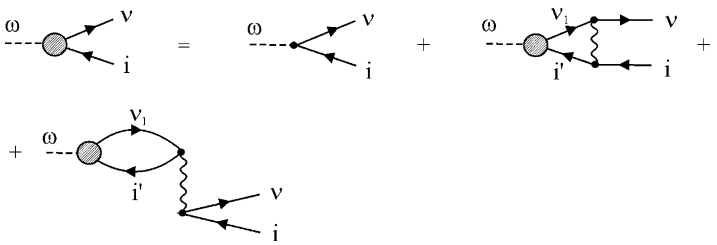

(1.65)

Those states i' are taken into account in (1.65) that have the same energy, i.e., $\varepsilon_i = \varepsilon_{i'}$. More details can be found in [AM] and [AC].

1.8 Angular Anisotropy Parameter

An important characteristic of the photoionization process is the angular distribution of photoelectrons. In dipole approximation, this is particularly simple and is presented for the unpolarized beam of photons by the following expression:

$$\frac{\mathrm{d}\sigma_{nl}(\omega)}{\mathrm{d}\Omega} = \frac{\sigma_{nl}(\omega)}{4\pi}[1 - \beta_{nl}(\omega) P_2(\cos\theta)], \tag{1.66}$$

here nl denotes the principal quantum number n and angular momentum l of the ionized subshell, Ω is the solid angle of photoelectron emission, $P_2(\cos\theta)$ is

the second-order Legendre polynomial, θ is the angle between the photoelectron momentum and photon beam directions, and $\beta_{nl}(\omega)$ is the angular anisotropy parameter. The angle, for which $P_2(\cos\theta_M) = 0$, is called the magic angle. This angle equals to $\theta_M \approx 54.7°$. For this angle, the corrections to $\mathrm{d}\sigma_{nl}(\omega)/\mathrm{d}\Omega$, defined by β, do not appear.

For polarized light, the formula for angular distribution of photoelectrons is written as:

$$\frac{\mathrm{d}\sigma_{nl}(\omega)}{\mathrm{d}\Omega} = \frac{\sigma_{nl}(\omega)}{4\pi}[1 + (-2)^{-|\mu|}\beta_{nl}(\omega)P_2(\cos\vartheta)], \tag{1.67}$$

here μ characterizes incoming light polarization. For linearly polarized light, $\mu = 0$ and for circularly polarized light, left and right, respectively, $\mu = \pm 1$. The angle ϑ is between the direction of polarization vector and photoelectron's momentum.

The partial photoionization cross-section $\sigma_{nl}^{R,V}(\omega)$ of nl-subshell in HF approximation is determined by the dipole matrix elements (1.60) calculated by making use of radial parts $P_{n(\varepsilon)l}(r)$ of HF wave functions (1.10) as follows [AM]:

$$\sigma_{nl}^{R,V}(\omega) = 2.689\frac{\omega N_{nl}}{2l+1}[l|d_{\varepsilon,l-1}^{R,V}|^2 + (l+1)|d_{\varepsilon,l+1}^{R,V}|^2], \quad (10^{-18}\,\mathrm{cm}^2). \tag{1.68}$$

Expression for the photoionization cross-section $\sigma_{nl}(\omega)$ of nl-subshell in RPAE is similar to (1.68) but the dipole matrix elements are calculated now in PRAE:

$$\sigma_{nl}(\omega) = 2.689\frac{\omega N_{nl}}{2l+1}[l|D_{\varepsilon,l-1}|^2 + (l+1)|D_{\varepsilon,l+1}|^2], \quad (10^{-18}\,\mathrm{cm}^2), \tag{1.69}$$

here the matrix elements $D_{\varepsilon l\pm1} \equiv D_{nl,\varepsilon l\pm1}^{V,R}(\omega)$ are solutions of RPAE equations for the radial matrix elements, obtained from (1.37) after integration over angular and summation over spin variables. The total photoionization cross-section $\sigma(\omega)$ is expressed via $\sigma_{nl}(\omega)$:

$$\sigma(\omega) = \sum_{nl}\sigma_{nl}(\omega), \tag{1.70}$$

where summation is performed over all subshells nl, whose ionization potential I_{nl} is smaller than ω.

In HF approximation, the angular anisotropy parameter $\beta_{nl}(\varepsilon)$ is expressed via the dipole radial matrix elements (1.60):

$$\beta_{nl}(\omega) = \frac{1}{(2l+1)[ld_{l-1}^2 + (l+1)d_{l+1}^2]}[l(l-1)d_{l-1}^2 + (l+1)(l+2)d_{l+1}^2$$
$$-6l(l+1)d_{l-1}d_{l+1}\cos(\delta_{l-1} - \delta_{l+1})]. \tag{1.71}$$

The scattering phases of the outgoing photoelectrons waves $\delta_{l\pm1} \equiv \delta_{l\pm1}(\varepsilon)$ are usually defined from the wave functions asymptotic. The definition of scattering phases is given by (3.8) and (3.10) (see, e.g., [LL]).

The $\beta_{nl}(\varepsilon)$ parameter in RPAE may be obtained from (1.71) by making use of the following replacement:

$$\begin{aligned} d_{l+1}d_{l-1}\cos(\delta_{l+1}-\delta_{l-1}) &\to [(\mathrm{Re}\, D_{l+1}\mathrm{Re}\, D_{l-1} \\ &+ \mathrm{Im}D_{l+1}\mathrm{Im}\, D_{l-1})\cos(\delta_{l+1}-\delta_{l-1}) \\ &- (\mathrm{Re}D_{l+1}\mathrm{Im}D_{l-1} - \mathrm{Im}D_{l+1}\mathrm{Re}\, D_{l-1})\sin(\delta_{l+1}-\delta_{l-1})] \\ &\equiv \tilde{D}_{l+1}\tilde{D}_{l-1}\cos(\delta_{l+1}+\Delta_{l+1}-\delta_{l-1}-\Delta_{l-1}), \\ d^2_{l\pm1} &\to \mathrm{Re}D^2_{l\pm1} + \mathrm{Im}D^2_{l\pm1} \equiv \tilde{D}^2_{l\pm1}. \end{aligned} \tag{1.72}$$

The following notation for the dipole matrix elements with correlations is used in the above formula:

$$D_{l\pm1}(\omega) \equiv \tilde{D}_{l\pm1}(\omega)\exp[i\,\Delta_{l\pm1}(\varepsilon)], \tag{1.73}$$

where $\tilde{D}_{l\pm1}(\omega)$ and $\Delta_{l\pm1}$ are the absolute values (modules) of the amplitudes of the corresponding transitions and the phases of photoelectrons with angular moments $l \pm 1$.

Finally, the parameter $\beta_{nl}(\varepsilon)$ is determined by the following formula:

$$\begin{aligned} \beta_{nl}(\varepsilon) &= \frac{1}{(2l+1)\,[l\,|D_{\varepsilon,l-1}|^2 + (l+1)|D_{\varepsilon,l+1}|^2]} \\ &\times \{l\,(l-1)\,|D_{\varepsilon,l-1}|^2 + (l+1)\,(l+2)\,|D_{\varepsilon,l+1}|^2 \\ &+ 6l\,(l+1)\,[(\mathrm{Re}D_{\varepsilon,l-1}\mathrm{Re}D_{\varepsilon,l+1} + \mathrm{Im}D_{\varepsilon,l-1}\mathrm{Im}D_{\varepsilon,l+1})\cos(\delta_{l+1}-\delta_{l-1}) \\ &- (\mathrm{Re}D_{\varepsilon,l-1}\mathrm{Im}D_{\varepsilon,l+1} - \mathrm{Im}D_{\varepsilon,l-1}\mathrm{Re}D_{\varepsilon,l+1})\sin(\delta_{l+1}-\delta_{l-1})]\} \\ &\equiv \frac{1}{(2l+1)\,[l\tilde{D}^2_{\varepsilon,l-1} + (l+1)\tilde{D}^2_{\varepsilon,l+1}]}[l\,(l-1)\,\tilde{D}^2_{\varepsilon,l-1} + (l+1)\,(l+2) \\ &\times \tilde{D}^2_{\varepsilon,l+1} - 6l\,(l+1)\,\tilde{D}_{\varepsilon,l-1}\tilde{D}_{\varepsilon,l+1}\cos(\tilde{\delta}_{l-1}-\tilde{\delta}_{l+1})], \end{aligned} \tag{1.74}$$

here $\tilde{\delta}_{l\pm1} = \delta_{l\pm1} + \Delta_{l\pm1}$.

In the vicinity of autoionization resonances, the angular anisotropy parameter as a function of ε varies rapidly. It can be represented by an expression similar to (1.34) [1.2]

$$\beta_{nl}(\zeta) = \frac{X\zeta^2 + Y\zeta + Z}{A\zeta^2 + B\zeta + c}, \tag{1.75}$$

here

$$X = \sum_{k,k'} a_{kk'} \mathrm{Re}[\breve{D}_k^* \breve{D}_{k'} \mathrm{e}^{i(\delta_k - \delta_{k'})}], \tag{1.76a}$$

$$Y = \frac{\mathrm{Im}\breve{D}_d}{\mathrm{Im}\breve{\Gamma}_{dd}} \sum_{k,k'} a_{kk'} \times \left\{ \mathrm{Re}[(q+i)\breve{\Gamma}_{dk'}^* \breve{D}_k + (q+i)\breve{\Gamma}_{dk} \breve{D}_{k'}^*] \mathrm{e}^{i(\delta_k - \delta_{k'})} \right\}, \tag{1.76b}$$

$$Z = \sum_{kk'} a_{kk'} \mathrm{Re} \left\{ \left[\breve{D}_{k'}^* \breve{D}_k + \frac{\mathrm{Im}\breve{D}_d}{\mathrm{Im}\breve{\Gamma}_{dd}} \times \left[(iq-1)\breve{\Gamma}_d^* k' \breve{D}_k - (iq+1)\breve{\Gamma}_{dk} \breve{D}_{k'}^* \right] + \left(\frac{\mathrm{Im}\breve{D}_d}{\mathrm{Im}\breve{\Gamma}_{dd}} \right) (q^2+1) \breve{\Gamma}_{dk'}^* \breve{\Gamma}_{dk} \right] \mathrm{e}^{i(\delta_k - \delta_{k'})} \right\}, \tag{1.76c}$$

$$\zeta = (\omega - \omega_d - \mathrm{Re}\breve{\Gamma}_{dd})/\mathrm{Im}\breve{\Gamma}_{dd}, \tag{1.76d}$$

$$A = \frac{\sigma_0}{4\pi},$$

$$B = 2q\rho^2 A, \tag{1.76e}$$

$$C = (1 - \rho^2 + q^2\rho^2)A,$$

$$a_{kk'} = \frac{1}{2l+1} \begin{pmatrix} l-1 & 3\sqrt{l(l+1)} \\ 3\sqrt{l(l+1)} & l+2 \end{pmatrix}. \tag{1.76f}$$

Parameters σ_0, ρ, and q are defined as in (1.50). The indices k and k' in the sums denote the transitions $l \to l \pm 1$. The notations $\breve{D}_k$ and $\breve{\Gamma}_{dk}$ are explained in connection to (1.52).

As it was mentioned earlier, the dipole approximation is valid if the wavelength of the ionizing radiation λ is much bigger than the radius of the atom r_A, in fact the radius of the ionized subshell r_i. Thus, the dipole approximation is valid if $\omega \ll 2\pi c/r_i$. However, the dipole parameter $r_i/\lambda \ll 1$ enters the photoionization cross-section in the second power while the angular anisotropy parameter β in the first. Due to this reason and because of some specific cancellations among relativistic corrections to the photoionization cross-section [1.3], with growth of ω the nondipole effects manifest themselves at first in angular distributions. The

formulae (1.66) and (1.67) are modified by including terms proportional to the first power of the dipole parameter [1.4]:

$$\frac{\mathrm{d}\sigma_{nl}(\omega)}{\mathrm{d}\Omega} = \frac{\sigma_{nl}(\omega)}{4\pi}[1 - \beta_{nl}(\omega)P_2(\cos\theta) + \kappa\gamma_{nl}(\omega)P_1(\cos\theta) + \kappa\eta_{nl}(\omega)P_3(\cos\theta)], \tag{1.77}$$

here $\kappa = \omega/c$ and $P_i(\cos\theta)$ are the Legendre polynomials. At the magic angle [see (1.66)] all corrections to the cross-section $\mathrm{d}\sigma_{nl}(\omega)/\mathrm{d}\Omega$ are due to nondipole contributions determined by the nondipole components.

The nondipole angular anisotropy parameters $\gamma(\omega)$ and $\eta(\omega)$ are determined in HF in the following way [1.5]:

$$\begin{aligned}\gamma_{nl}(\omega) = {} & \frac{6}{5[l\,d_{l-1}^2 + (l+1)d_{l+1}^2]} \\ & \times \left\{ \frac{l+1}{2l+3} d_{l+1}[3(l+2)q_{l+2}\cos(\delta_{l+2} - \delta_{l+1}) - l\,q_l\cos(\delta_l - \delta_{l+1})] \right. \\ & - \frac{l}{2l-1} d_{l-1}[3(l-1)q_{l-2}\cos(\delta_{l-2} - \delta_{l-1}) \\ & \left. - (l+1)q_l\cos(\delta_l - \delta_{l-1})] \right\},\end{aligned} \tag{1.78}$$

$$\begin{aligned}\eta_{nl}(\omega) = {} & \frac{6}{5[l\,d_{l-1}^2 + (l+1)d_{l+1}^2]} \\ & \times \left\{ \frac{(l+1)(l+2)}{(2l+1)(2l+3)} q_{l+2}\,[5l\,d_{l-1}\cos(\delta_{l+2} - \delta_{l-1}) \right. \\ & - (l+3)d_{l+1}\cos(\delta_{l+2} - \delta_{l+1})] \\ & - \frac{(l-1)l}{(2l+1)(2l-1)} q_{l-2}\,[5(l+1)d_{l+1}\cos(\delta_{l-2} - \delta_{l+1}) \\ & -(l-2)d_{l-1}\cos(\delta_{l-2} - \delta_{l-1})] \\ & + 2\,\frac{l(l+1)}{(2l-1)(2l+3)} q_l\,[(l+2)d_{l+1}\cos(\delta_l - \delta_{l+1}) \\ & \left. - (l-1)d_{l-1}\cos(\delta_l - \delta_{l-1})] \right\},\end{aligned} \tag{1.79}$$

here the matrix elements $d_{l\pm1}$ are defined by (1.60), while $q_{l\pm2,0}$ in the r-form are given by the following formula:

$$q_{l\pm2,0} = \frac{1}{2}\int_0^\infty P_{nl}(r)r^2 P_{\varepsilon l\pm2,l}(r)\mathrm{d}r. \tag{1.80}$$

We will not use the velocity form for $q_{l\pm2,0}$ but instead perform RPAE calculations of nondipole parameters. In this case, the results for the length and velocity forms coincide [see (1.2) and (1.3)].

Since in experiments on the investigations of photoelectron angular distribution the linearly polarized radiation is usually used, it is more convenient to employ the following formula instead of expression (1.77) [1.6–1.9]:

$$\frac{\mathrm{d}\sigma_{nl}(\omega)}{\mathrm{d}\Omega} = \frac{\sigma_{nl}(\omega)}{4\pi}[1 + \beta_{nl}P_2(\cos\Theta) + (\delta^{\mathrm{C}}_{nl} + \gamma^{\mathrm{C}}_{nl}\cos^2\Theta)\sin\Theta\cos\Phi], \quad (1.81)$$

here Θ is the polar angle between the directions of the photoelectron velocity $\mathbf{v}$ and photon polarization $\mathbf{e}$, Φ is the azimuthal angle, defined by the projection of $\mathbf{v}$ in the plane orthogonal to $\mathbf{e}$ and including to the vector of photon velocity. At magic angle Θ_M, where $P_2(\cos\Theta_M) = 0$, the corrections to dipolar cross-section are defined by the combination of the parameters $(\gamma^{\mathrm{C}}_{nl} + 3\delta^{\mathrm{C}}_{nl})$. It is called *magic combination*.

Nondipole parameters in (1.77) and (1.81) are connected by two simple relations [1.10]:

$$\frac{\gamma^{\mathrm{C}}_{nl}}{5} + \delta^{\mathrm{C}}_{nl} = \kappa\gamma_{nl}, \quad \frac{\gamma^{\mathrm{C}}_{nl}}{5} = -\kappa\eta_{nl}. \quad (1.82)$$

Expressions for $\gamma_{nl}(\omega)$ and $\eta_{nl}(\omega\}$ in RPAE can be obtained from (1.78) and (1.79) using the following substitutions:

$$\begin{aligned} &d_{l\pm1}q_{l\pm2.0}\cos(\delta_{l\pm2,0} - \delta_{l\pm1}) \to [(\mathrm{Re}D_{l\pm1}\mathrm{Re}Q_{l\pm2,0} \\ &\quad + \mathrm{Im}D_{l\pm1}\mathrm{Im}Q_{l\pm2,0})\cos(\delta_{l\pm2,0} - \delta_{l\pm1}) \\ &\quad + (\mathrm{Re}D_{l\pm1}\mathrm{Im}Q_{l\pm2,0} - \mathrm{Im}D_{l\pm1}\mathrm{Re}Q_{l\pm2,0})\sin(\delta_{l\pm2,0} - \delta_{l\pm1})], \\ &d^2_{l\pm1} \to \mathrm{Re}D^2_{l\pm1} + \mathrm{Im}D^2_{l\pm1}, \end{aligned} \quad (1.83)$$

here

$$Q_{l\pm2,0}(\omega) \equiv \tilde{Q}_{l\pm2,0}(\omega)\exp[i\Delta_{l\pm2,0}(\varepsilon)], \quad (1.84)$$

where $\tilde{Q}_{l\pm2,0}(\omega)$ and $\Delta_{l\pm2,0}$ are the absolute values (modules) and phases of corresponding transitions, and $\delta_{l\pm2,0}$ are the phases of photoelectrons with angular moments $l \pm 2, 0$.

The quadrupole matrix elements $Q_{l\pm2,0}$ are obtained from the solution of the radial part of the RPAE quadrupole equation, which is similar to (1.37)

$$\langle\nu_1|Q(\omega)|\nu_2\rangle = \langle\nu_1|\hat{q}|\nu_2\rangle + \sum_{\nu_3,\nu_4}\frac{\langle\nu_3|Q(\omega)|\nu_4\rangle(n_{\nu_4} - n_{\nu_3})\langle\nu_4\nu_1|U|\nu_3\nu_2\rangle}{\varepsilon_{\nu_4} - \varepsilon_{\nu_3} + \omega + i\eta(1 - 2n_{\nu_3})}, \quad (1.85)$$

here in r-form $\hat{q} = r^2P_2(\cos\theta)$. The numerical procedure to solve (1.85) is in principle similar to that for the dipole component. This equation can be generalized

in the same way as the equations for the dipole component in order to account for the effects of static and dynamic relaxation, i.e., the effects included in GRPAE and GRPAE II.

1.9 Other Characteristics of Photoionization

In this section, we will discuss some other characteristics of photoionization, namely, polarizabilities and polarization parameters of photoelectrons.

Atomic dipole polarizability $\alpha_d(\omega)$ is expressed via the oscillator strengths $f_{vv'}$ and photoionization cross-section $\sigma(\omega)$ using the following formula:

$$\alpha_d(\omega) = \sum_{j\le F, k>F} \frac{f_{jk}}{\omega_{jk}^2 - \omega^2} + \frac{c}{2\pi^2}\int_I^\infty \frac{\sigma(\omega')\mathrm{d}\omega'}{\omega'^2 - \omega^2 + i\omega\eta}, \quad \eta \to 0. \tag{1.86}$$

Calculating the oscillator strengths $f_{vv'}$ and photoionization cross-section $\sigma(\omega)$ using procedures described earlier, one can obtain atomic polarizabilities. As is seen from (1.86), $\alpha_d(\omega)$ is a complex quantity, its imaginary part being proportional to $\sigma(\omega)$. Dipole polarizability is of interest since it determines the photon–atom elastic scattering cross-section and electron–atom long-range interaction potential.

Interaction between two spherically symmetric atoms A and B at large distances R_{AB}, $V_{AB}(R_{AB}) = -C_6^{AB}/R_{AB}^6$ is also expressed via sums over oscillator strengths f_{jk} and integrals over densities of oscillator strengths $f_{j\varepsilon} \equiv c\sigma_j(\omega)/2\pi^2$ (with $\varepsilon = \omega - I_j$):

$$C_6^{AB} = -\frac{3}{2}\sum_{\substack{j\le F\\ k>F}}\sum_{\substack{j'\le F\\ k'>F}} \frac{f_{jk}^A f_{j'k'}^B}{\omega_{jk}\omega_{j'k'}(\omega_{jk} + \omega_{j'k'})}, \tag{1.87}$$

where $\omega_{jk} = \varepsilon_k + I_j$ and summation over $k, k' > F$ implies also integration over continuous spectrum one-electron–one-vacancy excitations of atoms A and B, respectively.

Important characteristics of photoionization process are photoelectron's polarization parameters that determine the orientation of photoelectrons spin. It was demonstrated that photoelectrons have nonzero average spin orientation [1.11,1.12]. The formulas for the photoelectron flux $I_{JJ'}(\vec{x},\vec{s})$, which originates from photoionization of an atom with initial total angular momentum J and final state ion momentum J', and for corresponding polarization parameters $A^j(\omega)$, $\zeta^j(\omega)$, $\xi^j(\omega)$, were derived in [1.13]. There the reader can find the necessary details. For circularly polarized light, one has [1.14]

$$I_{JJ'}(\omega) = \sum_j \frac{\sigma_{njl}}{8\pi} \left\{ 1 - \frac{1}{2}\beta_{nl}(\omega) \left[\frac{3}{2}(\vec{x}\vec{s})^2 - \frac{1}{2} \right] + A^j(\omega)(\vec{s}\vec{s}_\gamma) \right.$$
$$\left. -\zeta^j(\omega) \left[\frac{3}{2}(\vec{x}\vec{s}_\gamma)(\vec{x}\vec{s}) - \frac{1}{2}(\vec{s}\vec{s}_\gamma) \right] + \xi^j(\omega)[\vec{s}(\vec{x} \times k_\gamma)(\vec{x}\vec{k}_\gamma) \right\}, \quad (1.88)$$

here $\boldsymbol{s}_\gamma$ and $\boldsymbol{s}$ are unit vectors in photon and photoelectron spin directions, $\mathbf{x}$ is the direction of photoelectron's motion, and $\boldsymbol{k}_\gamma$ is the unit vector in the direction of photon motion. The photoelectron total momentum j can take two values, $j = l \pm 1/2$. A similar expression for linearly polarized light can be found in [1.14]. The parameters $A^j(\omega)$, $\zeta^j(\omega)$, and $\xi^j(\omega)$ are given by the following relations:

$$A^j(\omega) = \frac{(-1)^{j-l-1/2} l(l+1)}{2j+1} \frac{d_{l+1}^2 - d_{l-1}^2}{l d_{l-1}^2 + (l+1) d_{l+1}^2},$$
$$\zeta^j(\omega) = \frac{2(-1)^{j-l-1/2} l(l+1)}{(2j+1)(2l+1)}$$
$$\times \left[(l+2) d_{l+1}^2 - (l-1) d_{l-1}^2 - 3 d_{l+1} d_{l-1} \cos(\delta_{l+1} - \delta_{l-1}) \right]$$
$$\times [l d_{l-1}^2 + (l+1) d_{l+1}^2]^{-1},$$
$$\xi^j(\omega) = \frac{3(-1)^{j-l-1/2} l(l+1)}{2j+1} \frac{d_{l+1} d_{l-1} \sin(\delta_{l+1} - \delta_{l-1})}{l d_{l-1}^2 + (l+1) d_{l+1}^2}. \quad (1.89)$$

In RPAE, the parameters $A^j(\omega)$, $\zeta^j(\omega)$, and $\xi^j(\omega)$ can be obtained similar to (1.74), (1.78), and (1.77) by making use of substitutions (1.72) and (1.83).

1.10 Semiclosed Subshells Atoms

The application of the many-body theory to open shell atoms is complicated by the fact that the ground state of these objects is degenerate. As a result, the ground state must be rearranged before starting the calculations. However, there is one exception to this general rule, for which the many-body theory approach can be applied almost as easy as to the atoms with all closed subshells. Here we have in mind the semifilled shell atoms, where at least one of the subshells contains 1/2 of the total possible number of electrons.

It is known, that for these atoms so-called Hund rule is valid, which reads, that in such a subshell all electrons must have the same spin projection [1.15]. They can exchange only with electrons of the same spin projection including that from other subshells. As a result, each subshell splits into two levels, called "up" and "down." Thus, all electrons can be divided into two groups of different particles, "up" and "down" electrons. We emphasize that exchange exists only between electrons with the same spin projection.

The equations used before to describe photoionization must be generalized to a system of two kinds of different particles. So, instead of HF equation (1.10) we have a system of equations:

$$\left(\hat{H}^{\mathrm{HF}}_{\uparrow(\downarrow)} + \hat{V}^{H}_{\downarrow(\uparrow)}\right)\varphi^{\uparrow(\downarrow)}(\vec{r}) = \varepsilon^{\uparrow(\downarrow)}\varphi^{\uparrow(\downarrow)}(\vec{r}), \tag{1.90}$$

where $\uparrow$ ($\downarrow$) denotes "up" ("down") electrons, respectively.

In (1.90) $\hat{H}^{\mathrm{HF}}_{\uparrow(\downarrow)}$ is the Hartree–Fock one-electron Hamiltonian for the "up" ("down") electrons, $V^{H}_{\downarrow(\uparrow)}$ is the Hartree potential for the "down" ("up") electrons, $\varepsilon^{\uparrow(\downarrow)}$ and $\varphi^{\uparrow(\downarrow)}$ are the energies and wave functions of the "down" ("up") electrons, respectively.

In the HF approximation, the dipole $d^{R,V}_{l'\uparrow\downarrow}$ and quadrupole $q^{R,V}_{l'\uparrow\downarrow}$ matrix elements are given by relations similar to (1.60) and (1.80):

$$\begin{aligned} d^{R}_{l'\uparrow(\downarrow)} &\equiv \int_0^\infty P_{nl\uparrow(\downarrow)}(r)\, r\, P_{n'(\varepsilon)l'\uparrow(\downarrow)}(r)\mathrm{d}r, \\ d^{V}_{l'\uparrow(\downarrow)} &\equiv \int_0^\infty P_{nl\uparrow(\downarrow)}(r)\left(\frac{\mathrm{d}}{\mathrm{d}r} \pm \frac{l+l'+1}{2r}\right) P_{n'(\varepsilon)l\uparrow(\downarrow)}(r)\mathrm{d}r, \end{aligned} \tag{1.91}$$

$$q_{l'\uparrow(\downarrow)} = \frac{1}{2}\int_0^\infty P_{nl\uparrow(\downarrow)}(r) r^2 P_{\varepsilon l\pm 2,l\uparrow(\downarrow)}(r)\mathrm{d}r, \tag{1.92}$$

where $P_{nl\uparrow,\downarrow}(r)$ are the radial parts of solutions $\varphi^{\uparrow(\downarrow)}(\vec{r})$ of (1.90).

Introducing the changes, similar to that in HF equation, into equations of RPAE (GRPAE, GRPAE II), one can obtain corresponding spin-polarized (SP) equations SPRPAE (SPGRPAE, SPGRPAE II). The equation for the photoionization amplitude $\hat{D}(\omega)$ (141a) in SPRPAE may be represented as follows:

$$\begin{aligned} \left(\hat{D}_\uparrow(\omega)\ \ \hat{D}_\downarrow(\omega)\right) &= \left(\hat{d}_\uparrow(\omega)\ \ \hat{d}_\downarrow(\omega)\right) + \left(\hat{D}_\uparrow(\omega)\ \ \hat{D}_\downarrow(\omega)\right) \\ &\times \begin{pmatrix} \hat{\chi}_{\uparrow\uparrow} & 0 \\ 0 & \hat{\chi}_{\downarrow\downarrow} \end{pmatrix} \times \begin{pmatrix} U_{\uparrow\uparrow} & V_{\uparrow\downarrow} \\ V_{\downarrow\uparrow} & U_{\downarrow\downarrow} \end{pmatrix}. \end{aligned} \tag{1.93}$$

In the same way, the effective interelectron interaction $\hat{\Gamma}$ in SPRPAE may be presented in matrix form by generalizing equation (1.41b):

$$\begin{aligned} \begin{pmatrix} \hat{\Gamma}_{\uparrow\uparrow} & \hat{\Gamma}_{\uparrow\downarrow} \\ \hat{\Gamma}_{\downarrow\uparrow} & \hat{\Gamma}_{\downarrow\downarrow} \end{pmatrix} &= \begin{pmatrix} U_{\uparrow\uparrow} & V_{\uparrow\downarrow} \\ V_{\downarrow\uparrow} & U_{\downarrow\downarrow} \end{pmatrix} + \begin{pmatrix} U_{\uparrow\uparrow} & V_{\uparrow\downarrow} \\ V_{\downarrow\uparrow} & U_{\downarrow\downarrow} \end{pmatrix} \\ &\times \begin{pmatrix} \hat{\chi}_{\uparrow\uparrow} & 0 \\ 0 & \hat{\chi}_{\downarrow\downarrow} \end{pmatrix} \times \begin{pmatrix} \hat{\Gamma}_{\uparrow\uparrow} & \hat{\Gamma}_{\uparrow\downarrow} \\ \hat{\Gamma}_{\downarrow\uparrow} & \hat{\Gamma}_{\downarrow\downarrow} \end{pmatrix}. \end{aligned} \tag{1.94}$$

In (1.93) and (1.94), $U^{\uparrow\uparrow(\downarrow\downarrow)}$ are determined by (1.37), but for electrons with same spin projections while $V^{\uparrow\downarrow(\downarrow\uparrow)}$ are determined by (1.33), but for electrons with the opposite spin projections.

Equations (1.90), (1.93), and (1.94) can be solved numerically, just as (1.10) and (1.41a) and (1.41b). The photoionization cross-section is given by (1.69), where $N_{nl}|\hat{D}(\omega)|^2$ is substituted by the following expression:

$$N_{nl}|\hat{D}(\omega)|^2 \to N_{nl}^{\uparrow}|\hat{D}_{\uparrow}(\omega)|^2 + N_{nl}^{\downarrow}|\hat{D}_{\downarrow}(\omega)|^2, \tag{1.95}$$

where $N_{nl} = N_{nl}^{\uparrow} + N_{nl}^{\downarrow}$, with $N_{nl}^{\uparrow(\downarrow)}$ being the number of electrons on the nl "up" ("down") levels, respectively.

Partial photoionization cross-section of nl "up" ("down") levels in SP RPAE is given by the formula similar to (1.69):

$$\sigma_{nl\uparrow(\downarrow)}(\omega) = 2.689\frac{\omega N_{nl}}{2l+1}[l\,|D_{\varepsilon,l-1\uparrow(\downarrow)}|^2 + (l+1)|D_{\varepsilon,l+1\uparrow(\downarrow)}|^2], \quad (10^{-18}\ \mathrm{cm}^2). \tag{1.96}$$

Dipole angular anisotropy parameters for "up" ("down") nl-electrons in SP RPAE are obtained by the generalization of equation (1.74) as follows:

$$\begin{aligned}\beta_{nl\uparrow(\downarrow)}(\varepsilon) = {} & \frac{1}{(2l+1)\,[l\,\tilde{D}^2_{\varepsilon,l-1\uparrow(\downarrow)} + (l+1)\tilde{D}^2_{\varepsilon,l+1\uparrow(\downarrow)}]} \\ & \times\Big[l\,(l-1)\,\tilde{D}^2_{\varepsilon,l-1\uparrow(\downarrow)} + (l+1)\,(l+2)\,\tilde{D}^2_{\varepsilon,l+1\uparrow(\downarrow)} \\ & -6l\ \ (l+1)\,\tilde{D}_{\varepsilon,l-1\uparrow(\downarrow)}\tilde{D}_{\varepsilon,l+1\uparrow(\downarrow)}\cos(\tilde{\delta}_{l-1\uparrow(\downarrow)} - \tilde{\delta}_{l+1\uparrow(\downarrow)})\Big],\end{aligned} \tag{1.97}$$

where

$$D_{l\pm1\uparrow(\downarrow)}(\omega) \equiv \tilde{D}_{l\pm1\uparrow(\downarrow)}(\omega)\exp[i\,\Delta_{l\pm1\uparrow(\downarrow)}(\varepsilon)], \tag{1.98}$$

and $\tilde{\delta}_{l'\uparrow(\downarrow)} = \delta_{l'\uparrow(\downarrow)} + \Delta_{l'\uparrow(\downarrow)}$.

Nondipole angular anisotropy parameters for "up" ("down") nl-electrons in SP RPAE are obtained by the generalization of equations (1.78) and (1.79) as follows:

$$\begin{aligned}\gamma_{nl\uparrow(\downarrow)}(\omega) = {} & \frac{6}{5\Big[(l+1)\tilde{D}^2_{l+1\uparrow(\downarrow)} + l\,\tilde{D}^2_{l-1\uparrow(\downarrow)}\Big]} \\ & \times\Bigg\{\frac{(l+1)}{2l+3}\tilde{D}_{l+1\uparrow(\downarrow)}\Big[3\,(l+2)\,\tilde{Q}_{l+2\uparrow(\downarrow)}\cos\Big(\tilde{\delta}_{l+2\uparrow(\downarrow)} - \tilde{\delta}_{l+1\uparrow(\downarrow)}\Big) \\ & -l\,\tilde{Q}_{l\uparrow(\downarrow)}\cos\Big(\tilde{\delta}_{l\uparrow(\downarrow)} - \tilde{\delta}_{l+1\uparrow(\downarrow)}\Big)\Big] \\ & -\frac{l\,\tilde{D}_{l-1\uparrow(\downarrow)}}{2l-1}\Big[3\,(l-1)\,\tilde{Q}_{l-2\uparrow(\downarrow)}\cos\Big(\tilde{\delta}_{l-2\uparrow(\downarrow)} - \tilde{\delta}_{l-1\uparrow(\downarrow)}\Big)\end{aligned}$$

$$- \ (l+1)\,\tilde{Q}_{l\uparrow(\downarrow)} \cos\left(\tilde{\delta}_{l\uparrow(\downarrow)} - \tilde{\delta}_{l-1\uparrow(\downarrow)}\right)\Big]\Big\}, \tag{1.99}$$

$$\begin{aligned}
\eta_{nl\uparrow(\downarrow)}(\omega) = {} & \frac{6}{5\left[(l+1)\tilde{D}^2_{l+1\uparrow(\downarrow)} + l\,\tilde{D}^2_{l-1\uparrow(\downarrow)}\right]} \Big\{ \frac{(l+1)\,(l+2)}{(2l+1)\,(2l+3)}\,\tilde{Q}_{l+2\uparrow(\downarrow)} \\
& \times \Big[5l\,\tilde{D}_{l-1\uparrow(\downarrow)} \cos\left(\tilde{\delta}_{l+2\uparrow(\downarrow)} - \tilde{\delta}_{l-1\uparrow(\downarrow)}\right) \\
& - (l+3)\,\tilde{D}_{l+1\uparrow(\downarrow)} \cos\left(\tilde{\delta}_{l+2\uparrow(\downarrow)} - \tilde{\delta}_{l+1\uparrow(\downarrow)}\right)\Big] \\
& - \frac{(l-1)\,l}{(2l+1)\,(2l-1)}\,\tilde{Q}_{l-2\uparrow(\downarrow)} \\
& \times \Big[5\,(l+1)\,\tilde{D}_{l+1\uparrow(\downarrow)} \cos\left(\tilde{\delta}_{l-2\uparrow(\downarrow)} - \tilde{\delta}_{l+1\uparrow(\downarrow)}\right) \\
& - (l-2)\,\tilde{D}_{l-1\uparrow(\downarrow)} \cos\left(\tilde{\delta}_{l-2\uparrow(\downarrow)} - \tilde{\delta}_{l-1\uparrow(\downarrow)}\right)\Big] \\
& + 2\frac{l(l+1)\tilde{Q}_{l\uparrow(\downarrow)}}{(2l-1)(2l+3)} \\
& \times \Big[(l+2)\tilde{D}_{l+1\uparrow(\downarrow)}\tilde{D}_{l+1\uparrow(\downarrow)} \cos(\tilde{\delta}_{l\uparrow(\downarrow)} - \tilde{\delta}_{l+1\uparrow(\downarrow)}) \\
& - (l-1)\ \tilde{D}_{l-1\uparrow(\downarrow)}\tilde{D}_{l-1\uparrow(\downarrow)} \cos\left(\tilde{\delta}_{l\uparrow(\downarrow)} - \tilde{\delta}_{l-1\uparrow(\downarrow)}\right)\Big]\Big\}.
\end{aligned} \tag{1.100}$$

where

$$Q_{l\pm2,0\uparrow(\downarrow)}(\omega) \equiv \tilde{Q}_{l\pm2,0\uparrow(\downarrow)}(\omega) \exp[i\,\Delta_{l\pm2,0\uparrow(\downarrow)}(\varepsilon)], \tag{1.101}$$

and $\tilde{\delta}_{l_j\uparrow(\downarrow)} = \delta_{l_j\uparrow(\downarrow)} + \Delta_{l_j\uparrow(\downarrow)}$. [see (1.73)]

It is interesting to note that the distance between the "up" and "down" levels with the same quantum numbers n and l is much bigger than the spin-orbit splitting in all but the heaviest atoms. This is clear since exchange is usually bigger than relativistic spin–orbit interaction.

1.11 Open Shell Atoms

The theory of photoionization of open shell atoms technically is very complicated. The reason is the mentioned above the degeneracy of the ground state and the possibility of exchange of momentum between the excited electron–vacancy pair and the core. Only one RPAE generalization, presented in [1.16], seems to be reliable, because it gives the same results in "length" and "velocity" forms and fulfills the sum rule. It keeps the total angular momentum in initial (photon + atom), intermediate, and final states—photoelectron and residual ion—equal. For

simplicity, as everywhere in this book, we limit ourselves to the so-called *LS* coupling, in which the total momentum L and the total spin S are conserved separately.

Two cases, namely ionization of the open subshell itself and a closed subshell in the presence of an open one, have to be treated differently due to complications of the binding of all angular moments and spins into total ones. Let us start with the photoionization of the open shell. The amplitude of photoionization in HF is determined by the following expression [1.16, AC]:

$$\langle \varepsilon_3 l_3, L_3 S_3 || d || n_1 l_1, LS \rangle = \delta_{SS_3} \sqrt{2S+1} C^{l_1 L S_1}_{L' S', l_3 L_1 S_1} \langle \varepsilon_3 l_3 || d || n_1 l_1 \rangle , \quad (1.102)$$

here ε_3, l_3 are the energy and angular momentum of the photoelectron, while $n_1 l_1$ are the principal quantum number and angular momentum of the created vacancy, *LS* are the total angular momentum and spin of the open subshell, $(n_1 l_1)^q (LS), q < 4l_1 + 2$, where $4l_1 + 2$ is the total number of electrons in a closed subshell l_1 and $\langle \varepsilon_3 l_3 || d || n_1 l_1 \rangle$ is the usual reduced dipole matrix element given by (1.58).

The RPAE equations for an open shell are much more complicated than that for closed shells (1.37). They become more complex with the growth of the number of electrons in open shells. Therefore, these equations were solved only for atoms with one electron or one vacancy outside of a closed subshell like, Cl, I on one side [1.16, 1.17] and Al on the other. In all these cases, only open subshells were studied.

Now let us start with the photoionization of a closed shell in the presence of the open one. The approach developed in [1.16–1.18] was generalized [1.19] in such a way that permitted to take into account simultaneously several subshells, including the open one. The calculations were performed for Xe^+ and I.

Photoionization of a closed subshell in the presence of open ones leads to a rather complicated final state having three open subshells, including the outgoing electron. At first, the angular momentum l_1 of the ionized subshell $n_1 l_1$ and that of the photoelectron εl_3, l_3, are coupled to produce the final state with the term ^1P, as it is required by the dipole selection rules $[(n_1 l_1)^{4l_1+1} (L_1 S_1) \varepsilon l_3] (^1P)$, where $L_1 = l_1, S_1 = 1/2$. After that the angular and spin moments of the open subshell, $(n_2 l_2)^q (LS), q < 4l_2 + 2$, are added to give the total angular and spin moments of the final state $L_3 S_3$.

There are several possible values of $L_3 S_3$, which correspond to a number of channels in photoionization of the closed shell in the presence of an open one. The corresponding HF matrix element is given by the following formula [1.19]:

$$\langle \varepsilon_3 l_3, L_3 S_3 || d || n_1 l_1, LS \rangle = \delta_{SS_3} \sqrt{2S+1} W^{l_1 LS1}_{l_3 L_3 S_3} \langle \varepsilon_3 l_3 || d || n_1 l_1 \rangle , \quad (1.103)$$

where $W^{l_1 LSl}_{l_3 L_3 S_3} = \sqrt{2(2l_3+1)/(2l+1)} (-1)^{l_1 + L - L_3}$. Replacing coefficients $C^{l_1 LS1}_{L' S', l_2 L_1 S_1}$ in (7) and (9) from [1.20] by corresponding values $W^{l_1 LSl}_{l_3 L_3 S_3}$, one obtains the expression for the Coulomb matrix elements, which should be used in RPAE equations (1.37). The general procedure for the solution of these equations is

the same as for closed shell atoms [AC] and open shell atoms [1.18–1.21]. This approach is called the RPAE for open shell atoms or RPAEO.

1.12 Negative and Positive Ions

The photoionization cross-sections of negative ions are of additional interest from the point of view of their near threshold behavior. The outgoing electron "feels" the field of residual neutral atom, which has shorter interaction radius than the positive Coulomb "tail" of the ionized neutral atom. According to the Wigner law [LL], the photoionization cross-section of negative ion is given by the following formula, which is valid near threshold:

$$\sigma_{nl}^{(-)}(\omega) \sim (\omega - I^-)^l, \tag{1.104}$$

where l is the angular momentum of ionized subshell. There is no doubt that this law is valid near threshold, but the numerical value of the word "near" is not clear. From the first glance, near the threshold or in the vicinity of the threshold means that $(\omega - I^-) \leq I^-$. But it happens that it is not the case: the photoionization cross-section follows to the Wigner law only very close to the threshold: $(\omega - I^-) \leq 0.1 I^-$ [1.22].

There are two distinctive kinds of negative ions, namely, "simple" and "complex" or "polarization" negative ions. "Simple" are those that may be created already in the HF approximation frame [1.23]. Usually, however, the ionization potential I_{HF} in HF for these ions is too small. In order to improve the situation, we can either introduce the experimental value I_{exp} instead of the HF value, or add some extra charge $\mathrm{d}Z$ to the nuclear charge, so that the $I_{\mathrm{HF}}^{(Z+\mathrm{d}Z)} = I_{\mathrm{exp}}^{Z}$. This relation determines in fact the $\mathrm{d}Z$ value.

All HF (1.10) and RPAE (1.37) equations have to be solved for the effective charge $Z_{\mathrm{eff}} = (Z + \mathrm{d}Z)$. The other option is to solve the same equations, neglecting the difference between I_{HF} and I_{exp}. This approach is not good enough for the consideration of the extra electron itself.

The "complex" negative ions can be formed only if the polarization of the atomic core by the additional electron is taken into account [1.24]. This polarization and corresponding corrections to the interelectron effective interaction and to effective photon–electron interaction are outside HF and RPAE [AM, AC]. Extensive calculations of "complex" negative ions photoionization were performed quite a while ago (see [1.24, 1.25] and references therein).

It is nothing specific about positive ions photoionization if they belong to one of the following groups: they have only closed subshells, semiclosed subshells, and either an extra electron outside a closed shell or a hole in it. In all these cases, the methods described earlier can be used without any difficulty. In fact, positive ions

are simpler objects than the neutral atoms from the point of view of the convergence speed of the calculation procedure.

The approaches developed in previous section can be applied to atoms and ions not only in their ground states, but also in the excited states. This is especially simple if the state under consideration is the closed shell or semiclosed shell and has one electron or one vacancy in addition to closed or semiclosed shells.

The RPAE and MBPT methods discussed earlier could be applied also to the simple molecules consisting of several atoms. The decisive complexity in molecule consideration is the lack of spherical symmetry. As a result it is not possible to perform analytical integration over the angular variables. That is why the RPAE equations for molecules are not one dimensional: for molecules with cylindrical symmetry they are two dimensional, and for molecules without this symmetry they are three dimensional. Modern work stations and even PC are able to solve the RPAE equations by the "strong force" method, i.e., solving the three-dimensional RPAE equation directly.

1.13 Endohedral Atoms: The Effect of Electron Reflections

During last decade, new atomic-like objects consisting of many carbon atoms were discovered. These carbon atoms form closed almost empty two-dimensional surfaces, so-called fullerenes [1.26]. Much attention was paid to the investigations of their structure making use of the data on photon absorption. It turned out that all electrons of carbon atoms except $1s^2$-electrons are strongly hybridized. As a result, the photoabsorption spectra of these objects are characterized by a strong maximum called *Giant resonance* (see [1.27, 1.28] and references therein). Total power of this resonance, i.e., its total oscillator strength is close to the number of the fullerene valence electrons. Fullerenes are very complicated objects for ab initio calculations. That is why significant simplifications should be used for the investigations of their photoionization cross-sections and other properties.

Fullerenes are very specific and unusual, since almost each atom from the periodic table can be placed inside the fullerene, thus creating *endohedral* complexes. The endohedral complex consisting of fullerene and an atom A inside it is denoted as $A@C_n$, where n is the number of carbon atoms in the fullerene. In fact not only one atom, but also several atoms or a molecule can be placed inside the fullerene structure consisting of 60 or more carbon atoms. The properties and characteristics of the internal atom A, e.g., its photoionization cross-section and vacancy decay depend strongly on the fullerene shell. Note that for consideration below the fullerenes structure could be formed not necessarily of carbon atoms.

It is of interest to see how the photoionization cross-section and vacancy decays rate change from an isolated atom A to endohedral atom $A@C_{60}$. Our results are obtained in a very simple model and based on the present experimental data. The developed approach is also applicable to fullerenes with the number of atoms differing from 60.

We consider two most important types of influence on the photoionization cross-section of endohedral atom A: reflection of photoelectron wave due to the static field of fullerene shell and modification of incoming photon due to dynamic response of collectivized fullerene electrons.

The cross-sections of the processes under investigation in some cases are very small, but can be distinguished by the coincidence technique of electron spectroscopy.

To demonstrate our ideas we consider as an example only one fullerenes type, namely C_{60}, and suppose for simplicity the atom A is placed in the center of almost symmetrical shell C_{60}. Considerable displacement off the center eliminates the spherical symmetry of the problem and makes the calculation problem at least two dimensional. The same is correct if the fullerene is essentially nonspherical itself, as is, e.g., C_{87}.

It should be noted that the action of fullerene shell on the photoelectron wave results in an interference of direct and scattered waves from atom A.

Since the thickness of C_{60} shell Δ is less than its radius R_C, for low energy photoelectrons one can replace the C_{60} potential by the pseudopotential of zero thickness [1.29, 1.30]:

$$W(r) = -W_0\delta(r - R). \tag{1.105}$$

The parameter W_0 is defined from the condition that the binding energy of extra electron in negative ion C_{60}^- is equal to the experimentally observed value. The adding of potential (1.105) may be accounted for analytically [1.30, 1.31], by expression of partial wave with angular momentum l in terms of so-called regular $u_{kl}(r)$ and irregular $v_{kl}(r)$ at point $r \to 0$ solutions of atomic HF equation for photoelectron with momentum $k = \sqrt{2\varepsilon}$, where ε is the photoelectron energy connected with the photon frequency ω by the relation $\varepsilon = \omega - I_A$ and I_A is the ionization potential of atom A.

The adding of potential (1.105) results in the factor $F_{l'}(k)$ in one-electron photoionization amplitude, which depends on the photoelectron linear k and angular l' moments only [1.32]:

$$F_l(k) = \cos\Delta\delta_l(k)\left[1 - \tan\Delta\delta_l(k)\frac{v_{kl}(R)}{u_{kl}(R)}\right], \tag{1.106}$$

where $\Delta\delta_l(k)$ is the photoelectron elastic scattering phase due to action of the potential (1.105), which can be expressed by the following relation:

$$\tan\Delta\delta_l(k) = \frac{u_{kl}^2(R)}{u_{kl}(R)v_{kl}(R) - k/2W_0}. \tag{1.107}$$

If the effect of fullerenes shell is not too strong, the following relations for endohedral atom amplitudes $D^{AC(r)}$ and $Q^{AC(r)}$, expressed in terms of corresponding values of isolated atom for $nl \to \varepsilon l'$ transitions, are valid:

$$
\begin{aligned}
D^{\mathrm{AC}(r)}_{nl,kl'}(\omega) &= F_{l'}(k) D_{nl,kl'}(\omega) \exp[i\Delta\delta_{l'}(k)], \\
Q^{\mathrm{AC}(r)}_{nl,kl''}(\omega) &= F_{l''}(k) Q_{nl,kl''}(\omega) \exp[i\Delta\delta_{l''}(k)],
\end{aligned}
\tag{1.108}
$$

where superscript $\mathrm{AC}(r)$ denotes the value for endohedral atom $\mathrm{A@C}_n$, and index (r) denotes that the reflection from the fullerene shell is taken into account.

For endohedrals photoionization cross-sections, we have:

$$
\sigma^{\mathrm{AC}(r)}_{nl,kl'}(\omega) = F^2_{l'}(k)\sigma_{nl,kl'}(\omega). \tag{1.109}
$$

Note that the factor $F_{l'}(k)$ as a function of ω has strong resonances, which also appear in $\sigma^{\mathrm{AC}(r)}_{nl,kl'}(\omega)$ and are called *confinement resonances* [1.33, 1.34].

Making use of these amplitudes, formulae (1.71), (1.78), (1.79), and the replacement (1.72) and (1.83), one easily obtains photoionization cross-section and angular anisotropy parameters for $\mathrm{A@C}_n$.

Finally, we obtain from (1.74) the following formula for dipole angular anisotropy parameter of endohedral atom $\mathrm{A@C}_n$:

$$
\begin{aligned}
\beta^{\mathrm{AC}(r)}_{nl}(\omega) = {} & \frac{1}{(2l+1)\left[(l+1)F^2_{l+1}\tilde{D}^2_{l+1} + lF^2_{l-1}\tilde{D}^2_{l-1}\right]} \\
& \times[(l+1)(l+2)F^2_{l+1}\tilde{D}^2_{l+1} + l(l-1)F^2_{l-1}\tilde{D}^2_{l-1} \\
& -6l(l+1)F_{l+1}F_{l-1}\tilde{D}_{l+1}\tilde{D}_{l-1}\cos(\tilde{\tilde{\delta}}_{l+1} - \tilde{\tilde{\delta}}_{l-1})],
\end{aligned}
\tag{1.110}
$$

where $\tilde{\tilde{\delta}}_{l'} = \tilde{\delta}_{l'} + \Delta\delta_{l'} = \delta_{l'} + \Delta_{l'} + \Delta\delta_{l'}$ [see (1.73)].

Making use of (1.78), (1.79) and (1.72), (1.83), we obtain the following expression for angular anisotropy parameter:

$$
\begin{aligned}
\gamma^{\mathrm{AC}(r)}_{nl}(\omega) = {} & \frac{6}{5\left[(l+1)F^2_{l+1}\tilde{D}^2_{l+1} + lF^2_{l-1}\tilde{D}^2_{l-1}\right]} \\
& \times\left\{\frac{(l+1)F_{l+1}}{2l+3}\tilde{D}_{l+1}[3(l+2)F_{l+2}\tilde{Q}_{l+2}\cos\left(\tilde{\tilde{\delta}}_{l+2} - \tilde{\tilde{\delta}}_{l+1}\right)\right. \\
& -lF_l\tilde{Q}_l\cos\left(\tilde{\tilde{\delta}}_l - \tilde{\tilde{\delta}}_{l+1}\right)] - \frac{lF_{l-1}\tilde{D}_{l-1}}{2l-1} \\
& \times\left[3(l-1)F_{l-2}\tilde{Q}_{l-2}\cos\left(\tilde{\tilde{\delta}}_{l-2} - \tilde{\tilde{\delta}}_{l-1}\right)\right. \\
& \left.\left.-(l+1)F_l\tilde{Q}_l\cos\left(\tilde{\tilde{\delta}}_l - \tilde{\tilde{\delta}}_{l-1}\right)\right]\right\},
\end{aligned}
\tag{1.111}
$$

$$
\eta^{\mathrm{AC}(r)}_{nl}(\omega) = \frac{6}{5\left[(l+1)F^2_{l+1}\tilde{D}^2_{l+1} + lF^2_{l-1}\tilde{D}^2_{l-1}\right]}
$$

$$\times\left\{\frac{(l+1)(l+2)}{(2l+1)(2l+3)}F_{l+2}\tilde{Q}_{l+2}\left[5lF_{l-1}\tilde{D}_{l-1}\cos\left(\tilde{\tilde{\delta}}_{l+2}-\tilde{\tilde{\delta}}_{l-1}\right)\right.\right.$$
$$\left.-(l+3)\,F_{l+1}\tilde{D}_{l+1}\cos\left(\tilde{\tilde{\delta}}_{l+2}-\tilde{\tilde{\delta}}_{l+1}\right)\right]$$
$$-\frac{(l-1)\,l}{(2l+1)(2l-1)}F_{l-2}\tilde{Q}_{l-2}\left[5(l+1)\,F_{l+1}\tilde{D}_{l+1}\cos\left(\tilde{\tilde{\delta}}_{l-2}-\tilde{\tilde{\delta}}_{l+1}\right)\right.$$
$$\left.-(l-2)\,F_{l-1}\tilde{D}_{l-1}\cos\left(\tilde{\tilde{\delta}}_{l-2}-\tilde{\tilde{\delta}}_{l-1}\right)\right]$$
$$+2\frac{l(l+1)\,F_l\tilde{Q}_l}{(2l-1)(2l+3)}\left[(l+2)\,F_{l+1}\tilde{D}_{l+1}\tilde{D}_{l+1}\cos\left(\tilde{\tilde{\delta}}_l-\tilde{\tilde{\delta}}_{l+1}\right)\right.$$
$$\left.\left.-(l-1)\;F_{l-1}\tilde{D}_{l-1}\tilde{D}_{l-1}\cos\left(\tilde{\tilde{\delta}}_l-\tilde{\tilde{\delta}}_{l-1}\right)\right]\right\}. \tag{1.112}$$

The same parameters can be calculated also for atom A with semiclosed shells. In order to obtain the values $\sigma^{\mathrm{AC}(r)}_{nl,kl'\uparrow\downarrow}(\omega)$, $\beta^{\mathrm{AC}(r)}_{nl\uparrow\downarrow}(\omega)$, $\gamma^{\mathrm{AC}(r)}_{nl\uparrow\downarrow}(\omega)$, and $\eta^{\mathrm{AC}(r)}_{nl\uparrow\downarrow}(\omega)$, one can use (1.110–1.112), substituting there $\tilde{D}_{l'}(\omega)$, $\tilde{Q}_{l''}(\omega)$, $\tilde{\tilde{\delta}}_{l'''}$, and $F_{l'}(\omega)$ by $\tilde{D}_{l'\uparrow}(\omega)$, $\tilde{Q}_{l''\uparrow}(\omega)$, $\tilde{\tilde{\delta}}_{l'''\uparrow}$, and $F_{l'\uparrow}(\omega)$ or by $\tilde{D}_{l'\downarrow}(\omega)$, $\tilde{Q}_{l''\downarrow}(\omega)$, $\tilde{\tilde{\delta}}_{l'''\downarrow}$, and $F_{l'\downarrow}(\omega)$ for spin-up ($\uparrow$) and spin-down electrons ($\downarrow$) (see Sect. 1.10).

If the effect of $F_{l'}(k)$ is strong enough, it has to be taken nonperturbatively, so that (1.108) is not valid any more. Instead, one has to modify the amplitudes $D_{nl,kl'}(\omega)$ and $Q_{nl,kl'}(\omega)$. This can be achieved by solving (1.37) and (1.85) with account of F factors. Presenting these equations symbolically as

$$\left\langle\nu_1\left|\widehat{D}(\omega)\right|\nu_2\right\rangle=\left\langle\nu_1\left|\hat{d}\right|\nu_2\right\rangle+\sum_{\nu_3,\nu_4}$$
$$\times\frac{\left\langle\nu_3\left|\widehat{D}(\omega)\right|\nu_4\right\rangle\left[F^2_{\nu_3}n_{\nu_4}(1-n_{\nu_3})-F^2_{\nu_4}n_{\nu_3}(1-n_{\nu_4})\right]\langle\nu_4\nu_1\,|U|\,\nu_3\nu_2\rangle}{\varepsilon_{\nu_4}-\varepsilon_{\nu_3}+\omega+i\eta(1-2n_{\nu_3})}, \tag{1.113}$$

$$\left\langle\nu_1\left|\widehat{Q}(\omega)\right|\nu_2\right\rangle=\langle\nu_1|\hat{q}|\nu_2\rangle+\sum_{\nu_3,\nu_4}$$
$$\times\frac{\left\langle\nu_3\left|\widehat{Q}(\omega)\right|\nu_4\right\rangle\left[F^2_{\nu_3}n_{\nu_4}(1-n_{\nu_3})-F^2_{\nu_4}n_{\nu_3}(1-n_{\nu_4})\right]\langle\nu_4\nu_1\,|U|\,\nu_3\nu_2\rangle}{\varepsilon_{\nu_4}-\varepsilon_{\nu_3}+\omega+i\eta(1-2n_{\nu_3})}, \tag{1.114}$$

we obtain the proper amplitudes.

Here F_{ν_i} are the reflection factors, given by (1.107) with ν_i determined by photoelectron's linear momentum $k_{\nu_{i_i}}=\sqrt{2\varepsilon_{\nu_i}}$ and l_{ν_i}. The amplitudes with account of photoelectron scattering are presented as

$$D^{\mathrm{AC}(r)}_{nl,kl'}(\omega)=F_{l'}(k)\,\widehat{D}_{nl,kl'}(\omega)\exp[i\,\Delta\delta_{l'}(k)]$$
$$=F_{l'}(k)\,\widetilde{\widehat{D}}_{nl,kl'}(\omega)\exp[i\,(\widehat{\Delta}_{l'}(k)+\Delta\delta_{l'}(k)],$$

$$Q^{\mathrm{AC}(r)}_{nl,kl''}(\omega) = F_{l'}(k)\widehat{Q}_{nl,kl''}(\omega)\exp[i\Delta\delta_{l''}(k)]$$
$$= F_{l'}(k)\widetilde{\widehat{Q}}_{nl,kl''}(\omega)\exp[i(\widehat{\Delta}_{l''}(k) + \Delta\delta_{l''}(k)], \quad (1.115)$$

Reflection factors F_ν appear in (1.113) and (1.114) in intermediate, not directly ionized shells, representing the indirect influence of the fullerenes upon their photoionization cross-section. As a result, the confinement resonances [see (1.109), definition and references below it] could affect the cross-section of the directly ionized shell leading in it along to confinement also to *interference confinement resonances*.

Using these amplitudes, one calculates all the considered above characteristics of the photoionization process: cross-sections $\sigma_{nl}(\omega)$, angular anisotropy $\beta_{nl}(\omega)$, and spin polarization parameters $\gamma_{nl}(\omega)$, $\eta_{nl}(\omega)$ of photoelectron.

It is more accurate to substitute the static action of the fullerenes shell not by (1.105) but by a finite thickness potential

$$W(r) = -W_0 \quad \text{at} \quad R - \frac{\Delta_{\mathrm{C}}}{2} \le r \le R + \frac{\Delta_{\mathrm{C}}}{2},$$
$$W(r) = 0 \quad \text{at} \quad r < R - \frac{\Delta_{\mathrm{C}}}{2}, r > R + \frac{\Delta_{\mathrm{C}}}{2}. \quad (1.116)$$

where Δ_{C} is the thickness of the fullerenes shell. Inclusion of (1.116) modifies HF equations (1.10), by adding $W(r)$ to the potential of the nucleus $(-Z/r)$, thus modifying the one-electron states. Denoting these new wave functions as $\tilde{\varphi}_k(x)$ instead of $\varphi_k(x)$, we obtain (1.113) and (1.114), but with $\tilde{\varphi}_k(x)$ one-electron states. The same is valid if instead of (1.116) another, more sophisticated potential is taken into account. However, the additional accuracy of these potentials is questionable since all static potentials neglect the complex multiatomic structure of C_n and direct interaction between atomic and fullerenes electrons and between fullerene electrons themselves.

1.14 Endohedral Atoms: The Effect of Fullerene Polarization

The fullerene electronic shell effectively changes the intensity of incoming photon flux, which penetrates it and reaches the internal atom. This effect can be accounted for by the same way as the account of influence of one shell on the other. From physical point of view, the situation is the same, in addition to atomic shells, additional fullerene shell appears.

Significant simplification lays in relative weakness of interaction between the electrons of fullerene and atom A. Hence this interaction may be accounted for in the first order of MBPT. This is because the fullerene radius R is significantly larger than the atomic radius r_{A}. Hence, we have as a result, only the dipole–dipole contribution to the interaction between atomic and fullerene electrons:

$$V_{\mathrm{AC}} \approx \boldsymbol{r}_{\mathrm{A}} \cdot \frac{\boldsymbol{r}_{\mathrm{C}}}{R^3}, \tag{1.117}$$

here $\mathbf{r}_A$ and $\mathbf{r}_C$ are the radius vectors of electrons of atom A and fullerene, respectively. This relation is parametrically valid for atoms with ionization potential significantly less than that of a fullerene.

In the language of diagrammatic theory, the photoabsorption amplitude $\mathrm{A@C}_n$ is similar to (1.36), where wavy line denotes (1.117):

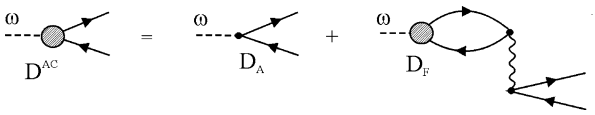

(1.118)

here D^{AC}, D_{A}, and D_{F} are photoionization amplitudes of $\mathrm{A@C}_n$, single atom A, and fullerene C_n, respectively. Note that the most frequently investigated case is $\mathrm{C}_n \equiv \mathrm{C}_{60}$, but nevertheless other fullerenes, e.g., C_{82}, could be also objects of investigation. Analytically, we have for (1.111):

$$D^{\mathrm{AC}}(\omega) \cong D_{\mathrm{A}}\left(1 - \frac{\alpha_{\mathrm{C}_n}(\omega)}{R^3}\right) \equiv D_{\mathrm{A}} G_{\mathrm{C}_n}(\omega), \tag{1.119}$$

where $\alpha_{\mathrm{C}_n}(\omega)$ is dipolar polarizability of fullerene shell. In framework of RPAE, D_{A} is the solution of (1.37). On the other hand, it is not essential for relation (1.119) what approximation is used to describe isolated atom.

The unified action of static fullerene potential represented by factor $F_l(k)$ from (1.108), which accounts for the reflection of photoelectron from atom A by the fullerene shell, and a factor $G_{\mathrm{C}_n}(\omega)$ from (1.119), which accounts for modification of the flux of incoming photons, acting on atom A due to fullerene polarization results in the following relation [1.34]:

$$\sigma^{\mathrm{AC}}_{nl,kl'}(\omega) = |F_{l'}(k)|^2 \left|1 - \frac{\alpha_{\mathrm{C}_n}(\omega)}{R^3}\right|^2 \widehat{\sigma}_{nl,kl'}(\omega) \equiv |F_{l'}(k)|^2 |G_{\mathrm{C}_n}(\omega)|^2 \widehat{\sigma}_{nl,kl'}(\omega). \tag{1.120}$$

here superscript AC without (r) denotes theoretical values, which account for scattering of photoelectron by fullerene static field and dynamic polarizability of fullerene; $\widehat{\sigma}_{nl,kl'}(\omega)$ is determined by the amplitude (1.115). Assuming that the modification of the atomic cross-section is not too strong, one can use in (1.120) experimental atomic photoionization cross-sections $\sigma_{nl,kl'}(\omega)$ and fullerene dipolar polarizability $\alpha_{\mathrm{C}_n}(\omega)$ with factors $F_{l'}(k)$, calculated in any model, including that, which are better than used above potential bubble model (1.105).

Factor $G_{\mathrm{C}_n}(\omega)$ in (1.119) changes the flux of dipole photons. It appeared that this factor as a function of ω has strong maxima, connected to the resonances in dipole polarizability, which also appear in $\sigma^{AC(r)}_{nl,kl'}(\omega)$ and are called *Giant endohedral resonances* [1.35].

The quadrupole matrix element $Q_{\mathrm{AC}}(\omega)$ may be modified in the same way accounting for the diagrams similar to (1.119) and resulting following expression, obtained with the help of (1.116):

$$Q_{\mathrm{AC}}(\omega) \cong \widehat{Q}\left(1 - \frac{\alpha^q_{\mathrm{C}_n}(\omega)}{4R^5}\right) \equiv \widehat{Q} G^q_{\mathrm{C}_n}(\omega), \tag{1.121}$$

where $\alpha^q_{\mathrm{C}_n}(\omega)$ is the fullerene quadrupole polarizability.

Multipliers $G_{\mathrm{C}_n}(\omega)$ and $G^q_{\mathrm{C}_n}(\omega)$ appear in nondipole parameters, resulting in additional ratios $G^q_{\mathrm{C}_n}(\omega)/G_{\mathrm{C}_n}(\omega)$. Note that $G_{\mathrm{C}_n}(\omega)$ and $G^q_{\mathrm{C}_n}(\omega)$ are complex values:

$$G^{q,d}_{\mathrm{C}_n}(\omega) = \tilde{G}^{q,d}_{\mathrm{C}_n}(\omega) \exp[i\Lambda^{q,d}(\omega)]. \tag{1.122}$$

In (1.120), $G_{\mathrm{C}_n}(\omega) \equiv G^d_{\mathrm{C}_n}(\omega)$.

As a result, the following formulae for angular anisotropy parameters are easily obtained:

$$\begin{aligned}
\gamma^{\mathrm{AC}}_{nl}(\omega) = {} & \frac{6\tilde{G}^q_{\mathrm{C}_n}(\omega)}{5\tilde{G}^d_{\mathrm{C}_n}(\omega)\left[(l+1)F^2_{l+1}\,\tilde{\tilde{D}}^2{}_{l+1} + lF^2_{l-1}\,\tilde{\tilde{D}}^2{}_{l-1}\right]} \times \left\{ \frac{(l+1)F_{l+1}}{2l+3}\tilde{\tilde{D}}_{l+1} \right. \\
& \times \left[3(l+2)\,F_{l+2}\tilde{\tilde{Q}}_{l+2}\cos\left(\bar{\delta}_{l+2} - \bar{\delta}_{l+1}\right) - lF_l\tilde{\tilde{Q}}_l\cos\left(\bar{\delta}_l - \bar{\delta}_{l+1}\right)\right] \\
& - \frac{lF_{l-1}\tilde{\tilde{D}}_{l-1}}{2l-1}\left[3(l-1)\,F_{l-2}\tilde{\tilde{Q}}_{l-2}\cos\left(\bar{\delta}_{l-2} - \bar{\delta}_{l-1}\right)\right. \\
& \left.\left. -(l+1)F_l\tilde{\tilde{Q}}_l\cos\left(\bar{\delta}_l - \bar{\delta}_{l-1}\right)\right]\right\},
\end{aligned} \tag{1.123}$$

$$\begin{aligned}
\eta^{\mathrm{AC}}_{nl}(\omega) = {} & \frac{6\tilde{G}^q_{\mathrm{C}_n}(\omega)}{5\tilde{G}^d_{\mathrm{C}_n}(\omega)\left[(l+1)F^2_{l+1}\,\tilde{\tilde{D}}^2{}_{l+1} + lF^2_{l-1}\,\tilde{\tilde{D}}^2{}_{l-1}\right]} \\
& \times \left\{ \frac{(l+1)(l+2)}{(2l+1)(2l+3)}F_{l+2}\tilde{\tilde{Q}}_{l+2}\left[5lF_{l-1}\tilde{\tilde{D}}_{l-1}\cos\left(\bar{\delta}_{l+2} - \bar{\delta}_{l-1}\right)\right.\right. \\
& \left. - (l+3)\,F_{l+1}\tilde{\tilde{D}}_{l+1}\cos\left(\bar{\delta}_{l+2} - \bar{\delta}_{l+1}\right)\right] - \frac{(l-1)l}{(2l+1)(2l-1)}F_{l-2}\tilde{\tilde{Q}}_{l-2} \\
& \times \left[5(l+1)\,F_{l+1}\tilde{\tilde{D}}_{l+1}\cos\left(\bar{\delta}_{l-2} - \bar{\delta}_{l+1}\right)\right. \\
& \left.\left. - (l-2)\,F_{l-1}\tilde{\tilde{D}}_{l-1}\cos\left(\bar{\delta}_{l-2} - \bar{\delta}_{l-1}\right)\right]\right\}
\end{aligned}$$

$$+2\frac{l\,(l+1)\,F_l\,\tilde{\tilde{Q}}_l}{(2l-1)\,(2l+3)}\left[(l+2)\,F_{l+1}\tilde{\tilde{D}}_{l+1}\cos\left(\bar{\delta}_l-\bar{\delta}_{l+1}\right)\right.$$
$$\left.-(l-1)\,F_{l-1}\tilde{\tilde{D}}_{l-1}\cos\left(\bar{\delta}_l-\bar{\delta}_{l-1}\right)\right]\Bigg\}, \tag{1.124}$$

here $\bar{\delta}_{l\pm1}=\tilde{\tilde{\delta}}_{l\pm1}+\Lambda^d=\tilde{\delta}_{l\pm1}+\Delta\delta_{l\pm1}+\Lambda^d=\delta_{l\pm1}+\widehat{\Delta}_{l\pm1}+\Delta\delta_{l\pm1}+\Lambda^d$ and $\bar{\delta}_{l\pm2,l}=\tilde{\tilde{\delta}}_{l\pm2,l}+\Lambda^q=\tilde{\delta}_{l\pm2,l}+\Delta\delta_{l\pm2,l}+\Lambda^q=\delta_{l\pm2,l}+\widehat{\Delta}_{l\pm2,l}+\Delta\delta_{l\pm2,l}+\Lambda^q$.

Polarizability $\alpha_F(\omega)$ may be obtained as a result of ab initio calculations that are quite complicated since it requires according to (1.85) calculation of oscillator strength and photoabsorption cross-section. Instead of this, one can substitute into (1.85) experimental fullerene photoabsorption cross-section $\sigma_{C_n}(\omega)$. We prefer to use the experimental cross-section $\sigma_{C_n}(\omega)$, which is directly proportional to the imaginary part of dipolar polarizability [BLP]:

$$\mathrm{Im}\alpha_{C_n}(\omega)=\frac{c\sigma_{C_n}(\omega)}{4\pi\omega}. \tag{1.125}$$

The cross-section $\sigma_{C_n}(\omega)$ is characterized by a strong maximum called Giant resonance. In C_{60} it is placed at about $\omega\approx 22$ eV. Experimenters usually do not present directly absolute values of $\sigma_{C_n}(\omega)$. Nevertheless, the absolute values may be estimated by making use of normalization procedure based on the sum rule:

$$\left(\frac{c}{2\pi^2}\right)\int\sigma_{C_n}(\omega)\mathrm{d}\omega=N, \tag{1.126}$$

here N is the number of collectivized electrons. For C_{60} it is equal to $N=240$, i.e., four collectivized electrons for each carbon atom. Note that for fullerene the contribution of discrete excitations is small and may be neglected.

The dispersion relation for the real part of $\alpha_{C_n}(\omega)$ is written as:

$$\mathrm{Re}\alpha_{C_n}(\omega)=\frac{c}{2\pi^2}\int_{I_F}^{\infty}\frac{\sigma_{C_n}(\omega')\mathrm{d}\omega'}{\omega'^2-\omega^2}, \tag{1.127}$$

where I_{C_n} is the fullerene ionization potential.

The examples of modifications of total and angular differential energy dependent photoionization cross-sections, resulting from the reflections of photoelectron wave by the static C_{60} potential and increasing of incoming electromagnetic fields due to polarization of electronic shell of C_{60} will be presented in Chap. 2. The results are obtained by using known from experiment fullerene characteristics, namely, its electron affinity, photoabsorption cross-section and the fact that the fullerene radius is significantly larger than the thickness fullerene shell and atomic radius.

Modification of the incoming photon flux and of vacancy decay probability is mainly due to the virtual and real excitation of giant dipole resonance of C_{60} [1.35].

1.15 Two-Shell Endohedrals

It is possible that fullerene has two, not one shell [1.36]. Thus, it can be considered in the simplest form as two spheres with considerably different radiuses R_1 and R_2 put one inside another [1.37]. Assume that they have the same center, so the fullerenes shell potential instead of (1.106) is of the form

$$W(r) = -V_1\delta(r - R_1) - V_2\delta(r - R_2). \tag{1.128}$$

At $r < R_1$ the solution of the Hartree–Fock (HF) equation for a photoelectron with linear momentum $k = \sqrt{2E}$ and angular l $\chi_{kl}(r)$, moving under the action of atomic HF potential [see (1.8)] and $W(r)$ can be presented as:

$$\chi_{kl}(r) = F_l(k)u_{kl}(r) \tag{1.129}$$

and the photoionization matrix elements defined in accord with (1.109). In (1.129) $u_{kl}(r)$ is the regular at $r = 0$ solution of the same equation, but without $V(r)$.

After some algebra we obtain the following expression for additional photoelectron's phase shift δ_l and the *reflection amplitude* $F_l(k)$:

$$\sin\Delta\delta = \frac{2}{\sqrt{\zeta}}\left\{kV_2u_2^2 + V_1u_1\left[ku_1 + 2V_2u_2(u_2\upsilon_1 - u_1\upsilon_2)\right]\right\}, \tag{1.130}$$

$$F_l(k) = \frac{k^2}{\sqrt{\zeta}}, \tag{1.131}$$

where

$$\begin{aligned}\zeta = {} & k^4 + 4k^3(V_1u_1\upsilon_1 + V_2u_2\upsilon_2) + 16V_1^2V_2^2u_1^2(u_2\upsilon_1 - u_1\upsilon_2)^2(u_2^2 + \upsilon_2^2)\\ & -16kV_1V_2u_1(u_1\upsilon_2 - u_2\upsilon_1)\left[V_1u_1(u_1u_2 + \upsilon_1\upsilon_2) + V_2u_2(u_2^2 + \upsilon_2^2)\right]\\ & +4k^2\{V_1^2u_1^2(u_1^2 + \upsilon_1^2) + V_2^2u_2^2(u_2^2 + \upsilon_2^2)\\ & +2V_1V_2u_1[2u_2\upsilon_1\upsilon_2 + \upsilon_1(u_2^2 - \upsilon_2^2)]\}.\end{aligned} \tag{1.132}$$

The following notations are employed in these formulas:

$$u_1 \equiv u_{kl}(R_1), \quad u_2 \equiv u_{kl}(R_2), \quad \upsilon_1 \equiv \upsilon_{kl}(R_1), \quad \upsilon_2 \equiv \upsilon_{kl}(R_2). \tag{1.133}$$

For a single-wall fullerene, the effect of its polarization upon incoming photon beam can be presented by diagrammatic equation (1.118) that leads to expression (1.119).

For two-shell fullerene, the corresponding expression is much more complex, since in principle the interaction between two group of electrons, belonging to fullerenes 1 and 2 must be taken into account. It is possible to apply for considered in [1.36] C_{60} and C_{240}, the following strong inequality $r \ll R_1 \ll R_2$. In this case, the amplitude $D_{AC}(\omega)$ can be presented as

$$D_{\mathrm{AC}}(\omega) \cong D_{\mathrm{A}}(\omega)\left[1-\left(\frac{\alpha_1}{R_1^3}+\frac{\alpha_2}{R_2^3}\right)\frac{1-\frac{\alpha_1\alpha_2}{\alpha_1 R_2^3+\alpha_2 R_1^3}\left(1+\frac{R_1^3}{R_2^3}\right)}{1-\frac{\alpha_1\alpha_2}{R_2^6}}\right]$$
$$\equiv G_{12}(\omega) D_{\mathrm{A}}(\omega), \tag{1.134}$$

where $G_{12}(\omega)$ is the *polarization amplitude factor* for two-shell fullerene. It follows from summation of diagrams much more complex than in (1.118):

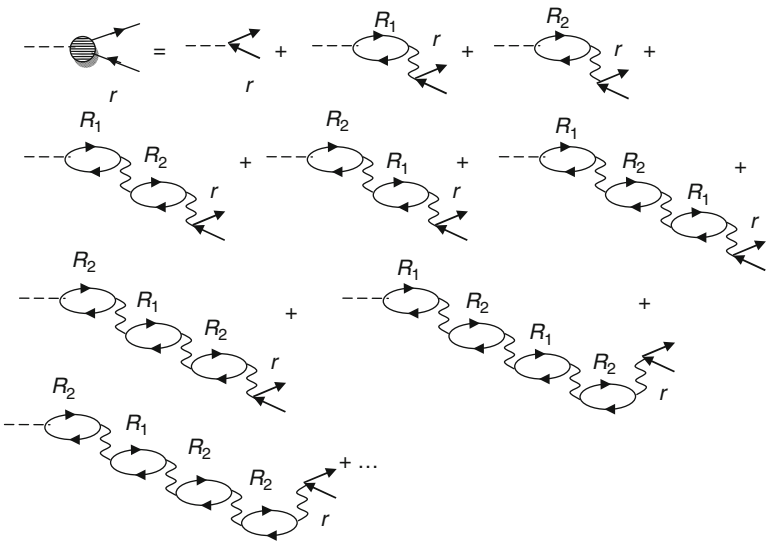

(1.135)

For simplicity of the drawings, we have omitted the so-called time-reverse diagrams.

It is seen that the correction due to simultaneous polarization of both fullerenes shells proportional to $\alpha_1\alpha_2$ considerably modifies a simple formula that would account only the sum of the shells' action.

Note that using the sequence of diagrams (1.135) and similar assumptions, one obtains for the quadrupole amplitude

$$Q_{\mathrm{AC}}(\omega) \cong Q_{\mathrm{A}}(\omega)\left[1-\left(\frac{\alpha_1^q}{4R_1^5}+\frac{\alpha_2^q}{4R_2^5}\right)\frac{1-\frac{\alpha_1^q\alpha_2^q}{4\alpha_1^q R_2^5+\alpha_2^q R_1^5}\left(1+\frac{R_1^5}{4R_2^5}\right)}{1-\frac{\alpha_1^q\alpha_2^q}{14R_2^6}}\right]$$
$$\equiv G_{12}^q(\omega) Q_{\mathrm{A}}(\omega), \tag{1.136}$$

where α_1^q and α_2^q are the dynamic quadrupole polarizabilities of the fullerenes, inner and outer, respectively. For one-shell fullerene, the quadrupole photoionization amplitude of the endohedral is given by (1.121).

It is essential to have in mind that (1.134) can in principle take into account electron correlations beyond the RPAE frame. Namely, each of the polarizabilities, α_1 or α_2, can include even *all* correlations inside each fullerene, 1 or 2, respectively. It means that as polarizabilities, precisely calculated or best experimentally obtained values can be used.

As it was mentioned in connection to one-shell polarization [see (1.119)], α_1 and α_2 can be calculated or taken from experiment. Directly determined in experiment are only static polarizabilities, namely, their values at $\omega \approx 0$. To obtain dynamic polarizability, calculations are needed. However, if photoionization cross-section $\sigma(\omega)$ of a considered object is measured, the dynamic polarizability can be derived using the relations (1.125) and (1.127).

To perform photoionization calculations we need to know the fullerenes potentials V_1 and V_2. They can be determined using for each of the shells the same formula that is usually employed for a single-shell fullerene

$$V_{1,2} = \frac{1}{2}\sqrt{2I_{1,2}}\left(1 + \coth\sqrt{2I_{1,2}}R_{1,2}\right), \tag{1.137}$$

where I is the ionization potential of the fullerene. By doing this we make a reasonable assumption that well separated shells are not essentially affecting each other so that a two-shell "onion" C_{N_1,N_2} really consists of two fullerenes C_{N_1} and C_{N_2}. For C_{60} and C_{240}, the values are $I_{60} = 0.195$ and $I_{240} = 0.280$ [1.38]. For completeness let us add $I_{540} = 0.386$. The radiuses of these fullerenes are also known, being equal to $R_{60} \cong 6.75$, $R_{240} \cong 13.5$, and $R_{540} \cong 19.8$. It is remarkable that for at least considered objects the ratio $\eta_n \equiv N_n/R_n^2$ are almost the same $\eta_{60} = 1.317$, $\eta_{240} = 1.317$, and $\eta_{540} = 1.38$. So, let us assume for η_n a universal value 1.32.

Analysis of the C_{60} polarizability permitted to conclude that at least for static value $\alpha_{C_{60}} \approx 60\alpha_C$. Since the electron density of all big enough fullerenes is the same, it seems natural to assume that $\alpha_{C_n} \approx N_n\alpha_C$. In order to estimate the contribution of the second fullerenes shell, let us assume also that the same relations are valid not only for static but also for dynamic polarizabilities. Using the ratio $\eta_n = 1.32$ and these assumptions, we obtain $\alpha_N(\omega)/R_N^3 \approx \alpha_{C60}(\omega)/45.5R_N \equiv \alpha_1(\omega)/45.5R_N$. With the help of this relation, we derive from (1.134)

$$D_{AC}(\omega) \approx D_A(\omega)\left[1 - 1.51\frac{\alpha_1}{R_1^3}\frac{1 - 0.380\alpha_1(\omega)/R_1^3}{1 - 0.0635[\alpha_1(\omega)/R_1^3]^2}\right] \equiv \bar{G}_{12}(\omega)D_A(\omega), \tag{1.138}$$

where $\bar{G}_{12}(\omega)$ is the approximate value of the polarization amplitude factor. The data on $\alpha_1(\omega)$ as well as on $S_1(\omega) = \left|\left(1 - \alpha_1(\omega)/R_1^3\right)\right|^2$ are taken from [1.32].

The formulas required to calculate the photoionization cross-sections and angular anisotropy parameters, both dipole and nondipole for two-shell endohedral atom $A@C_{N_1}@C_{N_2}$ are the same as for a single-shell endohedral (1.120), (1.111), (1.123), and (1.124) with $G_{12}^{d,q}(\omega)$ determined from (1.134), (1.135), and (1.138), $F_l(k)$ given by (1.131) and $\Delta\delta_l$ by (1.130).

1.16 Current Induced by Photon Momentum

Angular distribution asymmetry appearing due to the account of nondipolar corrections to photoelectron angular distribution (1.77) and (1.81) results in creation of nonzero total current $J(\omega)$, directed along or opposite to the photon flux [1.4, 1.39, 1.40].

In the photoabsorption process, gas volume absorbs photon flux energy $Q\omega$ as well as its momentum $Q\kappa = Q\omega/c$, where Q is the total number of absorbed photons. Momentum $Q\kappa$ *is* transferred to all ions and electrons originating due to the gas absorption of energy $Q\omega$. The sum of electron momentum $\vec{P}_{\text{el}}$ and ion momentum $\vec{P}_{\text{ion}}$ equals to total photon momentum $Q\kappa$: $Q\kappa = \left|\vec{P}_{\text{el}} + \vec{P}_{\text{ion}}\right|$. If the values $\left|\vec{P}_{\text{el}}\right|$ and $\left|\vec{P}_{\text{ion}}\right|$ are of the same order, the velocity of electron directed movement V_{el} is significantly larger than that for ions V_{ion}, and hence the electronic *induced current* is significantly larger than the ionic *induced current* $J_{\text{el}} \gg J_{\text{ion}}$. According to (1.66) in dipole approximation, photoelectron angular distribution is symmetrical with respect to replacement $\theta = 0$ to $\theta = \pi$. Hence it follows that in dipole approximation $V_{\text{el}} = 0$ and $J_{\text{el}} = 0$, and the description of induced current requires account of corrections beyond this approximations, i.e., quadrupole correction according to formulae (1.77) and (1.81).

All the photoelectrons form an induced increasing current until they collide with the gas atoms. The idea of existence of the induced current and calculation formula and its derivation are presented in [1.4, 1.39]. The formula for the density of induced current is written as:

$$j\,(\omega) = \sum_i \frac{W}{\sigma_{\text{el}}\,(\varepsilon_i)} \int \frac{\mathrm{d}\sigma_i\,(\omega)}{\mathrm{d}\Omega} \cos\theta \mathrm{d}\Omega = \sum_i \frac{W\kappa\sigma_i\,(\omega)\,\gamma_i\,(\omega)}{\sigma_{el}\,(\varepsilon_i)}, \qquad (1.139)$$

where W is the density of photon flux and integration over $\mathrm{d}\Omega$ is carried out making use of [IS]. The sum in (1.139) runs over all subshells i, ionized by photon of energy ω, $\sigma_{\text{el}}\,(\varepsilon_i)$ is scattering cross-section of electrons with energy $\varepsilon_i = \omega - I_i$ on gas atoms (see Chap. 3), and I_i is ionization potential of i-shell. It follows from (1.139) that the induced current is defined by nondipolar component of angular distribution $\gamma_i\,(\omega)$ determined by formulae (1.78), (1.83), and (1.123). The order of magnitude of this current is significant and its emergence is in principle an observable effect.

Indeed, according to (1.139) the flux $W = 10^{13}$ photons/s sm^2, which is easily realized in modern storage rings, results in a current density of about 10^{-9} A/cm^2. The value $j(\omega)$ increases significantly, if the electron scattering cross-section is small (see Chap. 3) and if photoionization cross-section $\sigma_i(\omega)$ and nondipolar parameter $\gamma_i(\omega)$ are large. Nondipolar parameter can be quite large in the cases of dipole and quadrupole resonances [1.41]. This result explicitly follows from the contribution of s-electrons into $\gamma_i(\omega)$, which is obtained from (1.78) and making use of (1.83)

$$\gamma_{ns}(\omega) = \frac{6}{5}\frac{\tilde{Q}_d(\omega)}{\tilde{D}_p(\omega)}\cos(\tilde{\delta}_d - \tilde{\delta}_p) \tag{1.140}$$

for an isolated atom, and

$$\gamma_{ns}^{\mathrm{AC}}(\omega) = \frac{6}{5}\frac{\tilde{G}^q_{\mathrm{C}_n}(\omega)}{\tilde{G}^d_{\mathrm{C}_n}(\omega)}\frac{\tilde{\tilde{Q}}_d(\omega)}{\tilde{\tilde{D}}_p(\omega)}\cos(\bar{\delta}_d - \bar{\delta}_p) \tag{1.141}$$

for an endohedral atom [see (1.20)].

The formula for contribution of all s-electron into induced current is written as:

$$j_0(\omega) = \sum_{ns} W\frac{6\kappa}{5}\frac{\tilde{G}^q_{\mathrm{C}_n}\tilde{\tilde{D}}_{np}(\omega)\tilde{\tilde{Q}}_{nd}(\omega)}{\tilde{G}^d_{\mathrm{C}_n}\sigma_{\mathrm{el}}(\varepsilon_{ns})}\cos[\bar{\delta}_d(\varepsilon_{ns}) - \bar{\delta}_p(\varepsilon_{ns})], \tag{1.142}$$

where $\tilde{D}_{np}(\omega)$ and $\tilde{Q}_{nd}(\omega)$ are dipole and quadrupole matrix elements, respectively, which are obtained as a solution of equation RPAE (1.37) and (1.85), respectively, and $\varepsilon_{ns} = \omega - I_{ns}$.

Calculation showed that $j(\omega)$ as a function of photon energy ω could change its sign at some frequency and the total photoelectron momentum is significantly different from the total photon momentum. This means that total momentum transferred to ions is large and depends upon ω.

The influence of many-electron correlations on the magnitude and sign of induced current is essential.

1.17 Inelastic Photoelectron Scattering

Photoelectron on the way from an atom may be inelastic scattered if its energy is sufficient for excitation or ionization of any atomic electron. Let us consider the role of this scattering. In diagram language, the discussed effect is represented as:

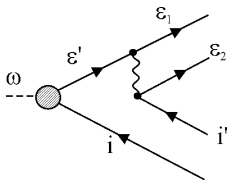

(1.143)

Physically, the diagram (1.143) represents the process of primary creation of vacancy i and photoelectron ε'. This process is described in the framework of RPAE. Then the photoelectron is inelastic scattered from state ε' to state ε_1 and creates electron–hole pair $\varepsilon_2 i'$. In the calculations, the diagram (1.143) accounts for the

interelectron interaction in the lowest order of perturbation theory. This process, called the *direct knock out*, was introduced and calculated for the first time in [1.42].

The *direct knockout* results in decrease of photoelectron energy and hence leads to the decrease of the observed photoionization cross-section of the main photoelectron line. The direct knock out increases the number of electrons that are removed from the atom. Corresponding cross-section is obtained by substituting amplitude (1.143) into formula (1.4).

For relatively deep shell i, formula for the cross-section of creation a single vacancy $\sigma_i^{(+)}(\omega)$ is simplified and can be written as [1.42, 1.43]:

$$\sigma_i^{(+)}(\omega) = \sigma_i(\omega) \exp\left[-2\mathrm{Im}\delta(\varepsilon)\right] \tag{1.144}$$

where $\sigma_i(\omega)$ is an experimental or a theoretical (e.g., RPAE or GRPAE) photoionization cross-section (see Sect. 1.8) and $\mathrm{Im}\delta(\varepsilon)$ is the imaginary part of electron inelastic scattering phase shift describing the probability of its inelastic scattering (see Chap. 3).

Correlation correction (1.143) in addition to photoionization cross-section changes significantly angular and spin distribution of electrons.

If photon energy is only a little above the ionization threshold of a subshell, the vacancy in which decays via Auger effect (see Sect. 5.8), an essential redistribution of energies between a "slow" photoelectron and "fast" Auger electron takes place. It occurs owing to interaction of the photoelectron with the new core that is created due to Auger decay of the initial vacancy. In the language of diagrams, it is represented as follows:

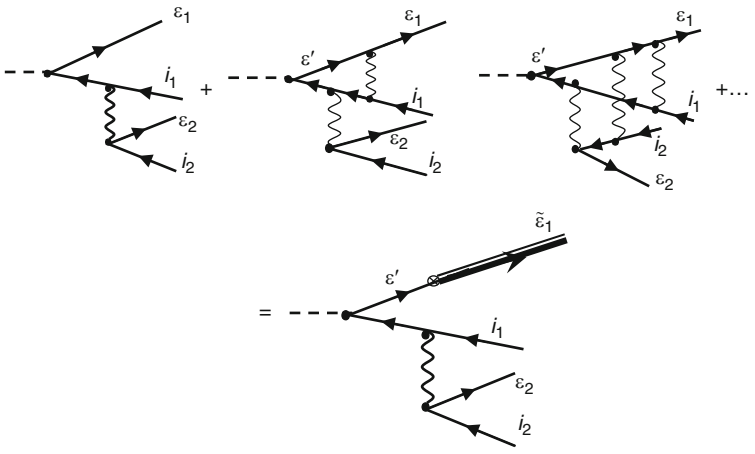

(1.145)

here $\varepsilon' \xrightarrow{\quad} \tilde{\varepsilon}_1$ denotes the overlap integral $\langle \varepsilon' | \tilde{\varepsilon}_1 \rangle$ of wave functions of a photoelectron with energies ε' and $\tilde{\varepsilon}_1$ in a field of vacancies j and $i_1 i_2$, respectively. Due to additional attraction to the two-vacancy state, the "slow" electron reduces its

speed v_1 while the fast electron accelerates and its speed v_2 increases. The respective energy shift $\Delta\varepsilon$ of each of them is equal but due to total energy conservation is of opposite sign and equal to

$$\varepsilon \sim \frac{\Gamma}{v_M}. \tag{1.146}$$

This entire phenomenon is a multielectronic effect named postcollision interaction (PCI). The change of energy of a slow photoelectron can be so great, that it will not leave the atom at all, and appears seized into a discrete highly excited level in a field of an ion with two vacancies formed after Auger decay [1.44]. A number of essential issues on PCI can be found in review [1.45].

1.18 Satellite Excitation

Photoionization of atomic i-shell is accompanied by the relaxation of ionic core resulting in origination, in addition to one-hole state i^{-1} of a number of double-hole–one-particle states $i^{-1}j^{-1}s$ with larger total energy, i.e., smaller kinetic energy in photoelectron spectrum. In photoelectron spectra, discrete excited states appear as shake-up satellites, and continuum states appear as low-kinetic energy background-shake-off satellites [1.46, 1.47]. For the relaxation with unchanged initial hole state, monopole selection rules are fulfilled and angular moments of the hole j and electron s are the same. The amplitude of photoionization with satellite excitation is given by the following diagram:

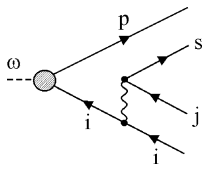

(1.147)

Since the intensities of satellites are usually <3% of the main line [1.46,1.47], the photoionization amplitudes may be calculated in the frame of perturbation theory [LL].

Making use of (1.147) one easily obtains the following formula for the shake-up satellites photoionization cross-section:

$$\sigma_{nljs}(\omega) = \left\{2.689\frac{\omega N_{nl}}{2l+1}[l|D_{nl,\varepsilon_{l-1}}(\omega)|^2 + (l+1)|D_{nl,\varepsilon_{l+1}}(\omega)|^2]\right\} \times \frac{|\langle si\,|U|\,ji\rangle|^2}{(\varepsilon_s - \varepsilon_j)} \left(10^{-18}\mathrm{cm}^2\right), \tag{1.148}$$

where nl stand for quantum numbers of the i-shell and $l \pm 1$ are orbital moments of photoelectron p and $\varepsilon_{l\pm1} = \omega - \varepsilon_s + \varepsilon_j + \varepsilon_i$. In formula (1.148), we introduce new values: RPAE photoionization amplitudes $D_{nl,\varepsilon_{l\pm1}}(\omega)$ depending on three energy parameters: initial state energy ε_i, final state energy $\varepsilon_{l\pm1}$, and photon energy ω. As distinct from formula (1.69), the energy conservation law does not connect these parameters in (1.148). The energy $\omega - \varepsilon_{l\pm1} + \varepsilon_i$ is transferred to satellite excitation.

Thus, the expression in curly brackets in (1.148) is the photoionization cross-section beyond the energy surface, which is denoted as $\sigma_{nl,\varepsilon_{l\pm1}}(\omega)$.

For complete description of photoionization of i-shell with satellite excitation, a two-dimensional array of photoionization cross-sections $\sigma_{nl,\varepsilon_{l\pm1}}(\omega)$ is required. These values are calculated within the RPAE program. A limited number of these supplementary curves can be plotted at the same coordinate system as the main photoionization curve as follows. Supplementary curves start from any point with abscissa ω_0 at the main photoionization curve $\sigma_{nl}(\omega)$, where all photon energy is transferred to photoelectron, i.e., $\omega_0 = \varepsilon_{nl\pm1} - \varepsilon_i$ and go to the left. At any point of this supplementary photoionization curve abscissa ω is also the energy transferred to photoelectron, and the value $\omega_0 - \omega$ is the energy transferred to the satellite excitation.

The supplementary curves for photoionization of Ne $2s$ and Ne $2p$ are shown in Figs. 7.1_Ne_p8–7.6_Ne_p13 and Figs. 7.7_Ne_p14–7.12_Ne_p19, respectively. These curves differ significantly. For Ne $2s$ they are considerably higher than the main photoionization curve, while for Ne $2p$ the supplementary curves almost coincide with the main photoionization curve. The latter means that the photoionization cross-section for $2p$-subshell for the photon energy ω with energy ΔE transferred to the satellite channel is almost equal to simple photoionization cross-section for the photon energy $\omega - \Delta E$.

Supplementary curves for angular anisotropy parameter β could be plotted in the same way as those for photoionization cross-section. These curves for angular anisotropy parameter for Ne $2p$ line almost coincide with the main curve for β.

Similar trends appear on the curves for photoionization cross-section of Ar $3s$ and Ar $3p$ subshells and for angular anisotropy parameter of Ar $3p$-line, shown in Diagrams 5.34, 5.35, and 5.36.

Diagram given by (1.147) also shows double photoionization cross-section if s corresponds to the continuum excitation (shake-off satellite). The formula for corresponding part of double photoionization cross-section is written as:

$$\sigma'_{ijs}(\omega) = \iint \frac{\sigma_{ip}(\omega)\delta(\omega - \varepsilon_p + \varepsilon_i - \varepsilon_s + \varepsilon_j)\,|\langle si\,|U|\,ji\rangle|^2}{(\varepsilon_s - \varepsilon_j)^2} \mathrm{d}\varepsilon_p \mathrm{d}\varepsilon_s. \quad (1.149)$$

The same excited atomic state originates also due to the interaction of outgoing electron with ionic core (direct knock-out), considered in Sect. 1.17. Diagram for the amplitude of this process is as follows:

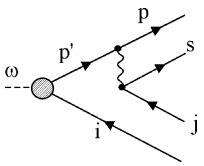

(1.150)

For a discrete state s, direct knock photoionization cross-section is written as:

$$\sigma''_{ijs} \sim \int \left| \int D_{ip'}(\omega) U_{sp',jp} \left[i\pi\delta\left(\omega - \varepsilon_{p'} + \varepsilon_i\right) + \frac{1}{\omega - \varepsilon_{p'} + \varepsilon_i} \right] \mathrm{d}\varepsilon_{p'} \right|^2 \mathrm{d}\varepsilon_s, \tag{1.151}$$

where $\varepsilon_p = \omega - \varepsilon_s + \varepsilon_i + \varepsilon_j$.

Note that in formulae (1.148) and (1.151) the possibility of interference of two channels of the excitation of the same final states was not taken into account explicitly.

The angular distributions of shake-up and direct knock satellites are essentially different. It follows from (1.147) that after photoionization the probability of the satellite excitation does not depend on the photoelectron angular momentum. Hence it follows that the amplitudes in channels $l \pm 1$ are proportional to the amplitudes of single photoionization of the shell under consideration and the angular anisotropy parameters for shake-off satellites are completely defined by supplementary β-curves. It also follows from these curves that the β-values for shake-off satellites will not differ significantly from that for the single ionization of the shell under consideration.

On the other hand, formula (1.151) contains matrix element with the outgoing electron wave function and the relation between photoelectron amplitudes in channels $l \pm 1$ will be completely different from that for the main line. Thus, the β-parameter for direct knock satellite will differ essentially from that for the main photoelectron line.

1.19 Two-Electron Photoionization and Recombination

Essential by magnitude and only correlation effects by nature are processes of two-electronic photoionization, i.e., removal of two electrons by a single photon, and two-electronic recombination—simultaneous capture by an ion—target of two electrons with emission of one photon. Both processes are possible only due to presence of the direct interelectronic interaction.

Let us start with two-electronic photoionization. The elementary diagrams, describing this process, look as follows [see also (1.35)]:

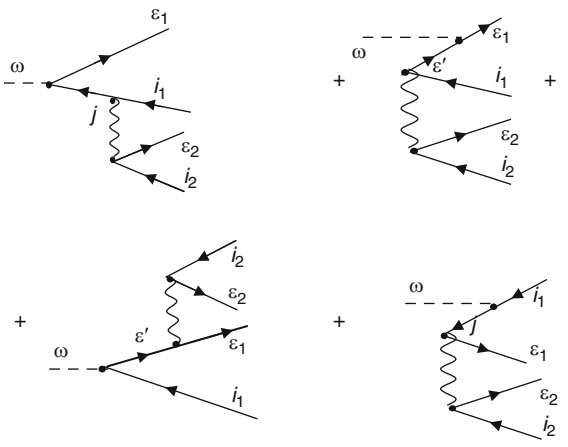

(1.152)

Amendments of higher orders include replacement of the operator $\hat{d}$ by $\hat{D}(\omega)$ in RPAE or GRPAE (see Sects. 1.5 and 1.6), the account of interaction between holes i_1 and i_2, that is to some extent achieved by replacement of the sum of ionization potentials $I_1 + I_2$ equal to by its exact value $I_{i_1 i_2}$. One has to take into account the interaction between electrons moving in a field of a hole. Now many papers are devoted to the problem of two-electron photoionization.

The mechanism of this process essentially simplifies at high photon energy, where almost all energy of a photon is absorbed by one electron, which quickly leaves the atom, suddenly changing the field acting upon the second electron. That leads to the so-called shake-off of the second electron that moves slowly. The process is characterized by the ratio $\sigma^{++}(\omega)/\sigma^{+}(\omega)$ of double-to-single photoionization cross-section that is ω-independent at high photon energies. This ratio for He is 1.65%, increasing for outer electrons in heavier atoms (see [1.48] and references therein).

The slow electron leaves the atom isotropic, while the fast is anisotropic. The direction of motion of both electrons is not connected. However, it has been shown [1.49] that with growth of ω another mechanism named *quasi-free knock-out* (QFK) becomes increasingly important. In the frame of this mechanism, a photon is absorbed by a pair of electrons, which share the incoming energy predominantly equally, moving in almost opposite directions. At relativistic energies $\omega \gg c^2$ this mechanism completely dominates [1.50]. Of interest is to follow how with increase of ω the energy distribution alters from a U-type curve to a curve with a powerful maximum in the middle, which then splits into two maximums [1.51]. Note that due to QFK mechanism the ratio $\sigma^{++}(\omega)/\sigma^{+}(\omega)$ starts to increase from its nonrelativistic value and reaches at $\omega \gg c^2$ another ω-independent value that is by a factor of six bigger than in the nonrelativistic region [1.50].

Now let us consider two-electronic recombination with emission of one photon. This process for the first time has been considered in [1.52, 1.53]. The elementary diagrams describing this process are the following:

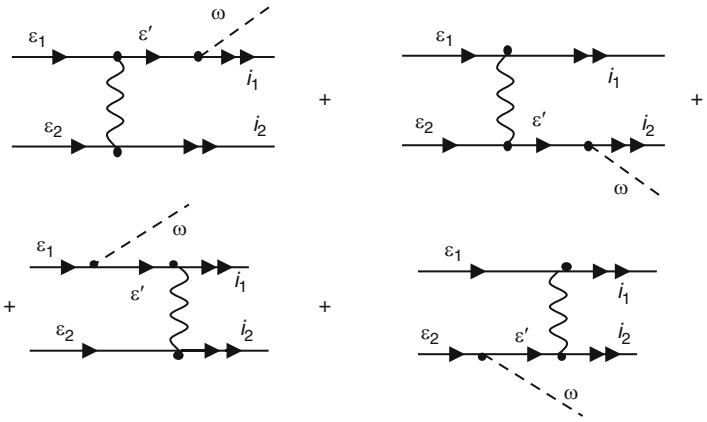

(1.153)

In this process, two electrons simultaneously pass from a continuous spectrum to vacant levels i_1 and i_2 in a field of a multiply charged ion. The transition energy is released as a single photon with the energy $\omega = \varepsilon_1 + \varepsilon_2 - \varepsilon_{i_1} - \varepsilon_{i_2}$. Emission of a single photon in recombination of two electrons is a process reversed in time to two-electronic photoionization. It is possible to calculate the cross-section of two-electronic recombination $\sigma_{\text{rec}}^{2e}(E)$ as function of incoming electron energy E, using the well-known principle *of detailed balance*. According to this principle, $\sigma_{\text{rec}}^{2e}(E)$ is proportional to a certain part of differential in energy and angle of the outgoing electrons double-electron photoionization cross-section:

$$\frac{d\sigma_{\text{rec}}^{2e}(E,\Omega_\gamma)}{d\Omega_\gamma} \sim \left[\frac{d^2\sigma^{++}(\omega_\gamma,\varepsilon_1,\Omega_1)}{d\varepsilon_1 d\Omega_1}\right]\Bigg|_{\substack{\varepsilon_1=\varepsilon_2=E \\ \Omega_1=\Omega_2\equiv\Omega}}, \tag{1.154}$$

where $\varepsilon_1 = \varepsilon_2 = E$ is the energy of photoelectrons, $\Omega_1 = \Omega_2 = \Omega$ and Ω_γ are the solid angles of emission of photoelectrons and the photon, respectively. So, to determine $\sigma_{\text{rec}}^{2e}(E)$ only that part of $\sigma^{++}(\omega_\gamma,\varepsilon_1,\Omega_1)$ is of interest that corresponds to big energy transfer from one electron to the other. For highly charged ions, it corresponds to big ω_γ. This part of $\sigma^{++}(\omega_\gamma,\varepsilon_1,\Omega_1)$ is determined by inter-electron correlations at short distances. However, as opposed to the mechanism QFK, this two-electronic ionization with its differential cross-section denoted $d^2\sigma^{++}(\omega_\gamma,E,\Omega)$ in (1.154) proceeds almost without an exchange of the linear moments between electrons since they move with equal speed in the same direction (experimental setup and results see in [1.54]). That is why interelectron interaction should be taken into account not only in the initial, but also in the final states.

1.20 Photoionization of the Excited Atoms

An elementary excited state of an atom is created when an atomic electron undertakes a transition to one of vacant excited levels located in general rather far from other electrons and the nucleus. However, despite of remoteness, the influence of the other electrons on the cross-section of ionization of the excited electron proved to be strong because of significant sensitivity of this cross-section to details of radial dependence of the self-coordinated field [1.55], and also because of effects of multielectron correlations [1.56, 1.57]. Such a state can be relatively long living, if the radiative decay of the excited state is forbidden due to angular momentum conservation.

The influence of correlations can be taken into account in the frameworks of RPAE or GRPAE, as was discussed earlier in connection to ionization of atoms in the ground state. Most simple from the photoionization cross-section calculations point of view are atoms with s-electrons excited to an s-state [1.56]. Influence of multielectronic correlations in RPAE proved to be very strong, leading to considerable displacement of position, number, and width of deep minima in the photoionization cross-section [1.57].

In Chap. 2, examples of a number of excited atoms photoionization cross-section are presented.

1.21 Electron Correlations in RPAE at High Photon Energy

It is known since the 1930s of last century that in one-electron approximation the photoionization cross-section is determined by a rather simple relation [1.58]

$$\sigma_{nl}(\omega) = \frac{c_{nl}}{\omega^{7/2+l}}. \tag{1.155}$$

This dependence follows from the definition of the one-electron photoionization amplitude (1.60) rightfully substituting the photoelectron's wave function $P_{\varepsilon l}(r)(\omega \approx \varepsilon = k^2/2)$ at high ω by a l component of the plane wave or the spherical Bessel function of the l–s order $j_l(kr)$ [LL]. Equation (1.155) was widely used to estimate the contribution of high photon energies into the sum rule (1.7) [1.59–1.61]. The contribution of this frequency region is important. Indeed, in He about 40% of the sum rule comes from $\omega \geq 8$ keV [1.62].

At first glance, the role of electron correlations has to decrease rapidly with the ω growth, since the interparticle interaction becomes smaller as compared to ω with the latter's growth. It appeared that this is not the case.

This was demonstrated by both direct numeric calculations [1.63] and analytically [1.64]. Let us show the main mechanism that is responsible for the contribution of correlations at high ω.

In this section, following [1.64], the strong influence will be demonstrated of s-electrons upon subshells with $l > 0$. It happens owing to two factors: first, in one-particle approach the $\sigma_{ns}^{(0)}(\omega)$ decreases with growth of ω more slowly than $\sigma_{nl}^{(0)}(\omega)$ for $l \neq 0$, second, the amplitude of intershell interaction, representing quasi-elastic scattering of s-vacancy with its transition into a closely located vacancy with $l \neq 0$, is almost independent upon ω at high ω.

Let us consider photoionization at high ω. We assume atomic electrons as nonrelativistic, since $\omega \ll c^2$ but $\omega \gg I$, I being the atomic ionization potential.

The diagram (1.36) represents the amplitude of photoionization in the lowest order d_{iv} and with corrections that we denote as $\Delta D_{iv}(\omega)$. Corrections of the first order in interelectron interaction $\Delta D_{iv}^{(2)}(\omega)$ along with d_{iv} are depicted in (1.156):

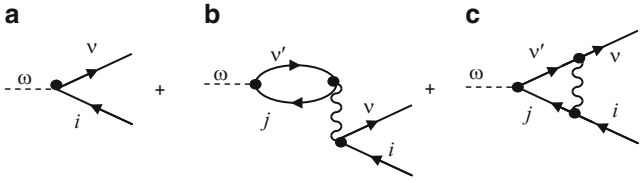

(1.156)

The shaded circles in (1.36) are substituted here by one-electron amplitude and only time-forward terms have to be taken into account [1.64].

Analytically, the matrix elements (1.156a) are given by the relation

$$d_{iv} \equiv \langle v|\vec{e}\vec{d}|i\rangle \tag{1.157}$$

For the diagram (1.156b) and (1.156c), an expression is valid

$$\Delta D_{iv}^{(2)}(\omega) = \sum_{j\leq F, v'>F} \frac{\langle v'|\vec{e}\vec{d}|i\rangle\left[\langle vj|\hat{V}|iv'\rangle - \langle vj|\hat{V}|v'i\rangle\right]}{\varepsilon_j - \varepsilon_{v'} + \omega + i\delta}\Bigg|_{\delta\to 0}, \tag{1.158}$$

where the first and second terms in square brackets correspond to diagrams (1.156b) and (1.156c), respectively.

In high ω limit, the wave functions of the outgoing electron and the virtually excited electrons can be taken as plane waves. This is correct even for slow electrons in the intermediate virtual state since the contribution of these states at high ω to the total sum is small because the respective energy denominator in (1.158) is big.

The amplitude of photoionization of electrons from the subshell $i \equiv nl, l \neq 0$ changes under the influence of the adjacent ns subshell. To show this, most transparent is to perform consideration in the velocity form, where $\hat{d} = \vec{e}\vec{\nabla}$ (1.2). Then for the one-partial amplitude of photoionization for $i_1 \equiv np(l = 1)$-electron$s$ [AM, 1.60] one has

$$d_{i_1,\varepsilon\vec{k}} = (\vec{e}\vec{k})\tilde{\varphi}_{np}(\vec{k}) = (\vec{e}\vec{k})\frac{4\pi Z}{k^4}\vec{k}\vec{\nabla}\varphi_{i_1}(\vec{r})\Big|_{\vec{r}=0}, \tag{1.159}$$

where $\vec{\hat{k}}$ is a unit vector in a direction of a electron linear momentum, Z is the charge of the atomic nucleus, $\varphi_{i_1}(\vec{r})$ is the one-partial wave function of the ionized electron in its initial state i_1, and $\tilde{\varphi}_i(\vec{k})$ is the Fourier image of $\varphi_{i_1}(\vec{r})$. In (1.158) it is taken into account that plane waves are normalized to a unit. Therefore, in the expression for the photoionization cross-section a density of final states appears that is proportional to $1/k$. As a result, the amplitude (1.158) leads to the following dependence of the photoionization cross-section upon ω: $\sigma_{nl}(\omega) \sim 1/\omega^{9/2}$.

It is easy to show that the contribution (1.156b) into $\Delta D^{(2)}_{if}(\omega)$ decreases with ω growth much faster than $d_{i_1,\varepsilon\vec{k}}$ given by (1.159). This is a direct consequence of that obvious fact, that it is difficult to transfer big energy via relatively weak Coulomb interelectron interaction.

The situation for (1.156c) is qualitative different since the matrix element $\langle \nu j|\hat{V}|\nu' i\rangle$ does not need big energy transfer at any ω. Retaining in expression for $\Delta D^{(2)}_{if}(\omega)$ only one term in the sum upon j ($j = n's$) and separating it into real and imaginary parts, we obtain

$$\Delta D^{(2)}_{i_1\to\varepsilon\vec{k}}(\omega) = \mathrm{Re}\Delta D^{(2)}_{i_1,\varepsilon\vec{k}}(\omega) + i\,\mathrm{Im}\Delta D^{(2)}_{i_1,\varepsilon\vec{k}}(\omega), \tag{1.160}$$

where

$$\mathrm{Re}\Delta D^{(2)}_{i_1,\varepsilon\vec{k}}(\omega) = \mathrm{P}\int (\vec{e}\vec{k})\frac{\tilde{\varphi}_{n's}(\vec{p})}{k^2 - k'^2}\frac{4\pi}{|\vec{k}-\vec{k}'|^2} \times \left\langle n's\left|\exp\left[i(\vec{k}-\vec{k}')\vec{r}\right]\right|i_1\right\rangle \frac{\mathrm{d}\vec{k}'}{(2\pi)^3}, \tag{1.161}$$

$$\mathrm{Im}\Delta D^{(2)}_{i_1,\varepsilon\vec{k}}(\omega) = \int (\vec{e}\vec{k})\tilde{\varphi}_{n's}(\vec{k})\frac{4\pi}{|\vec{k}-\vec{k}'|^2} \times \left\langle n's\left|\exp\left[i(\vec{k}-\vec{k}')\vec{r}\right]\right|i_1\right\rangle \delta(k^2 - \vec{k}'^2)\frac{\mathrm{d}\vec{k}'}{(2\pi)^3}, \tag{1.162}$$

here P denotes the principal value of integral.

To calculate the contributions of expressions (1.161) and (1.162), it is necessary to take into account the rapid decrease of Fourier images of one-electronic wave functions at least, as $1/p^4$, with increase of p. The main contribution to (1.161) and (1.162) comes from relatively small $\left|\vec{k}-\vec{k}'\right| \approx r_{n'}^{-1} \ll k$, where $r_{n'}$ is the mean radius of the n' subshell. Retaining the leading terms in $1/p$, one has

$$\mathrm{Re}\Delta D^{(2)}_{i_1,\varepsilon\vec{p}}(\omega) \sim (\vec{e}\vec{k})\left[\tilde{\varphi}_{n's}(\vec{k})\right]\frac{1}{k}\int_0^\infty \frac{\mathrm{d}q}{q}\langle n's||j_l(qr)||i_1\rangle, \tag{1.163}$$

here $\langle n's \,\|\, j_l\,(qr)\,\|\, i_1\rangle$ is the reduced matrix element of a spherical Bessel function $j_l\,(qr)$ and $q = |\vec{k}-\vec{k}'|$. In (1.143) integral over q does not depend upon k,

and hence $\tilde{\varphi}_{n's}(\vec{k})/k$ has the same order in $1/k$, as $\tilde{\varphi}_{i_1}(\vec{k})$. Therefore, the term Re $\Delta D^{(2)}_{i_1,\varepsilon\vec{k}}(\omega)$ is of the same order in $1/k$ as the amplitude $d_{i_1\to\varepsilon\vec{k}}$ in (1.159), thus leading to correction that exists at high ω also.

Note that the contribution $\mathrm{Im}\Delta D^{(2)}_{i_1,\varepsilon\vec{k}}(\omega)$ is by a factor $1/k$ less than $\mathrm{Re}\Delta D^{(2)}_{i_1,\varepsilon\vec{k}}(\omega)$. Indeed, using the same expansion in $1/k$ as for estimation of $\mathrm{Re}\Delta D^{(2)}_{i_1,\varepsilon\vec{k}}(\omega)$ in (1.163), we receive

$$\mathrm{Im}\Delta D^{(2)}_{i_1,\varepsilon\vec{k}}(\omega) \sim (\vec{e}\vec{k})\left[\tilde{\varphi}_{n's}(\vec{k})\right]\frac{1}{k^2}\int_0^\infty \mathrm{d}q\langle n's||j_l\,(qr)||i_1\rangle. \tag{1.164}$$

Comparison of (1.163) and (1.164) confirms that for $i_1 \equiv np$-electrons the main correction to the one-electron amplitude at high ω is Re $\Delta D^{(2)}_{i_1,\varepsilon\vec{k}}(\omega)$.

It is known that for photoionization of $i = nl$ electrons with $l > 1$ the one-electron amplitude at high ω behaves [1.65, 1.66] as:

$$d_{nl\to\varepsilon\vec{p}} = \left(\vec{e}\vec{k}\right)\frac{1}{k^{3+l}}. \tag{1.165}$$

At any l one has for $\Delta D^{(2)}_{if}(\omega)$ instead of (1.165) [1.64]

$$\Delta D^{(2)}_{if}(\omega) \approx i^{(l-1)}\left(\vec{e}\vec{k}\right)\left[\tilde{\varphi}_{n's}\left(\vec{k}\right)\right]\frac{1}{k}\int_0^\infty \frac{\mathrm{d}q}{q}\langle n's||j_l(qr)||nl\rangle. \tag{1.166}$$

According to (1.166), for subshells nl with $l \geq 2$ the term $\Delta D^{(2)}_{if}(\omega)$ starts to dominate over the one-electron term $d_{nl,\varepsilon\vec{k}}$ at big enough ω. Therefore, at high ω one has instead of (1.155) the cross-section simply proportional to $|\Delta D^{(2)}_{if}(\omega)|^2$. It means that instead of (1.155) for all *l it is*:

$$\sigma_{nl}(\omega) = \frac{C}{\omega^{9/2}} = \frac{1}{\omega}\sum_{n'<F} f_{n's,nl}\sigma_{ns}(\omega), \tag{1.167}$$

where the relation

$$f_{n's,nl} = \frac{1}{2}\left|\int_0^\infty \frac{\mathrm{d}q}{q}\langle n's||j_l(qr)||nl\rangle\right|^2, \tag{1.168}$$

determines the effect of interaction between $n's$ and nl levels.

It is interesting to find out the relative contribution of various intermediate $n's$ states. According to (1.168), the greatest contribution comes from subshells $n's$ mostly overlapping with nl, i.e., from state ns.

The matrix element $\langle n's||j_l(qr)||nl\rangle$ is proportional to the amplitude of the Generalized Oscillator strength of $n's \to nl$ transition, discussed at length in

Sect. 3.6. To take into account the effect of multielectron correlations in this matrix element, one has to substitute $j_l(qr)$ by $G_R^l(q,\omega)$ given by (3.66).

1.22 Electron Correlations at High Photon Energy Out of RPAE Frame

In this section, we consider photoionization of atoms that results in creation of complex states c due to interaction with one-electron s-state s. The cross-section of such a process $\sigma_c(\omega)$ decreases with ω growth having the lowest possible rate, namely $\sigma\,(\omega) \sim 1/\omega^{7/2}$ at high ω.

To show the physical reason of this result, assume [1.67, 1.68], that in an atom after photon absorption two states can appear—with wave function $\varphi_s(\vec{r})$ (a state with one vacancy), and complex c state with wave function $\varphi_c(\vec{r})$. The last state, in addition to a single vacancy, includes at least one extra electron–vacancy pair. The interaction between states s and c is determined by the matrix element V_{sc}. Assume for simplicity that while the unperturbed by V_{sc} cross-section of photoionization of an s-state $\sigma_s^{(0)}\,(\omega)$ is nonzero, direct photoionization of c-state c is impossible so that $\sigma_c^{(0)}\,(\omega) = 0$. Due to V_{sc} the states c and s are mixed thus forming new states with wave functions

$$\begin{aligned}\psi_s(r) &= F_s^{1/2}\varphi_s(r) + (1-F_s)^{1/2}\,\varphi_c(r),\\ \psi_c(r) &= -\,(1-F_s)^{1/2}\,\varphi_s(r) + F_s^{1/2}\varphi_c(r).\end{aligned} \tag{1.169}$$

here F_s characterizes the admixture of c to s and refers to as *the spectroscopic factor*. If V_{sc} is small as compared to the states s and c energy difference $|\varepsilon_s - \varepsilon_c|$, then

$$F_s \approx 1 - \frac{V_{sc}^2}{2(\varepsilon_c - \varepsilon_s)^2}. \tag{1.170}$$

From (1.169) it is seen that at high ω the cross-section $\sigma_c(\omega)$ is nonzero and the following relations are valid:

$$\sigma_s(\omega) = F_s\sigma_s^{(0)}\,(\omega)\,,\sigma_c\,(\omega) = (1-F_s)\,\sigma_s^{(0)}\,(\omega)\,. \tag{1.171}$$

That leads to ω-independence of the ratio

$$\frac{\sigma_c(\omega)}{\sigma_s(\omega)} = \frac{(1-F_s)}{F_s}. \tag{1.172}$$

The first example of a complex state or level is *two vacancies—one excited electron* $3p^{-2}3d$ combination in Ar that is connected via Coulomb interaction to $3s^{-1}$.

The corrections discussed in this section are out of the RPAE frame. The relation (1.171) predicts that the observable cross-section is smaller than the RPAE by the factor $F_{3s^{-1}}$ [1.68]. This behavior was confirmed by the results of numeric RPAE calculations of $\sigma^{(0)}_{3s^{-1}}(\omega)$ in Ar [1.69] and its comparison with experiment. Calculation value $F_{3s} \approx 0.79$ [1.68] gives reasonably good agreement with experiment.

Due to the described above mixing in, e.g., Ar, the ratio of cross-section $\sigma_{3p^{-2}3d}(\omega)$ of creating the ion's final state $3p^{-2}3d$ to the cross-sections $\sigma_{3p^{-1}}(\omega)$ of creating a final state with 3p-vacancy increases with ω growth:

$$\frac{\sigma_{3p^{-2}3d}(\omega)}{\sigma_{3p^{-1}}(\omega)} \sim \frac{\omega \left|\langle 3p3p \left|V\right| 3d3s\rangle\right|^2}{\left|\varepsilon_{3s^{-1}} - \varepsilon_{3p^{-2}3d}\right|^2}. \tag{1.173}$$

Note that increase of ω is able to compensate the smallness of the mixing factor.

For nd^{-2} states, one has $\sigma_{nd^{-2}n's}(\omega)/\sigma_{nd^{-1}}(\omega) \sim \omega^2 \left|\langle ndnd \left|V\right| n'sn''s\rangle\right|^2 / \left|\varepsilon_{n''s^{-1}} - \varepsilon_{nd^{-2}n's}\right|^2$, i.e., an extra power in ω as compared to (1.173). Note that creation of two-vacancy states is at the same time two-electron photoionization (see, e.g., [1.70, 1.71] and references therein)

Concluding this chapter, we consider it useful to present several references to relatively recent review-type papers that describe current status and develop presented methods employed in our calculations and data for a number of atoms, including endohedrals [1.72–1.83]. For convenience, these references go with their titles.

References

1.1. Fano U (1961) Effects of configuration interaction co intensities and phase shifts. Phys Rev 124:1866–1878
1.2. Kabachnik NM, Sazhina TJ (1976) Angular distribution and polarization of photoelectrons in the region of resonances. J Phys B 9:1681–1698
1.3. Ron A, Goldberg IB, Stein J, Manson ST, Pratt RH, Yin RY (1994) Relativistic, retardation, and multipole effects in photoionization cross sections: Z, n, and l dependence. Phys Rev A 50(2):1312–1320
1.4. Amusia MYa, Arifov PU, Baltenkov AS, Grinberg AA, Shapiro SG (1974) Calculation of current induced by photon momentum in gaseous Ar. Phys Lett A 47:66
1.5. Amusia MYa, Baltenkov AS, Chernysheva LV, Felfli Z, Msezane AZ (2001) Non-dipole parameters in angular distributions of electrons in photoionization of noble gas atoms. Phys Rev A 63:052506
1.6. Cooper JW (1990) Multipole corrections to the angular distribution of photoelectrons at low energies. Phys Rev A 42:6942–6945
1.7. Cooper JW (1992) Erratum: multipole corrections to the angular distribution of photoelectrons at low energies. Phys Rev A 45:3362
1.8. Cooper JW (1993) Photoelectron-angular-distribution parameters for rare-gas subshells. Phys Rev A 47:1841–1851

1.9. Bechler A, Pratt RH (1990) Higher multipole and retardation corrections to the dipole angular distributions of L-shell photoelectrons ejected by polarized photons. Phys Rev A 42:6400–6413
1.10. Amusia MYa, Baltenkov AS, Felfli Z, Msezane AZ (1999) Large non-dipole correlation effects near atomic photoionization thresholds. Phys Rev A 59(4): R1–R4
1.11. Cherepkov NA (1973) Angular distribution of photoelectrons with a given spin orientation. Sov JETP 65:933–946
1.12. Cherepkov NA (1972) Angular distribution and spin orientation of photoelectrons ejected by circularly polarized light. Phys Lett A 40:119–121
1.13. Cherepkov NA (1981) Angular distribution of molecular photoelectrons with defined spin orientation. J Phys B At Mol Opt Phys 14:L73–L78
1.14. Amusia MYa, Cherepkov NA, Chernysheva LV, Felfli Z, Msezane AZ (2004) Spin polarization of photoelectrons from 3d-electrons of Xe, Cs, and Ba. Phys Rev A 70:062709
1.15. Woodgate GK (1970) Elementary atomic structure. McGraw-Hill, New York
1.16. Cherepkov NA, Chernysheva LV (1977) Random phase approximation with exchange for open-shell atom. Phys Lett A 60(2):103–105
1.17. Amusia MYa, Cherepkov NA, Chernysheva LV, Manson ST (2000) Photoionization of atomic iodine and its ions. Phys Rev A 61:020701
1.18. Chernysheva LV (1977) Software package for atomic calculations. Izv USSR Acad Sci Ser. 41(12):2518–2528 (in Russian)
1.19. Amusia MYa, Cherepkov NA, Chernysheva LV, Manson ST (2000) Multielectron correlation effects in Xe^{++} formation resulting from the photoionization of Xe^{+} ions. J Phys B At Mol Opt Phys 33(1): L37–L42
1.20. Amusia MYa, Chernysheva LV, Ivanov VK, Manson ST (2002) Photoionization of 4d electrons in I^{+} and I^{++}. Phys. Rev. A 65(3):032714
1.21. Vesnicheva GA, Malyshev GM, Orlov VF, Cherepkov NA (1986) Sov Phys-Tech Phys 31:402
1.22. Mead RD., Lykke KR, Lineberger WC (1984) Photodetachment threshold laws. In: Eichler J, Hertel IV, Stolterfoht N (eds) Proceedings of the XIII ICPEAC on electronic and atomic collisions. Elsevier, Amsterdam, pp 721–730
1.23. Amusia MYa, Gribakin GF, Ivanov VK, Chernysheva LV (1986) Photodetachment of negative iodine ion. Izv USSR Acad Sci Ser Phys 50(7):1274–1278 (in Russian)
1.24. Gribakin GF, Gultsev BV, Ivanov VK, Kuchiev MYu (1990) Izv Vuzov USSR Phys 33:86–96 (in Russian)
1.25. Ivanov VK (1999) Many-body effects in negative ion photodetachment. J Phys B At Mol Opt Phys 32(12):R67–R101
1.26. Kroto HW, Heath JR, O'Brien SC, Curl RF, Smalley RE (1985) C_{60}: Buckminsterfullerene. Nature 318:162-163
1.27. Bertsch GF., Bulgac A, Tománek D, Wang Y (1991) Collective plasmon excitations in C_{60} clusters. Phys Rev Lett 67:2690–2693
1.28. Hertel IV, Steger H, de Vries J et al (1992) Giant plasmon excitation in free C_{60} and C_{70} molecules studied by photoionization. Phys Rev Lett 68:784–787
1.29. Amusia MYa, Baltenkov AS, Krakov BG (1998) Photodetachment of negative fullerenes ions. Phys Lett A 243:99–105
1.30. Baltenkov AS (1999) Resonances in the photoionization cross section of M@C_{60} endohedrals. Phys Lett A 254:203–209
1.31. Amusia MYa, Baltenkov AS (2006) Effect of plasma oscillations of C_{60} collectivized electrons on photoionization of endohedral noble-gas atoms. Phys Rev A 73:062723
1.32. Amusia MYa, Baltenkov AS (2006) Vacancy decay in endohedral atoms. Phys Rev A 73:063206
1.33. Amusia MYa, Baltenkov AS, Dolmatov VK, Manson ST, Msezane AZ (2004) Confinement resonances in photoelectron angular distributions from endohedral atoms. Phys Rev A 70:023201

1.34. Amusia MYa, Baltenkov AS, Chernysheva LV, Felfli Z, Msezane A (2006) Modification of the Xe 4d giant resonance by the C_{60} shell in molecular Xe@C_{60}. J Exper Theor Phys 206(1):53–60 (in Russian, JETP 102(1):56–60)
1.35. Amusia MYa, Baltenkov AS, Chernysheva LV (2008) Giant resonances of endohedral atoms. JETP Lett 89(6):275–279
1.36. Forró L, Mihály L (2001) Electronic properties of doped fullerenes. Rep Prog Phys 64(5):649
1.37. Amusia MYa, Chernysheva LV, Liverts EZ (2009) Photoionization of atoms stuffed inside a two-shell fullerene. Phys Rev A 80:032503-1–032503-12
1.38. Cabrera-Trujillo JM, Alonso JA, Iñiguez MP, López MJ, Rubio A (1996) Theoretical study of the binding of Na clusters encapsulated in the C_{240} fullerene. Phys Rev B 53:16059–16066
1.39. Amusia MYa, Baltenkov AS, Chernysheva LV, Felfli Z, Msezane AZ, Nordgren J (2001) Directed motion of electrons in gases under the action of photon flux. Phys Rev A 63:052512
1.40. Amusia MYa., Baltenkov AS, Grinberg AA, Shapiro SG (1975) Investigation of the current due to photon momentum in monoatomic gases. Zhur Exp Theor Phys 68:28–32 (in Russian, JETP, 41, 14)
1.41. Amusia MYa., Dolmatov VK (1980) Electron entrainment by resonance frequency light. Zhur Exp Theor Phys 79:1664–1670 (in Russian)
1.42. Amusia MYa., Gribakin GF, Tsemekhman KL (1989) Single and double photoionization of Xe atom above the 4d-subshell threshold. Izv USSR Acad Sci Phys Ser 53(9):1672–1676 (in Russian)
1.43. Amusia MYa, Gribakin GF, Tsemekhman KL, Tsemekhman VL (1990) Single and double photoionization in Xe and Ba above the 4d-threshold. J Phys B At Mol Opt Phys 23(3):393–402
1.44. Svensson S, Eriksson B, Martensson N, Wendin G, Gelius U (1988) Electron shake-up and correlation satellites and continuum shake-off distribution in X-ray photoelectron spectra of the rare gas atoms. J Electron Spectr Relat Phenom 47:327–384
1.45. Amusia MY, Kuchiev MYu, Sheinerman SA, Sheftel SI (1977) Intershell correlations in the formation of single charged ions near the Ar L-shell ionization threshold. J Phys B 10: L535–L539
1.46. Kuchiev MYu, Sheinerman SA (1989) Post-collision interaction in atomic processes. Sov Phys Usp 32:569–587
1.47. Kikas A, Osborne SJ, Ausmees A, Svensson S, Sairanen OP, Askela SJ (1996) High resolution study of the correlation satellites in photoelectron spectra of rare gases. J Electron Spectr Relat Phenom 77(3):241–266
1.48. Amusia MYa, Krivec R, Mandelzweig VB (2004) Two-electron photoionization of He and helium-like ions. In: Glöckle W, Tornow W (eds) Few body 17. Elsevier, Amsterdam, pp S301–S304
1.49. Amusia MY, Gorshkov VG, Drukarev EG, Kazachkov MP (1975) Two-electron photoionization of helium. J Phys B 8:1248–1266
1.50. Amusia MY, Drukarev EG, Krivec R, Mandelzweig VB (2003) Ultra-relativistic limit for the two-electron photoionization cross section. Phys Rev A 66(5) 052706-1–5
1.51. Amusia MY, Drukarev EG, Krivec R, Mandelzweig VB (2003) Shape variation of the two-electron photoionization spectrum with the photon energy growth (with E. Liverts, E.G. Drukarev, R. Krivec and V.B. Mandelzweig). Phys Rev A 71:012715 (2005)
1.52. Yakhontov VL, Amusia MYa (1996) Radiative double electron capture in fast heavy ion-atom collisions. Phys Lett A 221:328–334
1.53. Yakhontov VL, Amusia MYa (1997) Radiative double electron capture in collisions of fast heavy ions with solid carbon targets. Phys Rev A 55(3):1952–1961
1.54. Simon A, Warczak A, Elkafrawy T, Tanis JA (2010) Radiative double electron capture in collisions of O^{8+} ions with carbon. Phys Rev Lett 104(12):123001–123004
1.55. Amusia MYa, Lee IS, Sheftel SI (1977) Photoionization of excited states in Ar and Xe Atoms. Izv USSR Acad Sci Ser Fiz 41(12):2529–2537

1.56. Amusia MYa, Avdonina NB (1983) Characteristic features in photoionization of excited atomic states. J Phys B At Mol Phys 16(18):L543–545
1.57. Amusia MYa, Avdonina NB (1990) The role of intershell correlations in photoionization of excited ions and atoms. Sov Phys J Tech Fiz (USSR Acad Sci) 60(3):66–72
1.58. Bethe HA, Salpeter EE (1958) Quantum mechanics of one-and two-electron atoms. Springer, Berlin
1.59. Mehlhorn W, Starace AF (eds) (1982) Handbuch der Physik, vol 31. Springer, Berlin, p 46
1.60. Drake GWF, Starace AF (eds) (1996) Atomic, molecular, and optical physics handbook. AIP Press, Woodbury, NY, pp 305–320
1.61. Crasemann B, Cooper JW (eds) (1975) Atomic inner-shell processes, vol 1. Academic, NY, pp 170–181
1.62. Yan M, Sadedhpour HR, Dalgarno A (1998) Photoionization cross sections of He and H2. Astrophys J 496(2):1044–1050
1.63. Dias EWB, Chakraborty HS, Deshmukh PC, Manson ST, Hemmers O, Glans P, Hansen DL, Wang H, Whitfield SB, Lindle DW, Wehlitz R, Levin JC, Sellin IA, Perera RCC (1997) Breakdown of the independent particle approximation in high-energy photoionization. Phys Rev Lett 78:4553–4556
1.64. Amusia MYa, Avdonina NB, Drukarev EG, Manson ST, Pratt RH (2000) Modification of the high energy behavior of the atomic photoionization cross section. Phys Rev Lett 85(22):4703–4706
1.65. Jabbur RJ, Pratt RH (1964) High-frequency region of the spectrum of electron and positron Bremsstrahlung. II. Phys Rev 133: B1090–B1101
1.66. Rau ARP, Fano U (1967) Transition matrix elements for large momentum or energy transfer. Phys Rev 162:68–70
1.67. Amusia MYa (1981) Collective effects in an isolated atom. Izv USSR Acad Sci Ser Phys 45(12):2242–2254
1.68. Amusia MYa (1984) Interaction of complex atoms with radiation. Izv USSR Acad Sci Ser Phys 48(4):642–650
1.69. Hansen DL, Hemmers O, Wang H et al (1999) Validity of the independent-particle approximation in x-ray photoemission: The exception, not the rule. Phys Rev A 60: R2641–R2652
1.70. Amusia MYa, Gorshkov VG, Drukarev EG, Kazachkov MP (1975) Two-electron photoionization of helium. J Phys B 8:1248–1266
1.71. Amusia MYa, Drukarev EG, Krivec R, Mandelzweig VB (2003) Ultra-relativistic limit for the two-electron photoionization cross section. Phys Rev A 66:052706
1.72. Amusia MYa (1996) Theory of photoionization: VUV and soft X-ray frequency region. In: Becker U, Shirley D (eds) Photoionization in VUV and Soft X-Ray Energy Region. Plenum Press, NY, pp 1–46
1.73. Amusia MYa, Connerade J-P (2000) Collective motion probed by light. Rep Prog Phys 63:41–70
1.74. Amusia MYa (2004) Random phase approximation: from giant to intra-doublet resonances. Radiat Phys Chem 70:237–251
1.75. Amusia MYa, Baltenkov AS, Chernysheva LV, Felfli Z, Msezane AZ (2005) Near-threshold behavior of angular anisotropy parameters in negative ions photo-detachment. Phys Rev A 72:032727
1.76. Amusia MYa, Chernysheva LV (2006) Non-dipole angular anisotropy parameters of photoelectrons from semi-filled shell atoms. J Phys B At Mol Opt Phys 39:4627–4636
1.77. Amusia MYa (2007) Fast Electron scattering as a tool to study target's structure, review. J Electron Spectrosc Relat Phenom 159:81–90
1.78. Amusia MYa (2007) Photoionization and vacancy decay of endohedral atoms, review. J Electron Spectrosc Relat Phenom 161:112–120
1.79. Amusia MYa, Baltenkov AS, Chernysheva LV (2008) Photoionization of 3d electrons of Xe, Cs and Ba endohedral atoms: comparative analyses. Cent Eur J Phys 6(1):14–25

1.80. Amusia MYa, Chernysheva LV (2008) On the angular distribution and spin polarization of the photoelectrons from semi-filled shell atoms. http://arxiv.org/abs/physics/0701040
1.81. Amusia MYa, Baltenkov AS, Chernysheva LV (2008) On the photoionization of the outer electrons in noble gas endohedral atoms. JETP (Zhur Exp Theor Fyz) 134 2(8):221–230
1.82. Amusia MYa, Baltenkov AS, Chernysheva LV (2008) Photoionization of subvalent electrons in noble gas endohedrals: interference of three resonances. J Phys B At Mol Opt Phys 41:165201
1.83. Dolmatov VK (2009) Photoionization of atoms encaged in spherical fullerenes. In: Sabin JR, Brändas EJ (eds) Theory of confined quantum systems, Part 2. Advances in quantum chemistry, vol 58. Academic, USA, pp 13–68

Chapter 2
Results of Calculations

2.1 Data Representation and Used Formulas

In this chapter, we provide figures and tables that represent data collected in the study of total and partial photoionization cross-sections, relative cross-sections, dipole and non-dipole parameters of angular anisotropy and spin polarization of photoelectrons, as well as the oscillator strengths of discrete excitations. In some cases, experimental data are presented.

The numbering of figures is organized as follows. First goes the Chapter number, then the name of the element in the periodic table; then goes the sequential number of this figure in this Chapter, followed by letters denoting the atom in the periodic table. The final number marks the considered figure among all other that illustrate the considered characteristic or property of this atom. (e.g., Fig. 2.22_Ar_a1, denotes atom Ar 2.22 figure in Chapter 2). The next after element's name smaller letter indicates the corresponding values or characteristics:

(a) Denotes total photoionization cross-sections or quasi-photoionization cross-sections for excitations to discrete levels of atoms and ions in ground or excited states in HF approximation or RPAE and its modifications.
(b) Denotes ratio of partial photoionization cross-sections.
(c) Denotes dipole angular anisotropy parameters $\beta_{nl}(\omega)$.
(d) Denotes non-dipole angular anisotropy parameters $\gamma_{nl}(\omega)$ and $\eta_{nl}(\omega)$.
(e) Denotes spin-polarization parameters $A^j_{nl}(\omega)$, $\zeta^j_{nl}(\omega)$ and $\xi^j_{nl}(\omega)$ of photoelectron.
(f) Corresponds to other characteristics.

The last symbol is the number of the figure in the considered group.

However, not all data mentioned above are available for each atom or ion. In such cases, not every letter or number will be used in the presented figures.

To describe various characteristics of photon absorption by atoms, the following formulas of Chap. 1 were used:

M. Amusia et al., *Handbook of Theoretical Atomic Physics*,
DOI 10.1007/978-3-642-24752-1_2, © Springer-Verlag Berlin Heidelberg 2012

– Total cross-sections in HF and RPAE are obtained, using (1.70).
– Partial cross-sections in HF and RPAE are given by (1.68) and (1.69), respectively.
– Dipole angular anisotropy parameters in HF and RPAE are obtained using (1.71) and (1.74), respectively.
– Non-dipole angular anisotropy parameters $\gamma_{nl}(\omega)$ and $\eta_{nl}(\omega)$ in HF approximation are found using formulas (1.78), (1.79), (1.82), and in RPAE approximation replacement (1.83) is employed.
– Spin-polarization parameters of photoelectrons were obtained, using (1.89).
– Atomic dipole polarizabilities are calculated with the help of the formula (1.86).

Alongside with HF and RPAE, for intermediate and inner shells generalized approximation HF and RPAE or GHF, GRPAE and very seldom GRPAEII (see Sect. 1.6) are applied.

Calculations for atoms with half-filled shells are performed, using relations (1.95)–(1.99), within the framework of spin-polarized HF (SP HF) and RPAE (SP RPAE). Photoionization cross-sections for atoms with open shells in HF are obtained from (1.69) with amplitudes, given by formulas (1.102) and (1.103). The RPAE results for open shells (RPAEO) are derived using the approach described in Sect. 1.11.

Calculations of photoionization cross-sections of endohedral atoms were carried out, using (1.120), while angular anisotropy parameters are obtained using (1.110) for dipole and (1.123), (1.124)—for non-dipole. The approach employed in calculating the onion-type endohedral is described in Sect. 1.15.

"Drag" currents were calculated using (1.142). Photoionization cross-sections with account for inelastic scattering of the photoelectron escaping from ionizing atom were obtained using formula (1.144).

To achieve uniformity in the representation of discrete lines of photoexcitation and photoionization cross-sections, we have broaden discrete lines, using constant width of a line Δ. As a result, instead of oscillator strength f_{if} from (1.6), the quasi cross-section of excitation to discrete levels is represented by the following expression:

$$\sigma(\omega) = \frac{2\pi f_{if}\,\Delta}{c}\,\frac{1}{(\omega-\omega_{if})^2+(\Delta/2)^2}. \tag{2.1}$$

The parameter Δ is chosen, for definiteness, to be equal to 0.1 eV. The formula (2.1) is similar to that for the cross-section of excitation to isolated autoionization resonance, which follows from (1.50) at $\rho = 1$ and at very big value of parameter q. The meaning of $\Delta/2$ is the effective width of the discrete line Γ that is usually called the level's half width on its half-height (1.49).

Let us remind that our aim is to obtain not the best possible theoretical description of the experimental data for any special atom or ion but to present the results of mass calculations in the most suitable approach for such purpose—RPAE and its various generalizations. We intend to demonstrate, simultaneously, by comparison with the results in HF, the importance of inter-electron correlations. Actually, our purpose is creation of a new initial approximation that would stimulate the subsequent carrying

out of more exact measurement and more sophisticated calculations required for their interpretation.

Results are given in length and velocity forms [see (1.13)], marked as HF-l, HF-v, RPAE-l, RPAE-v, respectively. The results obtained earlier in the frames of used here theoretical approaches and published previously were recalculated for this book. That is why the reference to these results is given not simply by a number in the reference list, e.g., such as [1.3], but as (see [1.3]).

In the tables we will present the results for calculated value of the oscillator strength given in general by (1.6).

For close shell atoms their respective "length" and "velocity" HF-l, -v values are denoted as $f^{l,v}_{nl-n'l'}$ and RPAE-l, -v values are denoted as $F^{l,v}_{nl-n'l'}$. They are presented by the following formulas:

$$f^{l,v}_{nl-n'l'} = 2\omega_{nl-n'l'}|d^{l,v}_{nl-n'l'}|^2, \tag{2.2}$$

where nl is the initial and $n'l'$ is the final one-electron states, $\omega_{nl-n'l'} = \varepsilon_{nl} - \varepsilon_{n'l'}$ [see (1.54)], $d^{l,v}_{nl-n'l'}$ are determined by (1.59) and (1.60). In RPAE one has

$$F^{l,v}_{nl-n'l'} = 2\tilde{\omega}_{nl-n'l'}|D^{l,v}_{nl-n'l'}(\tilde{\omega}_{nl-n'l'})|^2, \tag{2.3}$$

where $\tilde{\omega}_{nl-n'l'}$ is the RPAE transition energy [see definition below (1.51)] and $D^{l,v}_{nl-n'l'}(\tilde{\omega}_{nl-n'l'})$ is determined using (1.37).

For semi-closed shell atoms, the applied approach is described in Sect. 1.10. The HF-l, -v values are denoted as $f^{l,v}_{nl-n'l'\uparrow(\downarrow)}$ and RPAE-l, -v and values are denoted as $F^{l,v}_{nl-n'l'\uparrow(\downarrow)}$. They are described by the following formulas:

$$f^{l,v}_{nl-n'l'\uparrow(\downarrow)} = 2\omega_{nl-n'l'\uparrow(\downarrow)}|d^{l,v}_{nl-n'l'\uparrow(\downarrow)}|^2, \tag{2.4}$$

where nl is the initial and $n'l'$ is the final one-electron states, $\omega_{nl-n'l'} = \varepsilon_{nl} - \varepsilon_{n'l'}$ [see (1.90)], $d^{l,v}_{nl-n'l'}$ are determined by (1.91). In RPAE, one has

$$F^{l,v}_{nl-n'l'\uparrow(\downarrow)} = 2\tilde{\omega}_{nl-n'l'\uparrow(\downarrow)}|D^{l,v}_{nl-n'l'\uparrow(\downarrow)}(\tilde{\omega}_{nl-n'l'\uparrow(\downarrow)})|^2, \tag{2.5}$$

where $\tilde{\omega}_{nl-n'l'\uparrow(\downarrow)}$ is the RPAE transition energy [see definition below (1.51)] and $D^{l,v}_{nl-n'l'\uparrow(\downarrow)}(\tilde{\omega}_{nl-n'l'\uparrow(\downarrow)})$ is determined using (1.93).

For convenience of the reader and regularity, we have presented the data for atoms and ions according to the element's position in the periodic table, with the only exception, that we start with atoms and some ions of noble gases.

Let us comment some used approaches and specific considered objects. We shall start the comments with half-filled shell atoms—Cr, Mn, and Eu. All of them are characterized by the presence of a relatively broad and intense resonance, which is a result of discrete transition from occupied half-filled level to a vacant half-filled level in continuous spectrum of ionization electron. Corresponding matrix element is very

large, so the width of this *Giant autoionizing resonance* is rather big. This resonance defines photoionization cross-sections also in all other subshells [2.1, 2.2][1] as well as the angular distributions and spin polarization of photoelectrons.

The method developed for consideration of atoms with half-filled shells has been also applied in calculations *of* $3d$-subshells of Xe, Cs, and Ba atoms [2.3]. Namely, it was suggested to treat $3d_{5/2}$ and $3d_{3/2}$ levels as "spin-up" and "spin-down" components of the $3d$-subshells. Then the interaction between "spin-up" and "spin-down" electrons can be taken into account easily, using the equations from Sect. 1.10. While calculating photoionization cross-section in these cases, it is necessary to add corrections to RPAE equations, since the numbers of electrons on levels 5/2 and 3/2 are not equal numbers of "spin-up" and "spin-down" electrons (namely, 5), but are 6 and 4, respectively. Therefore "spin-up" and "spin-down" components χ in (1.93) get multipliers 6/5 and 4/5, respectively.

Alkali atoms, for example, Li, Na, K, and Cs, form a special group of atoms with half-filled shells. They can be considered equally as atoms with open or half-filled shells. Since the influence of external valence electron on internal electrons is small, the choice of a particular method of consideration of the outer electron is not very important.

Let us notice that for negative ions the *Threshold Wigner law* (1.104) is often valid, as appeared from experimental data and calculations, in such a narrow photoelectron energy range that for not too detailed scale the figures look as if the cross-section would have a jump at the threshold.

We compare results for groups of atoms and ions of the same element with different ionicity, for example, K, K^-, K^+ (Fig. 2.108_KK$^-$K$^+$_a3), I, I^-, I^+ (Fig. 2.336_I$^-$I$^+$I_a3), to illustrate the role of interelectronic interaction. It is also of interest to compare negative ions with there isoelectronic (i.e. having the same electronic structure) neutral and positively charged neighbors, which form such set as Cs^+, Xe, I^-—Fig. 2.337_I$^-$XeCs$^+$_a4.

It should be noted that in ionization of one-electron ion, correlations could become stronger than in the next neutral atoms. However, with the further growth of the charge of an ion, the relative role of correlations becomes smaller. Indeed, larger part of total oscillator strength of the given subshell "moves" to its discrete excitation, while the cross-section of photo-absorption becomes smaller. It is visible already in cross-section of Ca^{2+} ion (see Fig. 2.156_Ca^{2+}_a1) and is even more pronounced in I^{2+} (Fig. 2.330_I^{2+}_a1) or Xe^{3+} Fig. 2.79_Xe^{3+}_a1, where the most part of huge 4d resonances is completely "eaten up" by discrete excitations $4d \rightarrow nf, np$.

We calculate photoionization of some excited states of atoms that can be considered within the framework of above-mentioned approximations, namely HF, RPAE, GRPAE, and SP RPAE. It is possible to calculate, for example, photoionization cross-section, as well as oscillator strength for highly excited *spin-saturated states* (SSS) in which all atomic electrons or at least those, which belong to an external

[1] In other chapters these and subsequent references are given with the number of chapter: so, reference [1, 2] of Chapter 2 is presented as [2.1, 2.2].

shells have the same spin projection, thus forming the highest possible total spin of atom under consideration.

Interest to SSS properties is determined by desire to understand possible influence of full change of quantum numbers of the occupied states on atomic properties. In comparison with corresponding atoms in their ground states, the SSS have much more electrons placed at large distance from a nucleus than in the ground state. Therefore, in SSS the role of interelectron interaction is much bigger that is why electron correlations become much stronger than in the ground states of atoms under consideration.

We present here results on photoionization of endohedral atoms $A@C_N$ that consist of an atom A stuffed inside the fullerenes shell C_N. The corresponding formulas are presented in Sects. 1.13 and 1.14; two main effects are taken into account—the reflection of photoelectron wave described by reflection factor $F_l(k)$ given by (1.106) and polarization of the fullerenes electron shell by the incoming photon beam described by the polarization factor $S(\omega) = |G_{C_N}(\omega)|^2$, where the polarization amplitude $G_{C_N}(\omega)$ is given by (1.120).

If reflection potential is week, the photoionization amplitude is calculated in the frame of RPAE (or GRPAE) that in the case of endohedral atoms takes into account electron correlations in A, and photoelectrons scattering by the static fullerenes potential (1.105). The respective amplitude is given by (1.108). If reflection is strong, and the fullerenes potential is approximated by (1.105), its effect upon virtually excited electrons has to be taken into account that is achieved in the frame of *FRPAE*, where the photoionization amplitudes are determined by (1.113) and (1.114). The same is the procedure for finite thickness strong fullerenes shell potential (1.116). The corresponding approximation is named *WRPAE*. Inclusion of polarization amplitude G is done in the frame of GWRPAE, with the photoionization amplitude given by (1.120).

The inclusion of reflection leads to endohedral partial photoionization cross-section $\sigma^{\mathrm{AC}(r)}_{nl,kl'}(\omega)$ determined by (1.109), and the dipole angular anisotropy parameter $\beta^{\mathrm{AC}(r)}_{nl}(\omega)$ given by (1.110). The non-dipole parameters $\gamma^{\mathrm{AC}(r)}_{nl}(\omega)$ and $\eta^{\mathrm{AC}(r)}_{nl}(\omega)$ are given by (1.111) and (1.112), respectively. Equation (1.120) determines the endohedral partial photoionization cross-section $\sigma^{\mathrm{AC}}_{nl,kl'}(\omega)$ with inclusion of the polarization factor $S(\omega)$ and reflection of the photoelectron wave. The corresponding non-dipole parameters $\gamma^{\mathrm{AC}}_{nl}(\omega)$ and $\eta^{\mathrm{AC}(r)}_{nl}(\omega)$ are given by (1.123) and (1.124), respectively. In the figures and their descriptions, the upper indexes $\mathrm{AC}(r)$ and AC are for simplicity of notations omitted.

Having in mind to illustrate qualitatively the effect of the fullerenes shell C_N on the photoionization of the atom A, we choose the best studied and in this sense most popular fullerene C_{60}. It consists of 60 carbon atoms with totally 240 electrons (four from each atom) being collectivized.

We consider also some onion-type endohedrals, in which a normal endohedral $A@C_{N1}$ is placed inside a much bigger fullerene C_{N2}. Being a rather exotic object, it deserves at least qualitative consideration. It is performed for $A@C_{60}@C_{240}$. The

reflection by both shells is taken into account using (1.131) and (1.132), while the polarization factor is given by $S(\omega) = |G_{12}(\omega)|^2$ determined using (1.134) and (1.136).

2.2 Atoms and Ions of Noble Gases

In this section, the results of our already known and new calculations of total and partial photoionization cross-sections, of dipole and non-dipole angular anisotropy parameters, of spin polarization parameters of photoelectrons, and of oscillator strength for noble gas atoms and of some their ions are presented.

Calculations have been carried out in one-electron HF approximation and with the account of many electron correlations in framework of RPAE. In some cases, our results are compared with the experimental data. If the difference between RPAE-l and RPAE-v is <2%, in figures only one curve is presented. In some cases, many-electron effects are calculated using RPAE (see Sect. 1.6).

Atoms of noble gases are considered especially in detail. Particularly, in this section we represent our results for external and intermediate subshells of atoms of noble gases He ($Z = 2$) $1s^2$; He*$1s^1$ $2s^1$ ($^3S_1$); Ne ($Z = 10$) $1s^2$, $2s^2$, $2p^6$; Ar ($Z = 18$) $1s^2$, $2s^2$, $2p^6$, $3s^2$, $3p^6$; Kr ($Z = 36$) $3s^2$, $3p^6$, $3d^{10}$, $4s^2$, $4p^6$; Xe ($Z = 54$) $3d^{10}$, $4s^2$, $4p^6$, $4d^{10}$, $5s^2$, $5p^6$ and some their ions Ne^{3+} $2s^2$, $2p^3$, Kr^{5+} $3d^{10}$, $4s^2$, $4p$, Xe^+ $4d^{10}$, $5s^2$, $5p^5$, Xe^{3+} $4d^{10}$, $5s^2$, $5p^3$; Xe^{5+} $4d^{10}$, $5s^2$, $5p$, Xe^{6+} $4d^{10}$, $5s^2$.

Figures 2.1_He_a1–2.4_He_g2 (He) present the data for He atom: ($Z = 2$) $1s^2$.

Figure 2.1_He_a1 shows photoionization cross-section $\sigma_{1s}(\omega)$ of He in HF and RPAE. The difference between HF-l and HF-v forms is small, while the negligible role of correlations is reflected in small distinction between results HF and RPAE. The agreement is within the limits of the accuracy of experimental data [2.4].

Figure 2.2_He_e1 presents non-dipole angular anisotropy parameter γ^{C}_{1s} for He in HF and RPAE (see [2.5]). This value is obtained making use of (1.142). Note a strong nonlinear increase in γ^{C}_{1s} near threshold with subsequent transformation to linear dependence.

Figure 2.3_He_g1 presents dipole polarizability $\alpha_{1s}(\omega)$ (in the units of a_0^3) for He in HF and RPAE. This value is positive at zero frequency and sharply increases until the energy of the first excitation. Beyond the ionization threshold, this value calculated in RPAE is negative and has a minimum at photon energy 2.5 Ry (see [2.6]).

Figure 2.4_He_g2 shows "drag" current density (in units of 10^{-11} A/cm^2) of $1s$-shell for He atom. This value is calculated making use of (1.142) (see [2.7]). The current density corresponds to photon flux 10^{13} photon/(s cm^2), which is easily achievable at synchrotron storage rings. There is a minimum at photon energy of 6 Ry.

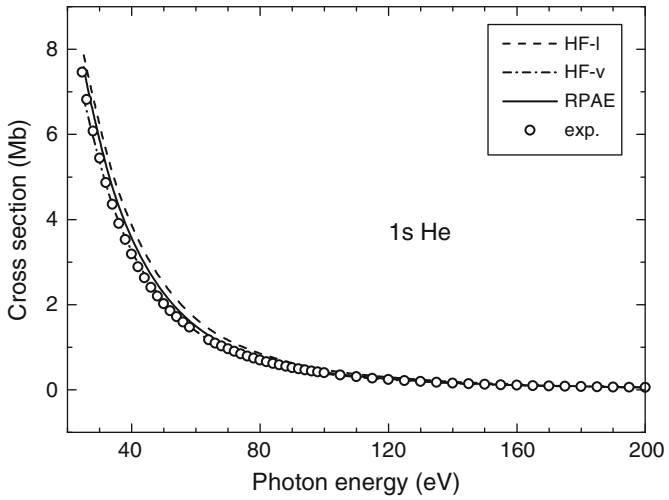

Fig. 2.1_He_a1 Photoionization cross section of He atom in HF and RPAE. Experiment is from [2.4]

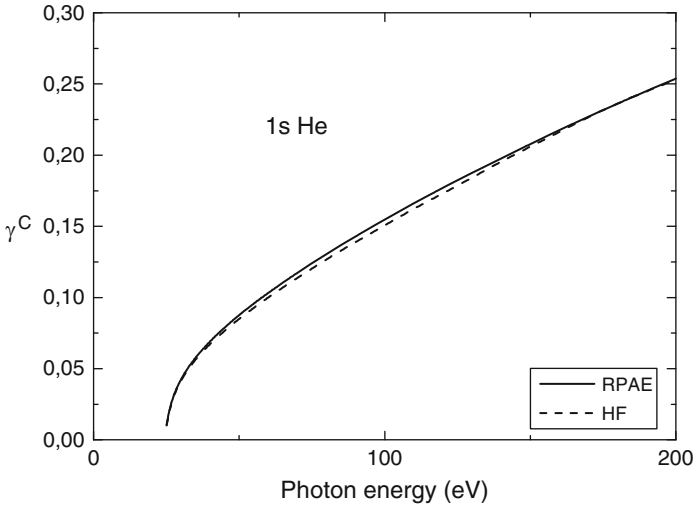

Fig. 2.2_He_e1 Non-dipole anisotropy parameter for He atom in HF and RPAE

Figure 2.5_He*_a1 (He*) presents data for He* atom in excited state: $(Z = 2)\ 1s^1\ 2s^1\ (^3S_1)$.

Figure 2.5_He*_a1 presents total photoionization cross-section $\sigma_{1s,2s}(\omega)$ for excited He* $1s^1\ 2s^1\ (^3S_1)$ in HF and SP RPAE.

Figures 2.6_Ne_a1–2.18_Ne_g2 (Ne) include all results of calculations for Ne atom: $(Z = 10)\ 1s^2 2s^2\ 2p^6$.

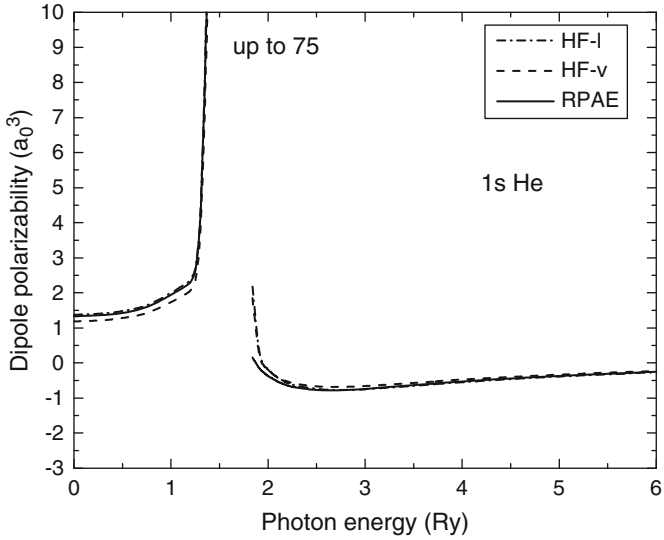

Fig. 2.3_He_g1 Dipole polarizability of He in HF and RPAE

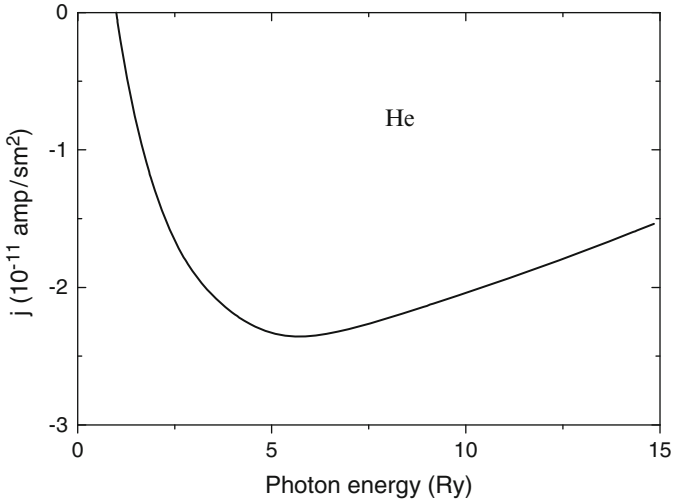

Fig. 2.4_He_g2 "Drag" current in He atomic gas

Figure 2.6_Ne_a1 presents total photoionization cross-section $\sigma(\omega)$ for Ne atom in HF and RPAE. Here the RPAE–correlation are taken into account in all dipole transitions $2p$–$n(\varepsilon)d$, $2p$–$n(\varepsilon)s$, $2s$–$n(\varepsilon)p$ and $1s$–$n(\varepsilon)p$. The role of transitions $2p$–$n(\varepsilon)d$ is rather significant, but only at $\omega \leq 25$ Ry. Influence of other transitions in this range of photon frequencies is not significant.

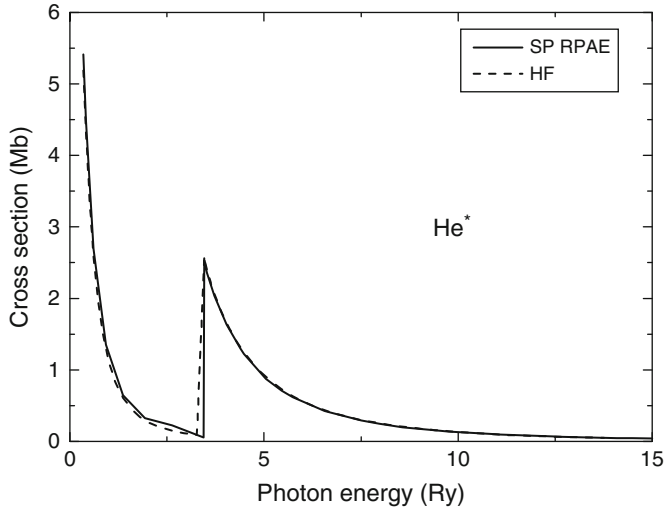

Fig. 2.5_He* _a1 Total photoionization cross section of He atom in excited state ($^3S_1$) in HF and SP RPAE

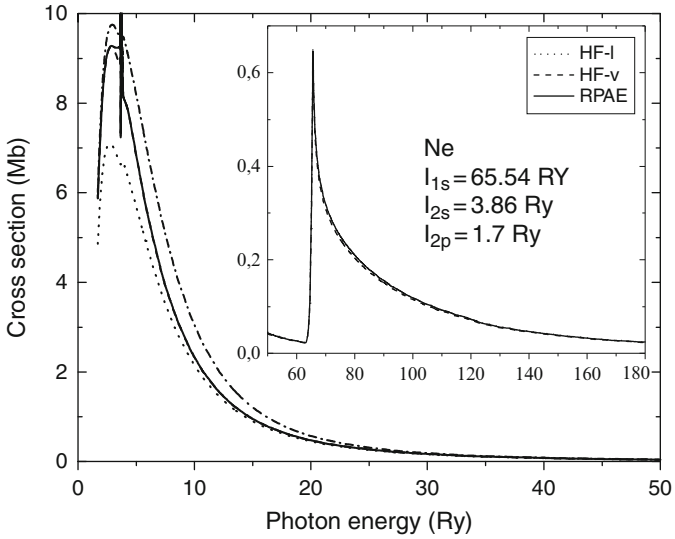

Fig. 2.6_Ne_a1 Total photoionization cross section of Ne atom in HF and RPAE. I—ionization potential of Ne subshells

Figure 2.7_Ne_b1 presents partial photoionization cross-section $\sigma_{1s}(\omega)$ of $1s$-subshell for Ne atom in HF (length and velocity forms) and RPAE. The role of electron correlations is very small.

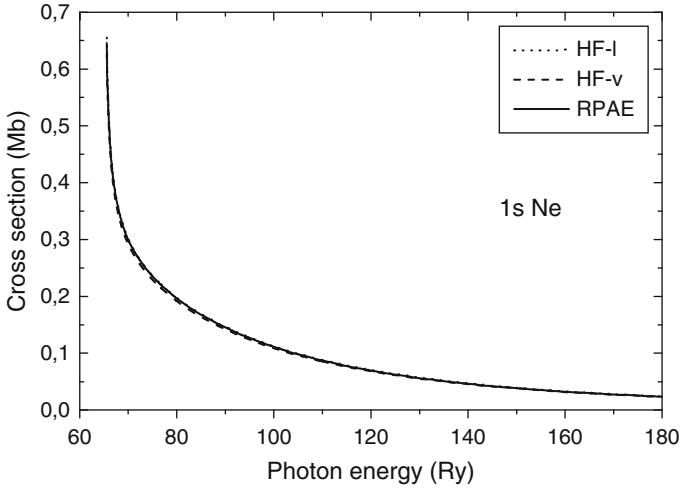

Fig. 2.7_Ne_b1 Photoionization cross section of $1s$-electrons for Ne atom in HF-l, HF-v, and RPAE

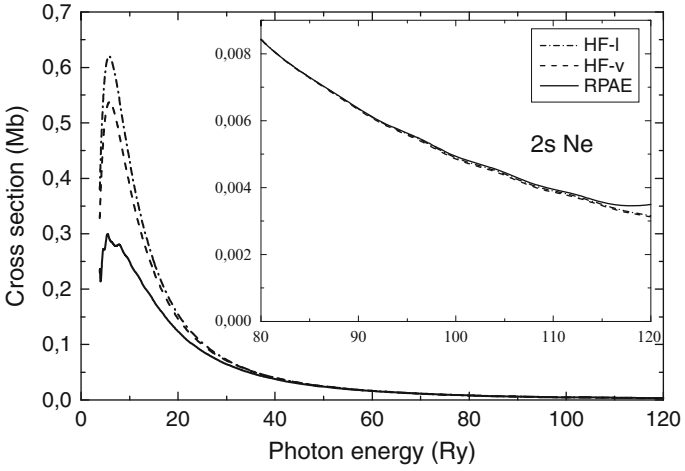

Fig. 2.8_Ne_b2 Photoionization cross section of $2s$-electrons for Ne atom in HF-l, HF-v, and RPAE

Figure 2.8_Ne_b2 depicts partial photoionization cross-section $\sigma_{2s}(\omega)$ of $2s$-subshell for Ne atom in HF and RPAE. Here the RPAE corrections are mainly because of $2p$–$n(\varepsilon)d$ transition and are great at $\omega \leq 25$ Ry.

Figure 2.9_Ne_b3 shows photoionization cross-section $\sigma_{2p}(\omega)$ of $2p$-subshells for Ne, in view of influence (and without it) of $2s$-subshell. The results in HF-l, HF-v, and RPAE are presented. We notice that the influence of $2s$- on $2p$-subshell becomes rather important at high frequencies. At the same time, with the growth of ω the influence of interaction between $2p$-electrons decreases rather quickly.

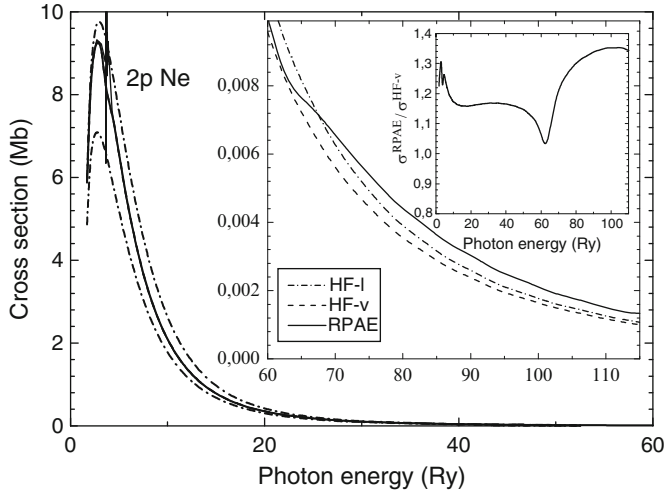

Fig. 2.9_Ne_b3 Photoionization cross section of $2p$-electrons for Ne atom in HF-l, HF-v, and RPAE

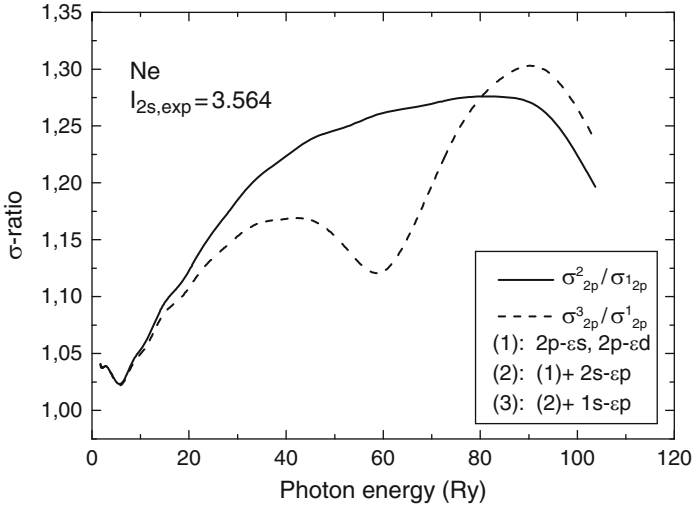

Fig. 2.10_Ne_c1 Photoionization cross section ratios of $2p$-electrons, obtained with account of RPAE-correlations $2p$-, $(2p + 2s)$- and $(2p + 2s + 1s)$-electrons in Ne atom

Importance of intershell RPAE-correlations at high photon energies is demonstrated in the second inset, where the ratio $\sigma^{\mathrm{RPAE}}/\sigma^{\mathrm{HF-v}}$ is presented.

Figure 2.10_Ne_c1 shows the cross-section ratio $\sigma^{\mathrm{RPAE}}_{2p}(\omega)/\sigma^{\mathrm{HF-v}}_{2p}(\omega)$ of $2p$-electrons. It has been calculated for Ne atom in [2.8] and shown in [2.9] on the basis of rather general considerations that at high frequencies this ratio should reach independent of frequency value, which is distinct from unity. Ionization potentials

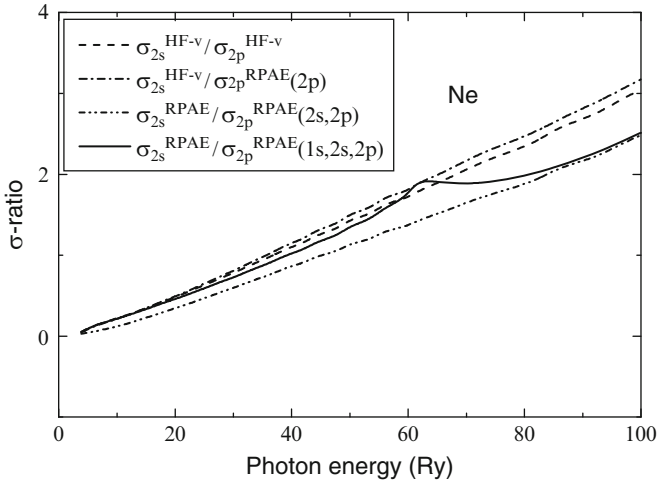

Fig. 2.11_Ne_c2 Photoionization cross section ratios of $2s$- and $2p$-electrons with account of RPAE correlations of $2p$-, $(2p + 2s)$- and $(2p + 2s + 1s)$-electrons in Ne atom

are taken equal to the following values: $I_{2s,\text{exp}} = 3.564$ Ry, $I_{2p,\text{theor}} = 1.7$ Ry, and $I_{1s,\text{theor}} = 65.54$ Ry. The threshold of $2s$-shell is taken from experiment in order to more precise account for the influence of $2s$-electrons on $2p$-electrons (see [AM]).

Figure 2.11_Ne_c2 shows the ratios of cross-sections of $2s$- and $2p$-shells with account of RPAE correlations between $2p$, $2p+2s$ and $2p+2s+1s$ electrons only.

Figure 2.12_Ne_c3 shows the ratio $\sigma_{2s}(\omega)/\sigma_{2p}(\omega)$ in various approximations—with account of RPAE correlations of $2p$, $2p + 2s$, and $2p + 2s + 1s$ electrons, respectively. Above the threshold the $2s$ cross-section is much less than the cross-section of $2p$-subshell. We notice that in all approximations this relation becomes more than one at $\omega \geq 40$ Ry. The appreciable variation of the ratio at $\omega \approx 40$ Ry is the result of action of $1s$-shell on the cross-section $\sigma_{2s}(\omega)$.

Figure 2.13_Ne_d1 presents dipole angular anisotropy parameter $\beta_{2p}(\omega)$ for $2p$-electrons with account of correlations between, respectively, $2p$, $2p+2s$, and $2p+2s+1s$ electrons in RPAE. A strong variation of this parameter due to influence of $1s$-electrons is seen.

Figure 2.14_Ne_e1 presents non-dipole angular anisotropy parameter γ^{C} of $1s$-electrons for Ne in HF and RPAE (see [2.10]). As distinct from He, a pronounced minimum appears immediately after threshold.

Figure 2.15_Ne_e2 presents a magic combination of non-dipole angular anisotropy parameters $(\gamma^{\text{C}} + 3\delta^{\text{C}})$ of $2p$-electrons of Ne in HF and RPAE [see discussion near (1.81)]. The curve looks like consisting of three linear parts—directly after threshold, until 600 eV and after this point.

Figure 2.16_Ne_e3 presents non-dipole angular anisotropy parameter γ^{C} of $2s$-electrons in Ne in HF and RPAE. The parameter changes rapidly near threshold

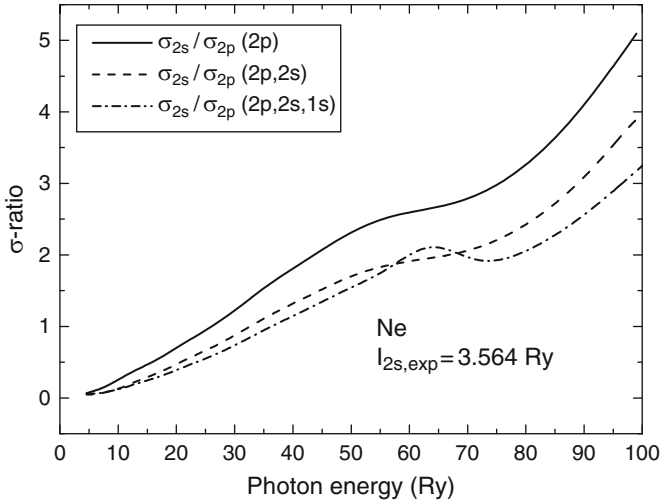

Fig. 2.12_Ne_c3 Photoionization cross section ratios of $2s$- and $2p$-electrons with account of $2p$, $(2p + 2s)$, $(2p + 2s + 1s)$-electrons in Ne atom

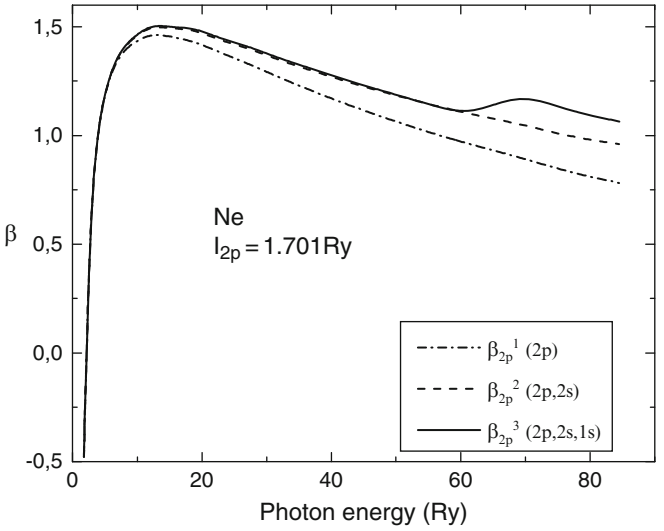

Fig. 2.13_Ne_d1 Dipole anisotropy parameter of $2p$, $(2p + 2s)$, $(2p + 2s + 1s)$-electrons with account of RPAE-correlations in Ne atom

reaching a maximum, then passes through a minimum at 10 Ry, and linearly increases further.

Figure 2.17_Ne_g1 presents "drag" current of $2p$-subshell normalized to unit photon flux W for Ne atom in RPAE in comparison with non-dipole parameter γ^{C} (see [2.10]).

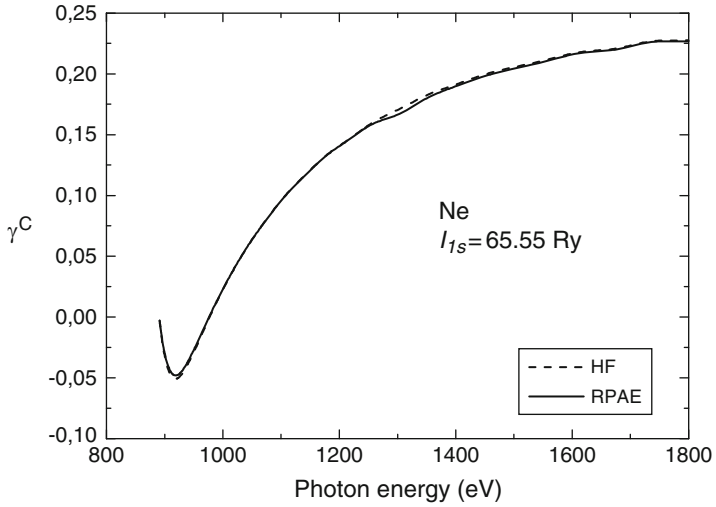

Fig. 2.14_Ne_e1 Non-dipole anisotropy parameter of 1s-electrons for Ne atom in HF and RPAE

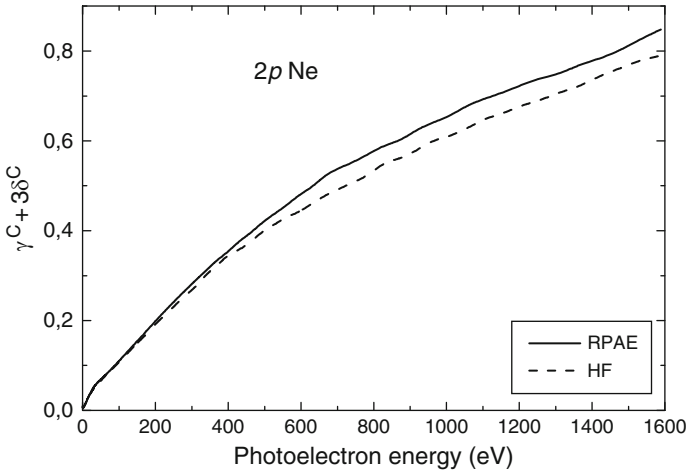

Fig. 2.15_Ne_e2 Magic combination of non-dipole parameters for 2p-electrons of Ne atom in HF and RPAE

Figure 2.18_Ne_g2 presents "drag" current of 2s-subshell normalized to unit photon flux W for Ne atom in RPAE in comparison with non-dipole parameter γ^C (see [2.10]). As distinct from the 2p-shell, there is a strong maximum near threshold. Here as in the previous case a coincidence of energy dependences of the current and the non-dipolar parameter attracts attention.

Figures 2.19_Ne^{3+}_a1–2.21_Ne^{3+}_d1 (Ne^{3+}) contain results of calculations for Ne^{3+} ion in a spin-polarized state: ($Z = 10$) $1s^2$, $2s^2$, $2p^3\uparrow$.

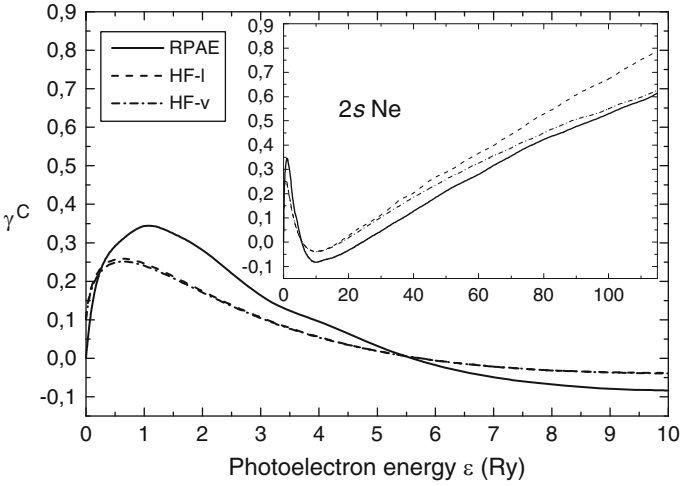

Fig. 2.16_Ne_e3 Non-dipole anisotropy parameter of 2*s*-electrons for Ne atom in HF and RPAE

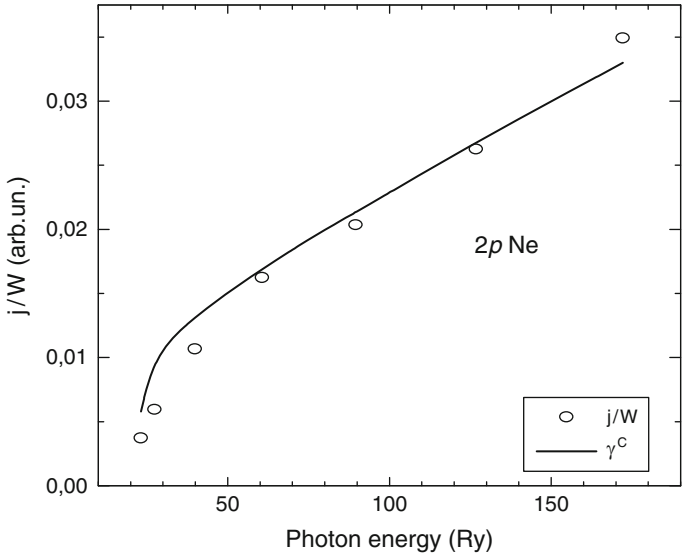

Fig. 2.17_Ne_g1 "Drag current" of 2*p*-shell in Ne atom in RPAE, normalized to unit photon flux *W*

Figure 2.19_Ne^{3+}_a1 presents total photoionization cross-section of Ne^{3+} ion from the threshold up to 20 Ry in SP RPAE. The sequence of maximums is the evidence of discrete excitations.

Figure 2.20_Ne^{3+}_a2 presents quasi cross-sections of discrete lines excitation for Ne^{3+} ion at frequencies from the threshold up to 10 Ry. In inserts are the resulted intensities of rather weak lines. This ion is an object with outer half-filled $2p^3$-shell.

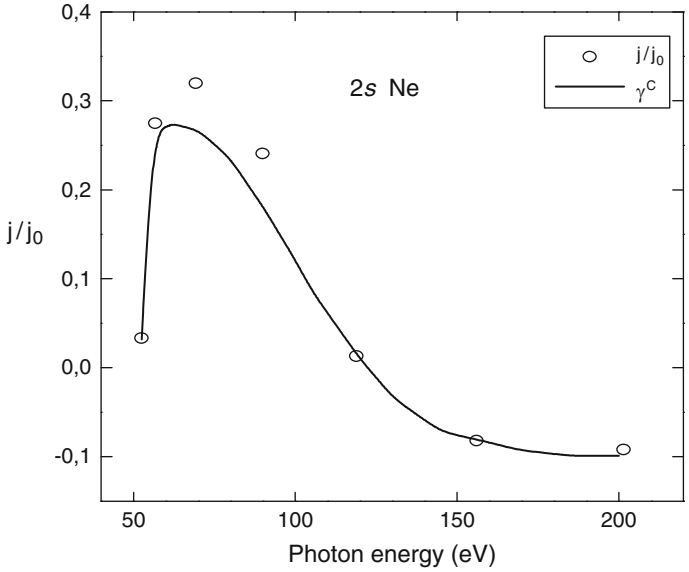

Fig. 2.18_Ne_g2 "Drag current" of 2*s*-shell for Ne atom in RPAE

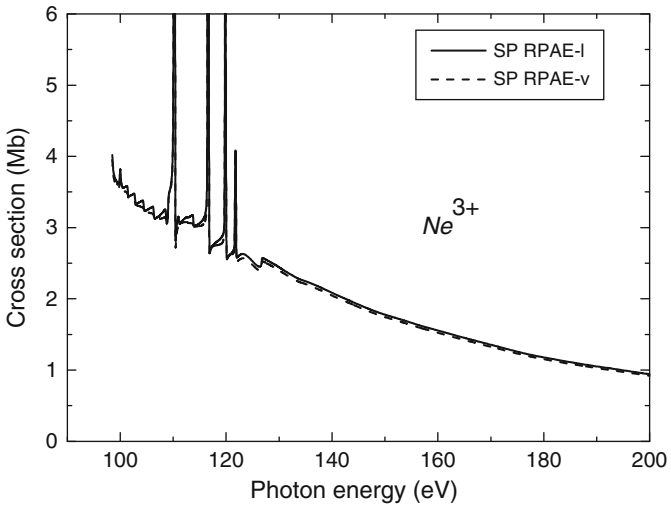

Fig. 2.19_Ne^{3+}_a1 Total photoionization cross section of Ne^{3+} ion in SP RPAE (length and velocity forms)

Figure 2.21_Ne^{3+}_d1 presents dipole angular anisotropy parameter $\beta_(\omega)$ for $2p$-electrons. Note strong variations of this parameter near discrete lines.

Figures 2.22_Ar_a1–2.39_Ar_g2 (Ar) contain results of calculations for Ar atom: ($Z = 18$) $1s^2$, $2s^2$, $2p^6$, $3s^2$, $3p^6$.

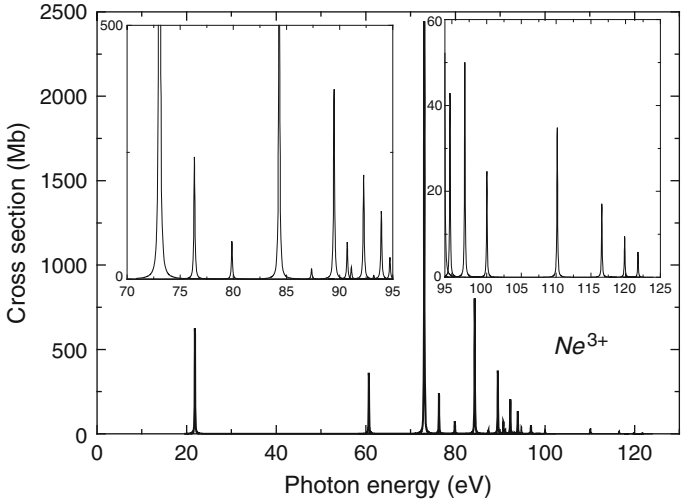

Fig. 2.20_Ne^{3+}_a2 Quasi cross section of excited discrete levels for Ne^{3+} ion

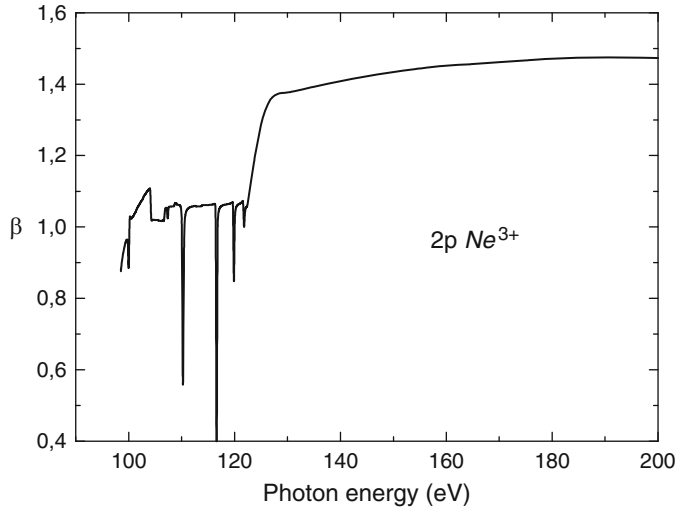

Fig. 2.21_Ne^{3+}_d1 Dipole anisotropy parameter of $2p$-electrons for Ne^{3+} ion

Figure 2.22_Ar_a1 presents total photoionization cross-section of Ar atom. RPAE correlations are taken into account in all dipole transitions $3p$–$n(\varepsilon)d$, $3p$–$n(\varepsilon)s$, $3s$–$n(\varepsilon)p$, $2p$–$n(\varepsilon)d$, $2p$–$n(\varepsilon)s$, $2s$–$n(\varepsilon)p$, and $1s$–$n(\varepsilon)p$. The considered range of ω is very large, approximately up to 900 Ry. The role of the channel $3p$–$n(\varepsilon)d$ is rather essential, but only for ω values close enough to the threshold of the $3p$-subshell. Influence of other transitions in this frequency range is not significant.

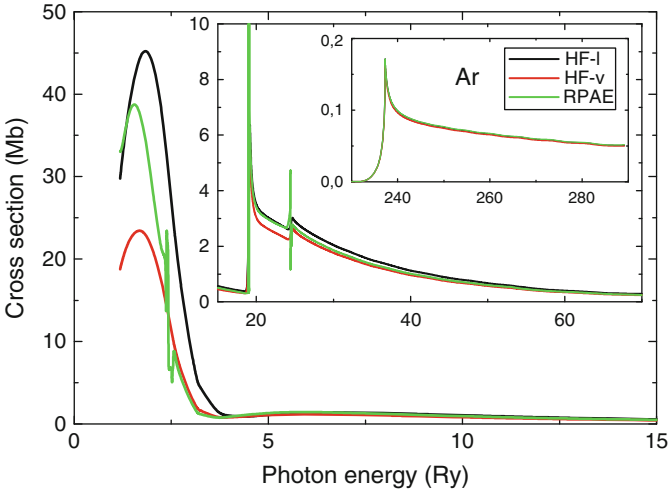

Fig. 2.22_Ar_a1 Total photoionization cross section of Ar atom in HF-l, HF-v, and RPAE

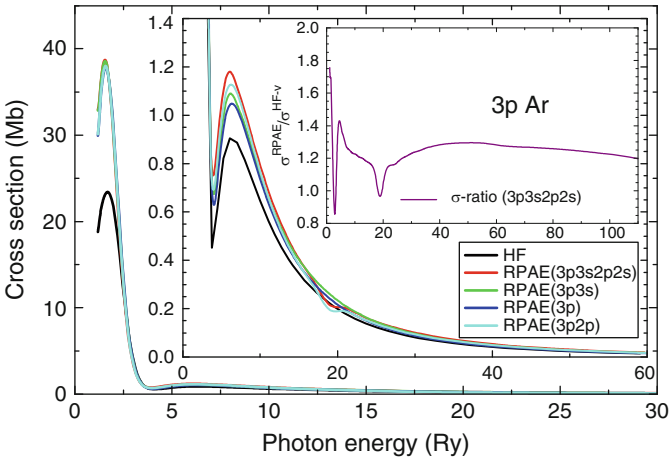

Fig. 2.23_Ar_b1 Photoionization cross section of $3p$-electrons for Ar atom in HF and RPAE with account of influence of different transitions

Figure 2.23_Ar_b1 depicts partial photoionization cross-sections of $3p$-subshell of Ar atom with and without taking into account the influence of some transitions, which are given in the figure. It is noticed that distinction between $\sigma_{3p}^{\mathrm{RPAE}}(\omega)$ and $\sigma_{3p}^{\mathrm{HF}}(\omega)$ is kept up to rather high ω and the most important is the influence *of* $3s$-on $3p$-subshell. It is essential that with growth of ω the influence of interaction between $3p$-electrons falls off rather quickly. Note a small maximum at 6 Ry.

Figure 2.24_Ar_b2 demonstrates partial photoionization cross-section of $3p$-electrons near the threshold. The large difference of results in "length" and

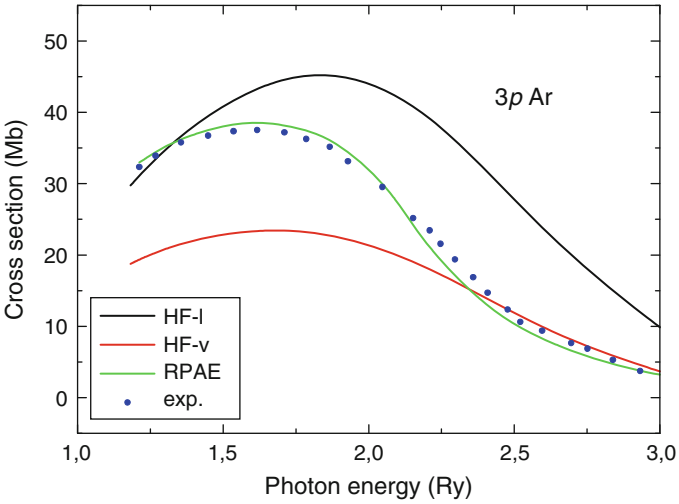

Fig. 2.24_Ar_b2 Photoionization cross section of $3p$-electrons for Ar atom in HF-l, HF-v, and RPAE. Experimental data are from [2.11]

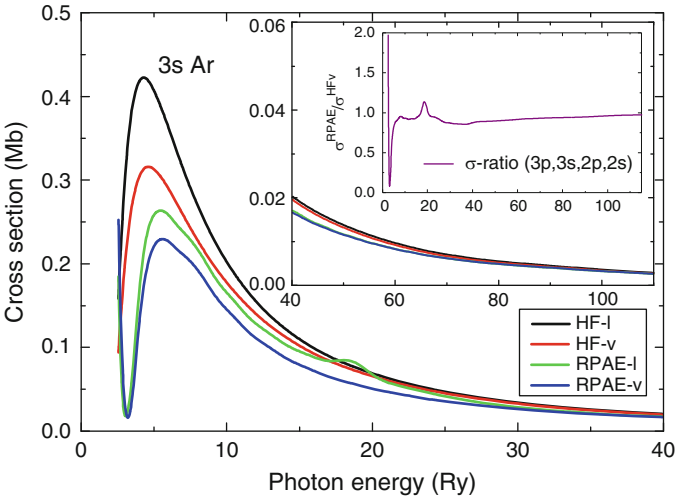

Fig. 2.25_Ar_b3 Photoionization cross section of $3s$-electrons for Ar atom in HF and RPAE (interference maximum is at about 6 Ry)

"velocity" forms and thus the large role of RPAE correlations is visible (see [2.11]). Experimental data are from [2.12].

Figure 2.25_Ar_b3 shows partial photoionization cross-section of $3s$-subshell for Ar atom. Here RPAE corrections are mainly due to the influence of $3p$–$n(\varepsilon)d$ transitions that are very strong everywhere in the considered region, up to $\omega \leq 25$ Ry.

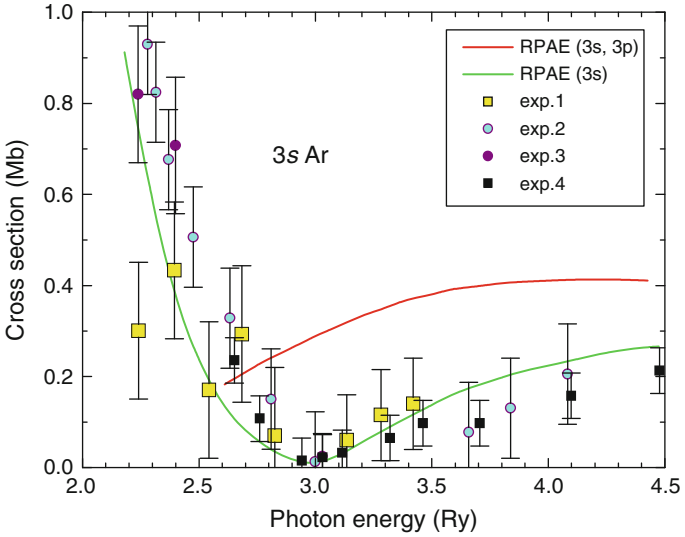

Fig. 2.26_Ar_b4 Photoionization cross section of 3*s*-electrons for Ar atom near interference minimum. Experiment is from [2.13]

Due to correlations there is a second maximum after threshold at $\omega \approx 6$ Ry, named *interference maximum*. Before it, at $\omega \approx 3$ Ry, there is *an interference minimum*.

Figure 2.26_Ar_b4 presents photoionization cross-section of 3*s*-subshell for Ar atom near so-called *interference minimum*. Experimental data are from [2.13]. Importance of RPAE corrections, which takes into account the interaction of electrons from different subshells at high photon energies, is illustrated in the inset of Fig. 2.23_Ar_b1 where the ratio $\sigma_{3p}^{\mathrm{RPAE}}(\omega)/\sigma_{3p}^{\mathrm{HF-v}}(\omega)$ is shown. In [2.14, 2.15] it was demonstrated that this ratio at high ω should reach the magnitude independent of frequency and distinct from that shown in the inset of Fig. 2.25_Ar_b3.

Figure 2.27_Ar_b5 shows partial photoionization cross-section of $2p$ electrons of Ar atom in HF, RPAE, HF with self-consistent account for $2p$-vacancy in the GHF and GRPAE approximations. It is seen that near the threshold photoionization cross-sections in HF and RPAE approximations has a narrow maximum, which is absent in GHF and GRPAE. The role of correlations in GHF and GRPAE is small as compared with HF and RPAE.

Figure 2.28_Ar_b6 demonstrates photoionization cross-section of $2p$- and $2s$-electrons for Ar atom in GRPAE (i.e., with rearrangement).

Figure 2.29_Ar_b7 presents photoionization cross-section of $1s$ electrons for Ar atom in HF, GRPAE, and GRPAEII. Experiment is from [2.16]. It is remarkable that even at the threshold of inner shell, the role of electron correlations beyond RPAE is large and correlations decrease the cross-section at the threshold approximately twice.

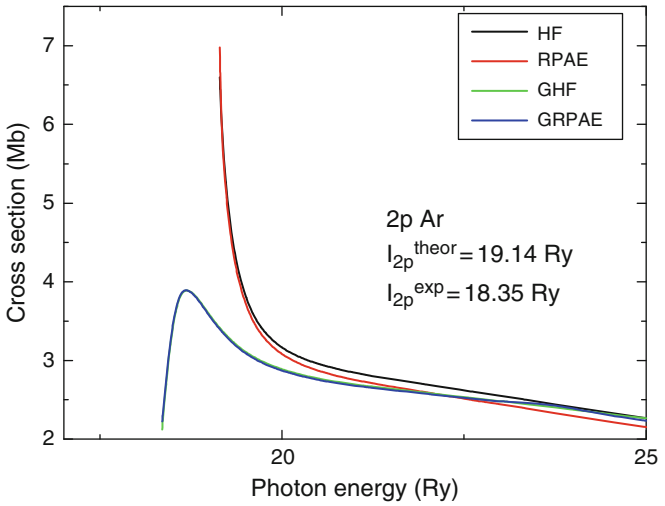

Fig. 2.27_Ar_b5 Photoionization cross section of $2p$-electrons for Ar atom in HF, RPAE and with rearrangement in GHF and GRPAE

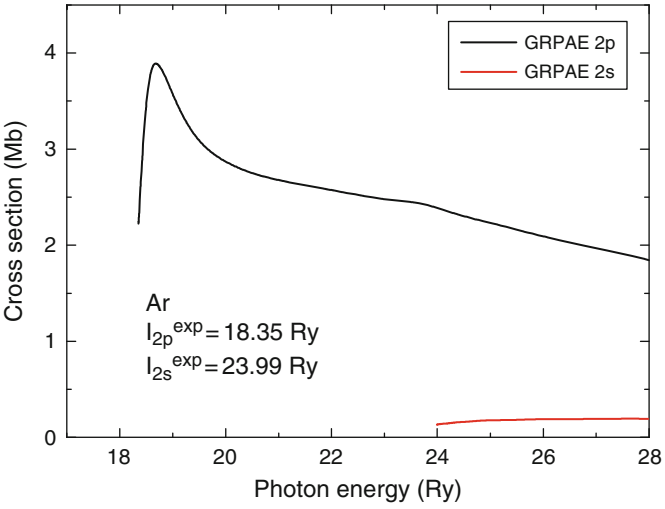

Fig. 2.28_Ar_b6 Photoionization cross section of $2p$- and $2s$-electrons for Ar atom with rearrangement in GRPAE

Figure 2.30_Ar_c1 illustrates the relative role of GRPAE correlations in photoionization cross-section of $3p$-electrons. Electron interaction is taken into account in GRPAE with experimental values of ionization thresholds of $3p$-, $3s$-, $2p$-, and $2s$-subshells.

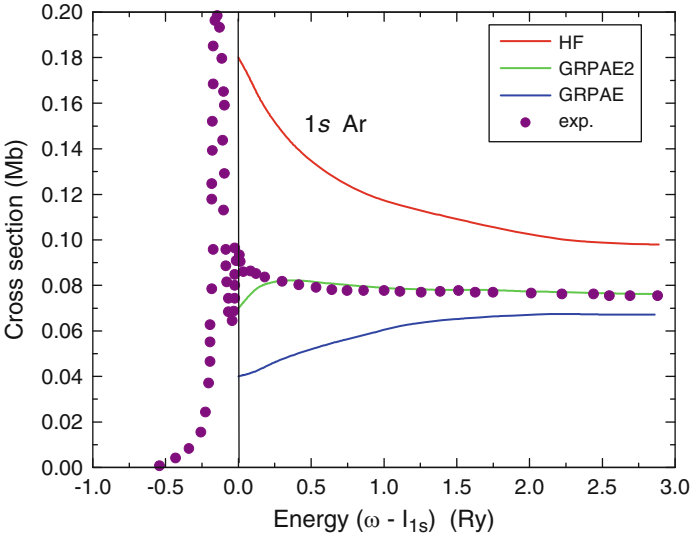

Fig. 2.29_Ar_b7 Photoionization cross section of 1*s*-electrons for Ar atom in HF and GRPAE. Experiment is from [2.16]

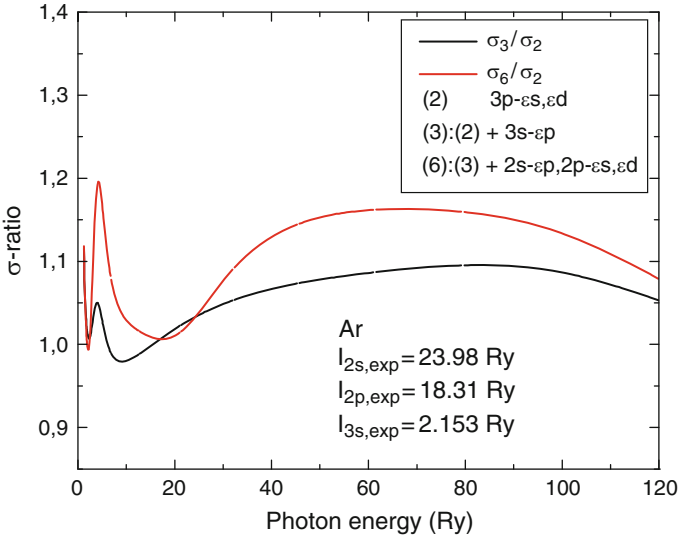

Fig. 2.30_Ar_c1 Relative role of GRPAE-correlations in photoionization cross section of 3*p*-electrons for Ar atom

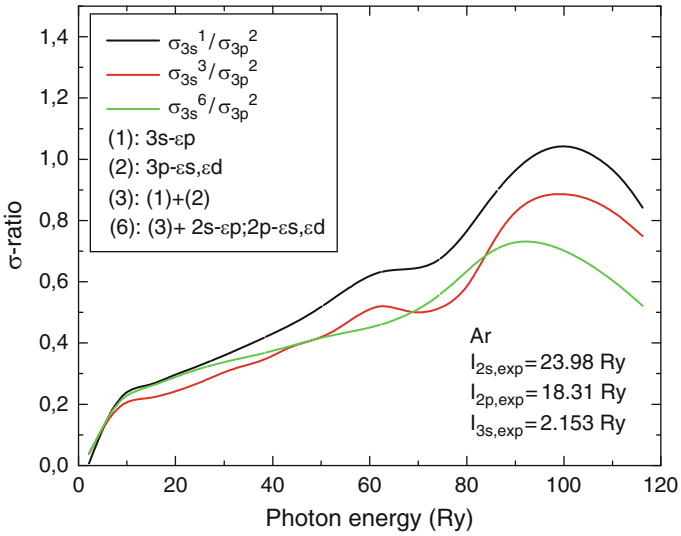

Fig. 2.31_Ar_c2 Photoionization cross section ratios for $3s$- and $3p$-electrons in GRPAE with account of influence of different shells for Ar atom

Figure 2.31_Ar_c2 presents the $\sigma_{3s}(\omega)/\sigma_{3p}(\omega)$ ratio calculated in GRPAE with account of the influence of various subshells. Near its threshold $3s$-cross-section is much less than the cross-section of $3p$-subshell. It is visible that in all approximations this ratio grows rather quickly but does not achieve such great values as $\sigma_{2s}(\omega)/\sigma_{2p}(\omega)$ in Ne.

Figure 2.32_Ar_d1 shows the dipole angular anisotropy parameter $\beta(\omega)$ of $3p$-electrons in GRPAE, in a rather broad range of frequencies ω and demonstrates the influence of correlations in various transitions. The variation in $\beta(\omega)$ at 18.5 Ry is a consequence of the influence of $2p$ electrons.

Figure 2.33_Ar_d2 shows the important role of RPAE correlations in $\beta(\omega)$ of $3p$-electrons in near-threshold area, where results in HF-l and experiment from [2.17, 2.18, 2.89] are given for comparison. The parameter $\beta(\omega)$ as function of ω has a pronounced maximum and a deep minimum. The agreement with experiment is quite good.

Figure 2.34_Ar_d3 compares the results of calculations of dipole angular anisotropy parameters $\beta_{3p}(\omega)$ and $\beta_{2p}(\omega)$ in RPAE. The parameter $\beta_{3p}(\omega)$ as compared with $\beta_{2p}(\omega)$ has an additional maximum in the vicinity of the threshold I_{3p} and a small minimum at about 350 eV.

Figure 2.35_Ar_d4 compares dipole angular anisotropy parameters $\beta_{2p}(\omega)$ in RPAE and GRPAE. The difference is not essential.

Figure 2.36_Ar_e1 presents the non-dipole angular anisotropy parameter γ^{C}_{3s} of $3s$-electrons in rather broad range of frequencies ω in HF and with account of correlations in RPAE. The parameter γ^{C}_{3s} has a maximum at 5 eV and a minimum at 9 eV.

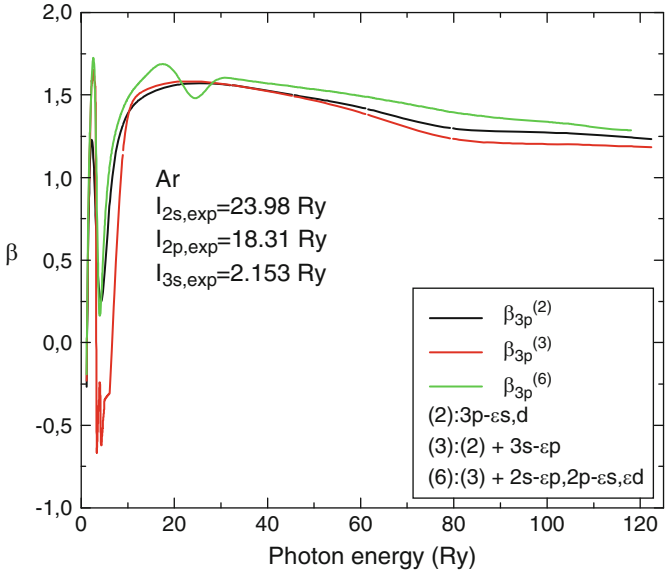

Fig. 2.32_Ar_d1 Dipole anisotropy parameter of $3p$-electrons for Ar atom in GRPAE with account of influence of different transitions

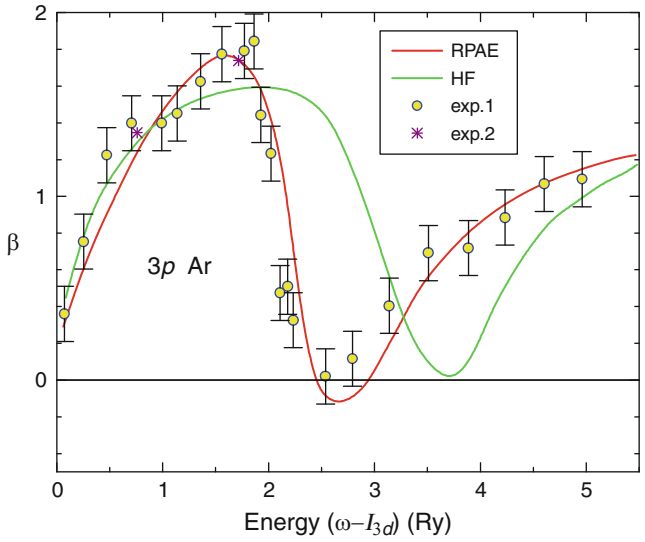

Fig. 2.33_Ar_d2 Dipole anisotropy parameter of $3p$-electrons for Ar atom. Experiment is from [2.17, 2.89, 2.18]

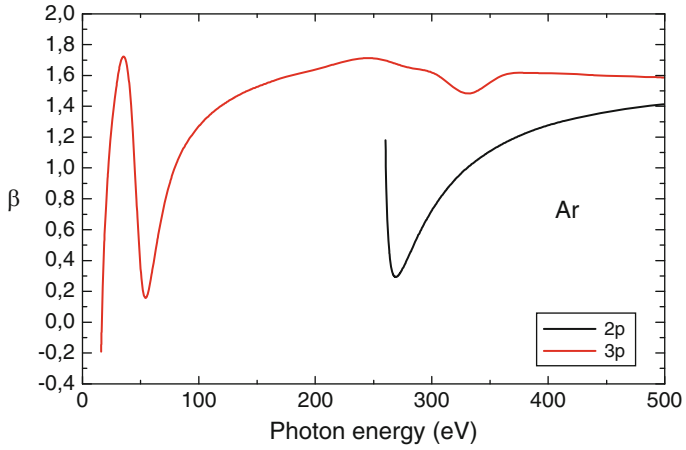

Fig. 2.34_Ar_d3 Dipole anisotropy parameter of $3p$- and $2p$-electrons for Ar atom in RPAE

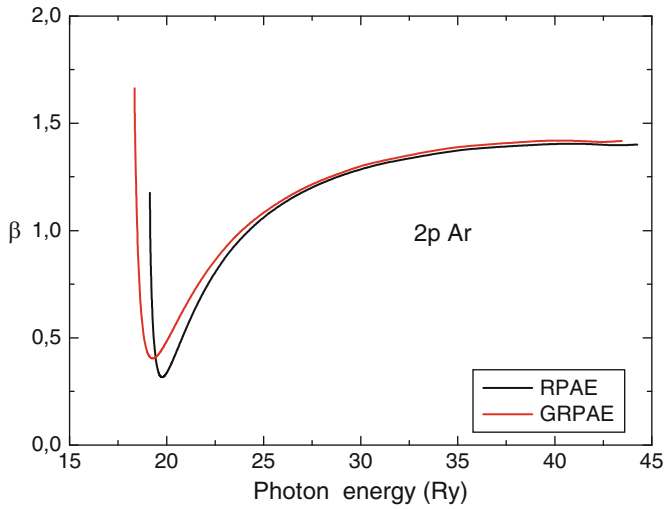

Fig. 2.35_Ar_d4 Dipole anisotropy parameter of $2p$-electrons for Ar atom in RPAE and GRPAE

Figure 2.37_Ar_e2 shows a magic combination [see discussion near (1.81)] of non-dipole parameters for $3p$ electrons of Ar atom in HF and RPAE. There is a rather narrow maximum quite near the ionization threshold of atom.

Figure 2.38_Ar_g1 presents the contribution of $3p$–εs transition to dipole polarizability in HF-l, HF-v, and RPAE (see [2.6]). At zero energy polarizability is positive and significantly larger than that of Ne. After the ionization threshold, it is negative and has a minimum at 1.5 Ry.

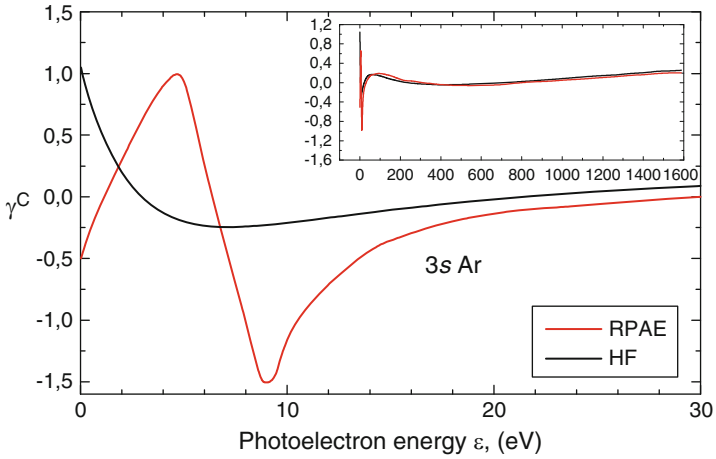

Fig. 2.36_Ar_e1 Non-dipole anisotropy parameter of 3*s*-electrons for Ar atom in HF and RPAE

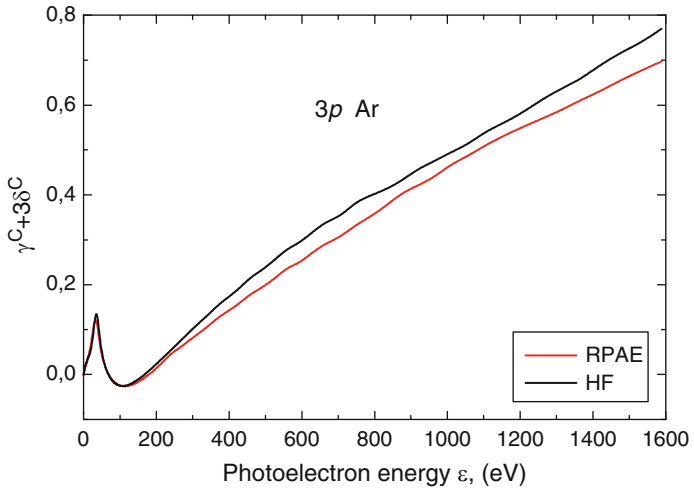

Fig. 2.37_Ar_e2 Magic combination of non-dipole anisotropy parameters of 3*p*-electrons for Ar atom

Figure 2.39_Ar_g2 depicts the contribution of $3p$–εd transition to dipole polarizability in HF-l, HF-v, and RPAE. The behavior of this contribution is similar to that shown in Fig. 2.38, but the amplitude is 5–10 times larger.

Figure 2.40_Ar*_a1 (Ar*) includes all results of calculations for excited Ar* atom: $(Z = 18)\, 3p^5\, 4p^1$.

Figure 2.40_Ar*_a1 demonstrates the photoionization cross-section of $(3p)^{-1}4p^1$ (^1D) state of Ar*. Dominative is the $4p(^1D) \to \varepsilon d(^1P)$ transition that has two deep minima, one of which close to threshold and the second at 3.5 Ry. The shape of $4p(^1S) \to \varepsilon d(^1P)$ is similar, but the first minimum is very shallow. The third

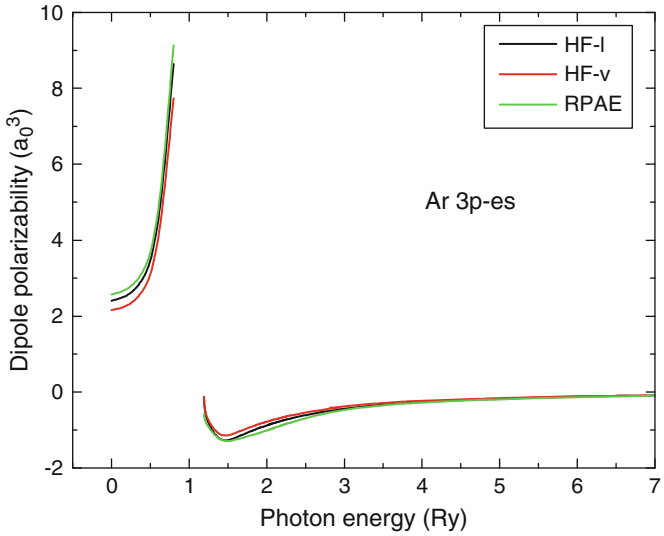

Fig. 2.38_Ar_g1 Contribution of $3p$-εs transition to dipole polarizability for Ar atom in HF (length and velocity forms) and RPAE

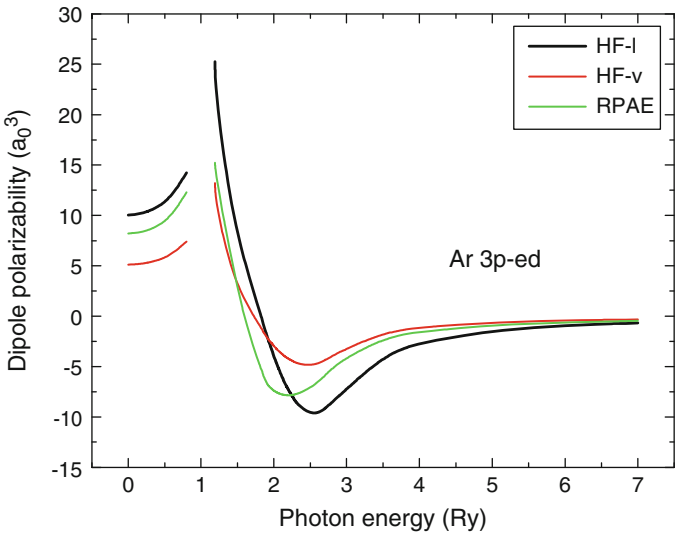

Fig. 2.39_Ar_g2 Contribution of $3p$-εd transition to dipole polarizability for Ar atom in HF and RPAE

contribution $4p(^1D) \rightarrow \varepsilon s(^1P)$ decreases almost monotonically. Note that the cross-sections are much smaller than that of $3p$ photoionization cross-section given in $3p(^1S) \rightarrow \varepsilon d(^1P)$.

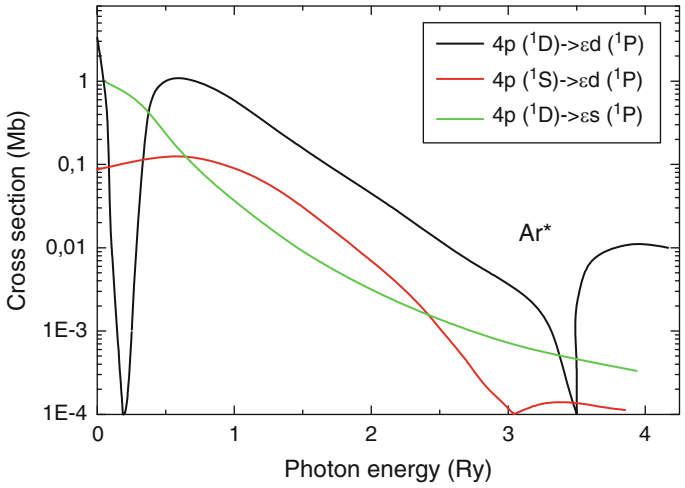

Fig. 2.40_Ar*_a1 Photoionization cross section of $(3p)^{-1}4p^1$ (^1D) state of Ar*

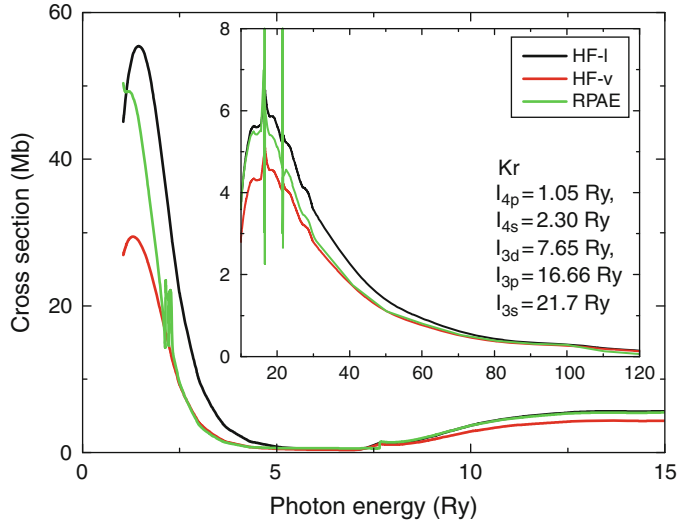

Fig. 2.41_Kr_a1 Total photoionization cross section of Kr atom in HF (length and velocity forms) and RPAE

Figures 2.41_Kr_a1–2.48_Kr_e2 (Kr) contain the results of calculations for Kr atom: $(Z = 36)\, 3p^6, 3d^{10}, 4s^2, 4p^6$.

Figure 2.41_Kr_a1 presents total photoionization cross-section of Kr in HF-l, HF-v, and RPAE. Here RPAE correlations are included in all dipole transitions $4p$–$n(\varepsilon)d$, $4p$–$n(\varepsilon)s$, $4s$–$n(\varepsilon)p$, $3d$–$n(\varepsilon)f$, $3d$–$n(\varepsilon)p$, $3p$–$n(\varepsilon)d$, $3p$–$n(\varepsilon)s$, and $3s$–$n(\varepsilon)p$. The considered range of ω is rather broad, approximately up to 120 Ry.

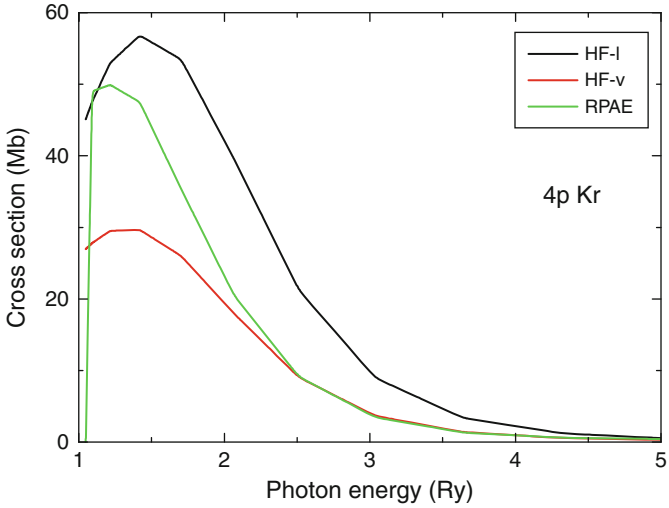

Fig. 2.42_Kr_b1 Photoionization cross section of $4p$-electrons for Kr atom in HF (length and velocity forms) and RPAE

The role of transition $4p$–$n(\varepsilon)d$ near the threshold of the $4p$-subshell is quite impressive. It is much stronger than that of $3p$–$n(\varepsilon)d$ in Ar atom. Note that due to transition $4p$–$n(\varepsilon)d$ there is a second minimum, at $\omega \approx 15$ Ry. Influence of other transitions in this frequency range is small.

Figure 2.42_Kr_b1 depicts partial photoionization cross-section for $4p$-subshell in HF (length and velocity forms) and RPAE. The role of RPAE correlations is quite large. A prominent maximum is seen. There is another maximum in the cross-section at larger photon energy (not demonstrated in the figure).

Figure 2.43_Kr_b2 shows partial photoionization cross-section for $4s$-subshell in RPAE where there are clearly visible interference minimum and maximum (see [2.19] and discussion in (1.47)).

Figure 2.44_Kr_b3 shows photoionization cross-section for $3d$-subshell in HF-l, HF-v, and RPAE. RPAE corrections are large at $\omega \leq 70$ Ry mainly due to $3p$–$n(\varepsilon)d$ transition. A change to a minimum is seen at $\omega = 110$ Ry.

Figure 2.45_Kr_b4 compares partial photoionization cross-section of $3p$- and $3s$-subshell in RPAE and GRPAE.

Figure 2.46_Kr_d1 presents angular anisotropy parameter $\beta(\omega)$ for $4p$- and $3d$-electrons. The role of RPAE correlations is significant. The curves are similar in shapes and look as just shifted in energy relative to each other.

Figure 2.47_Kr_e1 depicts non-dipole angular anisotropy parameter γ^{C} for $4s$-electrons in HF and RPAE. The account for RPAE correlations results in an appearance of a broad maximum above the threshold, which is followed by a deep minimum.

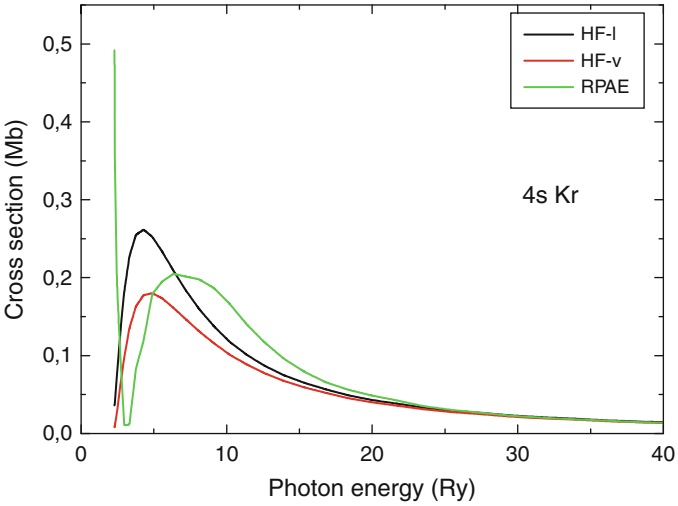

Fig. 2.43_Kr_b2 Photoionization cross section of 4*s*-electrons for Kr atom in HF (length and velocity forms) and RPAE

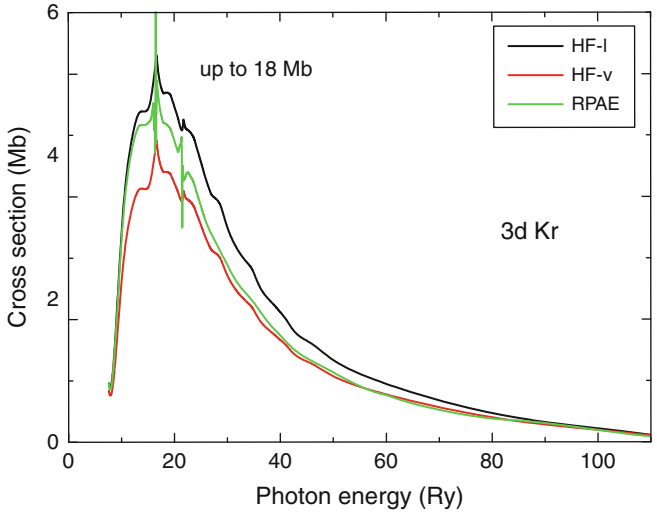

Fig. 2.44_Kr_b3 Photoionization cross section of 3*d*-electrons for Kr atom in HF (length and velocity forms) and RPAE

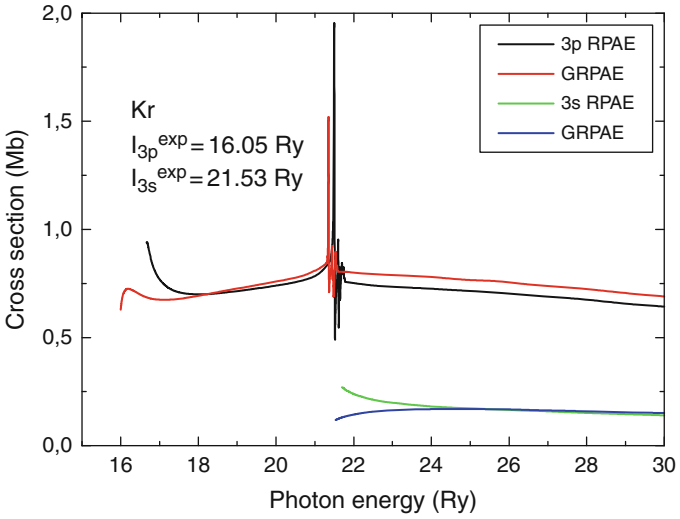

Fig. 2.45_Kr_b4 Photoionization cross section of $3p$- and $3s$-electrons for Kr atom in RPAE and GRPAE

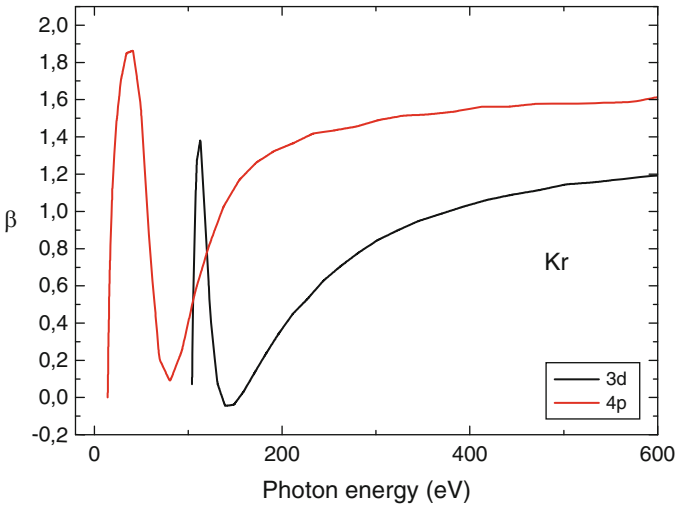

Fig. 2.46_Kr_d1 Dipole anisotropy parameter of $4p$- and $3d$-electrons for Kr atom in RPAE

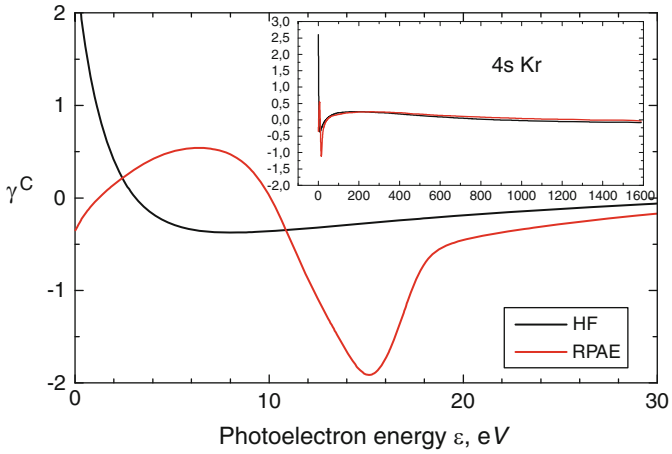

Fig. 2.47_Kr_e1 Non-dipole anisotropy parameter of 4*s*-electrons for Kr atom in HF and RPAE

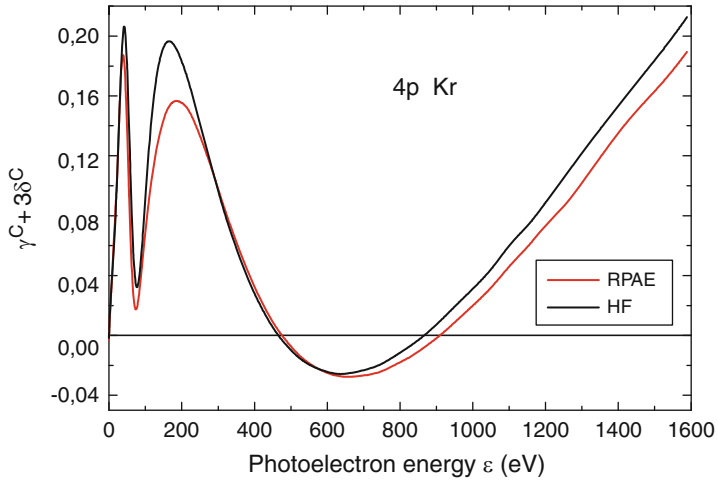

Fig. 2.48_Kr_e2 Magic combination of non-dipole anisotropy parameters of $4p$-electrons for Kr atom in HF and RPAE [see (1.81)]

Figure 2.48_Kr_e2 shows the magic combination of non-dipole angular anisotropy parameters $(\gamma^C + 3\delta^C)$ of $4p$-electrons (see discussion in (1.81)) in HF and RPAE. The energy dependence of this parameter is complex with two minimums and two maximums.

Figures 2.49_Kr^{5+}_a1–2.51_Kr^{5+}_d1 (Kr^{5+}) contain results of calculations for Kr^{5+} ion with configuration $(Z = 36)\ 3d^{10}\ 4s^2\ 4p^1$.

Figure 2.49_Kr^{5+}_a1 presents total photoionization cross-section and quasi cross-section of some discrete excitations of Kr^{5+} ion in HF-l, HF-v, and RPAE.

Figure 2.50_Kr^{5+}_a2 displaces discrete levels of excitation of Kr^{5+} ion in RPAE.

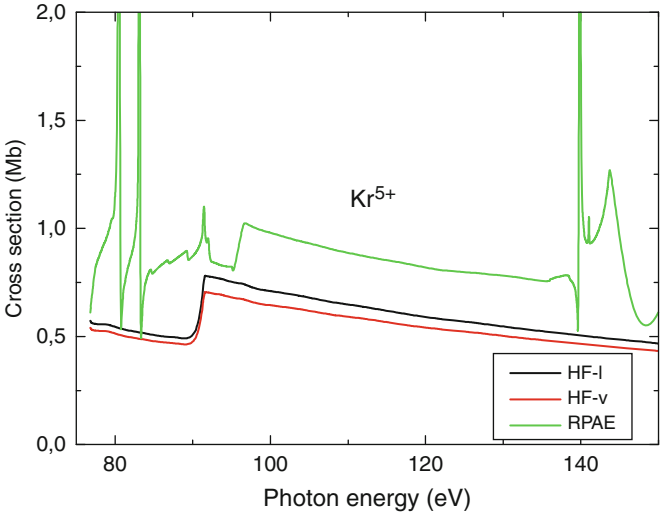

Fig. 2.49_Kr^{5+}_a1 Total photoionization cross section and some discrete excitations for Kr^{5+} ion in HF (length and velocity forms) and RPAE

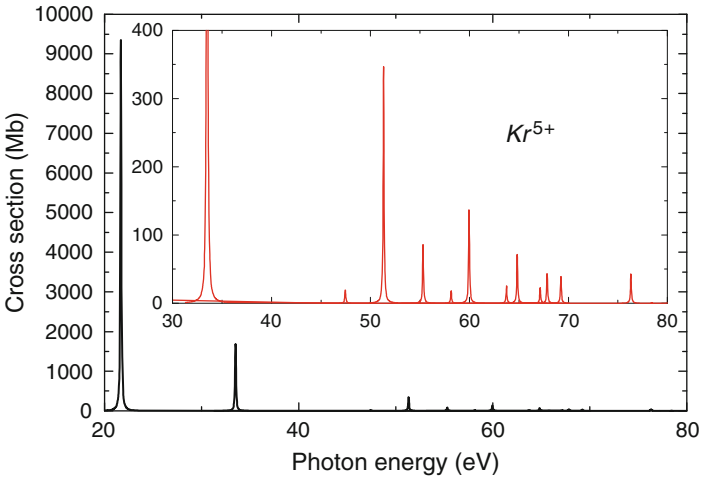

Fig. 2.50_Kr^{5+}_a2 Quasi-cross sections of discrete excitation levels for Kr^{5+} ion in RPAE

Figure 2.51_Kr^{5+}_d1 shows dipole angular anisotropy parameter $\beta(\omega)$ of $4p$-electrons in RPAE.

Figures 2.52_Xe_a1–2.71_Xe_g2 (Xe) contain results of calculations for Xe atom: $(Z = 54)\ 3d^{10}\ 4s^2\ 4p^6\ 4d^{10}\ 5s^2\ 5p^6$.

Figure 2.52_Xe_a1 presents total photoionization cross-section of Xe in HF (length and velocity forms) and RPAE. Here RPAE correlations are included

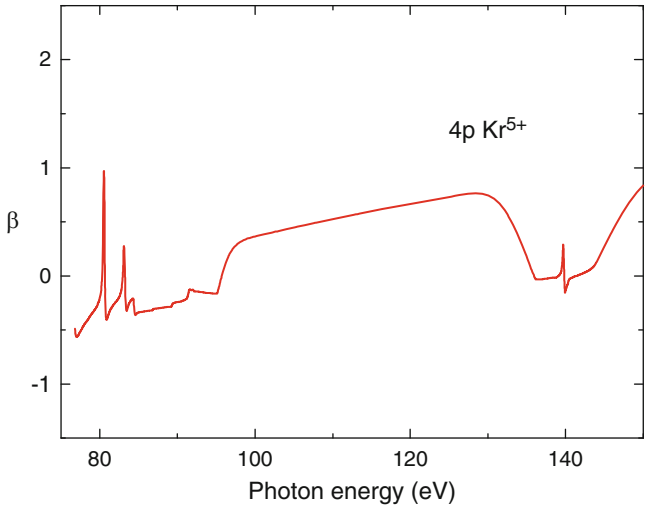

Fig. 2.51_Kr^{5+}_d1 Dipole anisotropy parameter of $4p$-electrons for Kr^{5+} ion in RPAE

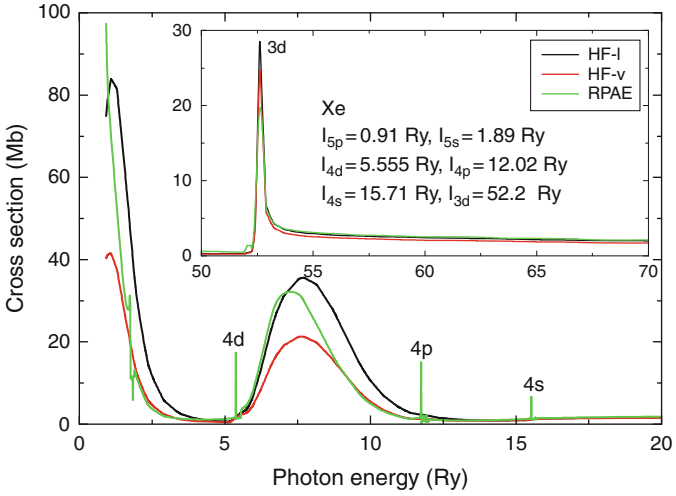

Fig. 2.52_Xe_a1 Total photoionization cross section of Xe atom in HF-l, HF-v, and RPAE

in all dipole transitions: $5p$–$n(\varepsilon)d$, $5p$–$n(\varepsilon)s$, $5s$–$n(\varepsilon)p$, $4d$–$n(\varepsilon)f$, $4d$–$n(\varepsilon)p$, $4p$–$n(\varepsilon)d$, $4p$–$n(\varepsilon)s$, $4s$–$n(\varepsilon)p$, $3d$–$n(\varepsilon)f$, and $3d$–$n(\varepsilon)p$. The considered range of ω is not too broad, approximately up to 700 Ry. The role of $5p$–$n(\varepsilon)d$ transition is rather impressive at values ω that are close to ionization threshold of $5p$-subshell. The influence of other transitions in this area of frequency is not significant. Strong correlations take place in the range 5–12 Ry where the powerful maximum is seen that is called Giant resonance.

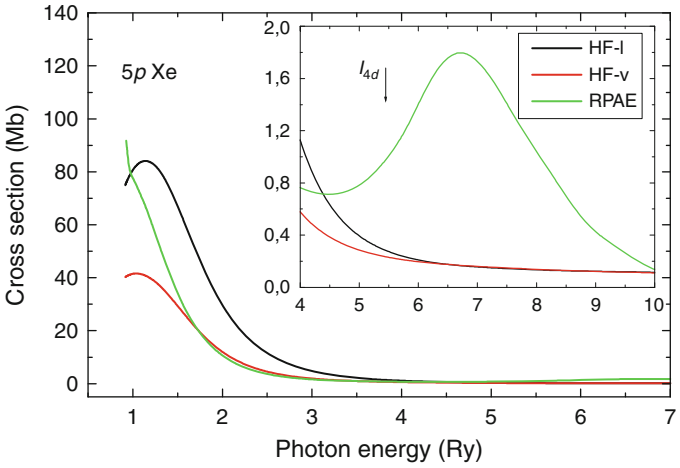

Fig. 2.53_Xe_b1 Photoionization cross section of $5p$-electrons for Xe atom in HF-l, HF-v, and RPAE. Influence of $4d$-electrons is strong (see inset) (see [2.19])

Figure 2.53_Xe_b1 shows partial photoionization cross-section of $5p$-subshells in HF-l, HF-v, and RPAE for Xe atom. RPAE corrections, mainly due to the influence of $5p$–$n(\varepsilon)d$ transition, are big enough at $\omega \leq 25$ Ry. The consequence of the influence of $4d$–$n(\varepsilon)f$ transition is the occurrence of a maximum at $\omega \approx 7$ Ry that is represented on insertion.

Figure 2.54_Xe_b2 presents partial photoionization cross-section of $5s$-subshell, with and without account of the influence of some transitions, which are given in the figure. The experimental data are from [2.20, 2.21, 2.22].

Figure 2.55_Xe_b3 shows photoionization cross-section of $4d$-subshell in HF-l, HF-v, and RPAE in the vicinity of the *Giant resonance*. It is seen that in RPAE appear additional minimum and maximum at $\omega \approx 20$ Ry. The ratio of cross-sections in RPAE and HF approximations, which significantly differs from unity up to 120 Ry, as is shown in the inset.

Figure 2.56_Xe_b4 shows photoionization cross-section of $4d$-subshell in the vicinity of the Giant resonance in HF-l, HF-v, and RPAE. Experiment is from [2.24].

Figure 2.57_Xe_b5 presents single electron photoionization cross-sections of Xe $4d$-subshell in RPAE and GRPAE with account for inelastic electron scattering on ion-remainder. Experiment is from [2.24].

Figure 2.58_Xe_b6 depicts partial photoionization cross-section of $4p$-subshell in HF-l, HF-v, and RPAE. The second maximum is seen at $\omega \approx 22$ Ry. In the inset, the ratio of cross-sections in RPAE and HF is given. It is visible that the role of correlations is appreciable at all considered ω. Note that the difference between $\sigma_{5p}^{\mathrm{RPAE}}(\omega)$ and $\sigma_{5p}^{\mathrm{HF}}(\omega)$ exists up to rather high ω and that the influence of $5s$ on $5p$-level is the most important. It is essential also that with growth of ω the influence of interaction between $5p$-electrons decreases rather quickly.

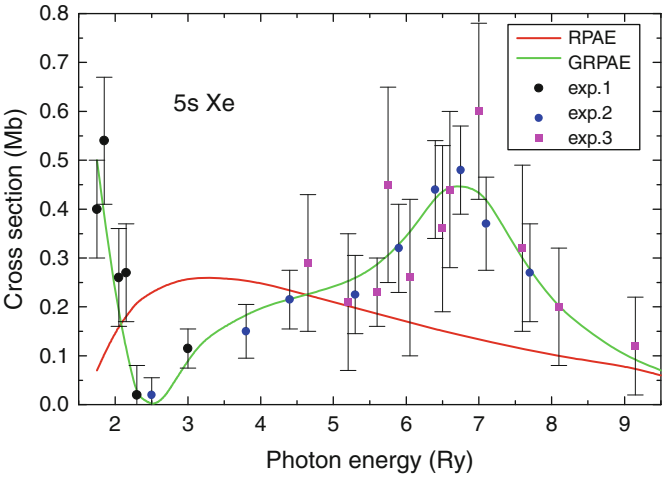

Fig. 2.54_Xe_b2 Photoionization cross section of 5*s*-electrons for Xe atom in RPAE and GRPAE. Experiment is from [2.20, 2.21, 2.22]

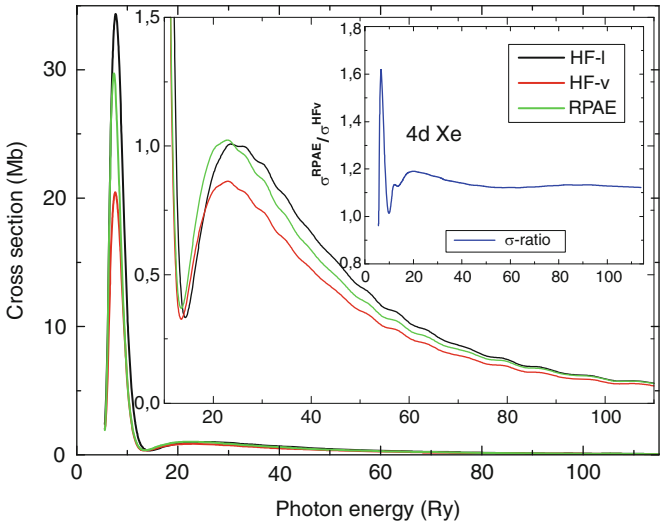

Fig. 2.55_Xe_b3 Photoionization cross section of 4*d*-electrons for Xe atom in HF-l, HF-v, and RPAE

Figure 2.59_Xe_b7 demonstrates photoionization cross-sections of $3d_{5/2}$ and $3d_{3/2}$ levels in HF and SP RPAE. The second maximum in photoionization cross-section of $3d_{5/2}$ electrons appears due to the influence of the $3d_{3/2}$ electrons that is called *intra-doublet* resonance, which is clearly seen [2.3]. Calculation is carried out on the basis of the assumption that 5/2 and 3/2 electrons can be considered as "up" and "down" electrons (see Sect. 1.10). This interaction is accounted for by formulas

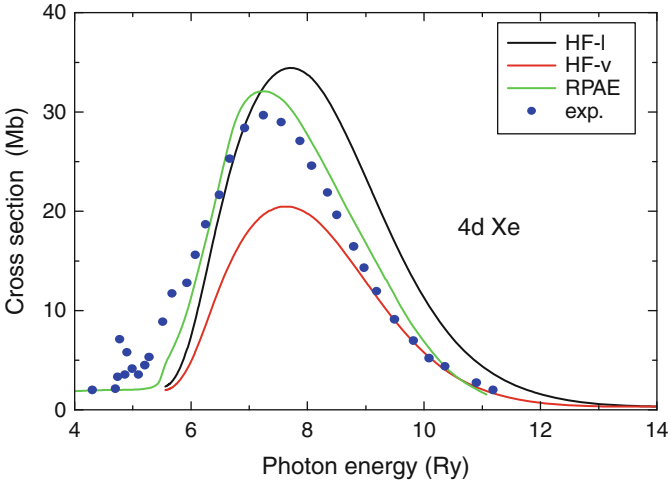

Fig. 2.56_Xe_b4 Photoionization cross section of $4d$-electrons for Xe in the vicinity of the Giant resonance, HF-l, HF-v, and RPAE. Experiment is from [2.23]

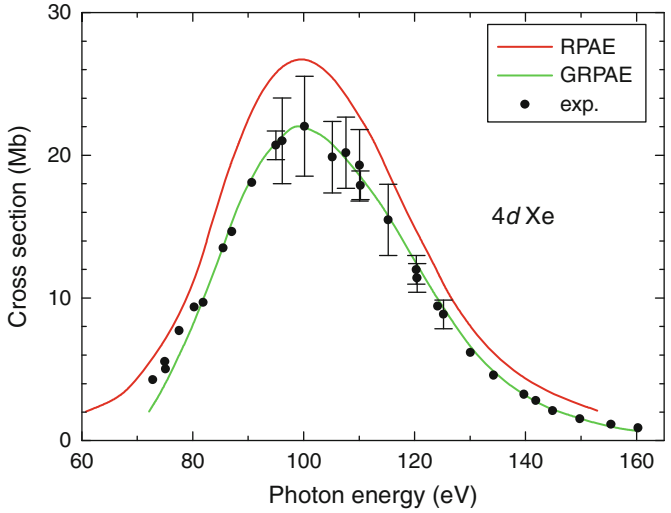

Fig. 2.57_Xe_b5 Single electron ionization of $4d$-electrons for Xe in RPAE and GRPAE. Experiment is from [2.24]

(1.96)–(1.99) with additional multipliers 6/5 and 4/5 in (1.93) for "up," and "down" terms, respectively. These multipliers account for real numbers of electrons at levels 5/2 and 3/2, i.e., 6 and 4, respectively [2.25]. The experimental data are from [2.26].

Figure 2.60_Xe_d1 presents dipole angular anisotropy parameters $\beta_{5p}(\omega)$ and $\beta_{4d}(\omega)$ in a rather broad frequency range. Both channels show oscillation, which is more contracted in energy for $\beta_{4d}(\omega)$ than for $\beta_{5p}(\omega)$.

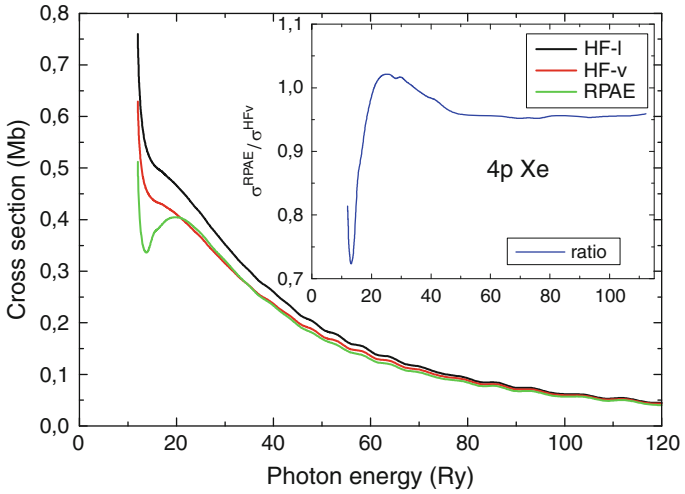

Fig. 2.58_Xe_b6 Photoionization cross section of $4p$-electrons for Xe atom in HF-l, HF-v, and RPAE

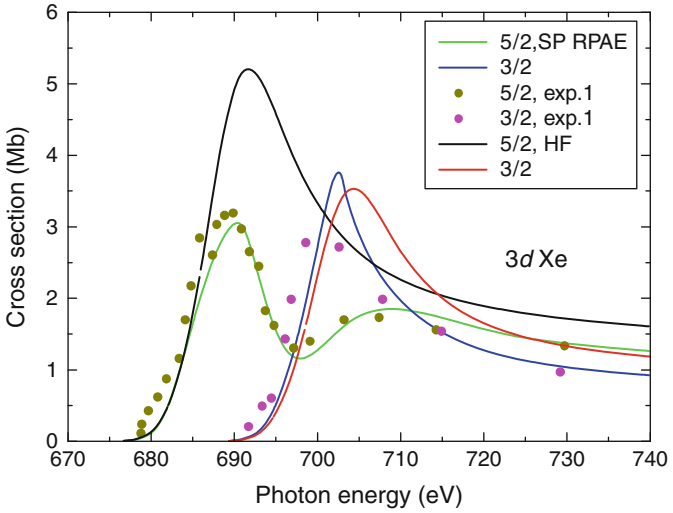

Fig. 2.59_Xe_b7 Photoionization cross section of $3d$-electrons for Xe atom in HF-l, HF-v, and RPAE [2.3, 2.25]. Experiment is from [2.26]

Figure 2.61_Xe_d2 shows dipole angular anisotropy parameter $\beta_{5p}(\omega)$ in HF and RPAE and shows significant role of RPAE correlations in near threshold region (see [2.27]). The energy dependence of β-parameter is oscillating. RPAE results agree well with the experiment [2.28–2.31].

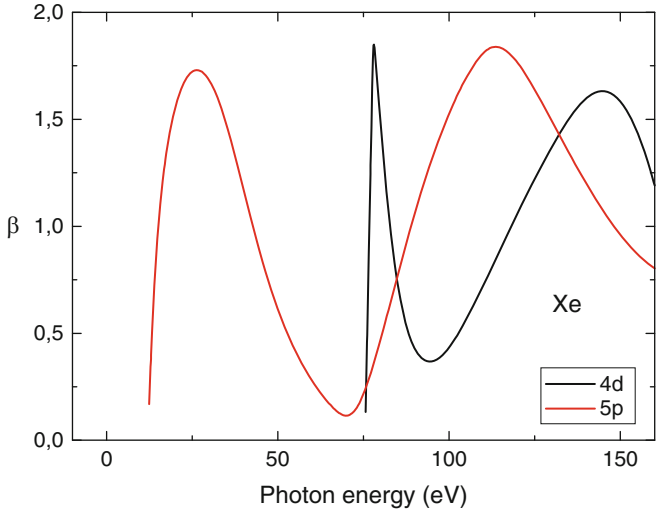

Fig. 2.60_Xe_d1 Dipole anisotropy parameter of $5p$- and $4d$-electrons for Xe atom in RPAE

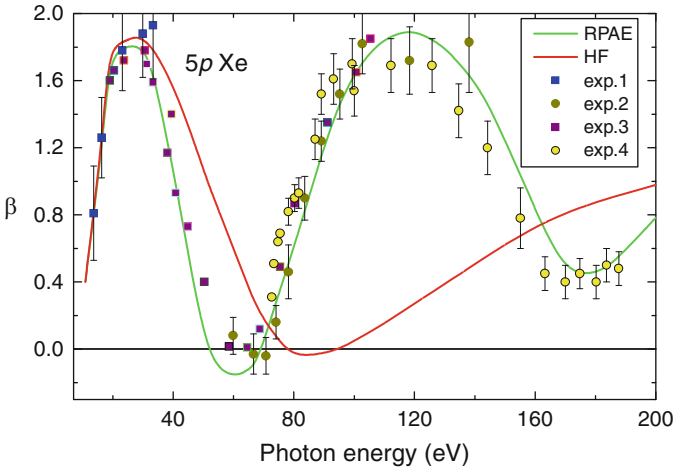

Fig. 2.61_Xe_d2 Dipole anisotropy parameter of $5p$-electrons for Xe atom in HF and RPAE [2.26]. Experiment is from [[2.28]–31], respectively

Figure 2.62_Xe_d3 depicts dipole angular anisotropy parameters $\beta_{3d_{5/2}}(\omega)$ and $\beta_{3d_{3/2}}(\omega)$ in SPRPAE (see [2.3]). The influence of intra-doublet interaction (see discussion of Fig. 2.59_Xe_b7) appears as a small maximum on a curve of $\beta_{3d_{5/2}}(\omega)$-parameter.

Figure 2.63_Xe_e1 shows the magic combination of non-dipole angular anisotropy parameters $(\gamma^{\mathrm{C}} + 3\delta^{\mathrm{C}})$ of $5p$-electrons in HF and RPAE for Xe atom (see [2.32]). The role of RPAE correlations is very large especially at small photoelectron energies.

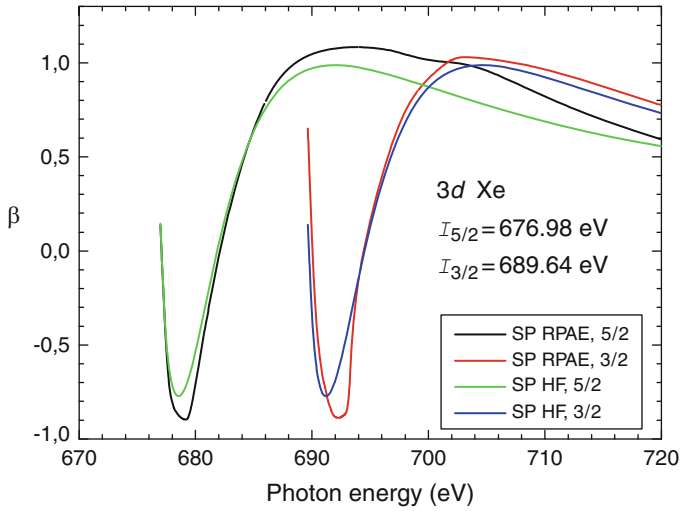

Fig. 2.62_Xe_d3 Dipole anisotropy parameter of $3d_{5/2}$- and $3d_{3/2}$-electrons for Xe atom in SP HF and SP RPAE (see [2.3])

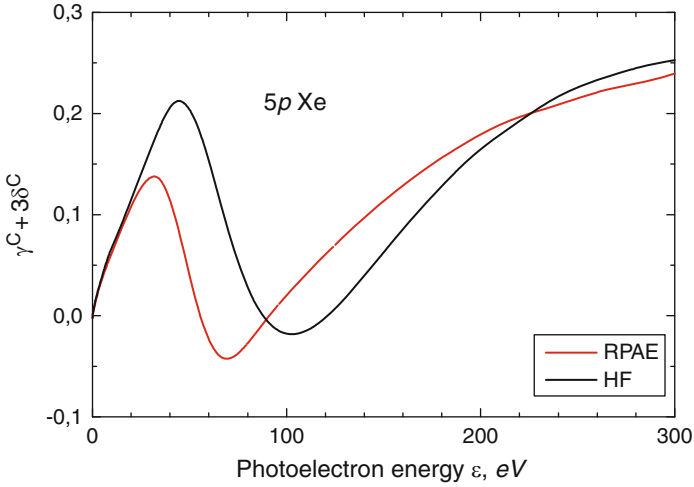

Fig. 2.63_Xe_e1 Magic combination of non-dipole anisotropy parameters of $5p$-electrons for Xe atom in HF and RPAE

Figure 2.64_Xe_e2 presents the non-dipole angular anisotropy parameter γ^{C} of $5s$-electrons in HF and RPAE near the ionization threshold. In the inset, the maximum reflecting influence of $4d$-subshell is seen. As in the case of $5p$-electrons, the role of RPAE correlations is significant.

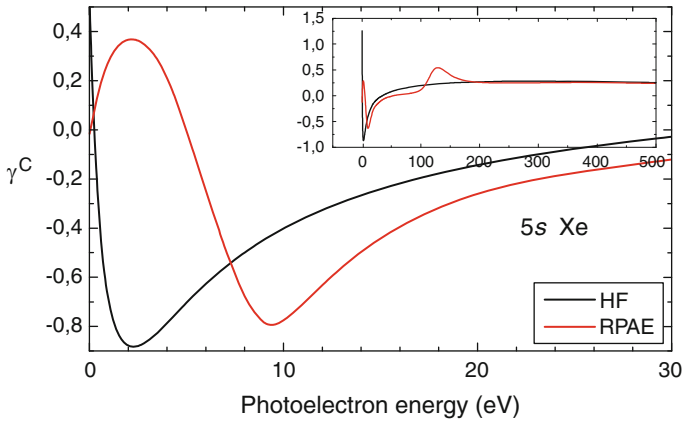

Fig. 2.64_Xe_e2 Non-dipole anisotropy parameter of 5*s*-electrons for Xe atom in HF and RPAE

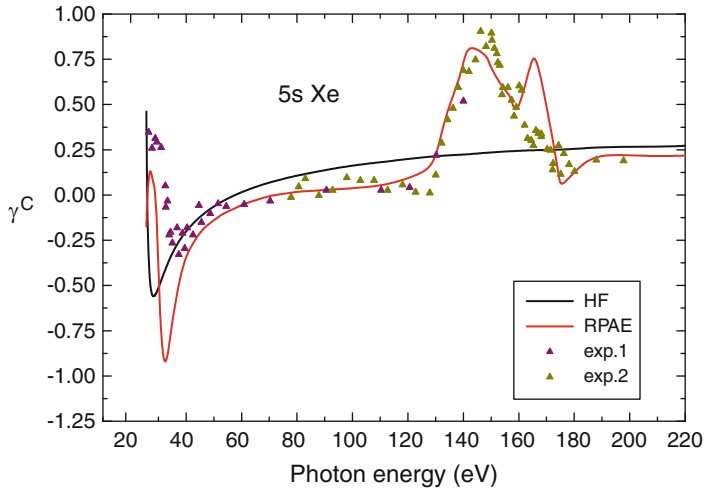

Fig. 2.65_Xe_e3 Non-dipole anisotropy parameter of 5*s*-electrons for Xe atom in HF and RPAE. Experiment is from [2.33]

Figure 2.65_Xe_e3 depicts non-dipole angular anisotropy parameter γ^{C} of 5*s*-electrons in HF and RPAE in a large range of photon energies. It is essential that the curve in RPAE is in agreement with the experiments [2.33].

Figure 2.66_Xe_e4 shows the non-dipole angular anisotropy parameters γ^{C}, δ^{C}, and their magic combination for 4*d*-electrons in HF and RPAE. The role of RPAE correlations is large only at $\omega > 80$ eV.

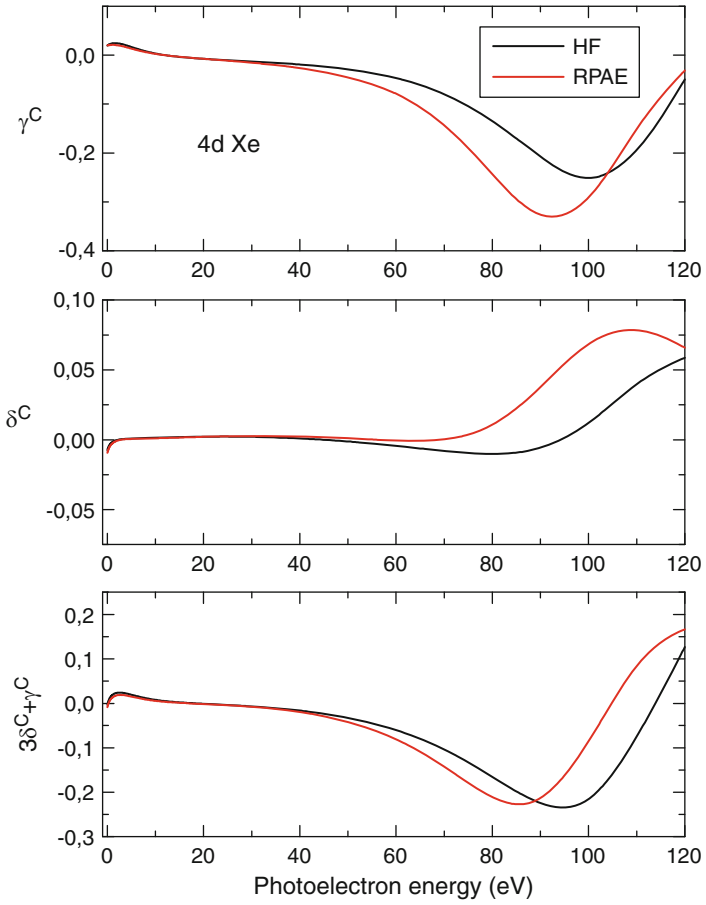

Fig. 2.66_Xe_e4 Non-dipole anisotropy parameter of $4d$-electrons and their magic combination for Xe atom in HF and RPAE

Figure 2.67_Xe_e5 shows the non-dipole angular anisotropy parameters γ^C, δ^C, and their magic combinations for $3d_{5/2}$- and $3d_{3/2}$-electrons of Xe atom in HF and SP RPAE (see [2.34]). The trace of an intra-doublet resonance is evident (see Fig. 2.59_Xe_b7).

Figure 2.68_Xe_f1 presents spin polarization parameters $A^j(\omega)$, $\alpha^j(\omega)$, and $\xi^j(\omega)$ of $4d$-electrons in RPAE. In all cases, the traces of giant resonance followed by a significantly smaller maximum at $\omega = 12$ Ry are seen.

Figure 2.69_Xe_f2 depicts spin polarization parameters $A^j(\omega)$, $\alpha^j(\omega)$, and $\xi^j(\omega)$ of $3d_{5/2}$ and $3d_{3/2}$ electrons of Xe in SP HF and SP RPAE (see discussion of a Fig. 2.59_Xe_b7). The role of intra-doublet correlations is small.

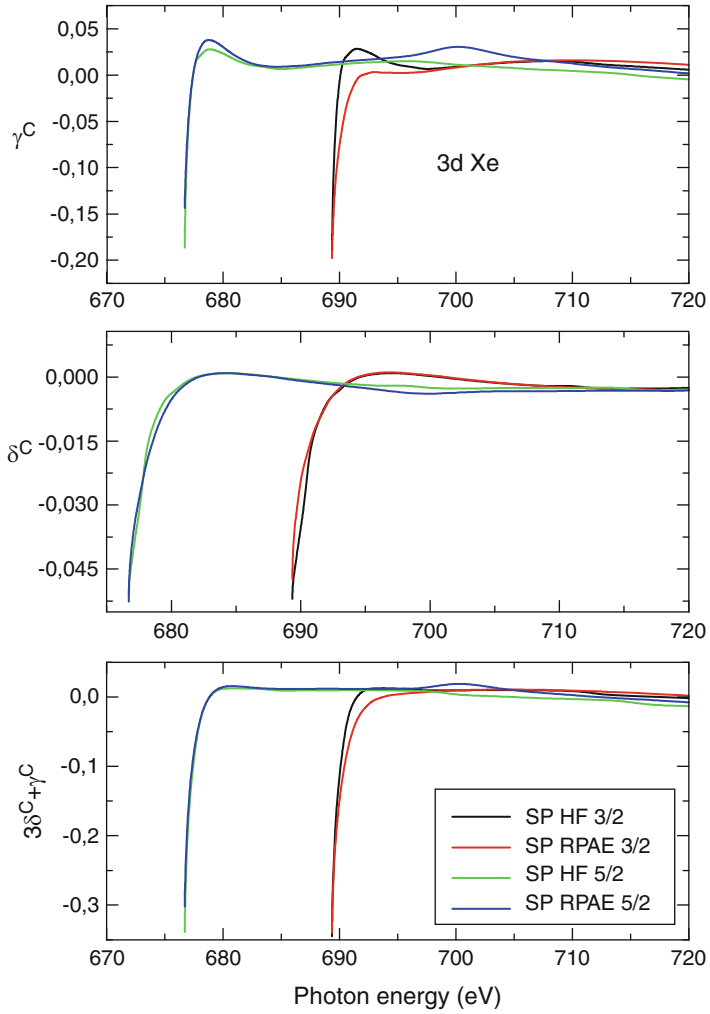

Fig. 2.67_Xe_e5 Non-dipole anisotropy parameter of $3d_{5/2}$ and $3d_{3/.2}$-electrons and their magic combination for Xe atom in SP HF and SP RPAE (see [2.34])

Figure 2.70_Xe_g1 shows single electron photoionization cross-section in the vicinity of $4d$-Giant resonance of Xe atom in HF and RPAE (see [2.35]). Experiment is from [2.20].

The Fig. 2.71_Xe_g2 presents "drag" currents in Xe atom in comparison with "drag" currents in Ar and He atoms (see [2.7]).

Figures 2.72_Xe*_a1 and 2.73_Xe*_a2 (Xe*) include all results of calculations for excited Xe* atom: $(Z = 54)\ 4d^{10}\ 5s^2\ 5p^5 5d^1\ (^1D)$.

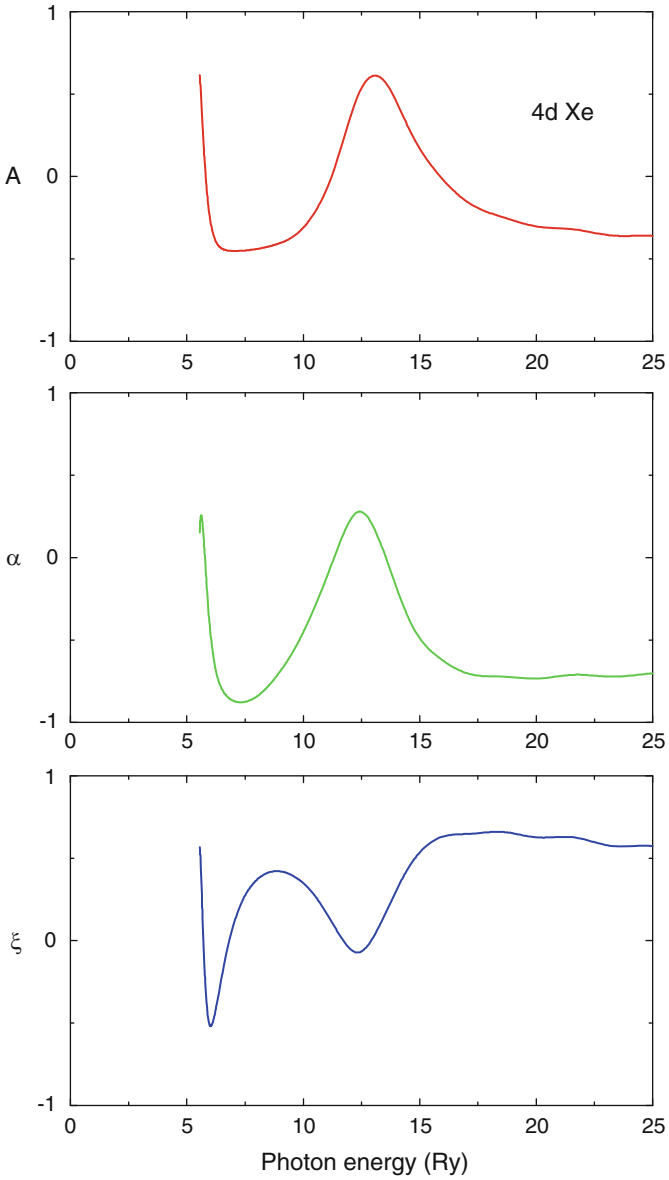

Fig. 2.68_Xe_f1 Spin polarization parameters of $4d$-electrons for Xe atom

Figure 2.72_Xe*_a1 shows photoionization cross-section of $5p$–$^1 5d^1$ (^1P) state of Xe*. The cross-section strongly depends upon the term of the final state: the ^1P has one deep and broad minimum, while ^1D has two, including a narrow and deep near threshold, at about 0.5 Ry, and is on the average bigger than the ^1D.

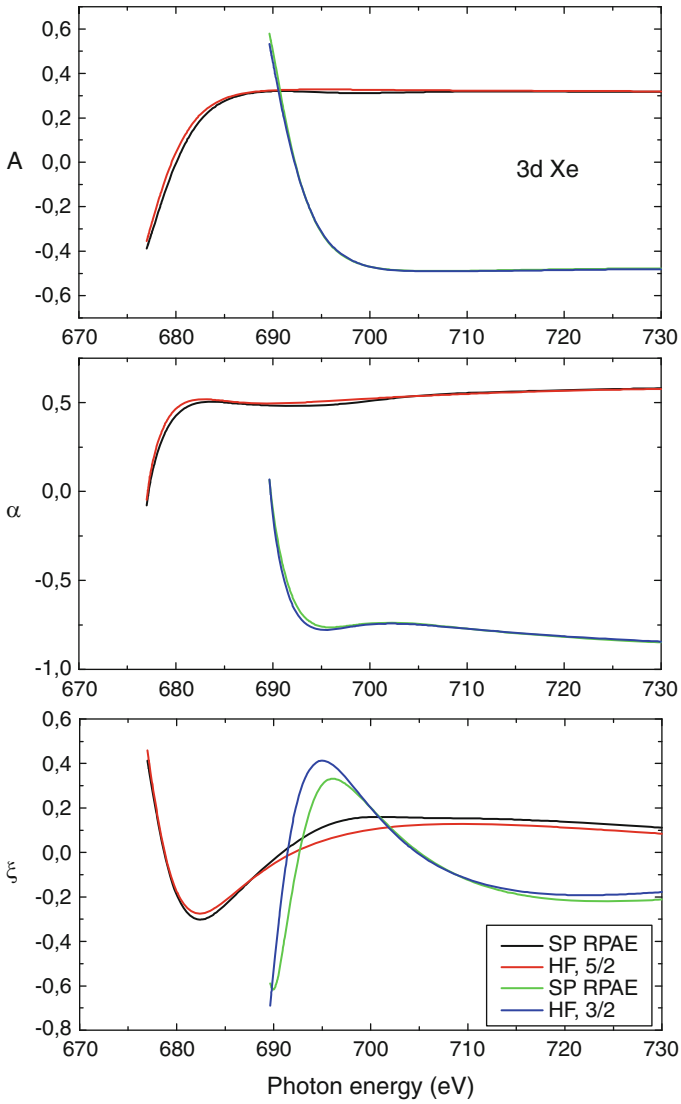

Fig. 2.69_Xe_f2 Parameters of spin polarization for $3d_{5/2}$- and $3d_{3/2}$-electrons of Xe atom in SP HF and SP RPAE

Figure 2.73_Xe*_a2 shows photoionization cross-section of $5p–^1 5d^1$ (^{1}F) state of Xe*. As in Fig. 2.72_Xe*_a1, the cross-section strongly depends on the term of the final state: the ^1D has one deep and narrow minimum near threshold, while ^{1}G has two, including a narrow and deep at about 1.3 Ry, and is on the average bigger than the ^1D.

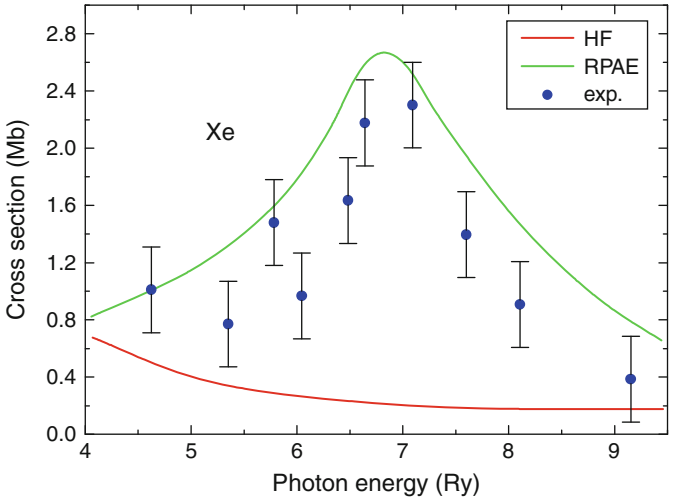

Fig. 2.70_Xe_g1 Single-charged ion yield in photon absorption by Xe atom in HF and RPAE (see [2.35]). Experiment is from [2.20]

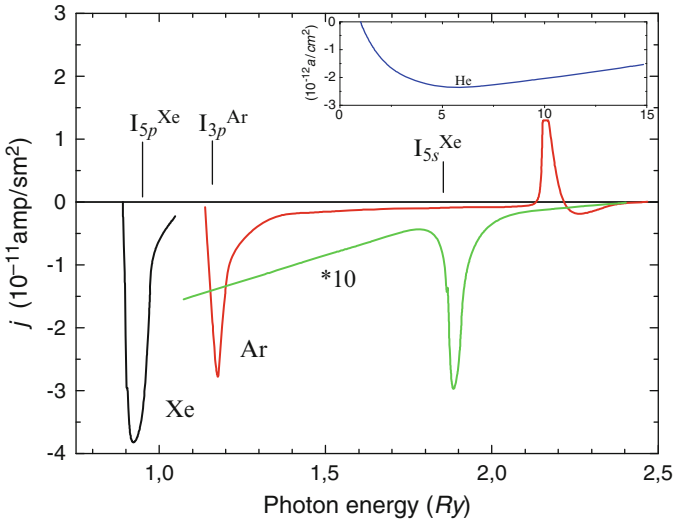

Fig. 2.71_Xe_g2 'Drag" currents for Xe in comparison with that for Ar and He (see [2.7]). In green are the Xe values multiplied by 10

Figures 2.74_Xe$^+$_a1–2.78_Xe$^+$_a2 (Xe$^+$) contain the results of calculations for Xe$^+$ ion: $Z = 54, 4d^{10}5s^2\,5p^5$.

Figure 2.74_Xe$^+$_a1 represents total photoionization cross-section of Xe$^+$ ion and contributions of various terms ^2S, ^2P, ^2D of the final state of an ion in HF.

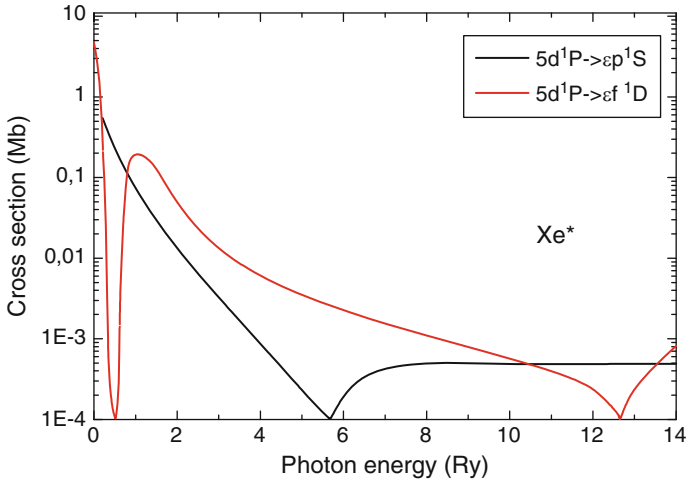

Fig. 2.72_Xe*_a1 Photoionization cross section of $5p^{-1}5d^1$ (^1P) state of Xe*

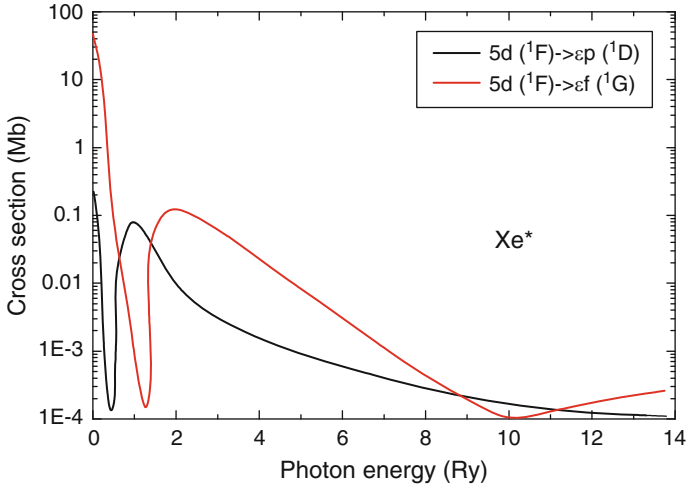

Fig. 2.73_Xe*_a2 Photoionization cross section of $5p^{-1}5d^1$ (^1F) state of Xe*

Figure 2.75_Xe^+_a2 depicts total cross-section of single photoionization of the ion Xe^+ in RPAEO (RPAE for open shells). The contribution of ^2D-, ^2P-, ^2S-terms of a final state and total cross-section are given (see [2.36]). It is seen that the Giant resonance is significantly changed by the set of quasi cross-sections of discrete excitations.

Figure 2.76_Xe^+_a3 shows the total cross-section of single photoionization of the ion Xe^+ (see [2.36]). Experimental data are from [2.37].

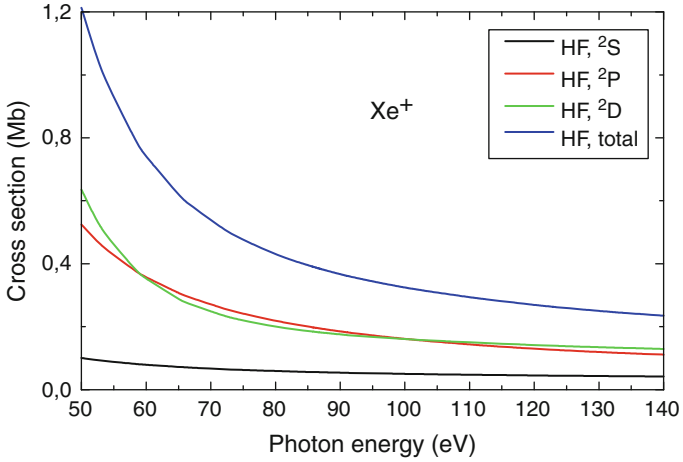

Fig. 2.74_Xe$^+$_a1 Total photoionization cross section and incomes of different terms in cross section of Xe^+ ion in HF

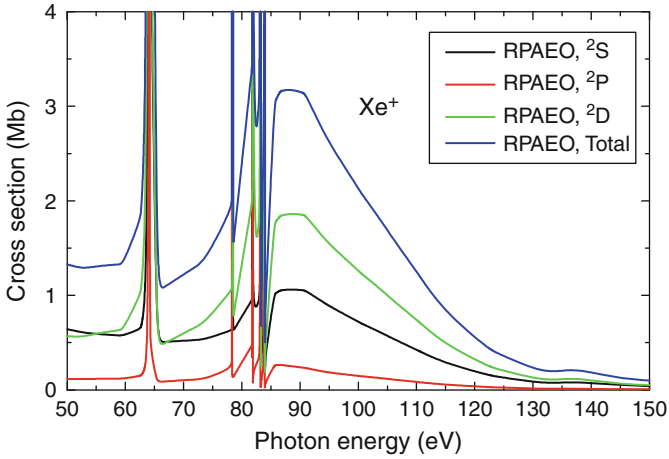

Fig. 2.75_Xe$^+$_a2 Total photoionization cross section and incomes of different terms into cross section of Xe^+ ion in RPAE for open shells (RPAEO) (see [2.36])

Figure 2.77_Xe$^+$_b1 presents photoionization cross-section of 5*s*-electrons in HF-l, HF-v, and RPAEO (with account of 4*d*-subshell). The difference from the case of Xe, shown in Fig. 2.54_Xe_b2, is in disappearance of interference minimum and in appreciable strengthening of the main maximum.

Figure 2.78_Xe$^+$_b2 depicts photoionization cross-section of 4*d* electrons in HF-l, HF-v, and RPAEO. The asymmetry of the Giant resonance is seen. This asymmetry is absent in Xe (see Fig. 2.57_Xe_b5).

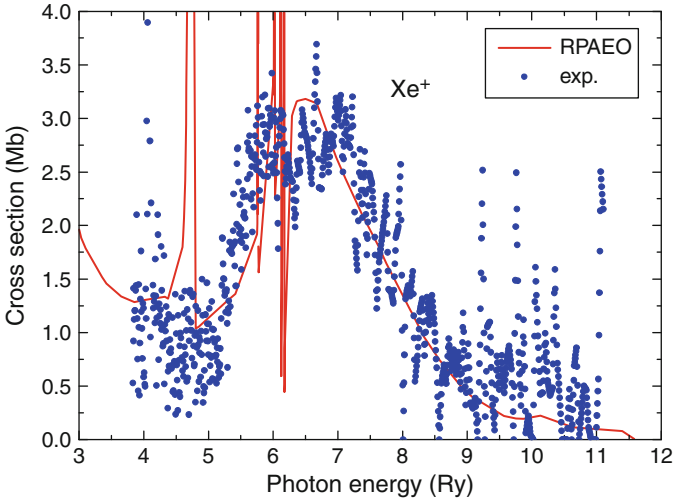

Fig. 2.76_Xe$^+$_a3 Total single-electron photoionization cross section for Xe^+ ion in RPAEO (see [2.36]). Experiment is from [2.37]

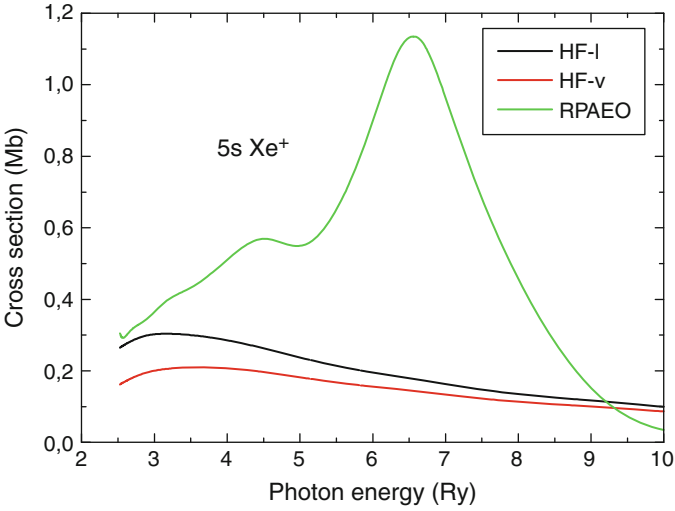

Fig. 2.77_Xe$^+$_b1 Photoionization cross section of 5*s*-electrons in HF-l, HF-v, and RPAEO

Figures 2.79_Xe^{3+}_a1–2.82_Xe^{3+}_d1 (Xe^{3+}) contain results of calculations for Xe^{3+} ion: $(Z = 54)\, 4d^{10}5s^2 5p^3 \uparrow$.

Figure 2.79_Xe^{3+}_a1 presents total photoionization cross-section of discrete excitations and photoionization cross-section of the ion Xe^{3+} in HF-l, HF-v, and SP RPAE. In this case, the Giant resonance is less than in neutral atom, but is visible.

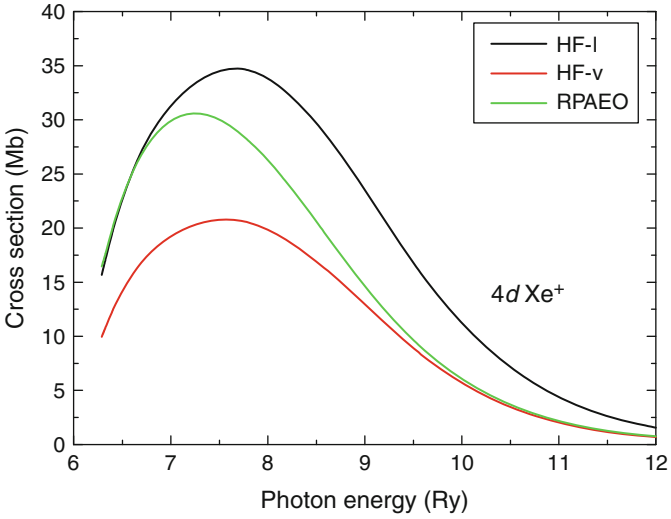

Fig. 2.78_Xe^{+}_b2 Photoionization cross section of 4*d*-electrons for Xe^{+} ion in HF-l, HF-v, and RPAEO

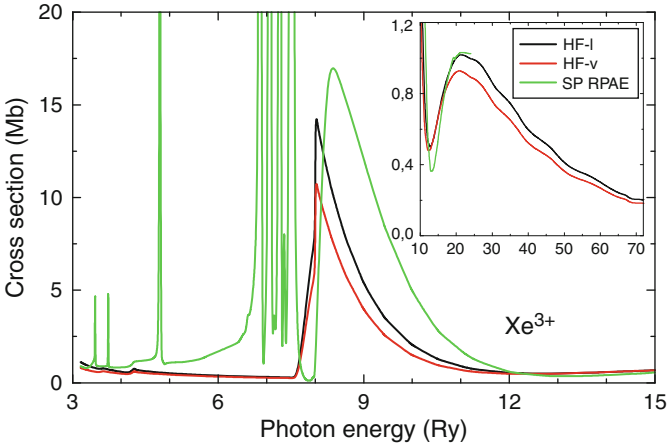

Fig. 2.79_Xe^{3+}_a1 Total photoionization cross section of Xe^{3+} ion in HF-l, HF-v, and SP RPAE

Figure 2.80_Xe^{3+}_a2 shows quasi cross-section of excitation of discrete levels of the ion Xe^{3+} in photon energy range from the first level up to 40 eV.

Figure 2.81_Xe^{3+}_a3 depicts quasi cross-section of excitation of discrete levels of ion Xe^{3+} in small photon energy range 40–55 eV.

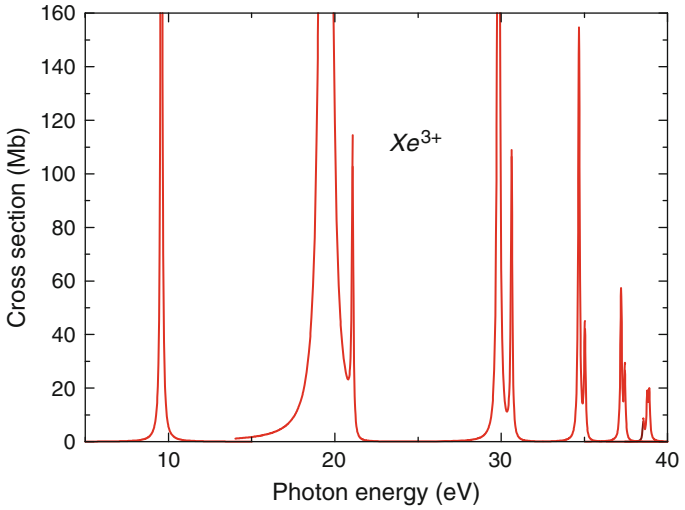

Fig. 2.80_Xe^{3+}_a2 Quasi cross-section of discrete level excitation for Xe^{3+} ion in low energy range

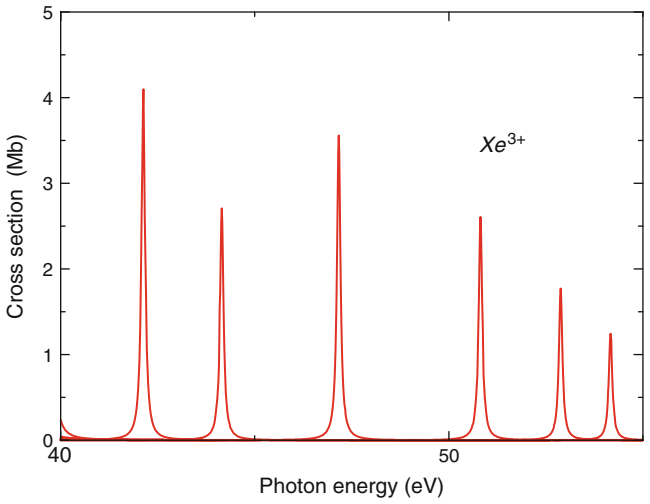

Fig. 2.81_Xe^{3+}_a3 Quasi cross section of discrete level excitation for Xe^{3+} ion

Figure 2.82_Xe^{3+}_d1 presents dipole angular anisotropy parameter of $5p$ "up" electrons, $4d$ "up" and $4d$ "down" electrons. The oscillating shapes of all parameters energy dependence are very similar.

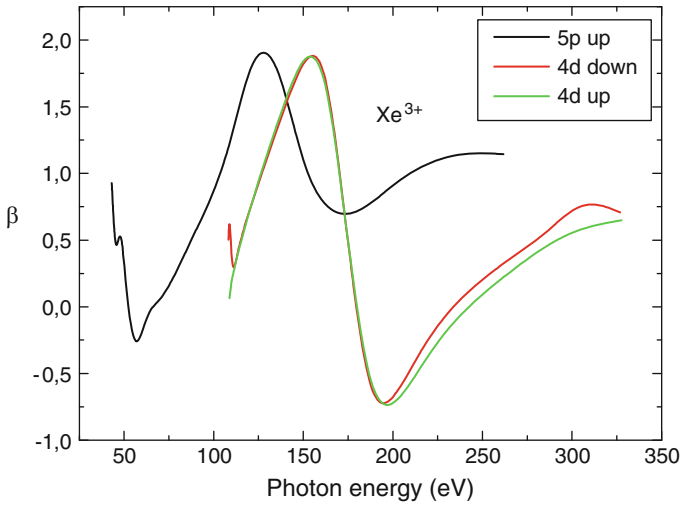

Fig. 2.82_Xe^{3+}_d1 Dipole anisotropy parameter of $5p$ "up"- and $4d$ "up" and "down"-electrons for Xe^{3+} ion

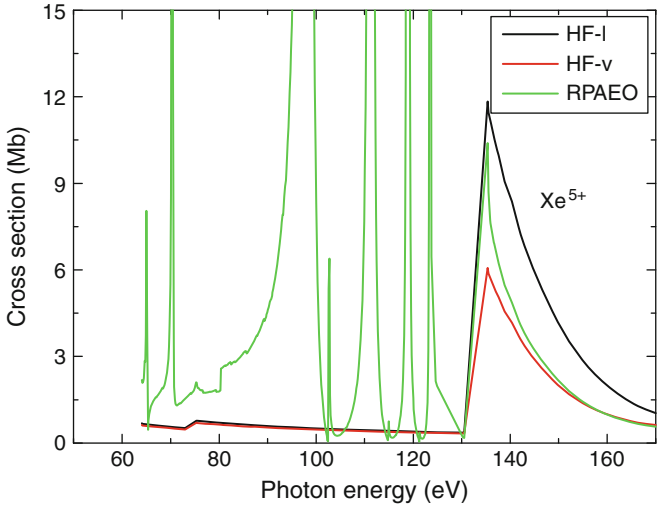

Fig. 2.83_Xe^{5+}_a1 Total photoionization cross section of Xe^{5+} ion in HF-l, HF-v, and RPAEO

Figures 2.83_Xe^{5+}_a1–2.86_Xe^{5+}_d1 (Xe^{5+}) contain results of calculations for Xe^{5+} ion: ($Z = 54$) $4d^{10}5s^25p^1$.

Figure 2.83_Xe^{5+}_a1 presents total cross-section of excitation to discrete levels of ion Xe^{5+} in HF and RPAEO. It is seen that Giant resonance is "entirely eaten" by discrete excitations.

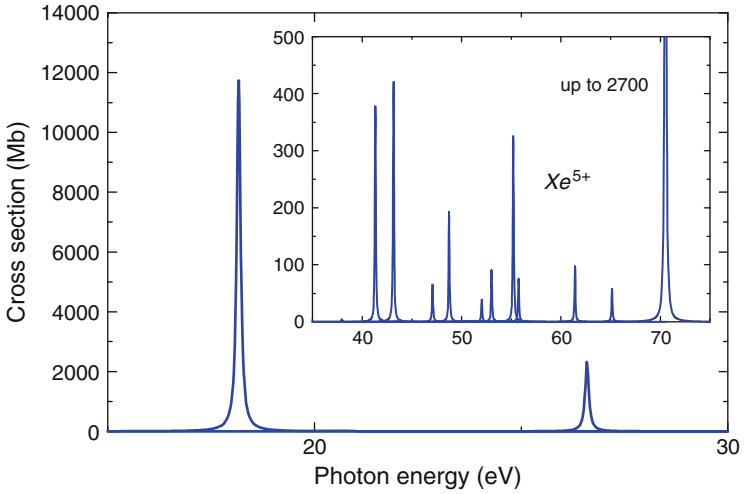

Fig. 2.84_Xe^{5+}_a2 Quasi cross section of discrete level excitation for Xe^{5+} ion in low energy field

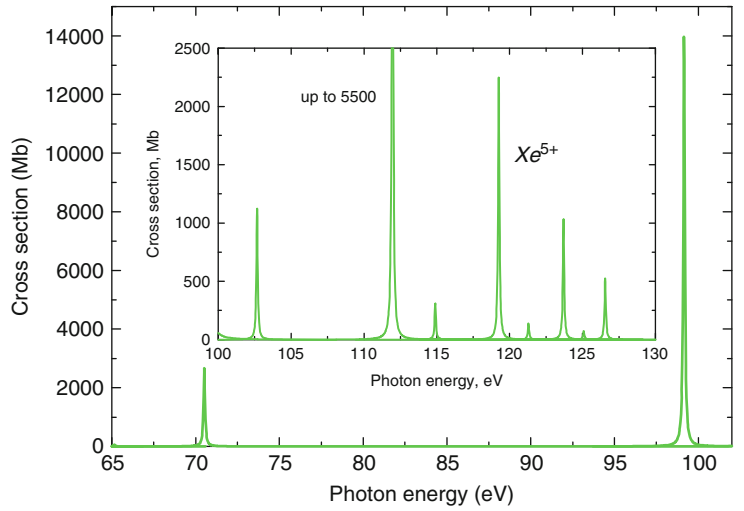

Fig. 2.85_Xe^{5+}_a3 Quasi cross section of discrete level excitation for Xe^{5+} ion

Figure 2.84_Xe^{5+}_a2 depicts quasi cross-section of excitation to discrete levels of ion Xe^{5+} in HF and RPAEO at $\omega < 30$ eV. On the insert quasi cross-section are presented for $(35 < \omega < 75)$ eV.

Figure 2.85_Xe^{5+}_a3 shows quasi cross-section of discrete excitations of Xe^{5+} in RPAEO at $65 < \omega < 130$ eV.

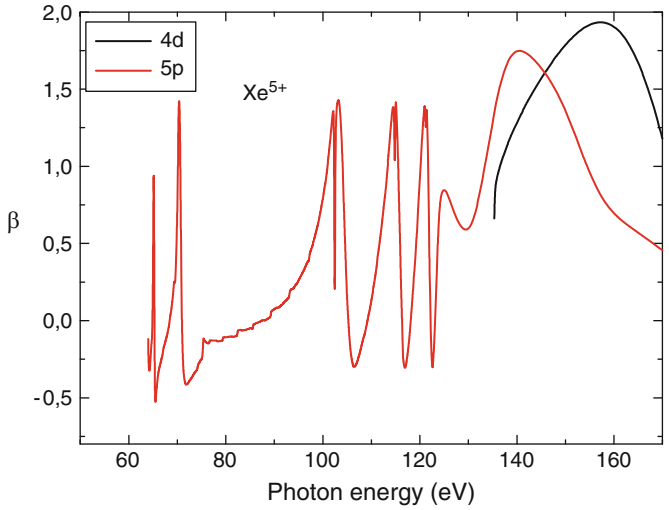

Fig. 2.86_Xe^{5+}_d1 Dipole anisotropy parameter of $5p$-, $4d$-electrons for Xe^{5+} ion in RPAE

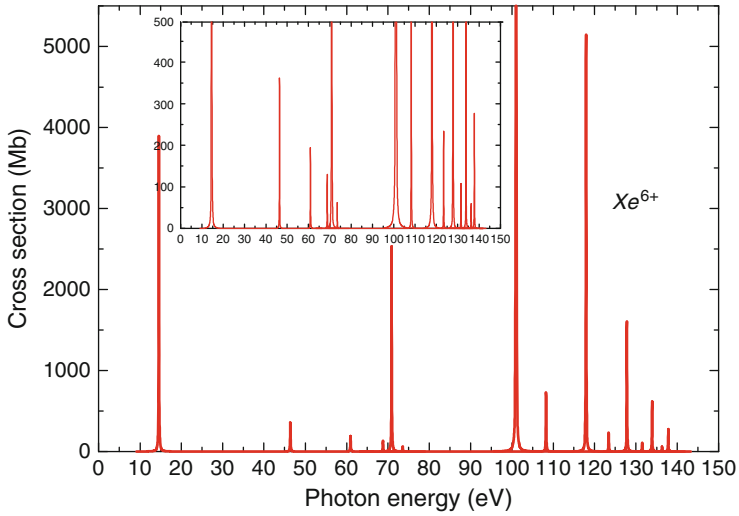

Fig. 2.87_Xe^{6+}_a1 Quasi cross section of discrete level excitation for Xe^{6+} ion

Figure 2.86_Xe^{5+}_d1 collects results on dipole angular anisotropy parameter of $5p$- and $4d$ electrons in RPAE. The influence of discrete excitations is large.

Figures 2.87_Xe^{6+}_a1 and 2.88_Xe^{6+}_d1 (Xe^{6+}) contain results of calculations for Xe^{6+} ion: $(Z = 54)\ 4d^{10}5s^2$.

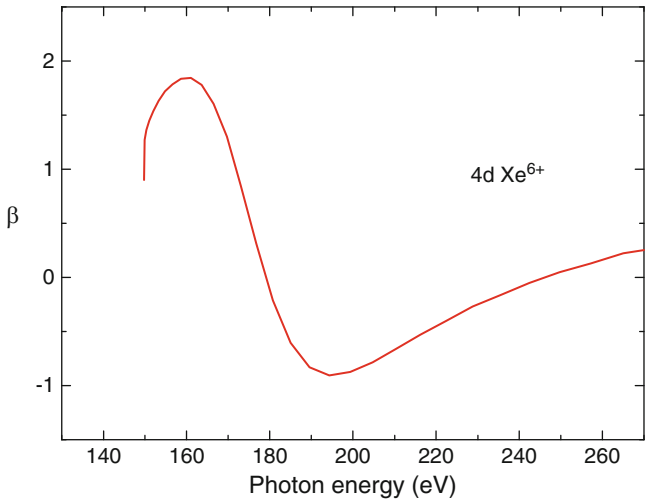

Fig. 2.88_Xe^{6+}_d1 Dipole anisotropy parameter of $4d$-electrons for Xe^{6+} ion in RPAE

Figure 2.87_Xe^{6+}_a1 presents quasi cross-sections of discrete excitation of Xe^{6+} ion in RPAE.

Figure 2.88_Xe^{6+}_d1 shows dipole angular anisotropy parameter of $4d$-electrons.

Table 2.1 includes calculated values of oscillator strengths in HF-l, HF-v, $f^{l,v}_{nl-n'l'}$, and $F^{l,v}_{nl-n'l'}$ in RPAE for several lowest discrete levels of excitation and for each considered subshell of each atom investigated in this section. Theoretical transition energies in RPAE $\tilde{\omega}_{nl-n'l'}$ are also given in this table.

The results for length and velocity forms in RPAE coincide with very good accuracy. In He the role of correlations is small. It considerably increases already in Ne, becoming bigger on the way to Xe. The biggest is the oscillator strength of the outer subshell np–$(n+1)$, s transition that dominates over the first p–d excitation. This domination decreases on the way from Ne to Xe, where slightly bigger is the outermost excitation $5p \rightarrow 5d$. The subvalent subshell excitations ns–$(n+1)$, p have oscillator strengths that are about 30 times smaller than that of np–$(n+1)$, s. For deeper subshells, the oscillator strengths are in general decreasing with decrease in principal quantum number of the exited electron.

Table 2.1 Oscillator strengths and transition energies of Noble gases He, Ne, Ar, and Xe

Transition	ω (Ry)	HF-l	HF-v	RPAE-l	RPAE-v
He					
$1s$–$2p$	1.59394	0.2602E+00	0.2295E+00	0.2518E+00	0.2517E+00
$1s$–$3p$	1.72721	0.7320E−01	0.6416E−01	0.7032E−01	0.7027E−01
$1s$–$4p$	1.77443	0.3033E−01	0.2653E−01	0.2902E−01	0.2900E−01
$1s$–$5p$	1.79643	0.1541E−01	0.1347E−01	0.1470E−01	0.1469E−01
$1s$–$6p$	1.80843	0.8894E−02	0.7768E−02	0.8438E−02	0.8432E−02
He*					
$2s$–$2p$ up	0.0846	0.5670E+00	0.6280E+00	0.5574E+00	0.5577E+00
$2s$–$3p$ up	0.2331	0.5603E−01	0.4979E−01	0.5904E−01	0.5890E−01
$2s$–$4p$ up	0.2842	0.2309E−01	0.2072E−01	0.2392E−01	0.2387E−01
$1s$–$2p$ up	2.8797	0.3241E+00	0.3348E+00	0.3355E+00	0.3333E+00
$1s$–$3p$ up	3.2953	0.5949E−01	0.5968E−01	0.5928E−01	0.5911E−01
$1s$–$4p$ up	3.3807	0.1583E−01	0.1585E−01	0.1578E−01	0.1574E−01
Ne					
$2p$–$3d$	1.58859	0.2328E−01	0.1789E−01	0.2193E−01	0.2194E−01
$2p$–$4d$	1.63787	0.1251E−01	0.9575E−02	0.1179E−01	0.1179E−01
$2p$–$5d$	1.66061	0.7009E−02	0.5354E−02	0.6622E−02	0.6625E−02
$2p$–$6d$	1.67250	0.4388E−02	0.3349E−02	0.4034E−02	0.4036E−02
$2p$–$3s$	1.34820	0.1564E+00	0.1438E+00	0.1653E+00	0.1651E+00
$2p$–$4s$	1.56349	0.2779E−01	0.2543E−01	0.2868E−01	0.2865E−01
$2p$–$5s$	1.62788	0.9917E−02	0.9062E−02	0.1029E−01	0.1028E−01
$2p$–$6s$	1.65564	0.4677E−02	0.4272E−02	0.4860E−02	0.4855E−02
$2s$–$3p$	3.64401	0.7524E−02	0.6553E−02	0.4604E−02	0.4634E−02
$2s$–$4p$	3.76087	0.2662E−02	0.2307E−02	0.1660E−02	0.1620E−02
$2s$–$5p$	3.80325	0.1211E−02	0.1048E−02	0.7639E−03	0.7373E−03
$2s$–$6p$	3.82339	0.6471E−03	0.5597E−03	0.4136E−03	0.3973E−03
$1s$–$3p$	65.27477	0.3269E−01	0.3127E−01	0.3231E−01	0.3220E−01
$1s$–$4p$	65.43138	0.6807E−02	0.6518E−02	0.6729E−02	0.6706E−02
$1s$–$5p$	65.48169	0.2660E−02	0.2548E−02	0.2629E−02	0.2620E−02
$1s$–$6p$	65.50458	0.1325E−02	0.1269E−02	0.1309E−02	0.1304E−02
Ar					
$3p$–$3d$	1.06774	0.1623E+00	0.9800E−01	0.1791E+00	0.1794E+00
$3p$–$4d$	1.11821	0.8250E−01	0.4911E−01	0.8865E−01	0.8877E−01
$3p$–$5d$	1.14137	0.4516E−01	0.2670E−01	0.4691E−01	0.4698E−01
$3p$–$6d$	1.15387	0.2700E−01	0.1591E−01	0.2418E−01	0.2422E−01
$3p$–$4s$	0.89669	0.2964E+00	0.2653E+00	0.3157E+00	0.3140E+00
$3p$–$5s$	1.06268	0.5571E−01	0.4956E−01	0.3734E−01	0.3713E−01
$3p$–$6s$	1.11636	0.2058E−01	0.1828E−01	0.1409E−01	0.1402E−01
$3p$–$7s$	1.14048	0.9929E−02	0.8815E−02	0.7130E−02	0.7099E−02
$3s$–$4p$	2.37042	0.1732E−02	0.9047E−03	0.7129E−02	0.7591E−02
$3s$–$5p$	2.46581	0.8093E−03	0.4533E−03	0.1822E−02	0.1873E−02
$3s$–$6p$	2.50217	0.4073E−03	0.2326E−03	0.7397E−03	0.7496E−03
$3s$–7p	2.52000	0.2292E−03	0.1320E−03	0.3795E−03	0.3818E−03
$2p$–$3d$	18.97943	0.2152E+00	0.1858E+00	0.2138E+00	0.2115E+00
$2p$–$4d$	19.05481	0.5945E−01	0.5135E−01	0.5691E−01	0.5628E−01

Table 2.1 (continued)

$2p$–$5d$	19.09018	0.2317E−01	0.2002E−01	0.2192E−01	0.2168E−01
$2p$–$6d$	19.10801	0.1157E−01	0.1000E−01	0.1074E−01	0.1062E−01
$2p$–$4s$	18.80062	0.1141E−01	0.1072E−01	0.2626E−01	0.2630E−01
$2p$–$5s$	19.01184	0.2136E−02	0.2004E−02	0.9772E−03	0.9934E−03
$2p$–$6s$	19.07273	0.8000E−03	0.7507E−03	0.5954E−03	0.6017E−03
$2p$–$7s$	19.09917	0.3873E−03	0.3634E−03	0.2720E−03	0.2750E−03
$2s$–$4p$	24.42482	0.1864E−01	0.1778E−01	0.1269E−01	0.1296E−01
$2s$–$5p$	24.54571	0.4411E−02	0.4211E−02	0.3046E−02	0.3108E−02
$2s$–$6p$	24.58765	0.1820E−02	0.1739E−02	0.1265E−02	0.1291E−02
$2s$–$7p$	24.60747	0.9345E−03	0.8926E−03	0.6559E−03	0.6691E−03
$1s$–$4p$	236.97464	0.8910E−02	0.8656E−02	0.8929E−02	0.8740E−02
$1s$–$5p$	237.11650	0.1677E−02	0.1629E−02	0.1681E−02	0.1645E−02
$1s$–$6p$	237.16181	0.6644E−03	0.6457E−03	0.6661E−03	0.6520E−03
$1s$–$7p$	237.18276	0.3348E−03	0.3254E−03	0.3356E−03	0.3285E−03
Kr					
$4p$–$4d$	0.93461	0.2672E+00	0.1530E+00	0.2614E+00	0.2607E+00
$4p$–$5d$	0.98482	0.1316E+00	0.7412E−01	0.1263E+00	0.1258E+00
$4p$–$6d$	1.00784	0.7115E−01	0.3979E−01	0.6358E−01	0.6329E−01
$4p$–$5s$	0.77984	0.3752E+00	0.3382E+00	0.3576E+00	0.3454E+00
$4p$–$6s$	0.93478	0.7049E−01	0.6319E−01	0.6592E−01	0.6463E−01
$4p$–$7s$	0.98501	0.2621E−01	0.2346E−01	0.2351E−01	0.2313E−01
$4s$–$5p$	2.13162	0.8616E−04	0.6070E−05	0.1164E−01	0.1130E−01
$4s$–$6p$	2.22055	0.1115E−03	0.9698E−05	0.3331E−02	0.3063E−02
$4s$–$7p$	2.25501	0.6989E−04	0.1013E−04	0.1436E−02	0.1290E−02
$4s$–$8p$	2.27208	0.4316E−04	0.7372E−05	0.7596E−03	0.6737E−03
$3d$–$4f$	7.58784	0.1185E−04	0.7287E−05	0.8819E−05	0.8829E−05
$3d$–$5f$	7.61038	0.1016E−04	0.6287E−05	0.7693E−05	0.7704E−05
$3d$–$6f$	7.62262	0.7380E−05	0.4580E−05	0.5802E−05	0.5815E−05
$3d$–$7f$	7.62993	0.5332E−05	0.3315E−05	0.4149E−05	0.4160E−05
$3d$–$5p$	7.44879	0.2891E−01	0.2543E−01	.2954E−01	.3009E−01
$3d$–$6p$	7.55727	0.7330E−02	0.6455E−02	0.7401E−02	0.7541E−02
$3d$–$7p$	7.59615	0.3089E−02	0.2721E−02	0.3100E−02	0.3159E−02
$3d$–$8p$	7.61483	0.1605E−02	0.1414E−02	0.1599E−02	0.1629E−02
$3p$–$5s$	16.34499	0.2237E−01	0.1905E−01	0.2177E−01	0.2184E−01
$3p$–$6s$	16.53819	0.4259E−02	0.3629E−02	0.4639E−02	0.4650E−02
$3p$–$7s$	16.59539	0.1620E−02	0.1380E−02	0.1755E−02	0.1759E−02
$3p$–$8s$	16.62057	0.7922E−03	0.6751E−03	0.8676E−03	0.8696E−03
$3p$–$4d$	16.50224	0.1891E−01	0.1757E−01	0.1621E−01	0.1593E−01
$3p$–$5d$	16.57873	0.5049E−02	0.4699E−02	0.4448E−02	0.4369E−02
$3p$–$6d$	16.61230	0.2083E−02	0.1940E−02	0.1862E−02	0.1828E−02
$3p$–$7d$	16.62926	0.1075E−02	0.1001E−02	0.9958E−03	0.9782E−03
$3s$–$5p$	21.49772	0.9903E−02	0.8810E−02	0.8604E−02	0.8565E−02
$3s$–$6p$	21.60601	0.2535E−02	0.2257E−02	0.2169E−02	0.2173E−02
$3s$–$7p$	21.64486	0.1074E−02	0.9565E−03	0.9231E−03	0.9245E−03
$3s$–$8p$	21.66353	0.5594E−03	0.4981E−03	0.4840E−03	0.4848E−03

Table 2.1 (continued)

Xe					
$5p$–$5d$	0.79773	0.4839E+00	0.2526E+00	0.4471E+00	0.4365E+00
$5p$–$6d$	0.84979	0.2307E+00	0.1178E+00	0.2104E+00	0.2054E+00
$5p$–$7d$	0.87346	0.1235E+00	0.6251E−01	0.1055E+00	0.1031E+00
$5p$–$8d$	0.88620	0.7304E−01	0.3679E−01	0.5761E−01	0.5628E−01
$5p$–$6s$	0.67252	0.4185E+00	0.3713E+00	0.4293E+00	0.4302E+00
$5p$–$7s$	0.80825	0.8240E−01	0.7270E−01	0.1257E+00	0.1256E+00
$5p$–$8s$	0.85441	0.3130E−01	0.2757E−01	0.4654E−01	0.4657E−01
$5p$–$9s$	0.87585	0.1538E−01	0.1354E−01	0.2213E−01	0.2217E−01
$5s$–$6p$	1.72627	0.1958E−03	0.2585E−05	0.1161E−01	0.9905E−02
$5s$–$7p$	1.80767	0.1877E−03	0.1487E−04	0.2730E−02	0.2414E−02
$5s$–$8p$	1.83993	0.1134E−03	0.1430E−04	0.1055E−02	0.9637E−03
$5s$–$9p$	1.85611	0.6936E−04	0.1026E−04	0.5187E−03	0.4843E−03
$4d$–$4f$	5.49297	0.2426E−03	0.1350E−03	0.2112E−03	0.2125E−03
$4d$–$5f$	5.51557	0.2122E−03	0.1187E−03	0.1894E−03	0.1906E−03
$4d$–$6f$	5.52785	0.1557E−03	0.8729E−04	0.1455E−03	0.1464E−03
$4d$–$7f$	5.53526	0.1117E−03	0.6272E−04	0.1019E−03	0.1026E−03
$4d$–$6p$	5.37156	0.5590E−01	0.4888E−01	0.4834E−01	0.4769E−01
$4d$–$7p$	5.46825	0.1505E−01	0.1317E−01	0.1246E−01	0.1229E−01
$4d$–$8p$	5.50404	0.6493E−02	0.5685E−02	0.5267E−02	0.5200E−02
$4d$–$9p$	5.52152	0.3420E−02	0.2995E−02	0.2726E−02	0.2692E−02
$4p$–$5d$	11.82496	0.2952E−02	0.2346E−02	0.1135E−02	0.1556E−02
$4p$–$6d$	11.92950	0.4634E−03	0.3754E−03	0.1154E−03	0.1665E−03
$4p$–$7d$	11.96523	0.1963E−03	0.1599E−03	0.3875E−04	0.5783E−04
$4p$–$8d$	11.98267	0.1034E−03	0.8443E−04	0.1555E−04	0.2438E−04
$4p$–$6s$	11.73533	0.3641E−01	0.2972E−01	0.2727E−01	0.2702E−01
$4p$–$7s$	11.90158	0.7294E−02	0.5962E−02	0.5355E−02	0.5280E−02
$4p$–$8s$	11.95310	0.2847E−02	0.2328E−02	0.2094E−02	0.2063E−02
$4p$–$9s$	11.97631	0.1414E−02	0.1156E−02	0.1040E−02	0.1024E−02
$4s$–$6p$	15.52875	0.8124E−02	0.6890E−02	0.5534E−02	0.5357E−02
$4s$–$7p$	15.62543	0.2204E−02	0.1870E−02	0.1527E−02	0.1478E−02
$4s$–$8p$	15.66121	0.9561E−03	0.8113E−03	0.6680E−03	0.6467E−03
$4s$–$9p$	15.67870	0.5051E−03	0.4286E−03	0.3561E−03	0.3447E−03
$3d$–$4f$	52.17514	0.1255E−03	0.1092E−03	0.1197E−03	0.1165E−03
$3d$–$5f$	52.19768	0.1233E−03	0.1072E−03	0.1171E−03	0.1140E−03
$3d$–$6f$	52.20994	0.9661E−04	0.8399E−04	0.9074E−04	0.8835E−04
$3d$–$7f$	52.21733	0.7219E−04	0.6276E−04	0.6820E−04	0.6641E−04
$3d$–$6p$	52.04121	0.3079E−02	0.2916E−02	0.5201E−02	0.5148E−02
$3d$–$7p$	52.14716	0.7333E−03	0.6945E−03	0.1302E−02	0.1288E−02
$3d$–$8p$	52.18475	0.3089E−03	0.2926E−03	0.5618E−03	0.5556E−03
$3d$–$9p$	52.20288	0.1609E−03	0.1524E−03	0.2959E−03	0.2927E−03

2.3 Atoms and Ions of Group I Elements of the Periodic Table

In this section, we present our results for outer and intermediate subshells of atoms and some ions of elements that belong to the first group of the periodic table, namely Li ($Z = 3$) $1s^2\ 2s\ \uparrow$; Na ($Z = 11$) $1s^2 2s^2\ 2p^6\ 3s\ \uparrow$; K ($Z = 19$) $2s^2\ 2p^6\ 3s^2\ 3p^6\ 4s\ \uparrow$; Cu ($Z = 29$) $2p^6\ 3s^2\ 3p^6\ 3d^{10}\ 4s\ \uparrow$; Rb ($Z = 37$) $3p^6 3d^{10}\ 4s^2\ 4p^6 5s\ \uparrow$; Ag ($Z = 47$) $3d^{10}\ 4s^2\ 4p^6\ 4d^{10} 5\ s\ \uparrow$; Cs ($Z = 55$) $3d^{10}\ 4s^2\ 4p^6\ 4d^{10}\ 5s^2\ 5p^6 6\ s\ \uparrow$, Cs* $4d^{10}\ 5s^2\ 5p^6 7s(8s, 6d)\ \uparrow$ and some ions $Li^+\ 1s^2$; $Li^- 1s^2 2s^2$, $Na^+\ 1s^2 2s^2 2p^6$, $Na^-\ 1s^2 2s^2 2p^6 3s^2$; $K^- 2s^2 2p^6 3s^2 3p^6 4s^2$; $K^+ 2s^2 2p^6 3s^2 3p^6$, $Cu^+\ 2p^6\ 3s^2\ 3p^6\ 3d^{10}$, $Rb^+\ 3p^6 3d^{10}\ 4s^2\ 4p^6$, $Rb^- 3p^6 3d^{10}\ 4s^2\ 4p^6 5s^2$, $Ag^+\ 3d^{10}\ 4s^2\ 4p^6\ 4d^{10}$, $Cs^+\ 3d^{10}\ 4s^2\ 4p^6\ 4d^{10}\ 5s^2\ 5p^6$, $Cs^-\ 3d^{10}\ 4s^2\ 4p^6\ 4d^{10}\ 5s^2\ 5p^6 6s^2$. Here $\uparrow$ denotes spin "up" electrons for SP RPAE (see Sect. 1.10). Atoms of this group have one electron in outermost shell, i.e., a half-filled subshell that is why we consider them within the framework of SP RPAE (see Sect. 1.10).

Formulas, using which the data were obtained here, and notations on figures are the same as for noble gases in Sect. 2.1.

Figures 2.89_Li_a1 and 2.90_Li_e1 contain data on Li atom: ($Z = 3$) $1s^2\ 2s^1\ \uparrow$.

Figure 2.89_Li_a1 presents total photoionization cross-section $\sigma(\omega)$ of Li in HF-l, HF-v, and SP RPAE. Difference of the results in forms HF-l and HF-v is small, and almost negligible role of correlations is reflected in rather small distinction between results of HF and SP RPAE.

Figure 2.90_Li_e1 shows non-dipole angular anisotropy parameters $\gamma^{\mathrm{C}}_{1s}(\omega)$, $\gamma^{\mathrm{C}}_{2s}(\omega)$ for Li atom in HF and SP RPAE. A small maximum is seen on the curve

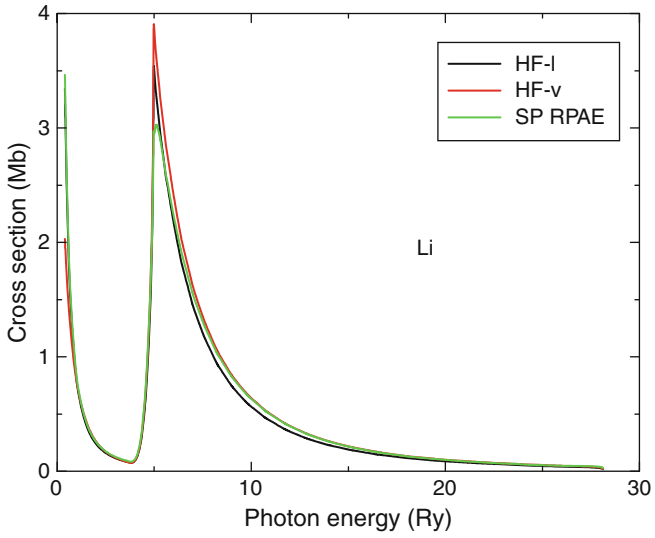

Fig. 2.89_Li_a1 Total photoionization cross section of Li atom in HF-l, HF-v, and SP RPAE

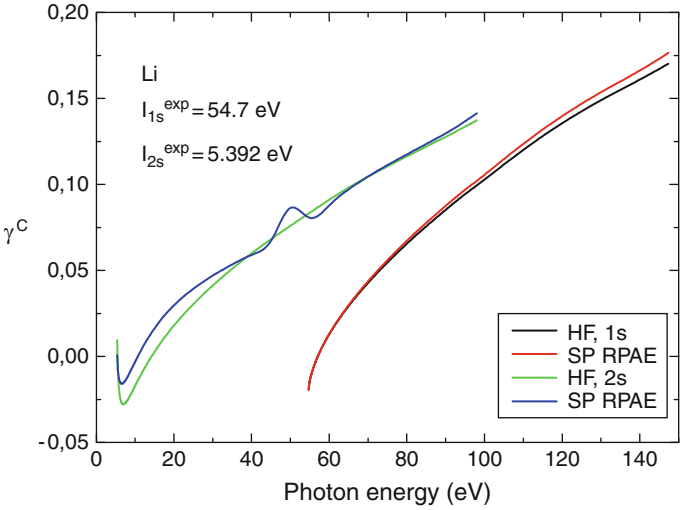

Fig. 2.90_Li_e1 Non-dipole anisotropy parameter of 1*s*- and 2*s*- electrons for Li atom in HF and SP RPAE

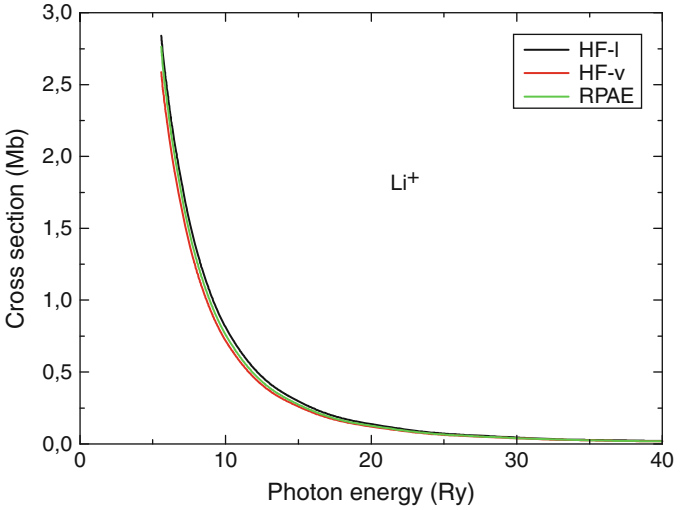

Fig. 2.91_Li^+_a1 Total photoionization cross section of Li^+ ion in HF-l, HF-v, and RPAE

$\gamma_{2s}^{C}(\omega)$ at 50 eV, which is the trace of influence of 1*s*-shell. There is also a small maximum near threshold on this curve.

Figure 2.91_Li^+ contains calculated data on Li^+ ion: $(Z = 3)\ 1s^2$.

Figure 2.91_Li^+_a1 presents total cross-section of photoionization of Li^+ ion in HF-l, HF-v, and RPAE. Since all curves merge in one, the role of correlations is small. The cross-section decreases significantly from the threshold.

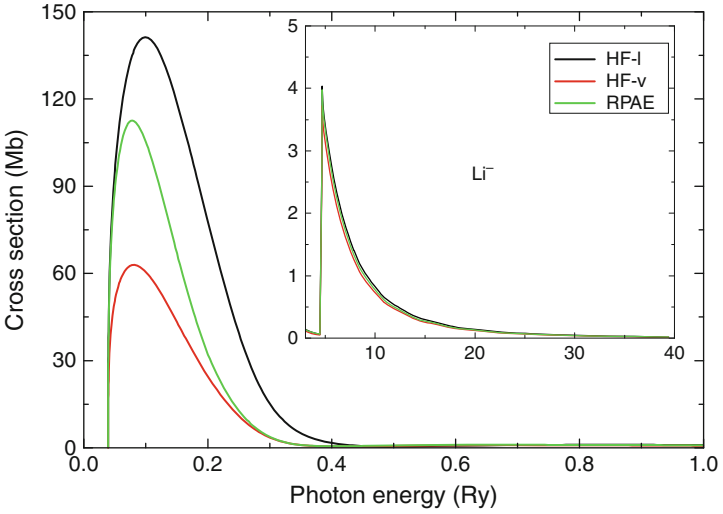

Fig. 2.92_Li⁻_a1 Total photodetachment cross section of Li^- ion in HF-l, HF-v, and RPAE

Figures 2.92_Li-_a1- 2.99_Li-_e6 (Li-) contains calculated data on Li^- ion: ($Z = 3$) $1s^2\ 2s^2$.

Figure 2.92_Li⁻_a1 shows total photodetachment cross-section of Li^- ion in HF-l, HF-v, and RPAE. Cross-section vanishes at the threshold reaching its maximum at 0.1–0.2 eV above threshold.

Figure 2.93_Li⁻_b1 presents photodetachment cross-section $\sigma_{1s}(\omega)$ of $1s$-electron for Li^- ion in GRPAE (see [2.38], [AICC]). The presence of one weakly bounded electron requires account for relaxation. It is remarkable that it is sufficient to obtain semi-quantitative agreement with experimental data. Experimental data are from [2.39, 2.40].

Figure 2.94_Li⁻_e1 includes angular anisotropy non-dipole parameters γ^{C}_{1s} and γ^{C}_{2s} for $1s$- and $2s$-electrons of Li^- ion in HF and RPAE. The variation of γ^{C}_{2s} near threshold is quite peculiar.

Figure 2.95_Li⁻_e2 shows angular anisotropy non-dipole parameters γ^{C}_{1s} and γ^{C}_{2s} of $1s$- and $2s$-electrons in Li^- in HF and GRPAE. The RPAE correlations result in decrease in parameter γ^{C}_{2s} in the vicinity of the resonance, which is quite near the threshold.

Figure 2.96_Li⁻_e3 compares non-dipole angular anisotropy parameters γ^{C}_{1s} of $1s$-electrons in Li^- ion (HF and GRPAE) and in Li atom (in HF as well as with rearrangement—in GRPAE frame).

Figure 2.97_Li⁻_e4 compares non-dipole angular anisotropy parameters γ^{C}_{1s} of $1s$-electrons Li^- ion (HF and RPAE) and Li atom (HF and SP RPAE). The curve for Li^- has a minimum near the Li$1s$ threshold.

Figure 2.98_Li⁻_e5 presents angular anisotropy non-dipole parameters γ^{C}_{2s} of $2s$-electrons for Li^- ion (HF and GRPAE) and Li atom (HF and SP GRPAE) with experimental thresholds. A clearly defined trace of $1s$-threshold is seen.

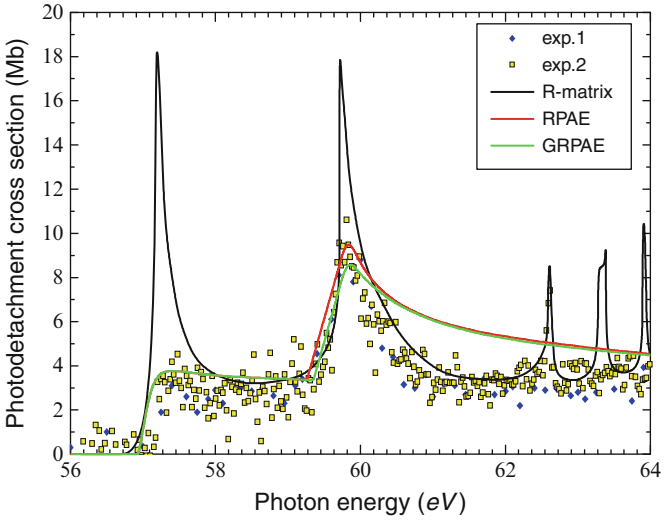

Fig. 2.93_Li⁻_b1 Photodetachment cross section of 1*s*-electrons for Li^- ion (see [2.38, AIChCh]). Experiment is from [2.39, 2.40]

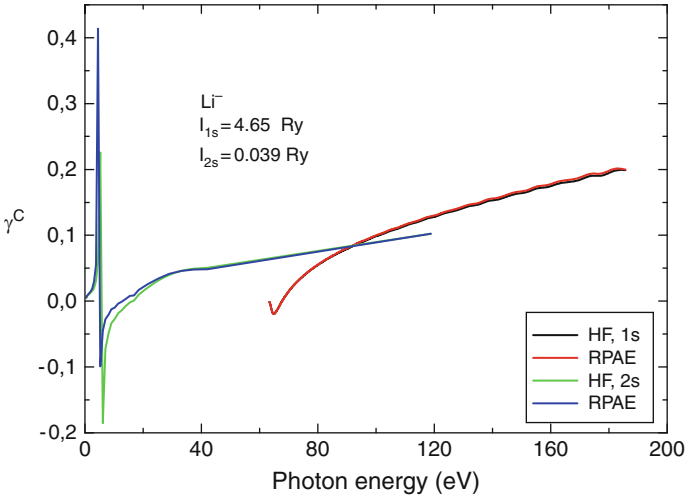

Fig. 2.94_Li⁻_e1 Non-dipole angular anisotropy parameter of 2*s*- and 1*s*-electrons for Li^- ion in HF and RPAE

Figure 2.99_Li⁻_e6 displays angular anisotropy non-dipole parameters γ_{2s}^{C} of 2*s*-electrons for Li^- ion (HF, RPAE) and Li atom (HF, SP RPAE). Theoretical threshold is used in calculations.

Figures 2.100_Na_a1 and 2.101_Na_d1 (Na) include all results of calculations for Na atom: $(Z = 11)\ 1s^2\ 2s^2\ 2p^6\ 3s\uparrow$.

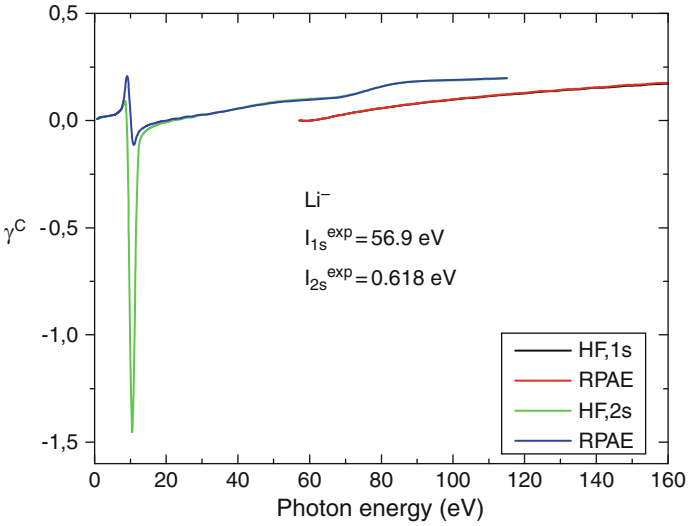

Fig. 2.95_Li⁻_e2 Non-dipole angular anisotropy parameter of Li^- ion with account of rearrangement in GRPAE

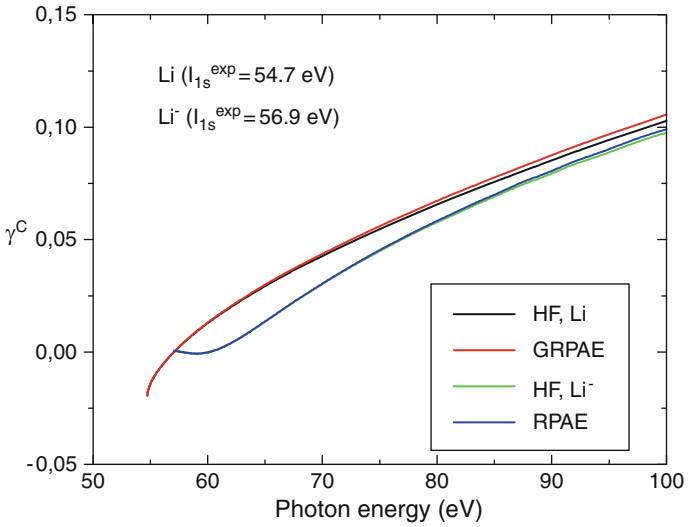

Fig. 2.96_Li⁻_e3 Non-dipole angular anisotropy parameter of 1s-electrons for Li^- ion (in HF and GRPAE) in comparison with the same for Li atom (in HF and GRPAE)

Figure 2.100_Na_a1 presents total photoionization cross-section of Na atom in HF-l, HF-v, and SP RPAE. Here correlations are taken into account in all dipole transitions $3s$–$n(\varepsilon)p$, $2p$–$n(\varepsilon)d$, $2p$–$n(\varepsilon)s$, $2s$–$n(\varepsilon)p$ and $1s$–$n(\varepsilon)p$. The role of $2p$–$n(\varepsilon)d$ is rather significant, but only at $\omega \leq 25$ Ry. Influence of other transitions

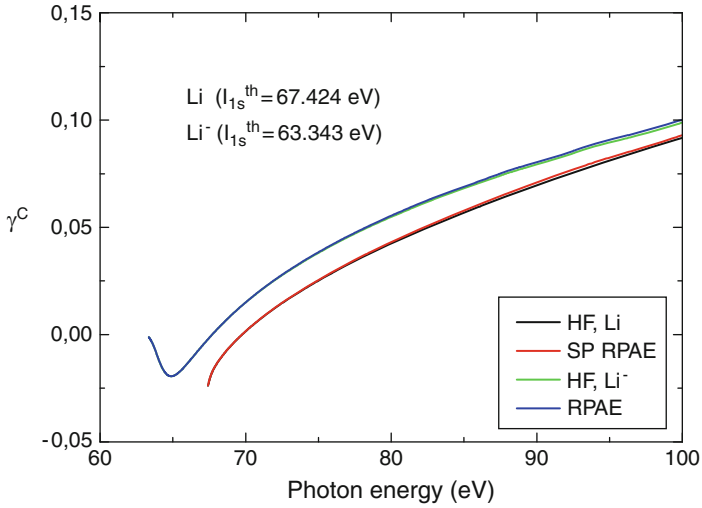

Fig. 2.97_Li⁻_e4 Non-dipole angular anisotropy parameter of 1*s*-electrons for Li^- ion (in HF and RPAE) in comparison with the same for Li atom (in HF and SP RPAE)

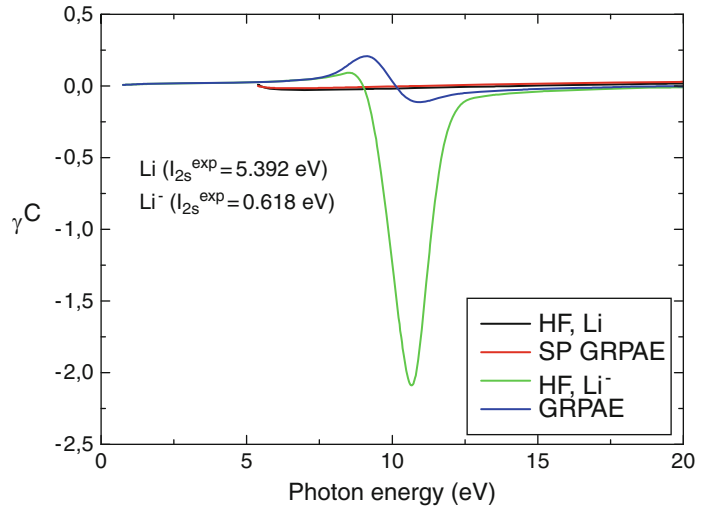

Fig. 2.98_Li⁻_e5 Non-dipole angular anisotropy parameter of 2*s*-electrons for Li^- ion (in HF and GRPAE) in comparison with the same for Li atom (in HF and SP GRPAE) with account of rearrangement

in this energy range is not essential with the only exception of appearance of resonance series $2s–n(\varepsilon)p$.

Figure 2.101_Na_d1 presents dipole angular anisotropy parameter $\beta_{2p}(\omega)$ for $2p$-electrons of Na atom in SP RPAE. There is a narrow maximum near threshold.

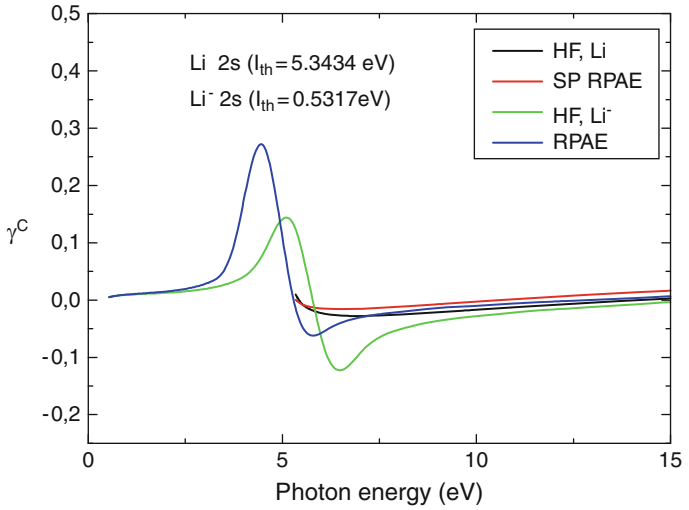

Fig. 2.99_Li$^-$_e6 Non-dipole angular anisotropy parameter of $2s$-electrons for Li^- ion (in HF and RPAE) in comparison with the same for Li atom (in HF and SP RPAE)

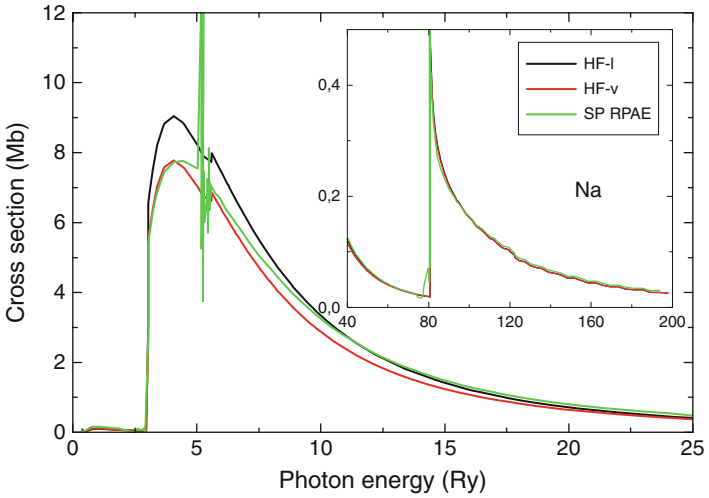

Fig. 2.100_Na_a1 Total photoionization cross section of Na atom in HF-l, HF-v, and SP RPAE

Figures 2.102_Na^+_a1 and 2.103_Na^+_d1 (Na^+) include all results of calculations for Na^+ ion ($Z = 11$)$1s^2 2s^2 2p^6$.

Figure 2.102_Na^+_a1 presents total photoionization cross-section of Na^+ ion in HF-l, HF-v, and RPAE. There is a pronounced maximum at the $1s$-threshold.

Figure 2.103_Na^+_d1 presents angular anisotropy dipole parameter $\beta_{2p}(\omega)$ of $2p$ electrons for Na^+ ion in RPAE.

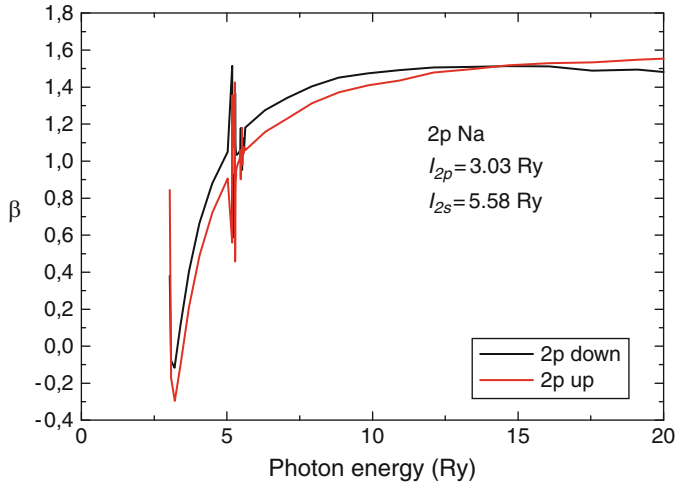

Fig. 2.101_Na_d1 Dipole anisotropy parameter of $2p$-electrons for Na atom in SP RPAE

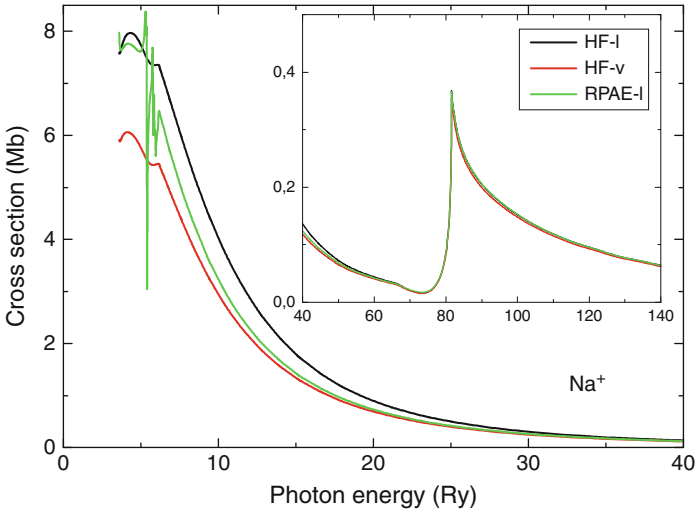

Fig. 2.102_Na^+_a1 Total photoionization cross section of Na^+ ion in HF-l, HF-v, and RPAE

Figures 2.104_Na^-_a1 and 2.105_Na^-_d1 (Na^-) include all results of calculations for Na^- ion: $Na^-(Z = 11)$ $1s^2\,2s^2\,2p^6 3s^2$.

Figure 2.104_Na^-_a1 presents total photoionization cross-section $\sigma(\omega)$ of Na^- ion in HF-l, HF-v, and RPAE. The role of electron correlations at small photon energies is large. Photoionization cross-section of $1s$-electrons is on the inner inset.

Figure 2.105_Na^-_d1 presents dipole angular anisotropy parameter $\beta_{2p}(\omega)$ of $2p$-electrons for Na^- ion in HF-l, HF-v, and RPAE. Near threshold there is a sharp maximum followed by a deep minimum.

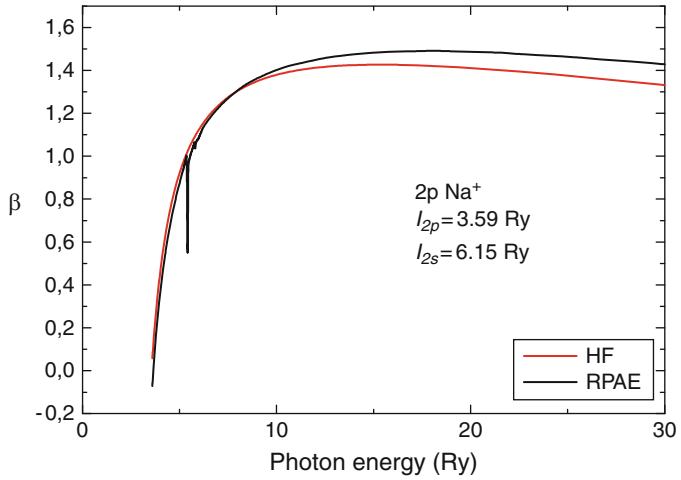

Fig. 2.103_Na$^+$_d1 Dipole anisotropy parameter of $2p$-electrons for Na^+ ion

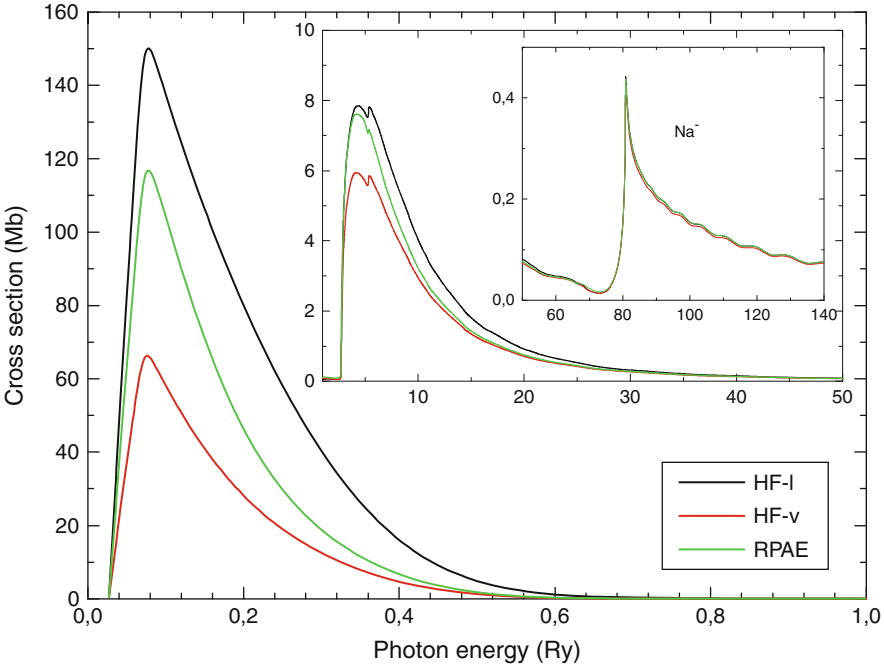

Fig. 2.104_Na$^-$_a1 Total photodetachment cross section of Na^- in HF-l, HF-v, and RPAE

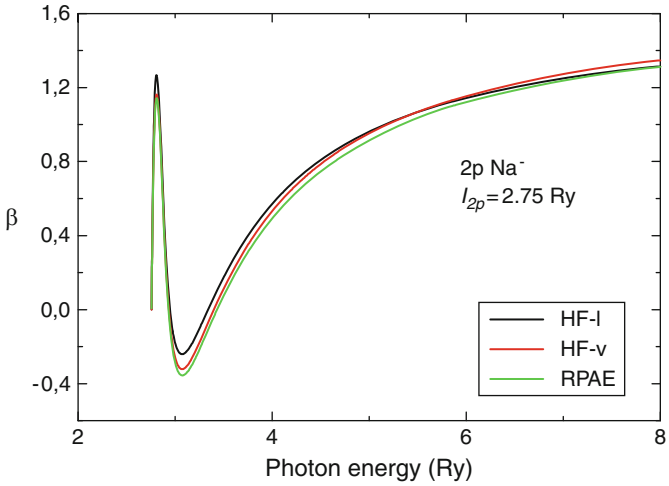

Fig. 2.105_Na$^-$_d1 Dipole angular anisotropy parameter of $2p$-electrons for Na^- ion in HF-l, HF-v, and RPAE

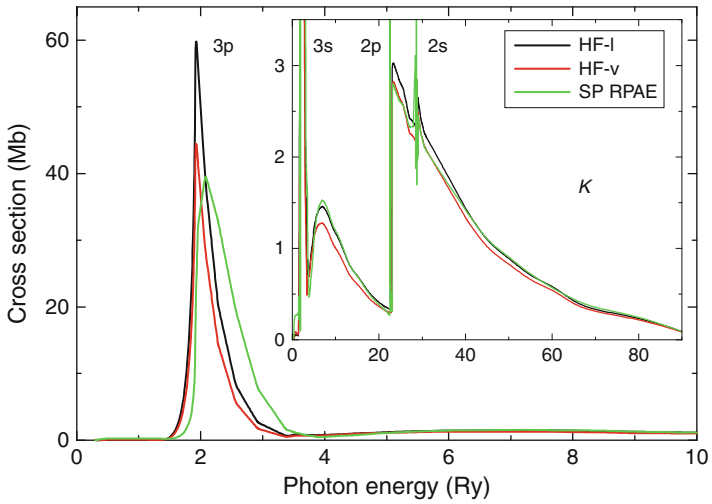

Fig. 2.106_K_a1 Total photoionization cross section of K atom in HF-l, HF-v, and SP RPAE

Figures 2.106_K_a1–2.110_KK^+Ar_f1 (K) include all results of calculations for K atom: $Z = 19, 2s^2 2p^6 3s^2 3p^6 4s \uparrow$.

Figure 2.106_K_a1 presents total cross-section $\sigma(\omega)$ of K atom in HF-l, HF-v, and SP RPAE. Maximum of $3p$ photoionization cross-section is seen on the figure and in inset there is another maximum at 7 Ry and a Cooper minimum before. The latter is due to change of sign of photoelectron amplitude in one-electron approximation.

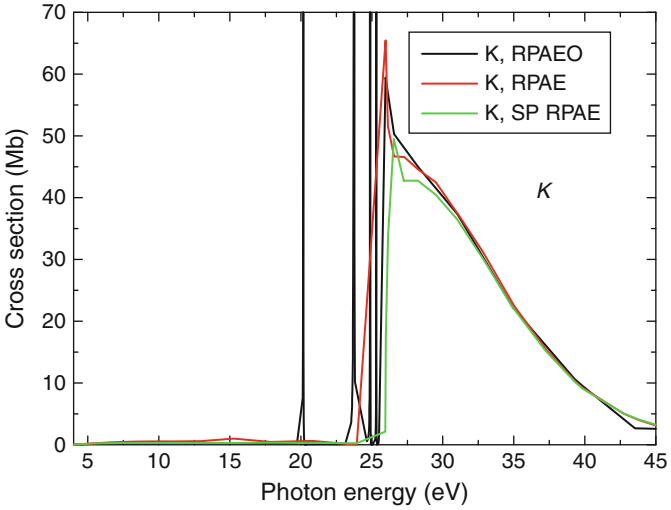

Fig. 2.107_K_a2 Total photoionization cross section of K in different approximations: RPAE for open shells (RPAEO), RPAE and SP RPAE

Figure 2.107_K_a2 compares total cross-sections of K atom, calculated in three various methods: RPAE for the open shells (RPAEO), RPAE, and SP RPAE. The agreement is quite satisfactory.

Figure 2.108_KK$^-$K$^+$_a3 displays photoionization cross-sections of K atom (SP RPAE) with the same data for K^- ion and K^+ ion (RPAE). There is a difference near the $2p$-threshold.

Figure 2.109_K_d1 shows dipole angular anisotropy parameter of $2p$- and $3p$-electrons for K atom.

Figure 2.110_KK$^+$Ar_f1 compares dipole angular anisotropy and spin polarization parameters $A_{3p1/2,3/2}$, $\alpha_{3p1/2,3/2}$, $\xi_{3p1/2,3/2}$ of K atom with Ar atom and K^+ ion in SP RPAE. While β_{3p} is similar for all three considered objects, a big difference is a typical feature for spin polarization parameters.

Figures 2.111_K$^+$_a1–2.113_K$^+$_d1 include all results of calculations for K^+ ion: $(Z = 19)\ 2s^2\ 2p^6\ 3s^2\ 3p^6$.

Figure 2.111_K$^+$_a1 shows total photoionization cross-section of K^+ in HF-l, HF-r, and RPAE. RPAE correlations are taken into account in all dipole transitions $3p$–$n(\varepsilon)d$, $3p$–$n(\varepsilon)s$, $3s$–$n(\varepsilon)p$, $2p$–$n(\varepsilon)d$, $2p$–$n(\varepsilon)s$, and $2s$–$n(\varepsilon)p$. The considered ω region is very broad, approximately up to 350 Ry. The role of the channel $3p$–$n(\varepsilon)d$ is great, but only for ω values close to a threshold of a $3p$-subshell. Influence of other transitions in this photon energy range is insignificant.

Figure 2.112_K$^+$_a2 shows a total photoionization cross-section of K^+ ion at small energies in RPAE. Experimental data are from [2.41, 2.42].

Figure 2.113_K$^+$_d1 shows angular anisotropy parameter $\beta_{2p,3p}$ of $3p$- and $2p$-subshells for K^+ ion in HF and RPAE. Parameter β_{3p} has a narrow pronounced

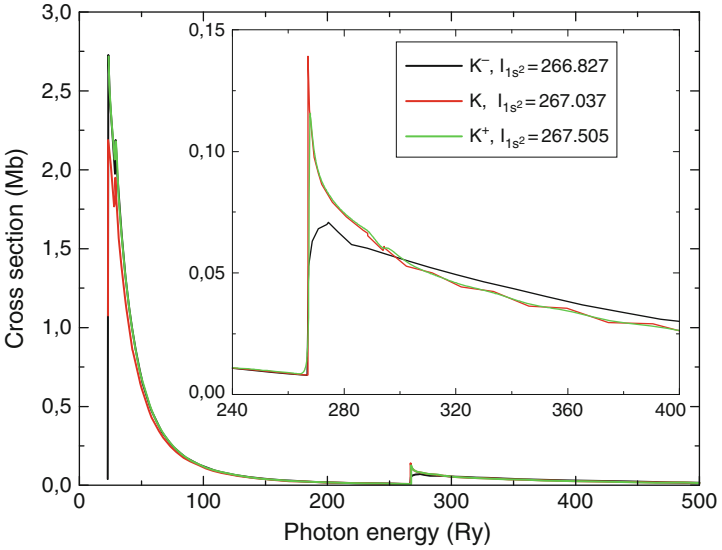

Fig. 2.108_KK$^-$K$^+$_a3 Photoionization cross section of K atom (in SP RPAE) in comparison with the same of K^+ and K^- ions (in RPAE)

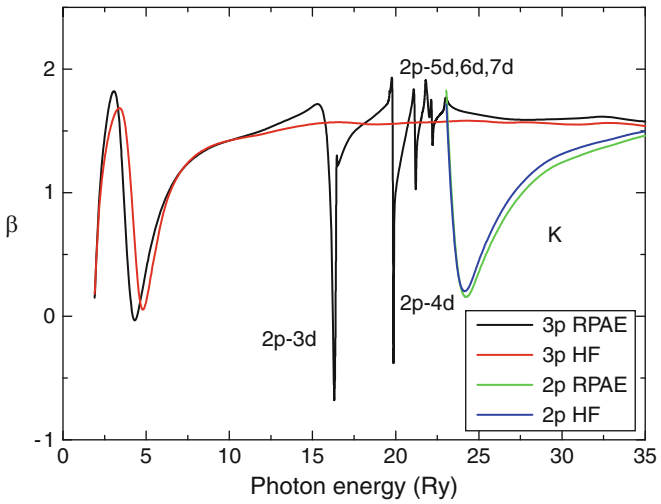

Fig. 2.109_K_d1 Dipole angular anisotropy parameter of $2p$- and $3p$-electrons for K atom in HF and RPAE (length forms)

maximum followed by a deep minimum. At $\omega = 300$ eV parameter β_{3p} has a maximum caused by the influence of $2p$-electrons.

Figures 2.114_K$^-$_a1–2.116_K$^-$_d1 include all results of calculations for K^- ion: $(Z = 19)\ 2s^2\ 2p^6\ 3s^2 3p^6\ 4s^2$.

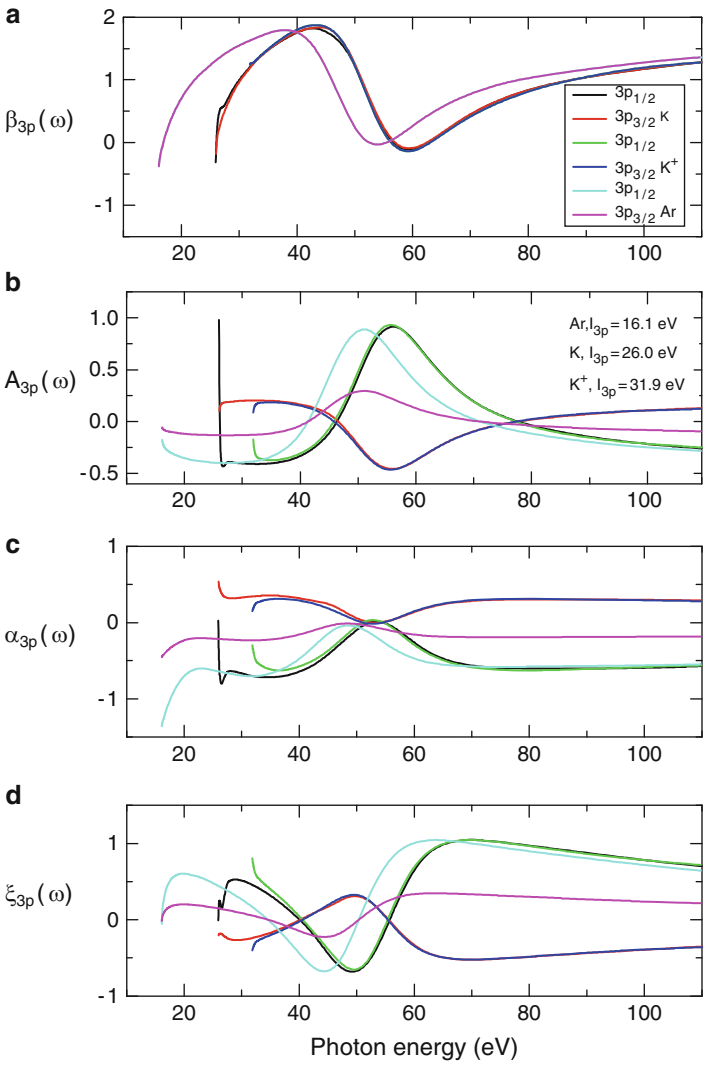

Fig. 2.110_KK$^+$Ar_f1 Dipole parameters of $3p$-electrons for K atom in comparison with the same of Ar atom and K^+ ion in SP RPAE: (**a**) angular anisotropy $\beta_{3p}(\omega)$; (**b**) spin polarization: $A_{3p}(\omega)$, (**c**) $\alpha_{3p}(\omega)$, and (**d**) $\xi_{3p}(\omega)$

Figure 2.114_K$^-$_a1 presents total photoionization cross-section $\sigma(\omega)$ of K^- ion in HF-l, HF-v, and RPAE. The role of correlations is significant. Cross-section is zero at the threshold, but very soon reaches a maximum.

Figure 2.115_K$^-$ArCl$^-$_a2 compares the results of calculations of photodetachment cross-sections of K^- ion (HF and SP RPAE), Ar and Cl^- (RPAE). The differences between three curves are large from threshold to 3.5 Ry, but they are essential also further.

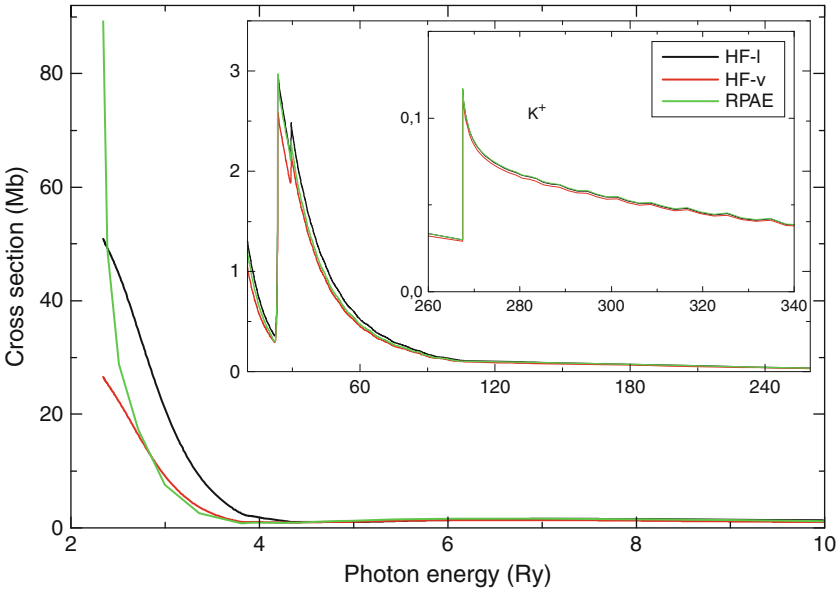

Fig. 2.111_K$^+$_a1 Total photoionization cross section of K^+ ion in HF-l, HF-v, and RPAE

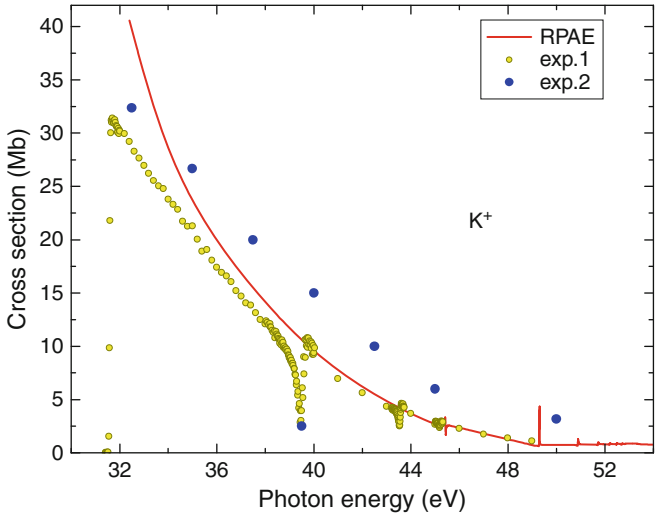

Fig. 2.112_K$^+$_a2 Total photoionization cross section of K^+ ion at small energies in RPAE. Experiment is from [2.41, 2.42]

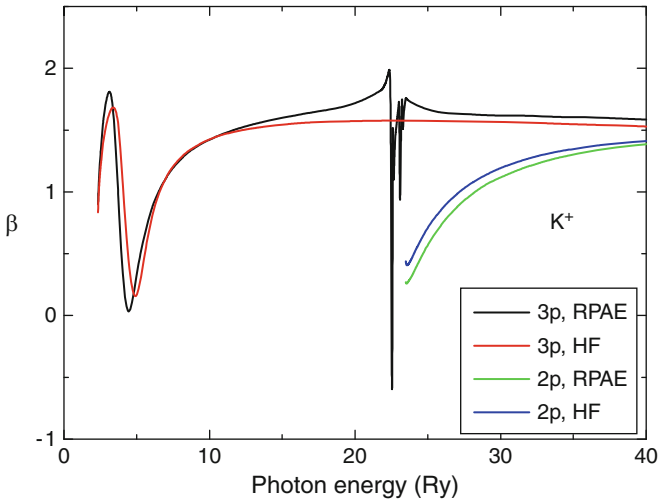

Fig. 2.113_K$^+$_d1 Dipole anisotropy parameter of $2p$- and $3p$-electrons for K^+ ion in HF and RPAE (length form)

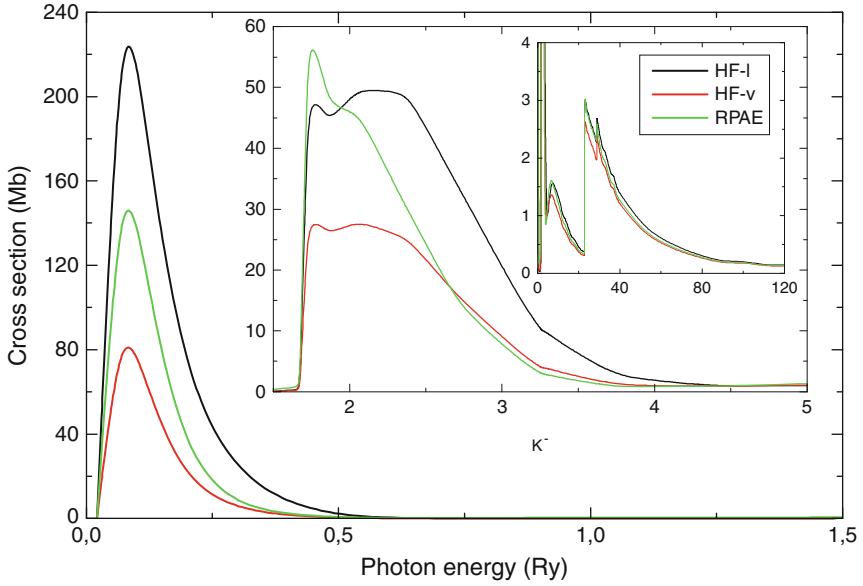

Fig. 2.114_K$^-$_a1 Total photodetachment cross section of K^- ion in HF-l, HF-v, and RPAE

Figure 2.116_K$^-$_d1 presents the dipole angular anisotropy parameters $\beta_{2p,3p}$ of $3p$- and $2p$-subshells of K^- ion in HF and RPAE. Both parameters reach maximums near thresholds and then have relatively narrow minimums.

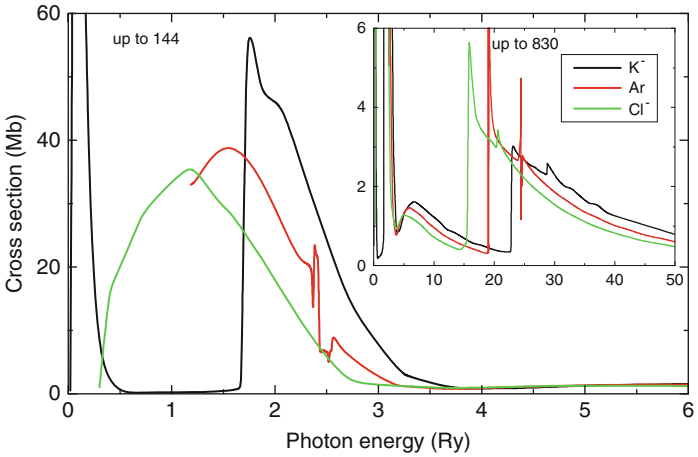

Fig. 2.115_K⁻ArCl⁻_a2 Photoionization cross section of K^- ion in comparison with the same of Ar atom and Cl^- ion

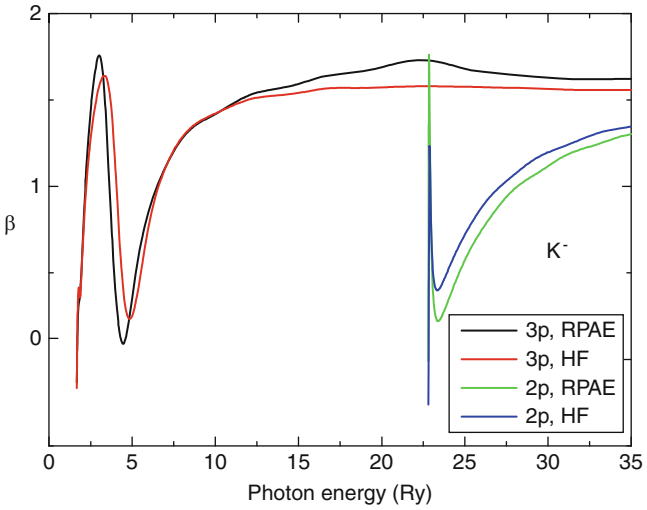

Fig. 2.116_K⁻_d1 Dipole angular anisotropy parameter of $2p$- and $3p$-electrons for K^- ion in HF and RPAE (length form)

Figures 2.117_Cu_a1 and 2.118_Cu_d1 include all results of calculations for Cu atom: $(Z = 29)\ 3s^2\ 3p^6 3d^{10}\ 4\,s\ \uparrow$.

Figure 2.117_Cu_a1 presents total photoionization cross-section of Cu atom in HF-l, HF-v, and SP RPAE. Discrete excitations of inner subshells are clearly seen.

Figure 2.118_Cu_d1 shows angular anisotropy parameters $\beta_{3d,3p}$ of $3d$- and $3p$-electrons for Cu atom in SP RPAE.

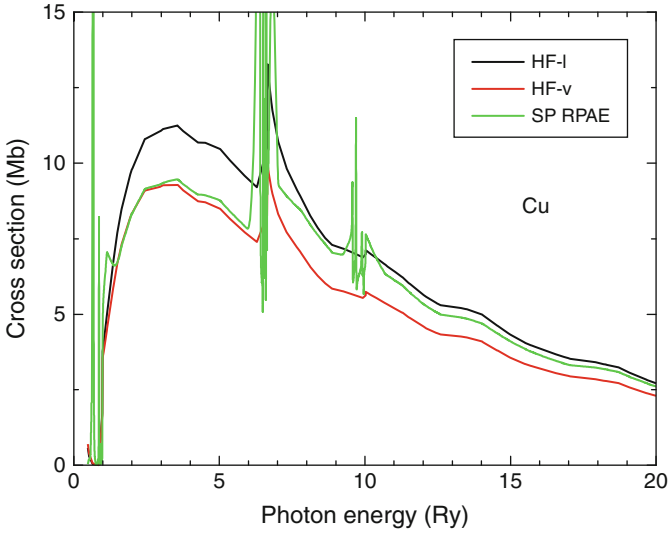

Fig. 2.117_Cu_a1 Total photoionization cross section of Cu atom in HF-l, HF-v, and SP RPAE

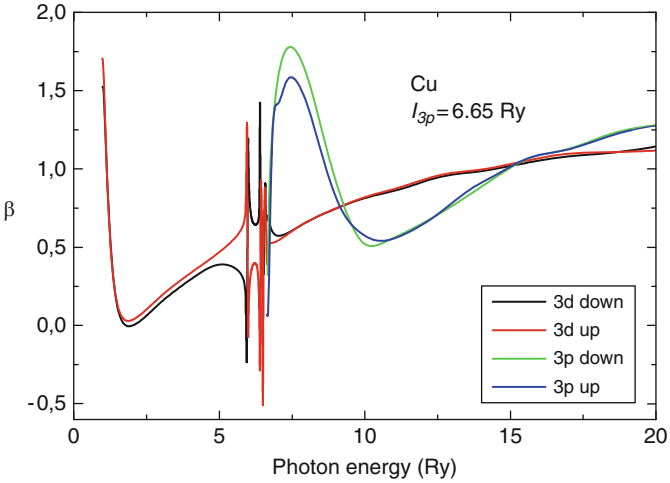

Fig. 2.118_Cu_d1 Dipole angular anisotropy parameter of $3d$- and $3p$-electrons of Cu atom

Figures 2.119_Cu$^+$_a1 and 2.120_Cu$^+$_d1 collects all results of calculations for Cu$^+$ ion: $(Z = 29)\ 3s^2\ 3p^6\ 3d^{10}$.

Figure 2.119_Cu$^+$_a1 presents total photoionization cross-section of Cu$^+$ ion in HF-l, HF-v, and RPAE.

Figure 2.120_Cu$^+$_d1 depicts dipole angular anisotropy parameters for $2p$-, $3p$- and $3d$-spin-polarized electrons of Cu$^+$ ion in SP RPAE. The curves $\beta_{3d\uparrow}$ and $\beta_{3d\downarrow}$

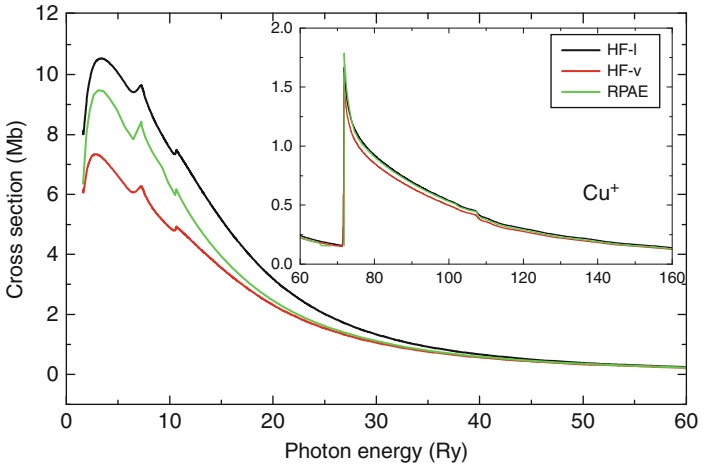

Fig. 2.119_Cu$^+$_a1 Total photoionization cross section of Cu$^+$ ion in HF-l, HF-v, and RPAE

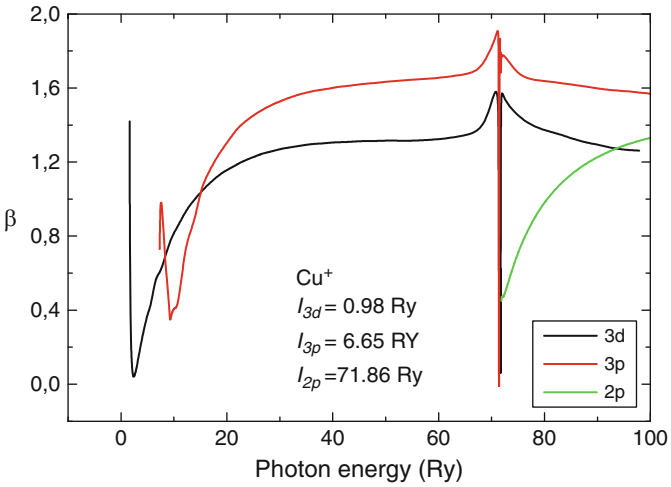

Fig. 2.120_Cu$^+$_d1 Dipole anisotropy parameter of $2p$-, $3p$-, $3d$-electrons Cu$^+$ ion

are characterized by minimums just above threshold and by strong variations near the $3p$-threshold.

Figures 2.121_Rb_a1–2.124_Rb_d2 include all results of calculations for Rb atom: $(Z = 37)\ 3d^{10}\ 4s^2\ 4p^6 5s\uparrow$.

Figure 2.121_Rb_a1 presents total photoionization cross-section of Rb atom in HF-l, HF-v, and SP RPAE. On the inset, the strong wide resonance in cross-section of $3d$-electrons is seen.

Figure 2.122_Rb_b1 shows Rb $3d$ photoionization cross-section in HF-l, HF-v, and SP GRPAE approximation.

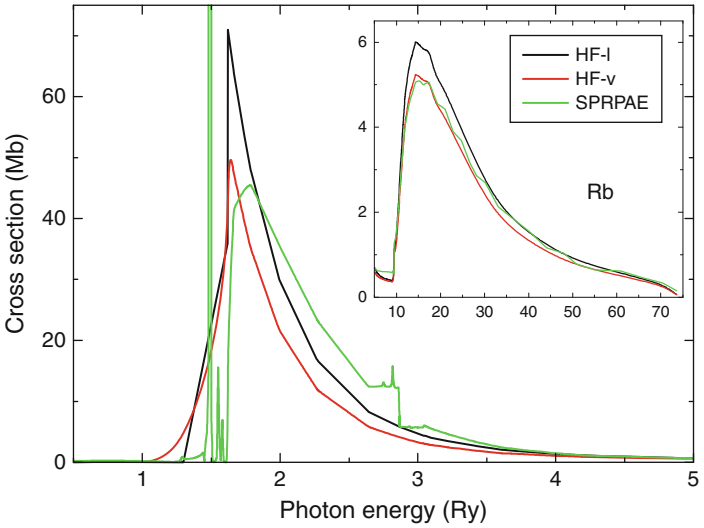

Fig. 2.121_Rb_a1 Total photoionization cross section of Rb atom in HF-l, HF-v, and SP RPAE

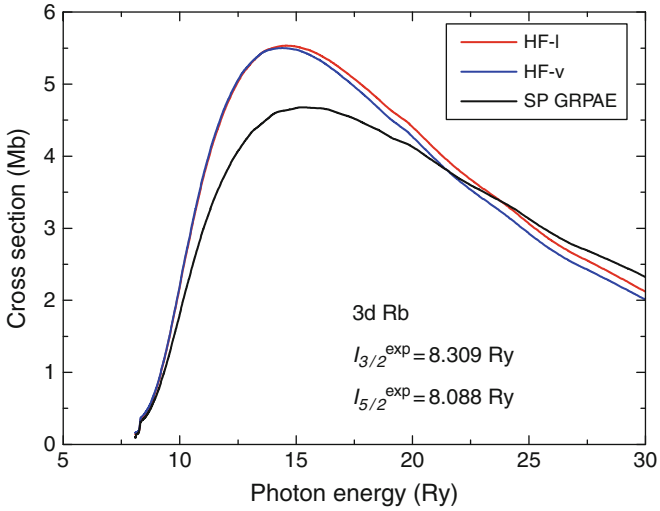

Fig. 2.122_Rb_b1 Partial photoionization cross section of Rb atom in HF-l, HF-v, and SP GRPAE

Figure 2.123_Rb_d1 depicts dipole angular anisotropy parameters $\beta_{3d}(\omega)$ and $\beta_{4p}(\omega)$ in SP RPAE.

Figure 2.124_Rb_d2 shows dipole angular anisotropy parameters of Rb$3d_{3/2}$ and Rb$3d_{5/2}$ levels in SP HF and SP RPAE.

Figures 2.125_Rb^+_a1 and 2.126_Rb^+_d1 include all results of calculations for Rb^+ ion: $(Z = 37)\ 3d^{10}\ 4s^2\ 4p^6$.

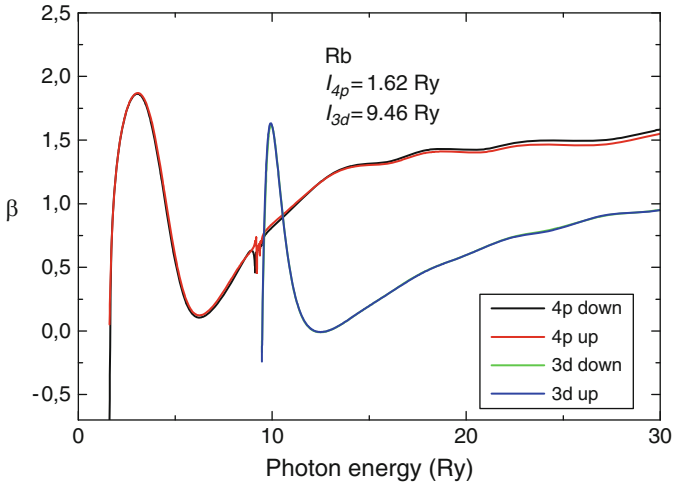

Fig. 2.123_Rb_d1 Dipole anisotropy parameter of $3d$- and $4p$-electrons for Rb atom in SP RPAE

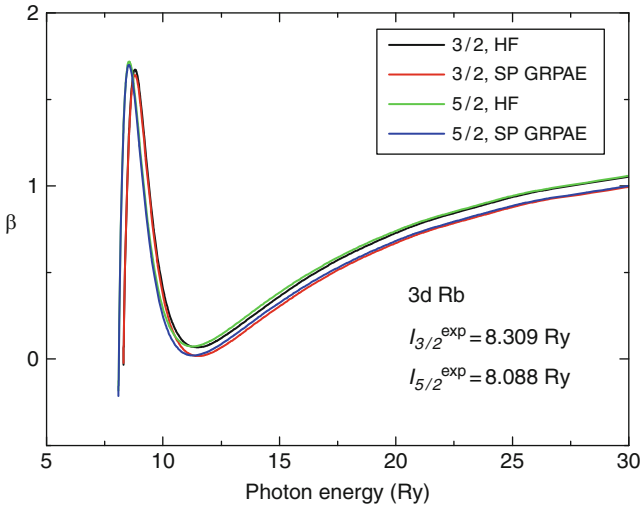

Fig. 2.124_Rb_d2 Dipole anisotropy parameter of $3d$-electrons for Rb atom in SP GRPAE

Figure 2.125_Rb^+_a1 presents total photoionization cross-section of Rb^+ ion in HF-l, HF-v, and RPAE. The cross-section is especially large at the threshold of $4d$-shell.

Figure 2.126_Rb^+_d1 shows dipole angular anisotropy parameters $\beta_{3p}(\omega)$, $\beta_{3d}(\omega)$, and $\beta_{4p}(\omega)$ for Rb^+ ion. The variations of parameters $\beta_{3d,4p}(\omega)$ near their thresholds are very similar, a maximum followed by a minimum.

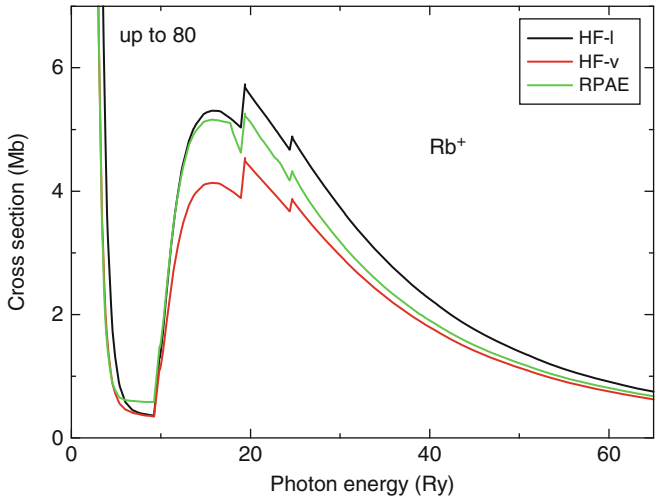

Fig. 2.125_Rb$^+$_a1 Total photoionization cross section of Rb$^+$ ion in HF-l, HF-v, and RPAE

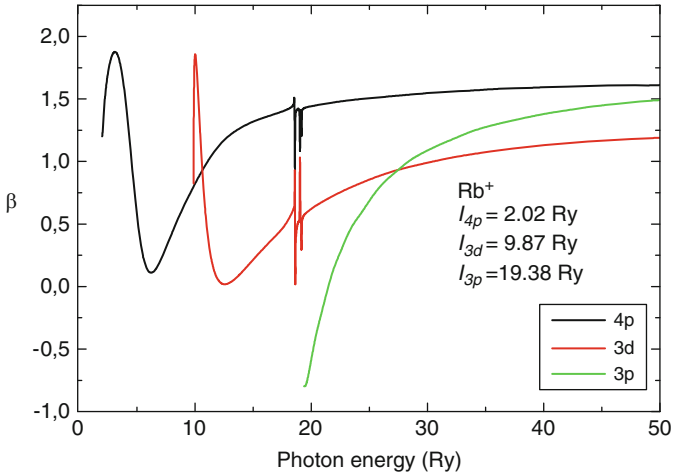

Fig. 2.126_Rb$^+$_d1 Dipole anisotropy parameter of $3p$-, $3d$- and $4p$-electrons for Rb$^+$ ion in RPAE

Figures 2.127_Rb$^-$_a1 and 2.128_Rb$^-$_d1 include all results of calculations for Rb$^-$ ion: $(Z = 37)\ 3d^{10}\ 4s^2\ 4p^6\ 5\ s^2$.

Figure 2.127_Rb$^-$_a1 presents total photoionization cross-section of Rb$^-$ ion in HF-l, HF-v, and RPAE.

Figure 2.128_Rb$^-$_d1 presents dipole angular anisotropy parameters $\beta_{3p}(\omega)$, $\beta_{3d}(\omega)$, and $\beta_{4p}(\omega)$ of Rb$^-$ ion. Parameters $\beta_{4p}(\omega)$ and $\beta_{3d}(\omega)$ rise from threshold to maximums and then go to minimums. The parameter $\beta_{3p}(\omega)$ falls down from threshold to a minimum.

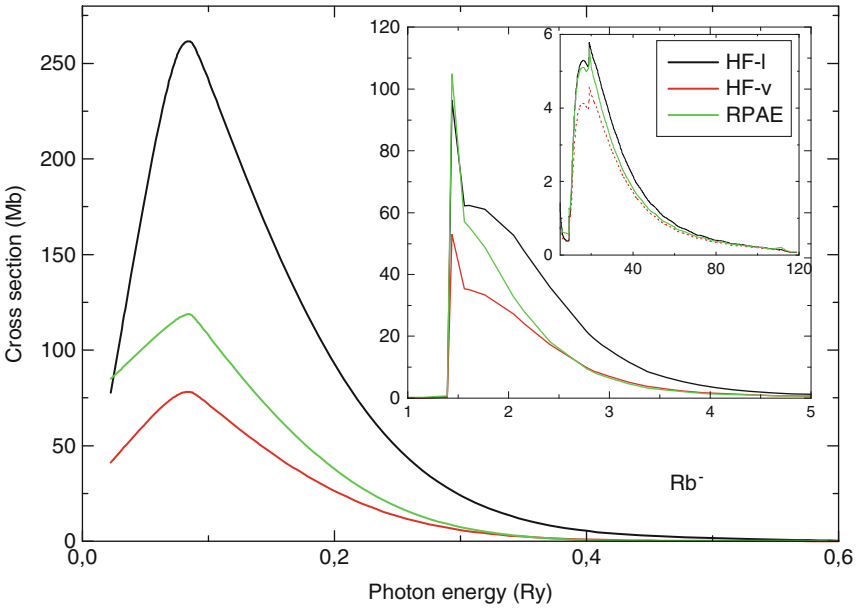

Fig. 2.127_Rb⁻_a1 Total photoionization cross section of Rb^- ion in HF-l, HF-v, and RPAE

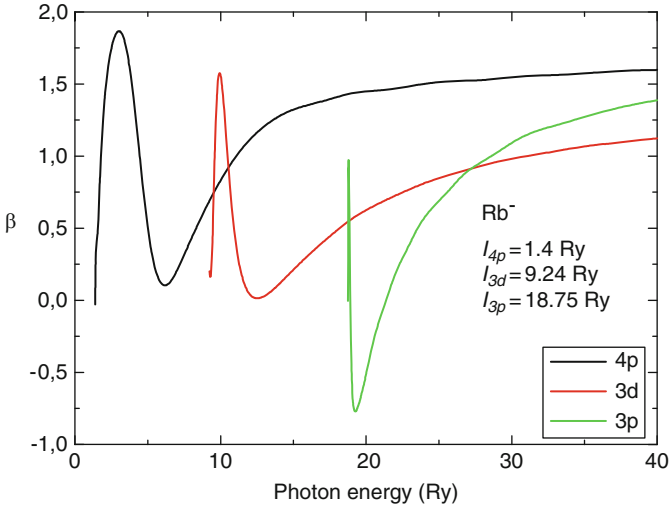

Fig. 2.128_Rb⁻_d1 Dipole anisotropy parameter of $4p$-, $3d$- and $3p$-electrons for Rb^- ion in RPAE

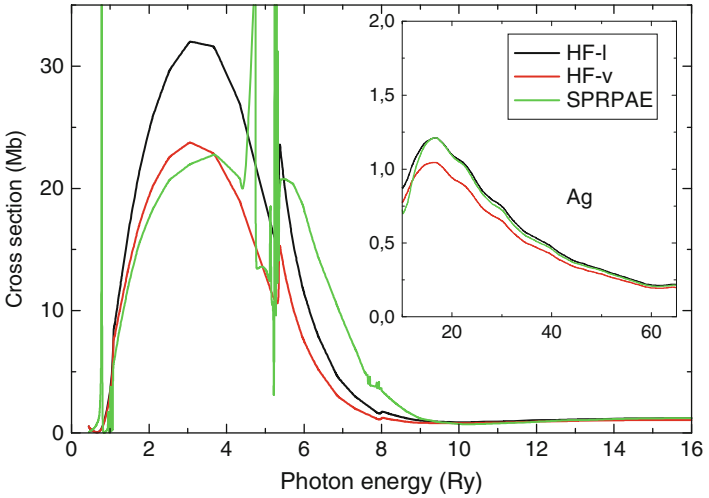

Fig. 2.129_Ag_a1 Total photoionization cross section of Ag atom in HF-l, HF-v, and SP RPAE

Figures 2.129_Ag_a1 and 2.130_Ag_d1 include all results of calculations for Ag atom: $(Z = 47)\, 4p^6, 4d^{10}, 5\, s^1\uparrow$.

Figure 2.129_Ag_a1 shows total photoionization cross-section of Ag in HF-l, HF-v, and SP RPAE. First maximum corresponds to cross-section of $4d^{10}$ electrons. A set of narrow maximums on its high-energy side corresponds to discrete excitations of $4p^6$ electrons. The second weak following after Cooper minimum is shown in the inset.

SP GRPAE Figure 2.130_Ag_d1 presents dipole angular anisotropy parameters $\beta_{4p}(\omega)$ and $\beta_{4d}(\omega)$ in SP GRPAE. Above the $4p$-threshold, the curves are very similar.

Figures 2.131_Ag^+_a1 and 2.132_Ag^+_d1 include all results of calculations for Ag^+ ion: $(Z = 47)\, 4p^6, 4d^{10}$.

Figure 2.131_Ag^+_a1 presents total photoionization cross-section of Ag^+ ion in HF-l, HF-v, and RPAE.

Figure 2.132_Ag^+_d1 presents dipole angular anisotropy parameters $\beta_{4d}(\omega)$, $\beta_{4p}(\omega)$, $\beta_{3d}(\omega)$ of $4d$-, $4p$-, $3d$-subshells for Ag^+ ion. The parameter is a very complex function with several maximums and minimums, the first of which is just above the threshold.

Figures 2.133_Cs_a1–2.141_Cs_f1 include all results of calculations for Cs atom: $(Z = 55)\, 4d^{10}, 5s^2, 5p^6, 6s^1\uparrow$.

Figure 2.133_Cs_a1 represents total photoionization cross-section of Cs atom in HF-l, HF-v, and SP RPAE. The huge resonance with a maximum is seen at 7.5 Ry. Its widths and position change significantly with account for RPAE correlations.

Figure 2.134_Cs_b1 depicts photoionization cross-section of $4d$-subshell for Cs atom in HF and SP GRPAE. One can see that the difference between respective curves is very big. In GRPAE the maximum shifts to the higher omega side, becomes broader and decreases in hight by about a factor of four.

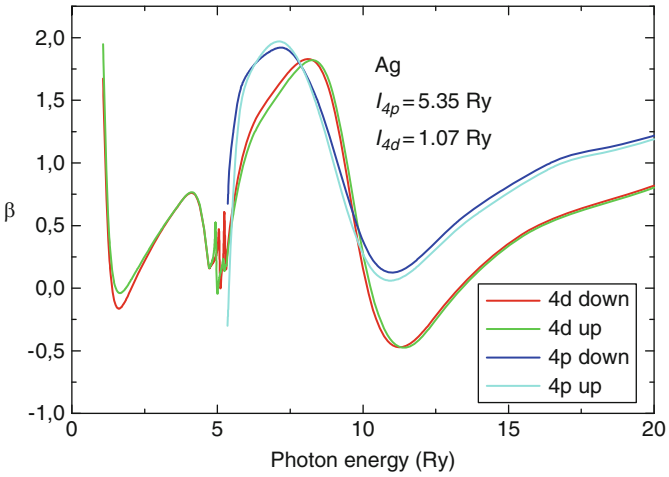

Fig. 2.130_Ag_d1 Dipole anisotropy parameter of $4d$- and $4p$-electrons for Ag atom in SP RPAE

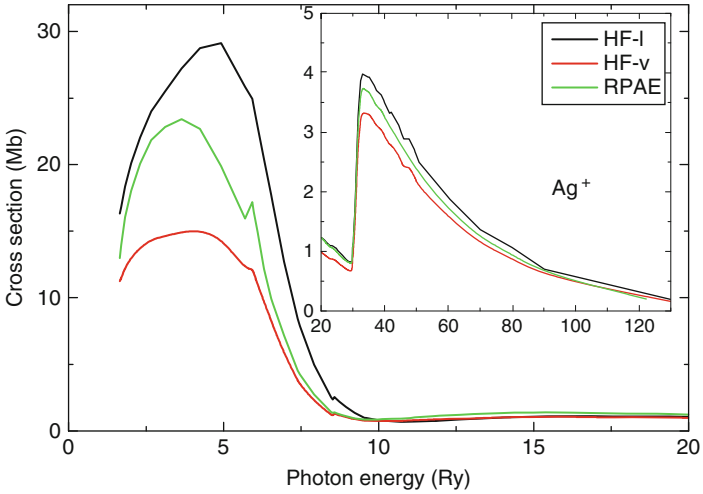

Fig. 2.131_Ag^+_a1 Total photoionization cross section of Ag^+ ion in HF-l, HF-v, and RPAE

Figure 2.135_Cs_b2 shows the photoionization cross-section of $3d_{5/2}$ and $3d_{3/2}$ levels in the frameworks SP HF and SP GRPAE. The second maximum in photoionization cross-section of 5/2 electrons, caused by influence on them by the electrons of level 3/2, called an intra-doublet resonance is clearly seen. Calculation, similar to that for $3d$ Xe, are carried out on the basis of the assumption that 5/2 and 3/2 electrons can be considered as electrons "up" and "down" (see Sect. 1.10).

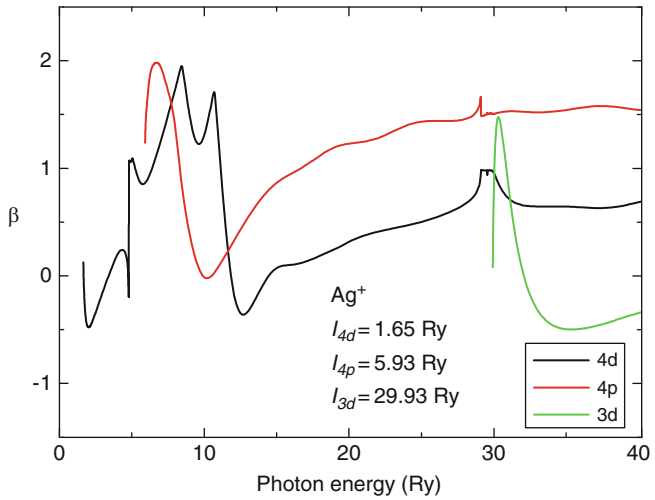

Fig. 2.132_Ag$^+$_d1 Dipole angular anisotropy parameter of $4d$-, $4p$-, and $3d$-electrons for Ag^+ ion in RPAE

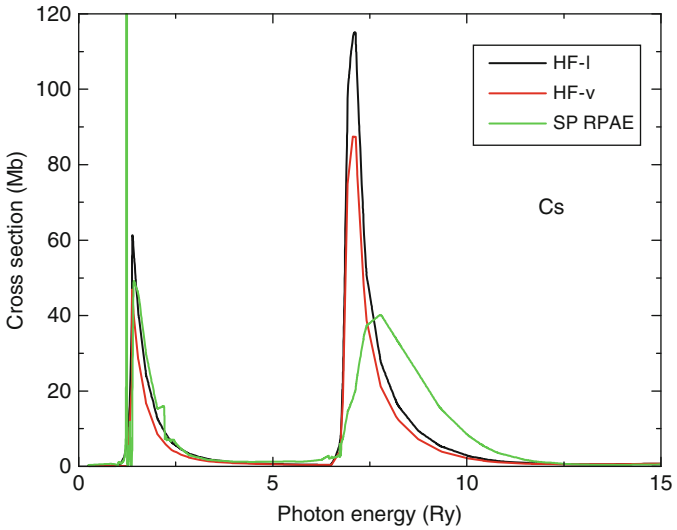

Fig. 2.133_Cs_a1 Total photoionization cross section of Cs atom in HF-l, HF-v, and SP RPAE

The cross-section was calculated making use of formulas (1.96)–(1.99), with that, however, difference, that "up" terms in (1.93) are multiplied by 6/5, and "down" terms are multiplied by 4/5, taking into the real numbers of electrons on levels 5/2 and 3/2 are 6 and 4, respectively [2.25]. Significant strengthening of a maximum in $\sigma_{3d\,5/2}$ is visible in comparison with a similar maximum in Xe—see Fig. 2.59_Xe_b7. It is noticeable that the difference of corresponding curves for $4d_{5/2}$ subshell in SP HF and SPRPAE is very important: a single maximum in SP HF is replaced in

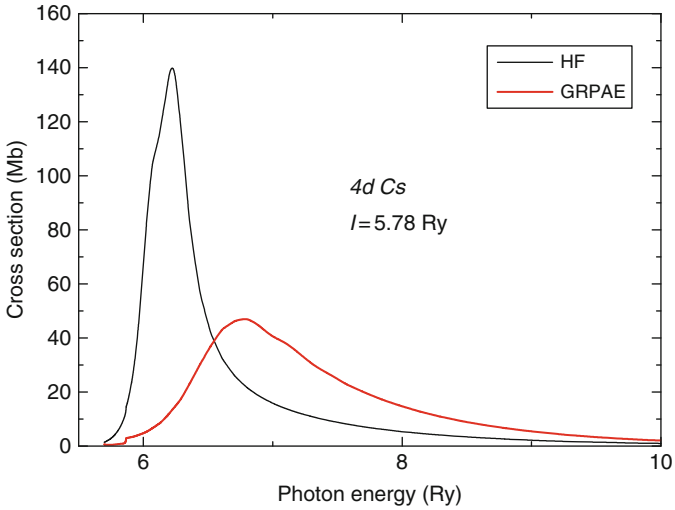

Fig. 2.134_Cs_b1 Photoionization cross section of $4d$-electrons for Cs atom in HF and GRPAE

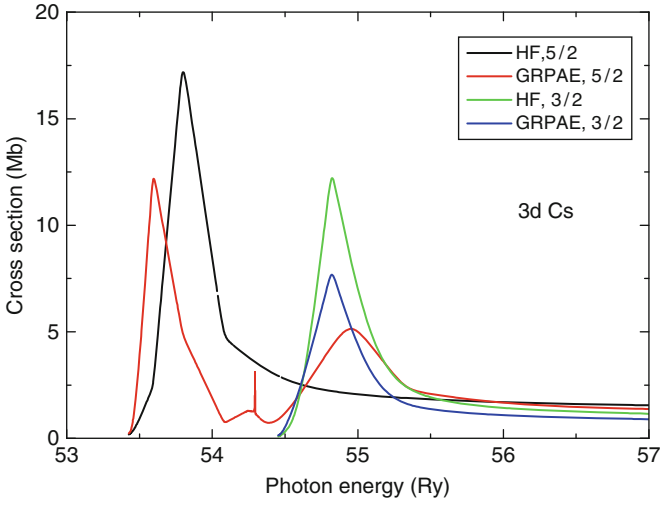

Fig. 2.135_Cs_b2 Photoionization cross section of $3d_{5/2}$ and $3d_{3/2}$-electrons Cs atom in SP HF and SP GRPAE (see [2.3])

SP GRPAE by three ones, whereas the $4d_{3/2}$ maximum under the influence of SP GRPAE correlations just decreases in height by several tens of percent.

Figure 2.136_Cs_d1 shows the dipole angular anisotropy parameters $\beta_{4d}(\omega)$ and $\beta_{5p}(\omega)$ of $4d$- and $5p$-electrons in a broad region of frequencies ω in SP RPAE. The curves of $\beta_{5p}(\omega)$ are very complex with two maximums and two minimums. The curves of $\beta_{4d}(\omega)$ "up" and "down" electrons differ significantly near threshold.

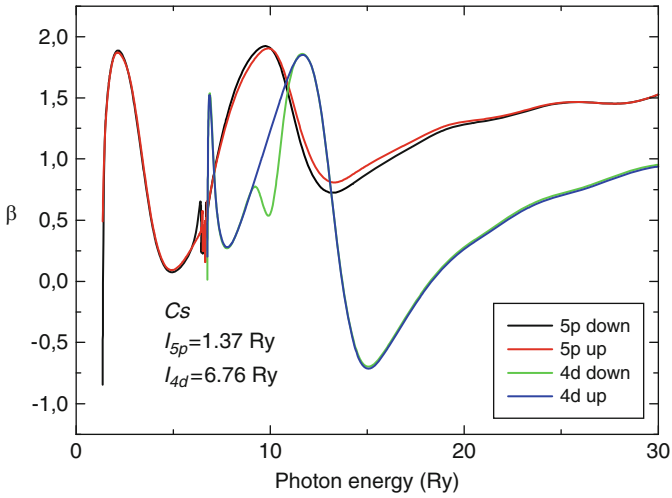

Fig. 2.136_Cs_d1 Dipole angular anisotropy parameter of $4d$- and $5p$-electrons for Cs atom in SP RPAE

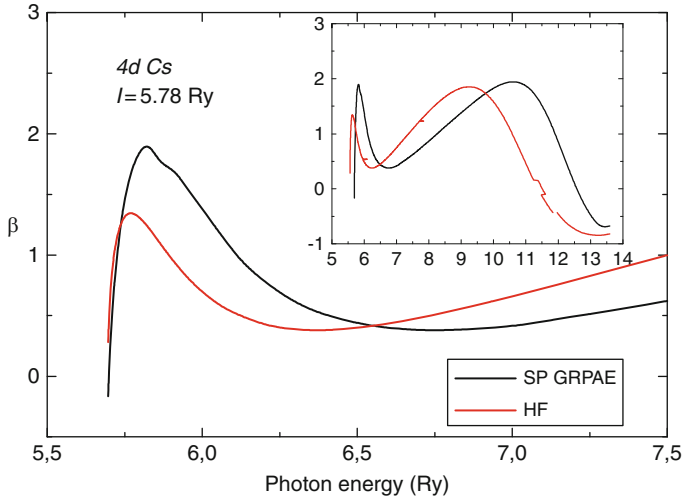

Fig. 2.137_Cs_d2 Dipole angular anisotropy parameter of $4d$-electrons for Cs atom in HF and SP GRPAE

SP GRPAE Figure 2.137_Cs_d2 presents dipole angular anisotropy parameter $\beta_{4d}(\omega)$ of $4d$-electrons in HF and SP GRPAE, in wide area of frequencies ω.

Figure 2.138_Cs_d3 depicts results of calculation of dipole angular anisotropy parameters $\beta_{3d5/2,3d3/2}(\omega)$ of $3d_{5/2}$ and $3d_{3/2}$ levels in HF and SP RPAE performed

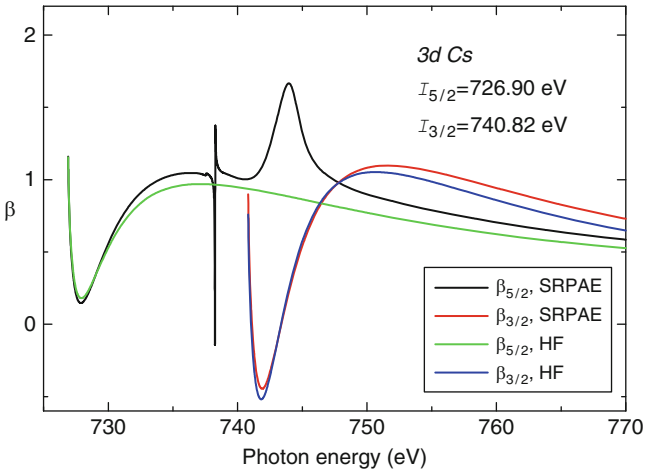

Fig. 2.138_Cs_d3 Dipole angular anisotropy parameter of $3d_{5/2}$ and $3d_{3/2}$-electrons Cs atom in SP HF and SP RPAE (see [2.43])

by the same technique as for partial cross-sections (see Fig. 2.135_Cs_b2) (see [2.43]). In comparison with $3d$ Xe, the influence of $3d_{3/2}$ on $3d_{5/2}$ levels increases considerably, leading to an impressing maximum in $\beta_{3d\,5/2}(\omega)$ as against the case of Xe presented in a Fig. 2.62_Xe_d3.

Figure 2.139_Cs_e1 shows non-dipole angular anisotropy parameters γ^{C}, δ^{C} and their magic combination $(\gamma^{\mathrm{C}} + 3\delta^{\mathrm{C}})$ of $4d$-levels for Cs atom in HF and RPAE. The significant maximums reflecting the influence of 3/2 electrons on 5/2 are visible.

Figure 2.140_Cs_e2 demonstrates the non-dipole angular anisotropy parameters γ^{C}, δ^{C}, and their magic combination $(\gamma^{\mathrm{C}} + 3\delta^{\mathrm{C}})$ for $3d_{5/2}$- and $3d_{3/2}$-levels for Cs atom in SP HF and SP GRPAE, with experimental ionization thresholds $I_{3d\ \mathrm{up}} = 53.43$ Ry, $I_{3d\ \mathrm{down}} = 54.45$ Ry. The significant maxima reflecting the influence of 3/2 electrons on 5/2 electrons are visible.

Figure 2.141_Cs_f1 presents spin polarization parameters $A^j(\omega)$, $\zeta^j(\omega)$, and $\xi^j(\omega)$ of $3d_{5/2}$- and $3d_{3/2}$-levels for Cs atom in HF and SP RPAE (see discussion of a Fig. 2.59_Xe_b7) (see. [2.44]). Strong effect of 3/2 level on 5/2 level is clearly visible.

Figures 2.142_Cs*_a1–2.146_Cs*_e1 (Cs*) include all results of calculations for excited Cs* atom: $(Z = 55)\ 4d^{10}\ 5s^2\ 5p^6 7s(8s, 6d)$.

Figure 2.142_Cs*_a1 demonstrates the total photoionization cross-section of outer electron in Cs atom in $7s$- and $8s$-excited states in HF and RPAE [2.45], along with 6s- in the ground state Cs. As is seen, the cross-section rapidly decreases on the way from $6s$ to $8s$. In the ground state $6s$ photoionization cross-section has one minimum [2.45].

Figure 2.143_Cs*_a2 shows the total cross section of Cs atom in $7s$- and $8s$-excited states in HF and RPAE. Note that in RPAE the cross-section is much

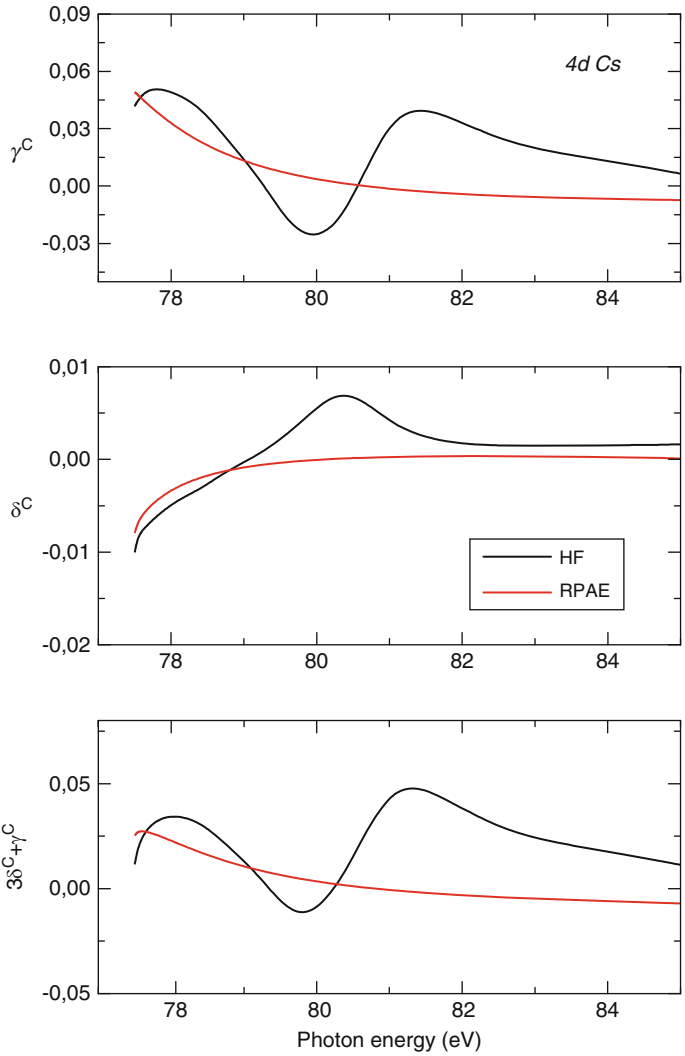

Fig. 2.139_Cs_e1 Non-dipole angular anisotropy parameters of $4d$-electrons and their magic combination for Cs atom in HF and RPAE

bigger and has two in $7s$ and one in $8s$ additional minima as compared to HF results. The photoionization cross-section of $7s$ is considerably bigger than the photoionization cross-section of $8s$ [2.45].

Figure 2.144_Cs*_a3 presents the photoionization cross-section of $6d$ excited electrons of Cs* in HF and RPAE (with inclusion of $4d^{10}$ electron action). Note that in RPAE the cross-section has a strong variation, with two maxima and minima, while in RPAE this is a smoothly decreasing curve.

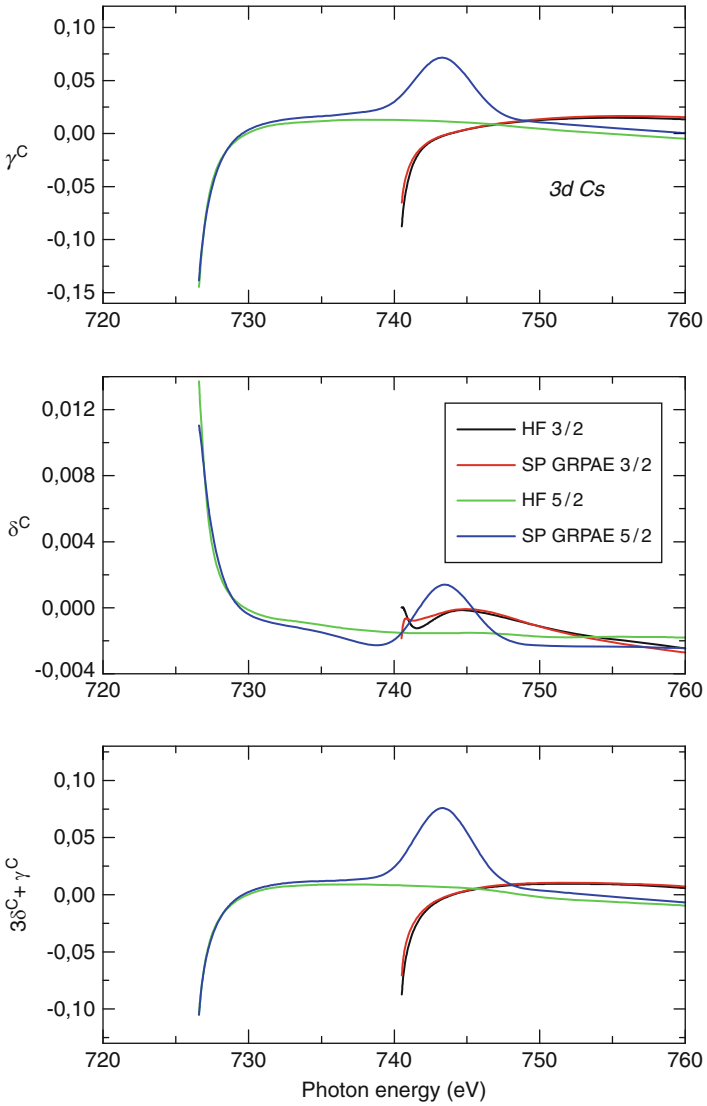

Fig. 2.140_Cs_e2 Non-dipole angular anisotropy parameter of $3d_{5/2}$ and $3d_{3/2}$-electrons and their magic combination for Cs atom in SP HF and SP GRPAE

Figure 2.145_Cs*_d1 depicts the dipole angular anisotropy parameter for $6d$-excited electron of Cs* [2.45]. Note that the RPAE effects are rather strong.

Figure 2.146_Cs*_e1 demonstrates the polarization of photoelectron ionized from $6d$-excited state of Cs* in HF and RPAE. The incoming photon is unpolarized. Note that the RPAE effects are rather strong.

Figures 2.147_Cs^+_a1 and 2.148_Cs^+_d1 (Cs^+) include all results of calculations for Cs^+ ion: $(Z = 55)\, 4d^{10}\, 5s^2\, 5p^6$.

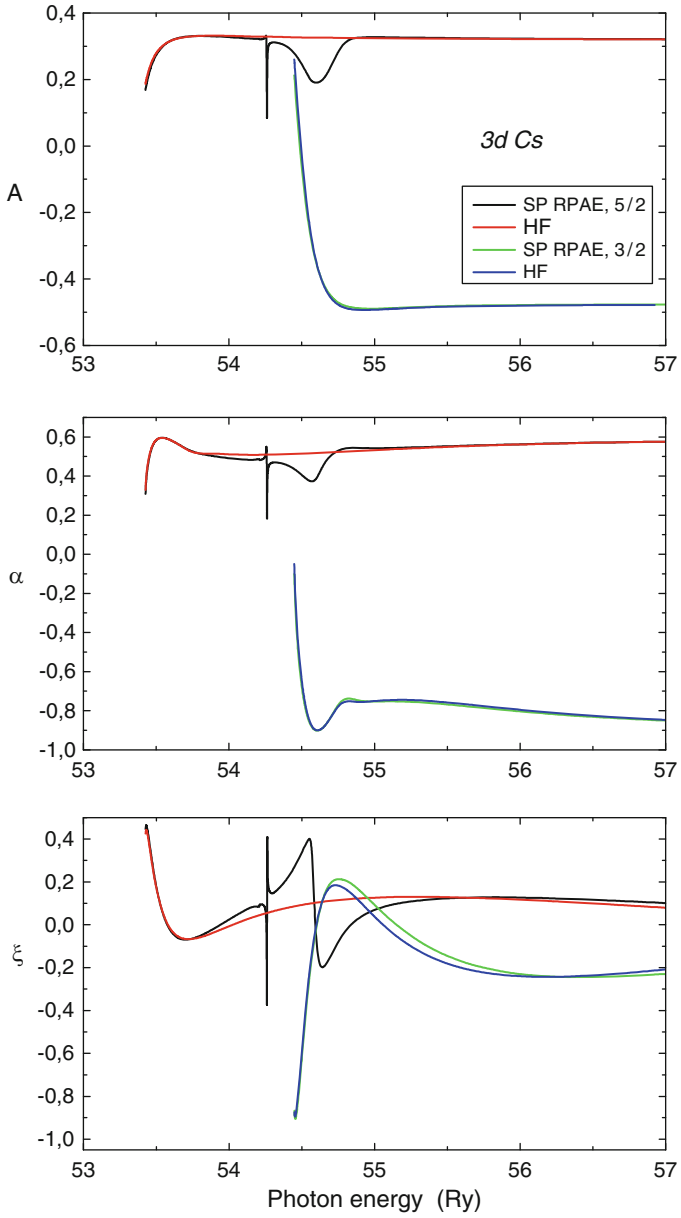

Fig. 2.141_Cs_f1 Spin polarization parameters $A^j(\omega)$, $\alpha^j(\omega)$, and $\xi^j(\omega)$ for $3d_{5/2}$ and $3d_{3/2}$ levels for Cs atom in HF and SP RPAE (see [2.43]

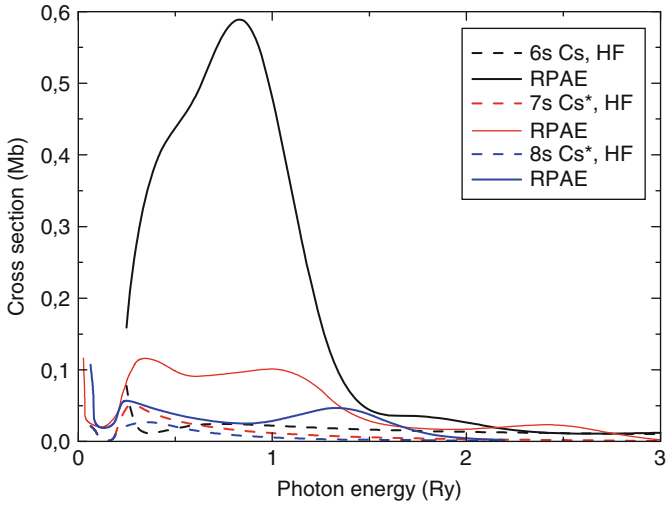

Fig. 2.142_Cs*_a1 Cross section of Cs atom in excited states in HF and RPAE

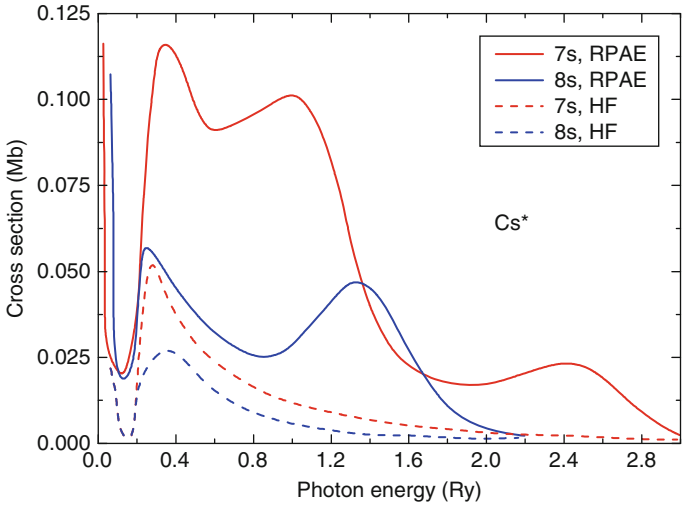

Fig. 2.143_Cs*_a2 Total cross section of Cs atom in $7s$- and $8s$-excited states in HF and RPAE

Figure 2.147_Cs^+_a1 presents total photoionization cross-section of Cs^+ ion in HF-l, HF-v, and RPAE. The Giant resonance is in $4d$-subshell where influence of correlations is seen.

Figure 2.148_Cs^+_d1 demonstrates dipole angular anisotropy parameter $\beta_{3d,4p,4d,5p}(\omega)$ of $3d$-, $4p$-, $4d$-, $5p$-subshells in RPAE, in a broad range of photon energy ω.

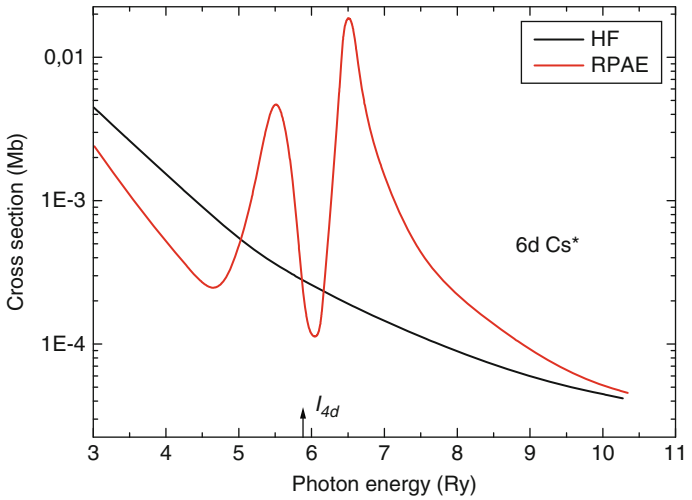

Fig. 2.144_Cs*_a3 The photoionization cross section of $6d$ excited electrons of Cs* in HF and RPAE (with inclusion of $4d^{10}$ electron action)

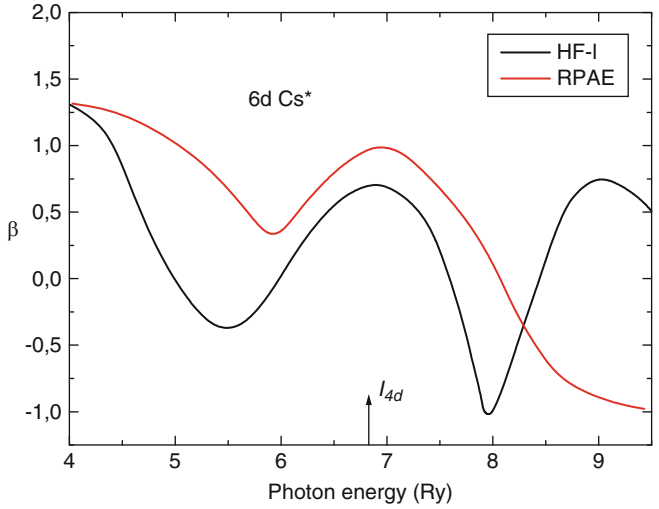

Fig. 2.145_Cs*_d1 Dipole angular anisotropy parameter for $6d$-excited electron of Cs*

Figures 2.149_Cs⁻_a1 and 2.150_Cs⁻_d1 (Cs^-) include all results of calculations for the ion Cs^- ion: $(Z = 55)\ 4d^{10}, 5s^2, 5p^6, 6\,s^2$.

Figure 2.149_Cs⁻_a1 presents total photodetachment cross-section of Cs^- ion in HF-l, HF-v, and RPAE. The influence of RPAE correlations is significant.

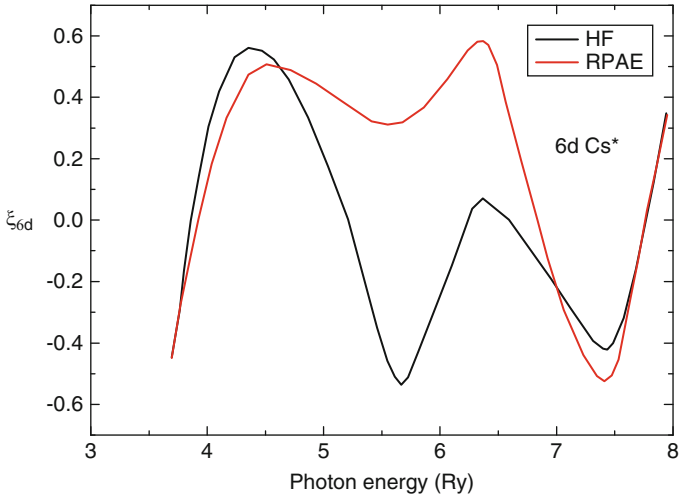

Fig. 2.146_Cs*_e1 Polarization of photoelectron ionized from $6d$-excited state of Cs* in HF and RPAE. The incoming photon is unpolarized

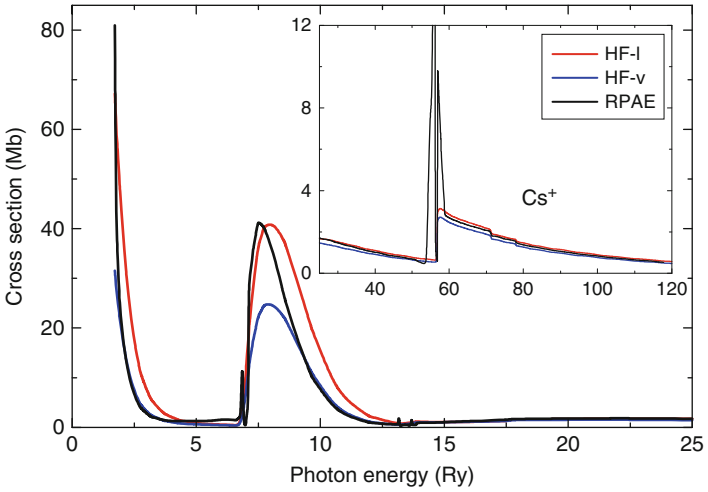

Fig. 2.147_Cs^+_a1 Total photoionization cross section of Cs^+ ion in HF-l, HF-v, and RPAE

Figure 2.150_Cs^-_d1 depicts dipole angular anisotropy parameter $\beta_{3d,4p,4d,5p}(\omega)$ of $3d$-, $4p$-, $4d$-, $5p$-subshells for Cs^- ion in RPAE, in wide range of frequencies ω. For $5p$ and $3d$ electrons the maximum is near threshold with a subsequent minimum, whereas the β-parameter for $4p$-electrons starts to decrease and reaches minimum quite near threshold.

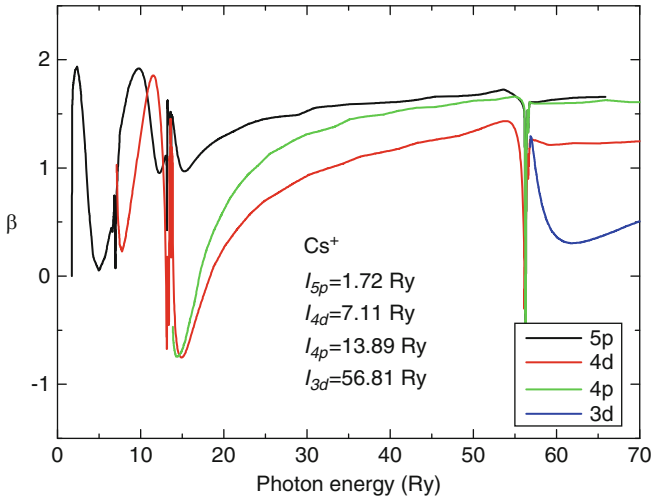

Fig. 2.148_Cs$^+$_d1 Dipole anisotropy parameter of $5p$-, $4d$-, $4p$-, and $3d$-electrons for Cs^+ ion

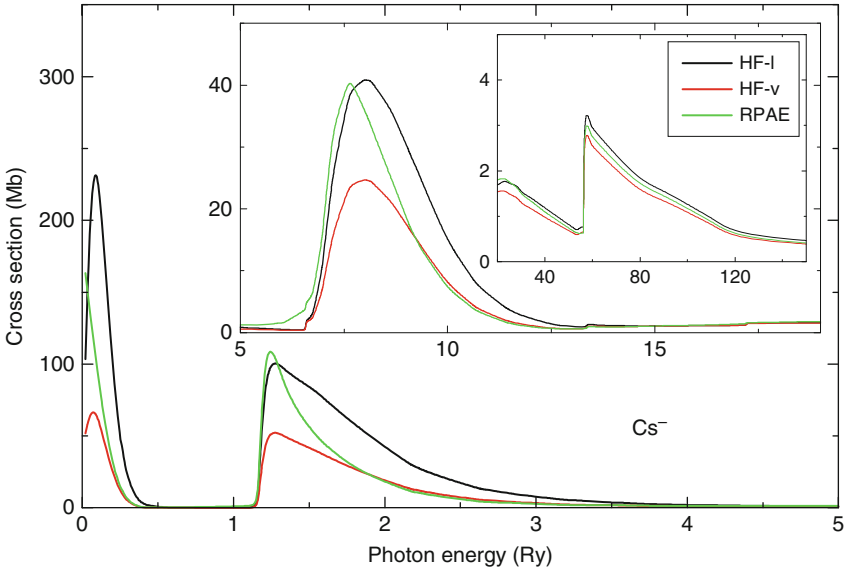

Fig. 2.149_Cs$^-$_a1 Total photoionization cross section of Cs^- ion in HF-l, HF-v, and RPAE

Table 2.2 includes calculated values of oscillator strengths in HF-l, HF-v $f^{l,v}_{nl-n'l'\uparrow(\downarrow)}$, and $F^{l,v}_{nl-n'l'\uparrow(\downarrow)}$ in RPAE for several lowest discrete levels of excitation and for each considered subshell of atoms and ions investigated in this section.

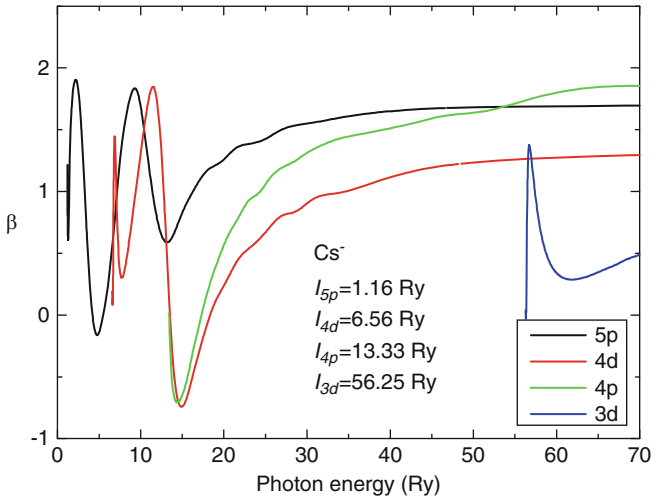

Fig. 2.150_Cs$^-$_d1 Dipole anisotropy parameter of $3d$-, $4p$-, $4d$-, and $5p$-electrons for Cs^- ion in RPAE

Theoretical transition energies in RPAE $\tilde{\omega}_{nl-n'l'\uparrow(\downarrow)}$ are also given in this table. The ions are treated similar to noble gases in Table 2.1.

The results for length and velocity forms in RPAE coincide with reasonable accuracy. For atoms Li, Na, K, Cu, and Ag, the dominative is the first discrete transition of the outer ns electron ns–np. The second in importance for Li, Na, and K is the transition $(n-1)$, p–ns, while for Cu and Ag it is $(n-1)$, d–np. For Rb and Cs the biggest is the subvalent subshell transition $(n-1)$, p–$(n-1)$, d. In ions Na^+, K^+, Rb^+, and Cs^+ dominates the outer p-electron transition. In K^+ the next in importance is the $2p$–$3d$ level. The second in importance in Rb^+, Ag^+, and Cs^+ is the outer electron np–$(n+1)s$ level. Only in Cu^+ dominates the subvalent transition $3p$–$5s$. In general, the role of correlations is bigger for higher transitions with smaller oscillator strengths. For deeper subshells, the oscillator strengths are, also in general, decreasing with decrease in principal quantum number of the exited electron.

Table 2.2 Oscillator strengths and transition energies of I group's elements and ions

Transition	ω (Ry)	HF-l	HF-v	RPAE-l	RPAE-v
Li					
$2s$–$2p$ do	0.04004	0.2211E+00	0.2359E+01	0.2176E+00	0.2242E+01
$2s$–$3p$ do	0.27055	0.5536E−01	0.2529E−01	0.5703E−01	0.2919E−01
$2s$–$4p$ do	0.32619	0.1774E−01	0.9408E−02	0.1822E−01	0.1075E−01
$1s$–$2p$ do	4.44256	0.2566E+00	0.2810E+00	0.3733E+00	0.4096E+00
$1s$–$3p$ do	4.77942	0.2798E−01	0.3077E−01	0.9241E−02	0.1020E−01
$1s$–$4p$ do	4.85820	0.9722E−02	0.1070E−01	0.9923E−02	0.1094E−01
$1s$–$2p$ up	4.32974	0.2278E+00	0.2556E+00	0.2332E−01	0.2531E−01
$1s$–$3p$ up	4.80740	0.3957E−01	0.4381E−01	0.4991E−01	0.5493E−01
$1s$–$4p$ up	4.89202	0.1148E−01	0.1270E−01	0.1337E−01	0.1473E−01
Li^+					
$1s$–$2p$	4.60952	0.4558E+00	0.4192E+00	0.4441E+00	0.4428E+00
$1s$–$3p$	5.14714	0.1144E+00	0.1046E+00	0.1107E+00	0.1104E+00
$1s$–$4p$	5.33754	0.4561E−01	0.4163E−01	0.4397E−01	0.4382E−01
Na					
$3s$–$3p$ up	0.14343	0.9882E+00	0.9724E+00	0.9679E+00	0.9552E+00
$3s$–$4p$ up	0.26329	0.1284E−01	0.1210E−01	0.9946E−02	0.9399E−02
$3s$–$5p$ up	0.30634	0.1870E−02	0.1698E−02	0.1222E−02	0.1104E−02
$2p$–$3d$ do	2.91274	0.1687E−01	0.1488E−01	0.1692E−01	0.1699E−01
$2p$–$4d$ do	2.96688	0.8892E−02	0.7837E−02	0.1393E−01	0.1394E−01
$2p$–$5d$ do	2.99137	0.4834E−02	0.4259E−02	0.2639E−02	0.2659E−02
$2p$–$3s$ do	2.47261	0.9796E−01	0.7473E−01	0.1080E+00	0.8598E−01
$2p$–$4s$ do	2.86433	0.1101E−01	0.8309E−02	0.1131E−01	0.8858E−02
$2p$–$5s$ do	2.94964	0.3613E−02	0.2720E−02	0.3969E−02	0.3134E−02
$2p$–$3d$ up	2.89924	0.3619E−01	0.2900E−01	0.2401E−01	0.2381E−01
$2p$–$4d$ up	2.96570	0.1271E−01	0.1044E−01	0.6016E−03	0.5834E−03
$2p$–$5d$ up	2.99345	0.6264E−02	0.5181E−02	0.6192E−02	0.6166E−02
$2s$–$3p$ do	5.27493	0.1597E−01	0.1470E−01	0.1140E−01	0.1114E−01
$2s$–$4p$ do	5.46560	0.3123E−02	0.2866E−02	0.7673E−03	0.8022E−03
$2s$–$5p$ do	5.52088	0.1241E−02	0.1139E−02	0.5662E−03	0.5866E−03
$2s$–$3p$ up	5.18537	0.1579E−01	0.1566E−01	0.8283E−02	0.8404E−02
$2s$–$4p$ up	5.47408	0.2963E−02	0.2836E−02	0.2446E−02	0.2519E−02
$2s$–$5p$ up	5.53289	0.1151E−02	0.1098E−02	0.7949E−03	0.8122E−03
$1s$–$3p$ do	80.55925	0.2277E−01	0.2230E−01	0.2477E−01	0.2487E−01
$1s$–$4p$ do	80.81891	0.2940E−02	0.2882E−02	0.8294E−03	0.8048E−03
$1s$–$5p$ do	80.88294	0.1088E−02	0.1066E−02	0.7364E−03	0.7295E−03
$1s$–$3p$ up	80.49684	0.1851E−01	0.1871E−01	0.3590E−02	0.3958E−02
$1s$–$4p$ up	80.82581	0.3250E−02	0.3285E−02	0.5734E−02	0.5896E−02
$1s$–$5p$ up	80.88889	0.1184E−02	0.1197E−02	0.1632E−02	0.1692E−02
Na^+					
$2p$–$3d$	3.14485	0.1894E+00	0.1470E+00	0.1710E+00	0.1704E+00
$2p$–$4d$	3.34253	0.9240E−01	0.7121E−01	0.1340E+00	0.1335E+00
$2p$–$5d$	3.43345	0.4965E−01	0.3814E−01	0.4630E−01	0.4613E−01
$2p$–$3s$	2.55813	0.1930E+00	0.1773E+00	0.2182E+00	0.2175E+00
$2p$–$4s$	3.14447	0.3561E−01	0.3253E−01	0.5280E−01	0.5262E−01
$2p$–$5s$	3.34282	0.1313E−01	0.1198E−01	0.8617E−04	0.8585E−04

Table 2.2 (continued)

2*s*–3*p*	5.39972	0.4489E−01	0.4011E−01	0.2453E−01	0.2440E−01
2*s*–4*p*	5.78743	0.1546E−01	0.1377E−01	0.9133E−02	0.8817E−02
2*s*–5*p*	5.93504	0.7052E−02	0.6278E−02	0.3749E−02	0.3715E−02
1*s*–3*p*	80.66526	0.4982E−01	0.4787E−01	0.4950E−01	0.4907E−01
1*s*–4*p*	81.13029	0.1223E−01	0.1176E−01	0.1216E−01	0.1206E−01
1*s*–5*p*	81.29477	0.5091E−02	0.4901E−02	0.5066E−02	0.5022E−02
K					
4*s*–4*p* up	0.09958	0.1075E+01	0.1031E+01	0.1011E+01	0.9898E+00
4*s*–5*p* up	0.20324	0.1004E−01	0.8318E−02	0.3864E−02	0.3273E−02
4*s*–6*p* up	0.24140	0.1326E−02	0.9542E−03	0.1848E−03	0.1068E−03
3*p*–3*d* do	1.75352	0.1223E+01	0.9226E+00	0.7907E+00	0.7794E+00
3*p*–4*d* do	1.83303	0.2593E+00	0.1932E+00	0.2595E+00	0.2555E+00
3*p*–5*d* do	1.84812	0.1071E+00	0.7940E−01	0.7568E−03	0.7482E−03
3*p*–4*s* do	1.47931	0.1738E+00	0.1627E+00	0.2091E+00	0.2068E+00
3*p*–5*s* do	1.76264	0.2074E−01	0.1938E−01	0.3098E−01	0.3056E−01
3*p*–6*s* do	1.83190	0.7104E−02	0.6636E−02	0.2737E−01	0.2697E−01
3*p*–3*d* up	1.75351	0.1250E+01	0.9108E+00	0.7909E+00	0.7796E+00
3*p*–4*d* up	1.83302	0.2449E+00	0.1828E+00	0.2599E+00	0.2558E+00
3*p*–5*d* up	1.86513	0.1051E+00	0.7845E−01	0.2874E+00	0.2828E+00
3*s*–4*p* do	3.24235	0.6536E−02	0.4950E−02	0.1117E−03	0.1063E−03
3*s*–5*p* do	3.38743	0.1551E−02	0.1180E−02	0.2219E−04	0.1829E−04
3*s*–6*p* do	3.43307	0.6580E−03	0.5014E−03	0.1353E−04	0.9673E−05
3*s*–4*p* up	3.17017	0.5374E−02	0.4981E−02	0.1890E−04	0.3149E−04
3*s*–5*p* up	3.39191	0.1338E−02	0.1128E−02	0.2089E−03	0.1761E−03
3*s*–6*p* up	3.44106	0.5614E−03	0.4691E−03	0.1244E−03	0.1027E−03
2*p*–3*d* do	22.52532	0.4253E+00	0.3980E+00	0.5667E+00	0.5670E+00
2*p*–4*d* do	22.92615	0.1033E−01	0.9678E−02	0.1619E−01	0.1622E−01
2*p*–5*d* do	22.97564	0.4586E−02	0.4299E−02	0.8213E−02	0.8222E−02
2*p*–4*s* do	22.54554	0.7242E−02	0.6922E−02	0.1266E+00	0.1264E+00
2*p*–5*s* do	22.88349	0.9710E−03	0.9273E−03	0.1256E−02	0.1271E−02
2*p*–6*s* do	22.95924	0.3385E−03	0.3232E−03	0.4062E−03	0.4110E−03
2*p*–3*d* up	22.52497	0.4146E+00	0.3881E+00	0.5150E+00	0.5154E+00
2*p*–4*d* up	22.91282	0.1871E−01	0.1749E−01	0.1152E−01	0.1147E−01
2*p*–5*d* up	22.97237	0.5909E−02	0.5525E−02	0.1860E−02	0.1849E−02
2*s*–4*p* do	28.67867	0.1343E−01	0.1293E−01	0.9889E−02	0.9873E−02
2*s*–5*p* do	28.86413	0.2158E−02	0.2080E−02	0.2289E−02	0.2303E−02
2*s*–6*p* do	28.91489	0.8452E−03	0.8146E−03	0.4349E−03	0.4321E−03
2*s*–4*p* up	28.59595	0.1424E−01	0.1374E−01	0.8444E−02	0.8686E−02
2*s*–5*p* up	28.86181	0.2352E−02	0.2271E−02	0.5899E−03	0.6162E−03
2*s*–6*p* up	28.91709	0.8632E−03	0.8334E−03	0.7658E−03	0.7843E−03
K^+					
3*p*–3*d*	1.86167	0.1612E+01	0.9215E+00	0.1608E+01	0.1506E+01
3*p*–4*d*	2.07054	0.7662E+00	0.4169E+00	0.6394E+00	0.5949E+00
3*p*–5*d*	2.16936	0.4022E+00	0.2136E+00	0.2638E+00	0.2446E+00
3*p*–4*s*	1.54345	0.3827E+00	0.3432E+00	0.4663E+00	0.4573E+00
3*p*–5*s*	1.96607	0.7347E−01	0.6557E−01	0.9303E−01	0.9059E−01
3*p*–6*s*	2.12226	0.2797E−01	0.2494E−01	0.3126E−01	0.3048E−01

Table 2.2 (continued)

3*s*–4*p*	3.33460	0.1864E−01	0.1360E−01	0.1342E−03	0.1640E−03
3*s*–5*p*	3.62319	0.7794E−02	0.5767E−02	0.1189E−02	0.1096E−02
3*s*–6*p*	3.74146	0.3868E−02	0.2877E−02	0.9786E−03	0.8522E−03
2*p*–3*d*	22.54462	0.6907E+00	0.6032E+00	0.6187E+00	0.6168E+00
2*p*–4*d*	23.10869	0.7327E−01	0.6405E−01	0.6636E−01	0.6609E−01
2*p*–5*d*	23.26199	0.3157E−01	0.2761E−01	0.2854E−01	0.2843E−01
2*p*–4*s*	22.59642	0.1544E−01	0.1468E−01	0.2016E−01	0.1989E−01
2*p*–5*s*	23.07814	0.3730E−02	0.3543E−02	0.8423E−02	0.8461E−02
2*p*–6*s*	23.24777	0.1542E−02	0.1464E−02	0.3202E−02	0.3217E−02
2*s*–4*p*	28.75262	0.3315E−01	0.3183E−01	0.2376E−01	0.2388E−01
2*s*–5*p*	29.09075	0.9161E−02	0.8806E−02	0.6523E−02	0.6575E−02
2*s*–6*p*	29.22056	0.4046E−02	0.3891E−02	0.2899E−02	0.2925E−02
1*s*–4*p*	266.79740	0.1294E−01	0.1260E−01	0.1293E−01	0.1277E−01
1*s*–5*p*	267.16808	0.3137E−02	0.3056E−02	0.3137E−02	0.3098E−02
1*s*–6*p*	267.30438	0.1350E−02	0.1315E−02	0.1350E−02	0.1334E−02
Cu					
4*s*–4*p* up	0.21314	0.9599E+00	0.9952E+00	0.7929E+00	0.8288E+00
4*s*–5*p* up	0.36663	0.2582E−01	0.2837E−01	0.4847E−02	0.5916E−02
4*s*–6*p* up	0.41645	0.5342E−02	0.6067E−02	0.2460E−03	0.3970E−03
3*d*–4*f* do	0.92381	0.5565E−03	0.5048E−03	0.6975E−03	0.6927E−03
3*d*–5*f* do	0.94644	0.4453E−03	0.4034E−03	0.4738E−03	0.4688E−03
3*d*–6*f* do	0.95873	0.3113E−03	0.2818E−03	0.3225E−03	0.3189E−03
3*d*–4*p* do	0.66151	0.1907E+00	0.1839E+00	0.3027E+00	0.3142E+00
3*d*–5*p* do	0.86173	0.2247E−01	0.2145E−01	0.2996E−01	0.3133E−01
3*d*–6*p* do	0.91883	0.7820E−02	0.7450E−02	0.9146E−02	0.9626E−02
3*d*–4*f* up	0.91520	0.9300E−03	0.7423E−03	0.7052E−03	0.7139E−03
3*d*–5*f* up	0.93786	0.7402E−03	0.5923E−03	0.6848E−03	0.6950E−03
3*d*–6*f* up	0.95018	0.5156E−03	0.4131E−03	0.4631E−03	0.4694E−03
3*d*–4*p* up	0.53086	0.2058E+00	0.2377E+00	0.9181E−01	0.8623E−01
3*d*–5*p* up	0.84565	0.1477E−01	0.1586E−01	0.5722E−02	0.5450E−02
3*d*–6*p* up	0.90822	0.5212E−02	0.5540E−02	0.3665E−02	0.3600E−02
3*p*–4*p* do	6.51868	0.3133E−01	0.1862E−01	0.1993E−01	0.1679E−01
3*p*–5*p* do	6.58775	0.1180E−01	0.6996E−02	0.1126E−01	0.9985E−02
3*p*–6*p* do	6.61166	0.5602E−02	0.3316E−02	0.5408E−03	0.4483E−03
3*p*–4*s* do	5.95550	0.9773E−01	0.7817E−01	0.7562E−01	0.8196E−01
3*p*–5*s* do	6.46841	0.8649E−02	0.7289E−02	0.8820E−02	0.9433E−02
3*p*–6*s* do	6.56461	0.2762E−02	0.2342E−02	0.3836E−02	0.4011E−02
3*p*–5*d* up	6.57240	0.5192E−02	0.3609E−02	0.7527E−03	0.7474E−03
3*p*–6*d* up	6.60096	0.2409E−02	0.1671E−02	0.2727E−02	0.2519E−02
3*p*–7*d* up	6.61560	0.1318E−02	0.9131E−03	0.3399E−02	0.3055E−02
3*p*–5*s* up	6.40214	0.3555E−01	0.2453E−01	0.3329E−01	0.3096E−01
3*p*–6*s* up	6.54620	0.4869E−02	0.3411E−02	0.3208E−02	0.3052E−02
3*p*–7*s* up	6.58833	0.1962E−02	0.1380E−02	0.5855E−03	0.6072E−03
3*s*–4*p* do	9.68873	0.1089E−01	0.8567E−02	0.1094E−01	0.9987E−02
3*s*–5*p* do	9.89724	0.1856E−02	0.1471E−02	0.2055E−02	0.1913E−02
3*s*–6*p* do	9.95527	0.7119E−03	0.5652E−03	0.9054E−03	0.8550E−03
3*s*–4*p* up	9.56792	0.1119E−01	0.9995E−02	0.9968E−02	0.1053E−01

Table 2.2 (continued)

3*s*–5*p* up	9.89123	0.1458E−02	0.1284E−02	0.1087E−02	0.1146E−02
3*s*–6*p* up	9.95421	0.5592E−03	0.4919E−03	0.3330E−03	0.3588E−03
Cu^+					
3*d*–4*p*	1.23956	0.7729E−01	0.5900E−01	0.5025E−01	0.3945E−01
3*d*–5*p*	1.39910	0.2818E−01	0.2139E−01	0.1880E−01	0.1490E−01
3*d*–6*p*	1.47561	0.1372E−01	0.1039E−01	0.9480E−02	0.7572E−02
3*d*–4*f*	1.36889	0.4754E−01	0.3696E−01	0.4322E−01	0.4382E−01
3*d*–5*f*	1.45970	0.3263E−01	0.2514E−01	0.3021E−01	0.3055E−01
3*d*–6*f*	1.50892	0.2114E−01	0.1621E−01	0.2104E−01	0.2110E−01
3*p*–5*s*	6.00722	0.2249E+00	0.1644E+00	0.2218E+00	0.1892E+00
3*p*–6*s*	6.78293	0.3586E−01	0.2789E−01	0.3773E−01	0.3569E−01
3*p*–7*s*	7.01225	0.1309E−01	0.1028E−01	0.1334E−01	0.1270E−01
3*p*–4*d*	6.85296	0.1474E−01	0.1122E−01	0.1545E−01	0.1445E−01
3*p*–5*d*	7.04131	0.4450E−02	0.3371E−02	0.4899E−02	0.5035E−02
3*p*–6*d*	7.12799	0.1922E−02	0.1449E−02	0.2502E−02	0.2525E−02
3*s*–4*p*	9.79408	0.3241E−01	0.2516E−01	0.2908E−01	0.2754E−01
3*s*–5*p*	10.26221	0.8895E−02	0.7003E−02	0.7716E−02	0.7445E−02
3*s*–6*p*	10.42613	0.3843E−02	0.3038E−02	0.3330E−02	0.3215E−02
2*p*–4*d*	71.39019	0.7435E−01	0.6730E−01	0.7062E−01	0.6961E−01
2*p*–5*d*	71.60137	0.2558E−01	0.2319E−01	0.2437E−01	0.2402E−01
2*p*–6*d*	71.69494	0.1227E−01	0.1113E−01	0.1205E−01	0.1188E−01
2*p*–5*s*	70.49065	0.6656E−02	0.6845E−02	0.1118E−01	0.1171E−01
2*p*–6*s*	71.33840	0.1289E−02	0.1297E−02	0.5390E−02	0.5443E−02
2*p*–7*s*	71.57893	0.4929E−03	0.4942E−03	0.1522E−02	0.1542E−02
Rb					
5*s*–5*p* up	0.09017	0.1128E+01	0.1067E+01	0.1037E+01	0.1033E+01
5*s*–6*p* up	0.18777	0.1348E−01	0.1077E−01	0.4137E−02	0.3968E−02
5*s*–7*p* up	0.22400	0.2161E−02	0.1508E−02	0.2317E−03	0.2006E−03
4*p*–4*d* do	1.45844	0.1436E+01	0.1069E+01	0.1223E+01	0.1214E+01
4*p*–5*d* do	1.54270	0.2658E+00	0.1956E+00	0.3347E+00	0.3324E+00
4*p*–6*d* do	1.56219	0.1102E+00	0.8074E−01	0.1023E−02	0.1023E−02
4*p*–5*s* do	1.21884	0.2202E+00	0.2179E+00	0.1577E+00	0.1664E+00
4*p*–6*s* do	1.48260	0.2658E−01	0.2613E−01	0.4812E−01	0.4916E−01
4*p*–7*s* do	1.54686	0.9215E−02	0.9042E−02	0.2516E−01	0.2541E−01
4*p*–5*d* up	1.54271	0.2540E+00	0.1871E+00	0.3395E+00	0.3372E+00
4*p*–6*d* up	1.57416	0.1076E+00	0.7930E−01	0.2566E+00	0.2548E+00
4*p*–6*s* up	1.45243	0.8068E−01	0.6949E−01	0.2492E−01	0.2374E−01
4*p*–7*s* up	1.54435	0.1257E−01	0.1096E−01	0.8531E−02	0.8190E−02
4*p*–8*s* up	1.57492	0.5433E−02	0.4754E−02	0.7220E−02	0.7067E−02
4*s*–5*p* do	2.81268	0.8283E−03	0.8708E−03	0.4998E−02	0.3938E−02
4*s*–6*p* do	2.94292	0.3089E−03	0.2899E−03	0.3703E−03	0.2608E−03
4*s*–7*p* do	2.98571	0.1465E−03	0.1343E−03	0.1479E−03	0.1141E−03
4*s*–5*p* up	2.74565	0.1256E−02	0.1100E−02	0.2104E−02	0.2343E−02
4*s*–6*p* up	2.94679	0.4735E−03	0.3475E−03	0.3687E−03	0.3755E−03
4*s*–7*p* up	2.99227	0.2142E−03	0.1556E−03	0.5917E−04	0.7472E−04
3*d*–4*f* do	9.40082	0.1423E−04	0.1076E−04	0.9963E−05	0.9887E−05
3*d*–5*f* do	9.42351	0.1274E−04	0.9658E−05	0.9588E−05	0.9560E−05

Table 2.2 (continued)

$3d$–$6f$ do	9.43592	0.9412E−05	0.7143E−05	0.6690E−05	0.6706E−05
$3d$–$5p$ do	9.19448	0.2240E−01	0.2100E−01	0.2576E−01	0.2771E−01
$3d$–$6p$ do	9.35752	0.3682E−02	0.3461E−02	0.5551E−02	0.5991E−02
$3d$–$7p$ do	9.40434	0.1453E−02	0.1367E−02	0.2339E−02	0.2528E−02
$3d$–$4f$ up	9.40010	0.2460E−04	0.1875E−04	0.1761E−04	0.1744E−04
$3d$–$5f$ up	9.42325	0.2114E−04	0.1615E−04	0.1583E−04	0.1573E−04
$3d$–$6f$ up	9.43597	0.1514E−04	0.1158E−04	0.1152E−04	0.1150E−04
$3d$–$5p$ up	9.11654	0.2178E−01	0.2086E−01	0.1556E−01	0.1703E−01
$3d$–$6p$ up	9.35242	0.3455E−02	0.3311E−02	0.1313E−02	0.1442E−02
$3d$–$7p$ up	9.40284	0.1311E−02	0.1256E−02	0.2367E−03	0.2613E−03
Rb^+					
$4p$–$4d$	1.54605	0.2167E+01	0.1199E+01	0.2039E+01	0.1930E+01
$4p$–$5d$	1.75337	0.9172E+00	0.4856E+00	0.7071E+00	0.6666E+00
$4p$–$6d$	1.84978	0.4593E+00	0.2383E+00	0.2877E+00	0.2707E+00
$4p$–$5s$	1.28607	0.4972E+00	0.4481E+00	0.5375E+00	0.5312E+00
$4p$–$6s$	1.66506	0.9496E−01	0.8518E−01	0.1239E+00	0.1213E+00
$4p$–$7s$	1.80880	0.3639E−01	0.3262E−01	0.4498E−01	0.4401E−01
$4s$–$5p$	2.89990	0.6858E−02	0.3832E−02	0.3422E−02	0.3213E−02
$4s$–$6p$	3.15784	0.3502E−02	0.2107E−02	0.1393E−03	0.1412E−03
$4s$–$7p$	3.26625	0.1858E−02	0.1142E−02	0.6087E−04	0.5143E−04
$3d$–$4f$	9.61430	0.1517E−02	0.1061E−02	0.1318E−02	0.1304E−02
$3d$–$5f$	9.70487	0.1326E−02	0.9348E−03	0.1174E−02	0.1162E−02
$3d$–$6f$	9.75442	0.9730E−03	0.6884E−03	0.8461E−03	0.8378E−03
$3d$–$5p$	9.26898	0.4577E−01	0.4062E−01	0.4629E−01	0.4683E−01
$3d$–$6p$	9.56488	0.1301E−01	0.1156E−01	0.1292E−01	0.1310E−01
$3d$–$7p$	9.68246	0.5818E−02	0.5169E−02	0.5709E−02	0.5792E−02
$3p$–$5s$	18.57033	0.3140E−01	0.2727E−01	0.1422E−01	0.1424E−01
$3p$–$6s$	19.00568	0.7768E−02	0.6750E−02	0.7812E−02	0.7849E−02
$3p$–$7s$	19.16070	0.3278E−02	0.2849E−02	0.3358E−02	0.3373E−02
$3p$–$4d$	18.59467	0.7950E−01	0.7496E−01	0.8118E−01	0.8212E−01
$3p$–$5d$	19.04107	0.1162E−01	0.1100E−01	0.1003E−01	0.1013E−01
$3p$–$6d$	19.17776	0.5145E−02	0.4877E−02	0.4455E−02	0.4498E−02
$3s$–$5p$	24.07086	0.1914E−01	0.1729E−01	0.1606E−01	0.1623E−01
$3s$–$6p$	24.36601	0.5682E−02	0.5138E−02	0.4803E−02	0.4853E−02
$3s$–$7p$	24.48339	0.2585E−02	0.2338E−02	0.2195E−02	0.2220E−02
Ag					
$5s$–$5p$ up	0.18333	0.1012E+01	0.1008E+01	0.8061E+00	0.8058E+00
$5s$–$6p$ up	0.33277	0.2406E−01	0.2394E−01	0.2691E−02	0.2697E−02
$5s$–$7p$ up	0.38076	0.4889E−02	0.4868E−02	0.6859E−04	0.6918E−04
$4d$–$4f$ do	1.00993	0.1304E−02	0.1105E−02	0.7990E−02	0.7818E−02
$4d$–$5f$ do	1.03256	0.1052E−02	0.8891E−03	0.1014E−02	0.9884E−03
$4d$–$6f$ do	1.04490	0.7388E−03	0.6234E−03	0.6844E−03	0.6672E−03
$4d$–$5p$ do	0.78312	0.3081E+00	0.2809E+00	0.3703E+00	0.3604E+00
$4d$–$6p$ do	0.95736	0.4401E−01	0.3997E−01	0.5054E−01	0.4949E−01
$4d$–$7p$ do	1.00963	0.1595E−01	0.1447E−01	0.7607E−02	0.7463E−02
$4d$–$4f$ up	1.01284	0.2110E−02	0.1575E−02	0.2820E−02	0.2803E−02
$4d$–$5f$ up	1.03559	0.1693E−02	0.1267E−02	0.1455E−02	0.1451E−02

Table 2.2 (continued)

$4d$–$6f$ up	1.04797	0.1183E−02	0.8869E−03	0.9697E−03	0.9680E−03
$4d$–$5p$ up	0.64873	0.3580E+00	0.4133E+00	0.1466E+00	0.1463E+00
$4d$–$6p$ up	0.94711	0.2918E−01	0.3149E−01	0.2463E−02	0.2432E−02
$4d$–$7p$ up	1.00961	0.1046E−01	0.1118E−01	0.7644E−02	0.7499E−02
$4p$–$5d$ do	5.24100	0.9164E−01	0.4970E−01	0.1124E+00	0.9750E−01
$4p$–$6p$ do	5.29082	0.3367E−01	0.1827E−01	0.5706E−01	0.4918E−01
$4p$–$7p$ do	5.31433	0.1598E−01	0.8676E−02	0.2952E−01	0.2534E−01
$4p$–$5s$ do	4.73837	0.1544E+00	0.1167E+00	0.1182E+00	0.1251E+00
$4p$–$6s$ do	5.18352	0.1368E−01	0.1091E−01	0.1442E−01	0.1496E−01
$4p$–$7s$ do	5.27090	0.4462E−02	0.3584E−02	0.4730E−02	0.4917E−02
$4p$–$5d$ up	5.22086	0.1605E−01	0.1208E−01	0.1059E+00	0.8420E−01
$4p$–$6d$ up	5.28087	0.6088E−02	0.4563E−02	0.2649E−02	0.2086E−02
$4p$–$7d$ up	5.30793	0.2942E−02	0.2202E−02	0.3029E−02	0.2978E−02
$4p$–$6s$ up	5.13552	0.4832E−01	0.3325E−01	0.5213E−01	0.4801E−01
$4p$–$7s$ up	5.25833	0.7506E−02	0.5253E−02	0.5529E−02	0.5254E−02
$4p$–$8s$ up	5.29692	0.3069E−02	0.2158E−02	0.2165E−02	0.2107E−02
$4s$–$5p$ do	7.69085	0.9194E−02	0.6388E−02	0.2420E−02	0.1568E−02
$4s$–$6p$ do	7.88097	0.1607E−02	0.1132E−02	0.4111E−03	0.3047E−03
$4s$–$7p$ do	7.93512	0.6248E−03	0.4419E−03	0.1303E−03	0.8889E−04
$4s$–$5p$ up	7.58514	0.9854E−02	0.7530E−02	0.4983E−03	0.5078E−03
$4s$–$6p$ up	7.87848	0.1314E−02	0.9922E−03	0.4687E−04	0.5735E−04
$4s$–$7p$ up	7.93736	0.5126E−03	0.3870E−03	0.9094E−04	0.8228E−04
Ag^+					
$4d$–$4f$	1.39824	0.1061E+00	0.7177E−01	0.1062E+00	0.1067E+00
$4d$–$5f$	1.48975	0.7226E−01	0.4819E−01	0.7674E−01	0.7705E−01
$4d$–$6f$	1.53902	0.4669E−01	0.3091E−01	0.4702E−01	0.4723E−01
$4d$–$5p$	0.90334	0.8512E+00	0.6802E+00	0.5861E+00	0.5834E+00
$4d$–$6p$	1.29423	0.1492E+00	0.1166E+00	0.6349E−01	0.6312E−01
$4d$–$7p$	1.44075	0.5638E−01	0.4388E−01	0.2395E−01	0.2380E−01
$4p$–$5s$	4.79411	0.3499E+00	0.2472E+00	0.3039E+00	0.3002E+00
$4p$–$6s$	5.46942	0.5439E−01	0.4110E−01	0.5970E−01	0.5882E−01
$4p$–$7s$	5.67523	0.2012E−01	0.1540E−01	0.2164E−01	0.2121E−01
$4p$–$5d$	5.52228	0.3249E−01	0.2677E−01	0.9453E−01	0.1005E+00
$4p$–$6d$	5.69877	0.1171E−01	0.9756E−02	0.3886E−01	0.3997E−01
$4p$–$7d$	5.78027	0.5594E−02	0.4684E−02	0.2038E−01	0.2065E−01
$4s$–$5p$	7.79397	0.2691E−01	0.1837E−01	0.5460E−02	0.5115E−02
$4s$–$6p$	8.21036	0.7488E−02	0.5250E−02	0.1962E−02	0.1873E−02
$4s$–$7p$	8.36003	0.3291E−02	0.2326E−02	0.9580E−03	0.9191E−03
$3d$–$4f$	29.67276	0.4565E−03	0.3801E−03	0.4175E−03	0.4175E−03
$3d$–$5f$	29.76326	0.4224E−03	0.3518E−03	0.3852E−03	0.3850E−03
$3d$–$6f$	29.81269	0.3187E−03	0.2654E−03	0.2912E−03	0.2910E−03
$3d$–$4p$	29.09291	0.1861E−01	0.1740E−01	0.2317E−01	0.2364E−01
$3d$–$5p$	29.54994	0.4388E−02	0.4102E−02	0.5513E−02	0.5620E−02
$3d$–$6p$	29.70726	0.1852E−02	0.1731E−02	0.2332E−02	0.2377E−02
Cs					
$6s$–$6p$ up	0.07308	0.1165E+01	0.1090E+01	0.1042E+01	0.1039E+01
$6s$–$7p$ up	0.16366	0.1002E−01	0.7289E−02	0.1141E−02	0.1086E−02

Table 2.2 (continued)

$6s$–$8p$ up	0.19763	0.1399E−02	0.7982E−03	0.4158E−05	0.7625E−05
$5p$–$5p$ do	1.18588	0.2340E+01	0.1659E+01	0.2139E+01	0.2114E+01
$5p$–$6p$ do	1.28581	0.2647E+00	0.1838E+00	0.5086E+00	0.5027E+00
$5p$–$7p$ do	1.30853	0.1048E+00	0.7235E−01	0.4437E−03	0.4372E−03
$5p$–$6s$ do	1.02359	0.2512E+00	0.2424E+00	0.2709E+00	0.2782E+00
$5p$–$7s$ do	1.24009	0.3210E−01	0.3068E−01	0.5584E−01	0.5627E−01
$5p$–$8s$ do	1.29803	0.1142E−01	0.1088E−01	0.2892E−01	0.2895E−01
$5p$–$5d$ up	1.18588	0.2304E+01	0.1577E+01	0.2139E+01	0.2114E+01
$5p$–$6d$ up	1.28581	0.3050E+00	0.2175E+00	0.5047E+00	0.4989E+00
$5p$–$7d$ up	1.31910	0.1144E+00	0.8115E−01	0.3445E+00	0.3405E+00
$5p$–$7s$ up	1.21452	0.9117E−01	0.7865E−01	0.1067E+00	0.1051E+00
$5p$–$8s$ up	1.29589	0.1501E−01	0.1314E−01	0.5101E−02	0.4981E−02
$5p$–$9s$ up	1.32391	0.6595E−02	0.5796E−02	0.7565E−02	0.7487E−02
$5s$–$6p$ do	2.24857	0.2347E−02	0.1164E−02	0.1052E−02	0.1059E−02
$5s$–$7p$ do	2.36585	0.6915E−03	0.3658E−03	0.1196E−03	0.1173E−03
$5s$–$8p$ do	2.40508	0.3142E−03	0.1690E−03	0.4392E−04	0.4419E−04
$5s$–$6p$ up	2.18730	0.1089E−02	0.8795E−03	0.1493E−02	0.1401E−02
$5s$–$7p$ up	2.36836	0.4917E−03	0.3219E−03	0.1460E−03	0.1508E−03
$5s$–$8p$ up	2.41051	0.2282E−03	0.1480E−03	0.5297E−04	0.4915E−04
$4d$–$4f$ do	6.69475	0.3202E−02	0.2373E−02	0.4359E−03	0.4389E−03
$4d$–$5f$ do	6.71761	0.3333E−02	0.2475E−02	0.2161E−03	0.2177E−03
$4d$–$6f$ do	6.73001	0.2668E−02	0.1983E−02	0.2156E−02	0.2167E−02
$4d$–$6p$ do	6.51836	0.4542E−01	0.3990E−01	0.4140E−01	0.3975E−01
$4d$–$7p$ do	6.65934	0.8091E−02	0.7129E−02	0.8769E−02	0.8448E−02
$4d$–$8p$ do	6.70200	0.3273E−02	0.2886E−02	0.3856E−02	0.3723E−02
$4d$–$4f$ up	6.69328	0.6060E−02	0.4500E−02	0.1416E−02	0.1420E−02
$4d$–$5f$ up	6.71699	0.5721E−02	0.4254E−02	0.1562E−02	0.1567E−02
$4d$–$6f$ up	6.73003	0.4294E−02	0.3195E−02	0.2305E−02	0.2317E−02
$4d$–$6p$ up	6.44395	0.4333E−01	0.3932E−01	0.2592E−01	0.2575E−01
$4d$–$7p$ up	6.65398	0.7351E−02	0.6676E−02	0.2537E−02	0.2531E−02
$4d$–$8p$ up	6.70043	0.2838E−02	0.2578E−02	0.5620E−03	0.5650E−03
Cs^+					
$5p$–$5d$	1.24448	0.3287E+01	0.1666E+01	0.2928E+01	0.2693E+01
$5p$–$6d$	1.45357	0.1276E+01	0.6112E+00	0.7972E+00	0.7272E+00
$5p$–$7d$	1.55047	0.6060E+00	0.2831E+00	0.2838E+00	0.2579E+00
$5p$–$6s$	1.07046	0.5660E+00	0.5036E+00	0.6196E+00	0.6130E+00
$5p$–$7s$	1.39544	0.1125E+00	0.9968E−01	0.1529E+00	0.1488E+00
$5p$–$8s$	1.52325	0.4396E−01	0.3893E−01	0.5648E−01	0.5488E−01
$5s$–$6p$	2.31981	0.7048E−02	0.3395E−02	0.1793E−02	0.1466E−02
$5s$–$7p$	2.54776	0.3693E−02	0.1973E−02	0.9539E−03	0.7109E−03
$5s$–$8p$	2.64615	0.1993E−02	0.1097E−02	0.5794E−03	0.5007E−03
$4d$–$4f$	6.85388	0.6450E−01	0.3849E−01	0.7715E−01	0.7609E−01
$4d$–$5f$	6.94581	0.6417E−01	0.3842E−01	0.8215E−01	0.8107E−01
$4d$–$6f$	6.99690	0.4944E−01	0.2965E−01	0.5728E−01	0.5647E−01
$4d$–$6p$	6.57887	0.9234E−01	0.8167E−01	0.7246E−01	0.7250E−01
$4d$–$7p$	6.83525	0.2763E−01	0.2446E−01	0.1295E−01	0.1306E−01
$4d$–$8p$	6.94074	0.1264E−01	0.1119E−01	0.1296E−02	0.1343E−02

Table 2.2 (continued)

$4p$–$5d$	13.13896	0.1370E−01	0.1201E−01	0.1474E−03	0.1593E−03
$4p$–$6d$	13.57328	0.2324E−02	0.2084E−02	0.4676E−03	0.4503E−03
$4p$–$7d$	13.70112	0.1088E−02	0.9802E−03	0.2428E−03	0.2370E−03
$4p$–$6s$	13.18677	0.5131E−01	0.4290E−01	0.3937E−01	0.3915E−01
$4p$–$7s$	13.55377	0.1320E−01	0.1106E−01	0.1006E−01	0.1003E−01
$4p$–$8s$	13.69063	0.5708E−02	0.4784E−02	0.4401E−02	0.4385E−02
$4s$–$6p$	17.21078	0.1615E−01	0.1403E−01	0.1192E−01	0.1191E−01
$4s$–$7p$	17.46695	0.5061E−02	0.4398E−02	0.3810E−02	0.3815E−02
$4s$–$8p$	17.57240	0.2364E−02	0.2054E−02	0.1780E−02	0.1787E−02
$3d$–$4f$	56.19383	0.1443E+01	0.1255E+01	0.1357E+01	0.1309E+01
$3d$–$5f$	56.56047	0.2760E−01	0.2398E−01	0.2570E−01	0.2478E−01
$3d$–$6f$	56.64936	0.1562E−01	0.1357E−01	0.1451E−01	0.1399E−01
$3d$–$6p$	56.25322	0.5074E−02	0.4858E−02	0.1966E−01	0.1870E−01
$3d$–$7p$	56.52312	0.1448E−02	0.1387E−02	0.9372E−03	0.9371E−03
$3d$–$8p$	56.63219	0.6614E−03	0.6334E−03	0.5634E−03	0.5608E−03

2.4 Atoms and Ions of Group II Elements of the Periodic Table

In this section, we present our results for external and intermediate subshells of atoms and some ions of the II group of the Periodic table, namely Be ($Z = 4$) $1s^2\ 2s^2$; Mg ($Z = 12$) $1s^2 2s^2\ 2p^6\ 3s^2$; Ca ($Z = 20$) $3s^2\ 3p^6\ 4s^2$; Ca^{2+} ($Z = 20$) $2p^6\ 3s^2 3p^6$, Ca^- ($Z = 20$) $2p^6$, $3s^2$, $3p^6$, $4s^2$, $4p$; Zn ($Z = 30$) $2p^6 3s^2\ 3p^6\ 3d^{10} 4s^2$; *Sr* ($Z = 38$) $3p^6 3d^{10}\ 4s^2\ 4p^6\ 5s^2$; Cd ($Z = 48$) $3d^{10}\ 4s^2 4p^6 4d^{10}\ 5s^2$; Ba ($Z = 56$) $3d^{10}\ 4s^2 4p^6\ 4d^{10} 5s^2 5p^6 6s^2$; Ba* $7s^2$,$8s^2$,$9s^2$. Formulas, which were used to obtain the data and notations in figures, are the same as for noble gases in Sect. 2.1.

Figure 2.151_Be_a1 (Be) shows the results of calculations on Be atom: ($Z = 4$) $1s^2$, $2s^2$.

Figure 2.151_Be_a1 presents total photoionization cross-section of Be in HF-l, HF-v, and RPAE. Maximums correspond to photoionization of $2s$ and $1s$ subshells. Difference between HF-l and HF-v results is small, while the inessential role of correlations is also reflected in almost negligible distinction between results in HF and RPAE.

Figures 2.152_Mg_a1 and 2.153_Mg_d1 (Mg) contain results of calculations for Mg atom: ($Z = 12$) $1s^2$, $2s^2$, $2p^6$, $3s^2$.

Figure 2.152_Mg_a1 presents total photoionization cross-section of Mg atom in HF-l, HF-v, and RPAE. At $\omega \approx 5$ Ry starts the contribution of $2p$-electrons, whose behavior is similar to that of Ne $2p$-shell. Note that the electron configuration of Mg is [Ne]$3s^2$.

Figure 2.153_Mg_d1 depicts dipole angular anisotropy parameter $\beta_{2p}(\omega)$ of $2p$-electrons for Mg atom. A maximum near threshold and subsequent maximum attract attention.

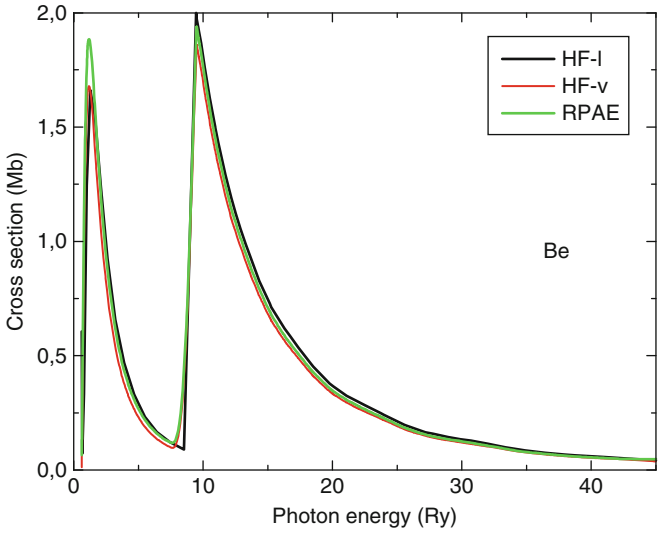

Fig. 2.151_Be_a1 Total photoionization cross section of Be atom in HF-l, HF-v, and RPAE

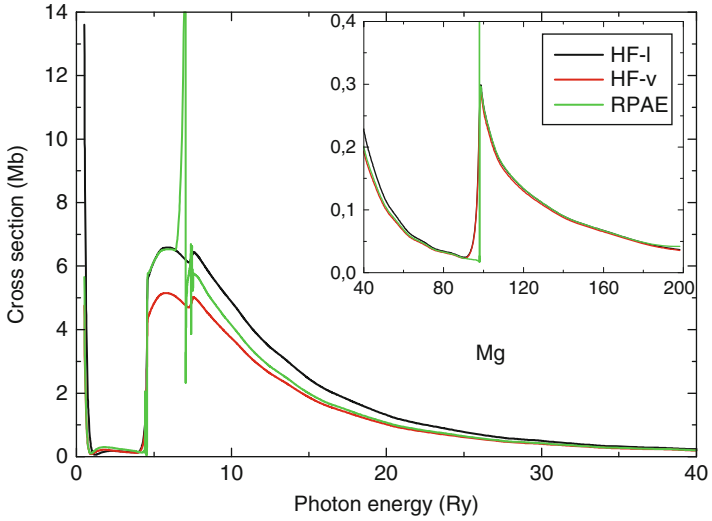

Fig. 2.152_Mg_a1 Total photoionization cross section of Mg atom in HF-l, HF-v, and RPAE

Figures 2.154_Ca_a1 and 2.155_Ca_d1 (Ca) contain results of calculations for Ca atom: ($Z = 20$) $2s^2$, $2p^6$, $3s^2$, $3p^6$, $4s^2$.

Figure 2.154_Ca_a1 presents total photoionization cross-section of Ca atom in HF-l, HF-v, and RPAE. In this case, maximum and subsequent deep minimum near threshold deserve attention.

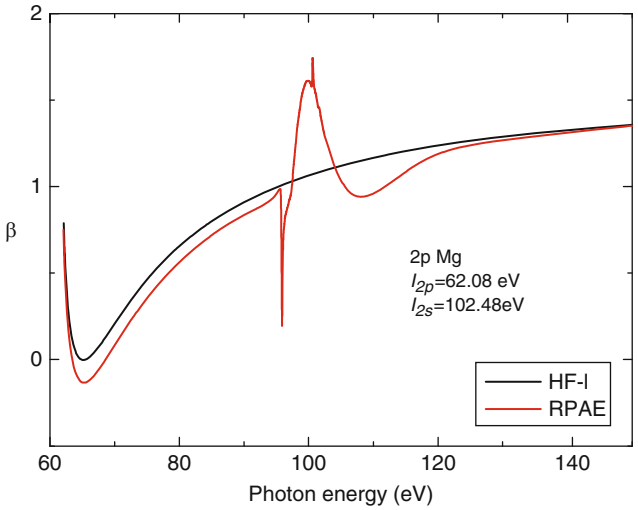

Fig. 2.153_Mg_d1 Dipole angular anisotropy parameter of $2p$-electrons for Mg

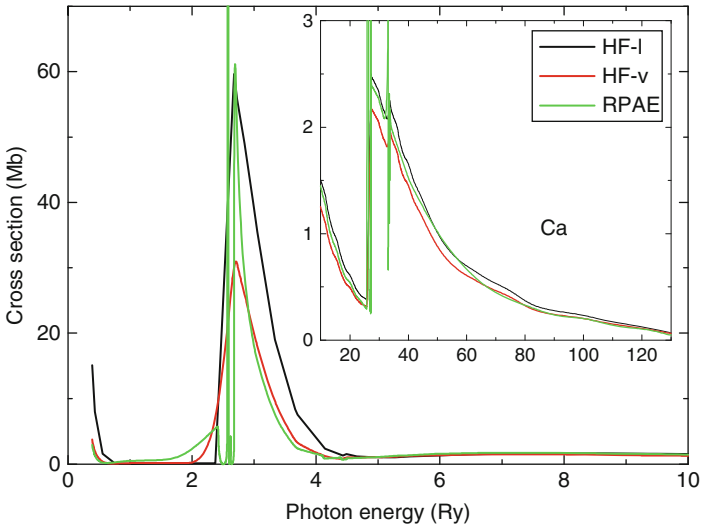

Fig. 2.154_Ca_a1 Total photoionization cross section of Ca atom in HF-l, HF-v, and RPAE

Figure 2.155_Ca_d1 depicts dipole angular anisotropy parameter $\beta_{2p,3p}(\omega)$ of $2p$- and $3p$-electrons of Ca atom in RPAE. The variations of parameter $\beta_{3p}(\omega)$ are strong near $3p$ threshold and near threshold of $2p$-shell.

Figures 2.156_Ca^{2+}_a1 and 2.157_Ca^{2+}_d1 (Ca^{2+}) contain results of calculations for Ca^{2+} ion: ($Z = 20$) $2p^6$, $3s^2$, $3p^6$.

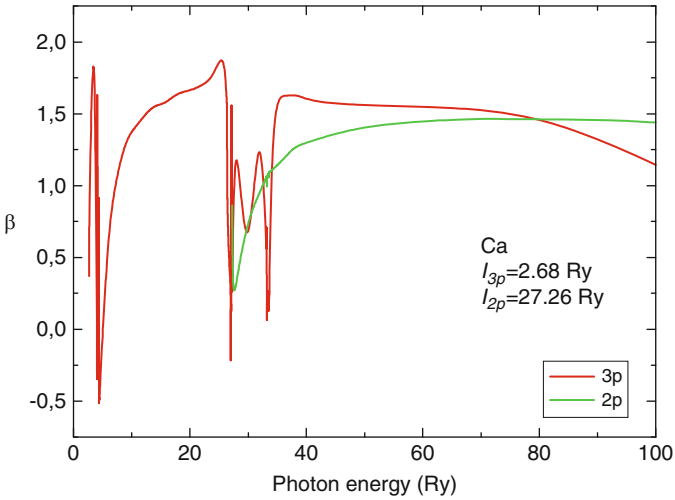

Fig. 2.155_Ca_d1 Dipole angular anisotropy parameter of $3p$- and $2p$-electrons for Ca atom in RPAE

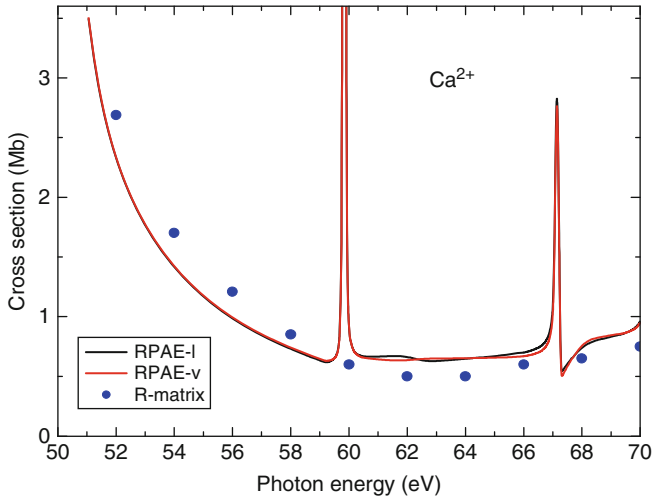

Fig. 2.156_Ca^{2+}_a1 Total photoionization cross section of Ca^{2+} atom in RPAE. R-matrix calculation is from [2.46]

Figure 2.156_Ca^{2+}_a1 presents total photoionization cross-section of Ca^{2+} ion in RPAE. Results of calculation by R-matrix method are from [2.46].

Figure 2.157_Ca^{2+}_d1 shows dipole angular anisotropy parameters $\beta_{3p}(\omega)$ of $3p$-electrons for Ca^{2+} ion. The β-parameter drops rapidly from threshold to a deep minimum.

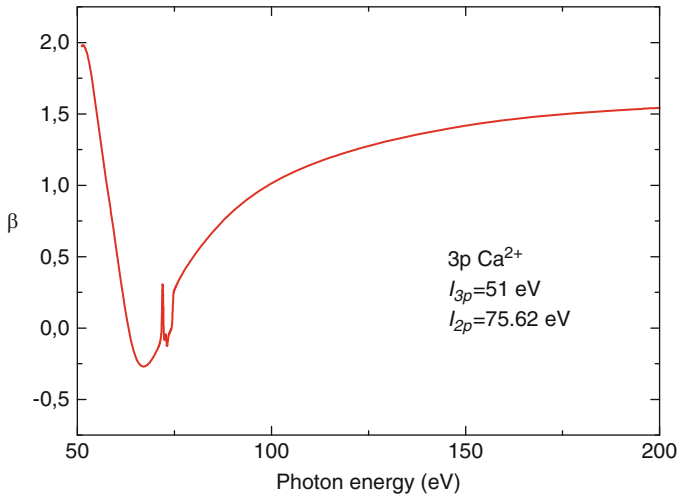

Fig. 2.157_Ca^{2+}_d1 Dipole angular anisotropy parameter of $3p$-electrons for Ca^{2+} ion in RPAE

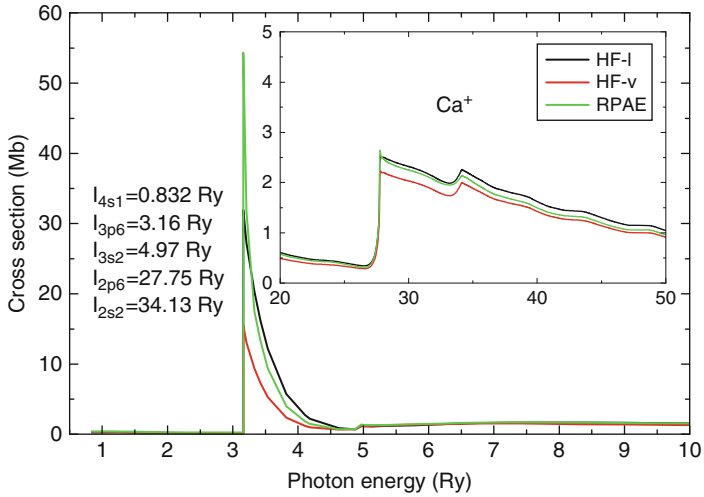

Fig. 2.158_Ca^{-}_a1 Total photoionization cross section of Ca^{+} ion in HF-l, HF-v, and RPAE

Figures 2.158_Ca^{+}_a1 and 2.159_Ca^{+}_d1 contain results of calculations for Ca^{+} ion: $(Z = 20)\, 2p^6, 3s^2, 3p^6, 4s^1$.

Figure 2.158_Ca^{+}_a1 demonstrates the total photoionization cross-section of Ca^{+} ion in HF-l, HF-v, and RPAE. The role of RPAE correlations is quite big and the increase at $3p$ threshold is fast as it would be in a neutral atom with its typical jumps of the photoionization cross-section at thresholds.

Figure 2.159_Ca^{+}_d1 depicts the dipole angular anisotropy parameter of $3p$- and $2p$-electrons for Ca^{+} ion in RPAE. Near $3p$ threshold β_{3p} is similar to Ar

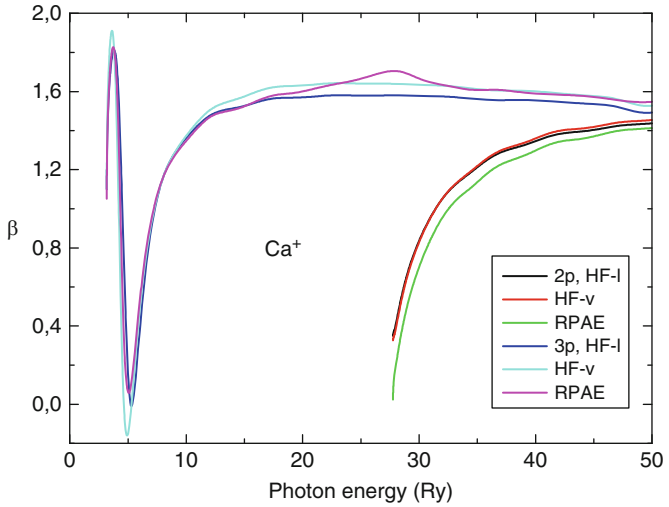

Fig. 2.159_Ca$^+$_d1 Dipole angular anisotropy parameter of $3p$- and $2p$-electrons for Ca^+ ion in RPAE

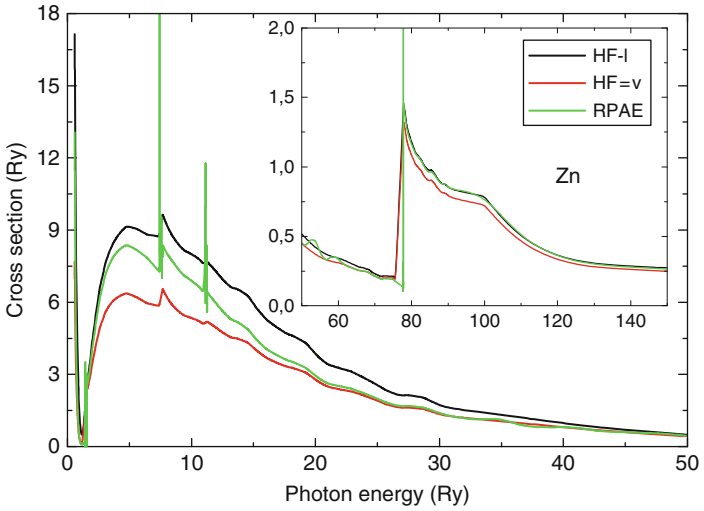

Fig. 2.160_Zn_a1 Total photoionization cross section of Zn atom in HF-l, HF-v, and RPAE

(see Fig. 2.32_Ar_d1). The variation of β_{3p} at the onset of $2p$ subshell ionization is stronger than in Ar.

Figures 2.160_Zn_a1 and 2.161_Zn_d1 (Zn) contain results of calculations for Zn atom: $(Z = 30)\, 2p^6, 3s^2, 3p^6, 3d^{10}, 4s^2$.

Figure 2.160_Zn_a1 presents total photoionization cross-section of Zn in HF-l, HF-v, and RPAE. The cross-section is defined mainly by the maximum of $3d$-electrons. Electron configuration of Zn is [Ar] $3d^{10}4s^2$.

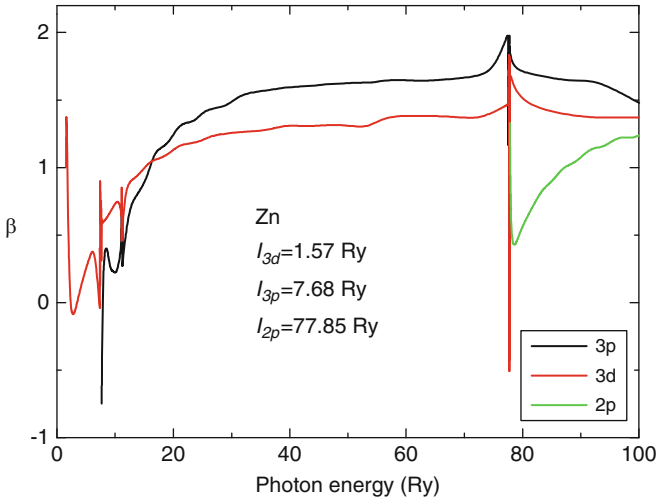

Fig. 2.161_Zn_d1 Dipole angular anisotropy parameter of $2p$-, $3p$-, $3d$-electrons for Zn atom in RPAE

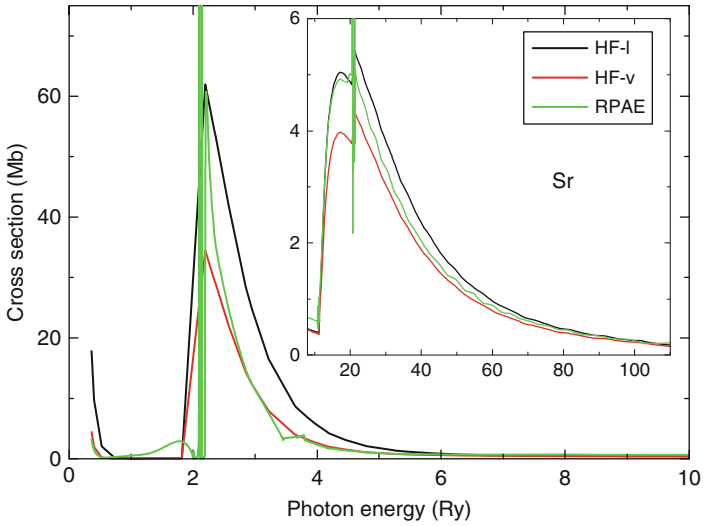

Fig. 2.162_Sr_a1 Total photoionization cross section of Sr atom in HF-l, HF-v, and RPAE

Figure 2.161_Zn_d1 presents dipole angular anisotropy parameters $\beta_{2p,3p,3d}(\omega)$ of $2p$-, $3p$-, and $3d$-electrons for Zn atom in RPAE. Note that the curve $\beta_{3d}(\omega)$ is especially complex.

Figures 2.162_Sr_a1–2.165_Sr_d2 (Sr) contain results of calculations for Sr atom: $(Z = 38)\ 3p^6, 3d^{10}, 4s^2, 4p^6, 5s^2$.

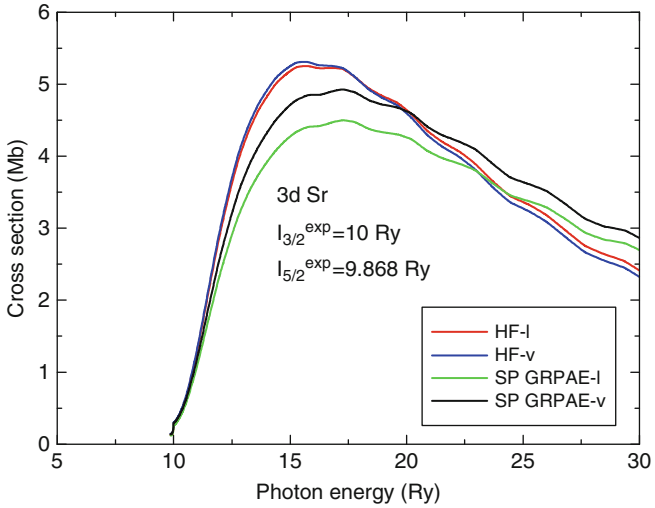

Fig. 2.163_Sr_b1 Partial photoionization cross section of $3d$-electrons for Sr atom in SP HF-l, SP HF-v, and SP GRPAE

Figure 2.162_Sr_a1 presents total photoionization cross-section of Sr atom in HF-l, HF-v, and RPAE. Note the maximum at 20 eV, which is due to the interaction of discrete levels of $4p$-electrons excitation with a continuous spectrum of $5s$-electrons ionization.

Figure 2.163_Sr_b1 shows partial photoionization cross-section of $3d$-electrons for Sr atom in SP HF-l, SP HF-v, and SP GRPAE. In all approximations, the curves increase from threshold reaching its maximum at 6–7 Ry above threshold, i.e., at 16–17 Ry.

Figure 2.164_Sr_d1 displays dipole angular anisotropy parameters $\beta_{4p,3d,3p}(\omega)$ of $4p$-, $3d$-, and $3p$-electrons for Sr atom in RPAE. The shapes of curves $\beta_{4p}(\omega)$ and $\beta_{3d}(\omega)$ are very similar and look as simply contracted in ω.

Figure 2.165_Sr_d2 illustrates the dipole angular anisotropy parameters of $3d_{5/2}$- and $3d_{3/2}$ electrons for Sr atom in SP GRPAE. A big narrow maxima near threshold that is followed by a second maximum dominates the curves. Rearrangement effects, as is seen from comparison with $3d$ data in Fig. 2.164_Sr_d1, are noticeable. The difference between $\beta_{3d_{5/2}}$ and $\beta_{3d_{3/2}}$ is observable.

Figures 2.166_Cd_a1 and 2.167_Cd_d1 (Cd) contain results of calculations for Cd atom: $(Z = 48)\, 4p^6, 4d^{10}, 5s^2$.

Figure 2.166_Cd_a1 shows total photoionization cross-section of Cd atom in HF-l, HF-v, and RPAE. Strong maximum in cross-section of $4d$-electrons shifted beyond ionization threshold is seen.

Figure 2.167_Cd_d1 illustrates dipole angular anisotropy parameters $\beta_{4p,3d,3p}(\omega)$ of $4p$-, $3d$-, and $3p$-electrons in RPAE ($I_{3d} = 32.14$ eV, $I_{4p} = 83.1$ eV, $I_{4d} = 20.81$ eV).

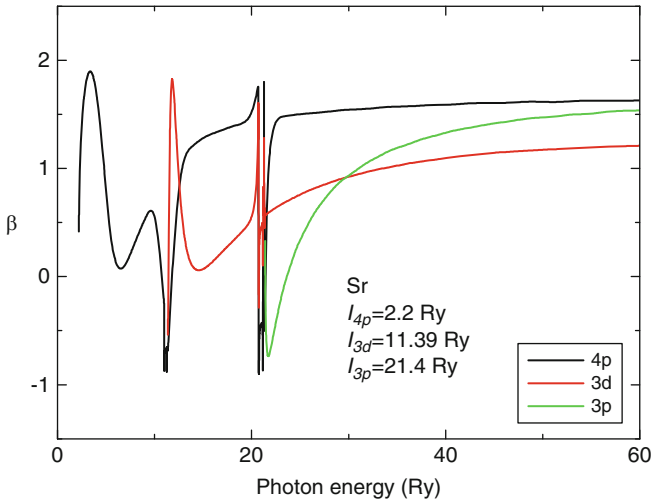

Fig. 2.164_Sr_d1 Dipole anisotropy parameter of $4p$-,$3d$-, $3p$-electrons for Sr atom in RPAE

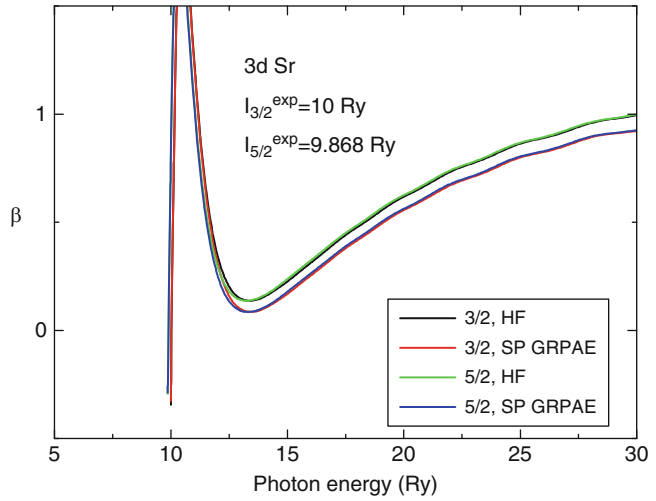

Fig. 2.165_Sr_d2 Dipole anisotropy parameters of $3d$-electrons for Sr atom in SP GRPAE

Figures 2.168_Ba_a1–2.180_Ba_f1 (Ba) contain results of calculations for Ba atom: $(Z = 56)\ 4d^{10}, 5s^2, 5p^6, 6s^2$.

Figure 2.168_Ba_a1 presents total photoionization cross-section of Ba atom in HF-l, HF-v, and RPAE. Giant resonance appears at $\approx$ 8.3 Ry.

Figure 2.169_Ba_b1 depicts photoionization cross-section of $4d$-electrons in RPAE and GRPAE. The given subshell defines the Giant resonance at $\approx$ 8.3 Ry. The difference between GRPAE and RPAE results is quite impressive with a clear

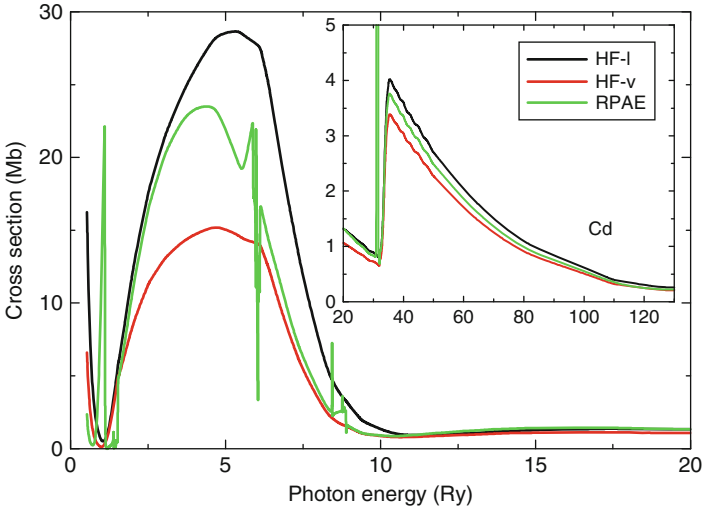

Fig. 2.166_Cd_a1 Total photoionization cross section of Cd atom in HF-l, HF-v, and RPAE

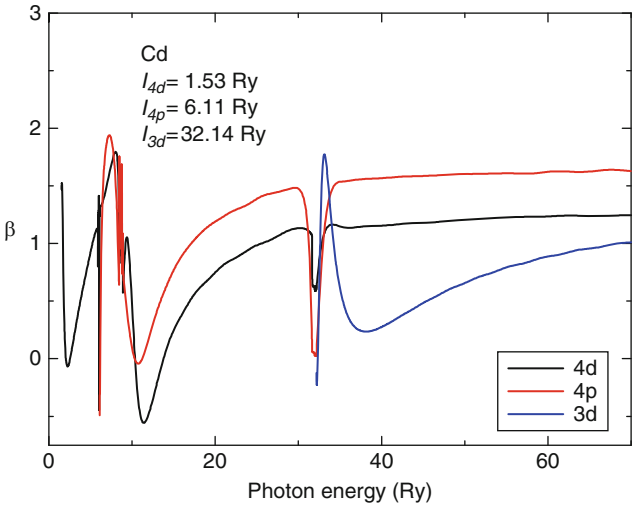

Fig. 2.167_Cd_d1 Dipole anisotropy parameter of $3p$-, $3d$-, $4p$-electrons for Cd atom in RPAE

experimental preference to the GRPAE approach. The experimental data are taken from [2.47].

Figure 2.170_Ba_b2 presents photoionization cross-section of Ba $4d$-electrons in GRPAE. It is seen that $4d$–εf transition absolutely dominated at all frequencies except the very threshold.

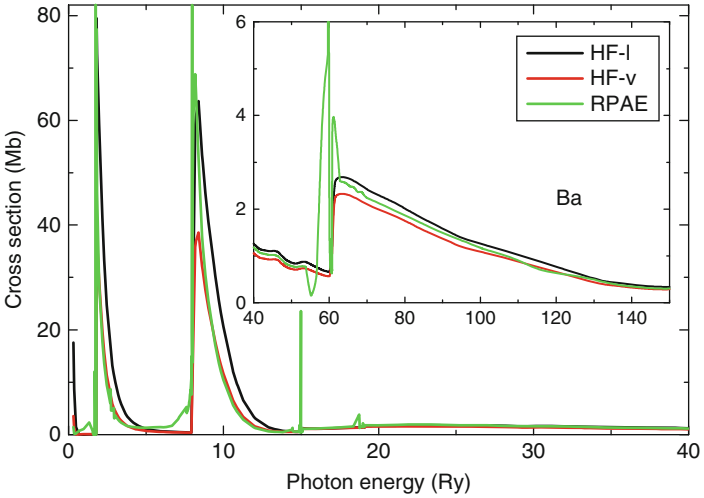

Fig. 2.168_Ba_a1 Total photoionization cross section of Ba atom in HF-l, HF-v, and RPAE

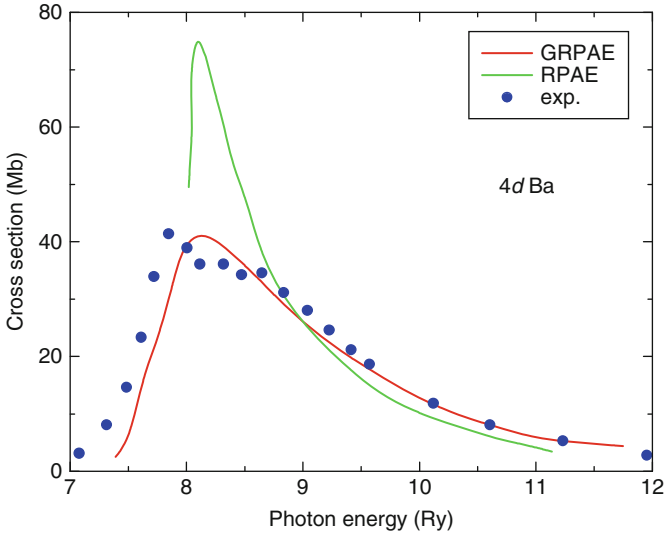

Fig. 2.169_Ba_b1 Photoionization cross section of $4d$-electrons for Ba atom in GRPAE and RPAE. Experiment is taken from [2.46]

Figure 2.171_Ba_b3 presents photoionization cross-section of $3d_{5/2}$ and $3d_{3/2}$ levels in HF and SP GRPAE (see [2.3] and [ACCI]). The ionization thresholds are $I_{3d\,\mathrm{up}} = 57.39$ Ry and $I_{3d\,\mathrm{down}} = 58.507$ Ry. The second maximum in photoionization cross-section of $3d_{5/2}$ electrons, caused by influence of $3d_{3/2}$ electrons, called intra-doublet resonance, is clearly seen. Its height is much more than for

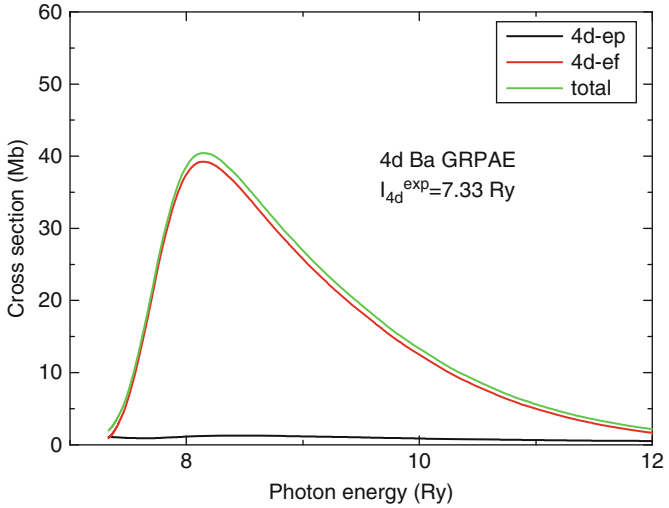

Fig. 2.170_Ba_b2 Photoionization cross section of $4d$-electrons for Ba atom in GRPAE

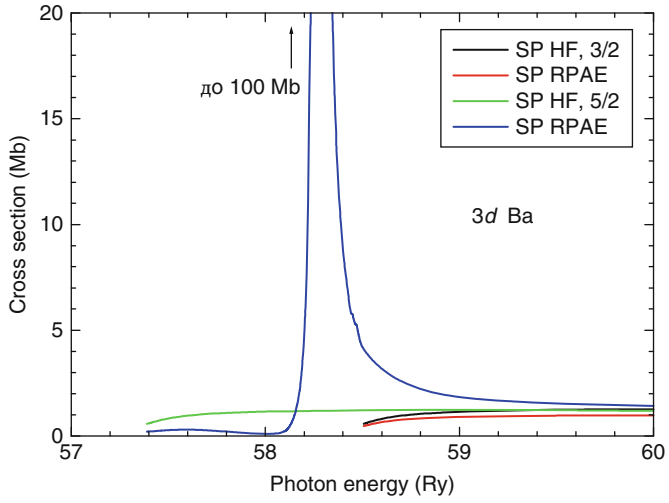

Fig. 2.171_Ba_b3 Photoionization cross section of $3d_{5/2}$- and $3d_{3/2}$-electrons for Ba atom in SP HF and SP RPAE. The ionization thresholds are $I_{3d\,\mathrm{up}} = 57.39$ Ry, $I_{3d\ \mathrm{down}} = 58.507$ Ry

a similar intra-doublet resonance in Cs (Fig. 2.135_Cs_b2) and, especially, in Xe (Fig. 2.59_Xe_b7). Calculation, as well as for $3d$ Xe, is carried out on the basis of the assumption that 5/2 and 3/2 electrons can be considered as "up" and "down" electrons (see Sect. 1.10). The cross-section is calculated according to formulas (1.96)–(1.99), with that, however, specification, that "up" terms in (1.93) are

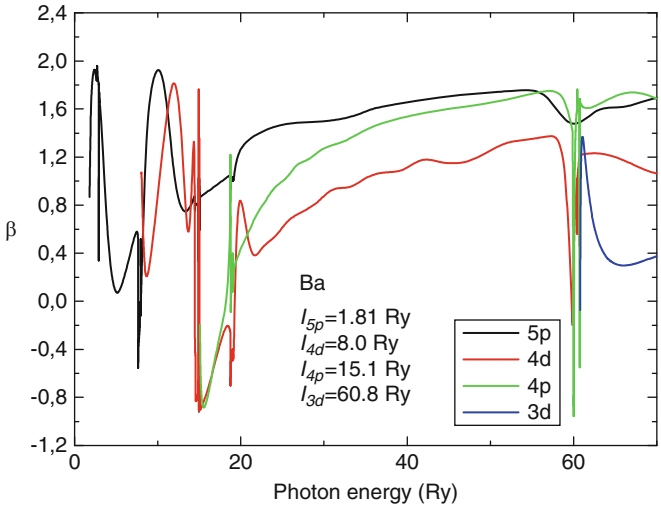

Fig. 2.172_Ba_d1 Dipole anisotropy parameter of $5p$-, $4d$-, $4p$-, and $3d$-electrons for Ba atom

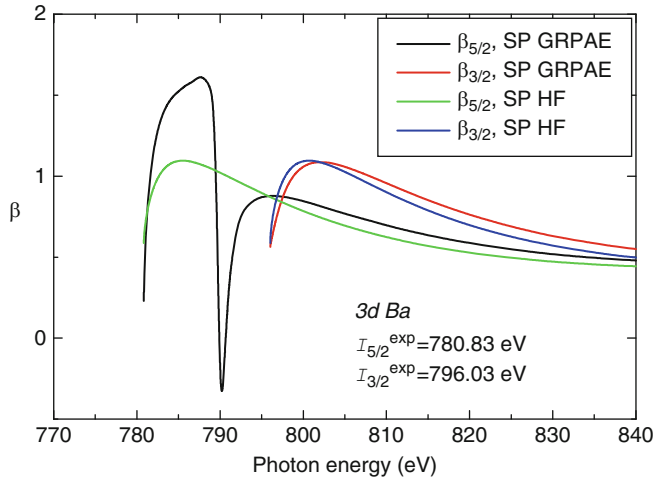

Fig. 2.173_Ba_d2 Dipole anisotropy parameter—electrons of $3d_{5/2}$- and $3d_{3/2}$-electrons for Ba in SP HF and SP GRPAE (see [2.43])

multiplied by 6/5, and "down"—are multiplied by 4/5, taking into account the real number electrons at levels 5/2 and 3/2, i.e., 6 and 4, respectively [2.25].

Figure 2.172_Ba_d1 shows the dipole angular anisotropy parameters $\beta_{5p,4d,4p,3d}(\omega)$ of $5p$-, $4d$-, $4p$-, and $3d$-electrons for Ba atom. Qualitatively, curves resemble the Fig. 2.167_Cd_d1.

Figure 2.173_Ba_d2 depicts dipole angular anisotropy parameters $\beta_{3d_{5/2},3d_{3/2}}(\omega)$ of 5/2- and 3/2-electrons for Ba atom in SP HF and SP GRPAE. The ionization

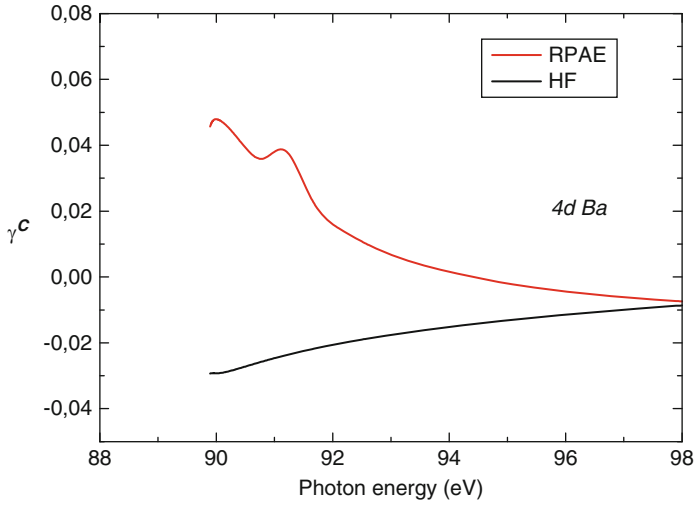

Fig. 2.174_Ba_e1 Non-dipole anisotropy parameter of $4d$-electrons for Ba atom in HF and RPAE

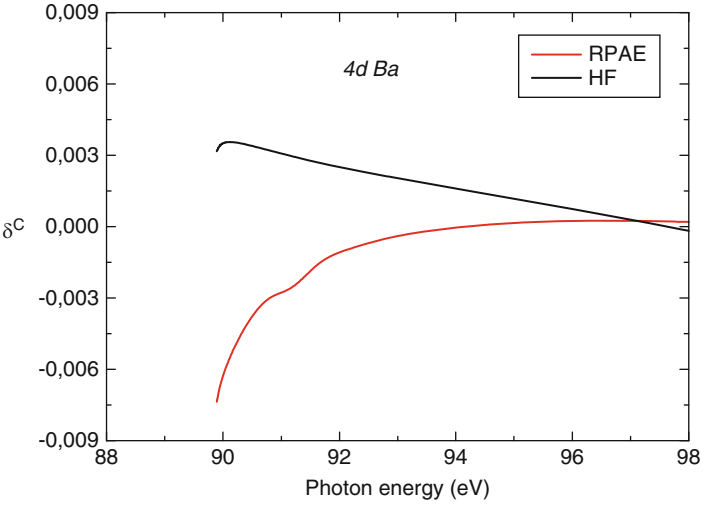

Fig. 2.175_Ba_e2 Non-dipole anisotropy parameter of $4d$-electrons for Ba atom in HF and RPAE

thresholds are $I_{3d5/2} = 57.39$ Ry and $I_{3d3/2} = 58.507$ Ry. Strong influence of 3/2-electrons on angular anisotropy parameter of 5/2-electrons is seen (see [2.43]).

Figure 2.174_Ba_e1 presents the non-dipole angular anisotropy parameter $\gamma^{\mathrm{C}}_{4d}(\omega)$ of Ba $4d$-electrons in HF and RPAE. The influence of correlations is large.

Figure 2.175_Ba_e2 illustrates the non-dipole angular anisotropy parameter $\delta^{\mathrm{C}}_{4d}(\omega)$ of Ba $4d$-electrons in HF and RPAE. Strong influence of correlations is visible.

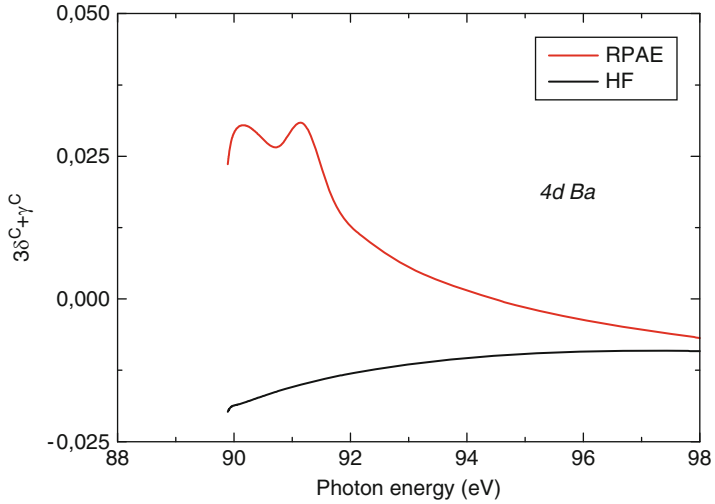

Fig. 2.176_Ba_e3 Non-dipole anisotropy parameter of $4d$-electrons for Ba atom in HF and RPAE (see [2.43])

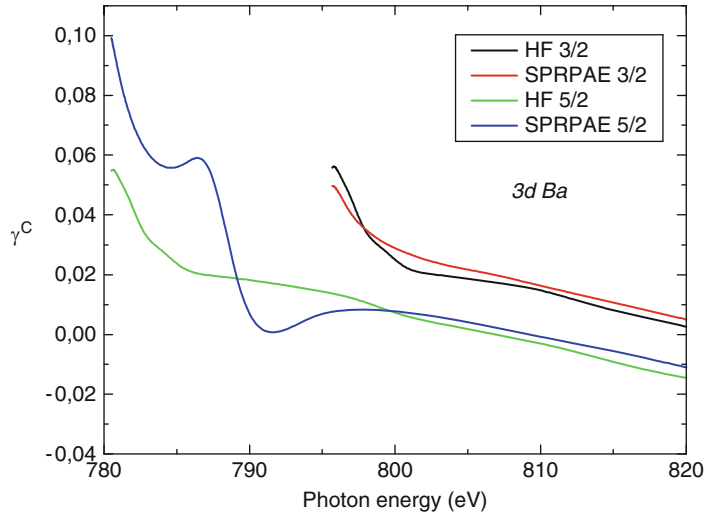

Fig. 2.177_Ba_e4 Non-dipole anisotropy parameter of $3d_{5/2}$- and $3d_{3/2}$-electrons for Ba atom in SP HF and SP GRPAE (see [2.43]). The ionization thresholds are $I_{3d5/2} = 57.39$ Ry, $I_{3d3/2} = 58.507$ Ry

Figure 2.176_Ba_e3 shows the magic combination of non-dipole angular anisotropy parameters $(\gamma^C_{4d} + 3\delta^C_{4d})$ of Ba $4d$-electrons in HF and RPAE (see [2.43]). Influence of correlations is great. In RPAE additional maximum appears at $\omega \approx 91$ eV.

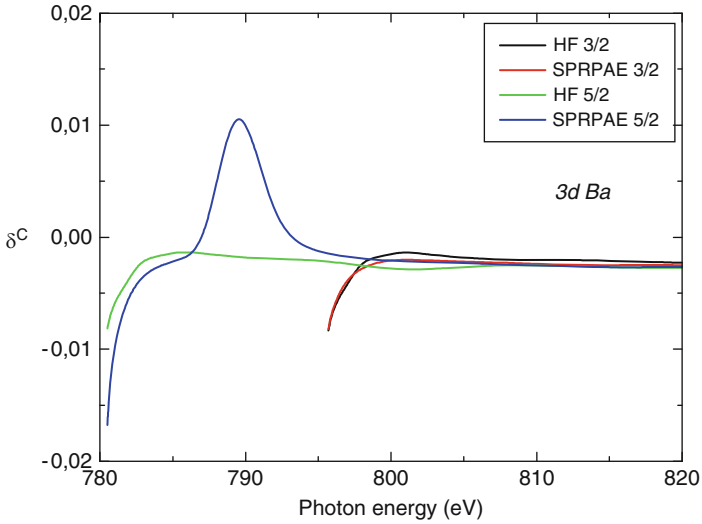

Fig. 2.178_Ba_e5 Non-dipole anisotropy parameter of $3d_{5/2}$- and $3d_{3/2}$-electrons for Ba atom in SP HF and SP GRPAE (see [2.43]). The ionization thresholds are $I_{3d5/2} = 57.39$ Ry, $I_{3d3/2} = 58.507$ Ry

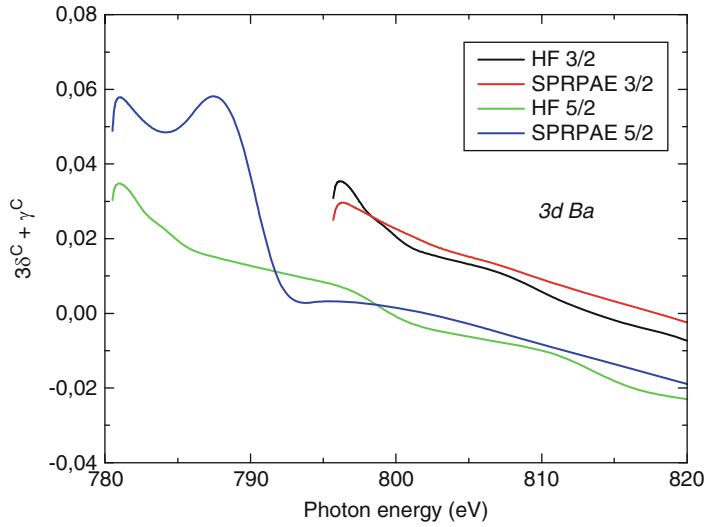

Fig. 2.179_Ba_e6 Magic combination of non-dipole anisotropy parameter of $3d_{5/2}$- and $3d_{3/2}$-electrons for Ba atom in SP HF and SP GRPAE (see [2.43]). The ionization thresholds are $I_{3d5/2} = 57.39$ Ry, $I_{3d3/2} = 58.507$ Ry

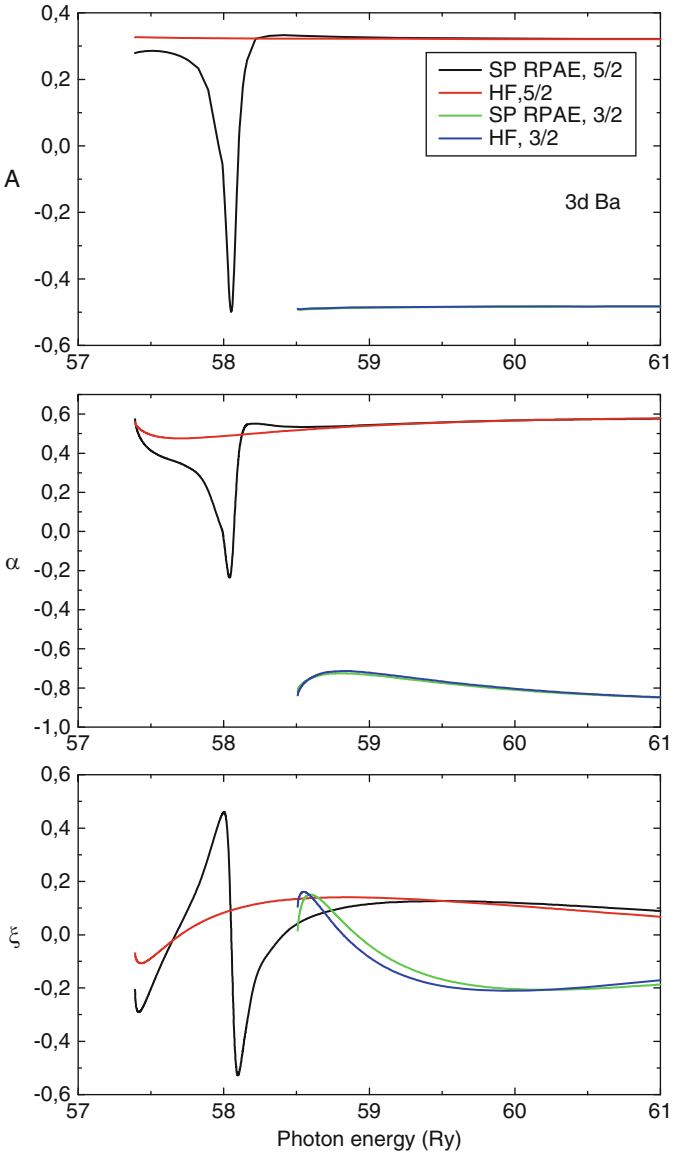

Fig. 2.180_Ba_f1 Spin polarization parameters $A^j(\omega)$, $\alpha^j(\omega)$, and $\xi^j(\omega)$ of $3d_{5/2}$ and $3d_{3/2}$-levels for Ba atom in HF and SP GRPAE (see [2.44]). The ionization thresholds are $I_{3d5/2} = 57.39$ Ry, $I_{3d3/2} = 58.507$ Ry

Figure 2.177_Ba_e4 presents non-dipole angular anisotropy parameter $\gamma^{\mathrm{C}}_{3d5/2,3d3/2}(\omega)$ of Ba $3d_{5/2}$- and $3d_{3/2}$-electrons in HF and SP GRPAE (see [2.43]). The ionization thresholds are $I_{3d5/2} = 57.39$ Ry and $I_{3d3/2} = 58.507$ Ry. Influence of 3/2-electrons on 5/2-electrons is appreciable.

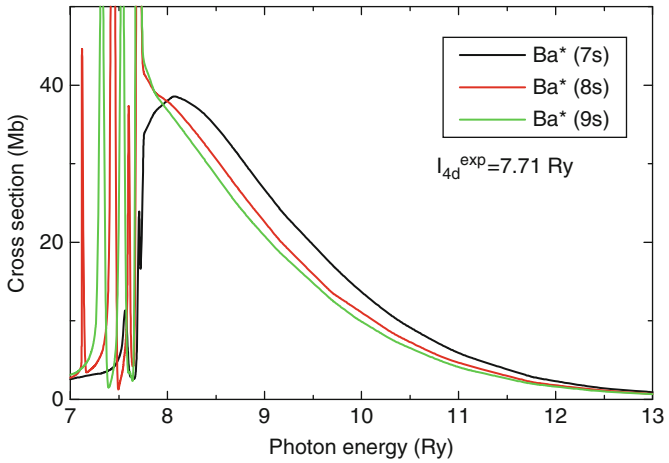

Fig. 2.181_Ba*_a1 Total photoionization cross sections of Ba atom in 7*s*-, 8*s*-, 9*s*-excited states in RPAE

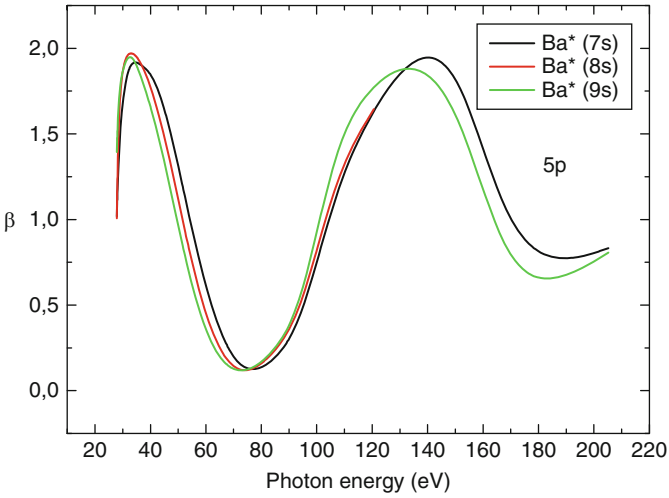

Fig. 2.182_Ba*_d1 Dipole anisotropy parameter of 5*p*-electrons for Ba* in excited states 7*s*, 8*s*, and 9*s*

Figure 2.178_Ba_e5 depicts non-dipole angular anisotropy parameter $\delta^{C}_{3d5/2,3d3/2}(\omega)$ of Ba $3d_{5/2}$- and $3d_{3/2}$-electrons in HF and SP GRPAE (see [2.43]). The ionization thresholds are $I_{3d5/2} = 57.39$ Ry and $I_{3d3/2} = 58.507$ Ry. The influence of 3/2-electrons on 5/2-electrons leads to an appreciable maximum.

Figure 2.179_Ba_e6 demonstrates the magic combination of non-dipole angular anisotropy parameters $(\gamma^{C}_{4d} + 3\delta^{C}_{4d})$ of Ba $3d_{5/2}$ and $3d_{3/2}$ electrons in HF and SP GRPAE (see [2.43]). The ionization thresholds are $I_{3d5/2} = 57.39$ Ry and $I_{3d3/2} = 58.507$ Ry. Influence of correlations is rather great.

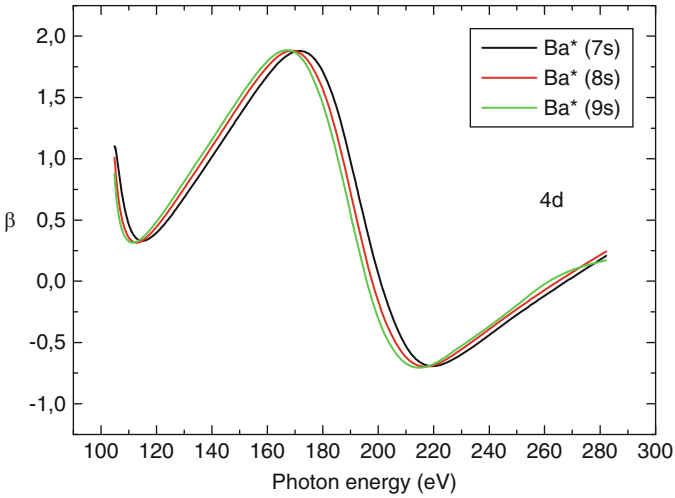

Fig. 2.183_Ba*_d2 Dipole anisotropy parameter of $4d$-electrons for Ba* in excited states $7s$, $8s$, and $9s$

Figure 2.180_Ba_f1 depicts spin polarization parameters $A^j(\omega)\zeta^j(\omega)\xi^j(\omega)$ of $3d_{5/2}$- and $3d_{3/2}$-electrons in GRPAE (see [2.44]). The ionization thresholds are $I_{3d\,\mathrm{up}} = 57.39$ Ry and $I_{3d\,\mathrm{down}} = 58.507$ Ry. The influence of 3/2-electrons on parameters of 5/2 electrons is seen in all cases.

Figures 2.181_Ba*_a1–2.183_Ba*_d2 (Ba*) contain results of calculations for Ba* atom in excited state with an external subshells: ($Z = 56$) $4d^{10}$, $5s^2$, $5p^6$, $7s^2$ ($8s^2$, $9s^2$)

Figure 2.181_Ba*_a1 presents total photoionization cross-section of Ba* atom with filled external subshell $7s^2$, $8s^2$, or $9s^2$ in RPAE. There is a displacement of the Giant resonance toward lower ω and significant strengthening of the discrete transitions $4d$–$6p$, $7p$, $8p$.

Figure 2.182_Ba*_d1 depicts dipole angular anisotropy parameters $\beta_{5p}(\omega)$ for excited levels $7s^2$, $8s^2$, $9s^2$ of Ba* atom calculated in SP RPAE.

Figure 2.183_Ba*_d2 demonstrates dipole angular anisotropy parameters $\beta_{4d}(\omega)$ for excited states $7s^2$, $8s^2$, $9s^2$ of Ba* in SP RPAE.

Table 2.3 includes calculated values of oscillator strengths in HF-l, HF-v, $f^{l,v}_{nl-n'l'}$, and $F^{l,v}_{nl-n'l'}$ in RPAE for several lowest discrete levels of excitation and for each considered subshell of atoms investigated in this section. Theoretical transition energies in RPAE $\tilde{\omega}_{nl-n'l'}$ are also given in this table.

The results for length and velocity forms in RPAE coincide with reasonable accuracy. In Be, Mg, and Cd, the outer electron *ns–np* transition dominates. In Ca, Sr, and Ba, the subvalent $(n-1)p-(n-1)d$ transitions absolutely dominate, while *ns–np* oscillator strengths are smaller, namely the second in Ca and Sr and even third in Ba. The role of correlations for several outer electrons excitations is big. Starting from Ca, the same is correct for the next subshell. For Cd and Ba correlations in the third subshell are also quite important. The oscillator strengths are, in general, decreasing with decrease in principal quantum number of the exited electron.

Table 2.3 Oscillator strengths and transition energies of II group's elements and ions

Transition	ω (Ry)	HF-l	HF-v	RPAE-l	RPAE-v
Be					
$2s$–$2p$	0.35361	0.1900E+01	0.1014E+01	0.1381E+01	0.1366E+01
$2s$–$3p$	0.49431	0.1064E+00	0.3173E−01	0.2412E−01	0.2339E−01
$2s$–$4p$	0.54998	0.1559E−01	0.2304E−02	0.1178E−02	0.1095E−02
$1s$–$2p$	8.69149	0.3752E+00	0.3611E+00	0.3745E+00	0.3744E+00
$1s$–$3p$	9.29261	0.3601E−01	0.3418E−01	0.3540E−01	0.3535E−01
$1s$–$4p$	9.38033	0.1191E−01	0.1129E−01	0.1169E−01	0.1167E−01
Mg					
$3s$–$3p$	0.29673	0.2099E+01	0.1159E+01	0.1661E+01	0.1607E+01
$3s$–$4p$	0.40304	0.3033E+00	0.1369E+00	0.1470E+00	0.1400E+00
$3s$–$5p$	0.44663	0.8745E−01	0.3580E−01	0.3373E−01	0.3183E−01
$2p$–$3d$	40.43151	0.4823E−01	0.3566E−01	0.4517E−01	0.4507E−01
$2p$–$4d$	4.49230	0.2072E−01	0.1550E−01	0.1923E−01	0.1918E−01
$2p$–$5d$	4.51953	0.1040E−01	0.7809E−02	0.9438E−02	0.9412E−02
$2p$–$4s$	4.31389	0.6187E−01	0.5337E−01	0.7717E−01	0.7684E−01
$2p$–$5s$	4.46476	0.7815E−02	0.6787E−02	0.9452E−02	0.9422E−02
$2p$–$6s$	4.50759	0.3106E−02	0.2701E−02	0.3728E−02	0.3719E−02
$2s$–$3p$	7.03720	0.5224E−01	0.5097E−01	0.3287E−01	0.3326E−01
$2s$–$4p$	7.39733	0.6447E−02	0.6131E−02	0.4048E−02	0.4026E−02
$2s$–$5p$	7.46311	0.2441E−02	0.2315E−02	0.1554E−02	0.1541E−02
$1s$–$3p$	97.46234	0.4345E−01	0.4190E−01	0.4326E−01	0.4269E−01
$1s$–$4p$	97.91425	0.4455E−02	0.4299E−02	0.4439E−02	0.4380E−02
$1s$–$5p$	97.98711	0.1575E−02	0.1520E−02	0.1569E−02	0.1548E−02
Ca					
$4s$–$4p$	0.20553	0.2523E+01	0.1226E+01	0.1839E+01	0.1773E+01
$4s$–$5p$	0.29642	0.3462E+00	0.1279E+00	0.1094E+00	0.1027E+00
$4s$–$6p$	0.33548	0.9524E−01	0.3056E−01	0.2021E−01	0.1861E−01
$3p$–$3d$	2.42559	0.2213E+01	0.1212E+01	0.2584E+01	0.2538E+01
$3p$–$4d$	2.58596	0.3629E+00	0.1977E+00	0.2306E+00	0.2260E+00
$3p$–$5d$	2.62599	0.1624E+00	0.8799E−01	0.8871E−01	0.8698E−01
$3p$–$5s$	2.48473	0.1208E+00	0.1006E+00	0.2697E−01	0.2664E−01
$3p$–$6s$	2.59528	0.1805E−01	0.1519E−01	0.5364E−02	0.5313E−02
$3p$–$7s$	2.63057	0.7471E−02	0.6299E−02	0.2296E−02	0.2281E−02
$3s$–$4p$	4.10109	0.2169E−01	0.2016E−01	0.5014E−02	0.4863E−02
$3s$–$5p$	4.37117	0.3493E−02	0.3045E−02	0.1295E−02	0.1219E−02
$3s$–$6p$	4.42580	0.1416E−02	0.1226E−02	0.5563E−03	0.5206E−03
$2p$–$3d$	26.31784	0.9311E+00	0.8207E+00	0.9079E+00	0.9139E+00
$2p$–$4d$	27.13029	0.2642E−01	0.2320E−01	0.2524E−01	0.2540E−01
$2p$–$5d$	27.19009	0.9255E−02	0.8131E−02	0.8759E−02	0.8815E−02
$2p$–$5s$	27.01496	0.8353E−02	0.7929E−02	0.1048E−01	0.1062E−01
$2p$–$6s$	27.16647	0.8518E−03	0.8089E−03	0.9992E−03	0.1013E−02
$2p$–$7s$	27.20522	0.3555E−03	0.3377E−03	0.3496E−03	0.3548E−03
$2s$–$4p$	33.18718	0.3228E−01	0.3111E−01	0.2320E−01	0.2312E−01
$2s$–$5p$	33.51740	0.3870E−02	0.3731E−02	0.2796E−02	0.2786E−02
$2s$–$6p$	33.57730	0.1443E−02	0.1392E−02	0.1031E−02	0.1029E−02

Table 2.3 (continued)

Zn					
$4s$–$4p$	0.47707	0.3088E+00	0.1604E+00	0.2851E+00	0.1774E+00
$4s$–$5p$	0.52361	0.9550E−01	0.4676E−01	0.6602E−01	0.3901E−01
$4s$–$6p$	0.54556	0.4188E−01	0.1991E−01	0.2406E−01	0.1385E−01
$3d$–$4p$	1.42787	0.3152E−01	0.2870E−01	0.2902E−01	0.2663E−01
$3d$–$5p$	1.49306	0.1119E−01	0.1012E−01	0.9848E−02	0.9001E−02
$3d$–$6p$	1.52050	0.5313E−02	0.4790E−02	0.4543E−02	0.4145E−02
$3d$–$4f$	1.50228	0.4248E−03	0.3065E−03	0.4778E−03	0.4121E−03
$3d$–$5f$	1.52489	0.3499E−03	0.2528E−03	0.4027E−03	0.3511E−03
$3d$–$6f$	1.53718	0.2484E−03	0.1796E−03	0.2589E−03	0.2264E−03
$3p$–$4d$	7.55878	0.8835E−03	0.8322E−03	0.1338E−02	0.1523E−02
$3p$–$5d$	7.61206	0.3961E−03	0.3684E−03	0.6247E−03	0.6854E−03
$3p$–$6d$	7.63656	0.2005E−03	0.1855E−03	0.2918E−03	0.3155E−03
$3p$–$5s$	7.43034	0.6214E−01	0.4638E−01	0.5943E−01	0.5428E−01
$3p$–$6s$	7.57686	0.9217E−02	0.6950E−02	0.8767E−02	0.8021E−02
$3p$–$7s$	7.62086	0.3644E−02	0.2755E−02	0.3453E−02	0.3165E−02
$3s$–$4p$	11.13603	0.3247E−02	0.2716E−02	0.3022E−02	0.2954E−02
$3s$–$5p$	11.20275	0.1223E−02	0.1022E−02	0.1136E−02	0.1110E−02
$3s$–$6p$	11.23065	0.5938E−03	0.4960E−03	0.5528E−03	0.5401E−03
$2p$–$4d$	77.72540	0.1049E−01	0.9510E−02	0.1061E−01	0.1055E−01
$2p$–$5d$	77.78090	0.4984E−02	0.4521E−02	0.4976E−02	0.4946E−02
$2p$–$6d$	77.80644	0.2568E−02	0.2329E−02	0.2508E−02	0.2492E−02
$2p$–$5s$	77.56570	0.2783E−02	0.2802E−02	0.5557E−02	0.5713E−02
$2p$–$6s$	77.74314	0.3250E−03	0.3264E−03	0.4779E−03	0.4928E−03
$2p$–$7s$	77.79001	0.1280E−03	0.1285E−03	0.1810E−03	0.1867E−03
Sr					
$5s$–$5p$	0.18261	0.2662E+01	0.1257E+01	0.1911E+01	0.1837E+01
$5s$–$6p$	0.26663	0.3876E+00	0.1401E+00	0.1149E+00	0.1074E+00
$5s$–$7p$	0.30337	0.1100E+00	0.3484E−01	0.2141E−01	0.1962E−01
$4p$–$4d$	1.94745	0.2677E+01	0.1439E+01	0.2728E+01	0.2679E+01
$4p$–$5d$	2.10384	0.3900E+00	0.2113E+00	0.2846E+00	0.2793E+00
$4p$–$6d$	2.14259	0.1726E+00	0.9329E−01	0.1064E+00	0.1044E+00
$4p$–$6s$	2.01566	0.1544E+00	0.1285E+00	0.1372E+00	0.1358E+00
$4p$–$7s$	2.11475	0.2468E−01	0.2076E−01	0.2310E−01	0.2290E−01
$4p$–$8s$	2.14757	0.1033E−01	0.8714E−02	0.9116E−02	0.9055E−02
$4s$–$5p$	3.44564	0.7582E−02	0.6781E−02	0.3956E−03	0.5090E−03
$4s$–$6p$	3.68166	0.1543E−02	0.1236E−02	0.1177E−03	0.9112E−04
$4s$–$7p$	3.73183	0.6581E−03	0.5220E−03	0.6999E−04	0.5163E−04
$3d$–$4f$	11.32503	0.5293E−04	0.3857E−04	0.5403E−04	0.5431E−04
$3d$–$5f$	11.34784	0.4863E−04	0.3546E−04	0.4279E−04	0.4300E−04
$3d$–$6f$	11.36035	0.3613E−04	0.2636E−04	0.3163E−04	0.3187E−04
$3d$–$5p$	10.98704	0.4069E−01	0.3627E−01	0.4168E−01	0.4236E−01
$3d$–$6p$	11.26978	0.4975E−02	0.4433E−02	0.5058E−02	0.5140E−02
$3d$–$7p$	11.32421	0.1910E−02	0.1702E−02	0.1921E−02	0.1952E−02
$3p$–$4d$	20.69861	0.1298E+00	0.1231E+00	0.1050E+00	0.1020E+00
$3p$–$5d$	21.28029	0.5637E−02	0.5286E−02	0.4521E−02	0.4395E−02
$3p$–$6d$	21.33523	0.2021E−02	0.1898E−02	0.1631E−02	0.1585E−02
$3p$–$6s$	21.18344	0.1685E−01	0.1463E−01	0.1750E−01	0.1738E−01

Table 2.3 (continued)

$3p$–$7s$	21.31344	0.1912E−02	0.1662E−02	0.1995E−02	0.1981E−02
$3p$–$8s$	21.34918	0.8126E−03	0.7063E−03	0.8623E−03	0.8562E−03
Cd					
$5s$–$5p$	0.30449	0.2149E+01	0.1220E+01	0.1543E+01	0.1492E+01
$5s$–$6p$	0.42302	0.3229E+00	0.1563E+00	0.7816E−01	0.7372E−01
$5s$–$7p$	0.46909	0.9671E−01	0.4366E−01	0.1387E−01	0.1288E−01
$4d$–$4f$	1.46430	0.1497E−02	0.9503E−03	0.1743E−02	0.1749E−02
$4d$–$5f$	1.48700	0.1232E−02	0.7828E−03	0.1195E−02	0.1199E−02
$4d$–$6f$	1.49934	0.8734E−03	0.5553E−03	0.8203E−03	0.8228E−03
$4d$–$5p$	1.09546	0.7097E+00	0.6712E+00	0.6659E+00	0.6748E+00
$4d$–$6p$	1.39745	0.5959E−01	0.5386E−01	0.4439E−01	0.4488E−01
$4d$–$7p$	1.45823	0.2162E−01	0.1941E−01	0.1457E−01	0.1473E−01
$4p$–$5d$	5.98704	0.4204E−02	0.4123E−02	0.1960E−01	0.1838E−01
$4p$–$6d$	6.04078	0.1853E−02	0.1799E−02	0.7745E−02	0.8435E−02
$4p$–$7d$	6.06514	0.9439E−03	0.9132E−03	0.3858E−02	0.4188E−02
$4p$–$6s$	5.88614	0.8732E−01	0.6311E−01	0.8158E−01	0.8065E−01
$4p$–$7s$	6.01182	0.1447E−01	0.1059E−01	0.1298E−01	0.1286E−01
$4p$–$8s$	6.05202	0.5840E−02	0.4288E−02	0.5195E−02	0.5149E−02
$4s$–$5p$	8.43933	0.2483E−01	0.1947E−01	0.6905E−02	0.6856E−02
$4s$–$6p$	8.76924	0.2763E−02	0.2136E−02	0.8549E−03	0.8434E−03
$4s$–$7p$	8.83127	0.1062E−02	0.8202E−03	0.3401E−03	0.3348E−03
$3d$–$4f$	32.08124	0.3872E−05	0.3259E−05	0.3536E−05	0.3516E−05
$3d$–$5f$	32.10379	0.3447E−05	0.2901E−05	0.3171E−05	0.3153E−05
$3d$–$6f$	32.11606	0.2552E−05	0.2148E−05	0.2353E−05	0.2340E−05
$3d$–$5p$	31.63068	0.1701E−01	0.1609E−01	0.2153E−01	0.2198E−01
$3d$–$6p$	32.00689	0.1604E−02	0.1516E−02	0.2045E−02	0.2087E−02
$3d$–$7p$	32.07218	0.5973E−03	0.5644E−03	0.7619E−03	0.7771E−03
Ba					
$6s$–$6p$	0.15158	0.2919E+01	0.1275E+01	0.1975E+01	0.1893E+01
$6s$–$7p$	0.22883	0.4114E+00	0.1307E+00	0.8890E−01	0.8223E−01
$6s$–$8p$	0.26346	0.1122E+00	0.3022E−01	0.1387E−01	0.1243E−01
$5p$–$7s$	1.64393	0.1794E+00	0.1475E+00	0.1927E+00	0.1891E+00
$5p$–$8s$	1.73149	0.3019E−01	0.2512E−01	0.3333E−01	0.3274E−01
$5p$–$9s$	1.76150	0.1290E−01	0.1076E−01	0.1341E−01	0.1320E−01
$5p$–$5d$	1.51681	0.4196E+01	0.2084E+01	0.3845E+01	0.3749E+01
$5p$–$6d$	1.71132	0.5221E+00	0.2605E+00	0.3036E+00	0.2956E+00
$5p$–$7d$	1.75252	0.2241E+00	0.1112E+00	0.1026E+00	0.9993E−01
$5s$–$6p$	2.70742	0.6413E−02	0.5577E−02	0.1417E−02	0.1624E−02
$5s$–$7p$	2.92020	0.1511E−02	0.1134E−02	0.7327E−03	0.6598E−03
$5s$–$8p$	2.96650	0.6624E−03	0.4913E−03	0.3800E−03	0.3266E−03
$4d$–$6p$	7.64417	0.8549E−01	0.7607E−01	0.5963E−01	0.6028E−01
$4d$–$7p$	7.89195	0.1118E−01	0.9949E−02	0.4464E−02	0.4523E−02
$4d$–$8p$	7.94176	0.4383E−02	0.3899E−02	0.1722E−02	0.1745E−02
$4d$–$4f$	7.93694	0.1444E−01	0.8695E−02	0.2632E−01	0.2643E−01
$4d$–$5f$	7.96011	0.1549E−01	0.9323E−02	0.3077E−01	0.3090E−01
$4d$–$6f$	7.97319	0.1229E−01	0.7395E−02	0.2390E−01	0.2400E−01
$4p$–$7s$	14.90677	0.2732E−01	0.2290E−01	0.2191E−01	0.2183E−01
$4p$–$8s$	15.01825	0.3381E−02	0.2839E−02	0.2729E−02	0.2718E−02

Table 2.3 (continued)

$4p$–$9s$	15.05063	0.1463E−02	0.1229E−02	0.1190E−02	0.1185E−02
$4p$–$5d$	14.44104	0.2777E−01	0.2522E−01	0.6914E−02	0.6259E−02
$4p$–$6d$	14.97998	0.1791E−02	0.1571E−02	0.7048E−03	0.6617E−03
$4p$–$7d$	15.03500	0.6006E−03	0.5305E−03	0.2444E−03	0.2298E−03
$4s$–$6p$	18.75511	0.1687E−01	0.1486E−01	0.1343E−01	0.1331E−01
$4s$–$7p$	19.00213	0.2307E−02	0.2027E−02	0.1839E−02	0.1825E−02
$4s$–$8p$	19.05175	0.9115E−03	0.8010E−03	0.7307E−03	0.7254E−03
$3d$–$6p$	60.42393	0.4899E−02	0.4690E−02	0.2817E−02	0.2885E−02
$3d$–$7p$	60.69081	0.6402E−03	0.6130E−03	0.5755E−03	0.5849E−03
$3d$–$8p$	60.74234	0.2464E−03	0.2359E−03	0.2166E−03	0.2202E−03
$3d$–$4f$	59.86615	0.1916E+01	0.1672E+01	0.1812E+01	0.1790E+01
$3d$–$5f$	60.73994	0.6839E−03	0.5953E−03	0.6494E−03	0.6412E−03
$3d$–$6f$	60.76303	0.5886E−03	0.5123E−03	0.5416E−03	0.5346E−03

2.5 Ions and Atoms of Group III Elements of the Periodic Table

In this section we present our results for outer and intermediate subshells of ions and some atoms belonging to the III group of periodic table. Here we have concentrated basically on the ions having all filled or one half-filled subshell, namely B ($Z=5$) $1s^2 2s^2 2p$; B* ($Z=5$) $1s\uparrow\ 2s\uparrow 2p^3\uparrow$ (^{6}S), B^+ ($Z=5$) $1s^2\ 2s^2$; Al^+ ($Z=13$) $2s^2\ 2p^6 3s^2$; Sc^{3+} ($Z=21$) $2p^6 3s^2 3p^6$; In^+ ($Z=49$) $3d^{10}4s^2 4p^6 4d^{10}5s^2$; La ($Z=57$) $4d^{10}5s^2 5p^6 5d 6s^2$; Ce^+ ($Z=58$) $4d^{10}5s^2 5p^6 5d 6s^2$; Ce^{3+} ($Z=58$) $4d^{10}5s^2 5p^6 5d$; Ce^{4+} ($Z=58$) $4d^{10}5s^2 5p^6$; Eu ($Z=63$) $3d^{10}\ 4d^{10}5s^2 5p^6 4f^7\uparrow 6s^2$; Eu^+ $3d^{10}\ 4d^{10}\ 5s^2 5p^6 4f^7\uparrow 6s^1$; Eu^{2+} $3d^{10}\ 4d^{10}\ 5s^2\ 5p^6 4f^7\uparrow$. Formulas used to obtain data and notations in figures are the same as for noble gases and are summarized in Sect. 2.1.

Here $\uparrow$ denotes "up" electrons for SP RPAE (see Sect. 1.10).

Figure 2.184_BB*_a1 (B) shows data on B atom: B ($Z=5$) $1s^2 2s^2\ 2p^1$.

Figure 2.184_BB*_a1 compares total photoionization cross-sections of B (in RPAEO) and B* (in SP RPAE). Interest to considered excited state B* is connected to the fact that it cannot decay via electron transitions without change of spin projection. As to the spin conserving transitions, they are forbidden due to Pauli Exclusion Principle an 1945.

Figures 2.185_B*_a1 and 2.186_B*_d1 (B*) show results of calculations on B* atom in excited state ($Z=5$) $1s\uparrow 2s\uparrow 2p^3\uparrow$.

Figure 2.185_B*_a1 presents total photoionization cross-section of B* in HF-l, HF-v, and SP RPAE.

Figure 2.186_B*_d1 demonstrates dipole angular anisotropy parameter $\beta_{2p}(\omega)$ of $2p$-electrons of B* atom in HF and SP RPAE.

Figure 2.187_B^+_a1 (B^+) shows results of calculations on B^+ ion: ($Z=5$) $1s^2 2s^2$.

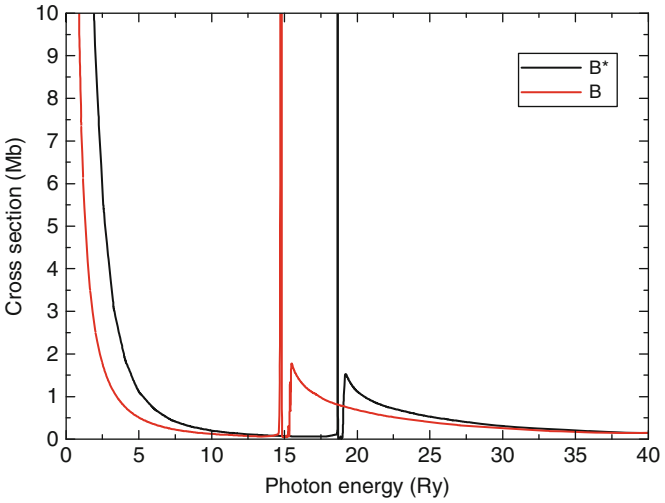

Fig. 2.184_BB*_a1 Total photoionization cross section of B atom (RPAEO) in comparison with the same of B* in excited state (SP RPAE)

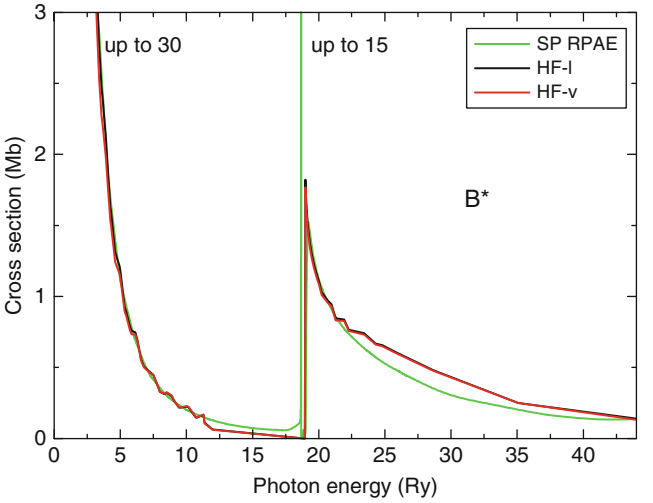

Fig. 2.185_B*_a1 Total photoionization cross section of B* atom in excited state in HF-l, HF-v, and SP RPAE

Figure 2.187_B^+_a1 presents data on total photoionization cross-section in HF-l, HF-v, and RPAE. The role of correlations is, as one could expect beforehand, quite small.

Figures 2.188_Al^+_a1 and 2.189_Al^+_d1 (Al^+) shows data on Al^+ ion: ($Z = 13$) $2s^2\,2p^6 3s^2$.

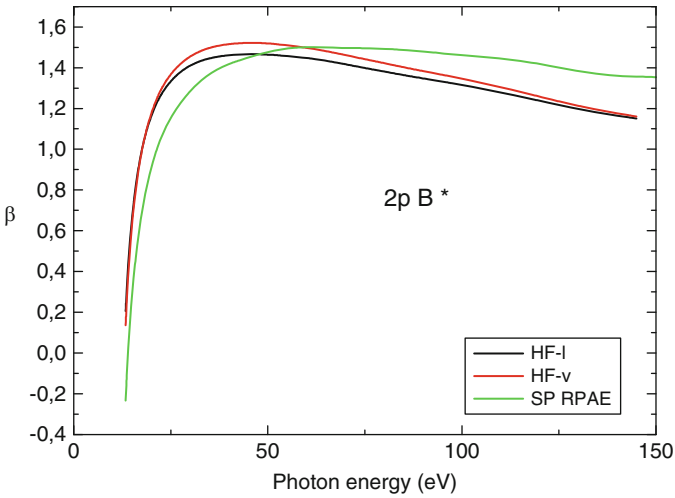

Fig. 2.186_B*_d1 Dipole angular anisotropy parameter of $2p$-electrons for B* atom in HF-l, HF-v, and SP RPAE

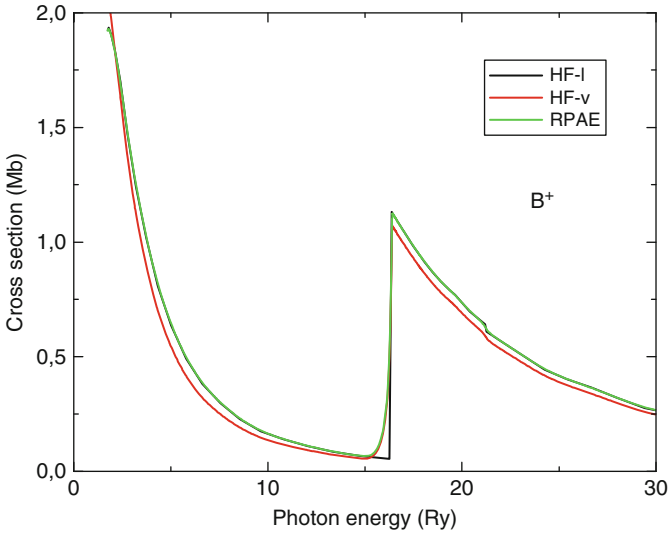

Fig. 2.187_B^+_a1 Total photoionization cross section of Be^+ ion in HF-l, HF-v, and RPAE

Figure 2.188_Al^+_a1 displays the total photoionization cross-section of Al^+ in HF-l, HF-v, and RPAE.

Figure 2.189_Al^+_d1 presents dipole angular anisotropy parameter $\beta_{2p}(\omega)$ of $2p$-electrons of Al^+ ion in RPAE.

Figures 2.190_Sc^{3+}_a1–2.193_Sc^{3+}_d1 (Sc^{3+}) show the data on Sc^{3+} ion: $(Z = 21)\, 2p^6\, 3s^2\, 3p^6$.

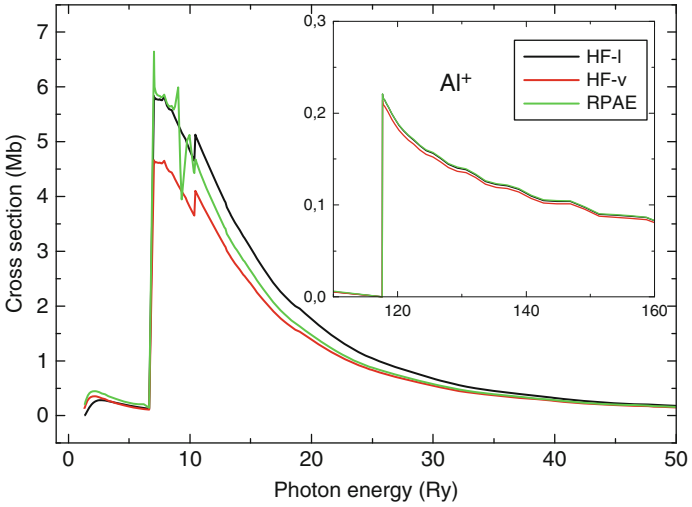

Fig. 2.188_Al$^+$_a1 Total photoionization cross section of Al^+ ion in HF-l, HF-v, and RPAE

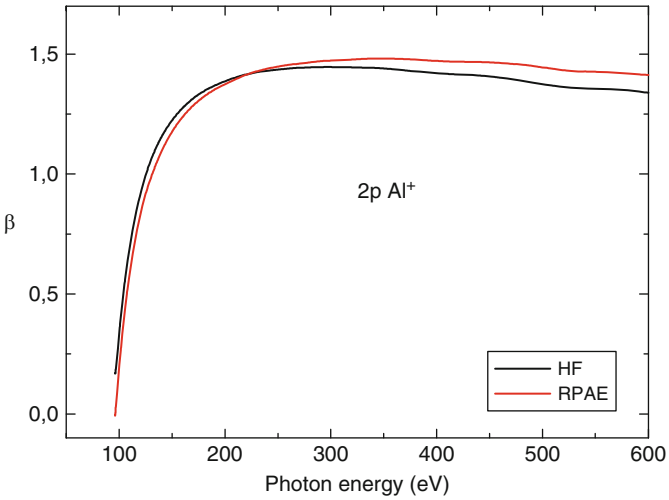

Fig. 2.189_Al$^+$_d1 Dipole anisotropy parameter of $2p$-electrons for Al^+ ion in HF and RPAE

Figure 2.190_Sc^{3+}_a1 demonstrates total photoionization cross-section of Sc^{3+} ion in RPAE. The range of autoionizing resonances is investigated as an example. Results of calculations by R-matrix method are taken from [2.46].

Figure 2.191_$Sc^{3+}Ca^{2+}K^+$_a2 shows total photoionization cross-sections of Sc^{3+} ion with the same of Ca^{2+} ion and K^+ ion in RPAE. At photon energy larger than 4.5 Ry the values of all cross-sections are close to each other. The Sc^{3+} cross-section differs from others by the series of discrete resonances—the traces of discrete excitations.

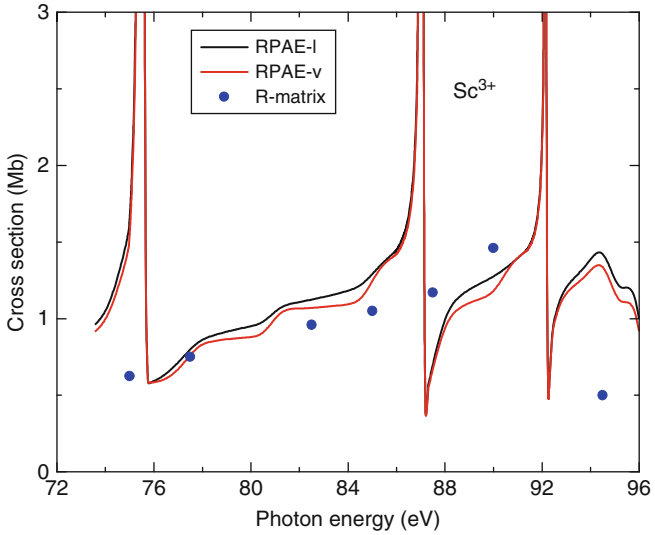

Fig. 2.190_Sc^{3+}_a1 Total photoionization cross section of Sc^{3+} ion in RPAE. *R* matrix calculations is from [2.46]

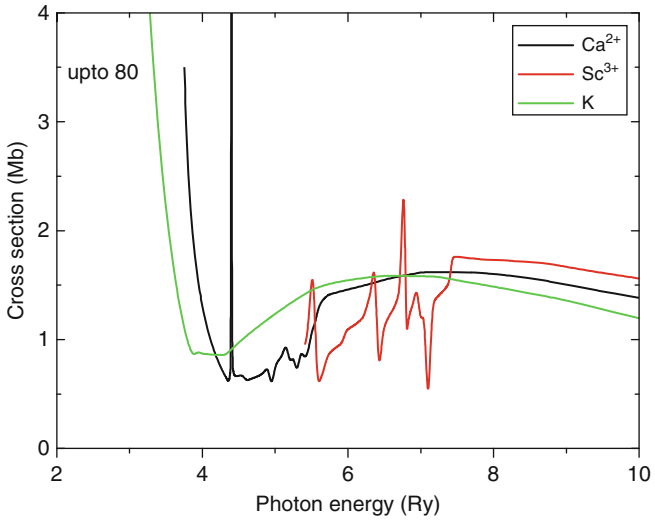

Fig. 2.191_Sc^{3+}Ca^{2+}K^{+}_a2 Total photoionization cross section of Sc^{3+} ion in comparison with the same of Ca^{2+}, K^{+} ions in RPAE

Figure 2.192_Sc^{3+}Ca^{2+}K^{+}Ar_b1 compares partial photoionization cross-sections of Sc^{3+} ion 3*s*-electrons with the same of Ca^{2+} ion, K^{+} ion and ar atom in RPAE. At photon energies larger then 4.5 Ry, the values of all cross-sections are close to each other.

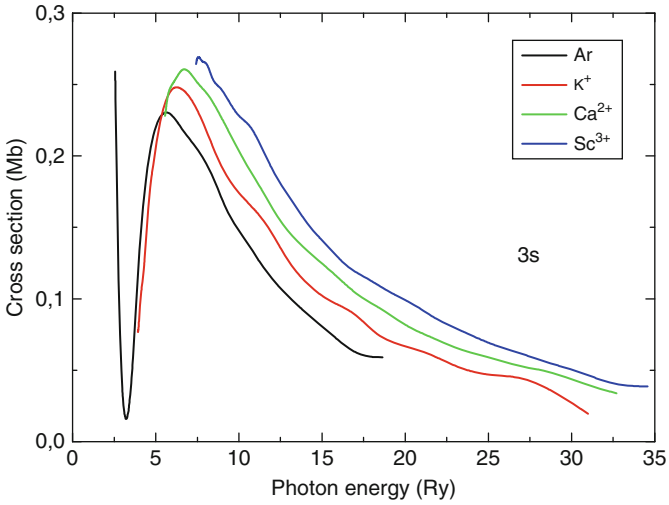

Fig. 2.192_$Sc^{3+}Ca^{2+}K^{+}$Ar_b1 Photoionization cross section of $3s$-electrons for Sc^{3+} ion in comparison with the same for Ca^{2+}, K^{+} ions and Ar atom in RPAE

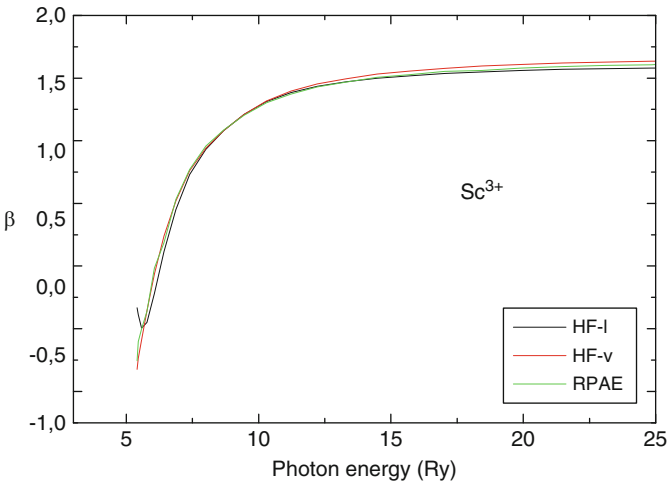

Fig. 2.193_Sc^{3+}_d1 Dipole anisotropy parameter of $3p$-electrons for Sc^{3+} ion in HF and RPAE

Figure 2.193_Sc^{3+}_d1 presents dipole angular anisotropy parameter $\beta_{3p}(\omega)$ of $3p$-electrons for Sc^{3+} ion in RPAE. The parameter is growing fast from threshold to almost flat variation with energy increase.

Figures 2.194_In^{+}_a1 and 2.195_In^{+}_d1 (In^{+}) contain results of calculations for In^{+} ion: In^{+} ($Z = 49$) $3d^{10}, 4s^2, 4p^6, 4d^{10}, 5s^2$.

Figure 2.194_In^{+}_a1 depicts total photoionization cross-section of In^{+} ion in HF-l, HF-v, and RPAE. The role of RPAE correlations is big in the region of the main maximum at 5–6 Ry.

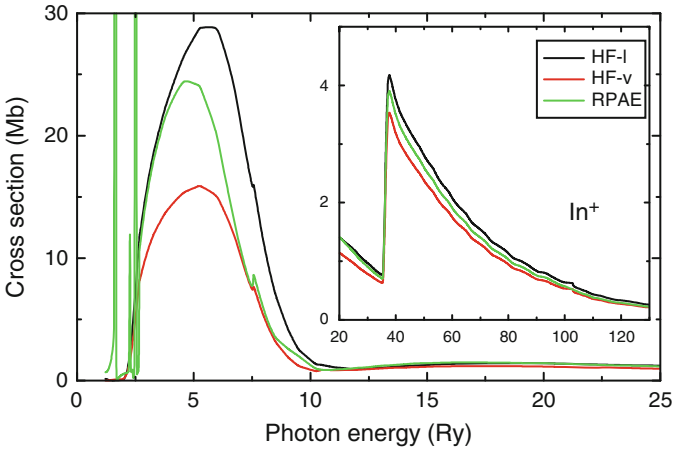

Fig. 2.194_In$^+$_a1 Total photoionization cross section of In$^+$ ion in HF-l, HF-v, and RPAE

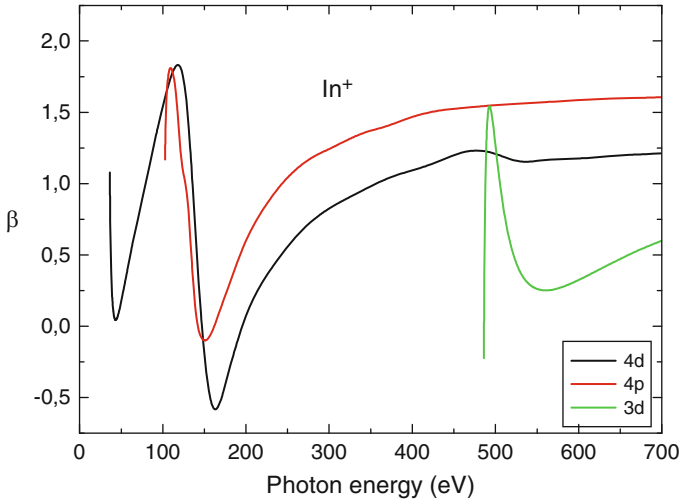

Fig. 2.195_In$^+$_d1 Dipole anisotropy parameter of $4d$-, $4p$-, $3d$-electrons for In$^+$ ion in RPAE

Figure 2.195_In$^+$_d1 presents the dipole angular anisotropy parameters $\beta_{4d,4p,3d}(\omega)$ of $4d$-, $4p$-, and $3d$-electrons for In$^+$ ion. The data for $4d$ has a two-minimum structure that for $4p$ looks similarly except that it is cut of due to higher ionization threshold; β_{3d} has a narrow maximum at threshold.

Figure 2.196_La_b1 (La) contains results of calculations for La atom: ($Z = 57$) $4d^{10}\,5s^2\,5p^6\,5d\,6s^2$.

Figure 2.196_La_b1 shows partial photoionization cross-section of $4d$-electrons for La atom in RPAE and GRPAE ($I_{4d}^{\text{exp}} = 7.64$ Ry) (see [2.47,2.48]). Experimental data are presented in [2.48].

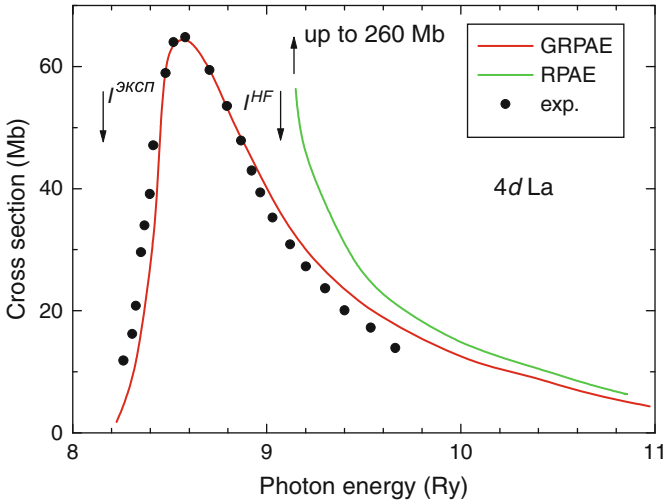

Fig. 2.196_La_b1 Partial photoionization cross section of $4d$-electrons for La atom in GRPAE and RPAE (see [2.48]). Experiment is from [2.47]

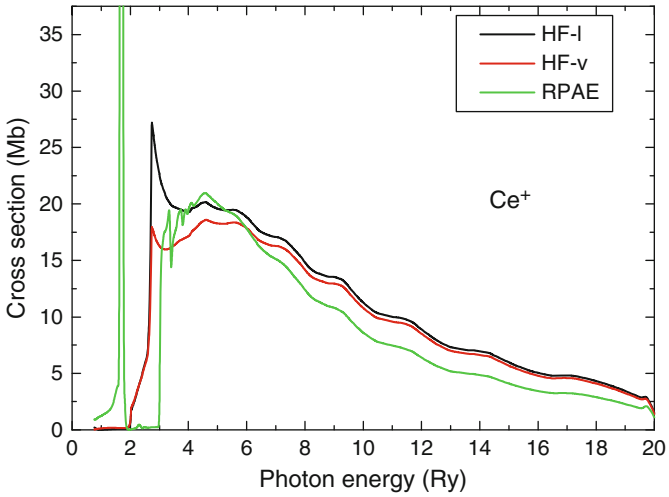

Fig. 2.197_Ce^+_a1 Total photoionization cross section of ion Ce^+ in HF-l, HF-v and RPAE

Figures 2.197_Ce^+_a1–2.200_Ce^+_b3 (Ce^+) contain results of calculations for Ce^+ ion: $(Z = 58)\, 4d^{10}\, 5s^2\, 5p^6\, 4f\, 6s^2$.

Figure 2.197_Ce^+_a1 includes the total photoionization cross-section of the Ce^+ ion in HF-l, HF-v, and RPAE. The role of correlations is moderate.

Figure 2.198_Ce^+_b1 displays photoionization cross-section of $5p$-electrons of Ce^+ ion in RPAE. The powerful maximum at 9.2 Ry is a result of discrete excitation $4d$–$4f$ decay into $5p$–εd continuous spectrum.

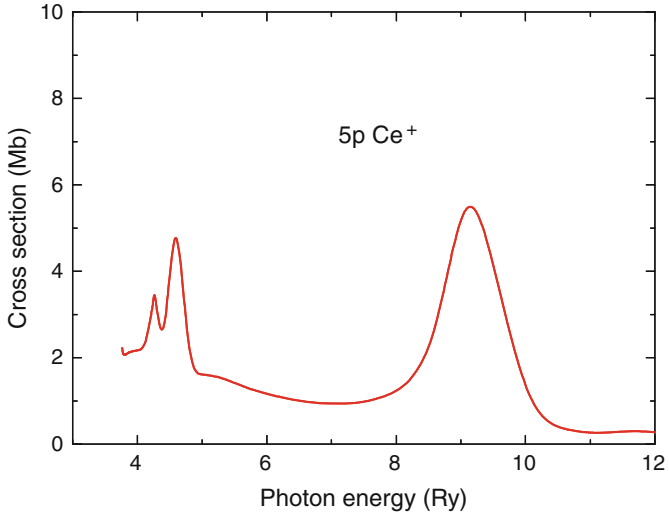

Fig. 2.198_Ce$^+$_b1 Photoionization cross section of $5p$-electrons of ion Ce$^+$ in RPAE

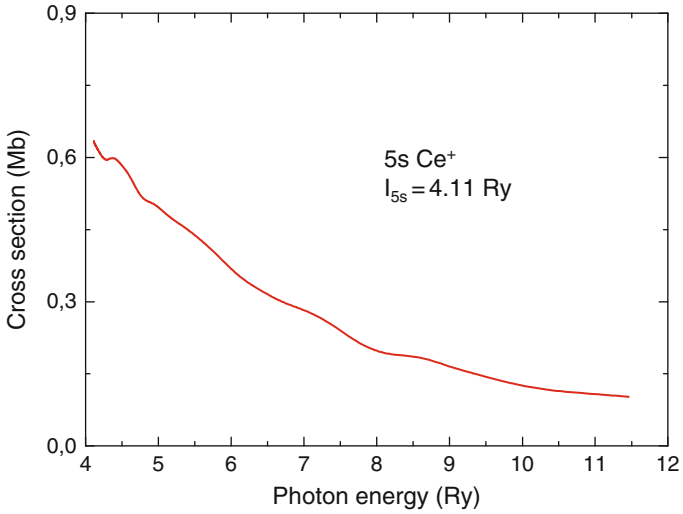

Fig. 2.199_Ce$^+$_b2 Photoionization cross section of $5s$-electrons of ion Ce$^+$ in RPAE

Figure 2.199_Ce$^+$_b2 presents photoionization cross-section of $5s$-electrons of Ce$^+$ ion in RPAE.

Figure 2.200_Ce$^+$_b3 shows photoionization cross-section of $4d$-electrons of ion Ce$^+$ in RPAE.

Figures 2.201_Ce^{3+}_a1–2.204_Ce^{3+}_b3 (Ce^{3+}) contain results of calculations for Ce^{3+} ion: ($Z = 58$) $4d^{10}\,5s^2\,5p^6\,4f$.

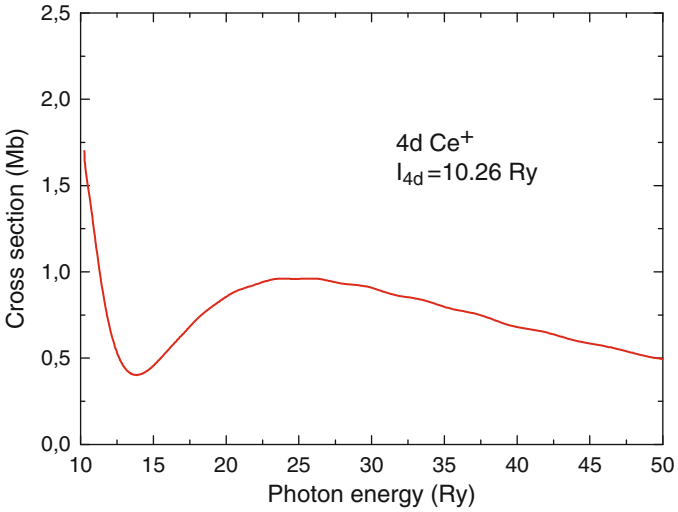

Fig. 2.200_Ce^{+}_b3 Photoionization cross section of $4d$-electrons of ion Ce^{+} in RPAE

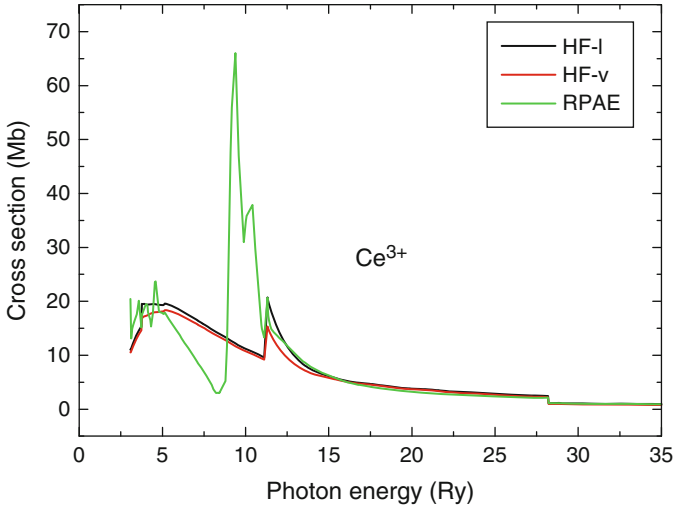

Fig. 2.201_Ce^{3+}_a1 Total photoionization cross section of ion Ce^{3+} in HF-l, HF-v, and RPAE

Figure 2.201_Ce^{3+}_a1 shows the total photoionization cross-section of ion Ce^{3+} in HF-l, HF-v, and RPAE. The RPAE corrections result in a powerful maximum at 9.2 Ry.

Figure 2.202_Ce^{3+}_b1 shows the photoionization cross-section of $5p$-electrons of Ce^{3+} ion in RPAE. The powerful maximum at 9.2 Ry is a result of discrete excitation $4d$–$4f$ that decays into $5p$–εd continuous spectrum. Qualitatively, the situation is similar to that in Fig. 2.198_Ce^{+}_b1.

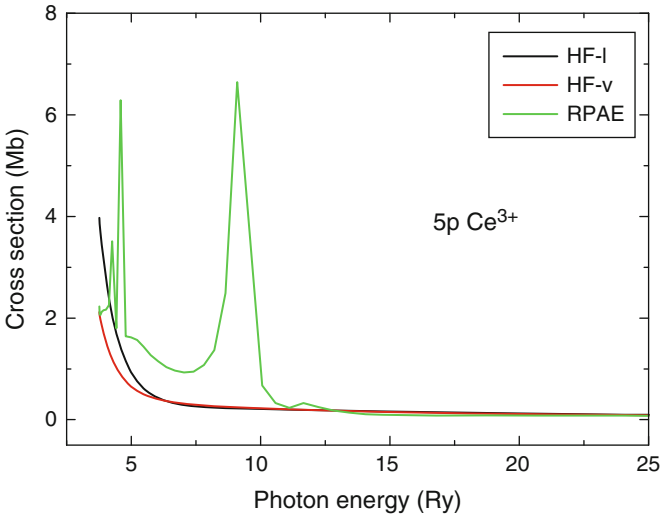

Fig. 2.202_Ce^{3+}_b1 Photoionization cross section of $5p$-electrons of ion Ce^{3+} in HF and RPAE

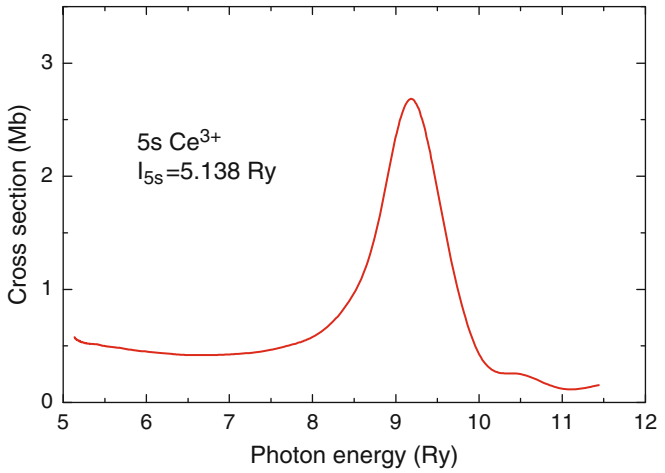

Fig. 2.203_Ce^{3+}_b2 Photoionization cross section of $5s$-electrons of ion Ce^{3+} in RPAE

Figure 2.203_Ce^{3+}_b2 demonstrates the photoionization cross-section of $5s$-electrons of Ce^{3+} ion in RPAE. Just as in $5p$, the powerful maximum at 9.2 Ry is a result of discrete excitation $4d$–$4f$ that decays into $5p$–εd and $5s$–εp continuous spectrum.

Figure 2.204_Ce^{3+}_b3 presents photoionization cross-section of $4d$-electrons of ion Ce^{3+} in RPAE. It has quite a big value at threshold and then a small but very broad maximum at 28 Ry.

Figures 2.205_Ce^{4+}_a1–2.211_Ce^{4+}_b6 (Ce^{4+}) contain results of calculations for Ce^{4+} ion: $(Z = 58)\ 4d^{10}\ 5s^2\ 5p^6$.

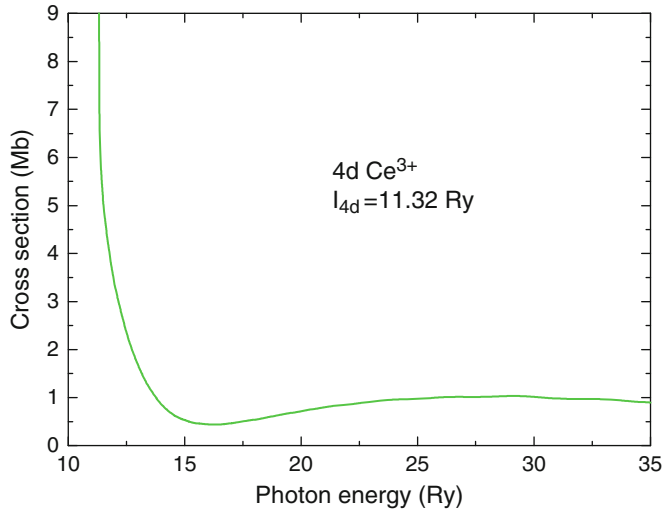

Fig. 2.204_Ce^{3+}_b3 Photoionization cross section of $4d$-electrons of ion Ce^{3+} in RPAE

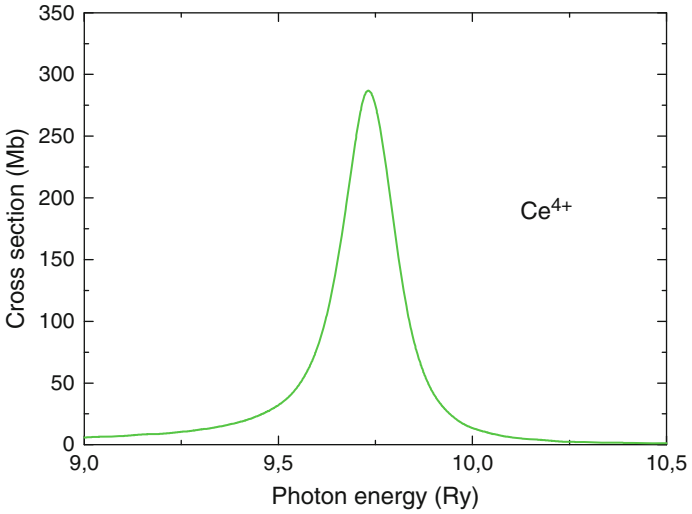

Fig. 2.205_Ce^{4+}_a1 Total photoionization cross section of ion Ce^{4+}

Figure 2.205_Ce^{4+}_a1 shows total photoionization cross-section of ion Ce^{4+} in RPAE. The curve is dominated by the Giant autoionization resonance, similar to what we see in Mn, Cr, and Eu.

Figure 2.206_Ce^{4+}_b1 displays partial photoionization cross-sections of $5p$-, $5s$-electrons of Ce^{4+} ion. The curves demonstrate the autoionization nature of the big maximum in the ion Ce^{4+}.

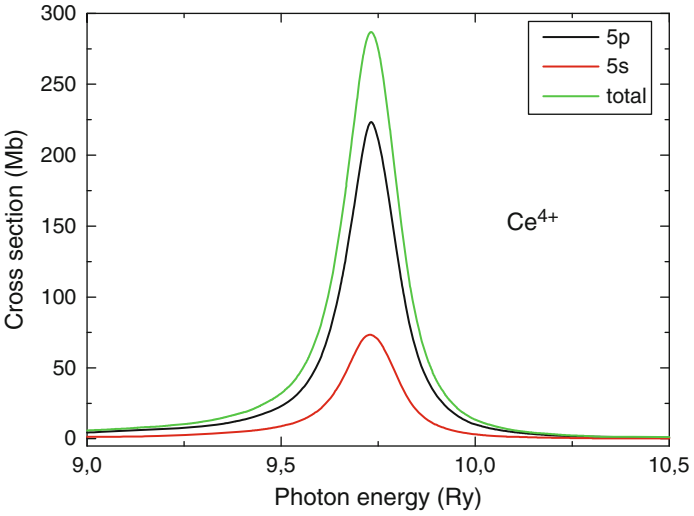

Fig. 2.206_Ce^{4+}_b1 Partial photoionization cross-sections of $5p$, $5s$-electrons of ion Ce^{4+} in RPAE

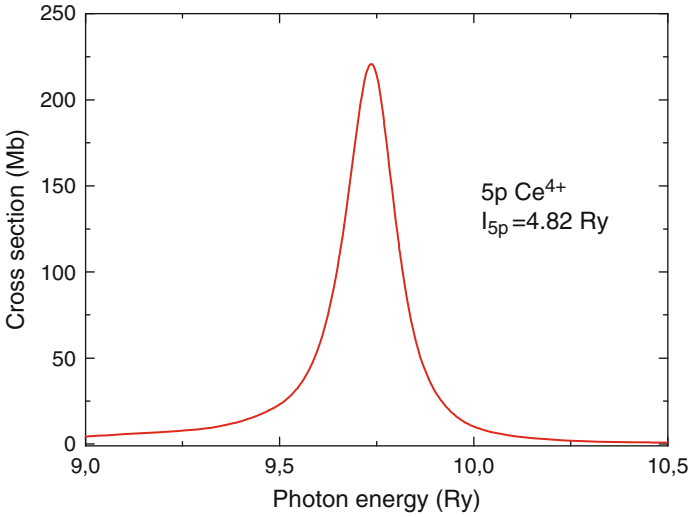

Fig. 2.207_Ce^{4+}_b2 Photoionization cross section of $5p$-electrons of ion Ce^{4+} in RPAE

Figure 2.207_Ce^{4+}_b2 shows photoionization cross-section of $5p$-electrons of ion Ce^{4+} in RPAE. As in the previous figure, the big maximum is a result of Giant autoionization of $4d$–$4f$ into $5p$–εd continuum.

Figure 2.208_Ce^{4+}_b3 depicts the partial photoionization cross-sections of $5p$-electrons of the ion Ce^4. Here the Giant autoionization resonance is of the same nature as in Figs. 2.206_Ce^{4+}_b1 and 2.207_Ce^{4+}_b2.

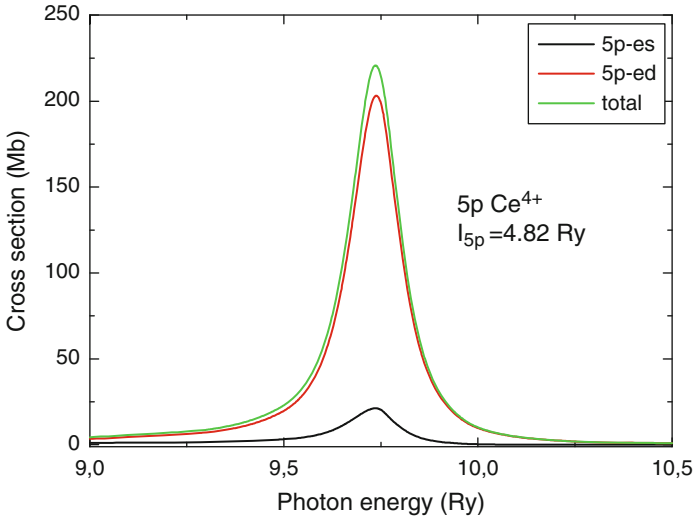

Fig. 2.208_Ce^{4+}_b3 Partial photoionization cross sections of $5p$-electrons of ion Ce^{4+} in RPAE

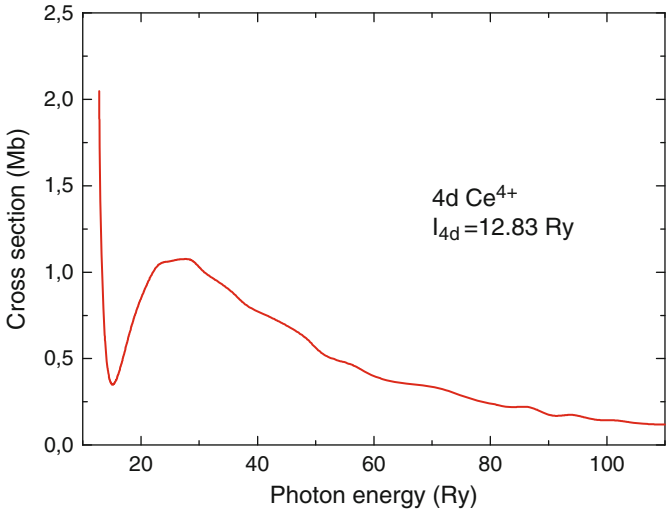

Fig. 2.209_Ce^{4+}_b4 Photoionization cross sections of $4d$-electrons of ion Ce^{4+} in RPAE

Figure 2.209_Ce^{4+}_b4 demonstrates the photoionization cross-sections of $4d$-electrons of ion Ce^{4+} in RPAE.

Figure 2.210_Ce^{4+}_b5 presents partial photoionization cross-sections of $4d$-electrons of ion Ce^{4+}. Note that direct $4d$ electron ionization has a small cross-section.

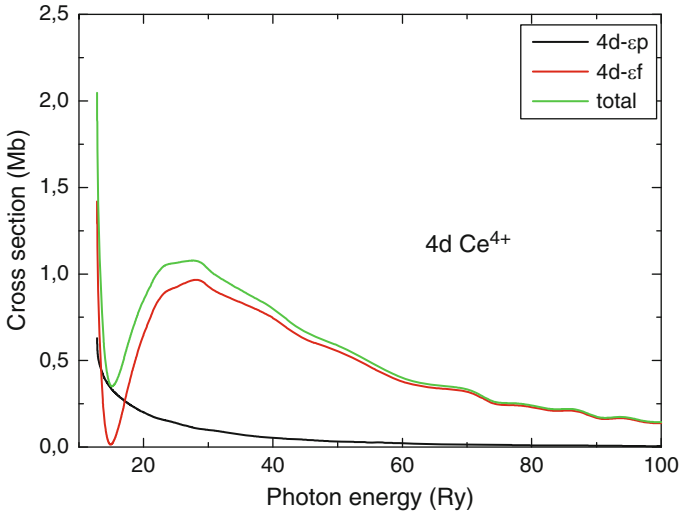

Fig. 2.210_Ce^{4+}_b5 Partial photoionization cross sections of $4d$-electrons of ion Ce^{4+} in RPAE

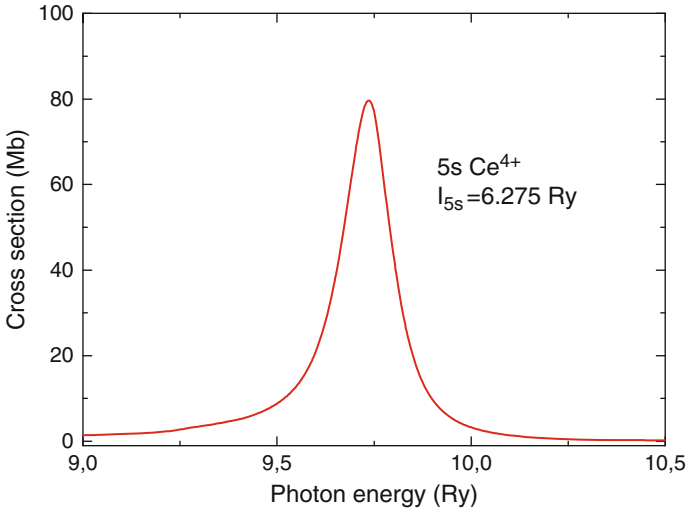

Fig. 2.211_Ce^{4+}_b6 Photoionization cross section of $5s$-electrons of ion Ce^{4+} in RPAE

Figure 2.211_Ce^{4+}_b6 displays photoionization cross-section of $5s$-electrons of ion Ce^{4+} in RPAE. Just as in Fig. 2.207_Ce^{4+}_b2, the cross-section is dominated by a big resonance that results from decay of $4d$–$4f$ excitation into $5s$–εp continuous spectrum. It is also affected strongly by the action of $5p$ electrons upon $5s$.

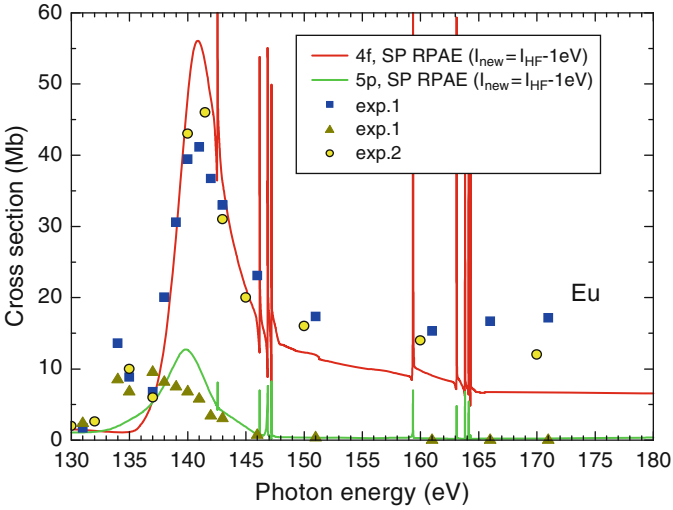

Fig. 2.212_Eu_b1 Partial photoionization cross section of $4f$ "up"- and $5p$ "up"- and "down"-electrons for Eu atom in SP RPAE (see [2.49, 2.50]). Experiment is from [2.51, 2.52]

Figures 2.212_Eu_b1–2.218_Eu_f1 (Eu) contain results of calculations for Eu atom: $(Z = 63)\ 3d^{10}\ 4d^{10}\ 4f^7 \uparrow 5s^2\ 5p^6,\ 6s^2$.

Figure 2.212_Eu_b1 presents photoionization cross-sections of $4f$ "up"- and $5p$ "up" and "down"-electrons for Eu atom in SP RPAE [2.49, 2.50]. The experimental data are from [2.51,2.52]. It is important to note that experimentally on the way from La to Eu near $4d$-threshold a big and almost identical maximum of photoabsorption cross-sections $\sigma(\omega)$ exists. Though by the form these resonances are similar, their nature in various atoms is completely different: in I, Cs, Ba atoms it is the Giant resonance, which decays emitting relatively low-energy electrons owing to $4d \rightarrow \varepsilon f(\varepsilon p)$ transition. In Eu atom it is instead *Giant autoionizing resonance* created by interaction of discrete excitation $4d\downarrow \rightarrow 4f\downarrow$ into half-filled $4f\downarrow$-level, which decays very rapidly via a continuous spectrum excitation of the half-filled level $4f\uparrow \rightarrow \varepsilon g(\varepsilon d)\uparrow$, with ejection of fast photoelectrons. This feature has been predicted in [2.2,2.53]. The matrix element of interaction of discrete excitation with a continuous spectrum is great owing to closeness of wave functions of occupied $4f$ "up"- and empty $4f$ "down"-states. The cross-section in the vicinity of a resonance is described directly by formulas of SP RPAE whereas near a normal autoionizing resonance the cross-section is described by (1.50).

Figure 2.213_Eu_b2 shows photoionization cross-section of $4f\uparrow$-electrons for Eu atom in SP RPAE (see [2.50]).

Figure 2.214_Eu_b3 compares photoionization cross-sections of $5s\uparrow\downarrow$-electrons for Eu atom with the same for Eu^+ and Eu^{2+} ions in SP RPAE [2.50]. The dominative relatively narrow maximum on these curves is due to interaction with the Giant autoionization resonance.

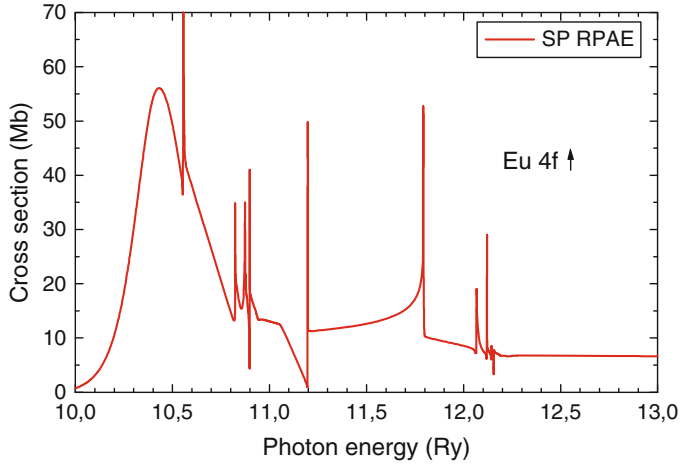

Fig. 2.213_Eu_b2 Photoionization cross section of $4f$ "up"-electrons for Eu atom in SP RPAE

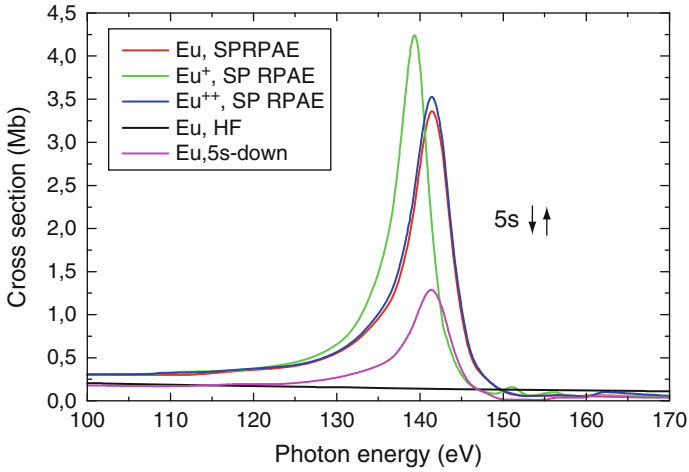

Fig. 2.214_Eu_b3 Photoionization cross section of $5s \uparrow\downarrow$-electrons for Eu atom and Eu^{+}, Eu^{2+} ions in SP RPAE

Figure 2.215_Eu_d1 presents dipole angular anisotropy parameters $\beta_{4d,4f,5p}(\omega)$ of $4d$-, $4f$-, $5p$-electrons for Eu atom in SP RPAE. The curves have rather complex structure in the area of $4d$-excitations.

Figure 2.216_Eu_d2 shows dipole angular anisotropy parameter of $4d$-, $5p\uparrow$ and $\downarrow$-, $4f\uparrow$-electrons for Eu atom in SP HF. Comparison with Fig. 2.215_Eu_d1 illustrates the role of interaction between different transitions, mainly the role of autoionization resonance.

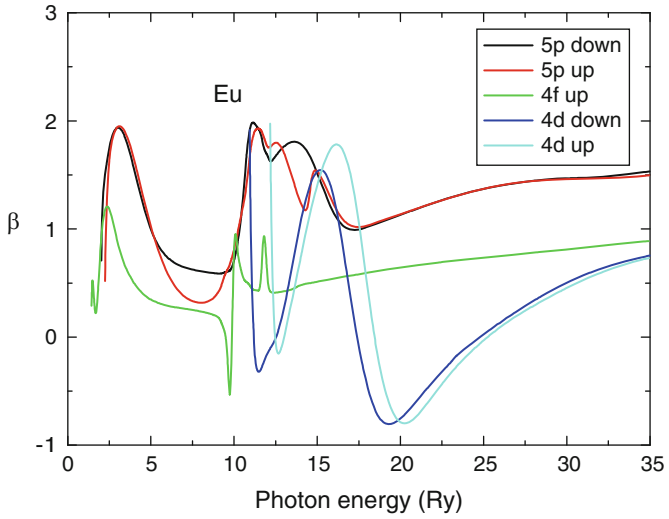

Fig. 2.215_Eu_d1 Dipole anisotropy parameter of $4d\uparrow\downarrow$-, $5p$ "up" and "down"-, $4f$ "up"-electrons for Eu atom in SP RPAE

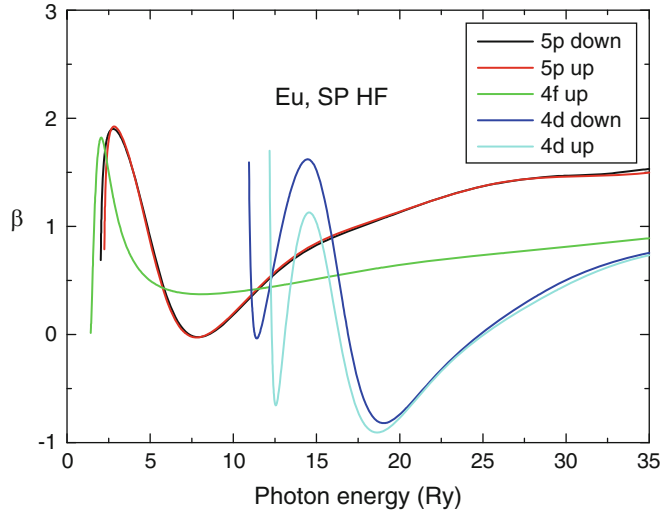

Fig. 2.216_Eu_d2 Dipole anisotropy parameter of $4d\uparrow\downarrow$-, $5p$ "up" and "down"-, $4f$ "up"-electrons for Eu atom in SP HF

Figure 2.217_Eu_e1 depicts non-dipole angular anisotropy parameters γ^{C} of $6s\downarrow\uparrow$-$e$lectrons for Eu atom in HF and SP RPAE. The "up" and "down" curves are essentially different in the photon energy region 5–10 Ry. For the "up" parameter the difference between HF and SP RPAE results is big.

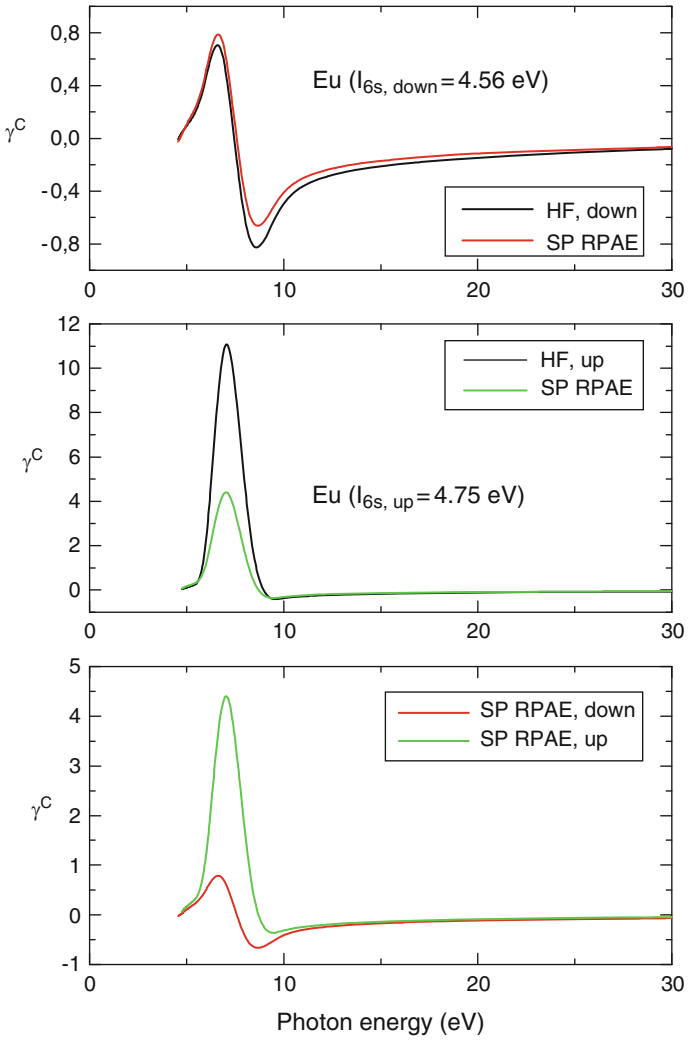

Fig. 2.217_Eu_e1 Non-dipole anisotropy parameter of 6*s*-electrons for Eu atom in HF and SP RPAE

Figure 2.218_Eu_f1 displays dipole angular anisotropy parameter $\beta_{4f}(\omega)$ and spin polarization parameters $A_{4f}^{7/2}$, $\alpha_{4f}^{7/2}$, and $\xi_{4f}^{7/2}$ for Eu atom in SP RPAE. Note the essential role of the $5p$-subshell.

Figures 2.219–2.224_Eu$^+$_d2 (Eu^+) contain results of calculations for Eu^+ ion: $(Z = 63)\ 3d^{10}, 4d^{10}, 4f^7 \uparrow 5s^2, 5p^6, 6s^1$.

Figure 2.219_Eu$^+$_a1 presents total photoionization cross-section of Eu^+ ion in SP RPAE (see [2.50]). In the cross-section the Giant autoionization resonance dominates. Experiment is from [2.54].

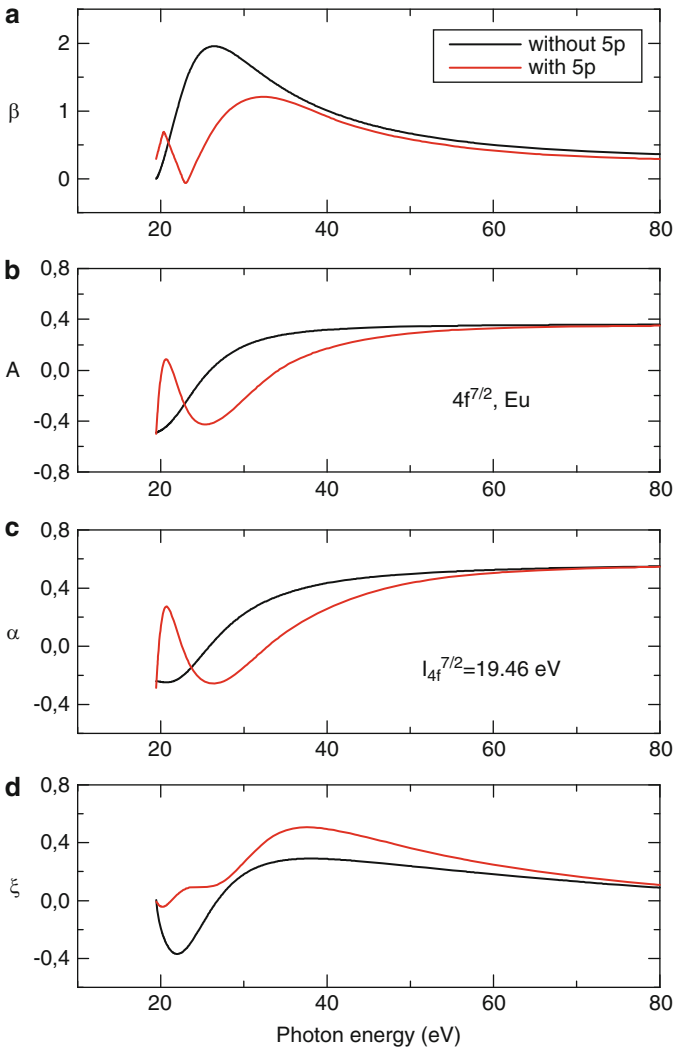

Fig. 2.218_Eu_f1 Dipole parameter of $4f$-electrons for Eu atom: (**a**) angular anisotropy $\beta_{4f}(\omega)$ and (**b**) spin polarization $A_{4f}^{7/2}(\omega)$, (**c**) $\alpha_{4f}^{7/2}(\omega)$, and (**d**) $\xi_{4f}^{7/2}(\omega)$

Figure 2.220_Eu$^+$_b1 demonstrates partial photoionization cross-section of $5p$-electrons for Eu^+ ion in SP RPAE. A maximum connected with the decay of discrete excited state $4d\uparrow \rightarrow 4f\uparrow$ into continuum of $5p$-ionization is seen.

Figure 2.221_Eu$^+$_b2 displays partial photoionization cross-section of $4d$-electrons for Eu^+ ion in SP RPAE. The shape of cross-section is very complex, but the value is small at high energies.

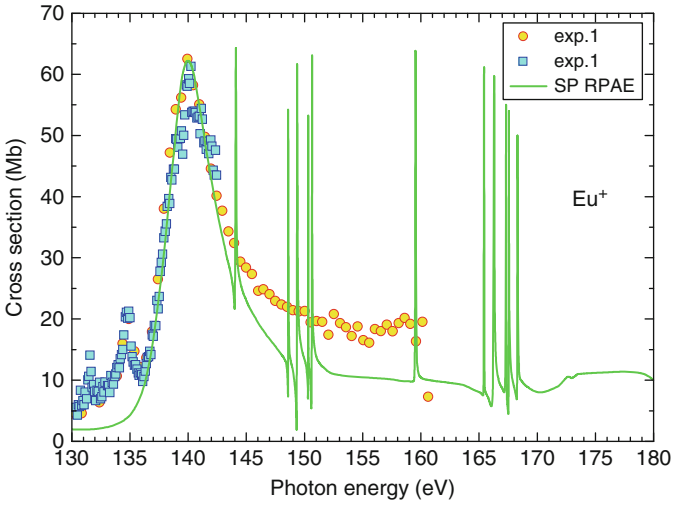

Fig. 2.219_Eu$^+$_a1 Total photoionization cross section of Eu$^+$ ion in SP RPAE (see [2.49]). Experiment is from [2.54]

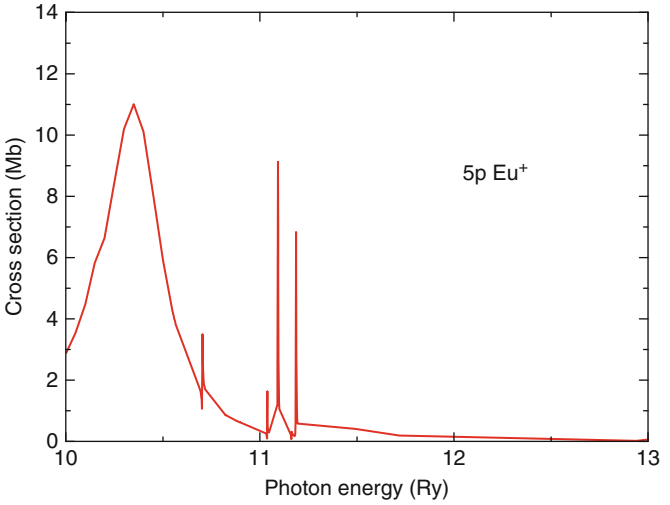

Fig. 2.220_Eu$^+$_b1 Photoionization cross section of $5p$-electrons for Eu$^+$ ion in SP RPAE

Figure 2.222_Eu$^+$_b3 shows partial photoionization cross-section of $4f\uparrow$-electrons for Eu$^+$ ion in SP RPAE, which differs not essentially from that of neutral atom.

Figure 2.223_Eu$^+$_d1 contains dipole angular anisotropy parameter of $5p\uparrow$, $5p\downarrow$, $4d\uparrow$, $4d\downarrow$, and $4f\uparrow$-electrons for Eu$^+$ ion in SP RPAE. All curves have

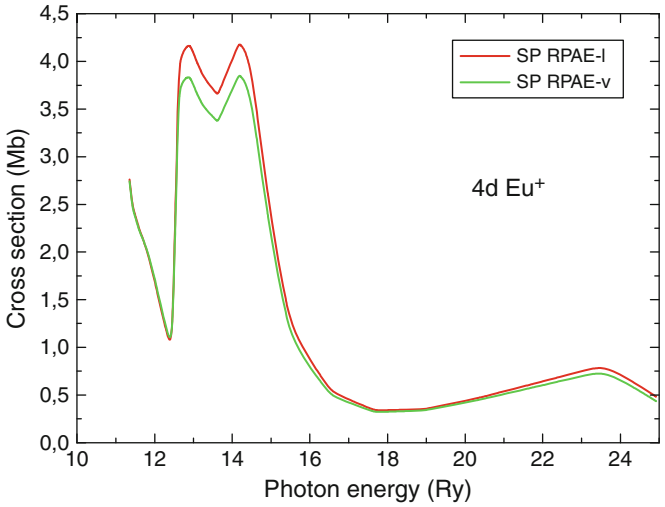

Fig. 2.221_Eu$^+$_b2 Photoionization cross section of $4d$-electrons for Eu$^+$ ion in SP RPAE

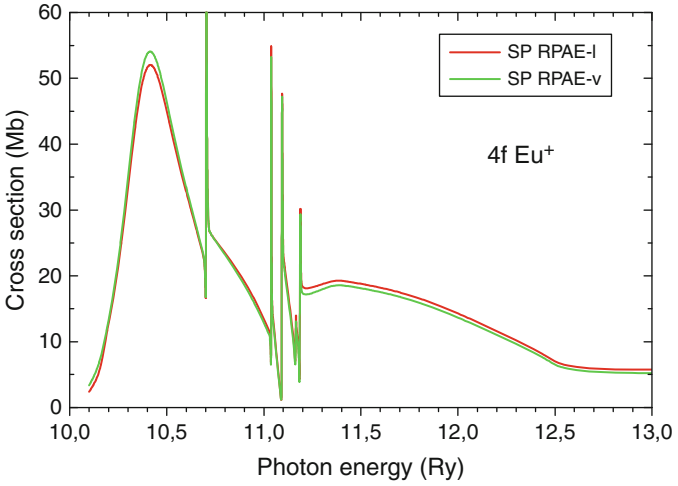

Fig. 2.222_Eu$^+$_b3 Photoionization cross section of $4f\uparrow$-electrons for Eu$^+$ ion in SP RPAE

maximums at threshold followed by minimum, with subsequent transfer to saturation.

Figure 2.224_Eu$^+$_d2 includes dipole angular anisotropy parameter of $5p\uparrow$, $5p\downarrow$, $4d\uparrow$, $4d\downarrow$, and $4f\uparrow$-electrons for Eu$^+$ ion in SP HF. Comparing this figure with Fig. 2.223_Eu$^+$_d1, one can see the effect of electron correlation that is prominent. Particularly essential is the difference in the broad region of $4d$ threshold.

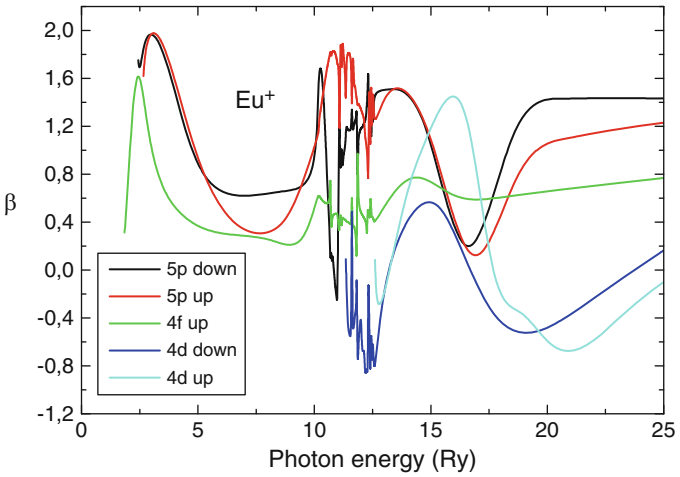

Fig. 2.223_Eu$^+$_d1 Dipole angular anisotropy parameter of $5p$ "up" and "down"-, $4f$ "up," $4d$ "up" and "down"-electrons for Eu^+ ion in SP RPAE

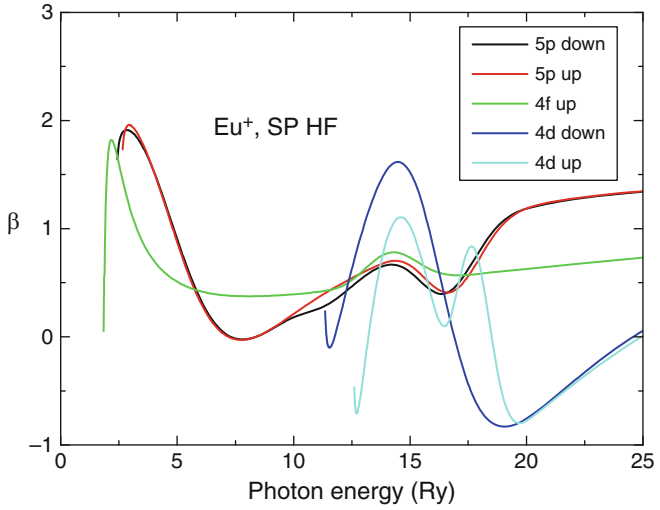

Fig. 2.224_Eu$^+$_d2 Dipole angular anisotropy parameter of $5p$ "up" and "down"-, $4f$ "up," $4d$ "up" and "down"-electrons for Eu^+ ion in SP HF

Figures 2.225_Eu^{2+}_a1–2.231_Eu^{2+}_d2 (Eu^{2+}) contain results of calculations for Eu^{2+} ion: ($Z = 63$) $3d^{10}$, $4d^{10}$, $4f^7\uparrow$, $5s^2$, $5p^6$.

Figure 2.225_Eu^{2+}_a1 presents total photoionization cross-section of Eu^{2+} ion in the vicinity of $4d$-subshell in SP RPAE. The difference from neutral Eu is due to more intense discrete transitions. Strong maximum is manifestation of the effect of the Giant autoionization $4d\downarrow - 4f\downarrow$ resonance.

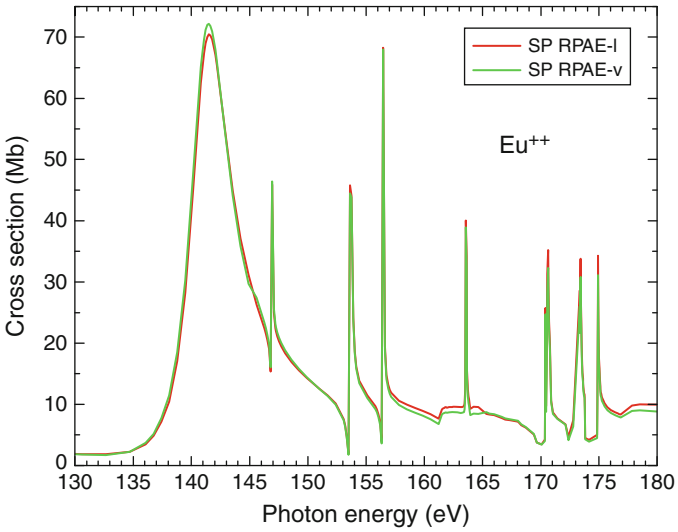

Fig. 2.225_Eu^{2+}_a1 Photoionization cross section of Eu^{2+} ion in the vicinity of $4d$-shell in SP RPAE

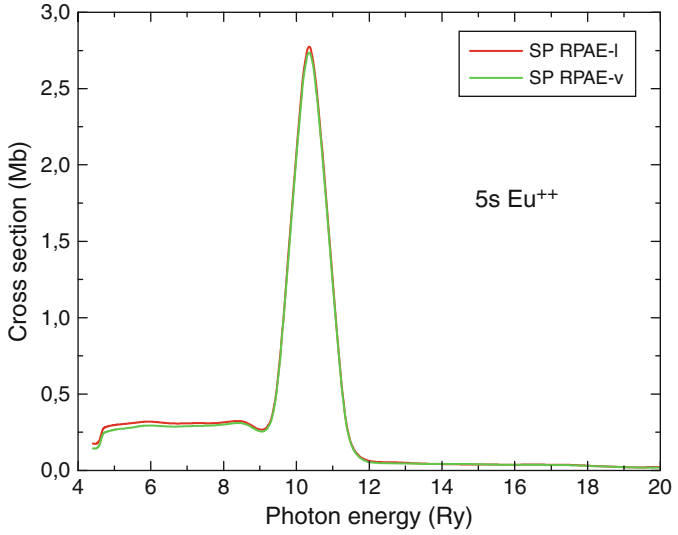

Fig. 2.226_Eu^{2+}_b1 Photoionization cross section of $5s$ "up"and "down"-electrons for Eu^{2+} ion in SP RPAE

Figure 2.226_Eu^{2+}_b1 shows photoionization cross-section of $5s\uparrow\downarrow$-electrons for Eu^{2+} ion in SP RPAE. The respective cross-sections are almost indistinguishable. The difference from neutral atom is small as in previous case.

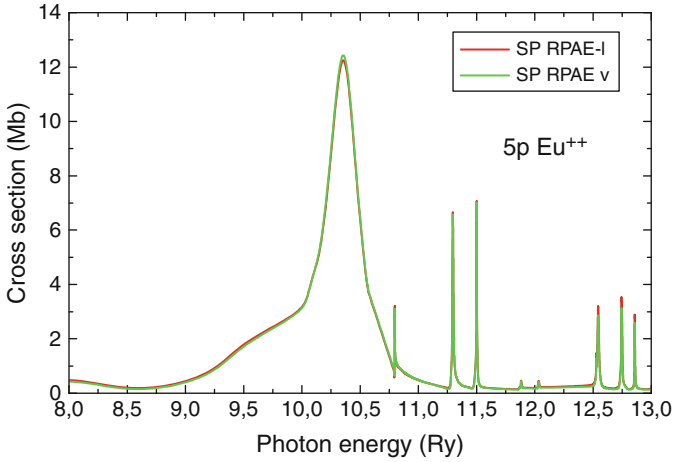

Fig. 2.227_Eu^{2+}_b2 Photoionization cross section of $5p$ "up"and "down"-electrons for Eu^{2+} ion in SP RPAE

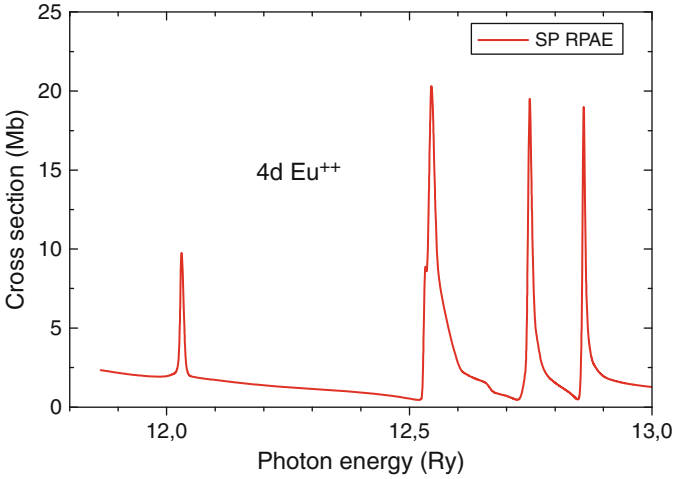

Fig. 2.228_Eu^{2+}_b3 Photoionization cross section of $4d$-electrons for Eu^{2+} ion in SP RPAE

Figure 2.227_Eu^{2+}_b2 displays photoionization cross-section of $5p\uparrow\downarrow$-electrons for Eu^{2+} ion in SP RPAE. This cross-section is close to the similar value of Eu^{+}. The powerful maximum is a trace of a big discrete excitation $4d\downarrow - 4f\downarrow$.

Figure 2.228_Eu^{2+}_b3 depicts photoionization cross-section of $4d$-electrons for Eu^{2+} ion in SP RPAE. Discrete excitations are dominating starting from 12 Ry.

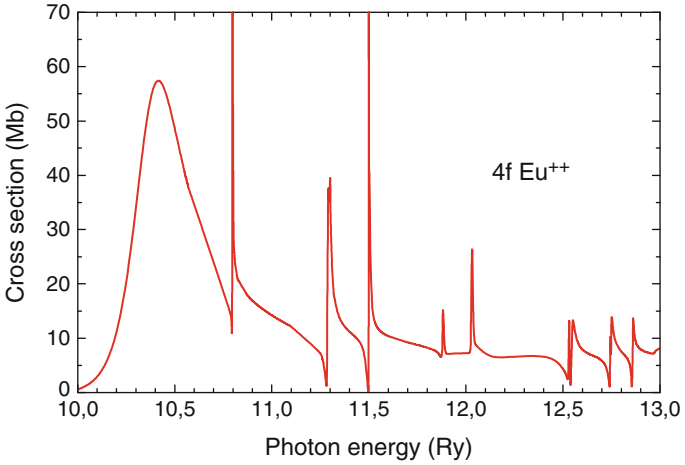

Fig. 2.229_Eu^{2+}_b4 Photoionization cross section of $4f$ "up"-electrons for Eu^{2+} ion in SP RPAE

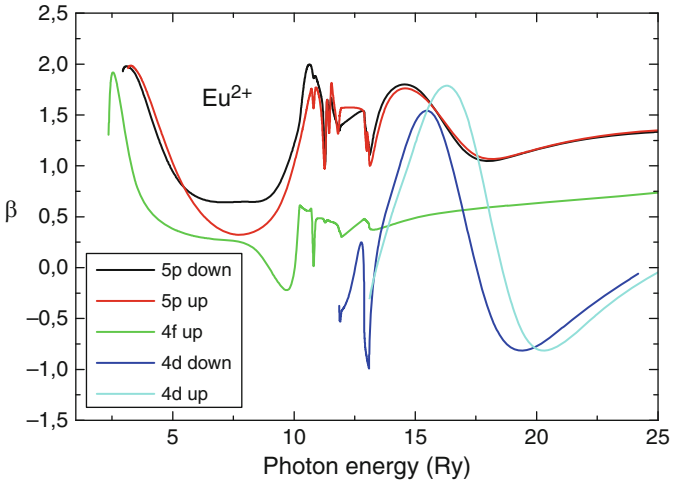

Fig. 2.230_Eu^{2+}_d1 Dipole angular anisotropy parameter of $4d\uparrow\downarrow$, $4f\uparrow$ "up"-, and $5p\uparrow\downarrow$-electrons for Eu^{2+} ion in SP RPAE

Figure 2.229_Eu^{2+}_b4 presents photoionization cross-section of $4f\uparrow$-electrons for Eu^{2+} ion in SP RPAE. The comparison with Fig. 2.225_Eu^{2+}_a1 shows that the main contribution to total cross-section is a result of direct ionization of the $4f$-subshell.

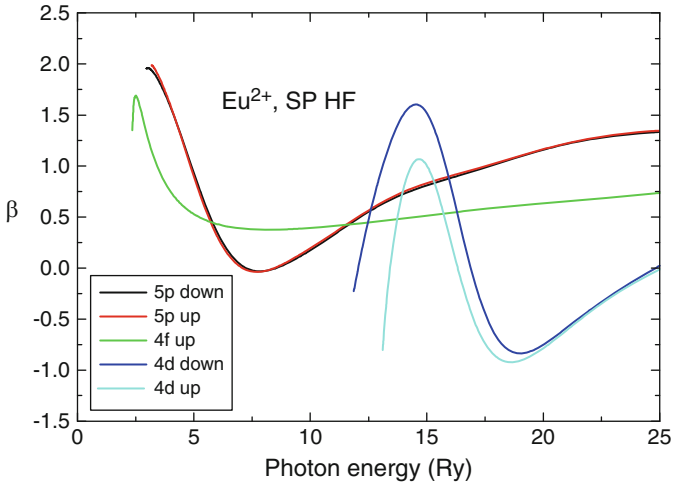

Fig. 2.231_Eu^{2+}_d2 Dipole angular anisotropy parameter of $4f$ "up"-, $4d$ "up" and "down"-, $5p$ "up" and "down"-electrons for Eu^{2+} ion in SP HF

Figure 2.230_Eu^{2+}_d1 shows dipole angular anisotropy parameter of $4d\uparrow\downarrow$-, $5p\uparrow\downarrow$-, and $4f\uparrow$-electrons for Eu^{2+} ion in SP RPAE. Absolute values and main features of these parameters are close to that shown in Fig. 2.223_Eu^{+}_d1.

Figure 2.231_Eu^{2+}_d2 shows dipole angular anisotropy parameter of $4d\uparrow\downarrow$, $5p\uparrow\downarrow$-, and $4f\uparrow$-electrons for Eu^{2+} ion in SP HF. The curves are close to each other, except additional maximum of $\beta_{4d\downarrow}$ at 180 eV.

Table 2.4 includes calculated values of oscillator strengths in HF-l, HF-v, $f^{l,v}_{nl-n'l'}, f^{l,v}_{nl-n'l'\uparrow(\downarrow)}$, and $F^{l,v}_{nl-n'l'}, F^{l,v}_{nl-n'l'\uparrow(\downarrow)}$ in RPAE for several lowest discrete levels of excitation and for each considered subshell of atoms investigated in this section. Theoretical transition energies in RPAE $\tilde{\omega}_{nl-n'l'}, \tilde{\omega}_{nl-n'l'\uparrow(\downarrow)}$ are also given in this table.

The results for length and velocity forms in RPAE coincide with reasonable accuracy. The role of correlations is big enough for almost all transitions in all considered objects. In Be* the biggest oscillator strength has outer electron $2p$–$3s$ up transition. In In^{+} the biggest is the oscillator strength of outer electron $5s$–$5p$, while that of $4d$–$5p$ is already two times smaller. In Eu, Eu^{+}, and Eu^{2+} the $4d$ electron transition into vacant state of the $4f$ semi-empty level dominate. Next in the oscillator strength are $5p$–$5d\uparrow$ and $5p$–$5d\downarrow$ levels. In Eu^{+} very intensive is $5p$–$5d\uparrow$ that is quite intensive also in Eu^{2+}, which is followed by $5p$–$5d\downarrow$. The oscillator strengths are, in general, decreasing with decrease in principal quantum number of the exited electron.

Table 2.4 Oscillator strengths and transition energies of III group's elements and their ions

Transition	ω (Ry)	HF-l	HF-v	RPAE-l	RPAE-v
B*					
$2p$–$3d$ up	0.8692	0.1431E+00	0.1099E+00	0.1427E−02	0.1517E−02
$2p$–$4d$ up	0.9185	0.6929E−01	0.5288E−01	0.4909E−01	0.4875E−01
$2p$–$5d$ up	0.9424	0.3691E−01	0.2809E−01	0.3211E−01	0.3203E−01
$2p$–$3s$ up	0.7107	0.1094E+00	0.9925E−01	0.1652E+00	0.1614E+00
$2p$–$4s$ up	0.8692	0.1869E−01	0.1690E−01	0.2997E−02	0.3146E−02
$2p$–$5s$ up	0.9201	0.6788E−02	0.6137E−02	0.8103E−03	0.8577E−03
$2s$–$3p$ up	1.4935	0.2597E−01	0.2833E−01	0.2401E−02	0.2304E−02
$2s$–$4p$ up	1.5965	0.8120E−02	0.8374E−02	0.1259E−02	0.1212E−02
$2s$–$5p$ up	1.6347	0.3615E−02	0.3671E−02	0.7156E−03	0.6648E−03
$1s$–$3p$ up	18.6691	0.2018E+00	0.1927E+00	0.1988E+00	0.2024E+00
$1s$–$4p$ up	18.8769	0.1946E−01	0.1871E−01	0.1916E−01	0.1955E−01
$1s$–$5p$ up	18.9274	0.7327E−02	0.7057E−02	0.7209E−02	0.7362E−02
In^+					
$5s$–$5p$	0.46336	0.2720E+01	0.1574E+01	0.1642E+01	0.1633E+01
$3s$–$6p$	0.84696	0.7166E−01	0.2179E−01	0.1221E−03	0.1039E−03
$5s$–$7p$	0.99885	0.1083E−01	0.1788E−02	0.1702E−02	0.1735E−02
$4d$–$4f$	2.40778	0.6243E−01	0.4001E−01	0.5761E−01	0.5770E−01
$4d$–$5f$	2.50016	0.4705E−01	0.3004E−01	0.4807E−01	0.4818E−01
$4d$–$6f$	2.55036	0.3163E−01	0.2015E−01	0.3115E−01	0.3122E−01
$4d$–$5p$	1.63660	0.8781E+00	0.8307E+00	0.7921E+00	0.7998E+00
$4d$–$6p$	2.26150	0.1040E+00	0.9386E−01	0.6613E−01	0.6688E−01
$4d$–$7p$	2.43521	0.3927E−01	0.3514E−01	0.2612E−01	0.2641E−01
$4p$–$5d$	7.09269	0.7098E−02	0.7638E−02	0.7332E−01	0.7053E−01
$4p$–$6d$	7.30040	0.1992E−02	0.2132E−02	0.1842E−01	0.1941E−01
$4p$–$7d$	7.39188	0.8610E−03	0.9236E−03	0.8701E−02	0.9089E−02
$4p$–$6s$	7.00657	0.8923E−01	0.6676E−01	0.8327E−01	0.8244E−01
$4p$–$7s$	7.26989	0.2300E−01	0.1745E−01	0.2083E−01	0.2055E−01
$4p$–$8s$	7.37691	0.1030E−01	0.7849E−02	0.9207E−02	0.9069E−02
$4s$–$5p$	9.43310	0.4042E−01	0.3309E−01	0.1491E−01	0.1471E−01
$4s$–$6p$	10.08759	0.7779E−02	0.6250E−02	0.3541E−02	0.3481E−02
$4s$–$7p$	10.26286	0.3291E−02	0.2641E−02	0.1583E−02	0.1557E−02
$3d$–$4f$	35.46157	0.1188E−02	0.1006E−02	0.1109E−02	0.1096E−02
$3d$–$5f$	35.55299	0.1164E−02	0.9851E−03	0.1077E−02	0.1064E−02
$3d$–$6f$	35.60333	0.8980E−03	0.7601E−03	0.8330E−03	0.8230E−03
$3d$–$5p$	34.58406	0.2241E−01	0.2131E−01	0.2915E−01	0.2963E−01
$3d$–$6p$	35.29983	0.3668E−02	0.3483E−02	0.4898E−02	0.4972E−02
$3d$–$7p$	35.48265	0.1498E−02	0.1422E−02	0.2010E−02	0.2041E−02
Eu					
$5p$–$7s$ do	1.8357	0.1200E+00	0.1028E+00	0.3417E−01	0.2986E−01
$5p$–$8s$ do	1.9428	0.1470E−01	0.1277E−01	0.2361E−01	0.2184E−01
$5p$–$9s$ do	1.9752	0.6118E−02	0.5331E−02	0.7119E−02	0.6554E−02
$5p$–$5d$ do	1.4467	0.2828E+01	0.2041E+01	0.1091E+00	0.1047E+00
$5p$–$6d$ do	1.9327	0.1583E+00	0.1185E+00	0.7905E+00	0.7768E+00
$5p$–$7d$ do	1.9689	0.5940E−01	0.4424E−01	0.3587E+00	0.3549E+00
$5p$–$7s$ up	2.0561	0.1077E+00	0.9156E−01	0.9807E−01	0.8885E−01

Table 2.4 (Continued)

5*p*–8*s* up	2.1627	0.1398E−01	0.1203E−01	0.1361E−01	0.1249E−01
5*p*–9*s* up	2.1956	0.5814E−02	0.5016E−02	0.5220E−02	0.4764E−02
5*p*–5*d* up	1.8487	0.3080E+01	0.2269E+01	0.2499E+01	0.2378E+01
5*p*–6*d* up	2.1342	0.1260E+00	0.9659E−01	0.2135E+00	0.2196E+00
5*p*–7*d* up	2.1830	0.4542E−01	0.3458E−01	0.7398E−01	0.7527E−01
4*f*–5*d* up	0.6862	0.3027E+00	0.4318E+00	0.6419E−01	0.8227E−01
4*f*–6*d* up	1.3073	0.6190E−02	0.8277E−02	0.1399E−02	0.1018E−02
4*f*–7*d* up	1.3637	0.2053E−02	0.2731E−02	0.1056E−02	0.8557E−03
4*f*–5g up	1.3891	0.1546E−05	0.1253E−05	0.7505E−06	0.6563E−06
4*f*–6g up	1.4013	0.1704E−05	0.1383E−05	0.7007E−06	0.6080E−06
4*f*–7g up	1.4087	0.1459E−05	0.1185E−05	0.5111E−06	0.4406E−06
4*d*–6*p* do	10.5562	0.3633E−01	0.3331E−01	0.1307E−01	0.1280E−01
4*d*–7*p* do	10.8227	0.4596E−02	0.4214E−02	0.3257E−02	0.3209E−02
4*d*–8*p* do	10.8752	0.1773E−02	0.1626E−02	0.1245E−02	0.1225E−02
4*d*–4*f* do	10.5454	0.4075E+01	0.3200E+01	0.4545E+01	0.4565E+01
4*d*–5*f* do	10.8743	0.8107E−02	0.6382E−02	0.1862E−02	0.1854E−02
4*d*–6*f* do	10.8972	0.5536E−02	0.4360E−02	0.1370E−02	0.1363E−02
4*d*–6*p* up	11.7914	0.3497E−01	0.2913E−01	0.3116E−01	0.3119E−01
4*d*–7*p* up	12.0667	0.4340E−02	0.3627E−02	0.4036E−02	0.4009E−02
4*d*–8*p* up	12.1199	0.1676E−02	0.1402E−02	0.1440E−02	0.1437E−02
4*d*–5*f* up	12.1196	0.2937E−03	0.2238E−03	0.1322E−02	0.1199E−02
4*d*–6*f* up	12.1425	0.2524E−03	0.1926E−03	0.9907E−03	0.8921E−03
4*d*–7*f* up	12.1550	0.1806E−03	0.1378E−03	0.7161E−03	0.6444E−03
Eu^+					
5*p*–6*s* do	1.61182	0.2669E+00	0.2589E+00	0.2580E+00	0.2664E+00
5*p*–7*s* do	2.05920	0.4351E−01	0.4173E−01	0.6503E−01	0.6554E−01
5*p*–8*s* do	2.21408	0.1645E−01	0.1572E−01	0.9723E−02	0.9935E−02
5*p*–5*d* do	1.47349	0.3073E+01	0.2268E+01	0.2269E−01	0.2269E−01
5*p*–6*d* do	2.10502	0.2905E+00	0.2056E+00	0.5965E+00	0.5837E+00
5*p*–7*d* do	2.22961	0.1005E+00	0.7017E−01	0.6570E−01	0.6260E−01
5*p*–6*s* up	2.24031	0.1051E+00	0.8831E−01	0.9786E−01	0.9427E−01
5*p*–7*s* up	2.43106	0.2326E−01	0.1976E−01	0.2575E−01	0.2507E−01
5*p*–8*s* up	2.51138	0.1061E−01	0.9034E−02	0.1027E−01	0.9991E−02
5*p*–5*d* up	1.89422	0.3225E+01	0.2370E+01	0.4067E+01	0.3993E+01
5*p*–6*d* up	2.30870	0.2676E+00	0.2026E+00	0.4316E+00	0.4485E+00
5*p*–7*d* up	2.44887	0.8161E−01	0.6070E−01	0.6975E−01	0.7269E−01
5*s*–6*p* do	3.29638	0.6065E−02	0.3890E−02	0.7697E−03	0.3894E−03
5*s*–7*p* do	3.59719	0.2290E−02	0.1520E−02	0.1997E−02	0.1303E−02
5*s*–8*p* do	3.71444	0.1120E−02	0.7515E−03	0.1154E−02	0.7866E−03
5*s*–6*p* up	3.47950	0.5040E−02	0.4419E−02	0.4401E−03	0.1099E−02
5*s*–7*p* up	3.87539	0.2010E−02	0.1544E−02	0.5117E−03	0.7635E−03
5*s*–8*p* up	4.00016	0.9969E−03	0.7557E−03	0.3967E−03	0.5176E−03
4*f*–5*d* up	0.69233	0.3057E+00	0.4360E+00	0.6759E−01	0.7952E−01
4*f*–6*d* up	1.45011	0.1571E−01	0.2065E−01	0.4378E−01	0.4236E−01
4*f*–7*d* up	1.62729	0.5115E−02	0.6614E−02	0.8083E−02	0.7801E−02
4*f*–5g up	1.68348	0.4508E−03	0.3706E−03	0.2671E−03	0.2517E−03
4*f*–6g up	1.73258	0.4671E−03	0.3843E−03	0.2276E−03	0.2143E−03
4*f*–7g up	1.76231	0.3844E−03	0.3163E−03	0.1550E−03	0.1457E−03

Table 2.4 (Continued)

$4d$–$4f$ do	10.50040	0.4153E+01	0.3262E+01	0.3725E+01	0.3727E+01
$4d$–$5f$ do	11.09527	0.5840E−01	0.4614E−01	0.1904E−01	0.1893E−01
$4d$–$6f$ do	11.18768	0.3148E−01	0.2489E−01	0.1137E−01	0.1125E−01
$4d$–$5f$ up	12.33148	0.9914E−02	0.7631E−02	0.3645E−01	0.3227E−01
$4d$–$6f$ up	12.42946	0.5731E−02	0.4429E−02	0.2241E−01	0.1975E−01
$4d$–$7f$ up	12.48243	0.3387E−02	0.2623E−02	0.1442E−01	0.1265E−01
Eu^{2+}					
$5p$–$6s$ do	1.67794	0.2950E+00	0.2859E+00	0.2988E+00	0.3095E+00
$5p$–$7s$ do	2.28375	0.5536E−01	0.5287E−01	0.1391E+00	0.1408E+00
$5p$–$8s$ do	2.53390	0.2155E−01	0.2047E−01	0.4720E−01	0.4769E−01
$5p$–$5d$ do	1.48278	0.3281E+01	0.2418E+01	0.7254E−01	0.6555E−01
$5p$–$6d$ do	2.29936	0.3424E+00	0.2375E+00	0.4206E+00	0.4205E+00
$5p$–$7d$ do	2.55325	0.1039E+00	0.7037E−01	0.3233E+00	0.3240E+00
$5p$–$6s$ up	1.86877	0.2769E+00	0.2631E+00	0.5286E+00	0.5519E+00
$5p$–$7s$ up	2.49616	0.5471E−01	0.5119E−01	0.2292E−01	0.2173E−01
$5p$–$8s$ up	2.74958	0.2156E−01	0.2006E−01	0.4198E−01	0.4310E−01
$5p$–$5d$ up	1.92433	0.3386E+01	0.2537E+01	0.9193E+00	0.9117E+00
$5p$–$6d$ up	2.49604	0.2793E+00	0.1978E+00	0.6948E−02	0.6426E−02
$5p$–$6d$ up	2.75394	0.8238E−01	0.5709E−01	0.8400E−01	0.8366E−01
$5s$–$6p$ do	3.39995	0.8820E−02	0.5786E−02	0.4596E−02	0.3202E−02
$5s$–$7p$ do	3.85376	0.4135E−02	0.2822E−02	0.3965E−02	0.3233E−02
$5s$–$8p$ do	4.05439	0.2167E−02	0.1499E−02	0.2204E−02	0.1802E−02
$5s$–$6p$ up	3.65871	0.1030E−01	0.6693E−02	0.1470E−02	0.1765E−02
$5s$–$7p$ up	4.12112	0.4581E−02	0.3080E−02	0.2024E−02	0.2188E−02
$5s$–$8p$ up	4.32480	0.2366E−02	0.1609E−02	0.1090E−02	0.1171E−02
$4f$–$5d$ up	0.72769	0.3224E+00	0.4502E+00	0.6785E−01	0.8311E−01
$4f$–$6d$ up	1.65709	0.1830E−01	0.2403E−01	0.4059E−01	0.4004E−01
$4f$–$7d$ up	1.92440	0.7102E−02	0.9085E−02	0.8797E+00	0.8725E+00
$4f$–5g up	1.99403	0.5349E−02	0.4499E−02	0.5955E−01	0.5939E−01
$4f$–6g up	2.10428	0.5067E−02	0.4246E−02	0.8387E−02	0.8342E−02
$4f$–7g up	2.17088	0.3977E−02	0.3325E−02	0.4823E−02	0.4793E−02
$4d$–$4f$ do	10.57958	0.4205E+01	0.3302E+01	0.3957E+01	0.3918E+01
$4d$–$5f$ do	11.30317	0.1350E+00	0.1068E+00	0.8030E−01	0.7975E−01
$4d$–$6f$ do	11.50412	0.6031E−01	0.4766E−01	0.3861E−01	0.3820E−01
$4d$–$5f$ up	12.53360	0.3903E−04	0.2364E−03	0.8218E−03	0.1159E−02
$4d$–$6f$ up	12.74098	0.4681E−03	0.7995E−04	0.8893E−03	0.4417E−03
$4d$–$7f$ up	12.85443	0.3560E−03	0.3613E−05	0.1291E−04	0.1115E−03

2.6 Ions and Atoms of Group IV Elements of the Periodic Table

In this section, we represent our results for external and intermediate subshells of ions and atoms that belong to the IV group of the Periodic Table. Here we concentrate mainly on the ions having all filled and one half-filled subshell, namely C* $(Z = 6)$ $1s^1 2s^1\ 2p^3 3s^1$all $\uparrow$; C^- $(Z = 6)$ $1s^2\ 2s^2 2p^3\ \uparrow$; Si* $(Z = 14)$ $1s 2s 2p^3\ 3s^1\ 3p^3\ 3d^5$, all $\uparrow$; Si^+ $(Z = 14)$ $2p^6\ 3s^2\ 3p$; Si^{2+} $(Z = 14)$ $2p^6\ 3s^2$; Si^{3+} $(Z = 14)\, 2p^3\ 3s^1$; Si^- $(Z = 14)\, 2s^2\ 2p^6\ 3s^2\ 3p^3\ \uparrow$; Ge^- $(Z = 32)\, 2p^6 3s^2\ 3p^6 3d^{10}\ 4s^2\ 4p^3\ \uparrow$. Formulas used in calculations and notations in figures are the same, as for noble gases and are collected in Sect. 2.1. Here $\uparrow$ denotes "up" electrons for SP RPAE (see Sect. 1.10).

Figures 2.232_C*_a1 and 2.233_C*_d1 (C*) contain results of calculations for C* atom in excited state $1s^1\ 2s^1\ 2p^3 3s^1\ \uparrow$.

Figure 2.232_C*_a1 presents total photoionization cross-section of C* atom in excited state in HF-l, HF-v, and SP RPAE. The main contribution is from $2p^3$ subshell.

Figure 2.233_C*_d1 shows dipole angular anisotropy parameter of $2p$-electrons for C* excited atom in HF-l, HF-v, and SP RPAE. The role of correlations is small.

Figures 2.234_C^-_a1–2.236_C^-_d1 (C^-) collect results of calculations for C^- ion $(Z = 6)$ $1s^2 2s^2 2p^3\ \uparrow$.

Figure 2.234_C^-_a1 presents total cross-section of photodetachment of C^- ion in HF-l, HF-v, and SP RPAE. Note the unexpectedly prominent role of electron correlations within the region 0.5 Ry above photodetachment threshold.

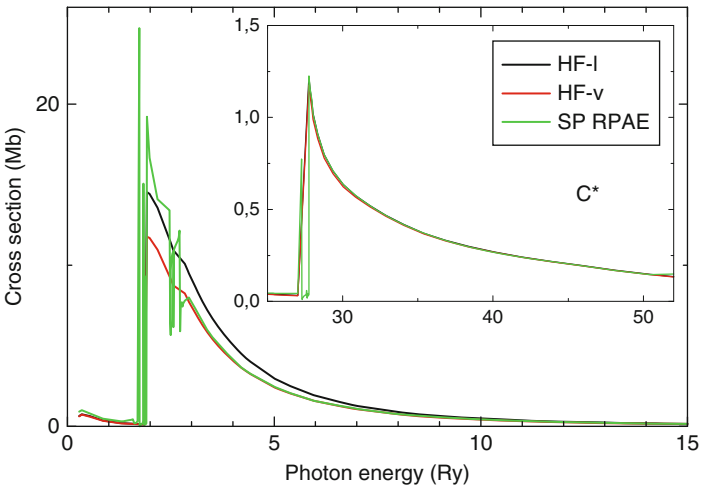

Fig. 2.232_C*_a1 Total photoionization cross section of C* atom in excited state in HF-l, HF-v, and RPAE

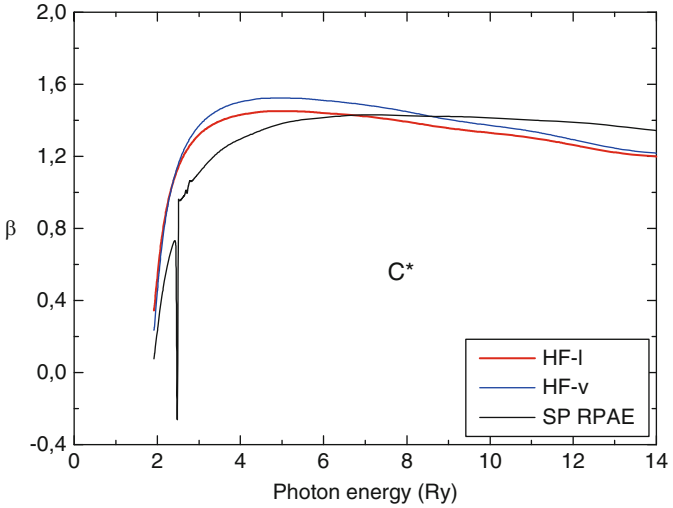

Fig. 2.233_C*_d1 Dipole anisotropy parameter of $2p$-electrons for C* atom in HF-l, HF-v, and SP RPAE

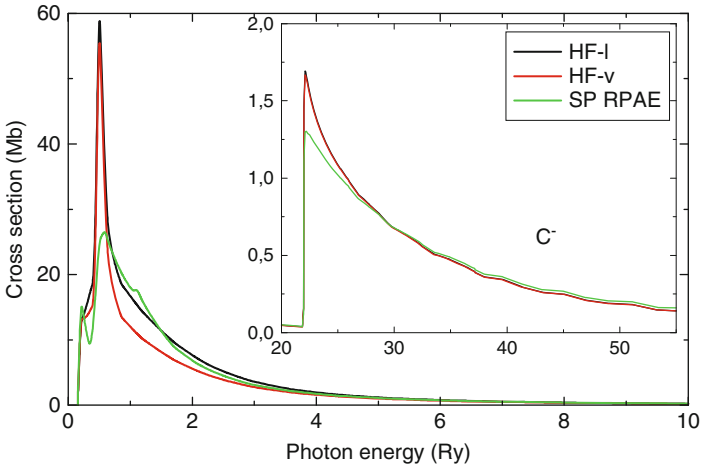

Fig. 2.234_C$^-$_a1 Total photoionization cross section of C^- ion in HF-l, HF-v, and SP RPAE

Figure 2.235_C$^-$_b1 presents cross-section of photodetachment of $1s$-electrons for C^- ion. Calculation data are from [2.57]. The maximum at threshold is a result of GRPAE calculations supplemented with account of polarization of the residual core by the photoelectron. Experiment is from [2.58]. They are normalized to the calculated cross-section at maximum.

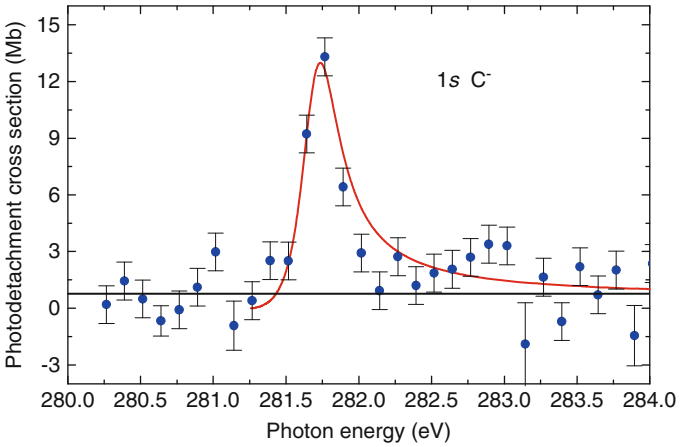

Fig. 2.235_C$^-$_b1 Photodetachment cross section of 1s-electrons for C$^-$ ion [2.56]. Experiment is from [2.58]

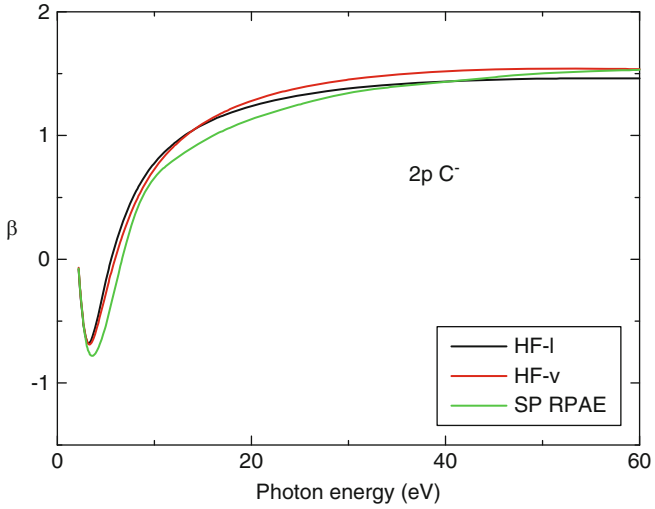

Fig. 2.236_C$^-$_d1 Dipole anisotropy parameter of 2p-electrons for C$^-$ ion

Figure 2.236_C$^-$_d1 depicts dipole angular anisotropy parameter of 2p-electrons for C$^-$ ion in HF-l, HF-v, and SP RPAE. The β-parameter has a minimum just after the threshold and the very soon reaches almost constant value.

Figures 2.237_Si*_a1 and 2.238_Si*_d1 (Si*) contain results of calculations for Si* atom in excited state ($Z = 14$) $1s^1\ 2s^1, 2p^3\ 3s^1\ 3p^3\ 3d^5\uparrow$.

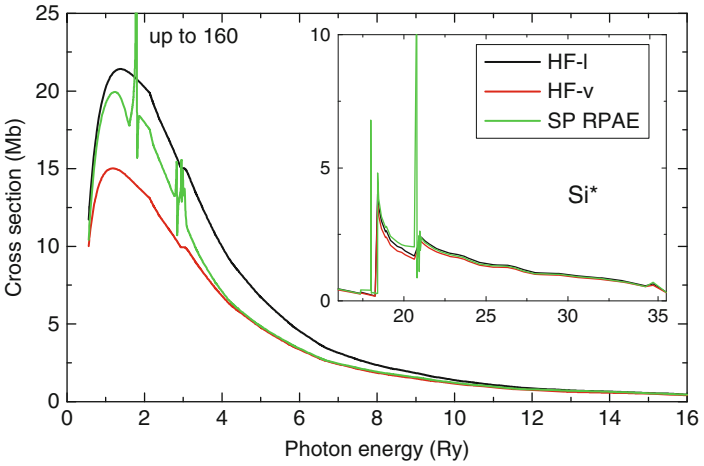

Fig. 2.237_Si*_a1 Total photoionization cross section of Si* atom in excited state in HF-l, HF-v, and SP RPAE

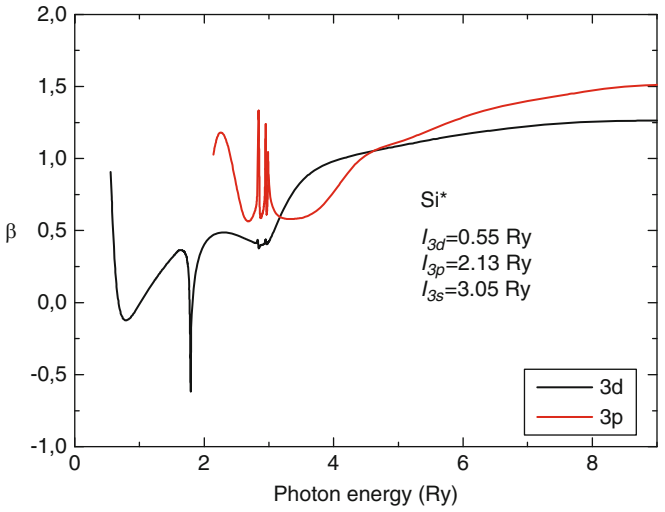

Fig. 2.238_Si*_d1 Dipole anisotropy parameter of $3d$-, $3p$-electrons for Si* excited atom in SP RPAE

Figure 2.237_Si*_a1 depicts total photoionization cross-section of Si* in HF-l, HF-v, and SP RPAE. The cross-section rises after the threshold and then decreases until it reaches the threshold of inner shell. The quasi cross-sections of discrete excitations are seen.

Figure 2.238_Si*_d1 shows dipole angular anisotropy parameter of $3d$- and $3p$-electrons for Si* atom in HF-l, HF-v, and SP RPAE.

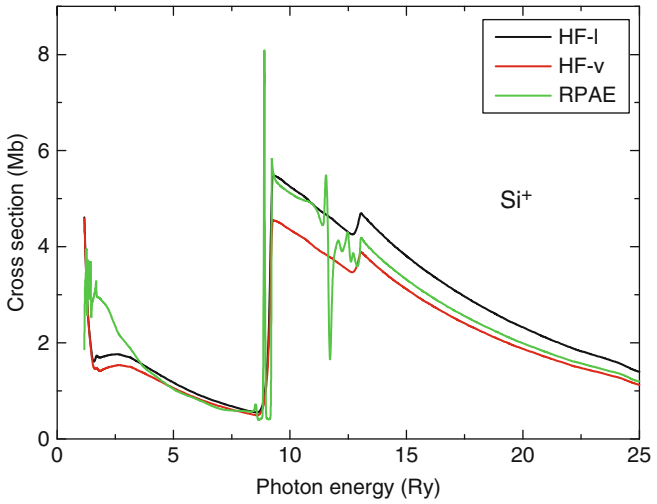

Fig. 2.239_Si$^+$_a1 Total photoionization cross section of Si$^+$ ion in HF-l, HF-v, and RPAE

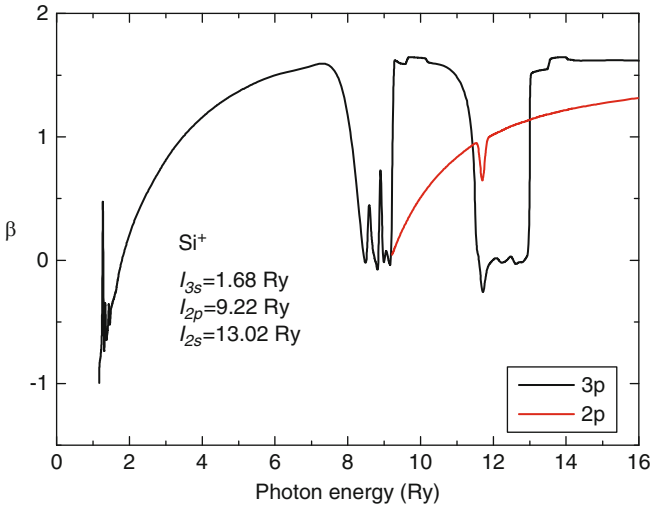

Fig. 2.240_Si$^+$_d1 Dipole anisotropy parameter of $3p$-, $2p$-electrons for Si$^+$ in RPAE

Figures 2.239_Si$^+$_a1 and 2.240_Si$^+$_d1 (Si$^+$) contain results of calculations for Si$^+$ ion ($Z = 14$)$1s^2 2s^2 2p^6 3s^2 3p$.

Figure 2.239_Si$^+$_a1 presents total photoionization cross-section of Si$^+$ ion in HF-l, HF-v, and RPAE. The role of electron correlations is noticeable, particularly in the region near threshold up to 2 Ry above it.

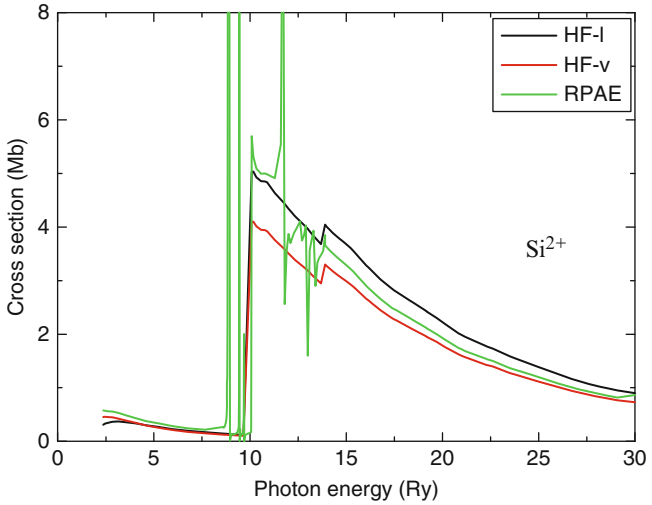

Fig. 2.241_Si^{2+}_a1 Total photoionization cross section of Si^{2+} ion in HF-l, HF-v, and RPAE

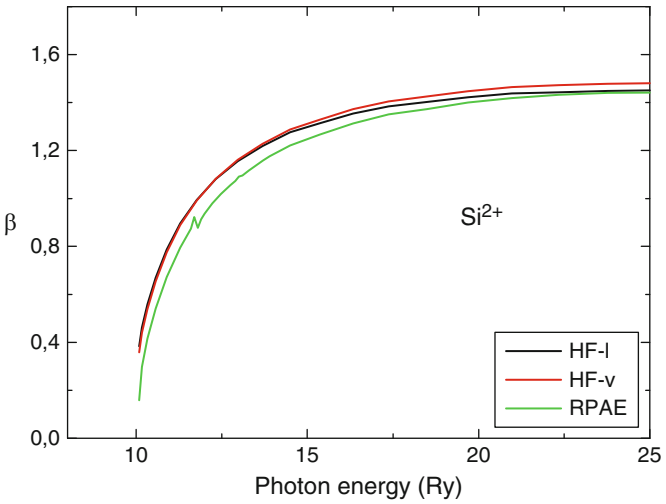

Fig. 2.242_Si^{2+}_d1 Dipole anisotropy parameter of $2p$-electrons for Si^{2+} in RPAE

Figure 2.240_Si^{+}_d1 displays dipole angular anisotropy parameter of $3p$-, $2p$-electrons for Si^{+} in RPAE.

Figures 2.241_Si^{2+}_a1 and 2.242_Si^{2+}_d1 (Si^{2+}) contain results of calculations for Si^{2+} ion $(Z = 14)1s^2 2s^2 2p^6 3s^2$.

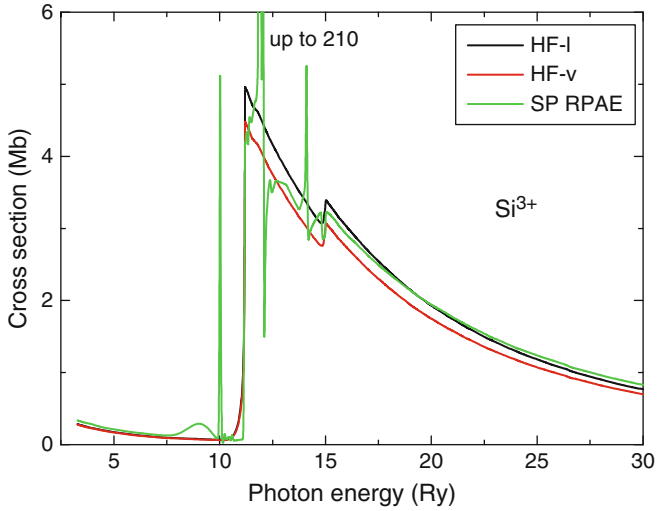

Fig. 2.243_Si^{3+}_a1 Total photoionization cross section of Si^{3+} ion in HF-l, HF-v, and SP RPAE

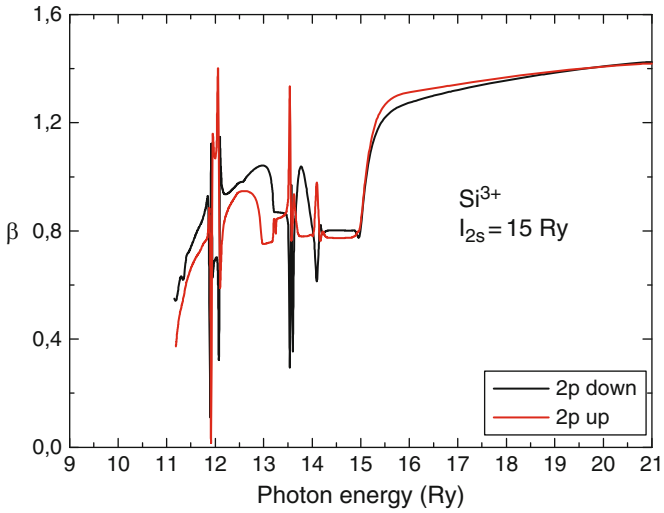

Fig. 2.244_Si^{3+}_d1 Dipole anisotropy parameter of $2p$-electrons for Si^{3+} in SP RPAE

Figure 2.241_Si^{2+}_a1 depicts total photoionization cross-section of Si^{2+} ion in HF-l, HF-v, and RPAE.

Figure 2.242_Si^{2+}_d1 presents dipole angular anisotropy parameter of $2p$-electrons for Si^{2+} in HF-l, HF-v, and RPAE. The role of electron correlations is essential only close to threshold.

Figures 2.243_Si^{3+}_a1 and 2.244_Si^{3+}_d1 (Si^{3+}) contain results of calculations for Si^{3+} ion ($Z = 14$) $1s^2 2s^2 2p^6 3s^1$.

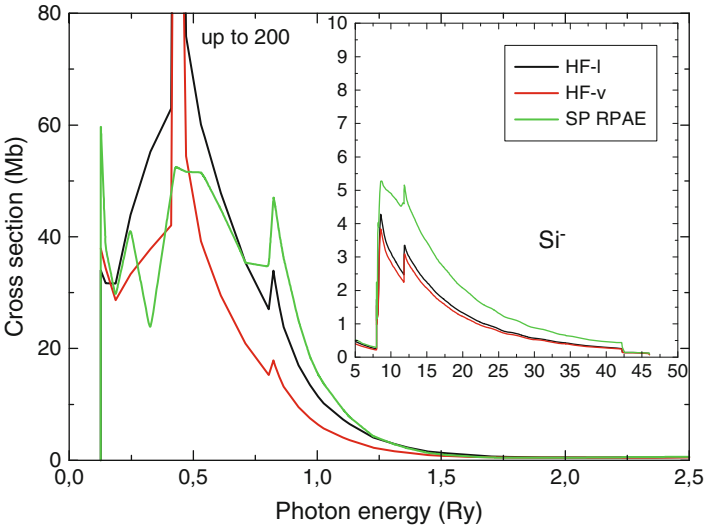

Fig. 2.245_Si⁻_a1 Total photodetachment cross section of Si^- ion in HF-l, HF-v, and SP RPAE

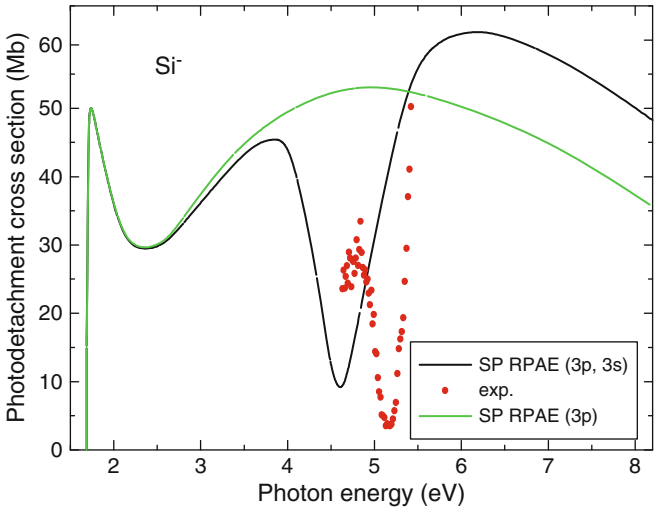

Fig. 2.246_Si⁻_b1 Photodetachment cross section of $3p$-electrons for Si^- ion in SP RPAE [2.55] Experiment is from [2.58]

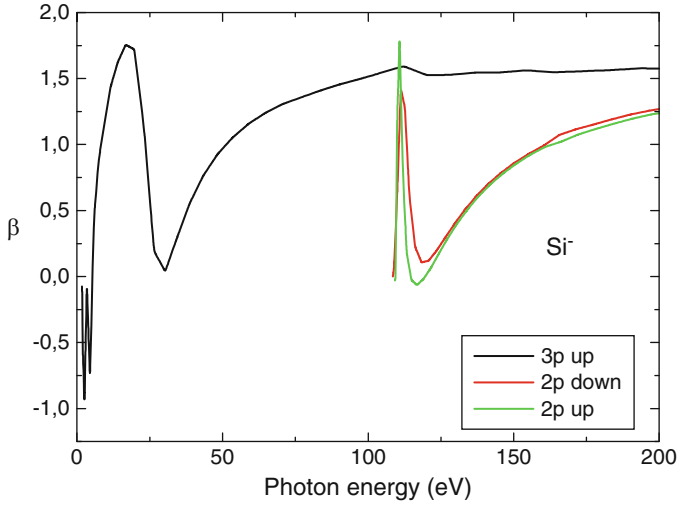

Fig. 2.247_Si⁻_d1 Dipole anisotropy parameter of $3p$ "up," $2p$ "up" and "down"-electrons for Si^- in SP RPAE

Figure 2.243_Si^{3+}_a1 presents total photoionization cross-section of Si^{3+} ion in HF-l, HF-v, and SP RPAE. Account of electron correlations brings in additional prominent structure, concentrated in the photon energy region 7–12 Ry.

Figure 2.244_Si^{3+}_d1 depicts dipole angular anisotropy parameter of $2p$-electrons for Si^{3+} in SP RPAE. The parameter is characterized by a peculiar structure from threshold at 11 Ry to almost 16 Ry that is due to effect of discrete excitations.

Figures 2.245_Si^-_a1–2.250_Si^-P_e2 (Si^-) contain results of calculations for Si^- ion ($Z = 14$) $2s^2\,2p^6\,3s^2\,3p^3\uparrow$.

Figure 2.245_Si^-_a1 shows total cross-section of photodetachment of Si^- ion in HF-l, HF-v, and SP RPAE. SP RPAE corrections lead to additional rather complex prominent structure.

Figure 2.246_Si^-_b1 presents cross-section of photodetachment of $3p$-electrons of Si^- ion. Cross-section in SP RPAE is under strong influence of $3s$-subshell [2.57]. Experimental data are taken from [2.59]. There are no discrete excitations in negative ions, however, the picture of cross-section is similar to that taking place in a vicinity of autoionizing "window" resonance [see (1.50)] that takes place at small Fano asymmetry parameter q. The role of discrete excitation is played by the effect of $3s$-ionization near their threshold.

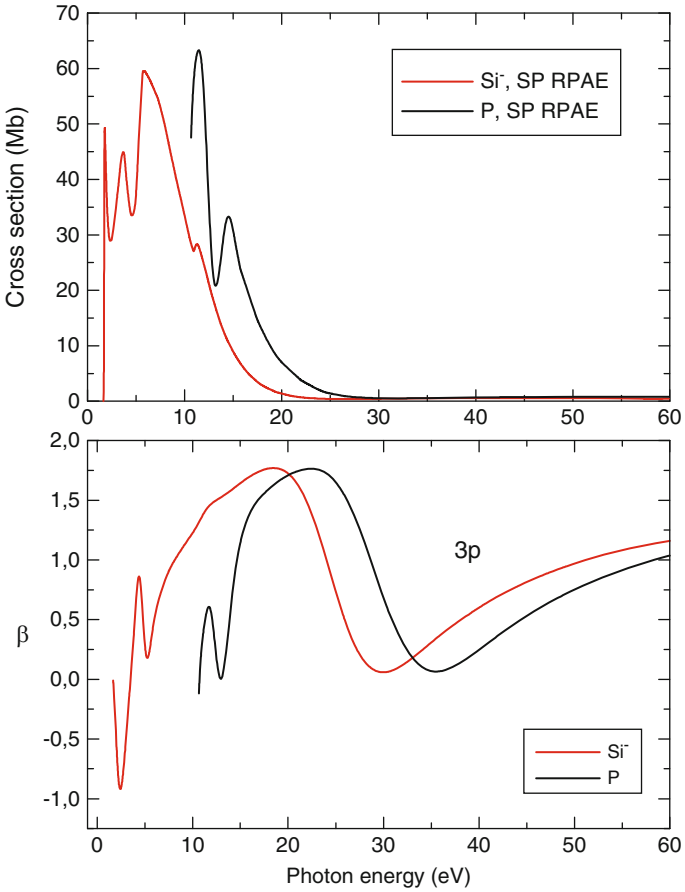

Fig. 2.248_Si⁻P_d2 Dipole anisotropy parameter and photoionization cross section and of $3p$-electrons for Si^- ion with the same for P atom in SP RPAE

Figure 2.247_Si⁻_d1 shows the dipole angular anisotropy parameter of $3p\uparrow$- and $2p\uparrow\downarrow$-electrons for Si^- ion in SP RPAE. As commonly, the energy dependence of the outermost $3p$-subshell is the most complex near threshold, where fast variation is seen. At the threshold, β_{2p}-parameter has a narrow and high maximum and after minimum $\beta_{3p}(\omega)$ rises gradually. Similar is the behavior of β_{2p}.

Figure 2.248_Si⁻P_d2 compares dipole angular anisotropy parameters of Si^- ion and P atom. Electron configurations of these objects are the same and their β_{3p}-parameters are close to each other.

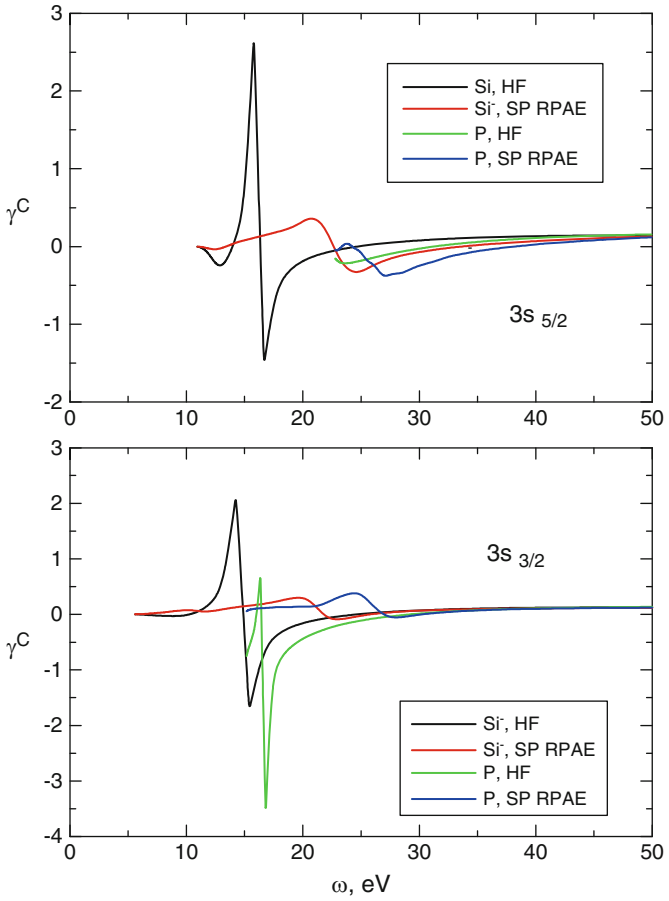

Fig. 2.249_Si⁻P_e1 Non-dipole anisotropy parameter of $3s$-electrons for Si^- ion in comparison with the same of P atom in HF and SP RPAE

Figure 2.249_Si⁻P_e1 compares non-dipole angular anisotropy parameters γ^C of $3s_{5/2}$- and $3s_{3/2}$-electrons for Si^- ion and P atom in HF-l, HF-v, and SP RPAE. As well as in a Fig. 2.248, the results for an ion and atom are close. It is remarkable that RPAE correlations considerably smooth the curves.

Figure 2.250_Si⁻P_e2 presents non-dipole angular anisotropy parameters and their magic combination for $3p$-electrons of Si^- ion and P atom. Again the ion and atom have close characteristics.

Figure 2.251_Ge⁻_b1 (Ge^-) contains results of calculations for Ge^- ($Z = 32$) $2p^6 3s^2 3p^6\ 3d^{10} 4s^2 4p^3\uparrow$.

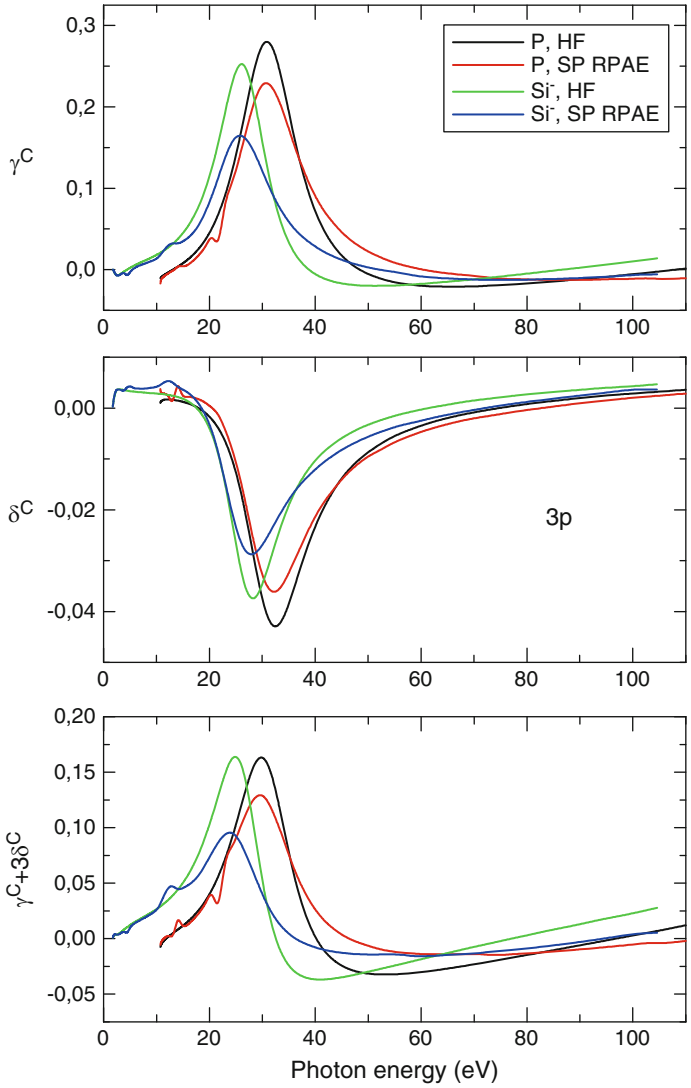

Fig. 2.250_Si⁻P_e2 Non-dipole anisotropy parameter of $3p$-electrons for Si^- ion in comparison with the same of P atom in HF and SP RPAE

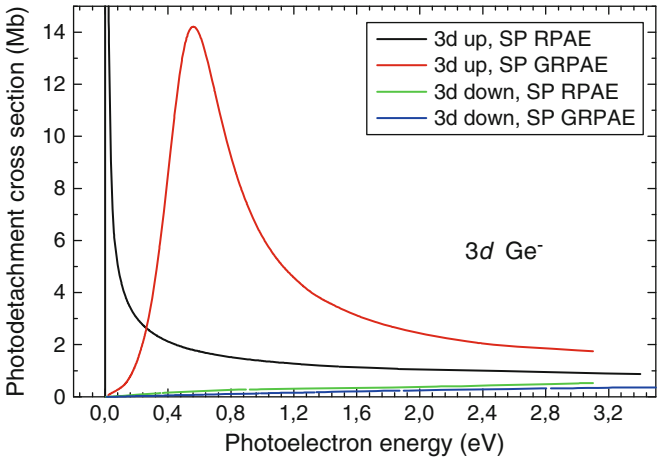

Fig. 2.251_Ge$^-$_b1 Photodetachment cross section of $3d$-electrons from Ge^- ion

Figure 2.251_Ge$^-$_b1 presents cross-section of photodetachment of $3d$-electrons of Ge^- ion in SP RPAE and SP GRPAE. The effects of rearrangement are quite strong.

Table 2.5 includes calculated values of oscillator strengths in HF-l, HF-v, $f^{l,v}_{nl-n'l'\uparrow(\downarrow)}$, and $F^{l,v}_{nl-n'l'\uparrow(\downarrow)}$ in RPAE for several lowest discrete levels of excitation and for each considered subshell of two excited atoms C* and Si*, investigated in this section. Respective theoretical transition energies in RPAE $\tilde{\omega}_{nl-n'l'\uparrow(\downarrow)}$ are also given in this table.

The results for length and velocity forms in RPAE coincide with reasonable accuracy. In C* the role of electron correlations is small for outer electrons and much bigger for the next to the outer subshell. The biggest oscillator strength has the outer subshell excitation $3s$–$3p$. In Si* all oscillator strengths are small. The oscillator strengths are, in general, decreasing with decrease in principal quantum number of the exited electron.

Table 2.5 Oscillator strengths and transition energies of IV group's elements and their ions

Transition	ω (Ry)	HF-l	HF-v	RPAE-l	RPAE-v
C*					
$3s$–$3p$ up	0.08190	0.9393E+00	0.9431E+00	0.9111E+00	0.9221E+00
$3s$–$4p$ up	0.18858	0.3351E−03	0.3020E−03	0.1243E−02	0.1155E−02
$3s$–$5p$ up	0.22787	0.1109E−02	0.1066E−02	0.1814E−02	0.1756E−02
$2p$–$3s$ up	1.74389	0.3126E+00	0.2395E+00	0.3327E+00	0.3331E+00
$2p$–$4s$ up	1.84081	0.7237E−01	0.5703E−01	0.4955E−01	0.4798E−01
$2p$–$5s$ up	1.87215	0.3419E−01	0.2705E−01	0.1978E−01	0.1895E−01
$2p$–$5p$ up	1.83668	0.4664E−02	0.4961E−02	0.3074E−01	0.3369E−01
$2p$–$6p$ up	1.87058	0.2003E−02	0.2138E−02	0.1301E−01	0.1406E−01
$2p$–$7p$ up	1.88713	0.1062E−02	0.1135E−02	0.1269E−02	0.1607E−02
$2s$–$3p$ up	2.47047	0.5220E−01	0.5781E−01	0.1134E−01	0.1301E−01
$2s$–$4p$ up	2.72229	0.1152E−01	0.1174E−01	0.1481E−02	0.1734E−02
$2s$–$5p$ up	2.77703	0.4238E−02	0.4280E−02	0.5959E−03	0.6928E−03
$1s$–$3p$ up	27.26785	0.1380E+00	0.1325E+00	0.1401E+00	0.1416E+00
$1s$–$4p$ up	27.62258	0.2153E−01	0.2078E−01	0.2158E−01	0.2187E−01
$1s$–$5p$ up	27.69215	0.6190E−02	0.5978E−02	0.6190E−02	0.6275E−02
Si*					
$3d$–$4f$ up	0.48142	0.1318E−01	0.1041E−01	0.1185E−01	0.1202E−01
$3d$–$5f$ up	0.50430	0.9614E−02	0.7542E−02	0.8842E−02	0.8983E−02
$3d$–$6f$ up	0.51670	0.6413E−02	0.5013E−02	0.6380E−02	0.6508E−02
$3d$–$5p$ up	0.44733	0.4104E−01	0.4192E−01	0.3782E−01	0.4216E−01
$3d$–$6p$ up	0.48851	0.1519E−01	0.1552E−01	0.1394E−01	0.1560E−01
$3d$–$7p$ up	0.50807	0.7428E−02	0.7596E−02	0.6811E−02	0.7613E−02
$3p$–$4s$ up	1.79586	0.1373E+00	0.8347E−01	0.1176E+00	0.8940E−01
$3p$–$5s$ up	2.00204	0.1990E−01	0.1301E−01	0.1522E−01	0.1357E−01
$3p$–$6s$ up	2.06080	0.7136E−02	0.4732E−02	0.5516E−02	0.4982E−02
$3s$–$4p$ up	2.82891	0.2339E−01	0.1518E−01	0.1245E−01	0.1033E−01
$3s$–$5p$ up	2.94905	0.5835E−02	0.3850E−02	0.3194E−02	0.2644E−02
$3s$–$6p$ up	2.99057	0.2455E−02	0.1628E−02	0.1409E−02	0.1165E−02
$2p$–$4s$ up	17.99262	0.9716E−02	0.1135E−01	0.2220E−01	0.2497E−01
$2p$–$5s$ up	18.24696	0.1477E−02	0.1671E−02	0.4261E−02	0.4589E−02
$2p$–$6s$ up	18.31203	0.5429E−03	0.6115E−03	0.1781E−02	0.1901E−02
$2s$–$4p$ up	20.78310	0.3970E−01	0.3770E−01	0.3168E−01	0.3155E−01
$2s$–$5p$ up	20.93561	0.7199E−02	0.6848E−02	0.5810E−02	0.5797E−02
$2s$–$6p$ up	20.98249	0.2852E−02	0.2714E−02	0.2292E−02	0.2291E−02

2.7 Atoms and Ions of Group V Elements of the Periodic Table

In this section we present our results for outer and intermediate subshells of atoms and some ions of V group elements. Here we have concentrated basically on the ions having all filled and one half-filled subshell, namely N $(Z = 7)\ 1s^2 2s^2 2p^3 \uparrow$; $N^{3+}(Z = 7)\ 1s^2 2s^2$; P $(Z = 15)\ 2s^2 2p^6 3s^2 3p^3 \uparrow$; As $(Z = 33)\ 3d^{10} 4s^2 4p^3 \uparrow$; Sb $(Z = 51)\ 4d^{10} 5s^2 5p^3 \uparrow$. Formulas used to obtain data and notations in figures the same as for noble gases and are resulted in Sect. 2.1. Here $\uparrow$ denotes "up" electrons for SP RPAE (see Sect. 1.10).

Figures 2.252_N_a1–2.254_N_f1 (N) contain results of calculations for N atom $(Z = 7)\ 1s^2\ 2s^2\ 2p^3 \uparrow$.

Figure 2.252_N_a1 shows total photoionization cross-section of N atom in HF-l, HF-v, and SP RPAE. The role of correlations is rather visible. The main contribution to cross-section is due to outer $2p$-electrons.

Figure 2.253_N_d1 presents dipole angular anisotropy parameters for N $2p$-elecrons in SP RPAE. The curve is smooth, increasing from zero at threshold to about $\beta \simeq 1.5$ at 4 Ry.

Figure 2.254_N_f1 includes dipole angular anisotropy and spin polarization parameters of N $2p$-electrons: (a) $\beta_{2p}(\omega)$, (b) $A_{2p}^{3/2}(\omega)$, (c) $\alpha_{2p}^{3/2}(\omega)$, and (d) $\xi_{2p}^{3/2}(\omega)$.

Figure 2.255_N^{3+}_a1 contains results of calculations for N^{3+} ion $(Z = 7)$ $1s^2\ 2s^2$.

Figure 2.255_N^{3+}_a1 shows total photoionization cross-section of N^{3+} ion in HF-l, HF-v, and SP RPAE. The role of electron correlations is decisively important in forming the maximum near the first ionization threshold.

Figures 2.256_P_a1–2.260_P_f1 (P) contain results of calculations for P atom $(Z = 15)\ 2s^2\ 2p^6\ 3s^2\ 3p^3 \uparrow$.

Figure 2.256_P_a1 depicts total photoionization cross-section of P atom in HF-l, HF-v, and SP RPAE. Strong narrow variations are manifestation of discrete excitations.

Figure 2.257_P_d1 presents dipole angular anisotropy parameter $2p\uparrow$, $2p\downarrow$, and $3p\uparrow$-electrons of P atom in SP RPAE. The $\beta_{3p\uparrow}(\omega)$ parameter has a narrow minimum near threshold, the second is at 10 eV from threshold and then there are two broader; two minimums are located at higher energies. Parameters $\beta_{2p\uparrow}(\omega)$ and $\beta_{2p\downarrow}(\omega)$ are close to each other and have a narrow maximum near threshold with a subsequent relatively slow increase.

Figure 2.258_P_e1 compares non-dipole angular anisotropy parameters γ^{C} of $3s\downarrow$- and $3s\uparrow$-electrons of P in SP HF and SP RPAE. It follows from this figure that the role of RPAE correlations is large and that the difference between two values near threshold is significant.

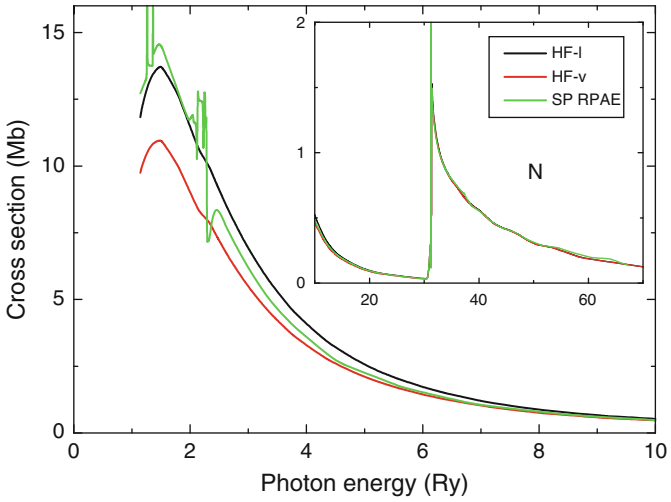

Fig. 2.252_N_a1 Total photoionization cross section of N atom in HF-l, HF-v, and SP RPAE

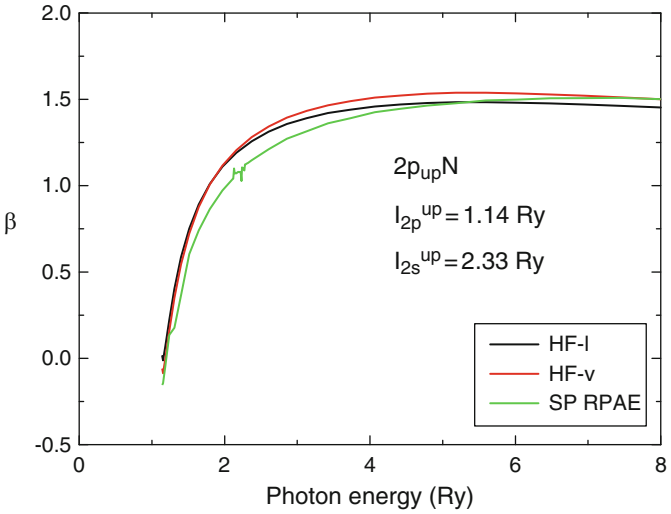

Fig. 2.253_N_d1 Dipole anisotropy parameter of $2p$-electrons for N in HF and SP RPAE

Figure 2.259_P_e2 presents non-dipole angular anisotropy parameters γ^{C} and δ^{C} and their magic combination $(\gamma^{\mathrm{C}} + 3\delta^{\mathrm{C}})$ for $3p\uparrow$-electrons of P. The role of RPAE correlations is modest.

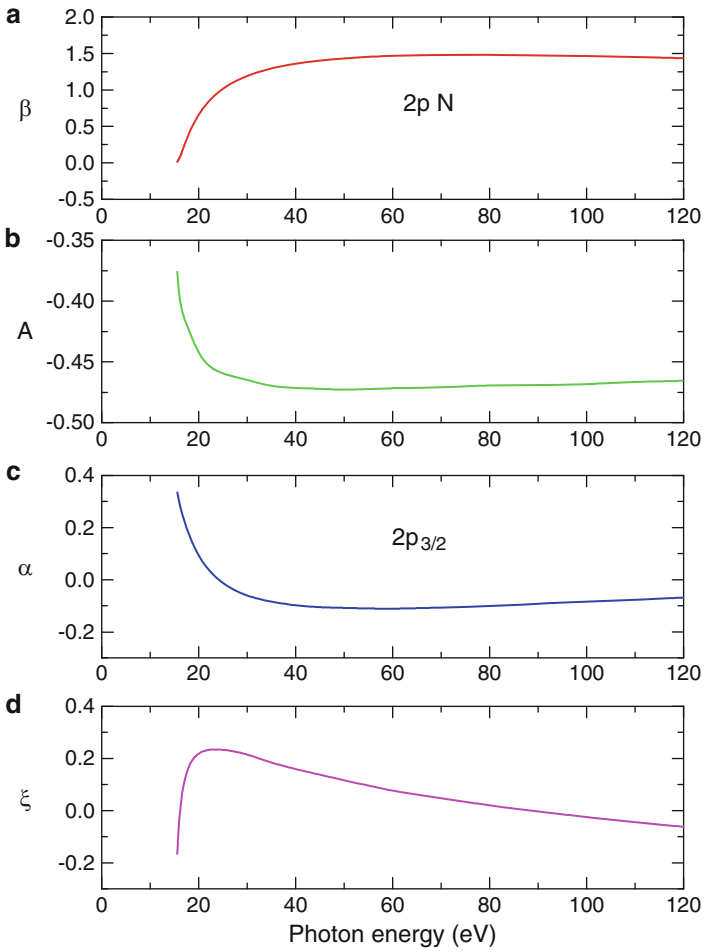

Fig. 2.254_N_f1 Dipole parameter of $2p$-electrons for N atom: (**a**) angular anisotropy $\beta_{2p}(\omega)$; (**b**) spin polarization $A_{2p}^{3/2}(\omega)$, (**c**) $\alpha_{2p}^{3/2}(\omega)$, and (**d**) $\xi_{2p}^{3/2}(\omega)$

Figure 2.260_P_f1 depicts dipole angular anisotropy parameters $3p\uparrow$-electrons of P: (a) angular anisotropy $\beta_{3p}(\omega)$; spin polarization (b) $A_{3p}^{3/2}(\omega)$, (c) $\alpha_{3p}^{3/2}(\omega)$, and (d) $\xi_{3p}^{3/2}(\omega)$—all in SP RPAE.

Figures 2.261_As_a1–2.264_As_f2 (As) contain results of calculations for As atom ($Z = 33$) $3d^{10}4s^2 4p^3\uparrow$.

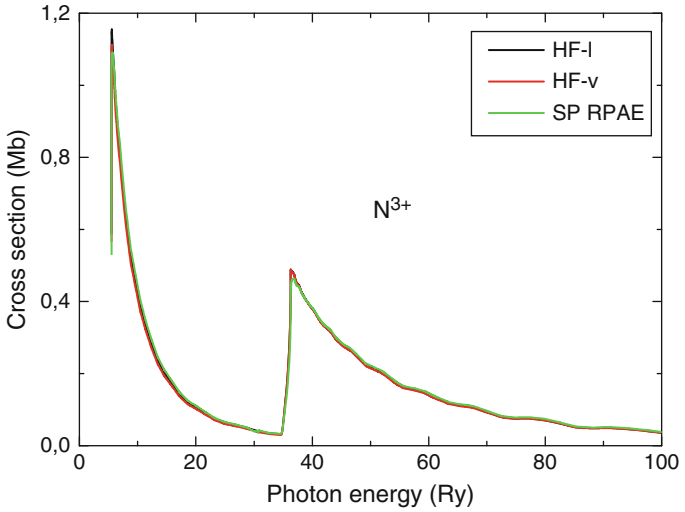

Fig. 2.255_N^{3+}_a1 Total photoionization cross section of N^{3+} ion in HF-l, HF-v, and SP RPAE

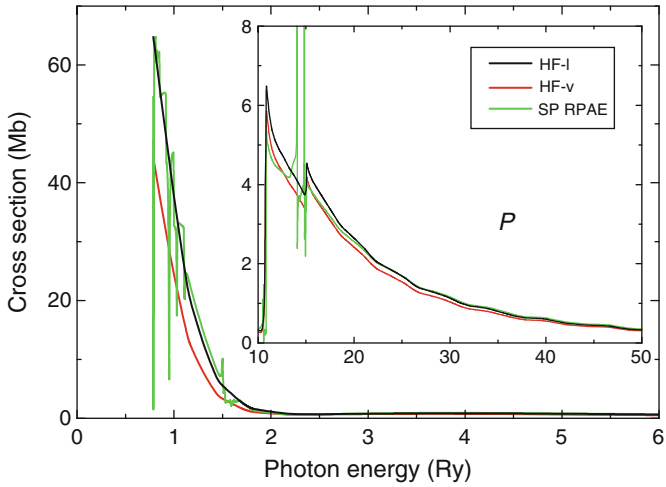

Fig. 2.256_P_a1 Total photoionization cross section of P atom in HF-l, HF-v, and SP RPAE

Figure 2.261_As_a1 presents total photoionization cross-section of As atom in HF-l, HF-v, and SP RPAE. Having a maximum at threshold, the cross-section slops down to zero rather fast and then at 10 Ry forms a broad maximum.

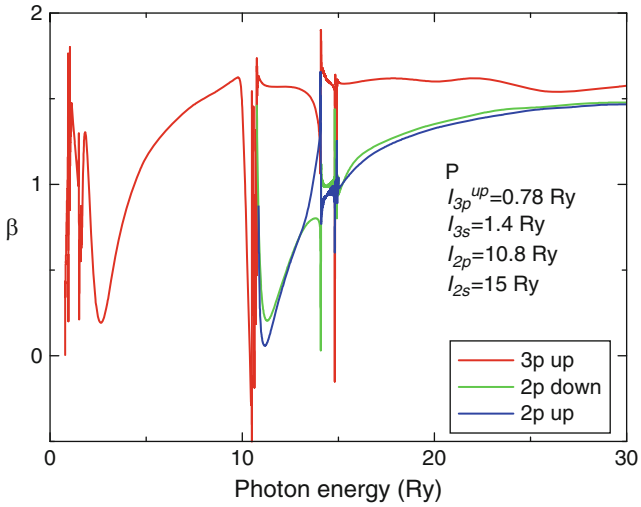

Fig. 2.257_P_d1 Dipole anisotropy parameter of $3p$, $2p$-electrons for P atom in SP RPAE

Figure 2.262_As_d1 presents dipole angular anisotropy parameter of $4p\uparrow$, $3d\uparrow$, and $3d\downarrow$ electrons of As atom in SP RPAE. Qualitatively all curves are similar and that of $\beta_{3d\uparrow}(\omega)$ and $\beta_{3d\downarrow}(\omega)$ are very close.

Figure 2.263_As_f1 contains dipole angular anisotropy parameters $4p$-electrons (a) angular anisotropy parameter $\beta_{4p}(\omega)$; spin polarization parameters (b) $A_{4p}^{3/2}(\omega)$, (c) $\alpha_{4p}^{3/2}(\omega)$, and (d) $\xi_{4p}^{3/2}(\omega)$ in SP RPAE. Note the variation at 30–70 eV.

Figure 2.264_As_f2 presents dipole angular anisotropy parameters of $3d$-electrons: (a) angular anisotropy parameter $\beta_{3d}(\omega)$; spin polarization parameters (b) $A_{3d}(\omega)$, (c) $\alpha_{3d}(\omega)$, and (d) $\xi_{3d}(\omega)$ in SP RPAE. The results of all parameters except $\beta_{3d}(\omega)$ differ significantly for 5/2- and 3/2-electrons.

Figures 2.265_Sb_a1–2.268_Sb_f2 (Sb) contain results of calculations for Sb atom $(Z = 51)\, 4d^{10}\, 5s^2\, 5p^3\uparrow$.

Figure 2.265_Sb_a1 presents total photoionization cross-section of Sb atom in HF-l, HF-v, and SP RPAE. This figure shows the Giant resonance of $4d$-electrons and significant role of correlations. The second maximum at about 20 Ry is remarkable.

Figure 2.266_Sb_d1 shows the dipole angular anisotropy parameter of $5p\uparrow$, $4d\uparrow$, and $4d\downarrow$-electrons of Sb atom in SP RPAE. Oscillating character of β-parameter and qualitative similarity of all curves are seen.

Figure 2.267_Sb_f1 presents dipole angular anisotropy parameters of $5p$-electrons: (a) angular anisotropy parameter $\beta_{5p}(\omega)$; spin polarization parameters (b) $A_{5p}(\omega)$, (c) $\alpha_{5p}(\omega)$, and (d) $\xi_{5p}(\omega)$ in SP RPAE.

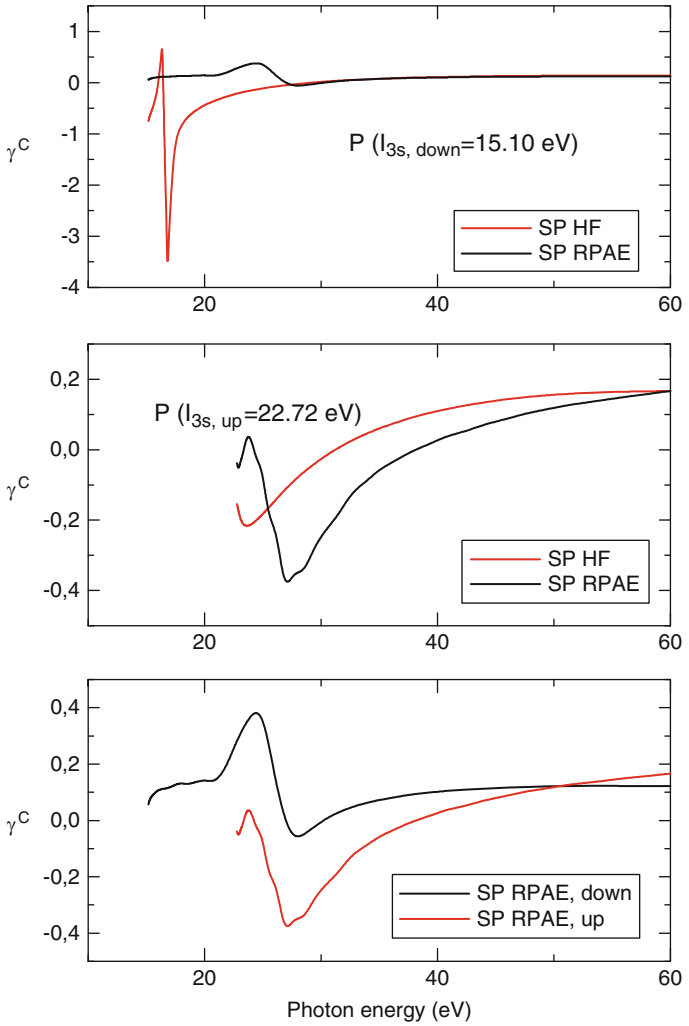

Fig. 2.258_P_e1 Non-dipole anisotropy parameter of 3*s* "down"- and "up"-electrons for P atom in SP HF and SP RPAE

Figure 2.268_Sb_f2 depicts dipole angular parameters of $4d$-electrons: (a) angular anisotropy parameter $\beta_{4d}(\omega)$, spin polarization parameters (b) $A_{4d}(\omega)$, (c) $\alpha_{4d}(\omega)$, and (d) $\xi_{4d}(\omega)$ in SP RPAE. All parameters, except $\beta_{4d}(\omega)$, for 5/2 and 3/2 electron are mirror images of each other.

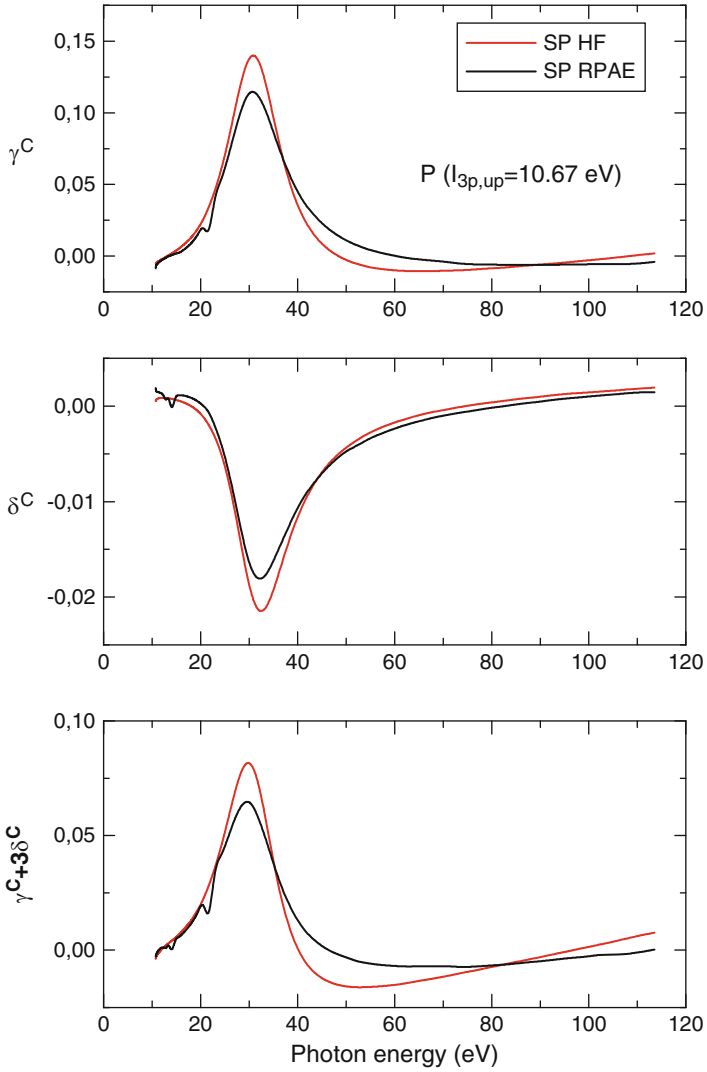

Fig. 2.259_P_e2 Dipole anisotropy parameters and their magic combination of $3p$ "up"-electrons for P atom in HF and SP RPAE

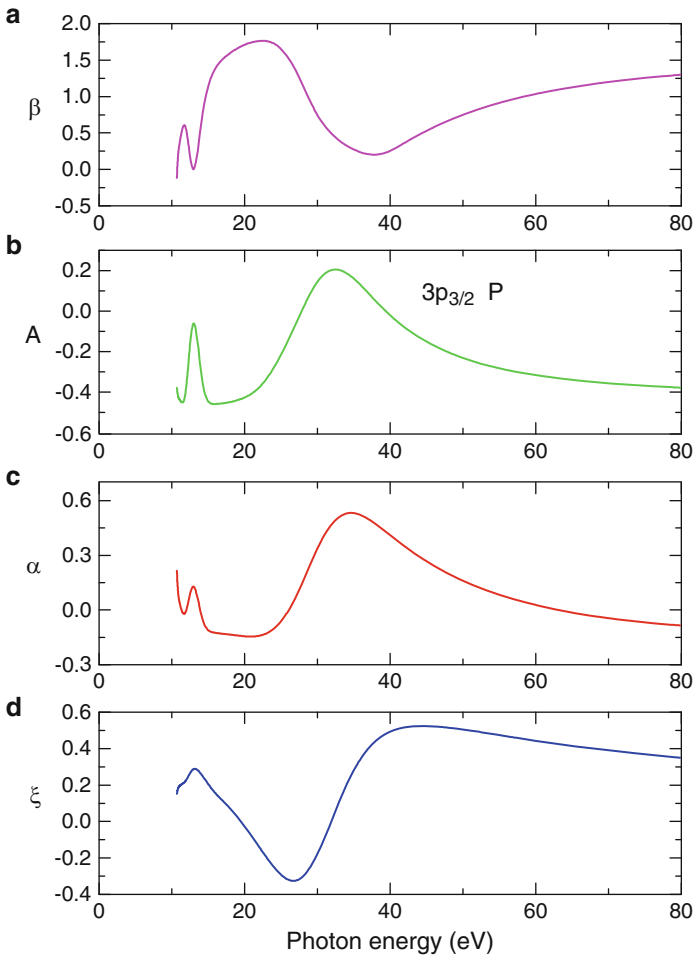

Fig. 2.260_P_f1 Dipole parameters of $3p$-electrons for P atom: (**a**) angular anisotropy $\beta_{3p}(\omega)$; (**b**) spin polarization $A_{3p}^{3/2}(\omega)$, (**c**) $\alpha_{3p}^{3/2}(\omega)$, and (**d**) $\xi_{3p}^{3/2}(\omega)$ in SP RPAE

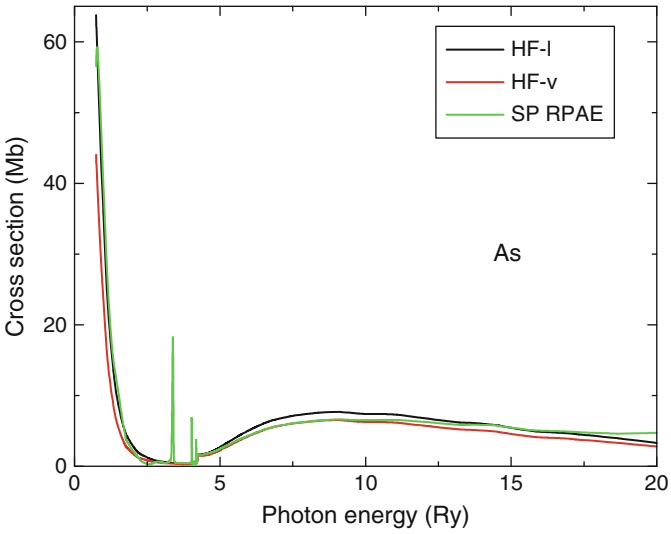

Fig. 2.261_As_a1 Total photoionization cross section of As atom in HF-l, HF-v, and SP RPAE

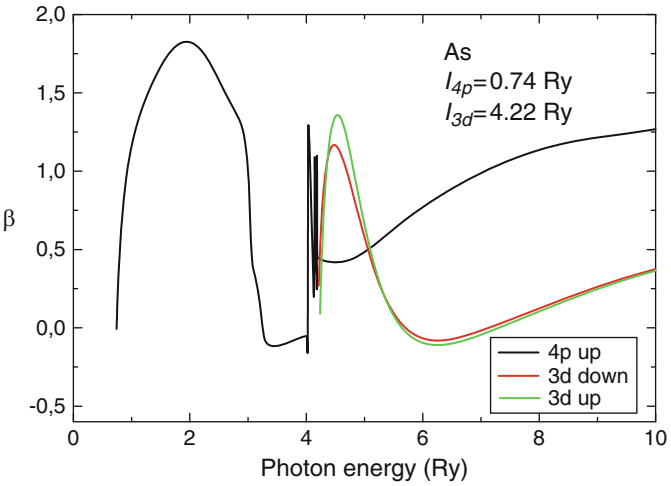

Fig. 2.262_As_d1 Dipole anisotropy parameter of $4p$ "up"-, $3d$ "up" and "down"-electrons for As atom in SP RPAE

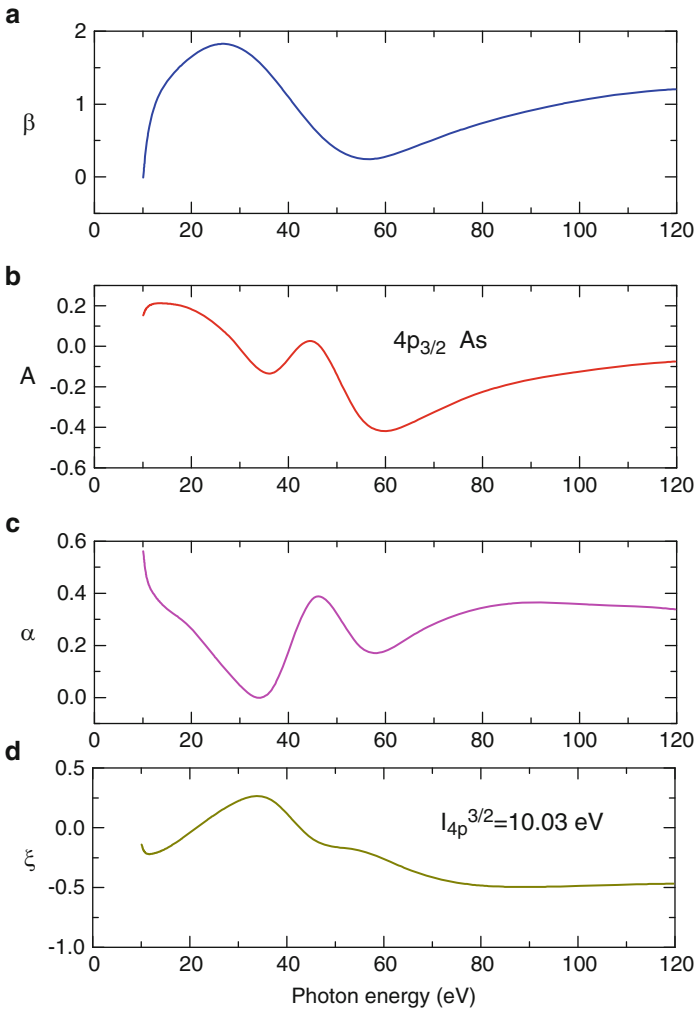

Fig. 2.263_As_f1 Dipole parameters of $4p$-electrons for As atom: (**a**) angular anisotropy $\beta_{4p}(\omega)$, (**b**) spin polarization $A_{4p}^{3/2}(\omega)$, (**c**) $\alpha_{4p}^{3/2}(\omega)$, and (**d**) $\xi_{4p}^{3/2}(\omega)$ in SP RPAE

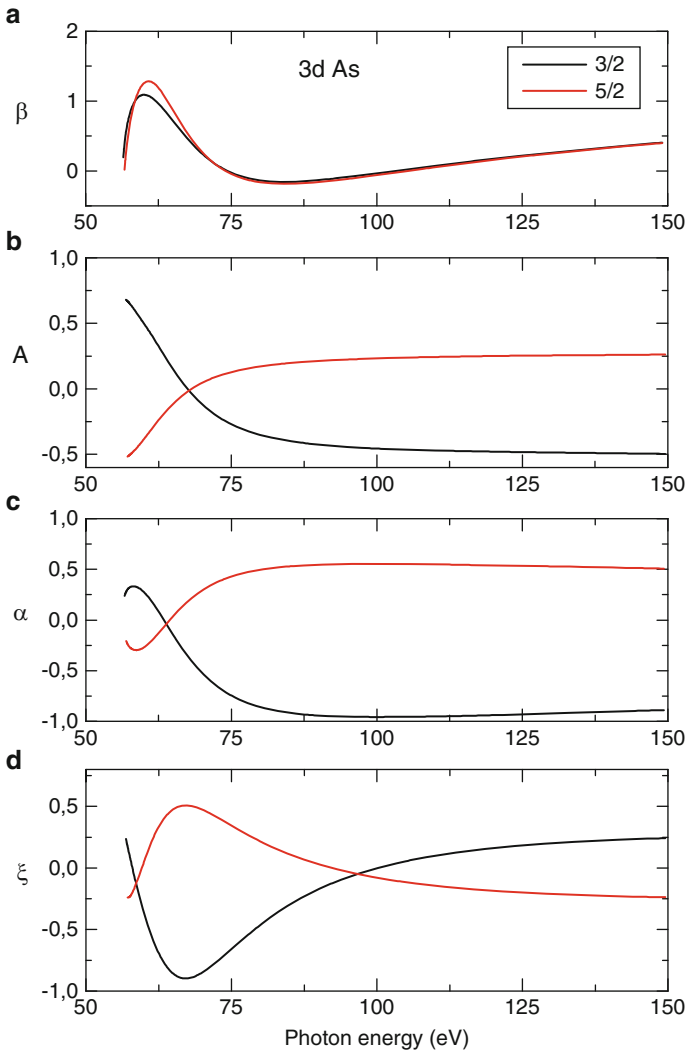

Fig. 2.264_As_f2 Dipole parameters of $3d$-electrons for As atom: (**a**) angular anisotropy $\beta_{3d}(\omega)$, (**b**) spin polarization $A_{3d}(\omega)$, (**c**) $\alpha_{3d}(\omega)$, and (**d**) $\xi_{3d}(\omega)$

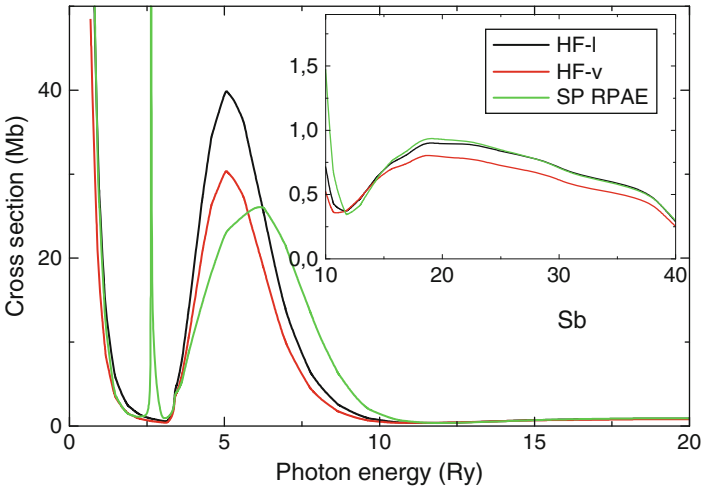

Fig. 2.265_Sb_a1 Total photoionization cross section of Sb atom in HF-l, HF-v, and SP RPAE

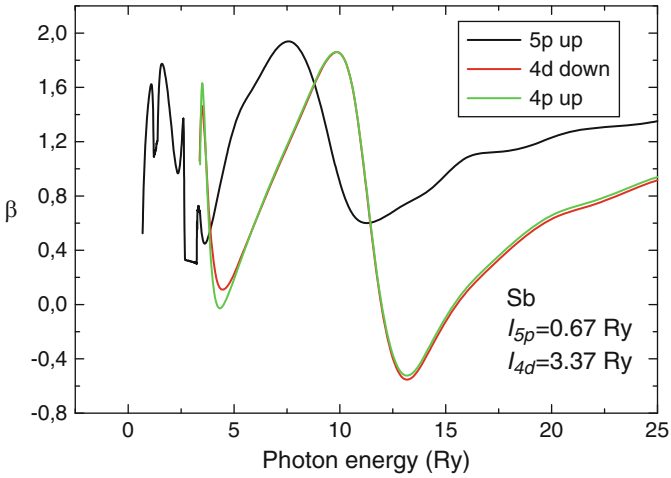

Fig. 2.266_Sb_d1 Dipole anisotropy parameter of $4d$ "up" and "down"- and $5p$ "up"-electrons for Sb atom in SP RPAE

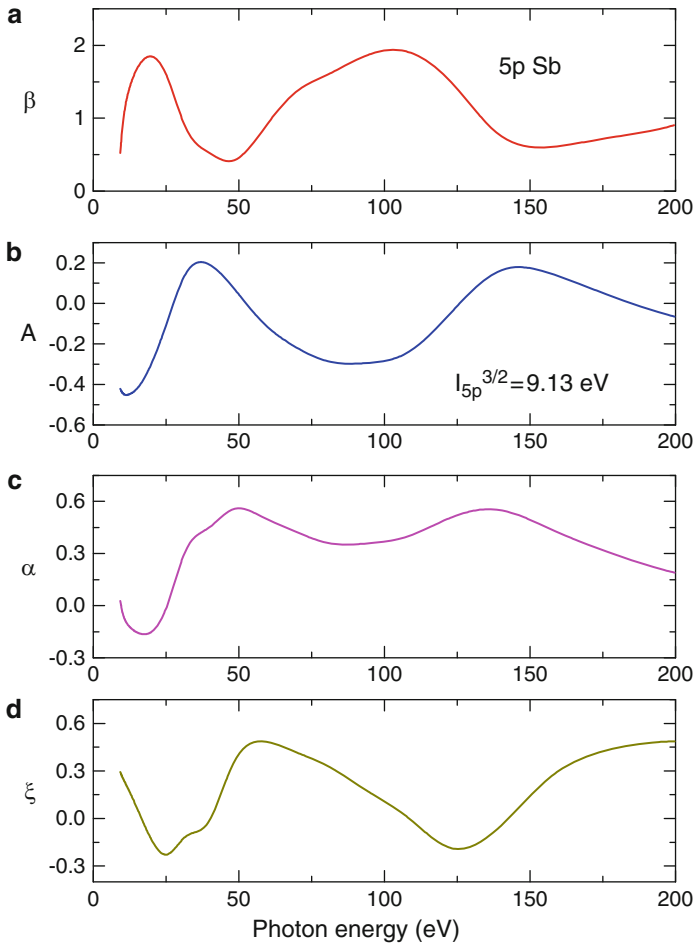

Fig. 2.267_Sb_f1 Dipole parameters of $5p$-electrons for Sb atom: (**a**) angular anisotropy $\beta_{5p}(\omega)$, (**b**) spin polarization $A_{5p}^{3/2}(\omega)$, (**c**) $\alpha_{5p}^{3/2}(\omega)$, and (**d**) $\xi_{5p}^{3/2}(\omega)$

Table 2.6 includes calculated values of oscillator strengths in HF-l, HF-v, $f_{nl-n'l'\uparrow(\downarrow)}^{l,v}$, and $F_{nl-n'l'\uparrow(\downarrow)}^{l,v}$ in RPAE for several lowest discrete levels of excitation and for each considered subshell of atoms, investigated in this section. Respective theoretical transition energies in RPAE $\tilde{\omega}_{nl-n'l'\uparrow(\downarrow)}$ are also given in this table.

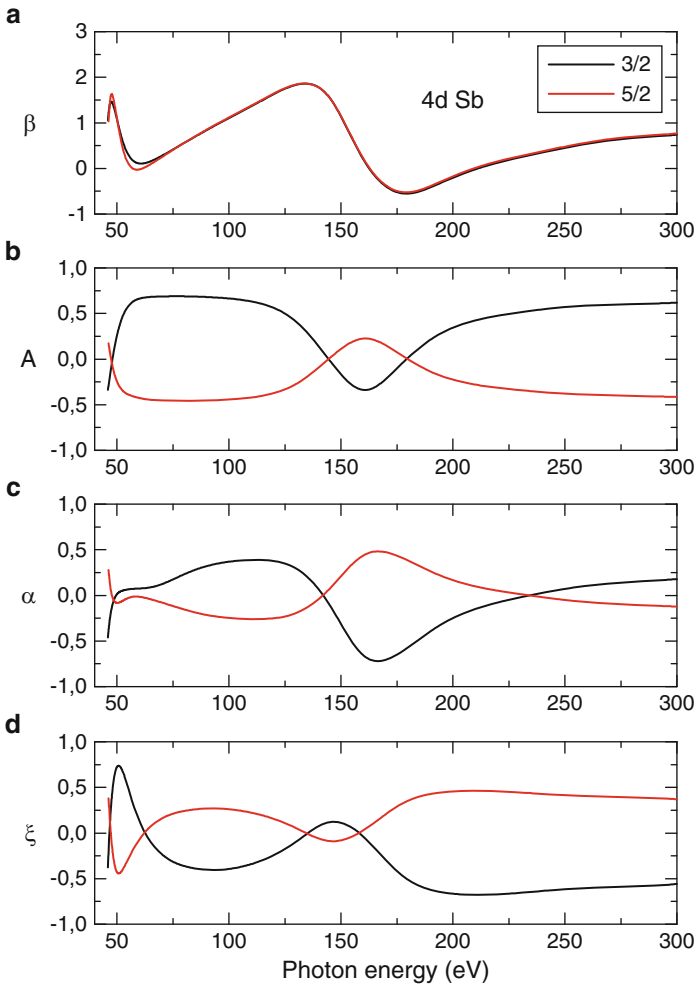

Fig. 2.268_Sb_f2 Dipole parameters of $4d$-electrons for Sb atom: (**a**) angular anisotropy $\beta_{4d}(\omega)$, (**b**) spin polarization $A_{4d}(\omega)$, (**c**) $\alpha_{4d}(\omega)$, and (**d**) $\xi_{4d}(\omega)$

The results for length and velocity forms in RPAE coincide with reasonable accuracy. The role of RPAE corrections for many levels is important. In N the biggest is $2s$–$2p\downarrow$ oscillator strength. For P and Sb the main are the outer subshell transitions $3p$–$4d\uparrow$ and $5p$–$5d\uparrow$. In As the biggest is the main transition $4s$–$4p\downarrow$ from the next to the outer subshell. The oscillator strengths are, in general, decreasing with decrease in principal quantum number of the exited electron.

Table 2.6 Oscillator strengths and transition energies of V group's elements and their ions

Transition	ω (Ry)	HF-l	HF-v	RPAE-l	RPAE-v
N					
$2p$–$3d$ up	1.02803	0.6895E−01	0.5616E−01	0.6757E−01	0.6757E−01
$2p$–$4d$ up	1.07818	0.3492E−01	0.2831E−01	0.3338E−01	0.3338E−01
$2p$–$5d$ up	1.10120	0.1903E−01	0.1540E−01	0.1994E−01	0.1993E−01
$2p$–$3s$ up	0.83530	0.1197E+00	0.1141E+00	0.9126E−01	0.8926E−01
$2p$–$4s$ up	1.01651	0.1933E−01	0.1838E−01	0.2812E−01	0.2769E−01
$2p$–$5s$ up	1.07370	0.6853E−02	0.6513E−02	0.1101E−01	0.1085E−01
$2s$–$2p$ do	0.71808	0.5764E+00	0.5999E+00	0.2879E+00	0.2885E+00
$2s$–$3p$ do	1.27272	0.2822E−03	0.1784E−03	0.1363E−01	0.1358E−01
$2s$–$4p$ do	1.36416	0.4050E−03	0.3309E−03	0.4498E−02	0.4451E−02
$2s$–$3p$ up	2.12015	0.8437E−02	0.9395E−02	0.2428E−02	0.1804E−02
$2s$–$4p$ up	2.23015	0.2941E−02	0.3077E−02	0.6094E−03	0.4739E−03
$2s$–$5p$ up	2.27031	0.1341E−02	0.1380E−02	0.2772E−03	0.2180E−03
$1s$–$2p$ do	29.62428	0.2159E+00	0.2186E+00	0.1801E+00	0.1794E+00
$1s$–$3p$ do	30.95215	0.6224E−02	0.6270E−02	0.7233E−04	0.6234E−04
$1s$–$4p$ do	31.06670	0.2035E−02	0.2049E−02	0.6086E−02	0.6116E−02
$1s$–$3p$ up	31.01621	0.1331E+00	0.1286E+00	0.1269E+00	0.1287E+00
$1s$–$4p$ up	31.22496	0.1407E−01	0.1365E−01	0.1307E−01	0.1330E−01
$1s$–$5p$ up	31.27763	0.5251E−02	0.5096E−02	0.4900E−02	0.4985E−02
P					
$3p$–$4d$ up	0.66853	0.6192E+00	0.4308E+00	0.4955E+00	0.4879E+00
$3p$–$5d$ up	0.71919	0.2737E+00	0.1871E+00	0.2662E+00	0.2617E+00
$3p$–$6d$ up	0.74289	0.1376E+00	0.9336E−01	0.1561E+00	0.1534E+00
$3p$–$4s$ up	0.52545	0.2473E+00	0.2383E+00	0.3087E+00	0.3011E+00
$3p$–$5s$ up	0.67376	0.3731E−01	0.3589E−01	0.1626E−01	0.1579E−01
$3p$–$6s$ up	0.72241	0.1332E−01	0.1281E−01	0.2665E−02	0.2586E−02
$3s$–$3p$ do	0.46064	0.8589E+00	0.8614E+00	0.3257E−01	0.3677E−01
$3s$–$4p$ up	0.95542	0.2981E−02	0.3019E−02	0.7791E−01	0.7591E−01
$3s$–$5p$ up	1.03319	0.4273E−03	0.4363E−03	0.2261E−01	0.1908E−01
$3s$–$4p$ up	1.50148	0.3361E−04	0.1299E−04	0.1051E−01	0.8093E−02
$3s$–$5p$ up	1.58867	0.5191E−04	0.8715E−04	0.1746E−02	0.1320E−02
$3s$–$6p$ up	1.62233	0.4894E−04	0.6091E−04	0.3651E−03	0.2871E−03
$2p$–$3d$ do	10.63305	0.2131E−01	0.1891E−01	0.1869E−01	0.1870E−01
$2p$–$4d$ do	10.68764	0.1402E−01	0.1247E−01	0.1052E−01	0.1052E−01
$2p$–$5d$ do	10.71422	0.7943E−02	0.7071E−02	0.4655E−02	0.4641E−02
$2p$–$4s$ do	10.47066	0.1105E−01	0.9915E−02	0.8132E−02	0.7882E−02
$2p$–$5s$ do	10.64309	0.2081E−02	0.1871E−02	0.2161E−02	0.2185E−02
$2p$–$6s$ do	10.69532	0.8007E−03	0.7203E−03	0.7562E−03	0.7591E−03
$2p$–$4d$ up	10.74779	0.1531E−01	0.1395E−01	0.9030E−02	0.9066E−02
$2p$–$5d$ up	10.78798	0.6580E−02	0.5999E−02	0.4140E−02	0.4154E−02
$2p$–$6d$ up	10.80703	0.3456E−02	0.3152E−02	0.2328E−02	0.2338E−02
$2p$–$4s$ up	10.50636	0.1369E−01	0.1434E−01	0.2803E−01	0.3038E−01
$2p$–$5s$ up	10.71828	0.1922E−02	0.2012E−02	0.3960E−02	0.4296E−02
$2p$–$6s$ up	10.77562	0.7150E−03	0.7484E−03	0.1115E−02	0.1223E−02
$2s$–$3p$ do	14.06547	0.6810E−01	0.6802E−01	0.4219E−01	0.4163E−01
$2s$–$4p$ do	14.82937	0.3222E−02	0.3167E−02	0.5359E−02	0.5273E−02

Table 2.6 (Continued)

2*s*–5*p* do	14.91522	0.1124E−02	0.1104E−02	0.7110E−03	0.7022E−03
2*s*–4*p* up	14.81307	0.4099E−01	0.3899E−01	0.2768E−01	0.2702E−01
2*s*–5*p* up	14.94741	0.6215E−02	0.5931E−02	0.5467E−02	0.5353E−02
2*s*–6*p* up	14.98829	0.2478E−02	0.2367E−02	0.2096E−02	0.2053E−02
As					
4*p*–5*s* up	0.48600	0.2860E+00	0.2798E+00	0.3416E+00	0.3398E+00
4*p*–6*s* up	0.63171	0.4191E−01	0.4093E−01	0.4131E−01	0.4061E−01
4*p*–7*s* up	0.67935	0.1494E−01	0.1459E−01	0.7884E−02	0.7753E−02
4*p*–4*d* up	0.62791	0.6675E+00	0.4661E+00	0.4856E+00	0.4816E+00
4*p*–5*d* up	0.67650	0.2769E+00	0.1903E+00	0.2794E+00	0.2766E+00
4*p*–6*d* up	0.69960	0.1365E+00	0.9313E−01	0.1691E+00	0.1674E+00
4*s*–4*p* do	0.62791	0.9558E+00	0.9488E+00	0.4852E+00	0.4812E+00
4*s*–5*p* do	0.96061	0.7602E−02	0.7472E−02	0.4563E−01	0.4077E−01
4*s*–6*p* do	1.03487	0.1606E−02	0.1573E−02	0.8110E−02	0.9193E−02
4*s*–5*p* up	1.46549	0.1476E−02	0.7867E−03	0.2092E−01	0.1783E−01
4*s*–6*p* up	1.54937	0.1008E−03	0.5666E−04	0.3975E−02	0.3466E−02
4*s*–7*p* up	1.58204	0.1893E−04	0.1108E−04	0.1363E−02	0.1263E−02
3*d*–4*p* do	3.37554	0.2603E+00	0.1600E+00	0.2634E+00	0.1584E+00
3*d*–5*p* do	4.05169	0.8974E−02	0.7515E−02	0.1733E−01	0.1502E−01
3*d*–6*p* do	4.13320	0.3057E−02	0.2484E−02	0.2096E−02	0.1682E−02
3*d*–4*f* do	4.15256	0.1565E−04	0.1312E−04	0.1611E−04	0.1555E−04
3*d*–5*f* do	4.17512	0.1341E−04	0.1125E−04	0.1201E−04	0.1165E−04
3*d*–6*f* do	4.18737	0.9724E−05	0.8165E−05	0.9498E−05	0.9187E−05
3*d*–5*p* up	4.03044	0.4017E−01	0.3383E−01	0.3123E−01	0.2889E−01
3*d*–6*p* up	4.14437	0.7282E−02	0.6176E−02	0.8490E−02	0.7744E−02
3*d*–7*p* up	4.18196	0.2943E−02	0.2501E−02	0.2974E−02	0.2734E−02
3*d*–4*f* up	4.17223	0.4435E−04	0.2666E−04	0.2906E−04	0.2755E−04
3*d*–5*f* up	4.19475	0.3790E−04	0.2305E−04	0.2522E−04	0.2396E−04
3*d*–6*f* up	4.20701	0.2745E−04	0.1679E−04	0.1797E−04	0.1717E−04
Sb					
5*p*–6*s* up	0.4423	0.3218E+00	0.2673E+00	0.4182E+00	0.3639E+00
5*p*–7*s* up	0.5700	0.5221E−01	0.4209E−01	0.6950E−01	0.5887E−01
5*p*–8*s* up	0.6135	0.1922E−01	0.1536E−01	0.1822E−01	0.1488E−01
5*p*–5*d* up	0.5533	0.1081E+01	0.7175E+00	0.8775E+00	0.8743E+00
5*p*–6*d* up	0.6050	0.3928E+00	0.2554E+00	0.4120E+00	0.4081E+00
5*p*–7*d* up	0.6292	0.1827E+00	0.1178E+00	0.2147E+00	0.2128E+00
5*s*–5*p* do	0.3844	0.1037E+01	0.1018E+01	0.1296E−01	0.2100E−01
5*s*–6*p* do	0.7955	0.7804E−02	0.7441E−02	0.3969E−01	0.3629E−01
5*s*–7*p* do	0.8640	0.1634E−02	0.1541E−02	0.6907E−02	0.7764E−02
5*s*–6*p* up	1.2342	0.1016E−02	0.6097E−03	0.1588E−01	0.1176E−01
5*s*–7*p* up	1.3111	0.4333E−04	0.3604E−04	0.3294E−02	0.2468E−02
5*s*–8*p* up	1.3417	0.3978E−05	0.5419E−05	0.7581E−03	0.7037E−03
4*d*–5*p* do	2.6379	0.4176E+00	0.4210E+00	0.3861E+00	0.3946E+00
4*d*–6*p* do	3.2106	0.1739E−01	0.1709E−01	0.1254E−01	0.1271E−01
4*d*–7*p* do	3.2864	0.6029E−02	0.5911E−02	0.4946E−02	0.5008E−02
4*d*–4*f* do	3.3015	0.1831E−03	0.1424E−03	0.1234E−03	0.1233E−03
4*d*–5*f* do	3.3241	0.1585E−03	0.1233E−03	0.1173E−03	0.1177E−03

Table 2.6 (Continued)

$4d$–$6f$ do	3.3364	0.1157E−03	0.9009E−04	0.8486E−04	0.8547E−04
$4d$–$6p$ up	3.2061	0.5955E−01	0.6005E−01	0.1250E−01	0.1500E−01
$4d$–$7p$ up	3.3019	0.1244E−01	0.1266E−01	0.1283E−01	0.1415E−01
$4d$–$8p$ up	3.3361	0.5166E−02	0.5269E−02	0.4416E−02	0.4922E−02
$4d$–$4f$ up	3.3232	0.5709E−03	0.3535E−03	0.3336E−03	0.3318E−03
$4d$–$5f$ up	3.3458	0.5009E−03	0.3133E−03	0.2883E−03	0.2867E−03
$4d$-$6f$ up	3.3582	0.3675E−03	0.2310E−03	0.2097E−03	0.2095E−03

2.8 Atoms and Ions of VI Group Elements

In this section we present our results for outer and intermediate subshells of ions and some atoms of VI group elements. Here we have concentrated basically on the ions having all filled or half-filled subshell, namely O^+ $(Z=8)$ $1s^22s^22p^3\uparrow$; Cr $(Z=24)$ $2p^63s^23p^63d^5\uparrow 4s\uparrow$; Cr* $(Z=24)$ $2p^63s^23p^63^5\uparrow 4s\downarrow$; Cr^+ $(Z=24)$ $2p^63s^23p^63d^5\uparrow$; Cr^- $(Z=24)$ $2p^63s^23p^63d^5\uparrow 4s^2\uparrow$; Mo $(Z=42)$ $3d^{10}4s^24p^64d^5\uparrow 5s\uparrow$; Mo* $(Z=42)$ $3d^{10}$ $4s^24p^64d^5\uparrow 5s\downarrow$. Formulas used to obtain the data and notations in figures are the same, as for noble gases, which are included in Sect. 2.1. Here $\uparrow$ denotes "up" electrons in SP RPAE (see Sect. 1.10).

Figures 2.269_O^+_a1 and 2.270_O^+_d1 (O^+) contain the results of calculations for O^+ ion: $(Z=8)1s^22s^2\,2p^3\uparrow$.

Figure 2.269_O^+_a1 presents total photoionization cross-sections in HF-l, HF-v, and SP RPAE. The role of correlations is small. Cross-section are large at thresholds and then rapidly decrease with increase in ω.

Figure 2.270_O^+_d1 shows the dipole angular anisotropy parameter of $2p$-electrons in SP RPAE. The β-parameter reaches maximum after threshold very soon and then decreases steadily.

Figures 2.271_Cr_a1–2.276_Cr_f2 (Cr) contain results of calculations for Cr atom: $(Z=24)\,2p^63s^23p^63d^5\uparrow 4s\uparrow$

Figure 2.271_Cr_a1 displays total photoionization cross-section of Cr atom in HF-l, HF-v, and SP RPAE. At $\omega\approx 3.5$ Ry it is seen that as well as in Mn Giant autoionizing resonance appear—a maximum arising owing to strong interaction of discrete transition $3p\downarrow$–$3d\downarrow$ with the continuous spectrum $3d\uparrow$–$\varepsilon f\uparrow$ (see and compare [2.60]).

Figure 2.272_Cr_d1 depicts dipole angular anisotropy parameter of $3d\uparrow$, $3p-\uparrow$-, and $\downarrow$-electrons for Cr atom in SP RPAE. Note qualitative similarity of curves for $3p$ "up"- and "down"-electrons (see [2.61]).

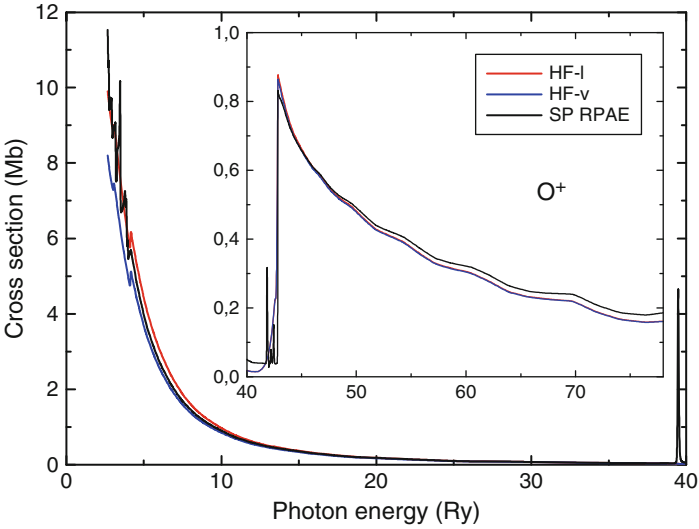

Fig. 2.269_O$^+$_a1 Total photoionization cross section of O^+ ion in HF-l, HF-v, and SP RPAE

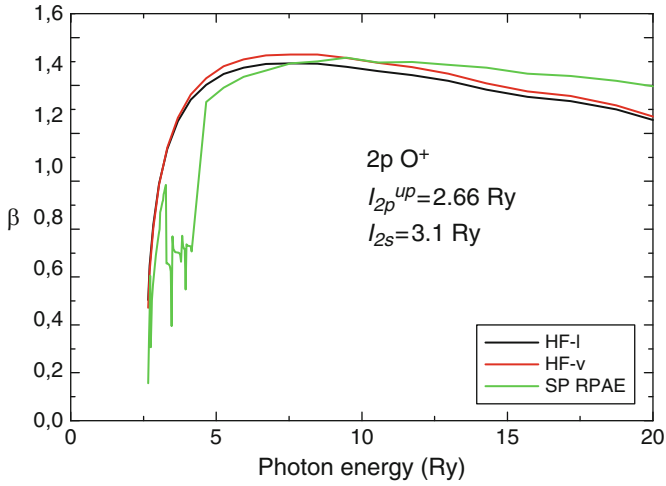

Fig. 2.270_O$^+$_d1 Dipole angular anisotropy parameter of $2p$-electrons for O^+ ion in SP RPAE

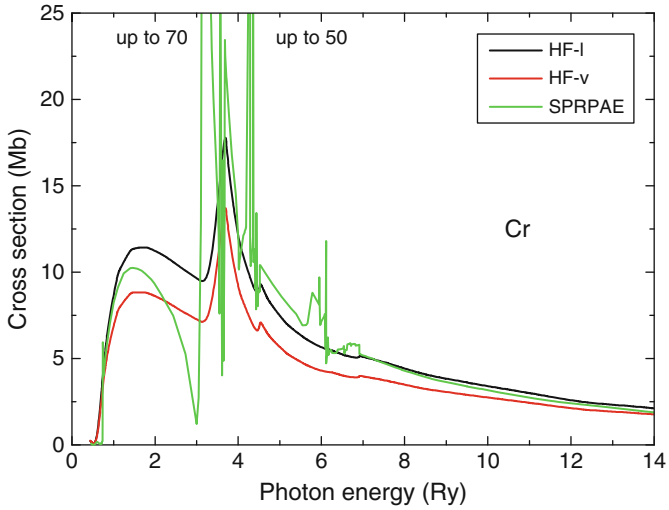

Fig. 2.271_Cr_a1 Total photoionization cross section of Cr atom in SP HF-l, SP HF-v, and SP RPAE (see [2.60–2.62])

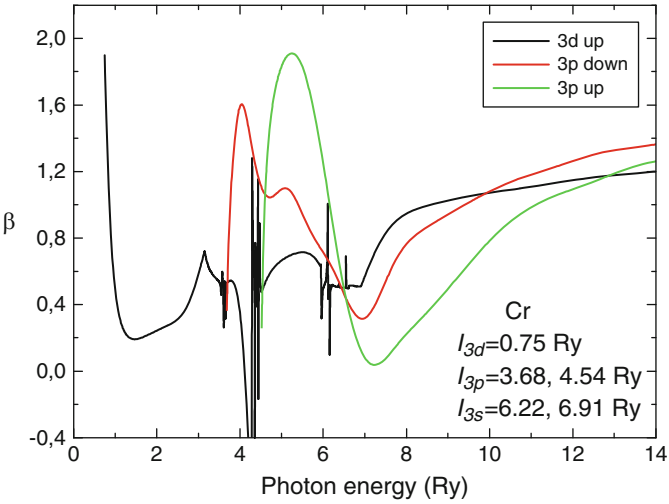

Fig. 2.272_Cr_d1 Dipole angular anisotropy parameter of $3d$ "up"- and $3p$ "up" and "down"-electrons for Cr atom in SP RPAE (see [2.60])

Figure 2.273_CrCr*_e1 compares non-dipole angular anisotropy parameters γ^{C} of $4s$ "up"-electrons for Cr atom and $4s$ "down"-electrons for excited Cr* atom (configuration $2p^6 3s^2 3p^6\, 3d^5 \uparrow 4s \downarrow$) in HF and SP RPAE. The difference between

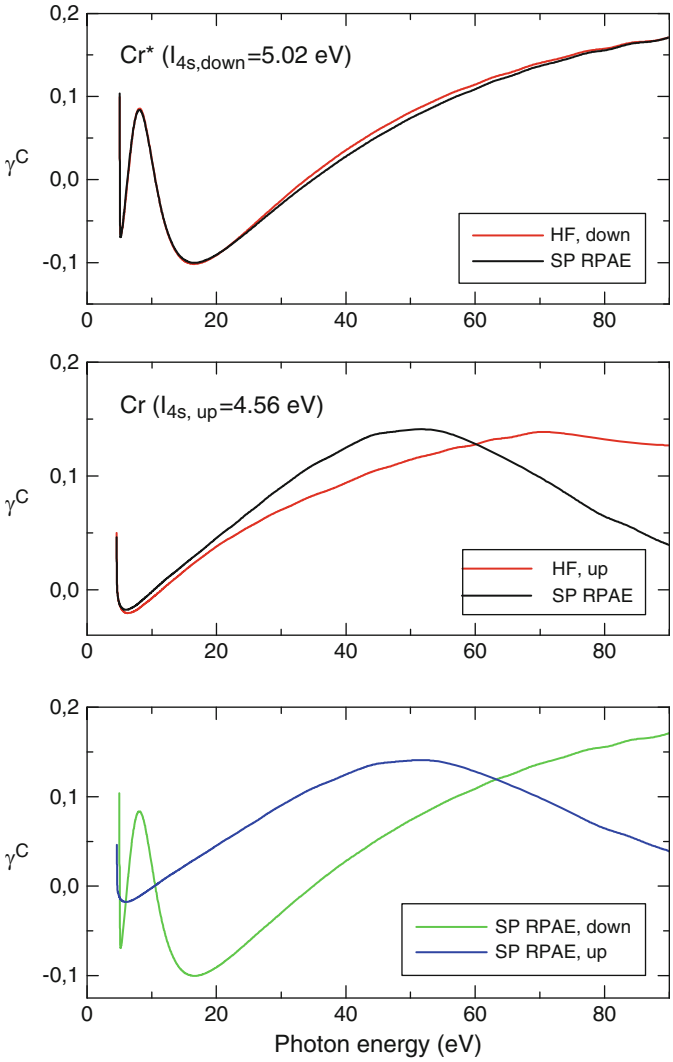

Fig. 2.273_CrCr*_e1 Non-dipole anisotropy parameters of 4*s* "up"-electrons for Cr atom and 4*s* "down"-electrons for Cr* atom in excited state (see [2.61, 2.62])

curves is rather big. The RPAE correlations are essential only for "up"-electrons. Parameter for "down"-electrons has an extra oscillation near the threshold.

Figure 2.274_Cr_e2 presents non-dipole angular anisotropy parameters γ^{C} and δ^{C} and their magic combination $(\gamma^{C} + 3\delta^{C})$ of $3d$-electrons in SP RPAE (see and compare [2.62]).

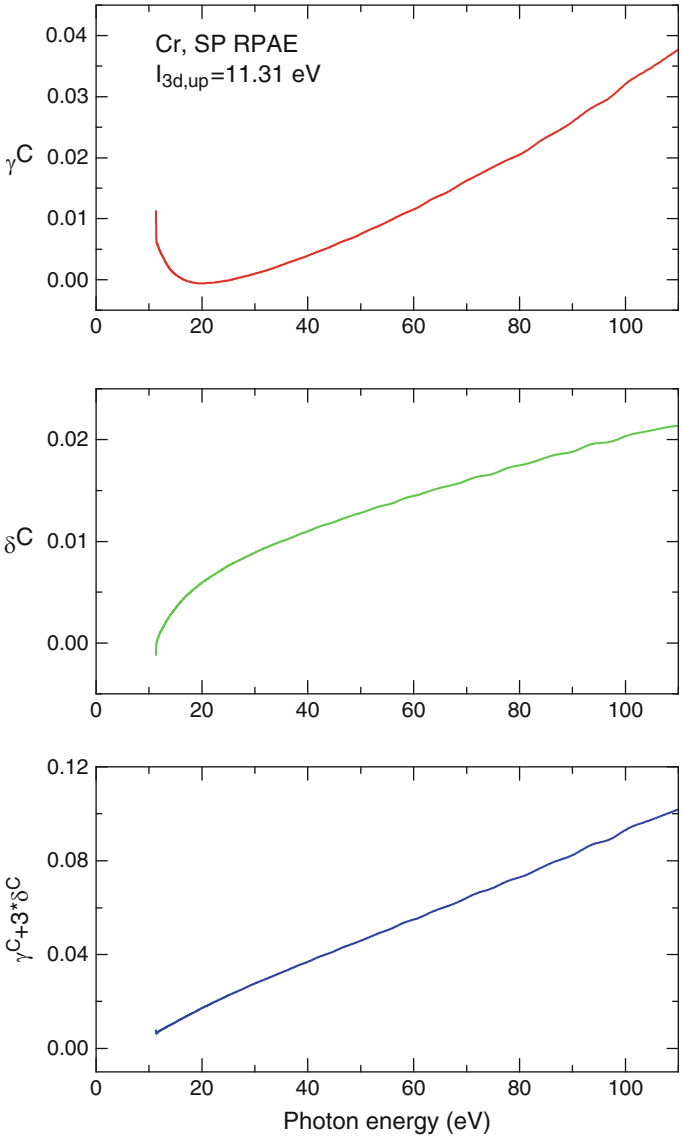

Fig. 2.274_Cr_e2 Non-dipole anisotropy parameters and their magic combination of $3d$-electrons Cr atom in SP RPAE (see and compare [2.60])

Figure 2.275_Cr_f1 demonstrates the dipole parameters of $3p$ "up"- and $3p$ "down"-electrons of Cr atom: (a) angular anisotropy parameter $\beta_{3p}(\omega)$, spin polarization parameters (b) $A_{3p}(\omega)$, (c) $\alpha_{3p}(\omega)$, and (d) $\xi_{3p}(\omega)$.

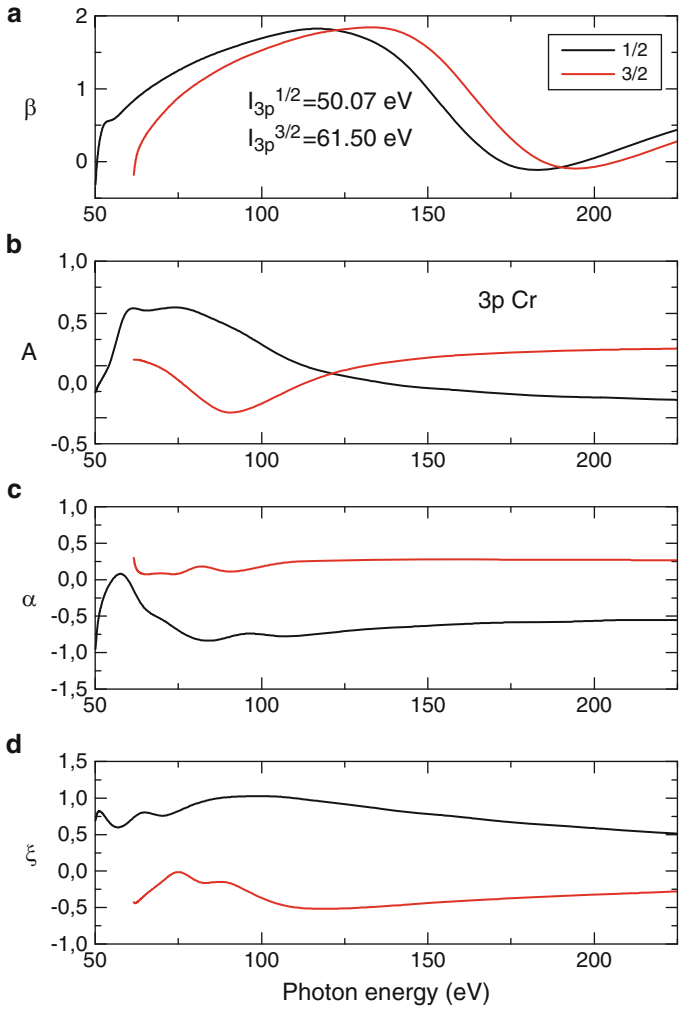

Fig. 2.275_Cr_f1 Dipole anisotropy parameter of $3p$ "up" and "down"-electrons for Cr atom: (**a**) angular anisotropy $\beta_{3p}(\omega)$, spin polarization (**b**) $A_{3p}(\omega)$, (**c**) $\alpha_{3p}(\omega)$, and (**d**) $\xi_{3p}(\omega)$

Figure 2.276_Cr_f2 shows the dipole angular anisotropy parameters of $3d$-electrons of Cr atom and Cr*: (a) angular anisotropy $\beta_{3d}(\omega)$; spin polarization (b) $A_{3d}^{5/2}(\omega)$, (c) $\alpha_{3d}^{5/2}(\omega)$, (d) $\xi_{3d}^{5/2}(\omega)$ (see and compare [2.61, 2.62]). The influence of considered excitation is small.

Figures 2.277_Cr*_a1 and 2.278_Cr*_d1 (Cr*) contain results of calculations for excited Cr* atom: ($Z = 24$) $2p^6, 3s^2, 3p^6, 3d^5 \uparrow 4s \downarrow$.

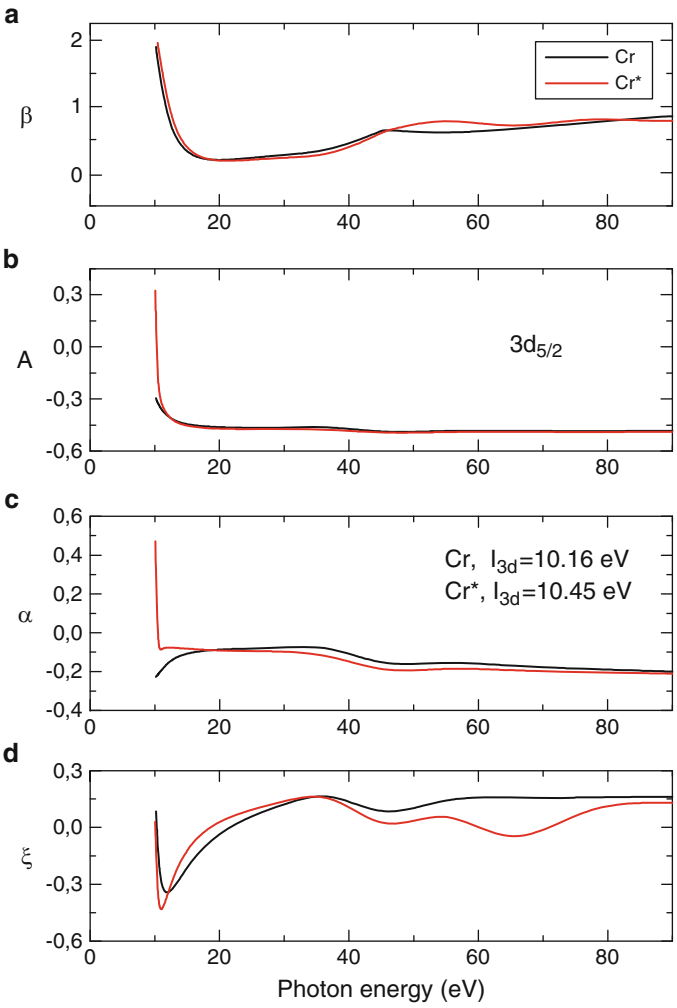

Fig. 2.276_Cr_f2 Dipole parameter of $3d$-electrons for Cr atom and Cr*: (**a**) angular anisotropy $\beta_{3d}(\omega)$, spin polarization (**b**) $A_{dp}^{5/2}(\omega)$, (**c**) $\alpha_{3d}^{5/2}(\omega)$, and (**d**)$\xi_{3d}^{5/2}(\omega)$ (see and compare [2.60–2.62])

Figure 2.277_Cr*_a1 depicts the total photoionization cross-section of Cr excited atom in SP HF-l, SP HF-v, and SP RPAE (see [2.62]). Note the strong maximum that reflects the contribution of the $3p$-electrons discrete excitations.

Figure 2.278_Cr*_d1 displays the dipole angular anisotropy parameter of $3d$ "up"- and $3p$ "up" and "down"-electrons for Cr* excited atom in SP RPAE (see [2.62]).

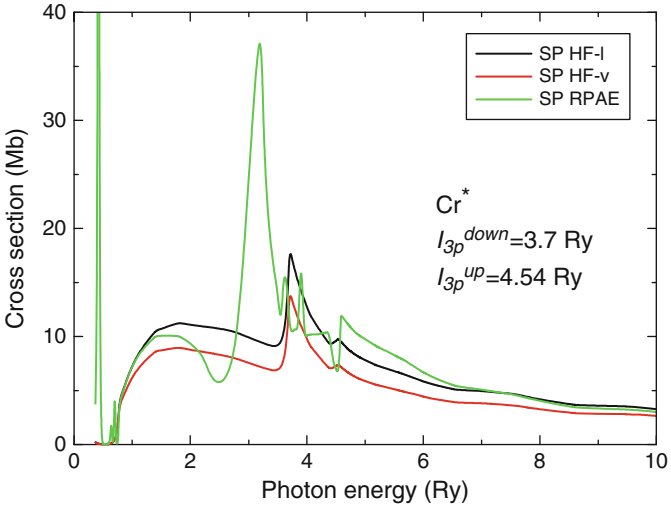

Fig. 2.277_Cr*_a1 Total photoionization cross section of Cr excited atom in SP HF-l, SP HF-v, and SP RPAE (see [2.61])

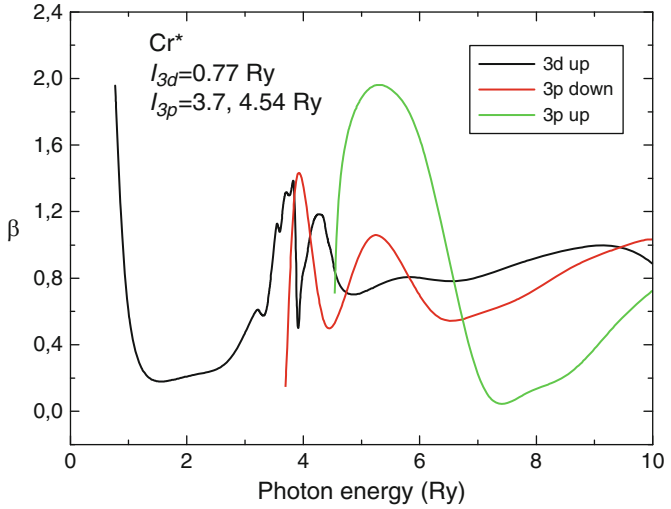

Fig. 2.278_Cr*_d1 Dipole angular anisotropy parameter of $3d$ "up"- and $3p$ "up" and "down"-electrons for Cr* excited atom in SP RPAE (see [2.61])

Figures 2.279_Cr^+_a1 and 2.280_Cr^+_d1 (Cr^+) contain results of calculations for Cr^+ ion: $(Z = 24)\, 2p^6, 3s^2, 3p^6, 3d^5 \uparrow$.

Figure 2.279_Cr^+_a1 depicts total photoionization cross-section of ion Cr^+ in SP RPAE. A strong maximum connected with excitation of $3p^3 \downarrow$ electrons is seen.

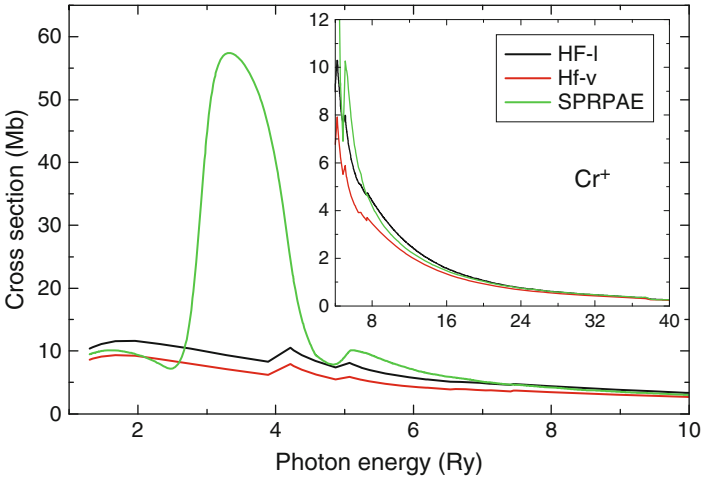

Fig. 2.279_Cr$^+$_a1 Total photoionization cross section of Cr^+ ion in HF-l, HF-v, and SP RPAE

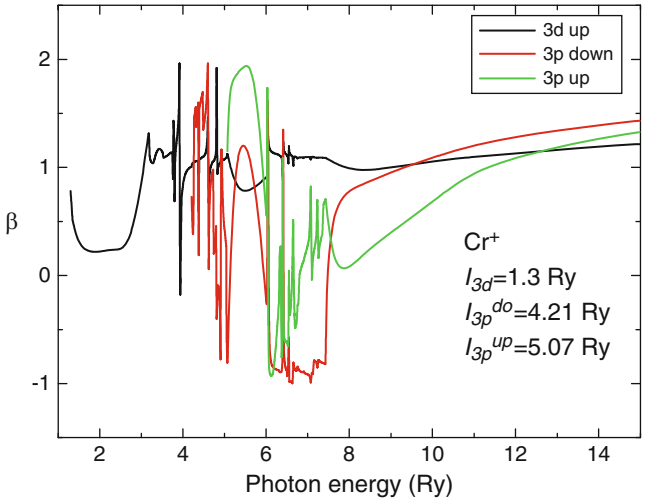

Fig. 2.280_Cr$^+$_d1 Dipole anisotropy parameter of $3d$ "up"- and $3p$ "up"-, "down"-electrons for Cr^+ ion

Figure 2.280_Cr$^+$_d1 presents dipole angular anisotropy parameter of $3d$ "up"-, $3p$ "up"-, and "down"-electrons for Cr^+ ion. The variations of parameters near thresholds are very strong (see [2.62]).

Figures 2.281_Cr$^-$_a1–2.283_Cr$^-$_d1 (Cr^-) contain results of calculations for Cr^- ion: $(Z = 24)\, 2p^6, 3s^2, 3p^6, 3d^5 \uparrow 4s^2$.

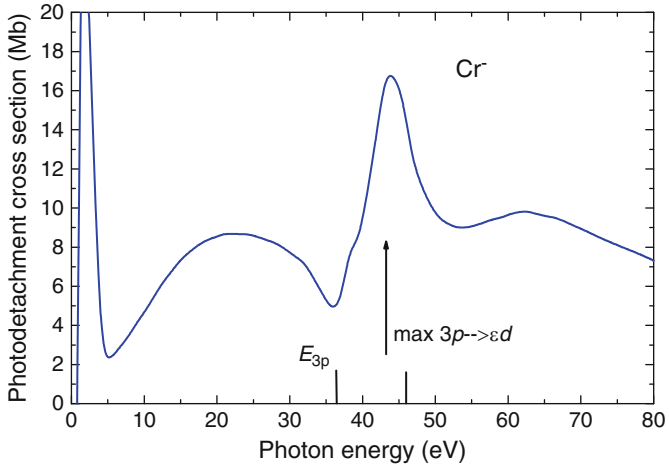

Fig. 2.281_Cr$^-$_a1 Total photodetachment cross section in GRPAE with account of polarization interaction between the photoelectron and the residual ion [2.62]

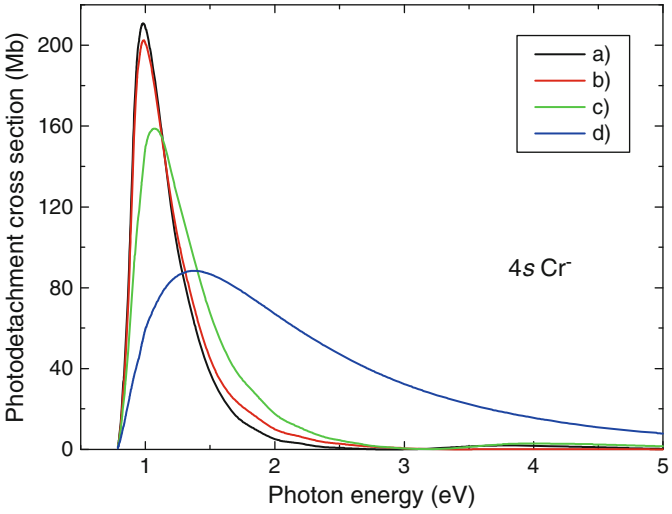

Fig. 2.282_Cr$^-$_b1 Polarization effects in the photo-detachment cross section of Cr^- (see [2.62])

Figure 2.281_Cr$^-$_a1 presents photodetachment cross-section of Cr^- ion near the threshold of inner shell $3p$. The calculations are performed in GRPAE with account of polarization interaction between the photoelectron and the residual ion [2.63].

Figure 2.282_Cr$^-$_b1 shows the cross-section of photodetachment cross-section of $4s$ electrons of Cr^-. Just as in Fig. 2.281_Cr$^-$_a1 the calculations are performed

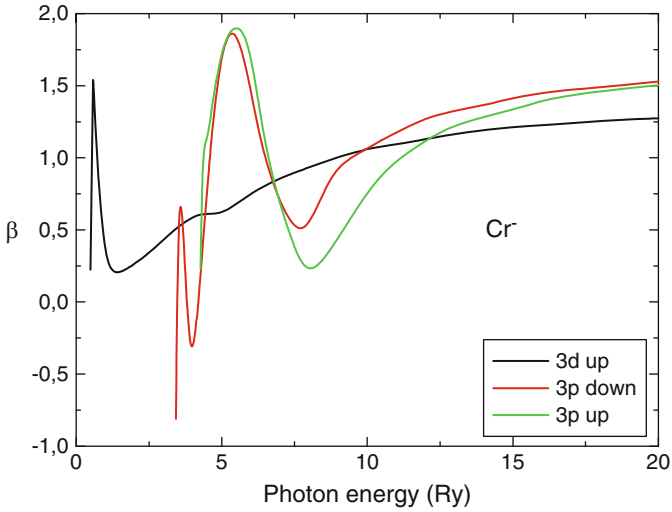

Fig. 2.283_Cr⁻_d1 Dipole anisotropy parameter of $3d$ "up"- and $3p$ "up"- "down"-electrons for Cr^- ion

in GRPAE with account of polarization interaction between the photoelectron and the residual ion [2.63]. Calculations are carried out using combined method that takes into account: (a) polarization in the ground state of $4s\downarrow$ electron; (b) RPAE combined with account of polarization potential, acting upon the outgoing photoelectron, (c) with operators l and v, respectively, and (d) the same with account for only several transitions from $4s\uparrow$ level.

Figure 2.283_Cr⁻_d1 depicts dipole angular anisotropy parameter of $3d\uparrow$- and $3p\uparrow\downarrow$ electrons for Cr^- ion. Parameter $\beta_{3d\uparrow}$ has a single narrow near threshold maximum. Parameter $\beta_{3p\uparrow}$ has a shape similar to $\beta_{3d\uparrow}$ energy dependence. The structure of $\beta_{3p\downarrow}$ is more complex, with a narrow maximum near threshold.

Figures 2.284_Mo_a1–2.287_MoMo*_f2 (Mo) contain results of calculations for Mo atom: $(Z = 42)\ 3d^{10}, 4s^2, 4p^6, 4d^5\uparrow, 5s\uparrow$.

Figure 2.284_Mo_a1 depicts total photoionization cross-section of Mo atom in HF-l, HF-v, and SP RPAE. The role of correlations is significant. The first maximum is due to photoionization cross-section of $4d^5\uparrow$ electrons, and the second is a trace of autoionizing resonance $4p\downarrow \rightarrow 4d\downarrow$, decaying with removal of $4d\uparrow$ electron.

Figure 2.285_Mo_d1 shows dipole angular anisotropy parameter of Mo $4d$ "up"-, $4p$ "up"- and "down"-electrons. The β_{4d}-parameter distinguishes by the minimum just above the threshold and by a small maximum at the threshold of $4p$-ionization. At high energies, all values of β are close to each other.

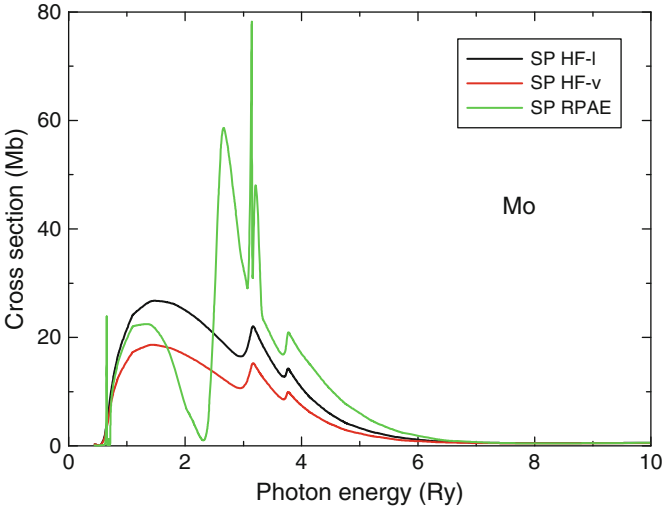

Fig. 2.284_Mo_a1 Total photoionization cross section of Mo atom in SP HF-l, SP HF-v, and SP RPAE

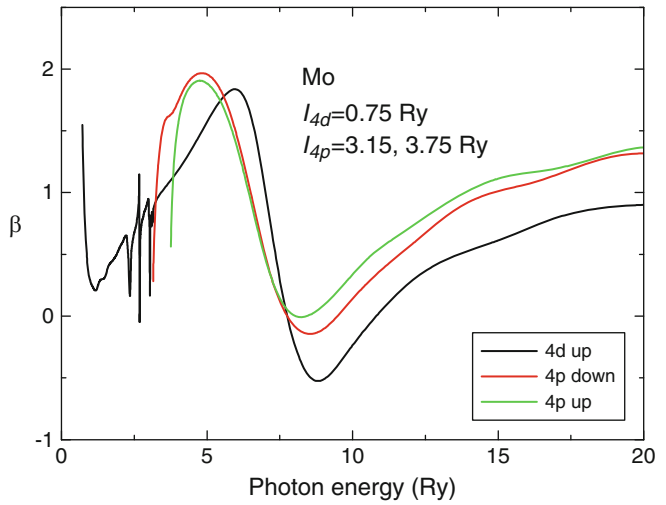

Fig. 2.285_Mo_d1 Dipole anisotropy parameter of $4d$ "up"- and $4p$ "up"-, "down"-electrons for Mo atom in SP RPAE

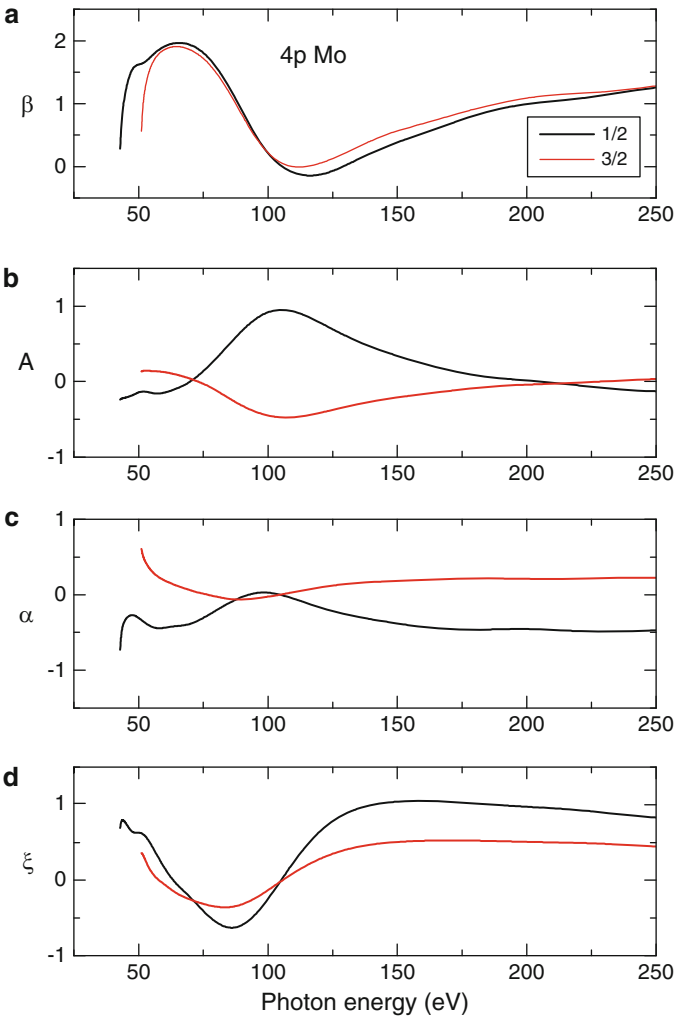

Fig. 2.286_Mo_f1 Dipole anisotropy parameters of $4p$ "up" and "down"-electrons for Mo atom: (**a**) angular anisotropy $\beta_{4p}(\omega)$, (**b**) spin polarization $A_{4p}(\omega)$, (**c**) $\alpha_{4p}(\omega)$, and (**d**) $\xi_{4p}(\omega)$ (see [2.61])

Figure 2.286_Mo_f1 presents dipole angular anisotropy parameters of $4p$ "up"- and "down"-electrons: (a) angular anisotropy $\beta_{4p}(\omega)$, spin polarization (b) $A_{4p}(\omega)$, (c) $\alpha_{4p}(\omega)$, and (d) $\xi_{4p}(\omega)$.

Figure 2.287_MoMo*_f2 presents dipole spin polarization parameters of $4d$-electrons for Mo and excited Mo* atoms: (a) angular anisotropy $\beta_{4d}(\omega)$, (b) $A_{4d}^{5/2}(\omega)$, (c) $\alpha_{4d}^{5/2}(\omega)$, and (d) $\xi_{4d}^{5/2}(\omega)$ (see [2.62]).

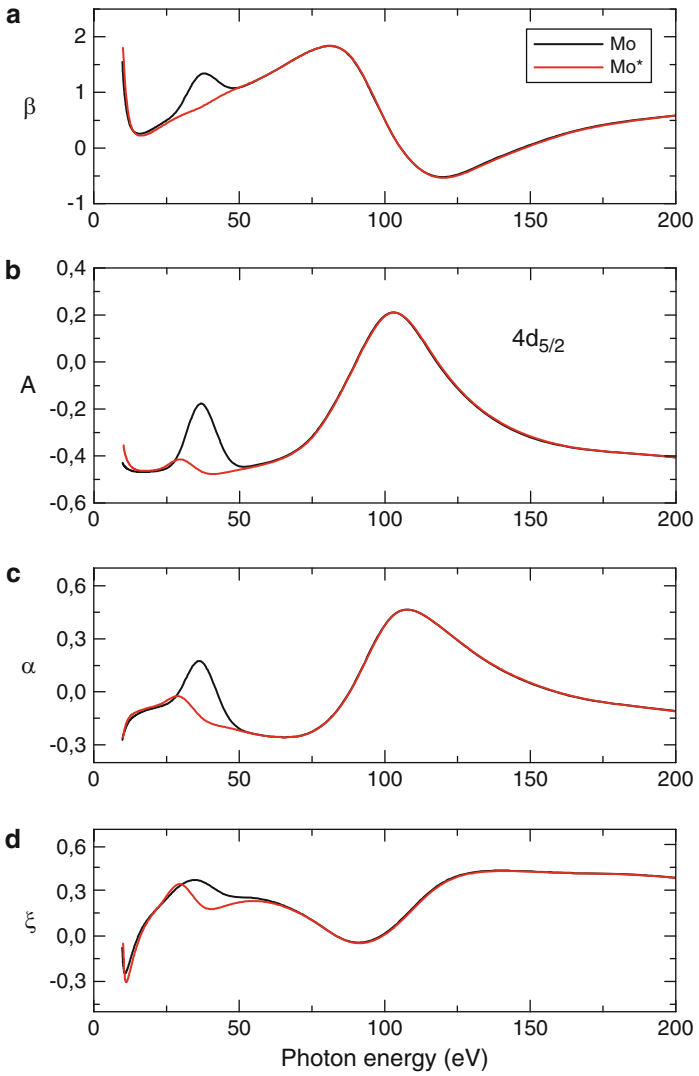

Fig. 2.287_MoMo*_f2 Dipole anisotropy parameters of $4d$-electrons for Mo and Mo* atoms: (**a**) angular anisotropy $\beta_{4d}(\omega)$, (**b**) spin polarization $A_{4d}^{5/2}(\omega)$, (**c**) $\alpha_{4d}^{5/2}(\omega)$, and (**d**) $\xi_{4d}^{5/2}(\omega)$ (see [2.61])

Figures 2.288_Mo*_a1 and 2.289_Mo*_d1 (Mo*) contain results of calculations for Mo* excited atom: $(Z = 42)\ 3d^{10}, 4s^2, 4p^6, 4d^5\uparrow, 5s\downarrow$.

Figure 2.288_Mo*_a1 displays total photoionization cross-section of Mo* atom in HF-l, HF-v, and SP RPAE.

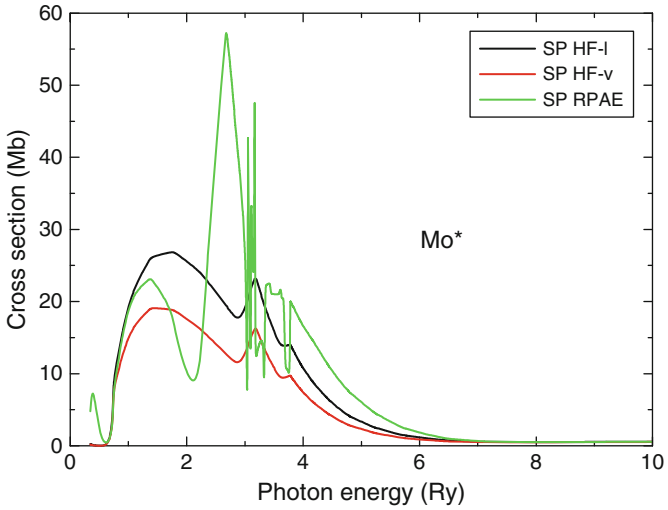

Fig. 2.288_Mo*_a1 Total photoionization cross section of Mo* atom in SP HF-l, SP HF-v, and SP RPAE

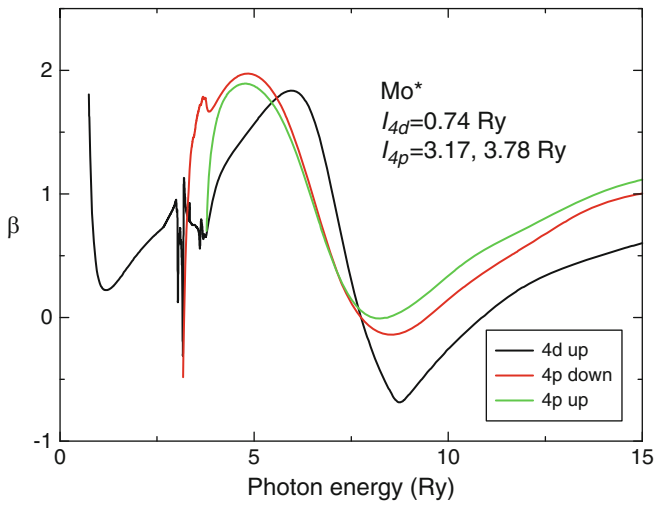

Fig. 2.289_Mo*_d1 Dipole anisotropy parameter of $4d$ "up"- and $4p$ "up"-, "down"-electrons for Mo* excited atom in SP RPAE

Figure 2.289_Mo*_d1 shows dipole angular anisotropy parameter of $4d$ "up"- and $4p$ "up"-, "down"-electrons for Mo* excited atom.

Table 2.7 includes calculated values of oscillator strengths in HF-l, HF-v $f^{l,v}_{nl-n'l'\uparrow(\downarrow)}$, and $F^{l,v}_{nl-n'l'\uparrow(\downarrow)}$ in RPAE for several lowest discrete levels of excitation and for each considered subshell of atoms investigated in this section. Respective theoretical transition energies in RPAE $\tilde{\omega}_{nl-n'l'\uparrow(\downarrow)}$ are also given in this table.

Table 2.7 Oscillator strengths and transition energies of VI group's elements and their ions

Transition	ω (Ry)	HF-l	HF-v	RPAE-l	RPAE-v
O^+					
$2p$–$3d$ up	2.19811	0.3556E+00	0.2965E+00	0.3828E+00	0.3804E+00
$2p$–$4d$ up	2.40255	0.1536E+00	0.1273E+00	0.1768E+00	0.1756E+00
$2p$–$5d$ up	2.49724	0.7767E−01	0.6419E−01	0.7214E−01	0.7164E−01
$2p$–$3s$ up	1.76382	0.1206E+00	0.1127E+00	0.1392E+00	0.1368E+00
$2p$–$4s$ up	2.25417	0.2096E−01	0.1954E−01	0.1294E−01	0.1259E−01
$2p$–$5s$ up	2.42530	0.7701E−02	0.7178E−02	0.9700E−03	0.1010E−02
$2s$–$2p$ do	1.01097	0.4758E+00	0.5003E+00	0.2740E+00	0.2760E+00
$2s$–$3p$ do	2.43700	0.2590E−01	0.2460E−01	0.3747E−01	0.3714E−01
$2s$–$4p$ do	2.74158	0.1051E−01	0.1004E−01	0.1709E−01	0.1702E−01
$2s$–$3p$ up	3.45729	0.4709E−01	0.4170E−01	0.7174E−02	0.6594E−02
$2s$–$4p$ up	3.80477	0.1517E−01	0.1338E−01	0.2612E−02	0.2429E−02
$2s$–$5p$ up	3.94080	0.6846E−02	0.6034E−02	0.1116E−02	0.1037E−02
$1s$–$2p$ do	39.50437	0.2315E+00	0.2342E+00	0.2107E+00	0.2097E+00
$1s$–$3p$ do	41.85195	0.1658E−01	0.1669E−01	0.6319E−02	0.6245E−02
$1s$–$4p$ do	42.21275	0.5602E−02	0.5634E−02	0.6403E−02	0.6385E−02
$1s$–$3p$ up	42.00043	0.9967E−01	0.9715E−01	0.1090E+00	0.1099E+00
$1s$–$4p$ up	42.44808	0.2115E−01	0.2067E−01	0.2056E−01	0.2079E−01
$1s$–$5p$ up	42.60409	0.8718E−02	0.8528E−02	0.7844E−02	0.7940E−02
Cr					
$4s$–$4p$ up	0.18243	0.1002E+01	0.1006E+01	0.7703E+00	0.7867E+00
$4s$–$5p$ up	0.33052	0.1550E−01	0.1593E−01	0.7458E−01	0.6576E−01
$4s$–$6p$ up	0.38321	0.2711E−02	0.2834E−02	0.7716E−02	0.7331E−02
$3d$–$4f$ up	0.68419	0.4666E−02	0.3579E−02	0.4878E−02	0.4922E−02
$3d$–$5f$ up	0.70696	0.3602E−02	0.2766E−02	0.3401E−02	0.3447E−02
$3d$–$6f$ up	0.71934	0.2469E−02	0.1897E−02	0.2304E−02	0.2335E−02
$3d$–$4p$ up	0.34624	0.2871E+00	0.3422E+00	0.3457E+00	0.3170E+00
$3d$–$5p$ up	0.62241	0.1575E−01	0.1689E−01	0.1520E−01	0.1377E−01
$3d$–$6p$ up	0.68016	0.5495E−02	0.5801E−02	0.4188E−02	0.3768E−02
$3p$–$4s$ do	3.15701	0.9893E−01	0.1008E+00	0.2356E+00	0.2530E+00
$3p$–$5s$ do	3.51654	0.1180E−01	0.1199E−01	0.7825E−02	0.8658E−02
$3p$–$6s$ do	3.59762	0.3972E−02	0.4036E−02	0.2879E−02	0.3167E−02
$3p$–$3d$ do	3.29127	0.1814E+01	0.1438E+01	0.1547E+01	0.1590E+01
$3p$–$4d$ do	3.57080	0.1150E+00	0.9006E−01	0.2153E−01	0.2137E−01
$3p$–$5d$ do	3.61849	0.4148E−01	0.3237E−01	0.7694E−02	0.7589E−02
$3p$–$5s$ up	4.28408	0.6718E−01	0.4971E−01	0.3754E−01	0.4066E−01
$3p$–$6s$ up	4.42889	0.7225E−02	0.5500E−02	0.4194E−02	0.4599E−02
$3p$–$7s$ up	4.46858	0.2897E−02	0.2219E−02	0.1708E−02	0.1870E−02
$3p$–$5d$ up	4.45533	0.1027E−02	0.1318E−02	0.8532E−02	0.9415E−02
$3p$–$6d$ up	4.48037	0.4670E−03	0.6021E−03	0.4169E−02	0.4596E−02
$3p$–$7d$ up	4.49366	0.2532E−03	0.3272E−03	0.2435E−02	0.2683E−02
$3s$–$4p$ do	5.94843	0.5900E−02	0.5792E−02	0.4884E−02	0.5288E−02
$3s$–$5p$ do	6.10906	0.1358E−02	0.1321E−02	0.2396E−02	0.2708E−02
$3s$–$6p$ do	6.15906	0.5537E−03	0.5369E−03	0.6574E−03	0.7213E−03
$3s$–$4p$ up	6.09334	0.2138E−01	0.1862E−01	0.5292E−02	0.6340E−02
$3s$–$5p$ up	6.54786	0.5288E−02	0.4737E−02	0.1991E−02	0.2458E−02
$3s$–$6p$ up	6.70208	0.2295E−02	0.2067E−02	0.8878E−03	0.1089E−02

Table 2.7 (Continued)

Cr*					
$4s$–$4p$ do	0.13256	0.1008E+01	0.9904E+00	0.7805E+00	0.7822E+00
$4s$–$5p$ do	0.26495	0.1628E−01	0.1534E−01	0.1408E−03	0.1423E−03
$4s$–$6p$ do	0.30965	0.2738E−02	0.2501E−02	0.1552E−02	0.1558E−02
$3d$–$4f$ up	0.70474	0.3082E−02	0.2667E−02	0.3980E−02	0.4047E−02
$3d$–$5f$ up	0.72747	0.2413E−02	0.2082E−02	0.2666E−02	0.2715E−02
$3d$–$6f$ up	0.73982	0.1666E−02	0.1436E−02	0.1803E−02	0.1837E−02
$3d$–$4p$ up	0.43148	0.3020E+00	0.2911E+00	0.4057E+00	0.4068E+00
$3d$–$5p$ up	0.64438	0.2499E−01	0.2366E−01	0.2248E−01	0.2242E−01
$3d$–$6p$ up	0.70098	0.8432E−02	0.7950E−02	0.6191E−02	0.6157E−02
$3p$–$6s$ do	3.60431	0.6030E−02	0.5828E−02	0.4185E−02	0.4561E−02
$3p$–$7s$ do	3.64274	0.2501E−02	0.2421E−02	0.1750E−02	0.1905E−02
$3p$–$8s$ do	3.66096	0.1300E−02	0.1259E−02	0.9544E−03	0.1036E−02
$3p$–$3d$ do	3.27216	0.1873E+01	0.1456E+01	0.1595E+01	0.1630E+01
$3p$–$4d$ do	3.58540	0.1030E+00	0.8169E−01	0.1967E−01	0.1968E−01
$3p$–$5d$ do	3.63394	0.3831E−01	0.3038E−01	0.7003E−02	0.6982E−02
$3s$–$4s$ up	3.89084	0.1556E+00	0.1085E+00	0.8249E−01	0.8196E−01
$3s$–$5s$ up	4.36573	0.1268E−01	0.9667E−02	0.7974E−02	0.7794E−02
$3s$–$6s$ up	4.45482	0.4071E−02	0.3131E−02	0.2626E−02	0.2595E−02
Mo					
$5s$–$5p$ up	0.17923	0.1077E+01	0.1071E+01	0.7459E+00	0.7585E+00
$5s$–$6p$ up	0.34046	0.1704E−01	0.1719E−01	0.1192E+00	0.1145E+00
$5s$–$7s$ up	0.38568	0.3285E−02	0.3354E−02	0.3343E−02	0.3228E−02
$4d$–$4f$ up	0.65510	0.1293E−01	0.9246E−02	0.1494E−01	0.1499E−01
$4d$–$5f$ up	0.67798	0.9901E−02	0.7075E−02	0.9617E−02	0.9803E−02
$4d$–$6f$ up	0.69045	0.6746E−02	0.4818E−02	0.6452E−02	0.6586E−02
$4d$–$5p$ up	0.32440	0.4835E+00	0.6590E+00	0.4476E+00	0.4252E+00
$4d$–$6p$ up	0.59715	0.2512E−01	0.3100E−01	0.1634E−01	0.1442E−01
$4d$–$7p$ up	0.65291	0.8746E−02	0.1061E−01	0.1980E−02	0.1573E−02

The results for length and velocity forms in RPAE coincide with reasonable accuracy. The role of RPAE corrections for many levels is important. In O^+, Cr, Cr*, and Mo the biggest oscillator strengths have the first excitation of the outer subshell—$2p$–$3d\uparrow$, $4s$–$4p\uparrow$, $4s$–$4p\uparrow$, and $5s$–$5p\uparrow$, respectively. The second in oscillator strength is the excitation of the next subshell. The oscillator strengths are, in general, decreasing with decrease in principal quantum number of the exited electron.

2.9 Atoms and Ions of VII and VIII Group Elements

In this section we present our results for outer and intermediate subshells of ions and of some atoms of elements VII and VIII groups. Here we have concentrated basically on the ions having all filled or one half-filled subshell, namely F $(Z=9)$ $1s^2 2s^2 2p^5$; F* $(Z=9)$ $1s^1 2s^1 2p^3 3s^1 3p^3\uparrow$; F^{2+} $(Z=9)$ $1s^2 2s^2 2p^3\uparrow$; $F^-(Z=9)$ $1s^2 2s^2 2p^6$; Cl $(Z=17)$ $2p^6 3s^2 3p^5$; $Cl^-(Z=17)$ $2p^6 3s^2 3p^6$; Mn $(Z=25)$ $3s^2 3p^6 3d^5\uparrow 4s^2$; Mn^+ $(Z=25)$ $3s^2 3p^6 3d^5\uparrow 4s\uparrow$; Br^- $(Z=35)$ $3s^2 3p^6 3d^{10} 4s^2 4p^6$; Tc $(Z=43)$ $4s^2 4p^6\ 4d^5\uparrow 5s^2$; Pd$(Z=46)$ $3s^2 3p^6 3d^{10} 4s^2 4p^6 4d^{10}$; $Pd^-(Z=46)$ $3s^2 3p^6 3d^{10} 4s^2 4p^6 4d^{10} 5s\uparrow$; I$(Z=53)$ $4s^2 4p^6 4d^{10} 5s^2\ 5p^5$; $I^+(Z=53)$ $4s^2 4p^6 4d^{10} 5s^2 5p^4$; $I^{2+}(Z=53)$ $4s^2 4p^6 4d\ 5s^2 5p^3\uparrow$; $I^-(Z=53)$ $4s^2 4p^6 4d^{10} 5s^2 5p^6$; $Fe^+(Z=26)$ $3s^2 3p^6 3d^5\uparrow 4s^2\uparrow$. Formulas used to obtain the data and notations in figures are the same as for noble gases resulted in Sect. 2.1. Here $\uparrow$ ($\downarrow$) denotes "up" ("down") electrons in SP RPAE (see Sect. 1.10).

Figure 2.290_F_a1 (F) contains results of calculations for F atom: $(Z=9)$ $1s^2 2s^2 2p^5$.

Figure 2.290_F_a1 shows total photoionization cross-section of F atom in RPAE for unfilled shells (RPAEO) with partial contributions of final state terms ^2S, ^2P, ^2D and their sum.

Figures 2.291_F*_a1–2.293_F*_d1 (F*) contain results of calculations for F* atom: $(Z=9)$ $1s^1 2s^1 2p^3 3s^1 3p^3\uparrow$.

Figure 2.291_F*_a1 shows total photoionization cross-section of F* atom in HF-l, HF-v, and SP RPAE. At 1.7 Ry the second maximum of section is seen.

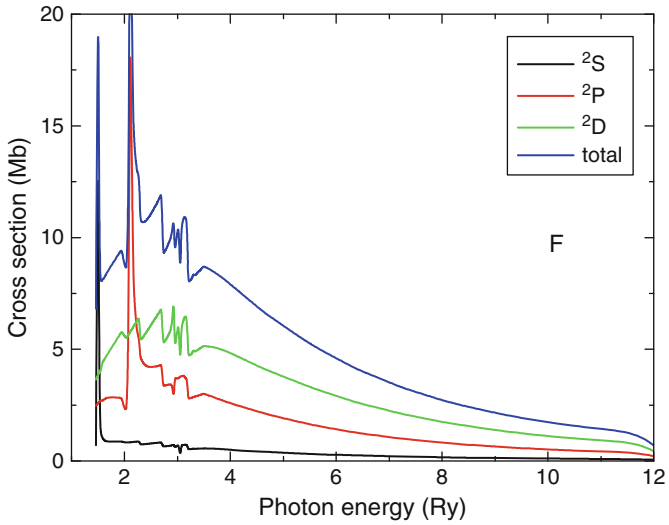

Fig. 2.290_F_a1 Total photoionization cross section of F atom RPAEO (for open shells) with terms ^2S,^2P,^2D and their sum

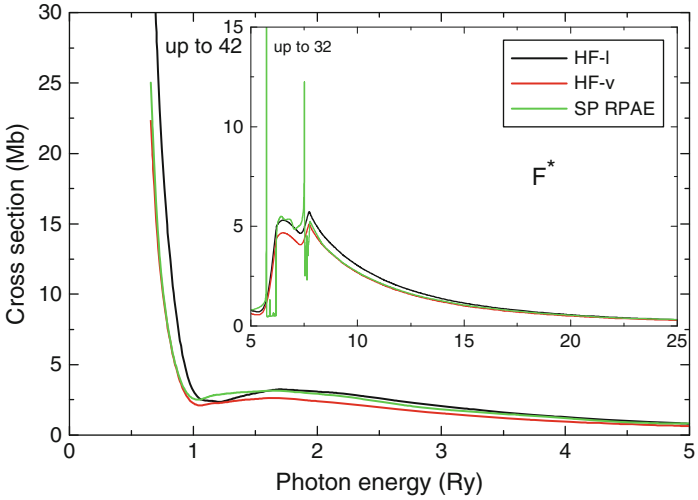

Fig. 2.291_F*_a1 Total photoionization cross section of excited F* atom in HF-l, HF-v, and SP RPAE

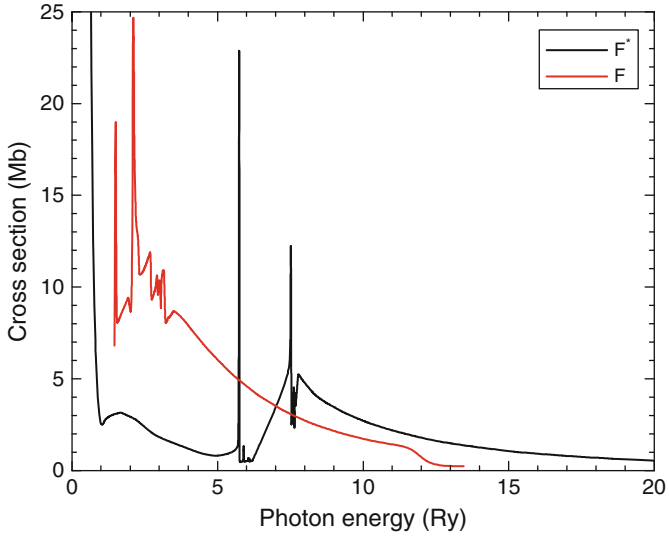

Fig. 2.292_F*F_a2 Photoionization cross section of F* atom in excited state in comparison with the same of F atom

Figure 2.292_F*F_a2 compares photoionization cross-sections of F atom in the ground and excited F* states in SP RPAE. Atomic excitation forms a maximum in a continuous spectrum at ≈ 8 Ry.

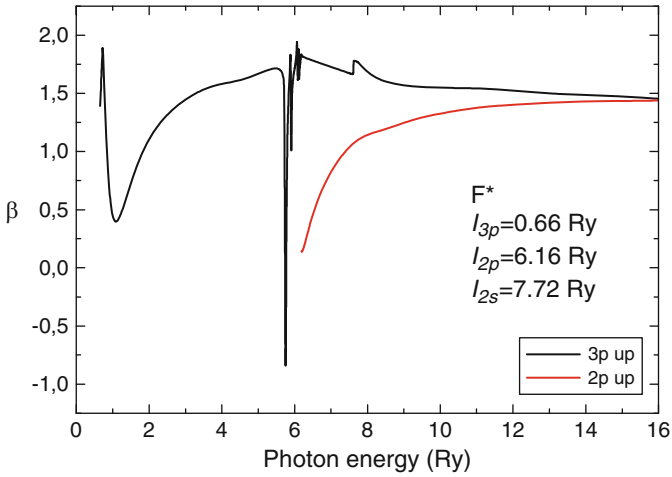

Fig. 2.293_F*_d1 Dipole angular anisotropy parameter of $3p$- and $2p$-electrons for F* atom in excited state in SP RPAE

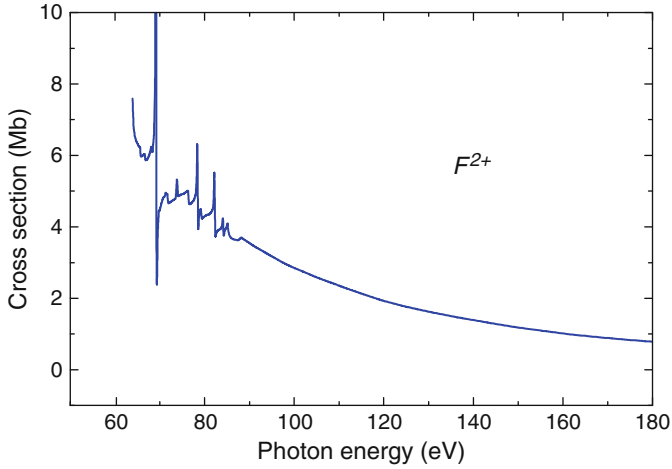

Fig. 2.294_F^{2+}_a1 Total photoionization cross section of F^{2+} ion in SP RPAE

Figure 2.293_F*_d1 presents dipole angular anisotropy parameter of $3p$- and $2p$-electrons for F* in SP RPAE. Note a narrow threshold maximum and a broad subsequent minimum at about 13 eV and a maximum at 75 eV, the latter arising owing to influence of $2p$-electrons on $3p$-electrons.

Figures 2.294_F^{2+}_a1–2.296_F^{2+}_d1 (F^{2+}) contain results of calculations for F^{2+} ion: ($Z = 9$) $1s^2 2s^2 2p^3 \uparrow$.

Figure 2.294_F^{2+}_a1 displays total photoionization cross-section of F^{2+} ion in SP RPAE. The cross-section has a prominent domain of discrete excitations.

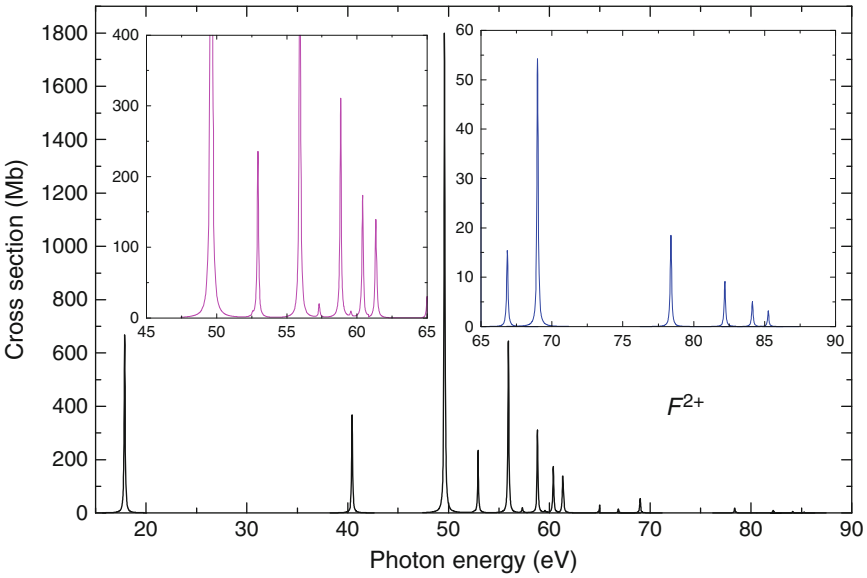

Fig. 2.295_F^{2+}_a2 Quasi-cross section of discrete levels for F^{2+} ion in SP RPAE

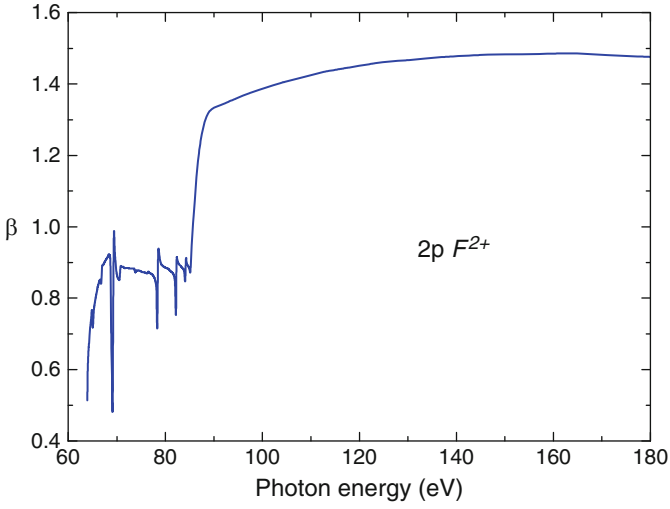

Fig. 2.296_F^{2+}_d1 Dipole angular anisotropy parameter of $2p$-electrons for F^{2+} ion in SP RPAE

Figure 2.295_F^{2+}_a2 presents quasi cross-section of excitation to discrete levels of F^{2+} ion in SP RPAE.

Figure 2.296_F^{2+}_d1 shows the dipole angular anisotropy parameter β_{2p} of $2p$-electrons of F^{2+} ion.

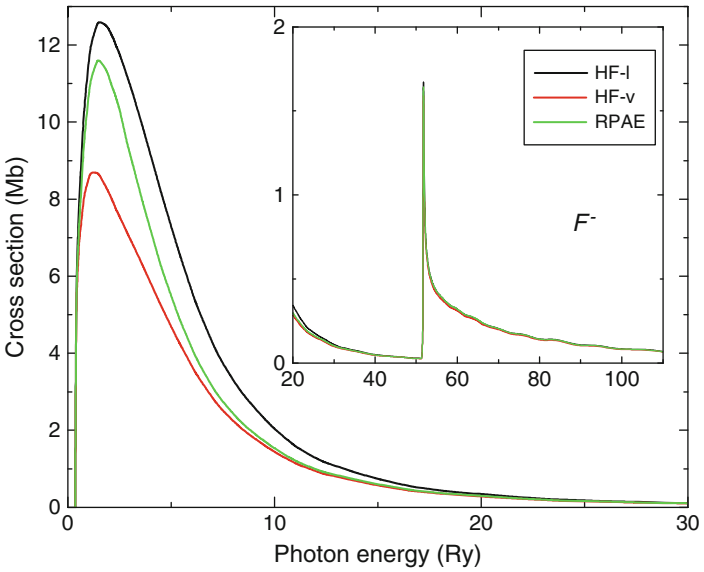

Fig. 2.297_F⁻_a1 Total photoionization cross section of F^- ion in HF-l, HF-v, and RPAE

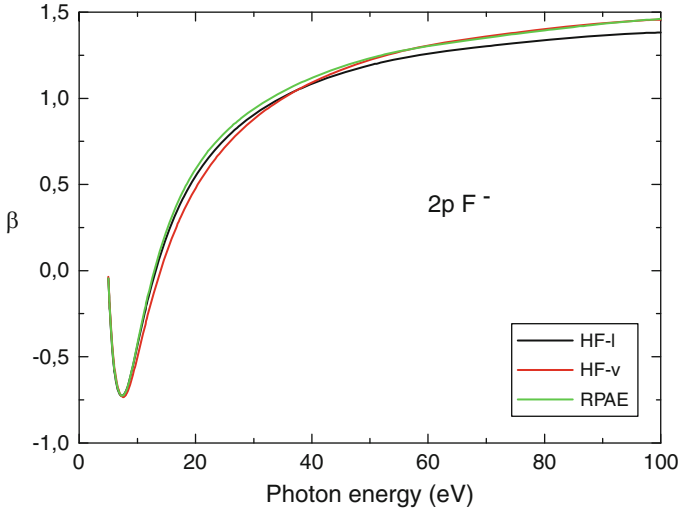

Fig. 2.298_F⁻_d1 Dipole angular anisotropy parameter of $2p$-electrons for F^- ion in HF-l, HF-v, and RPAE

Figures 2.297_F⁻_a1 and 2.298_F⁻_d1 (F^-) contain results of calculations for F^- ion: $(Z = 9)\ 1s^2 2s^2 2p^6$.

Figure 2.297_F⁻_a1 depicts total photodetachment cross-section of F^- ion in HF-l, HF-v, and RPAE. A sharp rise of photodetachment cross-section from

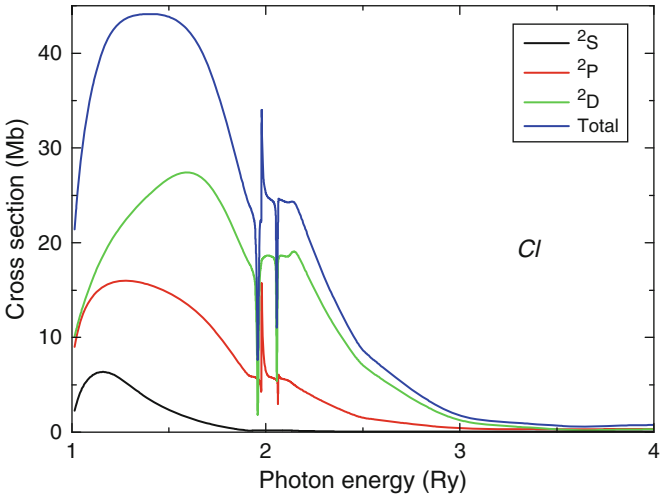

Fig. 2.299_Cl_a1 Total photoionization cross section of Cl atom in RPAEO with final terms ^2S, ^2P, ^2D and their sum (see [2.64])

threshold to maximum is similar to the behavior of the cross-section of the neutral atoms.

Figure 2.298_F$^-$_d1 presents dipole angular anisotropy parameter β_{2p} of $2p$-electrons for F^- ion in HF-l, HF-v, and RPAE. After narrow minimum near threshold β-parameter increases, but he slope of curve decreases.

Figures 2.299_Cl_a1 and 2.300_Cl_b1 (C1) contain results of calculations for Cl atom: $(Z = 17)\, 2p^6 3s^2 3p^5$.

Figure 2.299_Cl_a1 shows total photoionization cross-section of Cl atom in RPAEO with separate contributions of final state terms ^2S, ^2P, ^2D and their sum (see [2.64]). The cross-section is characterized by broad maximum at $\omega \approx 1.5$ Ry.

Figure 2.300_Cl_b1 shows photoionization cross-section of $3p$-electrons for Cl atom. Experiment is taken from [2.65]. The experimental ionization energies of terms of final states $3p^4\ ^3P$, ^1D and ^1S are as follows: $I_{^3P} = 0.959$ Ry, $I^1_D = 1.060$ Ry, and $I^1_S = 1.207$ Ry.

Figures 2.301_Cl$^-$_a1–2.304_Cl$^-$_d2 (Cl^-) contain results of calculations for Cl^- ion: $(Z = 17) 2p^6 3s^2 3p^6$.

Figure 2.301_Cl$^-$_a1 presents total photodetachment cross-section of Cl^- ion in HF-l, HF-v, and RPAE.

Figure 2.302_Cl$^-$_b1 depicts the photodetachment cross-section of $2p$-electrons for Cl^- ion in HF, RPAE, GHF, and GRPAE. The cross-section rises rapidly at threshold. In HF and RPAE there appears very high and narrow maximum, which is absent in GRPAE.

Figure 2.303_Cl$^-$_d1 displays the dipole angular anisotropy parameter of $2p$- and $3p$-electrons of Cl^- ion in HF and RPAE. Parameters $\beta_{3p,2p}(\omega)$ have a sharp

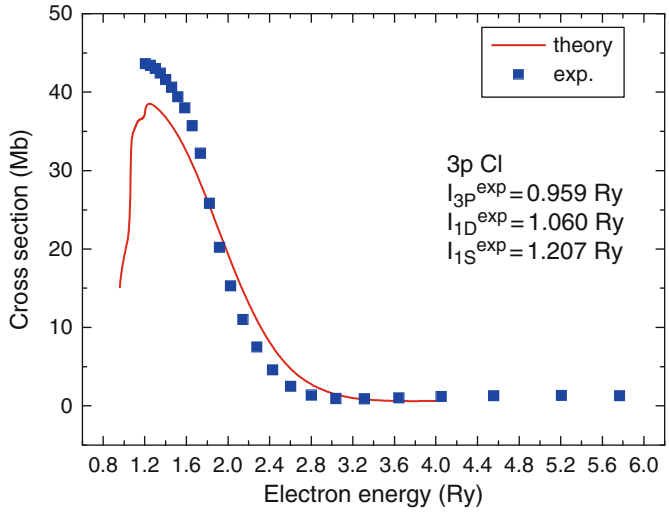

Fig. 2.300_Cl_b1 Photoionization cross section of $3p$-electrons for Cl atom. Experiment is from [2.65]

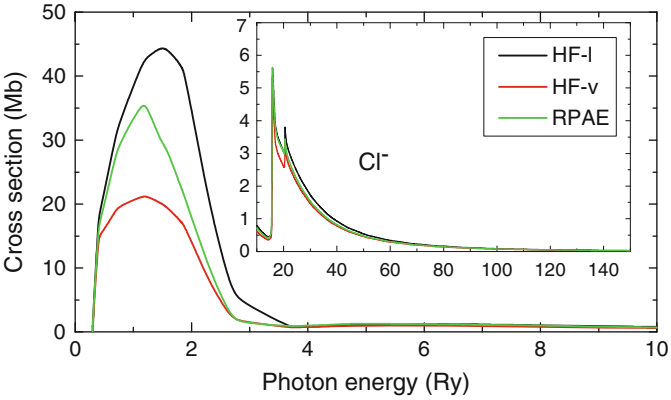

Fig. 2.301_Cl^-_a1 Total photoionization cross section of Cl^- ion in HF-l, HF-v, and RPAE

maximum near their thresholds that is followed by deep minimums. The influence of $2p$-shell near its threshold on $3p$ cross-section is evident.

Figure 2.304_Cl^-_d2 presents dipole angular anisotropy parameter of $2p$-electrons of Cl^- ion in RPAE and GRPAE. The narrow maximum near threshold existing in RPAE disappears in GRPAE.

Figures 2.305_Mn_a1–2.311_Mn_f2 (Mn) contain results of calculations for Mn atom: $(Z = 25)3s^2 3p^6 3d^5 \uparrow 4s^2$.

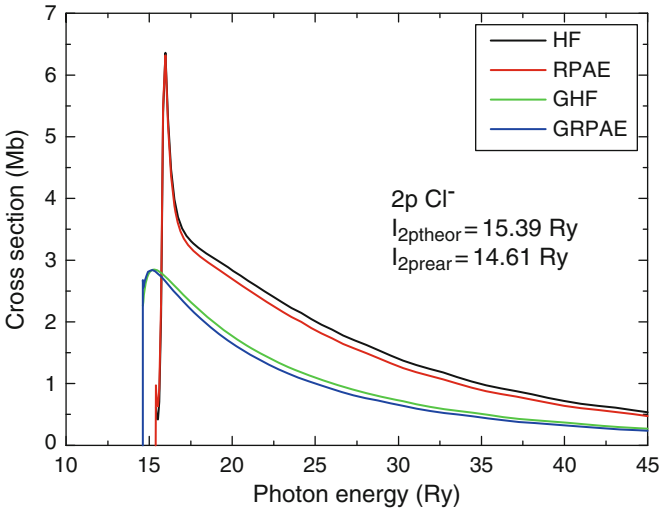

Fig. 2.302_Cl⁻_b1 Photoionization cross section of Cl^- ion of $2p$-electrons in HF, RPAE, GHF, and GRPAE

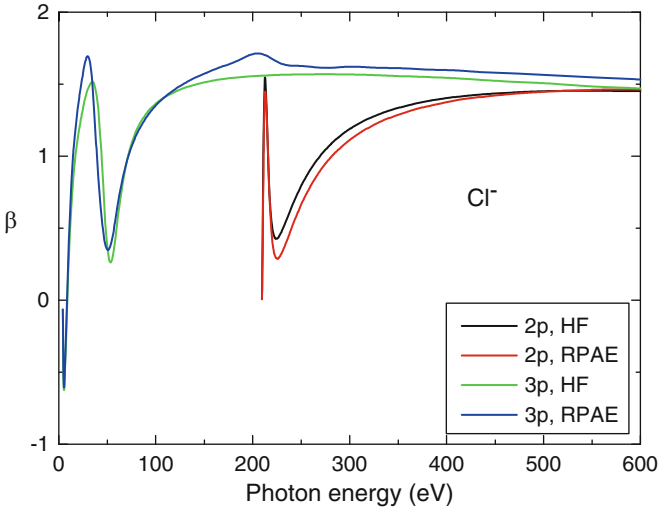

Fig. 2.303_Cl⁻_d1 Dipole angular anisotropy parameter of $2p$-, $3p$-electrons for Cl^- ion in HF and RPAE

Figure 2.305_Mn_a1 presents total photoionization cross-section of Mn atom in HF-l, HF-v, and SP RPAE. The structure of cross-sections is rich of resonances due to discrete excitations from intermediate subshell transitions.

Figure 2.306_Mn_b1 shows Giant autoionizing resonance in photoionization cross-section of $3d$ "up"-electrons of Mn atom [2.66, 2.67] with account of the

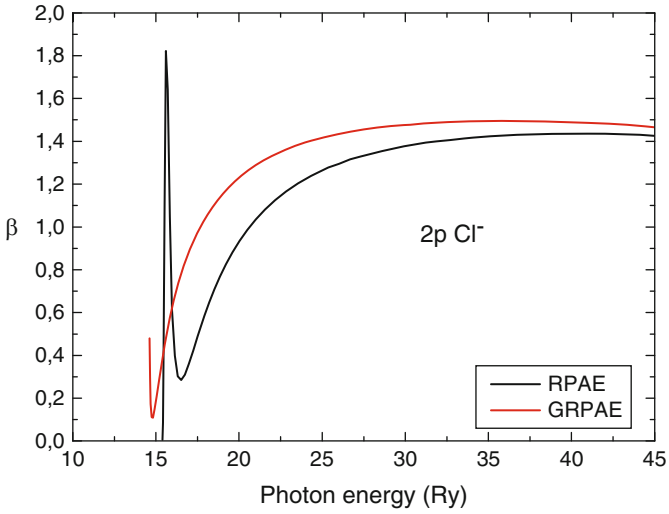

Fig. 2.304_Cl⁻_d2 Dipole angular anisotropy parameter of $2p$-electrons for Cl^- ion in RPAE and GRPAE

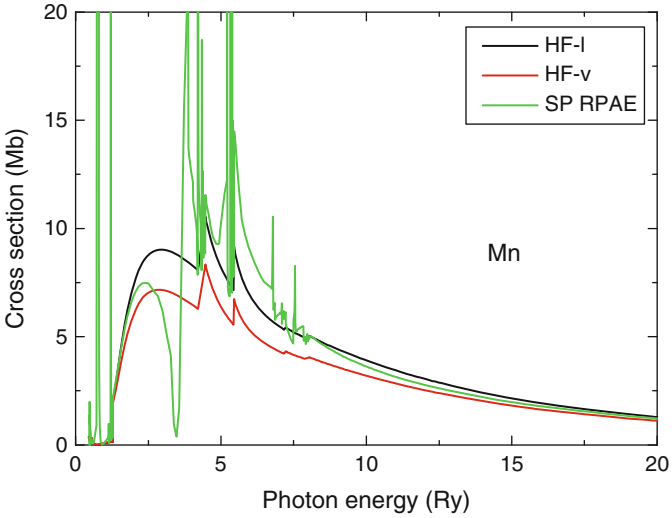

Fig. 2.305_Mn_a1 Total photoionization cross section of Mn atom in HF-l, HF-v, and SP RPAE

contribution of discrete excitation $3p\downarrow$–$3d\downarrow$. The experimental data are taken from [2.69, 2.70].

Figure 2.307_Mn_d1 presents dipole angular anisotropy parameter of $3d$ "up"-, $3p$ "up"- and "down"-electrons for Mn atom in SP RPAE. (see [2.61, 2.62]). The β_{3p}-parameter has a minimum near threshold, while the β_{2p}-parameter has a sharp maximum. At $\omega > 120$ eV both curves are close to each other.

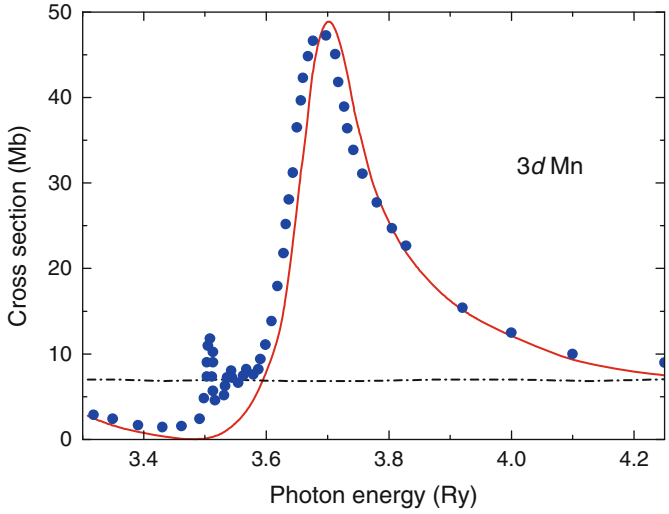

Fig. 2.306_Mn_b1 Photoionization cross section of $3d$-electrons for Mn atom (with account of $3p$ "down"-$3d$ "down" transition) in the vicinity of giant resonance (see [2.66]). Experiment is from [2.67, 2.69]

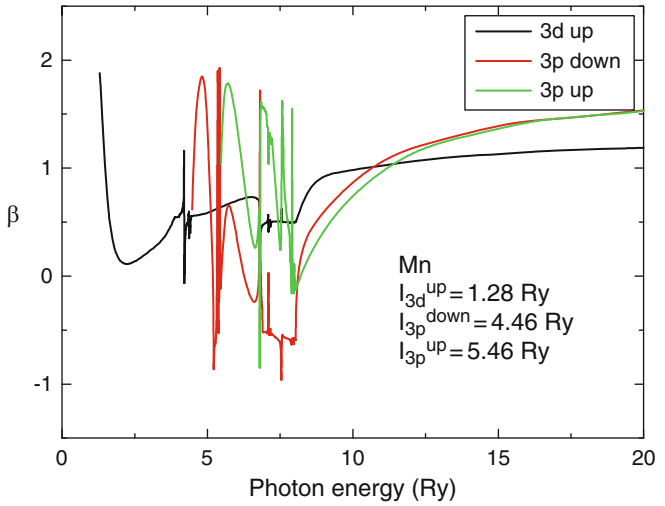

Fig. 2.307_Mn_d1 Dipole angular anisotropy parameter of $3d$ "up"-, $3p$ "up" and "down"-electrons for Mn atom in SP RPAE (see [2.60, 2.61])

Figure 2.308_Mn_e1 demonstrates non-dipole angular anisotropy parameter γ^{C} of $4s$ "up"- and "down"-electrons of Mn atom in HF and SP RPAE (see [2.68]). The role of correlations is not significant.

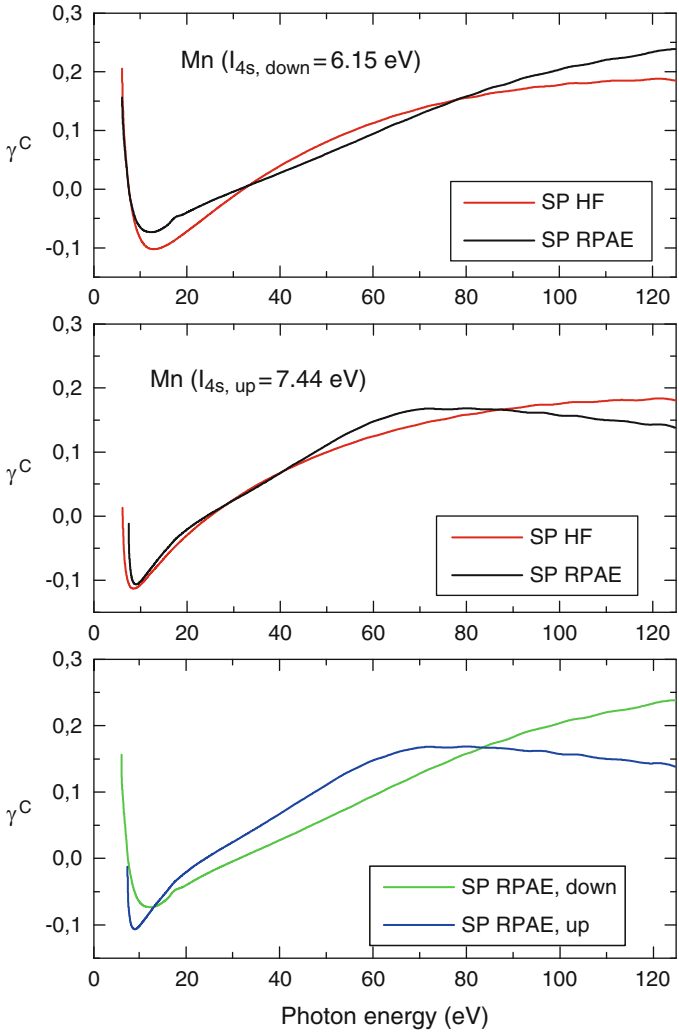

Fig. 2.308_Mn_e1 Non-dipole angular anisotropy parameter of 4*s* "up" and "down"-electrons for Mn atom inHF and SP RPAE (see [2.68])

Figure 2.309_Mn_e2 shows non-dipole angular anisotropy parameters γ^C and δ^C and their magic combination ($\gamma^C + 3\delta^C$) of $3d$ "up"-electrons in SP RPAE. The parameters rise rapidly from threshold and the energy dependence becomes slow linear (see [2.68]).

Figure 2.310_Mn_f1 depicts dipole anisotropy parameters of $3d$ "up"-electrons of Mn atom (a) angular anisotropy parameter $\beta_{3d}(\omega)$ (see [2.61, 2.62, 2.67]); spin

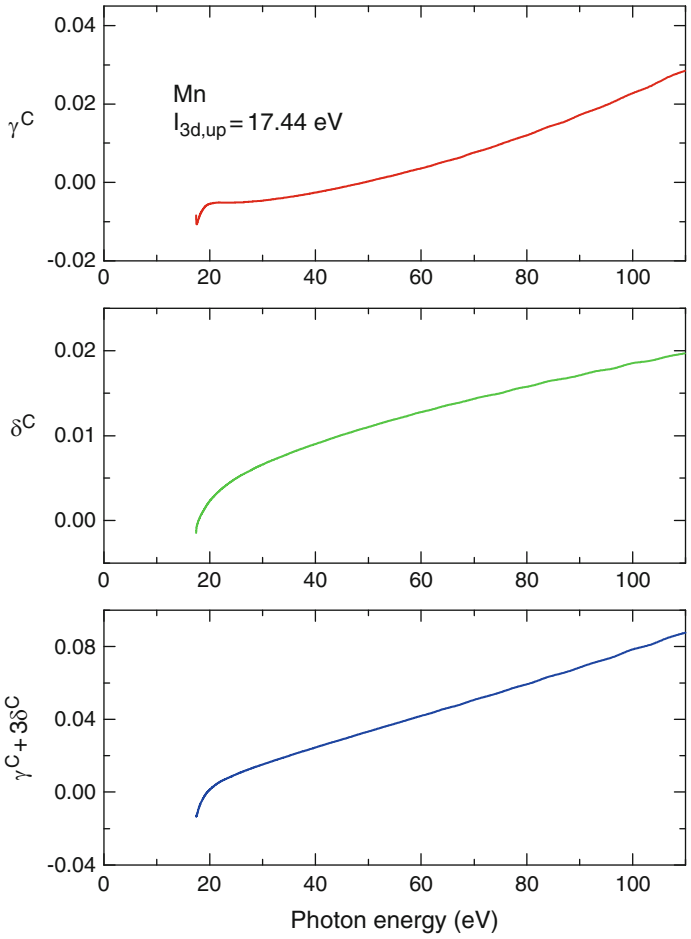

Fig. 2.309_Mn_e2 Non-dipole angular anisotropy parameters and their magic combination of $3d$ "up"-electrons for Mn atom in SP RPAE (see [2.68])

polarization parameters (b) $A_{3d}^{5/2}(\omega)$, (c) $\alpha_{3d}^{5/2}(\omega)$, and (d) $\xi_{3d}^{5/2}(\omega)$ in SP RPAE. The trace of influence of excitations of $3p$-electrons on spin-polarization is seen.

Figure 2.311_Mn_f2 demonstrates dipole angular anisotropy parameters of $3p$ "up"- and "down"-electrons: (a) angular anisotropy parameter $\beta_{3p}(\omega)$; spin polarization parameters (b) $A_{3p}(\omega)$, (c) $\alpha_{3p}(\omega)$, (d) $\xi_{3p}(\omega)$ in SP RPAE (see [2.62]).

Figures 2.312_Mn^+_a1–2.314_Mn^+_d2 (Mn^+) contain results of calculations for Mn^+ ion: ($Z = 25$) $3s^2 3p^6 3d^5 \uparrow 4s \uparrow$.

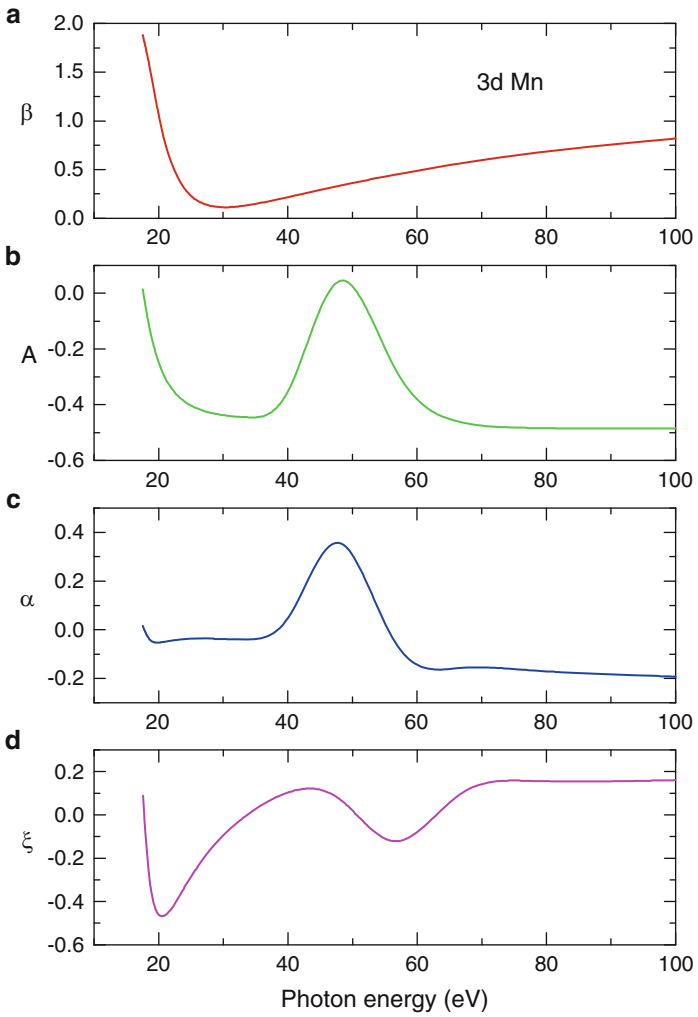

Fig. 2.310_Mn_f1 Dipole parameter of $3d$ "up"-electrons for Mn atom: (**a**) angular anizotropy $\beta_{3d}(\omega)$, (**b**) spin polarization $A_{3d}^{5/2}(\omega)$, (**c**) $\alpha_{3d}^{5/2}(\omega)$, and (**d**) $\xi_{3d}^{5/2}(\omega)$ (see [2.60, 2.61, 2.66])

Figure 2.312_Mn^+_a1 presents total photoionization cross-section of Mn^+ ion in HF-l, HF-v, and SP RPAE. A Giant autoionizing resonance is seen at 4 Ry. Before it, at energy ≈ 2.3 Ry, there is a maximum in cross-section of $3p$-electrons.

Figure 2.313_Mn^+_d1 displays dipole angular anisotropy parameters $\beta(\omega)$ of $3d$ "up"-, $3p$ "up" and "down"-electrons of Mn^+ ion. The difference between

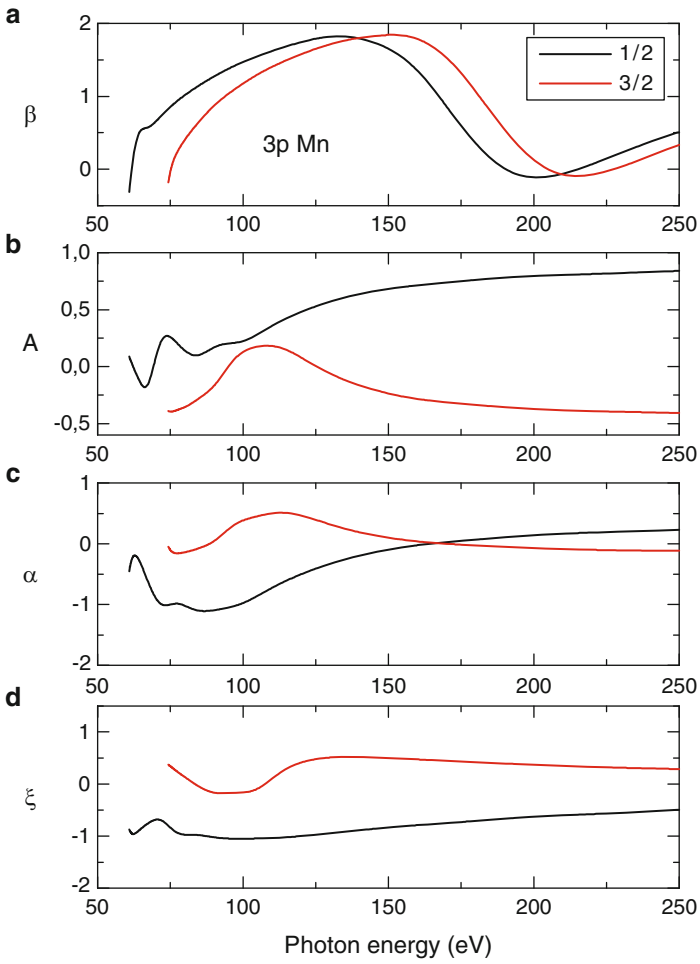

Fig. 2.311_Mn_f2 Dipole parameter of $3p$ "up" and "down"-electrons for Mn atom: (**a**) angular anisotropy $\beta_{3p}(\omega)$, (**b**) spin polarization $A_{3p}(\omega)$, (**c**) $\alpha_{3p}(\omega)$, and (**d**) $\xi_{3p}(\omega)$ (see [2.61])

parameters of $3p\uparrow$ and $3p\downarrow$ shells is large: $\beta_{3p\downarrow}(\omega)$ has additional with respect to $\beta_{3p\uparrow}(\omega)$, maximum beyond the threshold. Sharp variations of $\beta_{3d\uparrow}(\omega)$ obviously correlate with the specific features of photoionization cross-section (see Fig. 2.312_Mn^+_a1).

Figure 2.314_Mn^+_d2 shows dipole angular anisotropy parameter of $3d$-electrons of Mn^+ ion in SP RPAE. A strong oscillation due to influence of transition $3p\downarrow$–$3d\downarrow$ is seen (see [2.68]). The curve presents in details sharp variations of $\beta_{3d\uparrow}(\omega)$ at small energy range.

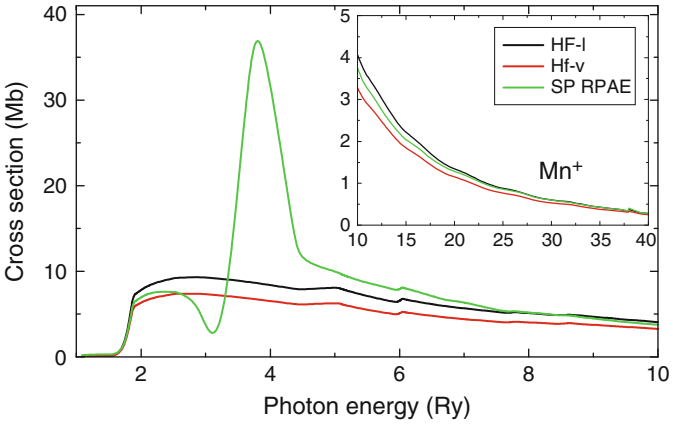

Fig. 2.312_Mn$^+$_a1 Total photoionization cross section of Mn^+ ion in HF-l, HF-v, and SP RPAE

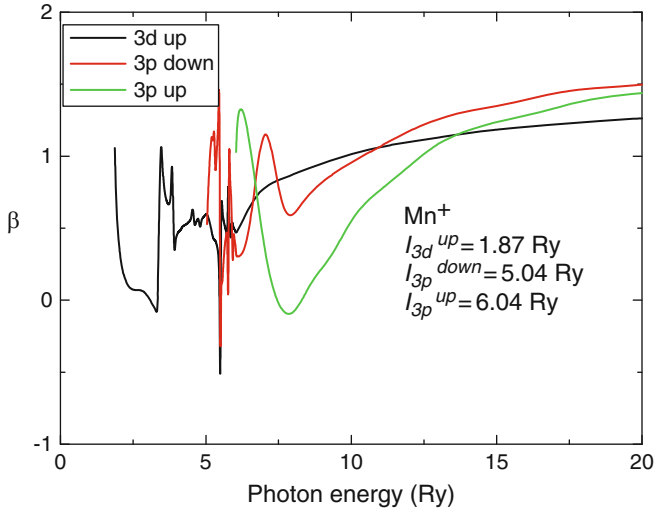

Fig. 2.313_Mn$^+$_d1 Dipole angular anisotropy parameter of $3d$ "up-, $3p$ "up" and "down"-electrons of Mn^+ ion

Figures 2.315_Br$^-$_a1 and 2.316_Br$^-$_d1 (Br^-) contain results of calculations for Br^- ion: $(Z = 35)\ 3s^2 3p^6 3d^{10} 4s^2 4p^6$.

Figure 2.315_Br$^-$_a1 presents total photoionization cross-section of Br^- ion in HF-l, HF-v, and RPAE. Two maxima at thresholds are visible, at 1 Ry, and at 15 Ry. Influence of electron correlations near thresholds is large.

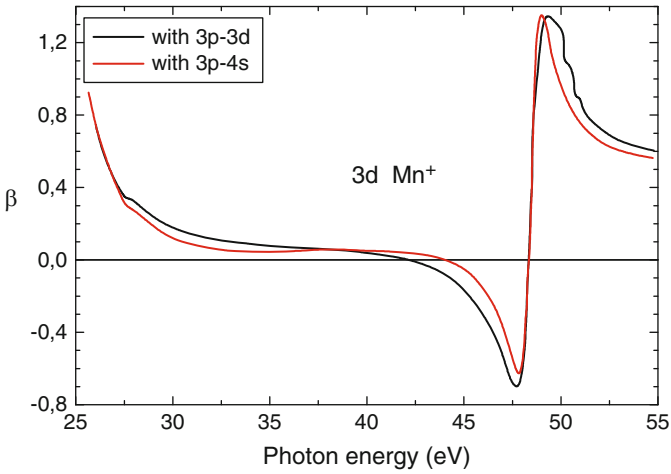

Fig. 2.314_Mn$^+$_d2 Dipole angular anisotropy parameter of $3d$-electrons for Mn^+ ion (see [2.67])

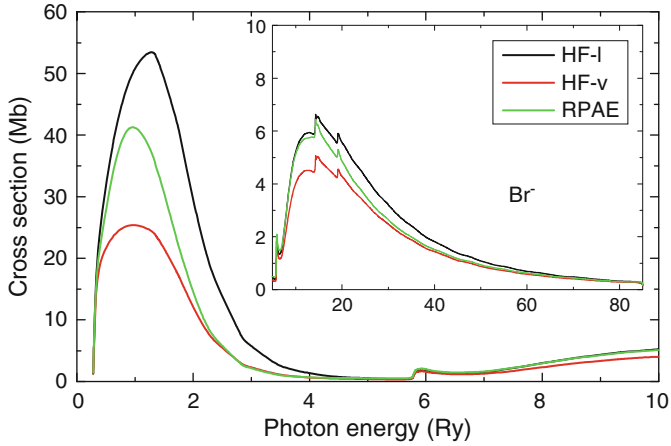

Fig. 2.315_Br$^-$_a1 Total photoionization cross section of Br^- ion in HF-l, HF-v, and RPAE

Figure 2.316_Br$^-$_d1 presents dipole anisotropy parameter of $3p$-, $4p$-electrons for Br^- ion. As in many other cases, β-parameter reveals oscillations starting immediately after the ionization threshold.

Figures 2.317_Tc_a1–2.320_Tc_f2 (Tc) contain results of calculations for Tc atom: $(Z = 43)\, 4s^2 4p^6 4d^5 \uparrow 5s^2$.

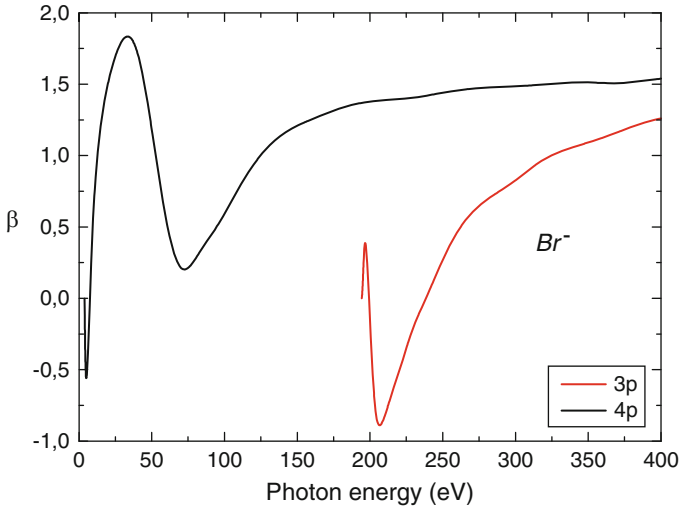

Fig. 2.316_Br⁻_d1 Dipole angular anisotropy parameter of $3p$- and $4p$-electrons for Br^- ion

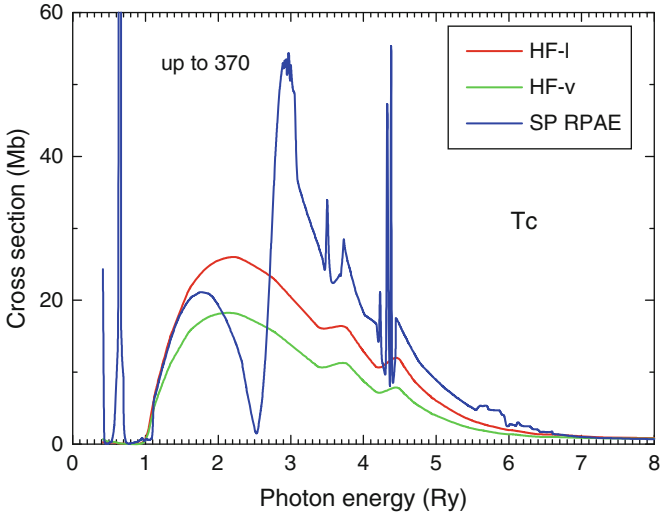

Fig. 2.317_Tc_a1 Total photoionization cross section of Tc atom in HF-l, HF-v, and SP RPAE

Figure 2.317_Tc_a1 depicts photoionization cross-section of Tc atom in HF-l, HF-v, and SP RPAE. It is seen that in SP RPAE there is a deep minimum at 2.5 Ry followed by a maximum at 3 Ry. The picture is similar to that of Mn (see Fig. 2.305_Mn_a1).

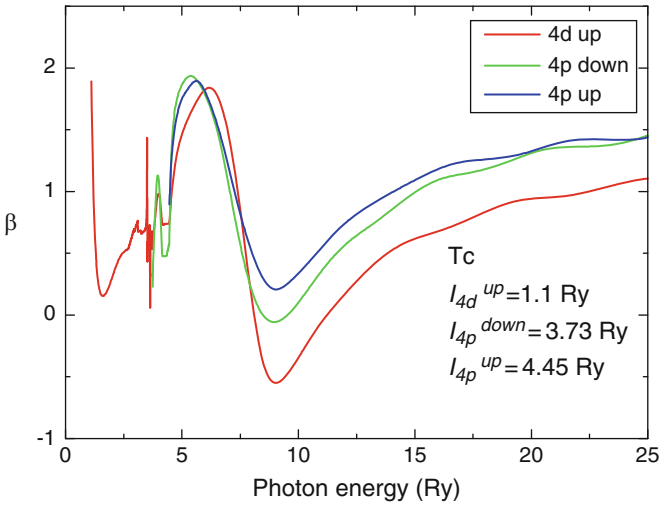

Fig. 2.318_Tc_d1 Dipole angular anisotropy parameter of $4d$ "up"-, $4p$ "up" and "down"-electrons for Tc atom in SP RPAE

Figure 2.318_Tc_d1 presents dipole angular anisotropy parameter of $4d$ "up"-, $4p$ "up"- and "down"-electrons of Tc atom in SP RPAE. At photon energy larger than 80 eV all curves are similar. Parameter $\beta_{4d\uparrow}$ has additional minimum just after the threshold.

Figure 2.319_Tc_f1 shows dipole angular anisotropy parameters of $4d$ "up"-electrons for Tc atom: (a) angular anisotropy $\beta_{4d}(\omega)$; spin polarization (b) $A_{4d}^{5/2}(\omega)$, (c) $\alpha_{4d}^{5/2}(\omega)$, (d) $\xi_{4d}^{5/2}(\omega)$. The behavior of all parameters except $\beta_{4d}(\omega)$, is similar to that for Mn—(see Fig. 2.310_Mn_f1), but the curve $\beta_{4d}(\omega)$ has additional maximum at 90 eV (see [2.62]).

Figure 2.320_Tc_f2 presents dipole anisotropy parameters of $4p$ "up"- and "down"-electrons of Tc atom: (a) angular anisotropy parameter $\beta_{4p}(\omega)$; spin polarization parameters (b) $A_{4p}(\omega)$, (c) $\alpha_{4p}(\omega)$, (d) $\xi_{4p}(\omega)$ (see [2.62]). The dependences on the photon energy are similar to that for Mn—(see Fig. 2.311_Mn_f2).

Figures 2.321_Pd_a1–2.323_Pd_d1 (Pd) contain results of calculations for Pd atom: $(Z = 46)\ 4s^2 4p^6 4d^{10}$.

Figure 2.321_Pd_a1 displays total photoionization cross-section of Pd atom in HF-l, HF-v, and RPAE. The cross-section of outermost $4d^{10}$-shell dominates. The role of RPAE correlations is large.

Figure 2.322_Pd_b1 depicts total photoionization cross-section of $4p$- and $4d$-electrons of Pd in HF-l, HF-v, and RPAE. It is seen that $4d^{10}$-cross-section forms Giant resonance, which is almost as high as Giant $4d$ resonance in Xe.

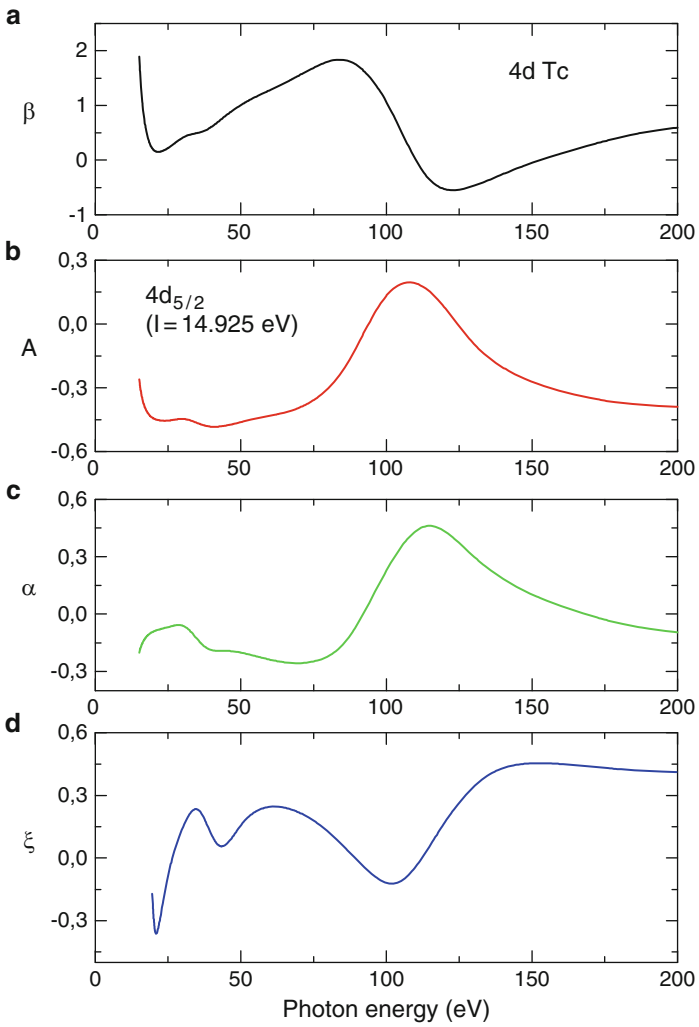

Fig. 2.319_Tc_f1 Dipole parameters of $4d$ "up"-electrons for Tc atom: (**a**) angular anisotropy $\beta_{4d}(\omega)$, (**b**) spin polarization $A_{4d}^{5/2}(\omega)$, (**c**) $\alpha_{4d}^{5/2}(\omega)$, and (**d**) $\xi_{4d}^{5/2}(\omega)$

Figure 2.323_Pd_d1 shows the dipole angular anisotropy parameter of $3d$-, $4p$-, and $4d$-electrons of Pd atom in RPAE. The cross-section is strongly deformed by effects of discrete transitions and intershell interaction.

Figure 2.324_Pd$^-$_b1 contains results of calculations for Pd$^-$ ion: $(Z = 46)\ 4s^2\ 4p^6 4d^{10} 5s^1 \uparrow$.

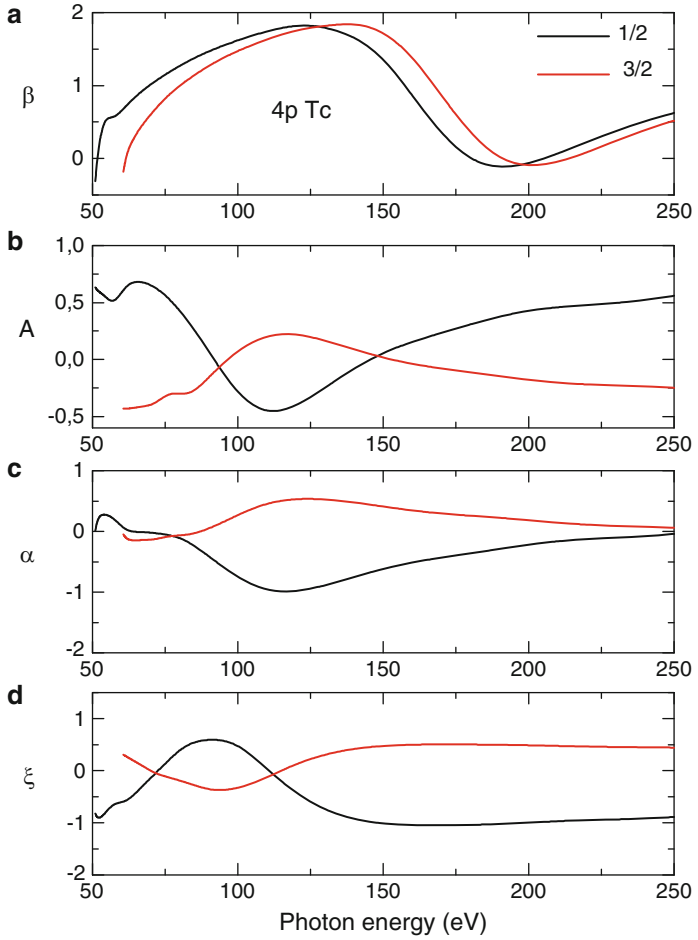

Fig. 2.320_Tc_f2 Dipole parameters of $4p$ "up" and "down"-electrons Tc atom: (**a**) angular anisotropy $\beta_{4p}(\omega)$, (**b**) spin polarization $A_{4p}(\omega)$, (**c**) $\alpha_{4p}(\omega)$, and (**d**) $\xi_{4p}(\omega)$ (see [2.61])

Figure 2.324_Pd$^-$_b1 presents partial photodetachment cross-sections of Pd^- ion in HF-l, HF-v, and RPAE near threshold: partial photodetachment cross-section of outer $5s$-electron with and without account for interaction with $4d^{10}$-shell and partial photodetachment of $4d$-electrons in RPAE.

Figure 2.325_I_a1 contains results of calculations for I atom: $(Z = 53)$ $4s^2 4p^6 4d^{10} 5s^2\, 5p^5$.

Figure 2.325_I_a1 represents total photoionization cross-section of atom I in RPAEO. The symmetric *Giant resonance* is seen and contributions of terms ^2S, ^2P, ^2D forming it and their sum are submitted (see [2.72]).

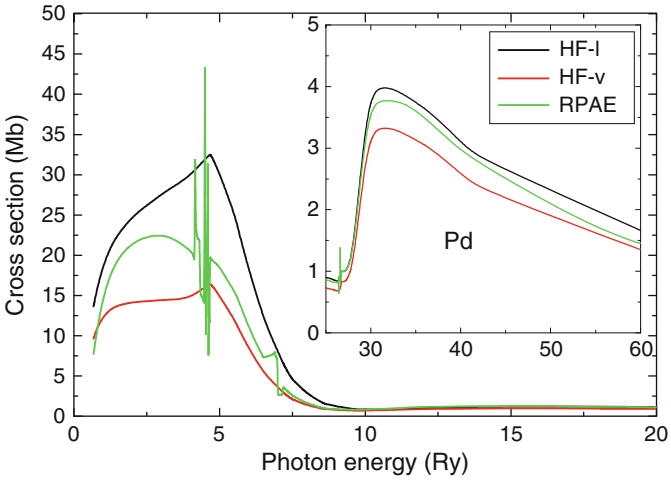

Fig. 2.321_Pd_a1 Total photoionization cross section of Pd atom in HF-l, HF-v, and RPAE

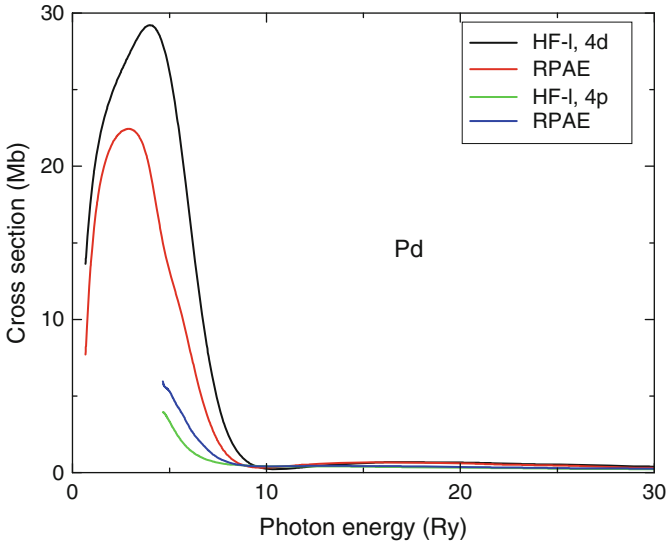

Fig. 2.322_Pd_b1 Photoionization cross section of $4p$- and $4d$-electrons for Pd atom in HF and RPAE

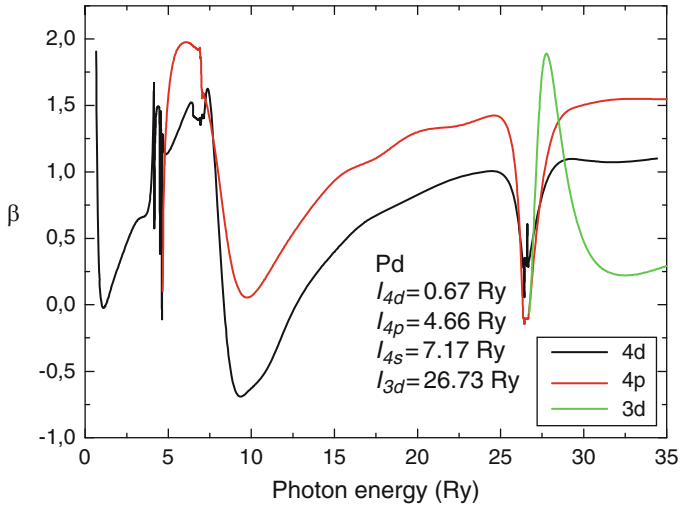

Fig. 2.323_Pd_d1 Dipole angular anisotropy parameter of $3d$-, $4d$-, $4p$-electrons for Pd atom

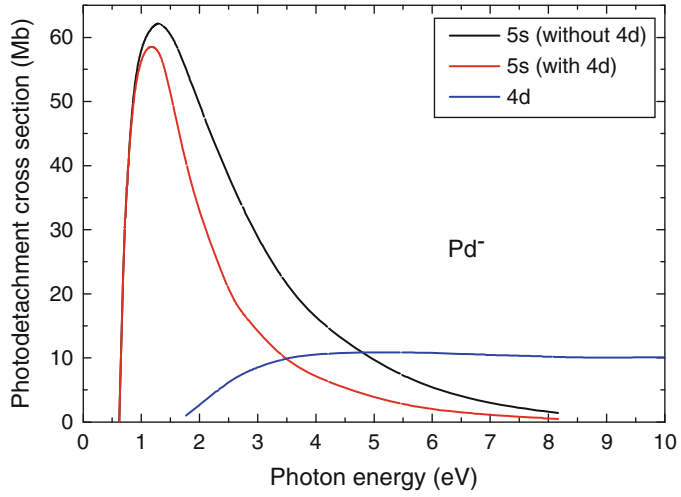

Fig. 2.324_Pd$^-$_b1 Partial photodetachment cross section of $5s$- and $4d$-electrons for Pd^- ion in HF-l, HF-v, and RPAE

Figures 2.326_I$^+$_a1–2.329_I$^+$_d1 (I^+) contain results of calculations for I^+ ion: $(Z = 53)\ 4s^2 4p^6 4d^{10} 5s^2 5p^4$.

Figure 2.326_I$^+$_a1 presents total photoionization cross-section of I^+ ion in RPAEO and in GRPAEO (see [2.72]). Experimental data are taken from [2.69]. Account for relaxation in GRPAEO improves agreement with experiment.

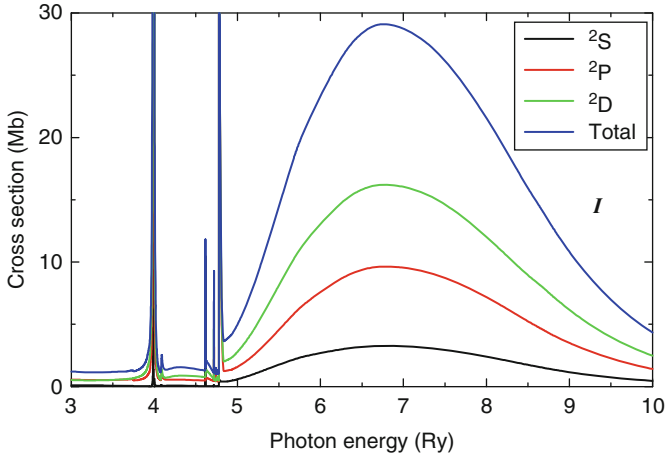

Fig. 2.325_I_a1 Total photoionization cross section and contribution of different terms into cross section of I atom in RPAEO (see [2.72])

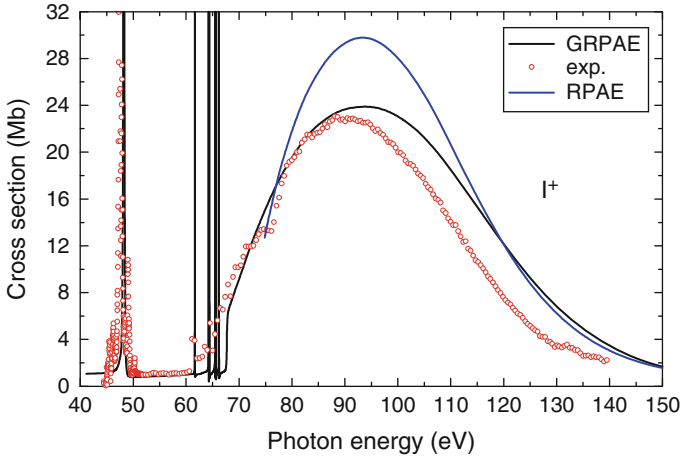

Fig. 2.326_I^+_a1 Total photoionization cross section of I^+ ion in RPAEO and GRPAEO (see [2.72]). Experiment is from [2.73]

Figure 2.327_I^+_a2 depicts the yield of double ions at photoabsorption by I^+ ion in RPAEO (see [2.72]). Experiment is from [2.73]. The maximum is seen at 80 eV which is qualitatively similar to that in Xe atom (see Fig. 2.57_Xe_b5).

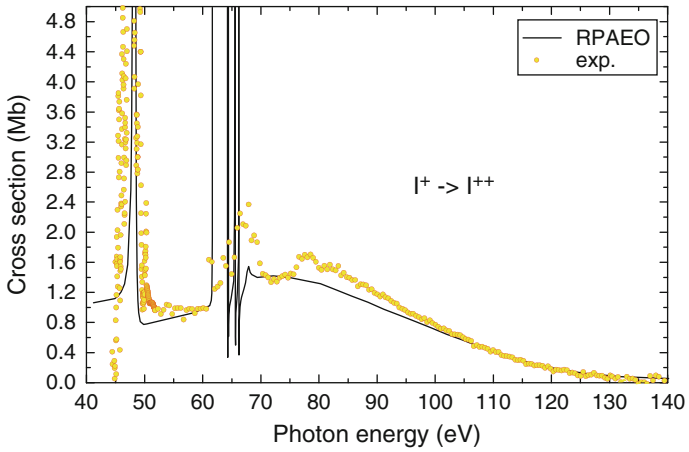

Fig. 2.327_I$^+$_a2 Cross-section of two-electron photoionization of I^+ ion in RPAEO. Experiment is from [2.73]

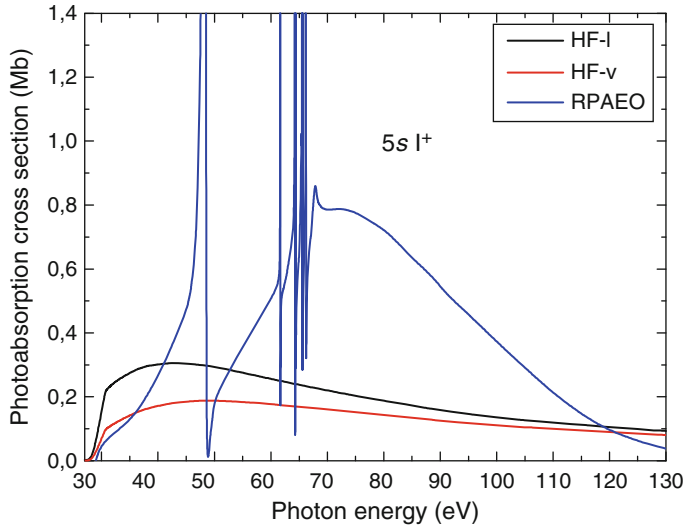

Fig. 2.328_I$^+$_b1 Interference resonance in photoionization cross section of 5*s*-electrons I^+ in HF-l, HF-v, and RPAEO

Figure 2.328_I$^+$_b1 presents photoionization cross-section of 5*s*-electrons of I^+ ion in the vicinity of the interference resonance in HF-l, HF-v, and RPAEO. The maximum is qualitatively similar to that taking place in photoionization cross-section of 5*s*-electrons for Xe (Fig. 2.54_Xe_b2) and is caused, as well as in Xe atom, by the influence of 4*d*-Giant resonance.

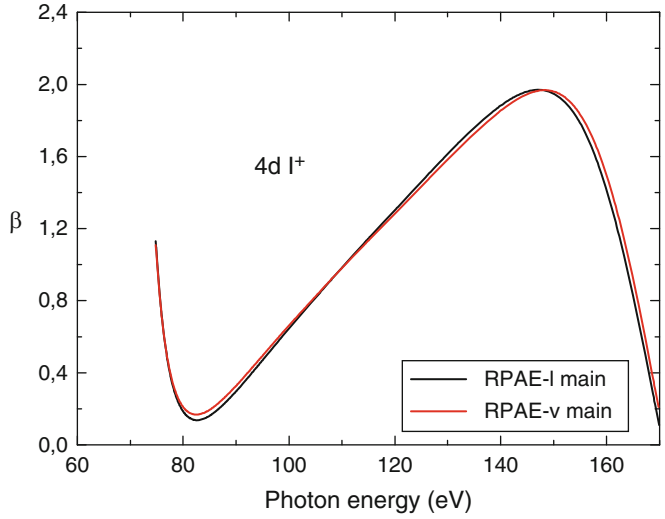

Fig. 2.329 I^+_d1 Dipole angular anisotropy parameter of $4d$-electrons for I^+ ion in RPAE (main term)

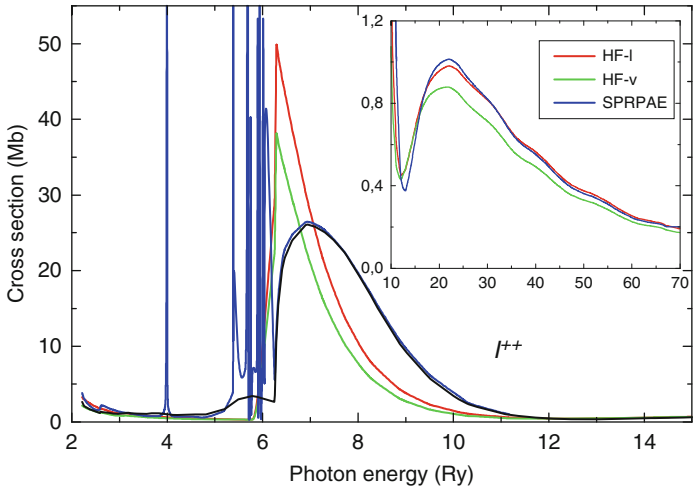

Fig. 2.330 I^{2+}_a1 Total photoionization cross section of I^{2+} ion in HF-l, HF-v, and SP RPAE (see [2.72])

Figure 2.329 I^+_d1 displays the dipole angular anisotropy parameter of $4d$-electrons for I^+ ion in RPAE in length and velocity forms. The curves are very close to each other.

Figures 2.330 I^{2+}_a1–2.333 I^{2+}_d1 (I^{2+}) contain results of calculations for I^{2+} ion: $(Z = 53)\ 4s^2 4p^6 4d^{10} 5s^2 5p^3 \uparrow$.

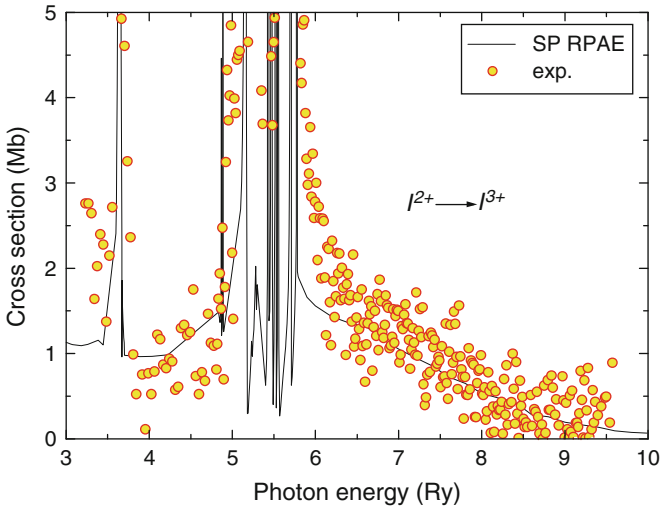

Fig. 2.331_I^{2+}_a2 Triple ions yield at photoabsorption by the I^{2+} ion in SP RPAE. Experiment is from [2.73]

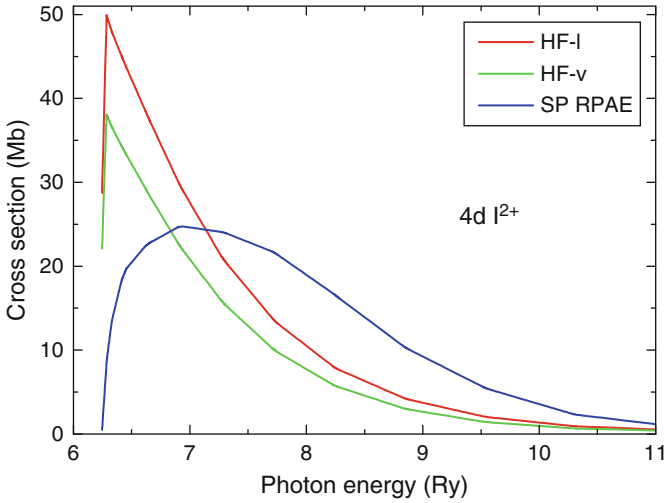

Fig. 2.332_I^{2+}_b1 Photoionization cross section of $4d$-electrons for I^{2+} ion in HF-l, HF-v, and SP RPAE

Figure 2.330_I^{2+}_a1 depicts total photoionization cross-section of I^{2+} ion in HF-l, HF-v, and SP RPAE. We see a strongly asymmetric Giant resonance of a $4d$-subshell and discrete level excitation with the large oscillator strength prior to this resonance (see [2.72]).

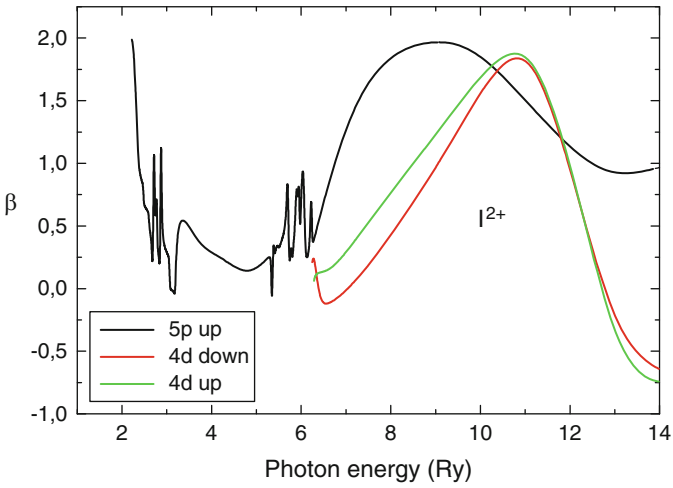

Fig. 2.333 I^{2+}_d1 Dipole angular anisotropy parameter of $4d$-, $5p$-electrons for I^{2+} ion in SP RPAE

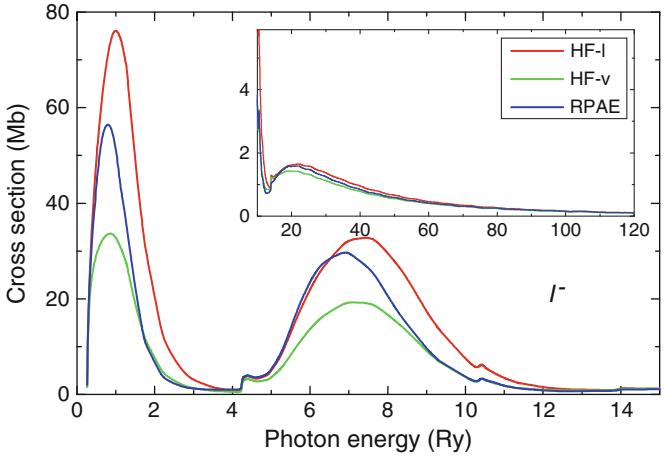

Fig. 2.334 I^{-}_a1 Total photoionization cross section of I^{-} ion in HF-l, HF-v, and RPAE (see [2.74])

Figure 2.331 I^{2+}_a2 displays a triple ions yield at photoabsorption by the I^{2+} ion in SP RPAE. Experiment is from [2.73]. Similarity of a situation for a double charged ion (Fig. 2.327 I^{+}_a2) is visible.

Figure 2.332 I^{2+}_b1 presents photoionization cross-section of $4d$-electrons for I^{2+} ion in HF-l, HF-v, and SP RPAE. It is remarkable that correlations remove a maximum at the threshold appearing in HF. This maximum is shifted significantly to higher energies. It is seen that the Giant resonance in continuous spectrum is strongly asymmetric. This asymmetry is bigger than that of I^{+} ion, shown in Fig. 2.326 I^{+}_a1.

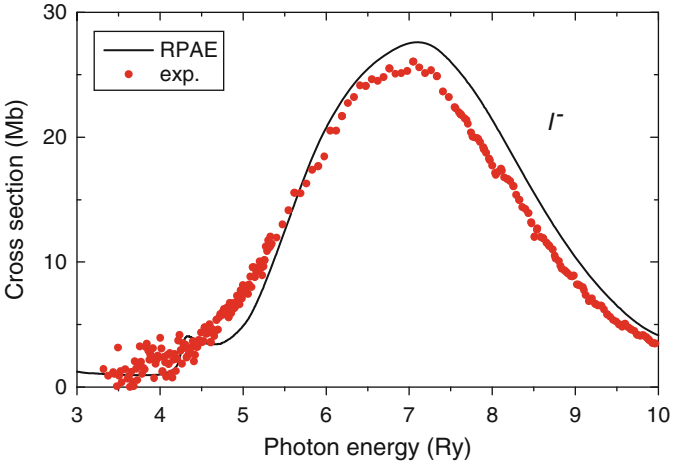

Fig. 2.335 I⁻_a2 Giant resonance in total photoionization cross section I^- ion (see [2.74]). Experiment seen in [2.74]

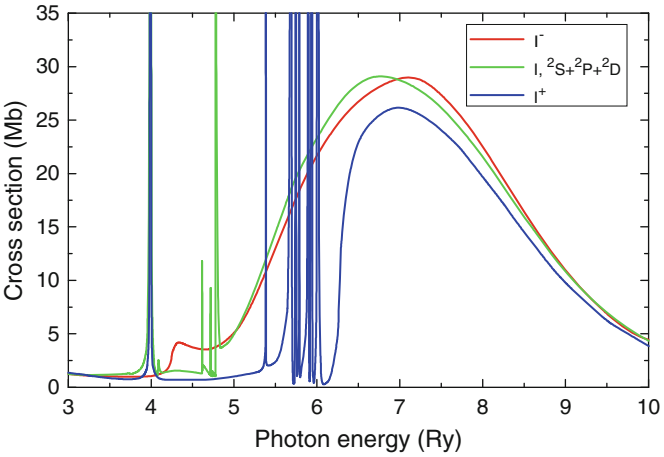

Fig. 2.336 I⁻I⁺I_a3 Total photoionization cross section in the vicinity of giant resonance for I^- ion (RPAE) in the comparison with the same for I atom (RPAEO) and I^+ ion (RPAEO) (see [2.72])

Figure 2.333 I^{2+}_d1 shows dipole angular anisotropy parameter of $4d$ "*up*" *and* "*down*"-, $5p$-"up"-electrons for I^{2+} ion.

Figures 2.334 I^-_a1–2.347 I^-_e6 (I^-) contain results of calculations for I^- ion: $(Z = 53)\ 4s^2, 4p^6, 4d^{10}, 5s^2, 5p^6$.

Figure 2.334 I^-_a1 presents total photoionization cross-section of I^- ion in HF-l, HF-v, and RPAE. Three maxima are visible, at 1, 7, and 20 Ry. A maximum at 7 Ry is the Giant resonance (see [2.74]).

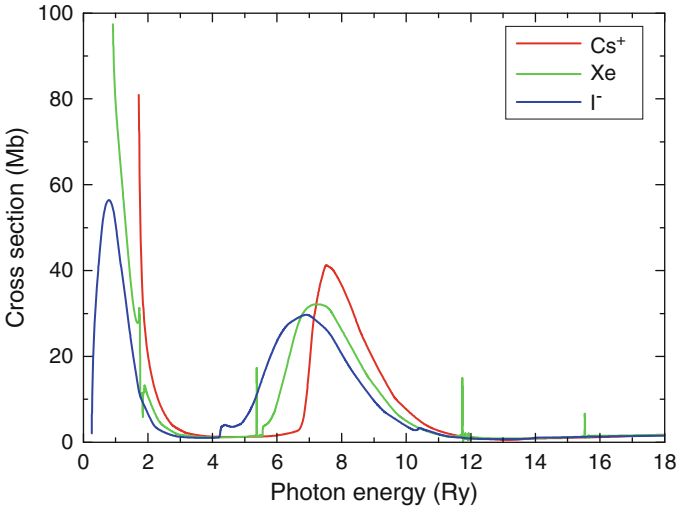

Fig. 2.337_I⁻XeCs⁺_a4 Photoionization cross section of I^- ion in comparison with the same for Xe atom and Cs^+ ion in RPAE

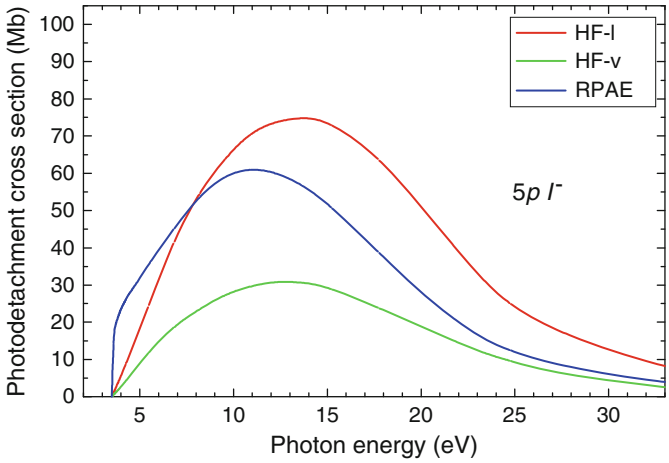

Fig. 2.338_I⁻_b1 Electron photodetachment cross section from $5p$-shell of I^- ion in HF-l, HF-v, and RPAE (see [2.74])

Figure 2.335_I⁻_a2 presents the Giant resonance in total photoionization cross-section of I^- ion in RPAE. Experiment can be found in [2.76].

Figure 2.336_I⁻I⁺I_a3 compares total photoionization cross-sections of I^- ion (in RPAE), I atom (in RPAEO) and I^+ ion (in RPAEO) in the vicinity of $4d$-Giant resonance (see [2.72]). The increase in contribution from discrete levels with decrease in number of electrons is seen.

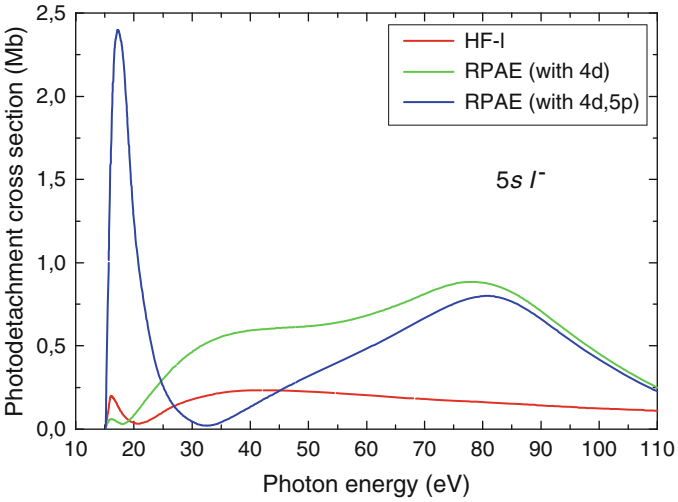

Fig. 2.339 I⁻_b2 Electron photodetachment cross section from $5s$-shell of I^- ion in HF-l, in RPAE (with the account $4d$-subshell and $4d$- and $5p$ electrons)

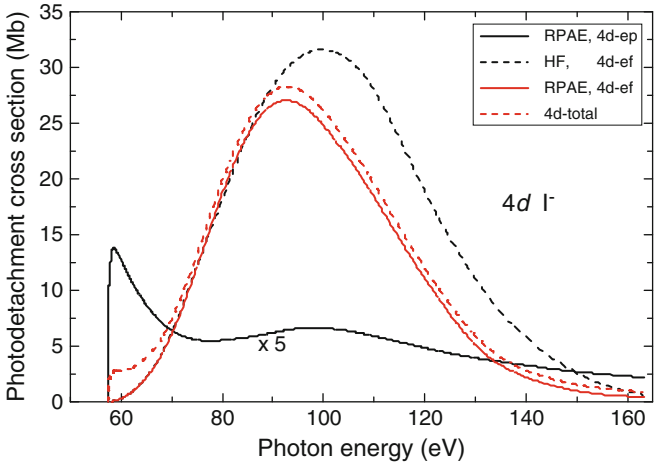

Fig. 2.340 I⁻_b3 $4d$-electron photodetachment cross section from I^- ion in HF (transition $4d–\varepsilon f$) and RPAE (transitions $4d–\varepsilon f$, εp and their sum)

Figure 2.337 I⁻XeCs⁺_a4 compares the photoionization cross-sections of I^- ion, Xe atom, and Cs^+ ion in RPAE. A trend of deformation of the first maximum and of the Giant resonance with increase in nucleus charge is seen. The cross-section for I^- is characterized by to rather broad maxima—the first at about 1 Ry and the second at about 7 Ry. The structure is considerably different even from that of Xe.

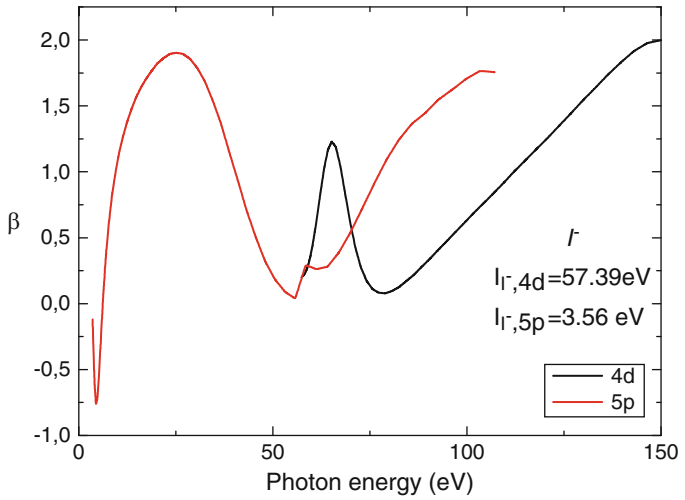

Fig. 2.341_I⁻_d1 Dipole angular anisotropy parameter of $4d$-, $5p$-electrons I^-, I—ionization potential of these shells

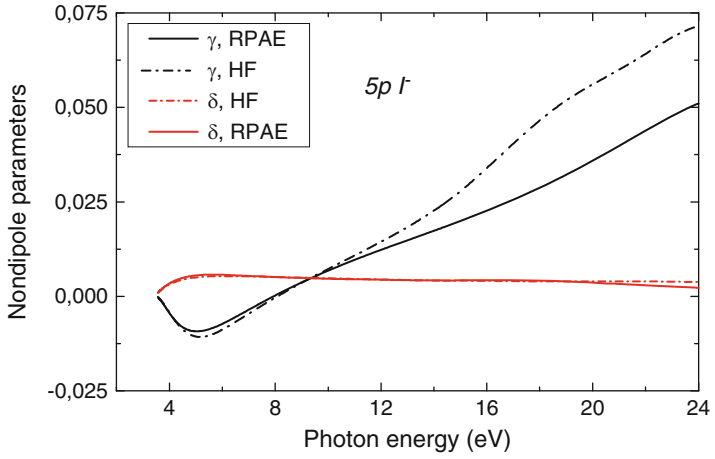

Fig. 2.342_I⁻_e1 Non-dipole angular anisotropy parameter of $5p$-electrons for I^- ion in near threshold field in HF and RPAE (see [2.76])

Figure 2.338_I⁻_b1 shows electron photodetachment cross-section from $5p$-shell of I^- ion in HF-l, HF-v, and RPAE. The role of electron correlations is big (see [2.72]).

Figure 2.339_I⁻_b2 depicts electron photodetachment cross-section from $5s$-shell of I^- ion in HF-l, in RPAE with the account of $4d$-subshell, in RPAE with

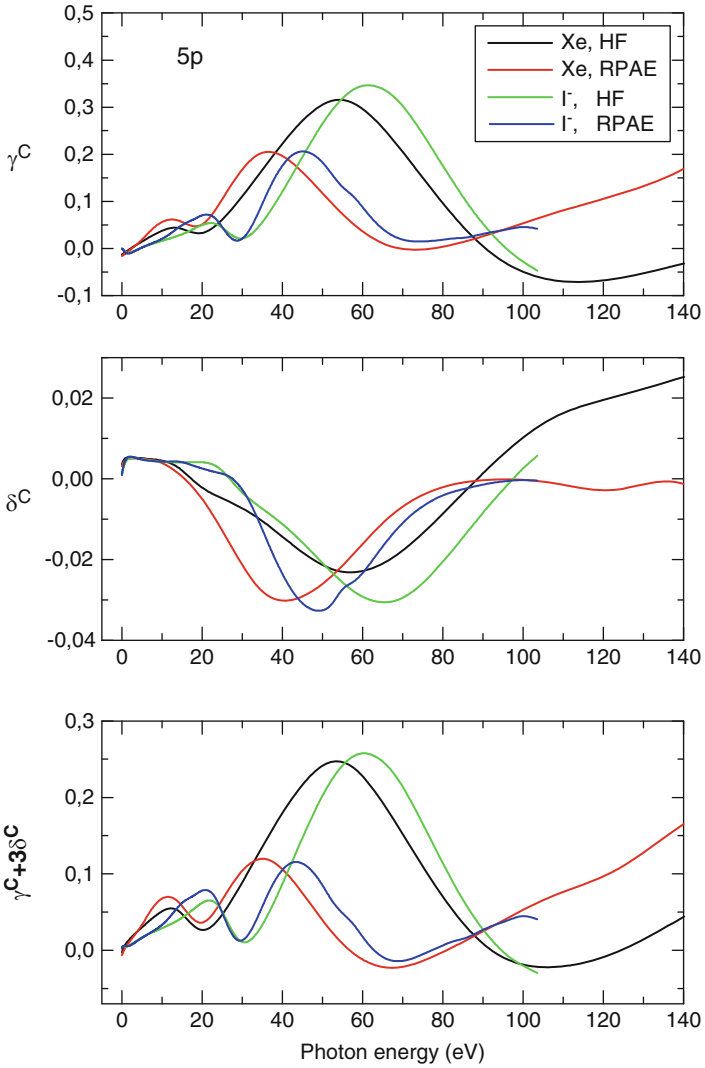

Fig. 2.343_I⁻_e2 Non-dipole angular anisotropy parameters and their magic combination of $5p$-electrons for I^- ion in comparison with analog data for Xe atom in HF and RPAE (see [2.76])

account of $4d$- and $5p$ electrons. Just as for the case of Xe, a complete collectivization of $5s^2$ electrons takes place due to the influence of their "neighbors"—$5p^6$ and $4d^{10}$ electrons. Note an almost symmetric maximum just above threshold that is a result of the effect of $5p$-electrons upon $5s$ cross-section.

Figure 2.340_I⁻_b3 presents $4d$-electron photodetachment cross-section from I^- ion in HF (transition $4d–\varepsilon f$) and RPAE (transitions $4d–\varepsilon f$, εp and their sum)—Giant resonance. A noticeable feature is the trace of a jump near threshold.

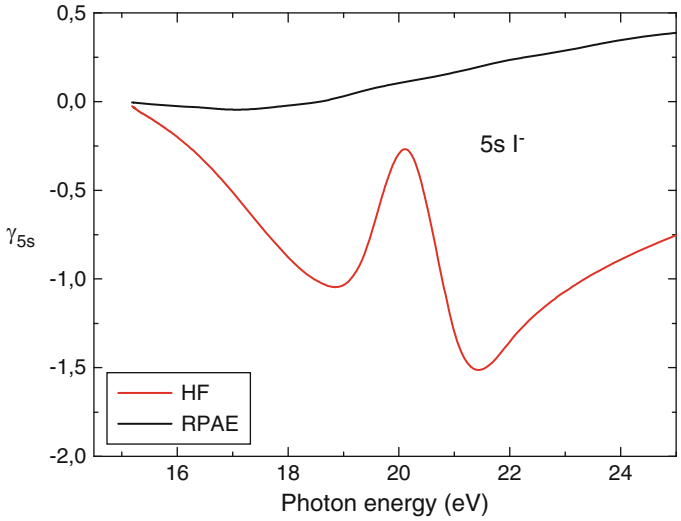

Fig. 2.344_I⁻_e3 Non-dipole angular anisotropy parameter of 5*s*-electrons for I^- ion in near threshold field in HF and RPAE

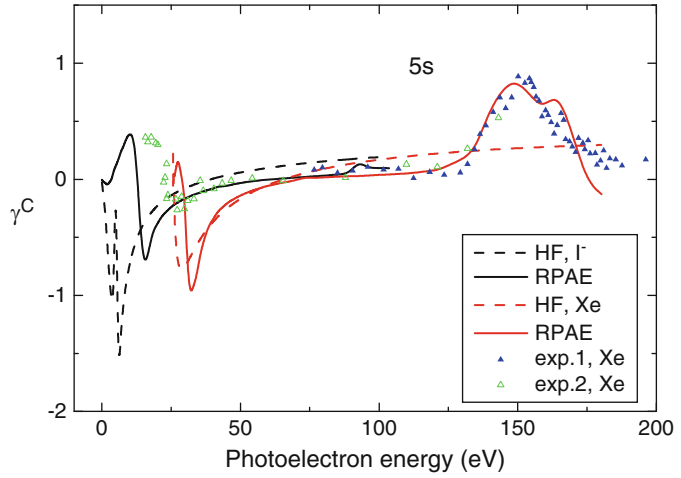

Fig. 2.345_I⁻_e4 Non-dipole angular anisotropy parameter of 5*s*-electrons for I^- in comparison with Xe atom in HF and RPAE (see [2.72, 2.33]). Experiment is from [2.33]

Figure 2.341_I⁻_d1 displays dipole angular anisotropy parameter of $4d$-, $5p$-electrons of I^- ion. A deep and narrow minimum of β_{5p} at threshold is remarkable, whereas β_{4d} has a maximum at threshold. A small maximum of β_{5p} at 67 eV is seen. Ionization potentials are equal $I_{4d} = 57.39$ eV and $I_{5p} = 3.56$ eV.

Figure 2.342_I⁻_e1 shows the non-dipole angular anisotropy parameters of $5p$-electrons for I^- ion in near threshold region in HF and RPAE. Small variations are steeply replaced by linear dependence (see [2.76]).

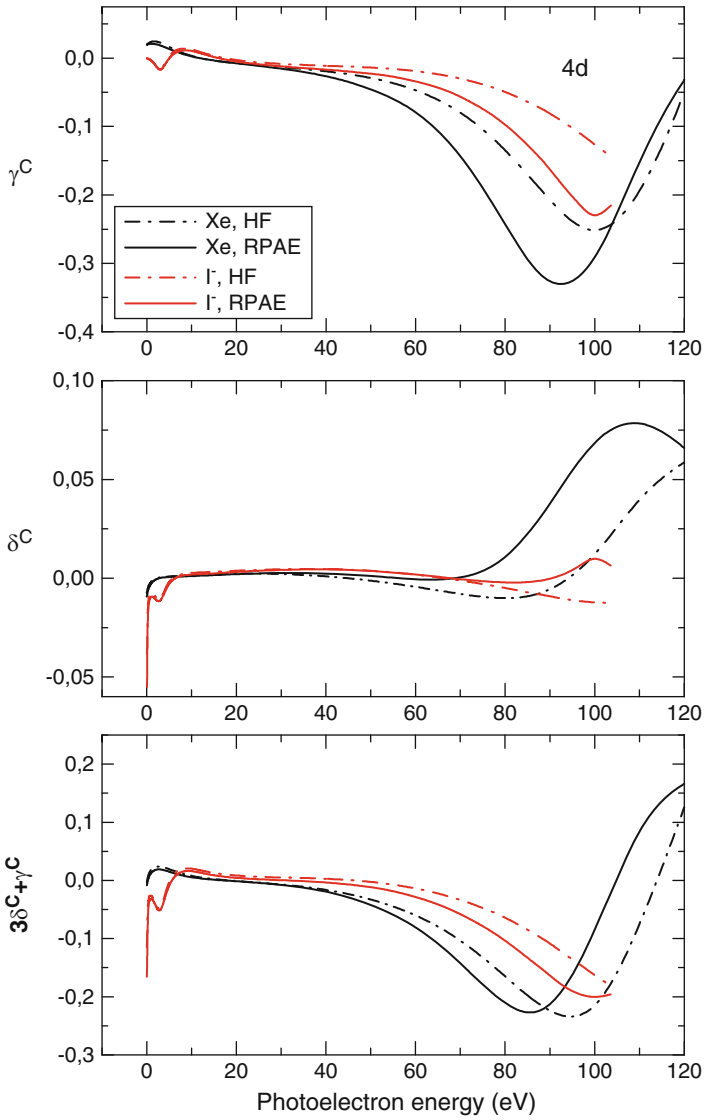

Fig. 2.346_I⁻_e5 Non-dipole angular anisotropy parameters and their magic combination of $4d$-electrons for I^- ion in comparison with analog data for Xe atom (see [2.10])

Figure 2.343_I⁻_e2 demonstrates the non-dipole angular anisotropy parameters γ^C and δ^C and their magic combination $(\gamma^C + 3\delta^C)$ of $5p$-electrons for I^- ion in comparison with similar data for Xe atom. Calculations are performed in HF and RPAE (see [2.76]).

Figure 2.344_I⁻_e3 depicts non-dipole angular anisotropy parameter γ^C of $5s$-electrons for I^- ion in near threshold region, calculated in HF and RPAE.

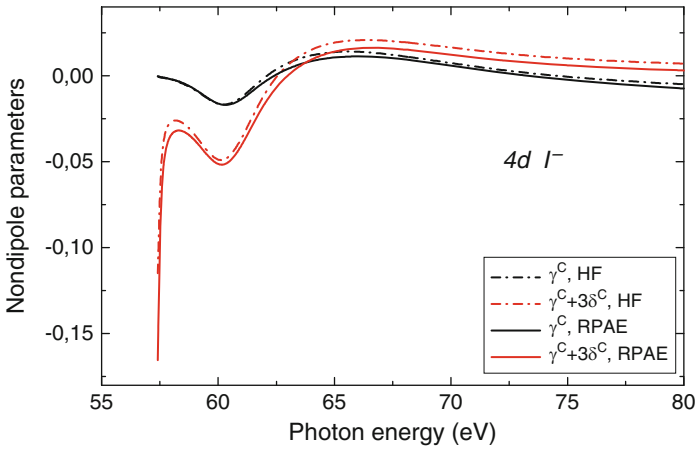

Fig. 2.347_I⁻_e6 Non-dipole angular anisotropy parameter γ^{C} and magic combination $(\gamma^{C} + 3\delta^{C})$ of $4d$-electrons for I^{-} ion in near threshold field for photon energy

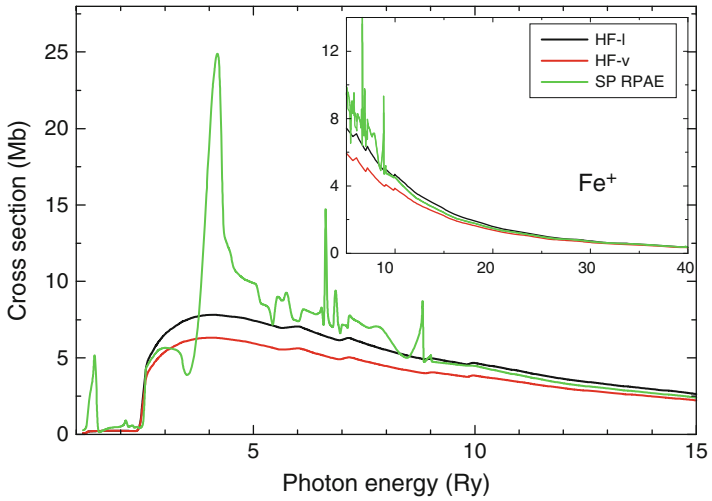

Fig. 2.348_Fe⁺_a1 Total photoionization cross section of Fe^{+} ion in HF-l, HF-v, and SP RPAE

Figure 2.345_I⁻_e4 shows the angular anisotropy parameter γ^{C} of $5s$-electrons of I^{-} ion in comparison with data for Xe atom [2.33, 2.76]. Experiment on Xe atom is from [2.33].

Figure 2.346_I⁻_e5 shows non-dipole angular anisotropy parameters γ^{C} and δ^{C} and their magic combination $(\gamma^{C} + 3\delta^{C})$ for $4d$-electrons of I^{-} ion in comparison with similar data for Xe atom (see [2.76]).

Figure 2.347_I⁻_e6 presents non-dipole angular anisotropy parameter γ^{C} and a magic combination $(\gamma^{C} + 3\delta^{C})$ of $4d$-electrons for I^{-} ion near-threshold photon energy region.

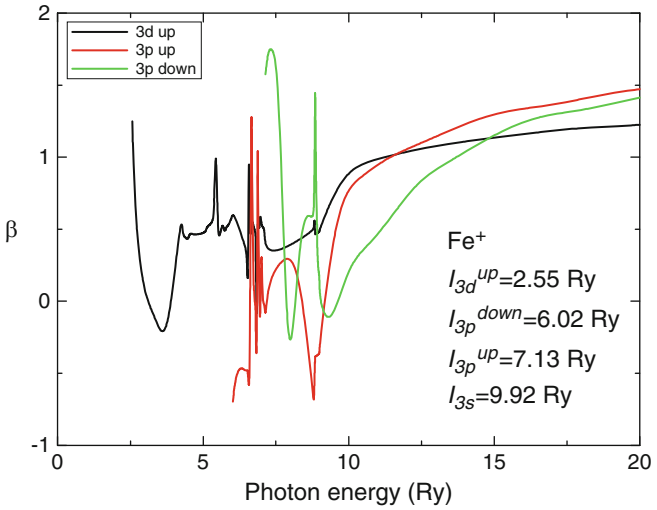

Fig. 2.349_Fe$^+$_d1 Dipole angular anisotropy parameter of $3d$ "up"-, $3p$ "up" and "down"-electrons for Fe^+ ion in SP RPAE

Figures 2.348_Fe$^+$_a1 and 2.349_Fe$^+$_d1 (Fe^+) contain results of calculations for Fe^+ ion: $(Z = 9)\ 1s^2 2s^2 2p^3 \uparrow$.

Figure 2.348_Fe$^+$_a1 shows the total photoionization cross-section of Fe^+ ion in HF-l, HF-v, and SP RPAE. The role of correlations is quite big. It gives a prominent narrow maximum at 1.3 Ry, and a high and narrow maximum at about 4.2 Ry with a subsequent rather complex structure. All this does not exist in HV, where the difference between results in length and velocity forms is not too big.

Figure 2.349_Fe$^+$_d1 shows the dipole angular anisotropy parameter of $3d$ "up"-, $3p$ "up" and "down"-electrons for Fe^+ ion in SP RPAE. All curves are quite complicated in the photon energy area between 3.7 and 10 Ry.

Table 2.8 includes calculated values of oscillator strengths in HF-l, HF-v, $f^{l,v}_{nl-n'l'}$, and $F^{l,v}_{nl-n'l'}$ in RPAE for several lowest discrete levels of excitation and for each considered subshell of some atoms, investigated in this section. The list of objects includes excited atom, open and closed shell atoms and one ion. Respective theoretical transition energies in RPAE $\tilde{\omega}_{nl-n'l'\uparrow(\downarrow)}$ are also given in this table.

The results for length and velocity forms in RPAE coincide with reasonable accuracy. The role of RPAE corrections for many levels is important. For F*, Cl(^2S), Cl(^2D), I(^2S) and I^{2+} is the outer electron lowest energy transition. In Mn is very big and in Tc dominates the transition to the semi-filled shell, $3p$–$3d\downarrow$ and $4p$–$4d\downarrow$, respectively. In Cl(^2P) most powerful is not the lowest level, but one of the levels with higher energy, $3p(^3P)$–$4d(^2P)$. In Mn dominates the $4s$–$4p\uparrow$ excitation. In I(^2D) the biggest is the transition from $4d$-subshell, $4d(^2D)$–$5p(^2D)$. In Pd most prominent is the outer electron transition with decreasing angular momentum, $4d$–$5p$. The oscillator strengths are, in general, decreasing with decrease in principal quantum number of the exited electron.

Table 2.8 Oscillator strengths and transition energies of VII and VIII group's elements and their ions

Transition	ω (Ry)	HF-l	HF-v	RPAE-l	RPAE-v
F*					
$3p$–$3d$ up	0.4978	0.2196E+01	0.1266E+01	0.1565E+01	0.1473E+01
$3p$–$4d$ up	0.5735	0.4933E+00	0.2664E+00	0.2381E+00	0.2226E+00
$3p$–$5d$ up	0.6061	0.1721E+00	0.8989E−01	0.6770E−01	0.6292E−01
$3p$–$4s$ up	0.4400	0.1934E+00	0.1998E+00	0.5814E+00	0.6369E+00
$3p$–$6s$ up	0.5590	0.3363E−01	0.3421E−01	0.3732E−01	0.4302E−01
$3p$–$7s$ up	0.6001	0.1259E−01	0.1274E−01	0.8904E−02	0.1060E−01
$3s$–$4p$ up	0.9764	0.8415E−02	0.8630E−02	0.2175E−02	0.4694E−02
$3s$–$5p$ up	1.0506	0.3597E−02	0.3237E−02	0.1331E−02	0.2190E−02
$3s$–$6p$ up	1.0805	0.1793E−02	0.1561E−02	0.1149E−02	0.1487E−02
$2p$–$3d$ up	5.7426	0.6236E+00	0.5470E+00	0.6516E+00	0.6605E+00
$2p$–$4d$ up	6.0718	0.2729E−01	0.2406E−01	0.2406E−01	0.2404E−01
$2p$–$5d$ up	6.1150	0.1278E−01	0.1127E−01	0.1121E−01	0.1120E−01
$2p$–$4s$ up	5.8993	0.1433E−01	0.1595E−01	0.7918E−02	0.1050E−01
$2p$–$5s$ up	6.0630	0.2160E−02	0.2395E−02	0.7002E−02	0.7931E−02
$2p$–$6s$ up	6.1112	0.8337E−03	0.9237E−03	0.2697E−02	0.3053E−02
$2s$–$4p$ up	7.5224	0.8588E−01	0.7948E−01	0.4724E−01	0.4598E−01
$2s$–$5p$ up	7.6376	0.1332E−01	0.1240E−01	0.7908E−02	0.7731E−02
$2s$–$6p$ up	7.6745	0.5424E−02	0.5055E−02	0.3309E−02	0.3242E−02
Cl(^2S)					
$3p(^1S)$–$4s(^2S)$	0.72063	0.20401E−01	0.20366E−01	0.34150E−01	0.61839E−01
$3p(^1S)$–$5s(^2S)$	0.89384	0.33399E−02	0.33301E−02	0.17445E−02	0.38928E−02
$3p(^1S)$–$6s(^2S)$	0.94723	0.12008E−02	0.11970E−02	0.13766E−02	0.26388E−02
$3p(^1D)$–$3d(^2S)$	0.87667	0.43596E−01	0.37253E−01	0.26079E−01	0.36109E−01
$3p(^1D)$–$4d(^2S)$	0.93549	0.20784E−01	0.17652E−01	0.41035E−02	0.57614E−02
$3p(^1D)$–$5d(^2S)$	0.96463	0.10757E−01	0.91106E−02	0.15325E−03	0.22833E−03
$3s(^2S)$–$3p(^2S)$	1.00307	0.22804E+00	0.14473E+00	0.64000E−02	0.79778E−02
$3s(^2S)$–$4p(^2S)$	1.96543	0.97385E−04	0.16151E−04	0.65805E−06	0.27109E−03
$3s(^2S)$–$5p(^2S)$	2.05867	0.58900E−04	0.17178E−04	0.81594E−05	0.43767E−04
Cl(^2P)					
$3p(^3P)$–$4s(^2P)$	0.74335	0.16421E+00	0.13961E+00	0.15641E+00	0.21127E+00
$3p(^3P)$–$5s(^2P)$	0.89763	0.31860E−01	0.26851E−01	0.78424E−02	0.18308E−01
$3p(^3P)$–$6s(^2P)$	0.94941	0.11908E−01	0.10014E−01	0.24524E−01	0.23385E−01
$3p(^3P)$–$3d(^2P)$	0.90079	0.42166E−01	0.29962E−01	0.71794E−01	0.56131E−01
$3p(^3P)$–$4d(^2P)$	0.94895	0.23514E−01	0.16541E−01	0.19264E+00	0.31091E+00
$3p(^3P)$–$5d(^2P)$	0.97060	0.13271E−01	0.92929E−02	0.17588E−02	0.23045E−04
$3p(^1D)$–$3d(^2P)$	0.86714	0.93403E−01	0.79750E−01	0.16931E−01	0.14861E−01
$3p(^1D)$–$4d(^2P)$	0.93301	0.47327E−01	0.40207E−01	0.22593E−02	0.10155E−02
$3p(^1D)$–$5d(^2P)$	0.96434	0.24995E−01	0.21186E−01	0.16744E−03	0.48845E−04
$3s(^2P)$–$3p(^2P)$	0.99916	0.66680E+00	0.38312E+00	0.37652E−01	0.94963E−01
$3s(^2P)$–$4p(^2P)$	1.97603	0.34441E−03	0.12646E−03	0.29019E−02	0.35184E−02
$3s(^2P)$–$5p(^2P)$	2.06162	0.19334E−03	0.86181E−04	0.66444E−03	0.86019E−03
Cl(^2D)					
$3p(^1D)$–$4s(^2D)$	0.72266	0.10200E+00	0.10183E+00	0.11316E+00	0.16509E+00
$3p(^1D)$–$5s(^2D)$	0.89457	0.16699E−01	0.16650E−01	0.17249E−01	0.29180E−01
$3p(^1D)$–$6s(^2D)$	0.94753	0.60040E−02	0.59851E−02	0.72237E−02	0.11579E−01

Table 2.8 (Continued)

$3p(^1S)$–$3d(^2D)$)	0.89335	0.61414E−01	0.58215E−01	0.18410E−01	0.17954E−01
$3p(^1S)$–$4d(^2D)$	0.94411	0.30898E−01	0.29307E−01	0.28851E−02	0.30537E−02
$3p(^1S)$–$5d(^2D)$	0.96903	0.15506E−01	0.14714E−01	0.62238E−03	0.73517E−03
$3p(^3P)$–$3d(^2D)$	0.89457	0.11572E+00	0.76043E−01	0.19983E−01	0.33852E−01
$3p(^3P)$–$4d(^2D)$	0.95345	0.57779E−01	0.37393E−01	0.35045E−01	0.31528E−01
$3p(^3P)$–$5d(^2D)$	0.97565	0.31321E−01	0.20131E−01	0.38588E−01	0.32116E−01
$3p(^1D)$–$3d(^2D)$	0.89454	0.71692E−01	0.62093E−01	0.70793E−01	0.11515E+00
$3p(^1D)$–$4d(^2D)$	0.94412	0.39545E−01	0.34148E−01	0.30898E−02	0.32768E−02
$3p(^1D)$–$5d(^2D)$	0.96896	0.21392E−01	0.18448E−01	0.10483E−02	0.13291E−02
$3s(^2D)$–$4p(^2D)$	0.82253	0.10998E+01	0.62982E+00	0.32090E−01	0.47554E−02
$3s(^2D)$–$5p(^2D)$	1.96019	0.91639E−03	0.42421E−03	0.42367E−01	0.30667E−01
$3s(^2D)$–$6p(^2D)$	2.05696	0.46386E−03	0.24587E−03	0.12519E−01	0.86639E−02
Mn					
$4s$–$4p$ do	0.08490	0.9994E+00	0.9816E+00	0.3084E−01	0.3110E−01
$4s$–$5p$ do	0.34676	0.2047E−01	0.1945E−01	0.1714E+00	0.1711E+00
$4s$–$6p$ do	0.39056	0.3934E−02	0.3664E−02	0.1410E−01	0.1405E−01
$4s$–$4p$ up	0.28261	0.1000E+01	0.9911E+00	0.1485E+01	0.1483E+01
$4s$–$5p$ up	0.43010	0.1488E−01	0.1461E−01	0.3647E−01	0.3638E−01
$4s$–$6p$ up	0.48213	0.2779E−02	0.2718E−02	0.5276E−02	0.5241E−02
$3d$–$4f$ up	1.21877	0.9669E−03	0.7538E−03	0.9730E−03	0.9663E−03
$3d$–$5f$ up	1.24146	0.7948E−03	0.6207E−03	0.7535E−03	0.7468E−03
$3d$–$6f$ up	1.25380	0.5629E−03	0.4400E−03	0.5263E−03	0.5213E−03
$3d$–$4p$ up	0.78441	0.2977E+00	0.3363E+00	0.3772E+00	0.3947E+00
$3d$–$5p$ up	1.14557	0.1723E−01	0.1824E−01	0.1908E−01	0.2022E−01
$3d$–$6p$ up	1.21032	0.5978E−02	0.6276E−02	0.6184E−02	0.6571E−02
$3p$–$3d$ do	3.66052	0.2204E+01	0.1739E+01	0.1375E+01	0.1428E+01
$3p$–$4d$ do	4.34220	0.2463E−01	0.1975E−01	0.5037E−02	0.5234E−02
$3p$–$5d$ do	4.39714	0.9415E−02	0.7489E−02	0.1707E−02	0.1763E−02
$3p$–$5s$ do	4.21375	0.5543E−01	0.5251E−01	0.5283E−01	0.5619E−01
$3p$–$6s$ do	4.36774	0.5951E−02	0.5685E−02	0.6000E−02	0.6354E−02
$3p$–$7s$ do	4.40866	0.2393E−02	0.2290E−02	0.2421E−02	0.2561E−02
$3p$–$4d$ up	5.32658	0.2744E−01	0.1387E−01	0.6976E−01	0.5913E−01
$3p$–$5d$ up	5.38502	0.8244E−02	0.4070E−02	0.2490E−01	0.2103E−01
$3p$–$6d$ up	5.41125	0.3593E−02	0.1754E−02	0.1191E−01	0.1002E−01
$3p$–$5s$ up	5.21621	0.4926E−01	0.3781E−01	0.2859E−01	0.3079E−01
$3p$–$6s$ up	5.35714	0.6644E−02	0.5179E−02	0.3836E−02	0.4194E−02
$3p$–$7s$ up	5.39901	0.2622E−02	0.2052E−02	0.1510E−02	0.1655E−02
$3s$–$4p$ do	6.78557	0.1213E−01	0.1165E−01	0.1209E−01	0.1228E−01
$3s$–$5p$ do	7.09505	0.1665E−02	0.1546E−02	0.1573E−02	0.1610E−02
$3s$–$6p$ do	7.15560	0.6469E−03	0.5985E−03	0.6138E−03	0.6263E−03
$3s$–$4p$ up	7.53920	0.2084E−01	0.1721E−01	0.1205E−01	0.1043E−01
$3s$–$5p$ up	7.90724	0.2146E−02	0.1744E−02	0.1128E−02	0.1002E−02
$3s$–$6p$ up	7.97176	0.8133E−03	0.6600E−03	0.4340E−03	0.3862E−03
Tc					
$5s$–$5p$ do	0.06906	0.1023E+01	0.1229E+01	0.5796E−01	0.1320E+00
$5s$–$6p$ do	0.30559	0.1803E−01	0.2949E−01	0.1739E+00	0.2251E+00
$5s$–$7p$ do	0.34690	0.3283E−02	0.6378E−02	0.1213E−01	0.2018E−01
$5s$–$5p$ up	0.25344	0.1083E+01	0.1062E+01	0.1391E+01	0.1512E+01

Table 2.8 (Continued)

$5s$–$6p$ up	0.41380	0.1582E−01	0.1524E−01	0.4381E−02	0.3494E−02
$5s$–$7p$ up	0.46837	0.3175E−02	0.3041E−02	0.1675E−02	0.2067E−02
$4d$–$4f$ up	1.03336	0.4689E−02	0.3404E−02	0.5400E−02	0.5370E−02
$4d$–$5f$ up	1.05620	0.3833E−02	0.2783E−02	0.3790E−02	0.3811E−02
$4d$–$6f$ up	1.06863	0.2703E−02	0.1964E−02	0.2616E−02	0.2635E−02
$4d$–$5p$ up	0.66401	0.5409E+00	0.5472E+00	0.6518E+00	0.5879E+00
$4d$–$6p$ up	0.97037	0.3123E−01	0.2965E−01	0.2595E−01	0.2273E−01
$4d$–$7p$ up	1.02914	0.1108E−01	0.1043E−01	0.7405E−02	0.6384E−02
$4p$–$4d$ do	2.92316	0.2964E+01	0.2294E+01	0.4693E+01	0.4860E+01
$4p$–$5d$ do	3.61029	0.4177E−01	0.3327E−01	0.5272E−01	0.5087E−01
$4p$–$6d$ do	3.66498	0.1582E−01	0.1250E−01	0.1888E−01	0.1797E−01
$4p$–$6s$ do	3.50548	0.7520E−01	0.6901E−01	0.7440E−01	0.8823E−01
$4p$–$7s$ do	3.64022	0.8780E−02	0.8129E−02	0.9331E−02	0.1065E−01
$4p$–$8s$ do	3.67796	0.3591E−02	0.3330E−02	0.4004E−02	0.4530E−02
$4p$–$5d$ up	4.32267	0.6110E−01	0.3676E−01	0.1510E+00	0.1323E+00
$4p$–$6d$ up	4.37893	0.2004E−01	0.1205E−01	0.5724E−01	0.4920E−01
$4p$–$7d$ up	4.40391	0.9161E−02	0.5504E−02	0.2777E−01	0.2390E−01
$4p$–$6s$ up	4.23465	0.6300E−01	0.4549E−01	0.3982E−01	0.4121E−01
$4p$–$7s$ up	4.35401	0.1013E−01	0.7451E−02	0.5925E−02	0.6250E−02
$4p$–$8s$ up	4.39264	0.4066E−02	0.3006E−02	0.2278E−02	0.2417E−02
$4s$–$5p$ do	5.63721	0.5723E−02	0.6370E−02	0.6968E−03	0.5175E−03
$4s$–$6p$ do	5.91027	0.9135E−03	0.9382E−03	0.7354E−04	0.7917E−04
$4s$–$7p$ do	5.96623	0.3676E−03	0.3738E−03	0.5934E−05	0.1770E−04
$4s$–$5p$ up	6.11723	0.1482E−01	0.1128E−01	0.3500E−02	0.2608E−02
$4s$–$6p$ up	6.46086	0.1508E−02	0.1129E−02	0.3994E−03	0.3346E−03
$4s$–$7p$ up	6.52143	0.5823E−03	0.4361E−03	0.1637E−03	0.1379E−03
$I(^2S)$					
$5p(^1S)$–$6s(^2S)$	0.55036	0.27586E−01	0.27189E−01	0.59579E−01	0.11078E+00
$5p(^1S)$–$7s(^2S)$	0.69896	0.46759E−02	0.45959E−02	0.39406E−02	0.80635E−02
$5p(^1S)$–$8s(^2S)$	0.74567	0.17235E−02	0.16928E−02	0.11676E−01	0.18127E−01
$5p(^1D)$–$5d(^2S)$	0.65163	0.12379E+00	0.10168E+00	0.33934E−01	0.52539E−01
$5p(^1D)$–$6d(^2S)$	0.71979	0.40496E−01	0.32917E−01	0.51762E−02	0.56897E−02
$5p(^1D)$–$7d(^2S)$	0.76917	0.17940E−01	0.14519E−01	0.91336E−01	0.12353E+00
$5s(^2S)$–$5p(^2S)$	0.74584	0.29941E+00	0.17162E+00	0.28267E−02	0.45358E−02
$5s(^2S)$–$6p(^2S)$	1.47726	0.11836E−05	0.29203E−04	0.13725E−03	0.75792E−04
$5s(^2S)$–$7p(^2S)$	1.56075	0.88464E−05	0.10766E−05	0.95768E−04	0.10256E−04
$4d(^2S)$–$5p(^2S)$	3.99239	0.11688E+00	0.97801E−01	0.10434E+00	0.10347E+00
$4d(^2S)$–$6p(^2S)$	4.61519	0.84410E−02	0.74379E−02	0.68124E−02	0.69234E−02
$4d(^2S)$–$7p(^2S)$	4.71475	0.20387E−02	0.17985E−02	0.15729E−02	0.16007E−02
$4d(^2S)$–$4f(^2S)$	4.73863	0.55211E−04	0.32257E−04	0.52718E−04	0.52374E−04
$4d(^2S)$–$5f(^2S)$	4.76169	0.47999E−04	0.28176E−04	0.44469E−04	0.44252E−04
$4d(^2S)$–$6f(^2S)$	4.77419	0.35047E−04	0.20622E−04	0.31992E−04	0.31914E−04
$I(^2P)$					
$5p(^3P)$–$6s(^2P)$	0.57234	0.22176E+00	0.18829E+00	0.16315E+00	0.21784E+00
$5p(^3P)$–$7s(^2P)$	0.70316	0.45118E−01	0.38008E−01	0.36324E−01	0.41844E−01
$5p(^3P)$–$8s(^2P)$	0.74736	0.17306E−01	0.14552E−01	0.64140E−05	0.14892E−06
$5p(^3P)$–$5d(^2P)$	0.68712	0.12159E+00	0.79025E−01	0.18485E−01	0.25524E−04

Table 2.8 (Continued)

$5p(^3P)$–$6d(^2P)$	0.74746	0.62430E−01	0.40033E−01	0.15333E−02	0.21865E−02
$5p(^3P)$–$7d(^2P)$	0.77030	0.33364E−01	0.21264E−01	0.14037E+00	0.15812E+00
$5p(^1D)$–$5d(^2P)$	0.63733	0.27326E+00	0.22290E+00	0.51618E−01	0.45805E−01
$5p(^1D)$–$6d(^2P)$	0.72832	0.94796E−01	0.76652E−01	0.35596E−01	0.72763E−01
$5p(^1D)$–$7d(^2P)$	0.75870	0.42343E−01	0.34112E−01	0.14270E−01	0.21068E−01
$5s(^2P)$–$5p(^2P)$	0.68712	0.89797E+00	0.49433E+00	0.18571E−01	0.25842E−04
$5s(^2P)$–$6p(^2P)$	1.49219	0.32706E−05	0.48621E−04	0.13024E−02	0.18683E−02
$5s(^2P)$–$7p(^2P)$	1.56527	0.19794E−04	0.15459E−05	0.25988E−03	0.43939E−03
$4d(^2P)$–$5p(^2P)$	3.99310	0.34921E+00	0.29141E+00	0.33133E+00	0.32775E+00
$4d(^2P)$–$6p(^2P)$	4.61994	0.23697E−01	0.20746E−01	0.21246E−01	0.20786E−01
$4d(^2P)$–$7p(^2P)$	4.71591	0.59725E−02	0.52332E−02	0.51536E−02	0.50549E−02
$4d(^2P)$–$4f(^2P)$	4.74002	0.91213E−04	0.50704E−04	0.83507E−04	0.82237E−04
$4d(^2P)$–$5f(^2P)$	4.76242	0.80014E−04	0.44711E−04	0.71167E−04	0.70143E−04
$4d(^2P)$–$6f(^2P)$	4.77462	0.58804E−04	0.32949E−04	0.51507E−04	0.50912E−04
$I(^2D)$					
$5p(^1D)$–$6s(^2D)$	0.55340	0.13793E+00	0.13594E+00	0.14123E+00	0.17829E+00
$5p(^1D)$–$7s(^2D)$	0.69954	0.23379E−01	0.22979E−01	0.17940E−01	0.30954E−01
$5p(^1D)$–$8s(^2D)$	0.74618	0.86173E−02	0.84638E−02	0.10404E−01	0.17597E−01
$5p(^1S)$–$5d(^2D)$	0.66689	0.16423E+00	0.14945E+00	0.55167E−02	0.93164E−03
$5p(^1S)$–$6d(^2D)$	0.73094	0.44202E−01	0.40120E−01	0.79285E−03	0.10724E−02
$5p(^1S)$–$7d(^2D)$	0.75989	0.17830E−01	0.16168E−01	0.74842E−04	0.16148E−03
$5p(^3P)$–$5d(^2D)$	0.67959	0.30584E+00	0.18100E+00	0.59750E−01	0.18670E−02
$5p(^3P)$–$6d(^2D)$	0.74824	0.14046E+00	0.81377E−01	0.19718E+00	0.22162E+00
$5p(^3P)$–$7d(^2D)$	0.76971	0.73454E−01	0.42164E−01	0.20016E+00	0.19500E+00
$5p(^1D)$–$5d(^2D)$	0.67959	0.21603E+00	0.17749E+00	0.59533E−01	0.18602E−02
$5p(^1D)$–$6d(^2D)$	0.73094	0.79269E−01	0.64734E−01	0.80371E−03	0.10868E−02
$5p(^1D)$–$7d(^2D)$	0.75991	0.35221E−01	0.28688E−01	0.92346E−04	0.19019E−03
$5s(^2D)$–$5p(^2D)$	0.67959	0.14897E+01	0.82277E+00	0.59205E−01	0.18510E−02
$5s(^2D)$–$6p(^2D)$	1.48050	0.32441E−04	0.51323E−04	0.31731E−02	0.52373E−02
$5s(^2D)$–$7p(^2D)$	1.56155	0.70901E−04	0.26512E−06	0.48647E−03	0.10499E−02
$4d(^2D)$–$5p(^2D)$	3.99389	0.56644E+00	0.46685E+00	0.55420E+00	0.54413E+00
$4d(^2D)$–$6p(^2D)$	4.62390	0.35778E−01	0.31067E−01	0.30968E−01	0.31626E−01
$4d(^2D)$–$7p(^2D)$	4.71685	0.95922E−02	0.83388E−02	0.79598E−02	0.81586E−02
$4d(^2D)$–$4f(^2D)$	4.73940	0.19032E−03	0.10740E−03	0.17637E−03	0.17863E−03
$4d(^2D)$–$5f(^2D)$	4.76210	0.16592E−03	0.94108E−04	0.14923E−03	0.15103E−03
$4d(^2D)$–$6f(^2D)$	4.77443	0.12145E−03	0.69070E−04	0.10768E−03	0.10918E−03
I^{2+}					
$5p$–$6s$ up	1.14022	0.3741E+00	0.3437E+00	0.2231E+01	0.2408E+01
$5p$–$7s$ up	1.63991	0.6504E−01	0.5973E−01	0.1233E−01	0.7611E−02
$5p$–$8s$ up	1.85034	0.2493E−01	0.2293E−01	0.8096E−01	0.7570E−01
$5p$–$5d$ up	1.16630	0.3749E+01	0.2576E+01	0.1880E+01	0.2180E+01
$5p$–$6d$ up	1.63991	0.3268E+00	0.2048E+00	0.1044E−01	0.6519E−02
$5p$–$7d$ up	1.85399	0.9432E−01	0.5697E−01	0.3886E−01	0.3366E−01
$5s$–$5p$ do	0.56943	0.1747E+01	0.2677E+01	0.2881E+00	0.7196E+00
$5s$–$6p$ do	1.77452	0.1652E+00	0.6396E−01	0.2402E+00	0.1204E+00
$5s$–$7p$ do	2.11989	0.4997E−01	0.1511E−01	0.5608E−01	0.1927E−01
$5s$–$6p$ up	2.32533	0.1199E−01	0.6988E−02	0.2132E−02	0.2471E−02

Table 2.8 (Continued)

$5s$–$7p$ up	2.69847	0.5608E−02	0.3444E−02	0.2261E−02	0.2525E−02
$5s$–$8p$ up	2.87056	0.2954E−02	0.1847E−02	0.1505E−02	0.1681E−02
$4d$–$5p$ do	4.00254	0.2673E+00	0.4879E+00	0.3560E+00	0.6750E+00
$4d$–$6p$ do	5.37966	0.4533E−01	0.5903E−01	0.9857E−01	0.1223E+00
$4d$–$7p$ do	5.74633	0.1877E−01	0.2283E−01	0.2344E−01	0.3056E−01
$4d$–$4f$ do	5.64677	0.6762E+00	0.5256E+00	0.6437E+00	0.6233E+00
$4d$–$5f$ do	5.87014	0.5870E+00	0.4542E+00	0.5130E+00	0.4945E+00
$4d$–$6f$ do	5.93696	0.3721E+00	0.2870E+00	0.7552E−01	0.7347E−01
$4d$–$6p$ up	5.35572	0.7734E−01	0.6932E−01	0.2349E−02	0.8625E−03
$4d$–$7p$ up	5.77076	0.2322E−01	0.2083E−01	0.2899E−01	0.3001E−01
$4d$–$8p$ up	5.95248	0.1087E−01	0.9755E−02	0.1145E−01	0.1134E−01
$4d$–$4f$ up	5.64674	0.1246E+01	0.9199E+00	0.6442E+00	0.6237E+00
$4d$–$5f$ up	5.87005	0.6190E+00	0.4622E+00	0.5192E+00	0.5004E+00
$4d$–$6f$ up	6.00259	0.3274E+00	0.2455E+00	0.5818E+00	0.5604E+00
Pd					
$4d$–$4f$	0.60897	0.7195E−02	0.5144E−02	0.4546E−02	0.4593E−02
$4d$–$5f$	0.63178	0.5416E−02	0.3844E−02	0.5774E−02	0.5803E−02
$4d$–$6f$	0.64410	0.3670E−02	0.2595E−02	0.3732E−02	0.3752E−02
$4d$–$5p$	0.42869	0.5111E+00	0.3733E+00	0.3436E+00	0.3396E+00
$4d$–$6p$	0.56490	0.9985E−01	0.7150E−01	0.4663E−01	0.4602E−01
$4d$–$7p$	0.61157	0.3792E−01	0.2704E−01	0.1788E−01	0.1766E−01
$4p$–$5s$	4.15283	0.2928E+00	0.1959E+00	0.2424E+00	0.2390E+00
$4p$–$6s$	4.50049	0.3140E−01	0.2273E−01	0.3110E−01	0.3083E−01
$4p$–$7s$	4.57943	0.1056E−01	0.7727E−02	0.1025E−01	0.1014E−01
$4p$–$5d$	4.55043	0.1674E−01	0.1298E−01	0.3093E−01	0.3229E−01
$4p$–$6d$	4.59864	0.7650E−02	0.5963E−02	0.1399E−01	0.1445E−01
$4p$–$7d$	4.62077	0.4015E−02	0.3136E−02	0.7320E−02	0.7515E−02
$4s$–$5p$	6.90800	0.1139E−01	0.7294E−02	0.1859E−02	0.1702E−02
$4s$–$6p$	7.06309	0.2543E−02	0.1664E−02	0.4002E−03	0.3920E−03
$4s$–$7p$	7.11247	0.1031E−02	0.6786E−03	0.1697E−03	0.1661E−03
$3d$–$4f$	26.66431	0.2264E−05	0.1868E−05	0.2031E−05	0.1945E−05
$3d$–$5f$	26.68683	0.1965E−05	0.1621E−05	0.1811E−05	0.1734E−05
$3d$–$6f$	26.69907	0.1435E−05	0.1184E−05	0.1327E−05	0.1270E−05
$3d$–$5p$	26.43173	0.1110E−01	0.1031E−01	0.1304E−01	0.1286E−01
$3d$–$6p$	26.60969	0.2032E−02	0.1889E−02	0.2393E−02	0.2359E−02
$3d$–$7p$	26.66243	0.7907E−03	0.7351E−03	0.9315E−03	0.9181E−03

2.10 Endohedral A@C_{60} Atoms and Ions

In this section we present our results for photoionization cross-sections, dipole and nondipole parameters of angular anisotropy of outer and intermediate subshells of some endohedral atoms A@C_{60} that means an atom A, stuffed inside a fullerenes shell. If reflection is considered as weak, the result is denoted as RPAE or GRPAE, the latter is if the atom A is calculated in GRPAE frame. If the polarization in this case is taken into account, the corresponding value is obtained in G-RPAE (or G-GRPAE). If the reflection is strong and C_{60} potential is approximated by a zero thickness potential, the results are obtained in FRPAE. Inclusion of polarization of C_{60} is denoted as GFRPAE. For finite thickness fullerenes shell potential, we have WRPAE and GWRPAE, respectively (see Sections 1.13 and 1.14).

Having in mind to illustrate qualitatively the effect of the fullerenes shell C_N upon the photoionization of the atom A, we choose the best studied and in this sense most popular fullerene C_{60}. It consist of 60 carbon atom with totally 240 electrons (four from each atom) being collectivized. The data are obtained for the following endohedral atoms Ne@$C_{60}2s^22p^6$; Ar@$C_{60}3s^23p^6$; Kr@$C_{60}4s^24p^6$; Xe@$C_{60}4d^{10}5s^25p^6$; Cs@$C_{60}4d^{10}5s^25p^66s$; Ba@$C_{60}4d^{10}5s^25p^66s^2$; La@$C_{60}4d^{10}5s^25p^65d6s^2$; Eu@$C_{60}4d^{10}5s^25p^64f^76s^2$; Na^+@$C_{60}2s^22p^6$; K^+@C_{60} $3s^23p^6$; Rb^+@$C_{60}3d^{10}4s^24p^6$; Cs^+@$C_{60}4d^{10}5s^25p^6$; Ce^+@$C_{60}4d^{10}4f5s^25p^66s^2$; Ce^{3+}@$C_{60}4d^{10}4f^15s^25p^6$; Ce^{4+}@$C_{60}4d^{10}5s^25p^6$; F^-@$C_{60}2s^22p^6$; Cl^-@$C_{60}3s^23p^6$; Br^-@$C_{60}4s^24p^6$; I^-@$C_{60}4d^{10}5s^25p^6$. Formulas used to receive the data, are mentioned at the beginning of this chapter, in Sect. 2.1.

Figures 2.350_C_{60}_g1 and 2.351_C_{60}_g2 (C_{60}) contain results of calculations for C_{60}.

Figure 2.350_C_{60}_g1 shows the absolute value of the amplitude $|G(\omega)|$ of the electromagnetic radiation polarization factor by the C_{60} electron shell, the polarization factor $S(\omega) = |G(\omega)|^2$ and the phase $\eta^d \equiv \arg G(\omega)$. The arrows mark the thresholds of outer *np* subshells of noble gas atoms. Quite peculiar is the "camel"-type shape. This is a direct consequence of the frequency-dependence of the C_{60} polarizability.

Figure 2.351_C_{60}_g2 shows the same as in Fig. 2.350_C_{60}_g1 polarization factor of the electromagnetic radiation by the electron shell of C_{60} $S(\omega) \equiv |G(\omega)|^2$. The arrows mark the thresholds of outer *ns* subshells.

Figures 2.352_Ne@C_{60}_a1–2.360_Ne@C_{60}_e3 (Ne@C_{60}) contain results of calculations for Ne@C_{60}.

Figure 2.352_Ne@C_{60}_a1 shows total photoionization cross-section of Ne free atom in RPAE and Ne@C_{60} in FRPAE, WRPAE, and GWRPAE. We see a series of resonances caused by reflection of the photoelectron wave off the Ne atom. These are called *confinement resonances*. It is natural that for finite thickness of the potential of the fullerenes shell the amplitudes of confinement resonances are smaller than for the zero-thickness (1.105). In GWRPAE the cross-section is considerably enhanced in comparison to WRPAE.

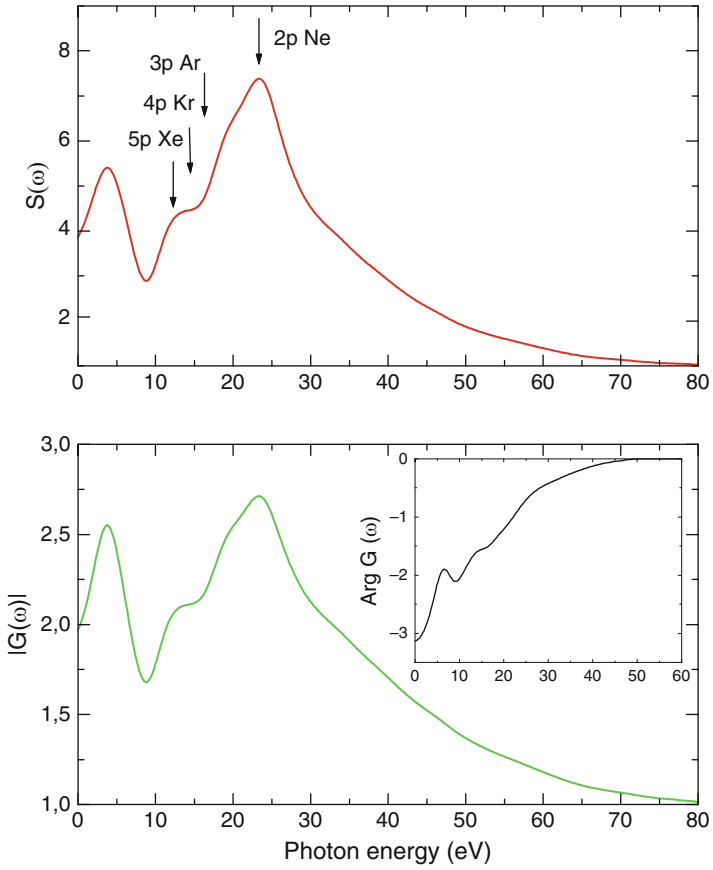

Fig. 2.350_C_{60}_g1 Polarization factor of the electromagnetic radiation by the electron shell of C_{60} $S(\omega) \equiv |G(\omega)|^2$, absolute value of its amplitude $\tilde{G}^d(\omega) \equiv |G(\omega)|$ and phase $\eta^d \equiv \arg G(\omega)$. The *arrows* mark the thresholds of outer *np* subshells

Figure 2.353_Ne@C_{60}_b1 shows photoionization cross-section of $2p$-electrons for Ne free atom in RPAE and Ne@C_{60} in RPAE, FRPAE, WRPAE, and GWRPAE. Note that inclusion of polarization of the fullerenes shell considerably enhances the first and the second maximum.

Figure 2.354_Ne@C_{60}_b2 presents photoionization cross-section of $2s$-electrons for Ne free atom in RPAE and Ne@C_{60} in RPAE, FRPAE, WRPAE, and GWRPAE. The effect of reflection is quite small.

Figure 2.355_Ne@C_{60}_b3 depicts photoionization cross-section of $2p$-elctrons for Ne@C_{60} with account of photoelectron reflection by C_{60} zero-thickness electron shell that leads to oscillations in comparison with smooth cross-section of free Ne. Due to polarization of C_{60}, these oscillations are enhanced by many times. The sharp

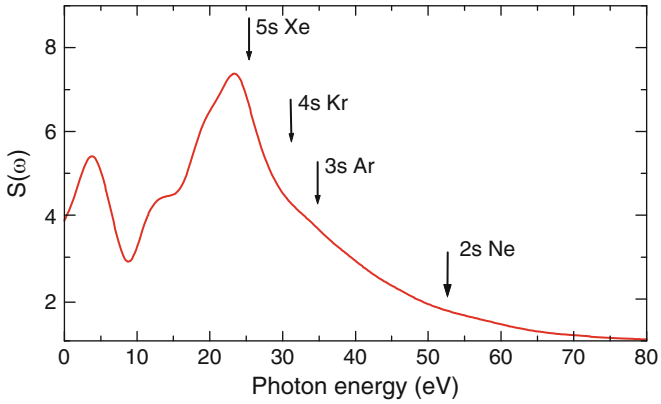

Fig. 2.351_C_{60}_g2 Polarization factor of the electromagnetic radiation by the electron shell of C_{60} $S(\omega) \equiv |G(\omega)|^2$. The *arrows* mark the thresholds of outer *ns* subshells

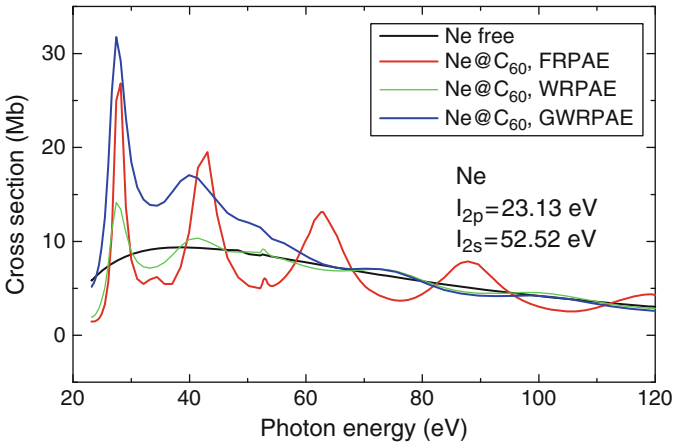

Fig. 2.352_Ne@C_{60}_a1 Total photoionization cross section of Ne free atom in RPAE and Ne@C_{60} in FRPAE, WRPAE, and GWRPAE

rise of cross-section is seen. The cross-section has three maximums, whose magnitudes are defined by polarization of fullerene electron shell (see Sect. 1.14).

Figure 2.356_Ne@C_{60}_b4 shows photoionization cross-section of 2*s*-electrons for Ne@C_{60} with account of photoelectron reflection by C_{60} zero-thickness electron shell and isolated Ne in RPAE. The same factors, as in a Fig. 2.355_Ne@C_{60}_b3 are taken into account. The amplification of electromagnetic radiation is not significant.

Figure 2.357_Ne@C_{60}_d1 displays the dipole angular anisotropy parameter β_{2p} of $2p$-electrons for Ne@C_{60} and Ne free atom in RPAE. The oscillations caused

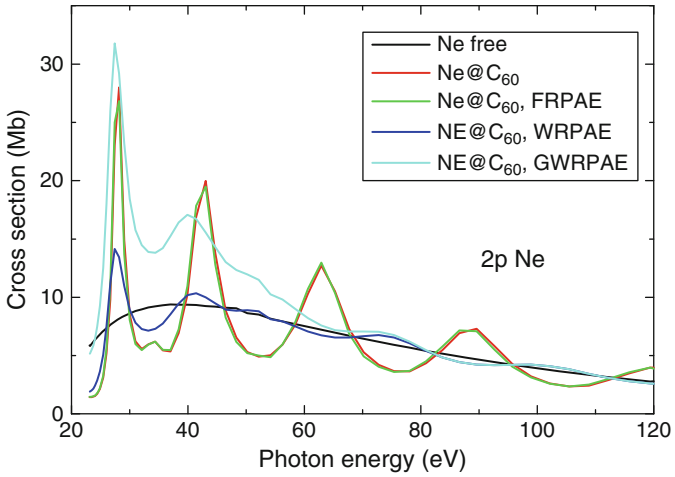

Fig. 2.353_Ne@C_{60}_b1 Photoionization cross section of $2p$-electrons for Ne free atom in RPAE and Ne@C_{60} in RPAE, FRPAE, WRPAE, and GWRPAE

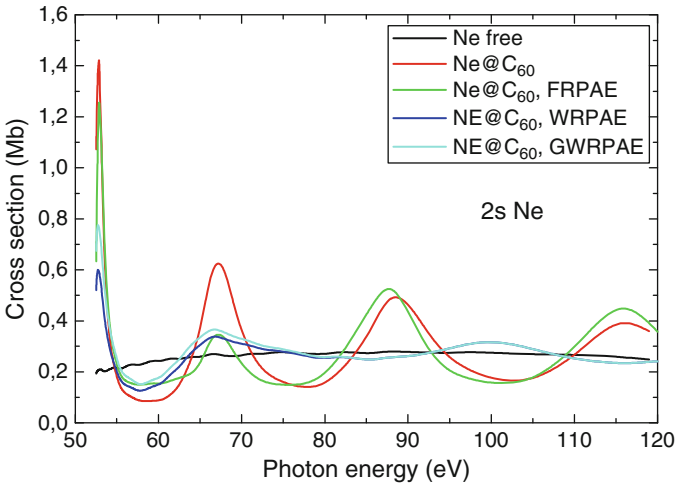

Fig. 2.354_Ne@C_{60}_b2 Photoionization cross section of $2s$-electrons for Ne free atom in RPAE and Ne@C_{60} in RPAE, FRPAE,WRPAE, and GWRPAE

by photoelectron reflection are seen. There is no influence of fullerene shell polarization on dipole angular anisotropy parameter.

Figure 2.358_Ne@C_{60}_e1 shows the non-dipole angular anisotropy parameter γ^{C}_{2p} of $2p$- electrons for Ne@C_{60} and Ne in RPAE. The role of photoelectron reflection is very large. The influence of fullerene polarization is neglected.

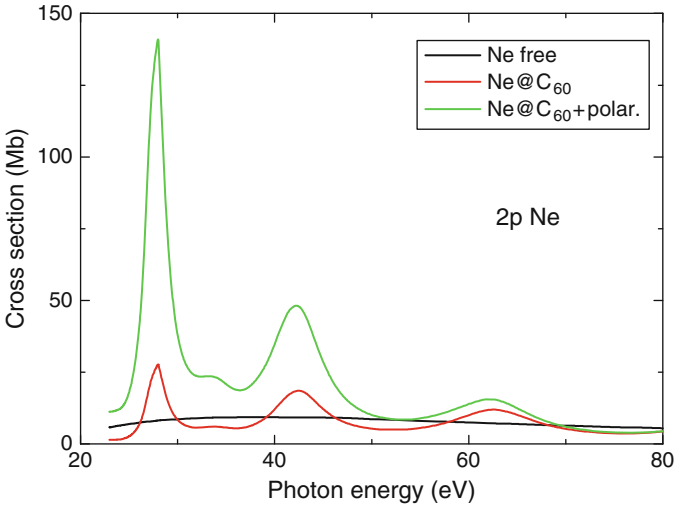

Fig. 2.355_Ne@C_{60}_b3 Photoionization cross section of $2p$-electrons of isolated atom Ne and Ne@C_{60} with account of photoelectrons reflection by C_{60} shell and its polarization by the incoming photon

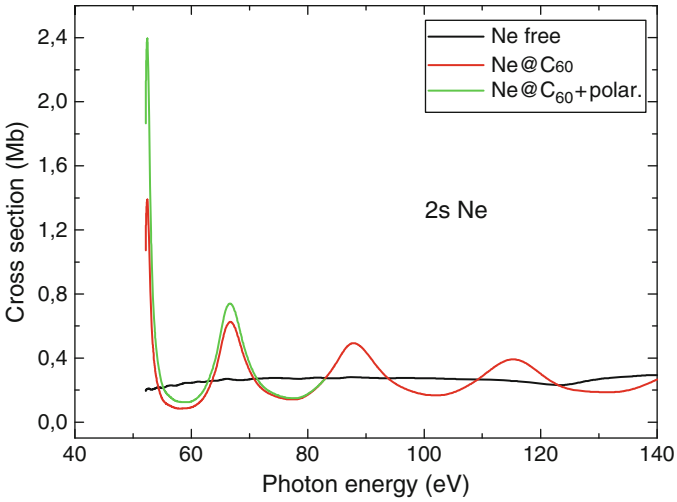

Fig. 2.356_Ne@C_{60}_b4 Photoionization cross section of $2p$-electrons in isolated atom Ne and Ne@C_{60} with account of photoelectron reflection and polarization of C_{60} shell by photon, respectively

Figure 2.359_Ne@C_{60}_e2 shows non-dipole angular anisotropy parameter γ_{2s}^{C} of $2s$- electrons for Ne@C_{60} and Ne in RPAE. The oscillations of the parameter near threshold are especially large, decreasing rapidly with increase in ω. The influence of fullerene polarization is neglected.

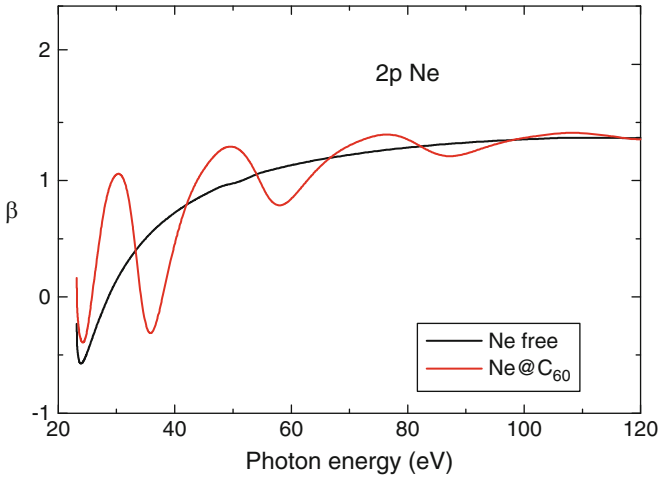

Fig. 2.357_Ne@C_{60}_d1 Dipole angular anisotropy parameter of $2p$-electrons for Ne@C_{60} and Ne free atom

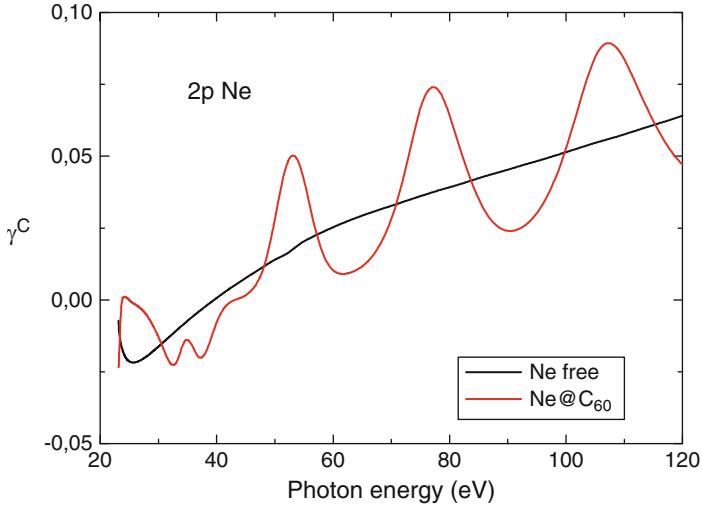

Fig. 2.358_Ne@C_{60}_e1 Non-dipole angular anisotropy parameter of $2p$-electrons for Ne@C_{60} and Ne in RPAE

Figure 2.360_Ne@C_{60}_e3 depicts non-dipole angular anisotropy parameter γ^{C}_{1s} of $1s$-electrons in Ne@C_{60} and Ne in RPAE. The oscillations of parameter are very strong at threshold, but decrease rapidly with increase in ω. The influence of fullerene polarization is neglected.

Figures 2.361_Ar@C_{60}_a1–2.368_Ar@C_{60}_e2 (Ar@C_{60}) contain results of calculations for Ar@C_{60} and Ar.

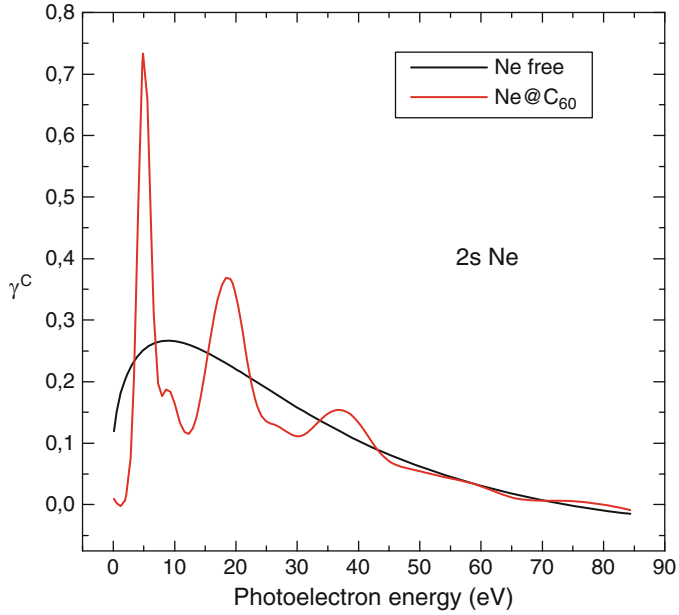

Fig. 2.359_Ne@C$_{60}$_e2 Non-dipole angular anisotropy parameter of 2*s*-electrons for Ne@C$_{60}$ and Ne in RPAE

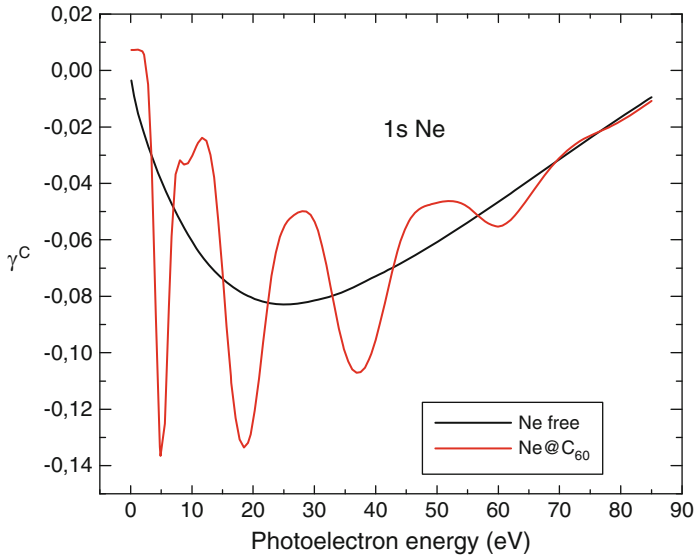

Fig. 2.360_Ne@C$_{60}$_e3 Non-dipole angular anisotropy parameter of 1*s*-electrons for Ne@C$_{60}$ and Ne

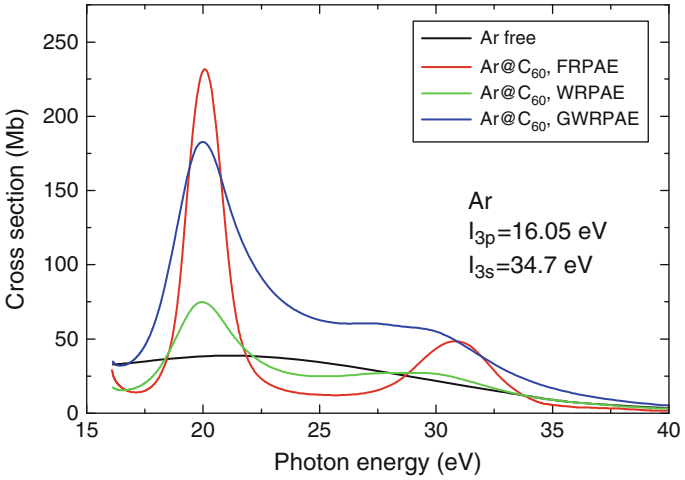

Fig. 2.361_Ar@C_{60}_a1 Total photoionization cross section of Ar free atom in RPAE and Ar@C_{60} in FRPAE, WRPAE, and GWRPAE. Giant endohedral resonance is seen

Figure 2.361_Ar@C_{60}_a1 shows total photoionization cross-section of Ar free atom in RPAE and Ar@C_{60} in FRPAE, WRPAE, and GWRPAE. One can see that near threshold a powerful structure called *Giant Endohedral resonance* [2.77] is formed. It has a big magnitude and exceeds the cross-section's pure atomic value by almost an order of magnitude.

Figure 2.362_Ar@C_{60}_b1 presents photoionization cross-section of $3p$-electrons for Ar free atom in RPAE and Ar@C_{60} in FRPAE, WRPAE, and GWRPAE. The cross-section is dominated by Giant endohedral resonance.

Figure 2.363_Ar@C_{60}_b2 shows photoionization cross-section of $3s$-electrons for Ar free atom in RPAE and Ar@C_{60} in FRPAE, WRPAE, and GWRPAE. The influence of polarization in GWRPAE brings the situation almost to that in WRPAE.

Figure 2.364_Ar@C_{60}_b3 shows photoionization cross-section of $3p$-electrons for Ar atom and of Ar@C_{60} in RPAE, with account for reflection of a photoelectron by C_{60} shell that leads to oscillations in comparison with smooth cross-section of Ar free atom, and polarization of C_{60} shell, rising cross-section in many times. The Giant endohedral resonance at 21 eV with oscillator strength of 20 units is seen.

Figure 2.365_Ar@C_{60}_b4 presents photoionization cross-section of $3s$-electrons for Ar and Ar@C_{60} in RPAE, with account for reflection of a photoelectron by C_{60} shell that leads to oscillations in comparison with smooth cross-section of free Ar, and polarization of C_{60} shell, rising cross-section in many times. In Ar@C_{60} $3s$-cross-section is approximately 400 times less than $3p$-one.

Figure 2.366_Ar@C_{60}_d1 shows dipole angular anisotropy parameter β_{3p} of $3p$-electrons for Ar@C_{60} and Ar. The role of photoelectron reflection is significant at threshold and after kinetic energy 50 eV.

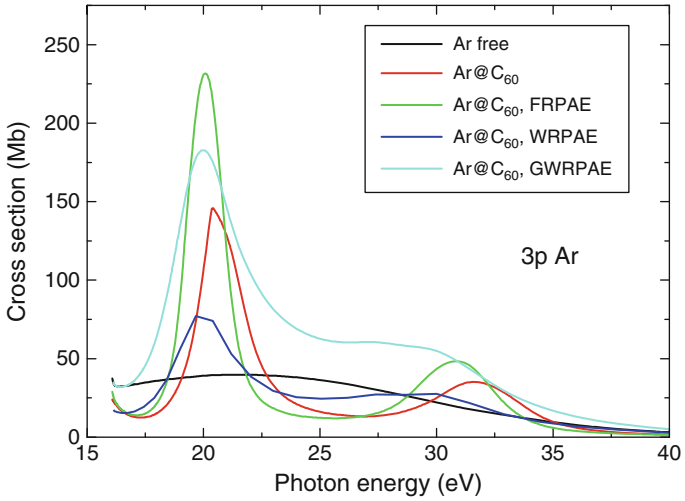

Fig. 2.362_Ar@C_{60}_b1 Photoionization cross section of $3p$-electrons for Ar free atom in RPAE and Ar@C_{60} in RPAE, FRPAE,WRPAE, and GWRPAE. Giant Endohedral resonance is seen

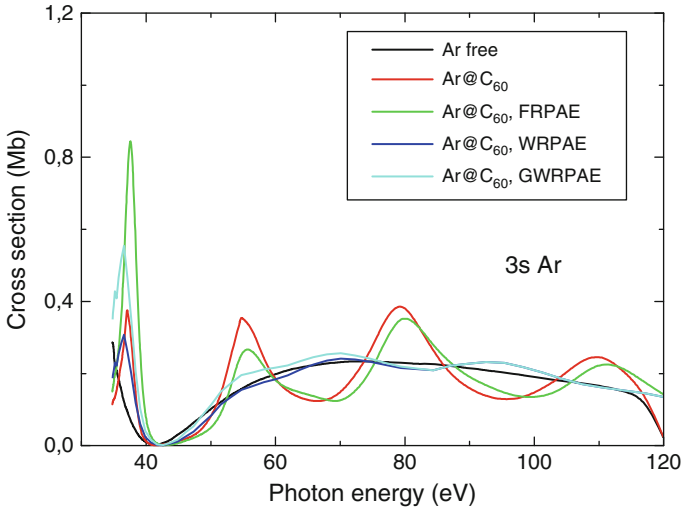

Fig. 2.363_Ar@C_{60}_b2 Photoionization cross section of $3s$-electrons for Ar free atom in RPAE and Ar@C_{60} in RPAE, FRPAE,WRPAE, and GWRPAE

Figure 2.367_Ar@C_{60}_e1 depicts non-dipole angular anisotropy parameter γ_{3p}^{C} of $3p$-electrons Ar@C_{60} and Ar. Photoelectron re-scattering on fullerenes shell results in moderate oscillations.

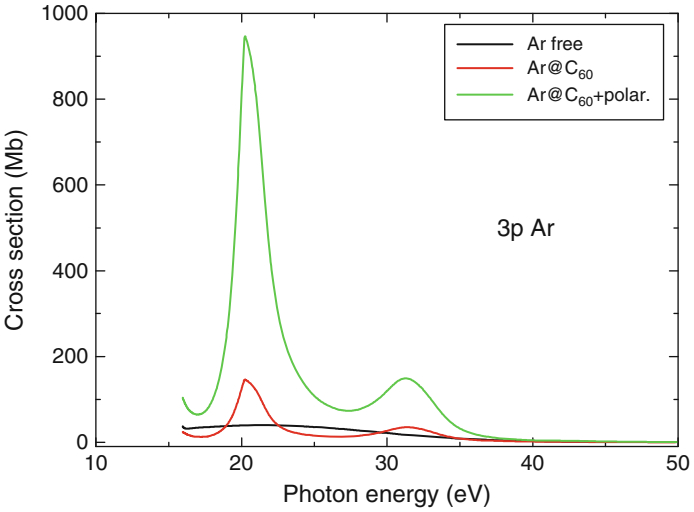

Fig. 2.364_Ar@C_{60}_b3 Photoionization cross section of $3p$-electrons for Ar@C_{60} and Ar in RPAE with account for photoelectron reflection by C_{60} shell and its polarization

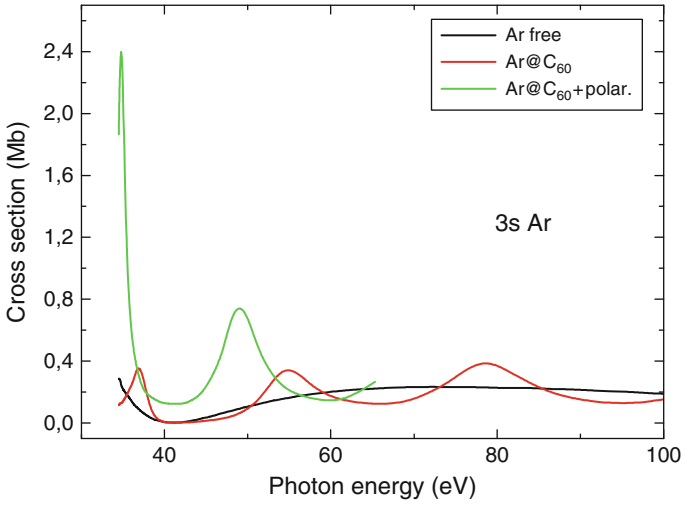

Fig. 2.365_Ar@C_{60}_b4 Photoionization cross section of $3s$-electrons for Ar@C_{60} and Ar in RPAE with account of photoelectron reflection by C_{60} shell and its polarization

Figure 2.368_Ar@C_{60}_e2 presents non-dipole angular anisotropy parameter γ_{3s}^{C} of $3s$-electrons Ar@C_{60} and Ar. The influence of fullerene is limited in the photon energy region $35 \leq \omega \leq 50$ eV.

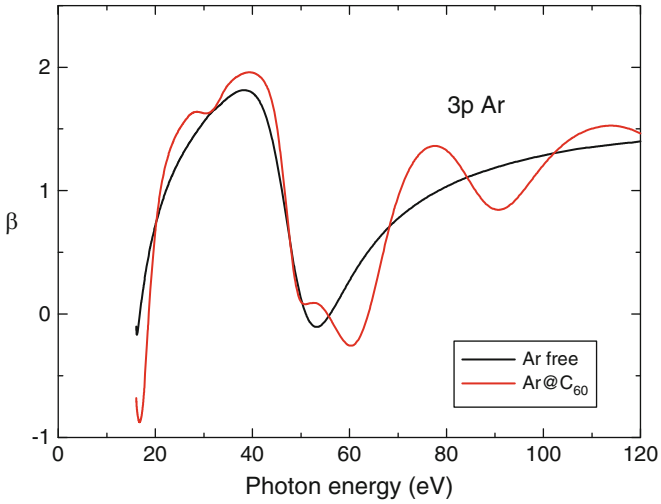

Fig. 2.366_Ar@C$_{60}$_d1 Dipole angular anisotropy parameter of 3p-electrons for Ar@C$_{60}$ and Ar in RPAE

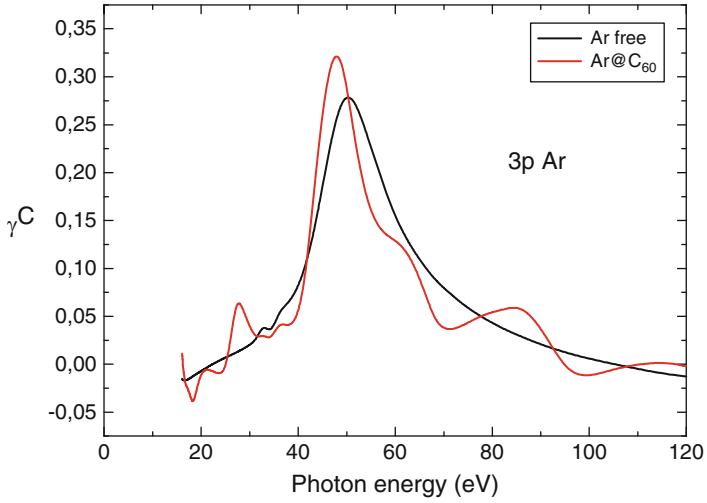

Fig. 2.367_Ar@C$_{60}$_e1 Non-dipole angular anisotropy parameter of 3p-electrons for Ar@C$_{60}$ and Ar in RPAE

Figures 2.369_Kr@C$_{60}$_a1–2.374_Kr@C$_{60}$_e2 (Kr@C$_{60}$) contain results of calculations for Kr@C$_{60}$.

Figure 2.369_Kr@C$_{60}$_a1 shows total photoionization cross-section of Kr free atom in RPAE and Kr@C$_{60}$ in FRPAE, WRPAE, and GWRPAE. One can see that near threshold a structure called *Giant Endohedral resonance* [2.77] is formed,

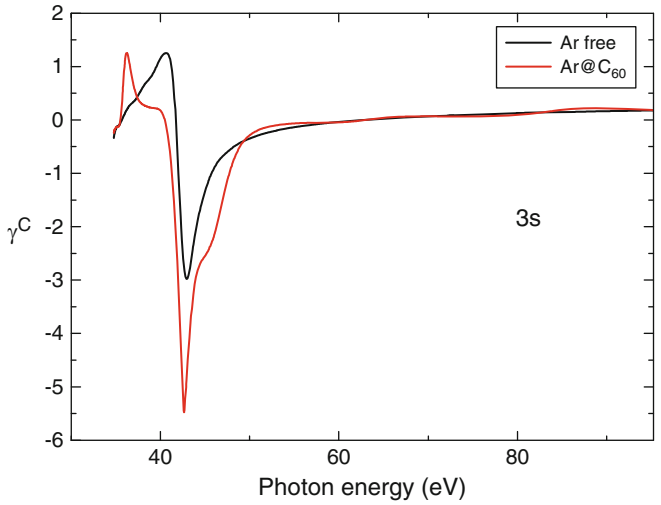

Fig. 2.368_Ar@C_{60}_e2 Non-dipole angular anisotropy parameter of 3*s*-electrons for Ar@C_{60} and Ar

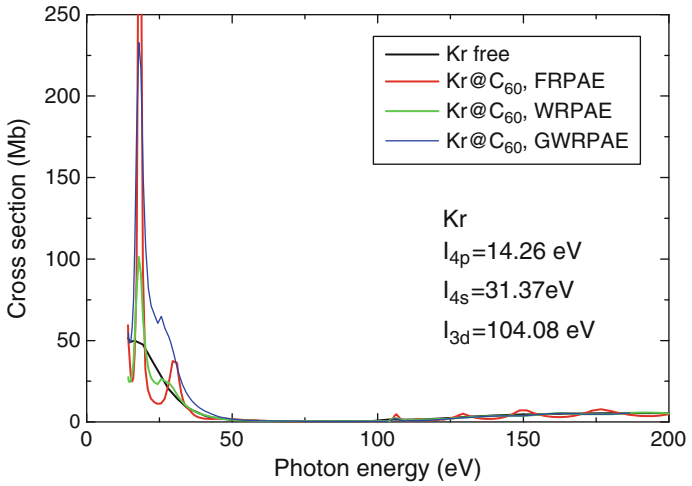

Fig. 2.369_Kr@C_{60}_a1 Total photoionization cross section of Kr free atom in RPAE and Kr@C_{60} in FRPAE, WRPAE, and GWRPAE

particularly powerful in GWRPAE. It has big magnitude and exceeds the cross-section's pure atomic value by more than five times.

Figure 2.370_Kr@C_{60}_b1 shows photoionization cross-section of 4*p*-electrons of Kr and Kr@C_{60} with account for photoelectron reflection by C_{60} shell that leads to oscillations in comparison with smooth cross-section of Kr free atom, and

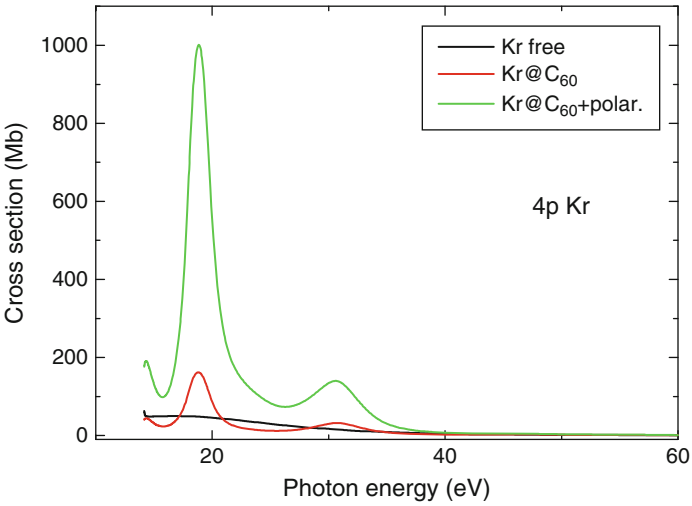

Fig. 2.370_Kr@C_{60}_b1 Photoionization cross section of 4*p*-electrons for Kr@C_{60} and Kr with account for photoelectron reflection by C_{60} shell and its polarization

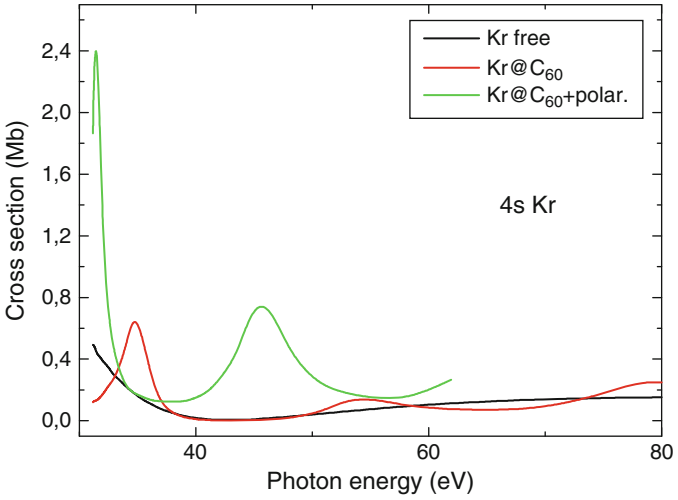

Fig. 2.371_Kr@C_{60}_b2 Photoionization cross section of 4*s*-forlectrons for Kr@C_{60} and Kr with account for photoelectron reflection by C_{60} shell and its polarization

polarization C_{60} shell, rising cross-section in many times. The most impressing result is the occurrence of *Giant endohedral resonance* at 19 eV with oscillator strength of 23 units (see [2.78]).

Figure 2.371_Kr@C_{60}_b2 depicts photoionization cross-section of 4*s*-electrons for Kr free atom and Kr@C_{60}, with account for photoelectron reflection by C_{60} shell that leads to oscillations in comparison with smooth cross-section of Kr free

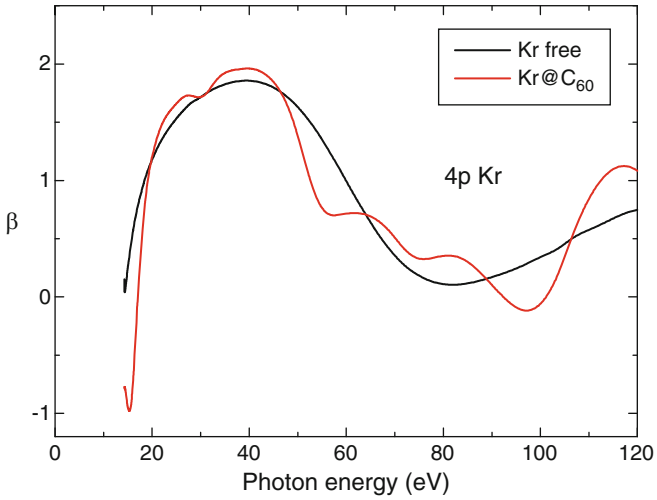

Fig. 2.372_Kr@C_{60}_d1 Dipole angular anisotropy parameter of $4p$-electrons for Kr@C_{60} and Kr in RPAE

atom, and polarization of C_{60} electron shell, rising the cross-section by many times. In Kr@C_{60} $4s$-cross-section is approximately 400 times less than that of $4p$, i.e., the situation is similar to taking place in Ar@C_{60}. In addition to near threshold maximum, there is a maximum at 47 eV.

Figure 2.372_Kr@C_{60}_d1 displays dipole angular anisotropy parameter β_{4p} of $4p$-electrons for Kr@C_{60} and Kr free atom. Oscillations caused by the fullerene shell are not large.

Figure 2.373_Kr@C_{60}_e1 presents non-dipole angular anisotropy parameter γ^{C}_{4p} of $4p$-electrons for Kr@C_{60} and Kr free atom in RPAE. The influence of fullerene polarization on non-dipole parameters is neglected.

Figure 2.374_Kr@C_{60}_e2 shows non-dipole angular anisotropy parameter γ^{C}_{4s} of $4s$-electrons Kr@C_{60} and Kr. The fullerene shell significantly changes the parameter, which acquires a sharp maximum at ionization threshold.

Figures 2.375_Xe@C_{60}_a1–2.399_Xe@C_{60}_g1 (Xe@C_{60}) contain results of calculations for Xe@C_{60}.

Figure 2.375_Xe@C_{60}_a1 presents total photoionization cross-section of Xe free atom in RPAE and Xe@C_{60} in, FRPAE, WRPAE, and GWRPAE. A powerful Giant endohedral resonance dominates the outer shell photoionization cross-section [2.77]. Prominent confinement resonances are seen above the $4d$-electrons threshold. In GWRPAE, the cross section is much bigger than in WRPAE.

Figure 2.376_Xe@C_{60}_b1 shows photoionization cross-section of $5p$-electrons for Xe free atom in RPAE and Xe@C_{60} in RPAE, FRPAE, WRPAE, and GWRPAE. Note that Giant endohedral resonance in GWRPAE is in total oscillator strength only a little less powerful than in FRPAE.

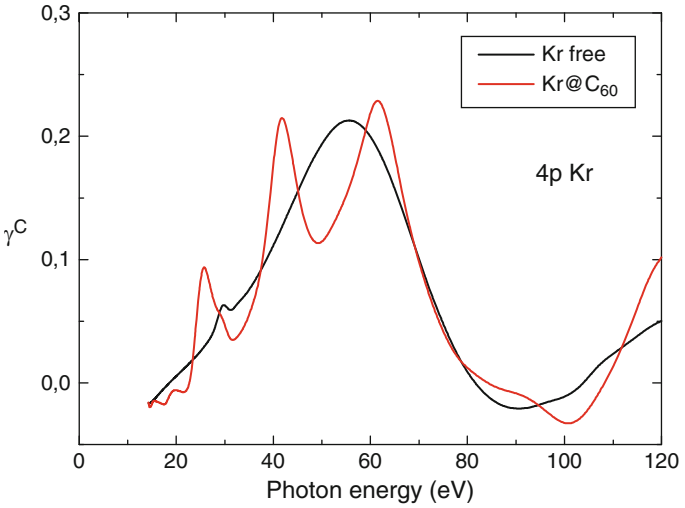

Fig. 2.373_Kr@C_{60}_e1 Non-dipole angular anisotropy parameter of 4p-electrons for Kr@C_{60} and Kr in RPAE

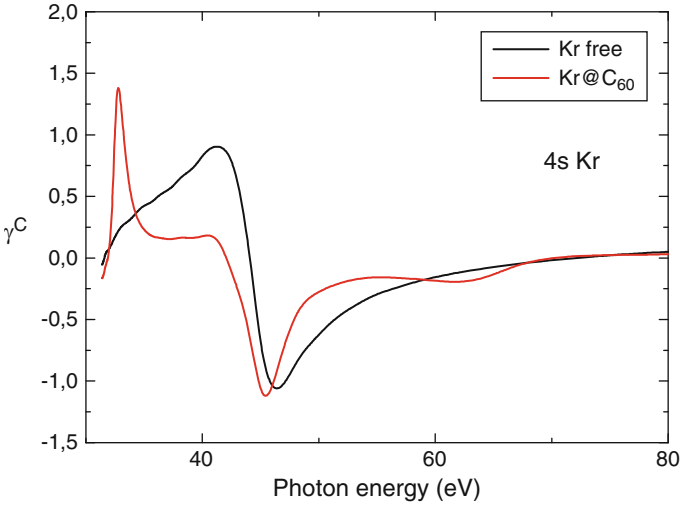

Fig. 2.374_Kr@C_{60}_e2 Non-dipole angular anisotropy parameter of 4s-electrons for Kr@C_{60} and Kr in RPAE

Figure 2.377_Xe@C_{60}_b2 depicts photoionization cross-section of 5s-electrons for Xe free atom in RPAE and Xe@C_{60} in RPAE, FRPAE, WRPAE, and GWRPAE [2.78]. Note that the structure in 5s cross-section reflects confinement resonances of 5s-electrons as well as resonances in 4d affecting in its turn the 5s cross-section due to intershell interaction. The results in GWRPAE are, as it should be, close to WRPAE and even RPAE for the free atom.

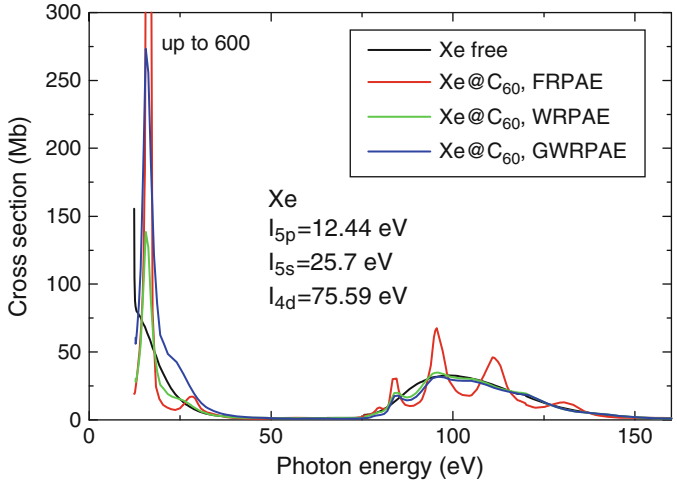

Fig. 2.375_Xe@C_{60}_a1 Total photoionization cross section of Xe free atom in RPAE and Xe@C_{60} in FRPAE, WRPAE, and GWRPAE

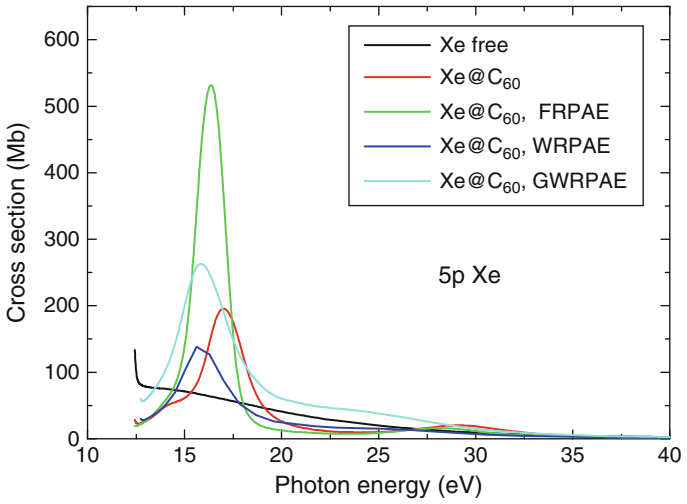

Fig. 2.376_Xe@C_{60}_b1 Photoionization cross section of $5p$-electrons for Xe free atom in RPAE and Xe@C_{60} in RPAE, FRPAE, WRPAE, and GWRPAE

Figure 2.378_Xe@C_{60}_b3 displays photoionization cross-section of $4d$-electrons for Xe free atom in RPAE and Xe@C_{60} in RPAE, FRPAE, WRPAE, and GWRPAE (see [2.80, 2.81]). The cross-section in GRPAE is very close to WRPAE, since polarization factor for high ω is close to one.

Figure 2.379_Xe@C_{60}_b4 shows photoionization cross-section of $5p$-electrons of Xe and Xe@C_{60}, with account for photoelectron reflection by C_{60} shell that

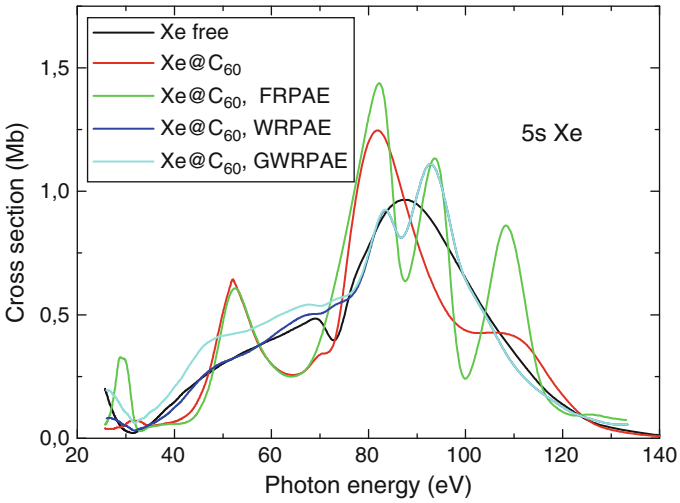

Fig. 2.377_Xe@C_{60}_b2 Photoionization cross section of 5*s*-electrons for Xe free atom in RPAE and Xe@C_{60} in RPAE, FRPAE, WRPAE, and GWRPAE

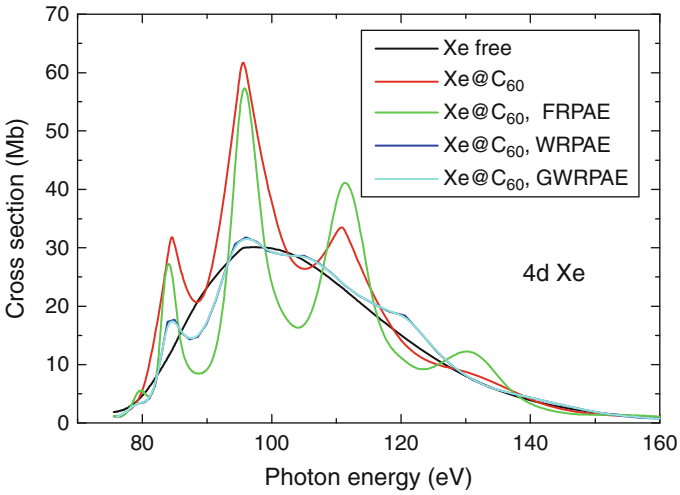

Fig. 2.378_Xe@C_{60}_b3 Photoionization cross section of 4*d*-electrons for Xe free atom in RPAE and Xe@C_{60} in RPAE, FRPAE, WRPAE, and GWRPAE

leads to oscillations in comparison with smooth cross-section of free Xe atom, and polarization of C_{60} shell that leads to rising of the cross-section by many times. The most impressing result is the occurrence of Giant endohedral resonance at 17 eV with oscillator strength of 25 units.

Figure 2.380_Xe@C_{60}_b5 presents photoionization cross-section of 5*s*-electrons of Xe and Xe@C_{60}, with account for photoelectron reflection by C_{60} shell that

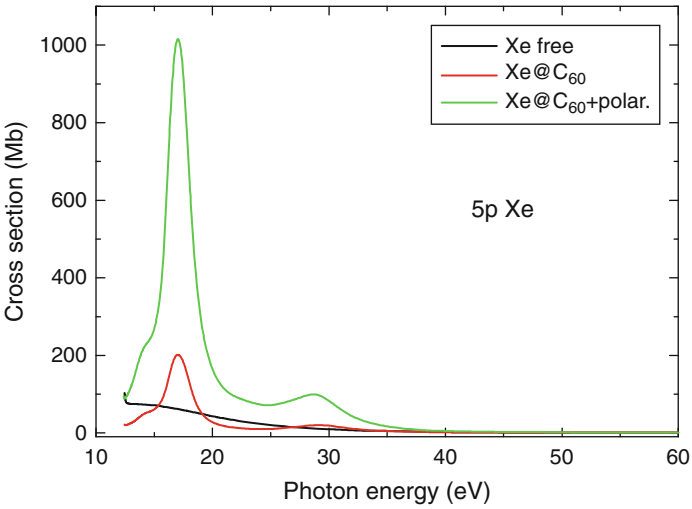

Fig. 2.379_Xe@C_{60}_b4 Photoionization cross section of $5p$-electrons for Xe@C_{60} and Xe in RPAE and GFRPAE

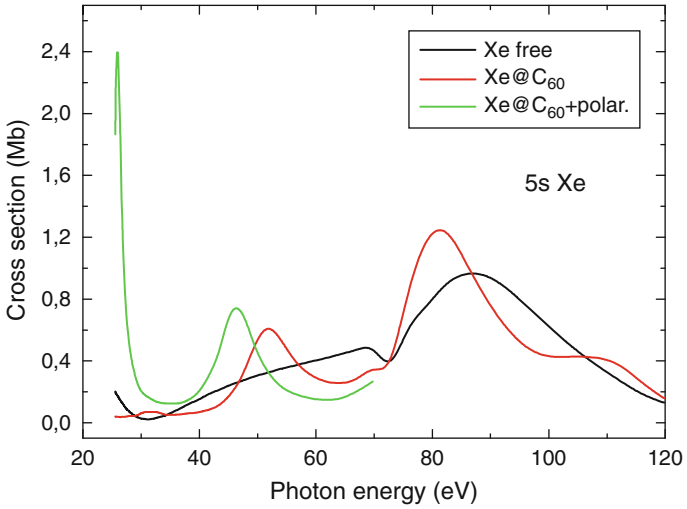

Fig. 2.380_Xe@C_{60}_b5 Photoionization cross section of $5s$-electrons for Xe@C_{60} and Xe atom in RPAE with account for photoelectron reflection by C_{60} shell and its polarization in GFRPAE

leads to oscillations in comparison with smooth cross-section of free Xe, and for polarization of C_{60} shell that increases the cross-section by about 20 times. In Xe@C_{60} the $5s$ cross-section is approximately 400 times less, than that of $5p$, i.e., the situation is similar to having a place in Ar@C_{60} and Kr@C_{60}.

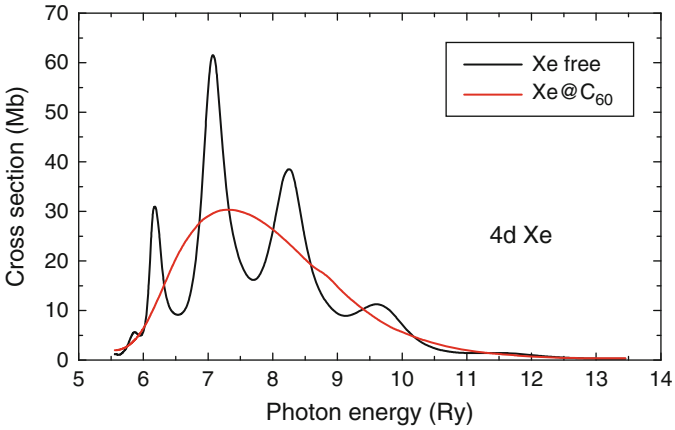

Fig. 2.381_Xe@C_{60}_b6 Photoionization cross section of $4d$-electrons for Xe@C_{60} and Xe in RPAE

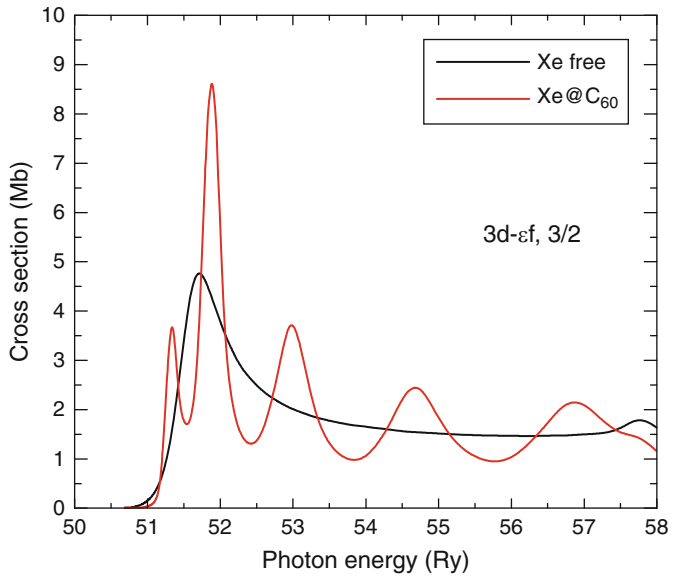

Fig. 2.382_Xe@C_{60}_b9 Photoionization cross section of $3d_{3/2}$-electrons for Xe@C_{60} and Xe in RPAE

Figure 2.381_Xe@C_{60}_b6 includes photoionization cross-section of $4d$-electrons for Xe@C_{60} and Xe (see [2.80, 2.81]) in RPAE. It is seen that photoelectron reflection results in a complete destruction of Giant resonance, which is replaced by four maximums.

fIGURE 2.382_Xe@C_{60}_b7 compares the experimental cross-section of Xe@C_{60}^{+} in the region of $4d$ subshell [2.82] with results for free Xe atom and Xe@C_{60} in RPAE and FRPAE (Fig. 2.381_Xe@C_{60}_b6). The measurements are the first

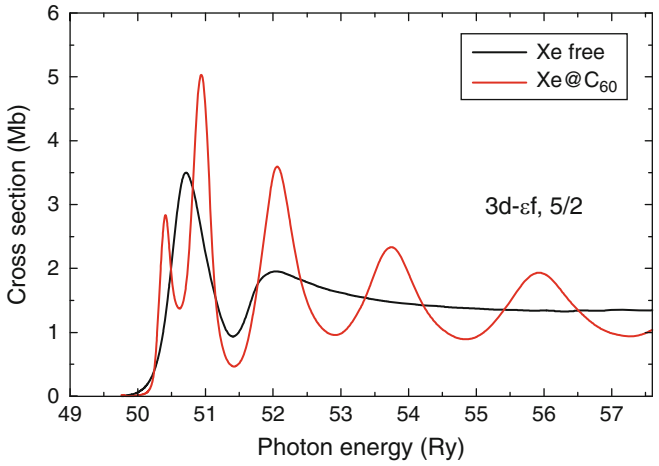

Fig. 2.383_Xe@C_{60}_b8 Photoionization cross section of $3d_{5/2}$-electrons for Xe@C_{60} and Xe, $3d–\varepsilon f$ transition in RPAE

confirmation of theoretic prediction, presented at the previous figure. Note that it confirms the multi-maxima structure in the $4d$ Xe@C_{60} Giant resonance. For such a crude model the agreement is reasonable.

Figure 2.383_Xe@C_{60}_b8 depicts photoionization cross-section of $3d_{5/2}$-electrons for Xe@C_{60} and Xe atom, $3d–\varepsilon f$ transition (see [2.83,2.84]). Polarization of fullerene shell at these photon energies is not essential. Photoelectron reflection results in strong oscillations of $3d_{5/2}$-electrons cross-section. The influence of $3d_{3/2}$ level is essential but masked by strong oscillations caused by photoelectrons reflection by fullerene shell.

Figure 2.384_Xe@C_{60}_b9 depicts photoionization cross-section of $3d_{3/2}$ electrons for Xe@C60 and Xe atom, 3d-epsilon f transition (see [2.83, 2.84]). Polarization of fullerenes shell at these photon energies is not essential. Photoelectron reflection results in strong oscillations of $3d_{3/2}$-electrons cross-section. The role of $3d_{5/2}$ is inessential.

Figure 2.385_Xe@C_{60}_d1 displays dipole angular anisotropy parameter β_{5p} of $5p$-electrons for Xe@C_{60} and Xe atom in RPAE. The photoelectron reflection results in appreciable oscillations of β_{5p} parameter (see [2.78]). Additional maximum immediately after threshold is quite remarkable.

Figure 2.386_Xe@C_{60}_d2 demonstrates dipole angular anisotropy parameter β_{4d} of $4d$-electrons Xe@C_{60} and Xe atom in RPAE (see [2.83, 2.81]). Photoelectron reflection results in additional maximum near threshold and oscillations far from it.

Figure 2.387_Xe@C_{60}_d3 presents dipole angular anisotropy parameter $\beta_{3d_{3/2}}$ of $3d_{3/2}$-electrons for Xe@C_{60} and Xe atom in RPAE (see [2.82, 2.84]). Note the complex structure with narrow minimums and maximum immediately above threshold.

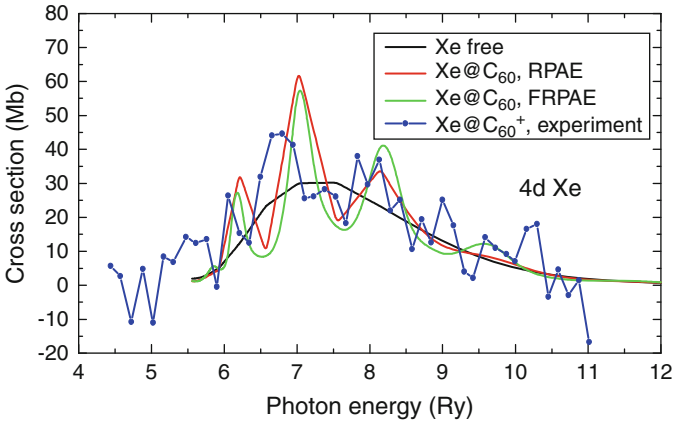

Fig. 2.384_Xe@C_{60}_b7 Comparison of experimental cross-section of Xe@C_{60}^{+} in the region of $4d$ subshell [2.82] of with results for free Xe atom and Xe@C_{60} in RPAE and FRPAE (**Fig.** 2.381_Xe@C_{60}_b6)

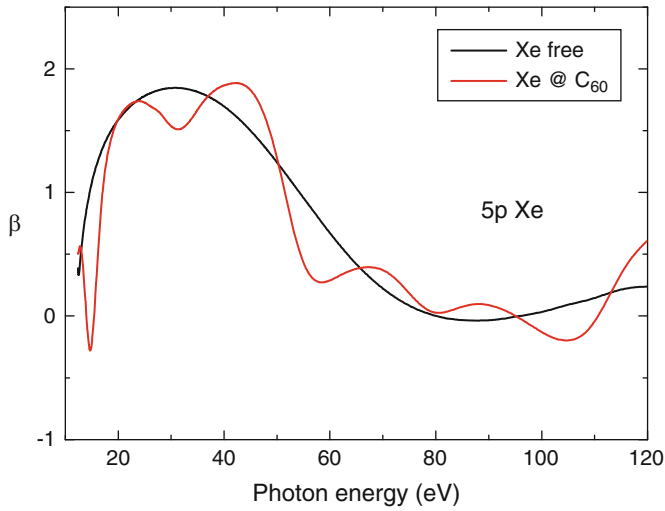

Fig. 2.385_Xe@C_{60}_d1 Dipole angular anisotropy parameter of $5p$-electrons for Xe@C_{60} and Xe atom in RPAE

Figure 2.388_Xe@C_{60}_d4 depicts dipole angular anisotropy parameter $\beta_{3d_{5/2}}$ of $3d_{5/2}$-electrons for Xe@C_{60} and Xe atom in RPAE (see [2.83, 2.84]). At threshold appear additional minimum and maximum.

Figure 2.389_Xe@C_{60}_e1 shows non-dipole angular anisotropy parameter γ_{5p}^{C} of $5p$-electrons for Xe@C_{60} and Xe free atom in RPAE. The role of photoelectron reflection by fullerene shell is significant, adding prominent new structure as compared to the isolated atom case.

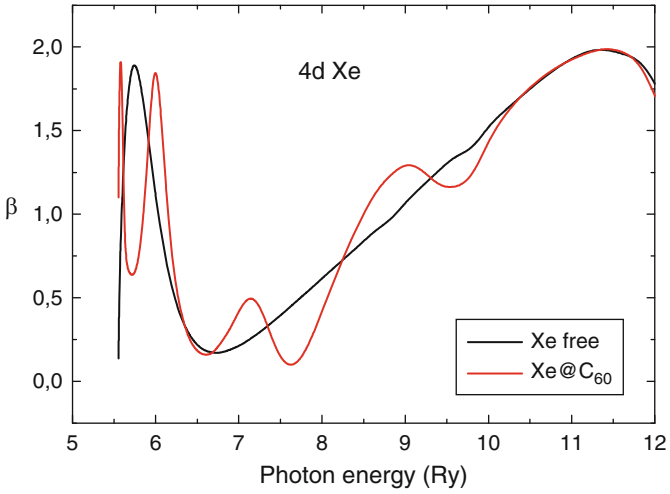

Fig. 2.386_Xe@C_{60}_d2 Dipole angular anisotropy parameter of $4d$-electrons for Xe@C_{60} and Xe atom in RPAE

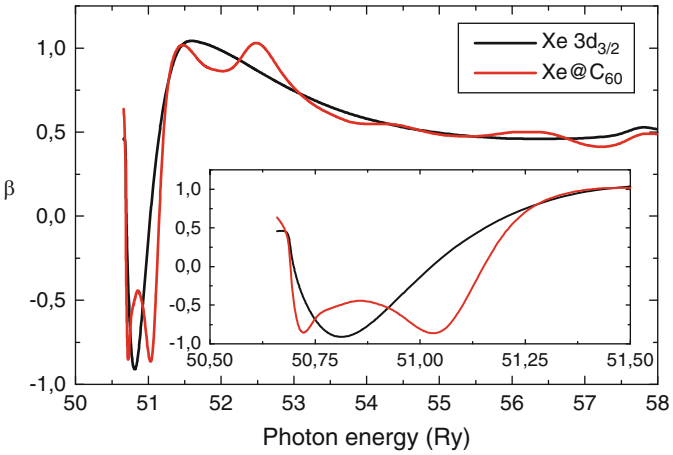

Fig. 2.387_Xe@C_{60}_d3 Dipole angular anisotropy parameter of $3d_{3/2}$-electrons for Xe@C_{60} and Xe atom in RPAE

Figure 2.390_Xe@C_{60}_e2 presents non-dipole angular anisotropy parameter γ^{C}_{5s} of $5s$-electrons Xe@C_{60} and Xe atom in RPAE. The photoelectron reflection sharply rises the amplitude of near threshold parameter oscillation.

Figure 2.391_Xe@C_{60}_e3 displays non-dipole angular anisotropy parameter γ^{C}_{4d} of $4d$-electrons for Xe@C_{60} and Xe free atom in RPAE (see [2.81]). Photoelectron reflection results in additional minimum at 85 eV and small oscillations.

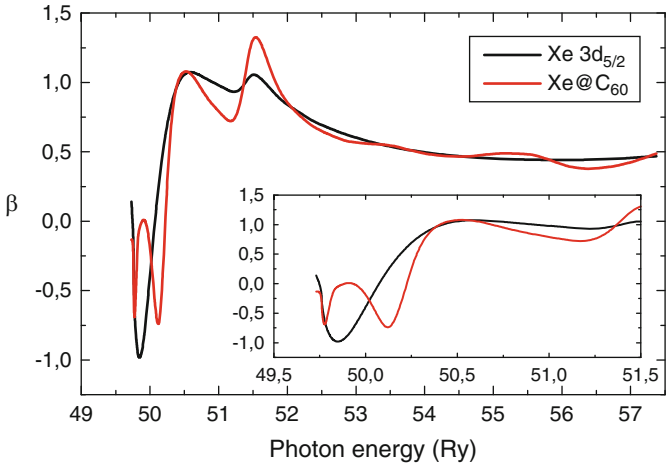

Fig. 2.388_Xe@C$_{60}$_d4 Dipole angular anisotropy parameter β of $3d_{5/2}$-electrons for Xe@C$_{60}$ and Xe in RPAE

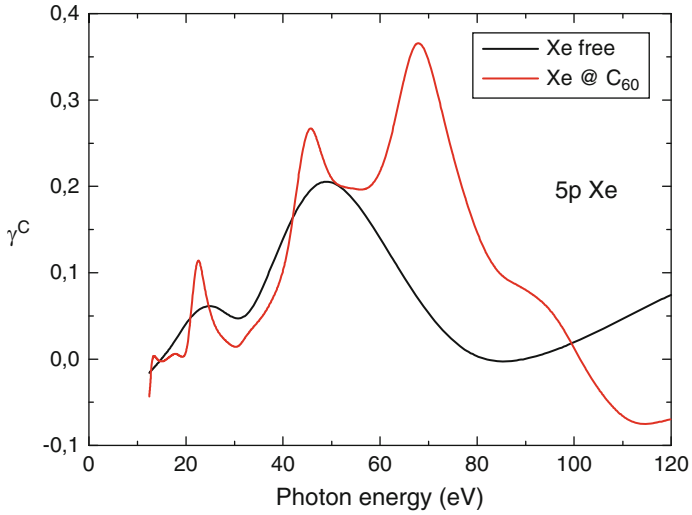

Fig. 2.389_Xe@C$_{60}$_e1 Non-dipole angular anisotropy parameter of $5p$-electrons for Xe@C$_{60}$ and Xe in RPAE

Figure 2.392_Xe@C$_{60}$_e4 shows non-dipole angular anisotropy parameter δ^{C}_{4d} of $4d$-electrons for Xe@C$_{60}$ and Xe free atom in RPAE (see [2.81]). Photoelectron reflection by fullerene shell results in appreciable oscillations.

Figure 2.393_Xe@C$_{60}$_e5 depicts non-dipole angular anisotropy parameter γ^{C} of $3d_{3/2}$-electrons for Xe@C$_{60}$ and Xe free atom in RPAE (see [2.83]). Photoelectron reflection by fullerene shell results in ripples of the parameter curve.

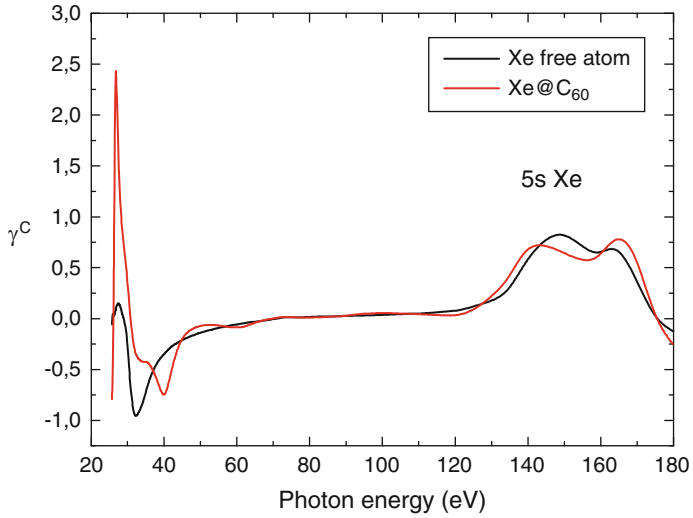

Fig. 2.390_Xe@C_{60}_e2 Non-dipole angular anisotropy parameter γ^C of 5*s*-electrons for Xe@C_{60} and Xe in RPAE

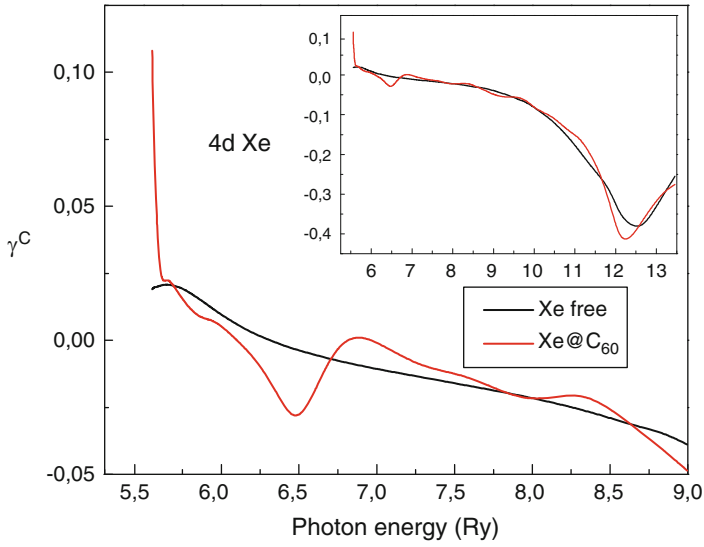

Fig. 2.391_Xe@C_{60}_e3 Non-dipole angular anisotropy parameter γ^C of 4*d* electrons for Xe@C_{60} and Xe in RPAE

Figure 2.394_Xe@C_{60}_e6 displays non-dipole angular anisotropy parameter δ^C of $3d_{5/2}$-electrons for Xe@C_{60} and Xe free atom in RPAE. Photoelectron reflection by fullerene shell results appreciable maximum at threshold.

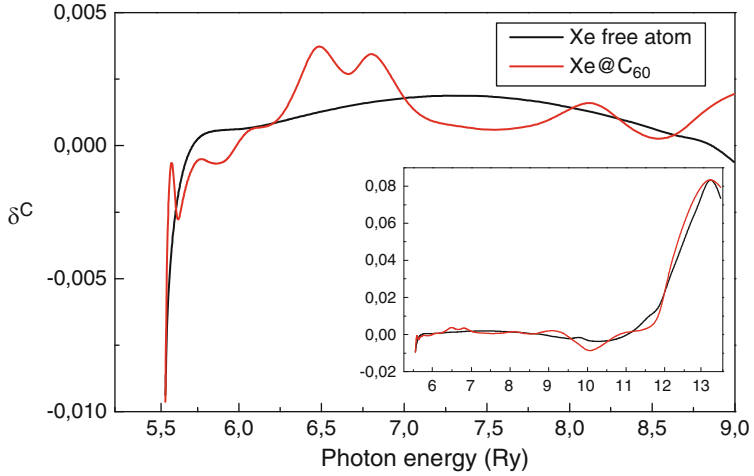

Fig. 2.392_Xe@C_{60}_e4 Non-dipole angular anisotropy parameter δ^C of $4d$ electrons for Xe@C_{60} and Xe in RPAE

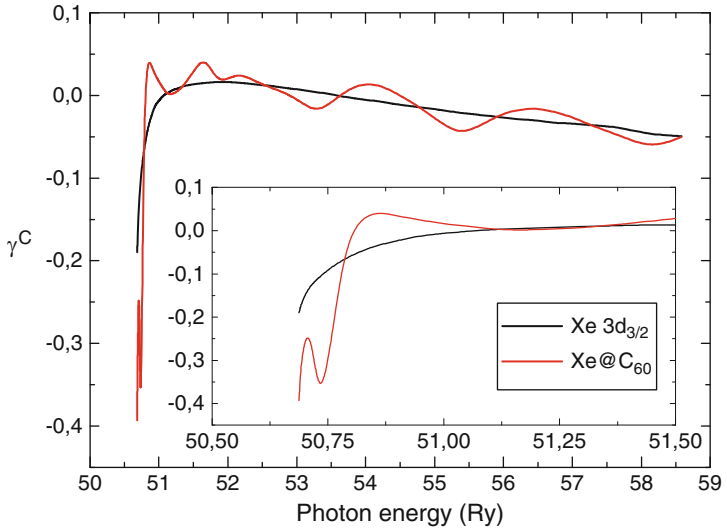

Fig. 2.393_Xe@C_{60}_e5 Non-dipole angular anisotropy parameter of $3d_{3/2}$-electrons for Xe@C_{60} and Xe in RPAE (see [2.84])

Figure 2.395_Xe@C_{60}_e7 shows the magic combination of non-dipole angular anisotropy parameter $3\delta^C + \gamma^C$ of $3d_{3/2}$-electrons for Xe@C_{60} and Xe free atom in RPAE. Photoelectron reflection manifests appreciably at threshold only.

Figure 2.396_Xe@C_{60}_e8 presents non-dipole angular anisotropy parameter γ^C of $3d_{5/2}$-electrons for Xe@C_{60} and Xe free atom in RPAE. Photoelectron reflection manifests appreciably 10 eV above the threshold.

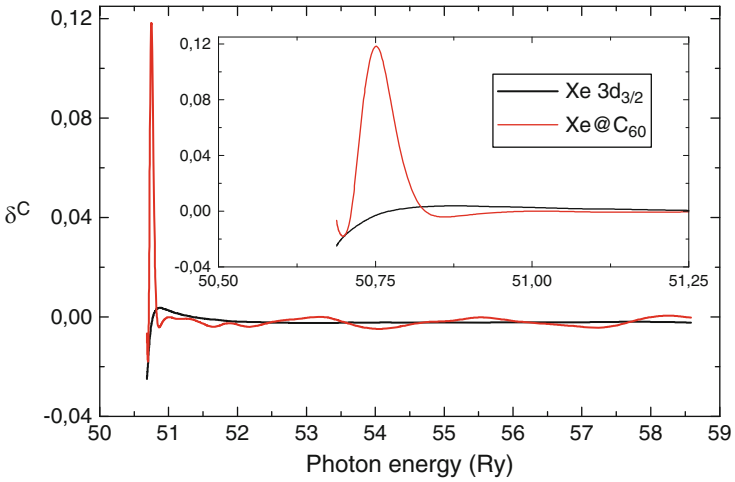

Fig. 2.394_Xe@C_{60}_e6 Non-dipole angular anisotropy parameter δ^C of $3d_{3/2}$-electrons for Xe@C_{60} and Xe in RPAE

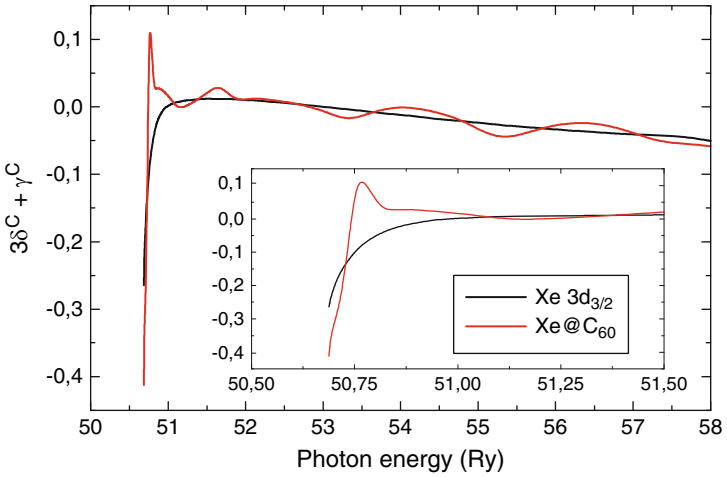

Fig. 2.395_Xe@C_{60}_e7 Magic combination of non-dipole angular anisotropy parameters of $3d_{3/2}$-electrons for Xe@C_{60} and Xe in RPAE

Figure 2.397_Xe@C_{60}_e9 depicts non-dipole angular anisotropy parameter δ^C of $3d_{5/2}$-electrons for Xe@C_{60} and Xe free atom in in RPAE. This figure has little in common to that for $4d$-electrons given by Fig. 2.392_Xe@C_{60}_e4.

Figure 2.398_Xe@C_{60}_e10 displays the magic combination of non-dipole angular anisotropy parameters ($3\delta^C + \gamma^C$) of $3d_{5/2}$-electrons for Xe@C_{60} and Xe free atom in RPAE. The influence of photoelectron reflection is especially large at threshold.

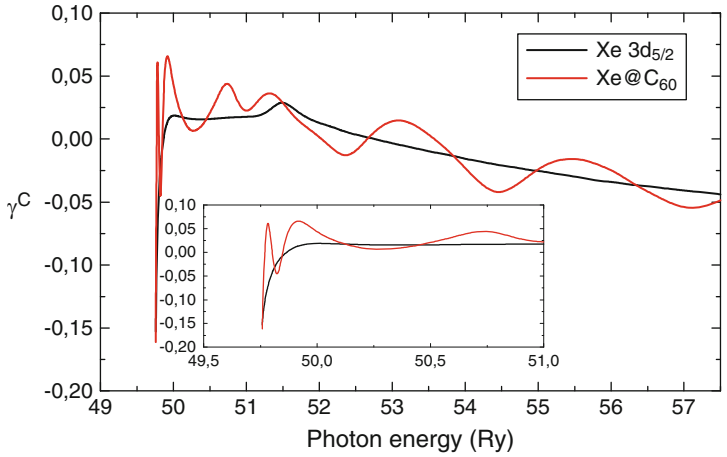

Fig. 2.396_Xe@C_{60}_e8 Non-dipole angular anisotropy parameter γ^{C} of $3d_{5/2}$-electrons for Xe in RPAE

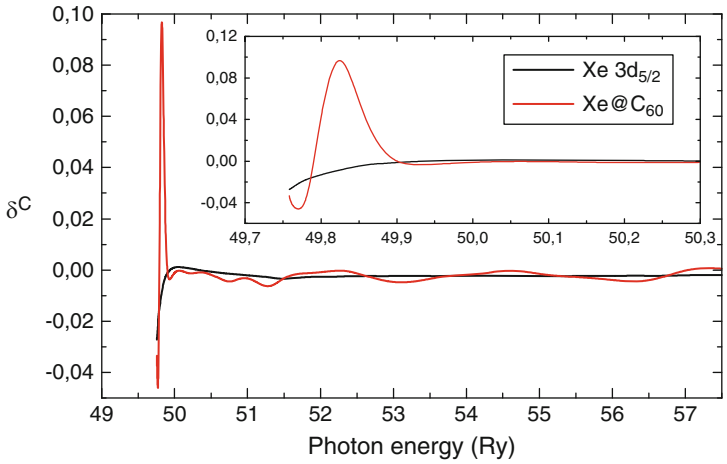

Fig. 2.397_Xe@C_{60}_e9 Non-dipole angular anisotropy parameter δ^{C} for $3d_{5/2}$-electrons in Xe@C_{60} and Xe free atom in RPAE

Figure 2.399_Xe@C_{60}_g1 shows reflection parameter $F_{l'}(\omega)$ [see formula (1.106)] of $4d$-electrons for Xe@C_{60} in RPAE. It is precisely these oscillations that define the structure of photoionization cross-sections of $4d$-subshell of Xe@C_{60}.

Figures 2.400_Cs@C_{60}_b1–2.402_Cs@C_{60}_e1 (Cs@C_{60}) contain results of calculations for Cs@C_{60}.

Figure 2.400_Cs@C_{60}_b1 depicts photoionization cross-section of $3d_{3/2}$ and $3d_{5/2}$-electrons for Cs@C_{60} and Cs free atom in SP RPAE (see [2.82]). Multitude of fullerene reflection maximums almost completely shields the influence of 3/2 electrons on 5/2 electrons.

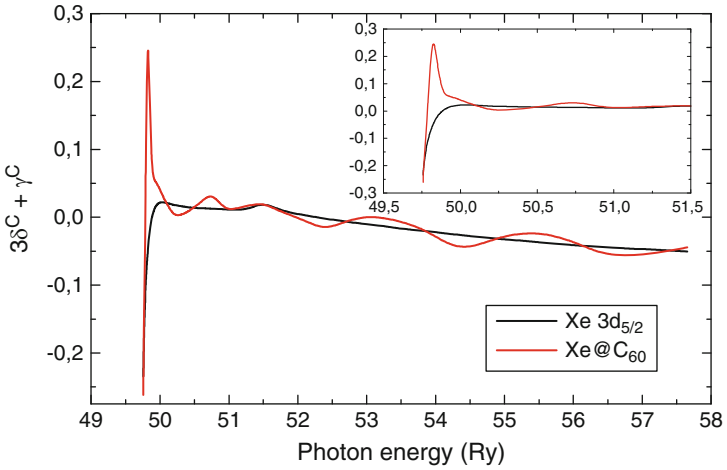

Fig. 2.398_Xe@C_{60}_e10 Magic combination of non-dipole angular anisotropy parameters $(3\delta^C + \gamma^C)$ of $3d_{5/2}$-electrons for Xe@C_{60} and Xe in RPAE

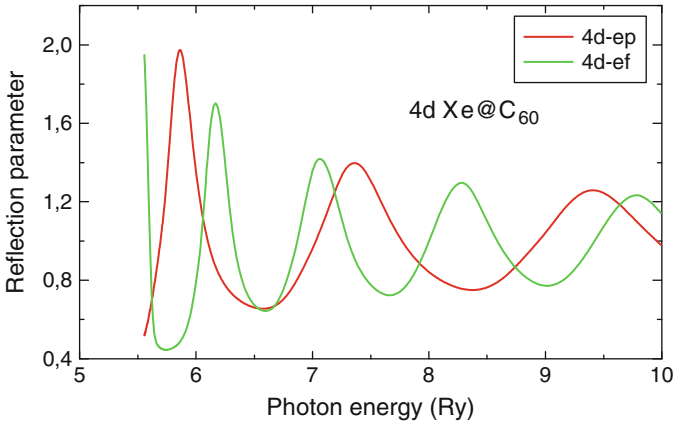

Fig. 2.399_Xe@C_{60}_g1 Reflection parameter $F_{l'}(\omega)$ (1.106) of photoelectrons from $4d$ level for Xe@C_{60} in RPAE

Figure 2.401_Cs@C_{60}_d1 shows dipole angular anisotropy parameter β of $3d_{3/2;5/2}$-electrons for Cs@C_{60} and Cs free atom in SP RPAE. As in the case of cross-section, complex variations of parameters shield the influence of 3/2 electrons on 5/2 electrons.

Figure 2.402_Cs@C_{60}_e1 displays non-dipole angular anisotropy parameter γ^C of $3d_{3/2;5/2}$-electrons for Cs@C_{60} and Cs in SP RPAE. Similar to the case shown in Fig. 2.401_Cs@C_{60}_d1, complex variations of parameters masks the influence of 3/2 electrons on 5/2 electrons.

Figures 2.403_Ba@C_{60}_b1–2.408_Ba@C_{60}_e2 (Ba@C_{60}) contain results of calculations for Ba@C_{60}.

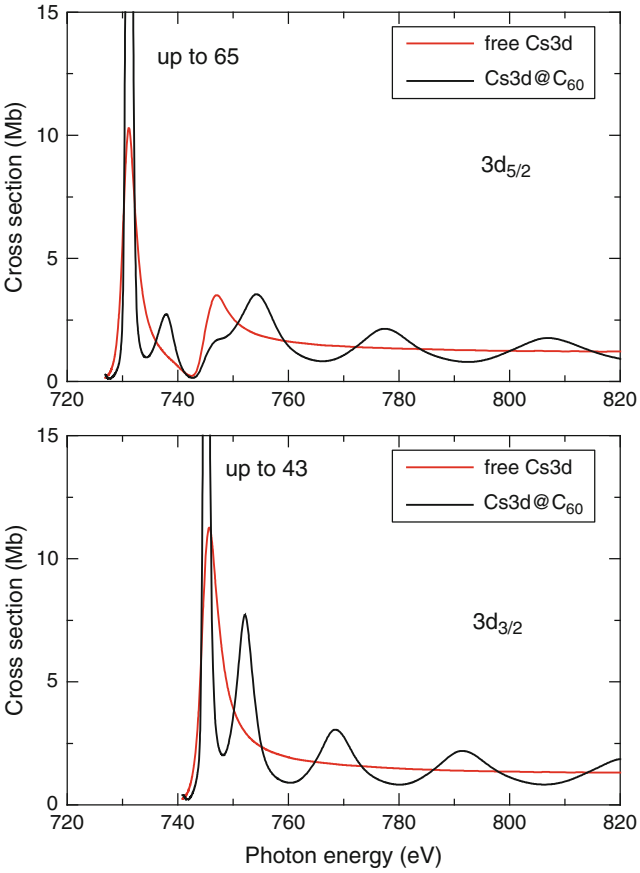

Fig. 2.400_Cs@C_{60}_b1 Photoionization cross-section of $3d_{5/2}$ and $3d_{3/2}$-electrons of Cs@C_{60} and Cs in SP RPAE

Figure 2.403_Ba@C_{60}_b1 presents photoionization cross-section of $4d$-electrons for Ba@C_{60} and Ba free atom in GRPAE (see [2.80]). There are five distinct maximums caused by photoelectron reflection from inner shell by the fullerene.

Figure 2.404_Ba@C_{60}_b2 presents partial photoionization cross-section of $4d$-electrons for Ba@C_{60} and Ba free atom in GRPAE.

Figure 2.405_Ba@C_{60}_b3 presents photoionization cross-section of $3d_{3/2}$ and $3d_{5/2}$-electrons for Ba@C_{60} and Ba free atom in GRPAE (see [2.82]).

Figure 2.406_Ba@C_{60}_d1 presents dipole angular anisotropy parameter β of $3d_{5/2}$- and $3d_{3/2}$ electrons for Ba@C_{60} and Ba free atom in GRPAE. Photoelectron reflection appends fairly sharp changes in behavior of β-parameter as a function of ω.

Figure 2.407_Ba@C_{60}_e1 shows non-dipole angular anisotropy parameter γ^{C} of $3d_{3/2;5/2}$-electrons for Ba@C_{60} and Ba free atom in GRPAE. Additional variations appreciably change the parameters.

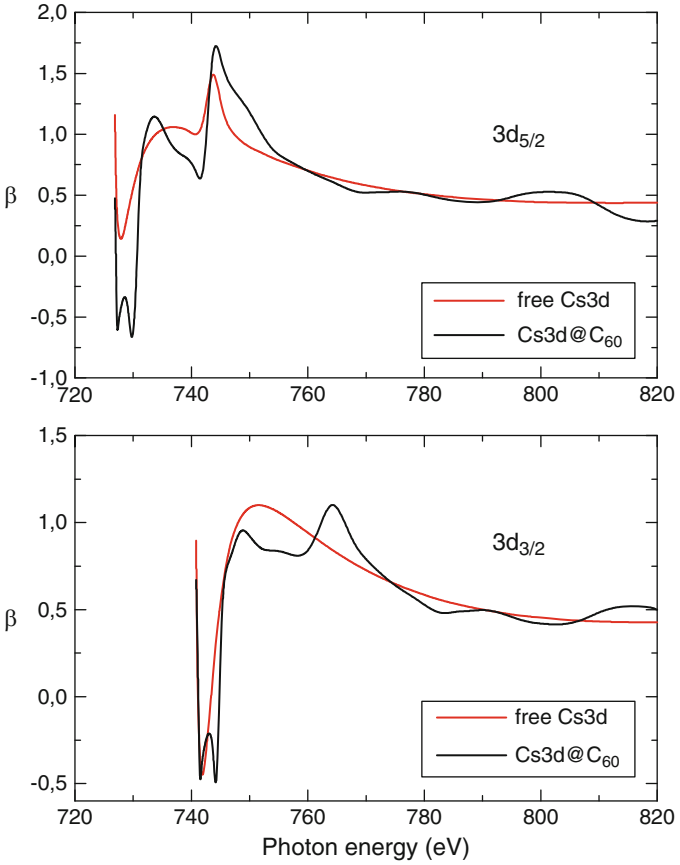

Fig. 2.401_Cs@C_{60}_d1 Dipole anisotropy parameter β for $3d_{5/2}$ and $3d_{3/2}$-electrons of Cs@C_{60} and Cs free atom in SP RPAE

Figure 2.408_Ba@C_{60}_e2 presents non-dipole angular anisotropy parameter δ^{C} of $3d_{3/2;5/2}$-electrons for Ba@C_{60} and Ba free atom. Photoelectron reflection not only appreciably enhances maximum caused by the influence of 3/2 electrons on 5/2 electrons, but created new oscillations.

Figures 2.409_La@C_{60}_b1–2.412_La@C_{60}_b4 (La@C_{60}) contain results of calculations for La@C_{60}.

Figure 2.409_La@C_{60}_b1 shows photoionization cross-section of $4d$-electrons of isolated atom La (see [2.85]) and La@C_{60} with account for reflection of photoelectrons by C_{60} shell, in RPAE.

Figure 2.410_La@C_{60}_b2 shows partial photoionization cross-sections of $4d$-electrons of isolated atom La (see [2.85]) and La@C_{60} with account for reflection of photoelectrons by C_{60} shell, in RPAE.

Figure 2.411_La@C_{60}_b3 demonstrates photoionization cross-section of $4d$-electrons of isolated atom La (see [2.85]) and La@C_{60} with account of reflection of photoelectrons by C_{60} shell and its polarization by the incoming photon, in GRPAE.

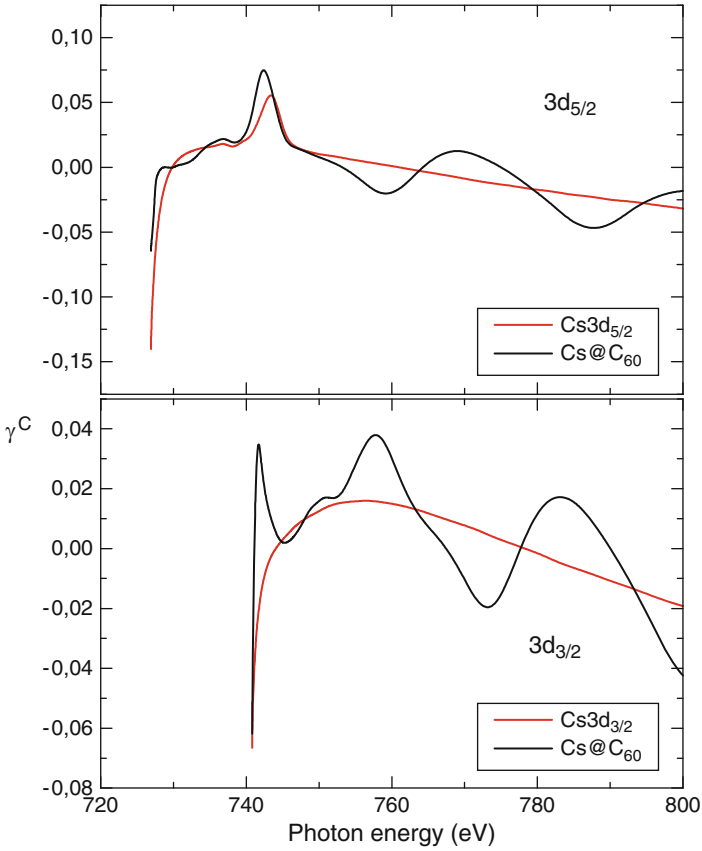

Fig. 2.402_Cs@C_{60}_e1 Non-dipole anisotropy parameter γ^{C} for $3d_{5/2}$- and $3d_{3/2}$-electrons of Cs free atom and Cs@C_{60} in SP RPAE

Figure 2.412_La@C_{60}_b4 depicts partial photoionization cross-sections of $4d$-electrons of isolated atom La and La@C_{60} with account for reflection of photoelectrons by C_{60} shell and its polarization by the incoming photon, in GRPAE.

Figures 2.413_Eu@C_{60}_b1–2.424_Eu@C_{60}_g1 Eu@C_{60} contain results of calculations for Eu@C_{60}.

Figure 2.413_Eu@C_{60}_b1 shows photoionization cross-section of $5p$ "down"-electrons for Eu@C_{60} and Eu free atom. Core polarization induces endohedral resonance at $\omega \approx 2.7$ Ry.

Figure 2.414_Eu@C_{60}_b2 presents photoionization cross-section of $5p$ "up"-electrons for Eu@C_{60} and Eu free atom in GRPAE. Core polarization induces endohedral resonance for $5p$"down," as well as for $5p$ "up" electrons at 2.7–2.8 Ry. Note, that amplification of cross-section in Eu@C_{60} is significantly smaller then in outer np-subshells of Ar@C_{60}, Kr@C_{60}, and Xe@C_{60}.

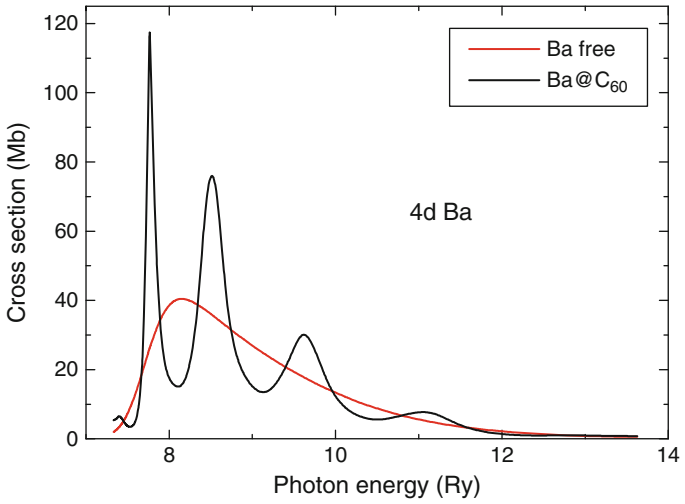

Fig. 2.403_Ba@C_{60}_b1 Photoionization cross section of 4*d*-electrons of Ba free atom and Ba@C_{60} in GRPAE

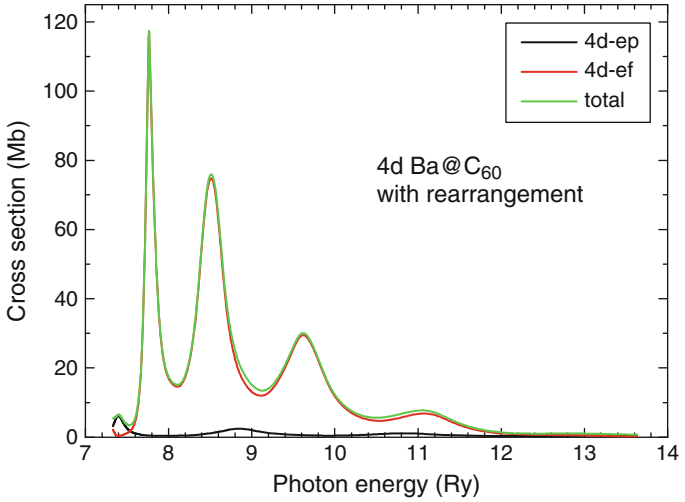

Fig. 2.404_Ba@C_{60}_b2 Partial photoionization cross section of 4*d*-electrons for Ba@C_{60} in GRPAE

Figure 2.415_Eu@C_{60}_b3 depicts photoionization cross-section of 5*s* "down"-electrons for Eu@C_{60} in GRPAE and FGRPAE and Eu free atom in GRPAE. The cross-section is changed mainly due to the effect of photoelectron reflection from the fullerene shell.

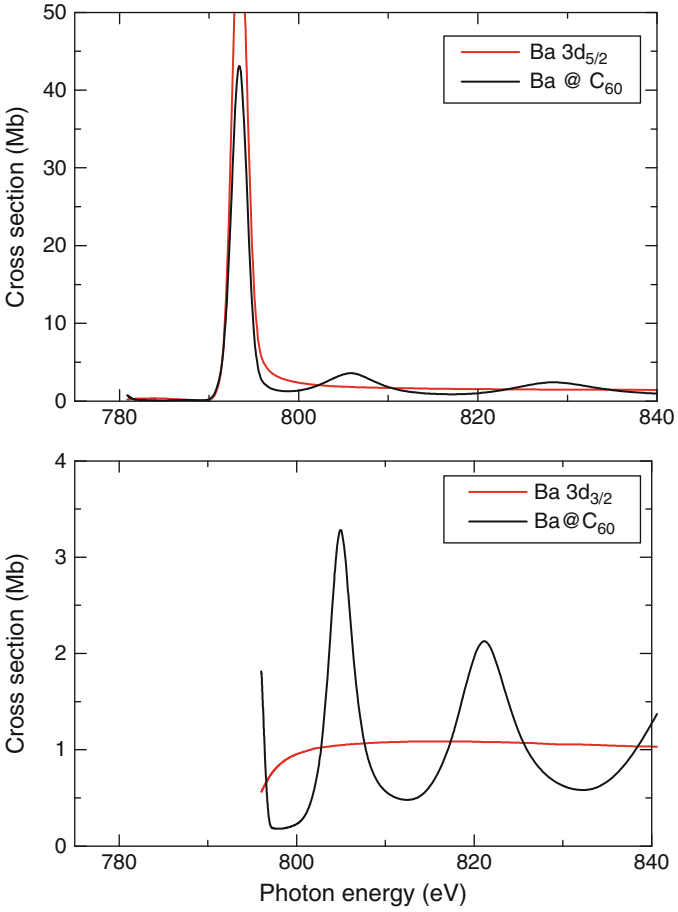

Fig. 2.405_Ba@C_{60}_b3 Photoionization cross section of $3d_{3/2}$, $3d_{5/2}$-electrons for Ba@C_{60} and Ba in GRPAE

Figure 2.416_Eu@C_{60}_b4 displays photoionization cross-section of $5s$ "up"-electrons for Eu@C_{60} in GRPAE and FGRPAE and Eu free atom in GRPAE. This cross-section as well as for "down" electrons is changed mainly due to the effect of photoelectron reflection from the fullerene shell, while fullerene shell polarization of the incoming photon is inessential.

Figure 2.417_Eu@C_{60}_b5 shows photoionization cross-section of $4f$ "up"-electrons for Eu@C_{60} and Eu free atom. The resonance in cross-section at 2.1 Ry is enhanced by an order of magnitude, increasing up to 130 Mb.

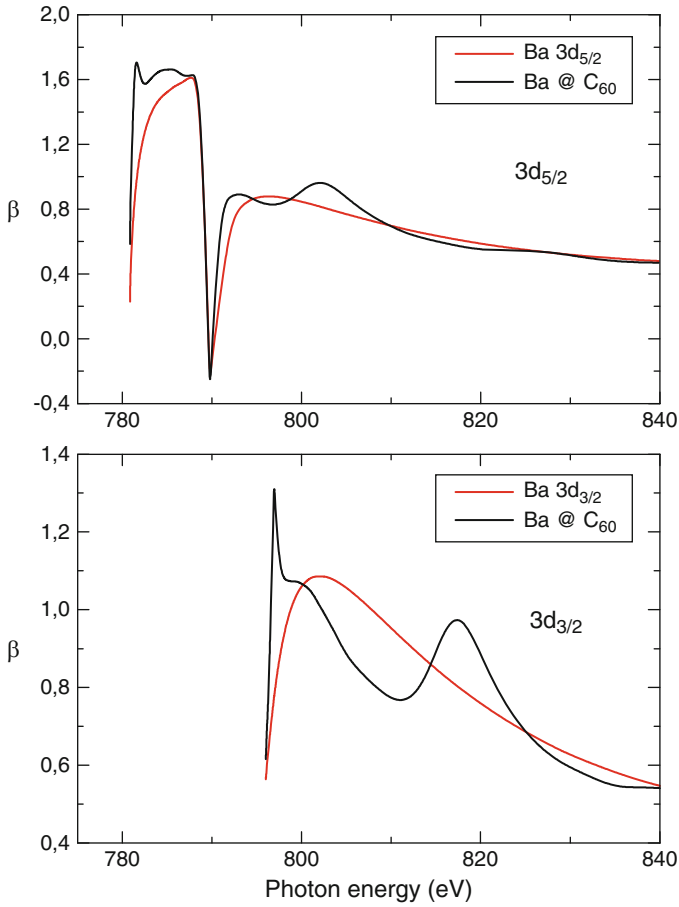

Fig. 2.406_Ba@C_{60}_d1 Dipole anisotropy parameter β of $3d_{5/2}$, $3d_{3/2}$-electrons for Ba@C_{60} and Ba in GRPAE

Figure 2.418_Eu@C_{60}_b6 shows photoionization cross-section of $4d$ "down"-electrons for Eu@C_{60} and Eu free atom. This transition is enhanced significantly due to photoelectrons' reflection. But its contribution to total photoionization cross-section is not very large.

Figure 2.419_Eu@C_{60}_b7 displays photoionization cross-section of $4d$ "up"-electrons for Eu@C_{60} and Eu free atom. Photoelectrons reflections generate several maximums on the photoionization curve within the energy interval 12–16 Ry.

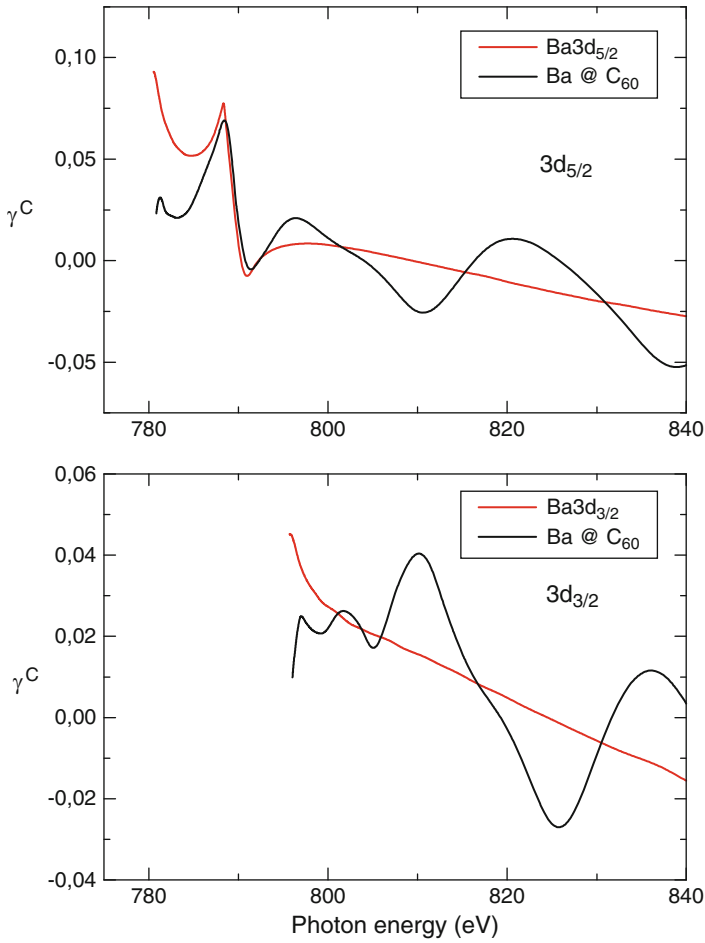

Fig. 2.407_Ba@C_{60}_e1 Non-dipole angular anisotropy parameter γ^C of $3d_{5/2}$, $3d_{3/2}$-electrons for Ba@C_{60} and Ba free atom in GRPAE

Figure 2.420_Eu@C_{60}_b8 collects photoionization cross-sections of $4d$ "up" and "down," $4f$ "up," $5p$ and $5p$ in the vicinity if Giant resonance for Eu@C_{60} and Eu free atom. It is seen that the influence of fullerene shell at Giant autoionizing resonance at 10.5 Ry is small.

Figure 2.421_Eu@C_{60}_d1 presents dipole angular anisotropy parameter β of $5p$-electrons for Eu@C_{60} and Eu. The influence of fullerene shell is small and it reveals in not too impressive oscillations of $\beta_{5p}(\omega)$.

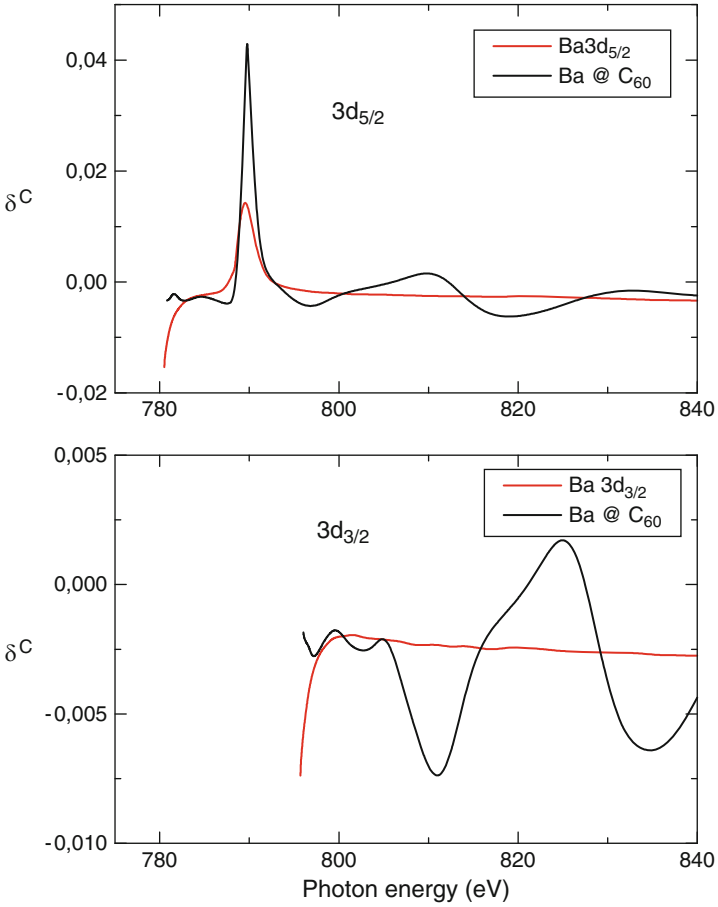

Fig. 2.408_Ba@C_{60}_e2 Non-dipole anisotropy parameter δ^C of $3d_{5/2}$ and $3d_{3/2}$-electrons for Ba@C_{60} and Ba

Figure 2.422_Eu@C_{60}_d2 displays the dipole angular anisotropy parameter β of $4f$-electrons for Eu@C_{60} and Eu. The influence of fullerene shell reveals at energy region of 3.5 Ry above photoionization threshold.

Figure 2.423_Eu@C_{60}_d3 presents dipole angular anisotropy parameter β_{4d} of $4d$-electrons for Eu@C_{60} and Eu atom. The fullerene shell effect is noticeable near the first minimum only.

Figure 2.424_Eu@C_{60}_g1 presents reflection parameter of $5p$-electrons for Eu@C_{60} and Eu free atom. It is precisely these oscillations define the structure of $5p$-subshell photoionization cross-section in Eu@C_{60} (see [2.86]).

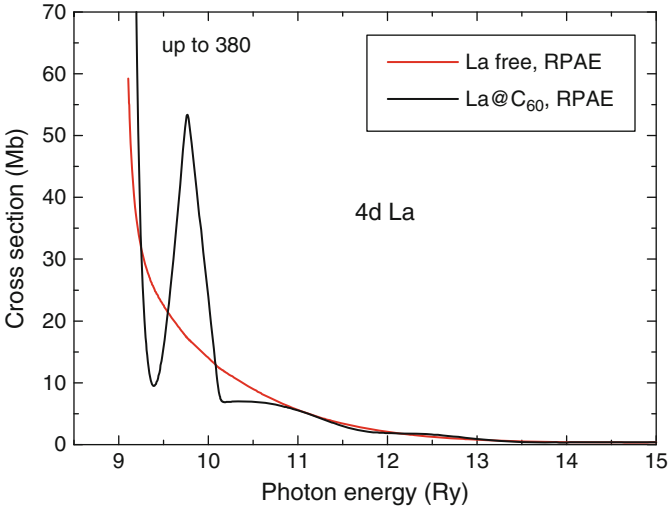

Fig. 2.409_La@C_{60}_b1 Photoionization cross section of 4*d*-electrons of isolated atom La (see [2.85]) and La@C_{60} with account for photoelectron reflection by C_{60} shell in RPAE

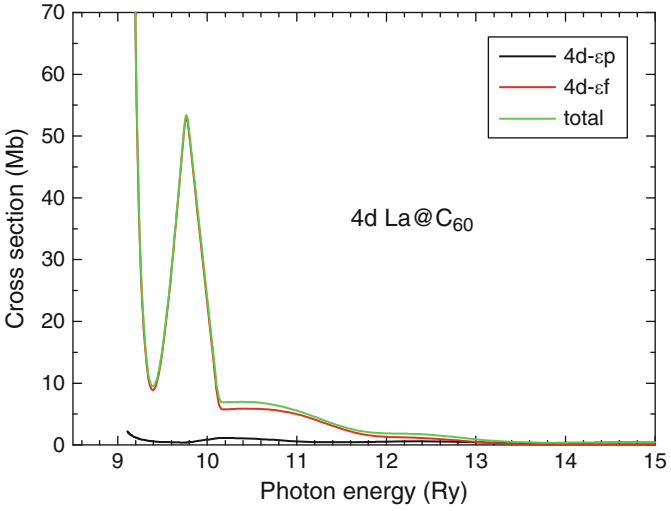

Fig. 2.410_La@C_{60}_b2 Partial photoionization cross sections of 4*d*-electrons of isolated atom La (see [2.85]) and La@C_{60} with account for photoelectron reflection by C_{60} shell in RPAE

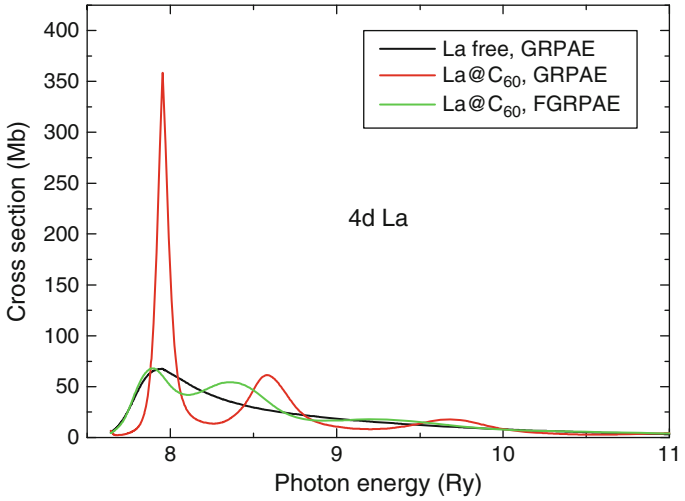

Fig. 2.411_La@C_{60}_b3 Photoionization cross section of $4d$-electrons of isolated atom La (see [2.85]) and La@C_{60} with account for photoelectrons reflection by C_{60} shell in GRPAE and FGRPAE

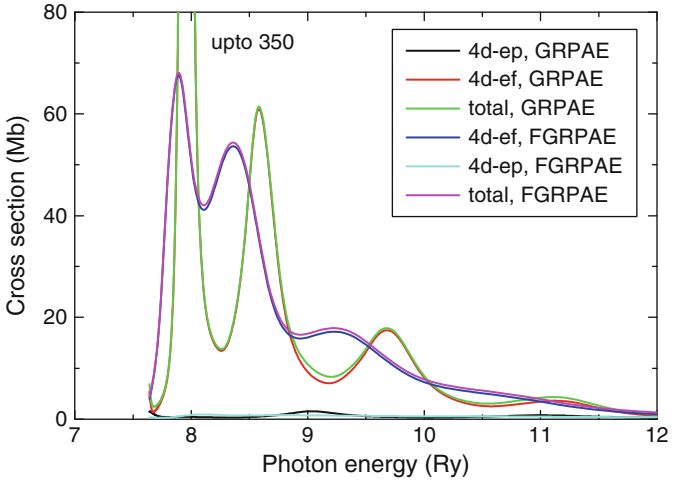

Fig. 2.412_La@C_{60}_b4 Partial photoionization cross sections of $4d$-electrons of isolated atom La and La@C_{60} with account for photoelectron reflection by C_{60} shell in GRPAE and FGRPAE

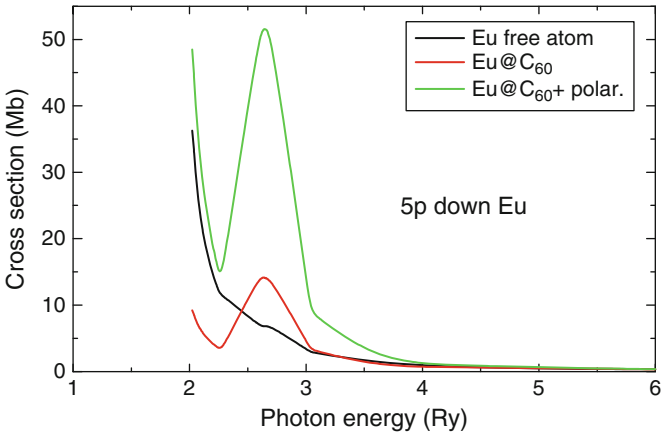

Fig. 2.413_Eu@C_{60}_b1 Photoionization cross section of $5p$ "down" electrons for Eu@C_{60}. and Eu in GRPAE with account of photoelectron reflection by C_{60} shell and its polarization by the incoming photon

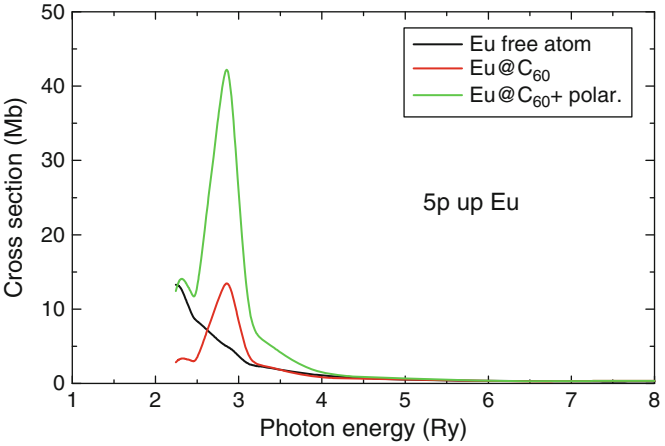

Fig. 2.414_Eu@C_{60}_b2 Photoionization cross section of $5p$ "up" electrons for Eu@C_{60} and Eu in GRPAE with account of photoelectron reflection by C_{60} shell and its polarization by the incoming photon

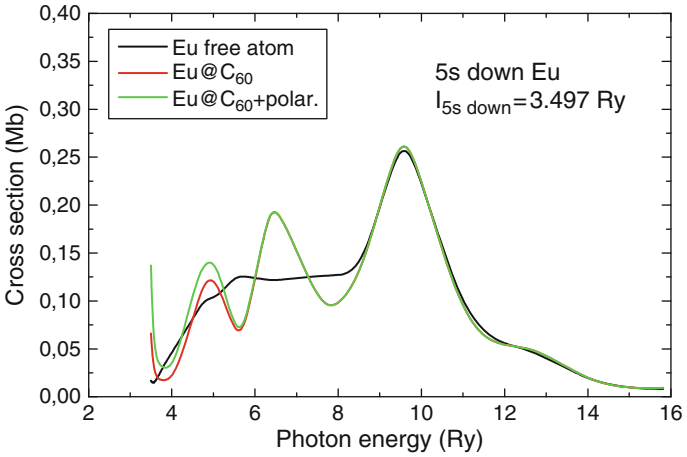

Fig. 2.415_Eu@C_{60}_b3 Photoionization cross section of 5*s* "down" electrons for Eu@C_{60}. and Eu

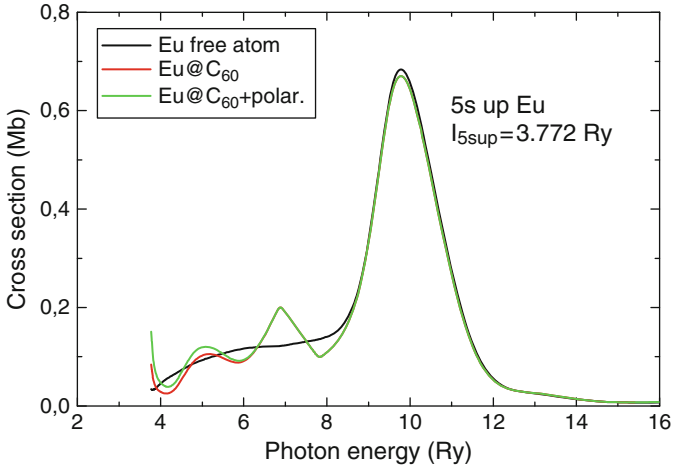

Fig. 2.416_Eu@C_{60}_b4 Photoionization cross section of 5*s* "up" electrons for Eu@C_{60} and Eu with account of photoelectron reflection by C_{60} shell and its polarization by the incoming photon

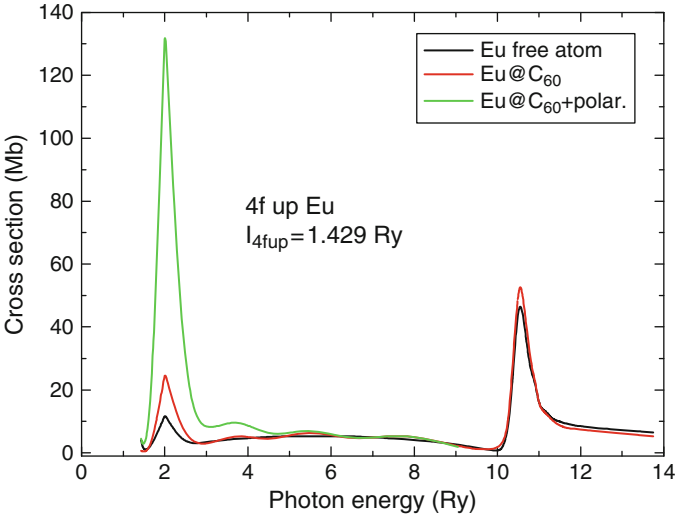

Fig. 2.417_Eu@C_{60}_b5 Photoionization cross section of $4f$ "up" electrons for Eu@C_{60}. and Eu with account of photoelectron reflection by C_{60} shell and its polarization by the incoming photon

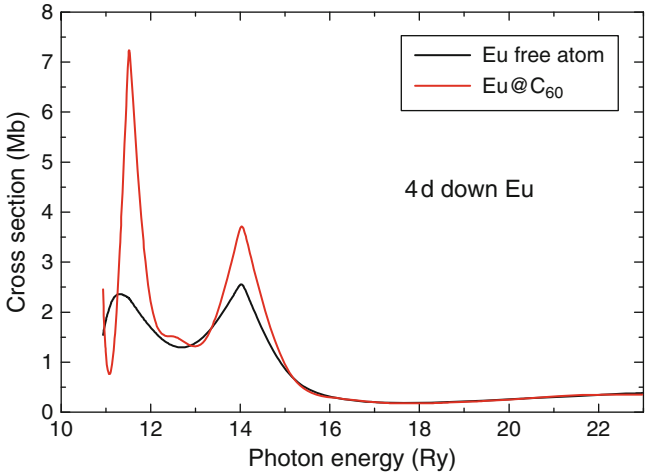

Fig. 2.418_Eu@C_{60}_b6 Photoionization cross section of $4d$ "down" electrons for Eu@C_{60}. and Eu

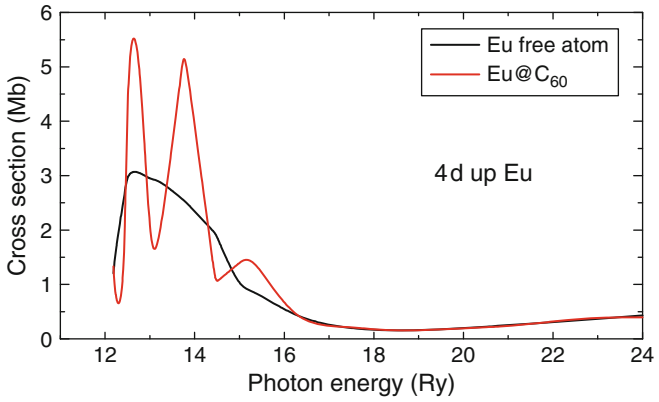

Fig. 2.419_Eu@C_{60}_b7 Photoionization cross-section of 4*d* "up" electrons for Eu@C_{60}. and Eu in SP RPAE

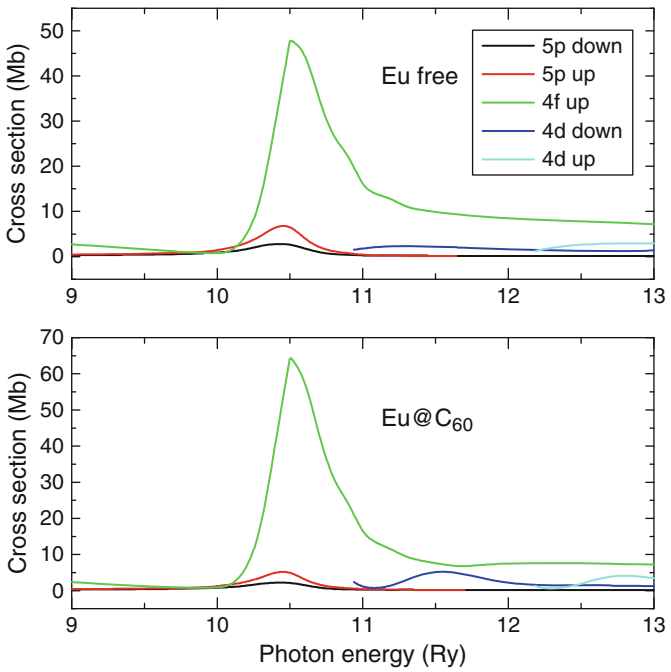

Fig. 2.420_Eu@C_{60}_b8 Photoionization cross section in the vicinity of Giant autoionization resonance for Eu and Eu@C_{60}

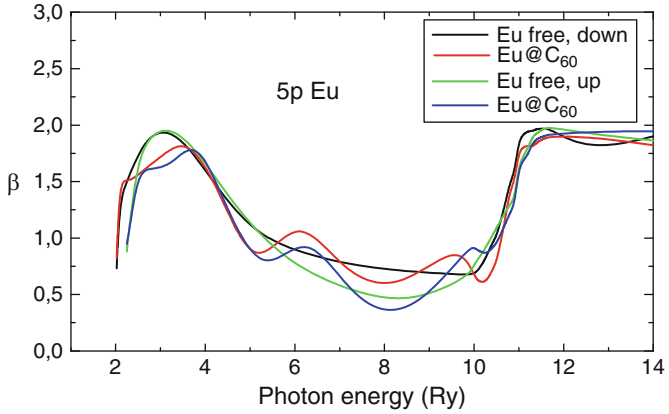

Fig. 2.421_Eu@C$_{60}$_d1 Dipole anisotropy parameter $\beta_{5p}(\omega)$ of $5p$ electrons for Eu@C$_{60}$ and Eu

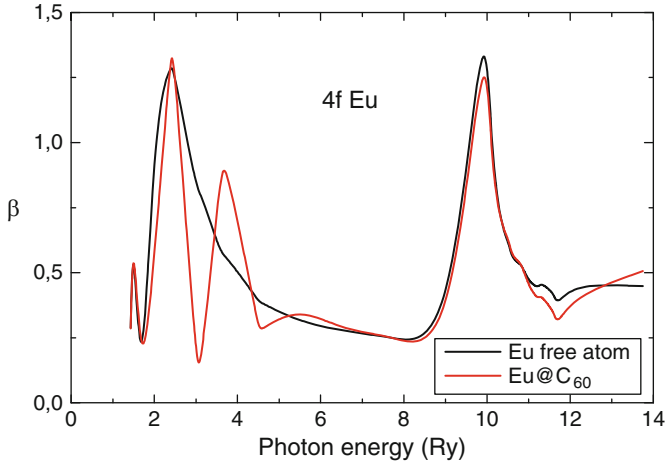

Fig. 2.422_Eu@C$_{60}$_d2 Dipole anisotropy parameter $\beta_{4f}(\omega)$ of $4f$ electrons for Eu@C$_{60}$ and Eu

Figures 2.425_C$_{60}$_g4 and 2.426_C$_{60}$_g5 (C$_{60}$) contain result of calculations for C$_{60}$.

Figure 2.425_C$_{60}$_g4 shows the absolute value of the amplitude $|G(\omega)|$ of the electromagnetic radiation enhancement factor of the C$_{60}$ electron shell. The arrows mark the thresholds of outer *np* subshells.

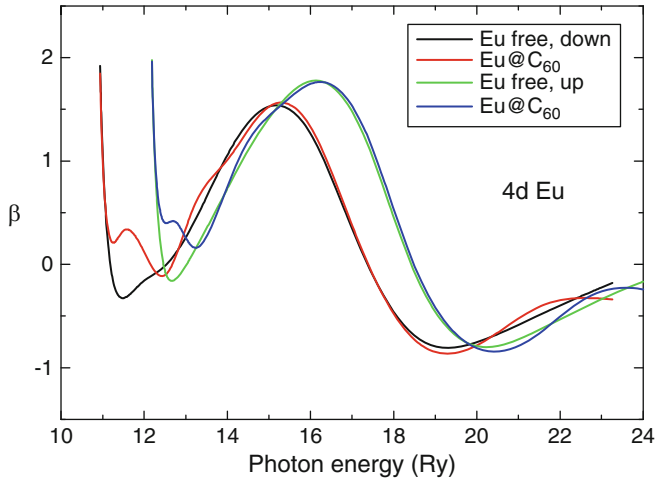

Fig. 2.423_Eu@C_{60}_d3 Dipole anisotropy parameter $\beta_{4d}(\omega)$ of $4d$ electrons for Eu@C_{60} and Eu

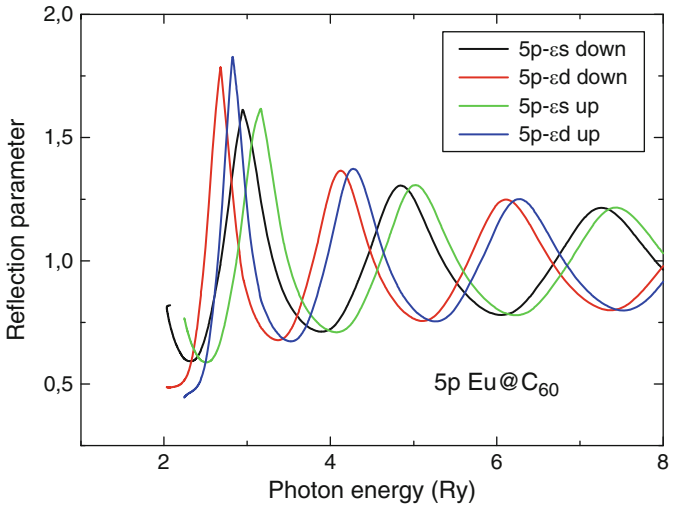

Fig. 2.424_Eu@C_{60}_g1 Reflection parameter $F_{l'}(\omega)$ (1.106) of photoelectrons from $5p$ level for Eu@C_{60}

Figure 2.426_C_{60}_g5 shows the absolute value of the polarization amplitude $|G(\omega)|$ of the electromagnetic radiation polarization factor of the C_{60} electron shell. The arrows mark the thresholds of outer ns subshells.

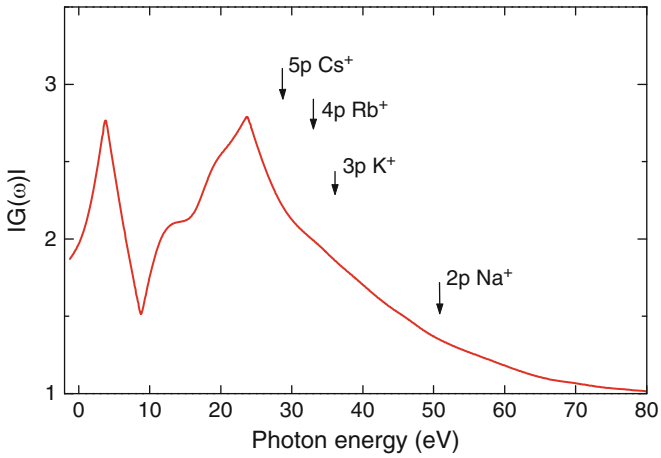

Fig. 2.425_C_{60}_g4 The absolute value of the amplitude $|G(\omega)|$ of the electromagnetic radiation enhancement factor by the C_{60} electron shell. The *arrows* mark the thresholds of outer *np* subshells

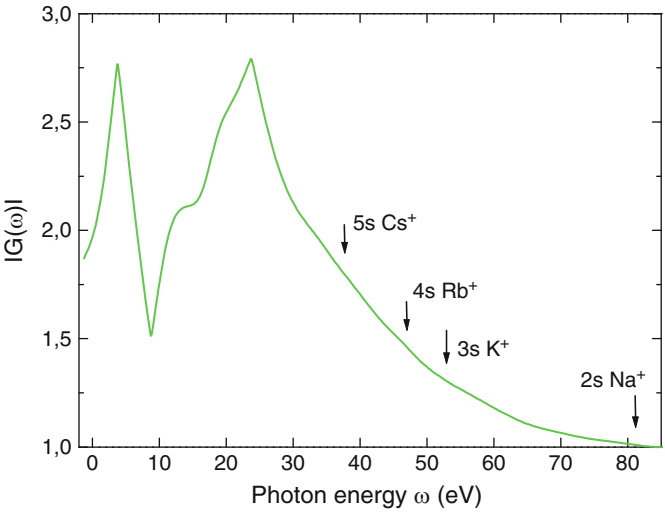

Fig. 2.426_C_{60}_g5 The absolute value of the amplitude $|G(\omega)|$ of the electromagnetic radiation enhancement factor by the C_{60} electron shell. The *arrows* mark the thresholds of outer *ns* subshells

Figures 2.427_Na^+@C_{60}_b1–2.431_Na^+@C_{60}_e2 (C_{60}) contain results of calculations for Na^+@C_{60}.

Figure 2.427_Na^+@C_{60}_b1 shows photoionization cross-section of $2p$-electrons of the ions Na^+ and Na^+@C_{60} with account of reflection of photoelectrons by C_{60} shell and its polarization by the incoming photon.

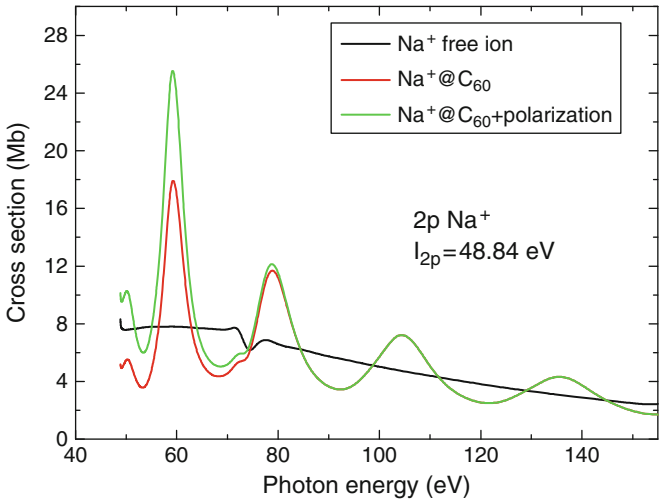

Fig. 2.427_Na^+@C_{60}_b1 Photoionization cross section of 2*p*-electrons of the ions Na^+ and Na^+@C_{60} with account of reflection of photoelectrons by C_{60} shell and its polarization by the incoming photon

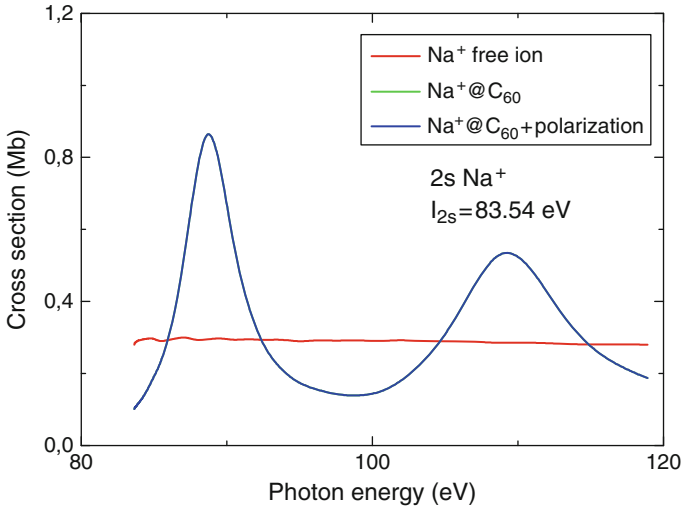

Fig. 2.428_Na^+@C_{60}_b2 Photoionization cross section of 2*s*-electrons of the ions Na^+ and Na^+@C_{60} with account of reflection of photoelectrons by C_{60} shell and its polarization by the incoming photon

Figure 2.428_Na^+@C_{60}_b2 displaces photoionization cross-section of 2*s*-electrons of the ions Na^+ and Na^+@C_{60} with account of reflection of photoelectrons by C_{60} shell and its polarization by the incoming photon.

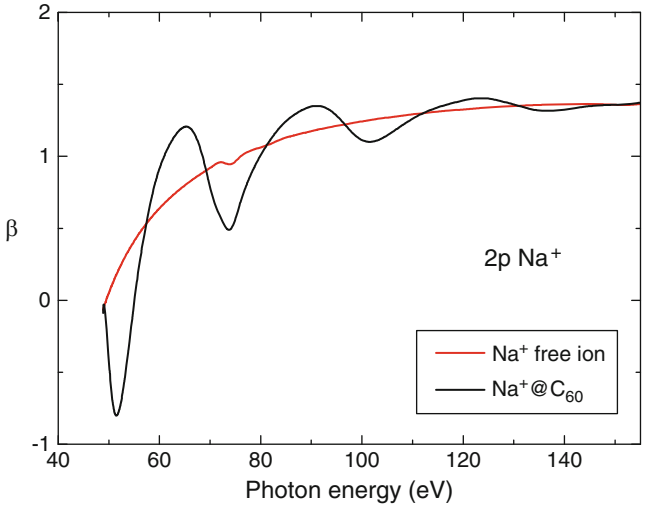

Fig. 2.429_Na$^+$@C$_{60}$_d1 Dipole angular anisotropy parameter β_{2p} of $2p$-electrons for Na$^+$@C$_{60}$ and Na$^+$

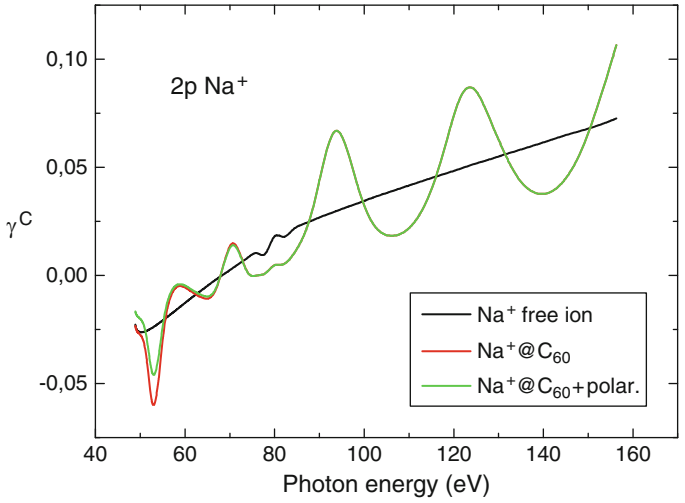

Fig. 2.430_Na$^+$@C$_{60}$_e1 Non-dipole angular anisotropy parameter γ^{C}_{2p} of $2p$-electrons for Na$^+$@C$_{60}$ and Na$^+$ with account of reflection of photoelectrons by C$_{60}$ shell and its polarization by the incoming photon

Figure 2.429_Na$^+$@C$_{60}$_d1 presents dipole angular anisotropy parameter β_{2p} of $2p$-electrons for Na$^+$@C$_{60}$ and Na$^+$ ions.

Figure 2.430_Na$^+$@C$_{60}$_e1 demonstrates non-dipole angular anisotropy parameter γ^{C}_{2p} of $2p$-electrons for Na$^+$@C$_{60}$ and Na$^+$ with account of reflection of photoelectrons by C$_{60}$ shell and its polarization by the incoming photon.

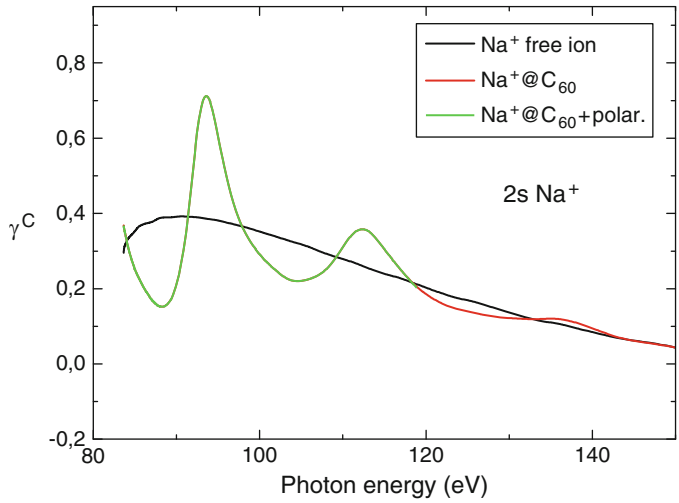

Fig. 2.431_Na^+@C_{60}_e2 Non-dipole angular anisotropy parameter γ_{2s}^{C} of $2s$-electrons for Na^+@C_{60} and Na^+ with account of reflection of photoelectrons by C_{60} shell and its polarization by the incoming photon

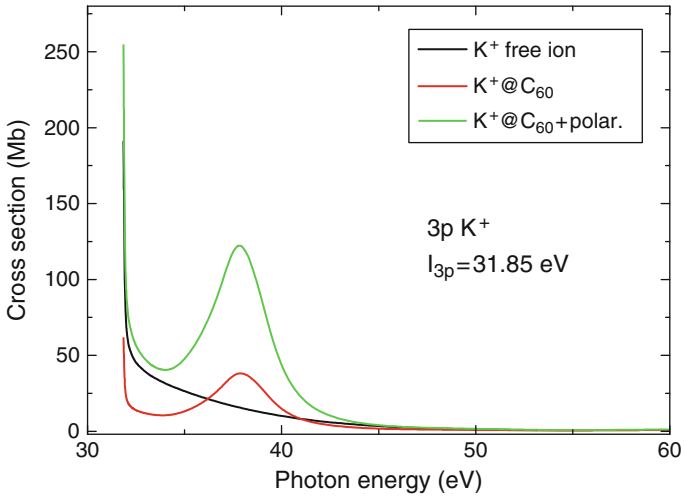

Fig. 2.432_K^+@C_{60}_b1 Photoionization cross section of $3p$-electrons of the ions K^+ and K^+@C_{60} with account of reflection of photoelectrons by C_{60} shell and its polarization by the incoming photon

Fig. 2.431_Na^+@C_{60}_e2 depicts non-dipole angular anisotropy parameter γ_{2s}^{C} of $2s$-electrons for Na^+@C_{60} and Na^+ with account of reflection of photoelectrons by C_{60} shell and its polarization by the incoming photon.

Figures 2.432_K^+@C_{60}_b1–2.436_K^+@C_{60}_e2 (K^+@C_{60}) contain results of calculations for K^+@C_{60}.

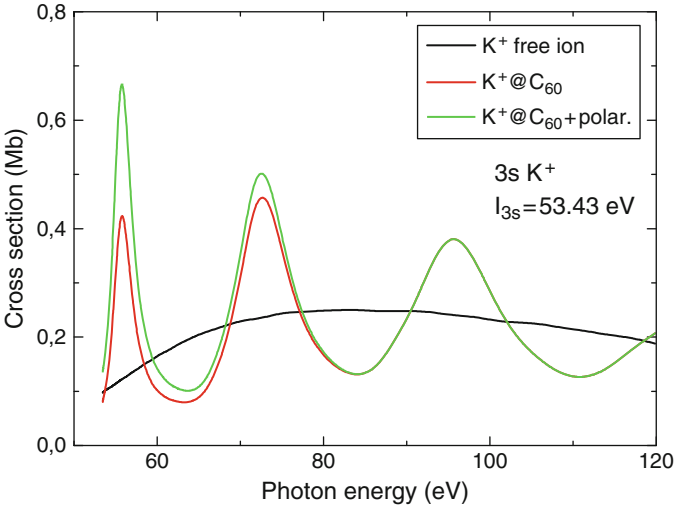

Fig. 2.433_K^+@C_{60}_b2 Photoionization cross section of 3*s*-electrons of the ions K^+ and K^+@C_{60} with account of reflection of photoelectrons by C_{60} shell and its polarization by the incoming photon

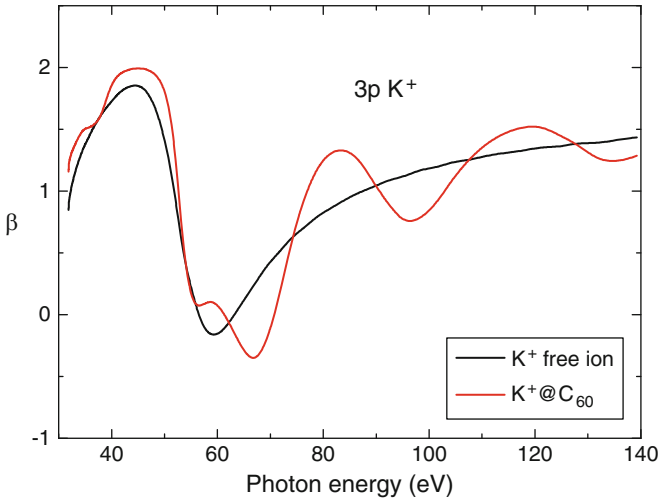

Fig. 2.434_K^+@C_{60}_d1 Dipole angular anisotropy parameter β_{3p} of 3*p*-electrons for K^+@C_{60} and K^+

Figure 2.432_K^+@C_{60}_b1 presents the photoionization cross-section of 3*p*-electrons of the ions K^+ and K^+@C_{60} with account of reflection of photoelectrons by C_{60} shell and its polarization by the incoming photon.

Figure 2.433_K^+@C_{60}_b2 shows photoionization cross-section of 3*s*-electrons of the ions K^+ and K^+@C_{60} with account of reflection of photoelectrons by C_{60} shell and its polarization by the incoming photon. The role of reflection is big.

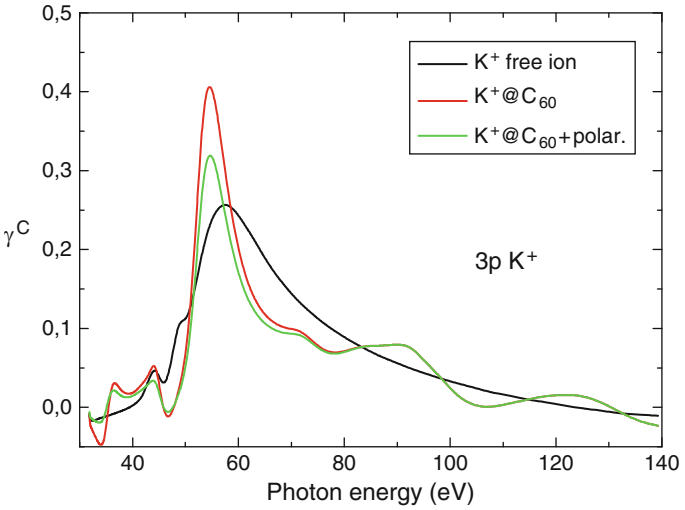

Fig. 2.435_K^+@C_{60}_e1 Non-dipole angular anisotropy parameter γ^C_{3p} of $3p$-electrons for K^+@C_{60} and K^+ with account of reflection of photoelectrons by C_{60} shell and its polarization by the incoming photon

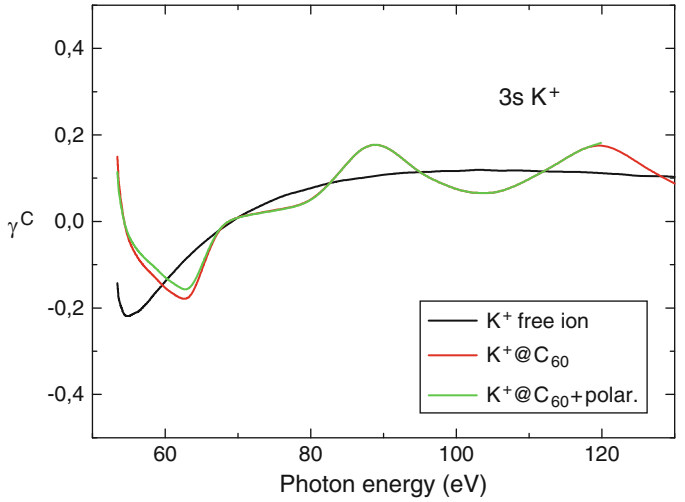

Fig. 2.436_K^+@C_{60}_e2 Non-dipole angular anisotropy parameter γ^C_{3s} of $3s$-electrons for K^+@C_{60} and K^+ with account of reflection of photoelectrons by C_{60} shell and its polarization by the incoming photon

Figure 2.434_K^+@C_{60}_d1 depicts the dipole angular anisotropy parameter β_{3p} of $3p$-electrons for K^+@C_{60} and K^+.

Figure 2.435_K^+@C_{60}_e1 demonstrates the non-dipole angular anisotropy parameter γ^C_{3p} of $3p$-electrons for K^+@C_{60} and K^+ with account of reflection of photoelectrons by C_{60} shell and its polarization by the incoming photon.

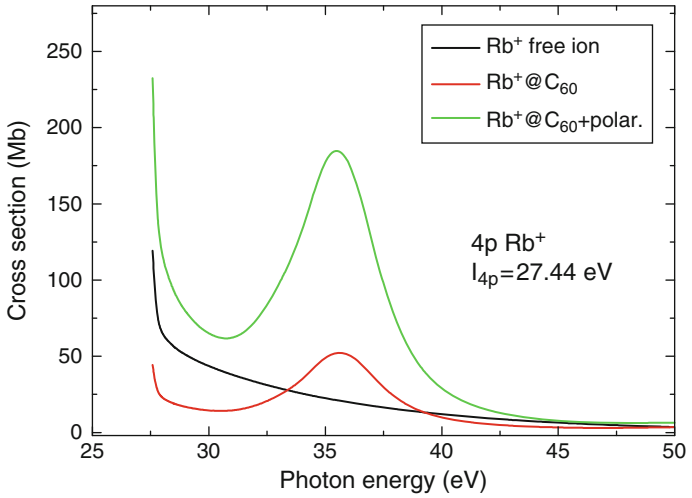

Fig. 2.437_$Rb^+@C_{60}$_b1 Photoionization cross section of $4p$-electrons of the ions Rb^+ and $Rb^+@C_{60}$ with account of reflection of photoelectrons by C_{60} shell and its polarization by the incoming photon

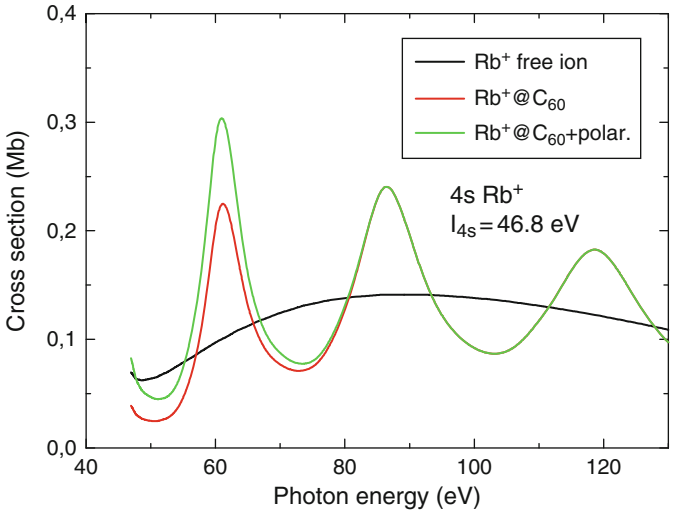

Fig. 2.438_$Rb^+@C_{60}$_b2 Photoionization cross section of $4s$-electrons of the ions Rb^+ and $Rb^+@C_{60}$ with account of reflection of photoelectrons by C_{60} shell and its polarization by the incoming photon

Figure 2.436_$K^+@C_{60}$_e2 displays non-dipole angular anisotropy parameter γ_{3s}^{C} of $3s$-electrons for $K^+@C_{60}$ and K^+ with account of reflection of photoelectrons by C_{60} shell and its polarization by the incoming photon.

Figures 2.437_$Rb^+@C_{60}$_b1–2.441_$Rb^+@C_{60}$_e2 ($Rb^+@C_{60}$) contain results of calculations for $Rb^+@C_{60}$.

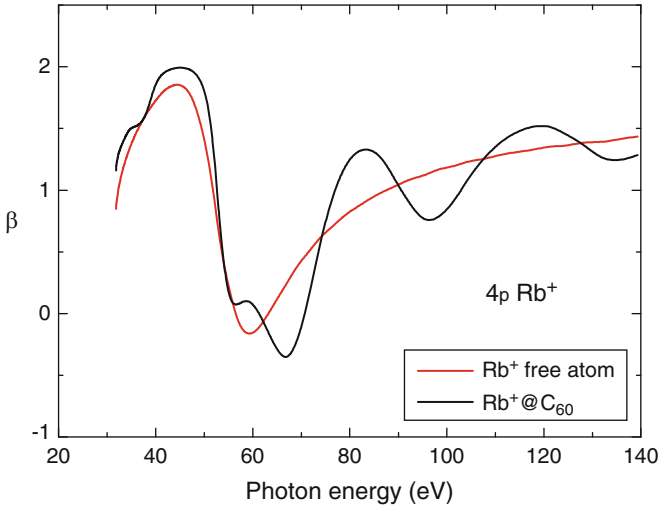

Fig. 2.439_Rb$^+$@C_{60}_d1 Dipole angular anisotropy parameter β_{4p} of $4p$-electrons for Rb^+@C_{60} and Rb^+

Figure 2.437_Rb$^+$@C_{60}_b1 depicts photoionization cross-section of $4p$-electrons of the ions Rb^+ and Rb^+@C_{60} with account of reflection of photoelectrons by C_{60} shell and its polarization by the incoming photon.

Figure 2.438_Rb$^+$@C_{60}_b2 presents photoionization cross-section of $4s$-electrons of the ions Rb^+ and Rb^+@C_{60} with account of reflection of photoelectrons by C_{60} shell and its polarization by the incoming photon.

Figure 2.439_Rb$^+$@C_{60}_d1 shows the dipole angular anisotropy parameter β_{4p} of $4p$-electrons for Rb^+@C_{60} and Rb^+. Fullerenes reflection adds quite prominent oscillations.

Figure 2.440_Rb$^+$@C_{60}_e1 presents non-dipole angular anisotropy parameter γ_{4p} of $4p$-electrons for Rb^+@C_{60} and Rb^+ with account for reflection of photoelectrons by C_{60} shell and its polarization by the incoming photon. As in most of the cases, reflection of photoelectrons by fullerene shell adds prominent oscillating structure.

Figure 2.441_Rb$^+$@C_{60}_e2 displays non-dipole angular anisotropy parameter γ_{4s} of $4s$-electrons for Rb^+@C_{60} and Rb^+ with account of reflection of photoelectrons by C_{60} shell and its polarization by the incoming photon.

Figures 2.442_Cs$^+$@C_{60}_b1–2.447_Cs$^+$@C_{60}_e3 (Cs^+@C_{60}) contain results of calculations for Cs^+@C_{60}.

Figure 2.442_Cs$^+$@C_{60}_b1 presents photoionization cross-section of $5p$-electrons for Cs^+ and Cs^+@C_{60} ions with account of reflection of photoelectrons by C_{60} shell and its polarization by the incoming photon. The effect of polarization is very big. It is remarkable that while reflection suppresses the threshold value, polarization increases it dramatic.

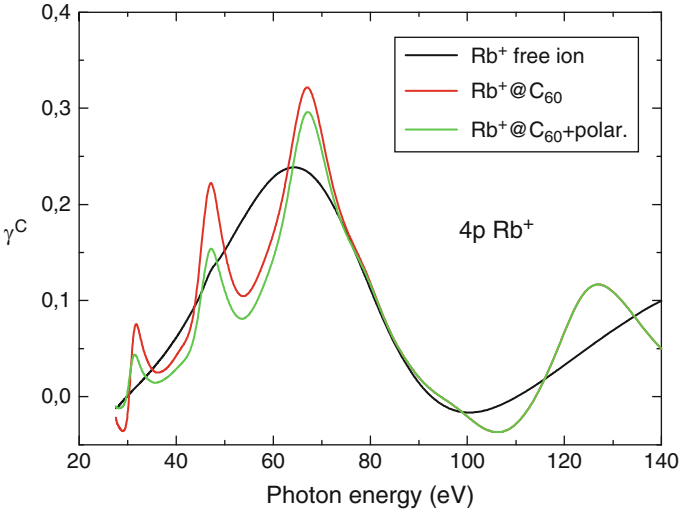

Fig. 2.440_Rb$^+$@C$_{60}$_e1 Non-dipole angular anisotropy parameter γ^{C}_{4p} of $4p$-electrons for Rb$^+$@C$_{60}$ and Rb$^+$ with account of reflection of photoelectrons by C$_{60}$ shell and its polarization by the incoming photon

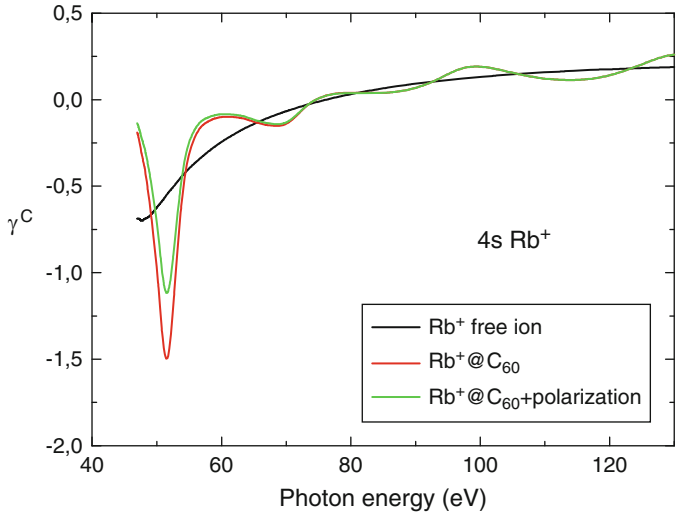

Fig. 2.441_Rb$^+$@C$_{60}$_e2 Non-dipole angular anisotropy parameter of $4s$-electrons for Rb$^+$@C$_{60}$ and Rb$^+$ with account of reflection of photoelectrons by C$_{60}$ shell and its polarization by the incoming photon

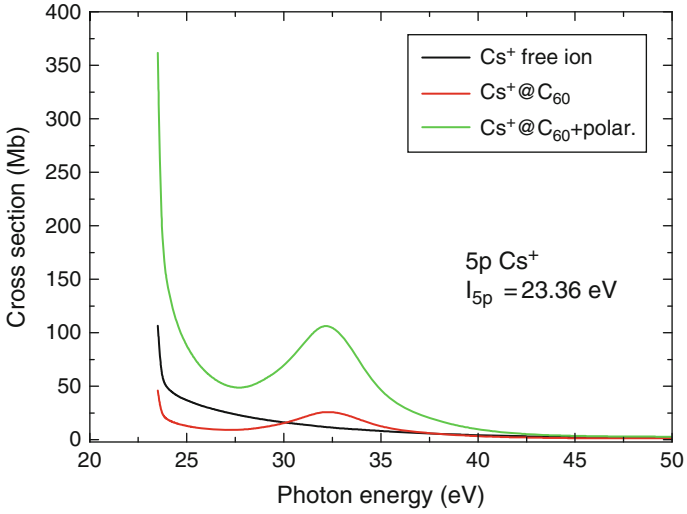

Fig. 2.442_Cs^+@C_{60}_b1 Photoionization cross section of 5*p*-electrons of the ions Cs^+ and Cs^+@C_{60} with account of reflection of photoelectrons by C_{60} shell and its polarization by the incoming photon

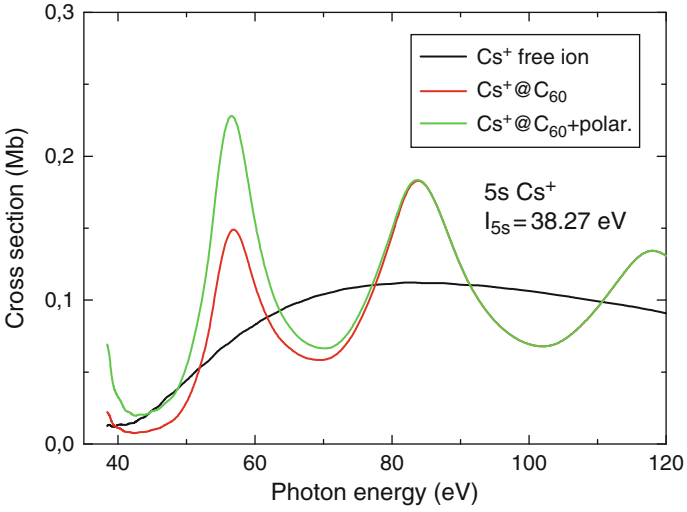

Fig. 2.443_Cs^+@C_{60}_b2 Photoionization cross section of 5*s*-electrons of ion Cs^+ and Cs^+@C_{60} with account of reflection of photoelectrons by C_{60} shell and its polarization by the incoming photon

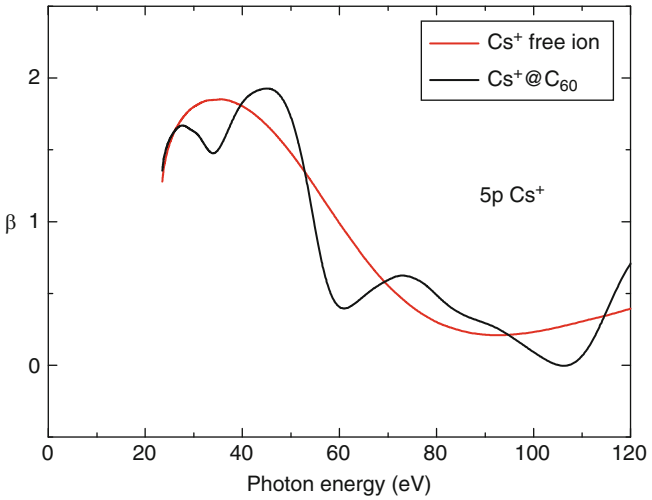

Fig. 2.444_Cs$^+$@C$_{60}$_d1 Dipole angular anisotropy parameter of $5p$-electrons for Cs$^+$@C$_{60}$ and Cs$^+$

Figure 2.443_Cs$^+$@C$_{60}$_b2 displays photoionization cross-section of $5s$-electrons for Cs$^+$ and Cs$^+$@C$_{60}$ ions with account of reflection of photoelectrons by C$_{60}$ shell and its polarization by the incoming photon. As usual, the role of polarization is much smaller than for the neighbor p-subshell.

Figure 2.444_Cs$^+$@C$_{60}$_d1 shows the dipole angular anisotropy parameter β_{5p} of $5p$-electrons for Cs$^+$@C$_{60}$ and Cs$^+$ ions. It has typical reflection oscillations.

Figure 2.445_Cs$^+$@C$_{60}$_e1 depicts non-dipole angular anisotropy parameter γ^{C}_{5p} of $5p$-electrons for Cs$^+$@C$_{60}$ and Cs$^+$ with account of reflection of photoelectrons by C$_{60}$ shell and its polarization by the incoming photon. Effect of polarization is small.

Figure 2.446_Cs$^+$@C$_{60}$_e2 displays the non-dipole angular anisotropy parameter γ^{C}_{5s} of $5s$-electrons for Cs$^+$@C$_{60}$ and Cs$^+$ ions with account of reflection of photoelectrons by C$_{60}$ shell and its polarization by the incoming photon.

Figure 2.447_Cs$^+$@C$_{60}$_e3 presents non-dipole angular anisotropy parameter δ^{C}_{5p} of $5p$-electrons for Cs$^+$@C$_{60}$ and Cs$^+$ with account of reflection of photoelectrons by C$_{60}$ shell and its polarization by the incoming photon. The role of polarization is noticeable at 30–50 eV.

Figures 2.448_Ce$^+$@C$_{60}$_b1–2.452_Ce$^+$@C$_{60}$_b5 (Ce$^+$@C$_{60}$) contain results of calculations for Ce$^+$@C$_{60}$ $Z = 58$ Ce$^+$@C$_{60}$ $4d^{10}4f5s^25p^66s^2$.

Figure 2.448_Ce$^+$@C$_{60}$_b1 displays photoionization cross-section of $5p$-electrons of ion Ce$^+$ and Ce$^+$@C$_{60}$ with account of reflection of photoelectrons by C$_{60}$ shell and its polarization by the incoming photon. Note that the reflection is not essential for all photon energies of 7 Ry and above. This is because the photoelectrons in this area are fast.

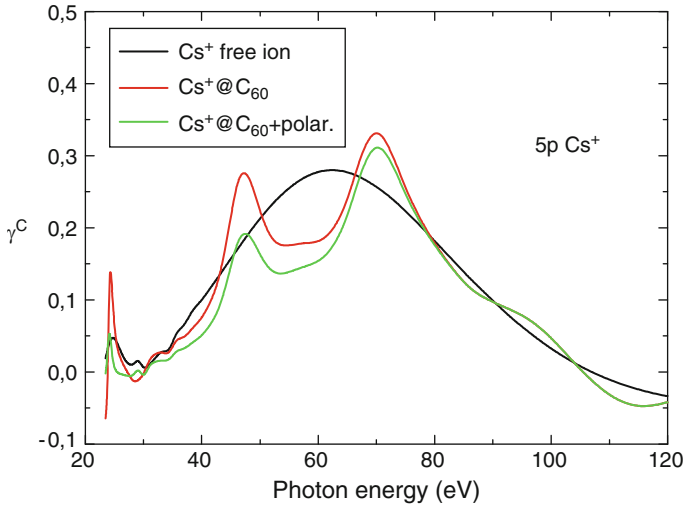

Fig. 2.445_Cs^+@C_{60}_e1 Non-dipole angular anisotropy parameter of 5*p*-electrons for Cs^+@C_{60} and Cs^+ ions with account of reflection of photoelectrons by C_{60} shell and its polarization by the incoming photon

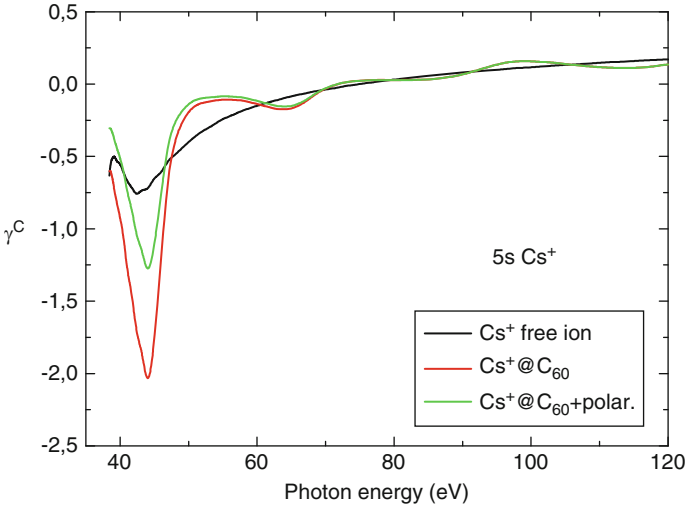

Fig. 2.446_Cs^+@C_{60}_e2 Non-dipole angular anisotropy parameter of 5*s*-electrons for Cs^+@C_{60} and Cs^+ ions with account of reflection of photoelectrons by C_{60} shell and its polarization by the incoming photon

Figure 2.449_Ce^+@C_{60}_b2 shows partial photoionization cross-section of 5*p*-electrons of isolated atom Ce^+ and Ce^+@C_{60} with account of reflection of photoelectrons by C_{60} shell and its polarization by the incoming photon.

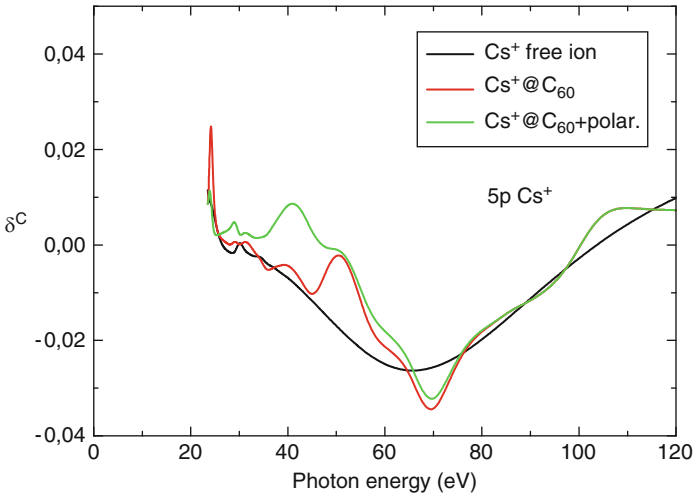

Fig. 2.447_Cs^+@C_{60}_e3 Non-dipole angular anisotropy parameter of $5p$-electrons for Cs^+@C_{60} and Cs^+ with account of reflection of photoelectrons by C_{60} shell and its polarization by the incoming photon

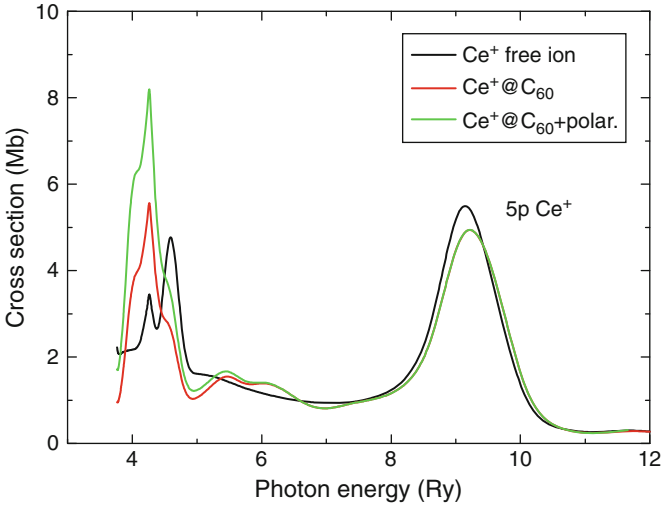

Fig. 2.448_Ce^+@C_{60}_b1 Photoionization cross section of $5p$-electrons of ion Ce^+ and Ce^+@C_{60} with account of reflection of photoelectrons by C_{60} shell and its polarization by the incoming photon

Figure 2.450_Ce^+@C_{60}_b3 demonstrates the photoionization cross-section of $5s$-electrons of ion Ce^+ and Ce^+@C_{60} with account of reflection of photoelectrons by C_{60} shell and its polarization by the incoming photon.

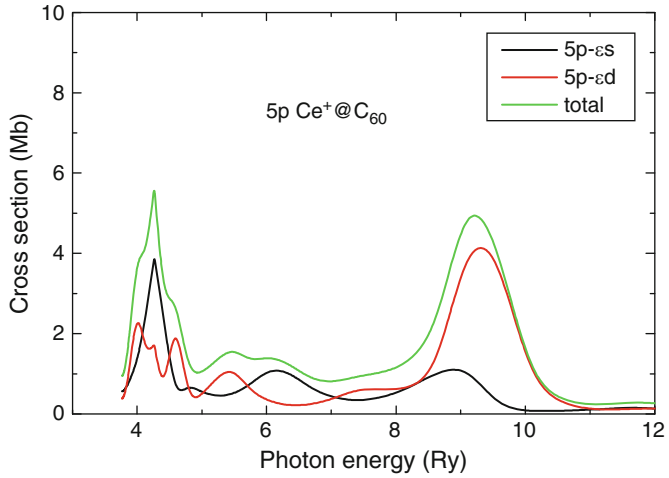

Fig. 2.449_Ce$^+$@C_{60}_b2 Partial photoionization cross section of 5*p*-electrons of isolated atom Ce^+ and Ce^+@C_{60} with account of reflection of photoelectrons by C_{60} shell and its polarization by the incoming photon

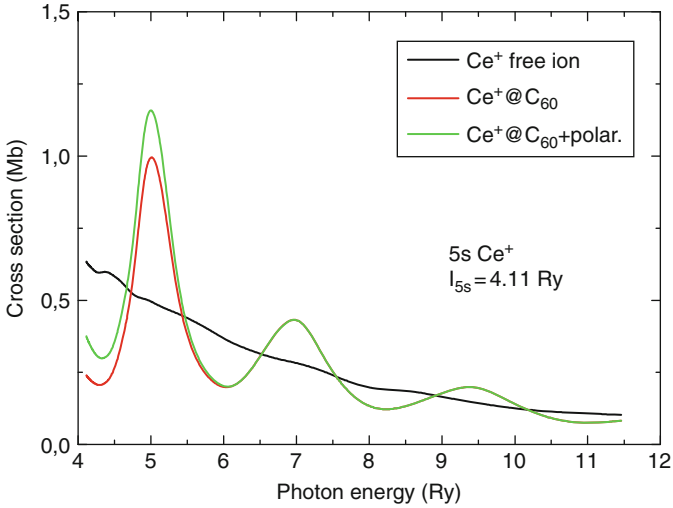

Fig. 2.450_Ce$^+$@C_{60}_b3 Photoionization cross section of 5*s*-electrons of ion Ce^+ and Ce^+@C_{60} with account of reflection of photoelectrons by C_{60} shell and its polarization by the incoming photon

Figure 2.451_Ce$^+$@C_{60}_b4 displays the photoionization cross-section of 4*d*-electrons of ion Ce^+ and Ce^+@C_{60} with account of reflection of photoelectrons by C_{60} shell and its polarization by the incoming photon. The effects of fullerene are quite small at any photon energy.

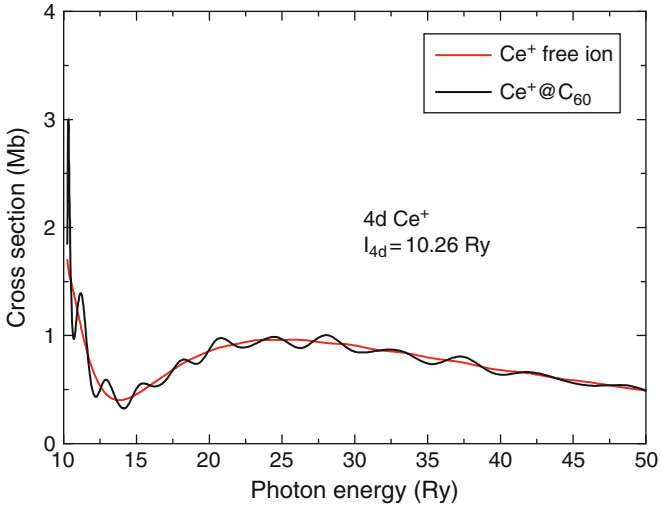

Fig. 2.451_Ce^+@C_{60}_b4 Photoionization cross section of $4d$-electrons of ion Ce^+ and Ce^+@C_{60} with account of reflection of photoelectrons by C_{60} shell and its polarization by the incoming photon

Figure 2.452_Ce^+@C_{60}_b5 presents partial photoionization cross-section of $4d$-electrons of ion Ce^+ and Ce^+@C_{60} with account of reflection of photoelectrons by C_{60} shell and its polarization by the incoming photon. The fullerene shell is responsible for all the small ripples on the curves.

Figures 2.453_Ce^{3+}@C_{60}_b1–2.457_Ce^{3+}@C_{60}_b5 (Ce^{3+}@C_{60}) contain results of calculations for Ce^{3+}@C_{60} $Z = 58$ Ce^{3+}@C_{60} $4d^{10}5s^25p^6$.

Figure 2.453_Ce^{3+}@C_{60}_b1 depicts photoionization cross-section of $5p$-electrons of ion Ce^{3+} and Ce^{3+}@C_{60} with account of reflection of photoelectrons by C_{60} shell and its polarization by the incoming photon. The curve is qualitatively similar to Fig. 2.449_Ce^+@C_{60}_b2.

Figure 2.454_Ce^{3+}@C_{60}_b2 shows partial photoionization cross-section of $5p$-electrons of ion Ce^{3+} and Ce^{3+}@C_{60} with account of reflection of photoelectrons by C_{60} shell and its polarization by the incoming photon.

Figure 2.455_Ce^{3+}@C_{60}_b3 shows photoionization cross-section of $5s$-electrons of ion Ce^{3+} and Ce^{3+}@C_{60} with account of reflection of photoelectrons by C_{60} shell and its polarization by the incoming photon in RPAE, FRPAE, and GFRPAE.

Figure 2.456_Ce^{3+}@C_{60}_b4 demonstrates the photoionization cross section of $4d$-electrons of ion Ce^{3+} and Ce^{3+}@C_{60} with account of reflection of photoelectrons by C_{60} shell in RPAE, FRPAE, and GFRPAE. One sees typical reflection oscillations.

Figure 2.457_Ce^{3+}@C_{60}_b5 shows the partial $4d$–εp and $4d$–εf photoionization cross-sections of $4d$-electrons of ion Ce^{3+} and Ce^{3+}@C_{60} with account of reflection of photoelectrons by C_{60} shell and its polarization by the incoming photon.

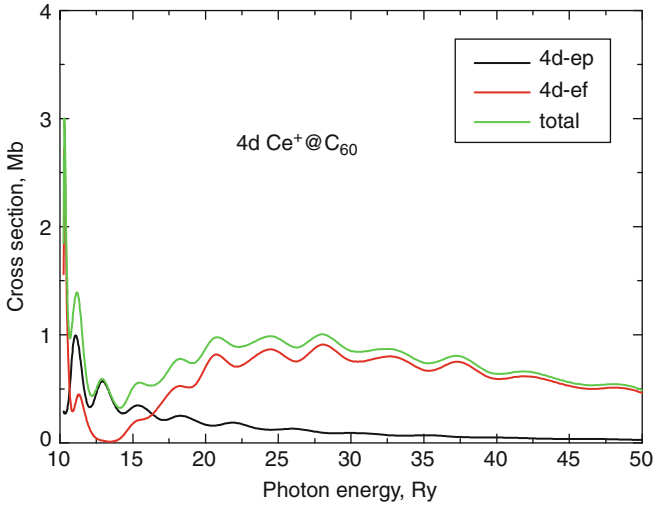

Fig. 2.452_Ce$^+$@C$_{60}$_b5 Partial photoionization cross section of $4d$-electrons of ion Ce^+ and Ce^+@C_{60} with account of reflection of photoelectrons by C_{60} shell and its polarization by the incoming photon

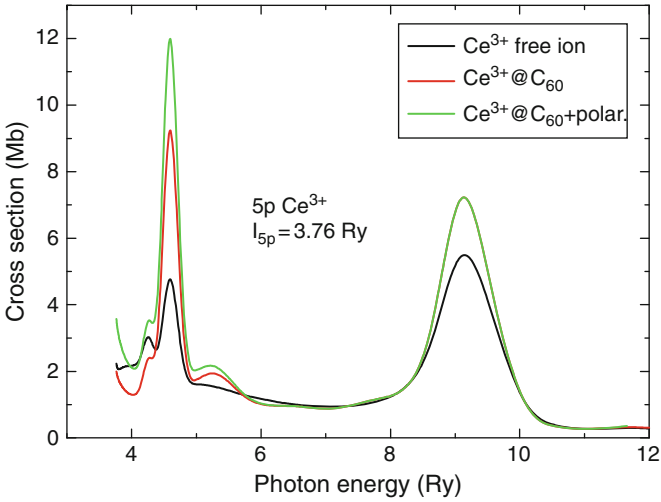

Fig. 2.453_Ce^{3+}@C$_{60}$_b1 Photoionization cross section of $5p$-electrons of ion Ce^{3+} and Ce^{3+}@C_{60} with account of reflection of photoelectrons by C_{60} shell and its polarization by the incoming photon in RPAE, FRPAE and GFRPAE

The cross-section $4d–\varepsilon f$ starting dominates from the threshold. For $\omega > 25$ Ry the domination becomes absolute.

Figures 2.458_Ce^{4+}@C$_{60}$_a1–2.464_Ce^{4+}@C$_{60}$_b6 (Ce^{4+}@C_{60}) contain results of calculations for Ce^{4+}@C_{60}. $Z = 58$ Ce^{4+}@C_{60} $4d^{10}5s^25p^6$.

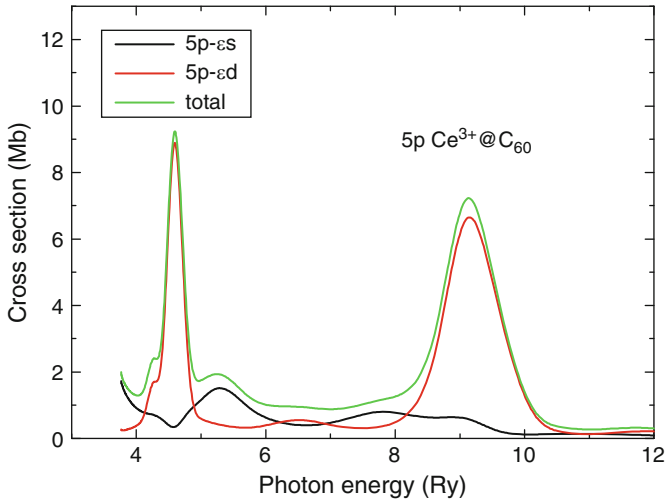

Fig. 2.454_Ce^{3+}@C_{60}_b2 Partial photoionization cross section of 5*p*-electrons of ion Ce^{3+} and Ce^{3+}@C_{60} with account of reflection of photoelectrons by C_{60} shell and its polarization by the incoming photon

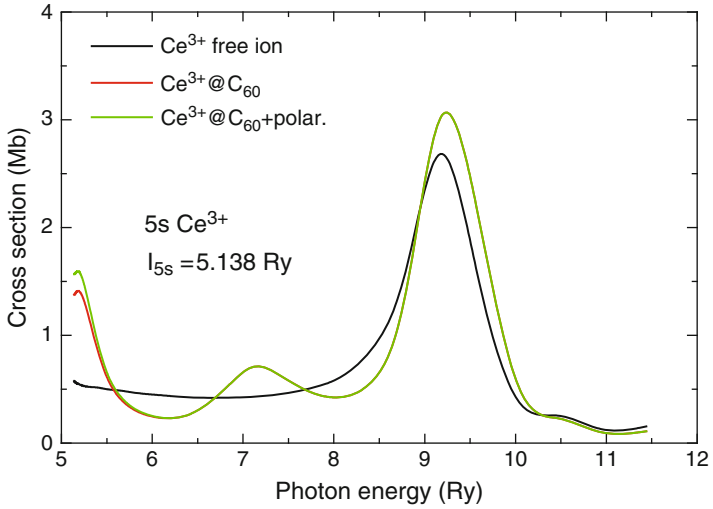

Fig. 2.455_Ce^{3+}@C_{60}_b3 Photoionization cross section of 5*s*-electrons of ion Ce^{3+} and Ce^{3+}@C_{60} with account of reflection of photoelectrons by C_{60} shell and its polarization by the incoming photon

Figure 2.458_Ce^{4+}@C_{60}_a1 demonstrates total photoionization cross-section of Ce^{4+} and Ce^{4+}@C_{60} ions with account of reflection of photoelectrons by C_{60} shell and its polarization by the incoming photon. A powerful maximum that is Giant autoionization resonance remains almost untouched by the fullerenes shell, because

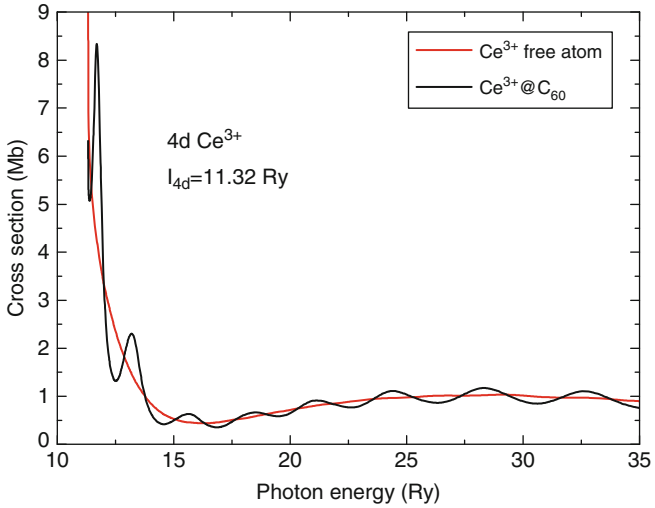

Fig. 2.456_Ce^{3+}@C_{60}_b4 Photoionization cross section of $4d$-electrons of ion Ce^{3+} and Ce^{3+}@C_{60} with account of reflection of photoelectrons by C_{60} shell

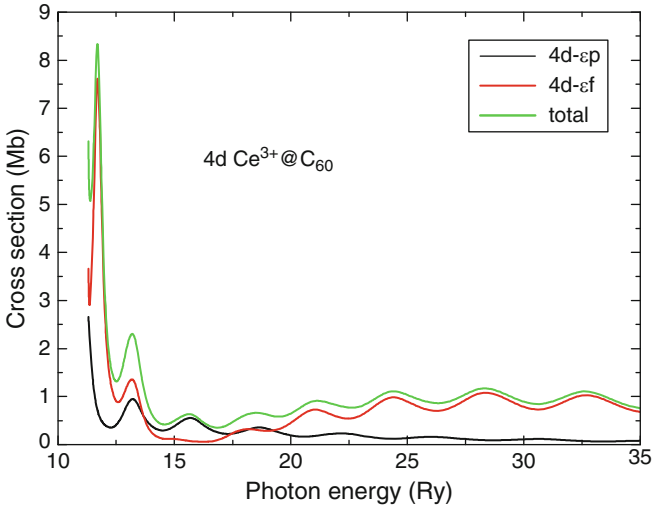

Fig. 2.457_Ce^{3+}@C_{60}_b5 Partial photoionization cross sections of $4d$-electrons of ion Ce^{3+} and Ce^{3+}@C_{60} with account of reflection of photoelectrons by C_{60} shell and its polarization by the incoming photon

fast electrons that originate from autoionization decay of $4d$–$4f$ level forms it (see [2.86]).

Figure 2.459_Ce^{4+}@C_{60}_b1 shows partial photoionization cross-sections of $5p$-, $5s$-electrons of ion Ce^{4+} and Ce^{4+}@C_{60} with account of reflection of

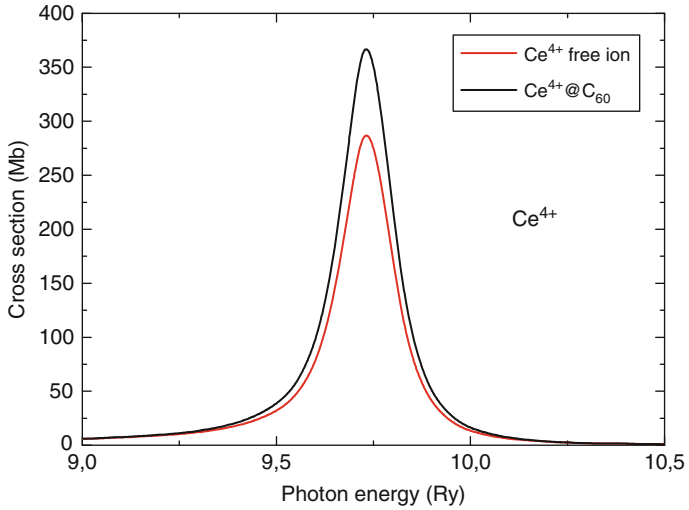

Fig. 2.458_Ce^{4+}@C$_{60}$_a1 Total photoionization cross section of ion Ce^{4+} and Ce^{4+}@C$_{60}$ with account of reflection of photoelectrons by C$_{60}$ shell

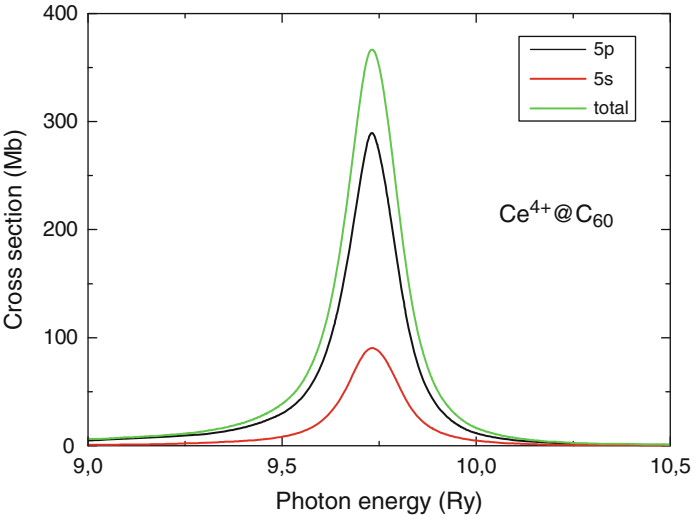

Fig. 2.459_Ce^{4+}@C$_{60}$_b1 Partial photoionization cross sections of $5p$, $5s$-electrons of ion Ce^{4+} and Ce^{4+}@C$_{60}$ with account of reflection of photoelectrons by C$_{60}$ shell

photoelectrons by C$_{60}$ shell and its polarization by the incoming photon. The small contribution of $4d$ electrons confirms the autoionization nature of the big maximum.

Figure 2.460_Ce^{4+}@C$_{60}$_b2 presents photoionization cross-section of $5p$-electrons for Ce^{4+} and Ce^{4+}@C$_{60}$ ions with account of reflection of photoelectrons

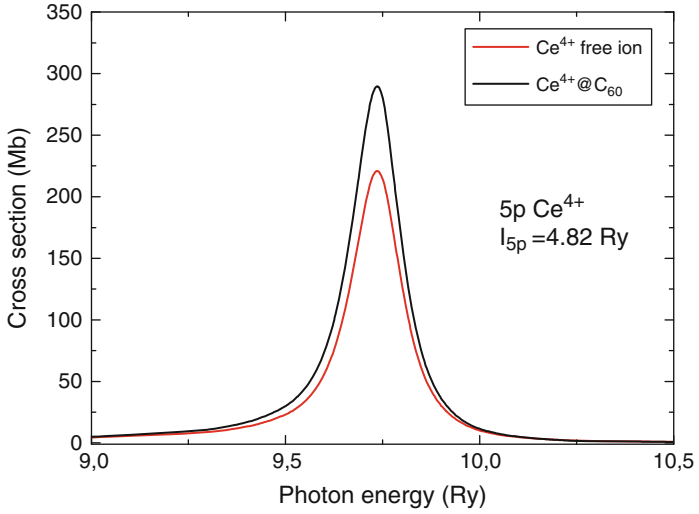

Fig. 2.460_Ce^{4+}@C_{60}_b2 Photoionization cross section of $5p$-electrons of ion Ce^{4+} and Ce^{4+}@C_{60} with account of reflection of photoelectrons by C_{60} shell and its polarization by the incoming photon

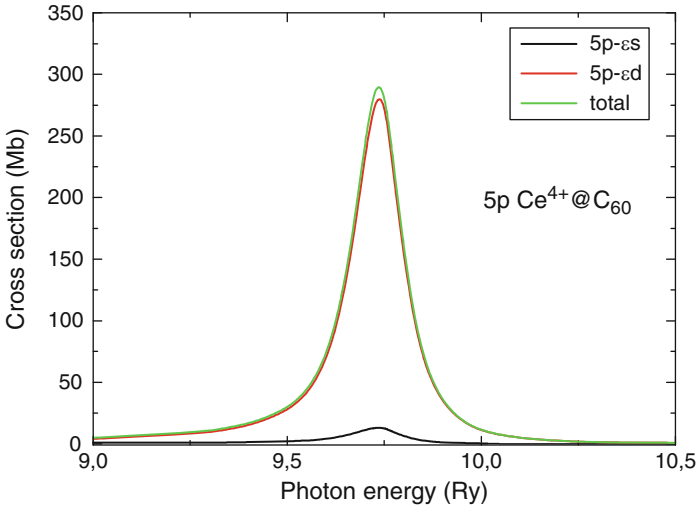

Fig. 2.461_Ce^{4+}@C_{60}_b3 Partial photoionization cross section of $5p$-electrons of ion Ce^{4+} and Ce^{4+}@C_{60} with account of reflection of photoelectrons by C_{60} shell

by C_{60} shell and its polarization by the incoming photon. It is these electrons the emission of which forms the powerful resonance.

Figure 2.461_Ce^{4+}@C_{60}_b3 shows the partial photoionization cross-section of $5p$-electrons of the ion Ce^{4+}@C_{60} with account of reflection of photoelectrons

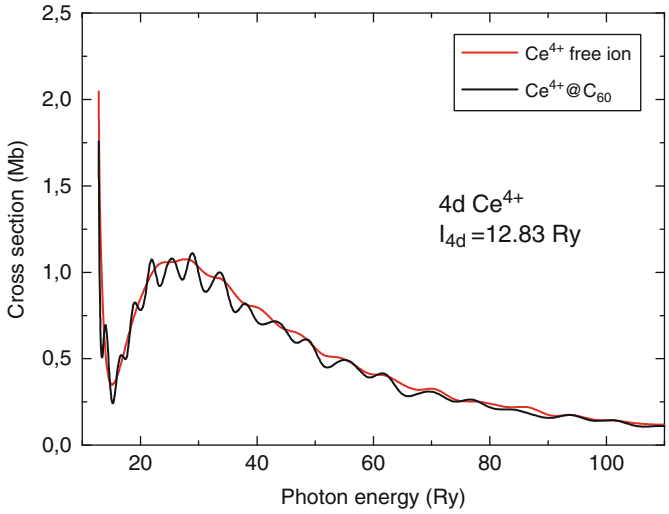

Fig. 2.462_Ce^{4+}@C$_{60}$_b4 Photoionization cross sections of $4d$-electrons of ion Ce^{4+} and Ce^{4+}@C_{60} with account of reflection of photoelectrons by C_{60} shell

by C_{60} shell and its polarization by the incoming photon. Note that a powerful maximum appears due to autoionization of the $4d$-$4f$ level.

Figure 2.462_Ce^{4+}@C$_{60}$_b4 presents photoionization cross-sections of $4d$-electrons of ion Ce^{4+} and Ce^{4+}@C_{60} with account of reflection of photoelectrons by C_{60} shell and its polarization by the incoming photon. The influence of fullerene is manifested in small ripples.

Figure 2.463_Ce^{4+}@C$_{60}$_b5 demonstrates the photoionization cross-sections of $4d$-electrons of the ion Ce^{4+}@C_{60} with account of reflection of photoelectrons by C_{60} shell and its polarization by the incoming photon. Note, however, that of some role is only reflection leading to small amplitude oscillations.

Figure 2.464_Ce^{4+}@C$_{60}$_b6 displays partial photoionization cross-section of $5s$-electrons of ion Ce^{4+} and Ce^{4+}@C_{60} with account of reflection of photoelectrons by C_{60} shell and its polarization by the incoming photon. Strong discrete excitation $4d$–$4f$ along with its decay into continuous spectrum $5p$–εd leads to a very big maximum in $5s$ electrons photoionization.

Figures 2.465_F$^-$NeNa$^+$@C$_{60}$_a1–2.472_F$^-$@C$_{60}$_e2 (F^-@C_{60}) contain results of calculations for F^-@C_{60}.

Figure 2.465_F$^-$NeNa$^+$@C$_{60}$_a1 shows the total photoionization cross-section of F^-@C_{60} in comparison with the same of Ne@C_{60} and Na^+@C_{60} in FRPAE. It is seen that on the way from F^- to Na^+ the oscillations of the cross-section became broader and lower.

Figure 2.466_F$^-$NeNa$^+$@C$_{60}$_b1 shows partial photoionization cross-section of $2p$-electrons for F^-@C_{60} ion in comparison with the same of Ne@C_{60}

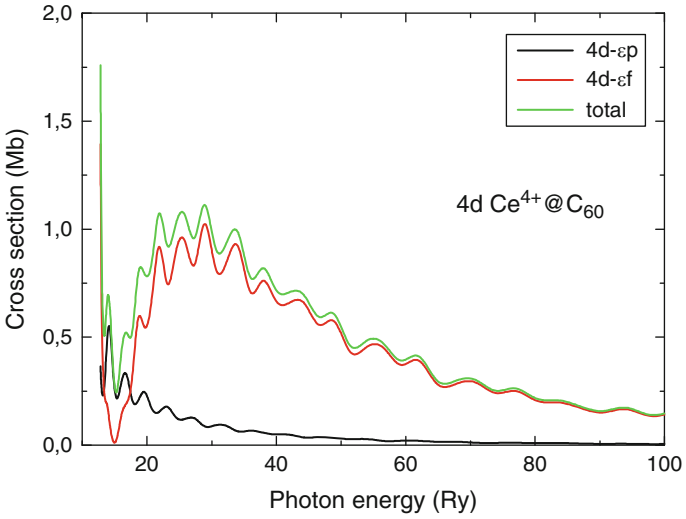

Fig. 2.463_Ce^{4+}@C_{60}_b5 Partial photoionization cross sections of $4d$-electrons of ion Ce^{4+} and Ce^{4+}@C_{60} with account of reflection of photoelectrons by C_{60} shell and its polarization by the incoming photon

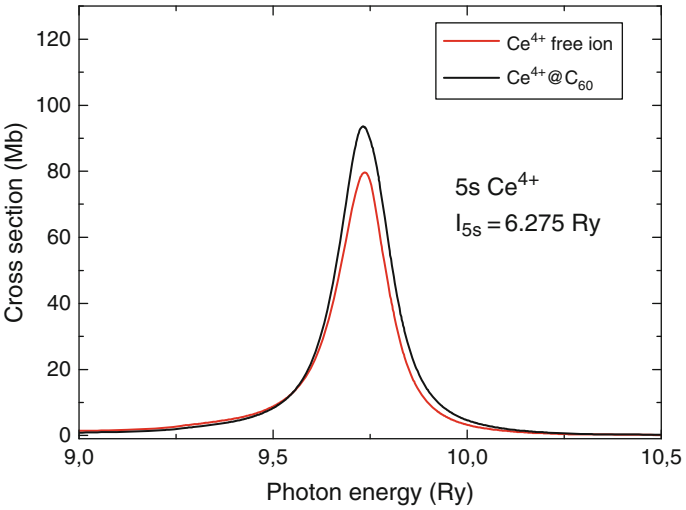

Fig. 2.464_Ce^{4+}@C_{60}_b6 Photoionization cross section of $5s$-electrons of ion Ce^{4+} and Ce^{4+}@C_{60} with account of reflection of photoelectrons by C_{60} shell

atom and Na^+@C_{60} ion in FRPAE. The figure, naturally, is similar to Fig. 2.465_F^-NeNa^+@C_{60}_a1.

Figure 2.467_F^-NeNa^+@C_{60}_b2 depicts partial photoionization cross-section of $2s$-electrons for F^-@C_{60} ion in comparison with the same of Ne@C_{60} atom and

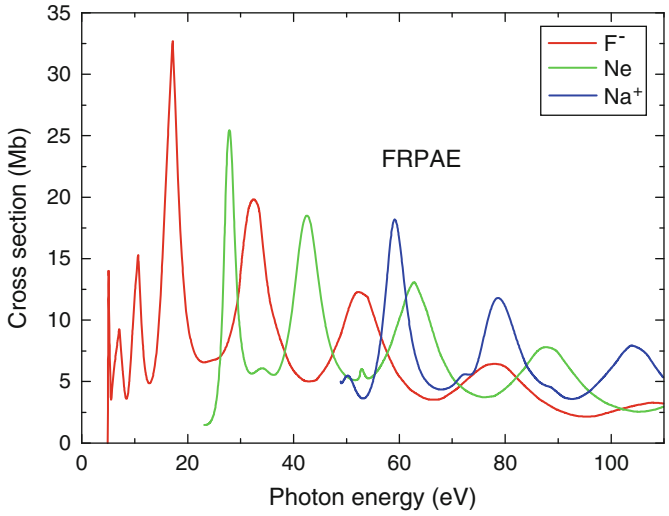

Fig. 2.465_F$^-$NeNa$^+$@C$_{60}$_a1 Total photoionization cross section of F$^-$@C$_{60}$ in comparison with the same of Ne@C$_{60}$ and Na$^+$@C$_{60}$ in FRPAE

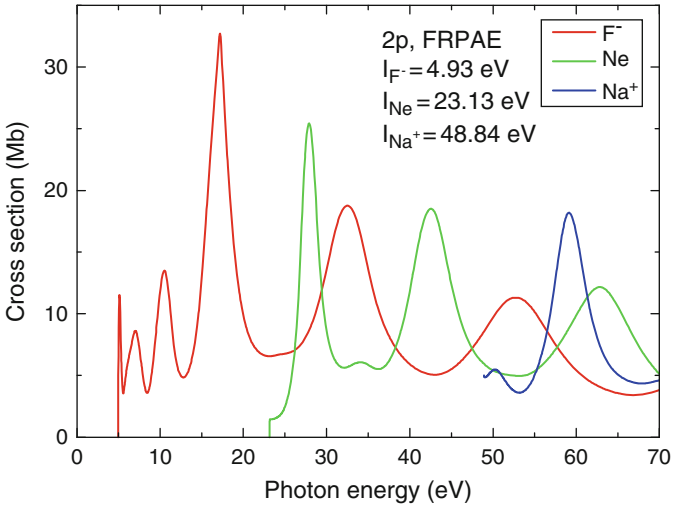

Fig. 2.466_F$^-$NeNa$^+$@C$_{60}$_b1 Photoionization cross section of 2p-electrons for F$^-$@C$_{60}$ ion in comparison with the same of Ne@C$_{60}$ atom and Na$^+$@C$_{60}$ ion in FRPAE

Na$^+$@C$_{60}$ ion in FRPAE. Peculiar is the narrow maximum at the threshold of Ne@C$_{60}$.

Figure 2.468_F$^-$@C$_{60}$_b1 presents partial photoionization cross-section of 2p-electrons of ions F$^-$ and F$^-$@C$_{60}$ with account of reflection of photoelectrons by C$_{60}$ shell and its polarization by the incoming photon. Powerful maxima appear in

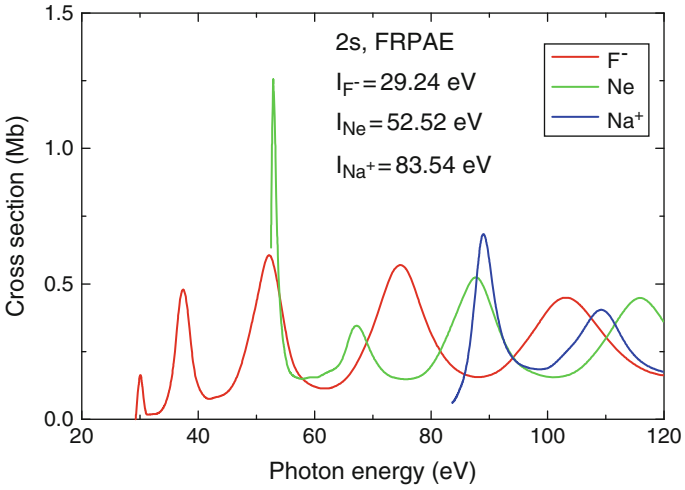

Fig. 2.467_F^-NeNa$^+$@C_{60}_b2 Photoionization cross section of 2*s*-electrons for F^-@C_{60} ion in comparison with the same of Ne@C_{60} atom and Na^+@C_{60} ion in FRPAE

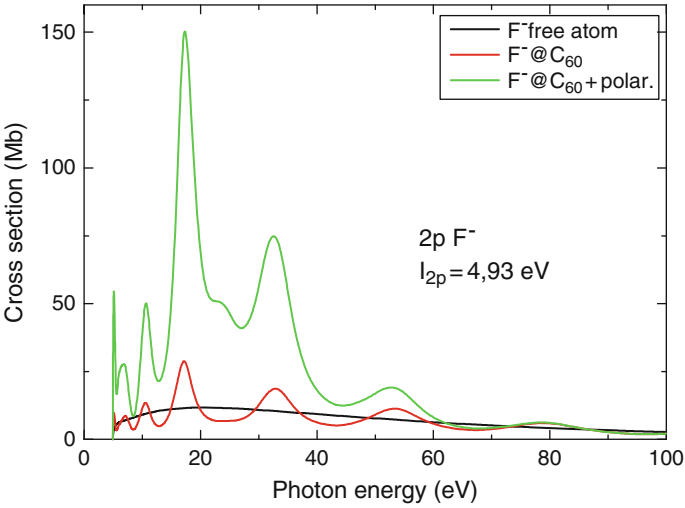

Fig. 2.468_F^-@C_{60}_b1 Photoionization cross section of 2*p*-electrons of ion F^- and F^-@C_{60} with account of reflection of photoelectrons by C_{60} shell and its polarization by the incoming photon, in RPAE and GF RPAE

the region 15–40 eV due to combined effect of reflection and mainly C_{60} electron shell polarization.

Figure 2.469_F^-@C_{60}_b2 displays partial photoionization cross-section of 2*s*-electrons of ions F^- and F^-@C_{60} with account of reflection of photoelectrons by

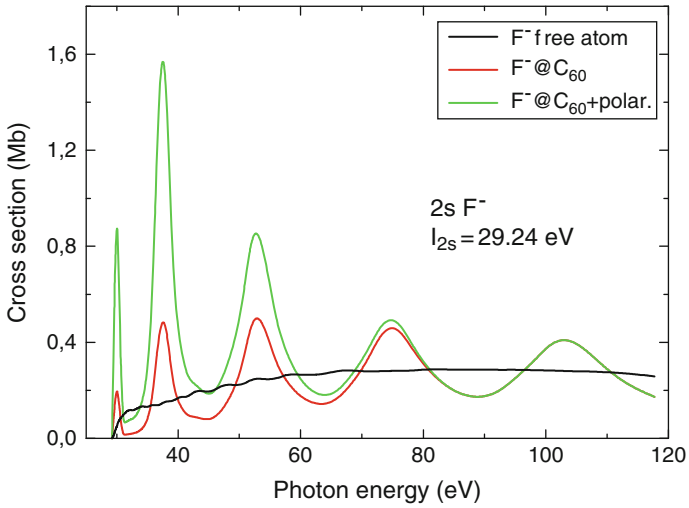

Fig. 2.469_F⁻@C$_{60}$_b2 Photoionization cross section of 2*s*-electrons of ion F^- and $F^-@C_{60}$ with account of reflection of photoelectrons by C_{60} shell and its polarization by the incoming photon in RPAE and in RPAE and GF RPAE

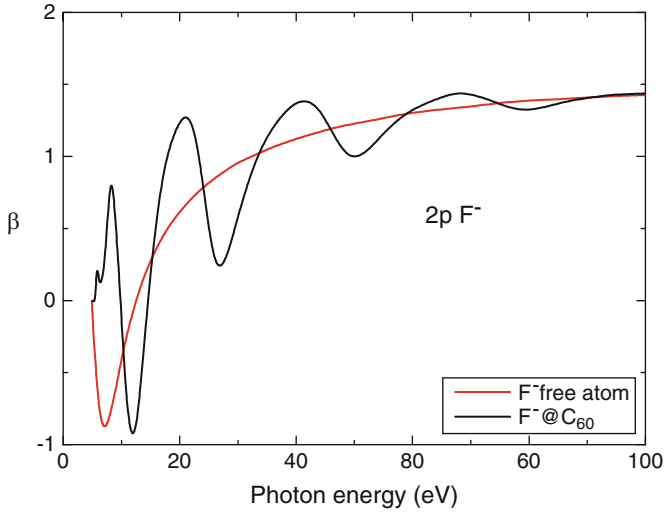

Fig. 2.470_F⁻@C$_{60}$_d1 Dipole angular anisotropy parameter of 2*p*-electrons for F^- and $F^-@C_{60}$ ions in RPAE

C_{60} shell and its polarization by the incoming photon. The role of polarization is smaller than for 2*p*.

Figure 2.470_F⁻@C$_{60}$_d1 demonstrates dipole angular anisotropy parameter of 2*p*-electrons for F^- and $F^-@C_{60}$ ions. Role of reflection by zero-thickness potential is very important.

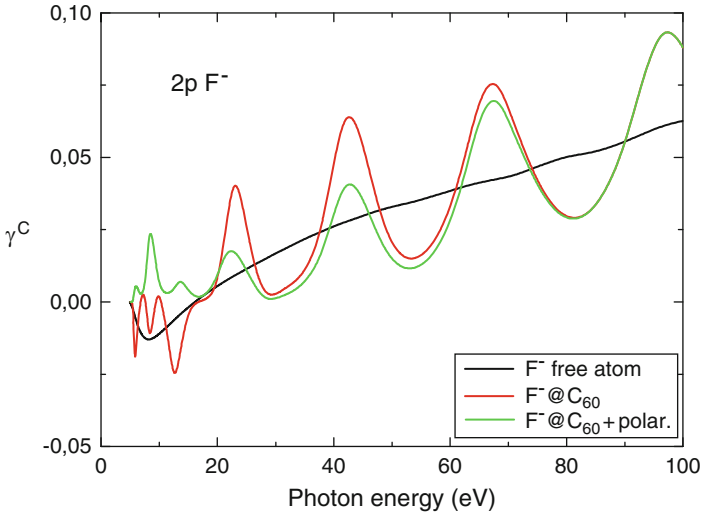

Fig. 2.471_F^-@C_{60}_e1 Non-dipole anisotropy parameter of $2p$-electrons of ion F^- and F^-@C_{60} with account of reflection of photoelectrons by C_{60} shell and its polarization by the incoming photon, in RPAE and GF RPAE

Figure 2.471_F^-@C_{60}_e1 depicts non-dipole angular anisotropy parameter of $2p$-electrons of ions F^- and F^-@C_{60} with account of reflection of photoelectrons by C_{60} shell and its polarization by the incoming photon. It is remarkable that C_{60} polarization even diminishes the amplitude of oscillations caused by reflections.

Figure 2.472_F^-@C_{60}_e2 shows non-dipole angular anisotropy parameter of $2s$-electrons of ions F^- and F^-@C_{60} with account of reflection of photoelectrons by C_{60} shell and its polarization by the incoming photon. Qualitatively, the situation is similar to that in Fig. 2.471_F^-@C_{60}_e1.

Figures 2.473_Cl^-ArK^+@C_{60}_a1–2.480_Cl^-@C_{60}_e2 (Cl^-@C_{60}) contain results of calculations for Cl^-@C_{60}.

Figure 2.473_Cl^-ArK^+@C_{60}_a1 presents total photoionization cross-section of Cl^-@C_{60} in comparison with the same of Ar@C_{60} and K^+@C_{60} in FRPAE. Most powerful here is the oscillation in Ar@C_{60}.

Figure 2.474_Cl^-ArK^+@C_{60}_b1 shows partial photoionization cross-section of $3p$-electrons of Cl^-@C_{60} ion in comparison with the same of Ar@C_{60} atom and K^+@C_{60} ion in FRPAE. The situation is similar to Fig. 2.473_Cl^-ArK^+@C_{60}_a1.

Figure 2.475_Cl^-ArK^+@C_{60}_b2 depicts partial photoionizaton cross-section of $3s$-electrons of Cl^-@C_{60} ion in comparison with the same of Ar@C_{60} atom and K^+@C_{60} ion in FRPAE. Here Cl^- has the most powerful near-threshold structure.

Figure 2.476_Cl^-@C_{60}_b3 displays partial photoionization cross-section of $3p$-electrons of ions Cl^- and Cl^-@C_{60} in RPAE with account of reflection of photoelectrons by C_{60} shell and its polarization by the incoming photon. Polarization enhances reflection oscillations into a really impressive multi-maximum structure.

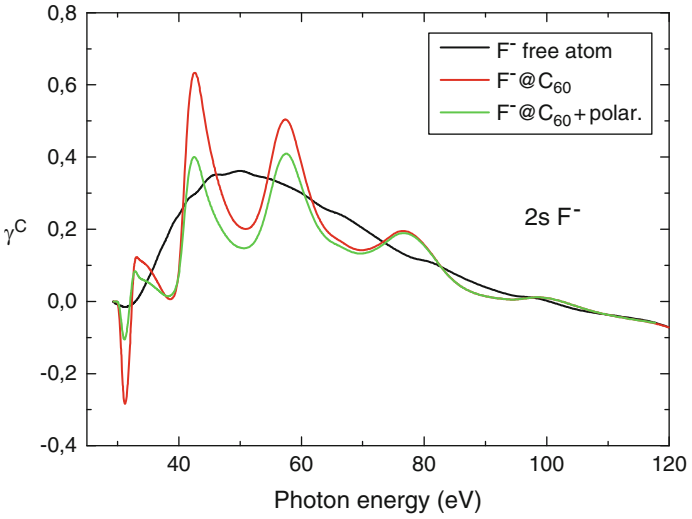

Fig. 2.472_F$^-$@C$_{60}$_e2 Non-dipole anisotropy parameter of 2*s*-electrons of ion F$^-$ and F$^-$@C$_{60}$ with account of reflection of photoelectrons by C$_{60}$ shell and its polarization by the incoming photon, in RPAE and GF RPAE

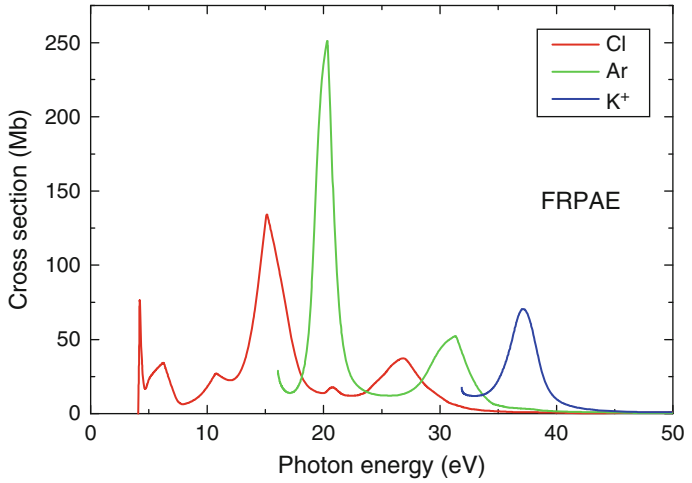

Fig. 2.473_Cl$^-$ArK$^+$@C$_{60}$_a1 Total photoionization cross section of Cl$^-$@C$_{60}$ in comparison with the same of Ar@C$_{60}$ and K$^+$@C$_{60}$ in FRPAE

Figure 2.477_Cl$^-$@C$_{60}$_b4 demonstrates photoionization cross-section of 3*s*-electrons of ions Cl$^-$ and Cl$^-$@C$_{60}$ with account of reflection of photoelectrons by C$_{60}$ shell and its polarization by the incoming photon. The cross-section, although much smaller than for 3*p* electrons, is big enough.

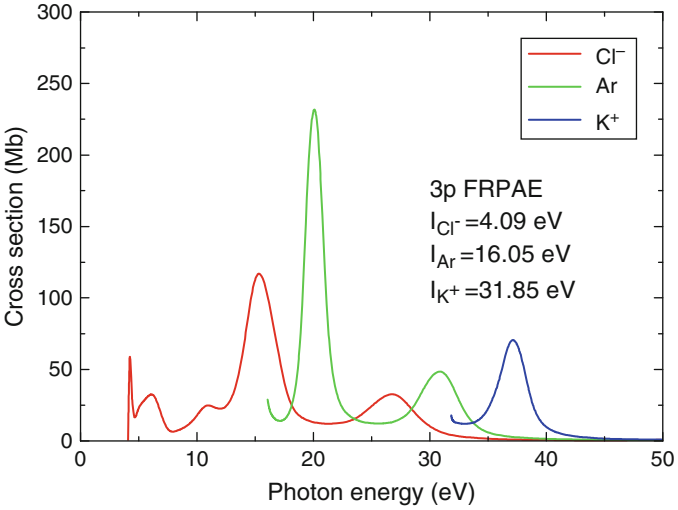

Fig. 2.474_$Cl^-ArK^+@C_{60}$_b1 Photoionization cross section of $3p$-electrons for $Cl^-@C_{60}$ ion in comparison with the same of $Ar@C_{60}$ atom and $K^+@C_{60}$ ion in FRPAE

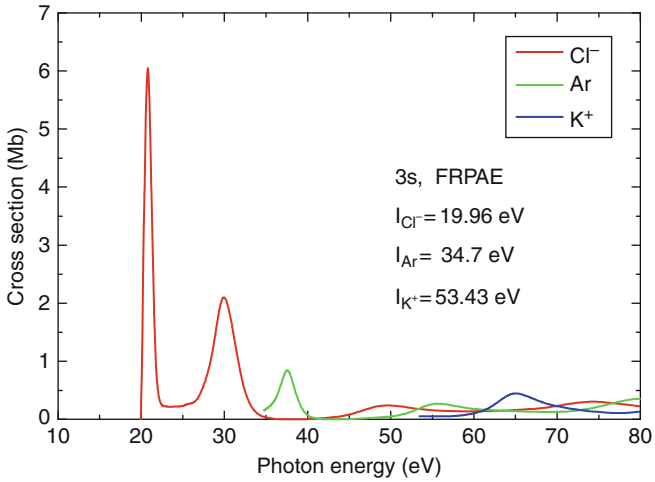

Fig. 2.475_$Cl^-ArK^+@C_{60}$_b2 Photoionization cross section of $3s$-electrons for $Cl^-@C_{60}$ ion in comparison with the same of $Ar@C_{60}$ atom and $K^+@C_{60}$ ion in FRPAE

Figure 2.478_$Cl^-@C_{60}$_d1 depicts dipole angular anisotropy parameter of $3p$-electrons of ion Cl^- and $Cl^-@C_{60}$. The effects of reflection are quite strong.

Figure 2.479_$Cl^-@C_{60}$_e1 presents non-dipole angular anisotropy parameter of $3p$-electrons of ion Cl^- and $Cl^-@C_{60}$ with account of reflection of photoelectrons by C_{60} shell and its polarization by the incoming photon.

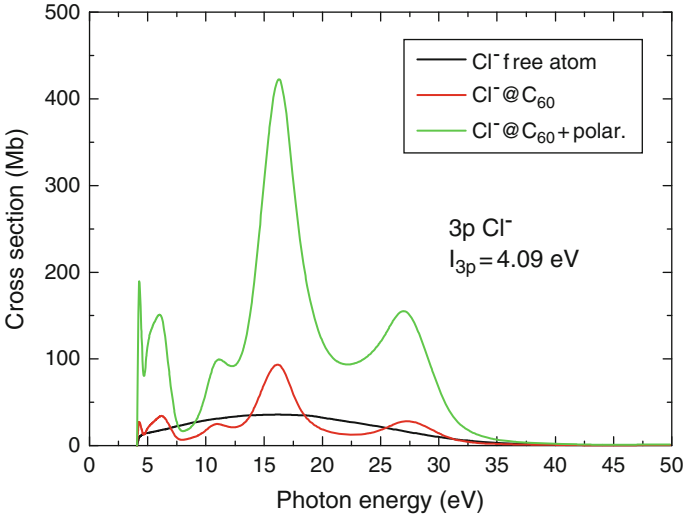

Fig. 2.476_Cl⁻@C$_{60}$_b3 Photoionization cross section of 3*p*-electrons of ion Cl^- and $Cl^-@C_{60}$ with account of reflection of photoelectrons by C_{60} shell and its polarization by the incoming photon, in RPAE and GF RPAE

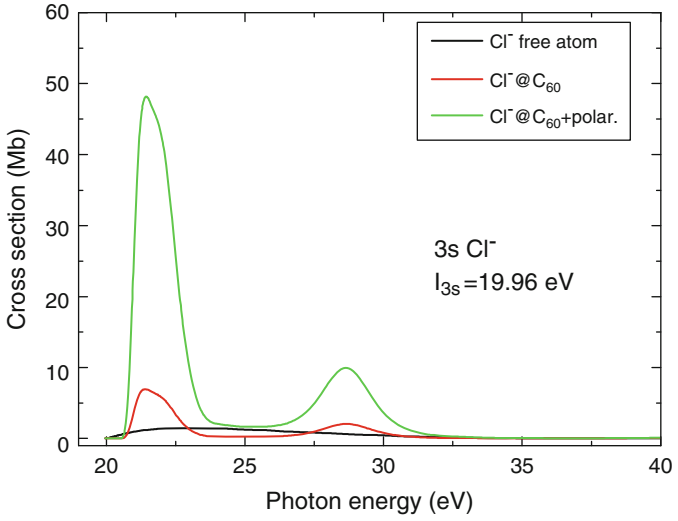

Fig. 2.477_Cl⁻@C$_{60}$_b4 Photoionization cross section of 3*s*-electrons of ion Cl^- and $Cl^-@C_{60}$ with account of reflection of photoelectrons by C_{60} shell and its polarization by the incoming photon, in RPAE and GF RPAE

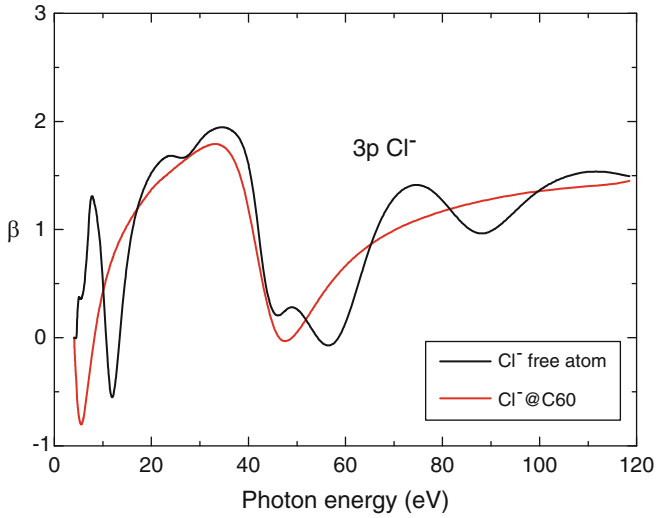

Fig. 2.478_Cl⁻@C_{60}_d1 Dipole anisotropy parameter of $3p$-electrons of ion Cl^- and $Cl^-@C_{60}$ in RPAE

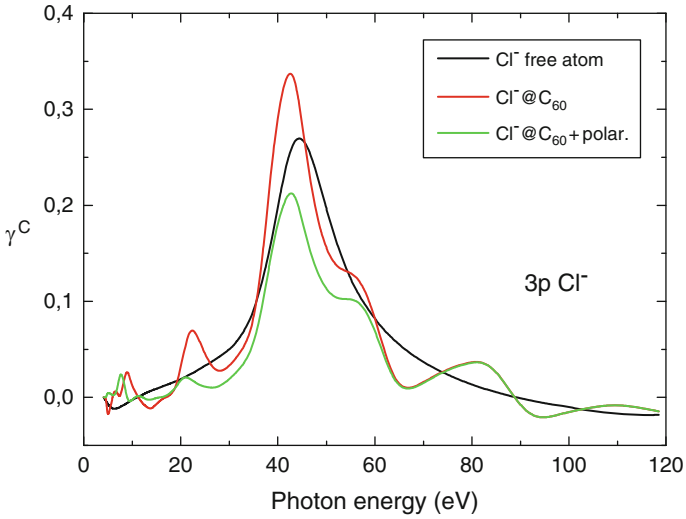

Fig. 2.479_Cl⁻@C_{60}_e1 Non-dipole anisotropy parameter of $3p$-electrons of ion Cl^- and $Cl^-@C_{60}$ with account of reflection of photoelectrons by C_{60} shell and its polarization by the incoming photon, in RPAE and GF RPAE

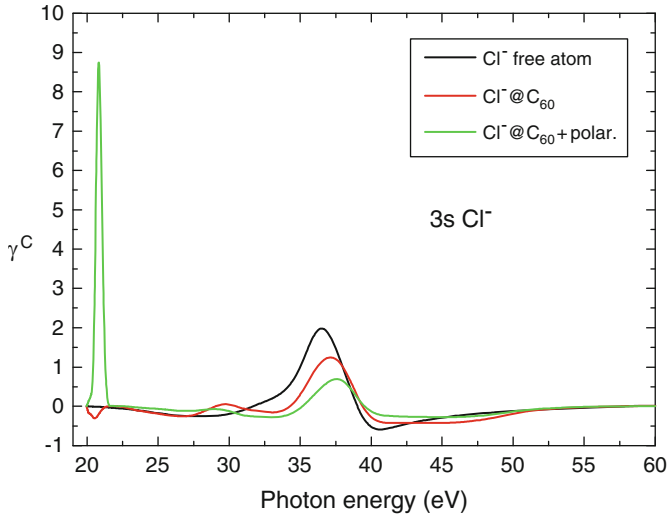

Fig. 2.480_Cl⁻@C60_e2 Non-dipole angular anisotropy parameter of 3*s*-electrons of ion Cl^- and $Cl^-@C_{60}$ with account of reflection of photoelectrons by C_{60} shell and its polarization by the incoming photon, in RPAE and GF RPAE

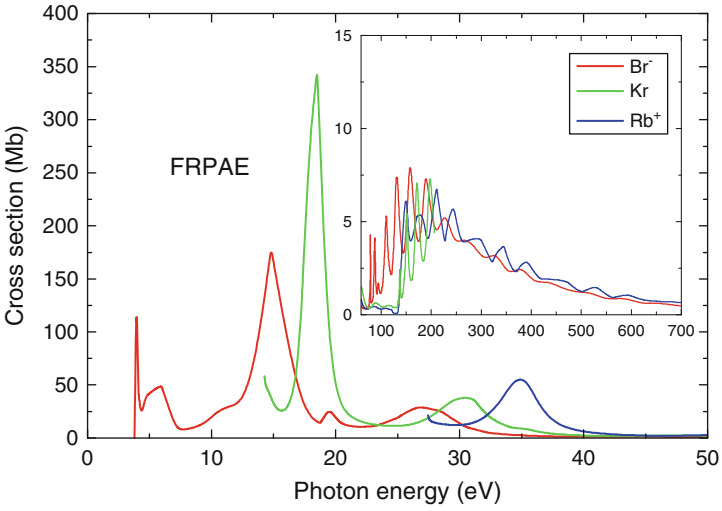

Fig. 2.481_Br⁻KrRb⁺@C60_a1 Total photoionization cross section of $Br^-@C_{60}$ ion in comparison with the same of $Kr@C_{60}$ atom and $Rb^+@C_{60}$ ion in FRPAE

Figure 2.480_Cl⁻@C60_e2 shows the non-dipole angular anisotropy parameter of 3*s*-electrons of ion Cl^- and $Cl^-@C_{60}$ with account of reflection of photoelectrons by C_{60} shell and its polarization by the incoming photon.

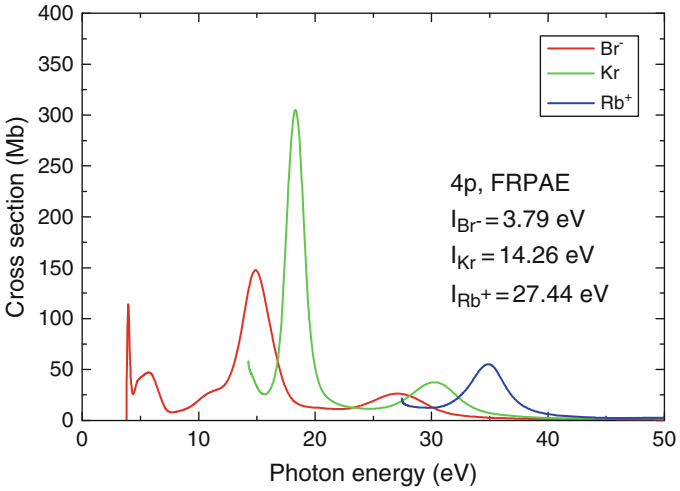

Fig. 2.482_Br$^-$KrRb$^+$@C_{60}_b1 Photoionization cross section of $4p$-electrons for Br$^-$@C_{60} ion in comparison with the same of Kr@C_{60} atom and Rb$^+$@C_{60} ion in FRPAE

Figures 2.481_Br$^-$KrRb$^+$@C_{60}_a1–2.489_Br$^-$@C_{60}_e2 (Br$^-$@C_{60}) contain results of calculations for Br$^-$@C_{60}.

Figure 2.481_Br$^-$KrRb$^+$@C_{60}_a1 demonstrates total photoionization cross-section of Br$^-$@C_{60} ion in comparison with the same of Kr@C_{60} atom and Rb$^+$@C_{60} ion in FRPAE. Most powerful here is the Kr@C_{60} maximum at threshold.

Figure 2.482_Br$^-$KrRb$^+$@C_{60}_b1 shows photoionization cross-section of $4p$-electrons of Br$^-$@C_{60} ion in comparison with the same of Kr@C_{60} atom and Rb$^+$@C_{60} ion in FRPAE. Just as in Fig. 2.481_Br$^-$KrRu$^+$@C_{60}_a1, most powerful is the Kr@C_{60} resonance.

Figure 2.483_Br$^-$KrRb$^+$@C_{60}_b2 depicts photoionization cross-section of $4s$-electrons of Br$^-$@C_{60} ion in comparison with the same of Kr@C_{60} atom and Rb$^+$@C_{60} ion in FRPAE. Just as in the case of Cl$^-$ArK$^+$ trio, most prominent is the threshold resonance in Br$^-$@C_{60}.

Figure 2.484_Br$^-$KrRb$^+$@C_{60}_b3 presents photoionization cross-section of $3d$-electrons of Br$^-$@C_{60} ion in comparison with the same of Kr@C_{60} atom and Rb$^+$@C_{60} ion in FRPAE. The photoelectron reflection gives a multi-maximum structure to the $3d$-resonance in the entire Br$^-$KrRu$^+$ trio.

Figure 2.485_Br$^-$@C_{60}_b4 illustrates photoionization cross-section of $4p$-electrons of Br$^-$ and Br$^-$@C_{60} ions with account of reflection of photoelectrons by C_{60} shell and its polarization by the incoming photon. Polarization enhances reflection oscillations into a really impressive multi-maximum structure.

Figure 2.486_Br$^-$@C_{60}_b5 displays photoionization cross-section of $4s$-electrons of ions Br$^-$ and Br$^-$@C_{60} with account of reflection of photoelectrons by

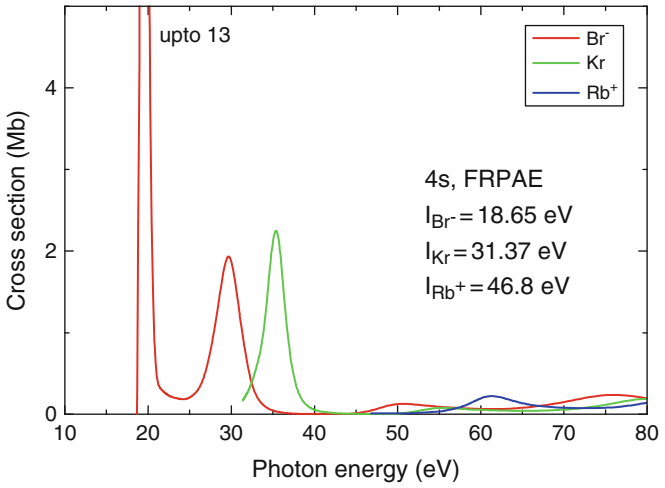

Fig. 2.483_Br$^-$KrRb$^+$@C$_{60}$_b2 Photoionization cross section of 4*s*-electrons for Br$^-$@C$_{60}$ ion in comparison with the same of Kr@C$_{60}$ atom and Rb$^+$@C$_{60}$ ion in FRPAE

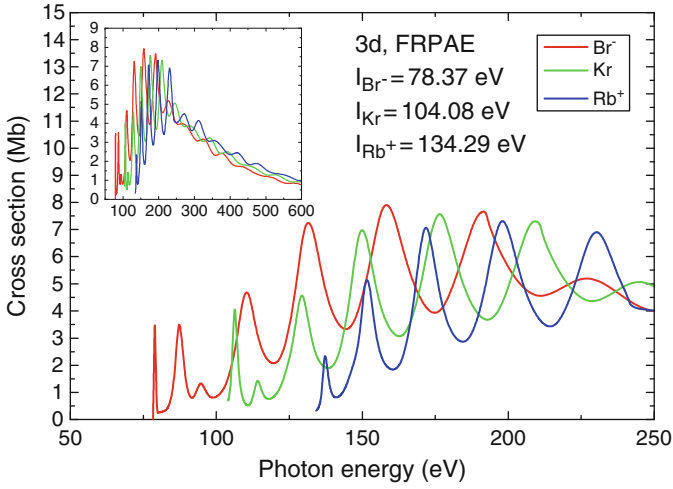

Fig. 2.484_Br$^-$KrRb$^+$@C$_{60}$_b3 Photoionization cross section of 3*d*-electrons for Br$^-$@C$_{60}$ ion in comparison with the same of Kr@C$_{60}$ atom and Rb$^+$@C$_{60}$ ion in FRPAE

C$_{60}$ shell and its polarization by the incoming photon. The cross-section, although much smaller than for 4*p* electrons, is big enough.

Figure 2.487_Br$^-$@C$_{60}$_d1 shows dipole angular anisotropy parameter β_{4p} of 4*p*-electrons of Br$^-$@C$_{60}$ and Br$^-$ ions. The effects of reflection are quite strong.

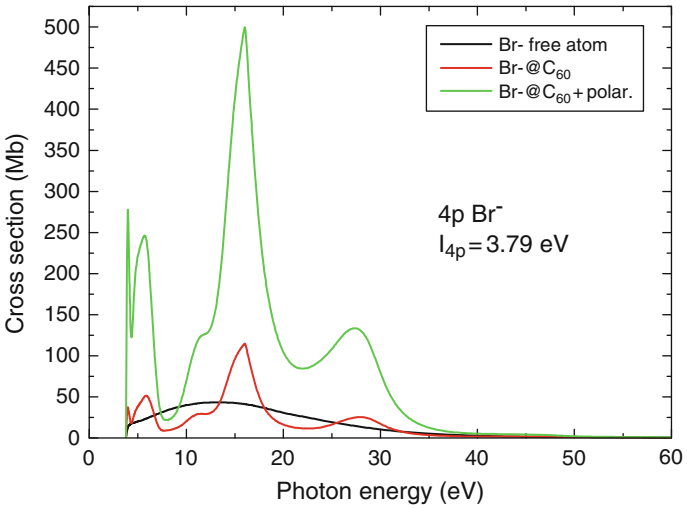

Fig. 2.485_Br$^-$@C_{60}_b4 Photoionization cross section of $4p$-electrons of ion Br^- and Br^-@C_{60} with account of reflection of photoelectrons by C_{60} shell and its polarization by the incoming photon, in RPAE and GF RPAE

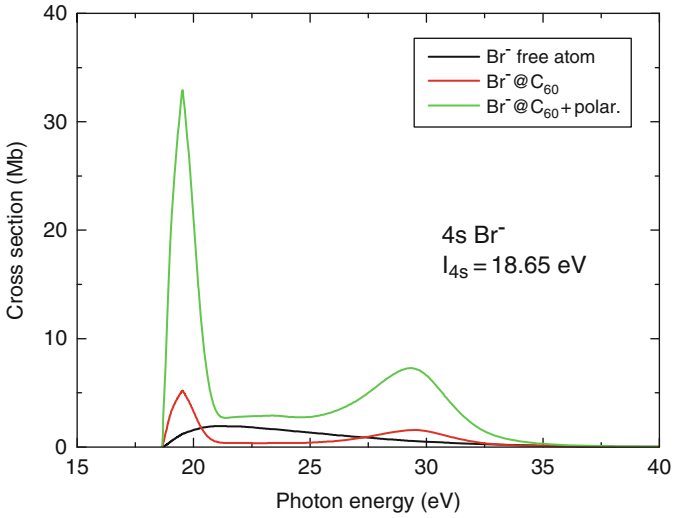

Fig. 2.486_Br$^-$@C_{60}_b5 Photoionization cross section of $4s$-electrons of ion Br^- and Br^-@C_{60} with account of reflection of photoelectrons by C_{60} shell and its polarization by the incoming photon, in RPAE and GF RPAE

Figure 2.488_Br$^-$@C_{60}_e1 presents non-dipole angular anisotropy parameter γ_{4p}^{C} of $4p$-electrons of Br^-@C_{60} and Br^- ions with account of reflection of photoelectrons by C_{60} shell and its polarization by the incoming photon.

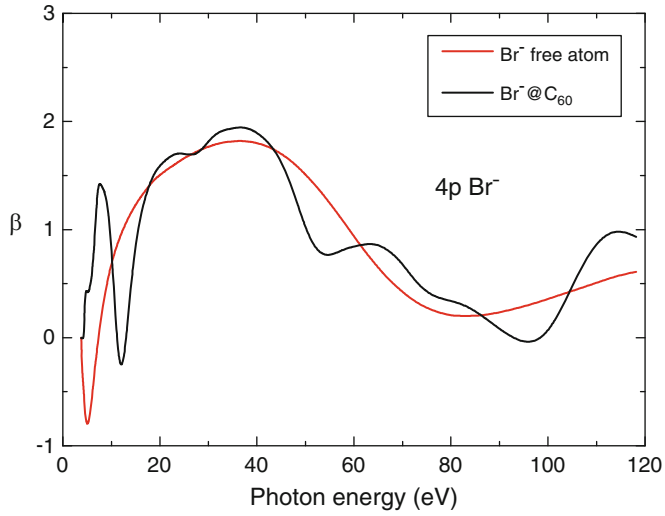

Fig. 2.487_Br$^-$@C$_{60}$_d1 Dipole angular anisotropy parameter of $4p$-electrons for Br$^-$@C$_{60}$ and Br$^-$ in RPAE

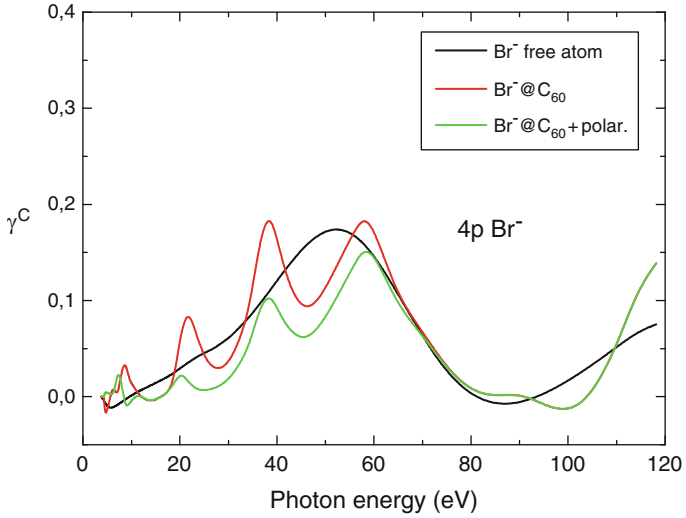

Fig. 2.488_Br$^-$@C$_{60}$_e1 Non-dipole angular anisotropy parameter of $4p$-electrons for Br$^-$@C$_{60}$ and Br$^-$ with account of reflection of photoelectrons by C$_{60}$ shell and its polarization by the incoming photon, in RPAE and GF RPAE

Figure 2.489_Br$^-$@C$_{60}$_e2 shows dipole angular anisotropy parameter γ^{C}_{4s} of $4s$-electrons of Br$^-$@C$_{60}$ and Br$^-$ with account of reflection of photoelectrons by C$_{60}$ shell and its polarization by the incoming photon. Fullerenes shell transforms the asymmetric Fano-type profile into an almost symmetric maximum.

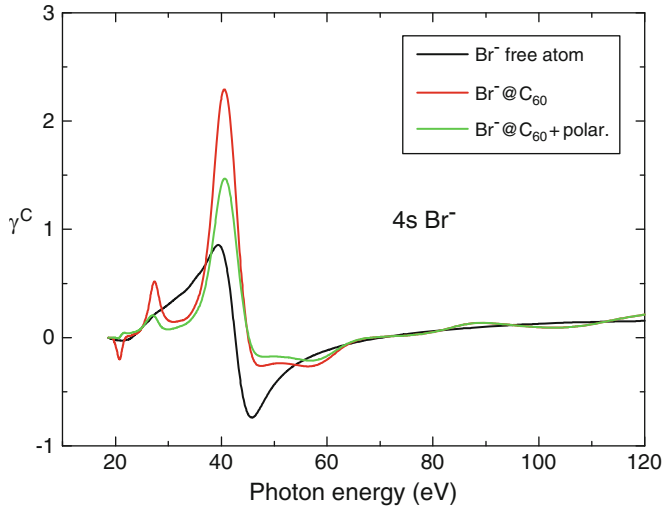

Fig. 2.489_Br$^-$@C_{60}_e2 Non-dipole angular anisotropy parameter of 4*s*-electrons for Br^-@C_{60} and Br^- with account of reflection of photoelectrons by C_{60} shell and its polarization by the incoming photon, in RPAE and GF RPAE

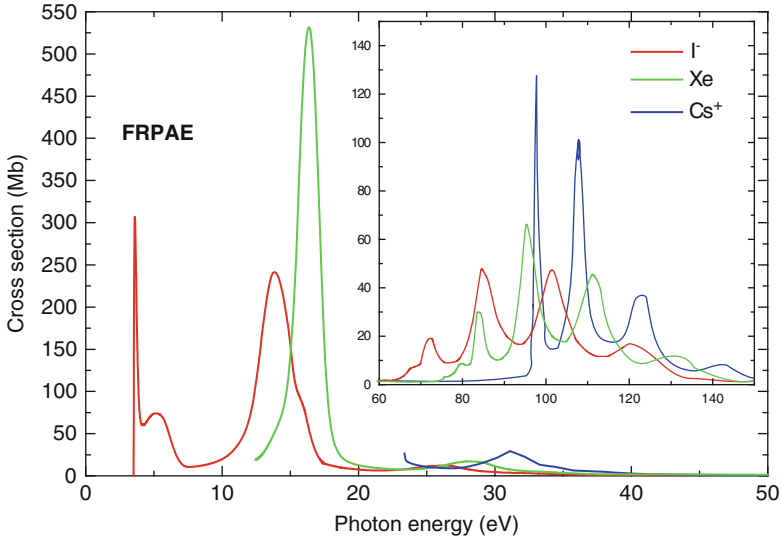

Fig. 2.490_I$^-$XeCs$^+$@C_{60}_a1 Total photoionization cross section of I^-@C_{60} ion in comparison with the same of Xe@C_{60} atom and Cs^+@C_{60} ion in FRPAE

Figures 2.490_I$^-$XeCs$^+$@C_{60}_a1–2.499_I$^-$@C_{60}_e3 (I^-@C_{60}) contain results of calculations for I^-@C_{60}.

Figure 2.490_I$^-$XeCs$^+$@C_{60}_a1 demonstrates total photoionization cross-section of I^-@C_{60} ion in comparison with the same of Xe@C_{60} atom and Cs^+@C_{60} ion in FRPAE. Most powerful here is the Xe@C_{60} maximum at threshold.

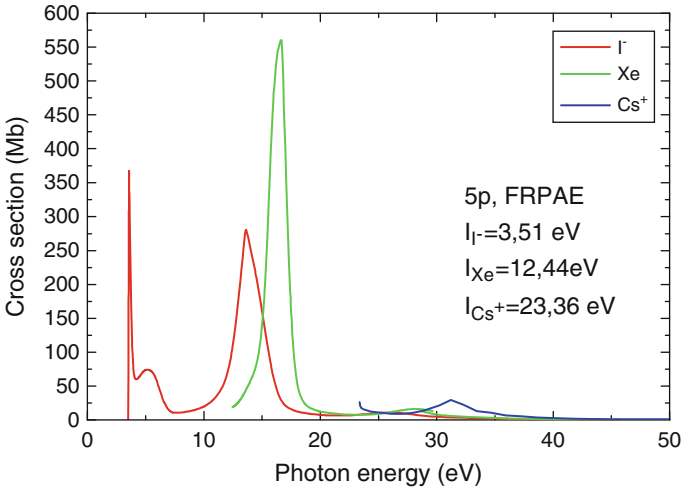

Fig. 2.491_I$^-$XeCs$^+$@C$_{60}$_b1 Photoionization cross section of 5*p*-electrons for I$^-$@C$_{60}$ ion in comparison with the same of Xe@C$_{60}$ atom and Cs$^+$@C$_{60}$ ion in FRPAE

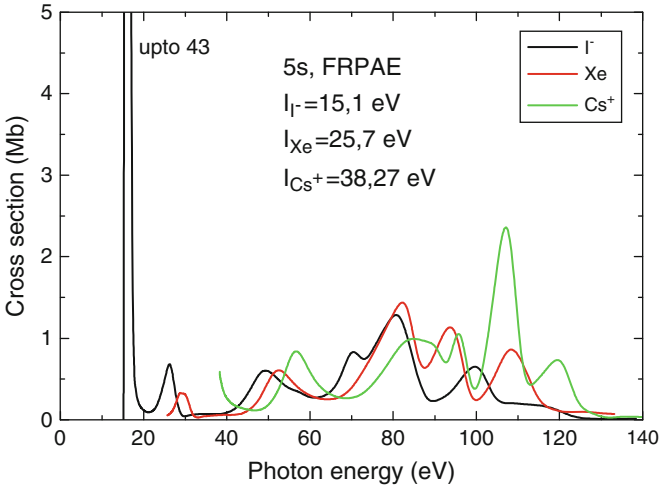

Fig. 2.492_I$^-$XeCs$^+$@C$_{60}$_b2 Photoionization cross section of 5*s*-electrons for I$^-$@C$_{60}$ ion in comparison with the same of Xe@C$_{60}$ atom and Cs$^+$@C$_{60}$ ion in FRPAE

Figure 2.491_I$^-$XeCs$^+$@C$_{60}$_b1 shows partial photoionization cross-section of 5*p*-electrons of I$^-$@C$_{60}$ ion in comparison with the same of Xe@C$_{60}$ atom and Cs$^+$@C$_{60}$ ion in FRPAE. Just as in Fig. 2.482_Br$^-$KrRb$^+$@C$_{60}$_a1, most powerful is the Xe@C$_{60}$ resonance.

Figure 2.492_I$^-$XeCs$^+$@C$_{60}$_b2 depicts partial photoionization cross-section of 5*s*-electrons of I$^-$@C$_{60}$ ion in comparison with the same of Xe@C$_{60}$ atom and Cs$^+$@C$_{60}$ ion in FRPAE. Just as in the case of Br$^-$KrCs$^+$ trio, most prominent is the threshold resonance in I$^-$@C$_{60}$.

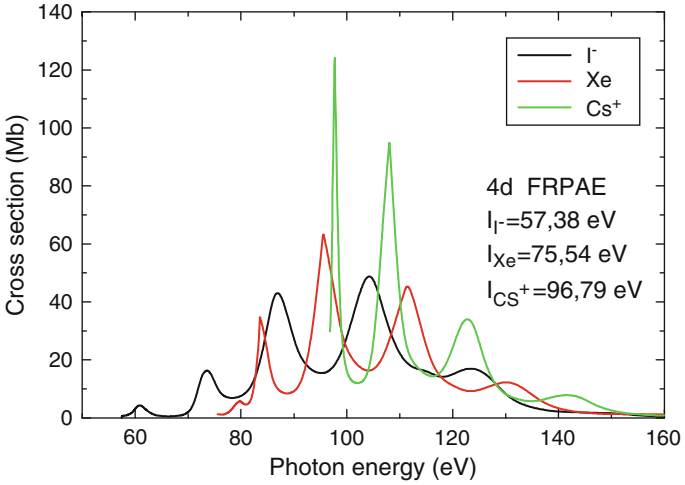

Fig. 2.493_$I^-XeCs^+@C_{60}$_b3 Photoionization cross section of $4d$-electrons for $I^-@C_{60}$ ion in comparison with the same of $Xe@C_{60}$ atom and $Cs^+@C_{60}$ ion in FRPAE

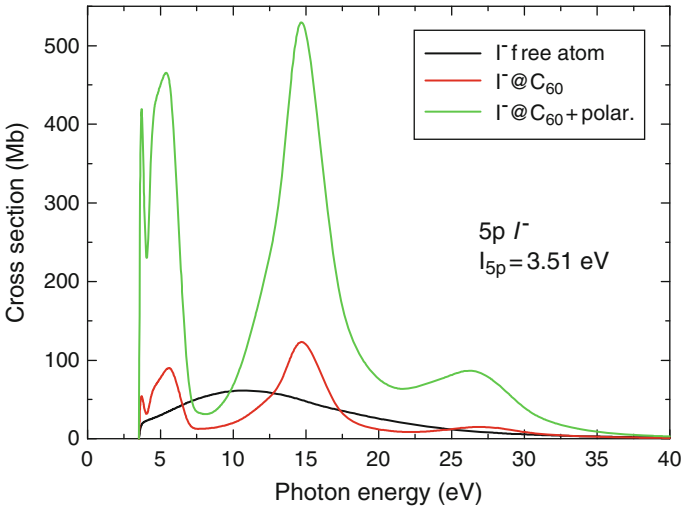

Fig. 2.494_$I^-@C_{60}$_b1 Photoionization cross section of $5p$-electrons of ion I^- and $I^-@C_{60}$ with account of reflection of photoelectrons by C_{60} shell and its polarization by the incoming photon, in RPAE and GF RPAE

Figure 2.493_$I^-XeCs^+@C_{60}$_b3 presents partial photoionization cross-section of $4d$-electrons of $I^-@C_{60}$ ion in comparison with the same of $Xe@C_{60}$ atom and $Cs^+@C_{60}$ ion in FRPAE. The photoelectron reflection gives a multi-maximum structure to the $4d$ Giant resonance in the entire I^-XeCs^+ trio.

Figure 2.494_$I^-@C_{60}$_b1 illustrates photoionization cross-section of $5p$-electrons of ion I^- and $I^-@C_{60}$ with account of reflection of photoelectrons by C_{60}

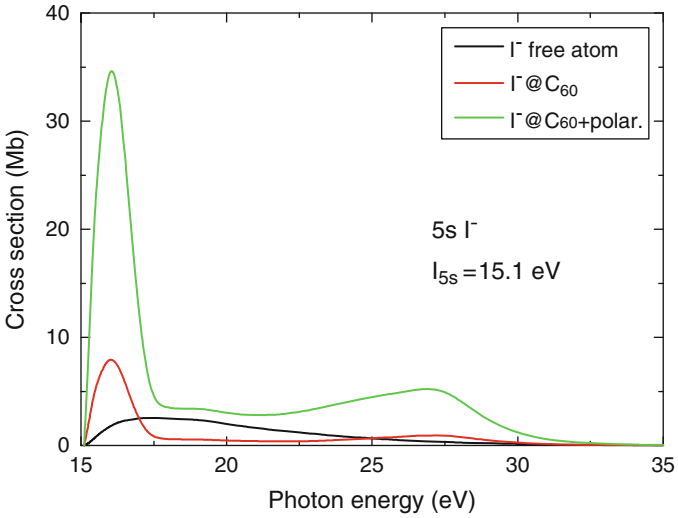

Fig. 2.495_I⁻@C60_b2 Photoionization cross section of 5*s*-electrons of ion I^- and $I^-@C_{60}$ with account of reflection of photoelectrons by C_{60} shell and its polarization by the incoming photon, in RPAE and GF RPAE

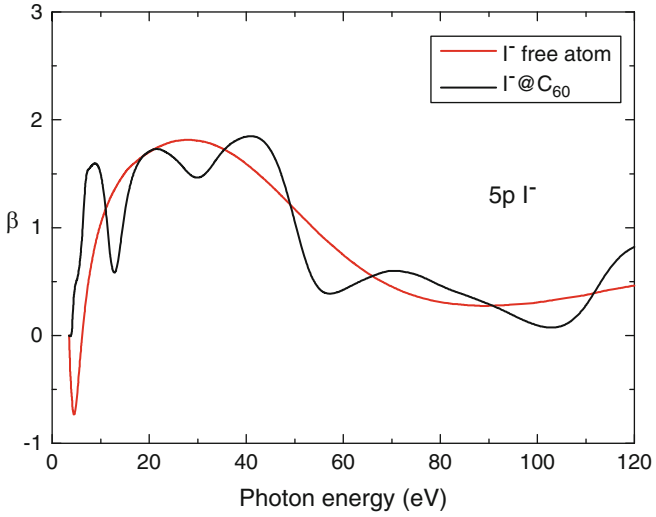

Fig. 2.496_I⁻@C60_d1 Dipole angular anisotropy parameter of 5*p*-electrons for $I^-@C_{60}$ and I^- in RPAE

shell and its polarization by the incoming photon. Polarization enhances reflection oscillations into a really impressive multi-maximum structure.

Figure 2.495_I⁻@C60_b2 depicts partial photoionization cross-section of 5*s*-electrons of I^- and $I^-@C_{60}$ ions with account of reflection of photoelectrons by

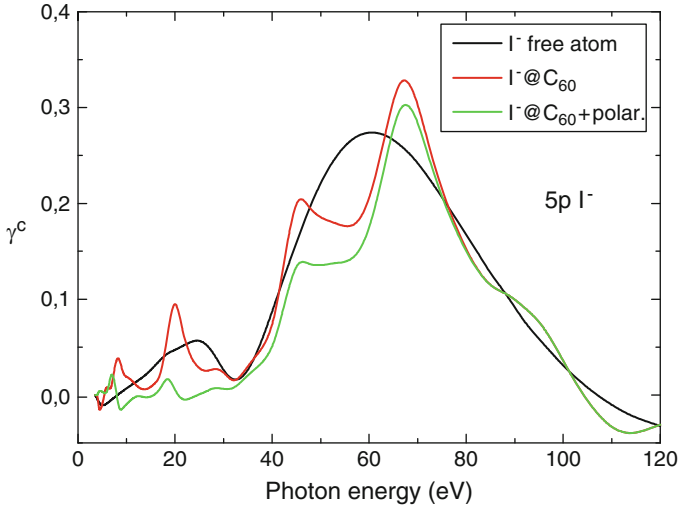

Fig. 2.497_I⁻@C_{60}_e1 Non-dipole angular anisotropy parameter γ^C of $5p$-electrons for $I^-@C_{60}$ and I^- ions with account of reflection of photoelectrons by C_{60} shell and its polarization by the incoming photon, in RPAE and GF RPAE

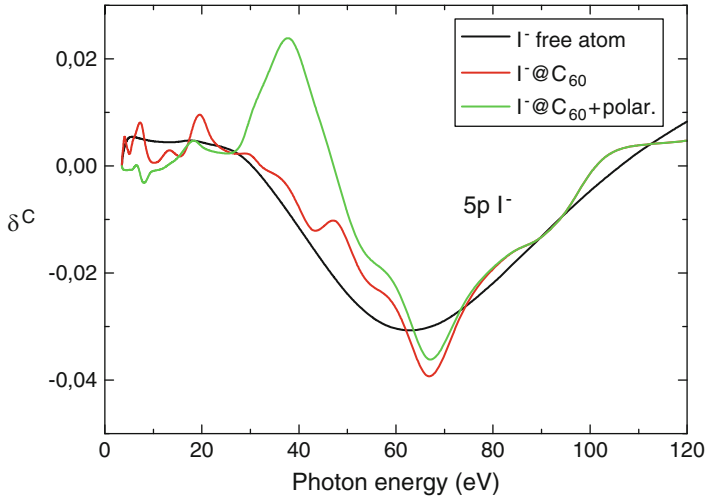

Fig. 2.498_I⁻@C_{60}_e2 Non-dipole angular anisotropy parameter δ^C of $5p$-electrons for $I^-@C_{60}$ and I^- with account of reflection of photoelectrons by C_{60} shell and its polarization by the incoming photon, in RPAE and GF RPAE

C_{60} shell and its polarization by the incoming photon. The cross-section, although much smaller than for $4p$ electrons, is big enough.

Figure 2.496_I⁻@C_{60}_d1 displays the dipole angular anisotropy parameter β_{5p} of $5p$-electrons of $I^-@C_{60}$ and I^- ions.

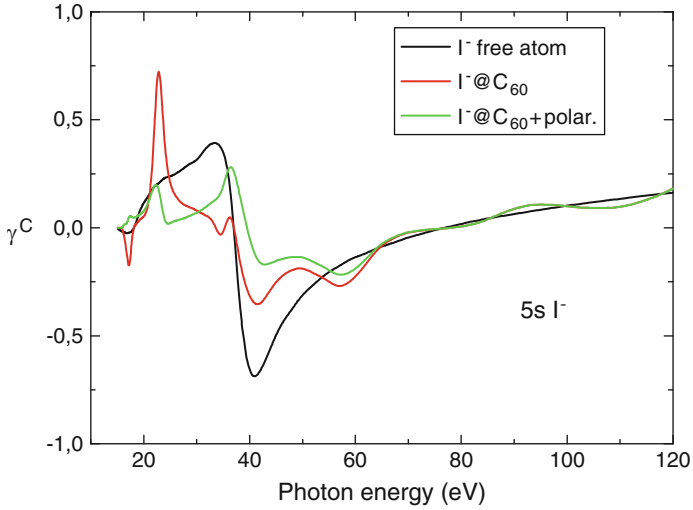

Fig. 2.499_I⁻@C$_{60}$_e3 Non-dipole angular anisotropy parameter γ^C of 5s-electrons for I$^-$@C$_{60}$ and I$^-$ with account of reflection of photoelectrons by C$_{60}$ shell and its polarization by the incoming photon, in RPAE and GF RPAE

Figure 2.497_I⁻@C$_{60}$_e1 presents non-dipole angular anisotropy parameter γ^C_{5p} of 5p-electrons of I$^-$@C$_{60}$ and I$^-$ ions with account of reflection of photoelectrons by C$_{60}$ shell and its polarization by the incoming photon. The fullerenes shell prominently alters the region of the big maximum.

Figure 2.498_I⁻@C$_{60}$_e2 shows non-dipole angular anisotropy parameter δ^C_{5p} of 5p-electrons for I$^-$@C$_{60}$ and I$^-$ ions with account of reflection of photoelectrons by C$_{60}$ shell and its polarization by the incoming photon. The polarization of the C$_{60}$ shell leads to a prominent maximum in δ^C_{5p}.

Figure 2.499_I⁻@C$_{60}$_e3 shows the non-dipole angular anisotropy parameter γ^C_{5s} of 5s-electrons of I$^-$@C$_{60}$ and I$^-$ ions with account of reflection of photoelectrons by C$_{60}$ shell and its polarization by the incoming photon.

2.11 Onion-Type Endohedral Atoms A@C$_{60}$@C$_{240}$

In this section we present our results for photoionization cross-sections, dipole and nondipole angular anisotropy parameters of outer and intermediate subshells of some onion-type endohedral atoms A@C$_{N1}$@C$_{N2}$ that means an atom A, stuffed inside a fullerenes shell C$_{N1}$. If reflection is considered as weak, the result is denoted as RPAE. Formulas for such an object are presented in Section 1.15.

Having in mind to study the problem qualitatively, we limit ourselves by example $N_1 = 60$ and $N_2 = 240$ (see [2.87, 2.88] and references their in). As examples of A we consider here noble gas atoms Ne, Ar, Kr, and Xe. A specific feature of these objects is interference interaction of atomic shells with two fullerenes shells

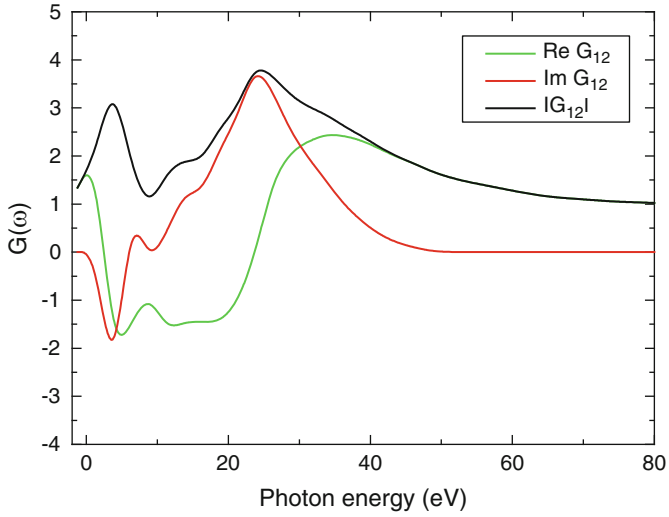

Fig. 2.500_C_{60}@C_{240}_g1 Polarization factor amplitude of the electromagnetic radiation $G_{12}(\omega)$ for C_{60}@C_{240}—real, imaginary, and absolute values

that lead to additional interference effects in the onion influence upon atomic photoionization characteristics.

Figures 2.500_C_{60}@C_{240}_g1 and 2.501_C_{60}@C_{240}_g2 (C60@C240) contain results of calculations for C_{60}@C_{240}.

Figure 2.500_C_{60}@C_{240}_g1 presents polarization factor amplitude of the electromagnetic radiation $G_{12}(\omega)$ for C_{60}@C_{240}—real, imaginary, and absolute values.

Figure 2.501_C_{60}@C_{240}_g2 shows polarization factor of the electromagnetic radiation by the electron shells $S_1(\omega)$ for C_{60}, $S_2(\omega)$ for C_{240} and $S_{12}(\omega)$ for C_{60}@C_{240}. It is seen that the combined effect of two shells, C_{60} and C_{240}, is far from being equal to a sum of partial contributions of these shells. It shows that interference effect in radiation interaction between two fullerenes shells is strong. The polarization factor from C_{240} is small enough, suppressing the photon intensity on the caged atom at $\omega \leq 5$ Ry by a factor of 2.

Figures 2.502_Ne@C_{60}@C_{240}_a1–2.504_Ne@C_{60}@C_{240}_b2 (Ne@C_{60}@C_{240}) contain results of calculations for Ne@C_{60}@C_{240}.

Figure 2.502_Ne@C_{60}@C_{240}_a1 displace the total photoionization cross-section of Ne, Ne@C_{60}, and Ne@C_{60}@C_{240} with account of reflection factor F in FRPAE and polarization G in GFRPAE. The effect of reflection from the second shell almost entirely compensates that by the first shell.

Figure 2.503_Ne@C_{60}@C_{240}_b1 presents the photoionization cross-section of $2p$-electrons for Ne, Ne@C_{60} and Ne@C_{60}@C_{240} with account of reflection factor F in RPAE and FRPAE and polarization G in GFRPAE. As in Fig. 2.502_Ne@C_{60}@C_{240}_a1, the effect of reflection from the second shell almost entirely compensates that by the first shell. Polarization leads to a profound maximum close to threshold.

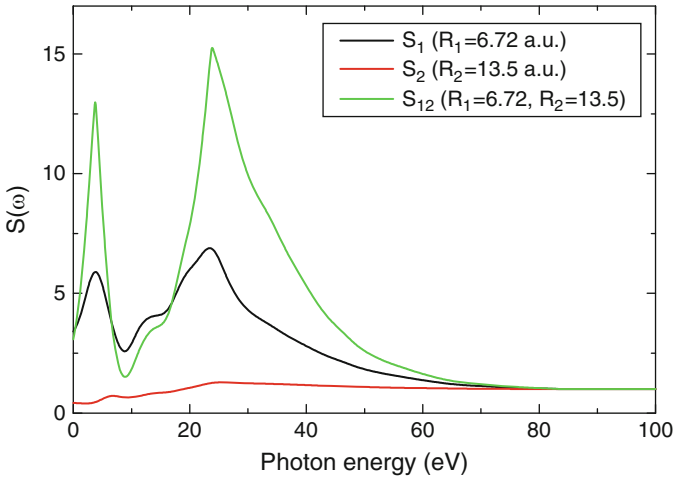

Fig. 2.501_C_{60}@C_{240}_g2 Polarization factor of the electromagnetic radiation by the electron shells $S_1(\omega)$ for C_{60}, $S_2(\omega)$ for C_{240} and $S_{12}(\omega)$ for C_{60}@C_{240}

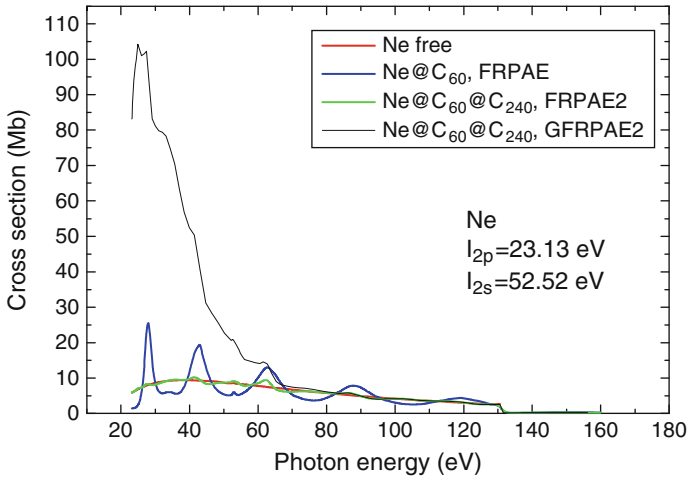

Fig. 2.502_Ne@C_{60}@C_{240}_a1 Total photoionization cross section of Ne, Ne@C_{60} and Ne@C_{60}@C_{240} with account of reflection factor F in FRPAE and polarization factor G in GFRPAE

Figure 2.504_Ne@C_{60}@C_{240}_b2 displays photoionization cross-section of 2s-electrons for Ne, Ne@C_{60} and Ne@C_{60}@C_{240} with account of reflection factor F in RPAE and FRPAE and polarization G in GFRPAE. Two-shell reflection is as strong as that by the C_{60}, but shifted in phase and a little bit modified in shape.

Figures 2.505_Ar@C_{60}@C_{240}_a1–2.514_Ar@C_{60}@C_{240}_e4 (Ar@C_{60}@C_{240}) contain results of calculations for Ar@C_{60}@C_{240}.

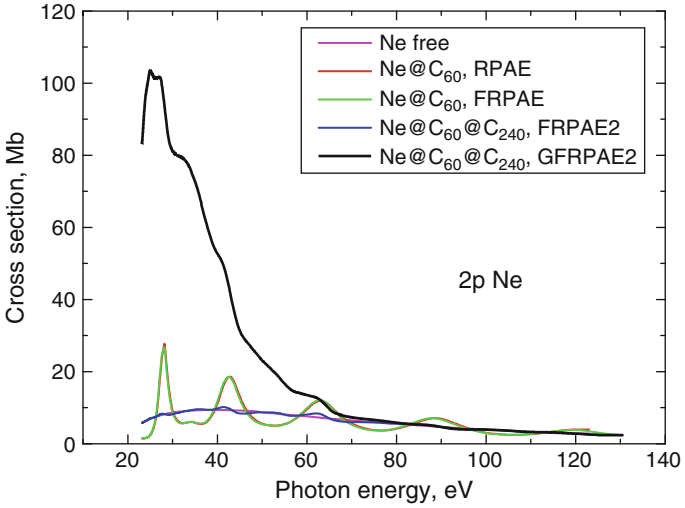

Fig. 2.503_Ne@C_{60}@C_{240}_b1 Photoionization cross section of $2p$-electrons for Ne, Ne@C_{60} and Ne@C_{60}@C_{240} with account of reflection factor F in RPAE and FRPAE and polarization factor G in GFRPAE

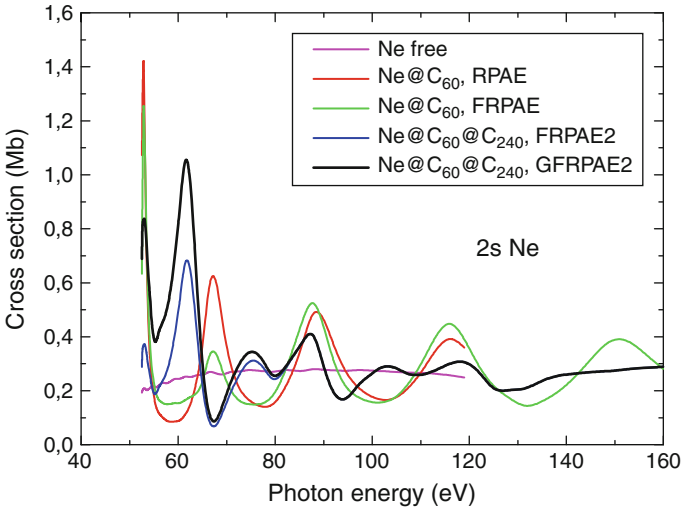

Fig. 2.504_Ne@C_{60}@C_{240}_b2 Photoionization cross section of $2s$-electrons for Ne, Ne@C_{60} and Ne@C_{60}@C_{240} with account of reflection factor F in RPAE and FRPAE and polarization factor G in GFRPAE

Figure 2.505_Ar@C_{60}@C_{240}_a1 demonstrates the total photoionization cross-section for Ar, Ar@C_{60} and Ar@C_{60}@C_{240} with account of reflection factor F in FRPAE and with polarization factor G in GFRPAE. Inclusion of only reflection of two shells leads to tremendous increase in the cross-section. In the main maximum,

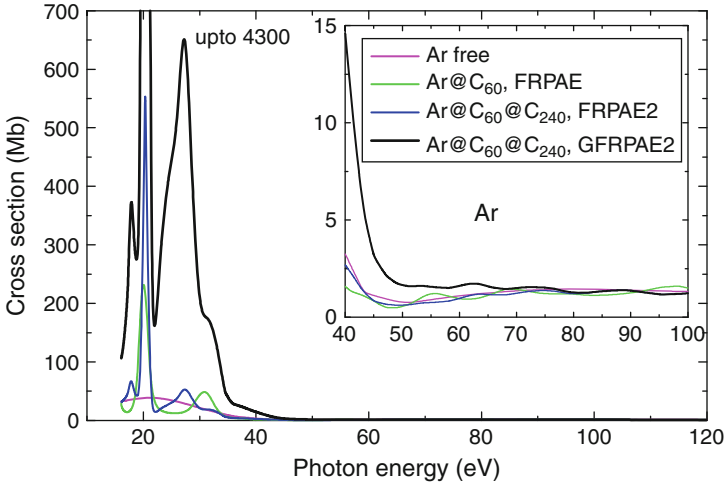

Fig. 2.505_Ar@C_{60}@C_{240}_a1 Total photoionization cross section for Ar, Ar@C_{60} and Ar@C_{60}@C_{240} with account of reflection factor F in FRPAE and with polarization factor G_{12} in GFRPAE

the increase is by a factor of almost 20. However, at photon energies higher than 40 eV the reflection adds only a fine oscillating structure. The polarization factor increases the cross-section to much bigger values, leading to two powerful maximums at 21 and 28 eV.

Figure 2.506_Ar@C_{60}@C_{240}_b1 shows the photoionization cross-section of $3p$-electrons in Ar in RPAE, Ar@C_{60}, Ar@C_{240} and Ar@C_{60}@C_{240} with account of reflection factor F in FRPAE. Naturally, the contribution of $3p$ dominates over the cross-section.

Figure 2.507_Ar@C_{60}@C_{240}_b2 presents photoionization cross-section of $3p$ electrons in Ar in RPAE, Ar@C_{60} and Ar@C_{60}@C_{240} with account of reflection factors F in FRPAE and the latter with account of polarization factor $G_{12}(\omega)$ in GFRPAE. It s seen that polarization leads to additional factor of three increase in the cross-section. In the main maximum, the increase is by a factor of about 70 and the cross-section exceeds 1,600 Mb.

Figure 2.508_Ar@C_{60}@C_{240}_b3 depicts photoionization cross-section of $3s$-electrons in Ar in RPAE, Ar@C_{60}, Ar@C_{240} and Ar@C_{60}@C_{240} with account of reflection factor F in FRPAE. Combination of two fullerenes almost cancels prominent effects of each other.

Figure 2.509_Ar@C_{60}@C_{240}_b4 demonstrates photoionization cross-section of $3s$ electrons in Ar in RPAE, Ar@C_{60} and Ar@C_{60}@C_{240} with account of reflection by factors F in FRPAE and the latter with account of polarization factor $G_{12}(\omega)$ in GFRPAE. By taking into account polarization the cross-section of Ar@C_{60}@C_{240} almost returns to the results of Ar@C_{60} in FRPAE.

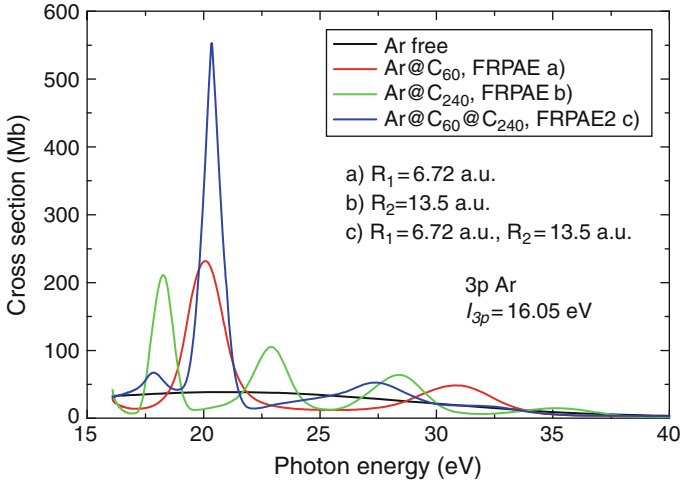

Fig. 2.506_Ar@C_{60}@C_{240}_b1 Photoionization cross section of $3p$-electrons in Ar, Ar@C_{60}, Ar@C_{240} and Ar@C_{60}@C_{240} with account of reflection factor F in FRPAE

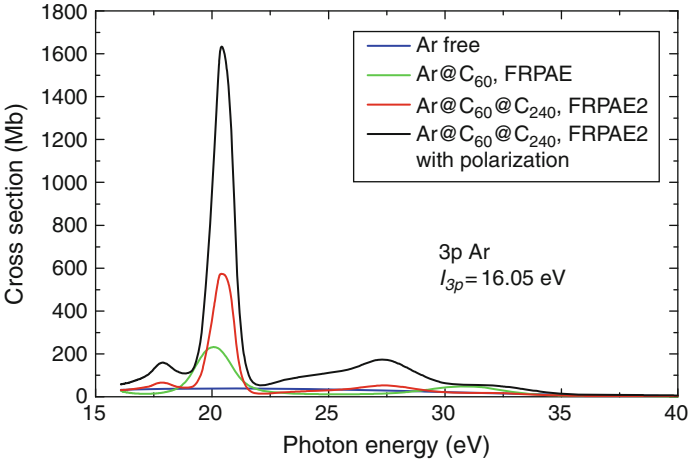

Fig. 2.507_Ar@C_{60}@C_{240}_b2 Photoionization cross-section of $3p$ electrons in Ar, Ar@C_{60}, and Ar@C_{60}@C_{240} with account of reflection factors F and the latter with account of polarization factor $G_{12}(\omega)$ in GFRPAE

Figure 2.510_Ar@C_{60}@C_{240}_d1 shows the dipole angular anisotropy parameter β^{C}_{3p} of $3p$ electrons for Ar in RPAE, Ar@C_{60}, Ar@C_{240}, and Ar@C_{60}@C_{240} in FRPAE. The FRPAE result in oscillations superimposed on the atomic value.

Figure 2.511_Ar@C_{60}@C_{240}_e1 illustrates the non-dipole angular anisotropy parameter γ^{C}_{3p} of $3p$ electrons for Ar in RPAE, Ar@C_{60} and Ar@C_{60}@C_{240} in GFRPAE. The GFRPAE result with two shells looks like a mirror reflection relative to the horizontal axis.

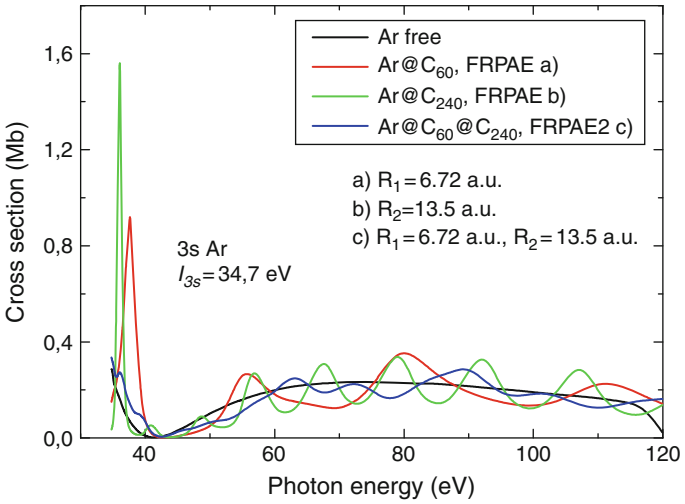

Fig. 2.508_Ar@C_{60}@C_{240}_b3 Photoionization cross section of 3*s*-electrons in Ar, Ar@C_{60}, Ar@C_{240}, and Ar@C_{60}@C_{240} with account of reflection factor F in FRPAE

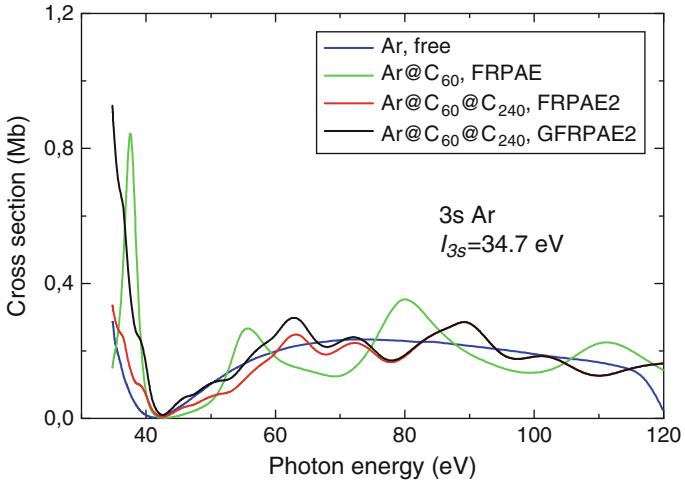

Fig. 2.509_Ar@C_{60}@C_{240}_b4 Photoionization cross-section of 3*s* electrons in Ar, Ar@C_{60} and Ar@C_{60}@C_{240} with account of reflection factors F in FRPAE and the latter with account of polarization factor $G_{12}(\omega)$ in GFRPAE

Figure 2.512_Ar@C_{60}@C_{240}_e2 shows the non-dipole angular anisotropy parameter δ^{C}_{3p} of $3p$ electrons for Ar in RPAE, Ar@C_{60}, and Ar@C_{60}@C_{240} in GFRPAE. As in Fig. 2.511_Ar@C_{60}@C_{240}_e1, the GFRPAE result with two shells, although being much smaller than γ^{C}_{3p} looks like a mirror reflection relative to the horizontal axis.

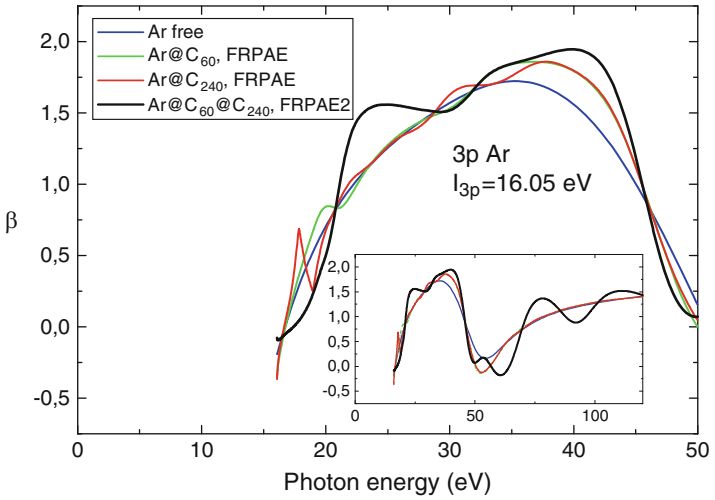

Fig. 2.510_Ar@C_{60}@C_{240}_d1 Dipole angular anisotropy parameter β^{C}_{3p} of $3p$ electrons for Ar in RPAE, Ar@C_{60}, Ar@C_{240} and Ar@C_{60}@C_{240} in FRPAE

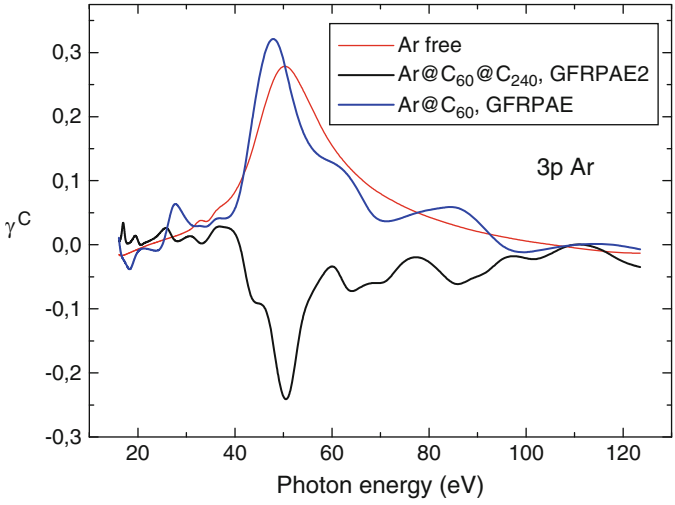

Fig. 2.511_Ar@C_{60}@C_{240}_e1 Non-dipole anisotropy parameter of $3p$ electrons for Ar in RPAE, Ar@C_{60} and Ar@C_{60}@C_{240} in GFRPAE

Figure 2.513_Ar@C_{60}@C_{240}_e3 represents the magic combination $\gamma^{C}_{3p} + 3\delta^{C}_{3p}$ of non-dipole angular anisotropy parameters of $3p$ electrons for Ar in RPAE, Ar@C_{60} and Ar@C_{60}@C_{240} in GFRPAE.

Figure 2.514_Ar@C_{60}@C_{240}_e4 demonstrates the non-dipole anisotropy parameter γ^{C}_{3s} of $3s$-electrons for Ar in RPAE, Ar@C_{60} and Ar@C_{60}@C_{240} in GFRPAE. The effects of GFRPAE are adding not too big oscillations only.

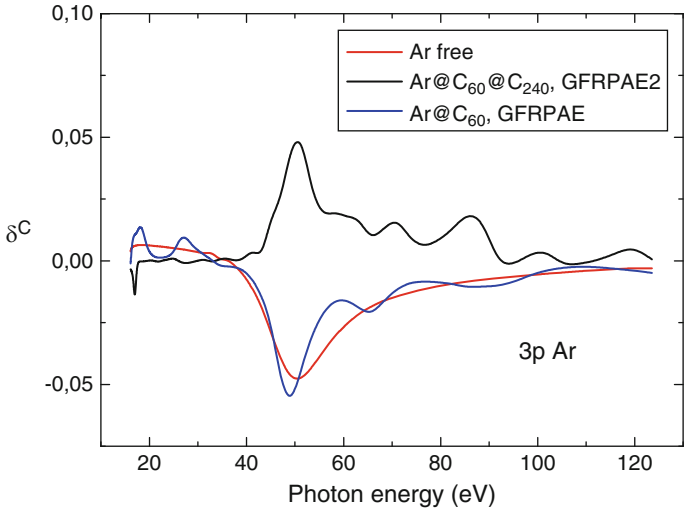

Fig. 2.512_Ar@C_{60}@C_{240}_e2 Non-dipole anisotropy parameter of $3p$ electrons for Ar in RPAE, Ar@C_{60} and Ar@C_{60}@C_{240} in GFRPAE

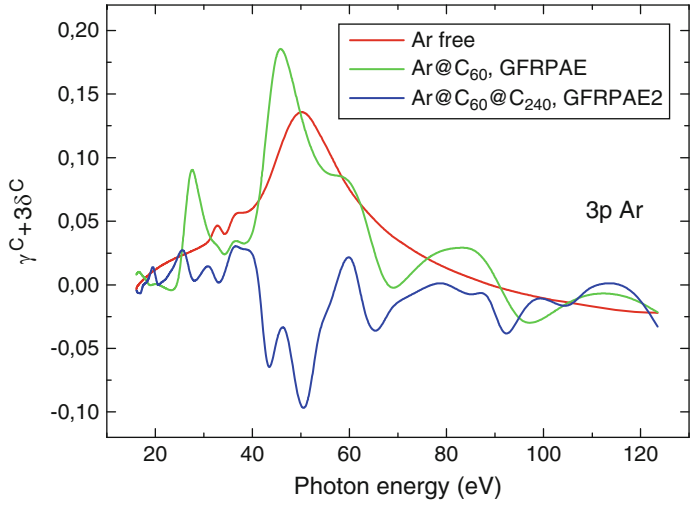

Fig. 2.513_Ar@C_{60}@C_{240}_e3 Magic combination of non-dipole anisotropy parameters of $3p$ electrons for Ar in RPAE, Ar@C_{60}, Ar@C_{60}@C_{240} in GFRPAE

Figures 2.515_Kr@C_{60}@C_{240}_a1–2.527_Kr@C_{60}@C_{240}_e7 (Kr@C_{60}@C_{240}) contain results of calculations for Kr@C_{60}@C_{240}.

Figure 2.515_Kr@C_{60}@C_{240}_a1 demonstrates the total photoionization cross-section for Kr in RPAE, Kr@C_{60} and Kr@C_{60}@C_{240} with account of reflection factor F in FRPAE and Kr@C_{60}@C_{240} with polarization factor in GFRPAE.

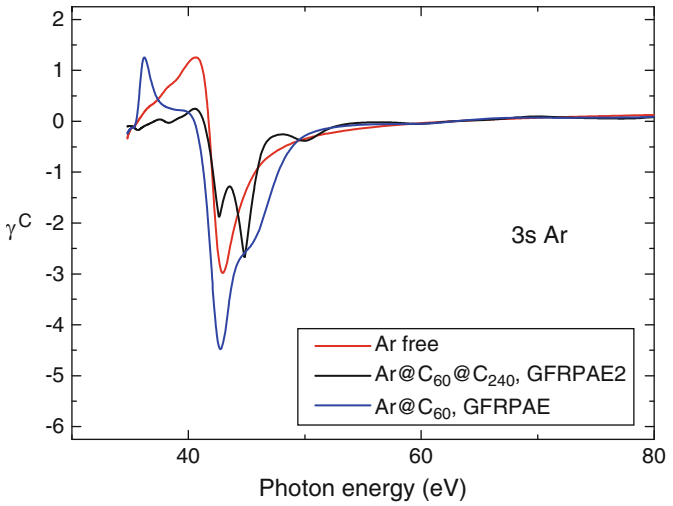

Fig. 2.514_Ar@C_{60}@C_{240}_e4 Non-dipole anisotropy parameter of 3*s*-electrons for Ar in RPAE, Ar@C_{60} and Ar@C_{60}@C_{240} in GFRPAE

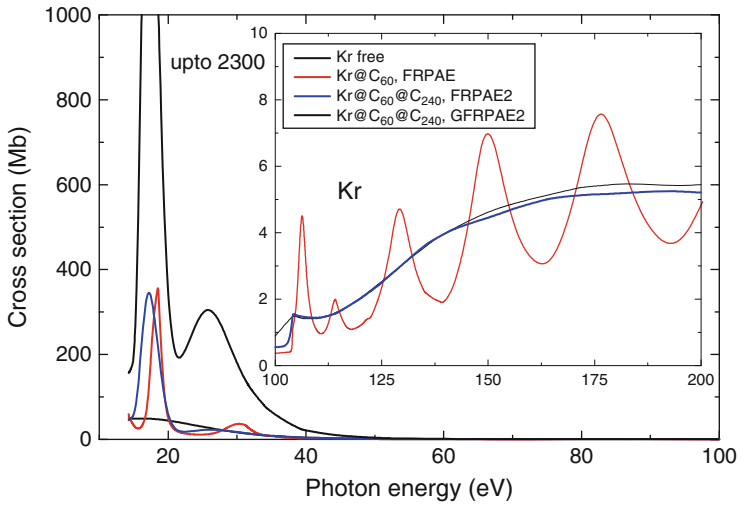

Fig. 2.515_Kr@C_{60}@C_{240}_a1 Photoionization cross section for Kr in RPAE, Kr@C_{60} and Kr@C_{60}@C_{240} with account of reflection factor F in FRPAE and Kr@C_{60}@C_{240} with polarization factor in GFRPAE

Inclusion of reflection by two shells leads to impressive increase in the cross-section. In the main maximum, the increase is by a factor of about 7, but almost the same for one and two fullerenes shells. At photon energies higher than 40 eV the reflection by the second shell eliminates the reflection by the first. It leads to pure atomic results for Kr@C_{60}@C_{240}.

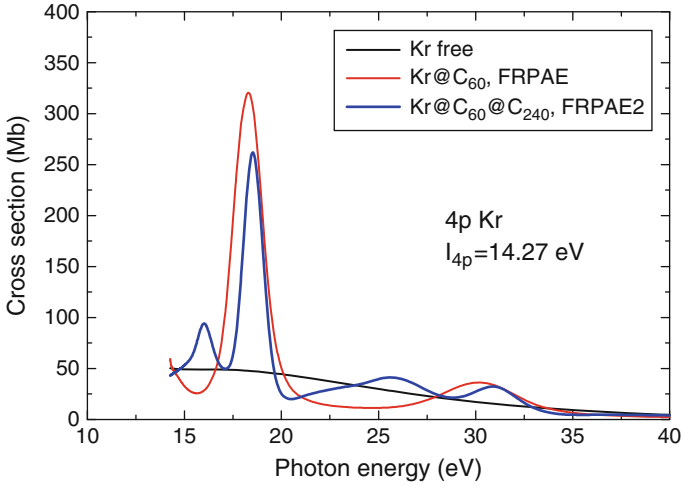

Fig. 2.516_Kr@C_{60}@C_{240}_b1 Photoionization cross section of $4p$-electrons for Kr, Kr@C_{60} and Kr@C_{60}@C_{240} with account of reflection factor F in FRPAE

Figure 2.516_Kr@C_{60}@C_{240}_b1 shows the photoionization cross-section of $4p$-electrons in Kr in RPAE, Kr@C_{60} and Kr@C_{60}@C_{240} with account of reflection factor F in FRPAE. Naturally, the contribution of $3p$ dominates over the cross-section. The influence of the second shell is small.

Figure 2.517_Kr@C_{60}@C_{240}_b2 depicts photoionization cross-section of $4s$-electrons in Kr in RPAE, Kr@C_{60} and Kr@C_{60}@C_{240} with account of reflection factor F in FRPAE. Combination of two fullerenes almost cancels prominent effects of each of them.

Figure 2.518_Kr@C_{60}@C_{240}_b3 represents the photoionization cross-section of $3d$-electrons for Kr, Kr@C_{60} and Kr@C_{60}@C_{240} with account of reflection factor F in FRPAE.

Figure 2.519_Kr@C_{60}@C_{240}_d1 shows the dipole angular anisotropy parameter β_{4p} of $4p$ electrons for Kr in RPAE, Kr@C_{60}, Ar@C_{240} and Kr@C_{60}@C_{240} in FRPAE. The reflection is inessential.

Figure 2.520_Kr@C_{60}@C_{240}_d2 shows the dipole angular anisotropy parameter β_{3d} of $3d$ electrons for Kr in RPAE, Kr@C_{60} and Kr@C_{60}@C_{240} in FRPAE. The reflection is inessential.

Figure 2.521_Kr@C_{60}@C_{240}_e1 illustrates the non-dipole angular anisotropy parameter γ^{C}_{4p} of $4p$ electrons for Kr, Kr@C_{60} and Kr@C_{60}@C_{240} in GFRPAE. The GFRPAE result is almost everywhere the smallest with a rather complex oscillating structure.

Figure 2.522_Kr@C_{60}@C_{240}_e2 shows the non-dipole angular anisotropy parameter δ^{C}_{4p} of $4p$ electrons for Kr in RPAE, Kr@C_{60} and Kr@C_{60}@C_{240} in GFRPAE. As in Fig. 2.521_Kr@C_{60}@C_{240}_e1, the GFRPAE result, although being much smaller than γ^{C}_{3p}, is characterized by a complex oscillating structure.

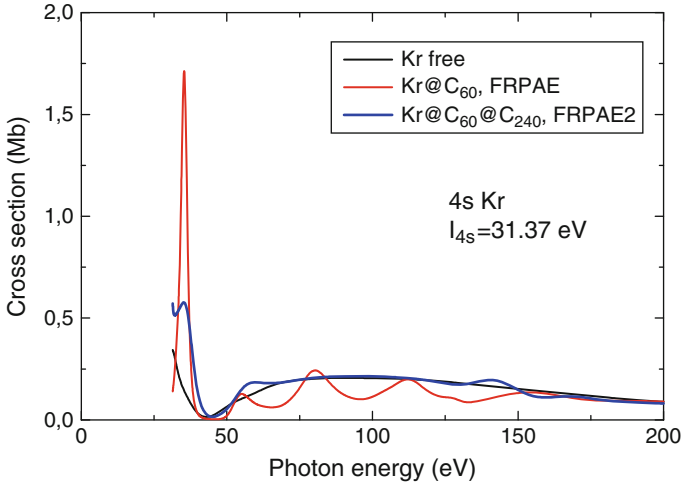

Fig. 2.517_Kr@C_{60}@C_{240}_b2 Photoionization cross section for Kr, Kr@C_{60} and Kr@C_{60}@C_{240} with account of reflection factor F in FRPAE

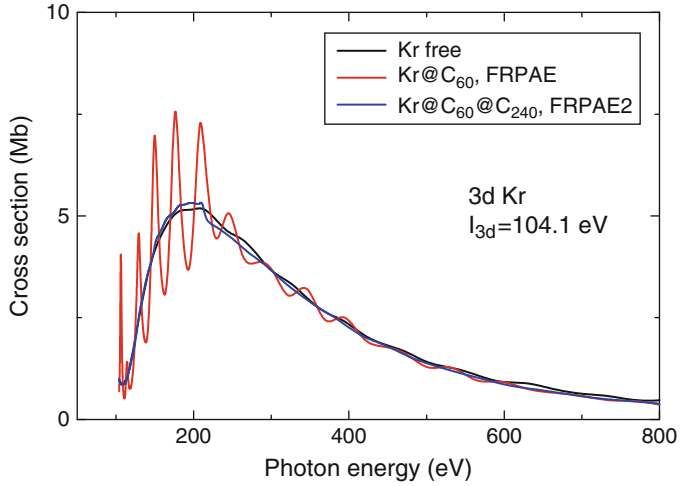

Fig. 2.518_Kr@C_{60}@C_{240}_b3 Photoionization cross section for Kr, Kr@C_{60} and Kr@C_{60}@C_{240} with account of reflection factor F in FRPAE

Figure 2.523_Kr@C_{60}@C_{240}_e3 represents the magic combination $\gamma^{C}_{4p} + 3\delta^{C}_{4p}$ of non-dipole angular anisotropy parameters of $4p$ electrons for Kr in RPAE, Kr@C_{60} and Kr@C_{60}@C_{240} in GRPAE. The GFRPAE value for onion-type fullerenes is the smallest and is strongly oscillating.

Figure 2.524_Kr@C_{60}@C_{240}_e4 demonstrates the non-dipole anisotropy parameter γ^{C}_{4s} of $4s$-electrons for Kr in RPAE, Kr@C_{60} in FRPAE and Kr@C_{60}@C_{240} in

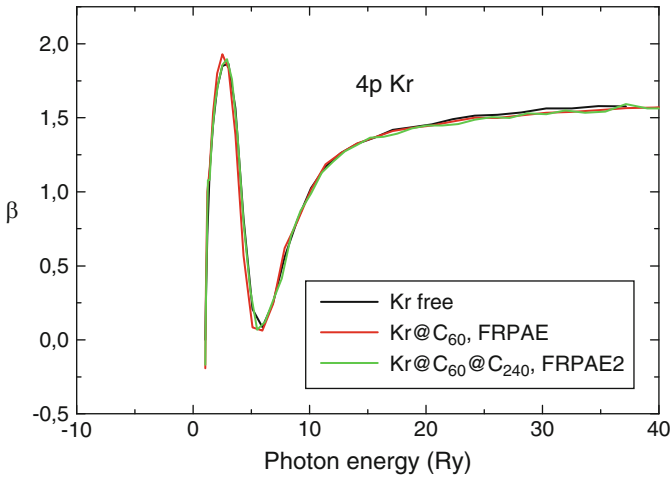

Fig. 2.519_Kr@C$_{60}$@C$_{240}$_d1 Dipole angular anisotropy parameter β^{C}_{4p} of $4p$ electrons for Kr in RPAE, Kr@C$_{60}$, Kr@C$_{240}$ and Kr@C$_{60}$@C$_{240}$ in FRPAE

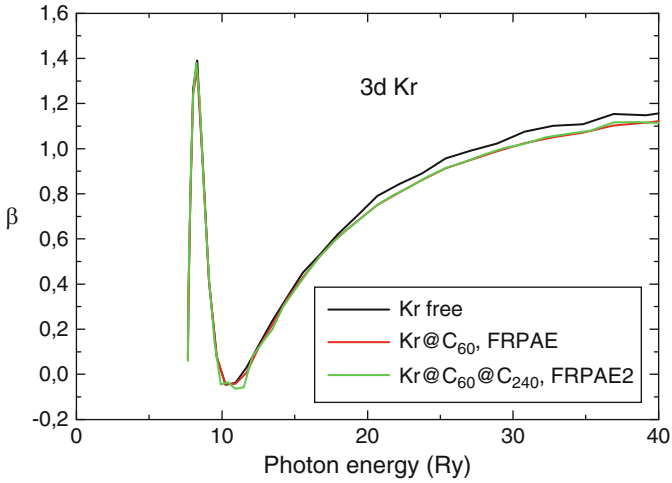

Fig. 2.520_Kr@C$_{60}$@C$_{240}$_d2 Dipole angular anisotropy parameter β^{C}_{3d} of $3d$ electrons for Kr in RPAE, Kr@C$_{60}$ and Kr@C$_{60}$@C$_{240}$ in FRPAE2

GFRPAE. The effect of GFRPAE is in creation of additional oscillating structure and in making the main GFRPAE maximum a mirror reflection of the main maximum in FRPAE.

Figure 2.525_Kr@C$_{60}$@C$_{240}$_e5 illustrates the non-dipole angular anisotropy parameter γ^{C}_{3d} of $3d$ electrons for Kr, Kr@C$_{60}$ and Kr@C$_{60}$@C$_{240}$. The inclusion of FRPAE adds strongly oscillating structure.

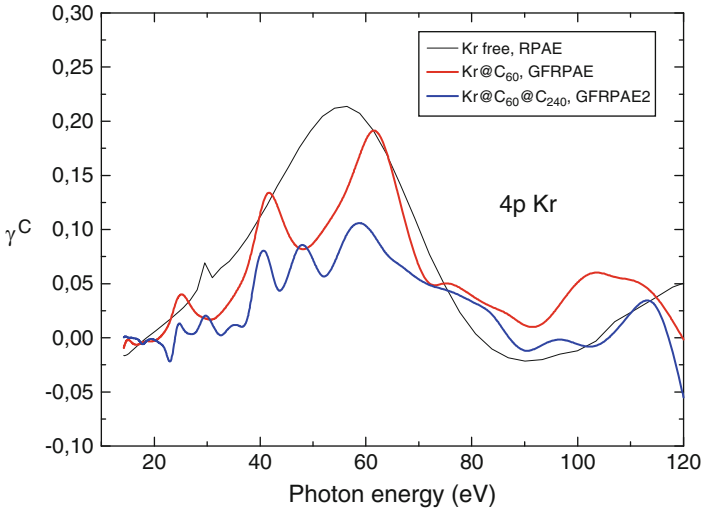

Fig. 2.521_Kr@C_{60}@C_{240}_e1 Non-dipole angular anisotropy parameter of $4p$ electrons for Kr in RPAE, Kr@C_{60} and Kr@C_{60}@C_{240} in GFRPAE

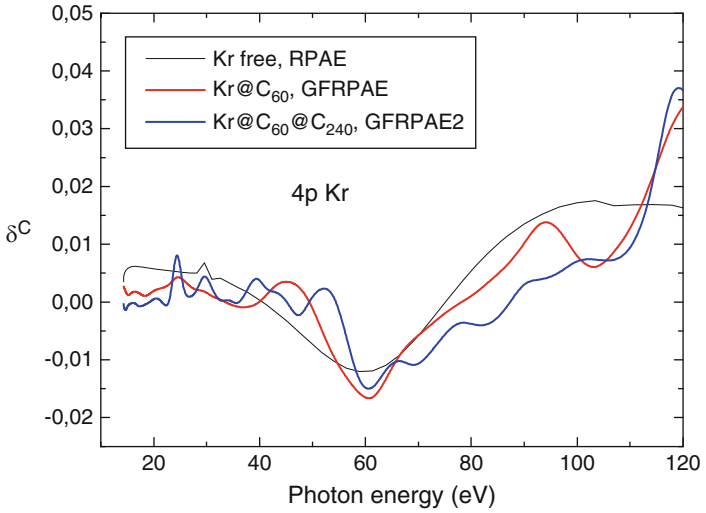

Fig. 2.522_Kr@C_{60}@C_{240}_e2 Non-dipole angular anisotropy parameter of $4p$ electrons for Kr in RPAE, Kr@C_{60} and Kr@C_{60}@C_{240} in GFRPAE

Figure 2.526_Kr@C_{60}@C_{240}_e6 shows the non-dipole angular anisotropy parameter δ^{C}_{3d} of $3d$ electrons for Kr, Kr@C_{60} and Kr@C_{60}@C_{240}. The FRPAE results are strongly oscillating and on the average a little bit smaller than the pure atomic value.

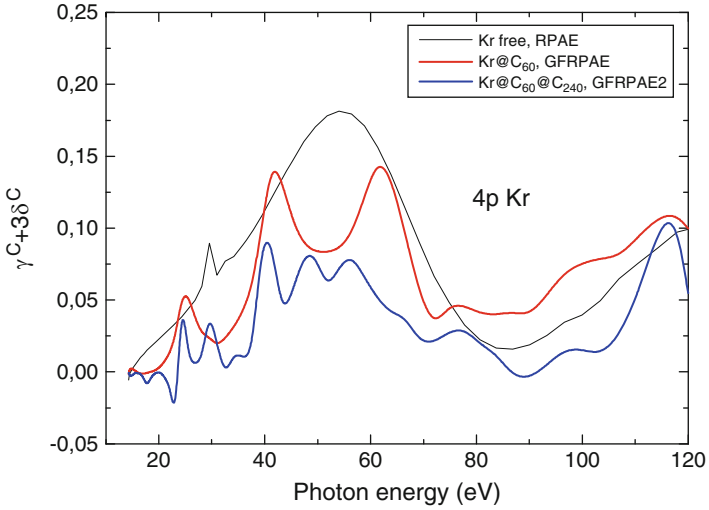

Fig. 2.523_Kr@C_{60}@C_{240}_e3 Magic combination of non-dipole angular anisotropy parameter of $4p$ electrons for Kr in RPAE, Kr@C_{60} and Kr@C_{60}@C_{240} in GFRPAE

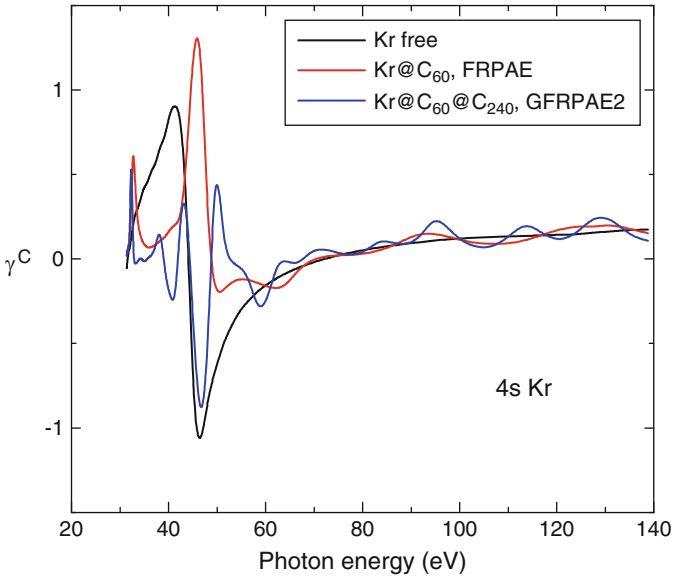

Fig. 2.524_Kr@C_{60}@C_{240}_e4 Non-dipole angular anisotropy parameter of $4s$ electrons for Kr in RPAE, Kr@C_{60} and Kr@C_{60}@C_{240} in GFRPAE

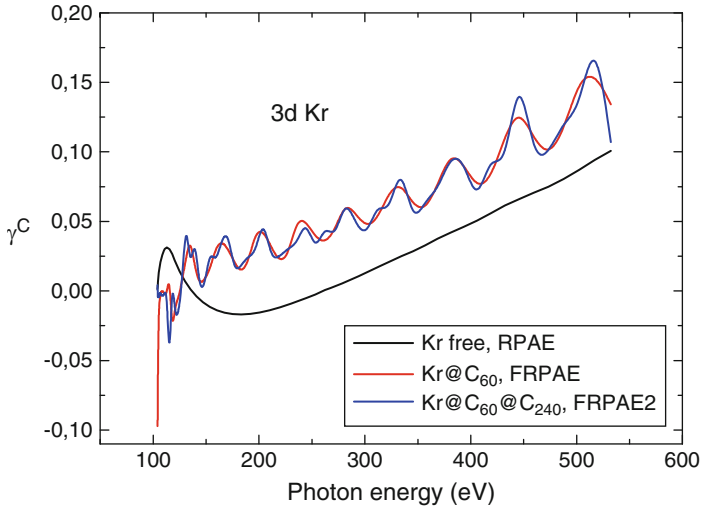

Fig. 2.525_Kr@C_{60}@C_{240}_e5 Non-dipole angular anisotropy parameter of 3*d* electrons for Kr in RPAE, Kr@C_{60} in FRPAE and Kr@C_{60}@C_{240} in FRPAE2

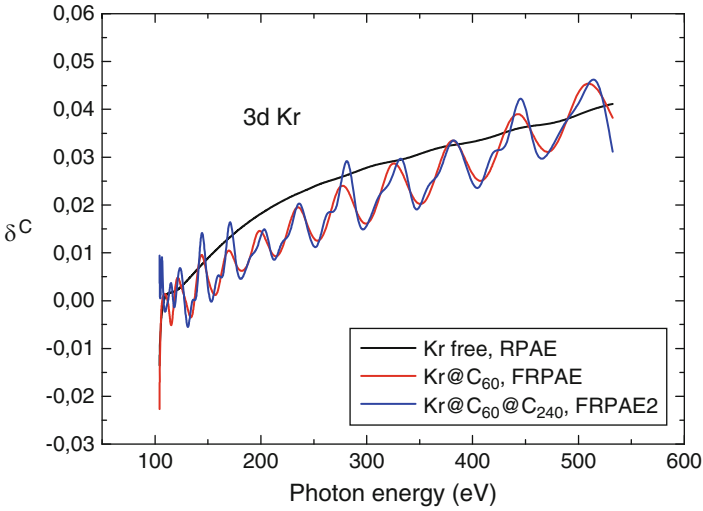

Fig. 2.526_Kr@C_{60}@C_{240}_e6 Non-dipole angular anisotropy parameter of 3*d* electrons for Kr in RPAE, Kr@C_{60} and Kr@C_{60}@C_{240} in FRPAE

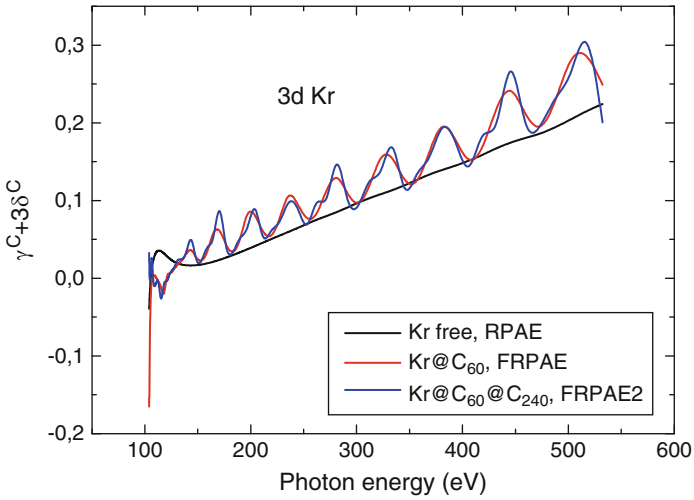

Fig. 2.527_Kr@C_{60}@C_{240}_e7 Non-dipole angular anisotropy parameter of 4*s* electrons for Kr in RPAE, Kr@C_{60} in FRPAE and Kr@C_{60}@C_{240} in FRPAE2

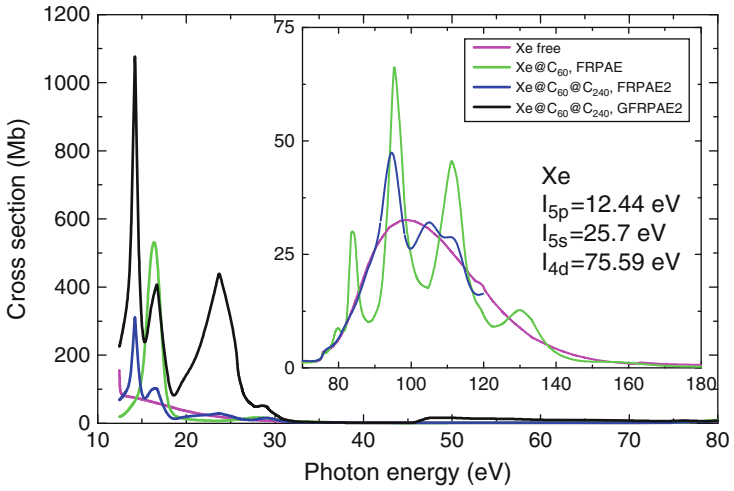

Fig. 2.528_Xe@C_{60}@C_{240}_a1 Total photoionization cross section for Xe in RPAE, Xe@C_{60} and Xe@C_{60}@C_{240} with account of reflection factor *F* in FRPAE and Xe@C_{60}@C_{240} with polarization factor in GFRPAE

Figure 2.527_Kr@C_{60}@C_{240}_e7 demonstrates the non-dipole angular anisotropy parameter of 4*s* electrons for Kr in RPAE, Kr@C_{60} and Kr@C_{60}@C_{240} in FRPAE. Being slightly bigger than the pure atomic value, the FRPAE results are strongly oscillating

Figures 2.528_Xe@C_{60}@C_{240}_a1–2.541_Xe@C_{60}@C_{240}_e7 (Xe@C_{60}@C_{240}) contain results of calculations for Xe@C_{60}@C_{240}.

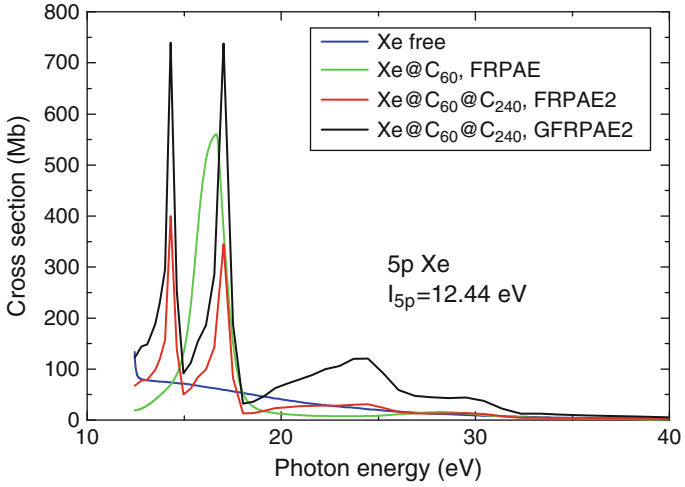

Fig. 2.529_Xe@C_{60}@C_{240}_b1 Photoionization cross section of $5p$-electrons for Xe in RPAE, Xe@C_{60} and Xe@C_{60}@C_{240} with account of reflection factor F in FRPAE and polarization factor G_{12} in GFRPAE

Figure 2.528_Xe@C_{60}@C_{240}_a1 demonstrates the total photoionization cross-section for Xe in RPAE, Xe@C_{60} and Xe@C_{60}@C_{240} with account of reflection factor F in FRPAE and for Xe@C_{60}@C_{240} also with polarization factor in GFRPAE. Inclusion of reflection of two shells leads to two prominent, but narrow maxima instead of one for C_{60}. The main maximum increases by a factor of 5 above the pure atomic level. At photon energies higher than 20 eV the reflection by the second shell eliminates the reflection by the first. This leads to pure atomic results. The $4d$ region is covered by oscillations, the second shell smoothing the effect of the first shell. The inclusion of the polarization factor enhances the cross-section at $\omega < 30$ eV dramatically.

Figure 2.529_Xe@C_{60}@C_{240}_b1 shows the photoionization cross-section of $5p$-electrons in Xe in RPAE, Xe@C_{60} and Xe@C_{60}@C_{240} with account of reflection factor F in FRPAE and FRPAE2, respectively. The polarization factor $G_{12}(\omega)$ is taken into account in GFRPAE. It s seen that polarization leads to additional factor of 1.5 increase in the cross-section. In the main maximum the increase is by a factor of about 10 and the cross-section exceeds 700 Mb. The influence of two shells at some frequencies compensates to large extend the big influence of the second shell.

Figure 2.530_Xe@C_{60}@C_{240}_b2 demonstrates photoionization cross-section of $5s$ electrons in Xe in RPAE, Xe@C_{60} and Xe@C_{60}@C_{240} with account of reflection by factors F in FRPAE and FRPAE2, respectively. The polarization factor $G_{12}(\omega)$ is included in the frame of GFRPAE. By taking into account polarization the cross-section of Xe@C_{60}@C_{240} is tremendously enhanced, particularly in the near threshold region. At the same time, in GFRPAE it has a sort of a fine structure.

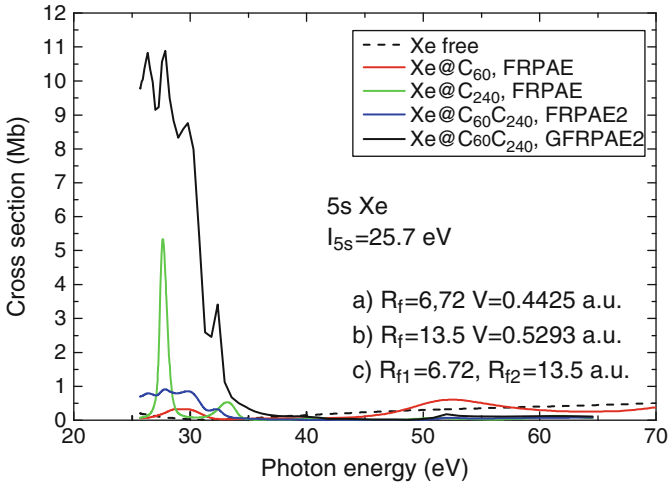

Fig. 2.530_Xe@C_{60}@C_{240}_b2 Photoionization cross section of 5*s*-electrons for Xe in RPAE, Xe@C_{60} and Xe@C_{60}@C_{240} with account of reflection factor F in FRPAE and with polarization of C_{60} in GFRPAE

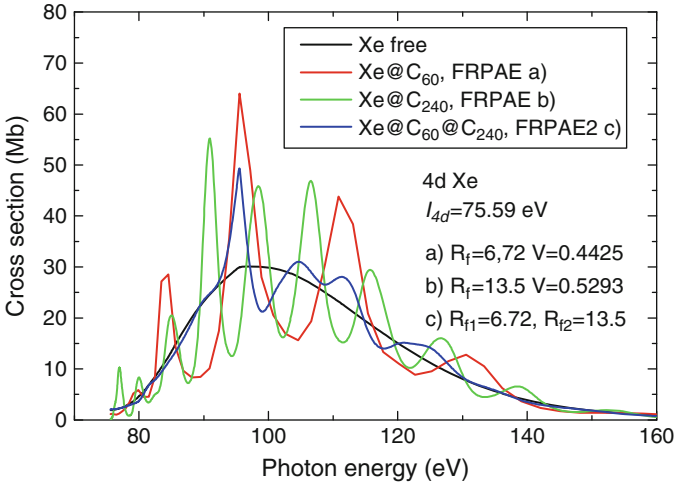

Fig. 2.531_Xe@C_{60}@C_{240}_b3 Photoionization cross section of 4*d*-electrons for Xe in RPAE, Xe@C_{60} and Xe@C_{60}@C_{240} with account of reflection factor F in FRPAE and with polarization of C_{60} in GFRPAE

Figure 2.531_Xe@C_{60}@C_{240}_b3 depicts photoionization cross-section of 4*d*-electrons in Xe, Xe@C_{60} and Xe@C_{60}@C_{240} with account of reflection factor F in FRPAE. Combination of two fullerenes considerably diminishes prominent effects of each of them.

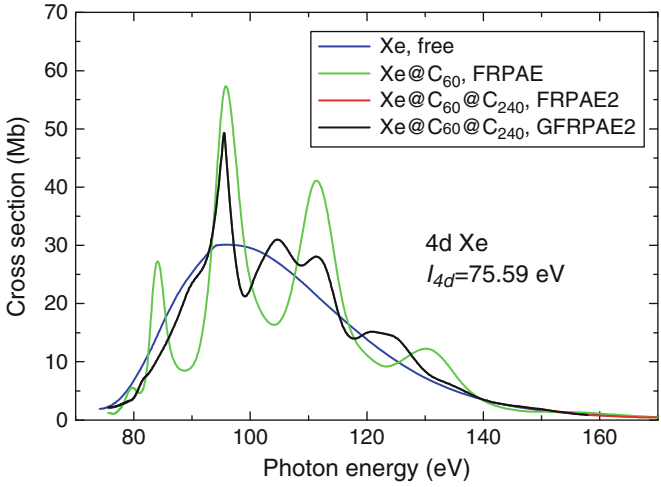

Fig. 2.532_Xe@C_{60}@C_{240}_b4 Photoionization cross-section of $4d$ electrons in Xe, Xe@C_{60} and Xe@C_{60}@C_{240} with account of reflection factors F and the latter with account of polarization factor $G_{12}(\omega)$ in GFRPAE2

Figure 2.532_Xe@C_{60}@C_{240}_b4 shows photoionization cross-section of $4d$ electrons in Xe, Xe@C_{60} and Xe@C_{60}@C_{240} with account of reflection by factors F in FRPAE and the latter with account of polarization factor $G_{12}(\omega)$ in GFRPAE2. By taking into account polarization the cross-section of Kr@C_{60}@C_{240} almost returns to the results of Kr@C_{60} in FRPAE.

Figure 2.533_Xe@C_{60}@C_{240}_d1 shows the dipole angular anisotropy parameter β_{5p} of $5p$ electrons for Xe in RPAE, Xe@C_{60} in FRPAE and Xe@C_{60}@C_{240} in FRPAE2. The FRPAE2 for two fullerenes shells adds oscillations that are much stronger than for each of the shells separately.

Figure 2.534_Xe@C_{60}@C_{240}_d2 shows the dipole angular anisotropy parameter β_{4d} of $4d$ electrons for Xe in RPAE, Xe@C_{60} in FRPAE and Xe@C_{60}@C_{240} in GFRPAE2. The FRPAE for two fullerenes shells adds, like in Fig. 2.533_Xe@C_{60}@C_{240}_d1, oscillations that are much stronger than for each of the shells separately.

Figure 2.535_Xe@C_{60}@C_{240}_e1 illustrates the non-dipole angular anisotropy parameter γ^{C}_{5p} of $5p$ electrons for Xe, Xe@C_{60} and Xe@C_{60}@C_{240} in RPAE for atom and FRPAE for endohedrals. FRPAE for onion endohedrals brings the result to almost zero with small oscillations around this value, while the FRPAE for inner fullerene only oscillates near the free atom value.

Figure 2.536_Xe_e2 shows the non-dipole angular anisotropy parameter δ^{C}_{5p} of $5p$ electrons for Xe, Xe@C_{60}, and Xe@C_{60}@C_{240} in RPAE for atom and FRPAE for endohedrals. As in Fig. 2.535_Xe@C_{60}@C_{240}_e1, the FRPAE for onion endohedrals brings the result to almost zero with oscillations around this value, while the FRPAE for inner fullerene only oscillates near the free atom value.

Figure 2.537_Xe@C_{60}@C_{240}_e3 represents the magic combination $\gamma^{C}_{5p} + 3\delta^{C}_{5p}$ of non-dipole angular anisotropy parameters of $5p$ electrons for Xe, Xe@C_{60} and

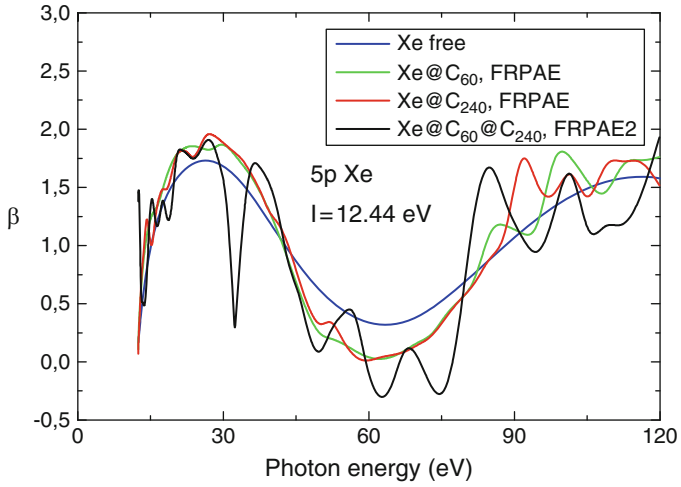

Fig. 2.533_Xe@C_{60}@C_{240}_d1 Dipole angular anisotropy parameter of $5p$ electrons for Xe in RPAE, Xe@C_{60}, Xe@C_{240} and Xe@C_{60}@C_{240} in FRPAE2

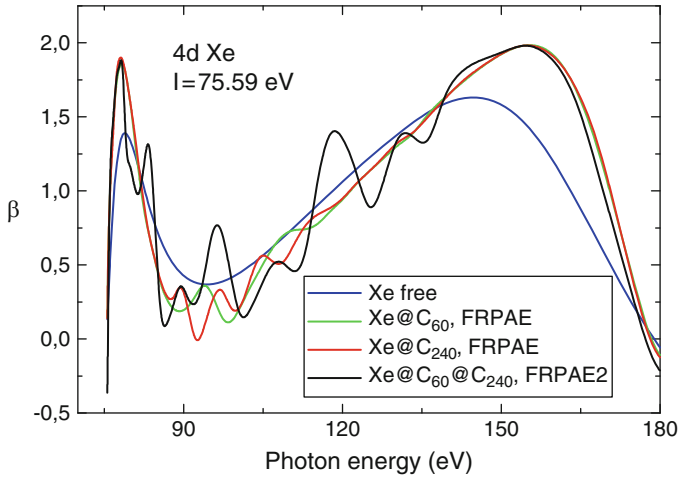

Fig. 2.534_Xe@C_{60}@C_{240}_d2 Dipole angular anisotropy parameter of $4d$ electrons for Xe in RPAE, Xe@C_{60}, Xe@C_{240} and Xe@C_{60}@C_{240} in FRPAE

Xe@C_{60}@C_{240} in RPAE for atom and FRPAE, FRPAE2 for endohedrals. For onion endohedrals the result are almost zero with small oscillations around this value, while the FRPAE for inner fullerene only oscillates higher with the average values higher than for the free atom.

Figure 2.538_Xe@C_{60}@C_{240}_e4 demonstrates the non-dipole anisotropy parameter γ_{5s}^{C} of $5s$-electrons for Xe in RPAE, Xe@C_{60} in FRPAE and Xe@C_{60}@C_{240} in FRPAE2. The effects of FRPAE are concentrated within a narrow area of 20 eV

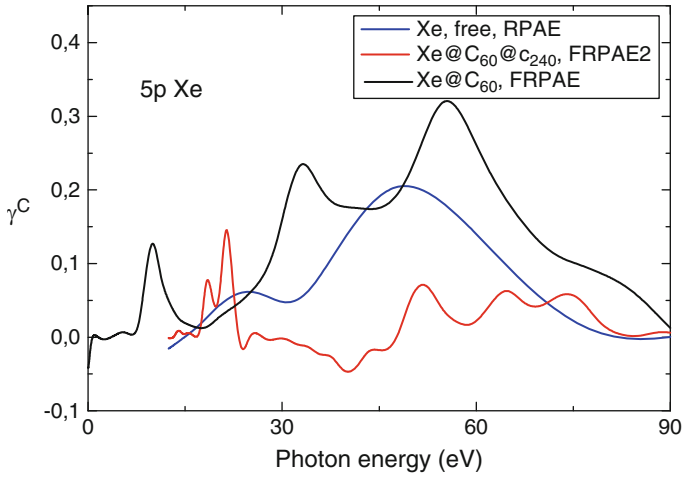

Fig. 2.535_Xe@C_{60}@C_{240}_e1 Non-dipole anisotropy parameter of $5p$ electrons for Xe in RPAE and Xe@C_{60}@C_{240} in FRPAE and FRPAE2

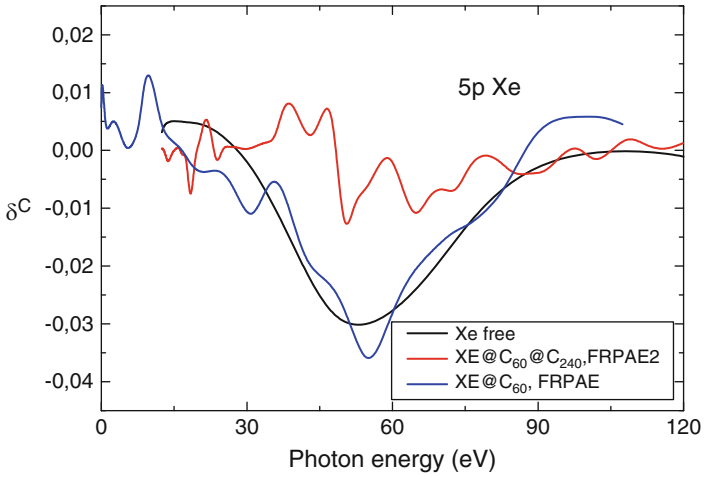

Fig. 2.536_Xe@C_{60}@C_{240}_e2 Non-dipole angular anisotropy parameter of $5p$ electrons for Xe in RPAE and Xe@C_{60}@C_{240} GFRPAE2

above threshold. The results for onion-type fullerenes are very close to zero except the threshold proximity.

Figure 2.539_Xe@C_{60}@C_{240}_e5 illustrates the non-dipole angular anisotropy parameter γ^{C}_{4d} of $4d$ electrons for Xe in RPAE, Xe@C_{60} in FRPAE and in FRPAE2 for Xe@C_{60}@. The FRPAE2 result looks like a mirror reflection relative to the horizontal axis. The reflection by two shells adds a narrow minimum close to 162 eV.

Figure 2.540_Xe@C_{60}@C_{240}_e6 shows the non-dipole angular anisotropy parameter δ^{C}_{4d} of $4d$ electrons for Xe in RPAE, Xe@C_{60} in FRPAE and

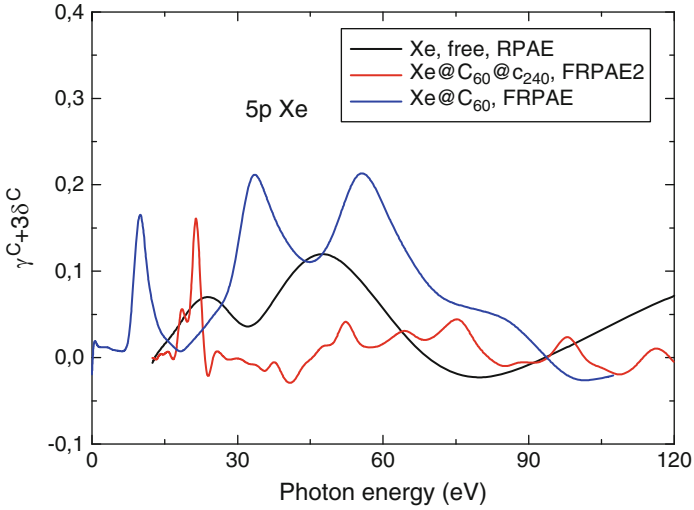

Fig. 2.537_Xe@C_{60}@C_{240}_e3 Magic combination of non-dipole angular anisotropy parameter of $5p$ electrons for Xe in RPAE, Xe@C_{60} in FRPAE and Xe@C_{60}@C_{240} in FRPAE2

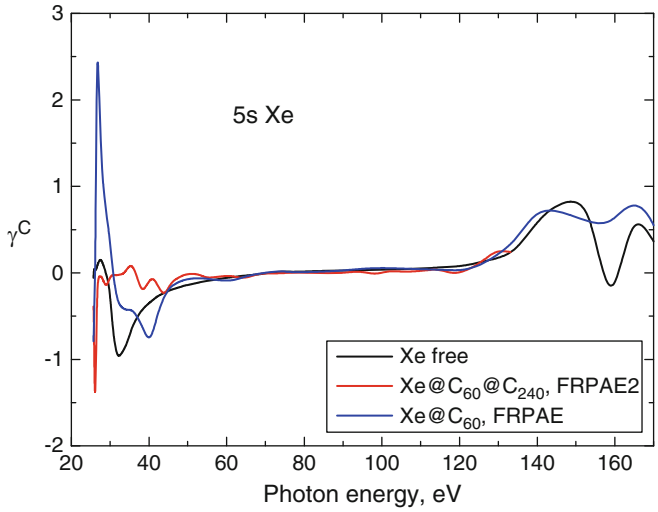

Fig. 2.538_Xe@C_{60}@C_{240}_e4 Non-dipole angular anisotropy parameter of $5s$ electrons for Xe in RPAE, Xe@C_{60} in FRPAE and Xe@C_{60}@C_{240} in FRPAE2

Xe@C_{60}@C_{240} in FRPAE2. As in Fig. 2.539_Xe@C_{60}@C_{240}_e5, the FRPAE2 result, although being much smaller than γ^C_{4d} looks like a mirror reflection relative to the horizontal axis. The reflection by two shells adds a narrow maximum close to 162 eV

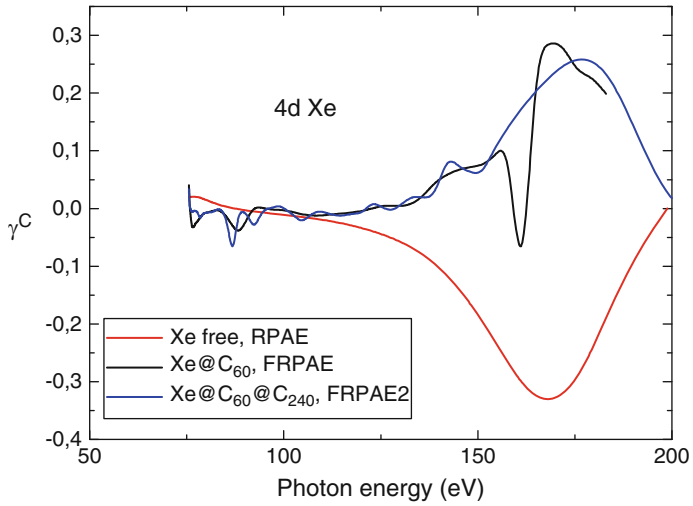

Fig. 2.539_Xe@C_{60}@C_{240}_e5 Non-dipole angular anisotropy parameter of 4*d* electrons for Xe in RPAE, Xe@C_{60} in FRPAE and Xe@C_{60}@C_{240} in FRPAE

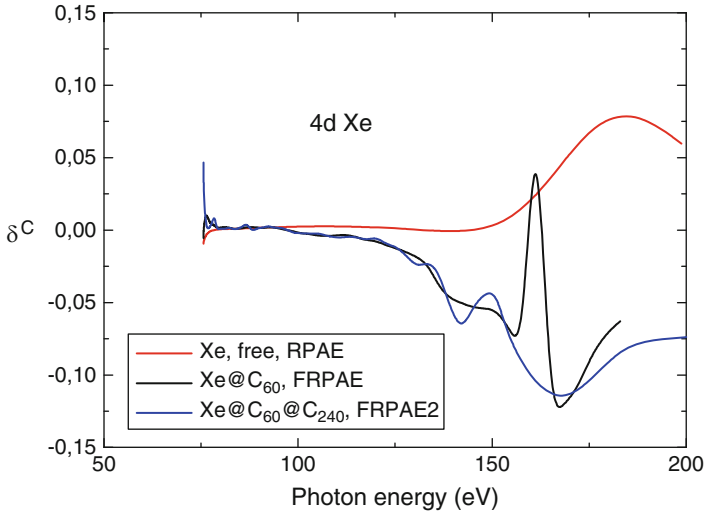

Fig. 2.540_Xe@C_{60}@C_{240}_e6 Non-dipole angular anisotropy parameter of 4*d* electrons for Xe RPAE, Xe@C_{60} in RPAE, Xe@C_{60}@C_{240} in FRPAE

Figure 2.541_Xe@C_{60}@C_{240}_e7 demonstrates the magic combination of non-dipole angular anisotropy parameters of 4*d* electrons for Xe in RPAE, Xe@C_{60} in FRPAE and Xe@C_{60}@C_{240} in FRPAE2. Except narrow vicinity of the threshold, FRPAE2 results presents relatively small oscillations near the corresponding free atomic value.

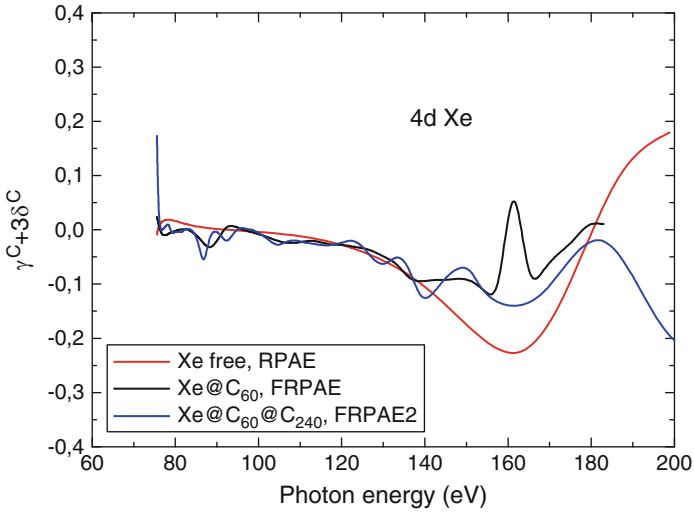

Fig. 2.541_Xe@C_{60}@C_{240}_e7 Magic combination of non-dipole angular anisotropy parameters of 4*d* electrons for Xe in RPAE, Xe@C_{60} in FRPAE and Xe@C_{60}@C_{240} in FRPAE2

References

2.1. Amusia MYa, Ivanov VK, Dolmatov VK (1978) Giant autoionization in Mn atom. JETP Lett 4:1305–1309 (in Russian)

2.2. Amusia MYa, Dolmatov VK, Ivanov VK, Sheftel SI (1981) Giant autoionization of the atoms with semi-occupied shells. in: autoionization phenomena in atoms. In: Proceedings of the 2nd scientific workshop, Moscow State University, pp 235–242 (in Russian)

2.3. Amusia MYa, Chernysheva LV, Manson ST, Msezane AZ, Radojevich V (2002) Strong electron correlations in photoionization of spin–orbit doublets. Phys Rev Lett 88:093002

2.4. Bizau JM, Wuilleumier FJ (1995) Redetermination of absolute partial photoionization cross-sections of He and Ne atoms between 20 and 300 eV photon energy. J Electron Spectrosc Relat Phenom 71:205–224

2.5. Amusia MYa, Baltenkov AS, Chernysheva LV, Felfli Z, Msezane AZ, Nordgren J (2001) Directed motion of electrons in gases under the action of photon flux. Phys Rev A 63:052512

2.6. Amusia MYa, Cherepkov NA, Shapiro SG (1972) Calculation of multipole polarizabilities and van-der-waals force constants. JETP 63:889 (in Russian)

2.7. Amusia MYa, Baltenkov AS, Greenberg AA, Shapiro SG (1975) Investigation of the current due to photon momentum in monoatomic gases. JETP 68:28–35

2.8. Dias E, Chakraborty H, Deshmukh P, Manson ST, Hemmers O, Glans P, Hansen D, Wang H, Whitfield S, Lindle D, Wehlits R, Levin J, Sellin I, Perera R (1997) Breakdown of the independent particle approximation in high-energy photoionization. Phys Rev Lett 78:4553–4556

2.9. Amusia MYa, Avdonina NB, Drukarev EG, Manson ST., Pratt RH (2000) Modification of the high energy behavior of the atomic photoionization cross section. Phys Rev Lett 85(22):4703–4706

2.10. Amusia MYa, Baltenkov AS, Chernysheva LV, Felfli Z, Msezane AZ (2001) Non-dipole parameters in angular distributions of electrons in photoionization of noble gas atoms. Phys Rev A 63:052506

2.11. Amusia MYa, Cherepkov NA, Chernysheva LV (1971) Noble-gas photoionization cross section with many-electron correlations. JETP 60:160–174 (in Russian)
2.12. West JB, Marr GV (1976) The absolute photoionization cross sections of helium, neon, argon and krypton in the extreme vacuum ultraviolet region of the spectrum. Proc Roy Soc. London A 349(1658):397–421
2.13. Tan KH, Brion CE (1978) Branching ratios and the partial photoionization cross-section for the 3s electron of argon. J. Electron Spectrosc Relat Phenom 13:77–82
2.14. Amusia MYa (1981) Collective effects in an isolated atom. Bull Russ Acad Sci Phys 45(12):2242–2254 (in Russian)
2.15. Amusia MYa (1984) Interaction of complex atoms with radiation. Bull Russ Acad Sci Phys 48(4):642–650
2.16. Shnopper HW (1963) Multiple excitation and ionization of inner atomic shells by X rays. Phys Rev 131:2558–2560
2.17. Houlgate RG, West JB, Codling K, Marr GV (1974) Angular distribution and photoionization cross section measurements on the 3p and 3s subshells of argon. J Phys B 7:L470–L473
2.18. Dehmer JL, Chupka WA, Berkowitz J, Jivery WT (1975) Wavelength dependence of the photoelectron angular distributions of the rare gases. Phys Rev A 12:1966–1977
2.19. West JB, Woodruff PR, Codling K, Houlgate RG (1976) The 4d, 5s and 5p partial photoionization cross sections of xenon above the 4d threshold. J Phys B At Mol Phys 9:407–410
2.20. Amusia MYa, Ivanov VK, Cherepkov NA, Chernysheva LV (1974) Intershell and intersubshell effects in atomic photoionization JETP 66:1537–1549
2.21. Samson JAR, Gardner JL (1974) Photoionization cross sections of the outer *s*-subshell electrons in the rare gases. Phys Rev Lett 33:671–674
2.22. Adam MY, Wuilleumier F, Sandner N, Krummacher S, Schmidt V, Mehlhorn W (1978) Jpn J Appl Phys 17:170–180
2.23. Haensel R, Keitel G, Kosuch N, Nielsen U, Schreiber P (1971) Optical absorption of solid neon and argon in the soft X-ray region. J De Physique:236–245 (32-C4)
2.24. Kammerling B, Kossman H, Schmidt V (1989) 4d photoionization in xenon: absolute partial cross section and relative strength of 4d many-electron processes. J Phys B At Mol Phys 22:841–854
2.25. Amusia MYa (2004) Random phase approximation: from Giant to intra-doublet resonances. Radiat Phys Chem 70:237–251
2.26. Kivimaki A, Hergenhahn U, Kempgens B, Hentges R, Piancastelli MN, Maier K, Ruedel A, Tulkki JJ, Bradshaw AM (2000) Near-threshold study of Xe 3*d* photoionization. Phys Rev A 63:012716
2.27. Amusia MYa, Ivanov VK (1976) The peculiarities of photoelectron angular distribution and ionization cross section of 5p subshell in Xe. Phys Lett A 59:194–196
2.28. Lynch MJ, Gardner JL, Codling K, Marr GV (1973) The photoionization of the 3s subshell of argon in the threshold region by photoelectron spectroscopy. Phys Lett A 43:237–238
2.29. Torop L, Morton J, West JB (1976) The angular distribution of photoelectrons from xenon. J Phys B At Mol Phys 9:2035–2041
2.30. Krause MO, Carlson TA, Woodruff PR (1981) Angular distribution of photoelectrons of Xe 5*p* spin–orbit components between 20 and 105 eV. Phys Rev A 24:1374–1385
2.31. Southworth S, Becker U, Truesdale CM, Kobrin PH, Lindle DW, Owaki S, Shirley DA (1983) Electron-spectroscopy study of inner-shell photoexcitation and ionization of Xe. Phys Rev A 28:261–273
2.32. Amusia MYa, Baltenkov AS, Chernysheva LV, Felfli Z, Manson ST, Msezane AZ (2003) On the effect of intra-doublet correlations upon the non-dipole parameters in Xe. INFN Frasc Phys Ser 32:3–8
2.33. Hemmers O, Guillemin R, Kanter EP, Krassig B, Lindle D, Southworth S H, Wehlitz R, Baker J, Hudson A, Lotrakul M, Rolles D, Stolte WC, Tran IC, Wolska A, Yu SW, Amusia MYa, Cheng KT, Chernysheva LV, Johnson WR, Manson ST (2003) Dramatic nondipole effects in low energy photoionization: experimental and theoretical study of Xe5s. Phys Rev Lett 91:053002

2.34. Amusia MYa, Baltenkov AS, Chernysheva LV, Felfli Z, Manson ST, Msezane AZ (2003) Correlation structure in nondipole photoionization. Phys Rev A 67:060702
2.35. Amusia MYa, Ivanov VK, Chernysheva LV (1973) Photoproduction of Kr^+ and Xe^+ ions in the vicinity of the outer d-subshell threshold. Phys Lett A 43:243
2.36. Amusia MYa, Cherepkov NA, Chernysheva LV, Manson ST (2000) Multielectron effects in Xe^{++} formation resulting from the photoionization of Xe^+ ions. J Phys B At Mol Opt Phys 33:L37–L42
2.37. Koizumi T, Awaya Y, Fujino A, Itoh T, Kitajima M, Kojima TM, Oura M. Sano, Sekioka T, Watanabe N, Koike F (1997) Phys Scripta T73:131–142
2.38. Ivanov VK, Lapkin KV, Kulov MA (2003) Electron photodetachment from the 1*s* shell of a negative lithium ion. Techn Phys Lett 29(8):620–623
2.39. Berrah N, Bozek JD, Wills AA, Turri G, Zhou HL, Manson ST, Akerman G, Rude B, Gibson ND, Walter CW, VoKy L, Hibbert A, Ferguson SM (2001) *K*-shell photodetachment of Li^-: experiment and theory. Phys Rev Lett 87(25):253002-1/4
2.40. Kjeldsen H, Andersen P, Folkmann F, Kristensen B, Andersen T (2001) Inner-shell photodetachment of Li^-. J Phys B At Mol Opt Phys 34(10):L353–L357
2.41. Kjeldsen H, Folkmann F, Knudsen H, Rasmussen MS, West JB, Andersen T (1999) Absolute photoionization cross section of K^+ ions from the 3p to the 3s threshold. J Phys B At Mol Opt Phys 32(18):4457–4465
2.42. van Kampen P, O'Sullivan G, Ivanov VK, Ipatov AN, Costello JT, Kennedy ET (1997) Dramatic changes in the 3*s* autoionization process at the beginning of the Ar I sequence. Phys Rev Lett 78:3082–3085
2.43. Amusia MYa, Baltenkov AS, Chernysheva LV, Felfli Z, Manson ST, Msezane AZ (2004) Intra-doublet correlation effect in dipole angular anisotropy parameters of 3d electrons. J Phys B At Mol Opt Phys 37:937–944
2.44. Amusia MYa, Cherepkov NA, Chernysheva LV, Felfli Z, Msezane AZ (2004) On spin polarization of photoelectrons from Xe, Cs, and Ba 3*d* spin-orbit components. Phys Rev A 70:062709
2.45. Amusia MYa, Avdonina NB (1988) Intershell interaction in excited atom and ion photoionization. Z Phys D Atoms Mol Clust 14:191–194
2.46. Wilson NJ, Donnelly D, Bell KL, Hibbert A (1999) R-matrix calculation of the photoabsorption of K II, Ca III and Sc IV. J Phys B At Mol Opt Phys 32(18):4495–4508
2.47. Rabe A, Radler K, Wolf HW. (1974) Photoabsorption of metallic and atomic barium between 80 eV and 160 eV. Vacuum ultraviolet radiation physics. Pergamon & Vieweg, Braunschweig, West Germany, pp. 247–249
2.48. Amusia MYa, Chernysheva LV, Ivanov VK, Kupchenko VA (1989) Photoionization of lanthanum and its ions in the region of the giant resonance. Z Phys D Atoms Mol Clust 14(3):215–217
2.49. Amusia MYa, Ivanov VK, Kupchenko VA (1989) The photoionization of atomic Eu in the vicinity of its giant resonance. Z Phys D Atoms Mol Clust 14(3):219–221
2.50. Amusia MYa, Chernysheva LV, Ivanov VK (2000) On the photoabsorption of atomic Eu, Eu^+ and Eu^{++} in the vicinity of 4d threshold radiation. Phys Chem 59:137–143
2.51. Becker U, Kerkhoff HG, Lindle DW, Kobrin PH, Ferret TA, Truesdale CM, Shirley DA (1986) Orbital-collapse effects in photoemission from atomic Eu. Phys Rev A 34:2858–2864
2.52. Richter M, Meyer M, Pahler M, Raven EV, Sonntag B (1989) Experimental study of atomic 4d giant resonances by photoabsorption and photoelectron spectroscopy: Sm, Eu, and Gd Phys Rev A 40:7007–7019
2.53. Amusia MYa, Sheftel SI, Chernysheva LV (1981) Nature of the giant resonance in photoionization cross section of Eu atom. J Techn Phys 51(11):2411 (in Russian)
2.54. Kojima TM, Oura M, Itoh Y, Koizumi T, Sano M, Sekioka T, Watanabe N, Yamaoka H, Awaya Y (1998) Photoion yield spectroscopy in the 4d photoionization of Eu^+. Phys B At Mol Opt Phys 31:1463–1468

2.55. Amusia MYa, Gribakin GF, Ivanov VK, Chernysheva LV (1990) Many-electron correlations in the negative ion photodetachment. J Phys B At Mol Opt Phys 23:385–391
2.56. Gribakin GF, Gribakina AA, Gultsev BV, Ivanov VK (1992) Correlational autodetachment of the low lying shape resonances in C^-, Si^- and Ge^- photodetachment. J Phys B At Mol Opt Phys 25:1757–1772
2.57. Lapkin CV, Ivanov VK (2004). In: Seventh International Workshop on Nondestructive Testing and Computer Simulations in Science and Engineering (NDTCS-2003, 9–15 June 2003, St. Petersburg, Russia). Ed. A.I. Melker/54, pp 42–46
2.58. Gibson ND, Walter CW, Zatsarinny O, Gorczyca T W, Akerman GD, Bozek JD, Martins M, McLaughlin BM, Berrah N (2003) K-shell photodetachment from C^-: Experiment and theory. Phys Rev A 67:030703(R)-1–030703(R)-4
2.59. Balling P, Kristensen P, Stapelfeldt H, Andersen T, Haugen HK (1993) Window resonance in photodetachment of the negative silicon ion: strong interaction of the 3p continuum with the 3s to 3p shape resonance. J Phys B At Mol Opt Phys 26:3531–3539
2.60. Amusia MYa, Dolmatov VK, Ivanov VK (1983) Photoionization of atoms with half-filled shells. JETP 85(1):115–123 (in Russian)
2.61. Amusia MYa, Dolmatov VK, Ivanov VK, Shapiro SG (1983) Angular distribution of $3p$-photoelectrons in Cr and Mn. J Phys B At Mol Phys 16(24):L753–L756
2.62. Amusia MYa, Chernysheva LV (2007) On the angular distribution and spin polarization of the photoelectrons from semi-filled shell atoms. http://arxiv.org/abs/physics/0701040
2.63. Ivanov VK, Krukovskaya LP, Kashenock GY (1996) Near-threshold shape resonance in Cr^- outer shell photodetachment. J Phys B At Mol Opt Phys 29(9):L313–L320
2.64. Cherepkov NA, Chernysheva LV (1977) Photoionization cross section of Cl atom in RPAE. Bull Russ Acad Sci Phys 41(12):2518–2528 (in Russian)
2.65. Samson JAR, Shefer Y, Angel GC (1986) A critical test of many-body theory: the photoionization cross section of Cl as an example of an open-shell atom. Phys Rev Lett 56:2020–2024
2.66. Amusia MYa, Ivanov VK, Chernysheva LV (1981) Peculiarities of the photoionization cross section of the Mn atom. J Phys B At Mol Phys 14:L19–L23
2.67. Amusia MYa, Dolmatov VK, Mansurov MM (1990) A new feature of 3p to 3d transitions in Mn atom. J Phys B At Mol Opt Phys 23:L491–L494
2.68. Amusia MYa, Dolmatov VK, Ivanov VK (1986) Non-dipole part of angular distribution of photoelectrons and entrainment current in atomic vapor of Mn. J Techn Phys 56(1):8–15 (in Russian)
2.69. Bruhn R, Schmidt E, Schroder H, Sonntag B (1982) Phys Lett A 90:41–44
2.70. Kobrin PH, Becker U, Truesdale CM, Lindle DW, Kerkhoff HG, Shirley DA (1984) Photoelectron asymmetries and two-electron satellites near the $3p - 3d$ giant resonance region in atomic Mn. J Electron Spectrosc Relat Phenom 34:129–139
2.71. Dolmatov VK, Amusia MYa (1994) Resonant structure of the 3d-electrons angular distribution in a free Mn^+ ion. J Phys B At Mol Opt Phys 27:L281–L285
2.72. Amusia MY, Cherepkov NA, Chernysheva LV, Manson ST (2000) On the photoionization of the iodine atom and its ions. Phys Rev A 61:R207–R211
2.73. Kjeldsen H, Andersen P, Folkmann F, Knudsen H, Kristensen B, West JB, Andersen T (2000) Absolute photoionization cross sections of I^+ and I^{2+} in the $4d$ ionization region. Phys Rev A 62:020702
2.74. Amusia MY, Gribakin GF, Ivanov VK, Chernysheva LV (1986) Photodetachment from outer subshells of negative iodine ion. Bull Russ Acad Sci Phys 50(7):1274–1278 (in Russian)
2.75. Kjeldsen H (2000) Measurements of absolute cross sections for photoionisation of ions. http://physics.nist.gov
2.76. Amusia MYa, Baltenkov AS, Chernysheva LV, Felfli Z, Msezane AZ (2005) Near-threshold behavior of angular anisotropy parameters in negative ions photo-detachment. Phys Rev A 72:032727
2.77. Amusia MYa, Baltenkov AS, Chernysheva LV (2008) Giant resonances of endohedral atoms. JETP Lett 87(4):230–233

2.78. Amusia MYa, Baltenkov AS, Chernysheva LV (2008) On the photoionization of the outer electrons in noble gas endohedral atoms. JETP 134(2):221–230
2.79. Amusia MYa, Baltenkov AS, Chernysheva LV (2008) Photoionization of subvalent electrons in noble gas endohedrals: interference of three resonances. J Phys B At Mol Opt Phys 41:165201
2.80. Amusia MYa, Baltenkov AS, Chernysheva LV, Felfli Z, Msezane AZ (2005) Dramatic distortion of 4*d* giant resonance by the fullerenes C_{60} shell. J Phys B At Mol Opt Phys 38:L169–L173
2.81. Amusia MYa, Baltenkov AS, Chernysheva LV, Felfli Z, Msezane AZ (2006) Modification of the Xe 4*d* giant resonance by the C_{60} shell in molecular Xe@C_{60}. JETP 129(1):63–70
2.82. Amusia MYa, Baltenkov AS, Chernysheva LV (2008) Photoionization of 3*d* electrons of Xe, Cs and Ba endohedral atoms: comparative analyses. Central Eur J Phys 6(1):14–25
2.83. Kilcoyne ALD, Aguilar A, Müller A, Schippers S, Cisneros C, Alna'Washi G, Aryal NB, Baral KK, Esteves DA, Thomas CM, and Phaneuf RA (2010) Confinement resonances in photoionization of Xe@C_{60}^{+}. Phys Rev Lett 105: 213001(4)
2.84. Amusia MYa, Baltenkov AS, Chernysheva LV (2007) Photoionization of Xe 3*d* electrons in molecule Xe@C_{60}: interplay of intra-doublet and confinement resonances. Phys Rev A 75:043201
2.85. Amusia MYa, Chernysheva LV, Ivanov VK, Kupchenko VA (1989) Photoionization of lanthanum and its ions in the region of the giant resonance. Z Phys D Atoms Mol Clust 14(3):215–217
2.86. Amusia MYa, Baltenkov AS, Chernysheva LV (2008) Distortion and preservation of giant resonances in endohedral atoms A@C_{60} JETP Lett 89(6):322–326
2.87. Amusia MYa, Liverz EZ, Chernysheva LV (2009) Photoionization of atoms stuffed inside a two-shell fullerene, (with L. V. Chernysheva and E. Z. Liverts). Phys Rev A 80:032503-1–032503-12
2.88. Amusia MYa, Liverz EZ, Chernysheva LV (2009) Photoionization of onion-type atoms (with L.V. Chernysheva, E.Z. Liverts). Pis'ma v ZhETF 90(5):393–397 (JETP Lett 90:350–354)
2.89. Houlgate RG, West JB, Codling K, Marr GV (1976) The angular distribution of the 3p electrons and the partial cross section of the 3s electrons of argon from threshold to 70 eV. J Electron Spectrosc Relat Phenom 9:205–209

Part II
Electron Scattering

Chapter 3
Main Points of the Electron Scattering Theory

3.1 Most Important on Electron–Atom Scattering

Electron–atom scattering is a process that takes place at natural conditions and in laboratory. The data of this process are required in other domains of physics and technology. They also serve as source of information on atomic structure and properties and on efficiency of different theoretical approaches that are used to describe the process of electron–atom scattering.

Even the scattering upon the simplest, hydrogen, atom presents considerable difficulties since is in essence a three-body problem. Its understanding requires a solution of a three-body problem—a description of two electrons moving in the Coulomb field of a nucleus. This problem has only a numerical solution, contrary to the photoionization of hydrogen, the cross section of which can be calculated pure analytically. This is why the e + H scattering is the most often considered case in electron–atom scattering studies.

For more complex atoms, the situation becomes much trickier. The next by the frequency of investigation object is He. There exist data on scattering upon more complicated atoms also.

Scattering can be *elastic*, *inelastic*, and *super-elastic*. In elastic scattering, the projectile's energy before and after scattering is precisely the same. In inelastic scattering, the energy, lost by the projectile, can be either emitted as a photon or transferred to the target atom, leading to its excitation or ionization. Ionization is a process in which one or several electrons can leave the target atom or ion while the residual ion is left in its lowest possible energy state. Ionization with excitation is a process, in which one or several electrons are eliminated from the target object and the latter is left in an excited state, on one of the discrete excited levels of the residual ion.

Super-elastic scattering takes place only on excited targets. In this process the projectile, whose energy is increased by value of the excitation energy, takes the excitation energy away. In photoionization, simultaneous ionization with excitation or ionization with excitation of two and more electrons can happen only due to

M. Amusia et al., *Handbook of Theoretical Atomic Physics*,
DOI 10.1007/978-3-642-24752-1_3, © Springer-Verlag Berlin Heidelberg 2012

inter-electron interaction. In electron (or any other charged particle) scattering, all these processes can proceed even without taking into account of the interaction between atomic electrons, only due to interaction of the projectile with all atomic electrons simultaneously.

All inelastic processes, except photon emission, start from some minimal, so-called *threshold energy I*.

The electron scattering can be treated in one-electron approximation and with accounting for the interaction between atomic electrons. In spite of limited accuracy of the one-electron approximation, we will perform and present results of calculations in its frame. In many cases, they can serve as a good initial step and mainly for orientation. As one-electron the Hartree–Fock approximation (HF) will be used, which is the best method compatible with the idea of independent motion of all atomic electrons in a common, so-called *self-consistent*, field. We will describe main features of HF in the next section.

However, in almost all processes considered in this book, the role of inter-electron interaction is essential, and in many instances is decisively important. The account of inter-electron interaction that leads to *correlations* in the atomic electron motion essentially modifies the electron–atom (or ion) scattering process. To take into account the inter-electron interaction, or as it is often called, the *multielectron correlations*, we will use in this book the random phase approximation with exchange (RPAE) or the many-body perturbation theory (MBPT). In essence, RPAE takes into account nonperturbatively, as a big correction, the dynamical variation of the self-consistent field acting upon each electron [AM]. In a number of cases, however, MBPT can be used to consider atomic processes, because the inter-electron interaction quite often can be treated as a relatively small perturbation.

Even considering the elastic scattering, the projectile–target interaction cannot be reduced to a potential. In fact, this interaction is nonlocal, energy-dependent, and only with considerable simplification can be presented as complex *optical potential* that depends upon the projectile's coordinate r and its energy $E = p^2/2$ [3.1]:

$$U(r, \vec{\sigma}, E) = V(r, \vec{\sigma}, E) + iW(r, \vec{\sigma}, E), \tag{3.1}$$

where $V(r, \vec{\sigma}, E)$ and $W(r, \vec{\sigma}, E)$ are real functions, the latter of which is primarily responsible for the absorption of the projectile wave $\psi_E(\vec{r}, \vec{\sigma})$. The equation for $\psi_E(\vec{r}, \vec{\sigma})$ looks in the following way:

$$\left[-\frac{\Delta}{2} - \frac{Z}{r} + V(r, \vec{\sigma}, E) + iW(r, \vec{\sigma}, E)\right]\psi_E(\vec{r}, \vec{\sigma}) = E\psi_E(\vec{r}, \vec{\sigma}). \tag{3.2}$$

Here Z is the nucleus charge.

This equation can be presented in integral form [3.2]:

$$\psi_E(\vec{r}) = \varphi_E(\vec{r}) + \int G_E^{(0)}(\vec{r}, \vec{r}')U(r, \vec{\sigma}, E)\psi_E(\vec{r}')\mathrm{d}\vec{r}', \tag{3.3}$$

where $\varphi_E(\vec{r})$ is the wave function of free movement of the projectile with energy E; $G_E^{(0)}(\vec{r},\vec{r}')$ is the Green's function of the Coulomb potential with charge Z that is a solution of the equation [3.2]

$$\left[-\frac{\Delta}{2}-\frac{Z}{r}-E\right]G_E^{(0)}(\vec{r},\vec{r'})=-\delta(\vec{r}-\vec{r}'). \tag{3.4}$$

If an extra potential $\delta U(r)$ acts upon the projectile, one has instead of (3.3) an integral equation [LL]

$$\psi_E(\vec{r})=\varphi_E(\vec{r})+\int G_E^{(U)}(\vec{r},\vec{r}')\delta U(r,\vec{\sigma},E)\psi_E(\vec{r}')\mathrm{d}\vec{r}', \tag{3.5}$$

where $G_E^{(U)}(\vec{r},\vec{r}')$ is a solution of (3.4) with $U(r,\vec{\sigma},E)$ added to $-Z/r$.

The expression (3.1) is considerably simplified in two limiting cases: that of very high, $E=p^2/2\gg I$, and very low, $0<E\ll I$, where I is the target's ionization potential, energies E. In both cases, one can put $W(r,\vec{\sigma},E)=0$. As to $V(r,\vec{\sigma},E)$, it becomes energy-independent and at $E\to\infty$ is equal to [3.3]

$$V(r,\vec{\sigma},E)|_{E\to\infty}=-\frac{Z}{r}+\int\frac{\rho(r')}{|\vec{r}-\vec{r}'|}\mathrm{d}\vec{r}', \tag{3.6}$$

where Z is the nuclear charge and $\rho(r)$ is the atomic electron density.

At $E\ll I$ the potential $V(r,\vec{\sigma},E)$ is presented at large r as

$$V(r,\vec{\sigma},E)=-\frac{\alpha_\mathrm{d}}{2r^4}, \tag{3.7}$$

where α_d is the dipole static polarizability of the target.

The scattering cross-section is expressed via the phase shifts $\delta_l(E)$ of the electronic partial waves that correspond to a given angular momentum l. Due to scattering on a short range potential, the radial part of the wave function $\psi_E(\vec{r},\vec{\sigma})$ [see (1.57)] can be presented at $r\to\infty$ as

$$P_{El}(r)|_{r\to\infty}\to\frac{1}{\sqrt{\pi k}}\sin\left[pr-l\pi/2+\delta_l(E)\right], \tag{3.8a}$$

The term "short range" means here decrease of the potential with r growth faster than $1/r^3$ [LL]. If the potential has a Coulomb part z/r then instead of (3.8a) one has

$$P_{El}(r)|_{r\to\infty}\to\frac{1}{\sqrt{\pi k}}\sin\left[pr+\frac{z}{p}\ln 2pr-\frac{l\pi}{2}+\delta_l^z(E)\right]. \tag{3.8b}$$

where $\delta_l^z(E) = \delta_l(E) + \arg\Gamma(l+1-iz/p)$, $\delta_l(E)$ originates from short range part of the potential $U(r, E)$ and $\Gamma(l+1-iz/p)$ is the Gamma-function of a complex argument $l+1-iz/p$.

Expressions (3.8a) and (3.8b) substitute the plane wave asymptotic

$$P_{El}^{(0)}(r)|_{r\to\infty} \to \frac{1}{\sqrt{\pi k}} \sin\left(pr - \frac{l\pi}{2}\right). \tag{3.9}$$

The phase shift $\delta_l(E)$, just as $\delta_l^z(E)$, is determined from either the asymptotic of the wave function [see (3.8a)] or from the following relation:

$$e^{i\delta_l(E)} \sin\delta_l(E) = \langle j_l(pr)|U(r, E)|P_{El}(r)\rangle, \tag{3.10}$$

where the spherical Bessel function $j_l\{pr)$ describes the radial part of the wave function of a free electron.

Of interest is a formula that gives the additional phase shift $\Delta\delta_l(E)$ if an additional potential $\delta U(r, E)$ acts upon the incoming particle [LL]:

$$e^{i\Delta\delta_l(E)} \sin\Delta\delta_l(E) = \langle P_{El}^{(U)}(r)|\delta U(r, E)|P_{El}^{(U+\delta U)}(r)\rangle, \tag{3.11}$$

where $P_{El}^{(U)}(r)$ and $P_{El}^{(U+\delta U)}(r)$ are the radial parts of the incoming particle wave functions calculated in the potentials $U(r, E)$ and $\delta U(r, E)$, respectively.

In general, the phases $\delta_l(E)$ are complex numbers

$$\delta_l(E) = \eta_l(E) + i\mu_l(E). \tag{3.12}$$

The differential in angle θ elastic scattering cross-section $d\sigma_E^{el}(\theta)/d\Omega$ is expressed via the phase shifts $\delta_l(E)$ using the following formula [LL]:

$$\frac{d\sigma^{el}(E)}{d\Omega} = \sum_{l,l'=0}^{\infty} \frac{1}{E}(2l+1)(2l'+1)\left(e^{2i\eta_l(E)-2\mu_l(E)} - 1\right)\left(e^{-2i\eta_{l'}(E)-2\mu_{l'}(E)} - 1\right)$$
$$\times P_l(\cos\theta) P_{l'}(\cos\theta). \tag{3.13}$$

For the total elastic scattering cross-sections one obtains after integration over $d\Omega$

$$\sigma^{el}(E) \equiv \sum_{l=0}^{\infty} \sigma_l^{el}(E) = \frac{2\pi}{E} \sum_{l=0}^{\infty} (2l+1) \sin^2\eta_l(E) e^{-2\mu_l(E)}. \tag{3.14}$$

Similarly, one can obtain expressions for inelastic and total scattering cross-sections [LL]:

$$\sigma^{in}(E) \equiv \sum_{l=0}^{\infty} \sigma_l^{in}(E) = \frac{2\pi}{E} \sum_{l=0}^{\infty} (2l+1)(1 - e^{-4\mu_l(E)}). \tag{3.15}$$

$$\sigma^{tot}(E) \equiv \sum_{l=0}^{\infty} \sigma_l^{tot}(E) = \frac{2\pi}{E} \sum_{l=0}^{\infty} (2l+1)[1 - \cos\eta_l(E) e^{-2\mu_l(E)}]. \tag{3.16}$$

If the phases $\delta_l(E)$ are real that happens when the inelastic scattering channels are closed, the elastic scattering cross-section is given by

$$\sigma^{\mathrm{el}}(E) = \frac{2\pi}{E}\sum_{l=0}^{\infty}(2l+1)\sin^2\delta_l(E). \tag{3.17}$$

Note that there exists an essential difference in scattering on objects with and without Coulomb asymptotic potential tale z/r. Namely, in the presence of such a tail the cross-sections (3.16) and (3.17) diverge.

Very often the *first Born* approximation is used to describe the elastic scattering. It takes into account the first order in $U(r, E)$ corrections to the free projectile's motion. The corresponding phase shifts $\delta_l^{(\mathrm{B})}(E)$ are obtained from (3.10) and are given by

$$\delta_l^{(\mathrm{B})}(E) = \langle j_l(pr)|U(r, E)|j_l(pr)\rangle. \tag{3.18}$$

First-order corrections to the phases, $\Delta\delta_l(E)$ due to a small additional potential $\delta U(r, E)$ are obtained from (3.11) and given by the relation [LL]

$$\Delta\delta_l(E) = \left\langle P_{El}^{(U)}(r)|\delta U(r, E)|P_{El}^{(U)}(r)\right\rangle. \tag{3.19}$$

Since at $E\to\infty$ one can neglect the projectile–atom interaction, it is natural to determine the phase in such a way that $\delta_l(E)|_{E\to\infty}\to 0$. Then there are two possibilities for the expression of $\delta_l(0)$. If there is no exchange between incoming particles and atomic electrons, i.e., they are not identical, one has [LL]

$$\delta_l(0) = n_l\pi, \tag{3.20}$$

where n_l is the number of vacant discrete levels with the angular momentum l in the potential $U(r, E)$ of the target.

If the incoming particle is an electron and exchange between the projectile and target electrons is taken into account, one has instead of (3.20) an essentially different relation, namely [3.4]

$$\delta_l(0) = (n_l + q_l)\pi, \tag{3.21}$$

where q_l is the number of occupied levels with momentum l in the target.

At $E\to 0$ for the phase shifts the following expansion [LL, 3.3] is valid:

$$\delta_l(E) - \delta_l(0) \approx a_l p^{2l+1}(1 + b_l p + \ldots). \tag{3.22}$$

Thus, we see that the elastic scattering cross-section at $E\to 0$ is a constant. However, the scattering cross-section due to quantum mechanical nature of the process can be and usually is essentially different from the geometrical value $4\pi r_{\mathrm{A}}^2$. It can also change very rapidly with small variation of p. As an example here serves

the Ramsauer minima [3.4, 3.5, LL], which appears in all but helium noble gas atoms scattering cross-sections at rather small energies. There the s-phase increases with growth of E from $E = 0$, but very soon reaches a maximum, then starting to decrease. It achieves a second zero value at $E > 0$, where the p-phase is still very small. The Ramsauer-type variation means that the real expansion parameter in (3.22) is not simply $r_A p < 1$, but a quantity that strongly depends upon the size and shape of $U(r, E)$.

The calculation of inelastic scattering cross-section is in general a rather complex problem, that, however, simplifies drastically at high energies $E \gg I$, or, more precise, at $p \gg \sqrt{I}$. In this case, the first Born approximation is valid and the projectile–target interaction can be considerably simplified. Indeed, at high E the total wave function of the system "projectile + atom" can be presented in the initial i(final f) state as a product of the projectile's plane wave and the target's wave function $\psi^{\mathrm{At}}_{i(f)}(x_1, \ldots, x_N)$

$$\Psi^{i(f)}_E(x, x_1, \ldots, x_N) = \mathrm{e}^{i\vec{p}_{i(f)}\vec{r}}\psi^{\mathrm{At}}_{i(f)}(x_1, \ldots, x_N). \tag{3.23}$$

The transition amplitude $M_{i\to f}$ is given by the expression

$$M_{i\to f}(q) = \left\langle \mathrm{e}^{i\vec{p}_i\vec{r}}\psi^{\mathrm{At}}_i(x_1, \ldots, x_N) \left| \sum_{j=1}^{N} \frac{1}{|\vec{r}_j - \vec{r}|} \right| \mathrm{e}^{-i\vec{p}_f\vec{r}}\psi^{\mathrm{At}}_f(x_1, \ldots, x_N) \right\rangle. \tag{3.24}$$

After integrating over r, the following is obtained [LL]:

$$\begin{aligned} M_{i\to f}(q) &= \frac{4\pi}{q^2}\sum_{j=1}^{N}\left\langle \psi^{\mathrm{At}}_i(x_1, \ldots x_j \ldots x_N)|\mathrm{e}^{i\vec{q}\vec{r}_j}|\psi^{\mathrm{At}}_f(x_1, \ldots, x_j \ldots x_N)\right\rangle \\ &= \frac{4\pi}{q^2}\sum_{j=1}^{N}\int \psi^{*\mathrm{At}}_i(x_1, \ldots, x_j \ldots x_N)\mathrm{e}^{i\vec{q}\vec{r}_j}\psi^{\mathrm{At}}_i(x_1, \ldots, x_j \ldots x_N) \\ &\times \mathrm{d}x_1 \ldots \mathrm{d}x_j \ldots \mathrm{d}x_N, \end{aligned} \tag{3.25}$$

where $\vec{q} = \vec{p}_f - \vec{p}_i$.

Differential in scattered electron angle Ω inelastic scattering cross-section is expressed via $M_{i\to f}(q)$ for excitation of a discrete level if or continuous energy ik in the following way, respectively:

$$\begin{aligned} \frac{\mathrm{d}\sigma_{if}(q)}{\mathrm{d}\Omega} &= \frac{p_f}{p_i}|M_{i\to f}(q)|^2 = \frac{4p_f}{q^2 p_i \omega_{if}}F_{i\to f}(q, \omega_{if}), \\ \frac{\mathrm{d}^2\sigma_{i\vec{k}}(q)}{\mathrm{d}\varepsilon\mathrm{d}\Omega\mathrm{d}\Omega_{\vec{k}}} &= \frac{p_f}{p_i}|M_{i\to\vec{k}}(q)|^2 = \frac{4p_f}{q^2 p_i \omega_{i\vec{k}}}F_{i\to\vec{k}}(q, \omega_{i\vec{k}}), \end{aligned} \tag{3.26}$$

here $\vec{k}$ is the knocked out electron linear moment and $\varepsilon = k^2/2$.

The following expression is called generalized oscillator strength (GOS):

$$F_{i\to f}(q,\omega_{if}) = \frac{\omega_{if}}{8\pi^2 q^2}|M_{i\to f}(q)|^2, \tag{3.27}$$

where $\omega_{fi} \equiv E_f - E_i$ is $i \to f$ transition energy. At $q \to 0$ one has $F_{i\to f}(q,\omega_{if}) \to F_{i\to f}$, with $F_{i\to f}$ given by (1.6). If the state f belongs to the continuous spectrum, the quantity $F_{i\to f}(q)$ is called the GOS density.

GOSes satisfy the sum rule, similar to that for $f_{i\to f}$, i.e., to the expression (1.7):

$$\Sigma \int_f F_{i\to f}(q,\omega_{if}) = N. \tag{3.28}$$

Note that summation over f in (3.28) implies also integration over ε.

Very often to describe not too fast electron–atom scattering, the *distorted wave Born approximation* (DWBA) is used. In this approximation the initial and final projectile's states are presented not by plane waves, but instead by solutions of (3.2) with $V(r,\sigma,E)$ being generally speaking different for initial and final states, $V_i(r,\sigma,E) \neq V_f(r,\sigma,E)$. Corresponding wave functions are substituted into (3.23) and (3.24) then via (3.26), determining the inelastic scattering cross-section in DWBA.

If the target atom A is in an excited state, A*, along with elastic and inelastic scattering, the *super-elastic scattering* can take place, in which the incoming particle can gain energy accepting the excitation energy of the target. The specific feature of super-elastic processes is that its cross-section $\sigma^{\sup}(E)$ diverges with decrease of $p = \sqrt{2E} \to 0$

$$\sigma^{\sup}(E)|_{p\to 0} = \frac{a}{p}. \tag{3.29}$$

3.2 Elastic Scattering in One-Electron Approximation

In one-electron approximation, the electron–atom elastic scattering cross-section is described using a relatively simple potential that is independent upon energy E and does not have an imaginary part, so that instead of (3.1) one has a potential $V(r)$. The dependence upon incoming electron spin s appears as a relativistic correction, being of the order of v/c to $V(r)$, where v is the incoming electron velocity and c is the speed of light. In the spherically symmetric potential of the atom, the vector of the angular momentum l characterizes electron states. Therefore, *spin–orbit* potential is presented as (see e.g., [IS]) in the following form:

$$V_{ls}(r) = \frac{1}{c}\frac{\partial}{\partial r}V(r)(\vec{l}\vec{s}). \tag{3.30}$$

Thus, the incoming electron wave function one-electron approximation is determined by the following equation:

$$\left[-\frac{\Delta}{2}-\frac{Z}{r}+V(r)+\frac{1}{c}\frac{\partial}{\partial r}V(r)(\vec{l}\vec{s})\right]\varphi_E(\vec{r},\vec{\sigma})=E\varphi_E(\vec{r},\vec{\sigma}). \tag{3.31}$$

In our calculations as one-electron we use Hartree–Fock (HF) approximation, which treats on equal grounds the incoming and atomic electrons. This approximation was described above, in Sect. 1.2. The incoming electron wave function $\varphi_E(x)$ is a solution of

$$-\frac{\Delta}{2}\varphi_E(x)-\frac{Z}{r}\varphi_E(x)+\sum_{k=1}^{N}\int \mathrm{d}x'\varphi_k^*(x')\frac{1}{|\vec{r}'-\vec{r}|}$$
$$\times\left[\varphi_k(x')\varphi_E(x)-\varphi_E(x')\varphi_k(x)\right]=E\varphi_E(x). \tag{3.32}$$

The wave functions of occupied states $\varphi_k(x)(1\le k\le N; x\equiv\vec{r},\vec{s})$ are determined by an equation similar to (3.32):

$$-\frac{\Delta}{2}\varphi_j(x)-\frac{Z}{r}\varphi_j(x)+\sum_{k=1}^{N}\int \mathrm{d}x'\varphi_k^*(x')\frac{1}{|\vec{r}'-\vec{r}|}$$
$$\times\left[\varphi_k(x')\varphi_j(x)-\varphi_j(x')\varphi_k(x)\right]=\varepsilon_j\varphi_j(x), \tag{3.33}$$

here j belongs to the states occupied in the target atom.

To obtain physical results, namely, phase shifts and then cross-sections, analytical and then numerical calculations have to be performed. As a first step, the one-electron wavefunctions $\varphi_k(x)\equiv\varphi_{\varepsilon(n)lm\sigma}(\vec{r},s)$—solutions of HF equations (3.32) and (3.33)—must be presented as a product of radial $R_{\varepsilon(n)l}(r)\equiv r^{-1}P_{\varepsilon(n)l}(r)$, angular $Y_{lm}(\vartheta,\varphi)$ and spin functions χ_σ:

$$\varphi_{\varepsilon(n)lm\sigma}(\vec{r},s)=r^{-1}P_{\varepsilon(n)l}(r)Y_{lm}(\vartheta,\varphi)\chi_\sigma, \tag{3.34}$$

where $Y_{lm}(\vartheta,\varphi)$ is the so-called spherical function, χ_σ is the spin function, $\varepsilon(n)$ is the one-electron energy (principal quantum number), l is the angular momentum quantum number, m is its projection upon a selected axis, σ is the electron spin projection, ϑ and φ are polar and azimuthal angles of the electron coordinate $\boldsymbol{r}$. Integration over polar angle and summation over spin projection can be performed analytically, while integration over r-numerically.

3.3 Polarization Interaction

Polarization interaction between the projectile electron and the target atom is a result of deformation of the target during the collision process. The incoming electron induces the displacement of charges inside the target atom, which results

in creation of a dipole moment. The latter in its turn acts upon the polarizing electron. Polarization interaction can be described classically. This leads to a potential that far from the target can be presented as (3.7), $\sim 1/r^4$. At small r, $r < r_A$ (r_A being the atomic radius) the $1/r^4$ singularity in (3.7) does not exist since $V(r, \vec{\sigma}, E) \to \text{Const}$ at $r \to 0$, so that at any r the potential $V(r, \vec{\sigma}, E)$ can be presented semi-phenomenologically as

$$V(r, \vec{\sigma}, E) = -\frac{\alpha_d}{2(r^2 + b^2)^2}, \tag{3.35}$$

with $b^4 = -\alpha_d/2V(0)$. The static dipole polarizability α_d of the target atom can be either calculated or taken from experiment. The parameter b can be chosen in such a way as to give good description of the low-energy scattering data. However, in such an approach one misses the energy dependence of the potential as well as the existence of its imaginary part. This is why in a number of papers, starting from old calculations in [3.6, 3.7] many-body theory approaches were used in calculations of the polarization interaction. The following diagrams describe the latter in the lowest order of perturbation theory:

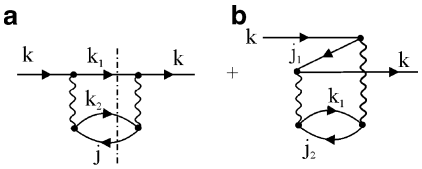

(3.36)

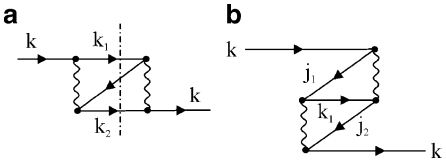

(3.37)

These diagrams must be supplemented by higher order corrections in inter-electron interaction. As those, we include the interaction between atomic excited electron and the vacancy j. One can see that only the diagram (3.36a) determines the $1/r^4$ behavior of the polarization interaction. All others affect the short-range part of the polarization interaction. But it appeared that the phase shift (3.10) is determined by all four terms. The imaginary part of the phase shift comes from diagrams (3.36a) and (3.37a), the intermediate states of which, denoted by the vertically oriented dash–dotted lines, can became a real physical states. Note that the intermediate states of diagrams (3.36b) and (3.37b) can be only virtual.

It appeared that in a broad region of incoming electron energies $E = p_k^2/2$ (p_k is the linear momentum of the state k), the interaction between the incoming (outgoing) and atomic electrons is sufficient to take into account in the second order of perturbation theory [3.7, 3.8]. As it was mentioned above, the interaction between

atomic electrons has to be taken in higher orders, including some summation of infinite subsequences of diagrams. As a result, one obtains the polarization interaction matrix that is presented in the following form $\langle k_i|\hat{\Sigma}(E)|k_f\rangle$ [3.8]. In the second order, the respective analytical expressions corresponding to diagrams of (3.36) and (3.37) are presented in the following way:

$$\left\langle E_i\ell \left\| \hat{\Sigma}^l(E) \right\| E_f\ell \right\rangle = \frac{1}{(2l+1)} \sum_{\substack{j \le F, L \\ \varepsilon_1\ell_1, \varepsilon_2 l_2 > F}} \times \int_0^\infty \frac{\left\langle E_i\ell, \varepsilon_j l_j \,\|V_L\| \, \varepsilon_1\ell_1, \varepsilon_2\ell_2 \right\rangle \left\langle \varepsilon_1\ell_1, \varepsilon_2\ell_2 \,\|U_L\| \, E_f\ell, \varepsilon_j l_j \right\rangle}{(2L+1)(E - \varepsilon_1 - \varepsilon_2 + \varepsilon_j + i\delta)} \mathrm{d}\varepsilon_1 \mathrm{d}\varepsilon_2, \quad (3.38)$$

$$\left\langle E_i\ell \left\| \hat{\Sigma}^l(E) \right\| E_f\ell \right\rangle = \frac{1}{(2l+1)} \sum_{\substack{j_1, j_2 \le F, L \\ \varepsilon_2 l_2 > F}} \times \int_0^\infty \frac{\left\langle E_i\ell, \varepsilon_{j_2} l_{j_2} \,\|V_L\| \, \varepsilon_{j_1} l_{j_1}, \varepsilon_2\ell_2 \right\rangle \left\langle \varepsilon_{j_1} l_{j_1} \varepsilon_2\ell_2 \,\|U_L\| \, E_f\ell, \varepsilon_{j_2} l_{j_2} \right\rangle}{(2L+1)(E - \varepsilon_{j_1} + \varepsilon_2 - \varepsilon_{j_2})} \mathrm{d}\varepsilon_2, \quad (3.39)$$

here $E_{i(f)}l$ denotes the energy and angular momentum of the initial (final) incoming electron state, $\varepsilon_1\ell_1, \varepsilon_2\ell_2$ are intermediate state electrons energy and angular momentum, $\varepsilon_{j_1} l_{j_1}, \varepsilon_{j_2} l_{j_2}$ are the respective values for vacancies; the electron and vacancies wave functions are determined in HF approximation, by solving equations (3.32) and (3.33), respectively. The inclusion of higher order RPAE corrections into (3.38) and (3.39) is discussed at length in [AC]. The reduced Coulomb matrix elements that are denoted by doubled vertical lines are defined in [AC].

The polarization interaction is nonlocal, energy-dependent, and is a complex function

$$\Sigma(\vec{r}, \vec{r}', E) \equiv \mathrm{Re}\Sigma(\vec{r}, \vec{r}', E) + i\,\mathrm{Im}\Sigma(\vec{r}, \vec{r}', E). \quad (3.40)$$

The imaginary part of $\Sigma(\vec{r}, \vec{r}', E)$ is determined by the $i\delta$ term in (3.38):

$$\mathrm{Im}\left\langle E_i\ell \left\| \hat{\Sigma}^l(E) \right\| E_f\ell \right\rangle = \frac{\pi}{(2l+1)} \times \sum_{\substack{j \le F, L \\ \varepsilon_1\ell_1, \varepsilon_2 l_2 > F}} \times \frac{1}{(2L+1)} \int_0^\infty \left\langle E_i\ell, \varepsilon_j l_j \,\|V_L\| \, \varepsilon_1\ell_1, \tilde{\varepsilon}_2\ell_2 \right\rangle \left\langle \varepsilon_1\ell_1, \tilde{\varepsilon}_2\ell_2 \,\|U_L\| \, E_f\ell, \varepsilon_j l_j \right\rangle \mathrm{d}\varepsilon_1, \quad (3.41)$$

where $\tilde{\varepsilon}_2 = E - \varepsilon_1 + \varepsilon_j$.

The expressions (3.38) and (3.39) determine the polarization interaction in what was called simplified RPAE or SRPAE [3.9–3.11].

3.4 Dyson Equation

Dyson equation determines the precise one-electron wave function. It includes the polarization interaction, not specifying its form. Since the polarization interaction is additional to the HF, the Dyson equation for electron–atom scattering is presented in the following way:

$$-\frac{\Delta}{2}\psi_E(x) - \frac{Z}{r}\psi_E(x) + \sum_{k=1}^{N}\int \mathrm{d}x'\psi_k^*(x')\frac{1}{|\vec{r}' - \vec{r}|}[\psi_k(x')\psi_E(x) - \psi_E(x')\psi_k(x)] + \int \mathrm{d}x'\Sigma(x, x', E)\psi_E(x') = E\psi_E(x). \tag{3.42}$$

Due to E-dependence, the wave function $\psi_E(x)$ has an unusual normalization

$$\int \mathrm{d}x\,\psi_k^*(x)\psi_{E'}(x) = Z(E)\delta(E - E'), \tag{3.43}$$

where $Z(E)$, that is called renormalization constant or spectroscopic factor, is determined by the relation [3.12]

$$Z(E) = \frac{1}{\left[1 - \partial\left\langle E|\hat{\Sigma}(E)|E\right\rangle\Big/\partial E\right]} < 1. \tag{3.44}$$

In real numerical calculations, however, the deviation of $Z(E)$ from 1 is neglected and $\psi_k(x)$ for $k \le F$ is substituted by HF wave function $\varphi_k(x)$.

The (3.42) is convenient to solve in integral form and in energy representation, where for partial wave l it looks like [3.8]:

$$\left\langle E\ell|\hat{\tilde{\Sigma}}^l(E_1)|E'\ell\right\rangle = \left\langle E\ell|\hat{\Sigma}^l(E_1)|E'\ell\right\rangle + \sum_{E''}\left\langle E\ell|\hat{\Sigma}^l(E_1)|E''\ell\right\rangle \times \frac{1}{E_1 - E'' + i\delta}\left\langle E''\ell|\hat{\tilde{\Sigma}}^l(E_1)|E'\ell\right\rangle. \tag{3.45}$$

where the sum over E'' includes also integration over continuous spectrum.

The additional scattering phase shift $\Delta\delta_l(E)$ due to polarization interaction $\hat{\Sigma}(E)$ is connected to the diagonal matrix element of (3.45) [3.8]:

$$\mathrm{e}^{i\Delta\delta_l(E)}\sin\Delta\delta_l(E) = \left\langle E\ell||\hat{\tilde{\Sigma}}^l(E)||E\ell\right\rangle. \tag{3.46}$$

If as $\left\langle E\ell|\hat{\Sigma}^l(E_1)|E''\ell\right\rangle$ in (3.45) the matrix elements (3.38) and (3.39) are used, the expression (3.46) then determines correction to scattering phases in the simplified

RPAE approximation (SRPAE). If the polarization potential is small, the correction to the phase is given instead of (3.46) by the following expression [3.10]:

$$\Delta\delta_l(E) = \left\langle E\ell||\hat{\Sigma}^l(E)||E\ell\right\rangle. \tag{3.47}$$

The methods described above are most convenient for closed shell atom. Just as in photoionization, the presence of an open shell adds a lot of complexity. There exists, however, a group of atoms, the consideration of which is almost as simple and coherent as that of closed shell atoms. We have in mind semi-filled shell atoms.

The idea of the approach used for their consideration in scattering processes is similar to that presented in Sect. 1.10 [3.13]. All electrons, including the incoming one, are presented as either "up" or "down" particles, denoted by arrows ↑ and ↓, respectively. To illustrate the difference with closed shell atoms let us consider the polarization interaction in the second order, which for "up" ("down") incoming electron is presented by four diagrams, similar to (3.36) and (3.37):

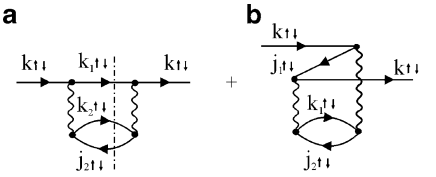

(3.48)

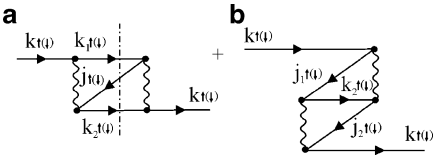

(3.49)

Note, that along the line of the incoming electron it is either in "up" or "down" states.

Matrix elements that give analytical formulas corresponding to (3.48) and (3.49), present the simplified spin-polarized RPAE expressions for the polarization interaction matrix elements $\langle E\ell \uparrow (\downarrow)|\hat{\Sigma}^l_{\uparrow(\downarrow)}(E_1)|E''\ell \uparrow (\downarrow)\rangle$. Thus, the (3.45) is separated into two independent ones that correspond to "up" and "down" electrons. Equation (3.46) gives two separate phase shifts, $\Delta\delta_{l_{\uparrow(\downarrow)}}(E)$, that after adding to the respective spin-polarized HF phase shifts permit to obtain with the help of (3.13)–(3.17) all electron–atom scattering cross-sections: cross-sections $\sigma^{\rm el}_{\uparrow(\downarrow)}(E)$, $\sigma^{\rm in}_{\uparrow(\downarrow)}(E)$, and $\sigma^{\rm tot}_{\uparrow(\downarrow)}(E)$, respectively.

3.5 Inelastic Scattering of Slow and Medium Energy Electrons

This process is usually treated in the so-called DWBA. The following diagram presents the respective amplitude:

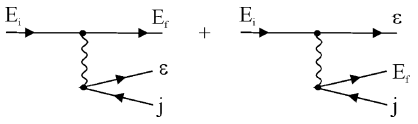

(3.50)

The states of the incoming and outgoing, as well as atomic electrons, are determined in HF approximation. The amplitude that corresponds to (3.50) is given by the following matrix element:

$$U_{i\to f\varepsilon j} \equiv \left\langle E_i\, j\,|U|\,E_f\,\varepsilon\right\rangle \equiv \left\langle E_i\, j\,|V|\,E_f\,\varepsilon\right\rangle - \left\langle E_i\, j\,|V|\,\varepsilon E_f\right\rangle. \tag{3.51}$$

The following relation gives the cross-section of inelastic scattering $\sigma_i^{(\mathrm{in})}$ in this approximation [LL]:

$$\sigma_i^{(\mathrm{in})} = \frac{2\pi}{E_i}\sum_{i\le F}\int_0^\infty |U_{i\to f\varepsilon j}|^2\delta(E_i - E_f - \varepsilon + \varepsilon_j)\mathrm{d}E_f\mathrm{d}\varepsilon. \tag{3.52}$$

The one-electron wave functions can be calculated with account of polarization interaction. It is relatively easy to include also the interaction between one of the final-state electrons and the vacancy j in RPAE frame. Much more complicated is to take into account simultaneously the interaction between both electrons and the vacancy.

The many-body diagram technique shows that the interaction between the initial and final state electrons also exists and in principle may become important. As an example let us present the following correction:

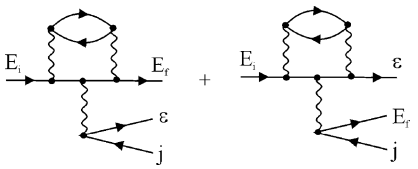

(3.53)

However, all such corrections are well out of the frame of our consideration in this book.

3.6 Inelastic Scattering of Fast Particles

The inelastic scattering cross-section of any incoming fast particle is expressed via the generalized oscillator strength given by (3.27). It follows from the GOS definition (3.27) that when $q \to 0$ the GOSes coincide with the optical oscillator strengths (1.6) or is simply proportional to the photoionization cross-section (1.5), depending upon the final state: whether it is a discrete excitation or belongs to the

continuous spectrum. The energy ω transferred to the atom in the collision process is equal to

$$\omega = \frac{p^2}{2M} - \frac{(\vec{p}-\vec{q})^2}{2M}. \tag{3.54}$$

where $E_\mathrm{p} = p^2/M$ is the incoming fast projectile energy. The energy ω enters GOSes directly via a factor in (3.27), and indirectly via the energy E_f of the state f.

In one-electron Hartree–Fock approximation (HF), (3.27) simplifies considerably, reducing to

$$f_{fi}(\omega, q) = \frac{2\omega}{q^2}\left|\int \varphi_f^*(\vec{r})\exp(i\vec{q}\vec{r})\varphi_i(\vec{r})\mathrm{d}\vec{r}\right|^2, \tag{3.55}$$

where $\varphi_{f,i}(\boldsymbol{r})$ are the HF wave functions. The transition operator $\hat{g}(\vec{q}) \equiv \exp(iqr)$ (q, r - vectors) can be presented as a sum of contributions with different multipolarities. Let us use the well-known expansion (see, e.g., [IS])

$$\exp(i\vec{q}\vec{r}) = \sum (2L+1) j_L(qr) P_L(\cos\theta), \tag{3.56}$$

here $j_L(qr)$ is the spherical Bessel function, $P_L(\cos\theta)$ is the Legandre polynomial, and θ is the angle between vectors $\boldsymbol{q}$ and $\boldsymbol{r}$. Separating the angular parts of the one-electron HF wave functions, using (3.56) and analytically performing integration over angles in matrix elements of (3.55), instead of $f_{fi}(\omega, q)$ partial one-electron GOSes $g^L_{nl,\varepsilon l'}(\omega, q)$ can be introduced, with l' within the following limits $|L-l| \le l' \le L+l$.

In the calculations presented in this book we retain the biggest ones, namely the dipole $L=1$, monopole $L=0$, quadrupole $L=2$, and octupole $L=3$ terms. Performing numerical integration of $\hat{g}_l(q)$ and a product of two HF wave functions, the GOSes amplitudes, which are matrix elements of $\hat{g}_l(q)$, are obtained.

The operator of the interaction between fast charged particle and atomic electrons can be presented in another than $\hat{g}(q) = \hat{g}^r(q) \equiv \exp(iqr)$ form. The latter, analogous to the case of photoionization [see (1.3)], can be called *length* form. The other one is similar to the *velocity* form in photoionization and looks like [AC, 3.14]

$$\begin{aligned} g^r(\omega, q) &= \exp(i\vec{q}\vec{r}), \\ g^v(\omega, q) &= \tfrac{1}{\omega}[\exp(i\vec{q}\vec{r})(\vec{q}\vec{\nabla} - (\vec{q}\overleftarrow{\vec{\nabla}})\exp(i\vec{q}\vec{r})], \end{aligned} \tag{3.57}$$

where the upper arrow in $\overleftarrow{\vec{\nabla}}$ implies that the function standing to the left is being operated on.

The GOS of a transition i–f with multipolarity L in HF length approximation $f^L_{fi}(q, \omega^{\mathrm{HF}}_{fi})$ follows from (3.55):

$$f_{fi}^{L}(q,\omega_{fi}^{\mathrm{HF}}) = \frac{2\omega_{fi}^{\mathrm{HF}}}{q^2}\left|\int \varphi_f^*(\vec{r})\, j_L(qr)\, P_L(\cos\vartheta))\varphi_i(\vec{r})\mathrm{d}\vec{r}\right|^2 \equiv \frac{2\omega_{fi}^{\mathrm{HF}}}{q^2}\left|\langle f\,|j_L(qr)|\,i\rangle\right|^2, \tag{3.58}$$

where $\varphi_{f,i}(\vec{r}) = R_{\varepsilon_f(n_{f,i})}(r)Y_{l_{f,i}m_{f,i}}(\theta_{\vec{r}},\phi_{\vec{r}})\chi_{s_{f,i}}$ are the HF one-electron wave functions with their radial, angular, and spin parts, respectively. The $i-f$ excitation energy is denoted as $\omega_{fi}^{\mathrm{HF}}$. Electron energy (principal quantum number), and angular momentum, its projection and spin quantum numbers of initial i and final f states are denoted as $\varepsilon_f(n_{f,i})$, $l_{f,i}$, $m_{f,i}$, and $s_{f,i}$, respectively.

Next step in GOSes calculation is to take into account the many-electron correlations [3.14]. This can be done only approximately due to very complicated nature of the exact wave functions $\psi_{f,i}(\vec{r}_1,\ldots,\vec{r}_N)$. Here we take into account the many-electron correlations in the frame of the RPAE, already described in Chap. 1, Sect. 1.5. This approximation was applied very successfully to photoionization studies during many years (see [AM] and Chap. 2) giving quantitatively good description of the cross-sections, including a number of their specific features, such as giant resonances (GRs) in the absolute cross-sections and interference, giant autoionization, and spin-doublet resonances in the partial ones (see Sect. 1.5)

In order to obtain the matrix elements of the transition operator in the RPAE frame $\hat{G}_{\mathrm{R}}(\omega,q)$, an integral equation similar to (1.37) had to be solved. This equation can be presented symbolically like (1.41a)

$$\hat{G}_{\mathrm{R}}(\omega,q) = \hat{g}(q) + \hat{G}_{\mathrm{R}}(\omega,q)\times\hat{\chi}(\omega)\times\hat{U}, \tag{3.59}$$

where the electron-vacancy propagator $\hat{\chi}(\omega,q)$ and the combination of the direct and exchange Coulomb inter-electron interaction $\hat{U}(q)$ are defined as in (1.41a). However, now they depend in principle upon q. Just as (1.41a), the (3.57) can be solved also symbolically leading to the following expression:

$$\hat{G}_{\mathrm{R}}(\omega,q) = \frac{\hat{g}(q)}{\hat{1}-\hat{\chi}(\omega,q)\times\hat{U}(q)}. \tag{3.60}$$

This equation permits to investigate qualitatively the general features of collective multielectron effects in the GOSes, just as it was done in Sect. 1.5 for photoionization. Indeed, we are looking for strong enhancement of GOSes that corresponds to zeroes of the denominator in (3.60). The frequencies $\Omega(q)$ that are solutions of equation

$$\hat{1}-\hat{\chi}(\omega,q)\times\hat{U}(q) = 0, \tag{3.61}$$

can be called GOSes GR that at $q\to 0$ coincides with the GRs in photoionization.

Just as in photoionization (see Sect. 1.5), multielectron correlations can manifest themselves also in *interference resonances* (IR) and *correlation minima* (CM). In IR the amplitude of, for example, an outer atomic subshell $\hat{G}_{\mathrm{R}}^{(\mathrm{o})}(\omega_{\mathrm{IR}},q)$ is much greater than $\hat{g}^{(\mathrm{o})}(q)$. This occurs because of the large amplitude $\hat{G}_{\mathrm{R}}^{(\mathrm{i})}(\omega_{\mathrm{IR}},q)$ for the

interaction of a fast charged particle with the inner subshell, which strongly couples to the outer subshell by the inter-subshell interaction $\hat{U}^{(\mathrm{io})}$, so that [see (1.47)]

$$\hat{G}_{\mathrm{R}}^{(\mathrm{o})}(\omega_{\mathrm{IR}}, q) \approx \hat{G}_{\mathrm{R}}^{(\mathrm{i})}(\omega_{\mathrm{IR}}, q) \times \hat{\chi}^{(\mathrm{i})}(\omega) \times \hat{U}^{(\mathrm{io})} \gg g^{(\mathrm{o})}(q). \tag{3.62}$$

At the correlation minima destructive interference occurs, so that $\hat{G}_{\mathrm{R}}(\omega_{\mathrm{CM}}, q) = 0$, while $g^{(\mathrm{o})}(q) \neq 0$.

Nonsymbolically (3.58) is usually presented in matrix form that, naturally, looks more complicated, as for the dipole photoionization amplitude is illustrated by (1.37):

$$\left\langle f|\hat{G}_{\mathrm{R}}(\omega, q)|i\right\rangle = \langle f|\hat{g}^{r,v}(q)|i\rangle + \left(\sum_{n' \leq F, k' > F} - \sum_{n' > F, k' \leq F}\right) \times \frac{\left\langle k'|\hat{G}_{\mathrm{R}}(\omega, q)|n'\right\rangle \langle n' f|U|k' i\rangle}{\omega - \varepsilon_{k'} + \varepsilon_{n'} + \mathrm{i}\eta(1 - 2n_{k'})}, \tag{3.63}$$

here, as in (1.37), $\leq F(> F)$ denotes occupied (vacant) HF states, ε_n are the one-electron HF energies, $\eta \to 0$ and $n_k = 1(0)$ for $k \leq F(> F)$; $\langle nf|U|ki\rangle = \langle nf|V|ki\rangle - \langle nf|V|ik\rangle$. The RPAE results for *length* and *velocity* forms must be the same, and this is why $\hat{G}_{\mathrm{R}}(\omega, q)$ has no upper index r or v.

The procedure of solving this equation is described in details in [AC, AM] and for photoionization RPAE equation presented in Sect. 1.7. The only difference is that the operator $\hat{g}^{r,v}(q)$ has to be expanded into an, in principle, infinite series

$$g^{r,v}(q) = \sum_{L=0}^{\infty} g_L^{r,v}(|q|) P_L(\cos\vartheta), \tag{3.64}$$

where $P_L(\cos\vartheta)$ is the LTH-order Legendre polynomial and ϑ is the angle between $\boldsymbol{r}$ and $\boldsymbol{q}$. After performing analytically integration over ϑ in (3.63), one obtains instead a system of decoupled equations, separately for each L.

Note that contrary to $\hat{g}(q)$, $\hat{G}_{\mathrm{R}}(\omega, q)$ is a nonlocal operator, which correspond to two space coordinates $\boldsymbol{r}$ and $\boldsymbol{r}\prime$ instead of only one, $\boldsymbol{r}$, in $\hat{G}\hat{g}(q)$. Using (3.58) and (3.63), one can present the GOSes with account of many-electron RPAE correlations in the following form:

$$F_{fi}^{\mathrm{R}}(\omega, q) = \frac{2\omega}{q^2} \left|\left\langle f|\hat{G}_{\mathrm{R}}(\omega, q)|i\right\rangle\right|^2, \tag{3.65}$$

here $\langle f|$ and $|i\rangle$ are, respectively, the final and initial HF states.

To take into account many-electron correlations in RPAE, the system of (3.63) has to be solved, that after separating of components with different L for the r-form looks as follows

$$\left\langle f\left|G_{\mathrm{R}}^{L}(\omega,q)\right|i\right\rangle = \langle f|j_L(qr)|i\rangle + \left(\sum_{n'\le F,k'>F} - \sum_{n'>F,k'\le F}\right) \times \frac{\left\langle k'\left|G_{\mathrm{R}}^{L}(\omega,q)\right|n'\right\rangle \langle n' f|U|k' i\rangle_L}{\omega - \varepsilon_{k'} + \varepsilon_{n'} + i\eta(1-2n_{k'})}. \tag{3.66}$$

The procedure of solving this equation is described in details in [AC] and Sect. 1.7.

A relation similar to (3.57) that follows from (3.55) determines the L-component of GOSes in RPAE $F_{fi}^{L}(q,\omega_{fi}^{\mathrm{R}})$:

$$F_{fi}^{L}(q,\omega) = \frac{2\omega_{fi}}{q^2}\left|\left\langle f\left|G_{\mathrm{R}}^{L}(q,\omega)\right|i\right\rangle\right|^2. \tag{3.67}$$

The calculations of GOSes for discrete transitions permit to determine their multipolarity quite reliable [3.15]. This interpretation is of particular interest for nondipole transitions since they cannot be observed in photon absorption. But even optically allowed dipole transitions can in principle have a noticeable admixture of other multipolarities, for example, of the octupole one that can be disclosed by studying their GOSes and performing accurately enough calculations.

Via GOSes one can express the cross section of ionization of nl subshell by fast electron, using in RPAE the following formulas:

$$\frac{\mathrm{d}F_{nl}(q,\omega)}{\mathrm{d}\omega} = \frac{4(2l+1)}{\pi k}\sum_{l'L}(2l'+1)(2L+1)F_{kl',nl}^{L}(q,\omega), \tag{3.68}$$

$$\frac{\mathrm{d}\sigma_{nl}(\omega)}{\mathrm{d}\varepsilon} = \frac{2\pi}{E\omega}\int_{\omega/p}^{2p}\frac{\mathrm{d}F_{nl}(q,\omega)}{\mathrm{d}\omega}\frac{\mathrm{d}q}{q}, \tag{3.69}$$

where ionized electron energy is $\varepsilon = k^2/2$, $\varepsilon = \omega - I_{nl}$, I_{nl} is the nl subshell ionization potential, and $E = p^2/2$ is the primary electron energy. Note that if ionization of an open shell is considered, one has to substitute $2(2l+1)$ in (3.68) by the number of electrons in the open subshell N_{nl}. In this case, however, a more complex equation than (3.66) has to be solved. The problem of RPAE equation for open shell atoms is discussed in Sect. 1.11.

The differential in ω GOS and cross section that includes contributions from all atomic subshells nl can be obtained from (3.68) and (3.69) by summing over all nl that correspond to subshell that can be ionized by the energy ω.

The total fast electrons inelastic scattering cross-section with ionization of the nl subshell can be expressed via its photoionization cross-section $\sigma_{nl}(\omega)$ given by (1.69) ([LL], [3.16, 3.17]):

$$\sigma_{nl,In}^{\mathrm{B}}(E) = \frac{c}{2\pi E}\int_{I_{nl}}^{E}\frac{\sigma_{nl}(\omega)}{\omega}\ln\left(\varsigma_n\frac{4E}{\omega}\right)\mathrm{d}\omega, \tag{3.70}$$

where $\ln \varsigma_n \sim 1$ cannot be determined without detailed calculations. The expression (3.70) we call Bethe cross-section for the nl subshell. It is derived in the frame of so-called logarithmic accuracy, i.e., assuming that $\ln(E/\omega) \gg 1$. The total fast electron inelastic scattering cross-section with ionization of any atomic electron in the same logarithmic approximation is given by the following equation:

$$\sigma_{In}^{\mathrm{B}}(E) = \frac{c}{2\pi E}\sum_{nl}\int_{I_{nl}}^{E}\frac{\sigma_{nl}(\omega)}{\omega}\ln\left(\varsigma_n\frac{4E}{\omega}\right)\mathrm{d}\omega \simeq \frac{c}{2\pi E}\int_{I}^{E}\frac{\sigma(\omega)}{\omega}\ln\left(\varsigma\frac{4E}{\omega}\right)\mathrm{d}\omega$$

$$\equiv \frac{c}{2\pi E}\int_{I}^{E}\frac{\sigma(\omega)}{\omega}\ln\left(\frac{4E}{\omega}\right)\mathrm{d}\omega + A\frac{c}{2\pi E}\int_{I}^{E}\frac{\sigma(\omega)}{\omega}\mathrm{d}\omega$$

$$\equiv \frac{c}{2\pi E}\int_{I}^{E}\frac{\sigma(\omega)}{\omega}\ln\left(\frac{4E}{\omega}\right)\mathrm{d}\omega + A\sigma_{In}^{(1)}(E) \equiv \sigma_{In}(E) + A\sigma_{In}^{(1)}(E) \quad (3.71)$$

where $\sigma_{nl}(\omega)$ and $\sigma(\omega)$ are the partial of subshell nl and absolute atomic photoionization cross-section: $A \equiv \ln\varsigma > 0$. We introduce here the cross-section $\sigma_{In}^{(1)}(E)$ of the atom that is defined according to (3.71). Introduction of $\sigma_{In}^{(1)}(E)$ permits going beyond the logarithmic approximation by choosing the parameter A. While performing calculations with the help of (3.70) and (3.71), the best of all is to put $\varsigma_n = \varsigma = 1$, thus obtaining $\sigma_{In}(E)$ and also find $\sigma_{In}^{(1)}(E)$ separately. This gives the cross-section with the so-called logarithmic accuracy $\sigma_{In}(E)$ and the first non-vanishing nonlogarithmic correction that is determined by $\sigma_{In}^{(1)}(E)$. The parameter A has to be chosen to improve the general agreement with experimental data.

The ω dependence for the dipole GOS at $q = 0$ is reasonably well known because for $q = 0$ the GOSes are simply proportional to the extensively studied photoionization cross-sections, the results for which are presented in Chap. 2. Extremely strong multielectron effects were found there in a very broad photon frequency region—from the outer shells to well above inner shell thresholds. It is known that the whole variety of correlation effects, namely the intra- and inter-shell interaction proved to be very important in photoionization. Most prominent among these effects are the dipole Giant and correlation (or interference) resonances. However, almost nothing is known about the variation of these resonances in GOSes with the growth of q even in the dipole channel. As to monopole and quadrupole GOSes, they were not studied from this point of view at all.

3.7 Angular Distribution of Knocked-out Electrons

Of interest is consideration of the angular distribution of the secondary electrons relative to the linear momentum q, lost by the fast projectile in the collision process. Most convenient is to study the GOS density differential in the solid angle $\mathrm{d}\Omega$ of the

secondary electron. For small q, the main contribution comes from dipole transitions and is similar but not identical to that of unpolarized light.

The expressions presented in this section are derived in [3.18]. For differential in the outgoing electron angle GOS density of nl subshell $\mathrm{d}F_{nl}(q,\omega)/\mathrm{d}\Omega$, the following relation is valid:

$$\begin{aligned}\frac{\mathrm{d}F_{nl}(q,\omega)}{\mathrm{d}\Omega} &= \sum_{L'L''}\frac{\mathrm{d}F_{nl}^{L',L''}(q,\omega)}{\mathrm{d}\Omega} = \frac{\omega\pi}{(\omega-I_{nl})q^2}\sum_{L'L''}(2L'+1)(2L''+1)i^{L'-L''}\\ &\times\sum_{l'=|L'-l|}^{L'+l}\sum_{l''=|L''-l|}^{L''+l}\tilde{G}_{kl'L'}(q)\tilde{G}_{kl''L''}(q)i^{l''-l'}(2l'+1)(2l''+1)\mathrm{e}^{i(\bar{\delta}_{l'}-\bar{\delta}_{l''})}\\ &\times\begin{pmatrix}L' l\ l'\\ 0\,0\,0\end{pmatrix}\begin{pmatrix}l''\ l\ L''\\ 0\ \ 0\,0\end{pmatrix}\sum_{L=|l'-l''|}^{l'+l''}P_L(\cos\theta)(-1)^{L+l}(2L+1)\begin{pmatrix}l'\ L\ l''\\ 0\ 0\ 0\end{pmatrix}\\ &\times\begin{pmatrix}L\ L'\ L''\\ 0\ 0\ \ 0\end{pmatrix}\begin{Bmatrix}L\ L'\ L''\\ l\ l''\ l'\end{Bmatrix},\end{aligned}\tag{3.72}$$

here $\bar{\delta}_{l'} = \delta_{l'} + \Delta_{l'}$, where the expressions $G_{kl'L'}(q) \equiv \tilde{G}_{kl'L'}(q)\exp(i\Delta_{l'})$ are solutions of the RPAE set of equations (3.63) [see (1.73)]. Legendre polynomials $P_L(\cos\theta)$ are functions of the angle θ between the transferred in collision linear momentum $\vec{q}$ and linear momentum of the outgoing atomic electron $\vec{k}$.

The partial value of GOS $F_{nl}(q,\omega)$ is obtained from (3.72) by integrating over $\mathrm{d}\Omega$, leading to the following expression:

$$\begin{aligned}F_{nl}(q,\omega) &= \sum_{L'}F_{nl}^{L'}(q,\omega) = \frac{4\omega\pi^2}{(\omega-I_{nl})q^2}\sum_{L'}(2L'+1)\sum_{l'=|L'-l|}^{L'+l}\\ &\times[\tilde{G}_{kl'L'}(q)]^2(2l'+1)\begin{pmatrix}L'\ l\ l'\\ 0\ \ 0\,0\end{pmatrix}^2\ \text{(a)},\\ F_{nl}^{(W)}(q,\omega) &= \sum_{L'}F_{nl}^{(W)L'}(q,\omega) = \frac{4\omega\pi^2}{q^2}\sum_{L'}(2L'+1)\sum_{l'=|L'-l|}^{L'+l}\\ &\times[\tilde{G}_{kl'L'}(q)]^2(2l'+1)\begin{pmatrix}L'\ l\ l'\\ 0\ \ 0\,0\end{pmatrix}^2\ \text{(b)}.\end{aligned}\tag{3.73}$$

Note that at small q the dipole contribution in $F_{nl}^{(W)}(q,\omega) = (\omega - I_{nl})F_{nl}(q,\omega)$ dominates and $F_{nl}^{(W)}(q,\omega)$ is simply proportional to the photoionization cross-section $\sigma_{nl}(\omega)$ given by (1.69). To compare the results obtained with known formulas for the photoionization with lowest order nondipole corrections taken into account, let us consider so small q that it is enough to take into account terms with $L', L'' \le 2$. In this case, GOS angular distribution (3.72) can be presented similar to the photoionization (1.77) as

$$\frac{\mathrm{d}F_{nl}(q,\omega)}{\mathrm{d}\Omega} = \frac{F_{nl}(q,\omega)}{4\pi}\left\{1 - \frac{\beta_{nl}^{(\mathrm{in})}(\omega,q)}{2}\,P_2(\cos\theta) + q\left[\gamma_{nl}^{(\mathrm{in})}(\omega,q)P_1(\cos\theta)\right.\right.$$
$$\left.\left. +\eta_{nl}^{(\mathrm{in})}(\omega,q)P_3(\cos\theta) + \varsigma_{nl}^{(\mathrm{in})}(\omega,q)P_4(\cos\theta)\right]\right\}. \qquad (3.74)$$

The obvious difference is the q - dependence of the coefficients and an extra term $\varsigma_{nl}^{(\mathrm{in})}(\omega,q)P_4(\cos\theta)$. Even in this case expressions for $\beta_{nl}^{(\mathrm{in})}(\omega,q)$, $\gamma_{nl}^{(\mathrm{in})}(\omega,q)$, $\eta_{nl}^{(\mathrm{in})}(\omega,q)$, and $\varsigma_{nl}^{(\mathrm{in})}(\omega,q)$ via $g_{kl'L'}(q)$ are too complex as compared to relations for $\beta_{nl}(\omega)$, $\gamma_{nl}(\omega)$, and $\eta_{nl}(\omega)$ in photoionization. Therefore, it is more convenient to present the results for s, p, and d subshells separately.

For s-subshells it is obtained

$$\frac{\mathrm{d}F_{n0}(q,\omega)}{\mathrm{d}\Omega} = \sum_{L',L''=0}^{2}\frac{\mathrm{d}F_{n0}^{L',L''}(q,\omega)}{\mathrm{d}\Omega} = \frac{F_{n0}(q,\omega)}{4\pi}$$
$$\times\left\{1 + \frac{6}{W_0}\tilde{G}_{11}\left[\tilde{G}_{00}\cos(\bar{\delta}_0-\bar{\delta}_1) + 2\tilde{G}_{22}\cos(\bar{\delta}_1-\bar{\delta}_2)\right]P_1(\cos\theta)\right.$$
$$+\frac{2}{7W_0}\left[21\tilde{G}_{11}^2 + 5\tilde{G}_{22}(7\tilde{G}_{00}\cos(\bar{\delta}_0-\bar{\delta}_2) + 5\tilde{G}_{22})\right]P_2(\cos\theta) \qquad (3.75)$$
$$\left.+\frac{18}{W_0}\tilde{G}_{11}\tilde{G}_{22}\cos(\bar{\delta}_1-\bar{\delta}_2)\;P_3(\cos\theta) + \frac{90}{7W_0}\tilde{G}_{22}^2P_4(\cos\theta)\right\}$$
$$\equiv \frac{F_{n0}(q,\omega)}{4\pi}\left\{1 + \sum_{i=1}^{4}A_{n0i}(q,\omega)P_i(\cos\theta)\right\},$$

where

$$F_{n0} = \frac{4\pi^2\omega}{(\omega - I_{n0})q^2}W_0; \quad W_0 = \tilde{G}_{00}^2 + 3\tilde{G}_{11}^2 + 5\tilde{G}_{22}^2, \qquad (3.76)$$

here and below for compactness of the expressions we use $\tilde{G}_{lL}$ instead of $\tilde{G}^{L}_{\mathbf{r}\,nl\to kl}(q,\omega)$ from (3.66).

For $l = 1$ it is obtained

$$\frac{\mathrm{d}F_{n1}(q,\omega)}{\mathrm{d}\Omega} = \sum_{L',L''=0}^{2}\frac{\mathrm{d}F_{n1}^{L',L''}(q,\omega)}{\mathrm{d}\Omega} = \frac{F_{n1}}{4\pi}\left\{1 + \frac{1}{5W_1}\left[10\tilde{G}_{01}(2\tilde{G}_{12} - \tilde{G}_{10})\right.\right.$$
$$\times\cos(\bar{\delta}_0-\bar{\delta}_1) + 4\tilde{G}_{21}\left((5\tilde{G}_{10} - \tilde{G}_{12})\cos(\bar{\delta}_1-\bar{\delta}_2)\right.$$
$$\left.\left.+9\bar{G}_{32}\cos(\bar{\delta}_2-\bar{\delta}_3)\right)\right]P_1(\cos\theta) + \frac{2}{7W_1}\left[7\tilde{G}_{21}(\tilde{G}_{21} - 2\tilde{G}_{01}\cos(\bar{\delta}_0-\bar{\delta}_2))\right.$$
$$\left.+7\tilde{G}_{12}(\tilde{G}_{12} - 2\tilde{G}_{10}) + 3\tilde{G}_{32}((7\tilde{G}_{10} - 2\tilde{G}_{12})\cos(\bar{\delta}_1-\bar{\delta}_3) + 4\tilde{G}_{32})\right]P_2(\cos\theta)$$

$$
\begin{aligned}
&-\frac{6}{5W_1}\left[6\tilde{G}_{21}\tilde{G}_{12}\cos(\bar{\delta}_1-\bar{\delta}_2)+\tilde{G}_{32}(5\tilde{G}_{01}\cos(\bar{\delta}_0-\bar{\delta}_3)-4\tilde{G}_{21}\cos(\bar{\delta}_2-\bar{\delta}_3))\right]\\
&\times P_3(\cos\theta)+\frac{18}{7W_1}\tilde{G}_{32}\left[\tilde{G}_{32}-4\tilde{G}_{12}\cos(\bar{\delta}_1-\bar{\delta}_3)\right]P_4(\cos\theta)\Bigg\}\\
&\equiv\frac{F_{n1}(q,\omega)}{4\pi}\left\{1+\sum_{i=1}^{4}A_{n1i}(q,\omega)P_i(\cos\theta)\right\},
\end{aligned}
\tag{3.77}
$$

where

$$
F_{n1}=\frac{4\pi^2\omega}{(\omega-I_{n1})q^2}W_1;\quad W_1=\tilde{G}_{10}^2+\tilde{G}_{01}^2+2\left[\tilde{G}_{21}^2+\tilde{G}_{12}^2\right]+3\tilde{G}_{32}^2. \tag{3.78}
$$

For $l=2$ it is obtained

$$
\begin{aligned}
&\frac{\mathrm{d}F_{n2}(q,\omega)}{\mathrm{d}\Omega}\\
&=\frac{F_{n2}}{4\pi}\Bigg\{1+\frac{6}{W_2}\left[14\tilde{G}_{11}(\tilde{G}_{22}-\tilde{G}_{20})\cos(\bar{\delta}_1-\bar{\delta}_2)-14\tilde{G}_{11}\tilde{G}_{02}\right.\\
&\quad\times\cos(\bar{\delta}_0-\bar{\delta}_1)+3\tilde{G}_{31}\left((7\tilde{G}_{20}-2\tilde{G}_{22})\cos(\bar{\delta}_2-\bar{\delta}_3)+12\tilde{G}_{42}\cos(\bar{\delta}_3-\bar{\delta}_4)\right)\Big]\\
&\quad\times P_1(\cos\theta)+\frac{2}{245W_2}\left[1,029(\tilde{G}_{11}^2+6\tilde{G}_{31}^2)-18,522\tilde{G}_{11}\tilde{G}_{31}\cos(\bar{\delta}_1-\bar{\delta}_3)\right.\\
&\quad+1,225\tilde{G}_{02}(7\tilde{G}_{20}-10\tilde{G}_{22})\cos(\bar{\delta}_0-\bar{\delta}_2)-125\tilde{G}_{22}(98\tilde{G}_{20}+15\tilde{G}_{22})\\
&\quad\left.+450\tilde{G}_{42}((49\tilde{G}_{20}-20\tilde{G}_{22})\cos(\bar{\delta}_2-\bar{\delta}_4)+25\tilde{G}_{42})\right]P_2(\cos\theta)\\
&\quad+\frac{18}{W_2}\left[2\tilde{G}_{11}(\tilde{G}_{22}\cos(\bar{\delta}_1-\bar{\delta}_2)-6\tilde{G}_{42}\cos(\bar{\delta}_1-\bar{\delta}_4))+\tilde{G}_{31}(7\tilde{G}_{02}\cos(\bar{\delta}_0-\bar{\delta}_3)\right.\\
&\quad\left.-8\tilde{G}_{22}\cos(\bar{\delta}_2-\bar{\delta}_3)+6\tilde{G}_{42}\cos(\bar{\delta}_3-\bar{\delta}_4))\right]P_3(\cos\theta)\\
&\quad+\frac{90}{49W_2}\left[20\tilde{G}_{22}^2+\tilde{G}_{42}\left(98\tilde{G}_{02}\cos(\bar{\delta}_0-\bar{\delta}_4)\right.\right.\\
&\quad\left.\left.-100\tilde{G}_{22}\cos(\bar{\delta}_2-\bar{\delta}_4)+27\tilde{G}_{42}\right)\right]P_4(\cos\theta)\Bigg\}\\
&\equiv\frac{F_{n2}(q,\omega)}{4\pi}\left\{1+\sum_{i=1}^{4}A_{n2i}(q,\omega)P_i(\cos\theta)\right\},
\end{aligned}
\tag{3.79}
$$

where

$$
F_{n2}=\frac{4\pi^2\omega}{35(\omega-I_{n2})Eq^2}W_2;\quad W_2=35\tilde{G}_{20}^2+42\tilde{G}_{11}^2+63\tilde{G}_{31}^2+35\tilde{G}_{02}^2+50\tilde{G}_{22}^2+90\tilde{G}_{42}^2. \tag{3.80}
$$

Thus, we have expressed the angular distribution of knocked-out electrons in fast projectile-atom scattering via anisotropy parameters $A_{nli}(q,\omega)$, both dipole and nondipole.

Let us compare the result obtained in the small q limit with the known formula for photoionization of an atom by nonpolarized light. To do this, we have to use the lowest order terms of the first three spherical Bessel functions:

$$j_0(qr) \cong 1 - \frac{(qr)^2}{6};\ j_1(qr) \cong \frac{qr}{3}\left(1 - \frac{(qr)^2}{10}\right);\ j_2(qr) \cong \frac{(qr)^2}{15}\left(1 - \frac{(qr)^2}{14}\right). \tag{3.81}$$

It follows from (3.81) that the lowest in powers of q term is $\tilde{G}_{11} \sim q \ll 1$.[1] Correction to $\tilde{G}_{11}$ is proportional to q^3. As to $\tilde{G}_{00}$ and $\tilde{G}_{22}$, they are proportional to q^2 with corrections of the order of q^4. Retaining in (3.72) terms of the order of q^2 and bigger, one has the following expression:

$$\begin{aligned}
\frac{\mathrm{d}F_{n0}(q,\omega)}{\mathrm{d}\Omega} &= \frac{F_{n0}(q,\omega)}{4\pi}\left\{1 + 2P_2(\cos\theta) + \frac{2\tilde{G}_{00}}{\tilde{G}_{11}}\cos(\bar{\delta}_0 - \bar{\delta}_1)P_1(\cos\theta)\right. \\
&\quad \left. + \frac{2\tilde{G}_{22}}{\tilde{G}_{11}}\cos(\bar{\delta}_1 - \bar{\delta}_2)\left[2P_1(\cos\theta) + 3P_3(\cos\theta)\right]\right\} \\
&\equiv \frac{F_{n0}(q,\omega)}{4\pi}\left\{1 + 2P_2(\cos\theta) + \frac{2}{\tilde{G}_{11}}\left[\tilde{G}_{00}\cos(\bar{\delta}_0 - \bar{\delta}_1)\right.\right. \\
&\quad \left.\left. + 2\tilde{G}_{22}\cos(\bar{\delta}_1 - \bar{\delta}_2)\right]P_1(\cos\theta) + \frac{6\tilde{G}_{22}}{\tilde{G}_{11}}\cos(\bar{\delta}_1 - \bar{\delta}_2)P_3(\cos\theta)\right\} \\
&\equiv \frac{F_{n0}(q,\omega)}{4\pi}\left\{1 + 2P_2(\cos\theta) + q\gamma_{n0}^{(\mathrm{in})}(q,\omega)P_1(\cos\theta)\right. \\
&\quad \left. + q\eta_{n0}^{(\mathrm{in})}(q,\omega)P_3(\cos\theta)\right\},
\end{aligned} \tag{3.82}$$

[compare with (3.74)]

One should compare this relation with the similar one for photoionization of $n0$ subshell that follows from (1.77)–(1.79) and (1.83)–(1.84):

$$\begin{aligned}
\frac{\mathrm{d}\sigma_{n0}(\omega)}{\mathrm{d}\Omega} &= \frac{\sigma_{n0}(\omega)}{4\pi}\left\{1 - P_2(\cos\theta) + \kappa\frac{6\tilde{Q}_2}{5\tilde{D}_1}\cos(\bar{\delta}_1 - \bar{\delta}_2)\left[P_1(\cos\theta) - P_3(\cos\theta)\right]\right\} \\
&\equiv \frac{\sigma_{n0}(\omega)}{4\pi}\left\{1 - P_2(\cos\theta) + \kappa\gamma_{n0}(\omega)P_1(\cos\theta) + \kappa\eta_{n0}(\omega)P_3(\cos\theta)\right\},
\end{aligned} \tag{3.83}$$

where $\gamma_{n0}(\omega) = -\eta_{n0}(\omega) = 6\tilde{Q}_2/5\tilde{D}_1\cos(\bar{\delta}_1 - \bar{\delta}_2)$.

[1] As is seen from (3.81), we have in mind such values of q that it is $qR_{nl} < 1$, where R_{nl} is the radius of the ionized subshell.

The difference between (3.82) and (3.83) is seen in the sign and magnitude of the dipole parameters and in different expressions for the nondipole.

The difference between angular distributions of knocked-out atomic electrons in fast projectile–atom scattering (3.82) and photoelectrons (3.83) exists and is essential even in the so-called optical limit $q \to 0$. According to (3.74), there are simple relations in $q \to 0$ limit between dipole $\tilde{D}_1$ and quadrupole $\tilde{Q}_2$ matrix elements and $\tilde{G}_{11}$, $\tilde{G}_{22}$: $\tilde{G}_{11} = q\tilde{D}_1/3$ and $\tilde{G}_{22} = 2q^2\tilde{Q}_2/15$. With the help of relations $\tilde{G}_{00} = -q^2\tilde{Q}_2/3 = -(5/2)\tilde{G}_{22}$, (3.83) is transformed into the following expression:

$$\begin{aligned}
\frac{\mathrm{d}F_{n0}(q,\omega)}{\mathrm{d}\Omega} &= \frac{F_{n0}(q,\omega)}{4\pi}\left\{1 + 2P_2(\cos\theta) + q\frac{4\tilde{Q}_2}{5\tilde{D}_1}\cos(\bar{\delta}_1 - \bar{\delta}_2)[2P_1(\cos\theta)\right. \\
&\quad \left. +3P_3(\cos\theta)] - q\frac{2\tilde{Q}_2}{\tilde{D}_1}\cos(\bar{\delta}_0 - \bar{\delta}_1)P_1(\cos\theta)\right\} \\
&= \frac{F_{n0}(q,\omega)}{4\pi}\left\{1 + 2P_2(\cos\theta) + q\frac{2}{3}\gamma_{n0}(\omega)[2P_1(\cos\theta) + 3P_3(\cos\theta)]\right. \\
&\quad \left. -q\frac{2\tilde{Q}_2}{\tilde{D}_1}\cos(\bar{\delta}_0 - \bar{\delta}_1)\ P_1(\cos\theta)\right\} \\
&\equiv \frac{F_{n0}(q,\omega)}{4\pi}\left\{1 + 2P_2(\cos\theta) + q\frac{2\tilde{Q}_2}{\tilde{D}_1}\left[\frac{4}{5}\cos(\delta_1 - \delta_2)\right.\right. \\
&\quad \left.\left. - \cos(\delta_0 - \delta_1)\right] P_1(\cos\theta) + 2q\gamma_{n0}(\omega)P_3(\cos\theta)\right\}. \qquad (3.84a)
\end{aligned}$$

The deviation from (3.83) is evident, since the angular distribution is not expressed via a single nondipole parameter $\gamma_{n0}(\omega)$: a new phase difference $\bar{\delta}_0 - \bar{\delta}_1$ appears. As a result, following relations are valid at very small q:

$$\begin{aligned}
\gamma_{n0}^{(\mathrm{in})}(\omega) &= \frac{2\tilde{Q}_2}{\tilde{D}_1}\left[\frac{4}{5}\cos(\delta_1 - \delta_2) - \cos(\delta_0 - \delta_1)\right], \\
\eta_{n0}^{(\mathrm{in})}(\omega) &= 2\gamma_{n0}(\omega) = \frac{12}{5}\frac{\tilde{Q}_2}{\tilde{D}_1}\cos(\delta_1 - \delta_2).
\end{aligned} \qquad (3.84b)$$

For $l > 0$, even at very small q, the relations between nondipole parameters in photoionization and inelastic fast electron scattering are rather complex.

The similarity of general structure and considerable difference between (3.83) and (3.84a) is evident. On the other hand, the contribution of the nondipole parameters can be enhanced, since the condition $\omega/c \ll q \ll R^{-1}$ is easy to achieve. Let us note that even neglecting the terms with q (3.83) and (3.84a) remain

different: while in photoionization the angular distribution is proportional to $\sin^2\theta$ [see (3.83)], in inelastic scattering it is proportional to $\cos^2\theta$ [see (3.84a)].

The reason for this difference is clear. In photoabsorption the atomic electron is "pushed" off the atom by the electric field of the photon, which is perpendicular to the direction of the light beam. In inelastic scattering the push comes along momentum q, so the preferential is the emission of the electrons along the $\vec{q}$ direction, with the maximum at $\theta = 0$. Similar reason explains the difference in the nondipole terms. Note that the last term due to monopole transition (3.84a) is absent in photoabsorption angular distribution (3.83). It confirms that the angular distribution of GOS densities is richer than that of photoionization.

3.8 The Compton Effect

In this section, it will be demonstrated that the Compton scattering cross-section can be expressed under some conditions via GOSes. The operator that describes the interaction of photons with N atomic electrons in the nonrelativistic approximation looks as follows [BLP]:

$$\hat{\mathrm{K}} = \sum_{i=1}^{N} \left(-\frac{1}{c} \hat{\vec{p}}_i \vec{A}(\vec{r}_i) + \frac{1}{2c^2} \vec{A}^2(\vec{r}_i) \right), \tag{3.85}$$

where $\boldsymbol{A}(\boldsymbol{r}_i)$ is the vector potential of the electromagnetic field, $\boldsymbol{r}_i$ and $\hat{\vec{p}}_i$ are ith electron's coordinate and momentum, and c is the speed of light. The cross section of inelastic or Compton scattering of a photon is expressed via the second power of $\hat{\vec{p}}_i \vec{A}(\vec{r}_i)/c$ and the first power of $\vec{A}^2(\vec{r}_i)/2c^2$ operators. But the contribution of the second power of $\hat{\vec{p}}_i \vec{A}(\vec{r}_i)/c$ term to Compton scattering by nonrelativistic electrons is small.

For external electromagnetic field, one has $\vec{A}(\vec{r}_i) \sim \vec{e} \exp(i\vec{k}\vec{r}_i)$. Therefore, the differential in photon scattering angle $\mathrm{d}\Omega$ cross-section of Compton scattering accompanied by atomic transition from initial state $\langle i|$ to the final $|f\rangle$ one $\mathrm{d}\sigma^{\mathrm{C}}_{if}(\omega)/\mathrm{d}\Omega$ can be expressed via matrix elements of the operator $\exp(i\vec{k}\vec{r}_i)$:

$$\frac{\mathrm{d}\sigma^{\mathrm{C}}_{if}(\omega)}{\mathrm{d}\Omega} = \left(\frac{\mathrm{d}\sigma}{\mathrm{d}\Omega}\right)_0 \frac{E-\omega}{E} \sum_f \left| \left\langle i \left| \sum_{j=1}^{N} \mathrm{e}^{i\vec{q}\vec{r}_j} \right| f \right\rangle \right|^2, \tag{3.86}$$

here E is the incoming photon energy and ω is the energy transferred to the atom in the scattering process, $(\mathrm{d}\sigma/\mathrm{d}\Omega)_0$ is the classical Thomson scattering cross-section of light upon an electron (see [BLP, 3.19]). The vector $\vec{q}$ is the momentum transferred to the atom in the process of Compton scattering, $\vec{q} = \vec{\kappa} - \vec{\kappa}'$ with $\vec{k}'$ being the outgoing photon momentum. Note that summation over final states f is

performed preserving the energy conservation, $\omega = E_f - E_i$, where E_f and E_i are the energy of the atom in initial and the system "ionized electron and the residual ion" in the final states, respectively.

The last term the right-hand side of (3.86) can be expressed via the GOSes given by (3.27), which determine the inelastic scattering cross-section of a fast charge particle upon an atom: Then (3.86) can be presented in the following way:

$$\frac{\mathrm{d}\sigma^{\mathrm{C}}_{if}(\omega)}{\mathrm{d}\Omega} = \left(\frac{\mathrm{d}\sigma}{\mathrm{d}\Omega}\right)_0 \frac{E-\omega}{E}\frac{q^2}{2\omega}\sum_f F_{fi}(\omega, q). \tag{3.87}$$

Compton scattering for medium and heavy atoms is of interest at high energies E, of about tens or even hundreds keV. At these energies it starts to dominate over photoabsorption in the total cross-section of "photon–atom" interaction [3.19]. Having in mind that from the point of view of understanding the atomic structure, of interest are not too high ω, $\omega \leq 100$ Ry Therefore, one has a limitation $\omega/E \ll 1$. Neglecting corrections of the $\omega/E \ll 1$ order one obtains the following relation:

$$q = \frac{2E}{c}\left(1 - \frac{\omega}{2E}\right)^{1/2} \sin\vartheta, \tag{3.88}$$

where $\vartheta = \theta/2$ and θ is the outgoing photon scattering angle.

In Hartree–Fock approximation, the Compton scattering cross-section is given by (3.86) with GOSes determined by (3.58):

$$\frac{\mathrm{d}\sigma^{\mathrm{C}}_{\mathrm{HF}}(\omega)}{\mathrm{d}\Omega} = \left(\frac{\mathrm{d}\sigma}{\mathrm{d}\Omega}\right)_0 \frac{E-\omega}{E}\frac{q^2}{2\omega}\sum_{s>F, t\leq F} f_{st}(\omega, q), \tag{3.89}$$

here summation is performed over all one-electron states $t \leq F$, occupied in the initial state i of the atom and excited states $s > F$, which satisfy the energy conservation restriction, $\varepsilon_t = \omega + \varepsilon_s$.

The Thompson classical elastic scattering cross-section is given by the following expression [BLP]:

$$\left(\frac{\mathrm{d}\sigma}{\mathrm{d}\Omega}\right)_0 = \frac{1}{2c^4}(1+\cos^2\theta) \approx \frac{1}{c^4}\left[1 - \frac{1}{2}\left(\frac{qc}{E}\right)^2\right], \tag{3.90}$$

where θ is the photon scattering angle. The second step in (3.90) is valid for small scattering angles.

The next step in our consideration of Compton scattering is to take into account many-electron correlations in the RPAE frame. This expression is obtained substituting g_{st} in (3.89) by G_{st} given by (3.67).

Equation (3.63) for $\hat{G}_{\mathrm{R}}(\omega, q)$ with the help of (3.65) decouples into a system of independent equations for partial contributions with given angular momentum L,

$\hat{G}^L_{\mathrm{R}}(\omega, q)$, which have to be solved numerically as it is described in [AC] and in Chap. 2, giving matrix elements $\langle nl|\hat{G}^{(L)}_{\mathrm{R}}(\omega, q)|\varepsilon l'\rangle$. With these matrix elements, one can obtain RPAE partial L-values

$$F^{\mathrm{R}L}_{nl,\varepsilon l'}(\omega, q) = \frac{2\omega}{q^2}\left|\left\langle nl\left|\hat{G}^L_{\mathrm{R}}(\omega, q)\right|\varepsilon l'\right\rangle\right|^2. \tag{3.91}$$

Then these values, $G^{\mathrm{R}L}_{nl,\varepsilon l'}(\omega, q)$, have to substitute $g_{st}(\omega, q)$ in (3.89) leading to

$$\frac{\mathrm{d}\sigma^{\mathrm{C}}_{\mathrm{R}}(\omega)}{\mathrm{d}\Omega} = \left(\frac{\mathrm{d}\sigma}{\mathrm{d}\Omega}\right)_0 \frac{E-\omega}{E}\frac{q^2}{2\omega}\sum_{s>F, l\le F, L>0} F^{\mathrm{R}L}_{nl,\varepsilon l'}(\omega, q), \tag{3.92}$$

i.e., to RPAE Compton scattering cross-sections (see [3.20] and references therein).

In Compton scattering discrete levels can be excited. The corresponding cross-section is given by expression similar to (3.91):

$$\frac{\mathrm{d}\sigma^{\mathrm{C}}_{\mathrm{R},i\to f,L_{if}}(\omega_{if})}{\mathrm{d}\Omega} = \left(\frac{\mathrm{d}\sigma}{\mathrm{d}\Omega}\right)_0 \frac{E-\omega_{if}}{E}\frac{q^2}{2\omega_{if}} F^{\mathrm{R}L_{if}}_{i,f}(\omega_{if}, q), \tag{3.93}$$

here $i \to f$ denotes the discrete transition from the state i to f, with the excitation energy ω_{if}.

In calculations of the Compton scattering cross-sections we will limit ourselves with monopole, dipole, quadrupole, and octupole, $L = 0,\ 1,\ 2,\ 3$ transitions. We calculate $g^L_{nl,\varepsilon l'}(\omega, q)$ and $G^{\mathrm{R}L}_{nl,\varepsilon l'}(\omega, q)$ in a rather broad region of q values, $0 \le q \le 8$ at.un. and ω up to 100–120 Ry. For reasonable values of E, $E > 1,000$ Ry with 1–2% accuracy, one can simplify (3.88), reducing it to $q = (E/c)\theta$. Then instead of (3.92) it is obtained

$$\begin{aligned}
&\left(\frac{\mathrm{d}\sigma^{\mathrm{RC}}_{nl,\varepsilon}(\omega)}{\mathrm{d}\Omega}\right)\Big/\left(\frac{\mathrm{d}\sigma}{\mathrm{d}\Omega}\right)_0 = \frac{q^2}{2\omega}F_{nl,\varepsilon}(\omega, q) \equiv \varsigma^{\mathrm{R}}_{nl,\varepsilon}(\omega, q) = \sum_{l=0}^{L_{\max}} \varsigma^{\mathrm{R}}_{nl,\varepsilon,L}(\omega, q),\\
&F_{nl,\varepsilon}(\omega, q) = \sum_{L=0}^{L_{\max}}\sum_{l'} F^L_{nl,\varepsilon l'}(\omega, q),\\
&\varepsilon = \omega - I_{nl}, q = \tfrac{E\theta}{c}.
\end{aligned} \tag{3.94}$$

The function $\varsigma^{\mathrm{R}}_{nl,\varepsilon,L}(\omega, q)$ we call the relative cross-section of Compton scattering. It is convenient to introduce a similar function for a discrete transition:

$$\varsigma^{\mathrm{R}L}_{nl,n'l'}(\omega, q) \equiv \frac{q^2 F^{\mathrm{R}L}_{nl,n'l'}(\omega, q)}{2\omega_{nl,n'l'}}. \tag{3.95}$$

The relative role of RPAE correlations in ionization of an atom in Compton scattering is determined, according to (3.89) and (3.92) by the following ratio:

$$\left(\frac{\mathrm{d}\sigma^{\mathrm{C,R}}_{nl,\varepsilon}(\omega)}{\mathrm{d}\Omega}\right)\Bigg/\left(\frac{\mathrm{d}\sigma^{\mathrm{C,HF}}_{nl,\varepsilon}}{\mathrm{d}\Omega}\right) = \frac{F_{nl,\varepsilon}(\omega,q)}{f_{nl,\varepsilon}(\omega,q)}. \tag{3.96}$$

We have also calculated total cross sections of the Compton scattering. For a given transferred angular momentum L, one has in HF and RPAE (denoted by R) the following formula:

$$\frac{\mathrm{d}^2\sigma^{\mathrm{CHF},L}(\omega,q)}{\mathrm{d}\omega\mathrm{d}q} = \frac{q^2}{2\omega c^4}\left[1-\frac{1}{2}\left(\frac{qc}{E}\right)^2\right]\sum_{nl,l'} f^L_{nl,\varepsilon l'}(\omega,q), \tag{3.97}$$

$$\frac{\mathrm{d}^2\sigma^{\mathrm{CR},L}(\omega,q)}{\mathrm{d}\omega\mathrm{d}q} = \frac{q^2}{2\omega c^4}\left[1-\frac{1}{2}\left(\frac{qc}{E}\right)^2\right]\sum_{nl,l'} F^L_{nl,\varepsilon l'}(\omega,q). \tag{3.98}$$

If we want to find partial contribution of a given subshell nl to the Compton scattering cross-section, only one corresponding term instead of the sum over nl has to be retained in the right-hand side of (3.97) and (3.98). In this case one has $\varepsilon = \omega - I_{nl}$.

The differential in ω and q Compton scattering cross-section one must sum over all angular moments L taken into account

$$\frac{\mathrm{d}^2\sigma^{\mathrm{CR,HF}}(\omega,q)}{\mathrm{d}\omega\mathrm{d}q} = \sum_{L=0}^{3}\frac{d^{\,2}\sigma^{\mathrm{CR,HF},L}(\omega,q)}{\mathrm{d}\omega\mathrm{d}q}. \tag{3.99}$$

The differential only in ω cross-section is obtained from (3.98) and (3.99) by integrating it over q:

$$\frac{\mathrm{d}\sigma^{\mathrm{CHF}}(\omega,q)}{\mathrm{d}\omega} = \frac{1}{2\omega c^2E^2}\int_0^{q_{\max}} q^3\left[1-\frac{1}{2}\left(\frac{qc}{E}\right)^2\right]\sum_{nl,l'L} f^L_{nl,\varepsilon l'}(\omega,q)\mathrm{d}q, \tag{3.100}$$

$$\frac{\mathrm{d}\sigma^{\mathrm{CR}}(\omega,q)}{\mathrm{d}\omega} = \frac{1}{2\omega c^2E^2}\int_0^{q_{\max}} q^3\left[1-\frac{1}{2}\left(\frac{qc}{E}\right)^2\right]\sum_{nl,l'L} F^L_{nl,\varepsilon l'}(\omega,q)\mathrm{d}q, \tag{3.101}$$

here $q_{\max}$ is the upper limit of q, which in our calculations will be taken equal to 8 at. un. Note that $q_{\max}c/E \ll 1$.

We performed also calculations for the Compton excitation cross-section of discrete levels in all noble gas atoms. The respective cross sections are similar to (3.100) and (3.101):

$$\sigma^{\mathrm{CHF}}_{nl,n'l'}(\omega_{nl,n'l'},q)=\frac{1}{2\omega_{nl,n'l'}c^2E^2}\int\limits_0^{q_{\max}}q^3\left[1-\frac{1}{2}\left(\frac{qc}{E}\right)^2\right]f^L_{nl,\varepsilon l'}(\omega_{nl,n'l'},q)q, \tag{3.102}$$

$$\sigma^{\mathrm{CR}}_{nl,n'l'}(\omega_{nl,n'l'},q)=\frac{1}{2\omega_{nl,n'l'}c^2E^2}\int\limits_0^{q_{\max}}q^3\left[1-\frac{1}{2}\left(\frac{qc}{E}\right)^2\right]F^L_{nl,\varepsilon l'}(\omega_{nl,n'l'},q)\mathrm{d}q. \tag{3.103}$$

If one sums in (3.102) and (3.103) over all $n'l'$ and L, the total contribution to the cross section from discrete-level excitations of the nl electrons is obtained. The formulas (3.102) and (3.103) will be used below to obtain the total discrete-level excitation cross section in the Compton scattering and to compare it to the total classical Thompson cross section of light scattering upon an electron

$$\sigma_{\mathrm{cl}}=\frac{8\pi}{3c^4}\approx 2.3755\times 10^{-8}\ \text{at. un.} \tag{3.104}$$

Let us note that the contribution of a group of discrete levels decreases with the growth of E as $1/E^2$, while the total Compton cross section is almost E-independent. It means that with increase of E the main contribution to the Compton cross section comes not from electron excitation but from atomic electrons ionization.

The values of the total cross sections $\sigma^{\mathrm{R}}_{nl}(\omega)$, according to (3.102) and (3.103) and following [3.21], can be presented as:

$$\sigma^{\mathrm{HF,R}}_{nl}(\omega)=\frac{c^2}{E^2}\sigma_{\mathrm{cl}}B^{\mathrm{HF,R}}_{nl}(\omega). \tag{3.105}$$

As an example, the factors $B^{\mathrm{HF,R}}_{nl}(\omega)$ were calculated in [3.22] and found to be equal to $B^{\mathrm{R}}_{2p}\approx 0.2210$ for Ne, $B^{\mathrm{R}}_{3p}\approx 0.1454$ for Ar, $B^{\mathrm{R}}_{4p}\approx 0.2084$ for Kr, and $B^{\mathrm{R}}_{5p}\approx 0.2413$ for Xe. For energies that are of interest for Compton scattering, namely for E bigger than tens of keV one has $c/E\ll 1$, $B_{nl}(\omega)<Z$ and therefore the discrete-level excitation cross section is much smaller than the total atomic classical Thompson scattering cross-section given by (3.104).

3.9 GOS for Semi-filled Shells

Most simple are the GOS calculations for atoms and ions with all closed shells. There, the presented above formulas are directly applicable. For semi-filled shells the method similar to described in Sect. 1.10 will be applied that permits to use similar, but properly modified formulas. The main idea of this method is to treat electrons with spins directed up and down (denote as $\uparrow$ and $\downarrow$) as different particles.

The one electron wave functions will be given by equation identical to (1.90)

$$\left(\hat{H}^{\mathrm{HF}}_{\uparrow(\downarrow)} + \hat{V}^{\mathrm{H}}_{\downarrow(\uparrow)}\right)\varphi^{\uparrow(\downarrow)}(\vec{r}) = \varepsilon^{\uparrow(\downarrow)}\varphi^{\uparrow(\downarrow)}(\vec{r}). \tag{3.106}$$

In the HF approximation the generalized oscillator strengths are of up and down types, being determined by relations similar to (3.55)

$$f^{r}_{fi\uparrow(\downarrow)}(\omega, q) = \frac{2\omega}{q^2}\left|\int \varphi^{*}_{f\uparrow(\downarrow)}(\vec{r})\exp(i\vec{q}\vec{r})\varphi_{i\uparrow(\downarrow)}(\vec{r})\mathrm{d}\vec{r}\right|^2, \tag{3.107}$$

Similarly, to what has been done in Sect. 1.10, we treat the electron correlations in the frame of spin-polarized RPAE that leads instead of (1.41a) in RPAE to the following equation for operators of GOSes:

$$\begin{aligned}\left(\hat{G}_{R\uparrow}(\omega, q)\ \hat{G}_{R\downarrow}(\omega, q)\right) = \left(\hat{g}^{r,v}_{\uparrow}(\omega, q)\ \hat{g}^{r,v}_{\downarrow}(\omega, q)\right) + \left(\hat{G}_{R\uparrow}(\omega, q)\ \hat{G}_{R\downarrow}(\omega, q)\right)\\ \times\begin{pmatrix}\hat{\chi}_{\uparrow\uparrow} & 0\\ 0 & \hat{\chi}_{\downarrow\downarrow}\end{pmatrix}\times\begin{pmatrix}U_{\uparrow\uparrow} & V_{\uparrow\downarrow}\\ V_{\downarrow\uparrow} & U_{\downarrow\downarrow}\end{pmatrix},\end{aligned} \tag{3.108}$$

where $\hat{\chi}_{\uparrow\uparrow}$ and $\hat{\chi}_{\downarrow\downarrow}$, $U_{\uparrow\uparrow(\downarrow\downarrow)}$ and $V_{\uparrow\downarrow(\downarrow\uparrow)}$ are given by the same expressions as for $\hat{D}_{\uparrow(\downarrow)}(\omega)$ in (1.93). Note that in the matrix form similar to (3.63), the following expressions for length r and velocity v that follow from (3.57) have to be used:

$$\begin{aligned}\hat{g}^{r}_{\uparrow(\downarrow)}(\omega, q) \to \langle i\uparrow(\downarrow)|g^{r}(\omega, q)|f\uparrow(\downarrow)\rangle = \left\langle i\uparrow(\downarrow)\left|\exp(i\vec{q}\vec{r})\right|f\uparrow(\downarrow)\right\rangle,\\ \hat{g}^{v}_{\uparrow(\downarrow)}(\omega, q) \to \langle i\uparrow(\downarrow)|g^{v}(\omega, q)|f\uparrow(\downarrow)\rangle = \left\langle i\uparrow(\downarrow)\left|\tfrac{1}{\omega}[\exp(i\vec{q}\vec{r})(\vec{q}\vec{\nabla}\right.\right.\\ \left.\left.-(\vec{q}\overleftarrow{\vec{\nabla}})\exp(i\vec{q}\vec{r})]\right|f\uparrow(\downarrow)\right\rangle.\end{aligned} \tag{3.109}$$

After separating components with different L for the r-form, one obtains instead of (3.66) the following equation:

$$\begin{aligned}\left\langle f\uparrow|G^{L}_{R\uparrow}(\omega, q)|i\uparrow\right\rangle = \langle f\uparrow|j_L(qr)|i\uparrow\rangle + \left(\sum_{n'\le F, k'>F} - \sum_{n'>F, k'\le F}\right)\\ \times\frac{\left\langle k'\uparrow|G^{L}_{R\uparrow}(\omega, q)|n'\uparrow\right\rangle\langle n'\uparrow f\uparrow|U|k'\uparrow i\uparrow\rangle_L}{\omega - \varepsilon_{k'} + \varepsilon_{n'} + i\eta(1-2n_{k'})}\\ + \left(\sum_{n'\le F, k'>F} - \sum_{n'<F, k'\le F}\right)\\ \times\frac{\left\langle k'\downarrow|G^{L}_{R\uparrow}(\omega, q)|n'\downarrow\right\rangle\langle n'\downarrow f\uparrow|V|k'\downarrow i\uparrow\rangle_L}{\omega - \varepsilon_{k'} + \varepsilon_{n'} + i\eta(1-2n_{k'})}.\end{aligned} \tag{3.110}$$

The equation for matrix elements $\langle f \downarrow |G^L_{\mathrm{R}\downarrow}(\omega, q)|i \downarrow\rangle$ can be obtained from (3.110) substituting everywhere $\uparrow$ by $\downarrow$. The expression for GOS is similar to (3.66)

$$F^L_{fi\uparrow(\downarrow)}(q,\omega) = \frac{2\omega_{fi\uparrow(\downarrow)}}{q^2}\left|\left\langle f \uparrow (\downarrow)\left|G^L_{\mathrm{R}\uparrow(\downarrow)}(q,\omega)\right|i \uparrow (\downarrow)\right\rangle\right|^2. \tag{3.111}$$

The differential in angle Ω fast electron inelastic scattering cross-section can be obtained using (3.26):

$$\frac{\mathrm{d}\sigma(q)}{\mathrm{d}\Omega} = \frac{4}{q^2}\left[\sum_{i,f\uparrow}\frac{4p_{f\uparrow}}{q^2 p_{i\uparrow}\omega_{if\uparrow}}F_{i\to f\uparrow}(q,\omega_{if\uparrow}) + \sum_{i,f\downarrow}\frac{4p_{f\downarrow}}{q^2 p_{i\downarrow}\omega_{if\downarrow}}F_{i\to f\downarrow}(q,\omega_{if\downarrow})\right]. \tag{3.112}$$

In a similar way one can treat other characteristics of the fast electron scattering, such as angular distributions of the primary inelastic scattered and knocked out from the target atom electrons and corresponding spin polarization. To do this, one has to substitute in expressions for these quantities the GOS amplitudes with their respective spin-polarized versions, just as we did it deriving (1.96) and (1.97).

The method developed for GOSes of semi-filled shell atoms will be applied in calculations also of spin-orbit doublets as it was done in connection to photoionization. The specifics of this case, as compared to what was described in Sect. 1.10, is discussed in connection to Fig. 2.59_Xe_b7 in Chap. 2.

GOSes of open shell atoms can be investigated as it was done for photoionization in Sect. 1.11, but generalizing this to transitions of other than only dipole multipolarity.

3.10 Inelastic Scattering of Fast Particles upon Endohedrals

In Sects. 1.13 and 1.14, we have discussed photoionization of endohedral atoms—fullerenes shells with atoms stuffed inside them. Some experiments, where the endohedrals' photoionization cross-sections were studied, were already performed. We believe that in not too distant future endohedrals will be objects of investigations using fast electron scattering.

As an example of fullerene just as in Sects. 1.13 and 1.14, we consider C_{60}. The endohedral atom is denoted $A@C_{60}$. We consider two types of effects of C_{60} upon ionization of the "caged" atom A in $A@C_{60}$. The first is reflection of the electron emitted by the atom A in the collision process. The second is modification of the interaction between projectile and atom A electrons due to polarization of the C_{60} shell in the collision process.

The reflection is taken into account similarly to the case of photoionization [Sect. 1.13 (1.108)]:

$$G^{\mathrm{AC}(r)L}_{nl,kl'}(\omega,q) = F_{l'}(k)\widehat{G}^{L}_{nl,kl'}(\omega,q)\exp[i\,\Delta\delta_{l'}(k)], \tag{3.113}$$

where superscript AC(r) denotes the value for endohedral atom A@C_N, and index (r) denotes that the reflection from the fullerene shell is taken into account; functions $F_{l'}(k)$ and $\Delta\delta_{l'}$ are determined by the (1.106) and (1.107). Similar to (1.113), the expression for $\widehat{G}^{L}_{nl,kl'}$ is determined by the following equation:

$$\left\langle f|\widehat{G}^{L}_{R}(\omega,q)|i\right\rangle = \langle f|j_L(qr)|i\rangle + \left(\sum_{n'\le F,k'>F}\frac{F^2_{l_{k'}}(k')\left\langle k'|\widehat{G}^{L}_{R}(\omega,q)|n'\right\rangle\langle n'f|U|k'i\rangle_L}{\omega-\varepsilon_{k'}+\varepsilon_{n'}+i\eta}\right.$$
$$\left. -\sum_{k'>F,n'\le F}\frac{F^2_{l_{k'}}(k')\left\langle n'|\widehat{G}^{L}_{R}(\omega,q)|k'\right\rangle\langle k'f|U|n'i\rangle_L}{\omega-\varepsilon_{n'}+\varepsilon_{k'}-i\eta}\right). \tag{3.114}$$

Summation in (3.114) includes integration over the continuous one-electron spectrum of the atom A.

A relation similar to (3.67) that follows from (3.55) determines the L-component of GOSes in RPAE $F^{L}_{fi}(q,\omega^{\mathrm{R}}_{fi})$

$$F^{\mathrm{AC}(r)L}_{fi}(q,\omega) = \frac{2\omega_{fi}}{q^2}F^2_{l_f}(k)\left|\left\langle f\left|\widehat{G}^{L}_{\mathrm{R}}(q,\omega)\right|i\right\rangle\right|^2. \tag{3.115}$$

Via GOSes one can express the cross section of ionization of *nl* subshell by fast electron, using in RPAE the following formulas:

$$\frac{\mathrm{d}^2F^{\mathrm{AC}(r)}_{nl}(q,\omega)}{\mathrm{d}\omega\mathrm{d}q} = \frac{4(2l+1)}{\pi k}\sum_{l'L}(2l'+1)(2L+1)F^{\mathrm{AC}(r)L}_{kl',nl}(q,\omega), \tag{3.116}$$

$$\frac{\mathrm{d}\sigma^{\mathrm{AC}(r)}_{nl}(\omega)}{\mathrm{d}\varepsilon} = \frac{2\pi}{E\omega}\int_{\omega/p}^{2p}\frac{\mathrm{d}F^{\mathrm{AC}(r)}_{nl}(q,\omega)}{\mathrm{d}\omega}\frac{\mathrm{d}q}{q}. \tag{3.117}$$

The effect of fullerenes polarization can be taken into account similar to how it is done for the dipole amplitude of photoionization that is described in Sect. 1.14. However, instead of polarizabilities, as in (1.119) and (1.121), we obtain expressions that include q-dependent generalized polarizabilities $\alpha^{L}_{C_N}(\omega,q)$. The inclusion of amplitudes with account of secondary electron's scattering and fullerenes polarization is achieved in the following relation that is denoted by superscript AC without (r):

$$F^{\mathrm{AC}}_{nl,kl'}(\omega) = |F_{l'}(k)|^2\left|1-\frac{\alpha^{L}_{C_N}(\omega,q)}{R^3}\right|^2F^{L}_{nl,kl'}(\omega) \equiv F^2_{l'l'}(k)|G^{L}_{C_N}(\omega,q)|^2F^{L}_{nl,kl'}(\omega,q). \tag{3.118}$$

where

$$\alpha^L_{C_N}(\omega,q)=\frac{1}{q^{2L}}\sum_{\substack{k_C>F_C\\ n_C\le F_C}}\left[\frac{\langle n_C|j_L(qr)|k_C\rangle\langle k_C|Q^L_C(\omega,q)|n_C\rangle}{\varepsilon_{k_C}+I_{n_C}-\omega-i\eta}\right.$$
$$\left.+\frac{\langle n_C|\exp(-i\vec{q}\vec{r})|k_C\rangle\langle k_C|Q^L_C(\omega,q)|n_C\rangle}{\varepsilon_{k_C}+I_{n_C}+\omega-i\eta}\right], \tag{3.119}$$

here $\langle k_C|Q^L_C(\omega,q))|n_C\rangle$ are solutions of RPAE equation for the C_N electron shell:

$$\langle f_C|Q^L_C(\omega,q)|i_C\rangle=\langle f_C|j_L(qr)|i_C\rangle+\left(\sum_{\substack{n_C\le F\\ k_C>F}}\frac{\langle k_C|Q^L_C(\omega,q)|n_C\rangle\langle nf|U|k'i\rangle_L}{\omega-\varepsilon_{k_C}+\varepsilon_{n_C}+i\eta}\right.$$
$$\left.-\sum_{\substack{k_C>F\\ n_C\le F}}\frac{\langle n_C|Q^L_C(\omega,q)|k_C\rangle\langle k_Cf_C|U|n_Ci_C\rangle_L}{\omega-\varepsilon_{n_C}+\varepsilon_{k_C}-i\eta}\right). \tag{3.120}$$

Polarization factor $G^L_{C_N}(\omega,q)$ is, as the polarizability, a complex number and can be presented as

$$G^L_{C_N}(\omega,q)=\left|G^L_{C_N}(\omega,q)\right|\exp[i\Lambda_L(\omega)], \tag{3.121}$$

where $|G^L_{C_N}(\omega,q)|\equiv\tilde{G}^L_{C_N}(\omega,q)$ is the real part of it.

All electron states in (3.119) and (3.120) are marked by subscript C that notes that they belong to the fullerene C_N shell, contrary to (3.114), where the states belong to atom A.

For differential in the outgoing electron angle GOS density of *nl* subshell $\mathrm{d}F^{AC}_{nl}(q,\omega)/\mathrm{d}\Omega$, the following relation is valid:

$$\frac{\mathrm{d}F^{AC}_{nl}(q,\omega)}{\mathrm{d}\Omega}=\sum_{L'L''}\frac{\mathrm{d}F^{ACL',L''}_{nl}(q,\omega)}{\mathrm{d}\Omega}=\frac{\omega\pi}{(\omega-I_{nl})q^2}$$
$$\times\sum_{L'L''}(2L'+1)(2L''+1)i^{L'-L''}\tilde{G}^{L'}_{C_N}(\omega,q)\tilde{G}^{L''}_{C_N}(\omega,q)$$
$$\times\sum_{l'=|L'-l|}^{L'+l}\sum_{l''=|L''-l|}^{L''+l}F_{l'}(k)F_{l''}(k)\tilde{\widehat{G}}_{kl'L'}(q)\tilde{\widehat{G}}_{kl''L''}(q)i^{l''-l'}(2l'+1)$$

$$\times(2l''+1)\mathrm{e}^{i(\tilde{\delta}_{l'}+\Lambda_{L'}-\tilde{\delta}_{l''}-\Lambda_{L''})}\times\begin{pmatrix}L' & l & l'\\ 0 & 0\,0\end{pmatrix}\begin{pmatrix}l'' & l & L''\\ 0 & 0\,0\end{pmatrix}\sum_{L=|l'-l''|}^{l'+l''}$$

$$\times P_L(\cos\theta)(-1)^{L+l}(2L+1)\begin{pmatrix}l' & L & l''\\ 0 & 0 & 0\end{pmatrix}\begin{pmatrix}L & L' & L''\\ 0 & 0 & 0\end{pmatrix}\begin{Bmatrix}L & L' & L''\\ l & l'' & l'\end{Bmatrix}, \tag{3.122}$$

here $\tilde{\delta}_l=\bar{\delta}_l+\Delta\delta_l=\delta_l+\Delta_l+\Delta\delta_l$, where the expression $\widehat{G}_{kl'L'}(q)\equiv\tilde{\widehat{G}}_{kl'L'}(q)\exp(i\Delta_{l'})$ are solutions of the RPAE set of equations (3.114) and $\Delta\delta_l$ is defined by (1.107). Legendre polynomials $P_L(\cos\theta)$ are functions of the angle θ between the transferred in collision linear momentum $\vec{q}$ and linear momentum of the outgoing atomic electron $\vec{k}$.

The partial value of GOS $F_{nl}^{\mathrm{AC}}(q,\omega)$ is obtained from (3.122) by integrating over $\mathrm{d}\Omega$, leading to the following expression:

$$F_{nl}^{\mathrm{AC}}(q,\omega)=\sum_{L'}F_{nl}^{\mathrm{AC}L'}(q,\omega)=\frac{4\omega\pi^2}{Eq^2}\sum_{L'}(2L'+1)\times\sum_{l=|L'-l|}^{L'+l}$$

$$\times[\tilde{G}_{C_N}^{L'}(\omega,q)F_{l'}(k)\tilde{\widehat{G}}_{kl'L'}(q)]^2(2l'+1)\begin{pmatrix}L' & l & l'\\ 0\,0\,0\end{pmatrix}^2 \tag{3.123}$$

Let us consider so small q that it is enough to take into account terms with L', $L''\leq 2$. In this case, GOS angular distribution (3.123) can be presented similar to the photoionization (1.77) as

$$\frac{\mathrm{d}F_{nl}^{\mathrm{AC}}(q,\omega)}{d\Omega}=\frac{F_{nl}^{\mathrm{AC}}(q,\omega)}{4\pi}\left\{1-\frac{\beta_{nl}^{\mathrm{AC(in)}}(\omega,q)}{2}P_2(\cos\theta)\right.$$

$$+q\left[\gamma_{nl}^{\mathrm{AC(in)}}(\omega,q)P_1(\cos\theta)+\eta_{nl}^{\mathrm{AC(in)}}(\omega,q)P_3(\cos\theta)\right.$$

$$\left.\left.+\varsigma_{nl}^{\mathrm{AC(in)}}(\omega,q)P_4(\cos\theta)\right]\right\}$$

$$=\frac{F_{nl}^{\mathrm{AC}}(q,\omega)}{4\pi}\left\{1+\sum_{i=1}^{4}A_{nli}^{\mathrm{AC}}(q,\omega)P_i(\cos\theta)\right\}. \tag{3.124}$$

Even in case of small q the expressions for $\beta_{nl}^{(\mathrm{in})}(\omega,q)$, $\gamma_{nl}^{(\mathrm{in})}(\omega,q)$, $\eta_{nl}^{(\mathrm{in})}(\omega,q)$, and $\varsigma_{nl}^{(\mathrm{in})}(\omega,q)$ via $G_{kl'L'}(q)$ are too complex. Therefore, it is more convenient to present the results for s, p, and d subshells separately, not limiting ourselves, however, by too small q.

For s-subshells it is obtained

$$\frac{\mathrm{d}F_{n0}^{\mathrm{AC}}(q,\omega)}{\mathrm{d}\Omega} = \sum_{L',L''=0}^{2} \frac{\mathrm{d}F_{n0}^{\mathrm{AC}L',L''}(q,\omega)}{d\,\Omega} = \frac{F_{n0}^{\mathrm{AC}}(q,\omega)}{4\pi}$$
$$\times\left\{1+\frac{6}{W_0}\bar{G}_{11}\left[\bar{G}_{00}\cos(\bar{\bar{\delta}}_0-\bar{\bar{\delta}}_1)+2\bar{G}_{22}\cos(\bar{\bar{\delta}}_1-\bar{\bar{\delta}}_2)\right]P_1(\cos\theta)\right.$$
$$+\frac{2}{7W_0^{\mathrm{AC}}}\left[21\bar{G}_{11}^2+5\bar{G}_{22}(7\bar{G}_{00}\cos(\bar{\bar{\delta}}_0-\bar{\bar{\delta}}_2)+5\bar{G}_{22})\right]P_2(\cos\theta)$$
$$\left.+\frac{18}{W_0^{\mathrm{AC}}}\bar{G}_{11}\bar{G}_{22}\cos(\bar{\bar{\delta}}_1-\bar{\bar{\delta}}_2)\;P_3(\cos\theta)+\frac{90}{7W_0^{\mathrm{AC}}}\bar{G}_{22}^2P_4(\cos\theta)\right\}$$
$$\equiv \frac{F_{n0}^{\mathrm{AC}}(q,\omega)}{4\pi}\left\{1+\sum_{i=1}^{4}A_{n0i}^{\mathrm{AC}}(q,\omega)P_i(\cos\theta)\right\}$$
$$\approx \frac{F_{n0}^{\mathrm{AC}}(q,\omega)}{4\pi}\left\{1+2P_2(\cos\theta)+q\gamma_{n0}^{\mathrm{AC(in)}}(\omega)P_1(\cos\theta)\right.$$
$$\left.+q\eta_{n0}^{\mathrm{AC(in)}}(\omega)P_3(\cos\theta)\right\}, \tag{3.125}$$

where $\bar{\bar{\delta}}_{0,1,2}=\tilde{\delta}_{0,1,2}+\Lambda_{0,1,2}=\bar{\delta}_{0,1,2}+\Delta\delta_{0,1,2}+\Lambda_{0,1,2}=\delta_{0,1,2}+\Delta_{0,1,2}+\Delta\delta_{0,1,2}+\Lambda_{0,1,2}$ with $\Lambda_{0,1,2}$ determined by (3.121) and

$$F_{n0}^{\mathrm{AC}}=\frac{4\pi^2\omega}{(\omega-I_{n0})q^2}W_0^{\mathrm{AC}};\quad W_0^{\mathrm{AC}}=\bar{G}_{00}^2+3\bar{G}_{11}^2+5\bar{G}_{22}^2. \tag{3.126}$$

Note that the last expression in (3.125) is valid only for small enough q, $q \ll R_{ns}^{-1}$, R_{ns} being the ns subshell radius.

Here and below for compactness of the expressions, we use the following notation $\bar{G}_{l'L}\equiv\tilde{G}_{C_N}^{L}(\omega,q)F_{l'}(k)\widetilde{\bar{G}}_{kl'L}(q)$ for the expression in (3.123)

For $l=1$ it is obtained

$$\frac{\mathrm{d}F_{n1}(q,\omega)}{\mathrm{d}\Omega} = \sum_{L',L''=0}^{2} \frac{\mathrm{d}F_{n1}^{L',L''}(q,\omega)}{\mathrm{d}\Omega} = \frac{F_{n1}}{4\pi}$$
$$\times\left\{1+\frac{1}{5W_1}\left[10\bar{G}_{01}(2\bar{G}_{12}-\bar{G}_{10})\cos(\bar{\bar{\delta}}_0-\bar{\bar{\delta}}_1)\right.\right.$$
$$\left.+4\bar{G}_{21}((5\bar{G}_{10}-\bar{G}_{12})\cos(\bar{\bar{\delta}}_1-\bar{\bar{\delta}}_2)+9\bar{G}_{32}\cos(\bar{\bar{\delta}}_2-\bar{\bar{\delta}}_3))\right]P_1(\cos\theta)$$
$$+\frac{2}{7W_1}\left[7\bar{G}_{21}(\bar{G}_{21}-2\bar{G}_{01}\cos(\bar{\bar{\delta}}_0-\bar{\bar{\delta}}_2))+7\bar{G}_{12}(\bar{G}_{12}-2\bar{G}_{10})\right.$$

$$
\begin{aligned}
&+ 3\bar{G}_{32}((7\bar{G}_{10} - 2\bar{G}_{12})\cos(\bar{\bar{\delta}}_1 - \bar{\bar{\delta}}_3) + 2\bar{G}_{32})\Big] P_2(\cos\theta) \\
&+\frac{6}{5W_1}\Big[6\bar{G}_{12}\bar{G}_{21}\cos(\bar{\bar{\delta}}_1 - \bar{\bar{\delta}}_2) + \bar{G}_{32}(5\bar{G}_{01}\cos(\bar{\bar{\delta}}_0 - \bar{\bar{\delta}}_3) \\
&-4\bar{G}_{21}\cos(\bar{\bar{\delta}}_2 - \bar{\bar{\delta}}_3))\Big] P_3(\cos\theta) \\
&+\frac{18}{7W_0}\bar{G}_{32}\Big[\bar{G}_{32} - 4\bar{G}_{12}\cos(\bar{\bar{\delta}}_1 - \bar{\bar{\delta}}_3)\Big] P_4(\cos\theta)\Big\} \\
&\equiv \frac{F_{n1}(q,\omega)}{4\pi}\left\{1 + \sum_{i=1}^{4} A_{n1i}(q,\omega) P_i(\cos\theta)\right\}, \qquad (3.127)
\end{aligned}
$$

where

$$
F_{n1} = \frac{4\pi^2\omega}{(\omega - I_{n1})q^2} W_1; W_1 = \bar{G}_{10}^2 + \bar{G}_{01}^2 + 2\left[\bar{G}_{21}^2 + \bar{G}_{12}^2\right] + 3\bar{G}_{32}^2. \qquad (3.128)
$$

For $l = 2$ it is obtained

$$
\begin{aligned}
\frac{\mathrm{d}F_{n2}(q,\omega)}{\mathrm{d}\Omega} &= \frac{F_{n2}}{4\pi}\Big\{1 + \frac{6}{W_2}\Big[14\bar{G}_{11}(\bar{G}_{22} - \bar{G}_{02}) - 14g_{11}g_{20}\cos(\bar{\bar{\delta}}_0 - \bar{\bar{\delta}}_1) \\
&+3\bar{G}_{31}\left((7\bar{G}_{20} - 2\bar{G}_{22})\cos(\bar{\bar{\delta}}_1 - \bar{\bar{\delta}}_2) + 12\bar{G}_{24}\cos(\bar{\bar{\delta}}_3 - \bar{\bar{\delta}}_4)\right)\Big] P_1(\cos\theta) \\
&+\frac{2}{245W_2}\Big[1,029(\bar{G}_{11}^2 + 6\bar{G}_{13}^2) - 18,522\bar{G}_{11}\bar{G}_{31}\cos(\bar{\bar{\delta}}_1 - \bar{\bar{\delta}}_3) \\
&+1,225\bar{G}_{02}(7\bar{G}_{02} - 10\bar{G}_{22})\cos(\bar{\bar{\delta}}_0 - \bar{\bar{\delta}}_2) \\
&-125\bar{G}_{22}(98\bar{G}_{20} + 15\bar{G}_{22}) + 450\bar{G}_{42}(7\bar{G}_{20} - 10\bar{G}_{22})\cos(\bar{\bar{\delta}}_0 - \bar{\bar{\delta}}_2) \\
&+25\bar{G}_{42})\Big] P_2(\cos\theta) \\
&+\frac{18}{W_2}\Big[2\bar{G}_{11}(\bar{G}_{22}\cos(\bar{\bar{\delta}}_1 - \bar{\bar{\delta}}_2) - 6\bar{G}_{42}\cos(\bar{\bar{\delta}}_1 - \bar{\bar{\delta}}_4)) \\
&+\bar{G}_{31}(7\bar{G}_{02}\cos(\bar{\bar{\delta}}_0 - \bar{\bar{\delta}}_3) \\
&-8\bar{G}_{22}\cos(\bar{\bar{\delta}}_2 - \bar{\bar{\delta}}_3) + 6\bar{G}_{42}\cos(\bar{\bar{\delta}}_3 - \bar{\bar{\delta}}_4))\Big] P_3(\cos\theta) \\
&+\frac{90}{49W_2}\Big[20\bar{G}_{22}^2 + \bar{G}_{42}(98\bar{G}_{20}\cos(\bar{\bar{\delta}}_0 - \bar{\bar{\delta}}_4) - 100\bar{G}_{22}\cos(\bar{\bar{\delta}}_2 - \bar{\bar{\delta}}_4) \\
&+ 27\bar{G}_{42})\Big] P_4(\cos\theta)\Big\} \\
&\equiv \frac{F_{n2}(q,\omega)}{4\pi}\left\{1 + \sum_{i=1}^{4} A_{n2i}(q,\omega) P_i(\cos\theta)\right\}, \qquad (3.129)
\end{aligned}
$$

where

$$F_{n2} = \frac{4\pi^2\omega}{(\omega - I_{n2})q^2} W_2; \quad W_2 = 35\bar{G}^2_{20} + 42\bar{G}^2_{11} + 63\bar{G}^2_{31} + 35\bar{G}^2_{02} + 50\bar{G}^2_{22} + 90\bar{G}^2_{42}. \tag{3.130}$$

Now only data on the dipole polarizability $\alpha^1_{C_N}(\omega, 0) \equiv \alpha_{C_N}(\omega)$ [see (1.125)–(1.127)] are available. So, we can correct dipole GOS at small q and determine only $G^1_{C_N}(\omega, 0) \equiv G_{C_N}(\omega)$. However, this GOS gives the main contribution to the absolute GOS value. The total fast electrons inelastic scattering cross-section with ionization of the nl subshell of the endohedral atom can be expressed via its photoionization cross-sections $\sigma_{nl,\varepsilon l\pm1}(\omega)$ given by

$$\sigma_{nl}(E) = \frac{c}{2\pi E} \int_{I_{nl}}^{E} |G_{C_N}(\omega)|^2 \left[|F_{l+1}(k)|^2 \sigma_{nl,\varepsilon l+1}(\omega) + |F_{l-1}(k)|^2 \sigma_{nl,\varepsilon l-1}(\omega) \right] \ln\left(\tilde{\varsigma}_n \frac{E}{\omega}\right) \frac{\mathrm{d}\omega}{\omega}, \tag{3.131}$$

where $\tilde{\varsigma}_n \sim 1$ is a constant that can be determined as a result of accurate calculations only.

To obtain the absolute cross section of inelastic scattering of a endohedral atom, one has to sum (3.131) over nl.

Just as (3.71), the expression (3.131) is valid in the frame of so-called logarithm accuracy, i.e., assuming that $\ln(E/\omega) \gg 1$.

As a by-product, one can obtain with the same logarithm accuracy the absolute inelastic scattering cross-section $\sigma_{C_N}(E)$ of a fast electron upon an empty fullerene. It is given by expression similar to (3.71)

$$\sigma_{C_N}(E) \simeq \frac{c}{2\pi E} \int_{I}^{E} \frac{\sigma_{C_N}(\omega)}{\omega} \ln\left(\varsigma_N \frac{4E}{\omega}\right) \mathrm{d}\omega, \tag{3.132}$$

where $\sigma_{C_N}(\omega)$ is the fullerenes photoionization cross-section.

While performing calculations with the help of (3.131) or (3.132), just as using (3.71), best of all is to put $\tilde{\varsigma}_N = 1$.

3.11 Bremsstrahlung of Fast Particles

One of most widely discussed inelastic scattering processes is Bremsstrahlung (BR)—emission of radiation in the process of deceleration of a charged particle in the field of atom [BLP]. We consider simultaneously two mechanisms—ordinary Bremsstrahlung (OR), in which target atom acts as a static potential and polarization radiation (PR) or "Atomic Bremsstrahlung" [3.23], where the photon is radiated by the target deformed in the scattering process.

In the lowest order of interaction between the projectile and deformed or polarized target, the amplitudes of both processes are depicted by the diagrams

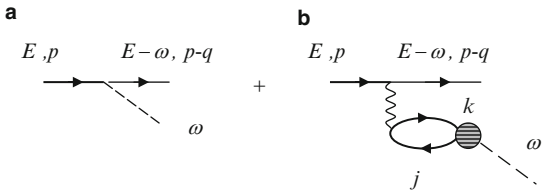

(3.133)

Analytic relation for the amplitude (3.133) of Bremsstrahlung can be presented according to [3.23] as

$$F_{\vec{p},\vec{p}-\vec{q}}(\omega) = \left\langle E, \vec{p} \left| \vec{e}\vec{d} \right| E-\omega, \vec{p}-\vec{q} \right\rangle + \sum_{\substack{k > F \\ j \le F}} \left\langle E, \vec{p}; j \left| U \right| E-\omega, \vec{p}-\vec{q}; k \right\rangle$$

$$\times \frac{2\omega_{kj}}{\omega^2 - \omega_{kj}^2 - i\omega\eta} \left\langle k \left| \vec{e}\vec{D}(\omega) \right| j \right\rangle. \tag{3.134}$$

where $\omega_{kj} = \varepsilon_k - \varepsilon_j$, $\eta \to +0$, $\vec{e}$ is the emitted photon polarization vector; $\vec{d}$ and $\vec{D}(\omega)$ are the dipole operator of electron–photon interaction in HF and RPAE [see (1.37)]. The first term in the right-hand side of (3.134) presents OB, while the second the PB contributions.

For intermediate electron energies the BR can be expressed via scattering phases, given by (3.8a) and (3.10), while the contribution of PR can be expressed via atomic polarizability, given by (1.86). For low velocities of the incoming and outgoing electrons, one can express the amplitude $F_{\vec{p},\vec{p}-\vec{q}}(\omega)$ via dipole polarizability of the atom given by (1.86) and the scattering shift $\delta_0(E)$ [see (3.8a)–(3.10)]

$$F_{\vec{p},\vec{p}-\vec{q}}(\omega) = \frac{2\pi}{\omega}\left[\frac{1}{\omega}\left(\frac{(\vec{e}\vec{p})-(\vec{e}\vec{q})}{p}\sin\delta_0(E) - \frac{(\vec{e}\vec{p})}{|\vec{p}-\vec{q}|}\sin\delta_0(E-\omega)\right) + 2\omega\frac{(\vec{e}\vec{q})}{q^2}\alpha_{\mathrm{d}}(\omega)\right]. \tag{3.135}$$

The expressions for fast electrons BR is simpler, being presented by the following amplitude:

$$F^{\nabla}_{\vec{p}\vec{q}}(\omega) = (\vec{p}\vec{q})\left[\frac{W(q)}{\omega} + \frac{4\pi\omega}{q^2}\alpha_{\mathrm{d}}(\omega, q)\right], \tag{3.136}$$

where $W(q)$ is the Fourier image of the Hartree field of the target atom $W(r)$:

$$W(r) = -\frac{Z}{r} + \int \frac{1}{|\vec{r}-\vec{r}'|}\rho(r')\mathrm{d}\vec{r}', \tag{3.137}$$

here $\rho(r)$ is the electron density. The generalized dipole polarizability $\alpha_{\rm d}(\omega, q)$ is defined by the expression similar to (3.119)

$$\alpha_{\rm d}(\omega,q) = \frac{3i}{(\vec{e}\vec{q})} \sum_{\substack{k>F \\ j\le F}} \left[\frac{\langle j \left| j_1(qr) P_1(\cos\theta_{qr}) \right| k \rangle \left\langle k \left| (\vec{e}\vec{D}(\omega)) \right| j \right\rangle}{\varepsilon_k + I_j - \omega - i\eta} \right.$$
$$\left. + \frac{\langle j \left| j_1(qr) P_1(\cos\theta_{qr}) \right| k \rangle \left\langle k \left| (\vec{e}\vec{D}(\omega)) \right| j \right\rangle}{\varepsilon_k + I_j + \omega - i\eta} \right], \tag{3.138}$$

here θ_{qr} is the angle between vectors $\vec{q}$ and $\vec{r}$. In the $q \to 0$ limit $\alpha_{\rm d}(\omega, q)_{q\to 0} \to \alpha_{\rm d}(\omega)$ that is given by (1.86). The BR spectrum $\mathrm{d}\sigma_{\rm BR}(\omega)/\mathrm{d}\omega$ is related to the BR amplitude $F^{\nabla}_{\vec{p}\vec{q}}(\omega)$ by the following equation:

$$\frac{\mathrm{d}\sigma_{\rm BR}(\omega)}{\mathrm{d}\omega} = \frac{\omega q}{16\pi^4 c^3 p^2} \int \left| F^{\nabla}_{\vec{p}\vec{q}}(\omega) \right|^2 \mathrm{d}\vec{q}\,\mathrm{d}\Omega_\gamma, \tag{3.139}$$

where $\mathrm{d}\Omega_\gamma$ is the solid angle of photon emission.

That leads to the following cross-section [3.24]:

$$\frac{\mathrm{d}\sigma_{\rm BR}(\omega)}{\mathrm{d}\omega} \approx \frac{16}{3}\frac{Z^2}{c^3 p^2 \omega} \ln 2pR + \frac{16}{3}\frac{\omega^3 |\alpha(\omega)|^2}{c^3 p^2} \ln\frac{p}{\omega R}. \tag{3.140}$$

Note that there is no interference term in (3.140), since PB is generated from long distances (small q), while OB comes from small distances (big q).

The expression for BR spectrum of fast electrons colliding with a fullerene can be obtained using (3.136), where $W(q)$ is substituted for the zero-thickness potential (1.105) by the following expression:

$$W(q) = -\frac{4\pi W_0 R}{q} \sin qR \tag{3.141}$$

For square well fullerenes potential (1.116) one has for

$$W(q) = -\frac{4\pi W_0}{q^3} \int_{q(R-\Delta_{\rm C}/2)}^{q(R+\Delta_{\rm C}/2)} t \sin t\,\mathrm{d}t. \tag{3.142}$$

The PR contribution can be obtained using (1.125) and (1.127).

3.12 Positron Scattering with Account of Polarization Interaction

Here, we will discuss the specifics of positron–atom scattering. The studies of positron–atom and positron–molecule scattering are a quite active area of research (see [3.25] and references therein). Of interest is to compare it to the electron collisions on the same objects. The mechanisms of projectile–target interaction are most transparent in the collision process at low energies. This is why we will concentrate here on this energy region.

In both cases, namely for the electron and positron scattering, the cross section is determined by the electrostatic and polarization potentials, by which the target acts upon the projectile. However, for incoming electrons, the exchange with the target's electrons is of importance. It does not exist for positrons at all. So, at first glance the positron scattering process looks as being simpler than that for electrons. Moreover, the positron–atom static potential, being in general repulsive, forces the positron to move into the areas of the target where the potential is the smallest, thus diminishing its overall action.

This is opposite to the case of electron–atom (molecule) collision. The contrast looks even stronger if one takes into account that, as it seems, the polarization potential for both, electrons and positrons, is attractive. Thus, for electrons the total potential had to be stronger than for positrons. Therefore, it seems at the first glance that any simple approach that is good for electrons had to work at least not worse for positrons. For instance, the second-order approximation to the polarization interaction, discussed in Sects. 3.3 and 3.4 is good for positron–atom scattering and only diagram (3.36a) contributes. One could expect this approach to be at least equally good in describing positron–atom scattering as for the electron–atom scattering. However, this view proved to be incorrect [3.26].

Indeed, the positron that is "pushed" out of the target can interact strongly with the temporarily, or virtually, excited electron that is outside the target. They form a kind of a bound state that can be called *virtual positronium*. This is a very important mechanism that dramatically affects the scattering cross section [3.26–3.31].

Diagrammatically, this mechanism is taken into account by going from (3.36a)—the only second-order diagram that describes positron polarization interaction—to the following one:

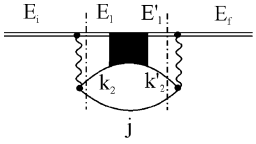

(3.143)

where the black square denotes the interaction of the positron, presented by a doubled line, that is taken into account nonperturbatively.

In the lowest order in the interaction between the incoming positron and atomic electrons, the analytical expression for positron scattering polarization interaction is given instead of (3.38) by

$$\left\langle E_i\ell \left\| \hat{\Sigma}^l(E) \right\| E_f\ell \right\rangle = \frac{1}{(2l+1)} \sum_{\substack{j \le F, L \\ \varepsilon_2 l_2 > F}} \times \int_0^\infty \frac{\left\langle E_i\ell, \varepsilon_j l_j \,\|V_L\|\, E_1\ell_1, \varepsilon_2\ell_2 \right\rangle \left\langle E_1\ell_1, \varepsilon_2\ell_2 \,\|V_\ell\|\, E_f\ell, \varepsilon_j l_j \right\rangle}{(2L+1)(E - E_1 - \varepsilon_2 + \varepsilon_j + i\delta)} \mathrm{d}E_1 \mathrm{d}\varepsilon_2. \quad (3.144)$$

where the second V_L substitutes U_L in (3.38).

The interaction between the positron and virtually excited atomic electron proved to be extremely important. Here, we will describe a method that permits to improve considerably the agreement with experiment and to give simple qualitative explanation of a large difference between cross sections for noble gases and their neighbors—alkali atoms. This method was suggested at first in [3.26] and developed further in [3.27–3.29]. The idea is to take into account all complexity of (3.89) simply by introducing the binding energy of the real *positronium* Ps, I_{Ps} into the energy denominator in (3.90):

$$\left\langle E_i\ell \left\| \hat{\Sigma}^l_{(\mathrm{Ps})}(E) \right\| E_f\ell \right\rangle = \frac{1}{(2l+1)} \sum_{\substack{j \le F, L \\ \varepsilon_2 l_2 > F}} \times \int_0^\infty \frac{\left\langle E_i\ell, \varepsilon_j l_j \,\|V_L\|\, E_1\ell_1, \varepsilon_2\ell_2 \right\rangle \left\langle E_1\ell_1, \varepsilon_2\ell_2 \,\|V_\ell\|\, E_f\ell, \varepsilon_j l_j \right\rangle}{(2L+1)(E - E_1 - \varepsilon_2 + \varepsilon_j + I_{\mathrm{Ps}} + i\delta)} \mathrm{d}E_1 \mathrm{d}\varepsilon_2. \quad (3.145)$$

Since the introduction of this approach in [3.26], a number of other calculations were performed (e.g., [3.30,3.31]), which exploit the idea of the virtual positronium formation but uses a much more complicated method, namely substituting the positron–electron wave function $E_1\ell_1, \varepsilon_2\ell_2\rangle$ in (3.140) by a wave function of a free positronium, that is not affected by the field of the remaining ion.

The elastic $\sigma^{\mathrm{el}+}(E)$, inelastic $\sigma^{\mathrm{in}+}(E)$, and total $\sigma^{\mathrm{in}+}(E)$ scattering cross sections of a positron with energy E is expressed via the partial scattering phases $\delta_\ell(E)$ as is presented by (3.14)–(3.16).

The first step of our approach is the HF calculations, which means HF for the target atom and frozen core for the incoming positron, naturally without exchange of the positron and the core electrons. Thus, to calculate the HF positron phase shifts $\delta^{\mathrm{HF}}_\ell(E)$, the following equation was solved for the positron wave function $\varphi_{e+}(\vec{r})$:

$$\left[-\frac{\Delta}{2} + \frac{Z}{r} - \int \frac{\mathrm{d}\vec{r}\rho(r')}{\left|\vec{r} - \vec{r'}\right|} \right] \varphi_{e+}(\vec{r}) = E\varphi_{e+}(\vec{r}), \quad (3.146)$$

here $\rho(r)$ is the atomic electron density. The asymptotes in r of the radial part $P^{e+}_{E\ell}(r)$ of $\varphi_{e+}(\vec{r})$ determines the phase shift (3.8a).

A prominent difference between the HF and experimental results at low positron energies in positron–atom elastic scattering exists for almost all up to now considered atoms, for example, in He. So, the polarization interaction must be taken into account. Assuming, that the polarization interaction $\hat{\sum}_{\mathrm{Ps}}$ is weak, one can express the correction $\Delta\delta_\ell(E)$ to the HF partial positron scattering phase due to the action of $\hat{\sum}_{\mathrm{Ps}}$ by the following formula:

$$\Delta\delta_\ell(E) = -\pi \left\langle E\ell \left\| \hat{\sum}{}^{l}_{\mathrm{Ps}}(E) \right\| E\ell \right\rangle, \tag{3.147}$$

where $\hat{\sum}{}^{l}_{\mathrm{Ps}}(E)$ is the ℓ-component of $\hat{\sum}_{(\mathrm{Ps})}$ determined by (3.145).

The scattering cross section with account of polarization interaction is determined by (3.14)–(3.16) where $\delta_l^{\mathrm{HF}}(E)$ is substituted by the phases $\delta_\ell(E) = \delta_\ell^{\mathrm{HF}}(E) + \Delta\delta_\ell(E)$ for E up to $E \le I \quad E < I$, I being the target atom ionization potential. For higher positron energies, the scattering phases given by (3.147) are complex and the imaginary part $\mathrm{Im}\Delta\delta_\ell(E) \equiv \mu_l(E)$ determines the inelastic scattering cross section of positron by an atom.

The elastic scattering cross section for $E > I$ is presented by (3.14). In fact, the method described in [3.26, 3.29], just as (3.145), can go in some aspects well beyond the simple second-order perturbation theory in inter-electron interaction. Namely, by calculating the HF wave function of the electron $\varepsilon_2 l_2$ in the atomic field with the vacancy i, it takes into account important higher order corrections.

Thus improved, polarization interaction even in its lowest order gives good results for elastic scattering of electrons on noble gases. This interaction depends upon projectile energy, is nonlocal and does not contain free adjustable parameters. Far from an atom it can be approximated as polarization potential

$$V_{\mathrm{pol}} = \frac{-\alpha(\varepsilon)}{2r^4}. \tag{3.148}$$

where $\alpha(\varepsilon)$, contrary to (3.7) and (3.35), is the atom's dipole *dynamical* polarizability, ε is the mean excitation energy of the incoming electron in the intermediate state.

The next after HF steps in our consideration of positron–atom scattering is the account of polarization interaction (3.38) in the lowest order, in the same manner as it is done for electron–atom scattering. The results obtained are improving the situation as to the correspondence to experimental data a little bit, but the inclusion of virtual positronium formation is required, which is achieved by using (3.143) as polarization interaction.

The account of virtual positronium binding performed in (3.143) leads instead of (3.146) to the following polarization potential:

$$V_{\mathrm{pol}} = \frac{-\alpha(\varepsilon + I_{\mathrm{Ps}})}{2r^4}. \tag{3.149}$$

This equation permits to predict an interesting phenomenon—the polarization interaction can be both, attractive, as it is usually believed, and repulsive [3.32,3.33]. The reason of this phenomenon is the possibility of alteration of the sign of polarizability. Static polarizability is always positive. Indeed, for negative effective energy $(\varepsilon - I_{\mathrm{Ps}})$ the polarizability can become negative thus leading to repulsion instead of attraction nature of the polarization interaction (3.7). In such a case, the polarization potential will enhance the action of the Hartree potential. It may affect upon the scattering cross section very essential.

The repulsive polarization potential V^{+}_{pol} takes place in alkali atoms. Perhaps it could explain the fact that positron scattering cross section at low energies on alkali atoms is much bigger than that on neighboring noble gas atoms.

Note that potential (3.149) leads to phases that do not obey prescriptions of either (3.20) or (3.21) formulas. This is a consequence of anomalous behavior of polarization interaction (3.145) that leads to imaginary part of the phase shift (3.147) already at $E = 0$ that signals a negative reaction threshold. In potential (3.149) it is reflected by the presence of $\mathrm{Im}\alpha(I_{\mathrm{Ps}}) \neq 0$.

Concluding this chapter, we find it proper to give some references to relatively recent review-type papers that describe modern state of the field and developing methods presented here [3.34–3.37].

References

3.1. Hodgson PE (1963) The optical model of elastic scattering. Clarendon Press, Oxford, p. 211
3.2. Baz' AI, Zeldovich YaB, Perelomov AM (1969) Scattering, Reactions and Decay in non-relativistic quantum mechanics. Israel Program for Scientific Translation, Jerusalem, p. 544
3.3. Drukarev GF (1987) Collisions of electrons with atoms and molecules. Plenum Press, New York, NY, p 252
3.4. Galitsky VM, Nikitin EE, Smirnov BM (1981) Theory of atomic particles collisions. Nauka, Moscow, p 255 (in Russian)
3.5. Mott NF, Massey HSW (1965) The theory of atomic collisions. Clarendon Press, Oxford, p. 858
3.6. Kelly HP (1968) Optical-potential calculation of electron–hydrogen singlet scattering. Phys. Rev. 171(1):54–60
3.7. Amusia MYa, Cherepkov NA (1975) Many-electron correlations in the scattering processes. Case Stud At Phys 5:47–179
3.8. Chernysheva LV, Amusia MYa, Davidovic D, Cherepkov NA (1980) Numerical calculation of scattering phases in the simplified random-phase approximation with exchange. The Ioffe Institute No. 663, Leningrad, p 48 (in Russian)
3.9. Amusia MYa, Cherepkov NA, Chernysheva LV, Shapiro SG (1974) Elastic scattering of slow electrons and level shifts in Ar. Phys Lett A 46(6):387–388
3.10. Amusia MYa, Tanchic A, Cherepkov NA, Chernysheva LV, Shapiro SG (1975) Slow electron–atom elastic scattering. Sov JETP 68(6):2023–2031
3.11. Amusia MYa, Cherepkov NA, Chernysheva LV, Davidovich DM, Radojevich V (1982) Slow electron elastic scattering on argon. Phys Rev A 25(1):219–225
3.12. Abrikosov AA, Gor'kov LP, Dzyaloshinskii IE (1965) Quantum field theoretical methods in statistical physics, 2nd edn. Pergamon Press, Oxford, p. 365 (xii)

3.13. Amusia MYa, Dolmatov VK (1990) Elastic scattering of electrons upon atoms with semi-filled shells. Sov JETP 97(4):1129–1139
3.14. Amusia MYa, Cherepkov NA, Yanev R, Sheftel SI, Zhivanovich Zh (1973) The role of many-electron correlations in fast electron–atom inelastic collisions. J Phys B At Mol Phys 6:1028–1039
3.15. Amusia MYa, Chernysheva LV, Felfli Z, Msezane AZ (2002) Reinterpretation of the recently measured absolute generalized oscillator strength for the Ar 3p–4p transition. Phys Rev A 65(5):54701
3.16. Inokuti M (1971) Inelastic collisions of fast charged particles with atoms and molecules—The Bethe theory revisited. Rev Mod Phys 43:297–347
3.17. Bethe H (1930) Zur Theorie des Durchgangs scneller Korpuskularstrahlen durch Materie Ann Phys 397:325–400
3.18. Amusia MYa, Chernysheva LV, Liverts E (2012) Angular distributions of secondary electrons in fast particle–atom scattering. Phys Rev A 85:042722-1-12
3.19. Pratt RH (2005) Recent theoretical developments in photon–atom scattering. Radiat Phys Chem 74(6):411–418
3.20. Amusia MYa, Chernysheva LV, Felfli Z, Msezane AZ (2002) Compton scattering upon heavy atoms with account of many-electron correlations. Surf Rev Lett 9(2):1155–1160
3.21. Amusia MYa, Chernysheva LV, Felfli Z, Msezane AZ (2002) Cross sections of discrete-level excitations of noble-gas atoms in compton scattering. Phys Rev A 65(6):62705
3.22. Amusia MYa, Chernysheva LV, Felfli Z, Msezane AZ (2007) Octupole contributions to the generalized oscillator strengths of discrete dipole transitions in noble gases. Phys Rev A 75:062703
3.23. Amusia MYa (1990) Bremsstrahlung. Energoatomizdat, Moscow, 204 pp (in Russian)
3.24. Amusia MYa, Buimistrov VM, Tsytovich VN, Zon BA (1992) In: Tsytovich VN, Oiringel IM (eds) Polarization bremsstrahlung. Plenum Press, New York, p. 367
3.25. Gribakin GF, Ludlow J (2004) Phys Rev A 70:0327203.
3.26. Amusia MYa, Cherepkov NA, Chernysheva LV, Shapiro SG (1976) The elastic scattering of slow positrons on He atom. J Phys B **9**:L531–L534
3.27. Ficocelli Varracchio E (1990) J Phys B At Mol Opt Phys 23:L779–L785
3.28. Ficocelli Varracchio E, Parcell LA (1992) Positron impact excitation of the $n = 2$ and $n = 3$ manifolds of He in the RPA formulation. J Phys B At Mol Opt Phys 25:3037–3048
3.29. Amusia MYa, Cherepkov NA, Chernysheva LV (2003) Elastic scattering of slow positrons on atoms. JETP 124, 1(7):1–9
3.30. Gribakin GF, King WA (1994) The effect of virtual positronium formation on positron–atom scattering. J Phys B At Mol Opt Phys 27:2639–2646
3.31. Dzuba VA, Flambaum VV, Gribakin GF, King WA (1996) Many-body calculations of positron scattering and annihilation from noble-gas atoms. J Phys B At Mol Opt Phys 29:3151–3176
3.32. Amusia MYa, Taulbjerg K (1995) The repulsive polarization potential of the "positron–alkali atom" Abstract of ICPEAC-XIX, p. 364
3.33. Batty CJ, Friedman E, Gal A (1997) Strong interaction physics from hadronic atoms. Phys Rep 287(5):385–445
3.34. Amusia MYa (1997) The many-body approach to electron–atom collisions. In: Boyle JJ, Pindzola MS (eds) Many-body atomic physics. Cambridge University Press, Cambridge, CA pp 185–212
3.35. Amusia MYa (2006) Many-body theory of atomic structure and processes. In: Drake G (ed) Atomic, molecular and optical physics handbook, 2nd edn. Springer, Hiedelberg (Chap. 23)
3.36. Amusia MYa (2007) Photoionization and vacancy decay of endohedral atoms, review. J Electron Spectr Relat Phenom 161:112–120
3.37. Amusia MYa (2007) Fast electron scattering as a tool to study target's structure, review. J Electron Spectr Relat Phenom 159:81–90

Chapter 4
Electron Scattering: Results of Calculations

4.1 Data Representation and Used Formulas

In this chapter, we collect figures and tables that present the data obtained in the investigation of elastic and inelastic scattering cross-sections of slow, medium-energy, and fast electrons e^- and relatively slow positrons e^+. We will present total and partial, different in angle and energy, Compton scattering cross-sections for a number of atoms and ions, both positive and negative. Where it is available, experimental data will be presented.

The numbering of figures is organized similar to Chap. 2, i.e., as follows: at first, goes the number of the respective Chapter, the next letter denotes the considered atom as in the periodic table of chemical elements; the next goes the consecutive number of the figure in this Chapter; the next small letter stands for the considered characteristic or property; the final number marks the considered figure among all other that illustrated the considered characteristic or property for this atom. For example, Fig. 4.51_Ar_a1 designates the first figure of the characteristic *a* of atom Ar. Denoted characteristics are as follows:

(a) Total elastic and inelastic electron or positron scattering cross-sections in Hartree–Fock and simplified RPAE–SRPAE version.
(b) Partial in angular momentum elastic or inelastic electron or positron scattering cross-sections in Hartree–Fock and simplified RPAE–SRPAE version.
(c) Differential elastic and inelastic electron scattering cross-sections in the same approximations.
(d) Electron or positron scattering cross-sections s, p, d, f, etc., phases.
(e) Densities of generalized oscillator strength (GOSes), total and partial, in Hartree–Fock and RPAE.
(f) Generalized oscillator strengths (GOSes) of discrete levels excitations, usually dipole and octupole, quadrupole and monopole; in some cases even of higher multipolarity, in Hartree–Fock and RPAE.

M. Amusia et al., *Handbook of Theoretical Atomic Physics*,
DOI 10.1007/978-3-642-24752-1_4, © Springer-Verlag Berlin Heidelberg 2012

(g) Differential in photon emission angle or energy total and partial Compton scattering cross-sections with ionization or excitation of discrete levels, in HF or in RPAE.
(h) Compton scattering cross-sections for discrete levels.
(i) Positron–atom scattering cross-sections—elastic and inelastic.
(j) Partial elastic and inelastic positron scattering cross-sections.
(k) Positron scattering cross-sections p-, d-, and f-phases.
(l) Fast electron inelastic scattering cross-sections.
(m) Secondary electron angular anisotropy parameters in fast electron–atom scattering.
(n) Characteristics of fullerenes and endohedral atoms.

The last digit presents the number of figure in the considered group. Not all mentioned above data are, however, available for each atom. In such cases, not all letters or digits will be used in numbering of a figure. In some cases we will compare the results of our calculations with experimental data.

The following formulas were employed to describe different characteristics of electron, Compton, and positron scattering.

The elastic, inelastic, and total scattering cross-sections are determined using (3.14) [(3.17)], (3.15), and (3.16), respectively. The differential in angle scattering cross-section is obtained using (3.13). The HF s-, p-, d-, and f-phase shifts are found from asymptotic presentation of the HF wave function of colliding electron or positron using (3.8a) or (3.8b). The polarization correction to it in the frame of simplified RPAE is obtained from (3.46) by solving (3.45) with polarization interaction taken from (3.38) and (3.39).

Densities of generalized oscillator strengths, both total and partial, in HF are obtained using (3.58) while in RPAE they are given by (3.63). GOSes for semifilled shells are obtained using (3.107) and (3.111). Good estimation for total fast electron inelastic scattering cross-sections is obtained using (3.70) and (3.71) with $\varsigma_n = \varsigma = 1$ in the so-called logarithmic approximation $\sigma_{\mathrm{In}}(E)$ and with the first nonvanishing nonlogarithmic correction to it $\sigma_{\mathrm{In}}^{(1)}(E)$.

Angular distribution of atomic electrons knocked out in fast electron–atom scattering is obtained using (3.75), (3.77), and (3.79). Angular anisotropy nondipole parameters for atomic electrons knocked out in fast electron–atom scattering are obtained using (3.82) at $q \to 0$. Nondipole parameters for GOSes and for photoionization are compared using (3.84a), (3.84b), and (3.83). It is more convenient to draw weighted GOS $F_{nl}^{(w)}(q,\omega)$ that differs from the GOS $F_{nl}(q,\omega)$ (3.73) by an extra factor $(\omega - I_{nl})$, so that $F_{nl}^{(w)}(q,\omega) = (\omega - I_{nl})F_{nl}(q,\omega)$ [see (3.73b)]. This permits to eliminate the sharp increase of $F_{nl}(q,\omega)$ at small $(\omega - I_{nl})$ on the corresponding figures.

GOSes for semifilled subshells in HF and RPAE are obtained using (3.107) and (3.111).

The differential in photon emission angle total and partial Compton scattering cross-section is determined by (3.89) and (3.91). The same, but partial in transferred to the target atom angular momentum Compton scattering cross-sections are

obtained using (3.78) and (3.79). The cross-section for discrete level Compton excitation is given by (3.93). Compton scattering cross-section ratios to Thomson scattering cross-sections are obtained using (3.94). The integrated over emitted photon scattering angle Compton s in HF and RPAE are given by (3.100) and (3.101).

GOSes for endohedrals A@C_{60} are obtained with account of reflection of the electron knocked out from A and with polarization of the virtual photon, by exchanging of which the fast electron interacts with the atom A from A@C_{60}. The reflection is taken into account using (3.115) and (3.116), while account of polarization with reflection is achieved using (3.123) and (3.124). In calculations only dipole polarization was taken into account, i.e., $|\tilde{G}^1_{C_{60}}(\omega, q)|^2 \equiv S_{C_{60}}(\omega, q) \neq 1$. The angular anisotropy parameters are found using (3.124)–(3.126). We substitute $S_{C_N}(\omega, q)$ by $S_{C_{60}}(\omega)$ determined by (1.120) and (1.125)–(1.127) (see Fig. 2.351_C_{60}_g2).

The elastic, inelastic, and total positron scattering cross-sections are obtained using (3.14)–(3.16) with Hartree phases and polarization corrections given by (3.147) and (3.145).

Let us remind, that as it was already noted in the Chap. 2, our purpose is not to obtain the currently most accurate theoretical description of the experimental data of a particular atom or an ion, but to carry out massive calculations in the best suitable for such purpose approximation, i.e., in RPAE or its simplified version SRPAE. We employ also some generalizations of it. Presenting data, we demonstrate by comparison with HF results the importance of multielectronic correlations.

In essence, our purpose is to create a new initial approach that would stimulate subsequent carrying out of measurements that are more exact and more sophisticated calculations that are necessary for new data interpretation.

As in Chap. 2 and for convenience of the reader, we consider atoms and ions according to the group they belong to in the periodic table of elements, and inside each group according to their atomic number, with the only exception that we start with atoms of noble gases.

4.2 Atoms of Noble Gases

In this section, we present results of our already published and new calculations of total and partial cross-sections of electrons and positrons elastic scattering on all atoms of noble gases in HF and with inclusion of polarization interaction calculated in the frame of simplified random phase approximation with exchange-SRPAE (see Sects. 3.3 and 3.4 and [AICC]). For positron scattering, we also improve SRPAE by including the virtual formation of positronium in intermediate states (see Sect. 3.12).

In formation of polarization interaction, the excitations of the following subshells are taken into account: $1s^2$ in He, $2s^2$, $2p^6$ in Ne, $3s^2$, $3p^6$ in Ar, $3d^{10}$, $4s^2$, $4p^6$ in Kr, and $4d^{10}$, $5s^2$, $5p^6$ in Xe. In the same approximation, s, p, d, f phases of scattering and corresponding partial cross-sections are calculated. Results of

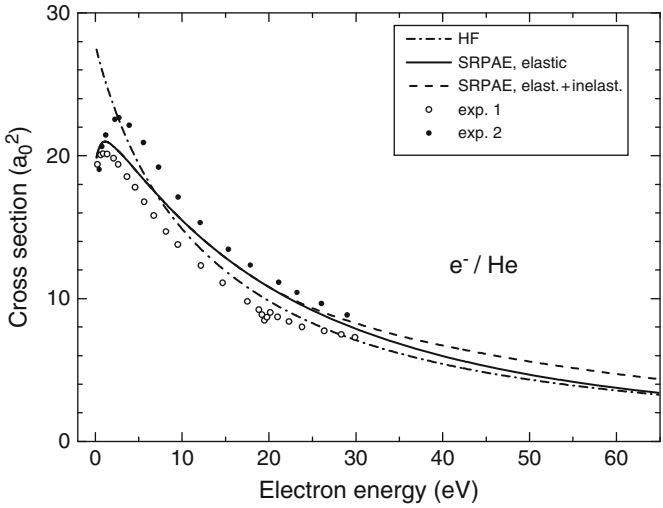

Fig. 4.1_He_a1 Cross-sections of elastic (in HF and SRPAE) and inelastic (in SRPAE) electron scattering on He atom [4.1, 4.2]. Experiment is from [4.3–4.5]

differential in scattering angle cross-sections for some energy are submitted. The generalized oscillator strengths (GOSes) and cross-sections of Compton scattering of photons with account of RPAE correlations of mentioned above electrons are presented. GOSes and cross-sections of Compton excitation of several first discrete levels of some atoms of noble gases are submitted. GOSes for $3d_{5/2}$, $3d_{3/2}$ electrons Xe are also given.

Figures 4.1–4.21 (He) show the results of calculations for He.

Figure 4.1_He_a1 shows the cross-section of elastic (in HF and SRPAE) and inelastic (in SRPAE) electron scattering on atom He (see [4.1, 4.2]). Experiment is from [4.3–4.5]. The SRPAE corrections are noticeable at small scattering energies, leading to a small maximum at $E = 0$. Inelastic cross-section is much smaller than the elastic.

Figure 4.2_He_b1 shows the contribution of s-, p-, d-, f-partial waves to elastic scattering cross-section of electrons on atom He. As it should be, at small energies the contribution of s-wave dominates. Contributions of other waves increase from energy $E = 0$. Particularly fast is the increase of the p-wave contribution.

Figure 4.3_He_c1 shows the differential in angle cross-sections of electron scattering on atom He for various linear incoming electron moment p. The cross-sections are dominated by forward scattering maxima and have much smaller backscattering maxima.

Figure 4.4_He_d1 shows the various partial wave phases of scattering of electrons upon He atom. At linear moment $p \to 0$ all but s-phases tend to zero. As to δ_s, at $p \to 0$ it tends to π [see (3.21)]. At $p \to 0$ the s-wave phase differs from others by the sign of it derivative as a function of E.

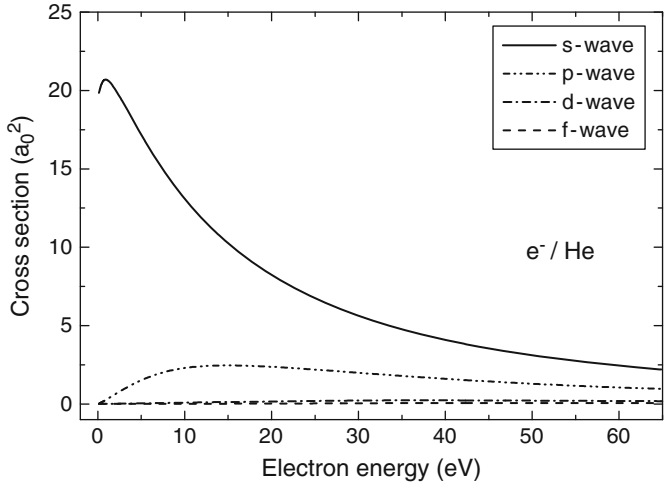

Fig. 4.2_He_b1 Contribution of partial waves to cross-section of elastic electron scattering on atom He

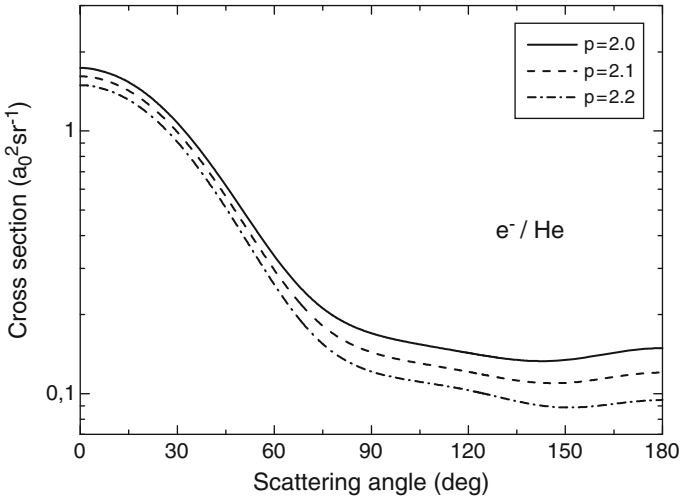

Fig. 4.3_He_c1 Differential in angle cross-section of electron scattering with various linear moments p on atom He

Figure 4.5_He_e1 shows the densities of monopole GOSes for He atom in RPAE as function of the energy transferred to the atom at various q (see [4.6, 4.7]). With growth of q at first appear a maximum at He ionization threshold that with subsequent q growth moves to higher and higher ω.

Figure 4.6_He_e2 shows the densities of dipole GOSes for He atom in RPAE as function of the energy transferred to the atom at various values q (see [4.7]). While

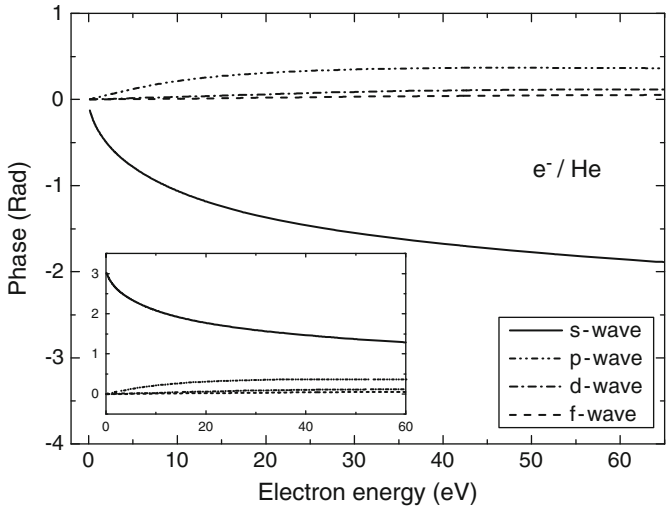

Fig. 4.4_He_d1 Phases of various partial waves in electron scattering on atom He

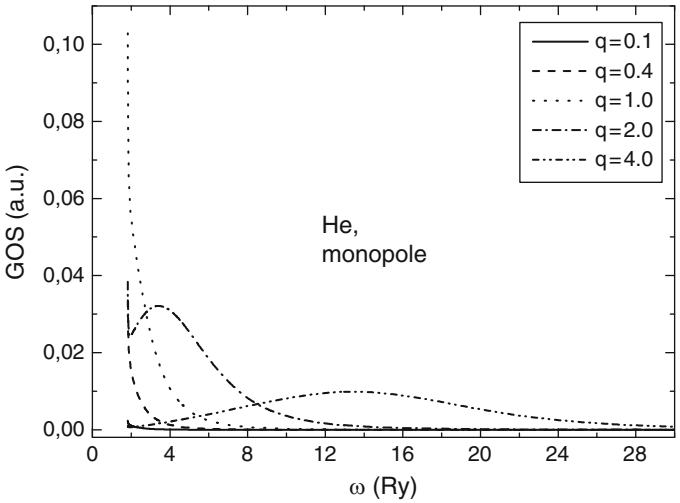

Fig. 4.5_He_e1 Density of monopole generalized oscillator strengths as a function of the energy transferred to atom at various q for He atom in RPAE (see [4.6, 4.7])

at small q GOSes are a rapidly decreasing function of ω, it acquires a maximum at ionization threshold with q growing. With subsequent increase of q the maximum rapidly moves toward higher and higher ω.

Figure 4.7_He_e3 shows the densities of quadrupole GOSes of He in RPAE as a function of the energy transferred to the atom at various values of q (see [4.7]).

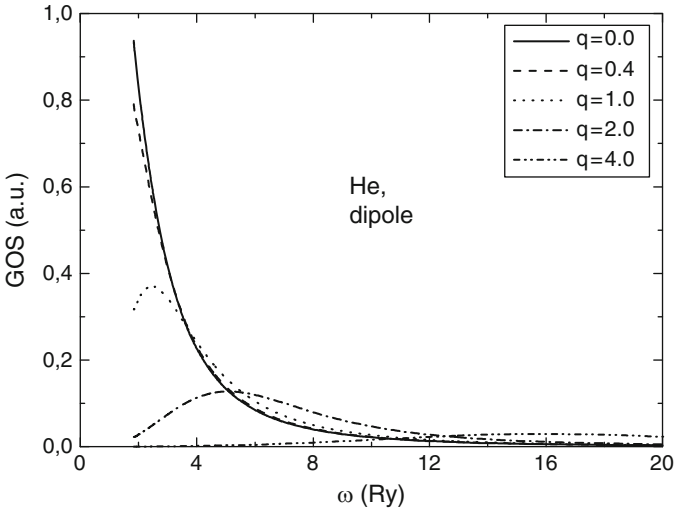

Fig. 4.6_He_e2 Density of dipole generalized oscillator strengths as function of the energy transferred to atom at various values q for He atom in RPAE (see [4.7])

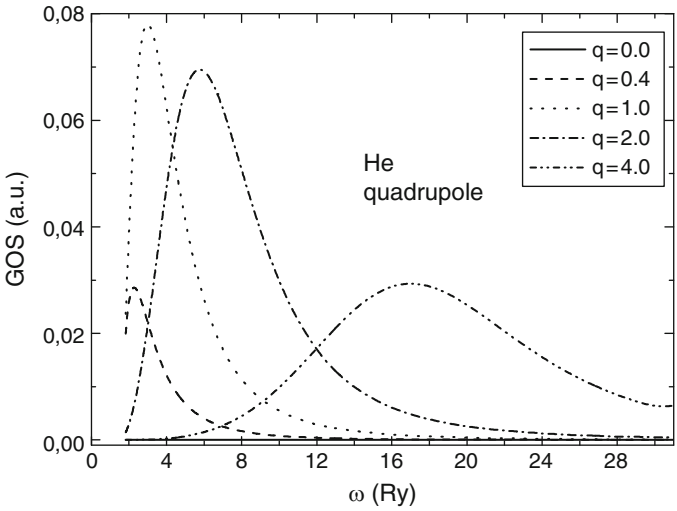

Fig. 4.7_He_e3 Density of quadrupole generalized oscillator strengths as function of the energy transferred to atom at various q of He in RPAE (see [4.7])

With q growth, a near threshold maximum appears that rapidly moves toward higher ω with growth of q.

Figure 4.8_He_f1 shows the results for GOSes of discrete monopole excitations for He from $1s$-state ($1s$–$2s$, $1s$–$3s$, $1s$–$4s$) as functions of q^2 transferred to the atom

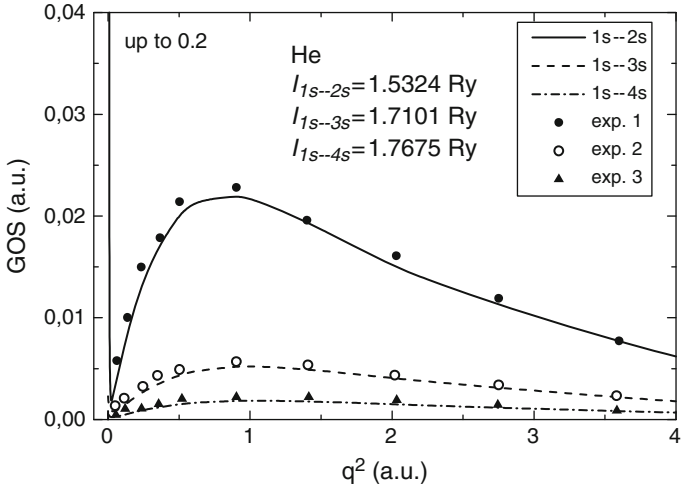

Fig. 4.8_He_f1 Generalized oscillator strengths of discrete monopole excitations from 1*s*-state (1*s*–2*s*, 1*s*–3*s*, 1*s*–4*s*) as functions of the square moment transferred to atom for He (see [4.8]). Experiment is from [4.8]

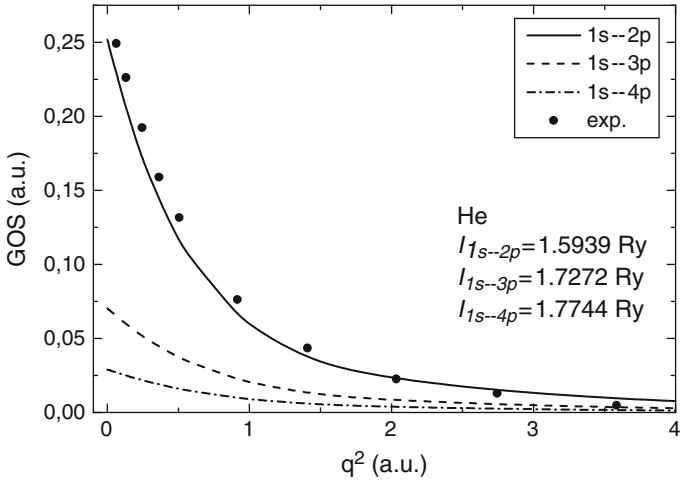

Fig. 4.9_He_f2 Generalized oscillator strengths of discrete dipole excitations from 1*s*-state as functions of square moment transferred to atom for He. Experiment is from [4.8]

(see [4.7]). Experimental data are taken from [4.8]. The agreement with experiment that is able to distinguish rather close laying discrete levels is very good.

Figure 4.9_He_f2 shows the GOSes of discrete dipole excitations for He from 1*s*-state (1*s*–2*p*, 1*s*–3*p*, 1*s*–4*p*) as functions of q^2 transferred to the atom. Experimental data are taken from [4.8]. The agreement "experiment–calculation" is good.

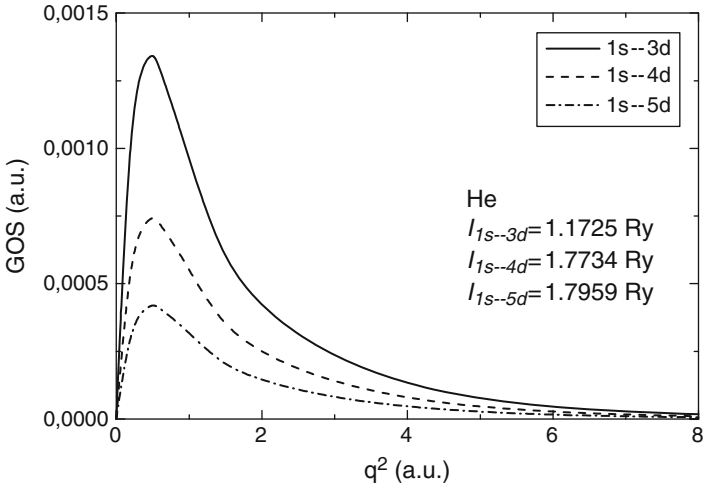

Fig. 4.10_He_f3 Generalized oscillator strengths of discrete quadrupole excitations from 1s-state as functions of square moment transferred to atom for He

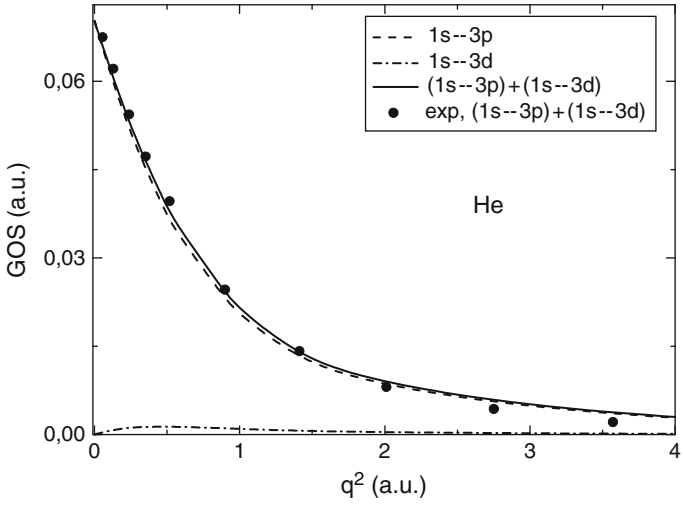

Fig. 4.11_He_f4 Generalized oscillator strengths of discrete dipole 1s–3p and quadrupole 1s–4d excitations as functions of square moment transferred to atom and their sum for He. Experiment is from [4.8]

Figure 4.10_He_f3 shows the GOSes of discrete quadrupole excitations for He from 1s-state (1s–3d, 1s–4d, 1s–5d) as functions of q^2 transferred to atom. It is seen as a quadrupole maximum the position of which is almost the same for all three levels.

Figure 4.11_He_f4 shows the GOSes of discrete dipole 1s–3p and quadrupole 1s–3d excitations for He as functions of q^2 transferred to the atom and their sum.

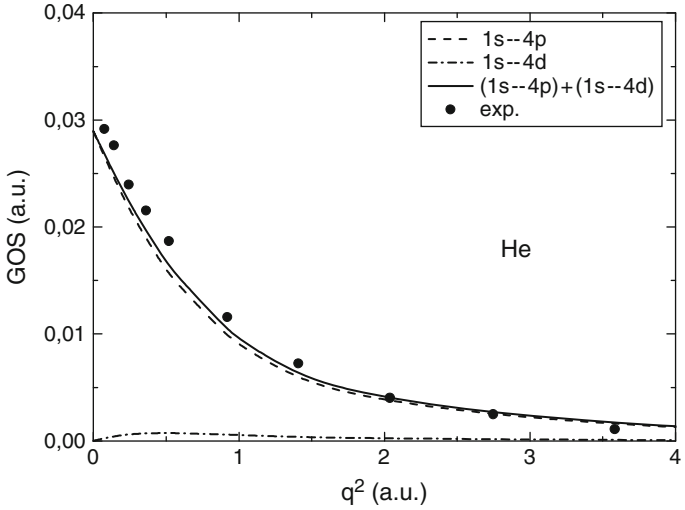

Fig. 4.12_He_f5 Generalized oscillator strengths of discrete dipole $1s$–$4p$ and quadrupole $1s$–$4d$ excitations as functions of square moment transferred to atom and their sum for He. Experiment is from [4.8]

Experimental data are taken from [4.8]. The combination of dipole and quadrupole levels is of interest, because they are experimentally almost indistinguishable since they have very close excitation energy. However, the contribution of quadrupole transition is small.

Figure 4.12_He_f5 shows the GOSes of discrete dipole $1s$–$4p$ and quadrupole $1s$–$4d$ excitations for He as functions of q^2 transferred to the atom and their sum. Experimental data are taken from [4.8]. The situation is similar to that shown in Fig. 4.11_He_f4.

Figure 4.13_He_i1 shows the cross-section of elastic (in HF and SRPAE) and inelastic (in SRPAE) scattering of positrons on He atom. Note that SRPAE for $(e^+ + A)$-scattering takes into account formation of virtual positronium (see [4.9, 4.10]). The contribution of inelastic scattering down to positron energy of about 16 eV is small. Experiment is taken from [4.11].

Figure 4.14_He_j1 shows the contribution of partial waves to the cross-section of elastic positron scattering on atom He in SRPAE. It is seen that s-wave contribution in the considered energy region dominates. The next in importance goes the p-wave with a maximum in the region of Ramsauer minimum in the s-wave contribution.

Figure 4.15_He_k1 shows the phases of various partial waves in positron scattering on He atom. The s-phase increases from $E = 0$ and after reaching a maximum at about 1 eV, being positive, starts to decrease, crosses the zero axis, and then continues decreasing. Other phases monotonically increase with growth of energy starting from $E = 0$. At some E they reach a maximum.

Figure 4.16_He_l1 shows the multiplied by incoming electron energy cross-section of inelastic scattering of fast electrons on atom He in logarithmic approximation $E\sigma_{\text{In}}(E)$. It is seen that this function at high E increases slowly.

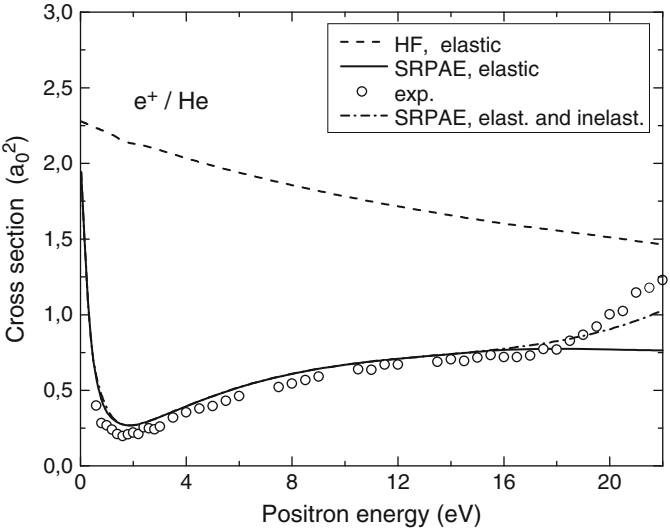

Fig. 4.13_He_i1 Cross-sections of elastic (in HF and SRPAE) and inelastic (in SRPAE) positron scattering on He atom (see [4.9, 4.10]). Experiment is from [4.11]

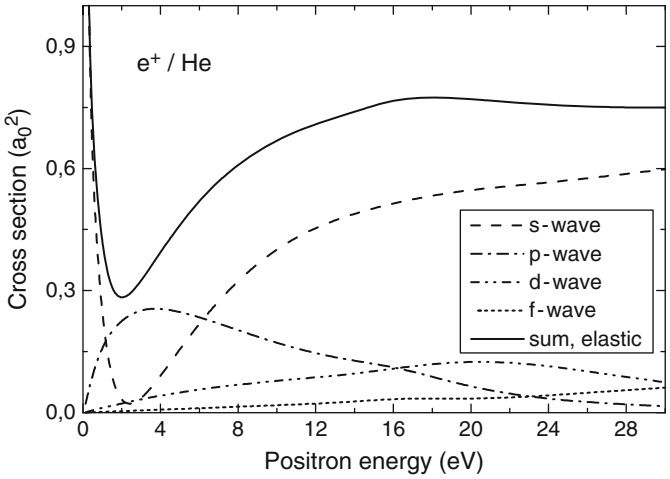

Fig. 4.14_He_j1 Contribution of partial waves to cross-section of elastic positron scattering on atom He in SRPAE

The cross-section is presented from $E = I$ for completeness only, since the logarithmic approximation is valid if $\ln(E/I) \gg 1$.

Figure 4.17_He_l2 shows the multiplied by incoming electron energy nonlogarithmic correction to the cross-section of inelastic scattering of fast electrons on He atom $E\sigma_{\text{In}}^{(1)}(E)$. It is seen that this function stops to grow already at $E = 10\,\text{Ry}$.

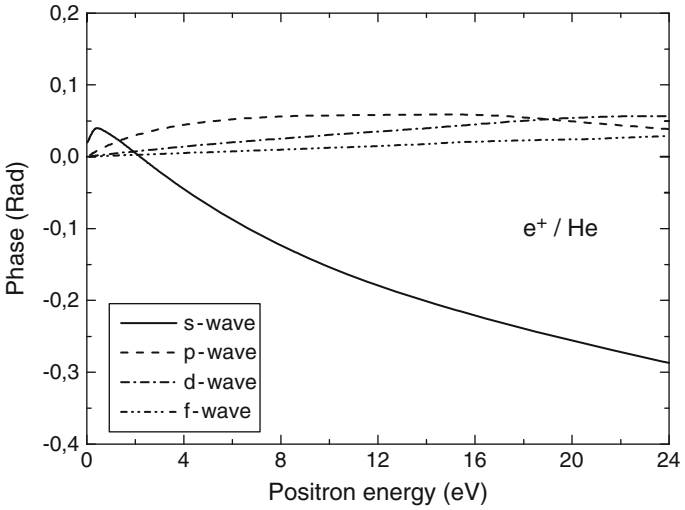

Fig. 4.15_He_k1 Phases of various partial waves in positron scattering on He atom

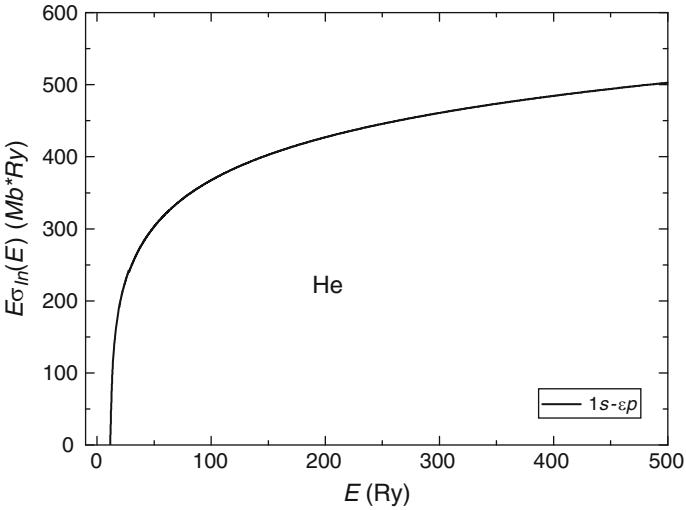

Fig. 4.16_He_l1 Multiplied by incoming electron energy cross-section of inelastic scattering of fast electrons in the logarithmic approximation

Figure 4.18_He_m1 shows the weighted differential in emission angle GOSes of knocked-out electron in fast projectile–He atom collision in HF, given by (3.73b) at magic angle $P_2(\cos\theta_m) = 0$ and a set of q values $q = 0.1$, 0.6, 1.1, 1.6, and 2.1. GOSes form a maximum that for small q is similar, as it should be, to the photoionization cross-section (see Fig. 2.1_He_a1). With ω growth one can see

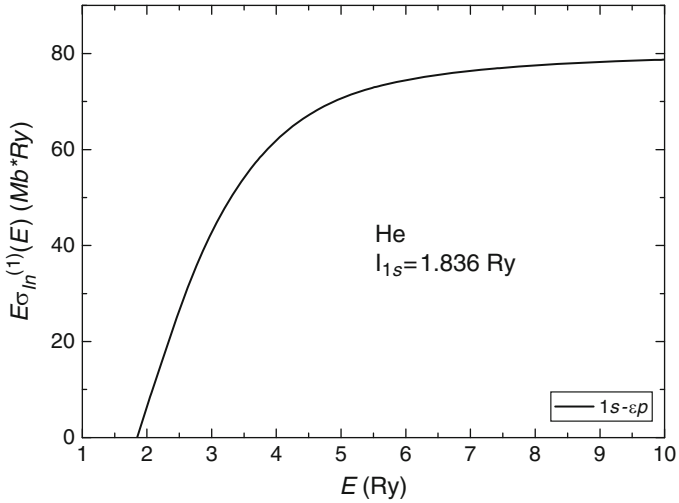

Fig. 4.17_He_l2 Nonlogarithmic correction to the multiplied by incoming electron energy cross-section of inelastic scattering of fast electrons

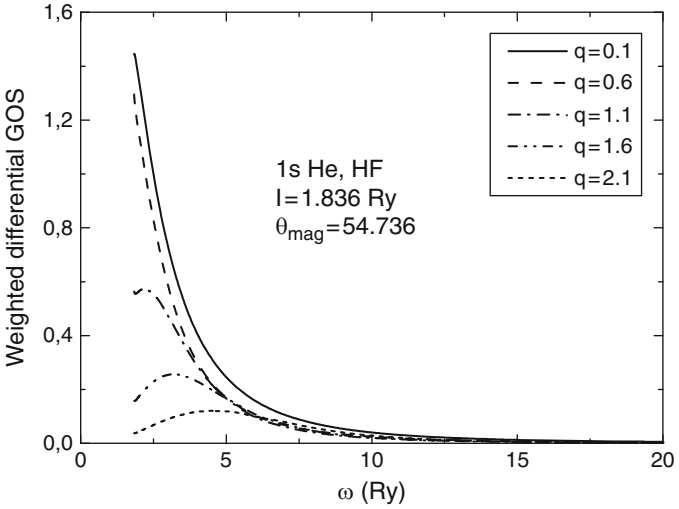

Fig. 4.18_He_m1 Weighted differential generalized oscillator strength in HF given by (3.73b) at magic angle $P_2(\cos\theta_m) = 0$ of He at different q

second and third maximums. With increase of q the GOS maximum decreases rather fast moving at the same time from $1s$ threshold to higher ω.

Figure 4.19_He_m2 shows the angular anisotropy parameters of knocked-out electrons in fast projectile–atom collision a_{1si} given by (3.75) as functions of ω at $q = 0.1$ in HF for He. The dipole parameter a_{1s2} is, as it should be for $q = 0.1$,

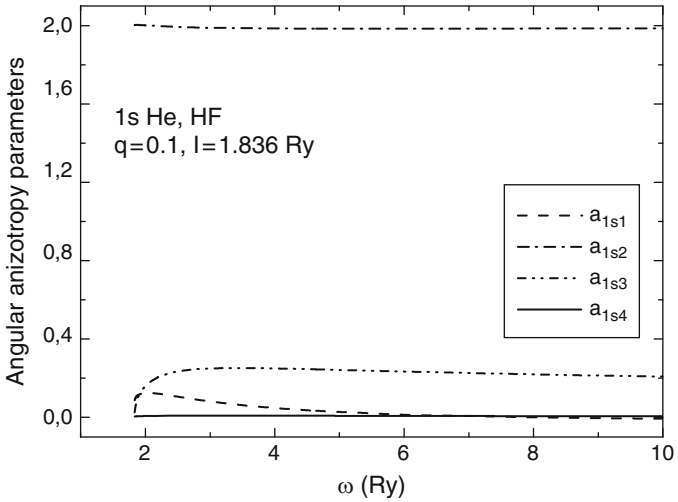

Fig. 4.19_He_m2 Angular anisotropy parameters of knocked-out electrons in fast projectile–atom collision a_{1si} given by (3.75) as functions of ω at $q = 0.1$ in HF for on He

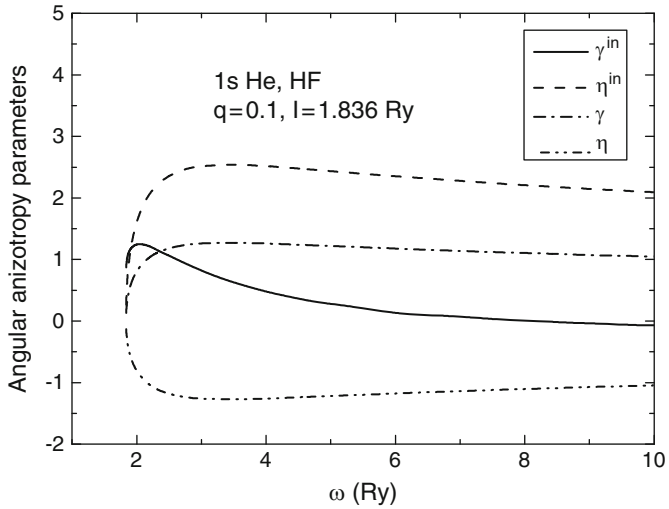

Fig. 4.20_He_m3 Angular anisotropy nondipole parameters of knocked-out electrons in fast projectile–atom collision in the optical limit compared to similar parameters in photoionization, given by (3.84a) and (3.84b) at $q = 0.1$ and (3.83) on He in HF

bigger than the nondipole parameters $a_{1s1}a_{1s3}$ by a factor of ten. Note that it is equal to 2 as in the optical limit $q \to 0$ [see (1.74) for $l = 0$]. The parameter a_{1s4} is smaller than the dipole a_{1s2} by two orders of magnitude.

Figure 4.20_He_m3 shows the angular anisotropy nondipole parameters of knocked-out electrons in fast projectile–atom collision in the optical limit $\gamma_{1s}^{(\mathrm{in})}(\omega)$

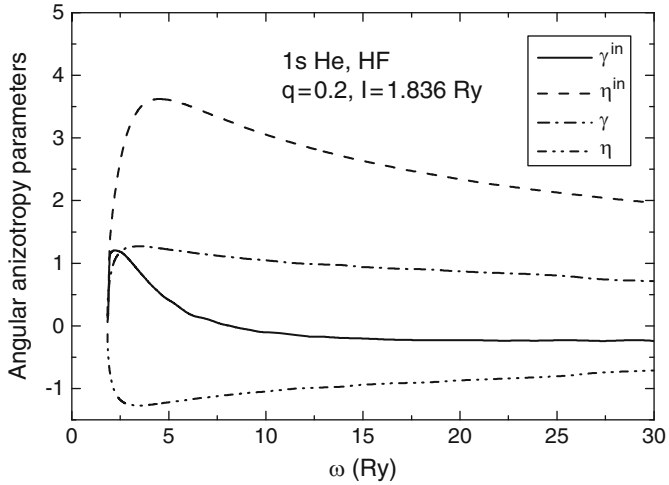

Fig. 4.21_He_m4 Angular anisotropy nondipole parameters of knocked-out electrons in fast projectile–atom collision in the optical limit compared to similar parameters in photoionization, given by (3.84a) and (3.84b) at $q = 0.2$ and (3.83) on He in HF

and $\eta_{1s}^{(\mathrm{in})}(\omega)$ given by (3.84a) and (3.84b) at $q = 0.1$ compared to similar parameters in photoionization $\gamma_{1s}(\omega)$ and $\eta_{1s}(\omega)$, given by (3.83) on He in HF. The ratio $\eta_{ns}^{(\mathrm{in})}(\omega) = 2\gamma_{ns}(\omega)$ is fulfilled with good accuracy.

Figure 4.21_He_m4 shows the angular anisotropy nondipole parameters of knocked-out electrons in fast projectile–atom collision in the optical limit $\gamma_{1s}^{(\mathrm{in})}(\omega)$ and $\eta_{1s}^{(\mathrm{in})}(\omega)$ given by (3.84a) and (3.84b) at $q = 0.2$ compared to similar parameters in photoionization $\gamma_{1s}(\omega)$ and $\eta_{1s}(\omega)$, given by (3.83) on He in HF. The ratio $\eta_{ns}^{(\mathrm{in})}(\omega) = 2\gamma_{ns}(\omega)$ starts to be violated due to growth of $\eta_{1s}^{(\mathrm{in})}(q, \omega)$.

Figures 4.22–4.50 (Ne) show the results of calculations for Ne atom.

Figure 4.22_Ne_a1 shows the cross-sections of elastic (in HF and SRPAE, see [4.1, 4.2]) and inelastic (in SRPAE) scattering of electrons on Ne atom. The role of correlations with decrease of energy from about 30 eV becomes more and more important.

Figure 4.23_Ne_b1 shows the contributions of first four partial waves to the cross-section of elastic electron scattering on Ne atom. The main contribution at low energy is from s-wave, but p- and d-waves overcome it from 50 eV. In fact, the shape of elastic cross-section is determined by combined contribution of p- and d-waves. With growth of electron energy the higher partial waves becomes more and more significant.

Figure 4.24_Ne_c1 shows the differential in angle cross-section of electron scattering on Ne atom with s-, p-, d-, f-waves taken into account in SRPAE. Experimental data are from [4.12].

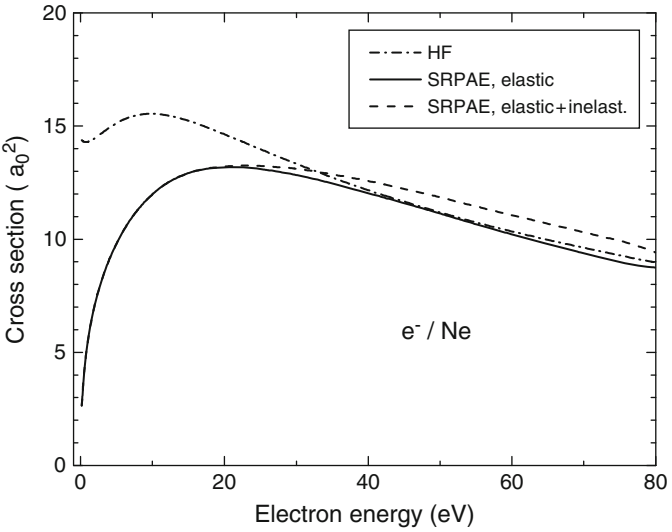

Fig. 4.22_Ne_a1 Cross-sections of elastic (in HF and SRPAE) (see [4.1, 4.2]) and inelastic (in SRPAE) electron scattering on Ne atom

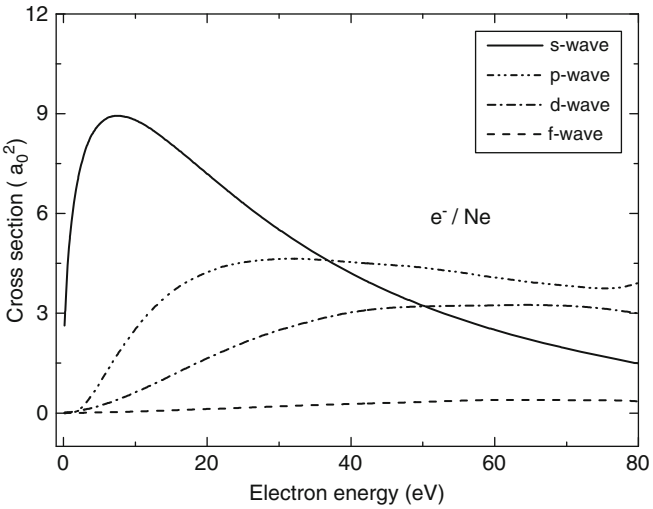

Fig. 4.23_Ne_b1 Contributions of partial waves to cross-section of elastic electron scattering on Ne atom in SRPAE

Figure 4.25_Ne_d1 shows the SRPAE phases of various partial waves in electron scattering on Ne. Here not only *s*-, but also *p*-phase has a negative derivative in all the considered range of energies.

Figure 4.26_Ne_e1 shows the density of the monopole GOSes for Ne in RPAE as a function of the energy transferred to the atom at various q (see [4.13]). It is seen, as

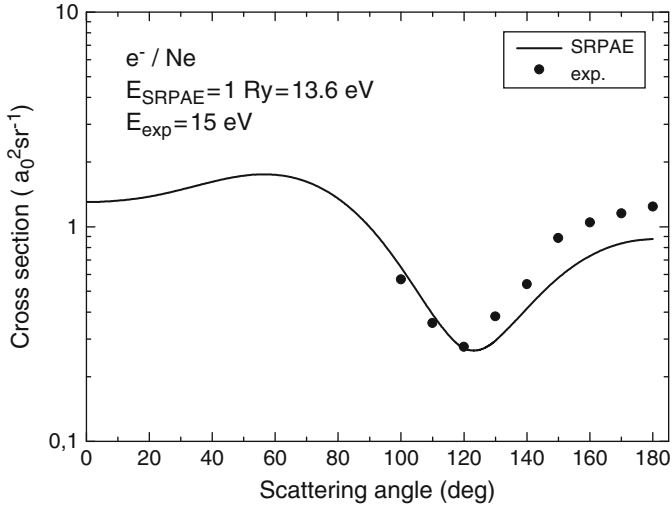

Fig. 4.24_Ne_c1 Differential in angle cross-section of electron scattering on Ne atom with *s*-, *p*-, *d*-, *f*-waves taken into account in SRPAE. Experimental data are taken from [4.12]

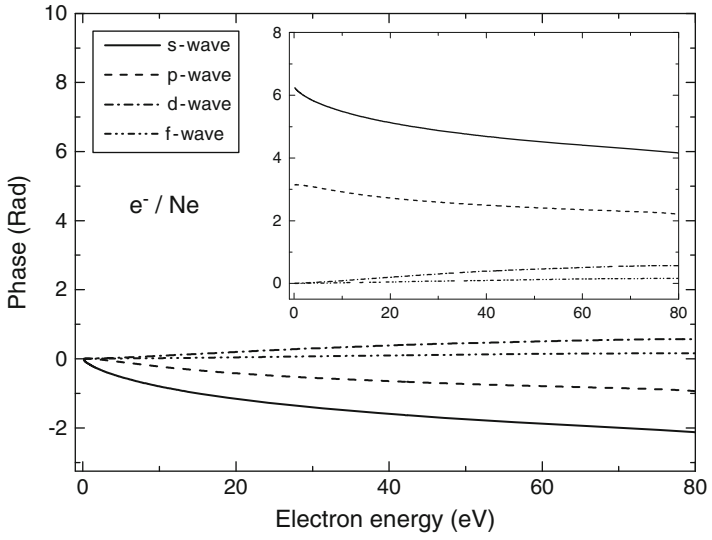

Fig. 4.25_Ne_d1 Phases of various partial waves in electron scattering on Ne atom in SRPAE

with growth of q the monopole GOSes quickly grow and clearly appears a maximum in GOSes, displaced with growth of q aside big energies. With increase of q, rapidly growth the maximum above the inner $1s$ shell threshold that is seen in the insert.

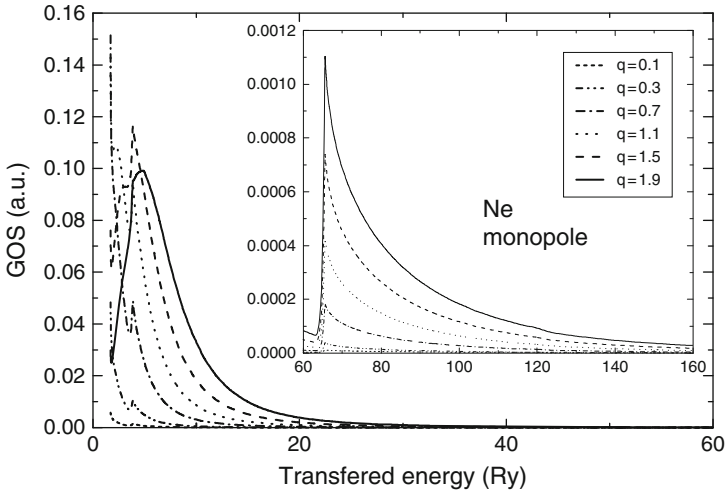

Fig. 4.26_Ne_e1 Density of monopole generalized oscillator strengths as function of the energy transferred to atom at various q for Ne in RPAE (see [4.13])

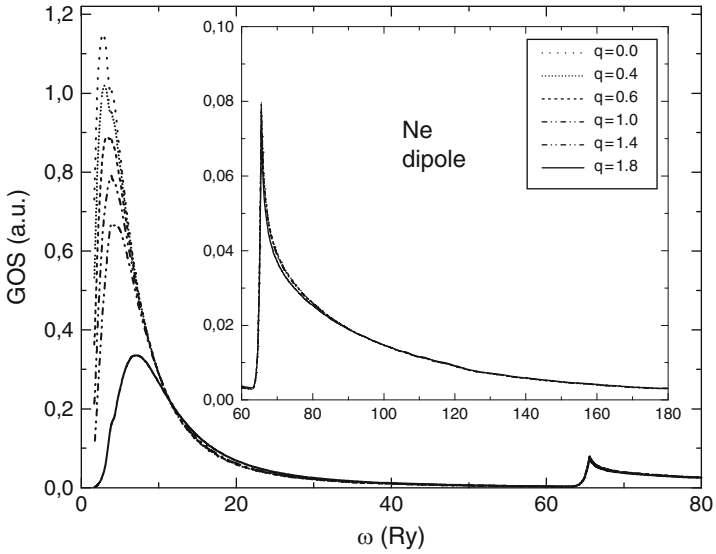

Fig. 4.27_Ne_e2 Density of dipole generalized oscillator strengths as function of the energy transferred to the atom at various q for Ne, in RPAE (see [4.14])

Figure 4.27_Ne_e2 shows the density of the dipole GOSes for Ne in RPAE as function of the energy transferred to the atom at various q (see [4.14]). As shown in Fig. 4.26_Ne_e1, the maximum is present at all values of q, being displaced slightly to the higher energy side with q growing. At the same time, the maximum becomes

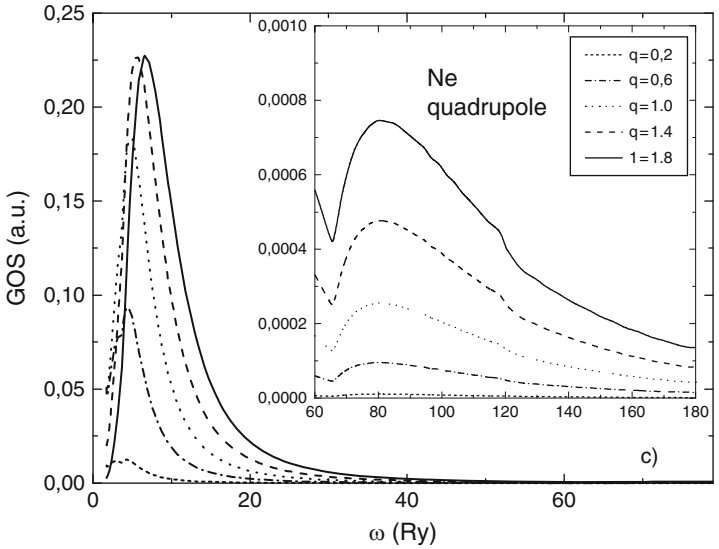

Fig. 4.28_Ne_e3 Density of at various q for Ne in quadrupole generalized oscillator strengths as function of the energy transferred to the atom, in RPAE (see [4.13])

broader and lower. The maximum at the inner $1s$ shell threshold is, as seen from the insert, q independent.

Figure 4.28_Ne_e3 shows the density of the quadrupole GOSes for Ne in RPAE as function of the energy transferred to the atom at various q (see [4.13]). The behavior of the second maximum (on the insert) considerably differs from the case of dipole and monopole GOSes (see Figs. 4.26_Ne_e1 and 4.27_Ne_e2).

Figure 4.29_Ne_e4 shows the density of octupole GOSes for Ne in RPAE as functions of the energy transferred to the atom at various q (see [4.14]). Here increase of q results in substantial growth of energy of the maximum with simultaneous prominent decrease of its height.

Figure 4.30_Ne_f1 shows the GOSes of two very close in energy discrete monopole and quadrupole excitations $2p$–$3p$ for Ne atom as function of q^2 transferred to the atom in RPAE (see [4.13]). It is seen that the second maximum belongs only to GOSes of the quadrupole level. To distinguish experimentally so closely located levels is extremely difficult that is why the sum of GOSes of two levels is given.

Figure 4.31_Ne_f2 shows the GOSes of discrete monopole and quadrupole excitations $2p$–$4p$ for Ne as functions of q^2 transferred to the atom, in RPAE (see [4.13]). The levels have very close excitation energy. Entirely, the picture is close to that shown in Fig. 4.30_Ne_f1.

Figure 4.32_Ne_f3 shows the GOSes of discrete quadrupole excitations $2p$–$4f$ and $2p$–$5f$ for Ne as functions of q^2 transferred to the atom in RPAE (see [4.13]).

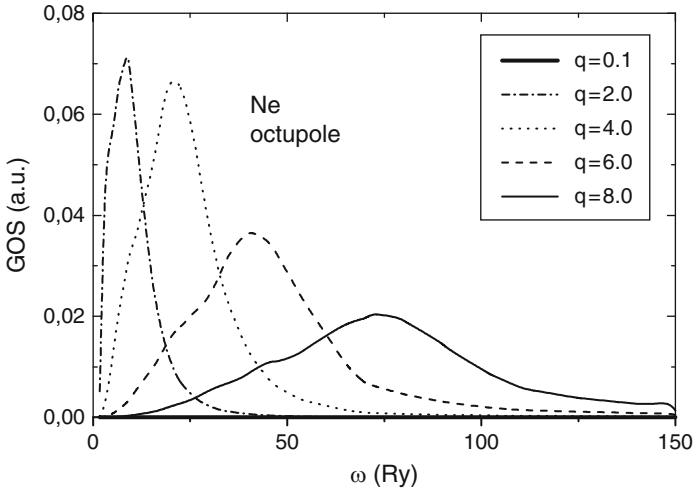

Fig. 4.29_Ne_e4 Density of octupole generalized oscillator strengths for Ne in RPAE as function of the energy transferred to the atom at various q (see [4.14])

Fast growth of GOSes with increase q^2 down to achievement of a maximum is seen at $q^2 \approx 0.3$.

Figure 4.33_Ne_f4 shows the GOSes strengths of discrete dipole excitations $2p$–$3s$, $2p$–$4s$ for Ne as functions of q^2 transferred to the atom, in HF and RPAE (see [4.14]). Forms of the curves in both approximations are similar while values are a little bit different. At $q^2 \approx 9$ GOSes for both levels have a maximum, but smaller than GOSes at $q^2 = 0$ by more than two orders of magnitude.

Figure 4.34_Ne_f5 shows the GOSes of discrete dipole excitations $2p$–$3d$, $2p$–$4d$ for Ne as function of q^2 transferred to the atom, in HF and RPAE (see [4.14]). With growth of q GOSes decrease monotonic and are much smaller than for the $2p$–$3s$, $4s$ transitions (see Fig. 4.33_Ne_f4).

Figure 4.35_Ne_f6 shows the GOSes of discrete octupole excitations $2p$–$3d$, $2p$–$4d$ for Ne as functions of q^2 transferred to the atom in HF and RPAE (see [4.14]). Shapes of GOSes for both transitions are simple and close to each other, while the magnitudes are essentially different.

Figure 4.36_Ne_f7 shows the GOSes of discrete dipole and octupole excitations $2p$–$3d$ for Ne as functions of q^2 transferred to the atom, in RPAE (see [4.14]). The behavior of GOSes of two considered levels is essentially different. But they are so close in energy that it is possible to investigate experimentally only the sum of their GOSes.

Figure 4.37_Ne_f8 shows the GOSes of discrete dipole and octupole excitations $2p$–$4d$ for Ne as a function of q^2 transferred to the atom, in RPAE (see [4.13]). As for $2p$–$3d$, they are so close in energy that it is possible to investigate experimentally only the sum of their GOSes.

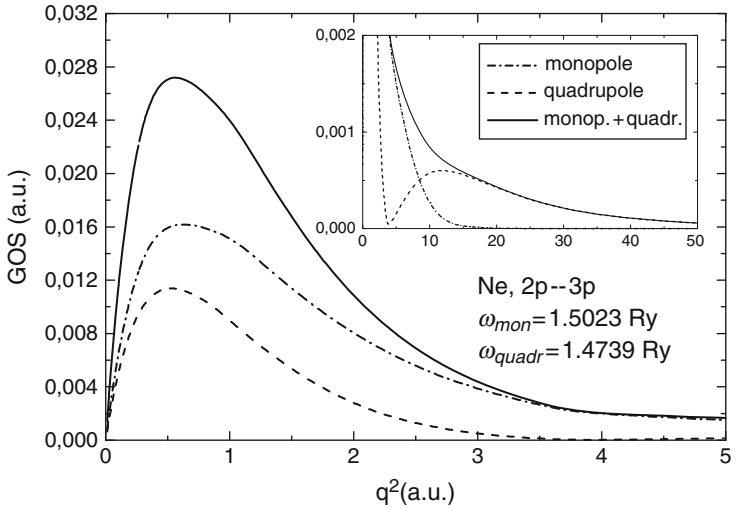

Fig. 4.30_Ne_f1 Generalized oscillator strengths of two very close in energy discrete monopole and quadrupole excitations $2p$–$3p$ for Ne as function of square linear momentum q transferred to the atom in RPAE (see [4.13])

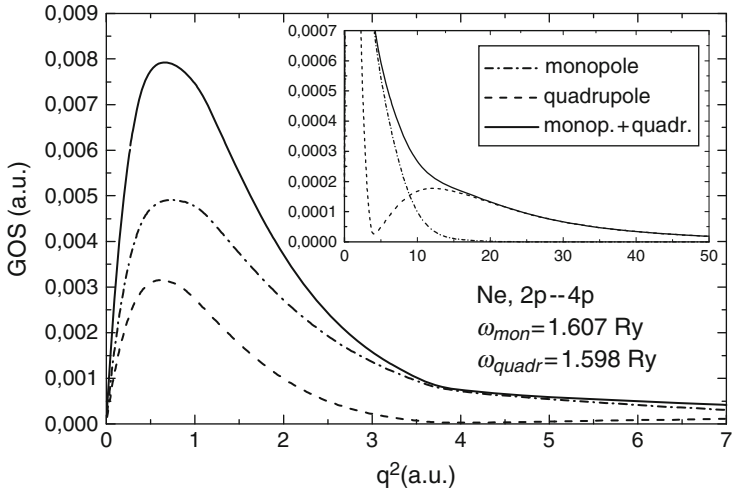

Fig. 4.31_Ne_f2 Generalized oscillator strengths of discrete monopole and quadrupole excitations $2p$–$4p$ for Ne as functions of square moment q transferred to the atom and their sum in RPAE (see [4.13])

Figure 4.38_Ne_g1 shows the results for cross-section of monopole Compton scattering of γ-quanta with energy $E = 2,000$ Ry on Ne in RPAE as function of transferred to the atom linear momentum q at various energies ω. The transferred angular momentum is $L = 0$ (see [4.15]). Note the big range of considered values of

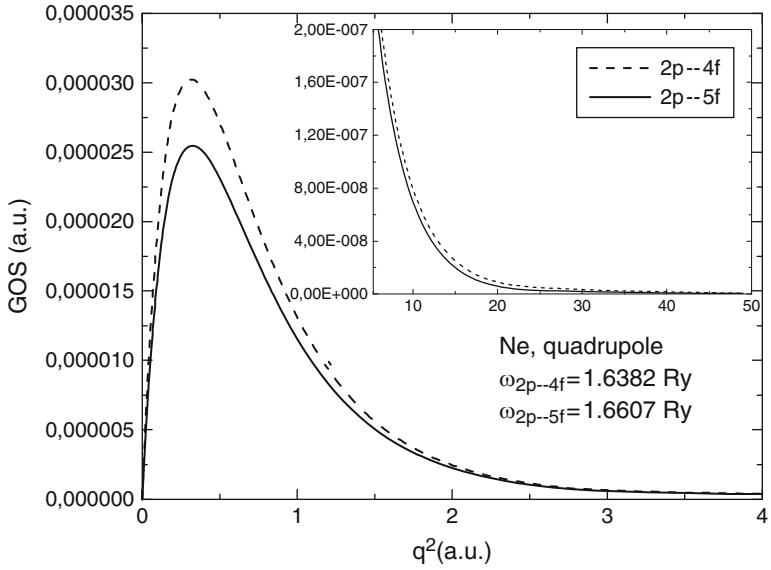

Fig. 4.32_Ne_f3 Generalized oscillator strengths of discrete quadrupole excitations of Ne as functions of q^2 transferred to the atom, in RPAE (see [4.13])

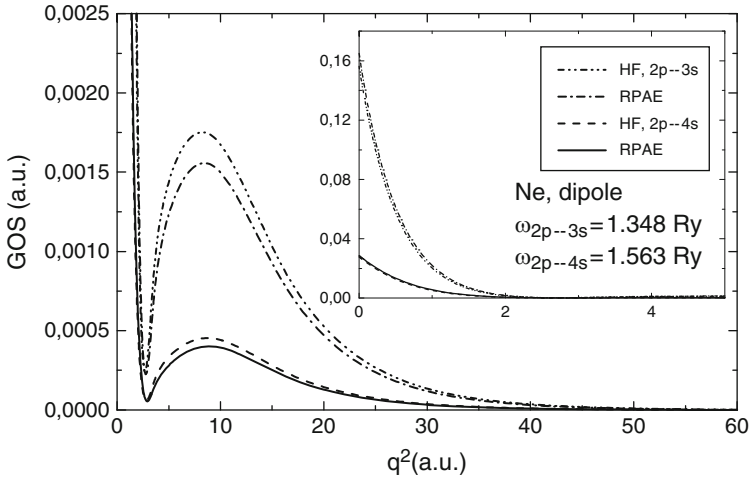

Fig. 4.33_Ne_f4 Generalized oscillator strengths of discrete dipole excitations of Ne as functions of q^2 transferred to the atom, in HF and RPAE (see [4.14])

$q, 0 < q < 8$ that corresponds to distances from much bigger than the atomic radius to much smaller than it. With growth of omega the maximum is reduced and moves the side of big q. There is an almost symmetric maximum that moves to higher q becoming lower and broader with ω growth.

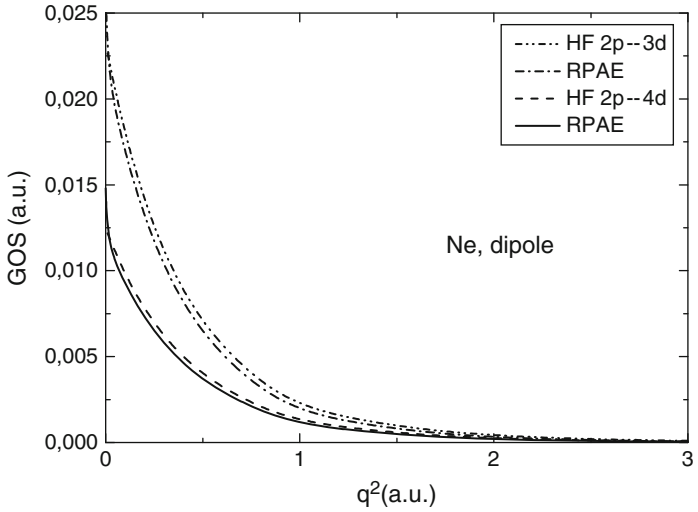

Fig. 4.34_Ne_f5 Generalized oscillator strengths of discrete dipole excitations of Ne as function of q^2 transferred to the atom, in HF and RPAE (see [4.14])

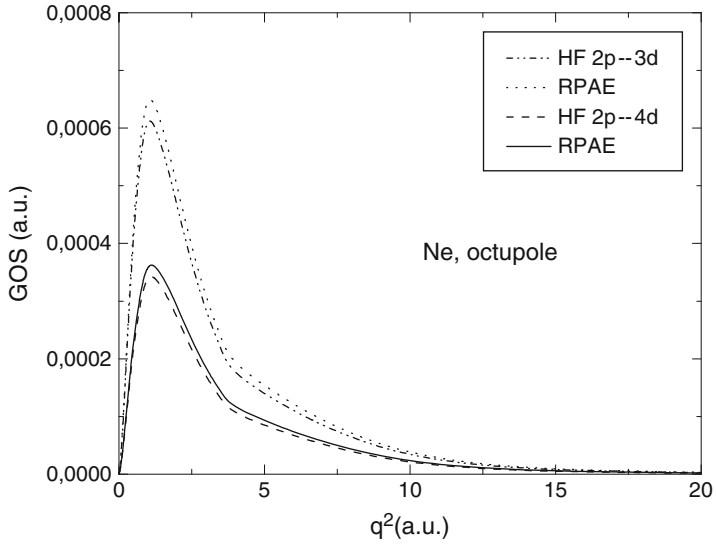

Fig. 4.35_Ne_f6 Generalized oscillator strengths of discrete octupole excitations as functions of square moment q transferred to atom for Ne in HF and RPAE (see [4.14])

Figure 4.39_Ne_g2 shows the cross-section of dipole Compton scattering of γ-quanta of energy $E = 2,000$ Ry on Ne in RPAE as function of the momentum q transferred to the atom at various energies ω. The transferred angular moment is

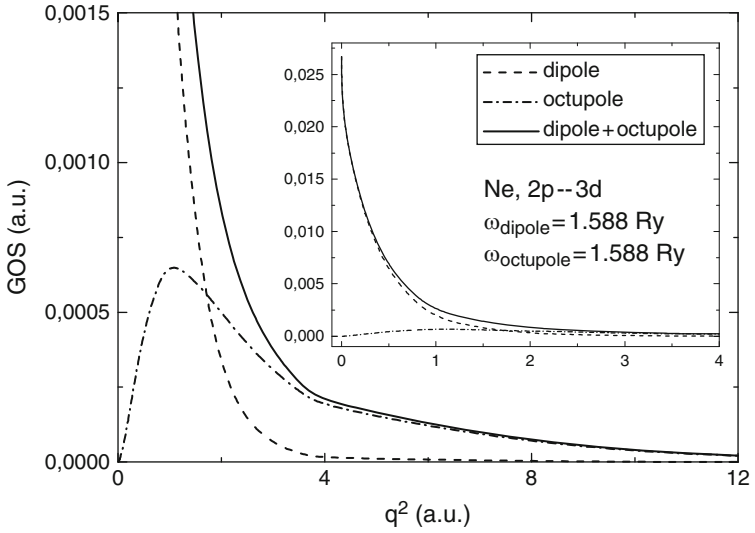

Fig. 4.36_Ne_f7 Generalized oscillator strengths of discrete dipole and octupole excitations as functions of square moment q transferred to atom for Ne in RPAE (see [4.14])

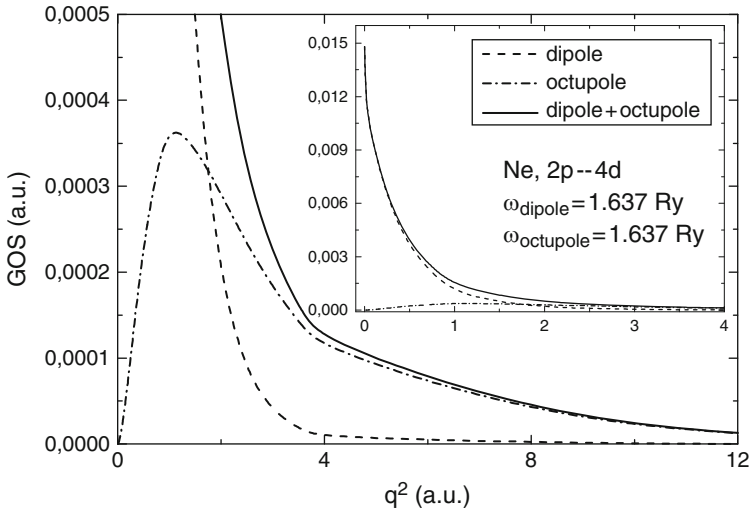

Fig. 4.37_Ne_f8 Generalized oscillator strengths of discrete dipole and octupole excitations as function of q^2 transferred to atom for Ne in RPAE (see [4.14])

$L = 1$ (see [4.15]). The curves have two maxima that move to higher q with increase of ω.

Figure 4.40_Ne_g3 shows the cross-section of quadrupole Compton scattering of γ-quanta with energy $E = 2,000$ Ry on Ne in RPAE as function of the momentum

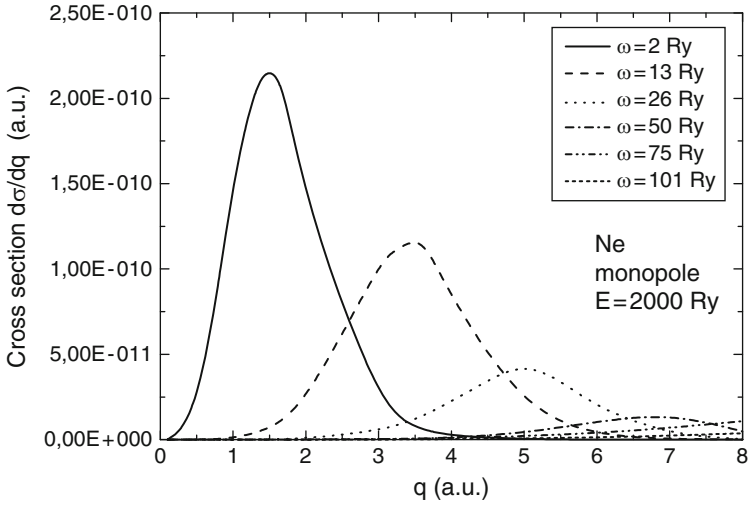

Fig. 4.38_Ne_g1 Cross-section of monopole Compton scattering of γ-quanta with energy $E = 2,000$ Ry as function transferred to atom of the moment q, at various energies ω on Ne in RPAE (see [4.15])

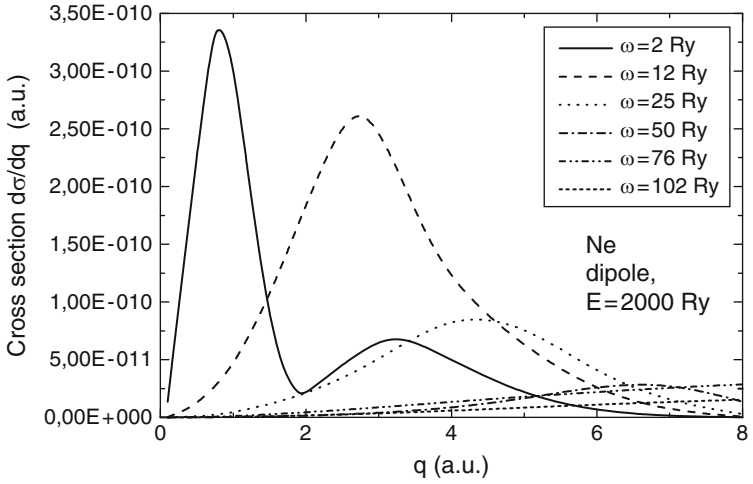

Fig. 4.39_Ne_g2 Cross-section of dipole Compton scattering of γ-quanta with energy $E = 2,000$ Ry as function of the moment q transferred to atom, at various energies ω on Ne in RPAE (see [4.15])

q transferred to the atom at various energies ω. The transferred angular momentum is $L = 2$ (see [4.15]). Just as for the dipole case, the curves have two maxima that move to higher q with increase of ω. Note that for small ω the maxima have almost the same height, but the situation rapidly changes with ω growing.

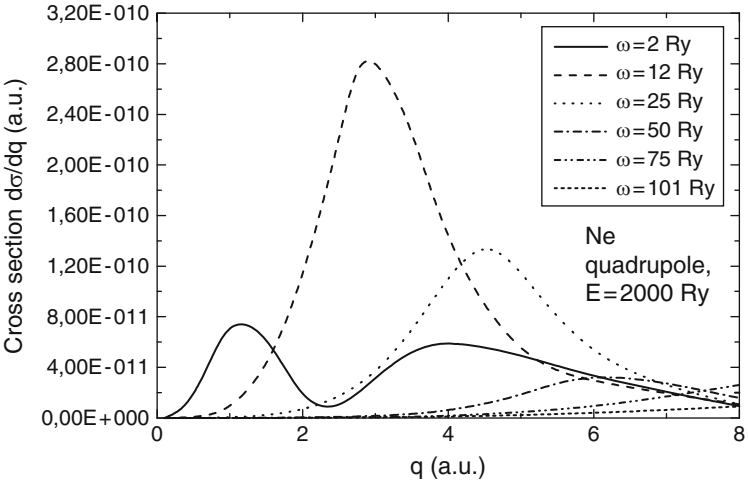

Fig. 4.40_Ne_g3 Cross-section of quadrupole Compton scattering of γ-quanta with energy $E = 2,000$ Ry as function of the moment q transferred to atom, at various energies ω on Ne in RPAE (see [4.15])

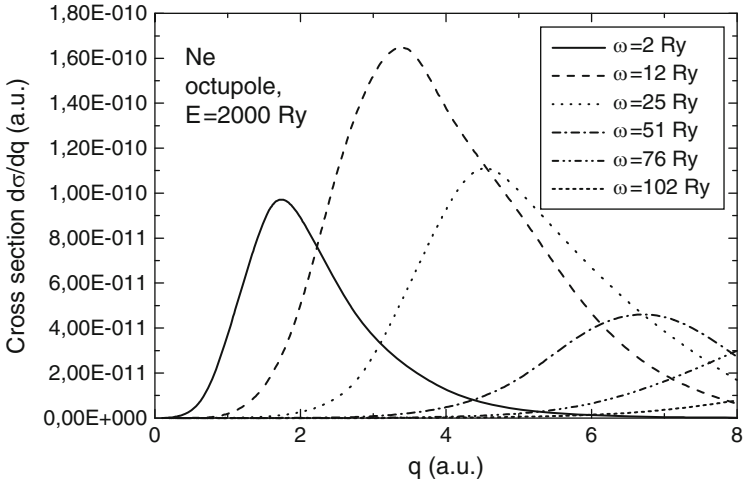

Fig. 4.41_Ne_g4 Cross-section of octupole Compton scattering of γ-quanta with energy $E = 2,000$ Ry as function of the moment q transferred to atom, at various energies ω on Ne in RPAE (see [4.15])

Figure 4.41_Ne_g4 shows the cross-section of octupole Compton scattering of γ-quanta with energy $E = 2,000$ Ry on Ne in RPAE as a function transferred to the atom the momentum q at various energies ω. The transferred angular momentum is $L = 3$ (see [4.15]). The second maximum is outside of the limits of the figure.

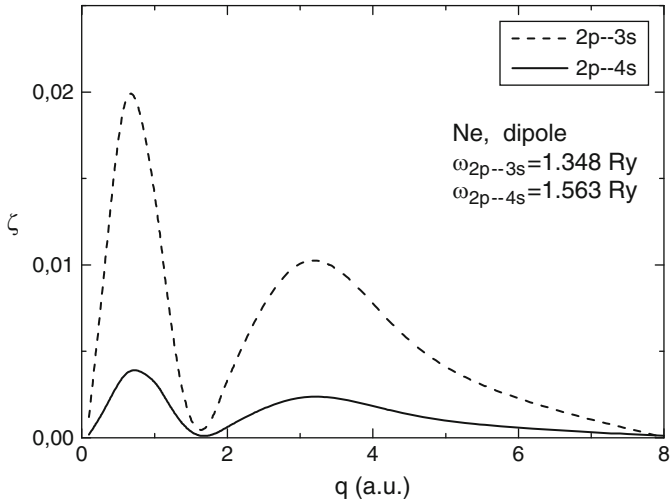

Fig. 4.42_Ne_h1 Relative cross-section of Compton excitation of dipole levels for Ne in RPAE (see [4.16])

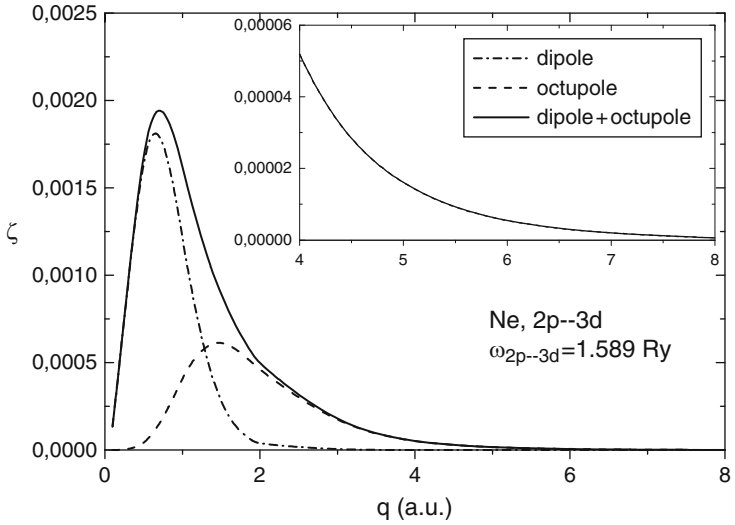

Fig. 4.43_Ne_h2 Relative cross-section of Compton excitation of dipole and octupole $2p$–$3d$ levels for Ne in RPAE (see [4.16])

Figure 4.42_Ne_h1 shows the cross-section of Compton excitation [defined by (3.94)], relative to Thomson cross-section, of dipole $2p$–$3s$ and $2p$–$4s$ levels for Ne in RPAE (see [4.16]). Note the presence of two maxima in the cross-section.

Figure 4.43_Ne_h2 shows the cross-section of Compton excitation [defined by (3.94)], relative to Thomson cross-section of the dipole and octupole levels $2p$–$3d$

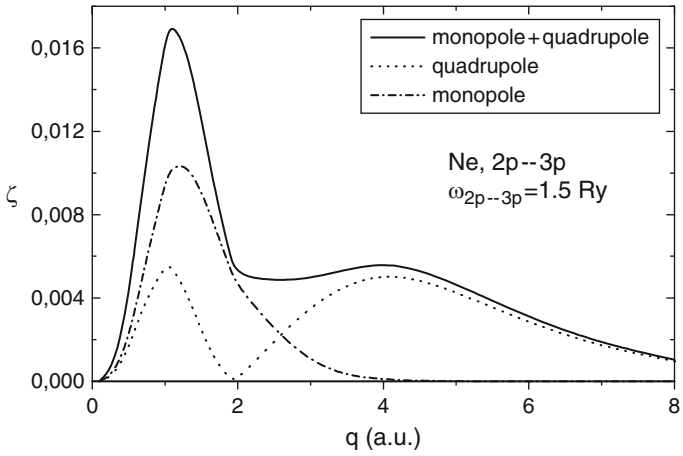

Fig. 4.44_Ne_h3 Relative cross-section of Compton excitation of quadrupole and monopole almost exactly degenerate $2p$–$3p$ levels for Ne in RPAE (see [4.16])

for Ne in RPAE (see [4.16]). Here, contrary to Fig. 4.42_Ne_h1, there is only one maximum in the cross-section.

Figure 4.44_Ne_h3 shows the relative cross-section of Compton excitation [defined by (3.94)] of quadrupole and monopole almost exactly degenerate $2p$–$3p$ levels for Ne in RPAE (see [4.16]). Two maxima in cross-section are distinctly visible.

Figure 4.45_Ne_h4 shows the relative cross-section of Compton excitation [defined by (3.94)] of some close in energy dipole, monopole, octupole, and quadrupole levels $2p$–$3d$, $2p$–$4p$, $2p$–$4d$, and $2p$–$4s$ for Ne in RPAE (see [4.16]). As well as shown in Fig. 4.44_Ne_h3, two maxima in the cross-section are clearly visible.

Figure 4.46_Ne_i1 shows the cross-section of elastic and inelastic positron scattering by Ne in HF and SRPAE (see [4.10]). Polarization interaction takes into account excitation of $2s$ and $2p$ subshells and formation of virtual positronium. Experimental data are taken from [4.17] and the agreement with it is very good. There is a Ramsauer minimum close to zero energy.

Figure 4.47_Ne_j1 shows the contributions of partial waves to the cross-section of elastic positron scattering by Ne in SRPAE. The main contribution is from the s-wave, while the p-wave contribution is essential in the Ramsauer minimum region.

Figure 4.48_Ne_k1 shows s-, p-, d-, f-phases of partial waves of elastic positron scattering by Ne in SRPAE. Note that that not only s but also p-phase becomes negative at relatively low energies.

Figure 4.49_Ne_l1 shows the multiplied by incoming electron energy total and partial cross-sections of inelastic scattering of fast electrons on atom Ne in logarithmic approximation $E\sigma_{\mathrm{In}}(E)$. Dominative is the contribution of scattering

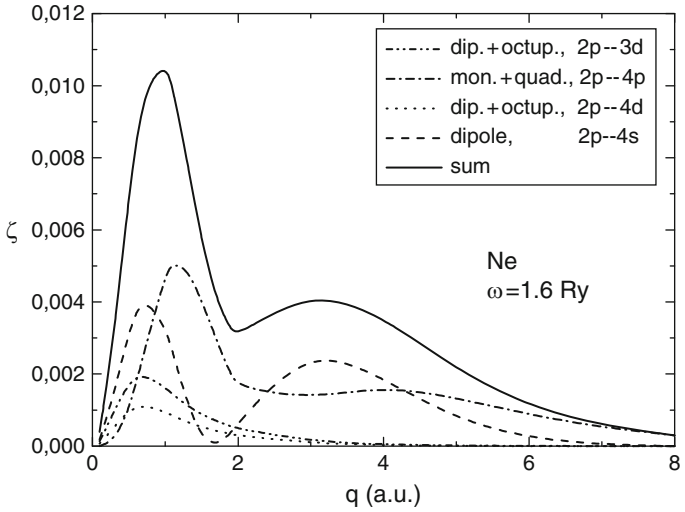

Fig. 4.45_Ne_h4 Relative cross-section of Compton excitation of some close on energy dipole, monopole, octupole, and quadrupole levels and their sum for Ne in RPAE (see [4.16])

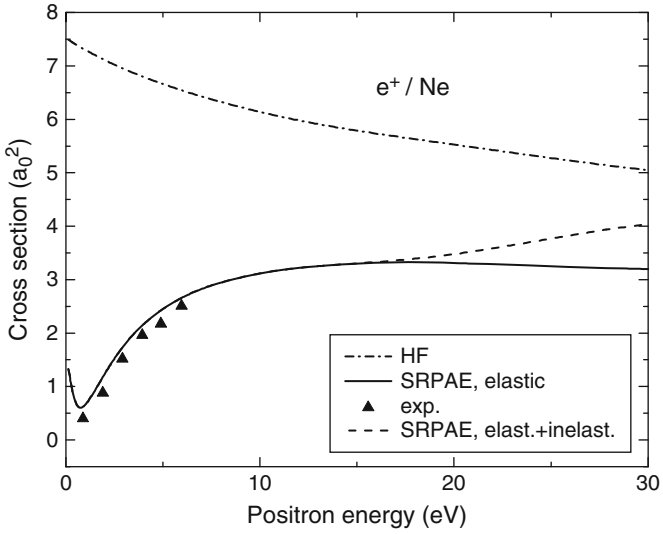

Fig. 4.46_Ne_i1 Cross-section of elastic and inelastic positron scattering for Ne in HF and SRPAE. Experimental data are taken from [4.17]

upon the outer $2p$ subshell, mainly from $2p$ to $3d$ transition. It is seen that all these functions at high E increase slowly. The fastest is the increase of the biggest partial cross-section. The cross-sections are presented from $E = I$ for completeness only, since the logarithmic approximation is valid if $\ln(E/I) \gg 1$.

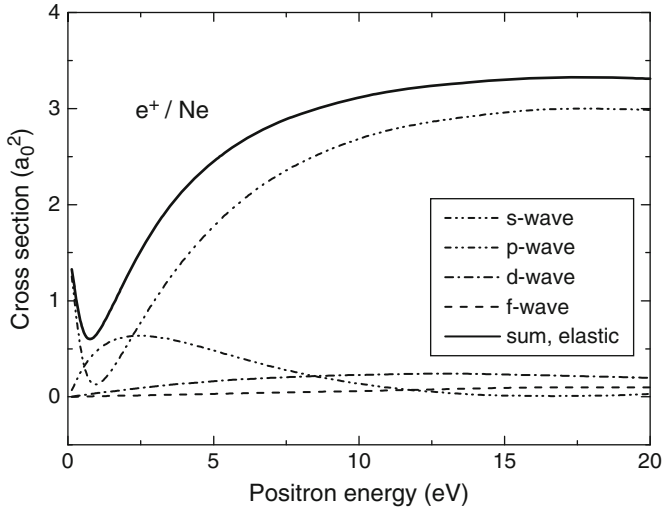

Fig. 4.47_Ne_j1 Contributions of partial waves to cross-section of elastic positron scattering on Ne atom in SRPAE

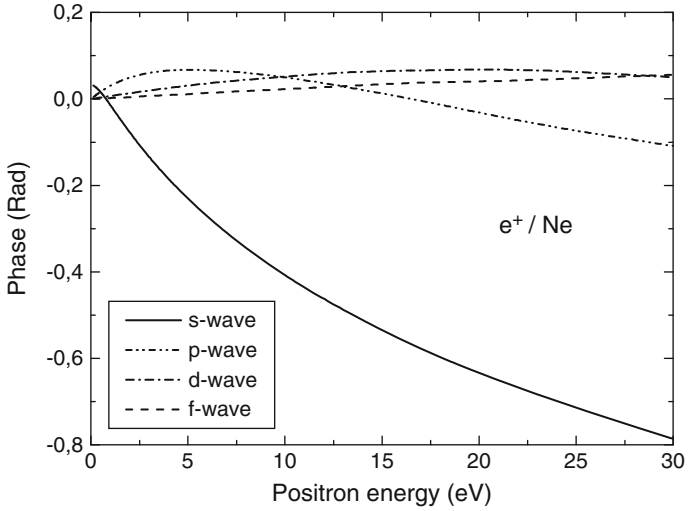

Fig. 4.48_Ne_k1 Phases of various partial waves in positron scattering on Ne atom in SRPAE

Figure 4.50_Ne_l2 shows the multiplied by incoming electron energy total and partial nonlogarithmic corrections to the cross-sections of inelastic scattering of fast electrons on Ne atom $E\sigma_{\mathrm{In}}^{(1)}(E)$. It is seen that these functions stop to grow already at $E = 10\,\mathrm{Ry}$.

Figures 4.51–4.101 (Ar) show the results of calculations for Ar.

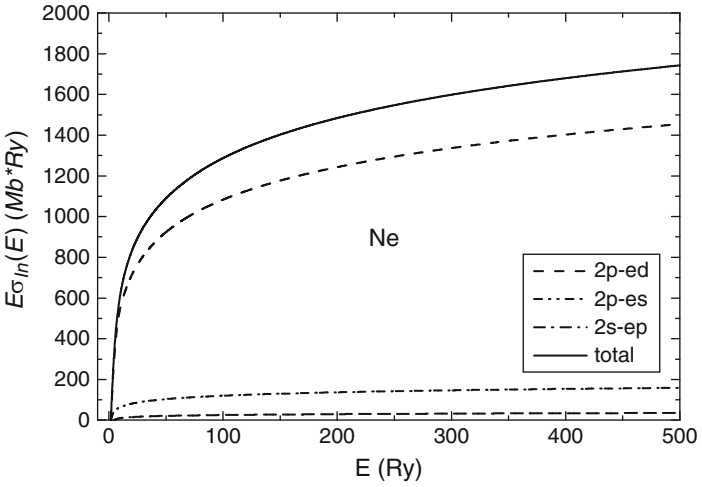

Fig. 4.49_Ne_l1 Multiplied by incoming electron energy cross-section of inelastic scattering of fast electrons in the logarithmic approximation

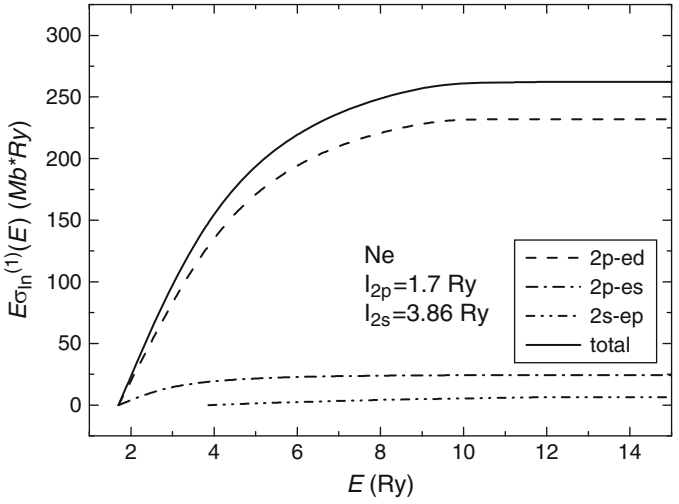

Fig. 4.50_Ne_l2 Nonlogarithmic correction to the multiplied by incoming electron energy cross-section of inelastic scattering of fast electrons

Figure 4.51_Ar_a1 shows the cross-section of elastic (in HF and SRPAE) and inelastic (in SRPAE) electron scattering on Ar (see [4.1, 4.2]). Experimental data are taken from [4.19]. The minimum in the cross-section, called Ramsauer minimum [4.20], arises only if the polarization interaction is taken into account.

Figure 4.52_Ar_b1 shows the contribution of partial waves in cross-section of electron elastic scattering on Ar in SRPAE. Note that the powerful maximum in

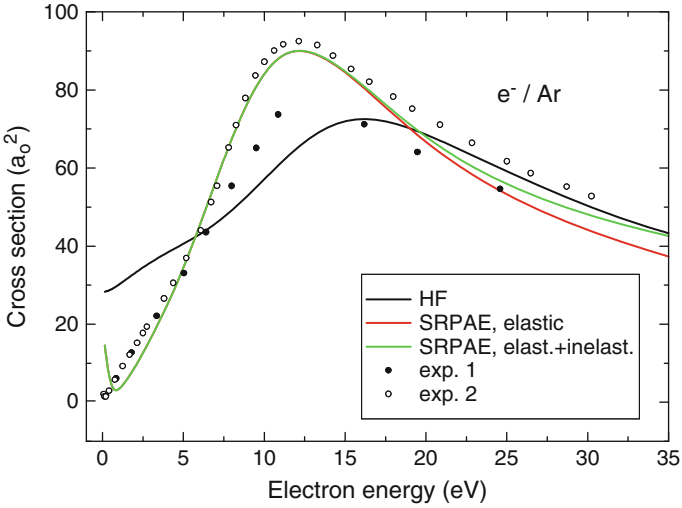

Fig. 4.51_Ar_a1 Cross-section of elastic (in HF and SRPAE) and inelastic (in SRPAE) electron scattering on Ar (see [4.1, 4.2]). Experiment is from [4.19]

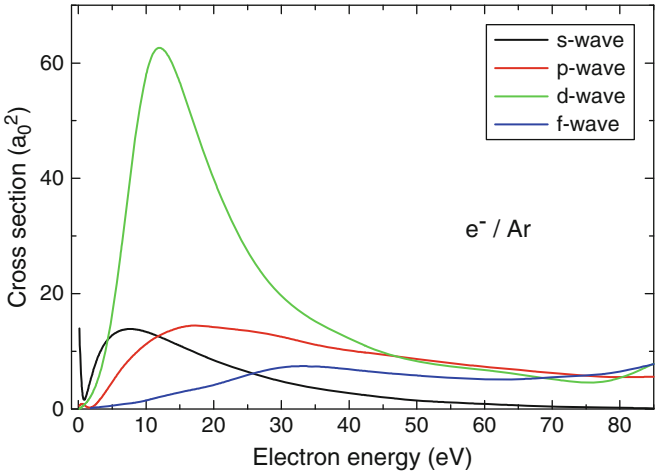

Fig. 4.52_Ar_b1 Contribution of partial waves in cross-section of electron elastic scattering on Ar, in SRPAE

d-wave with growth of the nuclear charge would transform into bound $3d$-level. This maximum determines the elastic scattering cross-section above the Ramsauer minimum [4.20].

Figure 4.53_Ar_c1 shows the differential in angle cross-section of electron scattering on Ar. The incoming electron energy is 39.3 eV. There are three maxima

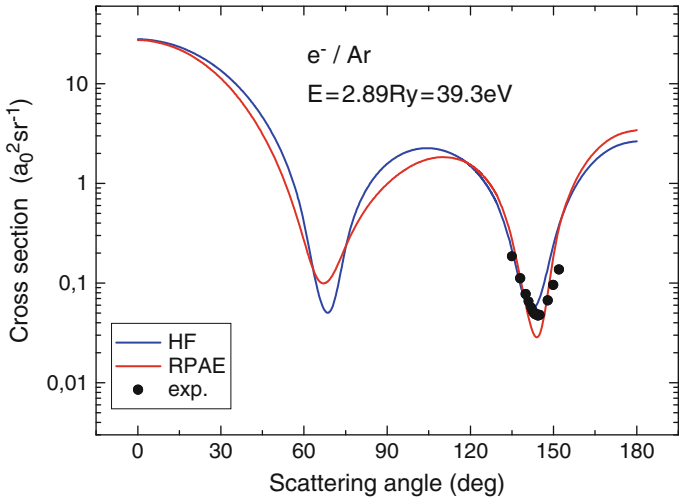

Fig. 4.53_Ar_c1 Differential on an angle cross-section of electron scattering on Ar. Experiment is from [4.21]

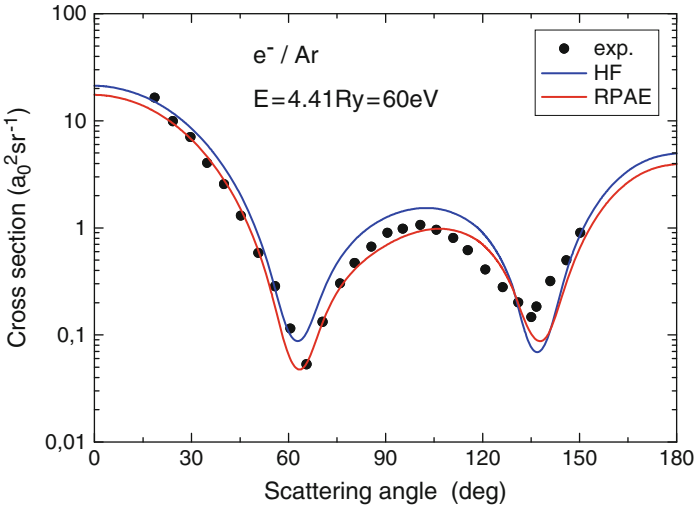

Fig. 4.54_Ar_c2 Differential on an angle cross-section of electron scattering on Ar. Experiment is from [4.21]

at 0°, 100°, and 180°. Experimental data are taken from [4.21]. The agreement with results of calculation is good.

Figure 4.54_Ar_c2 shows the differential in angle cross-section of electron scattering on Ar. The incoming electron energy is 60 eV. Results are close to submitted in Fig. 4.53_Ar_c1. The experimental data are taken from [4.21]. The role of correlations is appreciable and improves the agreement with experiment.

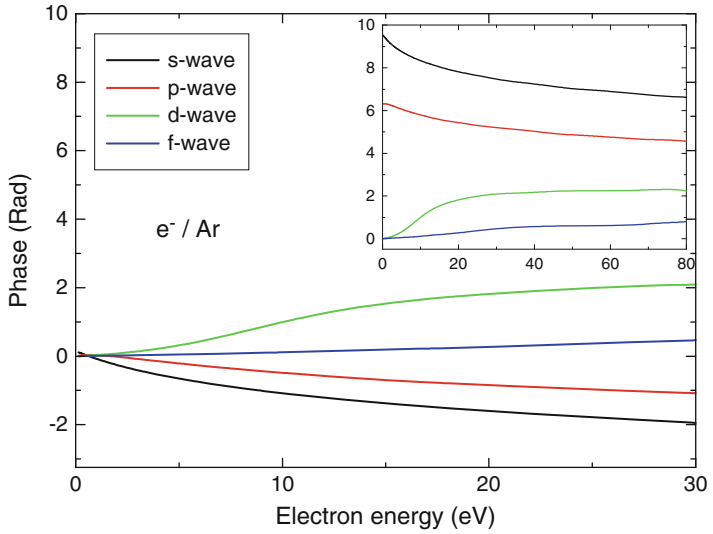

Fig. 4.55_Ar_d1 Phases of various partial waves in electron scattering on Ar, in SRPAE

Figure 4.55_Ar_d1 shows the SRPAE phases of various partial waves in electron scattering on Ar as functions of the projectile energy. As it should be in accord to (3.21), at zero electron energy s-phase is equal to 3π, p-phase—2π, and d-, f-phases reach zero, if all phases define in such a way that at $E \to \infty$ phases $\delta_l \to 0$.

Figure 4.56_Ar_d2 shows the phases for various partial waves in electron scattering on Ar in HF and SRPAE. Phases of s- and p-waves are decreasing already at low energies, while d- and f-phases are growing.

Figure 4.57_Ar_e1 shows the densities of the monopole GOSes for Ar in RPAE as functions of the energy ω transferred to the atom at various q (see [4.7]). The GOS curve maximum is moving to higher energies with q growth, simultaneously becoming broader and lower.

Figure 4.58_Ar_e2 shows the density of dipole GOSes for Ar in RPAE as function of the energy ω transferred to the atom at various q (see [4.7]). The value of dipole GOSes is an order of magnitude bigger than for both monopole (Fig. 4.57_Ar_e1) and quadrupole (Fig. 4.59_Ar_e3) cases.

Figure 4.59_Ar_e3 shows the density of quadrupole GOSes for Ar in RPAE as function of the energy ω transferred to the atom at various q (see [4.7]). The maximum is moving toward higher energies with q growing, simultaneously becoming broader and lower.

Figure 4.60_Ar_e4 shows the density of octupole GOSes for Ar in RPAE as function of the energy ω transferred to the atom at various q (see [4.7]). Displacement of a maximum to higher energies with growth of q is evident, similar to that shown in Figs. 4.57_Ar_e1 and 4.59_Ar_e3.

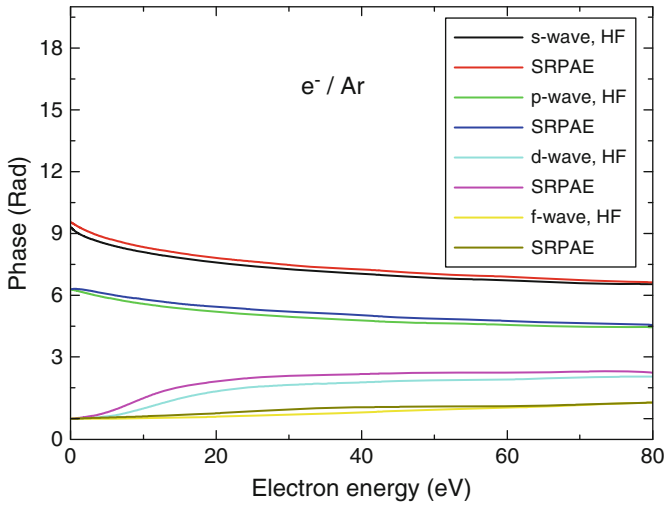

Fig. 4.56_Ar_d2 Comparison of phases for various partial waves in electron scattering on Ar, in HF and SRPAE

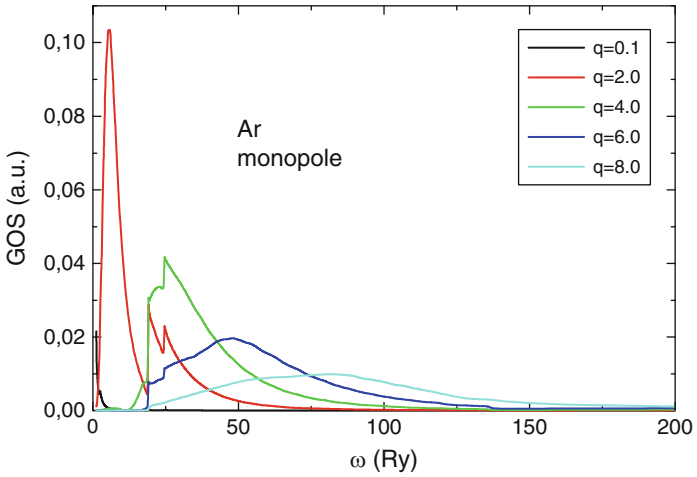

Fig. 4.57_Ar_e1 Density of monopole generalized oscillator strengths as function of the energy transferred to the atom at various q for Ar, in RPAE (see [4.7])

Figure 4.61_Ar_f1 shows the GOSes of discrete monopole and quadrupole $3p$–$4p$ excitations for Ar as functions of q^2 transferred by electron to the atom, in RPAE (see [4.13]). Quadrupole GOSes have two maxima, but owing to proximity in energy of monopole and quadrupole levels, only GOSes sums are measurable, where after maximum small excess is added (see the insert).

Figure 4.62_Ar_f2 shows the GOSes of discrete monopole and quadrupole $3p$–$4p$ excitations as functions of q^2 transferred to the atom Ar in RPAE (see [4.13]).

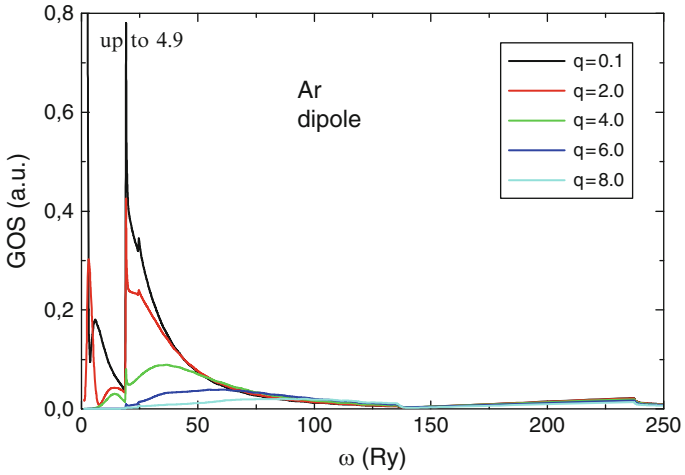

Fig. 4.58_Ar_e2 Density of dipole generalized oscillator strengths as function of the energy transferred to the atom at various q for Ar, in RPAE (see [4.7])

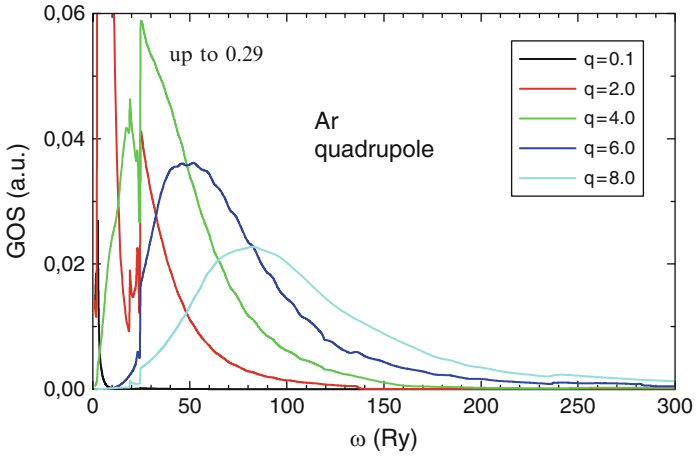

Fig. 4.59_Ar_e3 Density of quadrupole generalized oscillator strengths as function of the energy transferred to the atom at various q for Ar, in RPAE (see [4.7])

In considered area of q GOSes have one maximum. Experimental data are taken from [4.22]. Considerable difference between experiment and theory, increasing with growth $q^2 > 0.5$, is visible. We cannot exclude the possibility in experimental error as well.

Figure 4.63_Ar_f3 shows the GOSes of discrete monopole and quadrupole $3p$–$5p$ excitations for Ar as functions of q^2 transferred by electron to the atom in RPAE (see [4.13]). Both transitions have a maximum at $q^2 < 0.5$, whereas in quadrupole GOSes there is a second, small maximum at $q^2 < 10$.

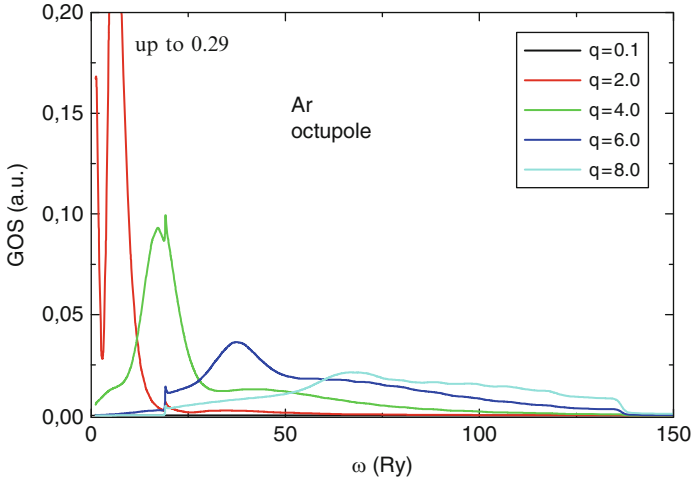

Fig. 4.60_Ar_e4 Density of octupole generalized oscillator strengths as function of the energy transferred to the atom at various q for Ar, in RPAE (see [4.7])

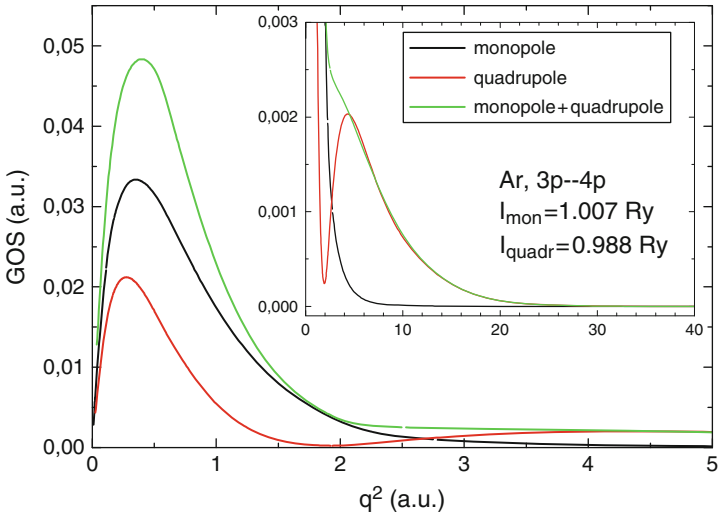

Fig. 4.61_Ar_f1 Generalized oscillator strengths of discrete monopole and quadrupole $3p$–$4p$ excitations as functions of square moment q transferred by electron to the atom for Ar, in RPAE (see [4.13])

Figure 4.64_Ar_f4 shows the GOSes of discrete quadrupole $3p$–$4f$ and $3p$–$5f$ excitations for Ar as function of q^2 transferred by electron to the atom, in RPAE (see [4.13]). In considered region of q GOSes have one maximum.

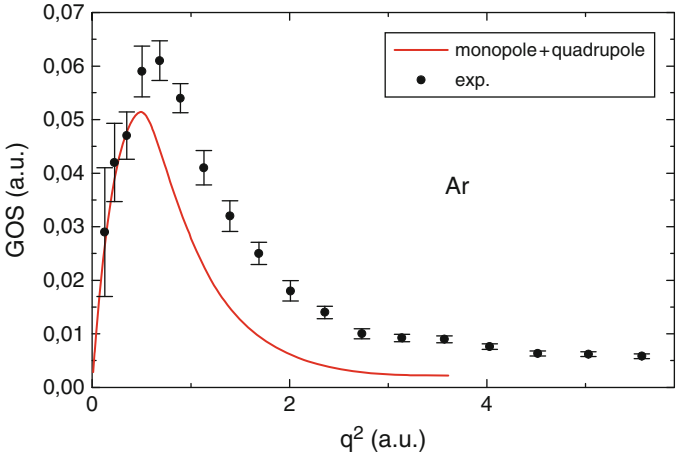

Fig. 4.62_Ar_f2 Generalized oscillator strengths of discrete monopole and quadrupole $3p$–$4p$ excitations as functions of square moment q transferred to the atom Ar, in RPAE (see [4.13]). Experiment is from [4.22]

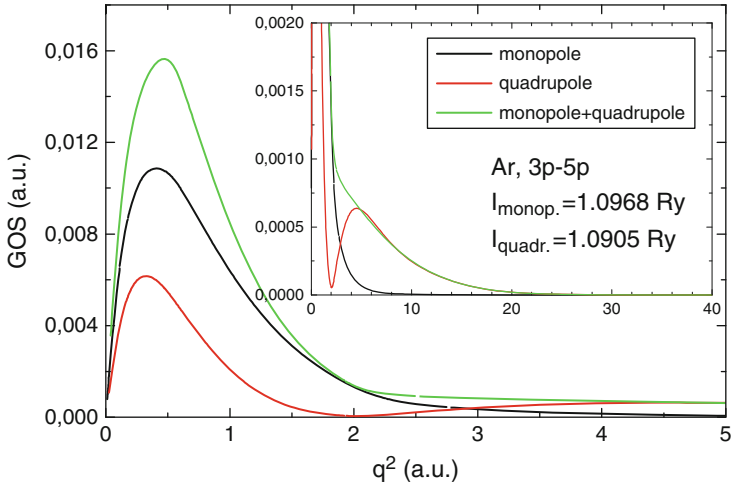

Fig. 4.63_Ar_f3 Generalized oscillator strengths of discrete monopole and quadrupole $3p$–$5p$ excitations as functions of a square moment transferred by electron to the atom Ar, in RPAE (see [4.13])

Figure 4.65_Ar_f5 shows the GOSes of discrete dipole $3p$–$4s$ and $3p$–$5s$ excitations for Ar as functions of q^2 transferred by electron to the atom, in RPAE (see [4.14]). For both levels GOSes have maximums, at the same q^2.

Figure 4.66_Ar_f6 shows the GOSes of discrete dipole $3p$–$3d$ and $3p$–$4d$ excitations for Ar as functions of q^2 by electron to the atom, in RPAE (see [4.14]). GOSes monotonously decrease with growth of q.

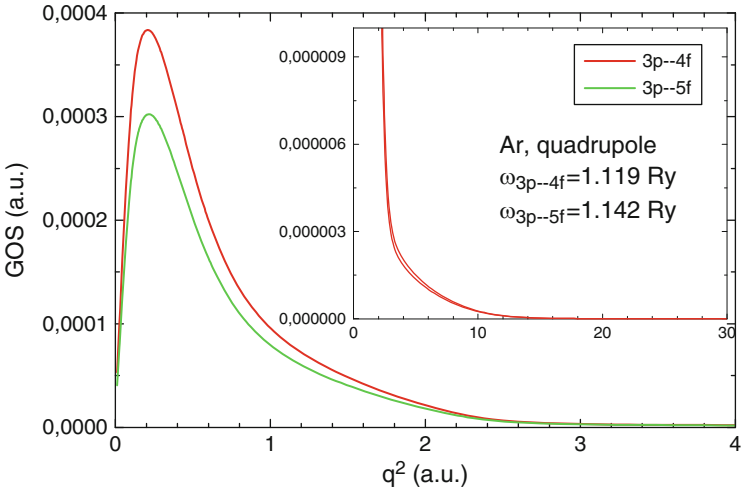

Fig. 4.64_Ar_f4 Generalized oscillator strengths of discrete quadrupole $3p$–$4f$ and $3p$–$5f$ excitations as function of square moment q transferred by electron to the atom Ar, in RPAE (see [4.13])

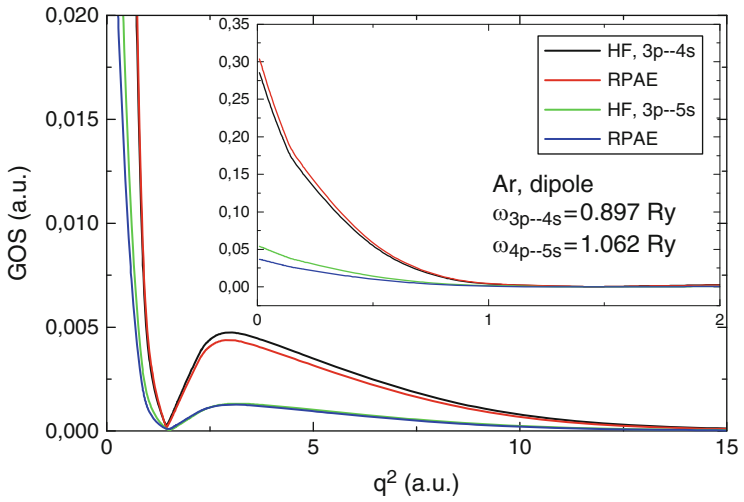

Fig. 4.65_Ar_f5 Generalized oscillator strengths of discrete dipole $3p$–$4s$ and $3p$–$5s$ excitations as functions of square moment q transferred by electron to the atom Ar, in RPAE (see [4.14])

Figure 4.67_Ar_f7 shows the GOSes of discrete octupole $3p$–$3d$ and $3p$–$4d$ excitations for Ar as function of q^2 transferred by electron to the atom, in RPAE (see [4.14]). As well as for all considered transitions, except dipole, GOSes grow with increase of q from $q = 0$, reaching a maximum at $q^2 \approx 1.7$.

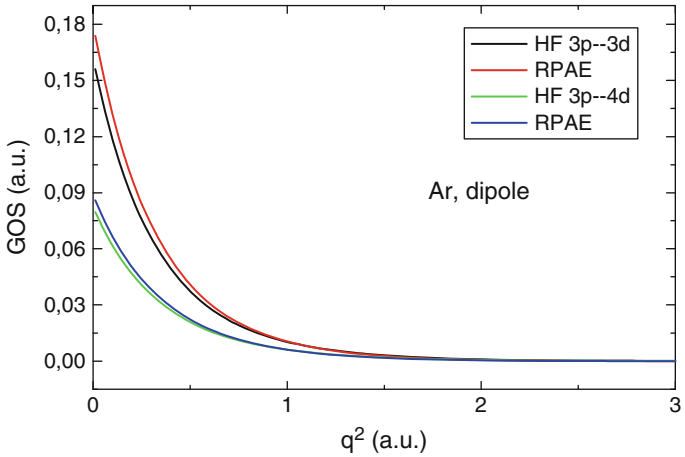

Fig. 4.66_Ar_f6 Generalized oscillator strengths of discrete dipole $3p$–$3d$ and $3p$–$4d$ excitations as functions of square moment q transferred by electron to atom for Ar in RPAE (see [4.14])

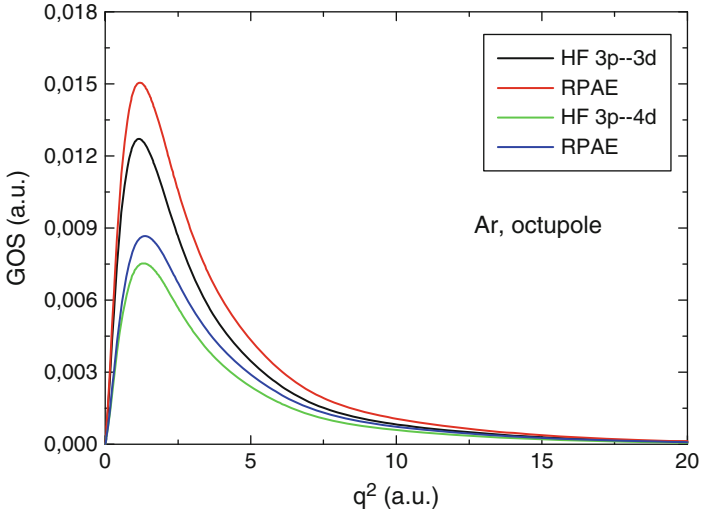

Fig. 4.67_Ar_f7 Generalized oscillator strengths of discrete octupole $3p$–$3d$ and $3p$–$4d$ excitations for Ar as functions of square moment q transferred by electron to the atom, in RPAE (see [4.14])

Figure 4.68_Ar_f8 shows the GOSes of discrete dipole and octupole $3p$–$3d$ excitations for Ar as function of q^2 square moment q transferred by electron to the atom, in RPAE (see [4.14]). As the levels are very close in energy, we present also the sum of their GOSes. Octupole GOS has one maximum at $q^2 \approx 1.25$, and dipole GOS promptly decreases with growth of q^2 up to 3 to form then a very broad and small maximum at $q^2 \approx 17$.

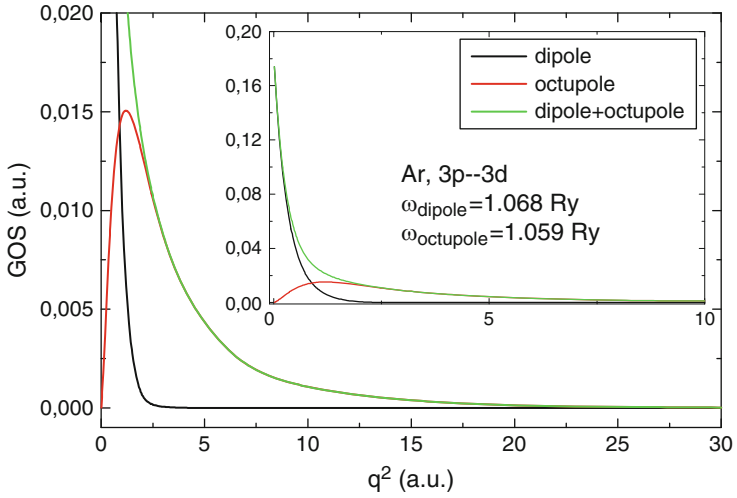

Fig. 4.68_Ar_f8 Generalized oscillator strengths of discrete dipole and octupole $3p$–$3d$ excitations as function of a square moment q transferred by electron to the atom Ar in RPAE (see [4.14])

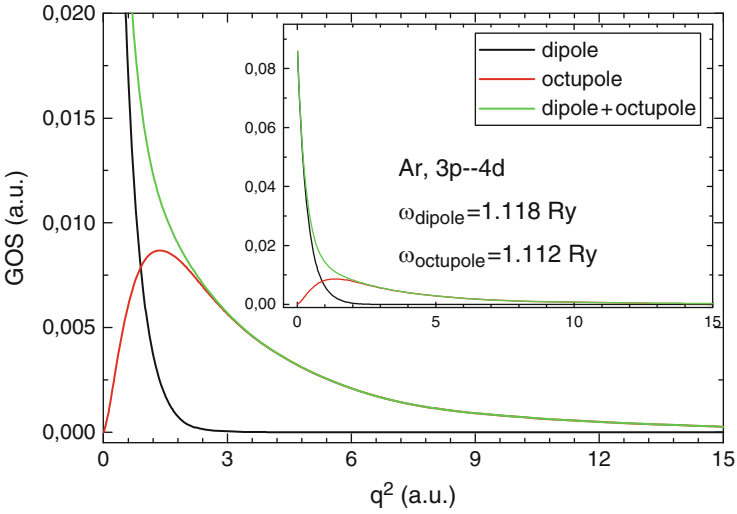

Fig. 4.69_Ar_f9 Generalized oscillator strengths of discrete dipole and octupole $3p$–$4d$ excitations as functions of square moment q transferred by electron to atom Ar, in RPAE (see [4.14])

Figure 4.69_Ar_f9 shows the GOSes of discrete dipole and octupole $3p$–$4d$ excitations as functions of q^2 transferred by electron to atom for Ar in RPAE (see [4.14]). Because of proximity of the levels in energy, the sum of their GOSes is in fact the only observable value.

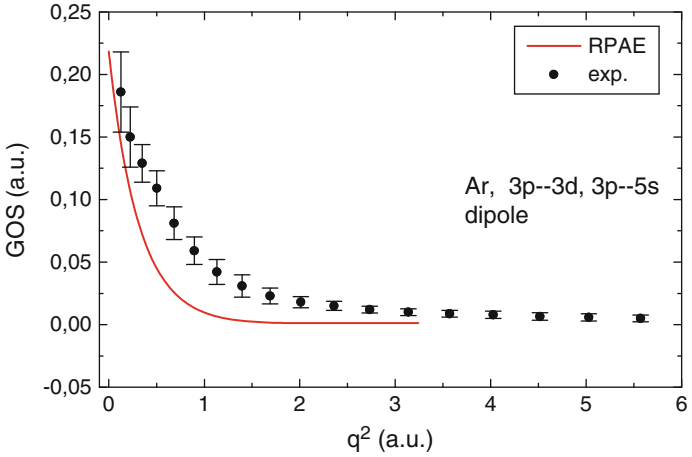

Fig. 4.70_Ar_f10 Generalized oscillator strengths of discrete dipole $3p$–$3d$, $3p$–$5s$ excitations as functions of square moment q transferred to atom Ar, in RPAE (see [4.14]). Experiment is from [4.24]

Figure 4.70_Ar_f10 shows the GOSes of discrete dipole $3p$–$3d$, $3p$–$5s$ excitations for Ar as functions of q^2 transferred to the atom, in RPAE (see [4.14]). The sum of GOSes quickly decreases with growth of q up to $q^2 \approx 1$ and then reaches a plateau. Experimental data are taken from [4.22]. The agreement between calculated and measured data is satisfactorily.

Figure 4.71_Ar_f11 shows the GOSes of discrete dipole $3p$–$4s$ excitation for Ar as function of q^2 square moment q transferred by electron to atom in HF and RPAE (see [4.23]). Experimental data are taken from [4.22]. Calculations reproduces well the position of a minimum in GOSes. Difference in the depths can be partly attributed to problems with resolution of experimental equipment (see [4.22]), but can be also reflection of necessity of going beyond the first Born approximation in the vicinity of a minimum.

Figure 4.72_Ar_f12 shows the GOSes of discrete monopole $3p$–$4p$ excitation for Ar as function of q^2 transferred by electron to the atom, in HF and RPAE (see [4.13]). Experimental data are taken from [4.24]. There is a qualitative agreement, but essential quantitative difference.

Figure 4.73_Ar_f13 shows the GOSes of discrete quadrupole $3p$–$4p$ excitation for Ar as function of q^2 transferred by electron to the atom, in HF and RPAE (see [4.13]). GOSes have two maxima, first of which, at smaller q, is by an order of magnitude bigger than the second. Experimental data are taken from [4.24]. Between theory and experiment there is a qualitative agreement, but essential quantitative difference.

Figure 4.74_Ar_g1 shows the cross-section of monopole Compton scattering of γ-quanta with energy $E = 2,000$ Ry on Ar as function of the moment q transferred to the atom, at various energies ω and at the transferred angular moment $L = 0$,

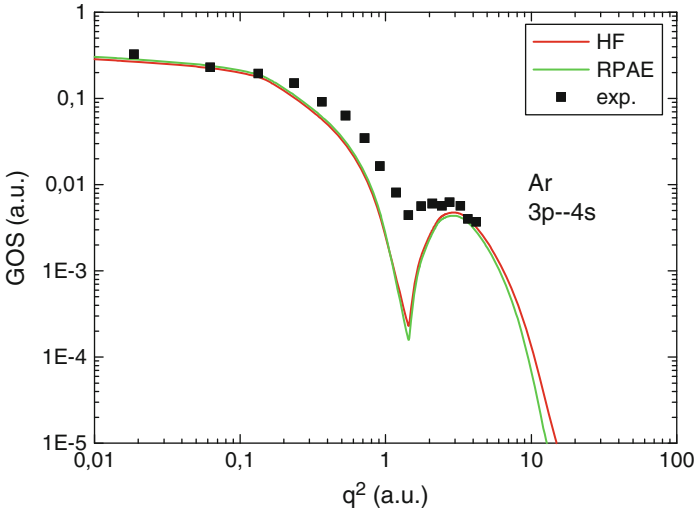

Fig. 4.71_Ar_f11 Generalized oscillator strengths of discrete dipole $3p$–$4s$ excitation as function of square moment q transferred by electron to atom Ar, in HF and RPAE (see [4.23]). Experiment is from [4.22]

in RPAE (see [4.15]). Note the big range of the considered values of q, $0 < q < 8$ and systematic shift of the maximums to the higher side of q values with growth of ω.

Figure 4.75_Ar_g2 shows the cross-section of dipole Compton scattering of γ-quanta with energy $E = 2,000$ Ry on Ar in RPAE as function of the moment q transferred to the atom, at various energies ω and at the transferred angular moment $L = 1$ (see [4.15]). The maximum moves to bigger values of q.

Figure 4.76_Ar_g3 shows the cross-section of quadrupole Compton scattering of γ-quanta with energy $E = 2,000$ Ry on Ar in RPAE as function of the moment q transferred to the atom, at various energies ω and at the transferred angular moment $L = 2$ (see [4.15]). The cross-section has two maxima, which with growth of ω leave aside big q.

Figure 4.77_Ar_g4 shows the cross-section of octupole Compton scattering of γ-quanta of energy $E = 2,000$ Ry on Ar in RPAE as function of the moment q transferred to the atom, at various energies ω and at the transferred angular moment $L = 3$ (see [4.15]). One maximum is seen, which with growth of ω decreases in value and moves to bigger q, just as in the previous figures.

Figure 4.78_Ar_h1 shows the cross-section of Compton excitation [defined by (3.94)], relative to Thomson cross-section, of dipole $3p$–$4s$, $3p$–$5s$ levels for Ar in RPAE (see [4.16]). Two-humped structure of GOSes is distinctly visible. On the way from $3p$–$4s$ to $3p$–$5s$ GOSes considerably decrease.

Figure 4.79_Ar_h2 shows the cross-section of Compton excitation [defined by (3.94)], relative to Thomson cross-section, of dipole and octupole $3p$–$3d$ levels for

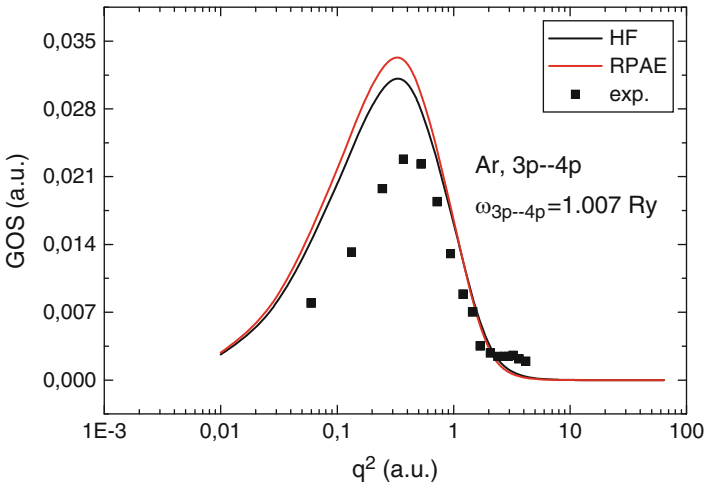

Fig. 4.72_Ar_f12 Generalized oscillator strengths of discrete monopole $3p$–$4p$ excitation as function of square moment q transferred by electron to the atom Ar in HF and RPAE (see [4.13]). Experiment is from [4.24]

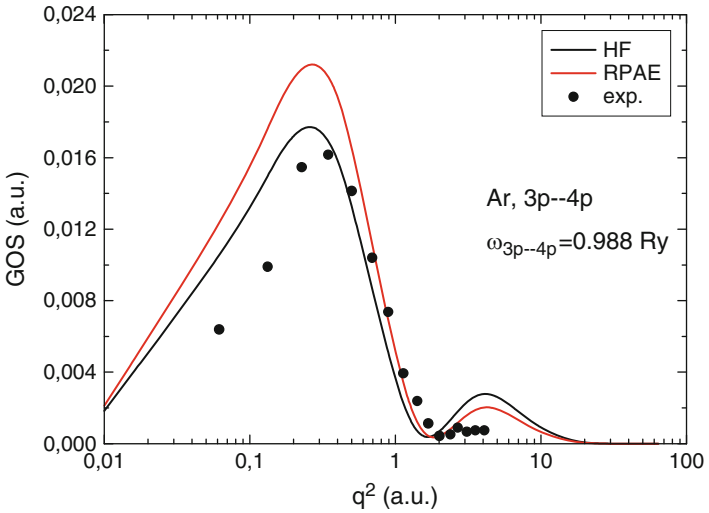

Fig. 4.73_Ar_f13 Generalized oscillator strengths of discrete quadrupole $3p$–$4p$ excitation as function of square moment q transferred by electron to atom Ar, in HF and RPAE (see [4.13]). Experiment is from [4.24]

Ar in RPAE (see [4.16]). Note that octupole transition is much stronger. This signals that higher transferred angular moments become important in Compton, contrary to the case of fast electron inelastic scattering, where dipole transition dominates.

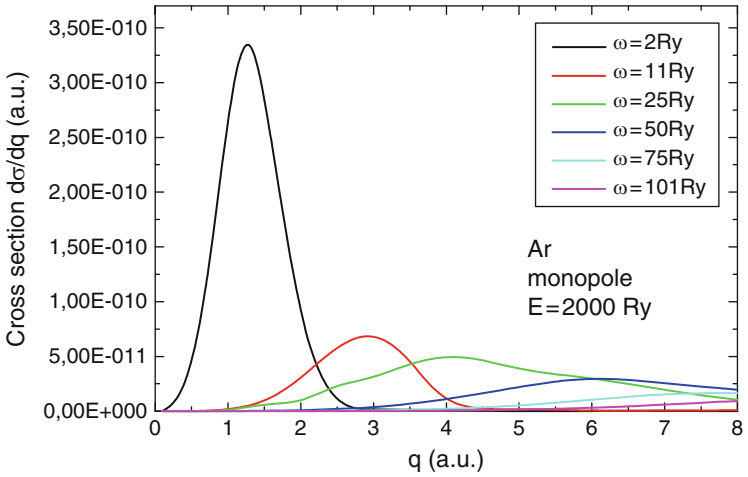

Fig. 4.74_Ar_g1 Cross-section of monopole Compton scattering of γ-quanta with energy $E = 2,000$ Ry on Ar as function of the moment q transferred to atom, at various energies ω, in RPAE (see [4.15])

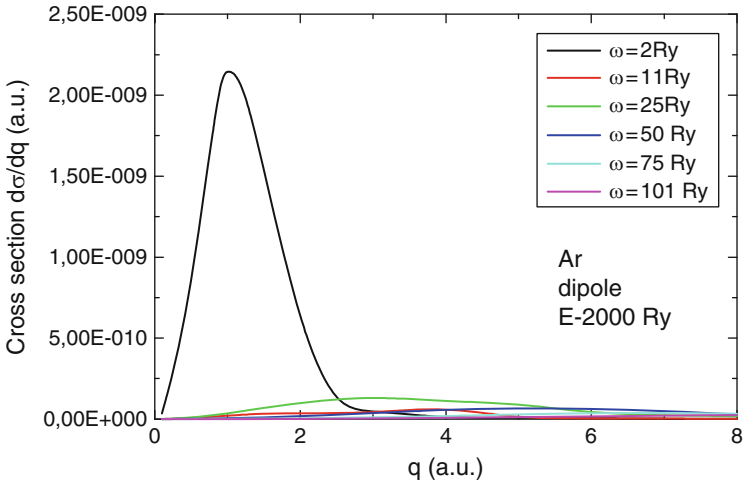

Fig. 4.75_Ar_g2 Cross-section of dipole Compton scattering of γ-quanta with energy $E = 2,000$ Ry on Ar as function of the moment q transferred to atom, at various energies ω, in RPAE (see [4.15])

Figure 4.80_Ar_h3 shows the relative to Thomson cross-section the cross-section of Compton excitation [defined by (3.94)] of quadrupole and monopole $3p$–$4p$ levels, almost exact degenerate, for Ar, in RPAE (see [4.16]). The trace of quadrupole maximum in cross-section is seen.

Figure 4.81_Ar_h4 shows the relative to Thomson cross-section the cross-section of Compton excitation [defined by (3.94)] of quadrupole and monopole $3p$–$5p$

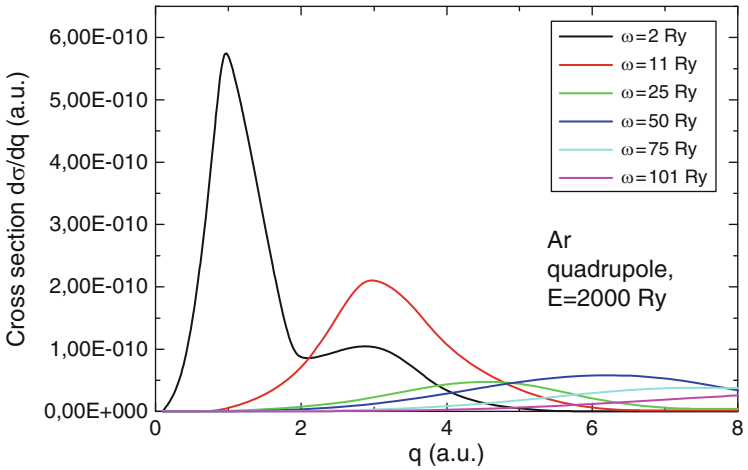

Fig. 4.76_Ar_g3 Cross-section of quadrupole Compton scattering of γ-quanta with energy $E = 2,000$ Ry on Ar as function of the moment q transferred to atom, at various energies ω in RPAE (see [4.15])

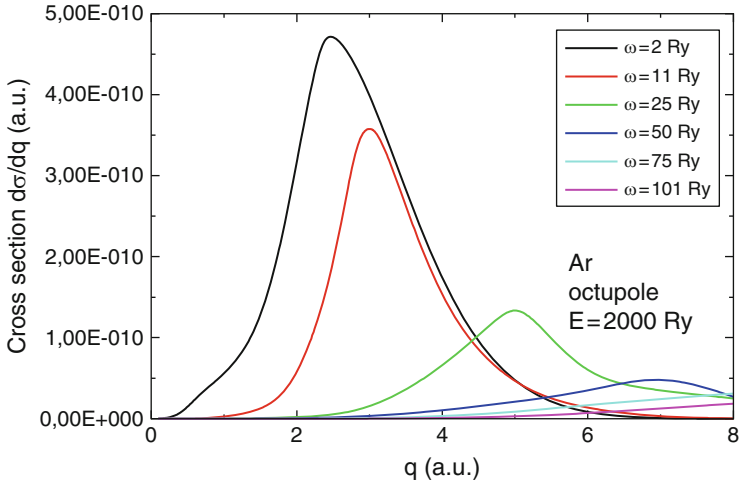

Fig. 4.77_Ar_g4 Cross-section of octupole Compton scattering of γ-quanta with energy $E = 2,000$ Ry on Ar as function of the moment q transferred to the atom, at various energies ω, in RPAE (see [4.15])

levels, almost exact degenerate, for Ar in RPAE (see [4.16]). The trace is seen of quadrupole maximum in total cross-section.

Figure. 4.82_Ar_h5 shows the relative to Thomson cross-section the cross-section of Compton excitation [defined by (3.94)] of $3p$–$5p$, $3p$–$3d$, $3p$–$4d$, $3p$–$5s$ levels: monopole, dipole, quadrupole, and octupole, and some of their combinations for Ar in RPAE (see [4.16]). All these levels are very close in energy. The presence of two

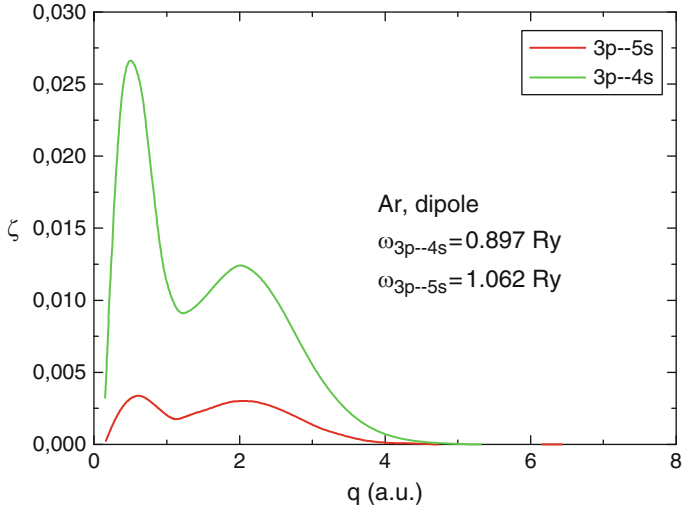

Fig. 4.78_Ar_h1 Relative cross-sections of Compton excitation of dipole $3p$–$4s$, $3p$–$5s$-levels for Ar in RPAE (see [4.16])

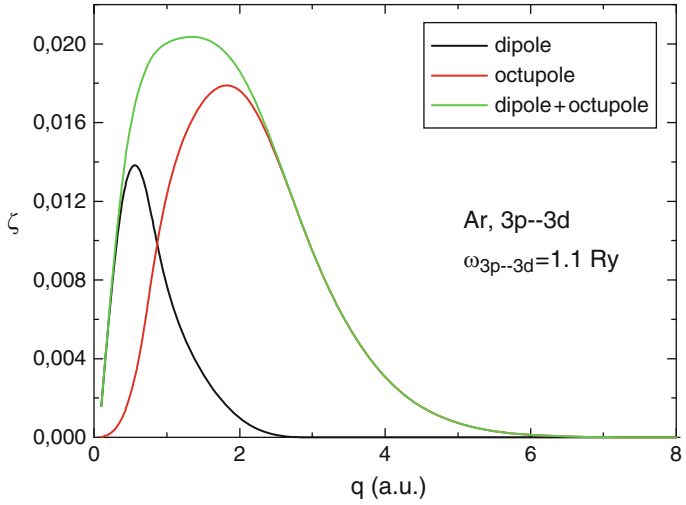

Fig. 4.79_Ar_h2 Relative cross-sections of Compton excitation of dipole and octupole $3p$–$3d$ levels for Ar, in RPAE (see [4.16])

maxima in "dipole + octupole" cross-section is not visible after summation of other closely located transitions is performed.

Figure 4.83_Ar_i1 shows the cross-section of elastic positron scattering on atom Ar in HF and SRPAE (see [4.10]). Experimental data are taken from [4.17]. Polarization interaction takes into account the virtual and real excitation of $3p$ and

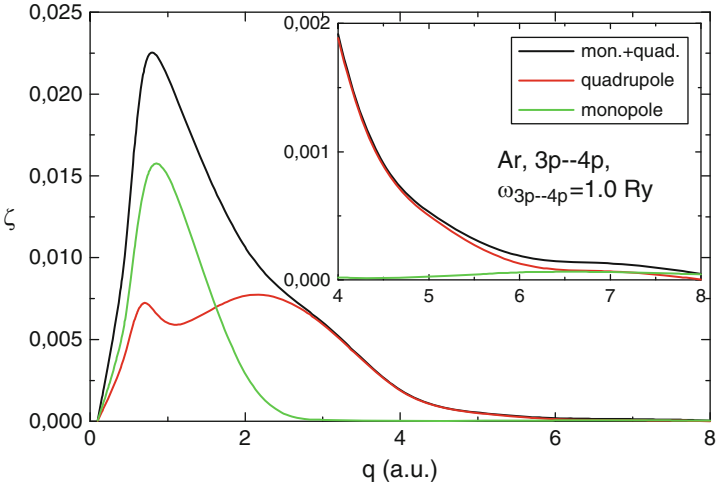

Fig. 4.80_Ar_h3 Relative cross-sections of Compton excitation quadrupole and monopole $3p$–$4p$ levels, almost exactly degenerate, for Ar in RPAE (see [4.16])

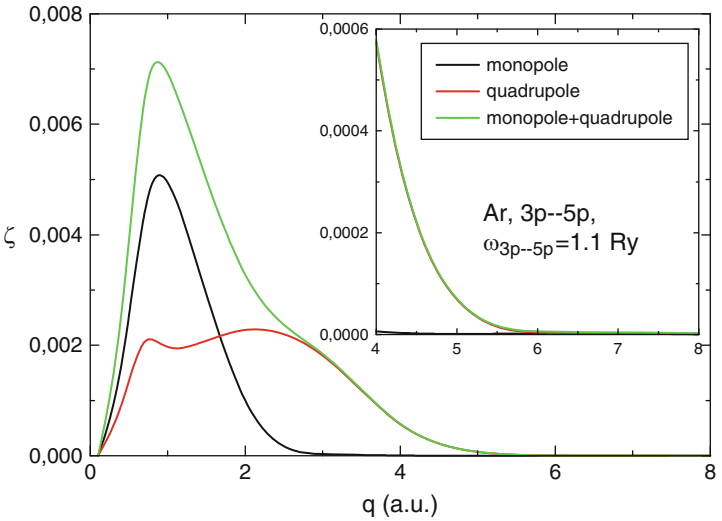

Fig. 4.81_Ar_h4 Relative cross-sections of Compton excitation of quadrupole and monopole $3p$–$5p$ levels, almost exactly degenerate, for Ar in RPAE (see [4.16])

$3p$ subshells and formation of virtual positronium. However, the deviation from experimental data is great, although the calculation reproduces significant change in speed of decrease of the cross-section at 2–2.5 eV.

Figure 4.84_Ar_j1 shows the contribution of partial waves to cross-section of elastic positron scattering on atom Ar in SRPAE. Polarization interaction takes into account the virtual and real excitation of $3p$ and $3s$ subshells and formation of

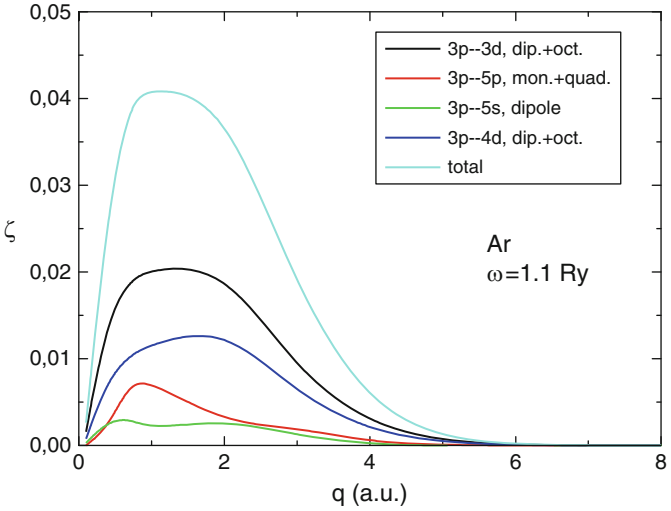

Fig. 4.82_Ar_h5 Relative cross-section of Compton excitation of $3p - 5p, 3p - 3d, 3p - 4d$, $3p - 5s$-levels: monopole, dipole, quadrupole, and octupole and their some combinations for Ar in RPAE (see [4.16])

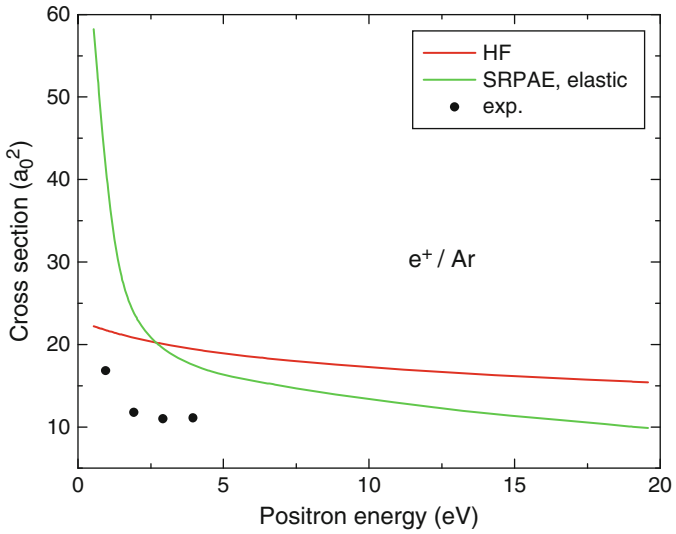

Fig. 4.83_Ar_i1 Cross-section of elastic positron scattering on Ar atom, in HF and SRPAE (see [4.10]). Experiment is from [4.17]

virtual positronium. Note that the s-wave contribution has a distinctive Ramsauer-type minimum that is, however, completely masked in the total cross-section mainly due to big p-wave contribution.

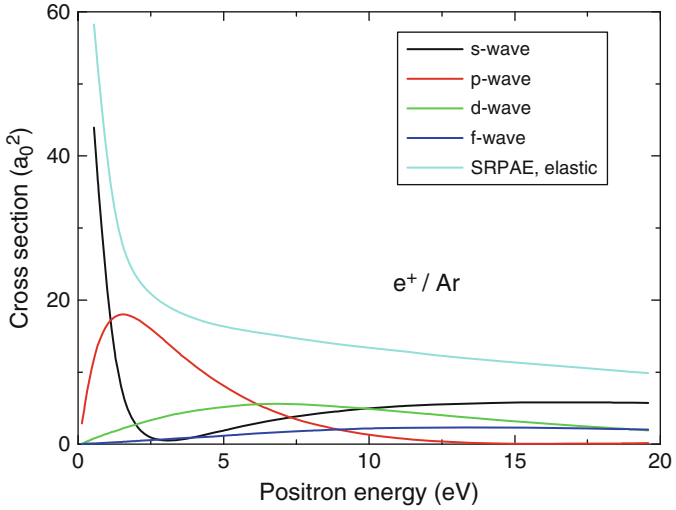

Fig. 4.84_Ar_j1 Contribution of partial waves in cross-section of positron elastic scattering on Ar in SRPAE

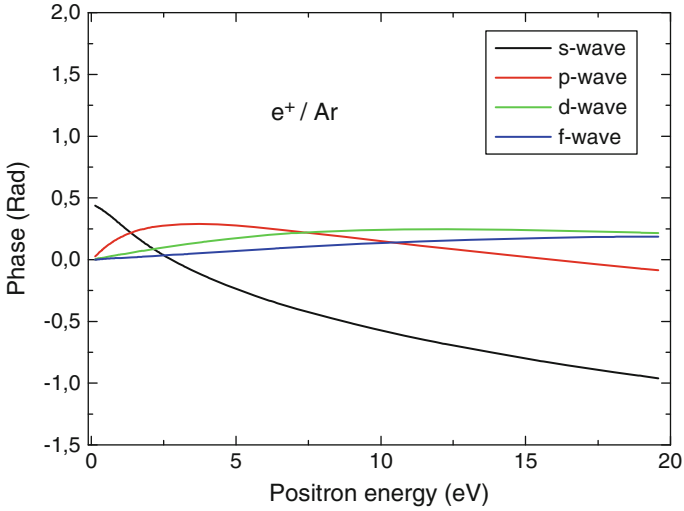

Fig. 4.85_Ar_k1 Phases of various partial waves in positron scattering on Ar in SRPAE

Figure 4.85_Ar_k1 shows the phases of various partial waves in positron scattering on Ar atom in SRPAE. The *s*-wave's phase starts, according to calculations, neither from zero, nor from any $n\pi$, thus contradicting to (3.21). Qualitatively, this is discussed at the end of Chap. 3.

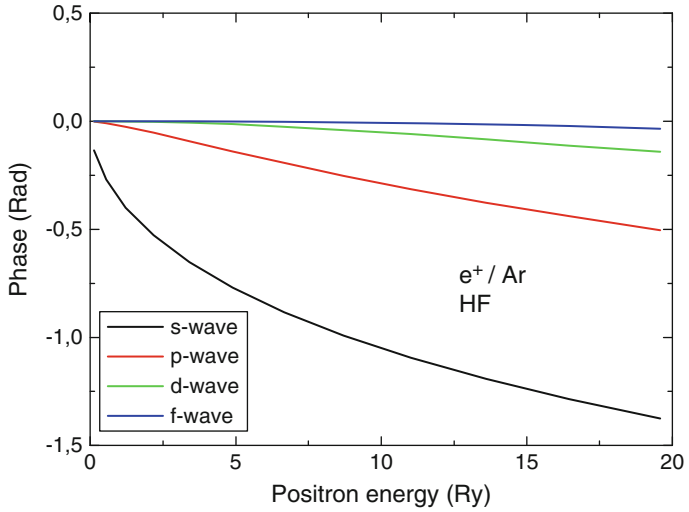

Fig. 4.86_Ar_k2 Phases of various partial waves in positron scattering on Ar in HF

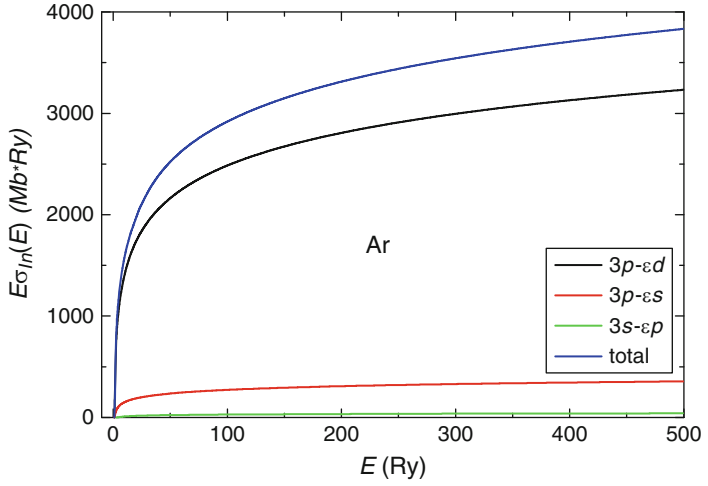

Fig. 4.87_Ar_l1 Multiplied by incoming electron energy cross-section of inelastic scattering of fast electrons in the logarithmic approximation

Figure 4.86_Ar_k2 shows the phases of various partial waves in positron scattering on Ar in HF. Note that all derivatives of the phases in energy at $E \to 0$ are negative.

Figure 4.87_Ar_l1 shows the total and partial cross-sections of inelastic scattering of fast electrons, multiplied by incoming electron energy, on atom Ar in logarithmic approximation $E\sigma_{\mathrm{In}}(E)$. Dominative is the contribution of scattering upon the outer $3p$ subshell, mainly from $3p$ to $3d$ transition. It is seen that all these functions

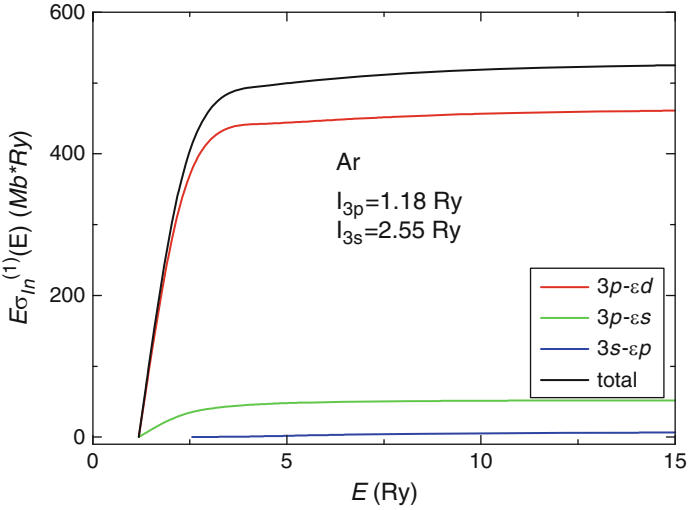

Fig. 4.88_Ar_l2 Nonlogarithmic correction to the multiplied by incoming electron energy cross-section of inelastic scattering of fast electrons

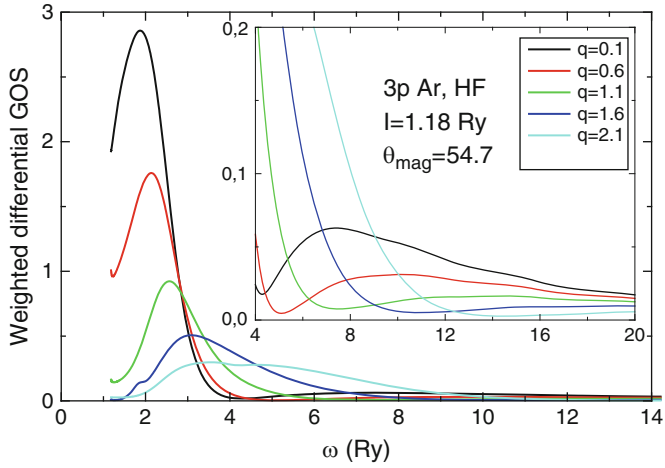

Fig. 4.89_Ar_m1 Weighted differential generalized oscillator strength given by (3.73b) at magic angle $P_2(\cos\theta_m) = 0$ of $3p$ subshell for Ar at different q in HF

at high E increase slowly. The fastest is the increase of the biggest partial cross-section. The cross-sections are presented from $E = I$ for completeness only, since the logarithmic approximation is valid if $\ln(E/I) \gg 1$.

Figure 4.88_Ar_l2 shows the multiplied by incoming electron energy total and partial nonlogarithmic corrections to the cross-sections of inelastic scattering of fast

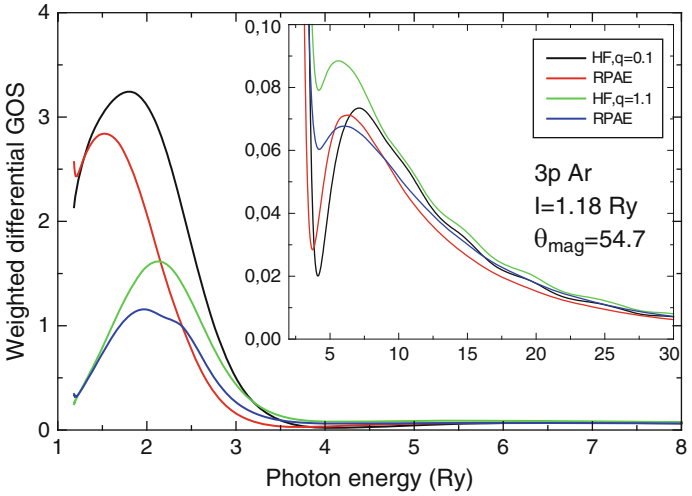

Fig. 4.90_Ar_m2 Weighted differential generalized oscillator strength given by (3.73b) at magic angle $P_2(\cos\theta_{\rm m}) = 0$ of $3p$ subshell for Ar at different q in HF and RPAE

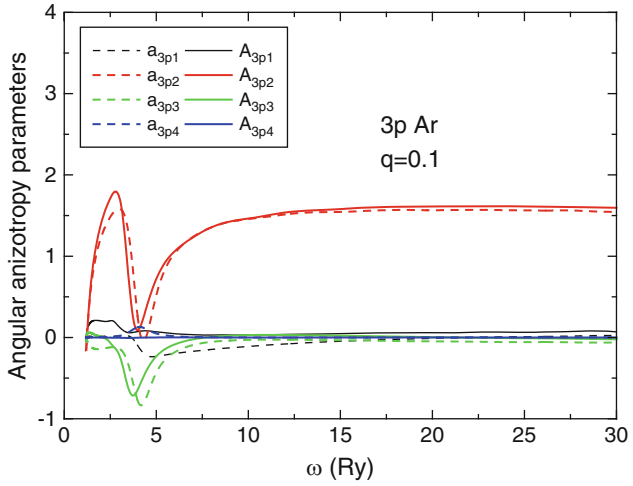

Fig. 4.91_Ar_m3 Angular anisotropy parameters of knocked-out electrons from $3p$ subshell of Ar in fast projectile–atom collision, given by (3.77) in HF (a_{3pi}) and RPAE (A_{3pi}) at $q = 0.1$ as functions of ω

electrons on Ar atom $E\sigma_{\rm In}^{(1)}(E)$. It is seen that these functions stop to grow already at $E = 7$ Ry.

Figure 4.89_Ar_m1 shows the weighted differential in emission angle GOSes of knocked-out electron in fast projectile–Ar atom collision in HF, given by (3.73b) at magic angle $P_2(\cos\theta_{\rm m}) = 0$ and a set of q values $q = 0.1$, 0.6, 1.1, 1.6, and

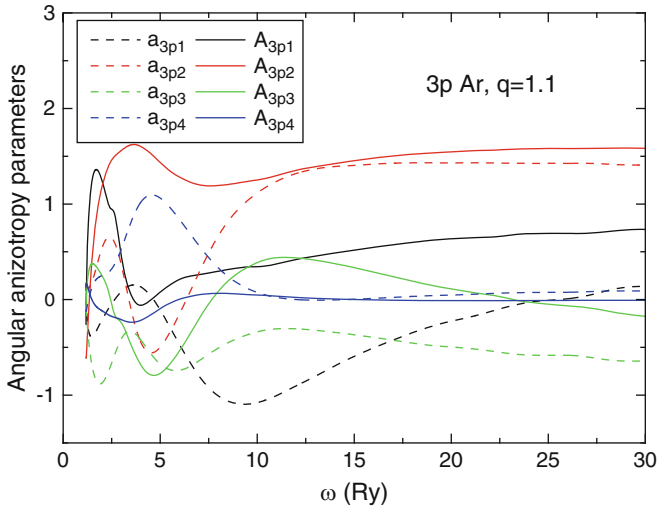

Fig. 4.92_Ar_m4 Angular anisotropy parameters of knocked-out electrons from $3p$ subshell of Ar in fast projectile–atom collision, given by (3.77), in HF (a_{3pi}) and RPAE (A_{3pi}) at $q = 1.1$ as functions of ω

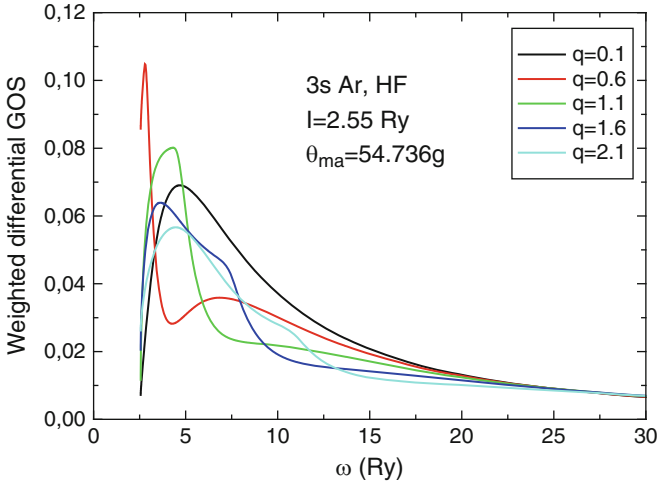

Fig. 4.93_Ar_m5 Weighted differential generalized oscillator strength given by (3.73b) at magic angle $P_2(\cos\theta_m) = 0$ of $3s$ subshell for Ar at different q in HF

2.1. Outer $3p$ subshell is considered. GOSes form a maximum that for small q is similar, as it should be, to the photoionization cross-section (see Fig. 2.22_Ar_a1). With ω growth one can see second and third maximums. With increase of q the first GOS maximum decreases rather fast slightly moving to higher ω. Other maximums remain almost unaffected.

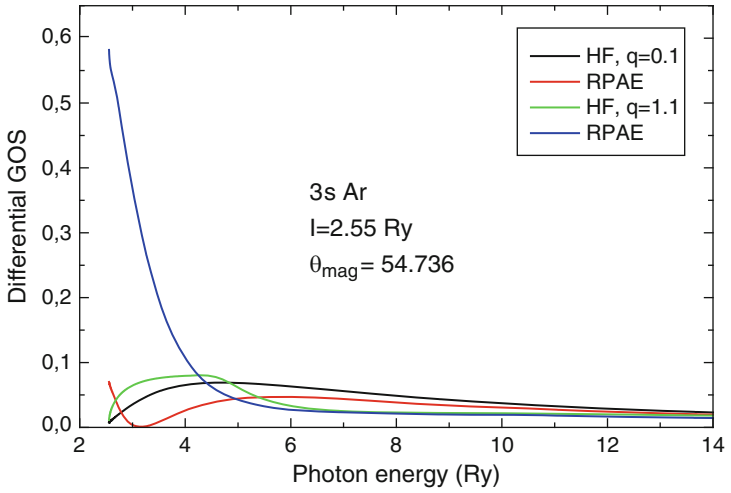

Fig. 4.94_Ar_m6 Weighted differential generalized oscillator strength (3.73b) at magic angle $P_2(\cos\theta_m) = 0$ of $3s$ subshell for Ar at different q in HF and RPAE

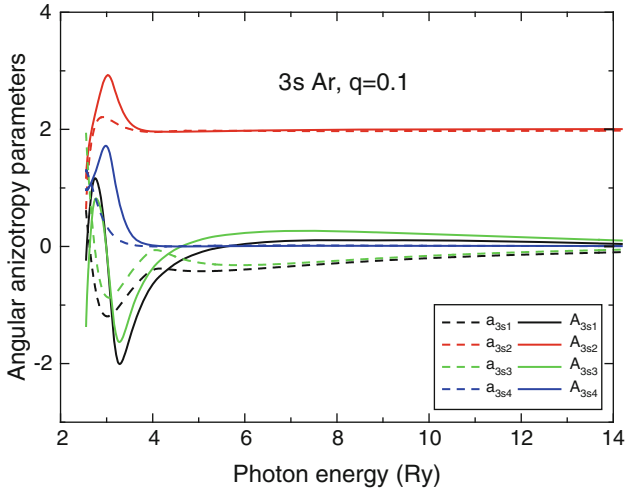

Fig. 4.95_Ar_m7 Angular anisotropy parameters of knocked-out electrons from $3s$ subshell of Ar in fast projectile–atom collision, given by (3.77) in HF (a_{3si}) and RPAE (A_{3si}) at $q = 0.1$ as functions of ω

Figure 4.90_Ar_m2 shows the weighted differential in electron emission angle GOSes given by (3.73b) at magic angle $P_2(\cos\theta_m) = 0$ of Ar $3p$ subshell in HF and RPAE for $q = 0.1$ and $q = 1.1$. As shown in Fig. 4.89_Ar_m1, GOSes are similar, as it should be, to the photoionization cross-section (see Fig. 2.22_Ar_a1). At $q = 1.1$, the main GOS maximum is much smaller than for $q = 0.1$. The minimum, which

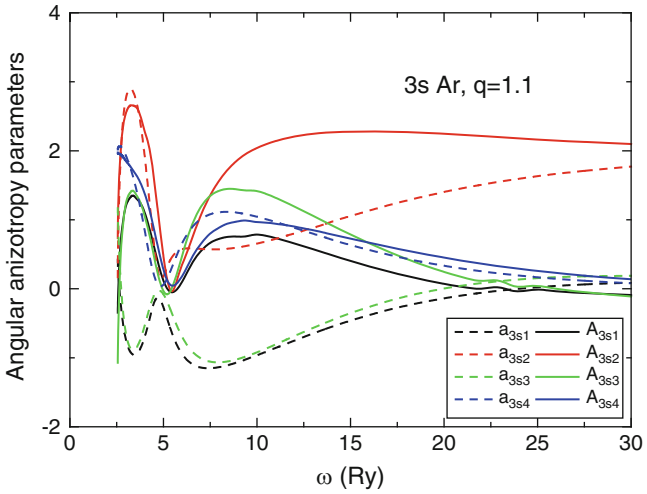

Fig. 4.96_Ar_m8 Angular anisotropy parameters of knocked-out electrons from $3s$ subshell of Ar in fast projectile–atom collision, given by (3.75) in HF (a_{3si}) and RPAE (A_{3si}) at $q = 1.1$ as functions of ω

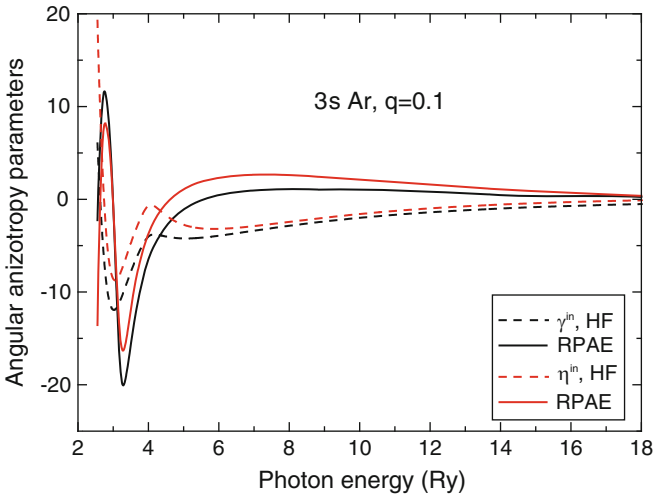

Fig. 4.97_Ar_m9 Angular anisotropy nondipole parameters of knocked-out electrons in fast projectile–atom collision in the optical limit given by (3.84a) and (3.84b) at $q = 0.1$ for $3s$ subshell of Ar

is similar to Cooper minimum in photoionization, is particularly deep in RPAE at $q = 0.1$.

Figure 4.91_Ar_m3 shows the angular anisotropy parameters of knocked-out electrons from $3p$ subshell of Ar in fast projectile–atom collision, given by (3.77) in HF (a_{3pi}) and RPAE (A_{3pi}) at $q = 0.1$ as functions of ω. The role of correlations

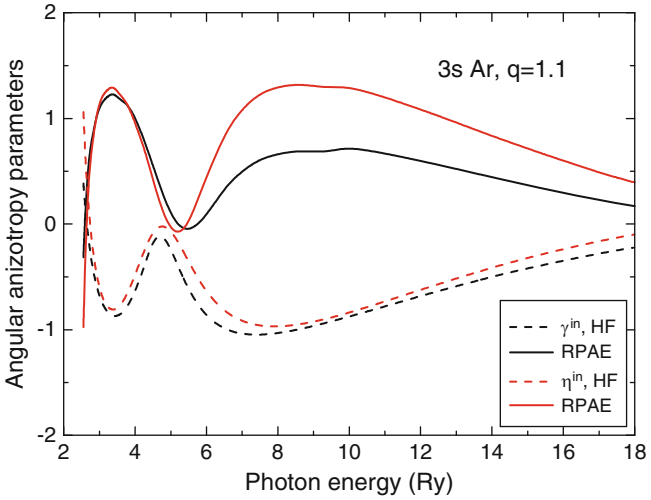

Fig. 4.98_Ar_m10 Angular anisotropy nondipole parameters of knocked-out electrons in fast projectile–atom collision in the optical limit given by (3.84a) and (3.84b) at $q = 1.1$ for $3s$ subshell of Ar

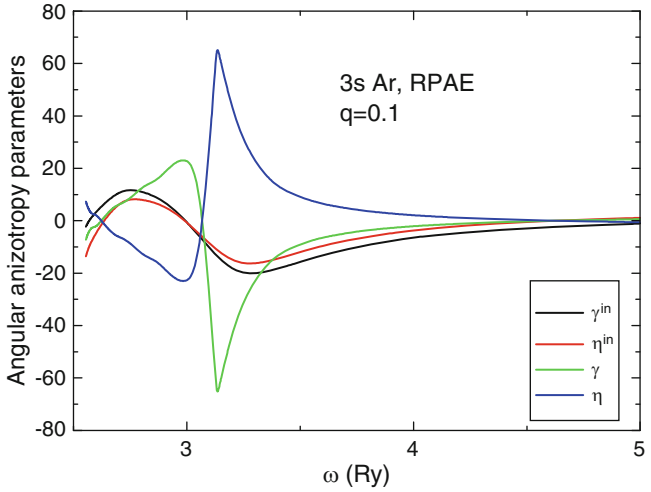

Fig. 4.99_Ar_m11 Angular anisotropy nondipole parameters of knocked-out electrons in fast projectile–atom collision in the optical limit compared to similar parameters in photoionization, given by (3.84a) and (3.84b) at $q = 0.1$ and (3.83) for $3s$ subshell of Ar in RPAE

is essential only for A_{3p1} that differs essentially from a_{3p1}. For other angular anisotropy parameters, correlations are small and energy dependence is in the vicinity of threshold. The dipole coefficients, as it should be, for small q by far exceed the nondipole.

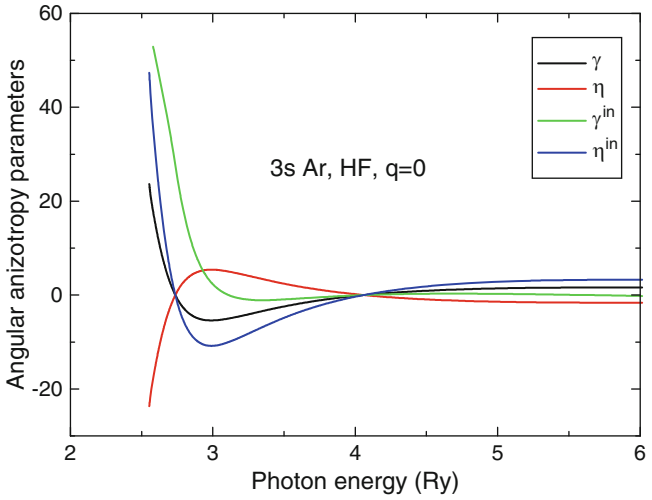

Fig. 4.100_Ar_m12 Comparison of nondipole anisotropy parameters of Ar $3s$ electrons in photoionization and fast electron inelastic scattering [see (3.84b)] at $q = 0$, calculated in HF

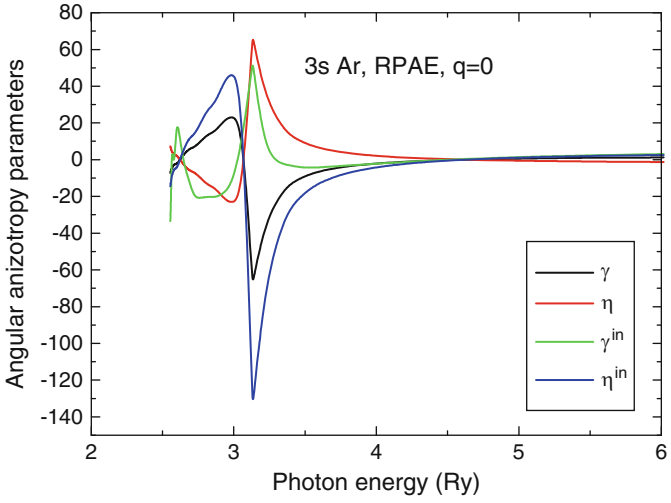

Fig. 4.101_Ar_m13 Comparison of nondipole anisotropy parameters of Ar $3s$ electrons in photoionization and fast electron inelastic scattering [see (3.84b)] at $q = 0$, calculated in RPAE

Figure 4.92_Ar_m4 shows the angular anisotropy parameters of knocked-out electrons from $3p$ subshell of Ar in fast projectile–atom collision, given by (3.77), in HF (a_{3pi}) and RPAE (A_{3pi}) at $q = 1.1$ as functions of ω. The increase of q from 0.1 to 1.1 leads to essential growth of the nondipole parameters with $i = 2$.

Figure 4.93_Ar_m5 shows the weighted differential in electron emission angle GOSes given by (3.73b) at magic angle $P_2(\cos\theta_m) = 0$ of $3s$ subshell for Ar at $q = 0.1, 0.6, 1.1, 1.6, 2.1$ in HF. They have maximums close to threshold and with increase of q became a structure more complex that at small q, where it is similar to photoionization cross-section shown in Fig. 2.25_Ar_b3 rapidly decrease with growth of ω forming a prominent minimum that becomes narrower and deeper with increase of q.

Figure 4.94_Ar_m6 shows the weighted differential in electron emission angle GOSes (3.73b) at magic angle $P_2(\cos\theta_m) = 0$ of $3s$ subshell for Ar at $q = 0.1$ and 1.1 in HF and RPAE. For $q = 0.1$ the situation is similar to photoionization where RPAE brings in a correlation or interference minimum (Fig. 2.25_Ar_b3). For $q = 1.1$, RPAE considerably decreases the height of the near threshold maximum.

Figure 4.95_Ar_m7 shows the angular anisotropy parameters of knocked-out electrons from $3s$ subshell of Ar in fast projectile–atom collision, given by (3.75), in HF (a_{3si}) and RPAE (A_{3si}) at $q = 0.1$ as functions of ω. Energy dependence of dipole parameter a_{3s2} and A_{3s2} disappear at about 4 Ry and they reach the value of the optical limit ($q \to 0$) $- a_{3s2} = A_{3s2} = 2$. Parameters with $i = 1, 3$ are by a factor of $q = 0.1$ smaller than that with $i = 2$. As to parameter $i = 4$, it is smaller than $a_{3s2} = A_{3s2} = 2$ by a factor $q^2 = 0.01$.

Figure 4.96_Ar_m8 shows the angular anisotropy parameters of knocked-out electrons from $3s$ subshell of Ar in fast projectile–atom collision, given by (3.75) in HF (a_{3si}) and RPAE (A_{3si}) at $q = 1.1$ as functions of ω. All parameters are of the same order of magnitude, essentially depend upon ω and that with $i = 1$ and 4 are mirror reflection relative to horizontal axis of the parameter with $i = 4$.

Figure 4.97_Ar_m9 shows the angular anisotropy nondipole parameters of knocked-out electrons in fast projectile–atom collision in the optical limit given by (3.84a) and (3.84b) at $q = 0.1$ for $3s$ subshell of Ar. Strong variations of parameters are located at $\omega < 2$ Ry. A strong and deep in RPAE minimum in $\eta^{(in)}$ should be compared to much smaller maximum in RPAE only for $\gamma^{(in)}$ at the same ω.

Figure 4.98_Ar_m10 shows the angular anisotropy nondipole parameters of knocked-out electrons in fast projectile–atom collision in the optical limit given by (3.84a) and (3.84b) at $q = 1.1$ for $3s$ subshell of Ar. Both parameters $\gamma^{(in)}$ and $\eta^{(in)}$ vary essentially and are of the same order of magnitude.

Figure 4.99_Ar_m11 shows the angular anisotropy nondipole parameters of knocked-out electrons in fast projectile–atom collision in the optical limit $\gamma_{3s}^{(in)}(\omega)$ and $\eta_{3s}^{(in)}(\omega)$ given by (3.84a) and (3.84b) at $q = 0.1$ compared to similar parameters in photoionization $\gamma_{3s}(\omega)$ and $\eta_{3s}(\omega)$, given by (3.83) for $3s$ subshell of Ar in RPAE. The ratio $\eta_{ns}^{(in)}(\omega) = 2\gamma_{ns}(\omega)$ is fulfilled with good accuracy.

Figure 4.100_Ar_m12 shows the comparison of nondipole anisotropy parameters of Ar $3s$ electrons in photoionization and fast electron inelastic scattering [see (3.84b)] at $q = 0$, calculated in HF. The ratio $\eta_{ns}^{(in)}(\omega) = 2\gamma_{ns}(\omega)$ is fulfilled with excellent accuracy. The relations between $\gamma_{ns}(\omega)$ and $\gamma_{ns}^{(in)}(\omega)$, $\eta_{ns}(\omega)$ and $\eta_{ns}^{(in)}(\omega)$

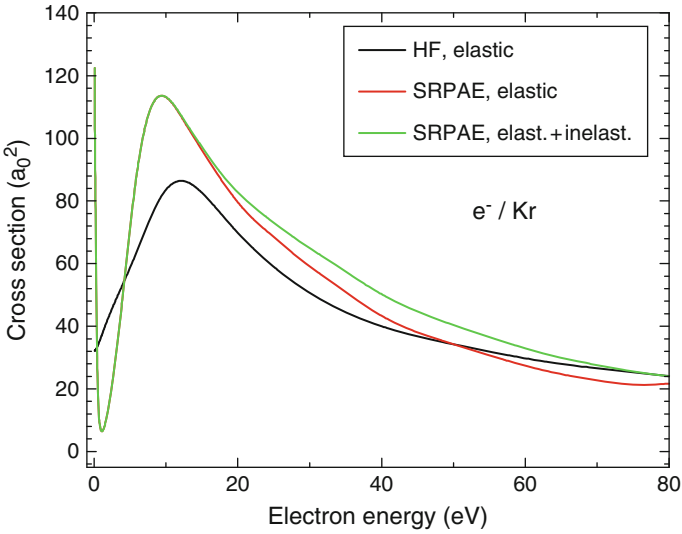

Fig. 4.102_Kr_a1 Cross-section of elastic (in HF and SRPAE) and inelastic (in SRPAE) electron scattering on Kr atom (see [4.1, 4.2])

are energy dependent. The $\gamma_{ns}^{(\mathrm{in})}(\omega)$ and $\eta_{ns}^{(\mathrm{in})}(\omega)$ are considerably bigger than $\gamma_{ns}(\omega)$ and $\eta_{ns}(\omega)$, and their contribution to the differential in angle oscillator strength can be increased by going to higher values of q [see (3.84a)].

Figure 4.101_Ar_m13 shows the comparison of nondipole anisotropy parameters of Ar $3s$ electrons in photoionization and fast electron inelastic scattering [see (3.84b)] at $q = 0$, calculated in RPAE. The effect of electron correlations is very big. The ratio $\eta_{ns}^{(\mathrm{in})}(\omega) = 2\gamma_{ns}(\omega)$ is fulfilled with excellent accuracy. The relations between $\gamma_{ns}(\omega)$ and $\gamma_{ns}^{(\mathrm{in})}(\omega)$, $\eta_{ns}(\omega)$, and $\eta_{ns}^{(\mathrm{in})}(\omega)$ are energy dependent, just as in HF (see Fig. 4.100_Ar_m12). The $\gamma_{ns}^{(\mathrm{in})}(\omega)$ and $\eta_{ns}^{(\mathrm{in})}(\omega)$ parameters are considerably bigger than $\gamma_{ns}(\omega)$ and $\eta_{ns}(\omega)$, and the (in) parameters in RPAE are much bigger than in HF. Nondipole parameters contribution to the differential in angle oscillator strength can be increased by going to higher values of q [see (3.84a)]

Figures 4.102–4.132 (Kr) show the results of calculations for Kr atom.

Figure 4.102_Kr_a1 shows the cross-section of elastic (in HF and SRPAE) and inelastic (in SRPAE) electron scattering on Kr atom (see [4.1, 4.2]). The role of electronic correlations is great down to energy of electron in about 20 eV. Ramsauer minimum [4.20] arises only if polarization interaction is taken into account. In calculations of this interaction, the contribution of virtual and real excitations of subshells $3d, 4s, 4p$ is taken into account. The inelastic cross-section is small in all considered energy region.

Figure 4.103_Kr_b1 shows the contribution of partial waves to cross-section of elastic electron scattering on Kr. Attention deserves a powerful maximum in d-wave, which with further increase of nuclear charge becomes a bound $4d$-level. Here not as usual the p-, but d-wave contribution defines the cross-section at the

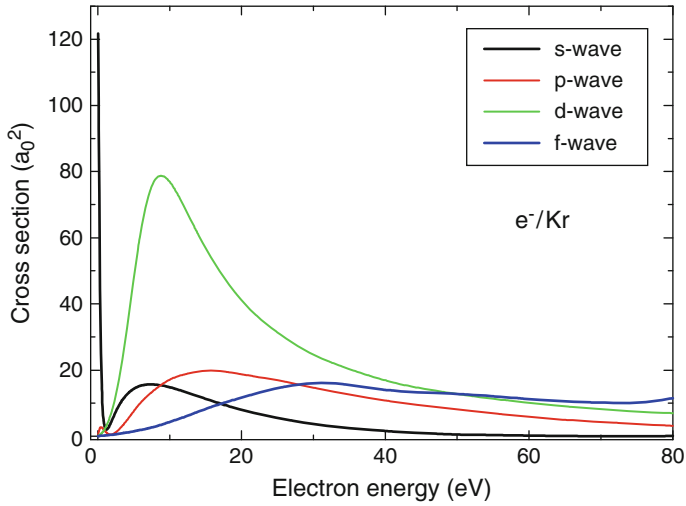

Fig. 4.103_Kr_b1 Contribution of partial waves to cross-section of elastic electron scattering on Kr

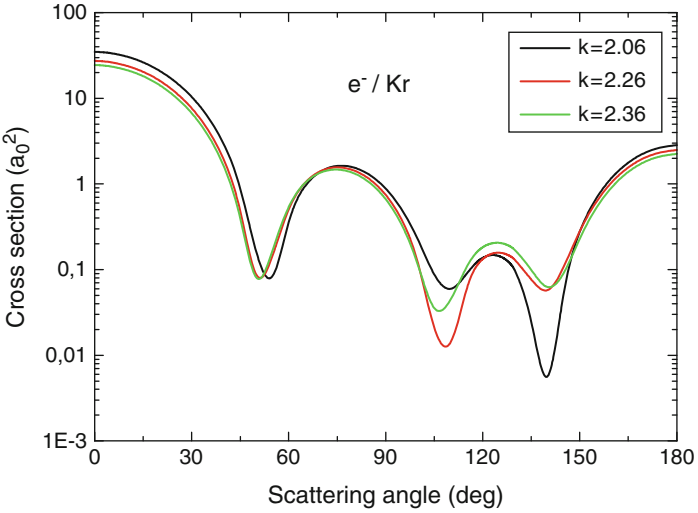

Fig. 4.104_Kr_c1 Differential in angle cross-section of electron scattering on Kr with s-, p- d-, and f-partial waves taken into account

Ramsauer minimum. The contribution to polarization interaction from subshells $3d, 4s, 4p$ was taken into account.

Figure 4.104_Kr_c1 shows the differential in angle cross-section of electron elastic scattering on Kr, with four partial waves of incoming electron taken into account: s-, p-, d-, and f. The data is presented for three incoming electron momentum κ, connected to its energy E by the relation $k = \sqrt{2E}$. Besides maxima

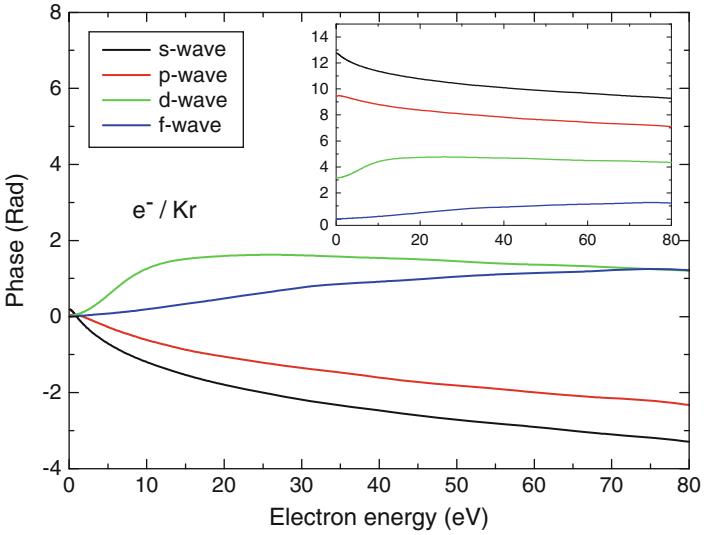

Fig. 4.105_Kr_d1 Phases of various partial waves in electron scattering on Kr, in SRPAE

in forward and backward scattering, the differential cross-section has two more maxima as compared to one in Ar (see Fig. 4.53_Ar_c1).

Figure 4.105_Kr_d1 shows the SRPAE phases of various partial waves in electron scattering on Kr. As it should be according to (3.21), at zero electron energy the s-phase is equal 4π, p-phase—3π, d-phase—2π, and f-phase approaches zero if the phases are defined in such a way that at $E \to \infty$ all phase $\delta_l \to 0$. Note that s- and p-phases are everywhere but the proximity of $E = 0$ negative, while d- and f-phases are positive .

Figure 4.106_Kr_e1 shows the density of monopole GOSes for Kr in RPAE as function of the energy ω transferred to the atom at various q (see [4.7]). Curves are rather complex. Their maxima with growth of q move to bigger energies.

Figure 4.107_Kr_e2 shows the density of dipole GOSes for Kr in RPAE as function of the energy ω transferred to the atom at various q (see [4.7]). The value of dipole GOS is by an order of magnitude bigger than both monopole (Fig. 4.106_Kr_e1) and quadrupole (Fig. 4.108_Kr_e3) GOSes. With growth of q, maximums decrease and move to bigger energies, becoming also broader.

Figure 4.108_Kr_e3 shows the density of quadrupole GOSes for Kr in RPAE as function of the energy ω transferred to the atom ω at various q (see [4.7]). GOSes in the considered region of q and ω have two maxima. The first, by about an order of magnitude bigger than the second, with growth of q is displaced to the bigger energy ω side. The second is shown on insert. Its motion to higher energies with growth of q is visible.

Figure 4.109_Kr_e4 shows the density of octupole GOSes for Kr in RPAE as function of the energy ω transferred to the atom at various q (see [4.7]). Behavior of GOSes is almost chaotic, being characterized by many maxima. At higher ω and q it is much bigger and more systematic.

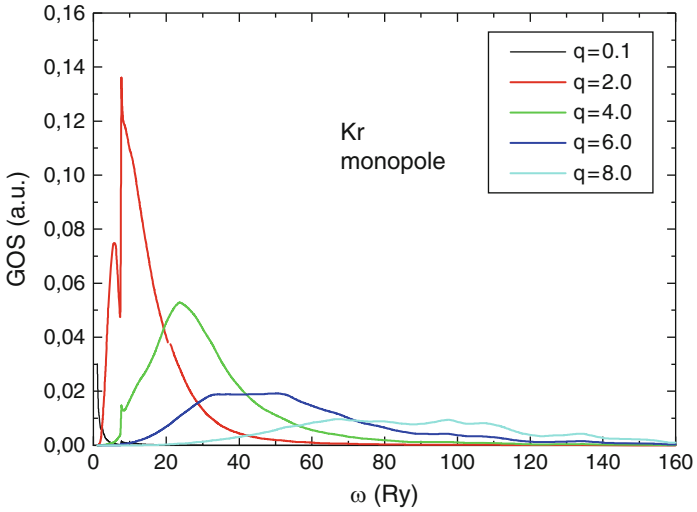

Fig. 4.106_Kr_e1 Density of monopole generalized oscillator strengths for Kr in RPAE as function of the energy ω transferred to the atom at various values of q (see [4.7])

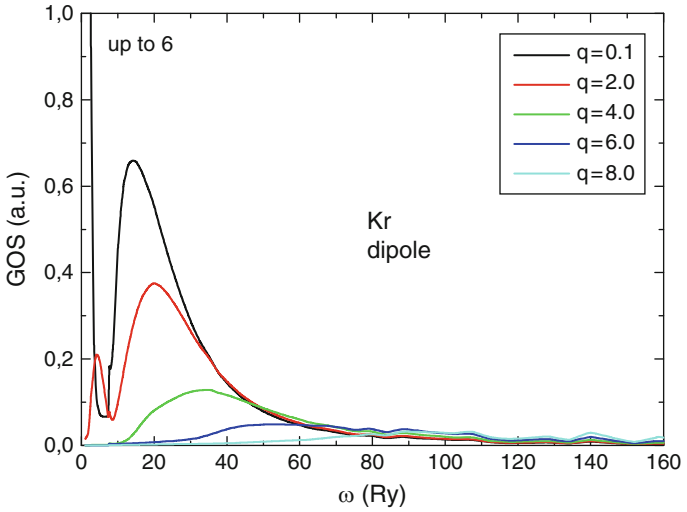

Fig. 4.107_Kr_e2 Densities of dipole generalized oscillator strengths for Kr in RPAE as function of the energy ω transferred to the atom at various q (see [4.7])

Figure 4.110_Kr_f1 shows the GOSes of discrete monopole and quadrupole $4p$–$5p$ excitations for Kr as functions of q^2 transferred to the atom, in RPAE (see [4.13]). Quadrupole GOSes have two maxima, but owing to proximity in excitation energy of monopole and quadrupole levels, it is possible to measure only the sum of GOSes, where after a maximum it is seen a very small excess (see insert).

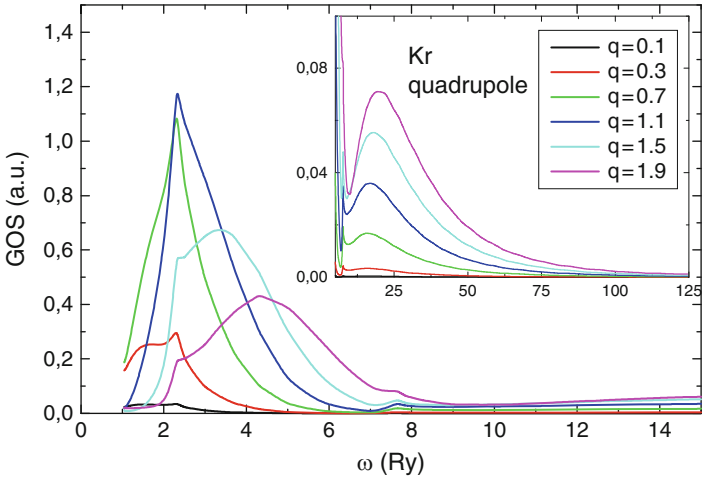

Fig. 4.108_Kr_e3 Density of quadrupole generalized oscillator strengths for Kr in RPAE as function of the energy ω transferred to the atom at various q (see [4.7])

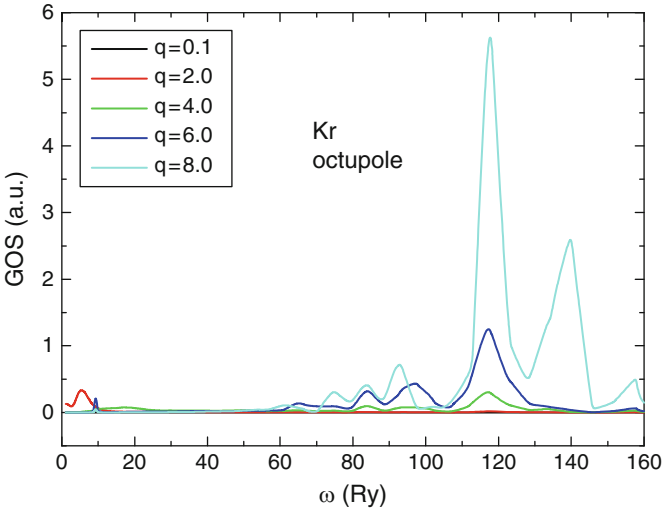

Fig. 4.109_Kr_e4 Density of octupole generalized oscillator strengths for Kr in RPAE as function of the energy ω transferred to the atom at various q (see [4.7])

Figure 4.111_Kr_f2 shows the GOSes of discrete monopole and quadrupole $4p$–$6p$ excitations for Kr as functions of q^2 transferred to the atom, in RPAE (see [4.13]). Quadrupole maximum is actually invisible in total GOSes of the level.

Figure 4.112_Kr_f3 shows the GOSes of discrete quadrupole $4p$–$4f$ and $4p$–$5f$ excitations for Kr as function of q^2 transferred to the atom, in RPAE (see [4.13]).

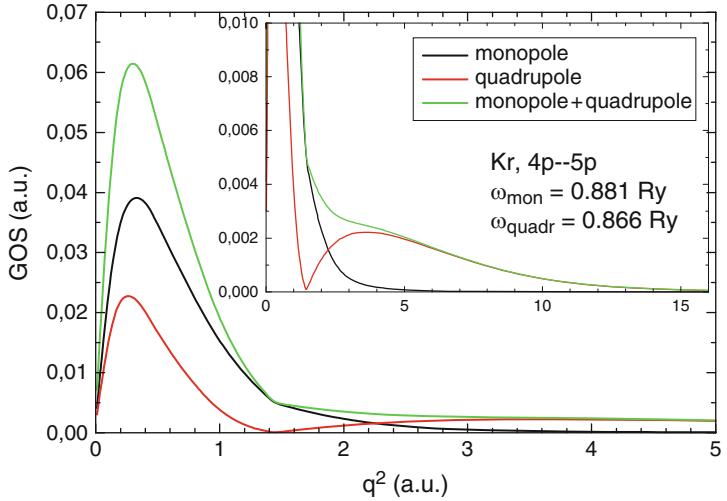

Fig. 4.110_Kr_f1 Generalized oscillator strengths of discrete monopole and quadrupole $4p$–$5p$ excitations for Kr as functions of square moment q transferred to the atom, in RPAE (see [4.13])

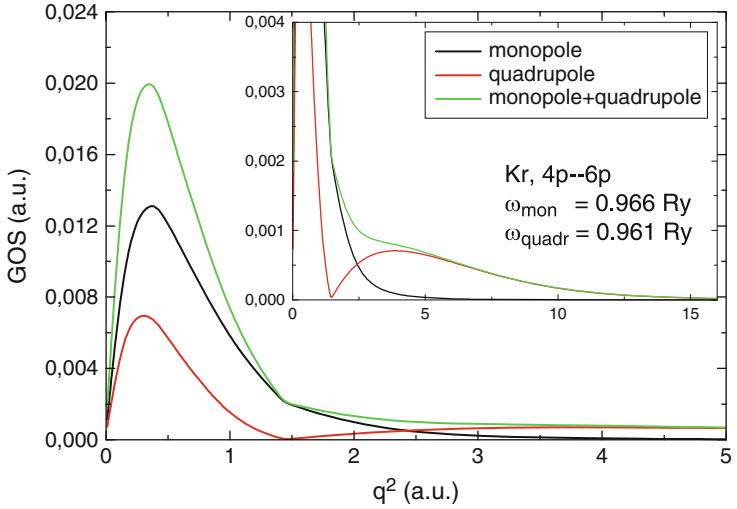

Fig. 4.111_Kr_f2 Generalized oscillator strengths of discrete monopole and quadrupole $4p$–$6p$ excitations for Kr as functions of square moment q transferred to the atom, in RPAE (see [4.13])

Figure 4.113_Kr_f4 shows the GOSes of discrete dipole $4p$–$5s$ and $4p$–$6s$ excitations for Kr as function of q^2 transferred to the atom, in HF and RPAE (see [4.14]). It is remarkable that in both levels GOSes are similar in shape and located almost at the same q^2, maximums.

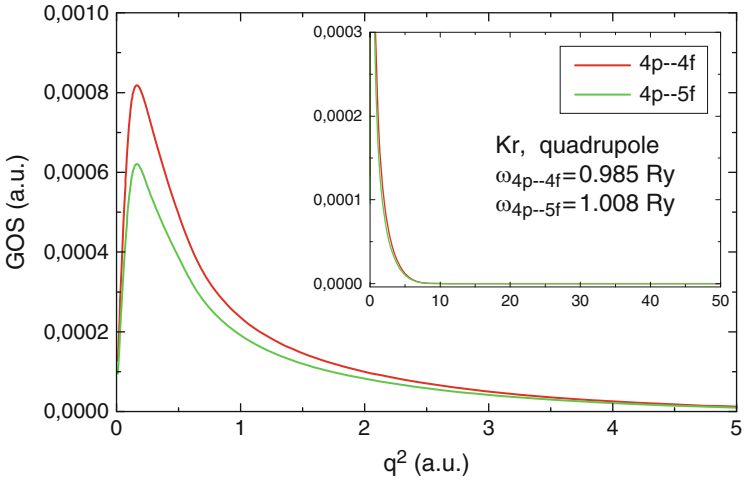

Fig. 4.112_Kr_f3 Generalized oscillator strengths of discrete quadrupole $4p$–$4f$ and $4p$–$5f$ excitations for Kr as function of square moment q transferred to the atom, in RPAE (see [4.13])

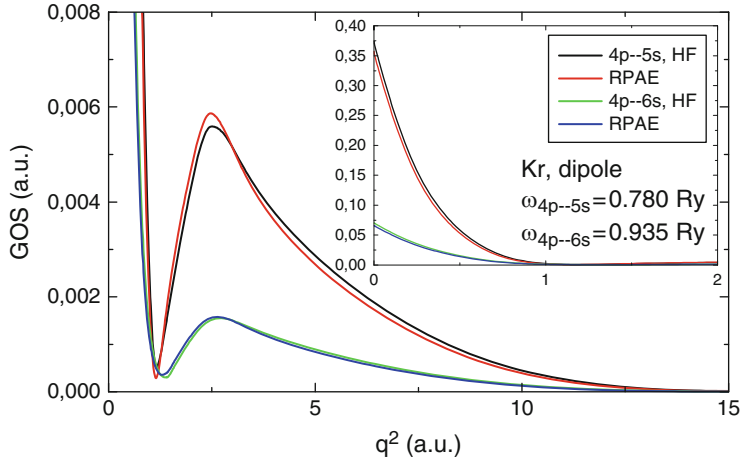

Fig. 4.113_Kr_f4 Generalized oscillator strengths of discrete dipole $4p$–$5s$ and $4p$–$6s$ excitations for Kr as function of square moment q transferred to the atom, in HF and RPAE (see [4.14])

Figure 4.114_Kr_f5 shows the GOSes of discrete dipole $4p$–$4d$ and $4p$–$5d$ excitations for Kr as functions of q^2 transferred to the atom, in HF and RPAE (see [4.14]). The role of correlations is insignificant.

Figure 4.115_Kr_f6 shows the GOSes of discrete octupole $4p$–$4d$ and $4p$–$5d$ excitations for Kr as functions of q^2 transferred to the atom, in HF and RPAE (see [4.14]). Curves have one maximum, at $q^2 \approx 1.25$. The role of correlations is appreciable, but insignificant.

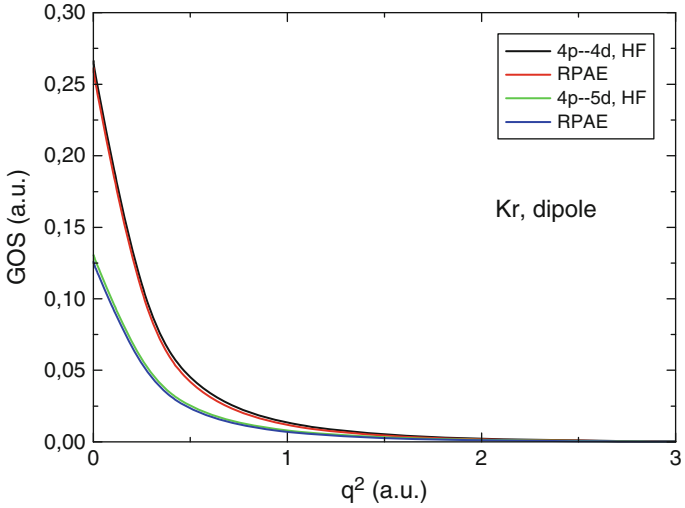

Fig. 4.114_Kr_f5 Generalized oscillator strengths of discrete dipole $4p$–$4d$ and $4p$–$5d$ excitations for Kr as functions of square moment q transferred to the atom, in HF and RPAE (see [4.14])

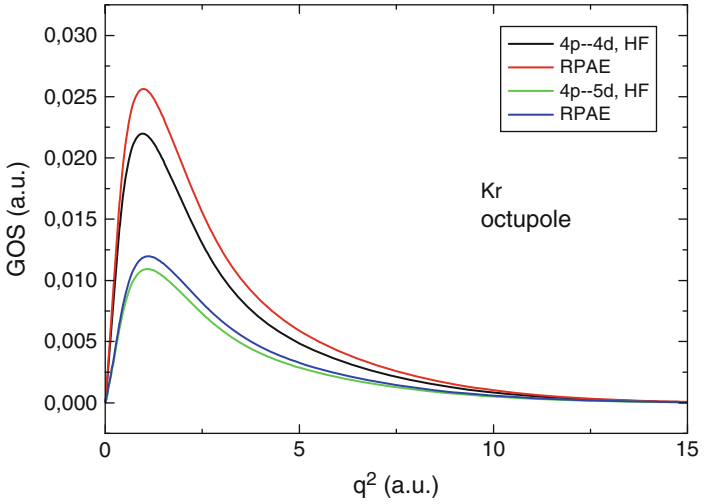

Fig. 4.115_Kr_f6 Generalized oscillator strengths of discrete octupole $4p$–$4d$ and $4p$–$5d$ excitations for Kr as functions of square moment q transferred to atom in HF and RPAE (see [4.14])

Figure 4.116_Kr_f7 shows the GOSes of discrete dipole and octupole $4p$–$4d$ excitations for Kr as function of q^2 transferred to the atom, in RPAE (see [4.14]). In octupole transition there is a maximum at $q^2 \approx 1$, and in dipole transition the maximum is located at $q^2 = 0$. As considered levels have almost the same energy, the sum of their GOSes is presented, which maximum is only at $q^2 = 0$.

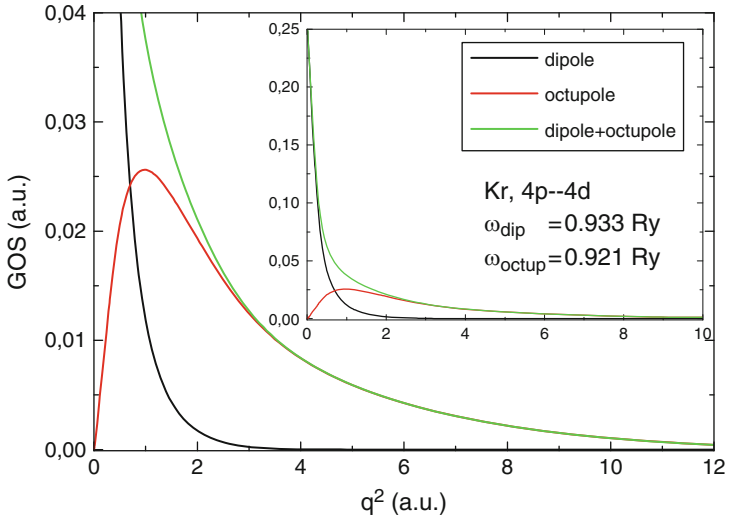

Fig. 4.116_Kr_f7 Generalized oscillator strengths of discrete dipole and octupole $4p$–$4d$ excitations for Kr as function of square moment q transferred to atom in RPAE (see [4.14])

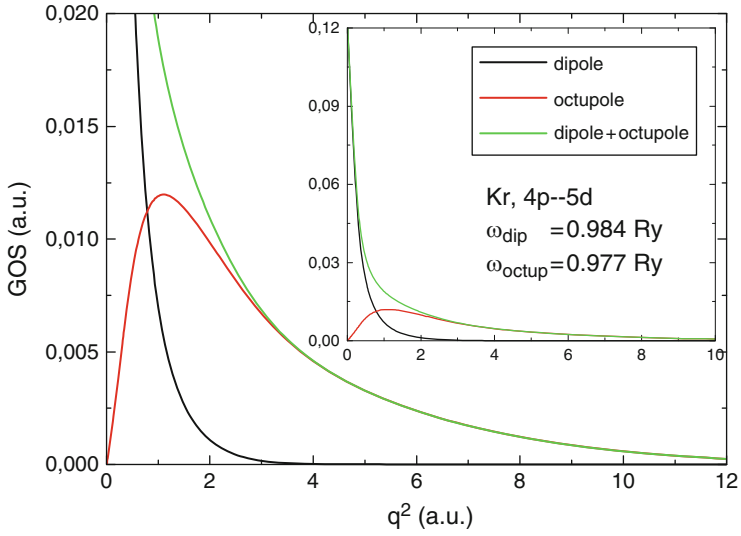

Fig. 4.117_Kr_f8 Generalized oscillator strengths of discrete dipole and octupole $4p$–$5d$ excitations for Kr as function of square momentum q transferred to atom in RPAE (see [4.14])

Figure 4.117_Kr_f8 shows the GOSes of discrete dipole and octupole $4p$–$5d$ excitations for Kr as function of q^2 transferred to the atom, in RPAE (see [4.14]). Because of proximity of the considered levels, the really observable value is only the sum of their GOSes.

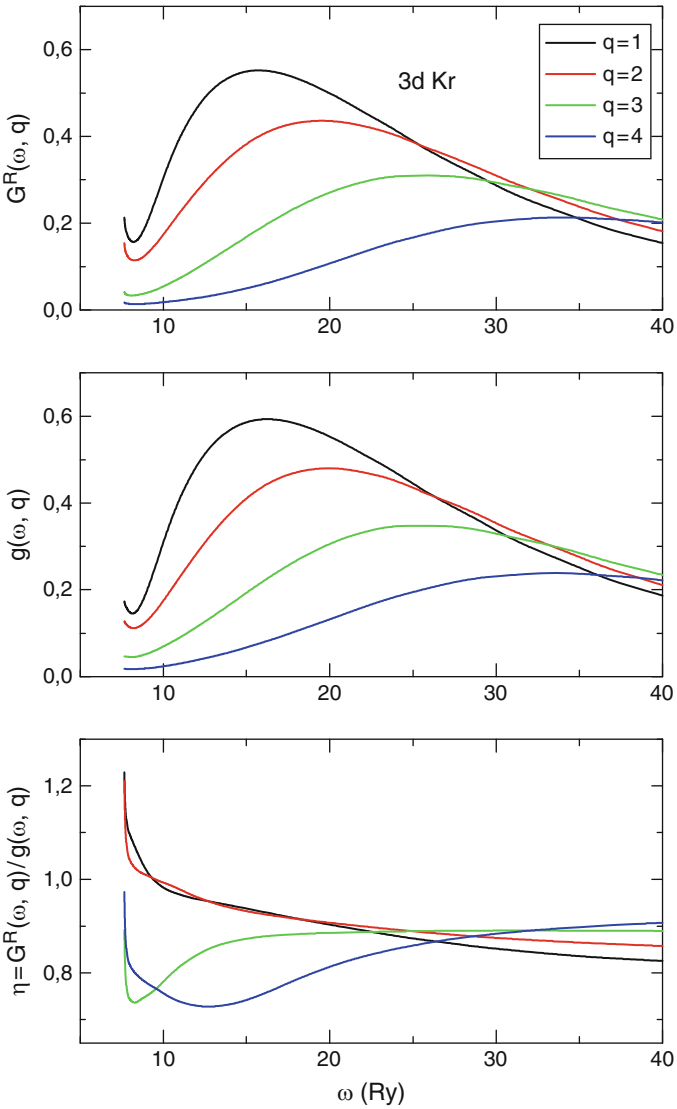

Fig. 4.118_Kr_f9 Generalized oscillator strengths and their ratio for $3d$-electrons of Kr, in HF and RPAE (see [4.7])

Figure 4.118_Kr_f9 shows the GOSes in RPAE and HF and their ratio for $3d$-electrons of Kr (see [4.7]). The role of RPAE corrections reaching in absolute value 20% is visible.

Figure 4.119_Kr_f10 shows the GOSes in HF and RPAE and their ratio for $4s$-electrons of Kr (see [4.7]). The role of RPAE corrections is greater than shown in Fig. 4.118_Kr_f9. At small energies and big q the ratio reaches quite an impressive value: it is equal to 4.

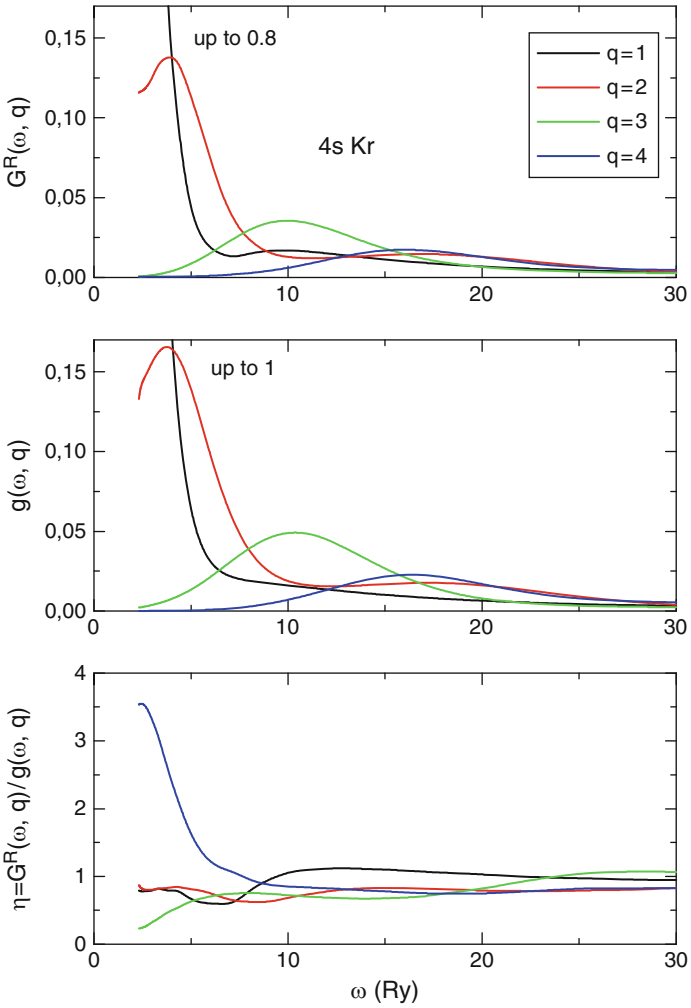

Fig. 4.119_Kr_f10 Generalized oscillator strengths and their ratio for 4*s*-electrons of Kr in HF and RPAE (see [4.7])

Figure 4.120_Kr_f11 shows the GOSes in HF and RPAE and their ratio for $4p$-electrons of Kr (see [4.7]). The role of RPAE corrections just as shown in Fig. 4.119_Kr_f10 is greater than that shown in Fig. 4.118_Kr_f9.

Figure 4.121_Kr_g1 shows the cross-section of monopole Compton scattering of γ-quanta with energy $E = 2,000$ Ry on Kr in RPAE as functions of the moment q transferred to the atom at various energies ω (the transferred angular moment is $L = 0$) (see [4.15]). A maximum that becomes broader and lower with growth of energy ω and moves toward big values of q characterize the cross-section. Note the big range of the considered values of q, $0 < q < 8$.

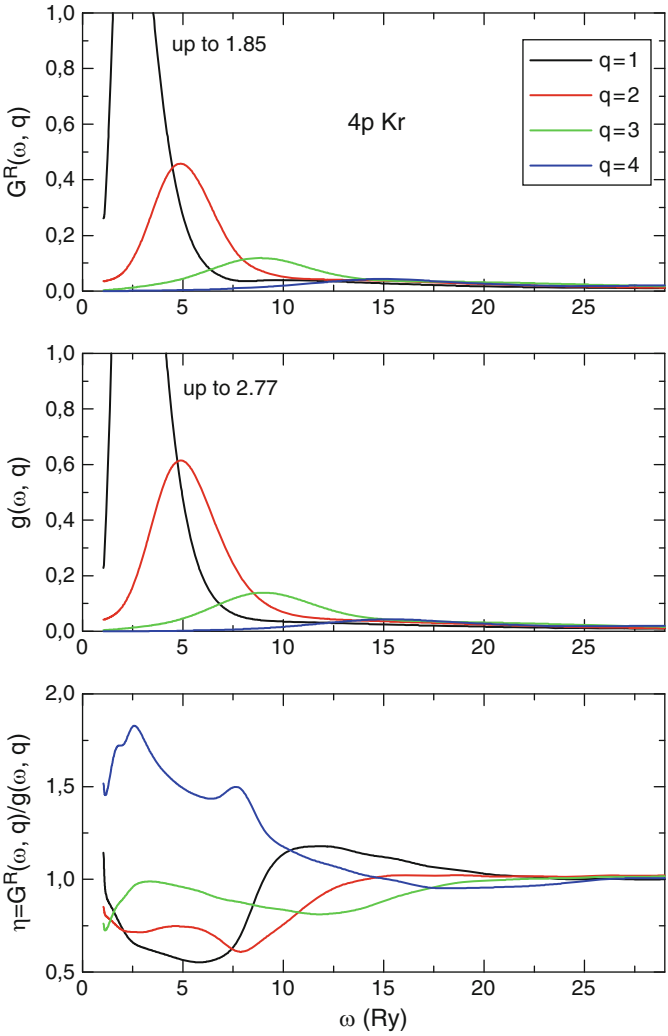

Fig. 4.120_Kr_f11 Generalized oscillator strengths and their ratio for $4p$-electrons of Kr in HF and RPAE (see [4.7])

Figure 4.122_Kr_g2 shows the cross-section of dipole Compton scattering of γ-quanta with energy $E = 2,000$ Ry on Kr in RPAE as function of the moment q transferred to the atom at various values of energy ω (the transferred angular moment is $L = 1$) (see [4.15]). The maximum with growth of ω becomes broader and lower, moving toward bigger values of q.

Figure 4.123_Kr_g3 shows the cross-section of quadrupole Compton scattering of γ-quanta with energy $E = 2,000$ Ry on Kr in RPAE as function of the linear moment q transferred to the atom, at various energies ω (the transferred angular

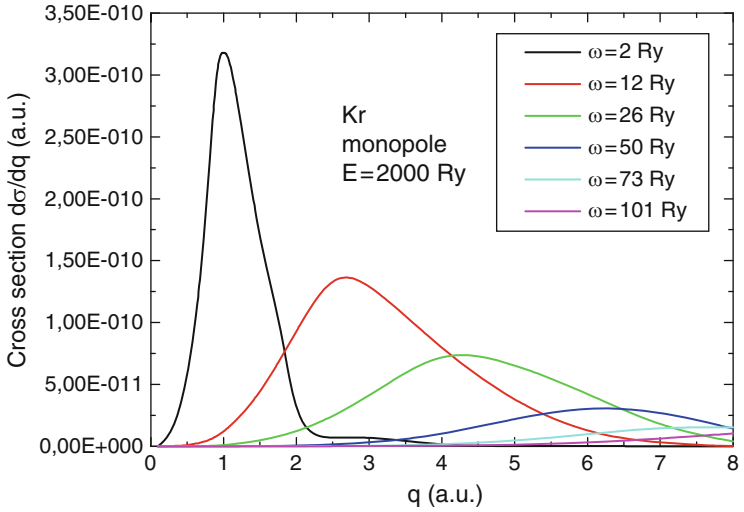

Fig. 4.121_Kr_g1 Cross-section of monopole Compton scattering of γ-quanta with energy $E = 2,000\,\text{Ry}$ as function of the linear moment q transferred to the atom, at various energies ω for Kr in RPAE (see [4.15])

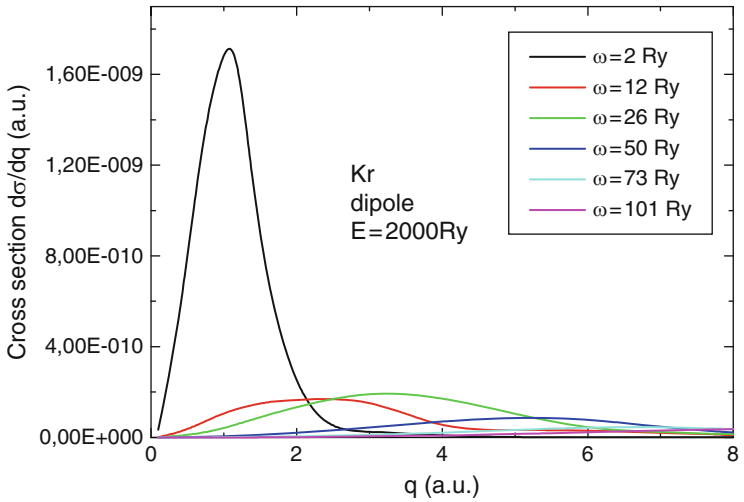

Fig. 4.122_Kr_g2 Cross-section of dipole Compton scattering of γ-quanta with energy $E = 2,000\,\text{Ry}$ as function of the linear moment q transferred to the atom, at various values of energy ω on Kr in RPAE (see [4.15])

moment $L = 2$) (see [4.15]). As shown in Fig. 4.122_Kr_g2, the maximum with growth of ω becomes broader and lower, moving toward bigger values of q.

Figure 4.124_Kr_g4 shows the cross-section of octupole Compton scattering of γ-quanta with energy $E = 2,000\,\text{Ry}$ on Kr in RPAE as function of the linear moment q transferred to the atom at various energies ω (the transferred angular

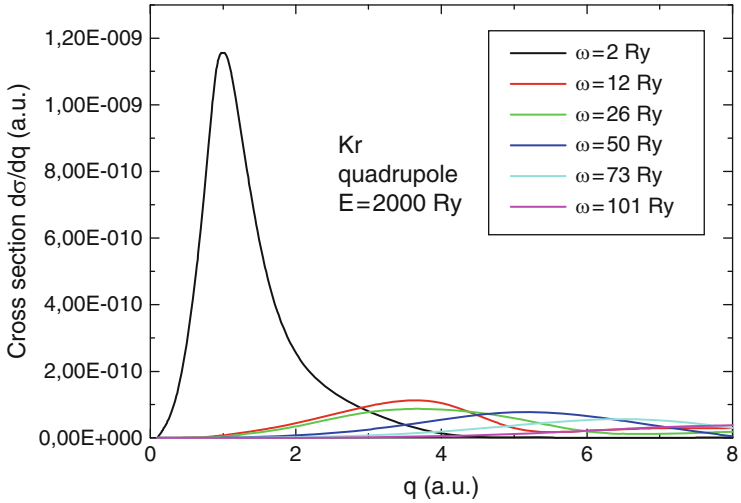

Fig. 4.123_Kr_g3 Cross-section of quadrupole Compton scattering of γ-quanta with energy $E = 2,000$ Ry as function of the linear moment q transferred to the atom, at various energies ω on Kr in RPAE (see [4.15])

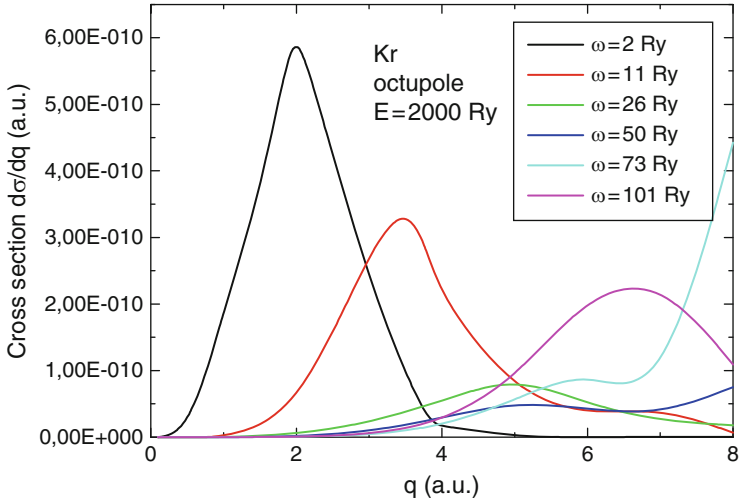

Fig. 4.124_Kr_g4 Cross-section of octupole Compton scattering of γ-quanta of energy $E = 2,000$ Ry as function of the linear moment q transferred to atom at various energies ω on Kr in RPAE (see [4.15])

moment is $L = 3$) (see [4.15]). The rapidly growing with increase of ω second maximum is outside the limits of the figure, except for $\omega = 50$ and 73 Ry.

Figure 4.125_Kr_h1 shows the cross-section of Compton excitation [defined by (3.94)], relative to Thomson cross-section, dipole and octupole $4p$–$4d$ levels for Kr in RPAE (see [4.16, 4.25]). Both distinct maximums merge in one.

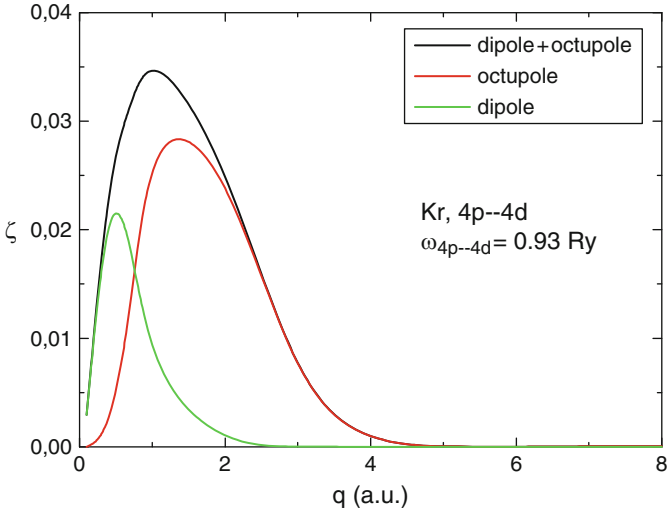

Fig. 4.125_Kr_h1 Relative cross-section of Compton excitation of dipole and octupole $4p$–$4d$-levels for Kr in RPAE (see [4.16, 4.25])

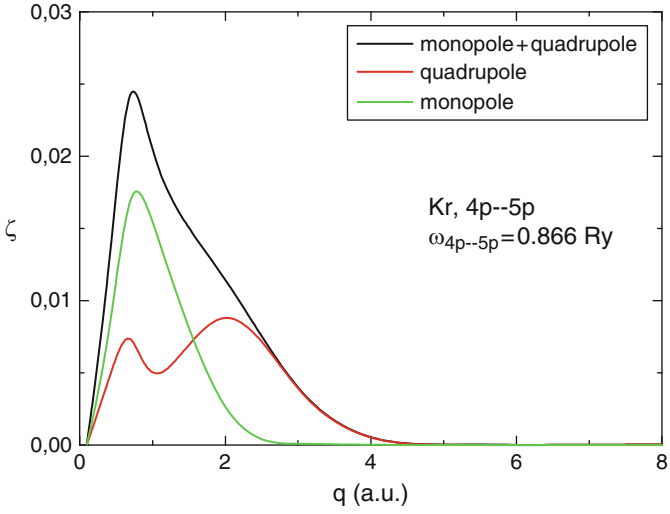

Fig. 4.126_Kr_h2 Relative cross-section of Compton excitation of quadrupole and monopole (almost exact degenerate) $4p$–$5p$-levels for Kr in RPAE (see [4.16, 4.25])

Figure 4.126_Kr_h2 shows the relative to Thomson cross-section the cross-section of Compton excitation [defined by (3.94)] of quadrupole and monopole (almost exact degenerate) $4p$–$5p$ levels for Kr in RPAE (see [4.16, 4.25]). Two distinctly visible maxima in quadrupole cross-section and one in monopole lead to an asymmetric profile for the sum.

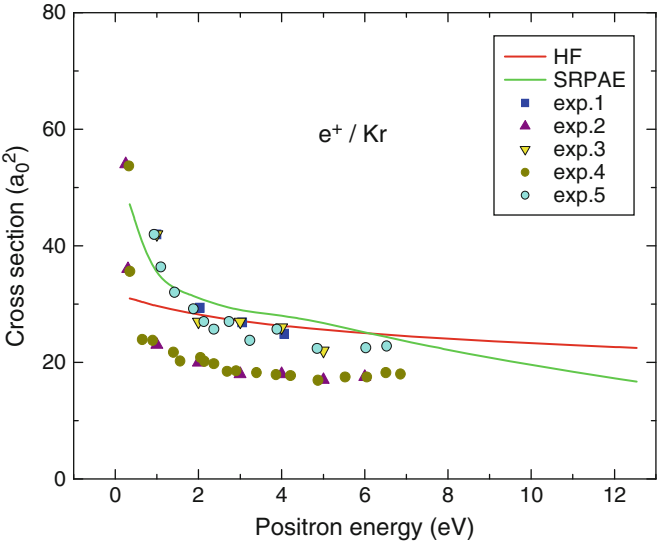

Fig. 4.127_Kr_i1 Cross-section of elastic positron scattering for Kr atom in HF and SRPAE (see [4.10]). Experimental data are taken from [4.17,4.26,4.27]

Figure 4.127_Kr_i1 shows the cross-section of elastic positron scattering for Kr atom in HF and SRPAE (see [4.10]). Experimental data are taken from [4.17,4.26,4.27], while results of more complex calculations can be found in [4.28]. Polarization interaction takes into account excitation of $4s$, $4p$ subshells and formation of virtual positronium.

Figure 4.128_Kr_j1 shows the contribution of different partial waves to total cross-section of elastic positron scattering on atom Kr in SRPAE. The main contribution comes from the s-wave, but the corresponding minimum is filled by big p-wave big contribution.

Figure 4.129_Kr_k1 shows the phases of various partial waves in positron scattering on Kr atom in SRPAE. The s-wave's phase starts, according to calculations, neither from zero, nor from any $n\pi$, thus contradicting to (3.21). Qualitatively, this is discussed at the end of Chap. 3. As one can see, the maximum in p-phase is considerably bigger than in Ar.

Figure 4.130_Kr_k2 shows the phases of various partial waves in positron scattering on Kr in HF. Note that all derivatives of the phases in energy at $E \to 0$ are, as it should be on pure theoretical ground, negative.

Figure 4.131_Kr_l1 shows the multiplied by incoming electron energy total and partial cross-sections of inelastic scattering of fast electrons on atom Kr in logarithmic approximation $E\sigma_{\mathrm{In}}(E)$. Dominative is the contribution of scattering upon the outer $4p$ subshell, mainly from $4p$ to εd dipole transition. It is seen that all these functions at high E increase slowly. The fastest is the increase of the biggest

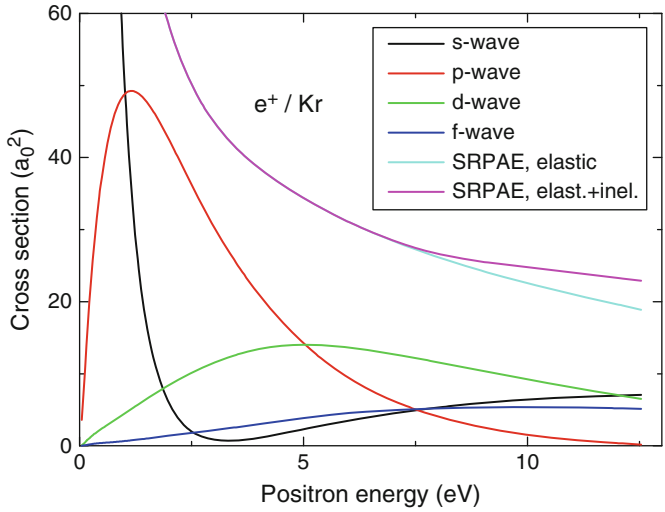

Fig. 4.128_Kr_j1 Contribution of partial waves to the cross-section of elastic positron scattering on Kr. The inelastic cross-section is also shown

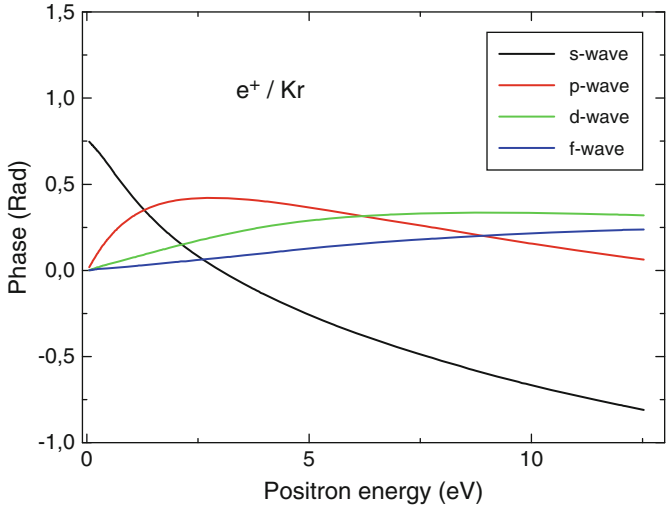

Fig. 4.129_Kr_k1 Phases of various partial waves in positron scattering on Kr in SRPAE

partial cross-section. The cross-sections are presented from $E = I$ for completeness only, since the logarithmic approximation is valid if $\ln(E/I) \gg 1$.

Figure 4.132_Kr_l2 shows the total and partial nonlogarithmic corrections to the cross-sections of inelastic scattering of fast electrons, multiplied by incoming electron energy, on Kr atom $E\sigma_{\mathrm{In}}^{(1)}(E)$. It is seen that these functions stop to grow already at $E = 5$ Ry.

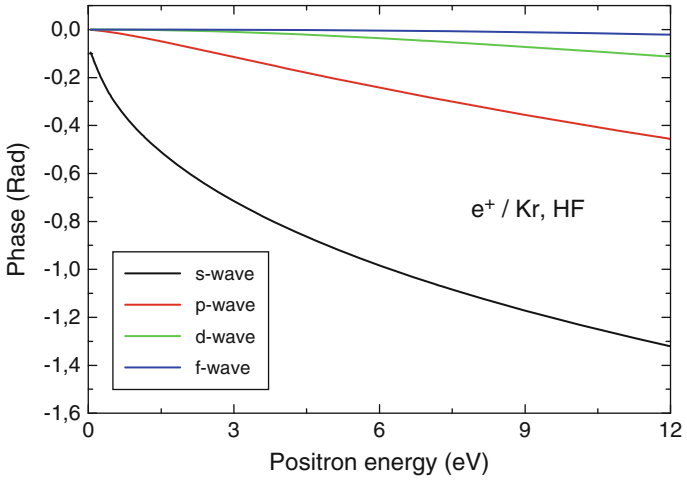

Fig. 4.130_Kr_k2 Phases of various partial waves in positron scattering on Kr in HF

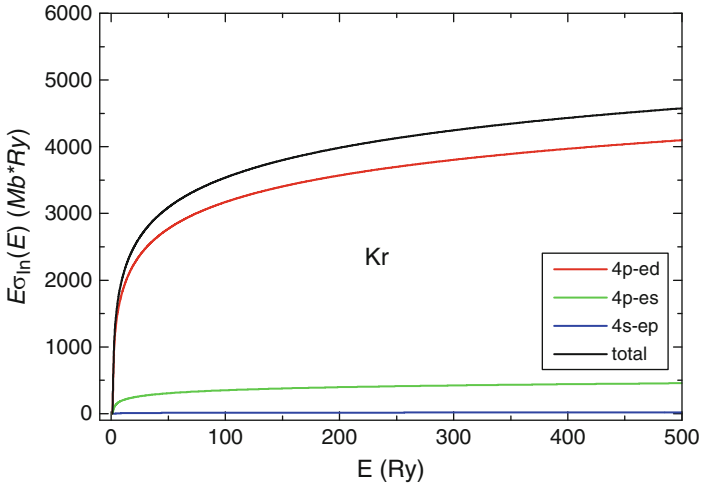

Fig. 4.131_Kr_l1 Multiplied by incoming electron energy cross-section of inelastic scattering of fast electrons in the logarithmic approximation

Figures 4.133–4.185 (Xe) show the results of calculations for Xe.

Figure 4.133_Xe_a1 shows the cross-section of elastic electron scattering on Xe atom in HF and SRPAE (see [4.1, 4.2]). The role of electronic correlations is great. After narrow Ramsauer minimum there is a two-humped maximum. Experimental data are taken from [4.29]. Ramsauer minimum [4.20] arises only if the polarization interaction is taken into account of. In calculations of this interaction, the contribution of virtual and real excitations from $4d, 5s, 5p$ subshells was included.

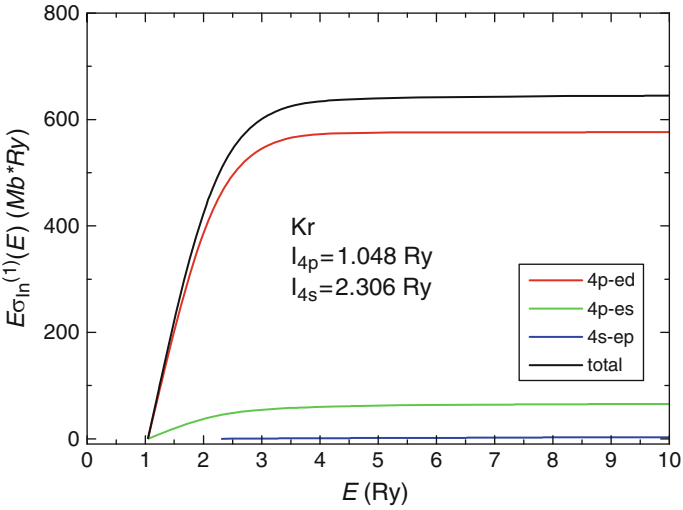

Fig. 4.132_Kr_l2 Nonlogarithmic correction to the multiplied by incoming electron energy cross-section of inelastic scattering of fast electrons

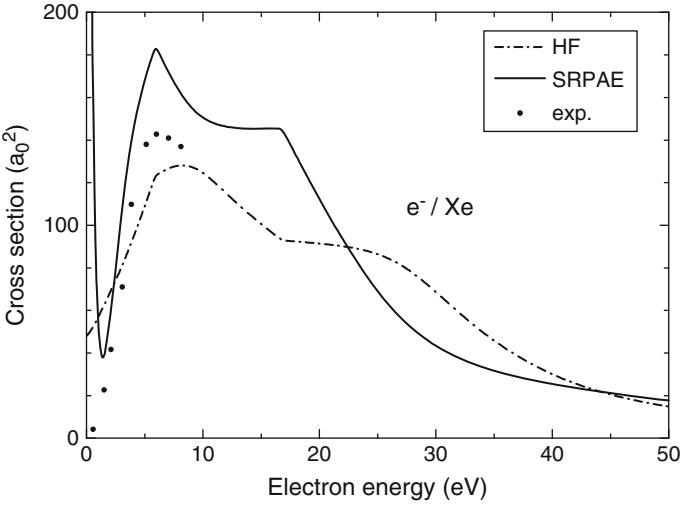

Fig. 4.133_Xe_a1 Cross-section of elastic electron scattering on Xe atom in HF and SRPAE (see [4.1, 4.2]). Experiment is from [4.29]

Figure 4.134_Xe_b1 shows the contribution of separate partial waves in cross-section of elastic electron scattering on Xe in SRPAE. Ramsauer minimum is narrow and deep because of the big value of a maximum in d-wave. It is also a maximum in p-wave while in f-wave there are two maximums. As well as shown in Fig. 4.133_Xe_a1, polarization interaction was taken into account.

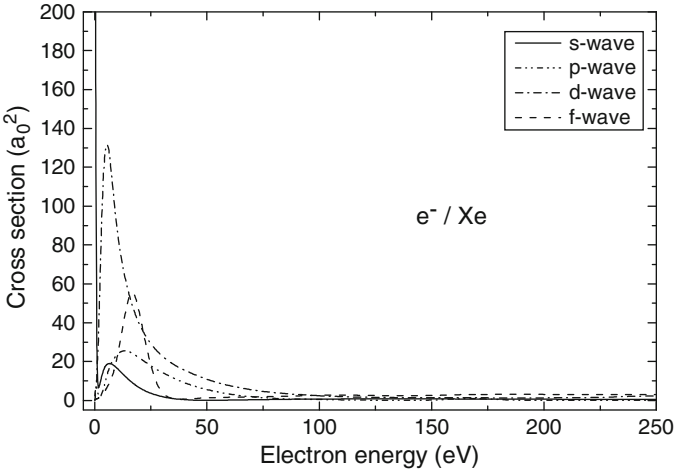

Fig. 4.134_Xe_b1 Contribution of separate partial waves in cross-section of elastic electron scattering on Xe in SRPAE

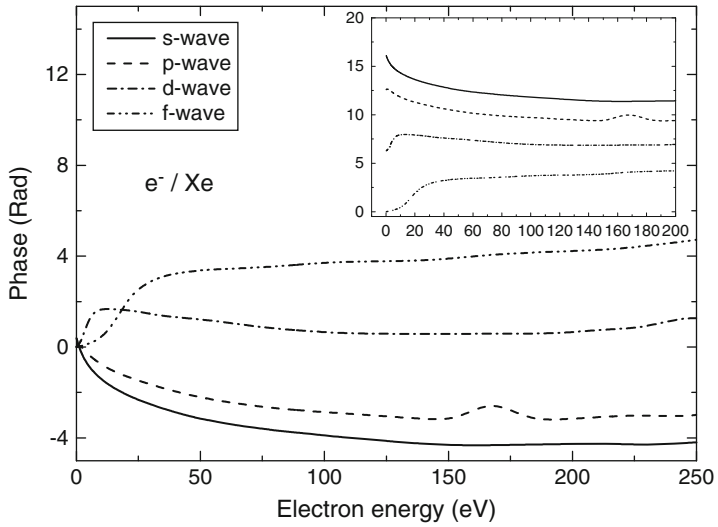

Fig. 4.135_Xe_d1 Phases of various partial waves in electron scattering on Xe in SRPAE

Figure 4.135_Xe_d1 shows the HF phases of various partial waves in electron scattering on Xe. As it should be in accord with (3.21), at zero electron energy s-phase is equal to 5π, p-phase—4π, d-phase—2π, and f-phase approaches zero if they are defined so that at $E \to \infty$ all phases $\delta_l \to 0$.

Figure 4.136_Xe_e1 shows the density of monopole GOSes for Xe in RPAE as function of the energy ω transferred to the atom at various q (see [4.7]). The maximums with growth of q move to bigger energies.

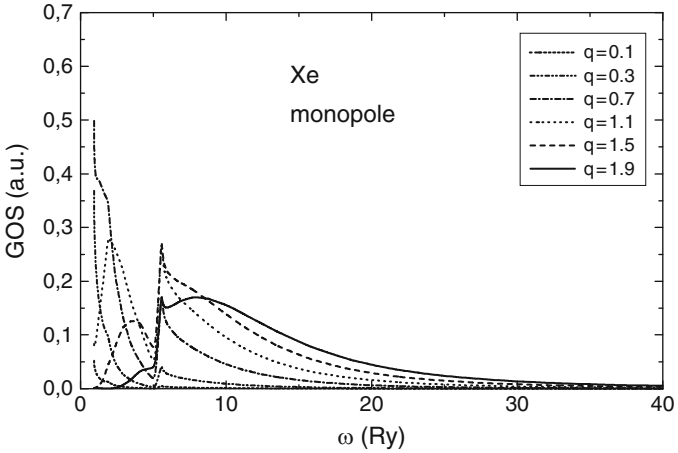

Fig. 4.136_Xe_e1 Density of monopole generalized oscillator strengths as function of the energy ω transferred to the atom at various q for Xe in RPAE (see [4.7])

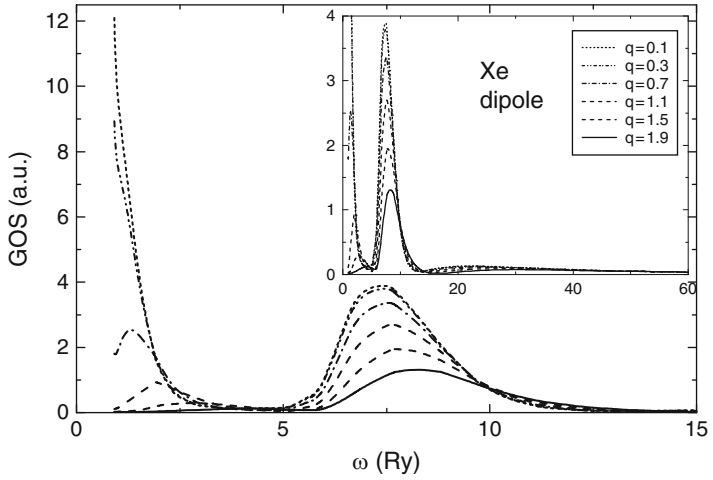

Fig. 4.137_Xe_e2 Density of dipole generalized oscillator strengths as function of the energy ω transferred to atom at various q for Xe in RPAE (see [4.7])

Figure 4.137_Xe_e2 shows the density of dipole GOSes for Xe in RPAE as function of the energy ω transferred to atom at various q (see [4.7]). The value of dipole GOSes is by an order of magnitude bigger than both monopole (Fig. 4.136_Xe_e1) and quadrupole (Fig. 4.138_Xe_e3) GOSes values. With growth of q the maximum at small ω moves to bigger energies. In the region of $\omega = 7$ Ry, huge dipole resonance is seen at all q that moves slowly to higher ω with growth of q.

Figure 4.138_Xe_e3 shows the density of quadrupole GOSes for Xe in RPAE as functions of the energy ω transferred to the atom at various q (see [4.7]). The

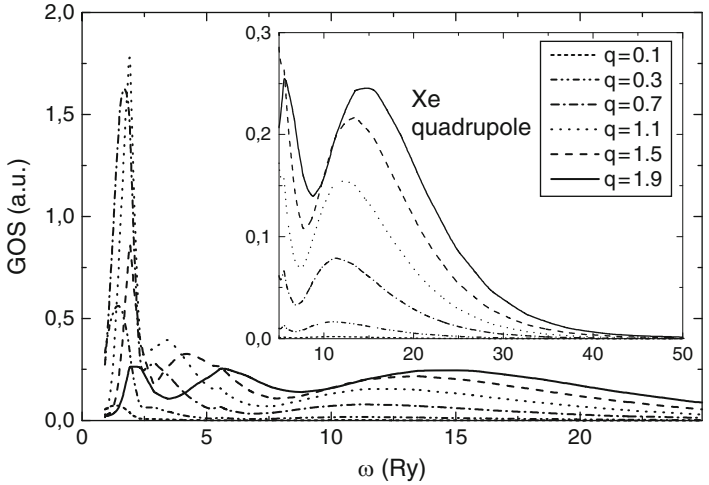

Fig. 4.138_Xe_e3 Density of quadrupole generalized oscillator strengths as function of the energy ω transferred to atom at various q for Xe in RPAE (see [4.7])

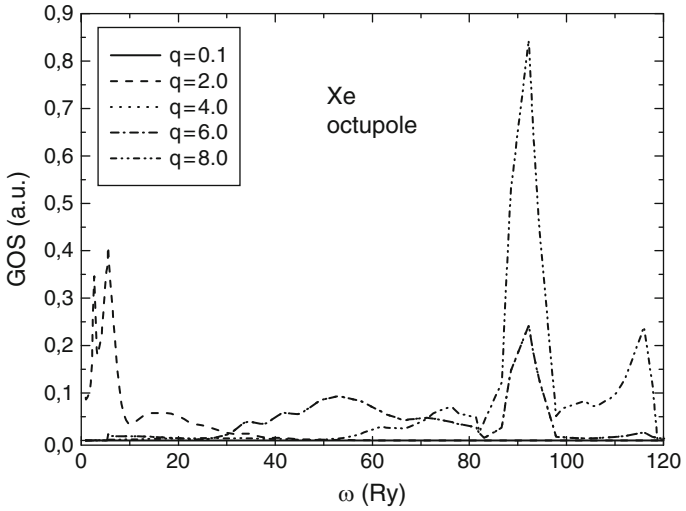

Fig. 4.139_Xe_e4 Density of octupole generalized oscillator strengths as function of the energy ω transferred to atom at various q for Xe in RPAE (see [4.7])

maximum is moving toward bigger energies with growth of q. Structure of GOSes as functions ω is rather complex. So, at significant q there are three maxima.

Figure 4.139_Xe_e4 shows the density of octupole GOSes for Xe in RPAE as function of the energy ω transferred to the atom at various q (see [4.7]). As well as in Kr, the behavior of GOSes is rather chaotic and is characterized for big q by several prominent maxima.

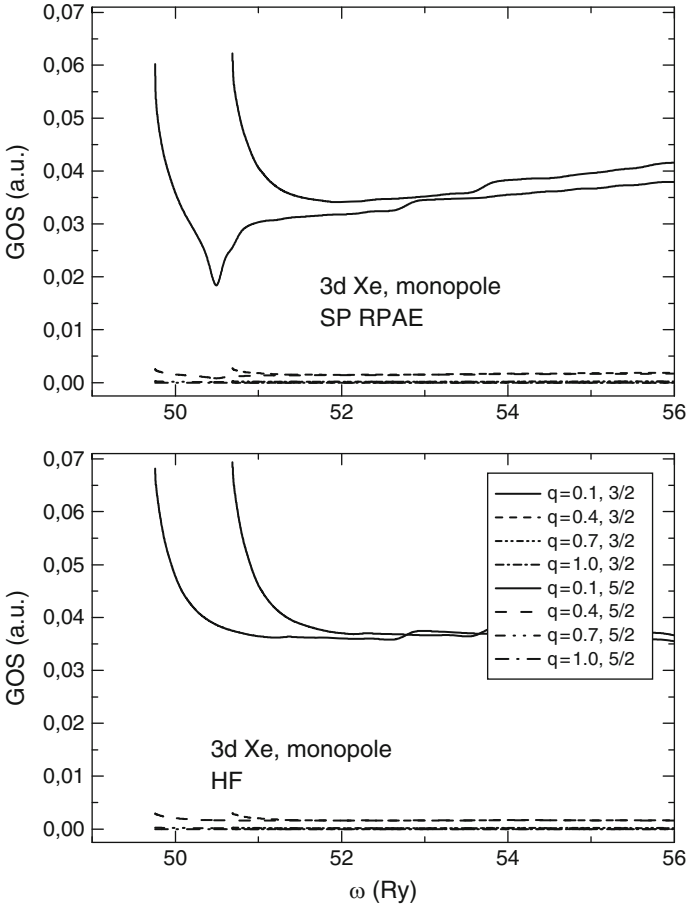

Fig. 4.140_Xe_e5 Density of monopole generalized oscillator strengths for $3d_{5/2}$- and $3d_{3/2}$-electrons as function of the energy ω transferred to atom at various q for Xe in HF and SP RPAE (see [4.30])

Figure 4.140_Xe_e5 shows the density of monopole GOSes of $3d_{5/2}$ and $3d_{3/2}$ electrons of Xe in HF and SP RPAE as function of the energy ω transferred to the atom at various q (see [4.30]). Calculation is carried out according to the description right at the end of Sects. 3.4 and 1.10. Strong influence of electrons on 3/2 level upon GOSes of 5/2 level is visible at small q.

Figure 4.141_Xe_e6 shows the density of dipole GOSes of $3d_{5/2}$- and $3d_{3/2}$-electrons for Xe in HF and SP RPAE as functions of the energy ω transferred to atom at various q (see [4.30]). As well as shown in Fig. 4.136_Xe_e1, the results are obtained according to description given in Sects. 1.10 and at the end of 3.4. The influence of 3/2-electrons leads to additional maximum in SP RPAE for GOSes of

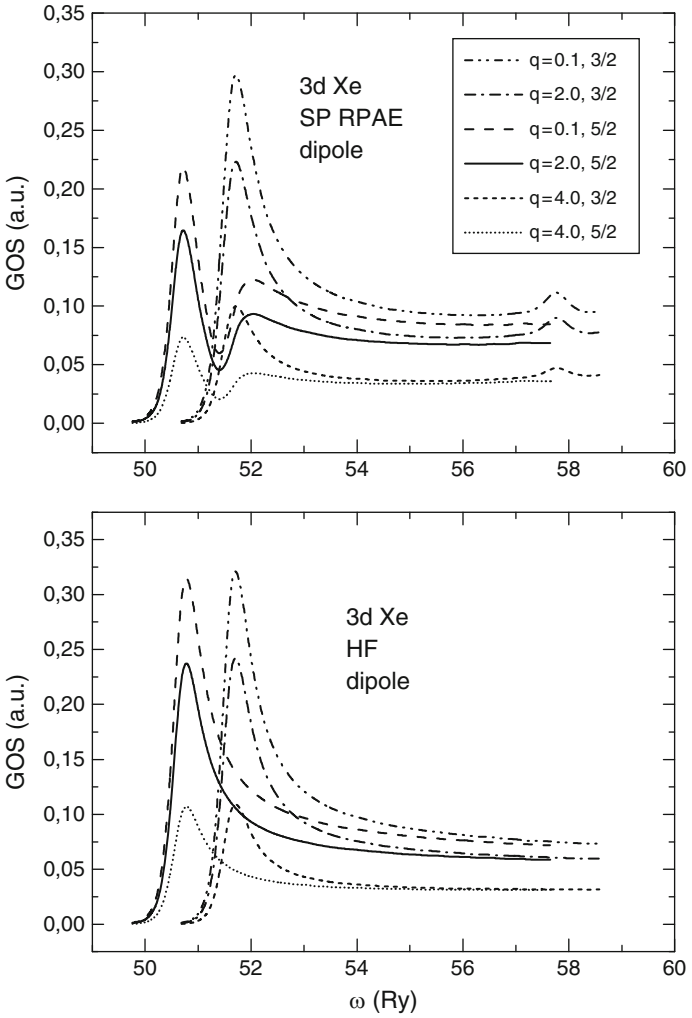

Fig. 4.141_Xe_e6 Density of dipole generalized oscillator strengths $3d_{5/2}$- and $3d_{3/2}$-electrons as function of the energy ω transferred to atom at various q for Xe in HF and SP RPAE (see [4.30])

electrons of 5/2-level at ≈52 eV for all considered q. The situation is similar to what takes place in photoeffect—see Fig. 2.59_Xe_b7.

Figure 4.142_Xe_e7 shows the density of quadrupole GOSes of $3d_{5/2}$- and $3d_{3/2}$-electrons for Xe in HF and SP RPAE as function of the energy ω transferred to atom at various q (see [4.30]). The role of interaction between 5/2- and 3/2-levels is manifested only in occurrence of a small additional maximum at ≈50.6 eV in GOSes of 5/2-level.

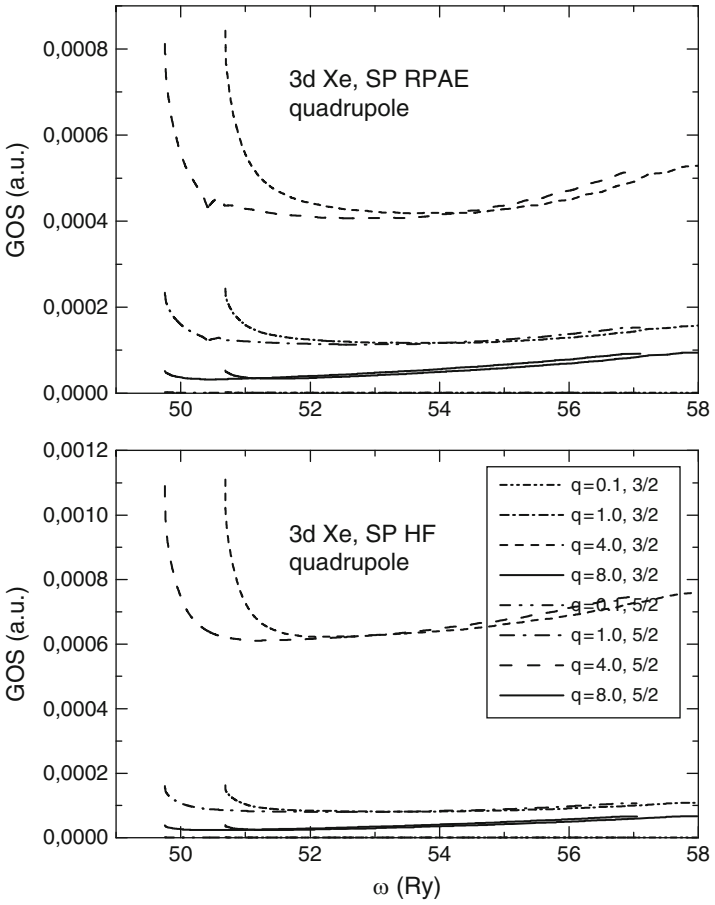

Fig. 4.142_Xe_e7 Density of quadrupole generalized oscillator strengths of $3d_{5/2}$- and $3d_{3/2}$-electrons as function of the energy ω transferred to atom at various q for Xe, in HF and SP RPAE (see [4.30])

Figure 4.143_Xe_f1 shows the GOS of discrete monopole and quadrupole $5p$–$6p$ excitations for Xe as function of q^2 transferred to the atom Xe, in RPAE (see [4.13]). Two prominent quadrupole maximums are visible in total GOSes also.

Figure 4.144_Xe_f2 shows the GOSes of discrete monopole and quadrupole $5p$–$7p$ excitations for Xe as function of q^2 transferred to the atom Xe, in RPAE (see [4.13]). Quadrupole maximum is seen in total GOSes also.

Figure 4.145_Xe_f3 shows the GOSes of discrete quadrupole $5p$–$4f$ and $5p$–$5f$ excitations for Xe as functions of q^2 transferred to the atom Xe, in HF and RPAE (see [4.13]).

Figure 4.146_Xe_f4 shows the GOSes of discrete dipole $5p$–$6s$ and $5p$–$7s$ excitations for Xe as function of q^2 transferred to the atom Xe, in HF and

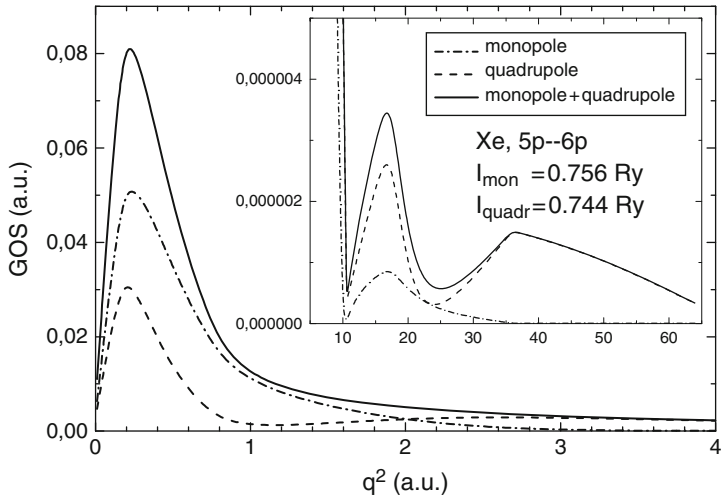

Fig. 4.143_Xe_f1 Generalized oscillator strengths of discrete monopole and quadrupole $5p$–$6p$ excitations as functions of square moment q transferred to the atom for Xe, in RPAE (see [4.13])

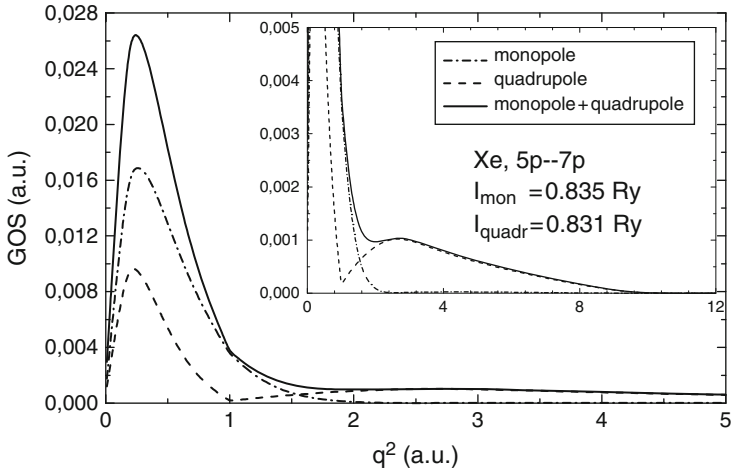

Fig. 4.144_Xe_f2 Generalized oscillator strengths of discrete monopole and quadrupole $5p$–$7p$ excitations as functions of square moment q transferred to atom for Xe, in RPAE (see [4.13])

RPAE (see [4.14]). It is remarkable that in Xe as well as in Kr (see Fig. 4.113_Kr_f4), GOSes of both levels have their maximum at almost the same q^2.

Figure 4.147_Xe_f5 shows the GOSes of discrete dipole $5p$–$5d$ and $5p$–$6d$ excitations for Xe as functions of q^2 transferred to the atom Xe, in RPAE (see [4.14]).

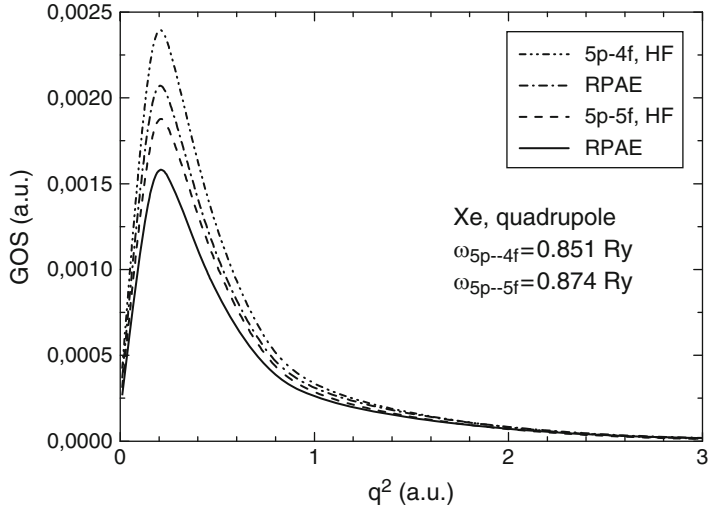

Fig. 4.145_Xe_f3 Generalized oscillator strengths of discrete quadrupole $5p$–$4f$ and $5p$–$5f$ excitations as functions of square moment q transferred to the atom Xe, in HF and RPAE (see [4.13])

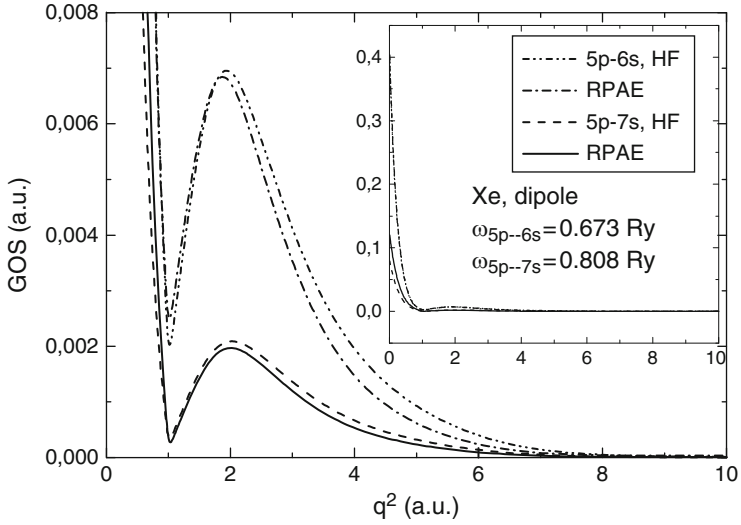

Fig. 4.146_Xe_f4 Generalized oscillator strengths of discrete dipole $5p$–$6s$- and $5p$–$7s$ excitations as to function of square moment q transferred to the atom Xe, in HF and RPAE (see [4.14])

Figure 4.148_Xe_f6 shows the GOSes of discrete octupole $5p$–$5d$ and $5p$–$6d$ excitations as functions of q^2 transferred to atom Xe, in RPAE (see [4.14]). GOSes of both levels have maxima at approximately same values of q.

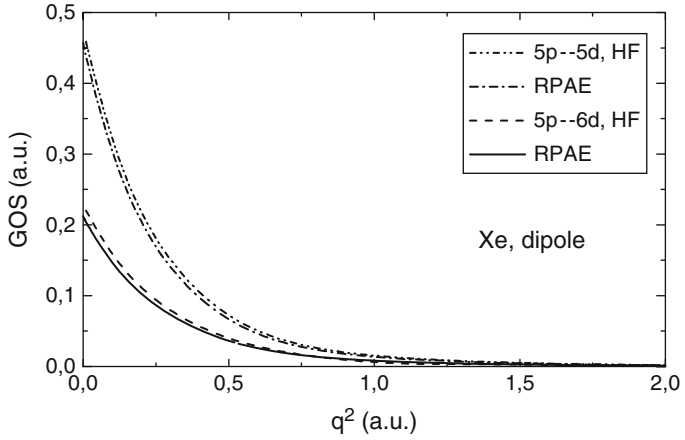

Fig. 4.147_Xe_f5 Generalized oscillator strengths of discrete dipole $5p$–$5d$- and $5p$–$6d$ excitations as functions of square moment q transferred to atom Xe, in RPAE (see [4.14])

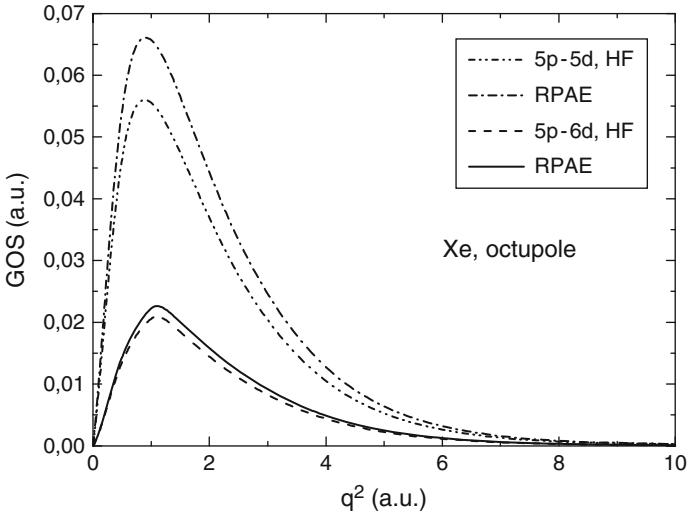

Fig. 4.148_Xe_f6 Generalized oscillator strengths of discrete octupole $5p$–$5d$- and $5p$–$6d$ excitations as to functions of square moment q transferred to the atom Xe, in RPAE (see [4.14])

Figure 4.149_Xe_f7 shows the GOSes of discrete dipole and octupole $5p$–$5d$ excitations for Xe as functions of q^2 transferred to the atom Xe, in RPAE (see [4.14]). As levels are closely located in energy, the sum of their GOSes is presented. Octupole maximum is masked in total GOS.

Figure 4.150_Xe_f8 shows the GOSes of discrete dipole and octupole $5p$–$6d$ excitations for Xe as functions of q^2 transferred to the atom Xe, in RPAE (see [4.14]). Because of the affinity of levels, in fact observable is the sum of their

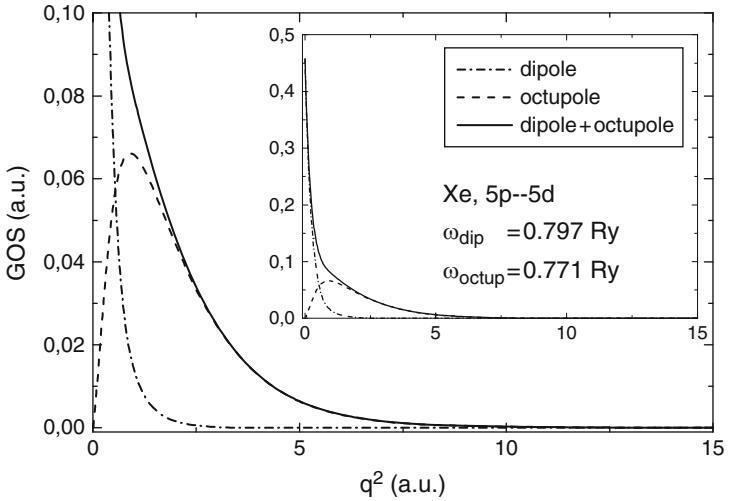

Fig. 4.149_Xe_f7 Generalized oscillator strengths of discrete dipole and octupole $5p$–$5d$ excitations as functions of square q transferred to the atom for Xe, in RPAE (see [4.14])

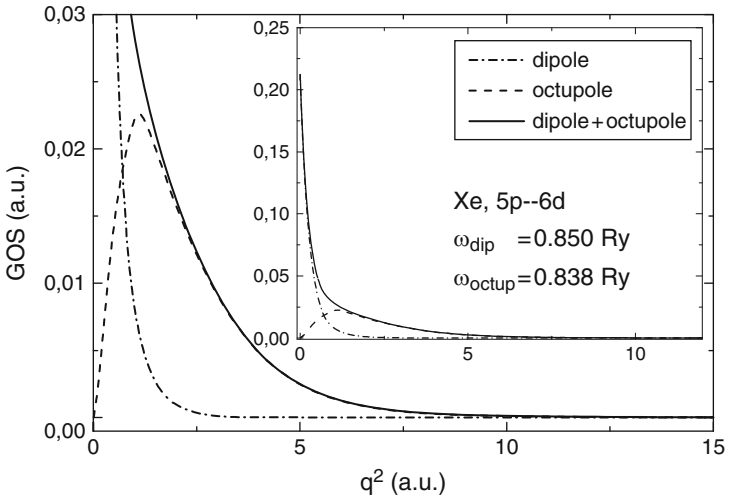

Fig. 4.150_Xe_f8 Generalized oscillator strengths of discrete dipole and octupole $5p$–$6d$ excitations as functions of square moment q transferred to atom for Xe in RPAE (see [4.14])

GOSes only. As shown in Fig. 4.149_Xe_f7, octupole maximum is masked in the total GOS.

Figure 4.151_Xe_f9 shows the GOSes in HF and RPAE and their ratio for $4d$-electrons of Xe. Considerable role of RPAE corrections is visible, particularly in the Giant resonance region.

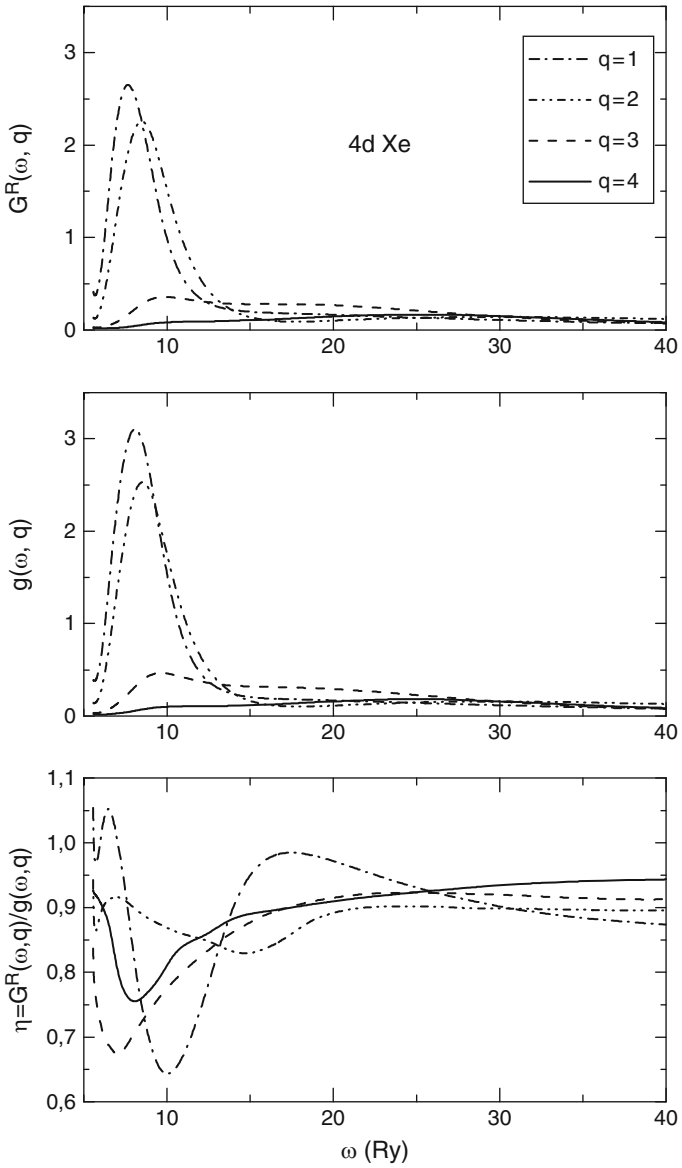

Fig. 4.151_Xe_f9 Generalized oscillator strengths in RPAE and HF and RPAE and their ratio for 4*d*-electrons for Xe

Figure 4.152_Xe_f10 shows the GOS and their ratio in HF and RPAE for 5*s*-electrons of Xe. Role of RPAE corrections is bigger than shown in Fig. 4.151_Xe_f9. It has a distinct maximum in the region of the Giant resonance.

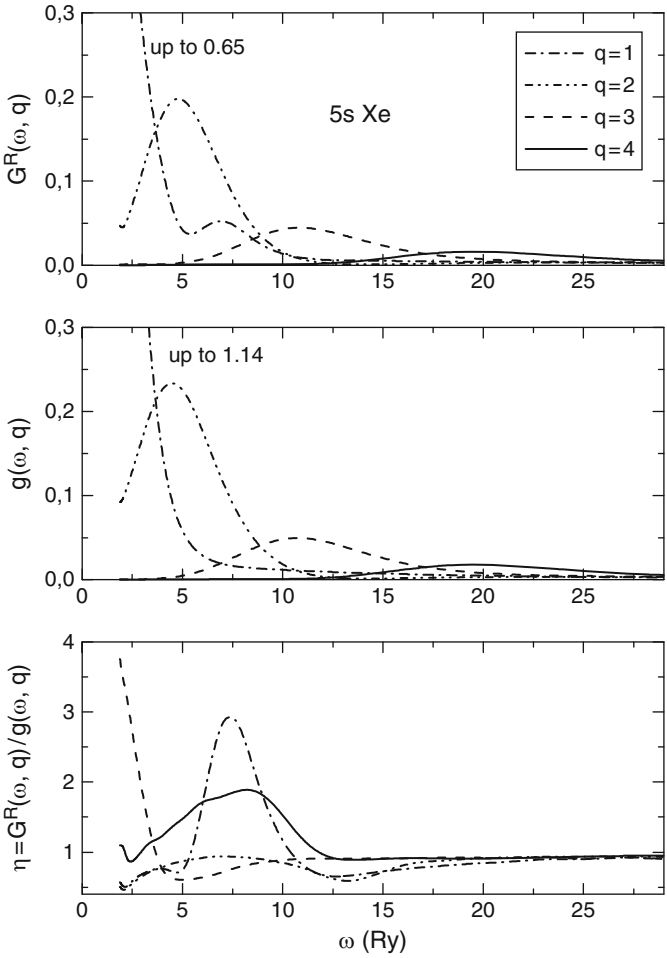

Fig. 4.152_Xe_f10 Generalized oscillator strengths and their ratio of 5*s*-electrons for Xe in HF and RPAE

Figure 4.153_Xe_f11 shows the GOSes and their ratio in HF and RPAE for $5p$-electrons of Xe. Role of RPAE corrections is significant, reaching the factor 1.7, again in the Giant $4d$ resonance region.

Figure 4.154_Xe_g1 shows the cross-section of monopole Compton scattering of γ-quanta with energy $E = 2,000$ Ry on Xe in RPAE as function of the moment q transferred to the atom Xe, at various values of energy ω (the transferred angular moment is $L = 0$) (see [4.15]). We pay attention to the big range of the considered values of q, $0 < q < 8$. With increase of ω, the maximum moves toward bigger q becoming lower and broader.

Figure 4.155_Xe_g2 shows the cross-section of dipole Compton scattering of γ-quanta with energy $E = 2,000$ Ry on Xe in RPAE as function of the moment

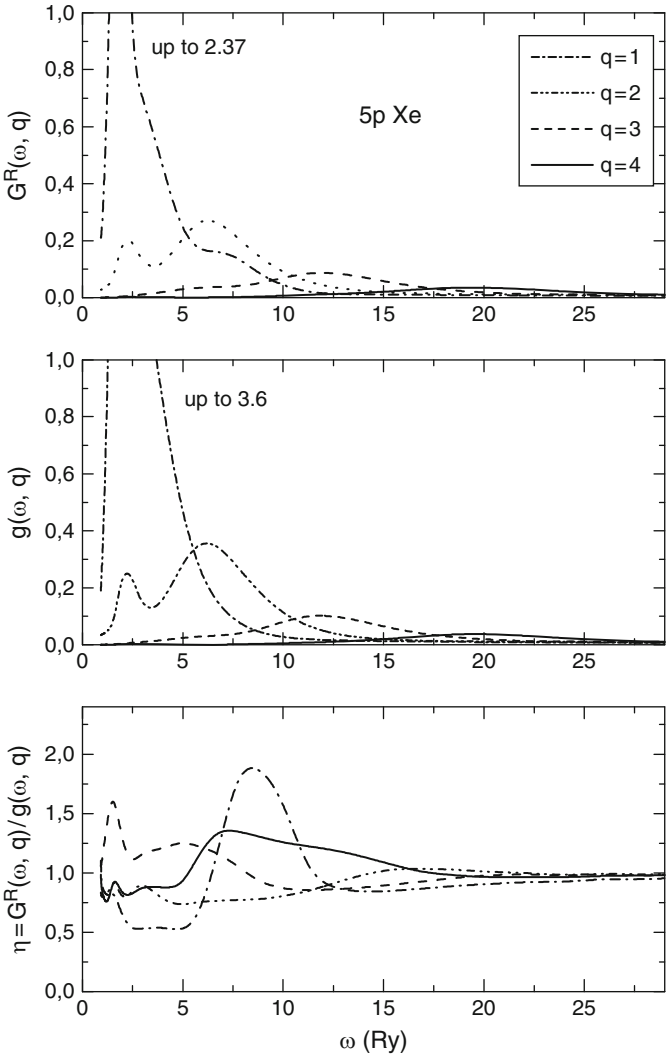

Fig. 4.153_Xe_f11 Generalized oscillator strengths and their ratio of $5p$-electrons for Xe, in HF and RPAE

q transferred to the atom Xe, at various values of energy ω (the transferred angular moment is $L = 1$) (see [4.15]). The maximum moves with growth of ω to higher q, outside the range of the figure, as shown in Fig. 4.154_Xe_g1 becoming broader and lower.

Figure 4.156_Xe_g3 shows the cross-section of quadrupole Compton scattering of γ-quanta with energy $E = 2,000$ Ry on Xe in RPAE as function of the moment q transferred to the atom Xe, at various values of energy ω (the transferred angular

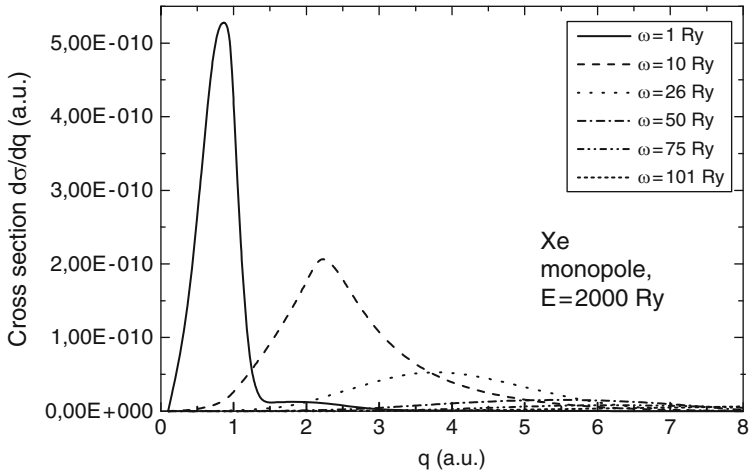

Fig. 4.154_Xe_g1 Cross-section of monopole Compton scattering of γ-quanta at energy $E = 2,000$ Ry as function of the moment q transferred to atom, at various values of energy ω on Xe, in RPAE (see [4.15])

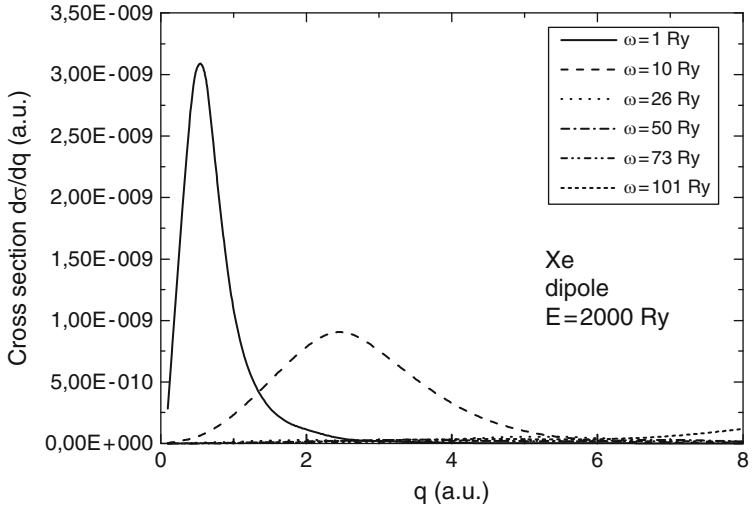

Fig. 4.155_Xe_g2 Cross-section of dipole Compton scattering of γ-quanta at energy $E = 2000Ry$ as function of the moment q transferred to atom, at various values of energy ω on Xe, in RPAE (see [4.15])

moment is $L = 2$) (see [4.15]). The two-maximum structure with growth of ω moves to bigger q, the maxima becoming broader and lower.

Figure 4.157_Xe_g4 gives the cross-section of octupole Compton scattering of γ-quanta with energy $E = 2,000$ Ry on Xe in RPAE as function of the moment q transferred to the atom Xe, at various values of energy ω (the transferred angular

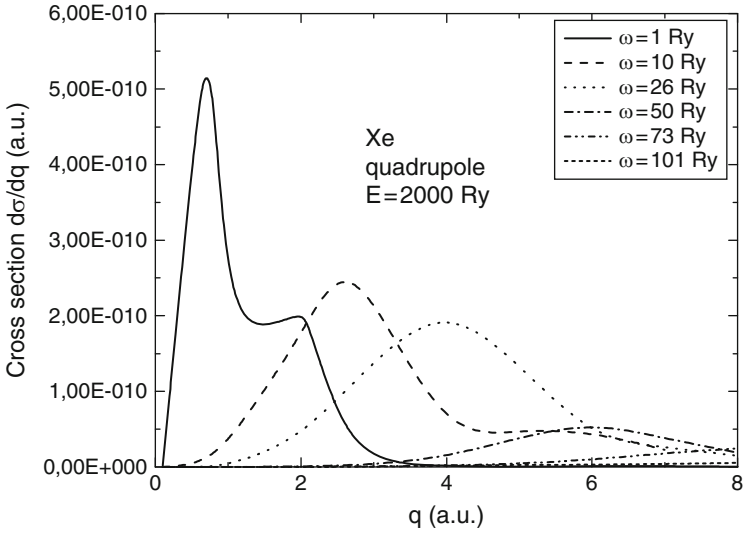

Fig. 4.156_Xe_g3 Cross-section of quadrupole Compton scattering of γ-quanta at energy $E = 2,000$ Ry as function of the moment q transferred to atom, at various values of energy ω on Xe, in RPAE (see [4.15])

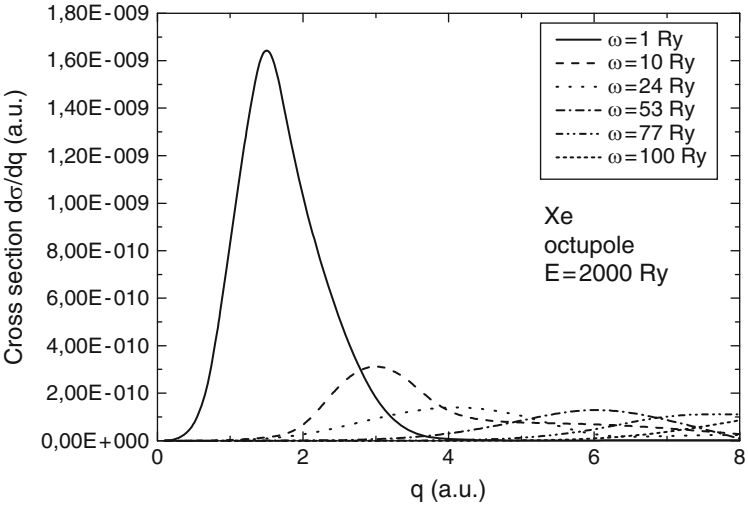

Fig. 4.157_Xe_g4 Cross-section of octupole Compton scattering of γ-quanta at energy $E = 2{,}000$ Ry as function of the moment q transferred to atom, at various values of energy ω on Xe, in RPAE (see [4.15])

moment is $L = 3$) (see [4.15]). The main maximum with increase of ω becomes broader and lower, moving to higher q. The second maximum is outside limits of the figure.

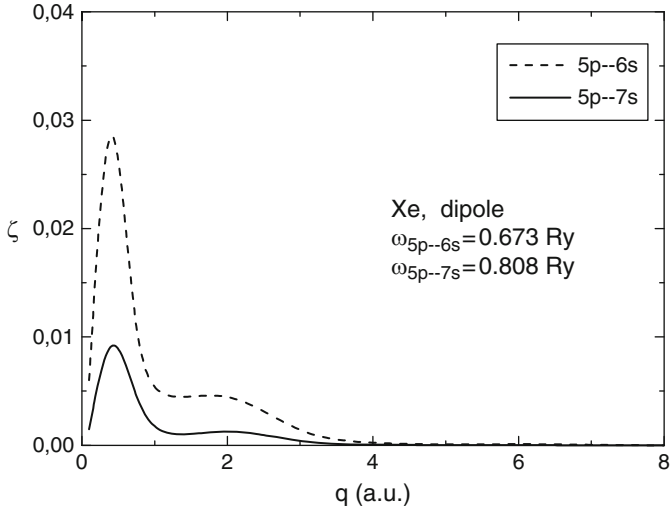

Fig. 4.158_Xe_h1 Relative cross-section of Compton excitation of dipole $5p$–$6s$- and $5p$–$7s$-levels of Xe, in RPAE (see [4.25])

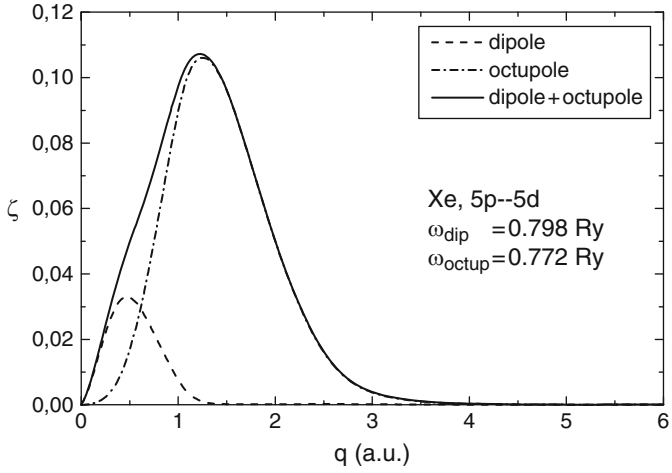

Fig. 4.159_Xe_h2 Relative cross-section of Compton excitation of dipole and octupole $5p$–$5d$-level for Xe, in RPAE (see [4.25])

Figure 4.158_Xe_h1 demonstrates the cross-section of Compton excitation of dipole $5p$–$6s$ and $5p$–$7s$ levels, relative to Thomson cross-section, Xe in RPAE (see [4.25]). Here there are two maxima in the cross-section.

Figure 4.159_Xe_h2 depicts the cross-section of Compton excitation of dipole and octupole $5p$–$5d$ level, relative to Thomson cross-section, for Xe in RPAE (see [4.25]). Here, contrary to the case of Fig. 4.158_Xe_h1, it is only one maximum in the cross-section.

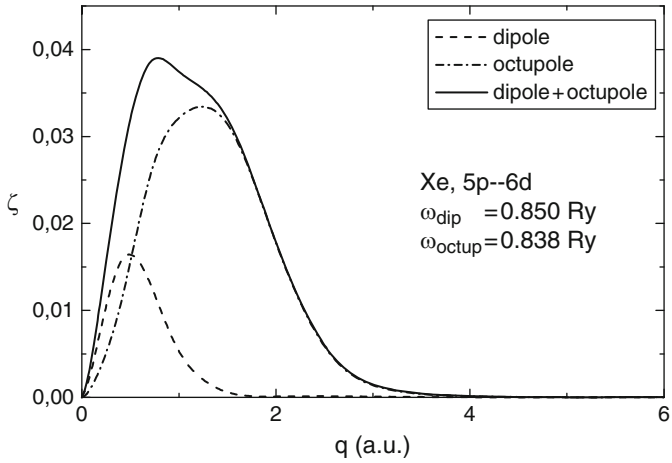

Fig. 4.160_Xe_h3 Relative cross-section of Compton excitation of dipole and octupole $5p$–$6d$-level for Xe, in RPAE (see [4.25])

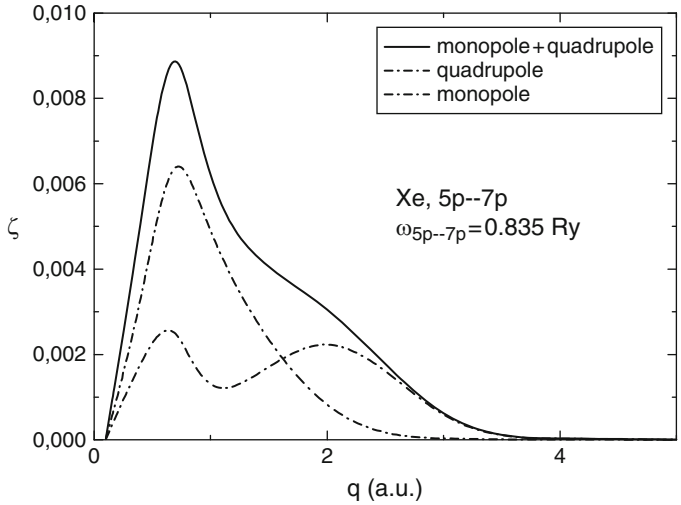

Fig. 4.161_Xe_h4 Relative cross-section of Compton excitation of some close on energy monopole and quadrupole $5p$–$7p$-levels for Xe, in RPAE (see [4.25])

Figure 4.160_Xe_h3 gives the cross-section of Compton excitation of dipole and octupole $5p$–$6d$ level, relative to Thomson cross-section, for Xe in RPAE (see [4.25]). The trace of second maximum in cross-section is seen.

Figure 4.161_Xe_h4 shows the cross-section of Compton excitation, relative to Thomson cross-section, of close in energy monopole and quadrupole ($5p$–$7p$) levels for Xe in RPAE (see [4.25]). As shown in Figs. 4.158_Xe_h1 and

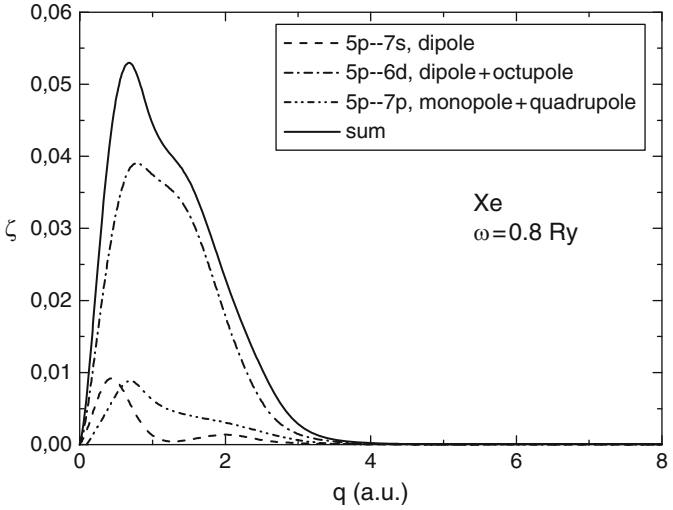

Fig. 4.162_Xe_h5 Relative cross-section of Compton excitation of dipole, octupole, monopole, and quadrupole ($5p$–$7s$, p—$6d$, $5p$–$7p$)-levels for Xe, in RPAE (see [4.25])

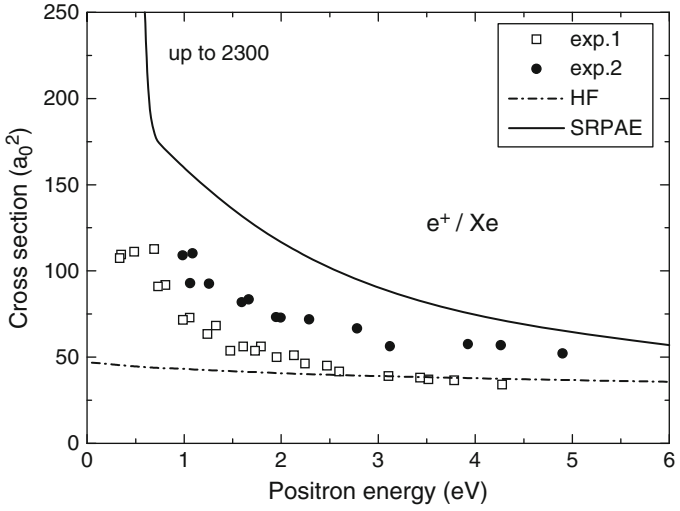

Fig. 4.163_Xe_i1 Cross-section of elastic positron scattering on Xe, in HF and SRPAE (see [4.10]). Experimental data are taken from [4.31, 4.17]

4.160_Xe_h3, traces of two maxima in the sum of cross-sections are visible. The hump at bigger q is caused by quadrupole transition.

Figure 4.162_Xe_h5 presents the cross-section of Compton excitation of dipole, octupole, monopole, and quadrupole ($5p$–$7s$, $5p$–$6d$, $5p$–$7p$) levels, relative to

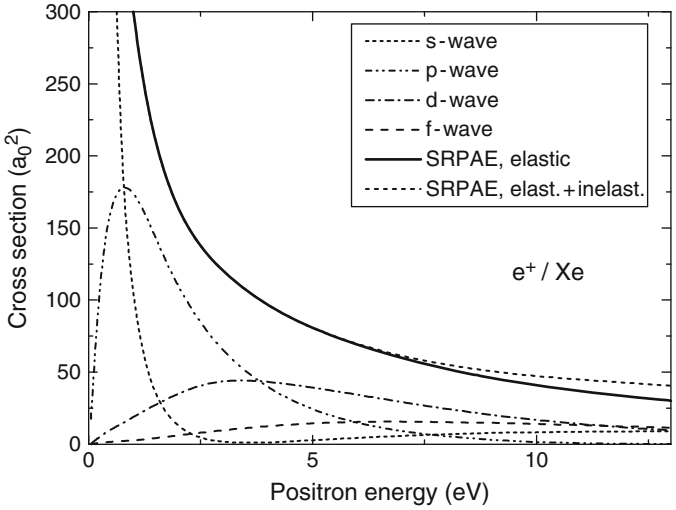

Fig. 4.164_Xe_j1 Contribution of separate partial waves in cross-section of elastic positron scattering on Xe, in SRPAE

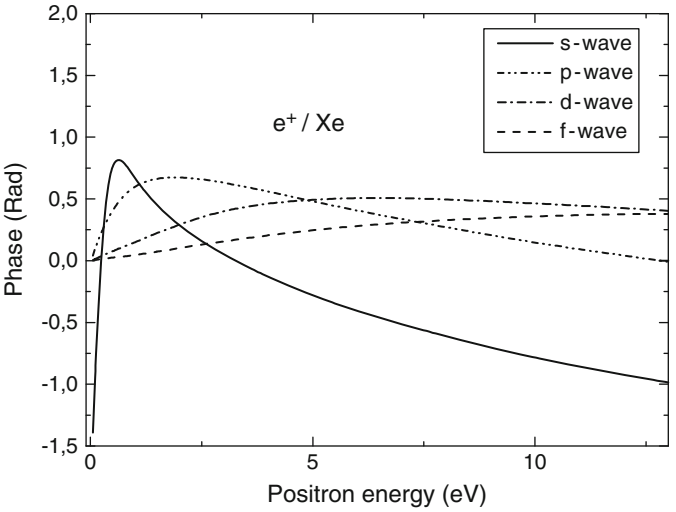

Fig. 4.165_Xe_k1 Phases of various partial waves in positron scattering on Xe, in SRPAE

Thomson cross-section, for Xe in RPAE (see [4.25]). Here again, as in all figures except Fig. 4.159_Xe_h2 a trace of the second maximum is seen.

Figure 4.163_Xe_i1 depicts the cross-section of elastic positron scattering on Xe in HF and SRPAE (see [4.10]). Experimental data are taken from [4.17, 4.31]. Polarization interaction takes into account excitations of $4d$, $5s$, $5p$ subshells and

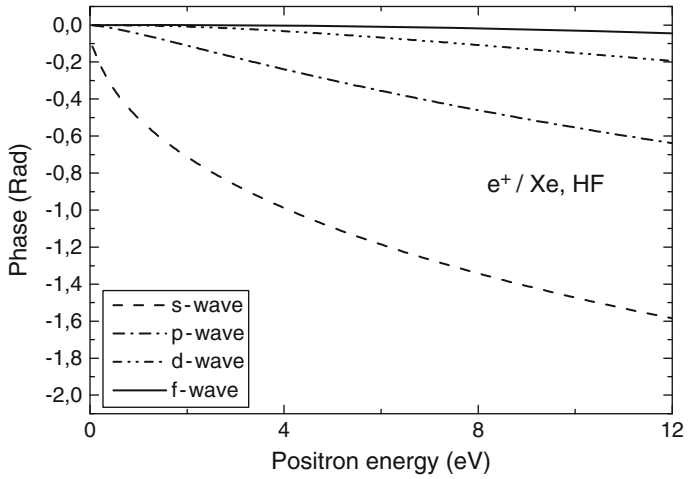

Fig. 4.166_Xe_k2 Phases of various partial waves in positron scattering on Xe, in HF

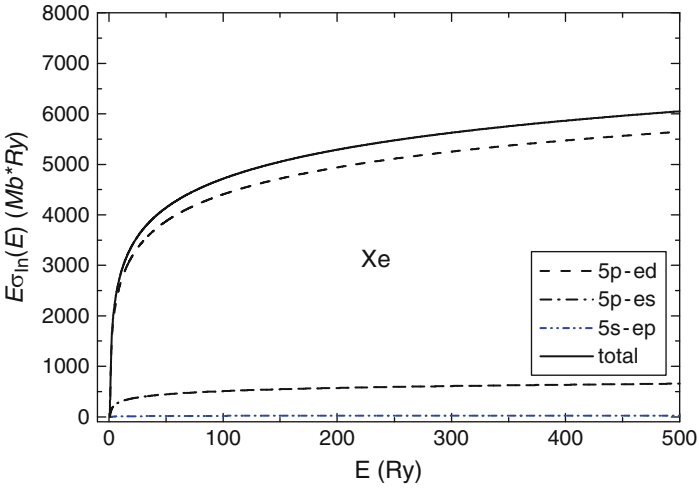

Fig. 4.167_Xe_l1 Multiplied by incoming electron energy cross-section of inelastic scattering of fast electrons in the logarithmic approximation

formation of virtual positronium. Note strong deviation of SRPAE from experiment. It seems that the employed method of virtual positronium formation is too crude.

Figure 4.164_Xe_j1 demonstrates the contribution of partial waves to cross-section of elastic positron scattering on Xe atom in SRPAE. While the mane is the *s*-wave, the *s*-wave Ramsauer minimum is eliminated by combined contribution of *p*- and *d*-waves. Inelastic cross-section is small.

Figure 4.165_Xe_k1 presents the phases of various partial waves in positron scattering on Xe atom in SRPAE. Note rather peculiar behavior of the *s*-phase, with fast increase from big negative values to a positive maximum at small energy

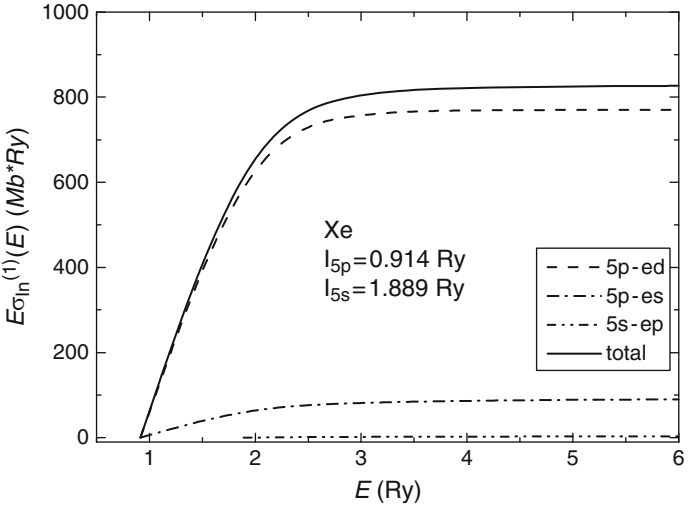

Fig. 4.168_Xe_l2 Nonlogarithmic correction to the multiplied by incoming electron energy cross-section of inelastic scattering of fast electrons

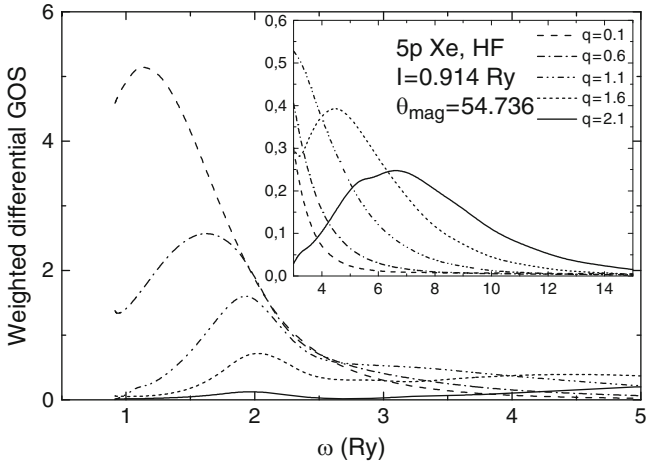

Fig. 4.169_Xe_m1 Weighted differential generalized oscillator strength (3.73b) at magic angle $P_2(\cos\theta_m) = 0$ of $5p$ subshell for Xe at different q in HF

(0.8 Ry) that is followed by monotonic decrease to negative values again. The s-wave's phase starts, according to calculations, neither from zero, nor from any $n\pi$, thus contradicting to (3.21). Qualitatively, this is discussed at the end of Chap. 3.

Figure 4.166_Xe_k2 gives the phases of various partial waves in positron scattering on Xe in HF. The behavior is in accord with general theoretical predictions for potential scattering.

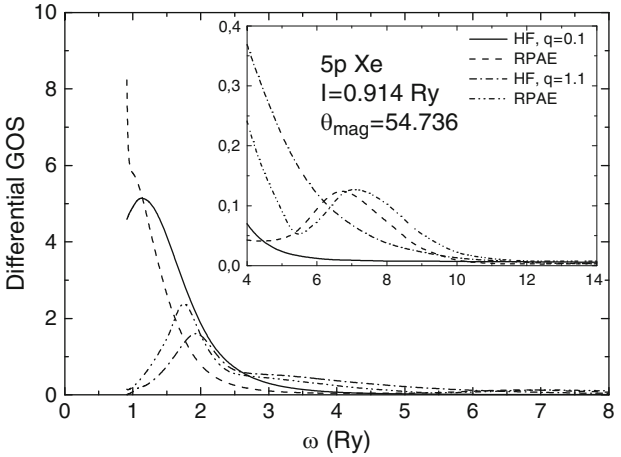

Fig. 4.170_Xe_m2 Weighted differential generalized oscillator strength (3.73b) at magic angle $P_2(\cos\theta_m) = 0$ of $5p$ subshell for Xe at different q in HF and RPAE

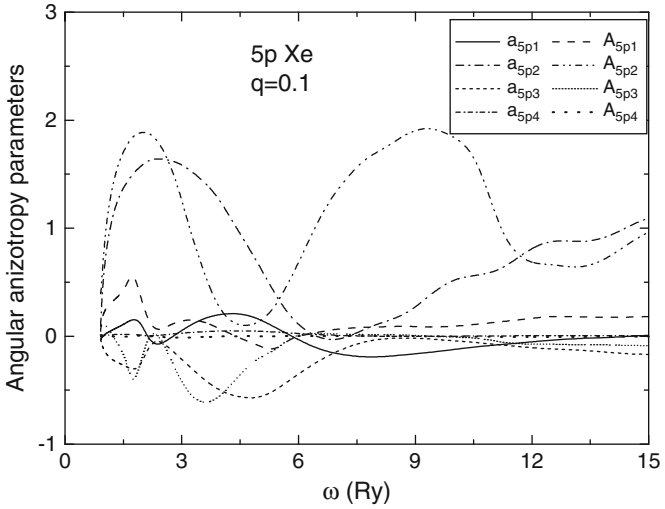

Fig. 4.171_Xe_m3 Angular anisotropy parameters of knocked-out electrons in fast projectile–Xe atom collision of $5p$ subshell, given by (3.77) in HF (a_{5pi}) and RPAE (A_{5pi}) at $q = 0.1$ as functions of ω

Figure 4.167_Xe_l1 shows the multiplied by incoming electron energy total and partial cross-sections of inelastic scattering of fast electrons on atom Xe in logarithmic approximation $E\sigma_{\text{In}}(E)$. Dominative is the contribution of scattering upon the outer $5p$ subshell, mainly from $5p$ to εd dipole transition. It is seen that all these functions at high E increase slowly. The fastest is the increase of the biggest

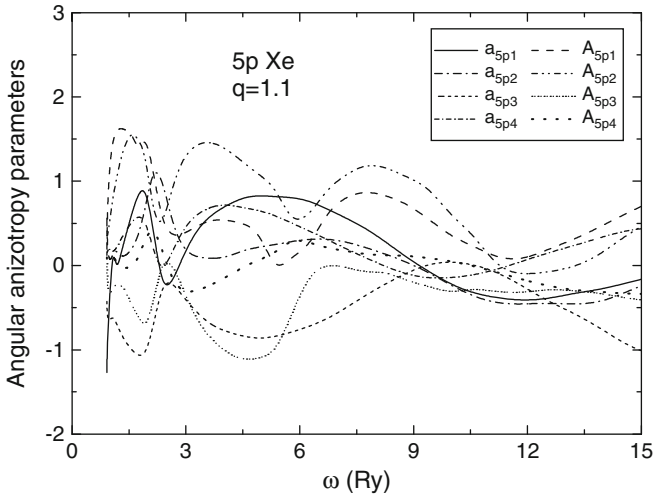

Fig. 4.172_Xe_m4 Angular anisotropy parameters of knocked-out electrons in fast projectile–atom collision given by (3.77), of $5p$ subshell on Xe in HF (a_{3pi}) and RPAE (A_{3pi}) at $q = 1.1$ as functions of ω

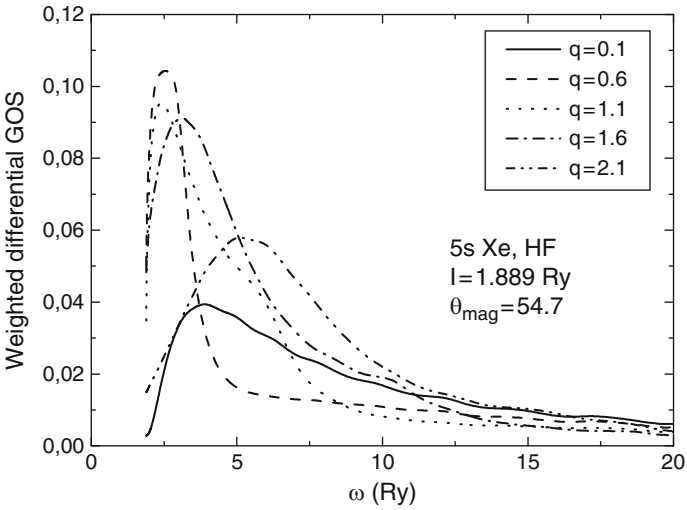

Fig. 4.173_Xe_m5 Weighted differential generalized oscillator strength (3.73b) at magic angle $P_2(\cos\theta_m) = 0$ of $5s$ subshell for Xe at different q in HF as functions of ω

partial cross-section. The cross-sections are presented from $E = I$ for completeness only, since the logarithmic approximation is valid if $\ln(E/I) \gg 1$.

Figure 4.168_Xe_l2 presents the total and partial nonlogarithmic corrections to the cross-sections of inelastic scattering of fast electrons on Xe atom multiplied by incoming electron energy $E\sigma_{\rm ln}^{(1)}(E)$. It is seen that these functions stop to grow

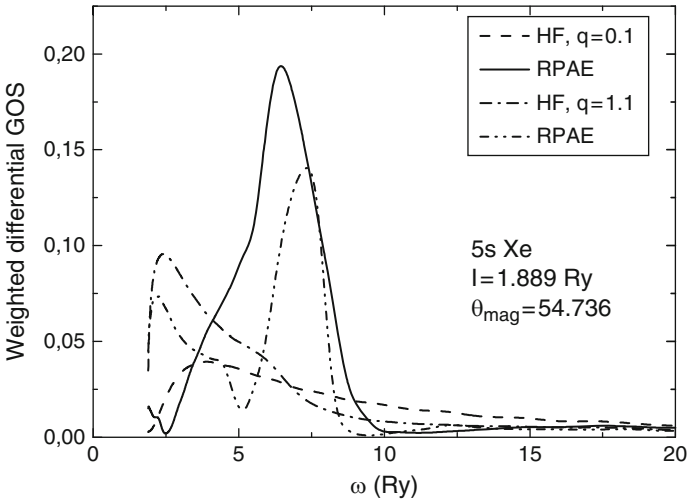

Fig. 4.174_Xe_m6 Weighted differential generalized oscillator strength (3.73b) at magic angle $P_2(\cos\theta_m) = 0$ of $5s$ subshell for Xe at different q in HF and RPAE

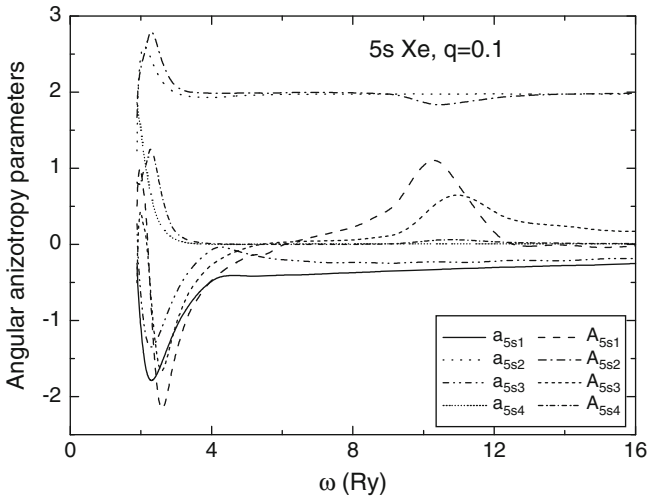

Fig. 4.175_Xe_m7 Angular anisotropy parameters of knocked-out electrons in fast projectile–atom collision as functions of ω given by (3.75) of $5s$ subshell on Xe in HF (a_{3pi}) and RPAE (A_{3pi}) at $q = 0.1$ as functions of ω

already at $E = 3$ Ry. Note that the asymptotic value is achieved at smaller and smaller values on the way from He to Xe.

Figure 4.169_Xe_m1 depicts the differential in electron emission angle weighted GOSes of knocked-out electron in fast projectile–Xe atom collision in HF, given by (3.73b) at magic angle $P_2(\cos\theta_m) = 0$ and a set of q values $q = 0.1, 0.6,$

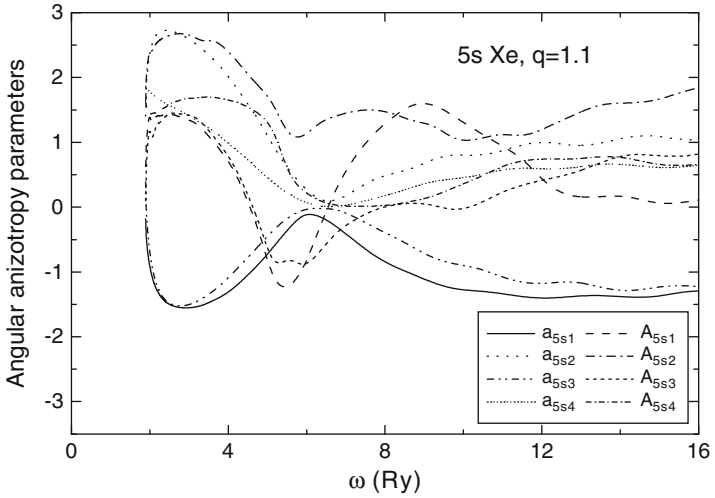

Fig. 4.176_Xe_m8 Angular anisotropy parameters of knocked-out electrons in fast projectile–atom collision given by (3.75) of 5*s* subshell on Xe in HF (a_{5si}) and RPAE (A_{5pi}) at $q = 1.1$ as functions of ω

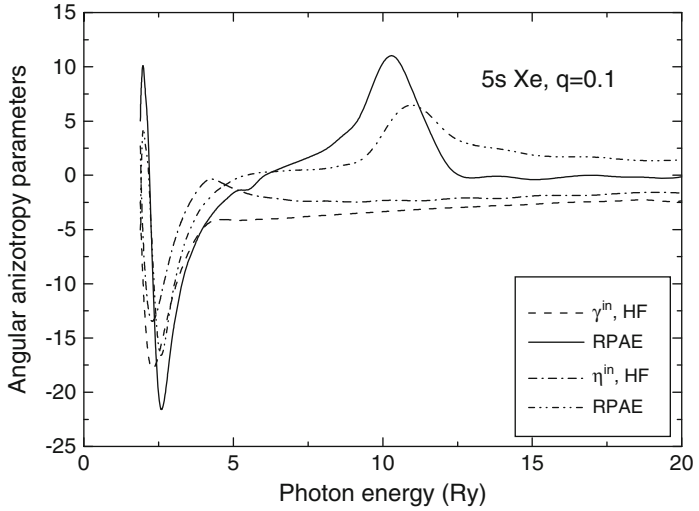

Fig. 4.177_Xe_m9 Angular anisotropy parameters nondipole parameters of knocked-out electrons in fast projectile–atom collision in the optical limit given by (3.84a) and (3.84b) at $q = 0.1$ for 5*s* subshell of Xe

1.1, 1.6, and 2.1. Outer 5*p* subshell is considered. GOSes for small q are similar to photoionization cross-section (see Fig. 2.134_Xe_b1) and their first maximum rapidly decreases with q growth, loosing its power. Additional maximums at higher ω are affected by increase of q not that effective.

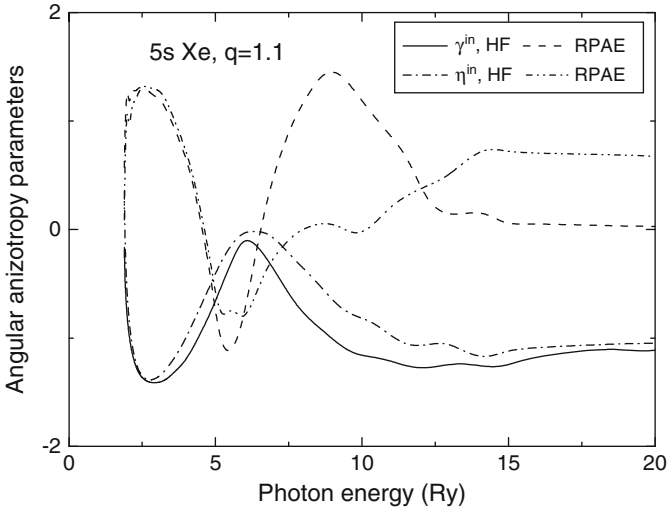

Fig. 4.178_Xe_m10 Angular anisotropy nondipole parameters of knocked-out electrons in fast projectile–atom collision in the optical limit given by (3.84a) and (3.84b) at $q = 1.1$ for $5s$ subshell of Xe

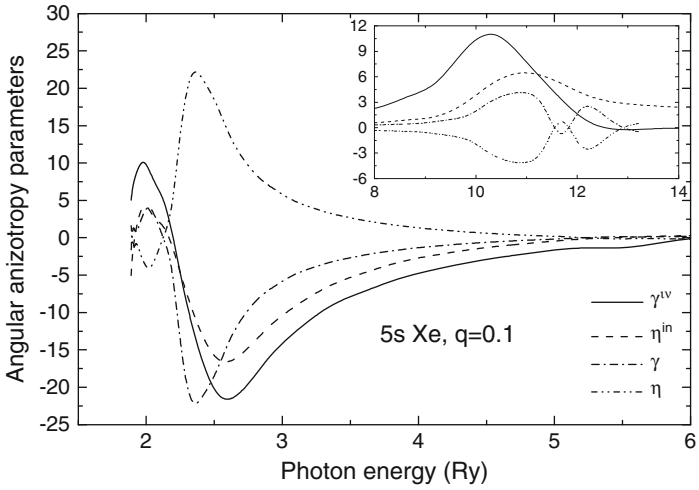

Fig. 4.179_Xe_m11 Angular anisotropy nondipole parameters of knocked-out electrons in fast projectile–atom collision in the optical limit $\gamma_{3s}^{(\mathrm{in})}(\omega)$ and given by (3.84a) and (3.84b) at $q = 0.1$ compared to similar parameters in photoionization $\gamma_{3s}(\omega)$ and $\eta_{3s}(\omega)$, given by (3.83) for $5s$ subshell of Xe in RPAE

Figure 4.170_Xe_m2 gives the weighted differential in electron emission angle GOSes given by (3.73b) at magic angle $P_2(\cos\theta_{\mathrm{m}}) = 0$ of $5p$ subshell for Xe at $q = 0.1$ and 1.1 in HF and RPAE. Role of RPAE correlations is quite impressive. GOSes curves in RPAE have several maximums at both q values.

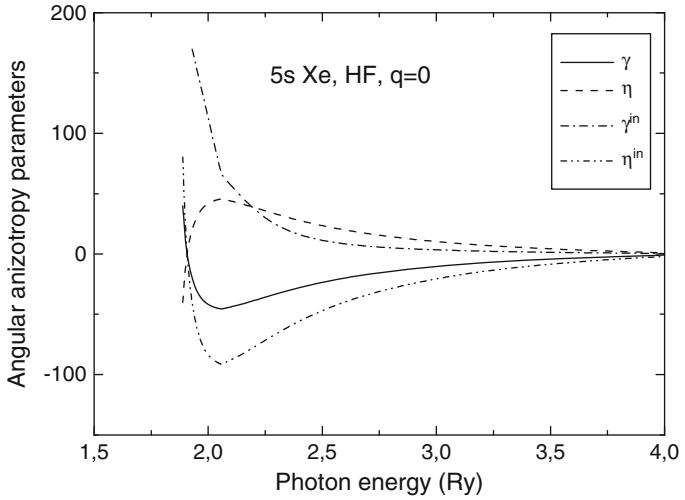

Fig. 4.180_Xe_m12 Comparison of nondipole anisotropy parameters of Xe $5s$ electrons in photoionization and fast electron inelastic scattering [see (3.84a) and (3.84b), respectively] at $q = 0$, calculated in HF

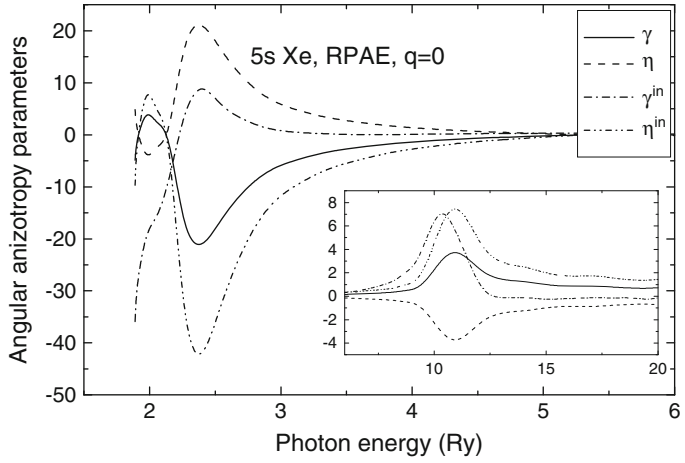

Fig. 4.181_Xe_m13 Comparison of nondipole anisotropy parameters of Xe $5s$ electrons in photoionization and fast electron inelastic scattering [see (3.84b)] at $q = 0$, calculated in RPAE

Figure 4.171_Xe_m3 shows the angular anisotropy parameters of knocked-out electrons in fast projectile–Xe atom collision of $5p$ subshell, given by (3.77) in HF (a_{5pi}) and RPAE (A_{5pi}) at $q = 0.1$ as functions of ω. Note that dipole parameters a_{5p2} and A_{5p2} are close to zero, as well as a_{5p1}, A_{5p1} and a_{5p4}, A_{5p4}. Very big is only the oscillating value of a_{5p1} and A_{5p1}.

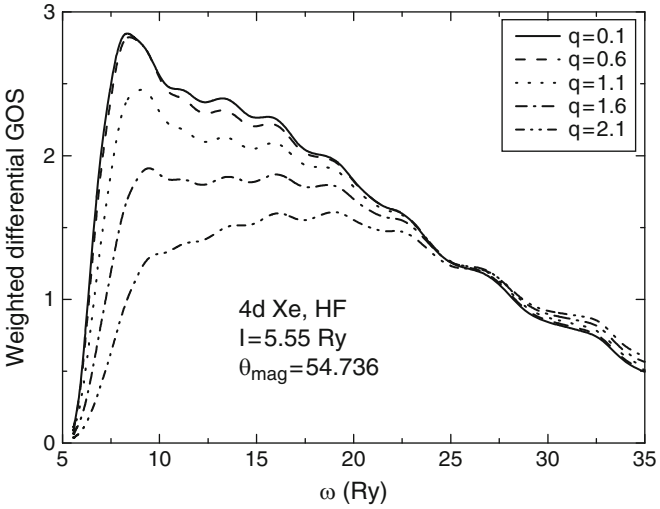

Fig. 4.182_Xe_m14 Weighted differential generalized oscillatorstrength (3.73b) at magic angle $P_2(\cos\theta_{\rm m}) = 0$ of $4d$ subshell for Xe at different q in HF

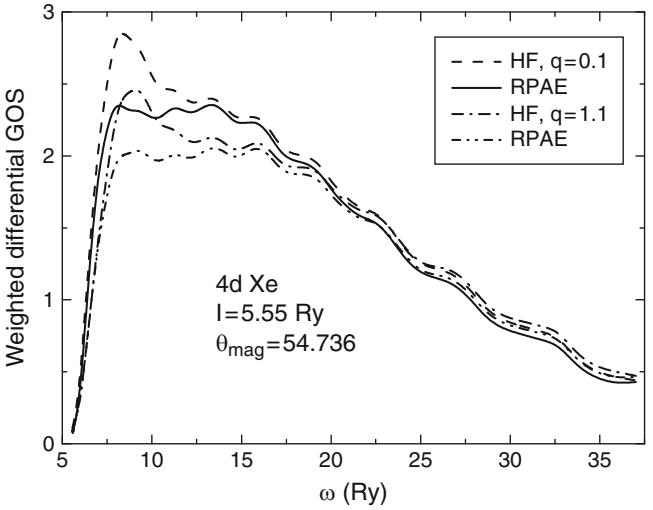

Fig. 4.183_Xe_m15 Weighted differential generalized oscillatorstrength (3.73b) at magic angle $P_2(\cos\theta_{\rm m}) = 0$ of $4d$ subshell for Xe at different q in HF and RPAE

Figure 4.172_Xe_m4 demonstrates the angular anisotropy parameters of knocked-out electrons in fast projectile–atom collision given by (3.77), of $5p$ subshell on Xe in HF (a_{3pi}) and RPAE (A_{3pi}) at $q = 1.1$ as functions of ω. Note that dipole parameters a_{5p2} and A_{5p2}, as well as a_{5p1}, A_{5p1} and a_{5p4}, A_{5p3} are considerably bigger than at $q = 0.1$. As to a_{5p1} and A_{5p1}, it becomes smaller.

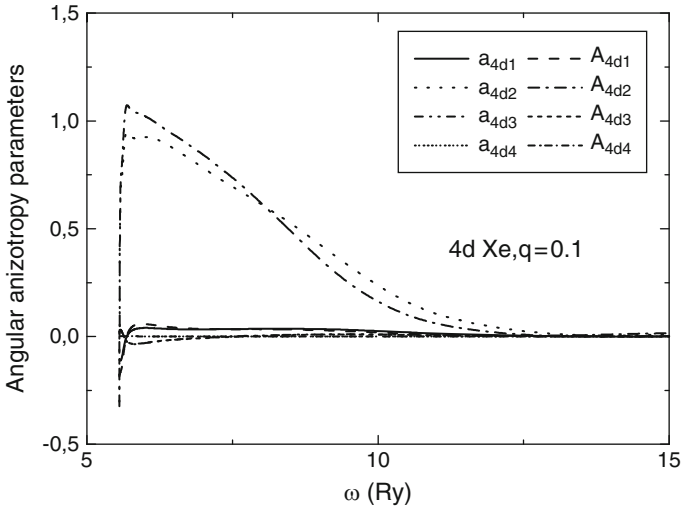

Fig. 4.184_Xe_m16 Angular anisotropy parameters given by of knocked-out electrons in fast projectile–atom collision as functions of ω (3.79) of $4d$ subshell on Xe in HF (a_{4di}) and RPAE (A_{4di}) at $q = 0.1$

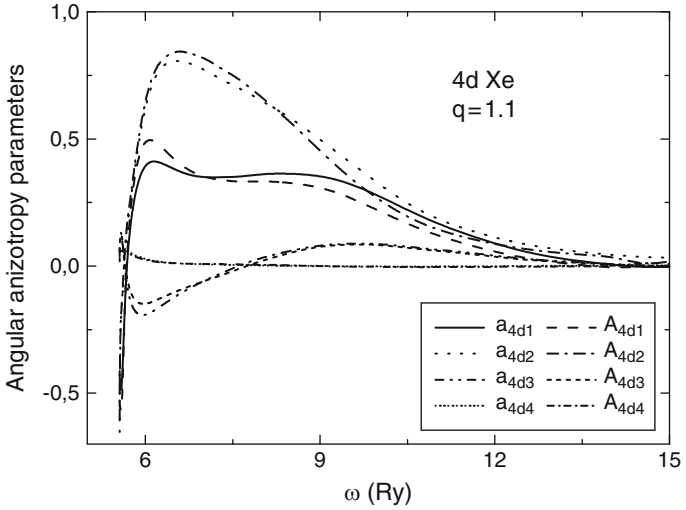

Fig. 4.185_Xe_m17 Angular anisotropy parameters of knocked-out electrons in fast projectile–atom collision as functions of ω given by (3.79) of $4d$ subshell on Xe in HF (a_{4di}) and RPAE (A_{4di}) at $q = 1.1$

Figure 4.173_Xe_m5 gives the weighted differential in electron emission angle GOSes given by (3.72) at magic angle $P_2(\cos\theta_m) = 0$ of $5s$ subshell for Xe at $q =$ 0.1, 0.6, 1.1, 1.6, and 2.1 in HF. GOSes for small q are similar to photoionization

cross-section (Fig. 2.54_Xe_b2). Contrary to the situation for $5p$, the maximum for $q > 0.1$ is bigger than for $q = 0.1$. With growth of q it increases and then starts to decrease.

Figure 4.174_Xe_m6 shows the weighted GOSes differential in emission angle of the knocked-out electron (3.73b) at magic angle $P_2(\cos\theta_m) = 0$ of $5s$ subshell for Xe at $q = 0.1$ and 1.1 in HF and RPAE. For small q, the GOSes are similar to the photoionization cross-section (see Fig. 2.54_Xe_b2). For $q = 1.1$, the near threshold maximum becomes much stronger. One see a broad and low RPAE maximums at 15 and 12 Ry for $q = 0.1$ and $q = 1.1$, respectively.

Figure 4.175_Xe_m7 presents the angular anisotropy parameters of knocked-out electrons in fast projectile–atom collision given by (3.75) of $5s$ subshell on Xe in HF (a_{5si}) and RPAE (A_{5pi}) at $q = 0.1$ as functions of ω. Note that the dipole parameters a_{5s2} and A_{5s2} are everywhere, except vicinity of $5s$ threshold and $4d$ Giant resonance, equal to 2, as it should be in the optical limit $q \to 0$. Near $5s$ threshold and in the $4d$ Giant resonance region other parameters essentially changes, whereas in other ω region they are smooth functions of ω. The ratio between parameters is natural: $100a_{5s4}, A_{5s4} \approx 10a_{5s1}, A_{5s1}; a_{5s3}, A_{5s3} \approx a_{5s2}, A_{5s2}$, in accord with $q = 0.1$ and $q^2 = 0.01$.

Figure 4.176_Xe_m8 depicts the angular anisotropy parameters of knocked-out electrons in fast projectile–atom collision given by (3.75) of $5s$ subshell on Xe in HF (a_{5si}) and RPAE (A_{5pi}) at $q = 1.1$ as functions of ω. All parameters are of the same order of magnitude and rapidly oscillate that is natural for big q.

Figure 4.177_Xe_m9 demonstrates the angular anisotropy nondipole parameters of knocked-out electrons in fast projectile–atom collision in the optical limit given by (3.84a) and (3.84b) at $q = 0.1$ for $5s$ subshell of Xe. Strong variations of parameters are located at $2 < \omega < 4$ Ry and at $8 < \omega < 12$ Ry, i.e., near threshold and in the $4d$ Giant resonance vicinity. The variation at $8 < \omega < 12$ Ry is a direct consequence of the action of $4d$ Giant resonance upon nondipole parameters of $5s$ Xe. A strong and deep minimum in $\eta^{(in)}$ should be compared to a much smaller maximum in RPAE only for $\gamma^{(in)}$ at the same ω.

Figure 4.178_Xe_m10 collects the angular anisotropy nondipole parameters of knocked-out electrons in fast projectile–atom collision in the optical limit given by (3.84a) and (3.84b) at $q = 1.1$ for $5s$ subshell of Xe. Both parameters, $\gamma^{(in)}$ and $\eta^{(in)}$, are essentially varying functions and of the same order of magnitude. This signals that $q = 1.1$ is far from the optical limit.

Figure 4.179_Xe_m11 shows the angular anisotropy nondipole parameters of knocked-out electrons in fast projectile–atom collision in the optical limit $\gamma_{5s}^{(in)}(\omega)$ and $\eta_{5s}^{(in)}(\omega)$ given by (3.84a) and (3.84b) at $q = 0.1$ compared to similar parameters in photoionization $\gamma_{5s}(\omega)$ and $\eta_{5s}(\omega)$, given by (3.83) for $5s$ subshell of Xe in RPAE. The ratio $\eta_{ns}^{(in)}(\omega) = 2\gamma_{ns}(\omega)$ is fulfilled with good accuracy.

Figure 4.180_Xe_m12 displace the nondipole anisotropy parameters of Xe$5s$ electrons in photoionization and fast electron inelastic scattering [see (3.84a)

and (3.84b), respectively] at $q = 0$, calculated in HF. The ratio $\eta_{ns}^{(\mathrm{in})}(\omega) = 2\gamma_{ns}(\omega)$ is fulfilled with excellent accuracy. The relations between $\gamma_{ns}(\omega)$ and $\gamma_{ns}^{(\mathrm{in})}(\omega)$, $\eta_{ns}(\omega)$ and $\eta_{ns}^{(\mathrm{in})}(\omega)$ are energy dependent. Parameters $\gamma_{ns}^{(\mathrm{in})}(\omega)$ and $\eta_{ns}^{(\mathrm{in})}(\omega)$ are considerably bigger than $\gamma_{ns}(\omega)$ and $\eta_{ns}(\omega)$, and their contribution to the differential in angle oscillator strength can be increased by going to higher values of q [see (3.84a)].

Figure 4.181_Xe_m13 shows the nondipole anisotropy parameters of Xe5s electrons in photoionization and fast electron inelastic scattering [see (3.84b)] at $q = 0$, calculated in RPAE. The effect of electron correlations is very big. The ratio $\eta_{ns}^{(\mathrm{in})}(\omega) = 2\gamma_{ns}(\omega)$ is fulfilled with excellent accuracy. The relations between $\gamma_{ns}(\omega)$ and $\gamma_{ns}^{(\mathrm{in})}(\omega)$, $\eta_{ns}(\omega)$ and $\eta_{ns}^{(\mathrm{in})}(\omega)$ are energy dependent, just as in HF (see Fig. 2.181_Xe_m13). The $\gamma_{ns}^{(\mathrm{in})}(\omega)$ and $\eta_{ns}^{(\mathrm{in})}(\omega)$ parameters are considerably bigger than $\gamma_{ns}(\omega)$ and $\eta_{ns}(\omega)$, and the (in) parameters in RPAE are much bigger than in HF. Nondipole parameters contribution to the differential in angle oscillator strength can be increased by going to higher values of q [see (3.84a)].

Figure 4.182_Xe_m14 shows the weighted GOSes differential in emission angle of the knocked-out electron (3.73b) at magic angle $P_2(\cos\theta_{\mathrm{m}}) = 0$ of 4d subshell for Xe at $q = 0.1$ and 1.1 in HF. GOSes have a powerful maximum in general similar to the photoionization cross-section of 4d shown in Fig. 2.56_Xe_b4.

Figure 4.183_Xe_m15 gives the weighted differential generalized oscillator strength (3.73b) at magic angle $P_2(\cos\theta_{\mathrm{m}}) = 0$ of 4d subshell for Xe at different q in HF and RPAE. The RPAE role is not too impressive.

Figure 4.184_Xe_m16 presents the angular anisotropy parameters of knocked-out electrons in fast projectile–atom collision as functions of ω given by (3.79) of 4d subshell on Xe in HF (a_{4di}) and RPAE (A_{4di}) at $q = 0.1$ as functions of ω. The dipole parameter $i = 2$ is of the order of one having a big and broad maximum at threshold. The difference between HF and RPAE is noticeable. All other parameters, except that with $i = 1$ are very close to zero.

Figure 4.185_Xe_m17 gives the angular anisotropy parameters of knocked-out electrons in fast projectile–atom collision given by (3.79) of 4d subshell on Xe in HF (a_{4di}) and RPAE (A_{4di}) at $q = 1.1$ as functions of ω. As it is for $q = 0.1$, here absolutely dominates the dipole parameter, but contrary to the case of $q = 0.1$ parameter $i = 1$ is also big. Noticeable is the $i = 3$ parameter. As to $i = 4$, it is very small, almost zero.

The GOSes at $q = 0.00001$ for Ne, Ar, Kr, and Xe. At so small q GOSes are close to optical values, i.e., dipole oscillator strengths (Table 4.1). Role of RPAE corrections is significant, in some cases even big. Coincidence of results in length and velocity forms in RPAE is quite good. Only in Xe the outer shell GOS of transition $nl - n(l+1)[5p - 5d]$ dominates. In other noble gas atoms, the dominative is the outer subshell $nl - n(l-1)$ transition. For all four atoms, the p–s transitions decrease much faster than p–d.

Table 4.1 Generalized oscillator strengths close to optical limit: Ne, Ar, Kr, and Xe at $q = 0.00001$

Transition	Energy (Ry)	HF-l	HF-v	RPAE-l	RPAE-v
Ne					
$2p$–$3d$	1.58864	0.2332E–01	0.1784E–01	0.2198E–01	0.2183E–01
$2p$–$4d$	1.63791	0.1254E–01	0.9551E–02	0.1182E–01	0.1174E–01
$2p$–$5d$	1.66061	0.7007E–02	0.5326E–02	0.6619E–02	0.6575E–02
$2p$–$6d$	1.67251	0.4390E–02	0.3334E–02	0.4037E–02	0.4008E–02
$2p$–$3s$	1.34836	0.1564E+00	0.1444E+00	0.1651E+00	0.1683E+00
$2p$–$4s$	1.56353	0.2779E–01	0.2553E–01	0.2866E–01	0.2928E–01
$2p$–$5s$	1.62790	0.9917E–02	0.9101E–02	0.1029E–01	0.1051E–01
$2p$–$6s$	1.65565	0.4677E–02	0.4290E–02	0.4862E–02	0.4968E–02
Ar					
$3p$–$3d$	1.06775	0.1624E+00	0.9698E–01	0.1812E+00	0.1795E+00
$3p$–$4d$	1.11820	0.8251E–01	0.4856E–01	0.8956E–01	0.8873E–01
$3p$–$5d$	1.14136	0.4514E–01	0.2639E–01	0.4754E–01	0.4710E–01
$3p$–$6d$	1.15387	0.2700E–01	0.1573E–01	0.2451E–01	0.2429E–01
$3p$–$4s$	0.89675	0.2964E+00	0.2598E+00	0.3161E+00	0.3107E+00
$3p$–$5s$	1.06269	0.5571E–01	0.4847E–01	0.3806E–01	0.3731E–01
$3p$–$6s$	1.11636	0.2058E–01	0.1787E–01	0.1424E–01	0.1396E–01
$3p$–$7s$	1.14048	0.9929E–02	0.8617E–02	0.7145E–02	0.7011E–02
Kr					
$4p$–$4d$	0.93330	0.2673E+00	0.1525E+00	0.2626E+00	0.2621E+00
$4p$–$5d$	0.98429	0.1316E+00	0.7385E–01	0.1284E+00	0.1280E+00
$4p$–$6d$	1.00758	0.7116E–01	0.3964E–01	0.6687E–01	0.6660E–01
$4p$–$7d$	1.02015	0.4230E–01	0.2347E–01	0.3687E–01	0.3672E–01
$4p$–$5s$	0.78016	0.3752E+00	0.3364E+00	0.3576E+00	0.3465E+00
$4p$–$6s$	0.93406	0.7049E–01	0.6282E–01	0.6562E–01	0.6426E–01
$4p$–$7s$	0.98480	0.2621E–01	0.2332E–01	0.2299E–01	0.2246E–01
$4p$–$8s$	1.00798	0.1271E–01	0.1131E–01	0.5974E–01	0.5790E–01
Xe					
$5p$–$5d$	0.79768	0.4834E+00	0.2507E+00	0.4633E+00	0.4580E+00
$5p$–$6d$	0.84976	0.2306E+00	0.1171E+00	0.2185E+00	0.2159E+00
$5p$–$7d$	0.87343	0.1235E+00	0.6210E–01	0.1108E+00	0.1094E+00
$5p$–$8d$	0.88618	0.7304E–01	0.3655E–01	0.6025E–01	0.5950E–01
$5p$–$6s$	0.67262	0.4185E+00	0.3675E+00	0.4290E+00	0.4188E+00
$5p$–$7s$	0.80827	0.8239E–01	0.7188E–01	0.1252E+00	0.1224E+00
$5p$–$8s$	0.85441	0.3130E–01	0.2726E–01	0.4608E–01	0.4505E–01
$5p$–$9s$	0.87585	0.1538E–01	0.1339E–01	0.2187E–01	0.2139E–01

4.3 Atoms and Some Ions of Group I Elements of the Periodic Table

In this section, results of our already known and new calculations of total and partial cross-sections of elastic scattering of electrons and positrons on some atoms and ions of I group's elements of the periodic system are presented. The calculations

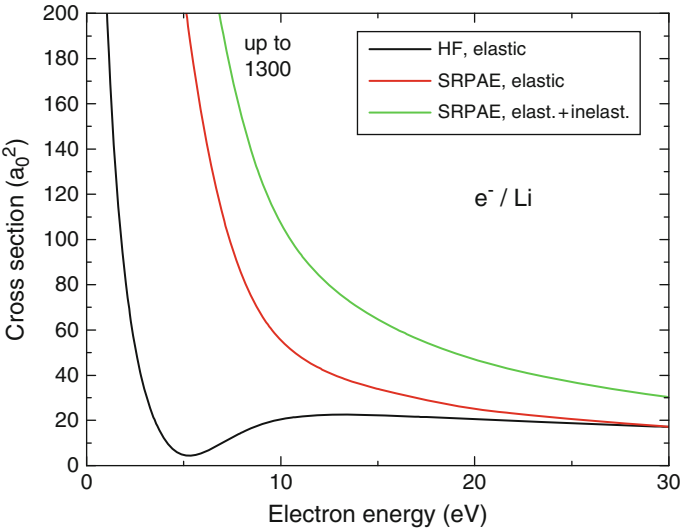

Fig. 4.186_Li_a1 Cross-section of elastic (in HF and SRPAE) and inelastic (in SRPAE) electron scattering on Li

are performed in one-electron HF approximation and with account of polarization interaction in the simplified random phase approximation with exchange-SRPAE (see Sects. 3.3 and 3.4 and [AICC]) including the effect of virtual formation of positronium (see Sect. 3.12). In polarization interaction, the excitation of following subshells of electrons was taken into account: $1s^2, 2s$ in Li, $1s^2$ in Li^+, $1s^2, 2s^2$ in Li^-, $2s^2, 2p^6, 3s$ in Na, $2s^2, 2p^6$ in Na^+, $2s^2, 2p^6, 3s^2$ in Na^-,$3s^2, 3p^6, 4s$ in K, $3s^2, 3p^6$ in K^+, $3s^2, 3p^6, 4s^2$ in K^-. In the same approximation, s, p, d, f phases of scattering and corresponding partial cross-sections are calculated. The generalized oscillator strengths with account of RPAE correlations for mentioned above electrons are presented. GOSes for $3d_{5/2}$, $3d_{3/2}$-electrons of Cs are given also.

Figures 4.186–4.194 (Li) show the results of calculations for Li.

Figure 4.186_Li_a1 illustrates the cross-section of elastic (in HF and SRPAE) and inelastic (in SRPAE) electron scattering on Li. The taken into account inelastic channel in Li is ionization of $2s$-electrons.

Figure 4.187_Li_b1 presents the contribution of partial waves to cross-section of elastic electron scattering on Li. The contribution of s-wave dominates only at very small energy. The contribution of p- and d-waves sharply grows, f-wave has a maximum. Starting from 5 eV p-wave dominates over all other. Note a small maximum at 2 eV in the s-wave.

Figure 4.188_Li_d1 depicts the phases of various partial waves in electron scattering in SRPAE on Li. Here s-phase has a negative derivative in all the considered range of energies. As it should be in accord with (3.21), at zero electron energy s-phase is equal to 2π, while p-, d-, f-phases approach zero value if all of them are defined so that $\delta_l \to 0$ at $E \to \infty$.

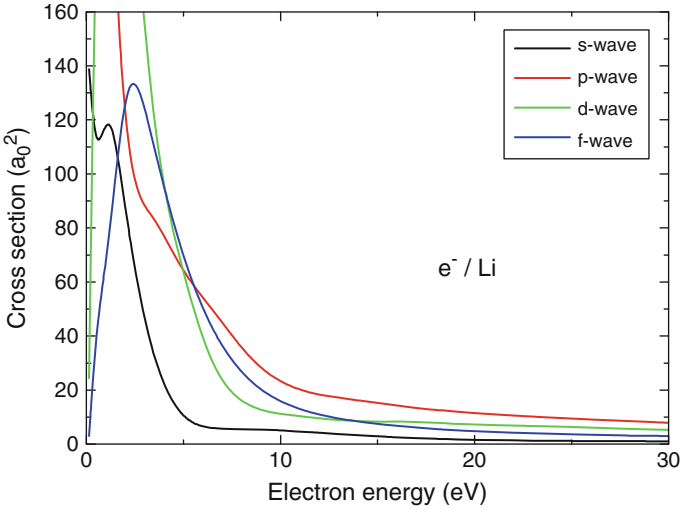

Fig. 4.187_Li_b1 Contribution of partial waves to cross-section of elastic electron scattering on Li

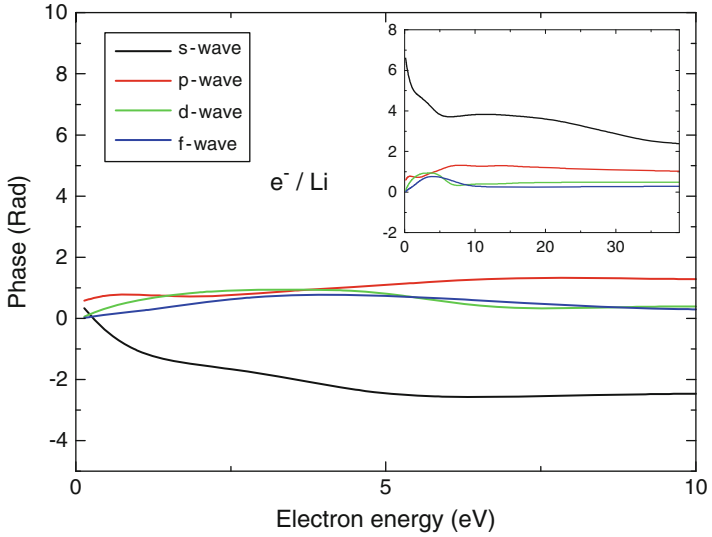

Fig. 4.188_Li_d1 SRPAE phases of various partial waves in electron scattering on Li in SRPAE

Figure 4.189_Li_e1 shows the density of the monopole GOSes for Li in RPAE as functions of the energy transferred to the atom Li at various q. Big radius of Li atom and, as a result, fast oscillations of $\exp(i\vec{q}\vec{r})$ already at rather small q lead to quite complex behavior of GOSes.

Figure 4.190_Li_e2 displays the density of dipole GOSes for Li in RPAE as function of the energy transferred to the atom at various q. The first maximum, from

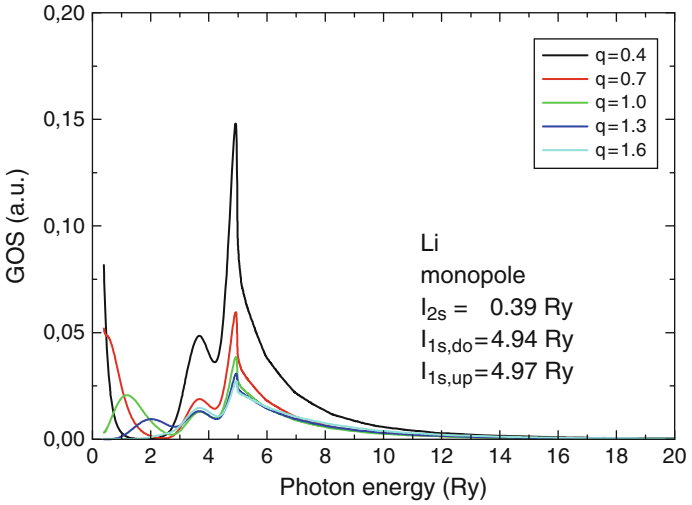

Fig. 4.189_Li_e1 Density of the monopole generalized oscillator strengths for Li in RPAE as functions of the energy transferred to the atom at various q

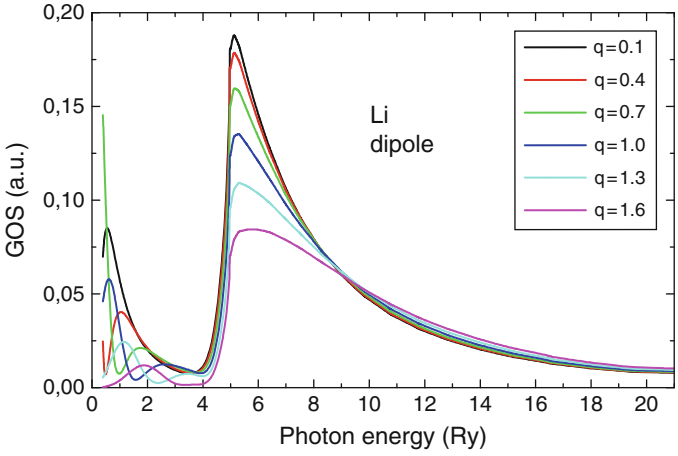

Fig. 4.190_Li_e2 Density of dipole generalized oscillator strengths as function of the energy transferred to the atom Li at various q, in RPAE

2s-electrons, moves to bigger energies with growth of q, whereas the second one that occurs from ionization of 1s-electrons remains at the same place. Dipole GOSes are much bigger than the monopole and quadrupole ones, as is seen from Figs. 4.189_Li_e1 and 4.191_Li_e3.

Figure 4.191_Li_e3 shows the density of quadrupole GOSes for Li in RPAE as functions of the energy transferred to the atom at various q. It is remarkable that with growth of q the first maximum decreases, whereas the second one grows.

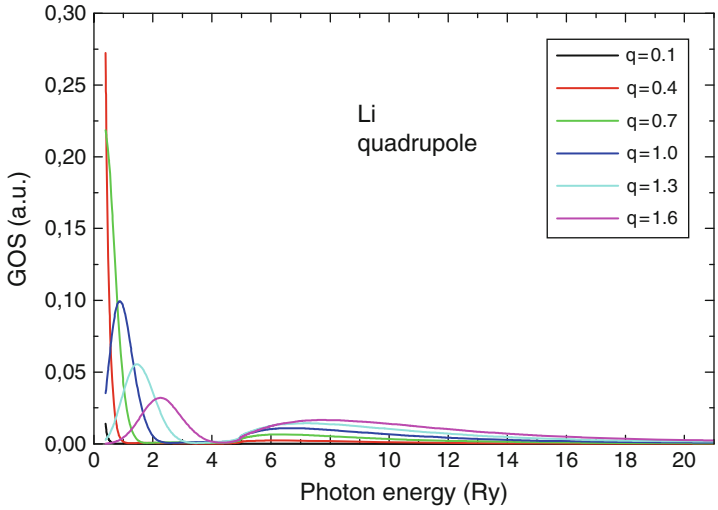

Fig. 4.191_Li_e3 Density of quadrupole generalized oscillator strengths as function of the energy transferred to the atom Li at various q, in RPAE

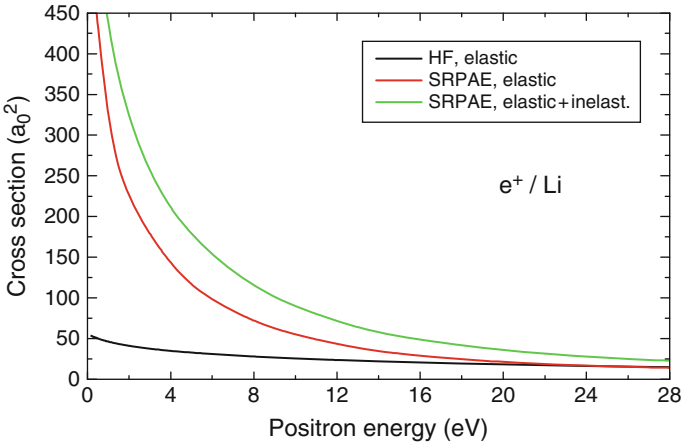

Fig. 4.192_Li_i1 Cross-section of elastic (in HF and SRPAE) and inelastic (in SRPAE) positron scattering for Li (see [4.10])

Figure 4.192_Li_i1 demonstrates the cross-section of elastic (in HF and SRPAE) and inelastic (in SRPAE) positron scattering for Li (see [4.10]). Polarization interaction, in which formation of virtual positronium is taken into account, sharply increases the cross-section (see discussion at the end of Sect. 3.12).

Figure 4.193_Li_j1 shows the contribution of several first partial waves to cross-section of elastic positron scattering on Li in SRPAE.

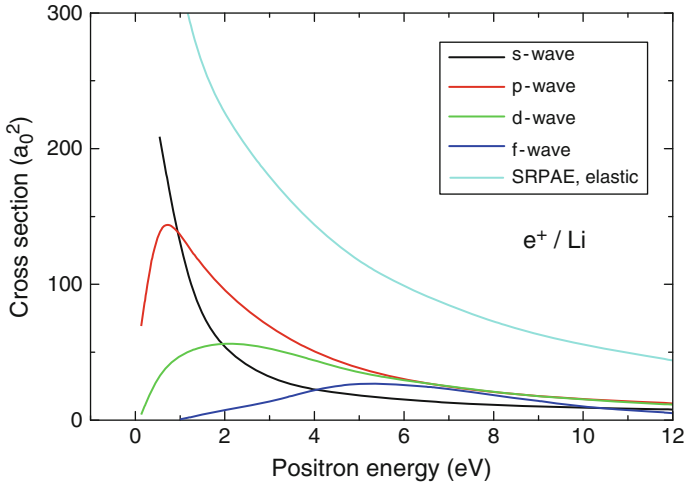

Fig. 4.193_Li_j1 Contribution of partial waves to cross-section of elastic positron scattering on Li in SRPAE

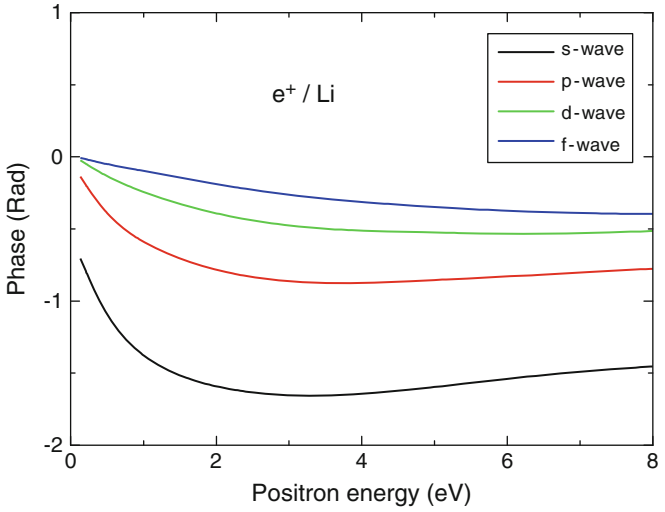

Fig. 4.194_Li_k1 Phases of various partial waves in positron scattering on Li, in SRPAE

Figure 4.194_Li_k1 gives the phases of various partial waves in electron scattering in SRPAE on Li. Note that all phases are negative in the considered region of positron energy.

Figures 4.195–4.202 (Li^+) show the results of calculations for Li^+ ion.

Figure 4.195_Li^+_a1 shows the contribution to the cross-section of elastic electron scattering on Li^+ ion in HF and SRPAE of *s*-, *p*-, *d*-, *f*-waves. Note, however, that for positive and negative ions the total cross-section diverges.

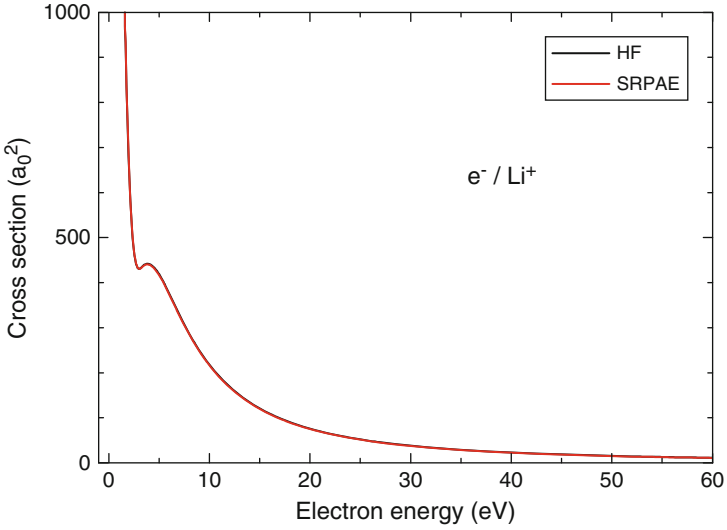

Fig. 4.195_Li$^+$_a1 Contribution from *s*-, *p*-, *d*-, *f*-partial waves to the cross-section of elastic electron scattering on Li^+ ion in HF and SRPAE

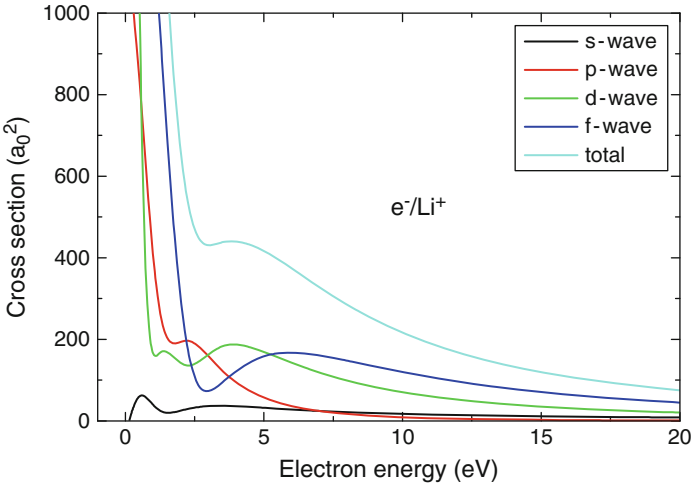

Fig. 4.196_Li$^+$_b1 Partial contributions of *s*-, *p*-, *d*-, *f*-waves of elastic electron scattering on Li^+ ion in SRPAE

Figure 4.196_Li$^+$_b1 collects the contributions to the cross-section of elastic electron scattering on Li^+ ion in SRPAE of *s*-, *p*-, *d*-, *f*-waves and their sum of. In the presented contribution to the cross-section, the second maximum results mainly from *d*-, *f*-waves.

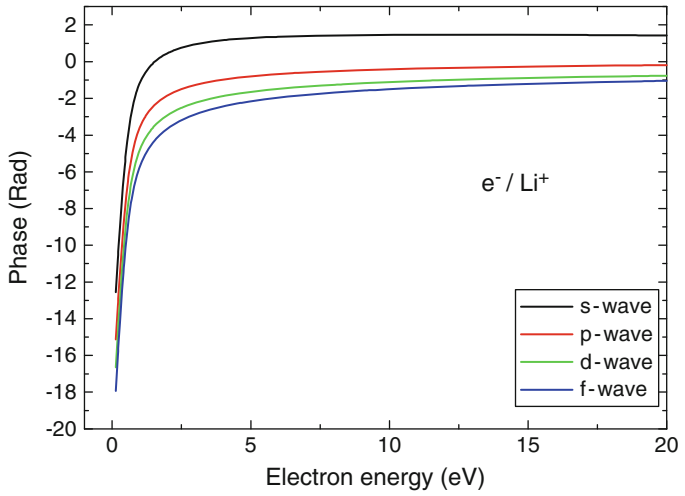

Fig. 4.197_Li$^+$_d1 HF phases of various partial waves in electron scattering on Li$^+$ ion

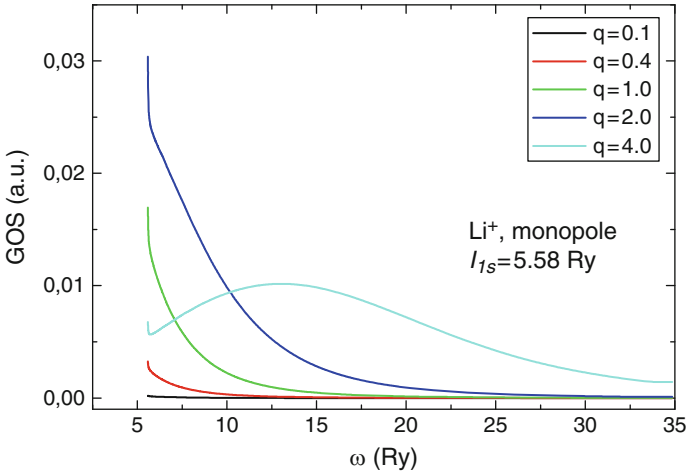

Fig. 4.198_Li$^+$_e1 Density of the monopole generalized oscillator strengths as function of the energy transferred to an ion at various q for Li$^+$ in RPAE

Figure 4.197_Li$^+$_d1 presents the HF phases of various partial waves in electron scattering on Li$^+$. The behavior of all phases as functions of energy is similar. Note that while the s-phase crosses zero and became at $E > 1$ eV positive, other considered phases approach zero from the negative side.

Figure 4.198_Li$^+$_e1 illustrates the density of monopole GOSes for Li$^+$ in RPAE as a function of the energy transferred to the ion at various q. With growth of q the maximum in GOSes moves from threshold to higher energies.

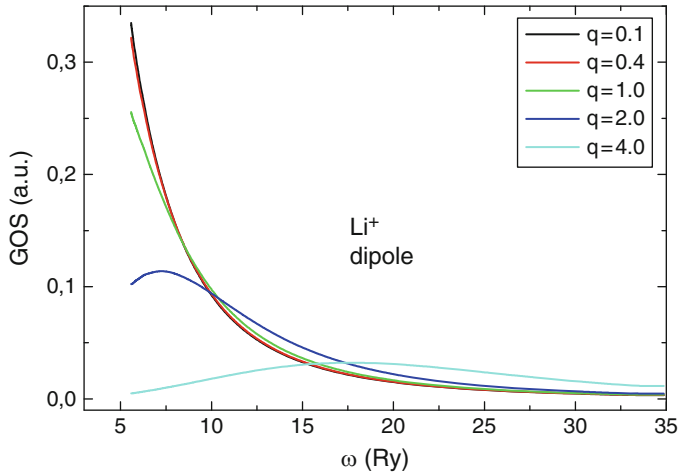

Fig. 4.199 Li^+_e2 Density of dipole generalized oscillator strengths as function of the energy transferred to an ion at various q for Li^+ in RPAE

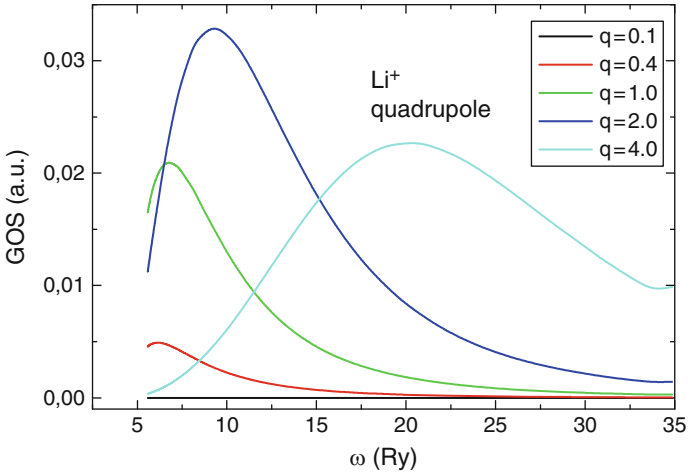

Fig. 4.200 Li^+_e3 Density of quadrupole generalized oscillator strengths as function of the energy transferred to ion at various q for Li^+ ion in RPAE

Figure 4.199 Li^+_e2 depicts the density of dipole GOSes for Li^+ in RPAE as function of the energy transferred to the ion at various q. The contribution of dipole GOSes is approximately one order bigger than the contribution of monopole and quadrupole ones—see Figs. 4.198 Li^+_e1 and 4.200 Li^+_e3.

Figure 4.200 Li^+_e3 shows the density of quadrupole GOSes for Li^+ ion in RPAE as functions of the energy transferred to the ion at various q. With growth of q the maximum is created that then moves to the higher ω side.

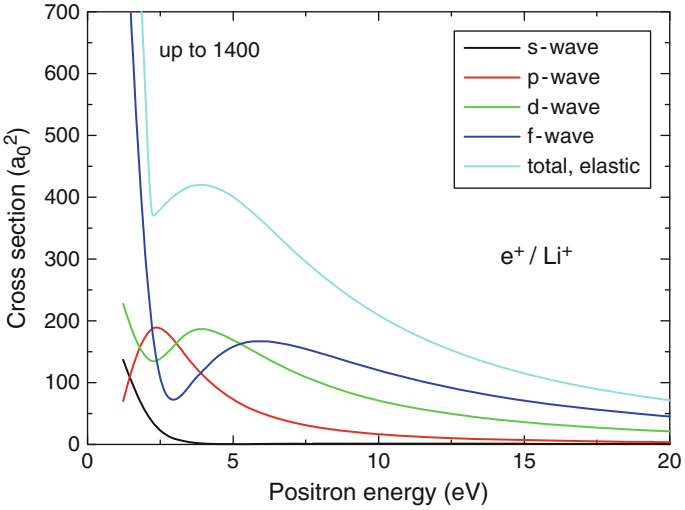

Fig. 4.201_Li$^+$_i1 Total cross-section of elastic positron scattering on Li^+ and the contribution to it of partial s-, p-,d-, f-waves in SRPAE, with account of virtual positronium formation

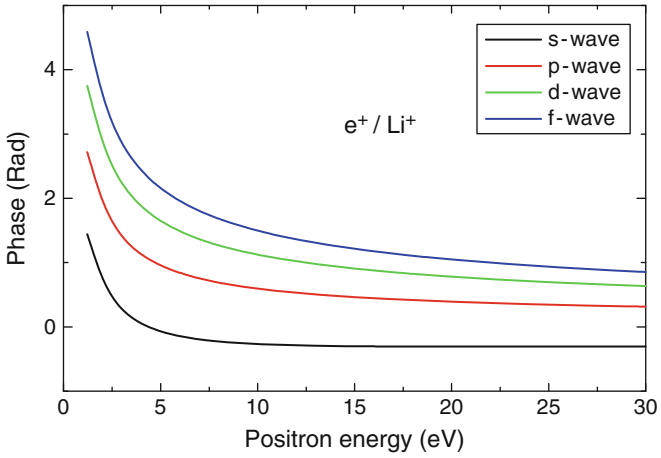

Fig. 4.202_Li$^+$_k1 Phases of various partial waves in positron scattering on Li^+ ion in SRPAE, with account of virtual positronium formation

Figure 4.201_Li$^+$_i1 gives the total cross-section of elastic positron scattering on Li^+ and the contribution to it of partial s-, p-, d-, f-waves in SRPAE, with account of virtual positronium formation. Remarkable is the second maximum that is formed by the contribution of d-, f-waves.

Figure 4.202_Li$^+$_k1 demonstrates the phases of various partial waves in positron scattering on Li^+ in SRPAE, with account of virtual positronium formation.

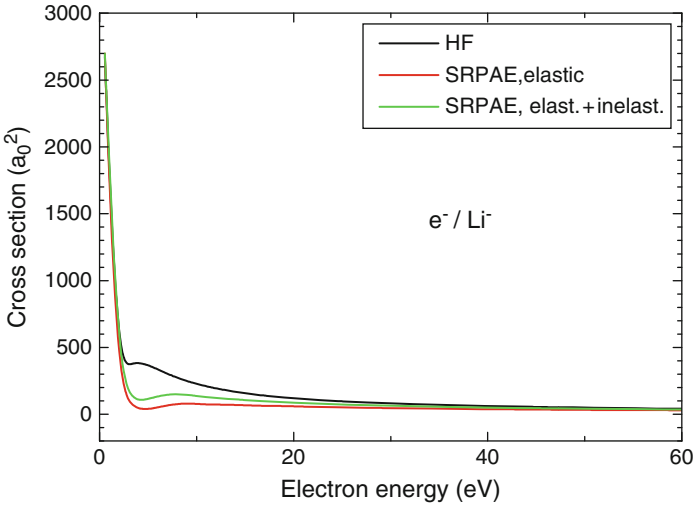

Fig. 4.203_Li$^-$_a1 Cross-section of elastic (in HF and SRPAE) and inelastic (in SRPAE) electron scattering on Li$^-$

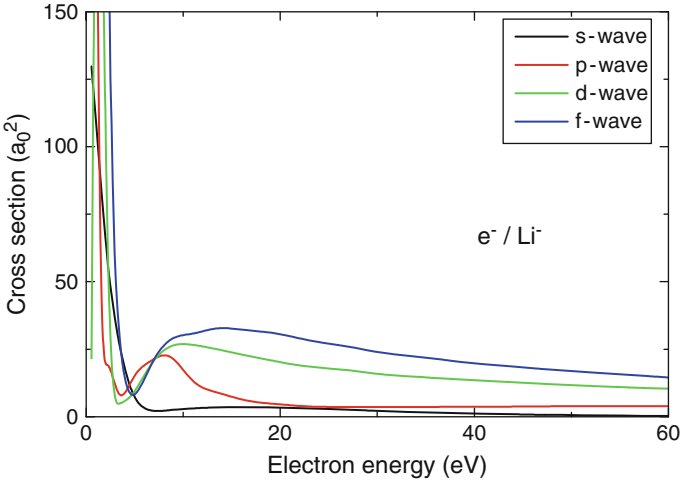

Fig. 4.204_Li$^-$_b1 Contribution of partial waves to the cross-section of elastic electron scattering on Li$^-$

Dependence of all considered phases on positron energy is similar. With growth of the orbital momentum the phases increase. They increase also with decrease of positron energy E.

Figures 4.203–4.210 (Li$^-$) show the results of calculations for Li$^-$ ion.

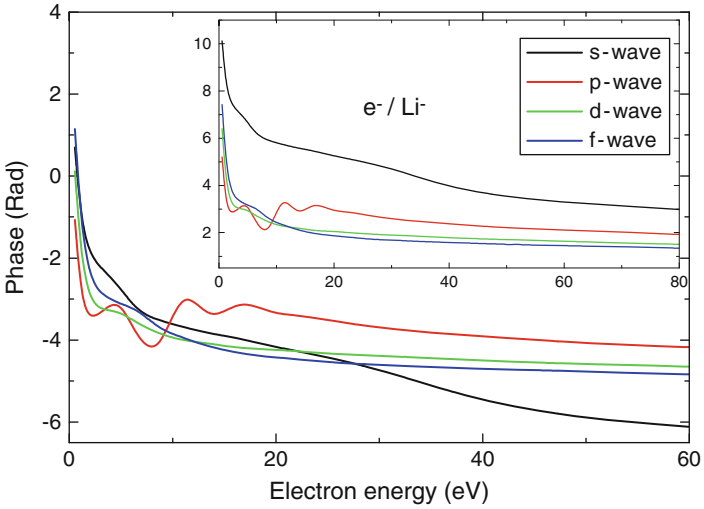

Fig. 4.205_Li$^-$_d1 Phases of various partial waves in electron scattering on Li^- ion

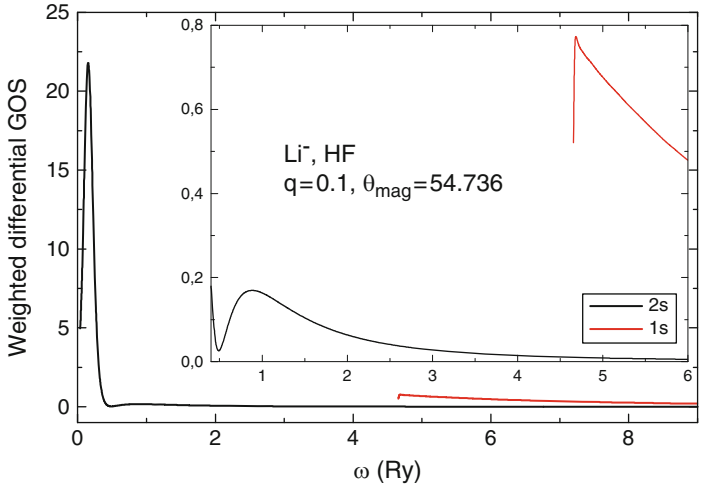

Fig. 4.206_Li$^-$_m1 Weighted differential generalized oscillator strength in HF given by (3.73b) at magic angle $P_2(\cos\theta_m) = 0$ of $2s$ and $1s$ subshells for Li^- at $q = 0.1$

Figure 4.203_Li$^-$_a1 gives the contribution to the cross-section of elastic (in HF and SRPAE) and inelastic (in SRPAE) electron scattering on Li^- from s-, p-, d-, f-scattering waves. It very quickly decreases with growth of electron energy. At 5 eV there is a small minimum. Note that the total cross-section diverges, just as all partial contributions in the limit $E \to 0$.

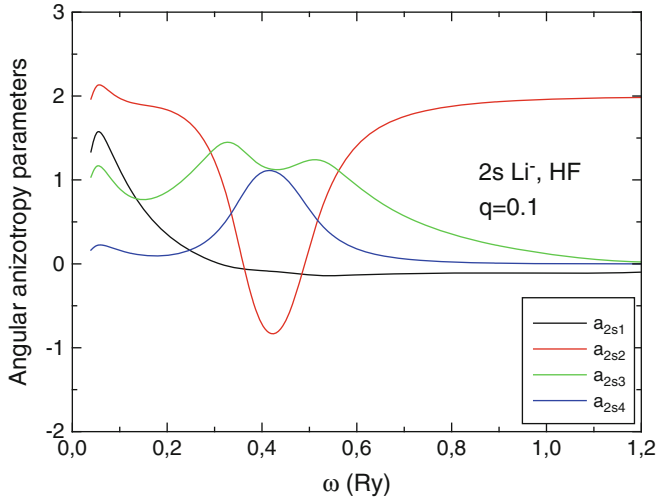

Fig. 4.207_Li⁻_m2 Angular anisotropy parameters of knocked-out electrons in fast projectile–atom collision (a_{2si}) given by (3.75) as functions of ω for $2s$ subshell on Li^- in HF at $q = 0.1$

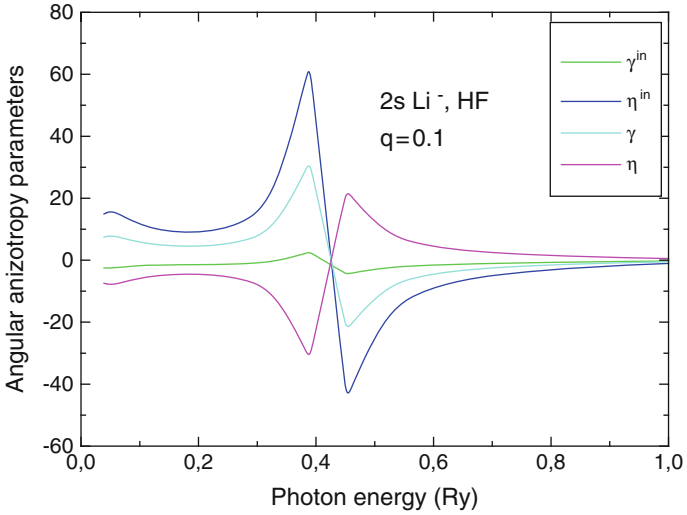

Fig. 4.208_Li⁻_m3 Angular anisotropy nondipole parameters of knocked-out electrons in fast projectile–atom collision in the optical limit compared to similar parameters in photoionization, given by (3.84a) and (3.84b) at $q = 0.1$ and (3.83) for $2s$ subshell on Li^- in HF at $q = 0.1$

Figure 4.204_Li⁻_b1 collects the contribution of partial waves to the cross-section of elastic electron scattering on Li^-. The greatest contributions are from scattering waves with biggest orbital moment.

Figure 4.205_Li⁻_d1 depicts the phases of various partial waves in electron scattering on Li^-. Behavior of s- and p-phases as functions of energy is rather complex.

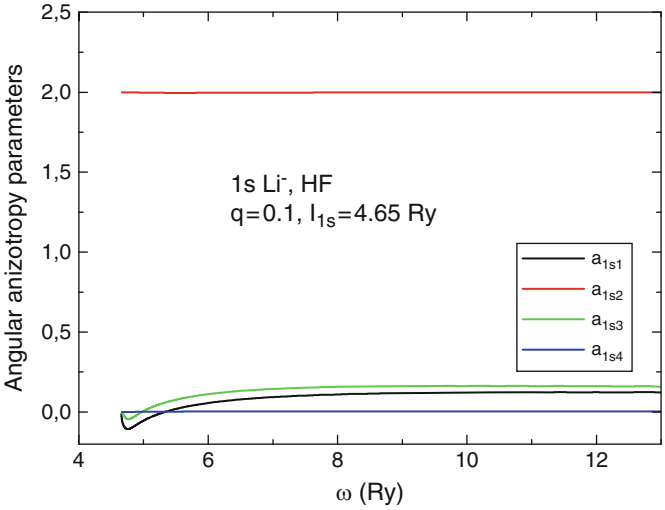

Fig. 4.209_Li$^-$_m4 Angular anisotropy parameters given by of knocked-out electrons in fast projectile–atom collision (a_{1si}) as functions of ω (3.75) for 1s subshell on Li$^-$ in HF at $q = 0.1$

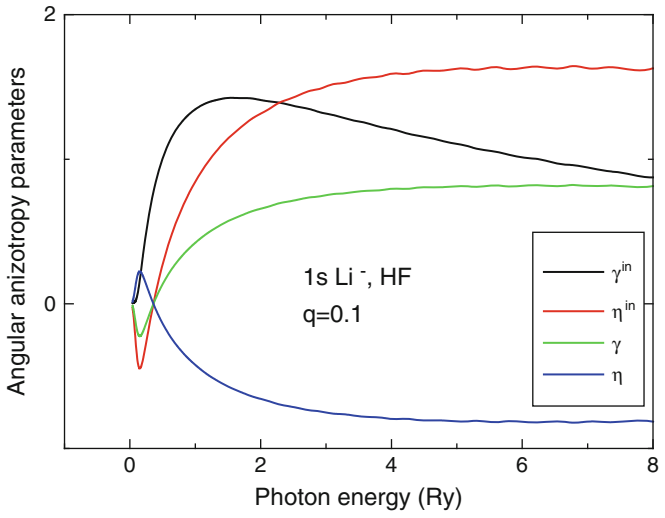

Fig. 4.210_Li$^-$_m5 Angular anisotropy nondipole parameters of knocked-out electrons in fast projectile–atom collision in the optical limit compared to similar parameters in photoionization, given by (3.84a) and (3.84b) at $q = 0.1$ and (3.83) for 1s subshell on Li$^-$ in HF at $q = 0.1$

Figure 4.206_Li$^-$_m1 demonstrates the weighted differential in angle GOSes of knocked-out electron in fast projectile–Li$^-$ ion collision in HF, given by (3.73b) at magic angle $P_2(\cos\theta_m) = 0$ and $q = 0.1$. Results are presented separately for 2s and 1s electrons. Note strong variation with maximums at 0.2 and near 1 Ry.

Figure 4.207_Li$^-$_m2 shows the angular anisotropy parameters of knocked-out electrons in fast projectile–atom collision (a_{2si}), determined by (3.75), as functions of ω for $2s$ subshell on Li^- in HF at $q = 0.1$. Starting from 2 Ry the parameters become energy independent (not shown in figure), with strong variations at $\omega < 1-1.5$ Ry. Note that at $\omega > 2$ Ry dominates the dipole parameter a_{2s2}, while nondipole a_{2s1} and a_{2s3} are, as it should be, by an order of magnitude smaller. As to a_{2s4}, it is only $q^2 \sim 0.01$ of a_{2s2}. Note that the dipole parameter is precisely equal to 2 in so-called optical limit, at $q \to 0$. We see that $q = 0.1$ is obviously close to this limit.

The dipole parameter is precisely equal to 2 in so-called optical limit, at $q \to 0$. We see that $q = 0.1$ is obviously close to this limit.

Figure 4.208_Li$^-$_m3 illustrates the angular anisotropy parameters of knocked-out electrons in fast projectile–atom collision (a_{2si}), given by (3.75), as functions of ω for $2s$ subshell on Li^- in HF at $q = 0.1$ in a much narrower region of ω than shown in Fig. 4.207_Li$^-$_m2. The variations of parameters are seen in details.

Figure 4.209_Li$^-$_m4 gives the angular anisotropy nondipole parameters of knocked-out electrons in fast projectile–atom collision in the optical limit $\gamma_{2s}^{(\mathrm{in})}(\omega)$ and $\eta_{2s}^{(\mathrm{in})}(\omega)$ given by (3.84a) and (3.84b) at $q = 0.1$ compared to similar parameters in photoionization $\gamma_{2s}(\omega)$ and $\eta_{2s}(\omega)$, given by (3.83) on He in HF. The ratio $\eta_{ns}^{(\mathrm{in})}(\omega) = 2\gamma_{ns}(\omega)$ is fulfilled with good accuracy. Note powerful resonance slightly above 0.42 Ry.

Figure 4.210_Li$^-$_m5 shows the angular anisotropy parameters given by of knocked-out electrons in fast projectile–atom collision (a_{nsi}) as functions of ω (3.75) for $1s$ subshell on Li^- in HF at $q = 0.1$. Starting from 6 Ry the parameters become energy independent, with small variations at $\omega < 6$ Ry. Note that at all considered ω the dipole parameter a_{1s2} dominates, while nondipole a_{1s1} and a_{1s3} are, as it should be, by an order of magnitude smaller. As to a_{1s4}, it is only $q^2 \sim 0.01$ of a_{1s2}. Note that the dipole parameter is precisely equal to 2 in so-called optical limit, at $q \to 0$ [see (1.74)]. We see that $q = 0.1$ is obviously close to this limit. For inner shells, the optical limit is achieved already at bigger q than for the inner.

Angular anisotropy nondipole parameters of knocked-out electrons in fast projectile–atom collision in the optical limit compared to similar parameters in photoionization, given by (3.84a) and (3.84b) at $q = 0.1$ and (3.83) on He in HF.

Figures 4.211–4.215 (Na) show the results of calculations for Na atom.

Figure 4.211_Na_a1 gives the elastic (in HF and SRPAE) and inelastic (in SRPAE) electron scattering cross-sections on Na atom. Polarization interaction is defined by the contribution of $2s$-, $3s$-electrons. The cross-section of elastic scattering quickly decreases with growth of incoming electron energy. Almost from the threshold inelastic and elastic cross-sections become comparable.

Figure 4.212_Na_b1 demonstrates the contribution of s-, p-, d-, f-partial waves to the cross-section of elastic electron scattering on Na. It is remarkable how quickly the contribution of s-wave decreases.

Figure 4.213_Na_d1 shows the phases of various partial waves in electron scattering on Na. The SRPAE corrections occur from the polarization interaction created by virtual excitation of $2p$-, $3s$-electrons. As it should be, in conformity

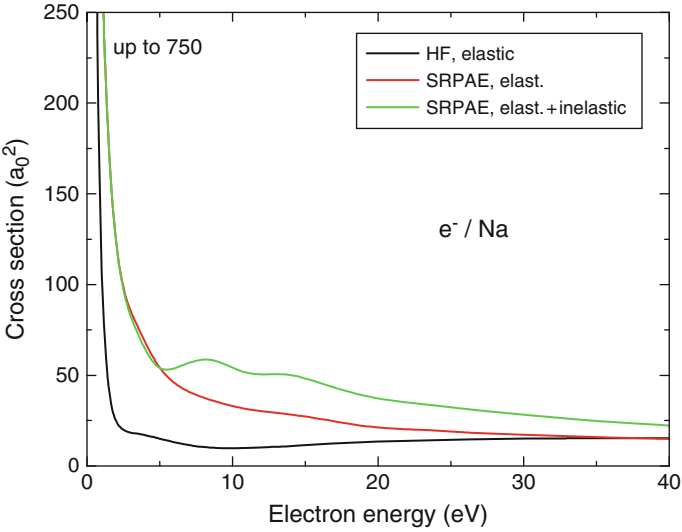

Fig. 4.211_Na_a1 Cross-section of elastic (in HF and SRPAE) and inelastic (in SRPAE) electron scattering on Na atom

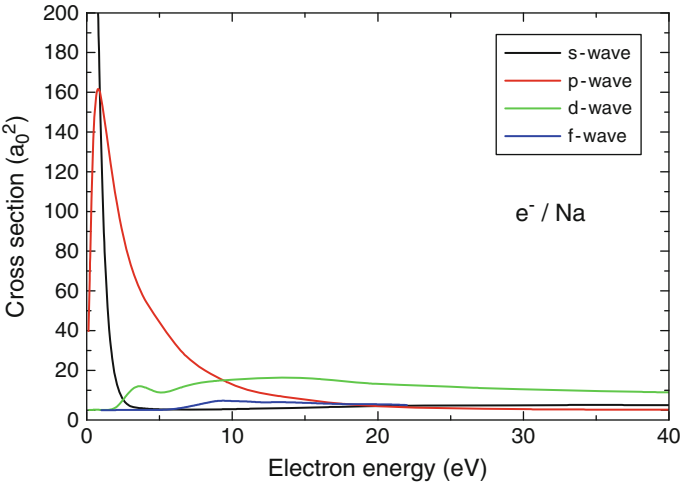

Fig. 4.212_Na_b1 Contribution of partial waves to the cross-section of elastic electron scattering on Na atom

with (3.21), at zero electron energy the s-phase is equal to 3π, p-phase- to π and d-, f-phases are zero if all of them are defined so that any phase $\delta_l \to 0$ at $E \to \infty$.

Figure 4.214_Na_j1 gives the contribution of partial waves to the cross-section of elastic positron scattering on Na. Note that at very small positron energy the

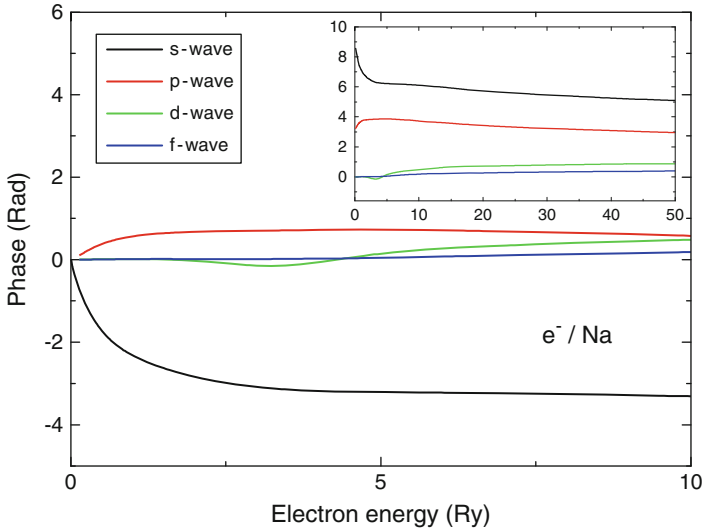

Fig. 4.213_Na_d1 Phases of various partial waves in electron scattering on Na

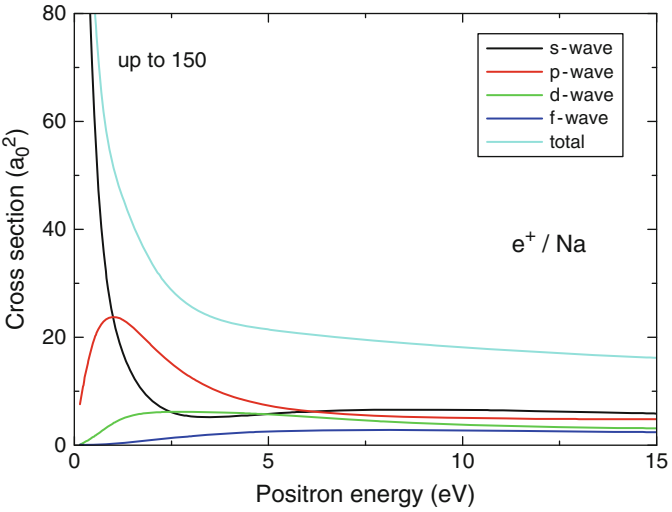

Fig. 4.214_Na_j1 Contribution of partial waves in cross-section of elastic positron scattering on Na in SRPAE

cross-section on Li is greater (see Fig. 4.192_Li_i1 and [4.10]). Note also the prominent maximum in the p-wave.

Figure 4.215_Na_k1 presents the phases of various partial waves in positron scattering on Na in SRPAE. Note nonzero negative value of the s-wave at $E \to 0$

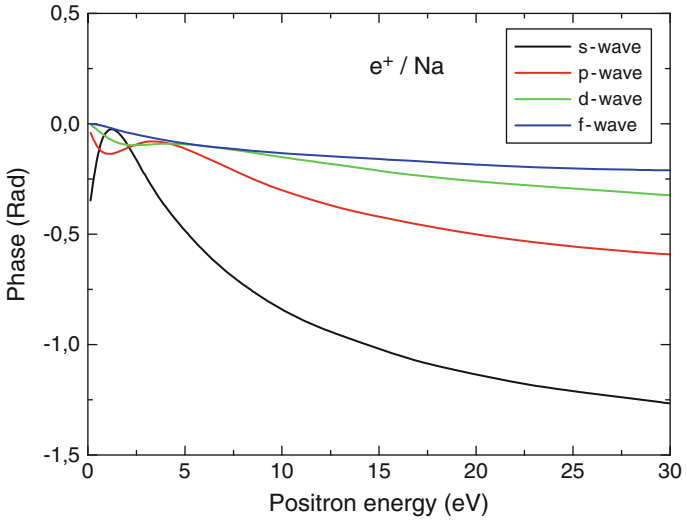

Fig. 4.215_Na_k1 Phases of various partial waves in positron scattering on Na in SRPAE

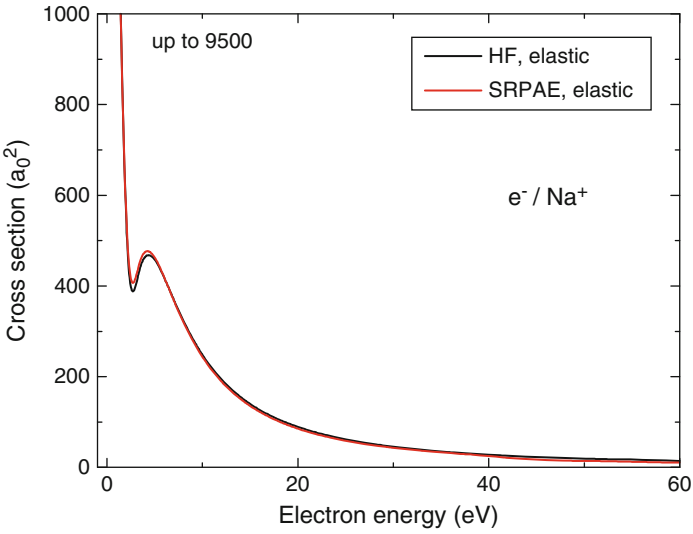

Fig. 4.216_Na^+_a1 Contribution from *s*-, *p*-, *d*-, *f*-partial waves to the cross-section of elastic electron scattering on Na^+ ion in HF and SRPAE

and a prominent maximum near $E = 0$, where the phase is zero. This behavior contradicts to (3.21) and is a consequence of employed by us polarization interaction (3.149).

Figures 4.216–4.220 (Na^+) show the results of calculations for Na^+ ion.

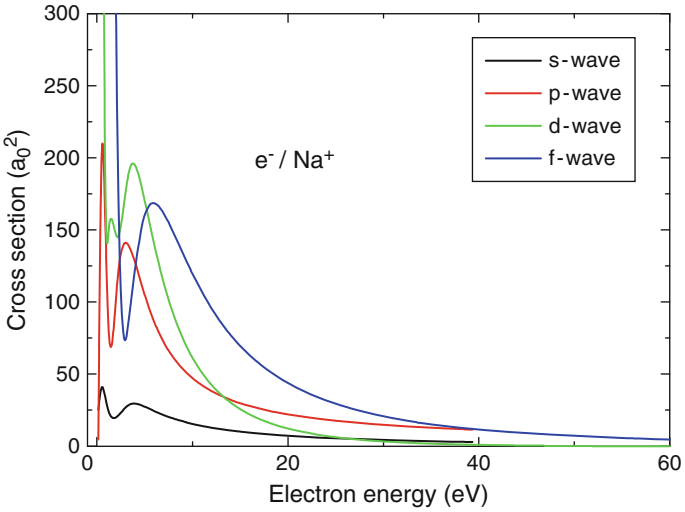

Fig. 4.217_Na$^+$_b1 Contribution of partial waves in cross-section of elastic electron scattering on Na^+ ion

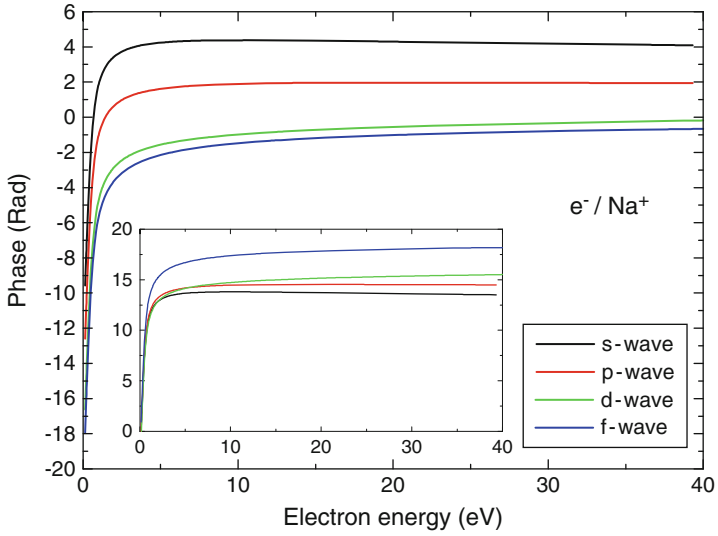

Fig. 4.218_Na$^+$_d1 Phases of various partial waves in electron scattering on Na^+ ion

Figure 4.216_Na$^+$_a1 illustrates the total contribution to the cross-section of elastic electron scattering on Na^+ in HF and SRPAE from *s*-, *p*-, *d*-, *f*-partial waves. There is an obvious similarity to Fig. 4.195_Li$^+$_a1—the cross-section of elastic electron scattering on Li^+.

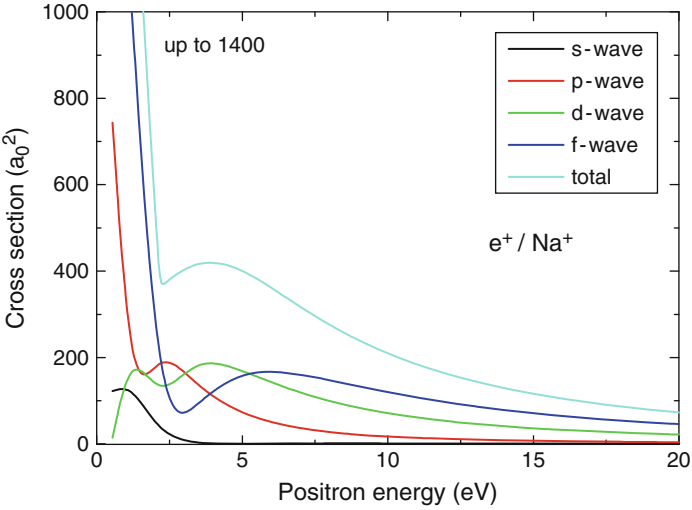

Fig. 4.219_Na$^+$_i1 Contributions from *s*-, *p*-, *d*-, *f*-partial waves to the cross-section of elastic positron scattering on Na^+

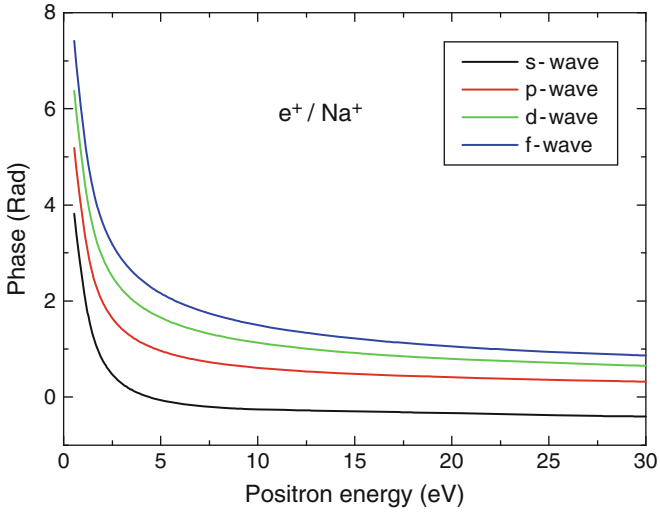

Fig. 4.220_Na$^+$_k1 Phases of various partial waves in positron scattering on Na^+ ion in SRPAE

Figure 4.217_Na$^+$_b1 demonstrates the contributions of *s*-, *p*-, *d*-, *f*-partial waves to the cross-section of elastic electron scattering on Na^+. The additional maximum in *s*-wave and two maxima in contributions of other waves is remarkable. Note growth of the contribution with increase in the angular moment of partial waves. It is essential to note that the total cross-section diverges. Partial contribution of any phase diverges at $E \to 0$.

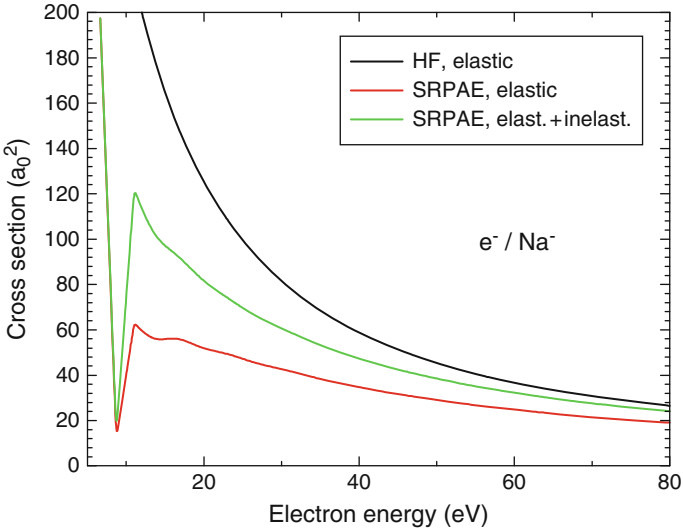

Fig. 4.221_Na$^-$_a1 Total contribution to the cross-section of elastic (in HF and SRPAE) and inelastic (in SRPAE) electron scattering on Na^- ion

Figure 4.218_Na$^+$_d1 gives the phases of various partial waves in electron scattering on Na^+. Growth of a phase is natural for Coulomb field at $E \to 0$.

Figure 4.219_Na$^+$_i1 shows the contributions of s-, p-, d-, f-partial waves to the total cross-section of elastic positron scattering on Na^+. The second maximum formed by the contribution of d-, f-waves is remarkable. Cross-section of Na^+ is rather similar to cross-section of Li^+ (see Fig. 4.201_Li$^+$_i1).

Fig 4.220_Na$^+$_k1 depicts the phases of various partial waves in positron scattering on Na^+. It is remarkable that phases increase with growth of the angular momentum and decrease with energy Egrowth. Note that here SRPAE and HF values almost coincide.

Figures 4.221–4.223 (Na^-)show the results of calculations for Na^- ion.

Figure 4.221_Na$^-$_a1 presents the total contribution to the cross-section of elastic electron scattering in HF and SRPAE and inelastic (in SRPAE) electron scattering on Na^- ion. Note the extremely strong influence of the SRPAE effects and big contribution of the inelastic scattering.

Figure 4.222_Na$^-$_b1 gives the contribution of partial waves to the cross-section of elastic electron scattering on Na^- ion. All curves are qualitatively similar. Most important are the contribution of p- and d-waves.

Figure 4.223_Na$^-$_d1 collects the phases of various partial waves in electron scattering on Na^- ion. For the ion case, there is no simple relation for phases at $E \to 0$, as is seen from the presented results of calculations.

Figures 4.224–4.229 (K) show the results of calculations for K atom.

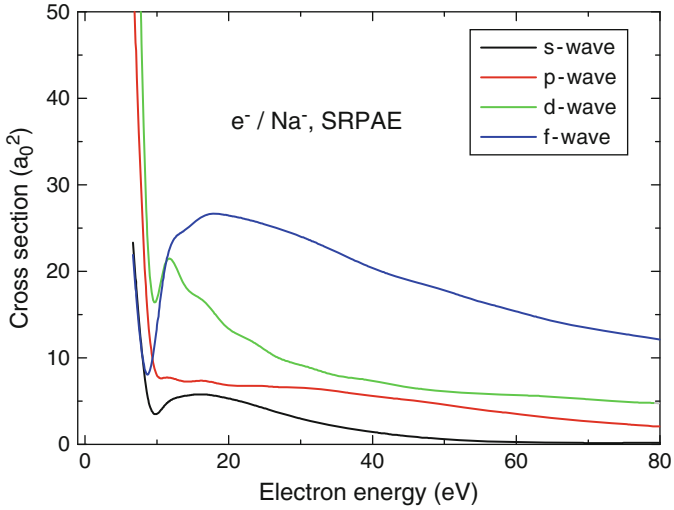

Fig. 4.222_Na$^-$_b1 Contribution of partial waves to the cross-section of elastic electron scattering on Na^- ion

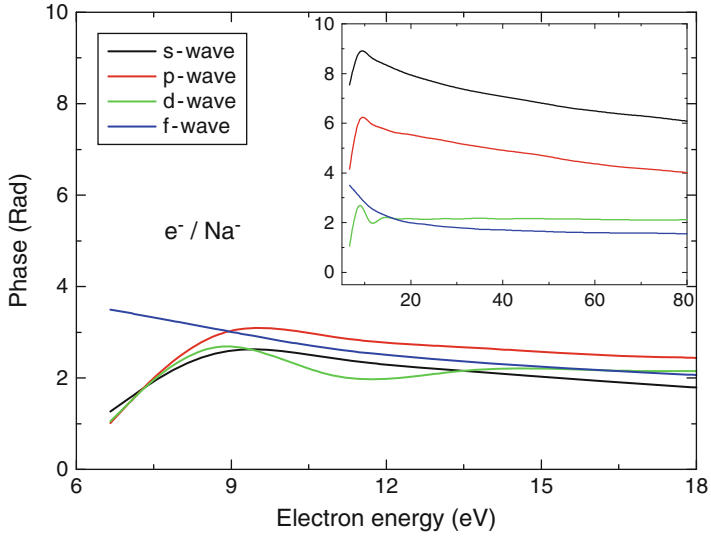

Fig. 4.223_Na$^-$_d1 Phases of various partial waves in electron scattering on Na^- ion

Figure 4.224_K_a1 gives the total cross-section of elastic (in HF and SRPAE) and inelastic (in SRPAE) electron scattering on K. HF maximum of elastic scattering disappears in SRPAE.

Figure 4.225_K_b1 presents the contribution of *s*-, *p*-, *d*-, *f*-partial waves in cross-section of elastic electron scattering on K. Except for extremely small E, the biggest contribution is from the higher orbital moments.

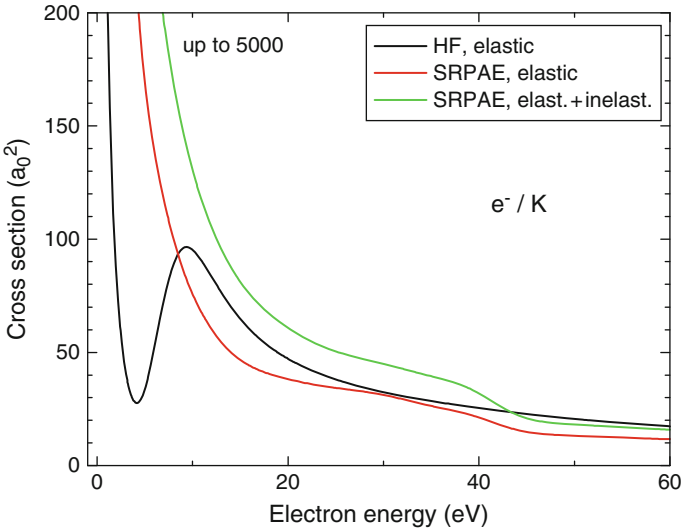

Fig. 4.224_K_a1 Total cross-section of elastic (in HF and SRPAE) and inelastic (in SRPAE) electron scattering on K atom

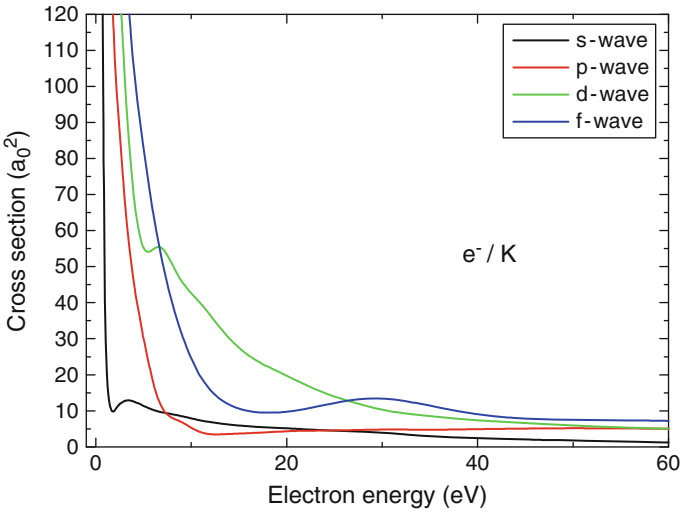

Fig. 4.225_K_b1 Contribution of partial waves in cross-section of elastic electron scattering on K atom

Figure 4.226_K_d1 shows the phases of s-, p-, d-, f-partial waves in electron scattering on K in SRPAE. At zero electron energy s-phase is equal to 4π, p-phase-to 2π and d-, f-phases are zero if all of them are defined so that $\delta_l \to 0$ at $E \to \infty$. Phases essentially vary at small energies.

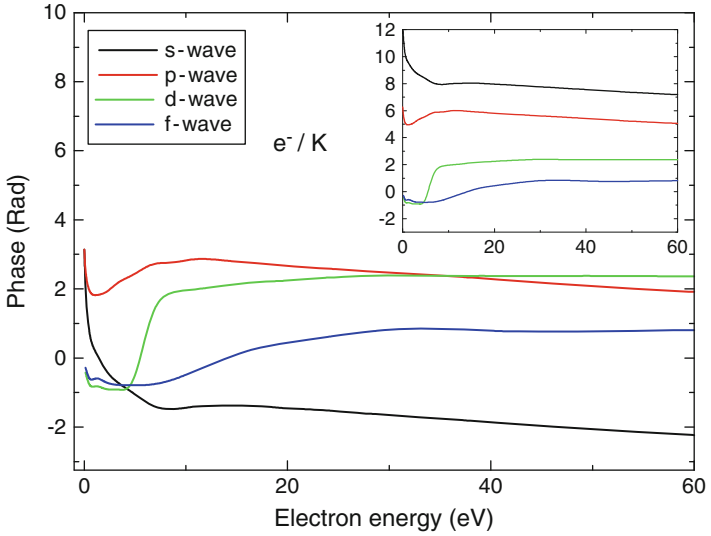

Fig. 4.226_K_d1 Phases of partial waves in electron scattering on K atom in SRPAE

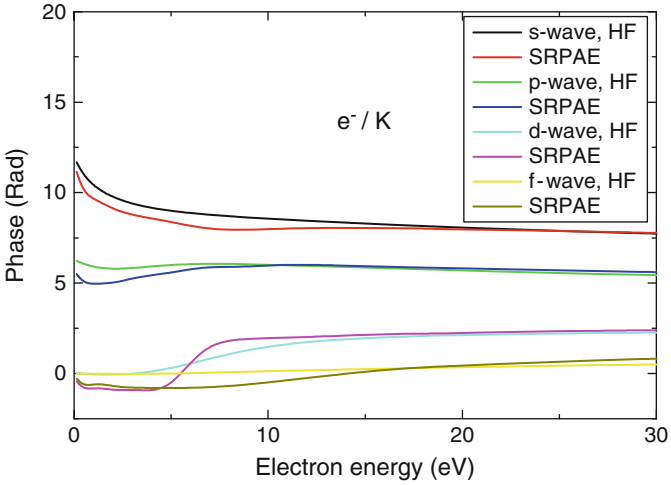

Fig. 4.227_K_d2 Comparison of phases of partial waves in electron scattering on K atom in HF and SRPAE

Figure 4.227_K_d2 demonstrates the comparison of phases of partial waves in electron scattering on K atom in HF and SRPAE. Particularly big is the difference for the d-wave that signals that due to polarization interaction a d-resonance will appear in electron scattering on Ca with subsequent transformation at much higher Z into a $3d$ subshell in Kr.

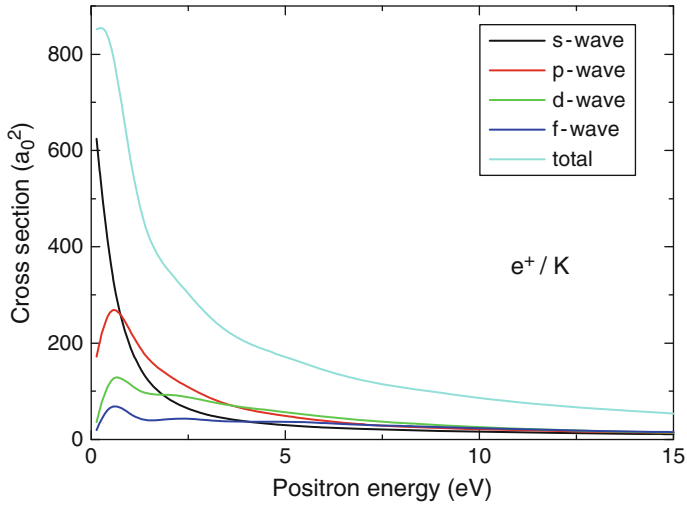

Fig. 4.228_K_i1 Total and partial cross-sections of elastic positron scattering on K atom

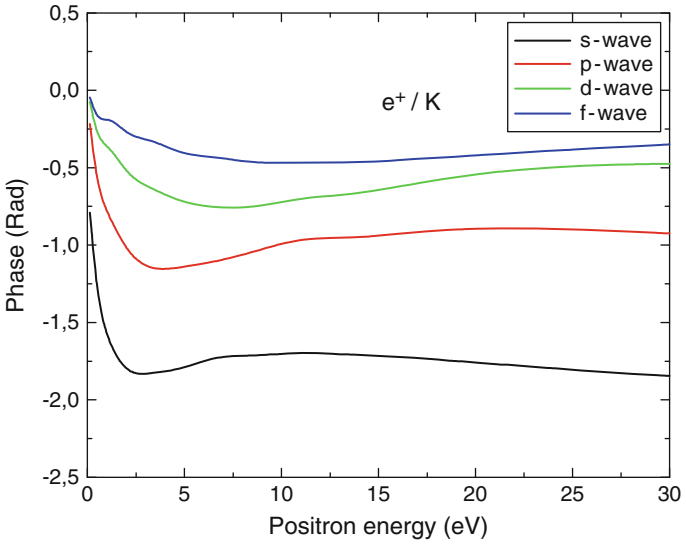

Fig. 4.229_K_k1 Phases of various partial waves in positron scattering on K in SRPAE

Figure 4.228_K_i1 shows the total and partial s-, p-, d-, f-cross-sections of elastic positron scattering on K. The contribution of $3s$, $3p$, $4s$ subshells to polarization interaction is taken into account along with formation of virtual positronium.

Figure 4.229_K_k1 depicts the phases of various partial waves in positron scattering on K in SRPAE. Note nonzero negative value of the s-wave at $E \to 0$

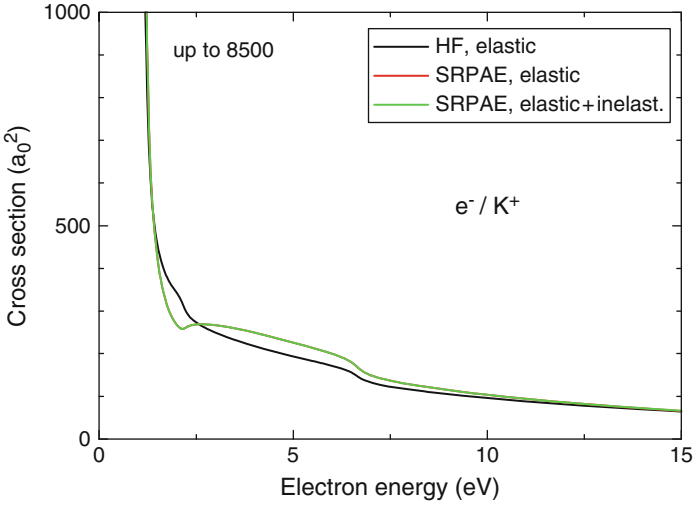

Fig. 4.230_K^+_a1 Partial contribution of s-, p- d-, f-waves to the cross-section of elastic (in HF and SRPAE) and inelastic (in SRPAE) electron scattering on ion K^+ ion

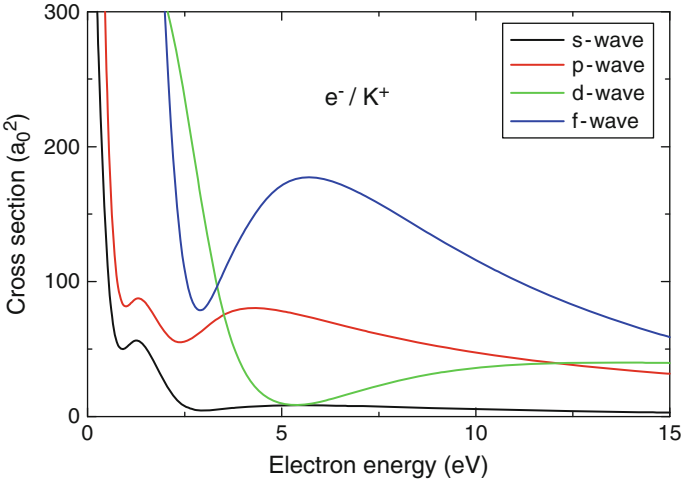

Fig. 4.231_K^+_b1 Contribution of partial waves in cross-section of elastic electron scattering on K^+ ion in SRPAE

and a prominent minimum near $E = 0$. This behavior contradicts to (3.21) and is a consequence of employed by us polarization interaction (3.149).

Figures 4.230–4.238 (K^+) show the results of calculations for K^+ ion.

Figure 4.230_K^+_a1 demonstrates the contribution of s-, p-, d-, f-incoming electron waves to the cross-section of elastic (in HF and SRPAE) and inelastic (in SRPAE) electron scattering on ion K^+. The polarization interaction is formed

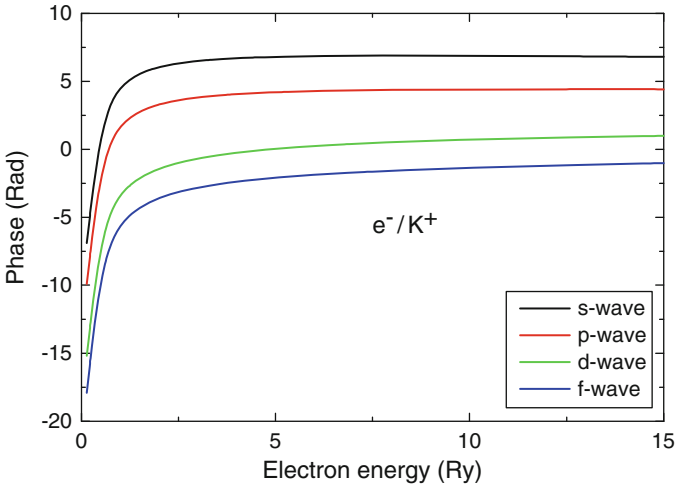

Fig. 4.232_K^+_d1 Phases of partial waves in electron scattering on K^+ ion in SRPAE

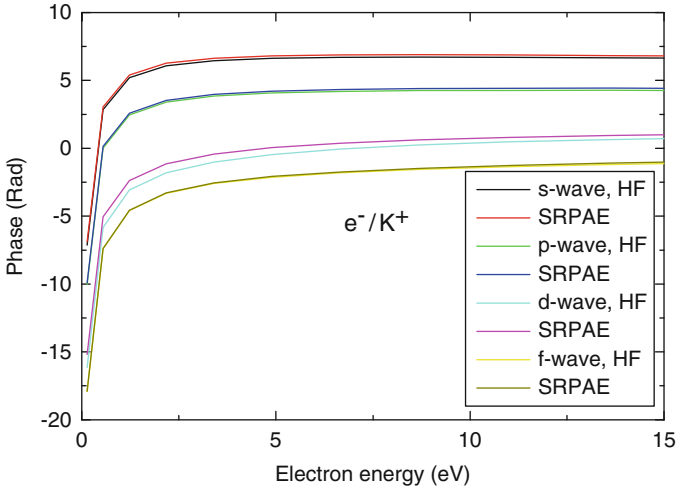

Fig. 4.233_K^+_d2 Phases of partial waves in electron scattering on K^+ ion in HF and SRPAE

from contributions of virtual and real excitations of $3s$, $3p$, $4s$ subshells. HF maximum of elastic scattering disappears in SRPAE. Note that the total cross-section diverges. It is a qualitative similarity to the situation with Na^+, as is seen from Fig. 4.216_Na^+_a1.

Figure 4.231_K^+_b1 represents the contribution of s-, p-, d-, f-partial waves to the cross-section of elastic electron scattering on K^+ in SRPAE. Polarization interaction occurs from $3s$, $3p$ subshells. At small energy E the contribution of f- and d-partial waves dominates. All partial contributions diverge at $E \to 0$.

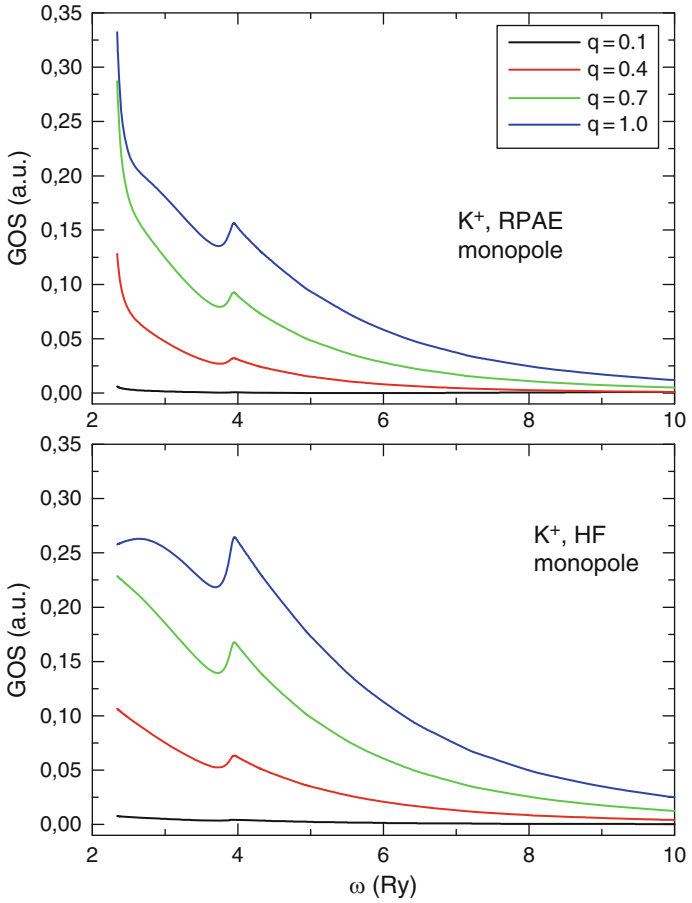

Fig. 4.234_K^+_e1 Density of the monopole generalized oscillator strengths as to function of the energy transferred to ion at various q for K^+ in HF and RPAE

Figure 4.232_K^+_d1 depicts the phases of s-, p-, d-, f-partial waves in electron scattering on K^+. Polarization interaction occurs from $3s$, $3p$ subshells.

Figure 4.233_K^+_d2 gives the phases of partial waves in electron scattering on K^+ ion in HF and SRPAE. The role of polarization interaction is not essential.

Figure 4.234_K^+_e1 contains the densities of the monopole GOSes for K^+ in HF and RPAE as function of the energy transferred to the ion at various q. GOSes grow with increase of q.

Figure 4.235_K^+_e2 presents the density of dipole GOSes for K^+ in HF and RPAE as function of the energy transferred to the ion at various q. At $\omega \leq 3\,\mathrm{Ry}$ dipole GOSes are bigger than monopole and quadrupole GOSes by more than an order (compare with Figs. 4.234_K^+_e1 and 4.236_K^+_e3).

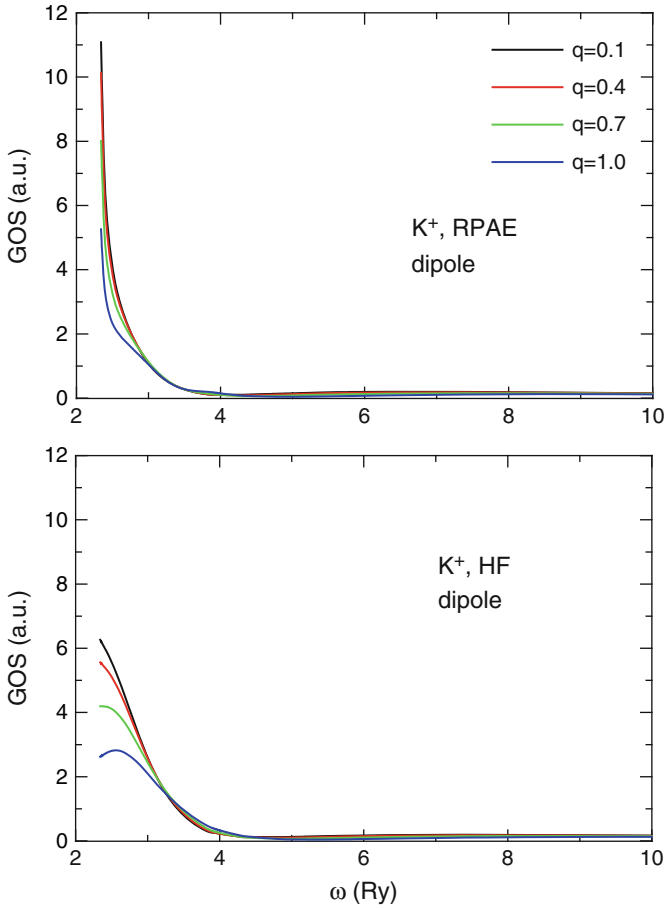

Fig. 4.235_K$^+$_e2 Density of dipole generalized oscillator strengths as to function of the energy transferred to ion at various q for K^+ ion in HF and RPAE

Figure 4.236_K$^+$_e3 depicts the density of quadrupole GOSes for K^+ in HF and RPAE as function of the energy transferred to the ion at various q. GOSes increases with growth of q.

Figure 4.237_K$^+$_i1 presents the contributions of partial s-, p-, d-, f-waves and total cross-section of elastic positron scattering on K^+. The second maximum formed by the contribution of d-, f-waves is remarkable. Cross-section of K^+ is very similar to the respective cross-section of Li^+ and Na^+ (see Figs. 4.201_Li$^+$_i1 and 4.219_Na$^+$_i1).

Figure 4.238_K$^+$_k1 shows the phases of partial waves in positron scattering on K^+ ion in SRPAE. Note rapid growth of the phases with energy decrease.

Figures 4.239–4.241 (Cs) show the results of calculations for Cs atom.

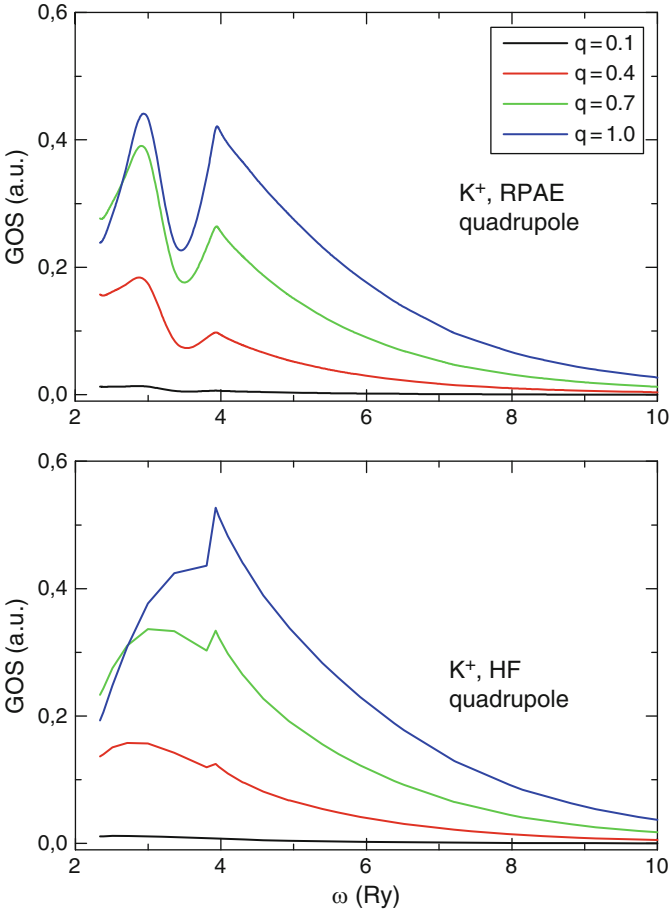

Fig. 4.236_K^+_e3 Density of quadrupole generalized oscillator strengths as to function of the energy transferred to ion at various q for K^+ ion in HF and RPAE

Figure 4.239_Cs_e1 depicts the density of monopole GOSes of $3d_{5/2}$ and $3d_{3/2}$ electrons for Cs in HF and SP RPAE as functions of the energy transferred to the atom at various q (see [4.30]). Calculations are carried out according to the description right at the end of Sects. 1.10 and 3.6. Strong influence of electrons of 3/2- on 5/2-level is visible at small q.

Figure 4.240_Cs_e2 represents the density of dipole GOSes of $3d_{5/2}$ and $3d_{3/2}$ electrons for Cs in HF and SP RPAE as functions of the energy transferred to the atom at various q (see [4.30]). As shown in Fig. 4.239_Cs_e1, results are obtained according to the procedure described in Sects. 1.10 and 3.6. The influence of 3/2-electrons leads to an additional maximum in SP RPAE GOSes of 5/2-electrons at ≈ 55 eV and at all considered q.

Figure 4.241_Cs_e3 gives the density of quadrupole GOSes of $3d_{5/2}$ and $3d_{3/2}$ electrons for Cs in HF and SP RPAE as functions of the energy transferred to the

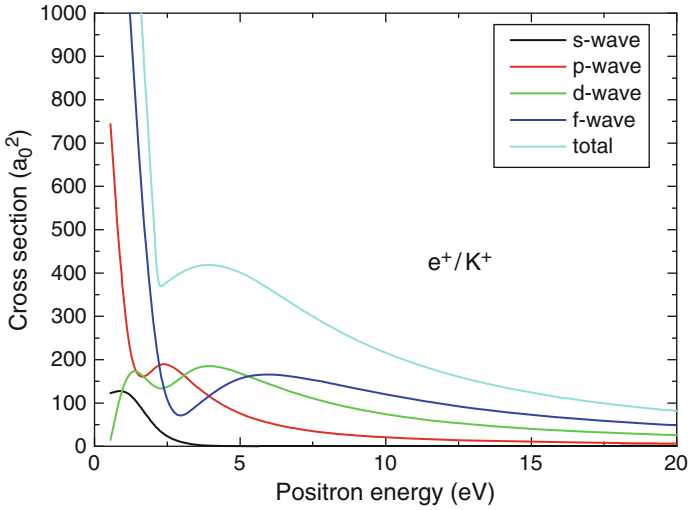

Fig. 4.237_K$^+$_i1 Total cross-section and contributions of partial waves for elastic electron scattering on K^+ ion

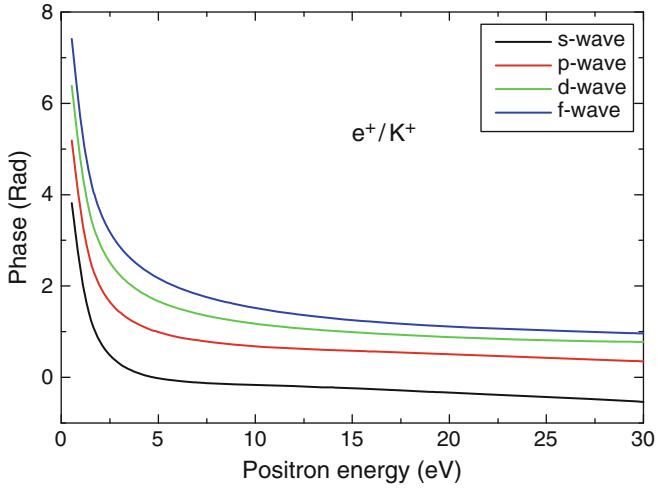

Fig. 4.238_K$^+$_k1 Phases of partial waves in positron scattering on K^+ ion in SRPAE

atom at various q (see [4.30]). The role of interaction between 5/2- and 3/2-levels is small and manifested only by a small additional maximum at ≈ 54.2 eV in GOSes of 5/2-level.

Table 4.2 presents quadrupole and monopole GOSes for Li atom and Li^+ ion at $q = 0.00001$. Because of small values GOSes, the error in calculations is great.

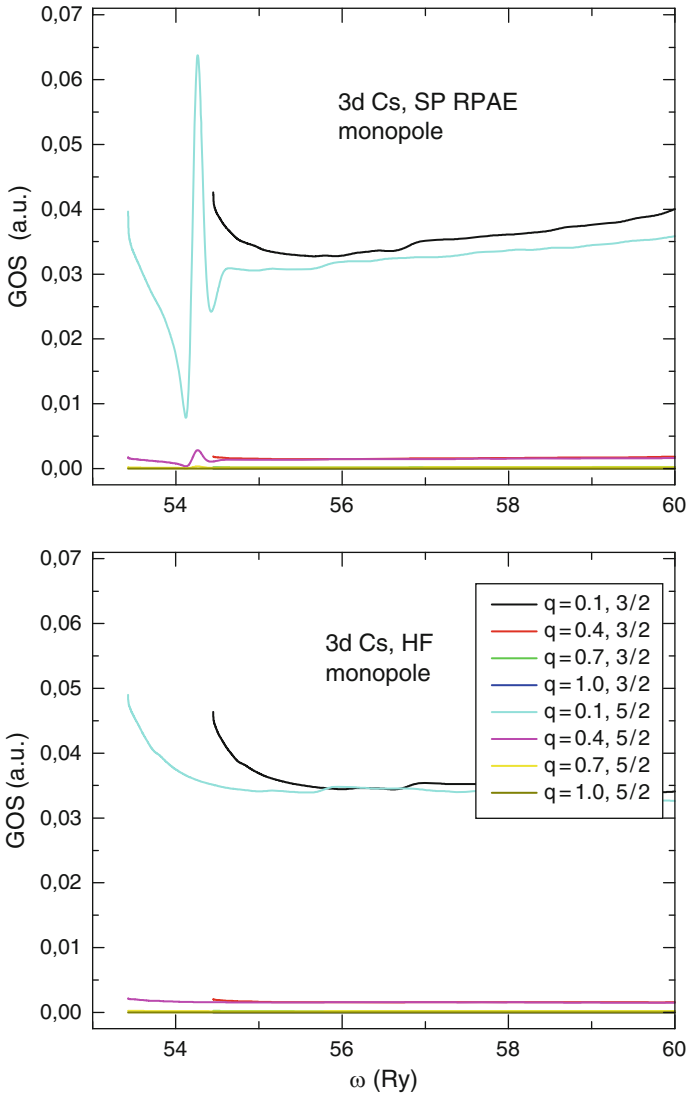

Fig. 4.239_Cs_e1 Density of monopole generalized oscillator strengths of $3d_{5/2}$ and $3d_{3/2}$ electrons as function of the energy transferred to atom at various q for Cs in HF and SP RPAE (see [4.30])

4.4 Atoms of Group II Elements of the Periodic Table

In this section, results are presented of our already known and new calculations of total and partial cross-sections of elastic electron scattering on atoms of II group elements of the Periodic Table in HF and with account of polarization interaction in the simplified random phase approximation with exchange SRPAE (see Sects. 3.3

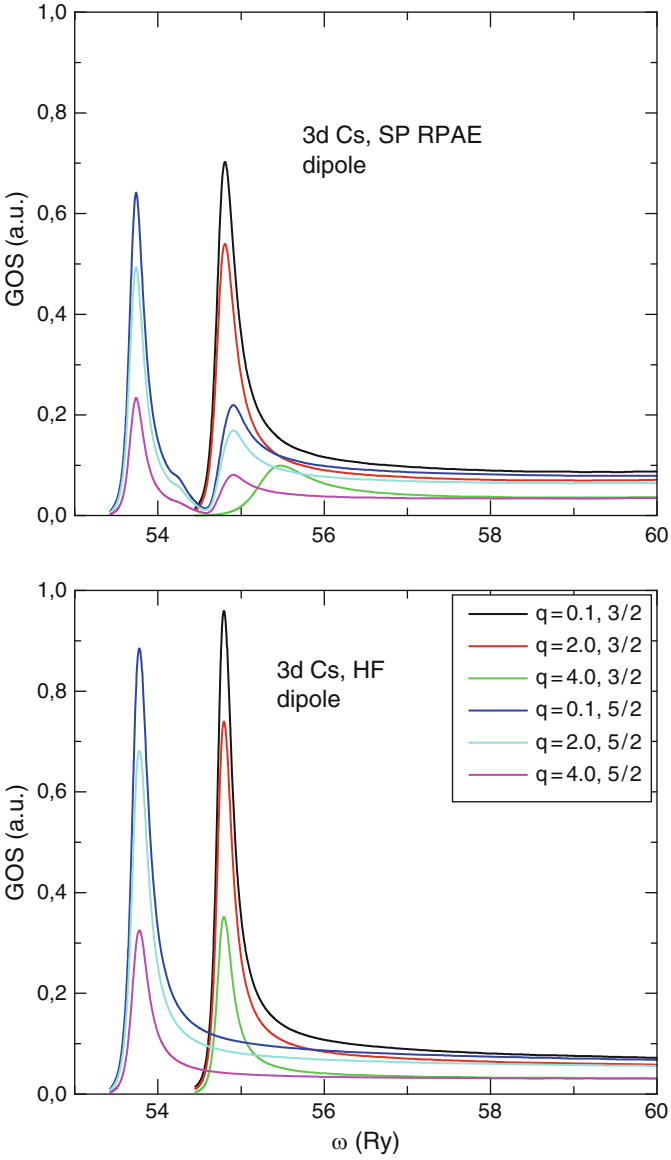

Fig. 4.240_Cs_e2 Density of dipole generalized oscillator strengths of $3d_{5/2}$ and $3d_{3/2}$ electrons as function of the energy transferred to atom at various q for Cs in HF and SP RPAE (see [4.30])

and 3.4 and [AICC]). In formation of polarization interaction, the excitation of following electrons are taken into account: $1s^2$ in Be, $2s^2, 2p^6, 3s^2$ in Mg, $3s^2, 3p^6, 4s^2$ in Ca, $3p^6, 3d^{10}, 4s^2$ in Zn, $4p^6, 4d^{10}, 5s^2$ in Cd, and $4d^{10}, 5s^2, 5p^6, 5s^2$ in Ba. In the same approximation, scattering phases and partial s-, p-, d-, f-contributions

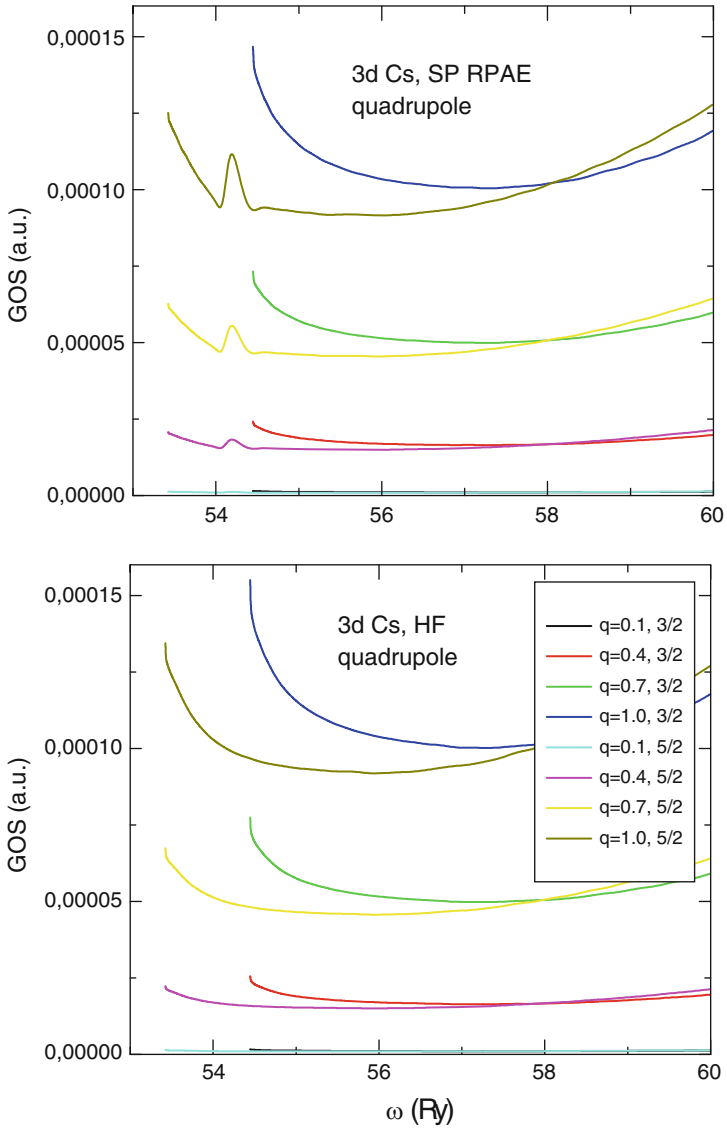

Fig. 4.241_Cs_e3 Density of quadrupole generalized oscillator strengths of $3d_{5/2}$ and $3d_{3/2}$ electrons as function of the energy transferred to atom at various q for Cs in HF and SP RPAE (see [4.30])

to cross-section are calculated. The generalized oscillator strengths (GOSes) with account of RPAE correlations of mentioned above electrons are also presented. Cross-sections of positron scattering upon Be and Mg are also given. GOSes for $3d_{5/2}$, $3d_{3/2}$ electrons for Ba are demonstrated also.

Table 4.2 Quadrupole and monopole generalized oscillator strengths of some discrete excitations of Li and Li^+

Transition	Energy (Ry)	HF-l	HF-v	RPAE-l	RPAE-v
Li, $L = 2$					
$2s$–$3d$ ↑	0.27156	0.1376E–09	0.1509E–09	0.1259E–09	0.1770E–09
$2s$–$4d$ ↑	0.32653	0.1942E–10	0.2228E–10	0.1498E–10	0.2463E–10
$2s$–$5d$ ↑	0.35069	0.6448E–11	0.7598E–11	0.4512E–11	0.8073E–11
$1s$–$3d$ ↓	4.82033	0.2150E–13	0.2042E–13	0.2097E–13	0.2024E–13
$1s$–$4d$ ↓	4.87189	0.1186E–13	0.1127E–13	0.1166E–13	0.1126E–13
$1s$–$5d$ ↓	4.89553	0.6733E–14	0.6395E–14	0.6560E–14	0.6332E–14
$1s$–$3d$ ↑	4.84377	0.4021E–13	0.3944E–13	0.3855E–13	0.3932E–13
$1s$–$4d$ ↑	4.90363	0.1664E–13	0.1628E–13	0.1600E–13	0.1626E–13
$1s$–$5d$ ↑	4.92964	0.8587E–14	0.8398E–14	0.8219E–14	0.8338E–14
Li^+, $L = 0$					
$1s$–$2s$	4.48977	0.3708E–02	0.3482E–11	0.3532E–02	0.4482E–11
$1s$–$3s$	5.11296	0.3932E–05	0.6877E–12	0.1693E–04	0.8365E–12
$1s$–$4s$	5.32340	0.1678E–05	0.2529E–12	0.5528E–05	0.2929E–12
Li^+, $L = 2$					
$1s$–$3d$	5.14053	0.7334E–14	0.7101E–14	0.7290E–14	0.7196E–14
$1s$–$4d$	5.33486	0.3592E–14	0.3476E–14	0.3569E–14	0.3524E–14
$1s$–$5d$	5.42480	0.1924E–14	0.1861E–14	0.1911E–14	0.1888E–14

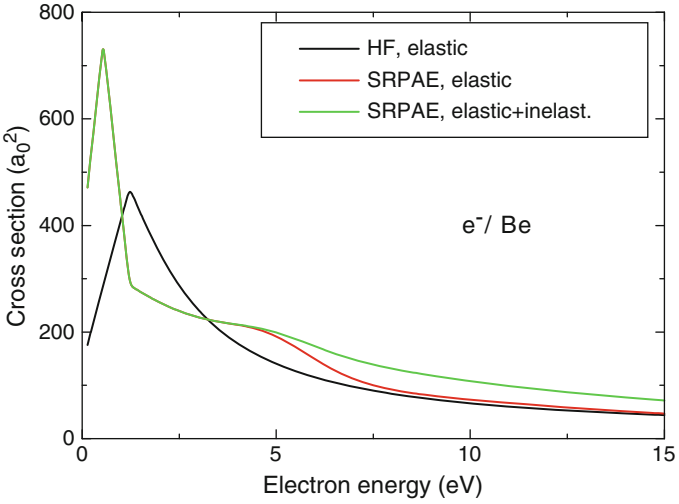

Fig. 4.242_Be_a1 Cross-section of elastic (in HF and SRPAE) and inelastic (in SRPAE) electron scattering on Be atom

Figures 4.242–4.254 (Be) show the results of calculations for Be atom.

Figure 4.242_Be_a1 gives the cross-section of elastic (in HF and SRPAE) and inelastic (in SRPAE) electron scattering on Be. The contributions of s-, p-, d-, f-waves are included. The polarization potential is taken into account by the solution

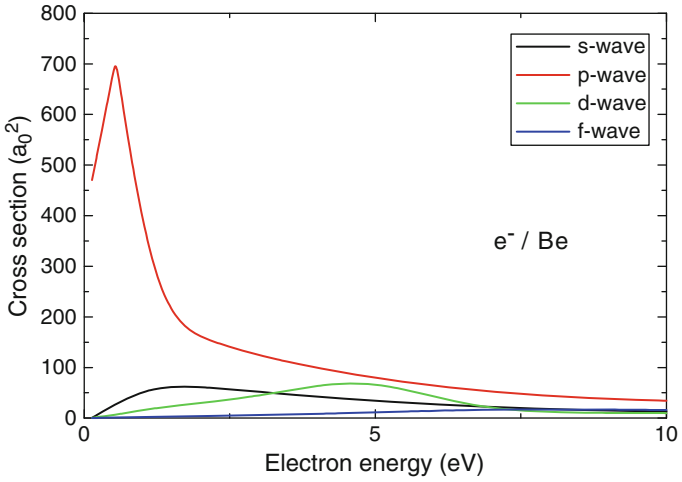

Fig. 4.243_Be_b1 Contributions of partial waves to cross-section of elastic electron scattering on Be atom

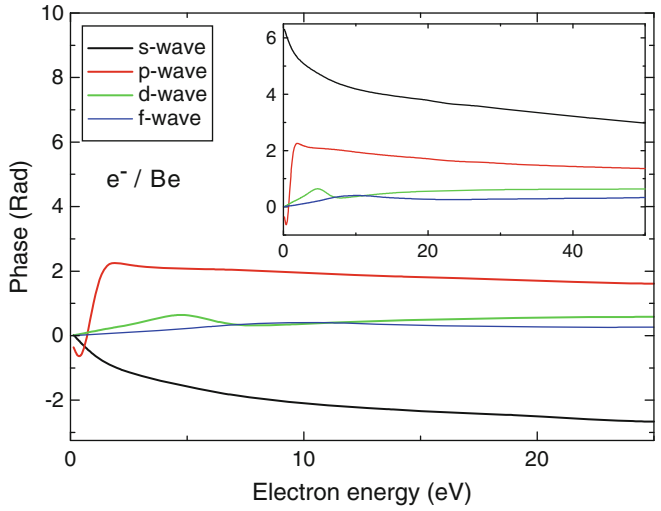

Fig. 4.244_Be_d1 Phases of various partial waves in electron scattering on Be atom in SRPAE

of Dayson equation from Sect. 3.4, whereas polarization interaction is determined approximately, in SRPAE. The cross-section has powerful maximum at 0.5 eV and prominent excess at energy $\approx$ 1 eV.

Figure 4.243_Be_b1 depicts the contributions of partial *s*-, *p*-, *d*-, *f*-waves to cross-section of elastic electron scattering on Be. It is visible that the main maximum at 0.5 eV is formed by the contribution of *p*-wave, while the contribution of

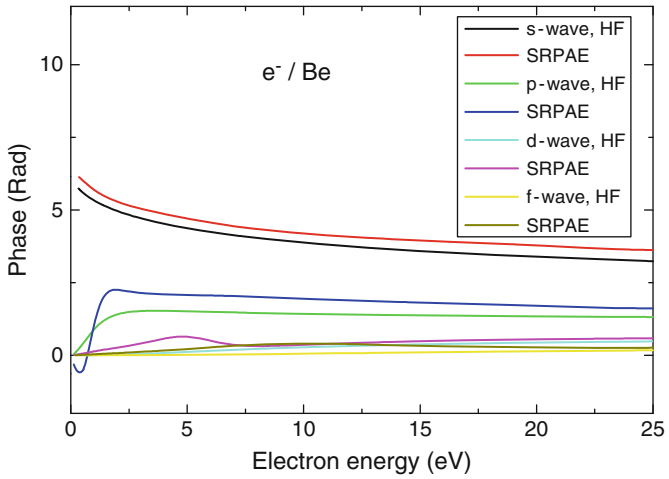

Fig. 4.245_Be_d2 Phases of various partial waves in electron scattering on Be atom in HF and SRPAE

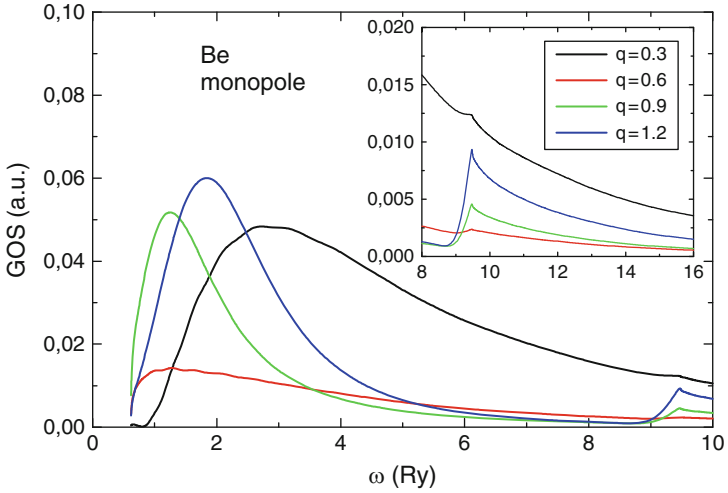

Fig. 4.246_Be_e1 Density of monopole generalized oscillator strengths as function of the energy transferred to atom at various q for Be in RPAE

d-wave has a maximum at 5 eV which is seen in the total cross-section also (Fig. 4.242_Be_a1).

Figure 4.244_Be_d1 shows the phases of various partial waves in electron scattering on Be, calculated as a result of the Dayson equations solution. On insert s-phase at $E = 0$ is equal to 2π, whereas other phases are equal to 0—in agreement with (3.21). In the basic figure, s-phase is shifted for compactness of curves by 2π.

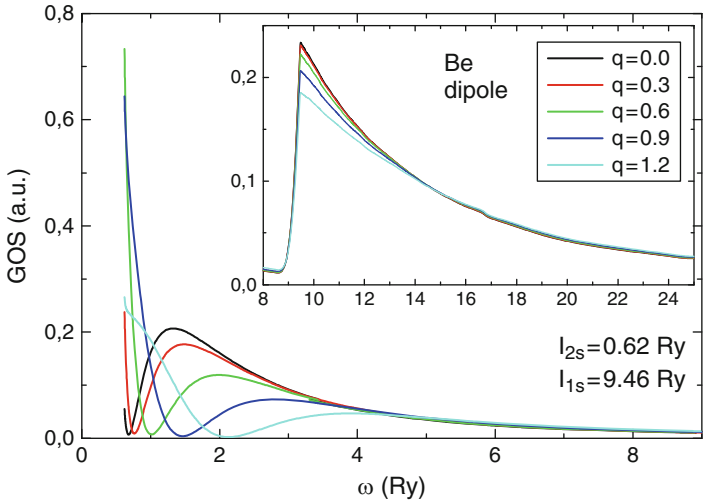

Fig. 4.247_Be_e2 Density of dipole generalized oscillator strengths as functions of the energy transferred to atom at various q for Be in RPAE (see [4.32])

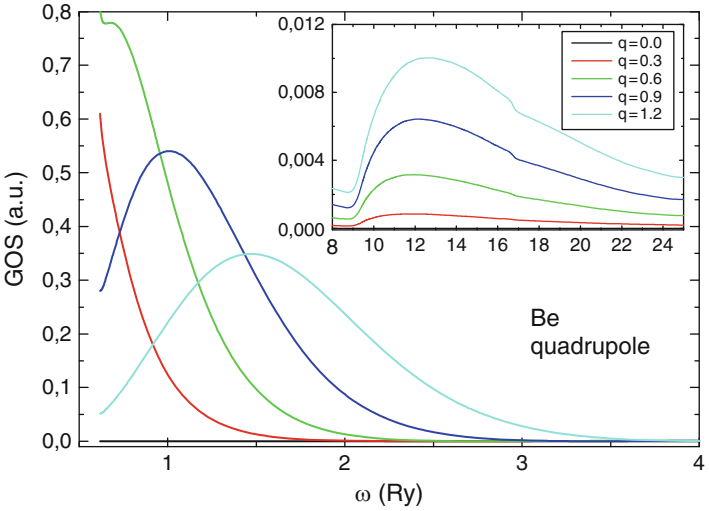

Fig. 4.248_Be_e3 Density of quadrupole generalized oscillator strengths as functions of the energy transferred to atom at various q for Be in RPAE

Figure 4.245_Be_d2 presents the phases of various partial waves in electron scattering on Be atom in HF and SRPAE. Particularly interesting is the SRPAE contribution to the d-wave.

Figure 4.246_Be_e1 demonstrates the density of monopole GOSes for Be in RPAE as function of the energy transferred to the atom at various q. With growth

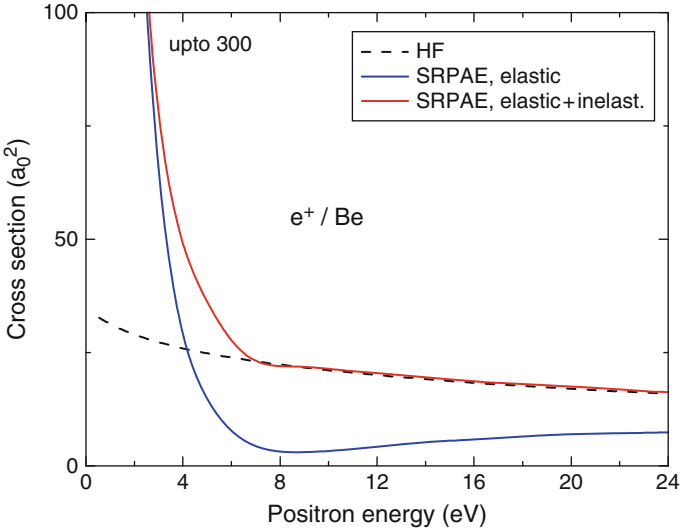

Fig. 4.249_Be_i1 Cross-section of elastic positron scattering on Be (see [4.10])

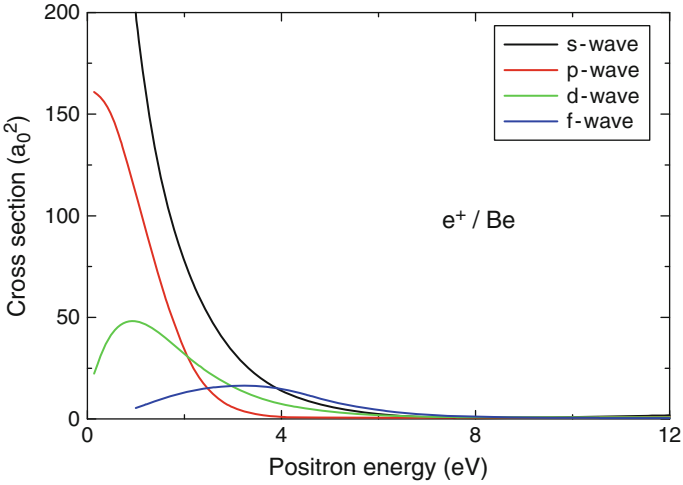

Fig. 4.250_Be_j1 Contributions of various partial waves in cross-section for Be atom

of q the maximum of GOSes moves, decreasing, to lower energy and then, starting from $q \approx 0.6$, a second, threshold maximum becomes prominent.

Figure 4.247_Be_e2 gives the density of dipole GOSes for Be in RPAE as functions of the energy transferred to the atom at various q (see [4.32]). With growth of q GOSes maximum moves to higher energies, becoming lower and broader. The threshold value at the same time increases.

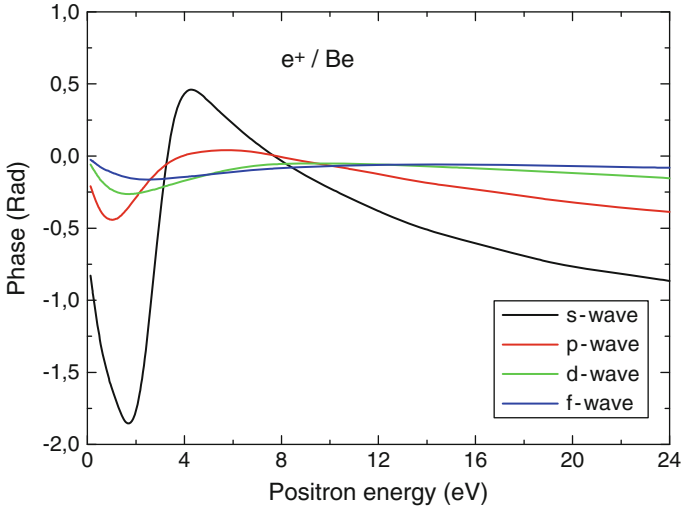

Fig. 4.251_Be_k1 Phases of various partial waves in positron scattering for Be atom in SRPAE

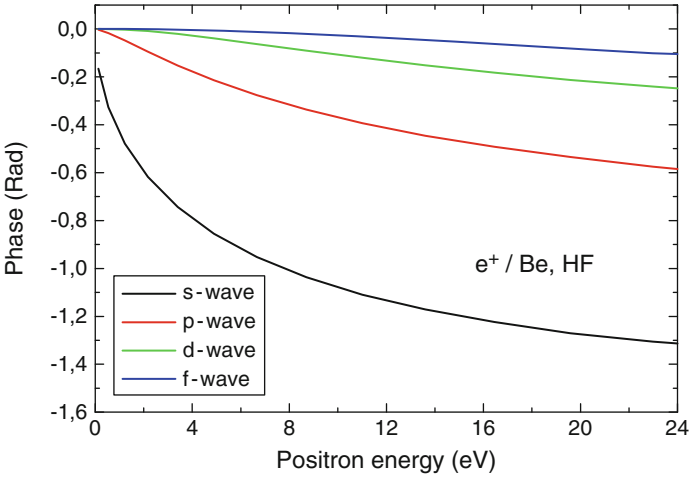

Fig. 4.252_Be_k2 Phases of various partial waves in positron scattering for Be atom in HF

Figure 4.248_Be_e3 shows the density of quadrupole GOSes for Be in RPAE as functions of the energy transferred to the atom at various q. With growth of q the first maximum in GOSes is moving to bigger values of ω, becoming lower and broader.

Figure 4.249_Be_i1 demonstrates the cross-section of elastic positron scattering on Be in HF and SRPAE (see [4.10]). The inclusion of electron correlations in SRPAE tremendously increases the cross-section at low energy. The contribution of inelastic scattering is very important with the dominative relative contribution at

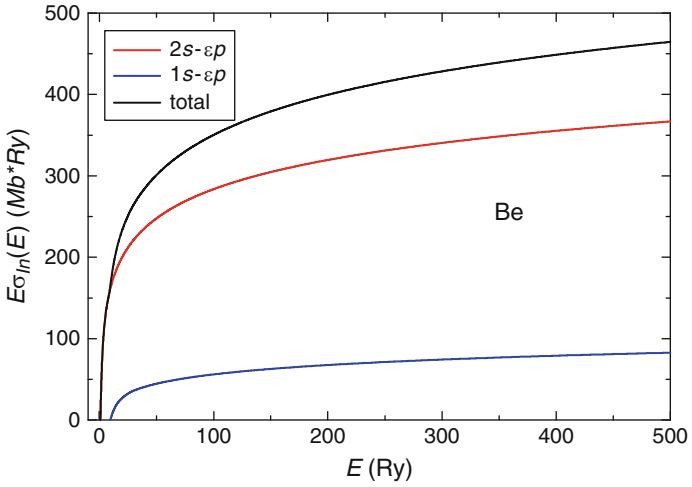

Fig. 4.253_Be_l1 Multiplied by incoming electron energy cross-section of inelastic scattering of fast electrons in the logarithmic approximation

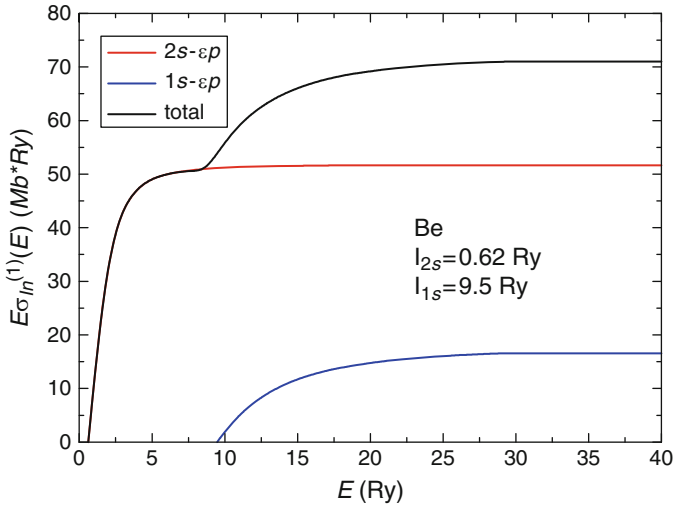

Fig. 4.254_Be_l2 Nonlogarithmic correction to the multiplied by incoming electron energy cross-section of inelastic scattering of fast electrons

$E \approx 3{-}4$ eV. The dominant contribution is $e^+ + \mathrm{Be} \rightarrow \mathrm{Ps} + \mathrm{Be}^+$. In calculation of polarization interaction, the formation of virtual positronium was taken into account. This was done as described in Sect. 3.12.

Figure 4.250_Be_j1 gives the contributions of various partial waves in cross-section of elastic positron scattering on Be. Dominative is the s-wave channel. It is overpassed by f-wave at 4 eV. Contribution of p- and d-waves is there smaller.

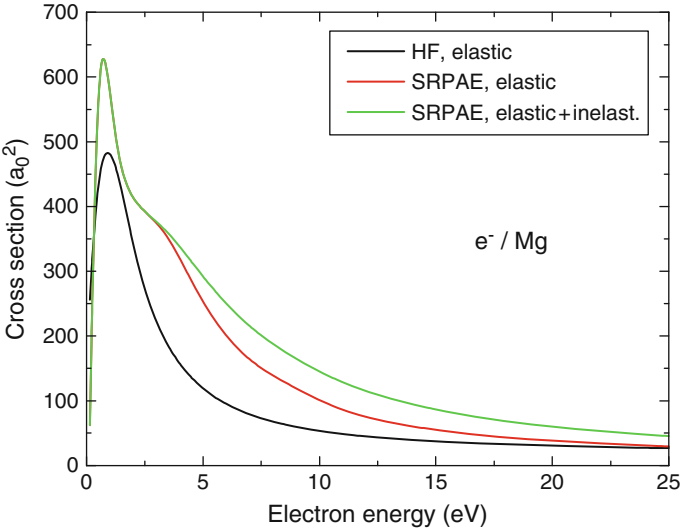

Fig. 4.255_Mg_a1 Cross-section of elastic (in HF and SRPAE) and inelastic (in SRPAE) electron scattering on Mg atom

Figure 4.251_Be_k1 demonstrates the s-, p-, d-, f-phase of partial waves for positron scattering upon Be in SRPAE with account of virtual positronium formation. Rather peculiar is the s-phase with pronounced minimum at 1.9 eV and prominent maximum at 4 eV. Note shape similarity of all phases as functions of positron energy. The s-phase at zero energy is nonzero. This peculiarity is explained at the end of Sect. 3.12.

Figure 4.252_Be_k2 depicts the phases of various partial waves in positron scattering upon Be atom in HF. All phases are negative and rapidly decrease from $E = 0$ with E growth. By comparing to Fig. 4.251_Be_k1, big role of polarization interaction, particularly for the s-phase, is seen.

Figure 4.253_Be_l1 represents the multiplied by incoming electron energy total and partial cross-sections of inelastic scattering of fast electrons on atom Be in logarithmic approximation $E\sigma_{\text{In}}(E)$ [see (3.71)]. Dominative is the contribution of scattering upon the outer $2s$ subshell, mainly from $2s$ to εp dipole transition. It is seen that these functions at high E increase slowly. Fastest is the increase of the bigger partial cross-section. The cross-sections are presented from $E = I$ for completeness only, since the logarithmic approximation is valid if $\ln(E/I) \gg 1$.

Figure 4.254_Be_l2 gives the multiplied by incoming electron energy total and partial nonlogarithmic corrections to the cross-sections of inelastic scattering of fast electrons on Be atom $E\sigma_{\text{In}}^{(1)}(E)$. It is seen that the outer shell contribution stops to grow already at $E = 5$ Ry, while for the inner shell contribution the almost constant value is reached at about $E = 30$ Ry.

Figures 4.255–4.263 (Mg) demonstrates the results of calculations for Mg atom.

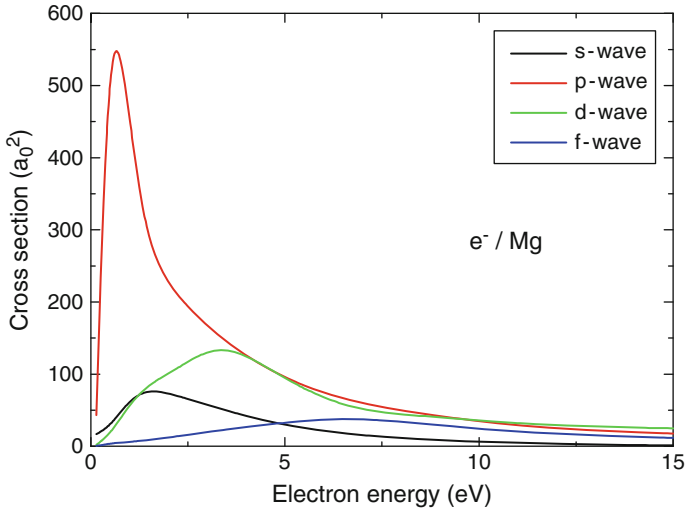

Fig. 4.256_Mg_b1 Contributions of partial waves in cross-section of elastic electron scattering on Mg atom

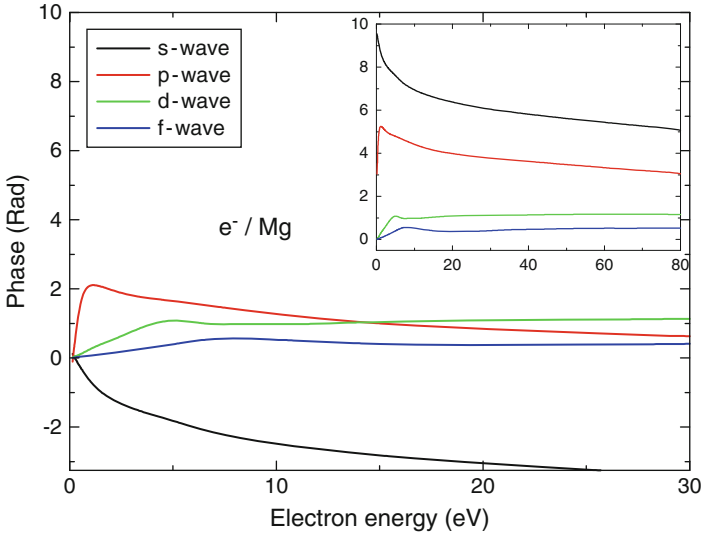

Fig. 4.257_Mg_d1 Phases of various partial waves in electron scattering on Mg

Figure 4.255_Mg_a1 depicts the cross-section of elastic (in HF and SRPAE) and inelastic (in SRPAE) electron scattering on Mg. The contribution of *s*-, *p*-, *d*-, *f*-waves is taken into account. It has a prominent maximum at 1 eV and includes noticeable inelastic scattering.

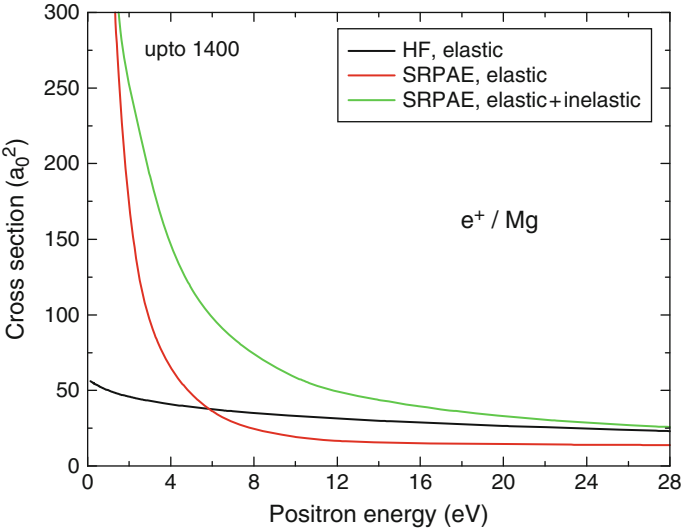

Fig. 4.258_Mg_i1 Cross-section of elastic (in HF and SRPAE) and inelastic (in SRPAE) scattering of a positron on Mg

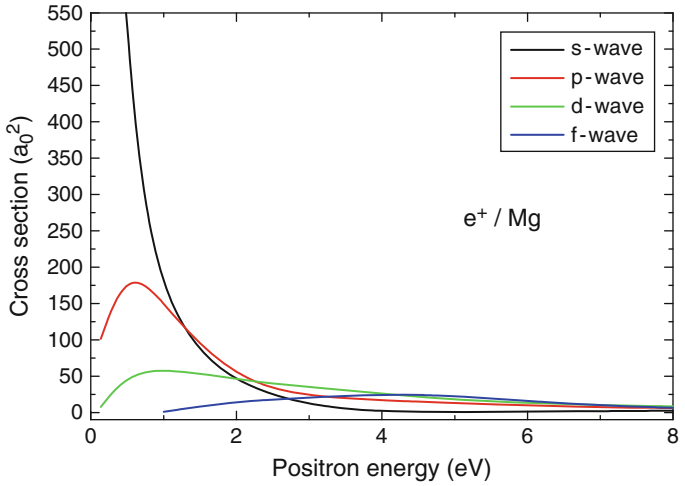

Fig. 4.259_Mg_j1 Contributions of partial waves in cross-section of elastic positron scattering on Mg

Figure 4.256_Mg_b1 shows the partial cross-sections of s-, p-, d-, f-waves of elastic electron scattering on Mg. It is visible that already at small energy E the p-wave term has a maximum at 0.7 eV that dominates, whereas the d-wave contribution has a maximum at 3.5 eV.

Figure 4.257_Mg_d1 collects the s, p, d, f-phases of various partial waves in electron scattering on Mg. Phases are determined in the frame of SRPAE.

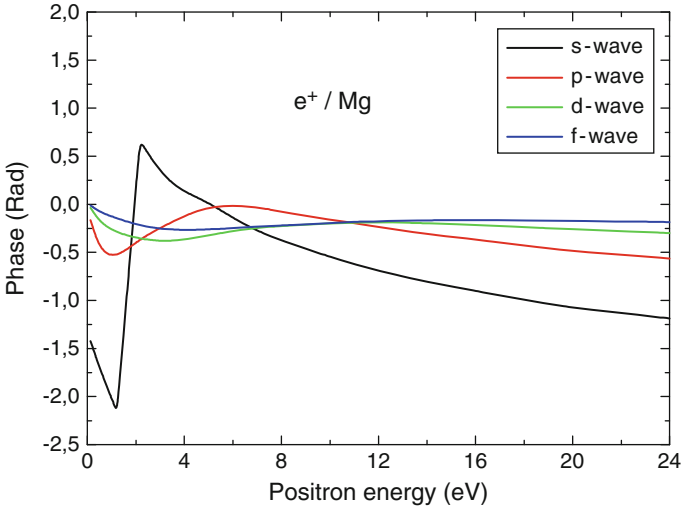

Fig. 4.260_Mg_k1 Phases of partial waves in positron scattering on Mg in SRPAE

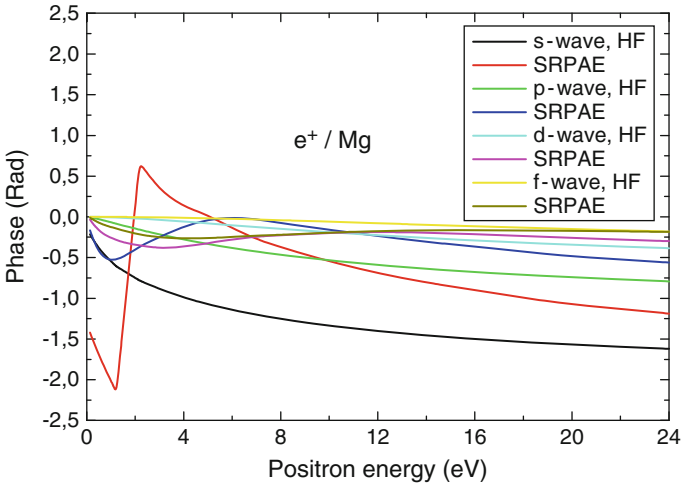

Fig. 4.261_Mg_k2 Phases of partial waves in positron scattering on Mg in HF and SRPAE

In conformity with (3.21), at zero electron energy s-phase is equal 3π, p-phase—π, and d-, f-phases are zero, if all of them are defined so that at $E \to \infty$ any phase $\delta_l \to 0$. Close to $E = 0$, p-phase quickly increases that speaks about approaching of $3p$-level already in the next atom Al. The polarization potential leads to a p-resonance in cross-section of elastic scattering that is a reflection of a possibility to form a negative ion Mg^-.

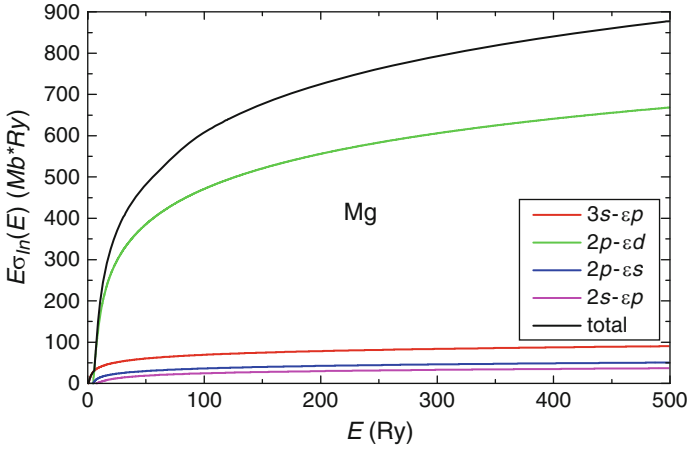

Fig. 4.262_Mg_i1 Multiplied by incoming electron energy cross-section of inelastic scattering of‘fast electrons in the logarithmic approximation

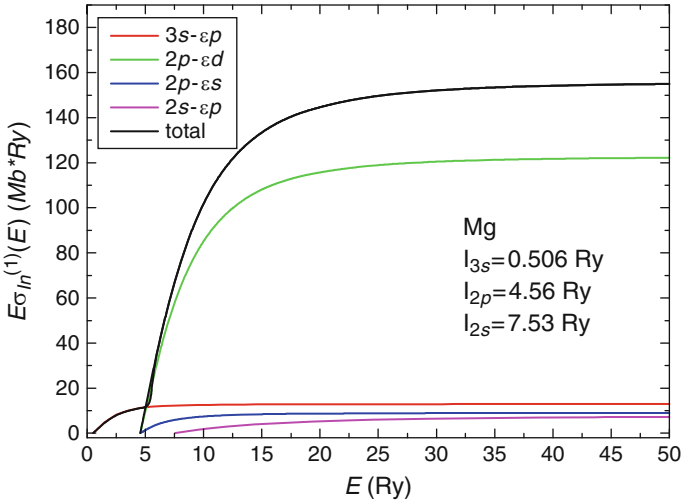

Fig. 4.263_Mg_i2 Nonlogarithmic correction to the multiplied by incoming electron energy cross-section of inelastic scattering of fast electrons

Figure 4.258_Mg_i1 presents the cross-section of elastic (in HF and SRPAE) and inelastic (in SRPAE) scattering of a positron on Mg. The inclusion of electron correlations in SRPAE tremendously increases the cross-section at low energy. The contribution of inelastic scattering is very important with the dominative relative contribution at $E \approx 3{-}4\,\mathrm{eV}$ and higher. The most important inelastic process is $e^+ + \mathrm{Mg} \to \mathrm{Ps} + \mathrm{Mg}^+$. In calculation of polarization interaction, the formation of virtual positronium was taken into account. This was done as described in Sect. 3.12.

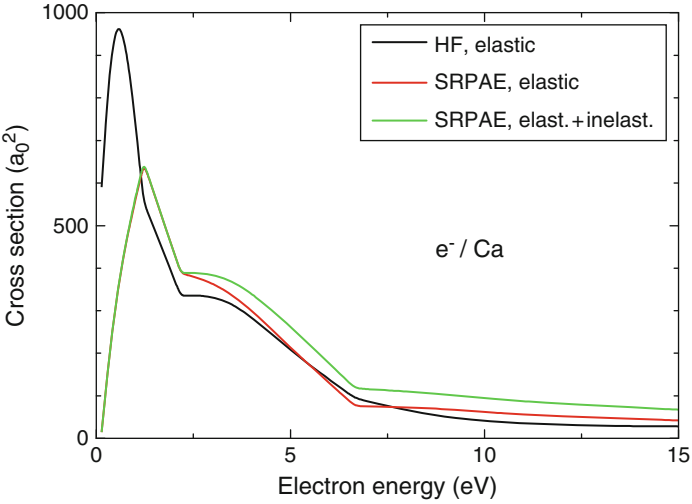

Fig. 4.264_Ca_a1 Cross-section of elastic (in HF and SRPAE) and inelastic (in SRPAE) electron scattering on Ca atom

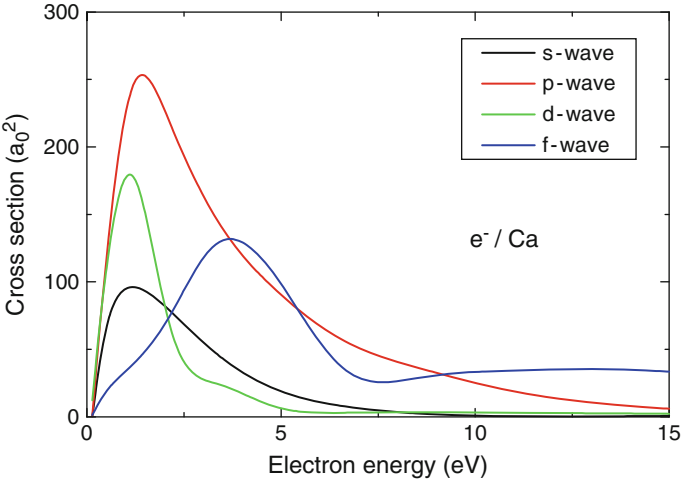

Fig. 4.265_Ca_b1 Contribution of partial waves in cross-section of elastic electron scattering on Ca

Figure 4.259_Mg_j1 presents the contributions of partial s-, p-, d-, f-waves in cross-section of elastic scattering of positrons on Mg. The contribution of s-wave absolutely dominates at $E < 1$ eV. Starting from $E \approx 2$ eV, other partial waves become increasingly important.

Figure 4.260_Mg_k1 gives the phases of partial s-, p-, d-, f-waves in positron scattering on Mg in SRPAE. Note shape similarity of all phases as functions of

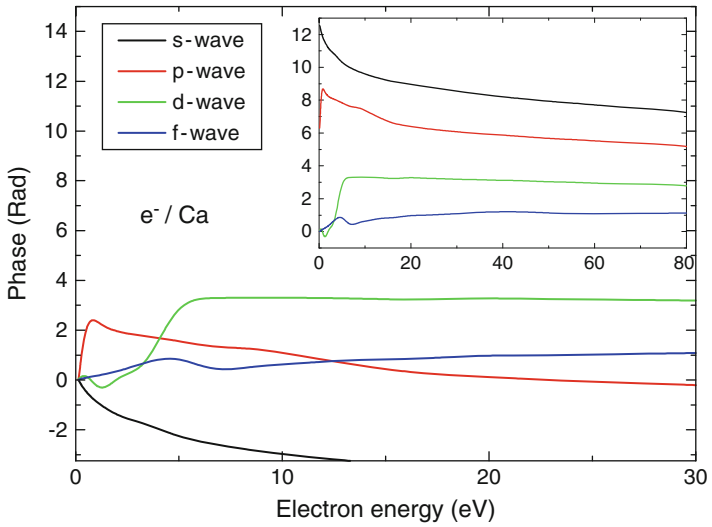

Fig. 4.266_Ca_d1 Phases of various partial waves in electron scattering on Ca in SRPAE

positron energy. The s-phase at zero energy is nonzero. This peculiarity is explained at the end of Sect. 3.12. The variation as big as in 2.5 rad in s-phase at energy 0–3 eV deserves attention.

Figure 4.261_Mg_k2 represents the phases of partial waves in positron scattering on Mg in HF and SRPAE. The difference between SRPAE and HF values is especially big for the s-wave.

Figure 4.262_Mg_l1 illustrates the multiplied by incoming electron energy the total and partial cross-sections of inelastic scattering of fast electrons on atom Mg in logarithmic approximation $E\sigma_{\rm ln}(E)$ [see (3.71)]. Absolutely dominative is the contribution of scattering upon the outer $2p$ subshell, mainly from $2p$ to εd dipole transition. It is seen that these functions at high E increase slowly. Fastest is the increase of the bigger partial cross-section. The cross-sections are presented from $E = I$ for completeness only, since the logarithmic approximation is valid if $\ln(E/I) \gg 1$.

Figure 4.263_Mg_l2 gives the total and partial nonlogarithmic corrections to the cross-sections of inelastic scattering of fast electrons, multiplied by incoming electron energy, on Mg atom $E\sigma^{(1)}_{\rm ln}(E)$. It is seen that the outer shell contribution stops to grow already at $E = 5\,$Ry, while for the bigger $2p$ subshell contribution the almost constant value is reached at about $E = 20{-}25\,$Ry.

Figures 4.264–4.276 (Ca) show the results of calculations for Ca atom.

Figure 4.264_Ca_a1 depicts the cross-section of elastic (in HF and SRPAE) and inelastic (in SRPAE) electron scattering on Ca. The contribution of s-, p-, d-, f-waves (see also [4.33, 4.34]) is taken into account. Note that the main maximum in SRPAE is lower than in HF.

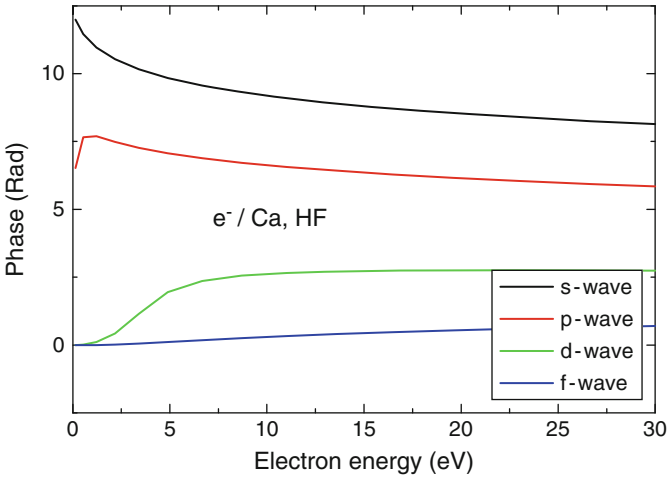

Fig. 4.267_Ca_d2 Phases of various partial waves in electron scattering on Ca in HF

Figure 4.265_Ca_b1 depicts the the contribution of partial waves in cross-section of elastic electron scattering on Ca. The contribution of s-, p-, d-, f-waves is taken into account. Calculations are carried out in SRPAE by solving the Dayson equation (3.45) with use of (3.46) (see also [4.35, 4.36]). The polarization potential includes contributions of virtual and real excitations of $3s$-, $3p$-, and $4s$-electrons. Note a powerful p-resonance that reflects the possibility to form a negative ion Ca^- with an outer p-electron.

Figure 4.266_Ca_d1 represents the phases of various partial waves in electron scattering on Ca in SRPAE. Phases at zero energy, in accord with (3.21) are equal: s-phase—4π and p-phase—2π. One should pay attention to the fact that p-phase very quickly increases, almost reaching 3π. It means that at a little stronger polarization interaction formation of a bound state e + Ca (i.e., negative ion Ca^-) is possible. In the main part of the figure, the phases are normalized so that all of them approach zero at $E = 0$. More accurate calculation of polarization interaction with use of Dayson equations (Sect. 3.4) has allowed to describe negative ions of Ca and of some other atoms of the second group of the periodic table [4.35, 4.36].

Figure 4.267_Ca_d2 demonstrates the phases of various partial waves in electron scattering on Ca in HF. They obey the requirement of (3.21). Note a maximum in p-wave that signals a possibility of a bound negative ion state Ca^- with outer p-electron.

Figure 4.268_Ca_e1 gives the density of monopole GOSes for Ca in HF and RPAE as function of the energy transferred to the atom at various q. With growth of q the first maximum is displaced to the bigger ω side.

Figure 4.269_Ca_e2 depicts the density of dipole GOSes for Ca in HF and RPAE as function of the energy transferred to the atom at various q. As is evident by

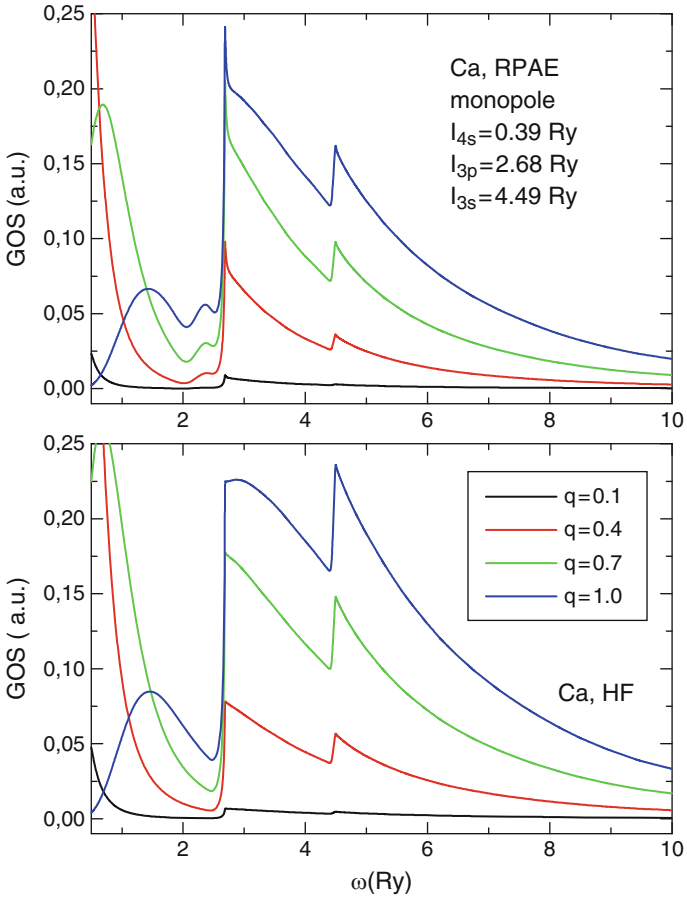

Fig. 4.268_Ca_e1 Density of monopole generalized oscillator strengths as function of the energy transferred to atom at various q for Ca in HF and RPAE

comparison with Figs. 4.268_Ca_e1 and 4.270_Ca_e3, the dipole GOSes absolutely dominate even at not small q, even up to $q = 1$.

Figure 4.270_Ca_e3 shows the density of quadrupole GOSes for Ca in HF and RPAE as functions of the energy transferred to the atom at various q. With increase of q GOS forms a maximum that moves from threshold to higher energy, becoming lower and broader.

Figure 4.271_Ca_i1 illustrates the cross-section of elastic (in HF and SRPAE) and inelastic (in SRPAE) positron scattering on Ca atom. Note the very big role of the polarization interaction that takes into account the virtual positronium formation. This was done as described in Sect. 3.12. The contribution of inelastic scattering is quite important. The dominant inelastic process is $e^+ + \mathrm{Ca} \to \mathrm{Ps} + \mathrm{Ca}^+$.

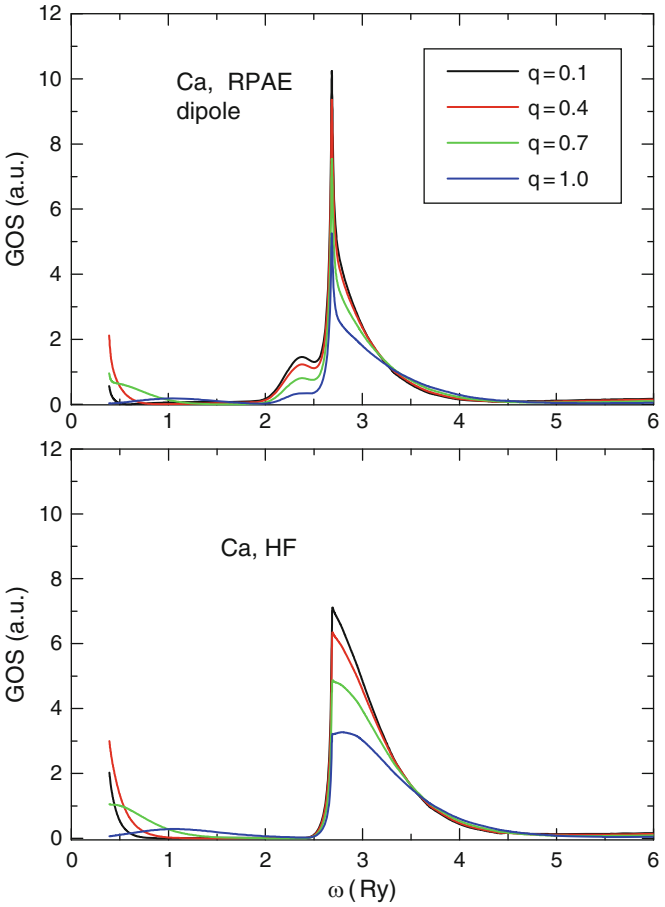

Fig. 4.269_Ca_e2 Density of dipole generalized oscillator strengths as function of the energy transferred to atom at various q for Ca in HF and RPAE

Figure 4.272_Ca_j1 collects the contributions of partial waves to cross-section of elastic electron scattering on Ca atom. While at low E dominates the s-wave, the contribution of p- and d-waves increase rapidly.

Figure 4.273_Ca_k1 illustrates the phases of various partial waves in positron scattering on Ca atom in HF. All phases are negative. In the considered energy region absolutely dominates the s-phase.

Figure 4.274_Ca_k2 demonstrates the phases of various partial waves in positron scattering on Ca atom in SRPAE. Rather peculiar is the s-phase with pronounced minimum at about 3 eV and noticeable maximum at 11 eV. The s-phase at zero energy is nonzero. This peculiarity is explained at the end of Sect. 3.12. Note that on the way from s-wave to f-wave the phases become smaller and the minimum step-by-step disappear.

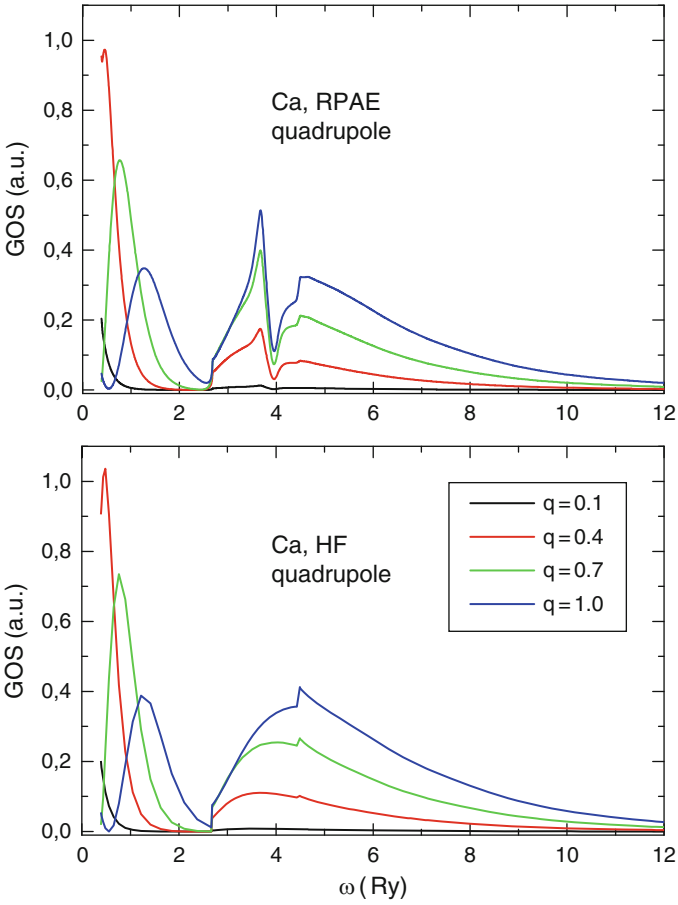

Fig. 4.270_Ca_e3 Density of quadrupole generalized oscillator strengths as function of the energy transferred to atom at various q for Ca in HF and RPAE

Figure 4.275_Ca_l1 presents the multiplied by incoming electron energy total and partial cross-sections of inelastic scattering of fast electrons on atom Ca in logarithmic approximation $E\sigma_{\mathrm{ln}}(E)$ [see (3.71)]. Dominative is the contribution of scattering upon the outer $3p$ subshell, mainly from $3p$ to εd dipole transition. It is seen that these functions at high E increase slowly. Fastest is the increase of the bigger partial cross-section. The cross-sections are presented from $E = I$ for completeness only, since the logarithmic approximation is valid if $\ln(E/I) \gg 1$.

Figure 4.276_Ca_l2 gives the total and partial nonlogarithmic corrections to the cross-sections of inelastic scattering of fast electrons, multiplied by incoming electron energy, on Ca atom $E\sigma_{\mathrm{ln}}^{(1)}(E)$. It is seen that the outer shell contribution

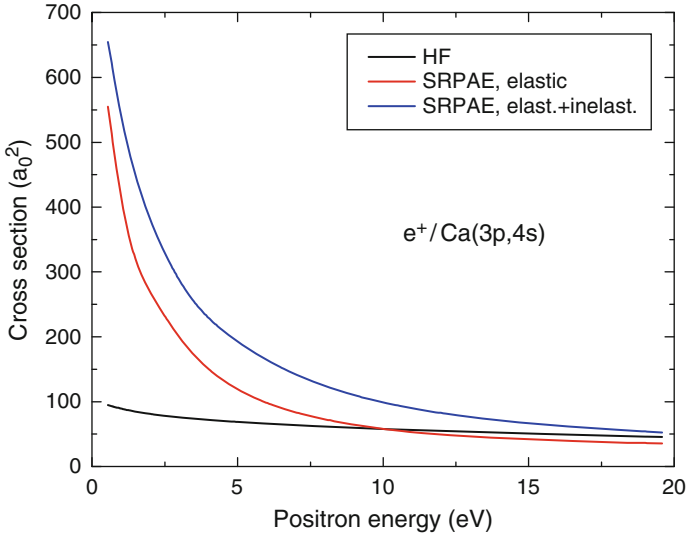

Fig. 4.271_Ca_i1 Cross-section of elastic (in HF and SRPAE) and inelastic (in SRPAE) positron scattering on Ca atom

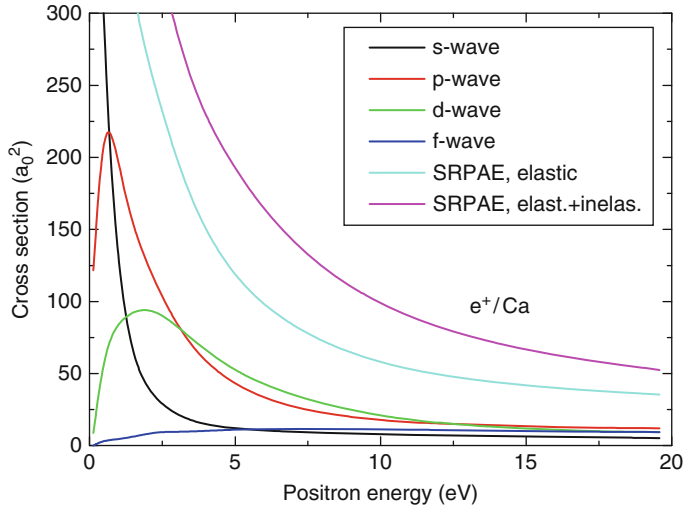

Fig. 4.272_Ca_j1 Contributions of partial waves to cross-section of elastic electron scattering on Ca atom

stops to grow already at $E = 5\,\mathrm{Ry}$, while for the bigger $2p$ subshell contribution the almost constant value is reached at about $E = 20{-}25\,\mathrm{Ry}$.

Figures 4.277–4.279 (Zn) show the results of calculations for Zn atom.

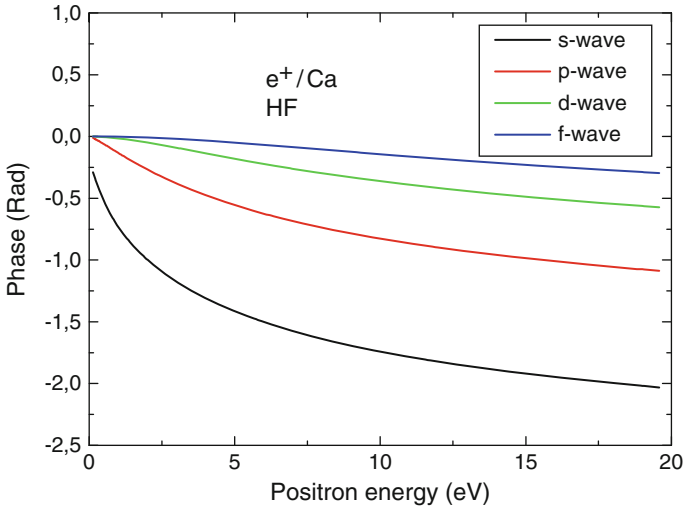

Fig. 4.273_Ca_k1 Phases of various partial waves in positron scattering on Ca atom in HF

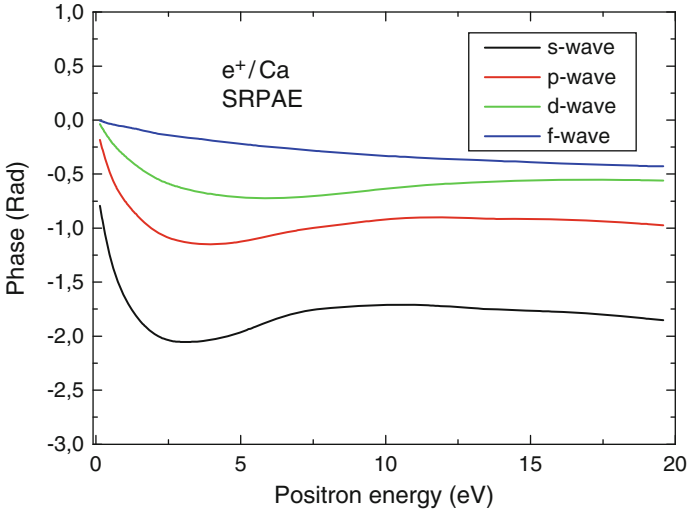

Fig. 4.274_Ca_k2 Phases of various partial waves in positron scattering on Ca atom in SRPAE

Figure 4.277_Zn_a1 presents the cross-section of elastic (in HF and SRPAE) and inelastic (in SRPAE) electron scattering on Zn. The incoming electron s-, p-, d-, f-waves are taken into account, and the polarization interaction includes contribution of virtual and real excitations and ionization of $3d$ and $4s$-electrons. Influence of the electronic correlations resulting in difference of SRPAE and HF results is essential, leading to a bigger cross-section in the entire considered energy region. The inelastic cross-section is small enough.

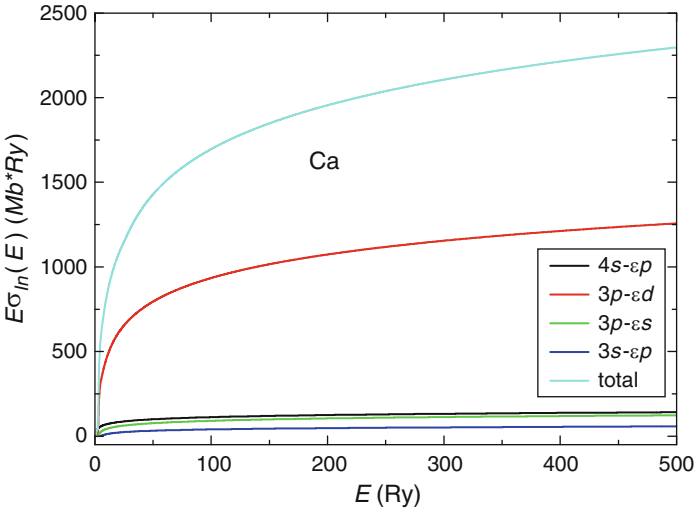

Fig. 4.275_Ca_l1 Multiplied by incoming electron energy cross-section of inelastic scattering of fast electrons in the logarithmic approximation

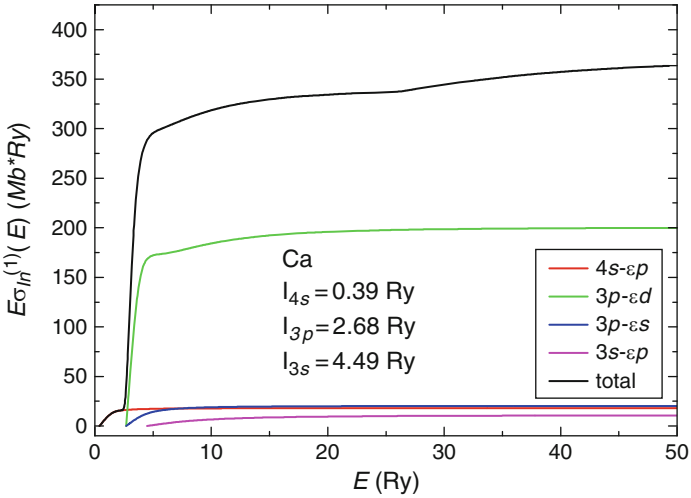

Fig. 4.276_Ca_l2 Nonlogarithmic correction to the multiplied by incoming electron energy cross-section of inelastic scattering of fast electrons

Figure 4.278_Zn_b1 gives the contributions of partial s-, p-, d-, f-waves into the cross-section of elastic electron scattering on Zn. Polarization interaction is created by virtual excitation $3d$- and $4s$-electrons. The main maximum is in p-wave, signaling about occurrence of bound $4p$-electron level in the neighbor atom-Gallium. Other maxima are smaller.

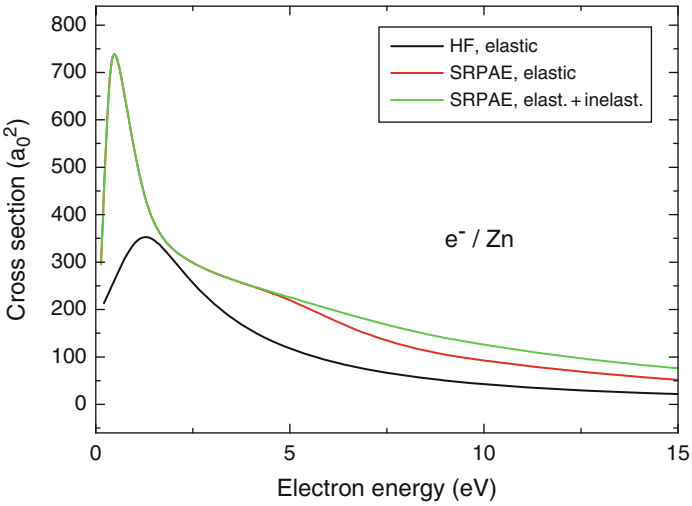

Fig. 4.277_Zn_a1 Cross-section of elastic (in HF and SRPAE) and inelastic (in SRPAE) electron scattering on Zn atom

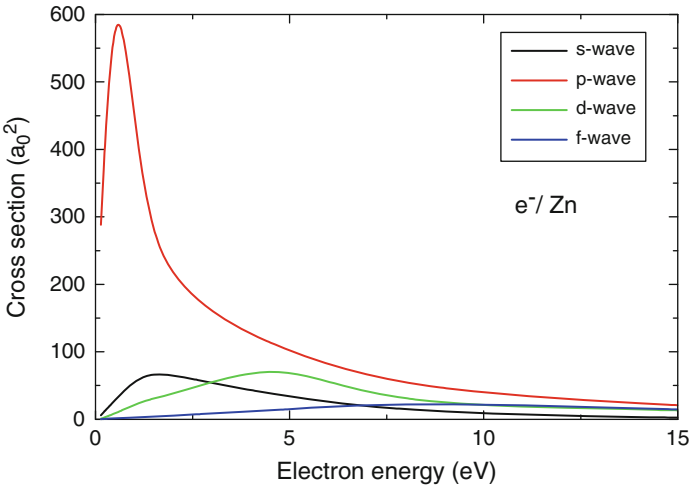

Fig. 4.278_Zn_b1 Contributions of partial waves in cross-section of elastic electron scattering on Zn atom

Figure 4.279_Zn_d1 collects the phases of partial s-, p-, d-, f-waves in electron scattering on Zn in SRPAE. Phases on insert at zero energy, in agreement with (3.21), are equal: s-phase—4π, p-phase—2π, and d-phase—π. In the main figure, phases are normalized so that all of them approach zero at $E = 0$.

Figures 4.280–4.282 (Cd) show the results of calculations for Cd atom.

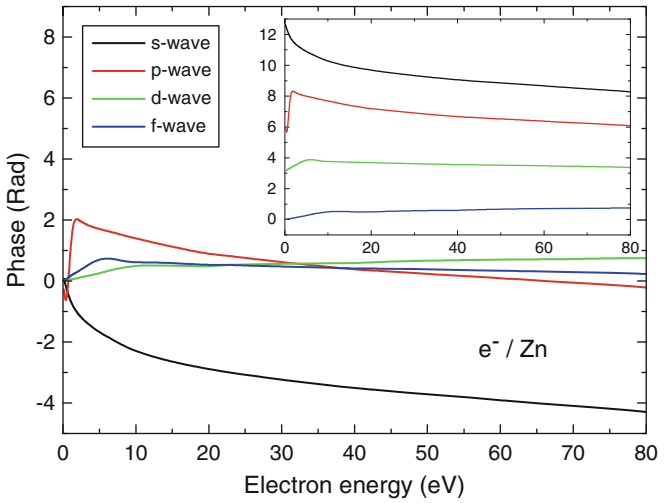

Fig. 4.279_Zn_d1 Phases of partial waves in electron scattering on Zn atom in SRPAE

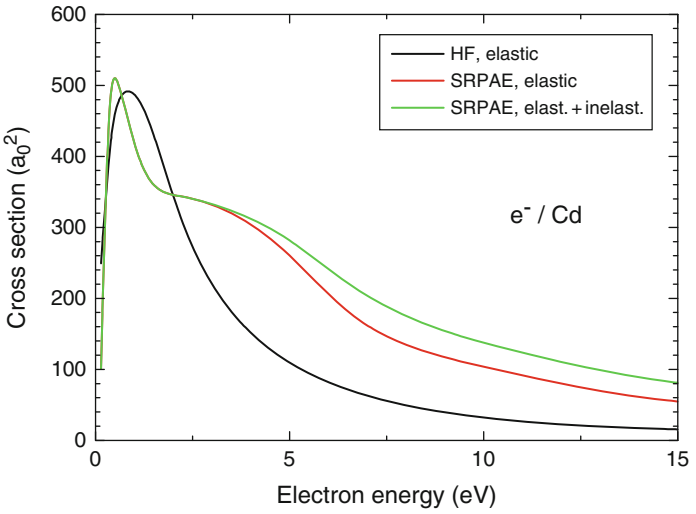

Fig. 4.280_Cd_a1 Cross-sections of elastic (in HF and SRPAE) and inelastic (in SRPAE) electron scattering on Cd atom

Figure 4.280_Cd_a1 demonstrates the cross-sections of elastic (in HF and SRPAE) and inelastic (in SRPAE) electron scattering on Cd. The contribution of s-, p-, d-, f-waves is taken into account. The polarization interaction includes virtual and real excitations of $4d$ and $5s$-electrons. Influence of the electronic correlations resulting in difference between SRPAE and HF results is big enough.

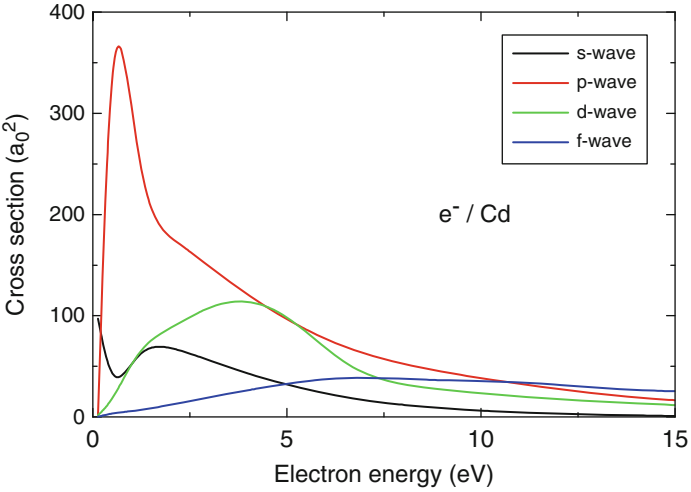

Fig. 4.281_Cd_b1 Contributions of partial waves to cross-section of elastic electron scattering on Cd atom in SRPAE

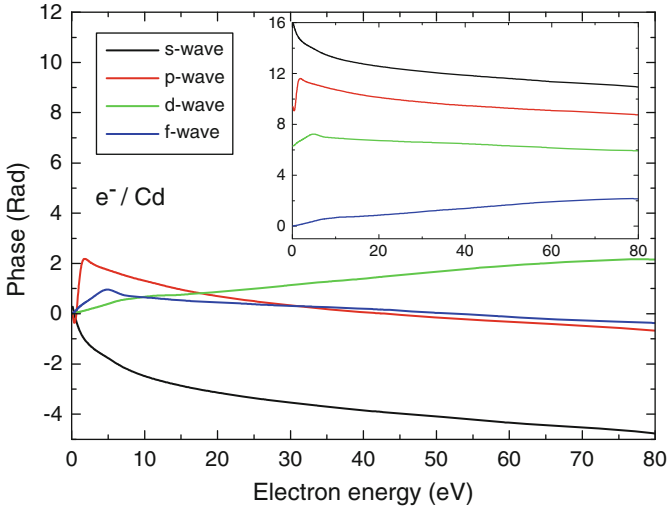

Fig. 4.282_Cd_d1 Phases of partial waves in electron scattering on Cd atom in SRPAE

Figure 4.281_Cd_b1 gives the contribution of partial s-, p-, d-, f-waves to cross-section of elastic electron scattering on Cd. Polarization interaction is created by virtual excitation of $4d$- and $5s$-electrons. The main maximum in Cd, as well as in other elements of II group, is in p-wave. The contribution of wide d-maximum is noticeable also. Presence of the second maximum in the s-wave is remarkable.

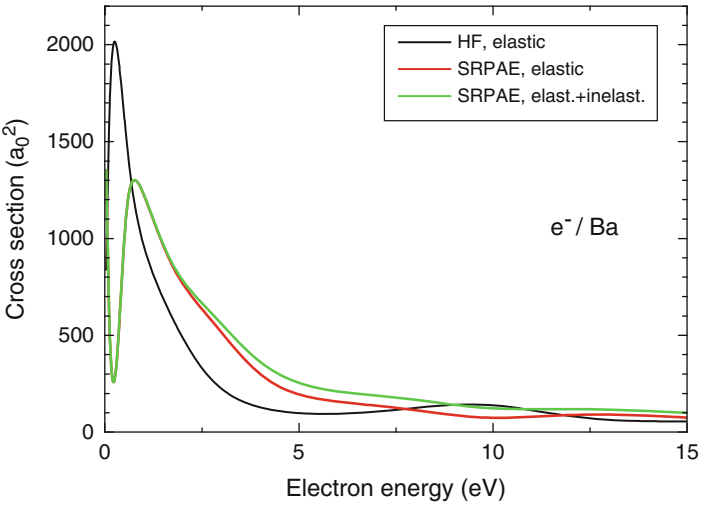

Fig. 4.283_Ba_a1 Cross-sections of elastic (in HF and SRPAE) and inelastic (in SRPAE) electron scattering on Ba atom

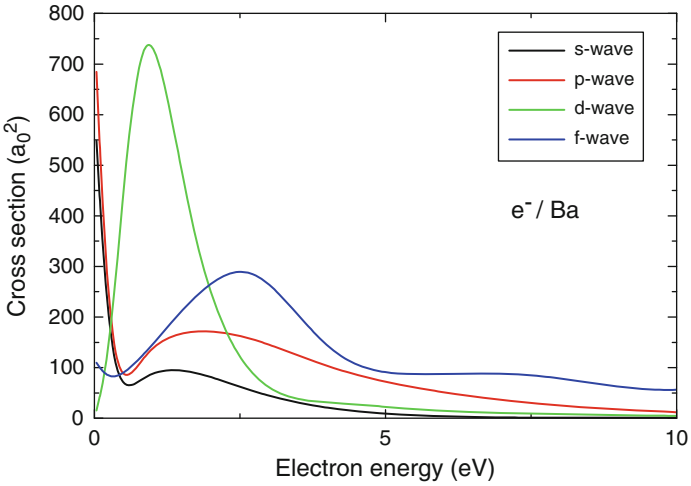

Fig. 4.284_Ba_b1 Contributions of partial waves to cross-section of elastic electron scattering on Ba atom

Figure 4.282_Cd_d1 contains the phases of partial s-, p-, d-, f-waves in electron scattering on Cd. Phases on insert at zero energy, in agreement with (3.21), are equal, respectively: s-phase—5π, p-phase—3π, and d-phase—2π. In the main figure, phases are normalized so that each of them is zero at $E = 0$.

Figures 4.283–4.292 (Ba) show the results of calculations for Ba atom.

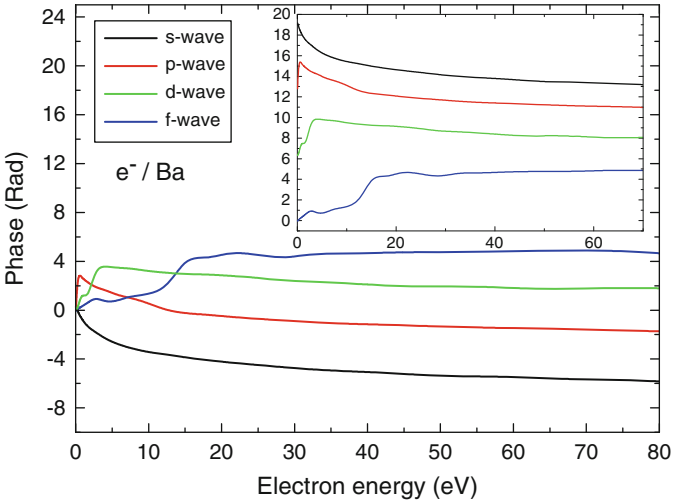

Fig. 4.285_Ba_d1 Phases of various partial waves in electron scattering on Ba atom in SRPAE

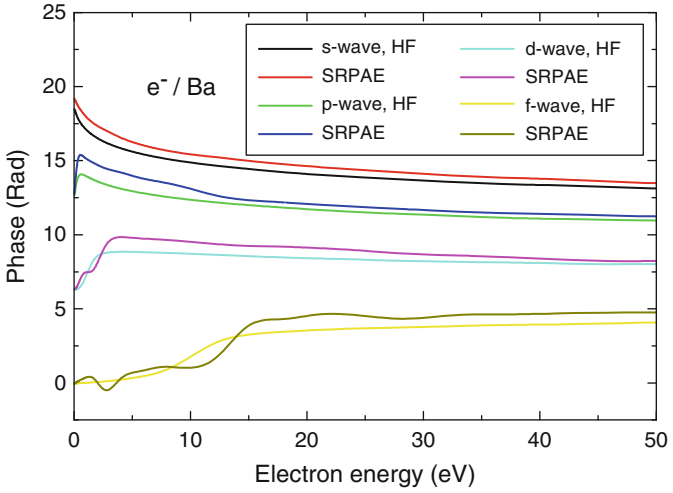

Fig. 4.286_Ba_d2 Phases of various partial waves in electron scattering on Ba atom in HF and SRPAE

Figure 4.283_Ba_a1 depicts the cross-sections of elastic (in HF and SRPAE) and inelastic (in SRPAE) electron scattering on Ba. The influence of electronic correlations results in occurrence of a minimum (such, as Ramsauer minimum [4.20]) and a maximum in SRPAE cross-section that are absent in HF.

Figure 4.284_Ba_b1 presents the contributions of partial s-, p-, d-, f-waves to cross-section of elastic electron scattering on Ba. Polarization interaction is created by virtual excitation of $5d$- and $6s$-electrons. Along with strong variation of the

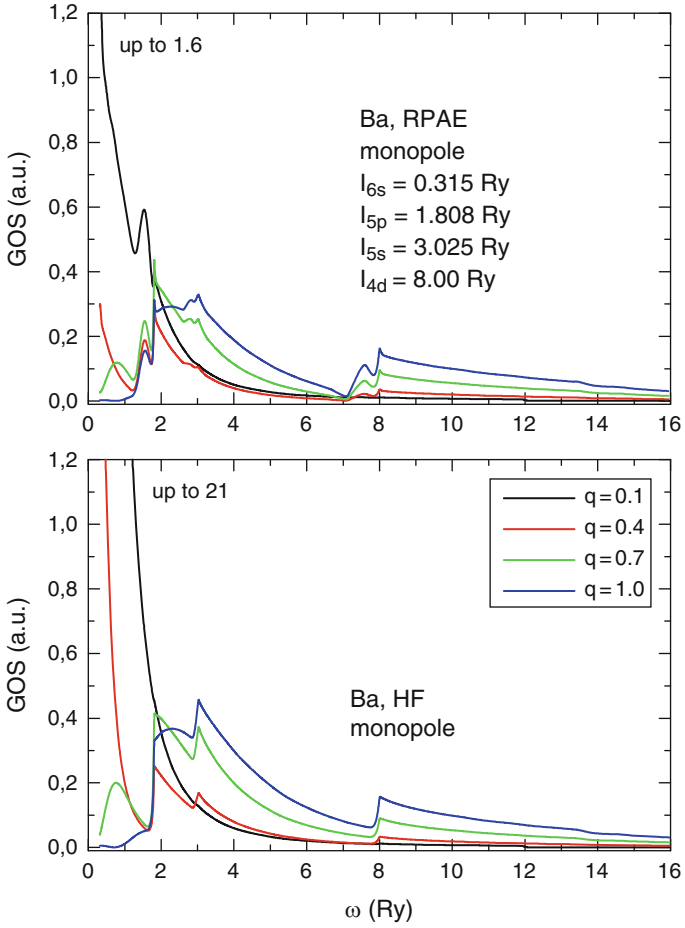

Fig. 4.287_Ba_e1 Density of monopole generalized oscillator strengths as function of the energy transferred to the atom at various q for Ba in HF and RPAE

s-wave contribution, prominent maximums appear in all other waves. As to f-phase contribution, we see in it even two maximums. However, most important are the maximum in p- and d-waves, while the contribution of broad second maximum, it is invisible in the cross-section. As in Cd, there is a second maximum in s-wave.

Figure 4.285_Ba_d1 offers the phases of various partial waves in electron scattering on Ba. Phases at zero energy, in agreement with (3.21), are equal to the following values, respectively: s-phase—6π, p-phase—4π, and d-phase—2π. The p-phase near $E = 0$ changes rapidly, almost reaching 5π. It means that at a little stronger polarization interaction formation of the connected state e + Ba (i.e., negative ion Ba^-) [4.35, 4.36] becomes possible. In the main figure, phases are normalized so that all of them are zero at $E = 0$.

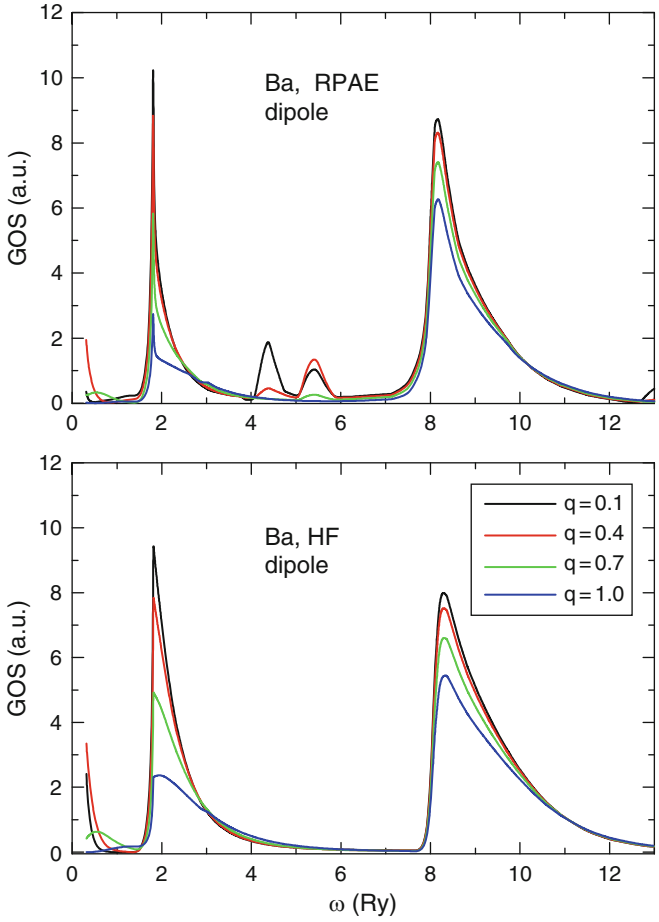

Fig. 4.288_Ba_e2 Density of dipole generalized oscillator strengths as function of the energy transferred to the atom at various q for Ba in HF and RPAE

Figure 4.286_Ba_d2 shows the phases of various partial waves in electron scattering on Ba atom in HF and SRPAE. One can see prominent role of polarization potential. Attention deserves almost irregular variations in the increasing from zero with energy growth f-phase due to polarization interaction.

Figure 4.287_Ba_e1 demonstrates the density of monopole GOSes for Ba in HF and RPAE as functions of the energy transferred to the atom at various q. With growth of energy, starting at $\omega \geq 2$ Ry, contributions of big q dominate.

Figure 4.288_Ba_e2 presents the density of dipole GOSes for Ba in HF and RPAE as function of the energy transferred to the atom at various q. With growth of q GOSes at a given energy, decrease.

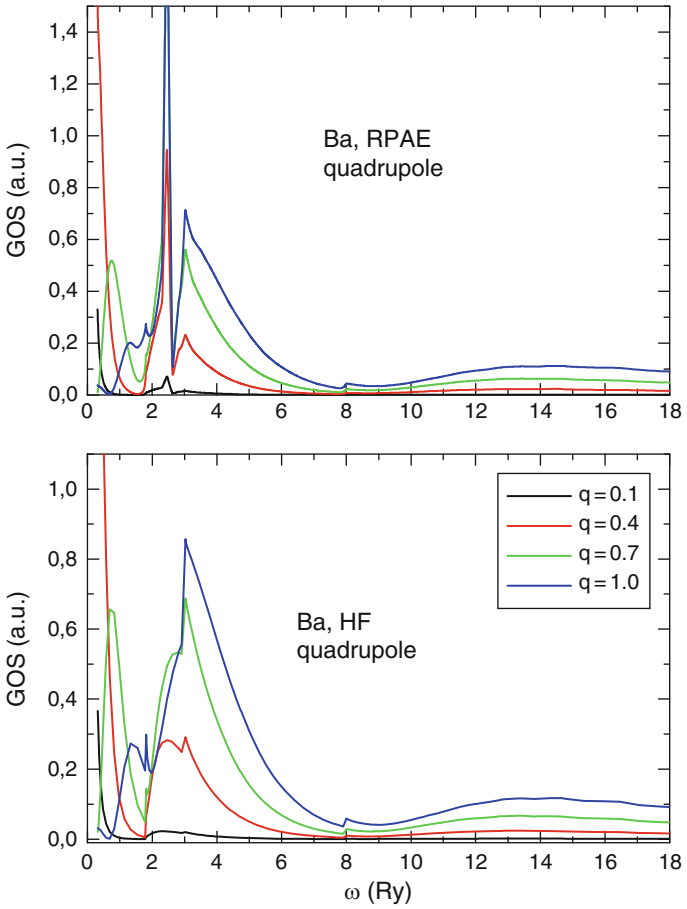

Fig. 4.289_Ba_e3 Density of quadrupole generalized oscillator strengths as function of the energy transferred to the atom at various q for Ba in HF and RPAE

Figure 4.289_Ba_e3 offers the density of quadrupole GOSes for Ba in HF and RPAE as functions of the energy transferred to the atom at various q. At almost any values of ω, contributions are become bigger at large q.

Figure 4.290_Ba_e4 represents the density of monopole GOSes of $3d_{5/2}$- and $3d_{3/2}$-electrons for Ba in HF and SP RPAE as functions of the energy transferred to the atom at various q (see [4.30]). Calculation is carried out according to the description given at the end of Sects. 3.6 and 1.10. Strong influence of 3/2-upon 5/2-level is visible at small q.

Figure 4.291_Ba_e5 demonstrates the density of dipole GOSes of $3d_{5/2}$- and $3d_{3/2}$-electrons for Ba in HF and SP RPAE as functions of the energy transferred to the atom at various q (see [4.30]). As shown in Fig. 4.287_Ba_e1, results are obtained according to description given in Sects. 1.10 and 3.6. Influence of 3/2-electrons leads to an additional prominent maximum of GOSes-electrons for 5/2-level in SP RPAE

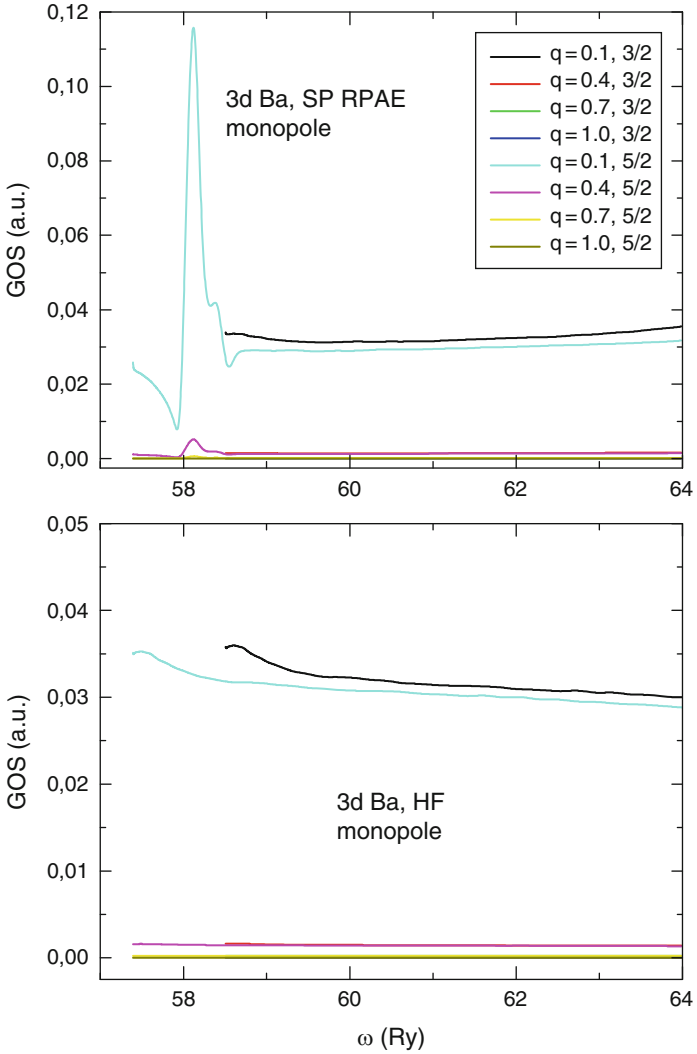

Fig. 4.290_Ba_e4 Density of monopole generalized oscillator strengths of $3d_{5/2}$- and $3d_{3/2}$-electrons as function of the energy transferred to the atom at various q for Ba in HF and SP RPAE (see [4.30])

in the area $\approx 58.3-59$ eV for all considered values of q. In the presented area of ω and q, dipole GOSes are greater than the monopole and quadrupole by an order of magnitude. SP RPAE corrections are large, as it can be seen if we compare data of the upper and lower parts of the figure.

Figure 4.292_Ba_e6 gives the density of quadrupole GOSes of $3d_{5/2}$- and $3d_{3/2}$-electrons for Ba in HF and SP RPAE as functions of the energy transferred to

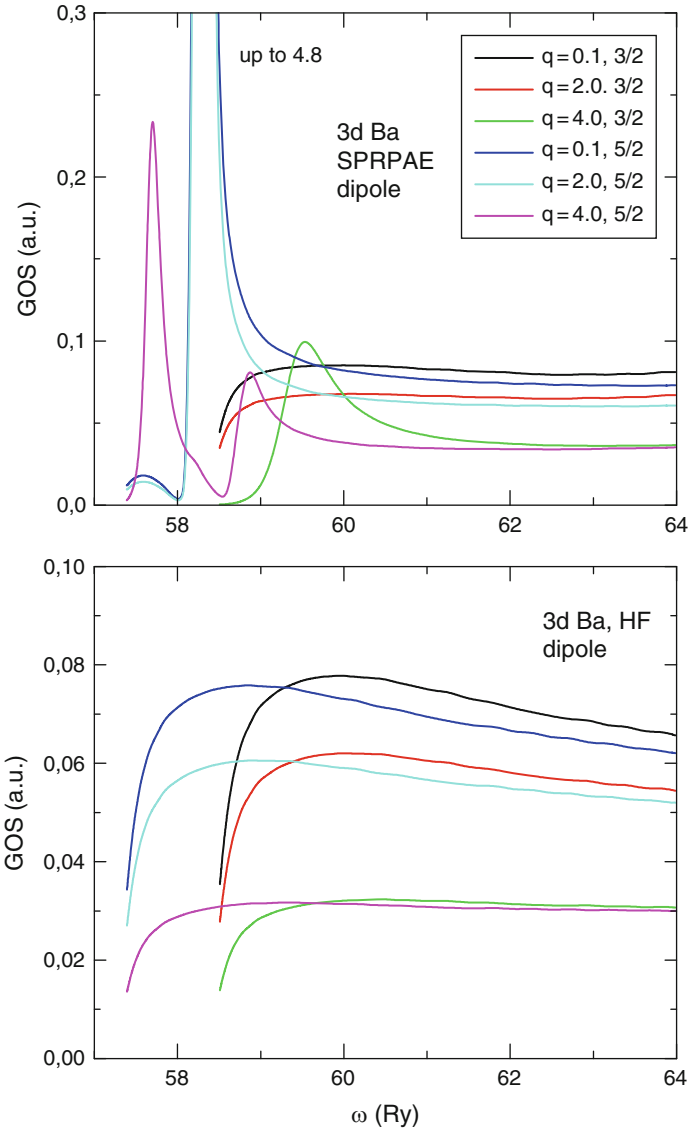

Fig. 4.291_Ba_e5 Density of dipole generalized oscillator strengths of $3d_{5/2}$- and $3d_{3/2}$-electrons as function of the energy transferred to the atom at various q for Ba in HF and SP RPAE (see [4.30])

the atom at various q (see [4.30]). The role of interaction of 5/2 and 3/2 levels is reduced and manifests itself by a small additional oscillation at ≈58.2 eV in GOSes of 5/2-level.

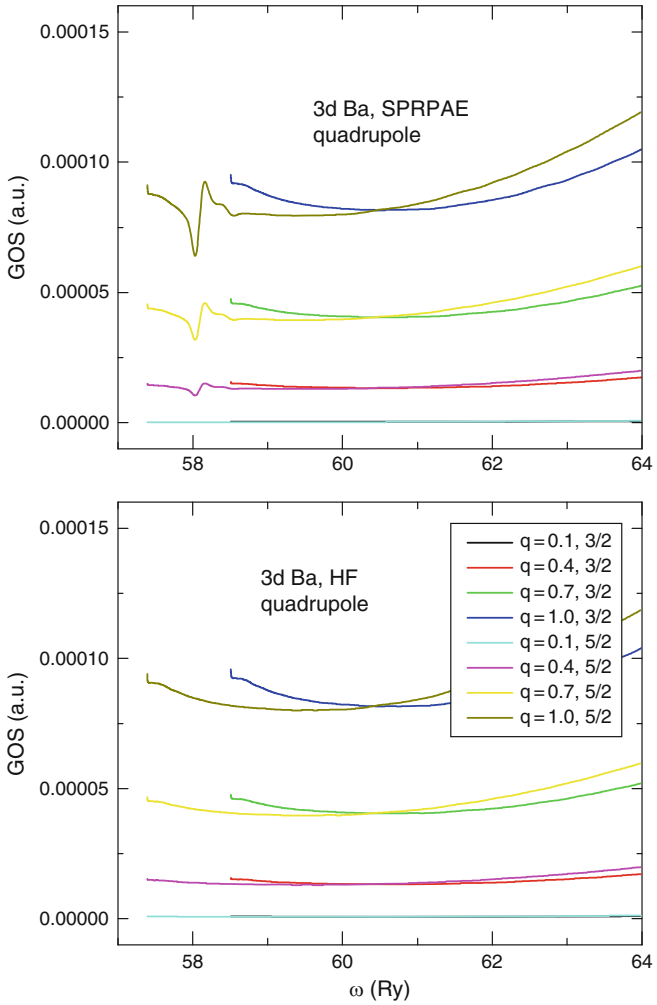

Fig. 4.292_Ba_e6 Density of quadrupole generalized oscillator strengths of $3d_{5/2}$- and $3d_{3/2}$-electrons as function of the energy transferred to the atom at various q for Ba in HF and SP RPAE (see [4.30])

4.5 Atoms and Ions of Groups IV and V Elements of the Periodic Table

In this section, the results of our calculations of the generalized oscillator strengths (GOSes) in HF and with account of RPAE correlations in the following interacting subshells are submitted: $2p^3\uparrow, 2p^3\downarrow, 3s\uparrow, 3s\downarrow, 3p^3\uparrow$ in Si^-, $2s\uparrow, 2s\downarrow, 2p^3\uparrow$ in N, and $2p^3\uparrow, 2p^3\downarrow, 3s\uparrow, 3s\downarrow, 3p^3\uparrow$ in P.

Figures 4.293–4.295 (Si^-) show the results of calculations for Si^- ion.

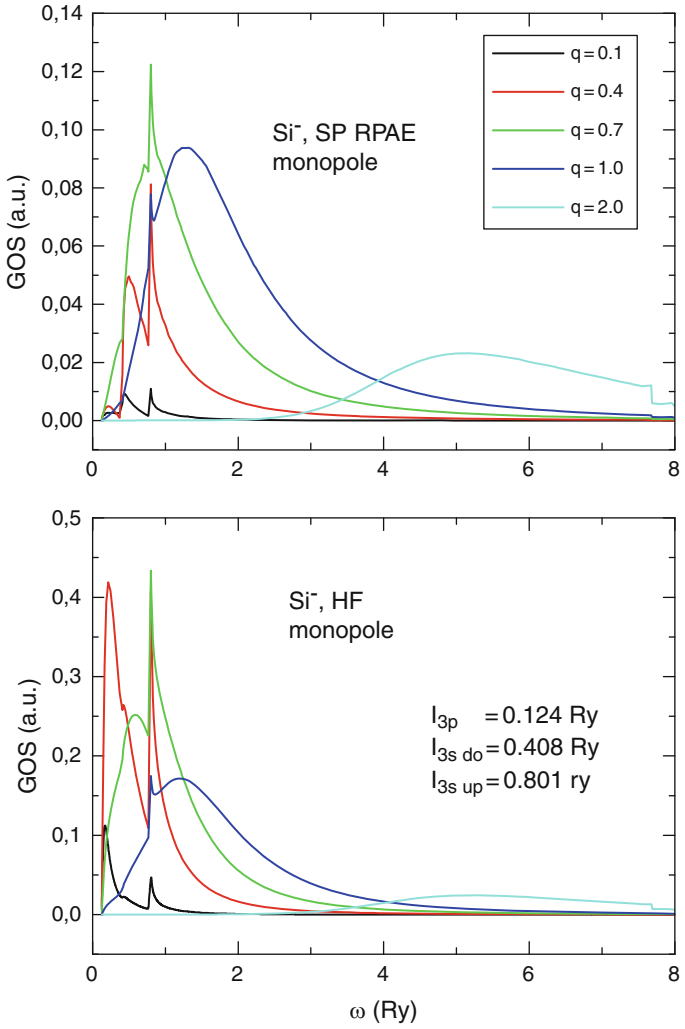

Fig. 4.293_Si⁻_e1 Density of monopole generalized oscillator strengths as function of the energy transferred to the ion at various q for Si^- in HF and SP RPAE

Figure 4.293_Si⁻_e1 contains the density of monopole GOSes for Si^- in HF and SP RPAE as functions of the energy transferred to the ion at various q. With growth of q the maximum in GOSes moves to the higher energy side. "Jumps" in GOSes are at ionization thresholds.

Figure 4.294_Si⁻_e2 represents the density of dipole GOSes for Si^- in HF and SP RPAE as to function of the energy transferred to the ion at various q. "Jumps" in GOSes are at ionization thresholds. Influence of electron correlations taken into account within the framework of SP RPAE is great. As usual, dipole GOSes are in general much bigger than the monopole and quadrupole ones.

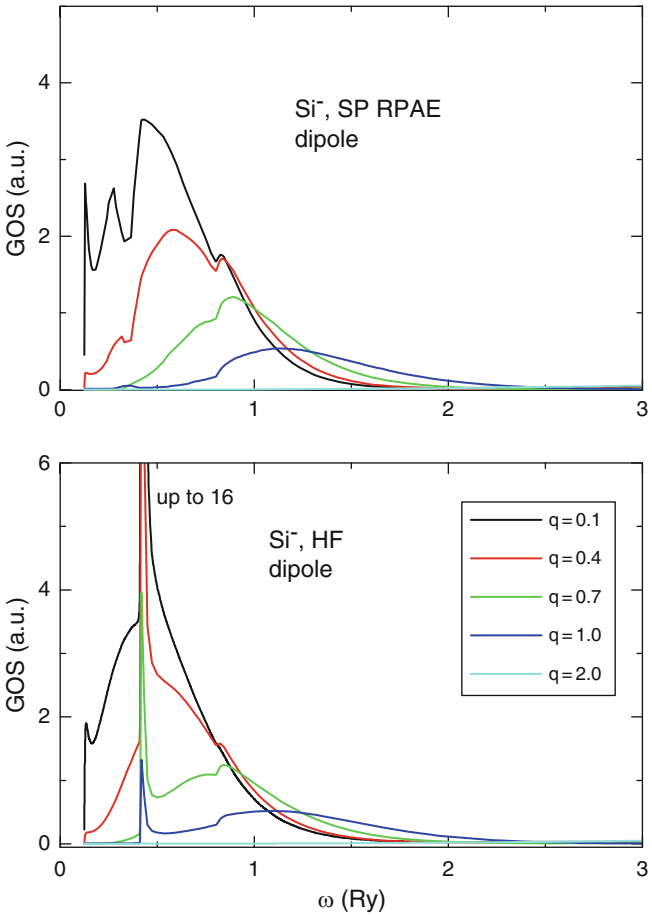

Fig. 4.294_Si⁻_e2 Density of dipole generalized oscillator strengths as function of the energy transferred to the ion at various q for Si^- in HF and SP RPAE

Figure 4.295_Si⁻_e3 gives the density of quadrupole GOSes for Si^- in HF and SP RPAE as functions of the energy transferred to the ion at various q. With growth of q a distinct maximum is formed, which becomes broader and lower, moving to higher ω.

Figures 4.296–4.298 (N) show the results of calculations for N atom.

Figure 4.296_N_e1 demonstrates the density of monopole GOSes for N in SP HF and SP RPAE as functions of the energy transferred to the atom at various q. "Jumps" in GOSes are at ionization thresholds. With growth of q GOSes at given ω increase.

Figure 4.297_N_e2 contains the density of dipole GOSes for N in HF and SP RPAE as a function of the energy transferred to the atom at various q. "Jumps" in GOSes are reflections of ionization thresholds. As it is rather typical for GOSes,

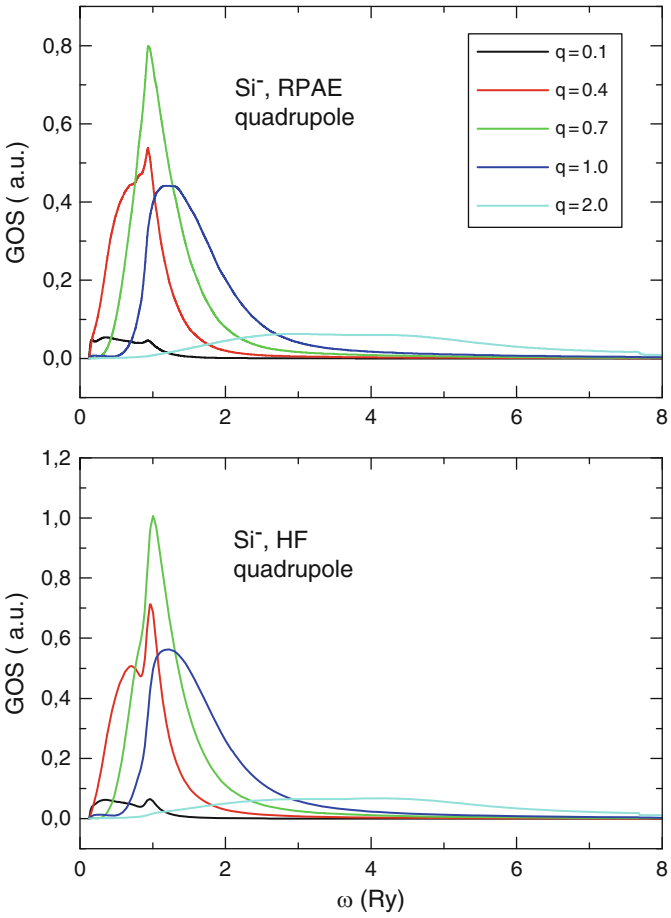

Fig. 4.295_Si⁻_e3 Density of quadrupole generalized oscillator strengths as function of the energy transferred to ion at various q for Si^- ion in HF and SP RPAE

the maximum with growth of q is displaced aside big transferred energies. As usual, dipole GOSes are about an order of magnitude bigger than the monopole (see Fig. 4.296_N_e1) and quadrupole (see Fig. 4.298_N_e3) GOSes. Contrary to monopole and quadrupole GOSes, dipole GOSes decrease with growth of q.

Figure 4.298_N_e3 gives the density of quadrupole GOSes for N in HF and SP RPAE as functions of the energy transferred to the atom at various q. "Jumps" in GOSes are at ionization thresholds. With q growing, GOSes at given ω increase.

Figures 4.299–4.301 (P) show the results of calculations for P atom.

Figure 4.299_P_e1 offers the density of monopole GOSes for P in HF and SP RPAE as function of the energy transferred to the atom at various q. With growth of q the picture of GOSes behavior as functions of ω becomes simpler and a single remaining maximum moves to higher energies with growth of q. "Jumps" in GOSes are at ionization thresholds.

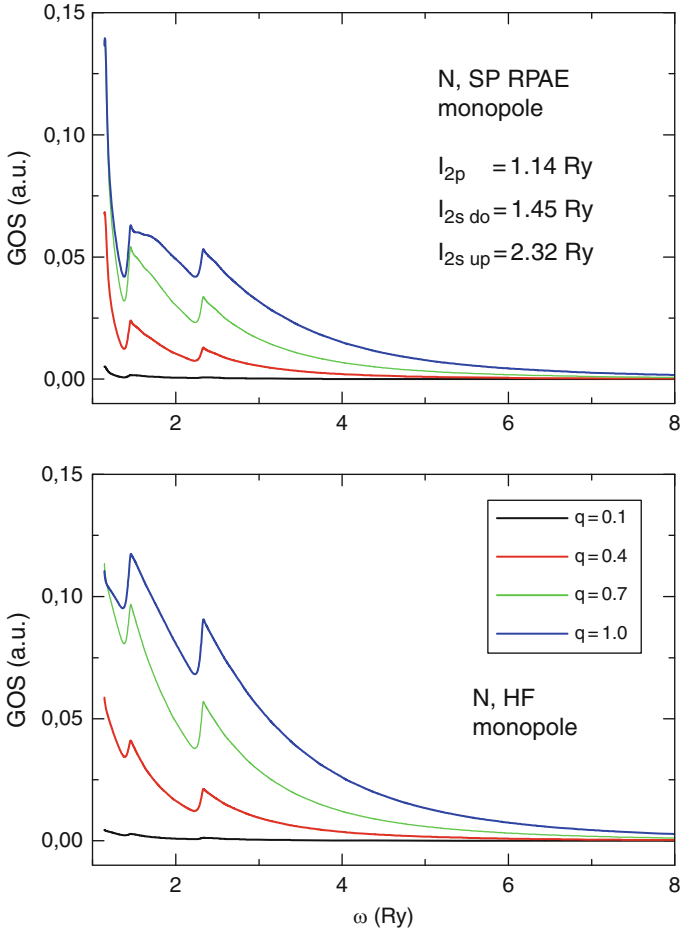

Fig. 4.296_N_e1 Density of monopole generalized oscillator strengths as function of the energy transferred to ion at various q for N atom in HF and SP RPAE

Figure 4.300_P_e2 represents the density of dipole GOSes for P in HF and SP RPAE as functions of the energy transferred to the atom at various q. "Jumps" in GOSes are reflections of ionization thresholds. Under the influence of electronic correlations there appears a specific two-maxima structure, which relative strength varies with growth of q. Dipole GOSes are higher than monopole and octupole GOSes approximately by the order of magnitude (see Figs. 4.299_P_e1 and 4.301_P_e3).

Figure 4.301_P_e3 gives the density of quadrupole GOSes for P in HF and SP RPAE as function of the energy transferred to the atom at various q. The role of correlations is insignificant. With growth of q the maximum in GOSes at first starts to increase and then decreases.

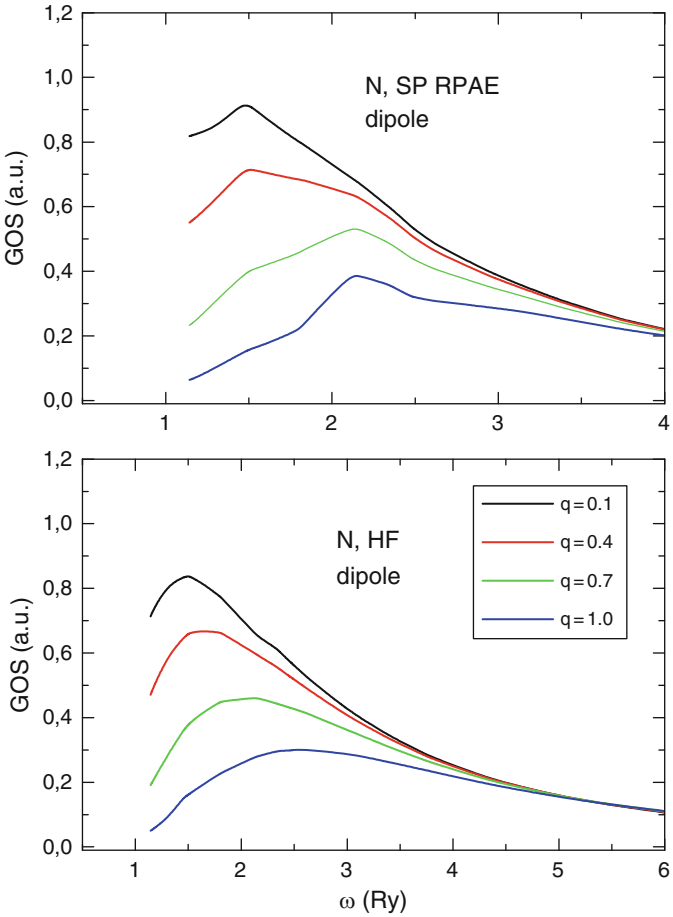

Fig. 4.297_N_e2 Density of dipole generalized oscillator strengths as function of the energy transferred to ion at various q for N atom in HF and SP RPAE

4.6 Ions of Group VII Elements of the Periodic Table

In this section, the results of our calculations of total and partial cross-sections of elastic electron scattering on a negative ion of fluorine $F^-(2s^2, 2p^6)$ are presented in HF and with account of polarization interaction in the simplified random phase approximation with exchange SRPAE (see Sects. 3.3 and 3.4 and [AICC]). In formation of polarization interaction, the virtual and real excitations of $2s^2$, $2p^6$ electrons are taken into account. In SRPAE s-, p-, d-, f-phases of scattering are calculated. The generalized oscillator strengths (GOSes) with account of RPAE correlations $4d$-, $5s$-, $5p$-electrons in I^- $(4d^{10}, 5s^2, 5p^6)$ ion are presented.

Figures 4.302–4.305 (F^-) show the results of calculations for F^- negative ion.

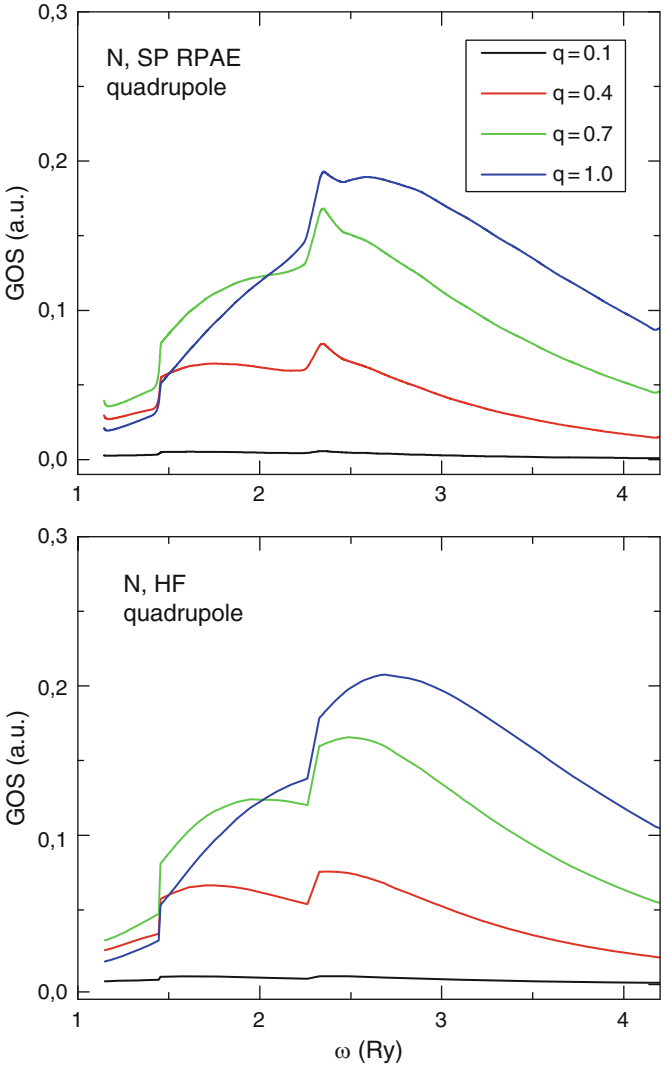

Fig. 4.298_N_e3 Density of quadrupole generalized oscillator strengths as function of the energy transferred to ion at various q for N atom in HF and SP RPAE

Figure 4.302_F⁻_a1 contains the contribution of s-, p-, d-, f-incoming electron waves to the cross-section of elastic (in HF and SRPAE) and inelastic (in SRPAE) electron scattering on F^- ion. At 5 eV there is a small maximum connected to the resonance in d-wave. Note that the total cross-section diverges.

Figure 4.303_F⁻_b1 depicts the contributions of partial s, p, d, f-waves to cross-section of elastic electron scattering on F^- in SRPAE. In p-, d-, f-waves, there is two maxima in cross-sections. All partial contributions diverge at $E \to 0$.

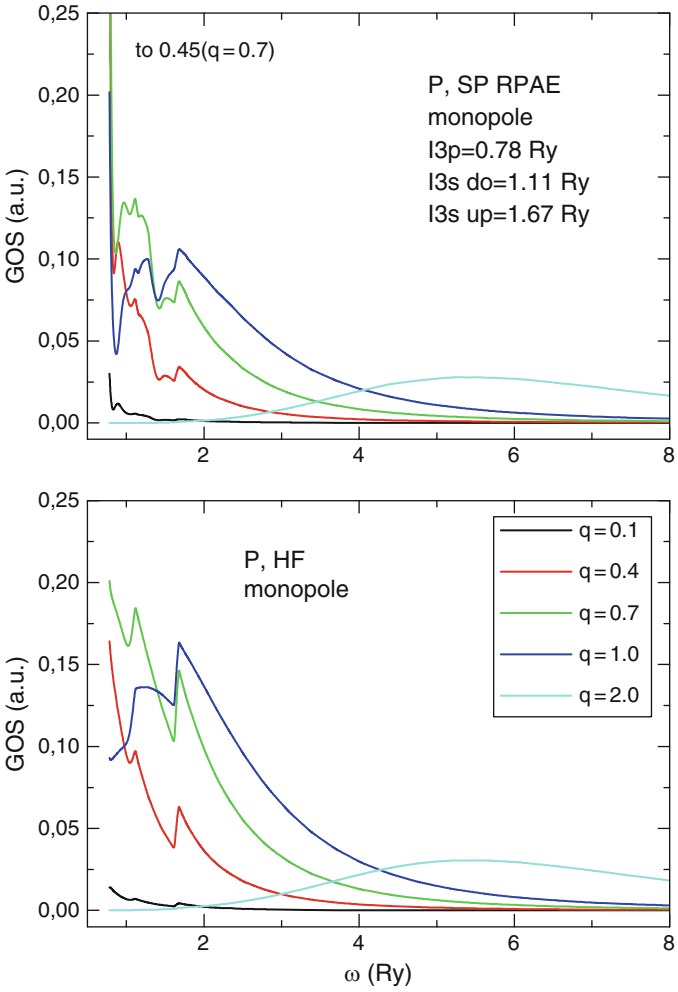

Fig. 4.299_P_e1 Density of monopole generalized oscillator strengths as function of the energy transferred to the atom P at various q in HF and SP RPAE

Figure 4.304_F^-_d1 gives the phases of partial s-, p-, d-, f-waves in electron scattering on F^- ion in SRPAE. As it should be, all Coulomb phases diverge at $E = 0$.

Figure 4.305_F^-_d2 contains the phases of partial waves in electron scattering on F^- ion in HF. The role of polarization interaction is considerable.

Figures 4.306–4.308 (I^-) show the results of calculations for I^- ($4d^{10}, 5s^2, 5p^6$) negative ion.

Figure 4.306_I^-_e1 offers the density of monopole GOSes for I^- in HF and RPAE as function of the energy transferred to the ion at various q. Displacement

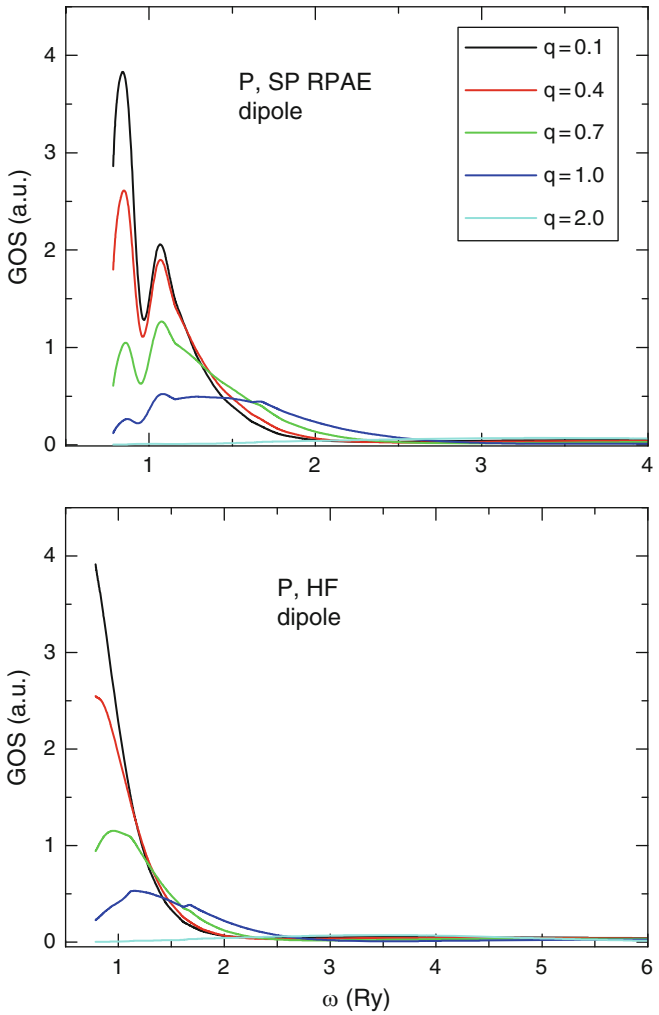

Fig. 4.300_P_e2 Density of dipole generalized oscillator strengths as function of the energy transferred to the atom at various q for P in HF and SP RPAE

of maxima with growth of q to higher energies is visible. The smallest value of GOSes is achieved already at $q = 2$, where it is almost zero up to $\omega \approx 4$ Ry.

Figure 4.307_I⁻_e2 gives the density of dipole GOSes for I^- in HF and RPAE as function of the energy transferred to the ion at various q. Upper curves are dominated by two resonances connected to ionization of multielectronic outer $5p$- and intermediate $4d$ subshells. Both maxima are rather powerful and look as two, instead of one, as in Xe, a huge resonance. Dipole GOSes, as usual, approximately by an order are bigger than monopole (Fig. 4.306_I⁻_e1) and quadrupole (Fig. 4.308_I⁻_e3).

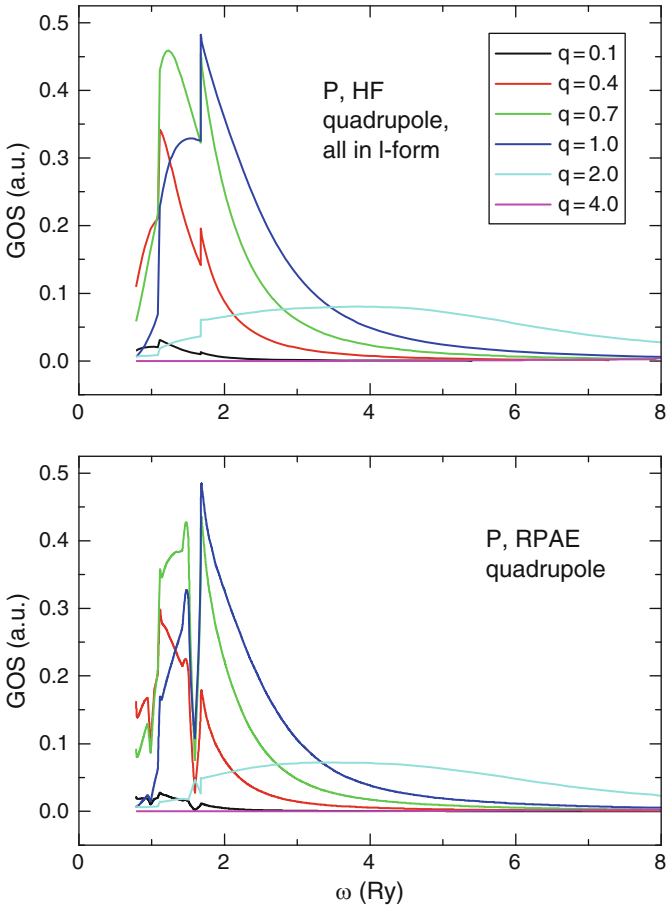

Fig. 4.301_P_e3 Density of quadrupole generalized oscillator strengths as function of the energy transferred to the atom P at various q in HF and SP RPAE

Figure 4.308_I⁻_e3 represents the density of quadrupole GOSes for I^- in HF and RPAE as function of the energy transferred to the ion at various q. Here with increase of q GOSes at first grow at low energies and then become functions with two and even three maximums. At $q > 0.7$ GOSes start to decrease, and the main maximum becomes broader and lower.

4.7 Endohedral A@C_{60} Atoms

In this section, we present our results for differential GOSes, their dipole and nondipole parameters of angular anisotropy for outer and intermediate subshells of some endohedral atoms A@C_{60} that means an atom A, stuffed inside a fullerenes shell. If reflection is considered as weak, the result is denoted as RPAE. If the

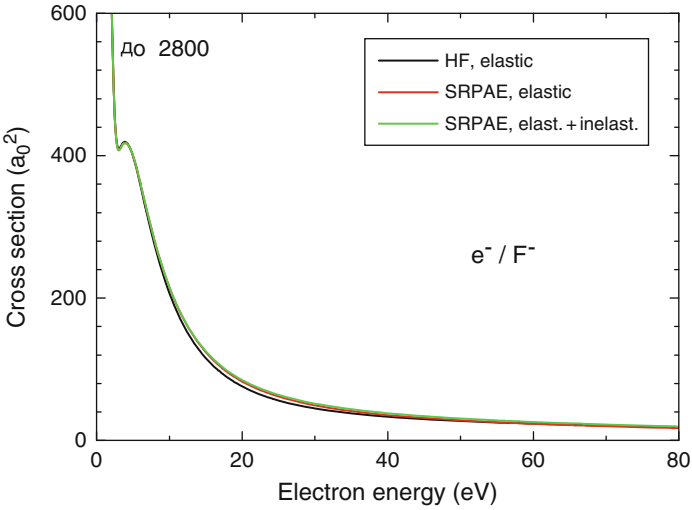

Fig. 4.302_F⁻_a1 Contribution of *s*-, *p*-, *d*-, and *f*-phases to the cross-section of elastic (in HF and SRPAE) and inelastic (in SRPAE) electron scattering on F^- ion

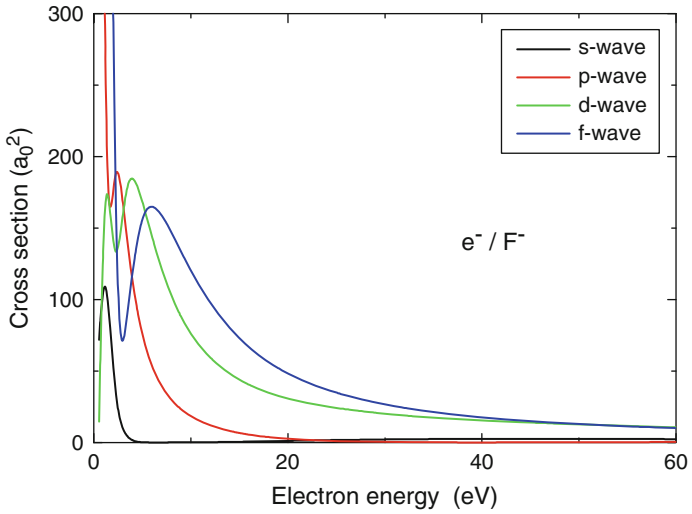

Fig. 4.303_F⁻_b1 Contributions of partial waves to cross-section of elastic electron scattering on F^- ion in SRPAE

reflection is strong and C_{60} potential is approximated by a zero thickness potential, the results are obtained in FRPAE. Inclusion of polarization of C_{60} is denoted as GFRPAE.

Having in mind to illustrate qualitatively the effect of the fullerenes shell C_N upon the photoionization of the atom A, we choose the best studied and in this

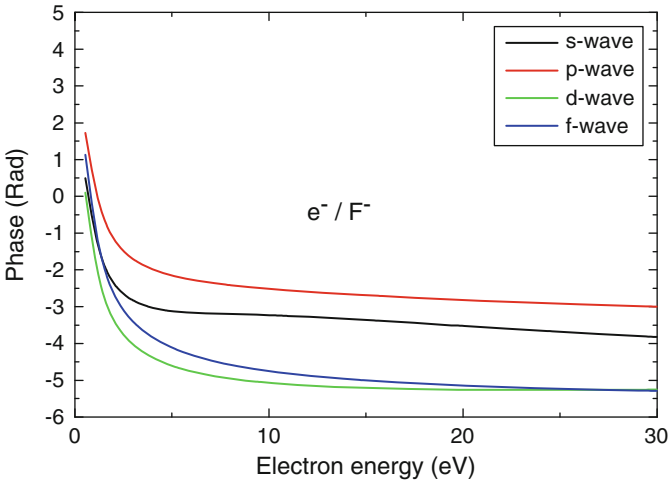

Fig. 4.304_F⁻_d1 Phases of partial waves in electron scattering on F^- ion in SRPAE

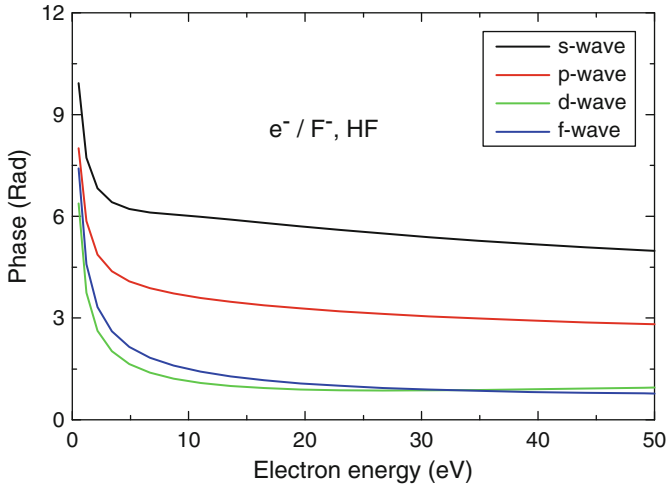

Fig. 4.305_F⁻_d2 Phases of partial waves in electron scattering on F^- ion in HF

sense most popular fullerene C_{60}. It consist of 60 carbon atoms with totally 240 electrons (four from each atom) being collectivized. The data are obtained for the following endohedral atoms $Ar@C_{60}$ $3s^2 3p^6$ and $Xe@C_{60}$ $4d^{10}5s^2 5p^6$. Formulas used in order to receive the data are mentioned at the beginning of this chapter, in Sect. 4.1.

Figure 4.309 (C_{60}) shows the results of calculations for C_{60}.

Figure 4.309_C_{60}_n1, similar to Fig. 2.351_C_{60}_g1, contains the absolute value of the amplitude $|G(\omega)|$ of the electromagnetic radiation polarization factor by the C_{60}

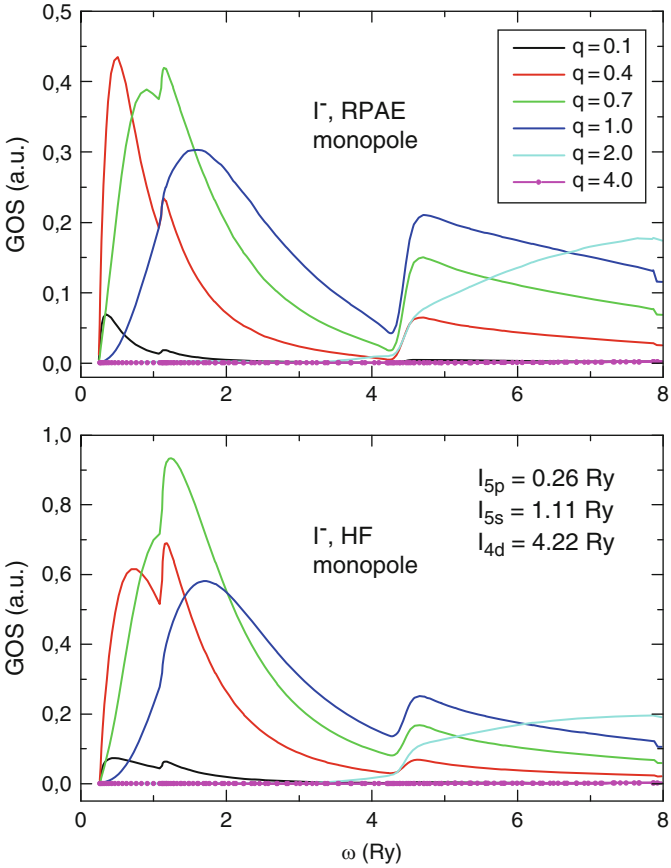

Fig. 4.306_I⁻_e1 Density of monopole generalized oscillator strengths as function of the energy transferred to ion at various q for I^- in HF and RPAE

electron shell, the polarization factor $S(\omega) = |G(\omega)|^2$ and the phase $\eta^{\mathrm{d}} \equiv \arg G(\omega)$. The arrows mark the thresholds of outer np and ns subshells of noble gas atoms Ar and Xe. Quite peculiar is the "camel"-type shape. This is a direct consequence of the frequency dependence of the C_{60} polarizability.

Figures 4.310–4.323 ($Ar@C_{60}$) show the results of calculations for $Ar@C_{60}$.

Figure 4.310_Ar@C_{60}_n1 presents the weighted GOSes differential in emission angle of the knocked-out electron (3.123) at magic angle $P_2(\cos\theta_{\mathrm{m}}) = 0$ of $3p$ subshell for $Ar@C_{60}$ at $q = 0.1$ in FRPAE, GFRPAE, and free Ar (see Fig. 4.90_Ar_m2). The amplification due to polarization of fullerenes shell is huge. Oscillations due to reflection by this shell are noticeable.

Figure 4.311_Ar@C_{60}_n2 depicts the GOSes differential in emission angle of the knocked-out electron (3.123) at magic angle $P_2(\cos\theta_{\mathrm{m}}) = 0$ of $3p$ subshell for $Ar@C_{60}$ at $q = 1.1$ in FRPAE, GFRPAE. The same value for Ar is shown in

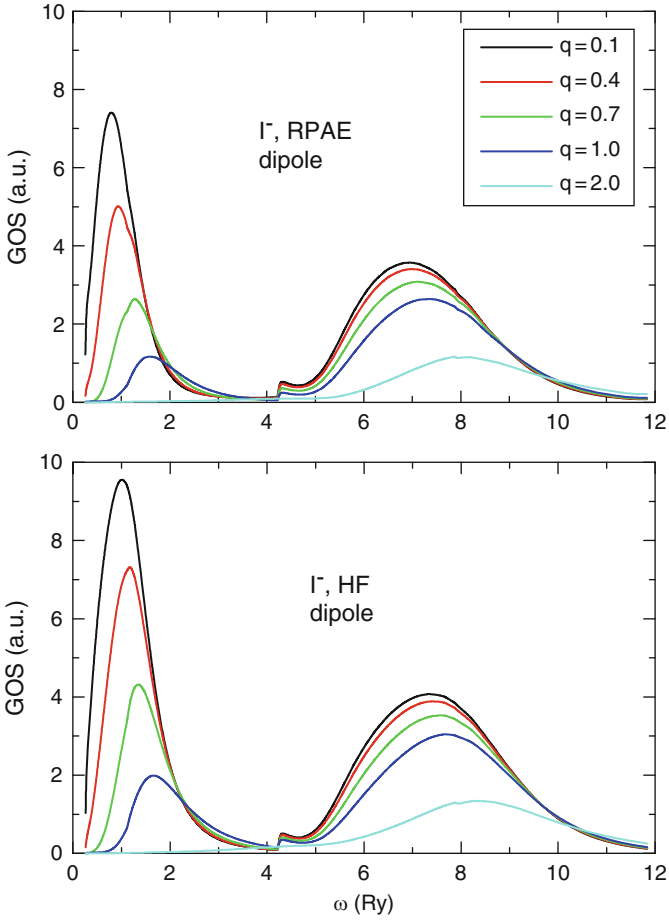

Fig. 4.307_I⁻_e2 Density of dipole generalized oscillator strengths as function of the energy transferred to ion at various q for I^- in HF and RPAE

Fig. 4.90_Ar_m2. Oscillations are due to reflection of knocked-out electron by the fullerenes shell. Its polarization above 4 Ry is weak.

Figure 4.312_Ar@C_{60}_n3 demonstrates the angular anisotropy parameter A^{AC}_{3p1} of knocked-out electrons from $3p$ subshell of Ar@C_{60} in fast projectile–atom collision, given by (3.124) in FRPAE and GFRPAE at $q = 0.1$ as functions of ω. The same value for Ar is shown in Fig. 4.91_Ar_m3. The main structure is the same as in the free atom.

Figure 4.313_Ar@C_{60}_n4 shows the angular anisotropy parameter A^{AC}_{3p2} of knocked-out electrons from $3p$ subshell of Ar@C_{60} in fast projectile–atom collision, given by (3.124) in RPAE, FRPAE, and GFRPAE at $q = 0.1$ as functions of ω. The same value for Ar is shown in Fig. 4.91_Ar_m3. Oscillations are due

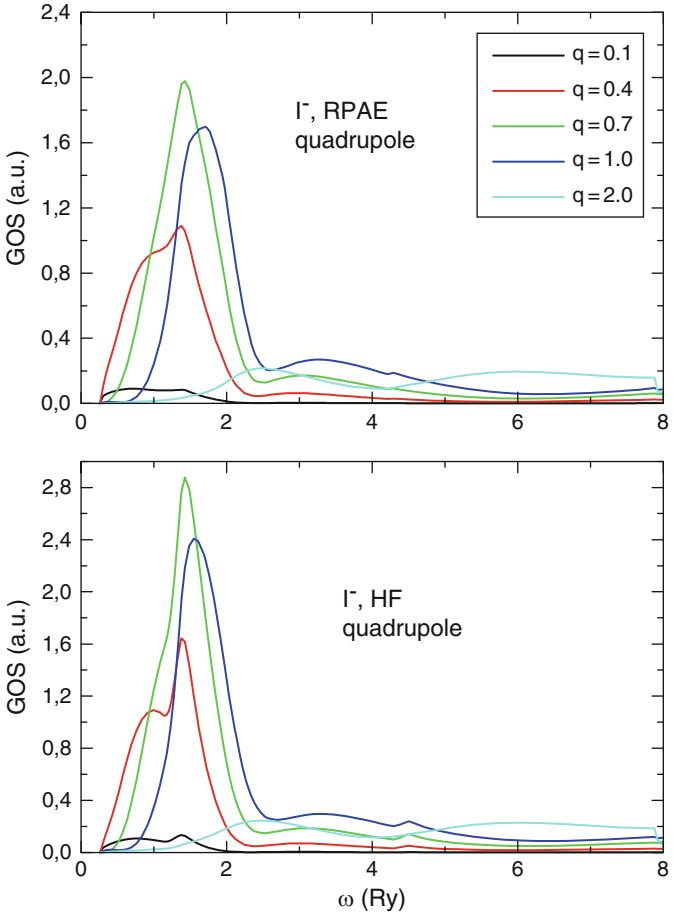

Fig. 4.308_I⁻_e3 Density of quadrupole generalized oscillator strengths as function of the energy transferred to ion at various q for I^- in HF and RPAE

to reflections that at $\omega < 3$ Ry are strongly amplified by the polarization of the fullerenes shell by the fast incoming electron. Note that A^{AC}_{3p2} is several times smaller than A^{AC}_{3p1}.

Figure 4.314_Ar@C_{60}_n5 gives the angular anisotropy parameter A^{AC}_{3p3} of knocked-out electrons from $3p$ subshell of Ar@C_{60} in fast projectile–atom collision, given by (3.124) in FRPAE and GFRPAE at $q = 0.1$ as functions of ω. The same value for Ar is shown in Fig. 4.91_Ar_m3. Effects of the fullerenes shell are noticeable. Note that A^{AC}_{3p3} is several times smaller than A^{AC}_{3p2}.

Figure 4.315_Ar@C_{60}_n6 displays the angular anisotropy parameter A^{AC}_{3p4} of knocked-out electrons from $3p$ subshell of Ar@C_{60} in fast projectile–atom collision, given by (3.124) in FRPAE and GFRPAE at $q = 0.1$ as functions

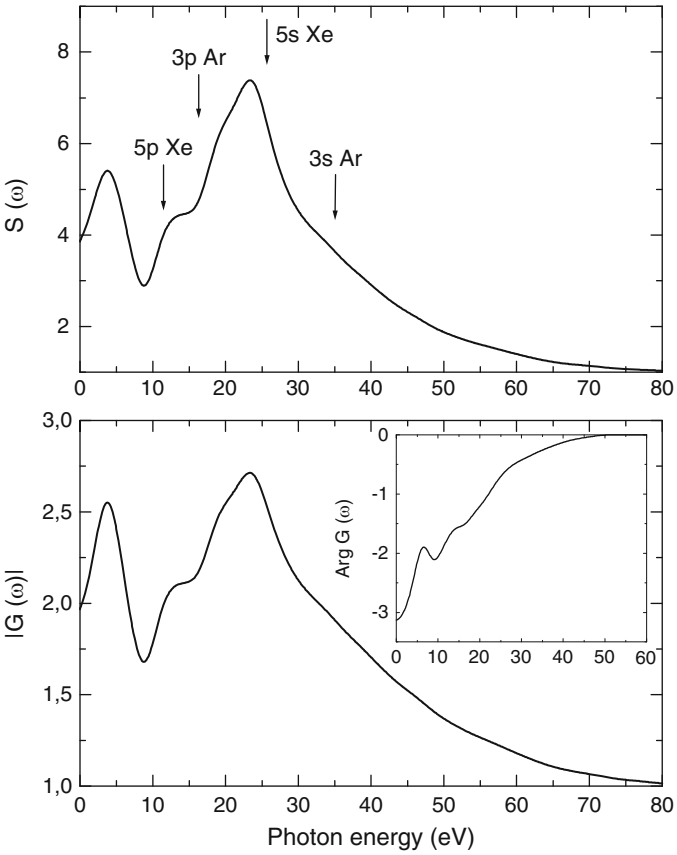

Fig. 4.309_C_{60}_n1 Polarization factor of the electromagnetic radiation by the electron shell of C_{60} $S(\omega) \equiv |G(\omega)|^2$, absolute value of its amplitude $\tilde{G}^{\mathrm{d}}(\omega) \equiv |G(\omega)|$ and phase $\eta^{\mathrm{d}} \equiv \arg G(\omega)$. The arrows mark the thresholds of Ar $3p$ and $3s$ and Xe $5p$, $5s$, and $4d$ subshells

of ω. The same value for free Ar is shown in Fig. 4.91_Ar_m3. As shown in Fig. 4.314_Ar@C_{60}_n5, the effects of the fullerenes shell are noticeable. Note that A^{AC}_{3p4} is several times smaller than A^{AC}_{3p3}.

Figure 4.316_Ar@C_{60}_n7 represents the weighted GOSes differential in emission angle of the knocked-out electron (3.123) at magic angle $P_2(\cos\theta_{\mathrm{m}}) = 0$ of $3s$ subshell for Ar@C_{60} at $q = 0.1$ in FRPAE, GFRPAE. The same value for free Ar is shown in Fig. 4.94_Ar_m6. Effect of the fullerenes shell is quite small, except a prominent increase in GFRPAE at about 4 Ry.

Figure 4.317_Ar@C_{60}_n8 demonstrates the GOSes differential in emission angle of the knocked-out electron (3.122, 4) at magic angle $P_2(\cos\theta_{\mathrm{m}}) = 0$ of $3s$ subshell for Ar@C_{60} at $q = 1.1$ in FRPAE, GFRPAE. The same value for Ar in RPAE is shown in Fig. 4.94_Ar_m6. Note that at such considerable q reflection prominently decreases, not increase, the GOS, giving it as usual oscillating structure.

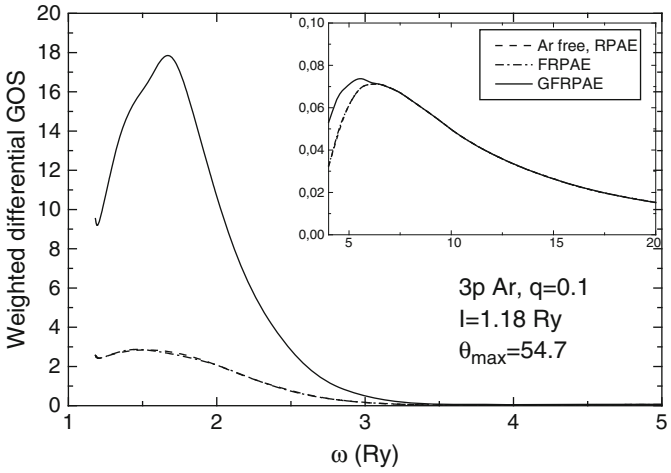

Fig. 4.310_Ar@C_{60}_n1 Weighted generalized oscillator strength differential in emission angle of the knocked-out electron (3.124) at magic angle $P_2(\cos\theta_m) = 0$ of $3p$ subshell for Ar@C_{60} at $q = 0.1$ in FRPAE, GFRPAE, and free Ar (see Fig. 4.90_Ar_m2)

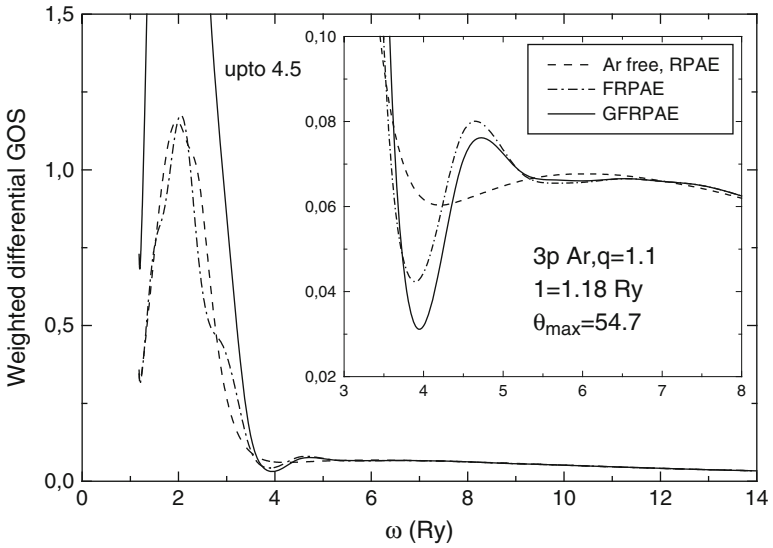

Fig. 4.311_Ar@C_{60}_n2 Generalized oscillator strength differential in emission angle of the knocked-out electron (3.124) at magic angle $P_2(\cos\theta_m) = 0$ of $3p$ subshell for Ar@C_{60} at $q = 1.1$ in FRPAE, GFRPAE and free Ar in RPAE (see Fig. 4.90_Ar_m2)

Figure 4.318_Ar@C_{60}_n9 shows the angular anisotropy parameter A^{AC}_{3s1} of knocked-out electrons from $3s$ subshell of Ar@C_{60} in fast projectile–atom collision, given by (3.124) in FRPAE and GFRPAE at $q = 0.1$ as functions of ω. The same value for Ar in RPAE is shown in Fig. 4.95_Ar_m7. Particularly important is

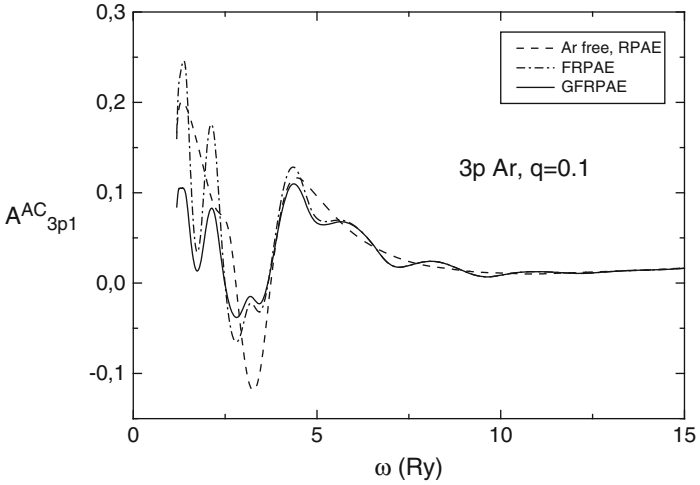

Fig. 4.312_Ar@C_{60}_n3 Angular anisotropy parameter A^{AC}_{3p1} of knocked-out electrons from $3p$ subshell of Ar@C_{60} in fast projectile–atom collision, given by (3.124) in FRPAE and GFRPAE at $q = 0.1$ and free Ar in RPAE (see Fig. 4.91_Ar_m3) as functions of ω

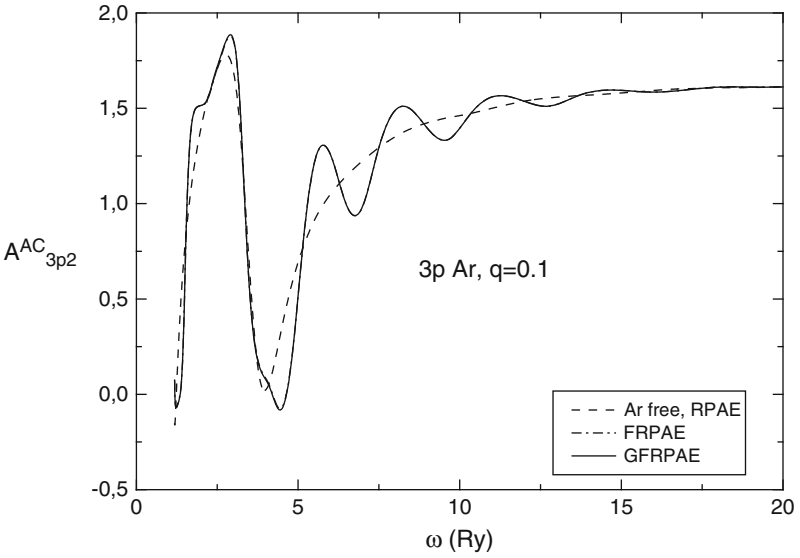

Fig. 4.313_Ar@C_{60}_n4 Angular anisotropy parameter A^{AC}_{3p2} of knocked-out electrons from $3p$ subshell of Ar@C_{60} in fast projectile–atom collision, given by (3.124) in FRPAE and GFRPAE at $q = 0.1$ and free Ar in RPAE (see Fig. 4.91_Ar_m3)

reflection of knocked-out electrons by the fullerenes shell. GFRPAE enhances FRPAE oscillations moderately.

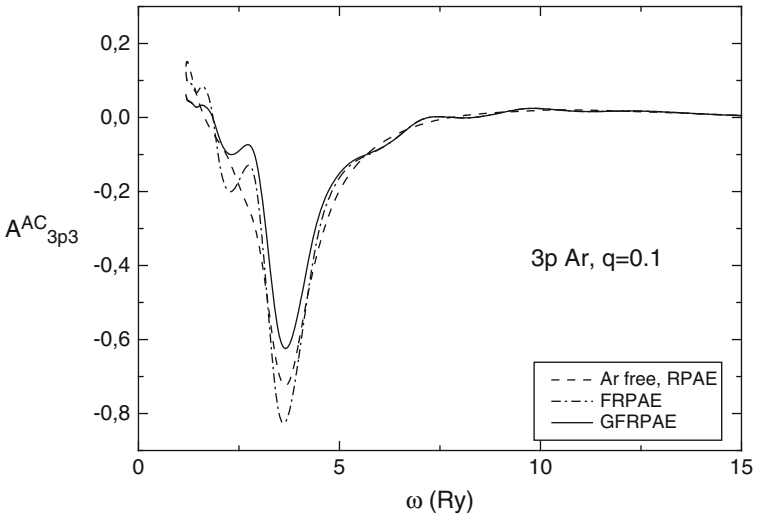

Fig. 4.314_Ar@C_{60}_n5. Angular anisotropy parameter A^{AC}_{3p3} of knocked-out electrons from $3p$ subshell of Ar@C_{60} in fast projectile–atom collision, given by (3.124) in FRPAE and GFRPAE at $q = 0.1$ and free Ar (see Fig. 4.91_Ar_m3)

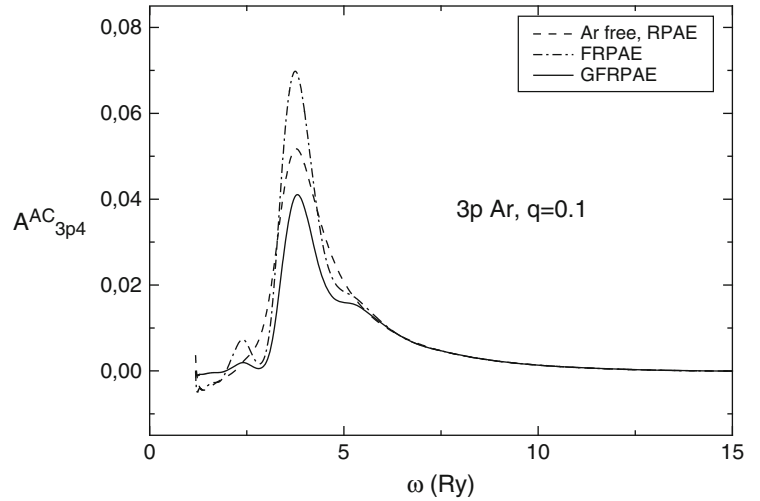

Fig. 4.315_Ar@C_{60}_n6 Angular anisotropy parameter A^{AC}_{3p4} of knocked-out electrons from $3p$ subshell of Ar@C_{60} in fast projectile–atom collision, given by (3.124) in FRPAE and GFRPAE at $q = 0.1$ and free Ar (see Fig. 4.91_Ar_m3)

Figure 4.319_Ar@C_{60}_n10 gives the angular anisotropy parameter A^{AC}_{3s2} of knocked-out electrons from $3s$ subshell of Ar@C_{60} in fast projectile–atom collision, given by (3.124) in FRPAE and GFRPAE at $q = 0.1$ as functions of ω. The same

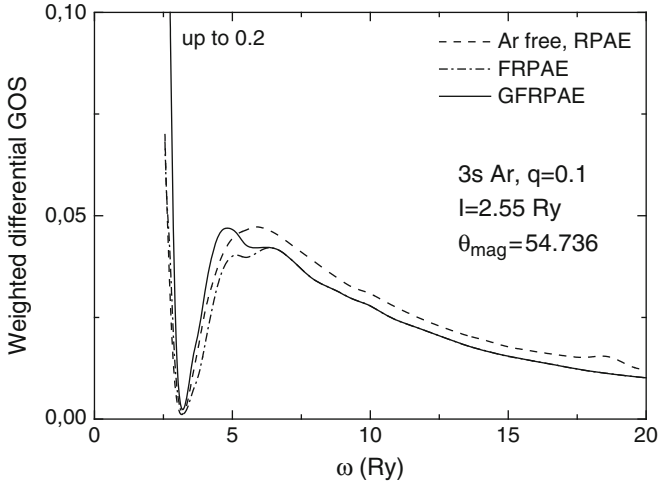

Fig. 4.316_Ar@C_{60}_n7 Weighted generalized oscillator strength differential in emission angle of the knocked-out electron (3.73b and 3.122) at magic angle $P_2(\cos\theta_m) = 0$ of $3s$ subshell for Ar@C_{60} at $q = 0.1$ in FRPAE and GFRPAE and free Ar in RPAE (see Fig. 4.94_Ar_m6)

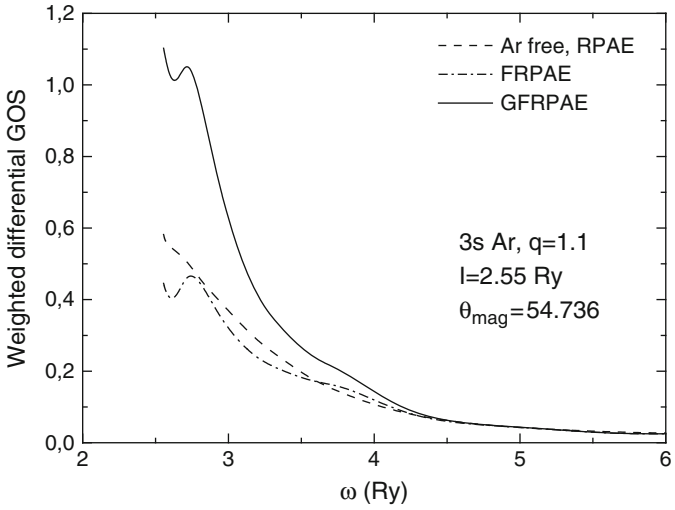

Fig. 4.317_Ar@C_{60}_n8 Generalized oscillator strength differential in emission angle of the knocked-out electron (3.124) at magic angle $P_2(\cos\theta_m) = 0$ of $3s$ subshell for Ar@C_{60} at $q = 1.1$ in FRPAE and GFRPAE and free Ar in RPAE (see Fig. 4.94_Ar_m6)

value for Ar in RPAE is shown in Fig. 4.95_Ar_m7. Role of fullerenes shell is small. Note that A^{AC}_{3s2} is several times bigger than A^{AC}_{3s1}.

Figure 4.320_Ar@C_{60}_n11 displays the angular anisotropy parameter A^{AC}_{3s3} of knocked-out electrons from $3s$ subshell of Ar@C_{60} in fast projectile–atom collision,

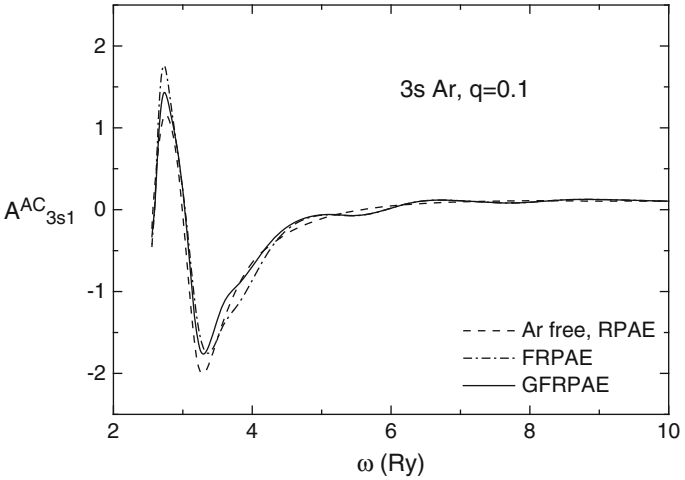

Fig. 4.318_Ar@C_{60}_n9 Angular anisotropy parameter A^{AC}_{3s1} of knocked-out electrons from 3s subshell of Ar@C_{60} in fast projectile–atom collision, given by (3.124) in FRPAE and GFRPAE at $q = 0.1$ and free Ar in RPAE (see Fig. 4.95_Ar_m7), as functions of ω

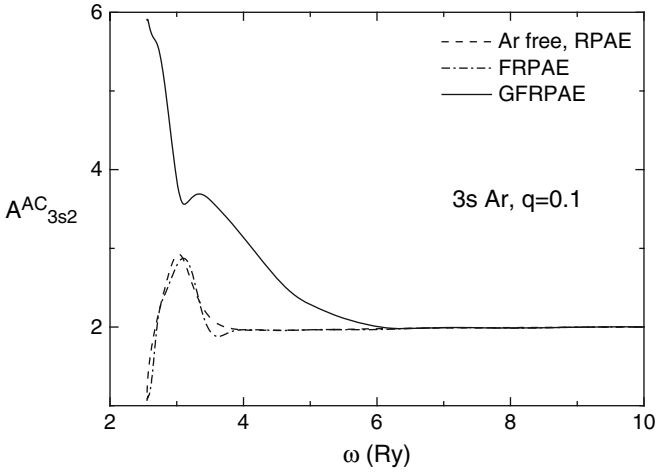

Fig. 4.319_Ar@C_{60}_n10 Angular anisotropy parameter A^{AC}_{3s2} of knocked-out electrons from 3s subshell of Ar@C_{60} in fast projectile–atom collision, given by (3.124) in FRPAE and GFRPAE at $q = 0.1$ and free Ar in RPAE (see Fig. 4.95_Ar_m7), as functions of ω

given by (3.124) in RPAE, FRPAE, and GFRPAE at $q = 0.1$ as functions of ω. The same value for Ar in RPAE is shown in Fig. 4.95_Ar_m7. The GRPAE effects amplify strong enough the FRPAE data, the latter having similar shape to that for isolated atom. Note that A^{AC}_{3s3} is of the same order of magnitude as A^{AC}_{3s2}.

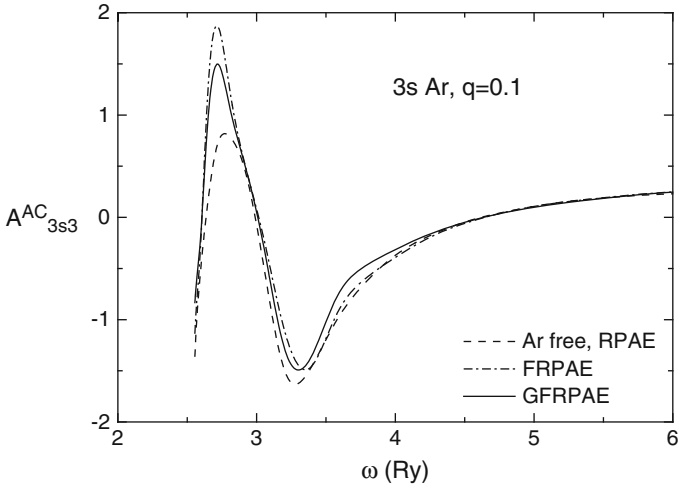

Fig. 4.320_Ar@C_{60}_n11 Angular anisotropy parameter A^{AC}_{3s3} of knocked-out electrons from 3s subshell of Ar@C_{60} in fast projectile–atom collision, given by (3.124) in FRPAE and GFRPAE at $q = 0.1$ and free Ar in RPAE (see Fig. 4.95_Ar_m7), as functions of ω

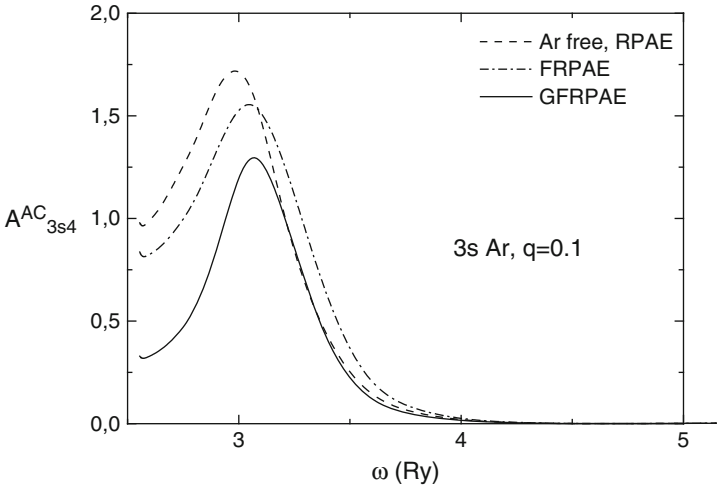

Fig. 4.321_Ar@C_{60}_n12 Angular anisotropy parameter A^{AC}_{3s4} of knocked-out electrons from 3s subshell of Ar@C_{60} in fast projectile–atom collision, given by (3.124) in FRPAE and GFRPAE at $q = 0.1$ and free Ar in RPAE (see Fig. 4.95_Ar_m7), as functions of ω

Figure 4.321_Ar@C_{60}_n12 presents the angular anisotropy parameter A^{AC}_{3s4} of knocked-out electrons from 3s subshell of Ar@C_{60} in fast projectile–atom collision, given by (3.124) in FRPAE and GFRPAE at $q = 0.1$ as functions of ω. The same

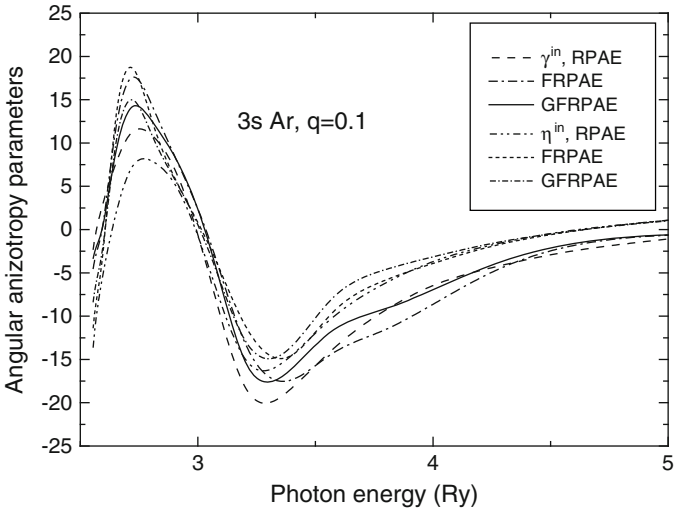

Fig. 4.322_Ar@C_{60}_n13 Angular anisotropy nondipole parameters of knocked-out electrons in fast projectile–atom collision in the optical limit given by (3.125) at $q = 0.1$ for $3s$ subshell of Ar@C_{60} and free Ar in RPAE (see Fig. 4.97_Ar_m9)

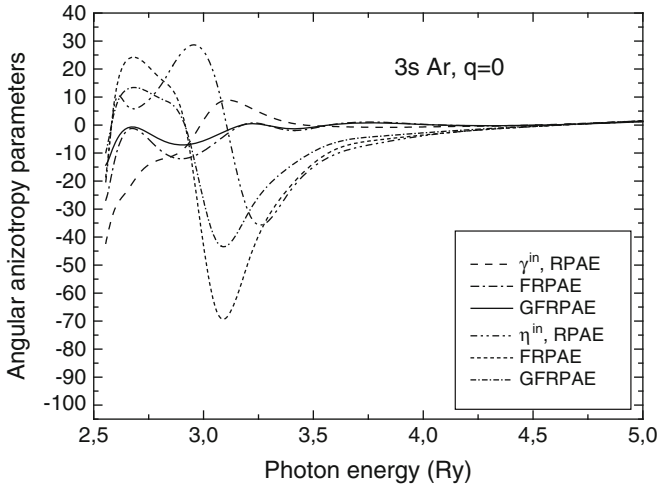

Fig. 4.323_Ar@C_{60}_n14 Angular anisotropy nondipole parameters of knocked-out electrons in fast projectile–atom collision in the optical limit given by (3.125) at $q = 0$ for $3s$ subshell of Ar@C_{60} and free Ar in RPAE (see Fig. 4.97_Ar_m9)

value for Ar is shown in Fig. 4.95_Ar_m7. The GFRPAE values are by a factor of 2 bigger than results for free atom and results in FRPAE.

Figure 4.322_Ar@C_{60}_n13 demonstrates the angular anisotropy nondipole parameters of knocked-out electrons in fast projectile–atom collision in the optical

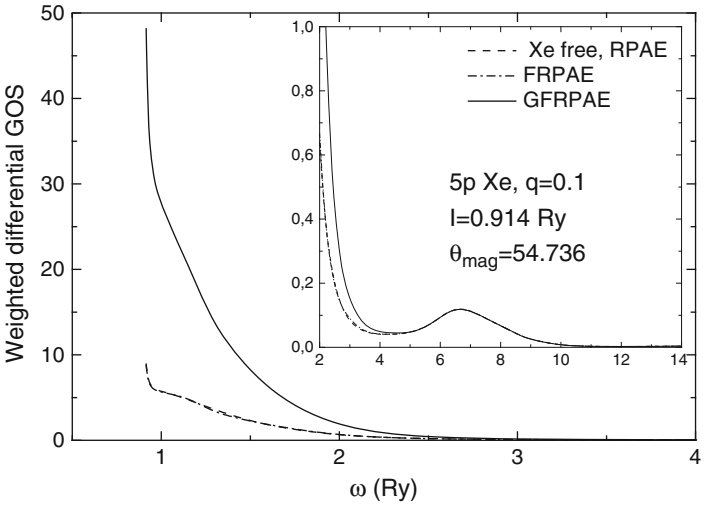

Fig. 4.324_Xe@C_{60}_n1 Weighted generalized oscillator strength differential in emission angle of the knocked-out electron (3.73 and 3.123) at magic angle $P_2(\cos\theta_m) = 0$ of $5p$ subshell for Xe@C_{60} at $q = 0.1$ in FRPAE, GFRPAE and free Xe in RPAE

limit given by (3.125) at $q = 0.1$ for $3s$ subshell of Ar@C_{60}. The same values for Ar in RPAE are shown in Fig. 4.97_Ar_m9.

Figure 4.323_Ar@C_{60}_n14 contains the angular anisotropy nondipole parameters of knocked-out electrons in fast projectile–atom collision in the optical limit given by (3.125) at $q = 0$ for $3s$ subshell of Ar@C_{60} and free Ar in RPAE (see Fig. 4.97_Ar_m9). The GFRPAE results are considerably different from both FRPAE and the free atom value in RPAE. The main variation is in the photon energy region $2.5 < \omega < 3.5$ Ry.

Figures 4.324–4.335 (Xe@C_{60}) show the results of calculations for Xe@C_{60}.

Figure 4.324_Xe@C_{60}_n1 contains the weighted GOSes differential in emission angle of the knocked-out electron (3.73 and 3.123) at magic angle $P_2(\cos\theta_m) = 0$ of $5p$ subshell for Xe@C_{60} at $q = 0.1$ in FRPAE, GFRPAE, and free Xe in RPAE. We see strong amplification of the weighted generalized oscillator strength due to polarization of the fullerenes shell under the action of the incoming photon beam.

Figure 4.325_Xe@C_{60}_n2 depicts the angular anisotropy parameter A^{AC}_{5p1} of knocked-out electrons from $5p$ subshell of Xe@C_{60} in fast projectile–atom collision, given by (3.124) in FRPAE, GFRPAE, and free Xe in RPAE at $q = 0.1$ as functions of ω. Note that nondipole parameter A^{AC}_{5p1} acquires only a small additional structure due to reflection, slightly amplified at low ω by polarization of the fullerenes shell—in GFRPAE.

Figure 4.326_Xe@C_{60}_n3 gives the angular anisotropy parameter A^{AC}_{5p2} of knocked-out electrons from $5p$ subshell of Xe@C_{60} in fast projectile–atom collision, given by (3.124) in FRPAE, GFRPAE, and free Xe in RPAE at $q = 0.1$

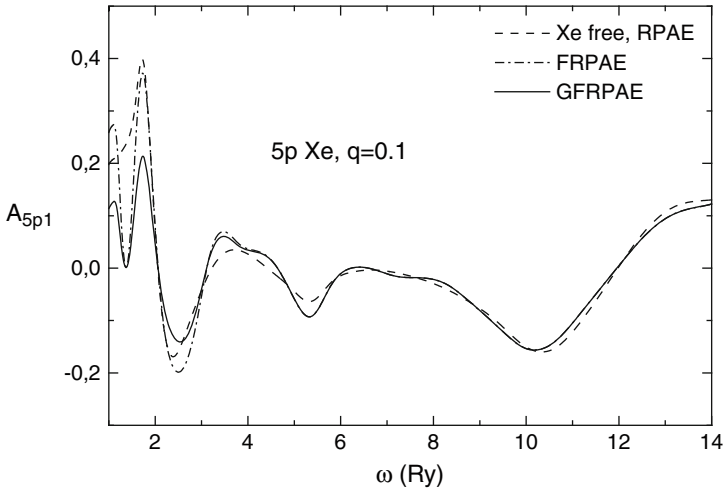

Fig. 4.325_Xe@C_{60}_n2 Angular anisotropy parameter A_{5p1}^{AC} of knocked-out electrons from $5p$ subshell of Xe@C_{60} in fast projectile–atom collision, given by (3.124) in FRPAE and GFRPAE at $q = 0.1$ and free Xe in RPAE, as functions of ω

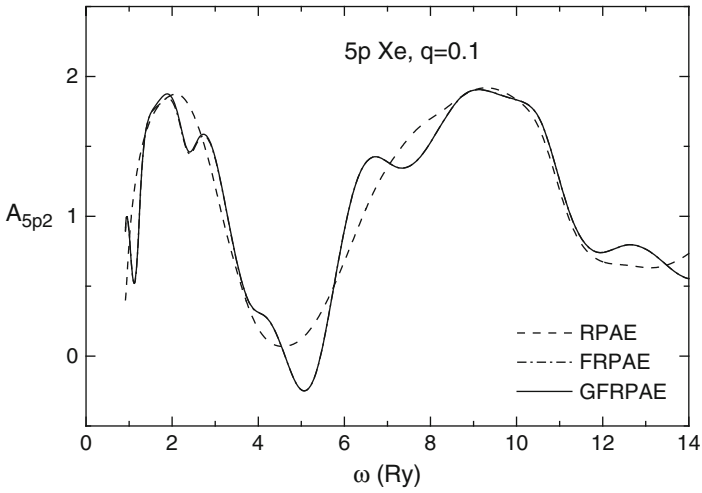

Fig. 4.326_Xe@C_{60}_n3 Angular anisotropy parameter A_{5p2}^{AC} of knocked-out electrons from $5p$ subshell of Xe@C_{60} in fast projectile–atom collision, given by (3.124) in FRPAE and GFRPAE at $q = 0.1$ and free Xe in RPAE, as functions of ω

as functions of ω. The parameter A_{5p2}^{AC} is by a factor of 10 smaller than A_{5p1}^{AC}. The effect of fullerene shell upon A_{5p2}^{AC} is quite big, particularly of GFRPAE.

Figure 4.327_Xe@C_{60}_n4 displays the angular anisotropy parameter A_{5p3}^{AC} of knocked-out electrons from $5p$ subshell of Xe@C_{60} in fast projectile–atom

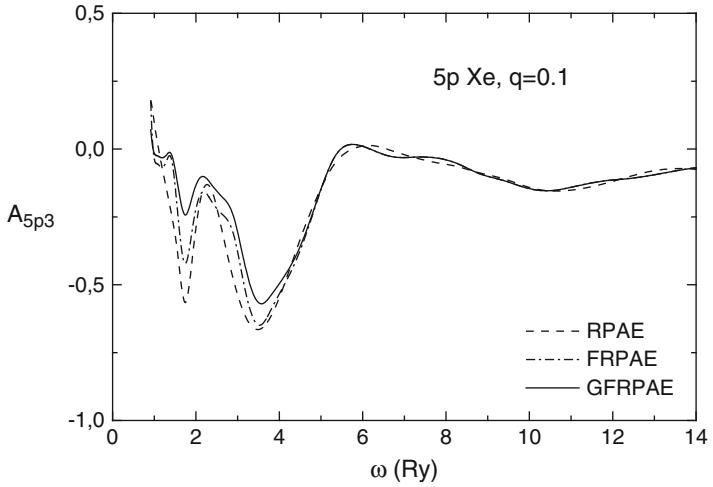

Fig. 4.327_Xe@C$_{60}$_n4 Angular anisotropy parameter A^{AC}_{5p3} of knocked-out electrons from $5p$ subshell of Xe@C$_{60}$ in fast projectile–atom collision, given by (3.124) in FRPAE and GFRPAE at $q = 0.1$ and free Xe in RPAE, as functions of ω

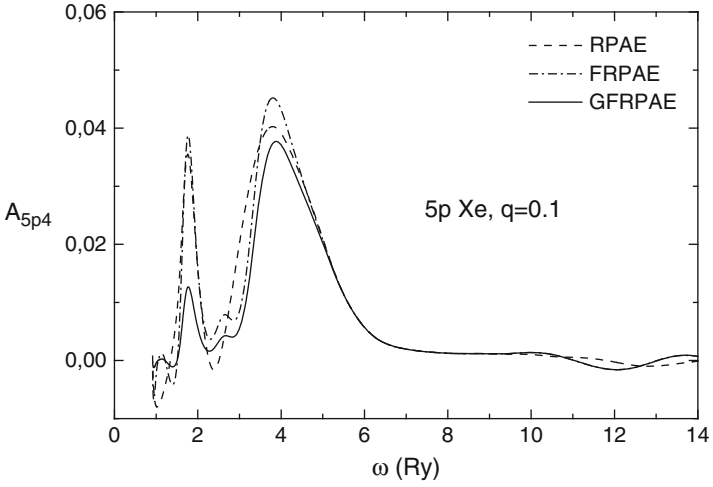

Fig. 4.328_Xe@C$_{60}$_n5 Angular anisotropy parameter A^{AC}_{5p4} of knocked-out electrons from $5p$ subshell of Xe@C$_{60}$ in fast projectile–atom collision, given by (3.124) in FRPAE and GFRPAE at $q = 0.1$ and free Xe in RPAE, as functions of ω

collision, given by (3.124) in FRPAE, GFRPAE, and free Xe in RPAE at $q = 0.1$ as functions of ω. The parameter A^{AC}_{5p3} is by a factor of 10 smaller than A^{AC}_{5p2}. Account of photoelectron reflection leads in A^{AC}_{5p3} to oscillations that are amplified, at $\omega \approx 1.5$ Ry, particularly strong by polarization of fullerenes shell by the photon beam, taken into account in GFRPAE.

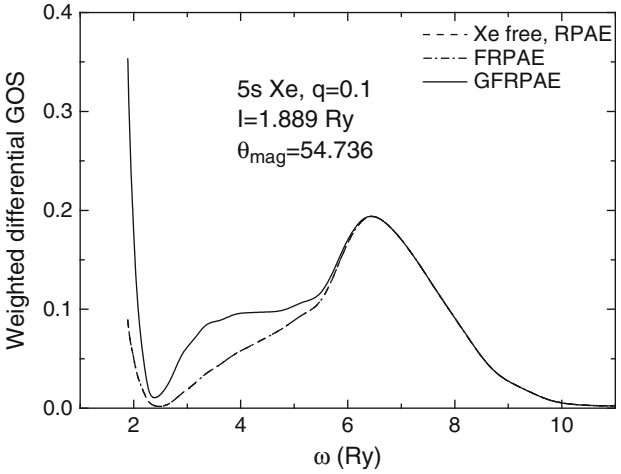

Fig. 4.329_Xe@C_{60}_n6 Weighted generalized oscillator strength differential in emission angle of the knocked-out electron (3.73 and 3.123) at magic angle $P_2(\cos\theta_m) = 0$ of $5s$ subshell for Xe@C_{60} at $q = 0.1$ in FRPAE, GFRPAE and free Xe in RPAE

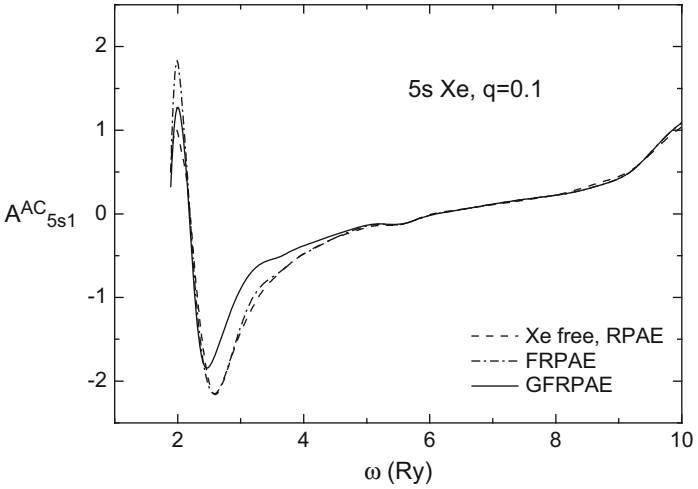

Fig. 4.330_Xe@C_{60}_n7 Angular anisotropy parameter A^{AC}_{5s1} of knocked-out electrons from $5s$ subshell of Xe@C_{60} in fast projectile–atom collision, given by (3.124) in FRPAE and GFRPAE at $q = 0.1$ and free Xe in RPAE, as functions of ω

Figure 4.328_Xe@C_{60}_n5 shows the angular anisotropy parameter A^{AC}_{5p4} of knocked-out electrons from $5p$ subshell of Xe@C_{60} in fast projectile–atom collision, given by (3.124) in FRPAE, GFRPAE, and free Xe in RPAE at $q = 0.1$ as functions of ω. The parameter A^{AC}_{5p4} is by a factor of 5 smaller than A^{AC}_{5p3}. GRPAE strongly increases the amplitude of oscillations that already exists in RPAE.

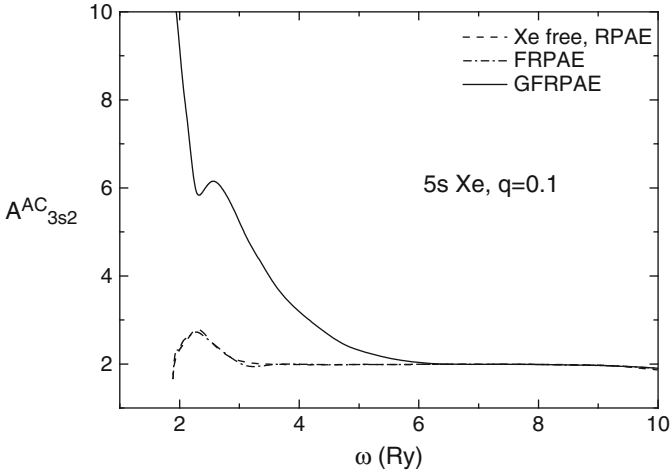

Fig. 4.331_Xe@C$_{60}$_n8 Angular anisotropy parameter A^{AC}_{5s2} of knocked-out electrons from $5s$ subshell of Xe@C$_{60}$ in fast projectile–atom collision, given by (3.124) in FRPAE and GFRPAE at $q = 0.1$ and free Xe in RPAE, as functions of ω

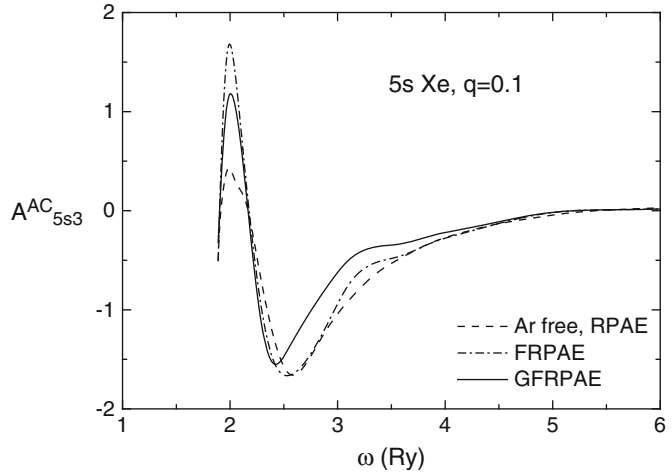

Fig. 4.332_Xe@C$_{60}$_n9 Angular anisotropy parameter A^{AC}_{5s3} of knocked-out electrons from $5s$ subshell of Xe@C$_{60}$ in fast projectile–atom collision, given by (3.124) in FRPAE and GFRPAE at $q = 0.1$ and free Xe in RPAE, as functions of ω

Figure 4.329_Xe@C$_{60}$_n6 represents the weighted GOSes differential in emission angle of the knocked-out electron (3.73 and 3.123) at magic angle $P_2(\cos\theta_{\mathrm{m}}) = 0$ of $5s$ subshell for Xe@C$_{60}$ at $q = 0.1$ in FRPAE, GFRPAE, and free Xe in RPAE. We see strong amplification of the weighted generalized

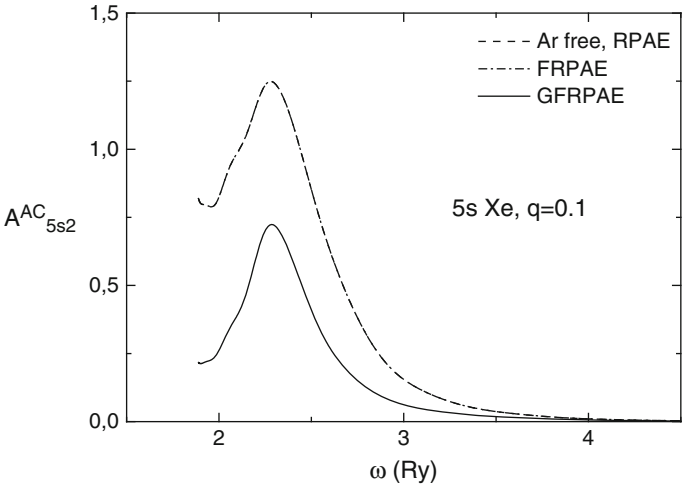

Fig. 4.333_Xe@C_{60}_n10 Angular anisotropy parameter A^{AC}_{5s4} of knocked-out electrons from 5*s* subshell of Xe@C_{60} in fast projectile–atom collision, given by (3.124) in FRPAE and GFRPAE at $q = 0.1$ and free Xe in RPAE, as functions of ω

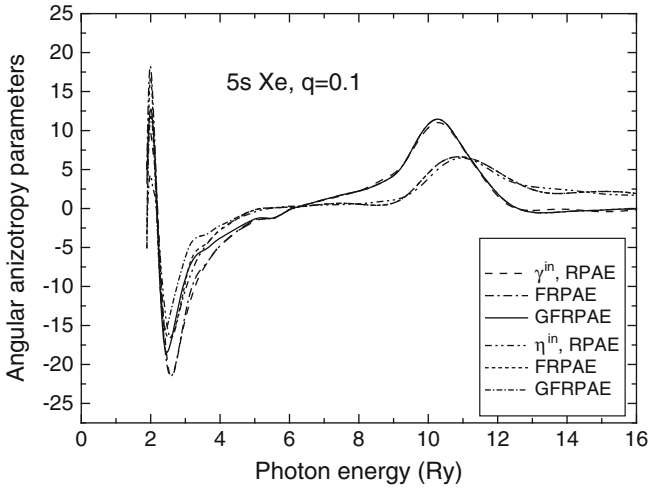

Fig. 4.334_Xe@C_{60}_n11 Angular anisotropy nondipole parameters of knocked-out electrons in fast projectile–atom collision in the optical limit given by (3.125) in FRPAE and GFRPAE at $q = 0.1$ for 5*s* subshell of Xe@C_{60} and free Xe in RPAE

oscillator strength due to polarization of the fullerenes shell under the action of the incoming photon beam near ionization threshold.

Figure 4.330_Xe@C_{60}_n7 depicts the angular anisotropy parameter A^{AC}_{5s1} of knocked-out electrons from 5*s* subshell of Xe@C_{60} in fast projectile–atom collision, given by (3.124) in FRPAE, GFRPAE, and free Xe in RPAE at $q = 0.1$ as functions

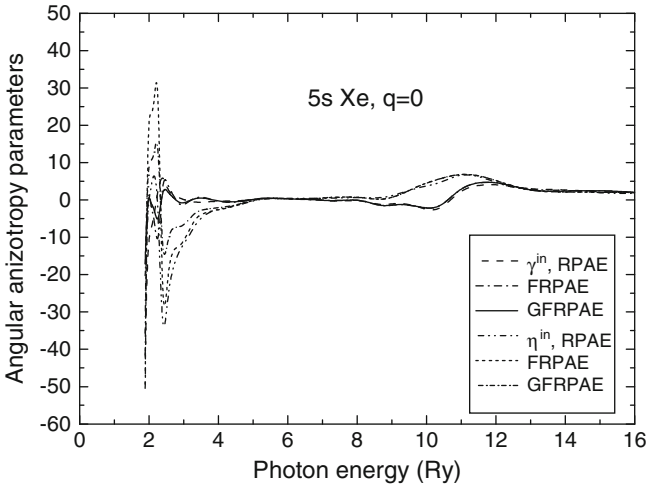

Fig. 4.335_Xe@C_{60}_n12 Angular anisotropy nondipole parameters of knocked-out electrons in fast projectile–atom collision in the absolute optical limit given by (3.125) at $q = 0$ for $5s$ subshell of Xe@C_{60} and free Xe in RPAE (see Fig. 4.177_Xe_m9)

of ω. Polarization of the fullerenes shell under the action of the photon beam strongly amplifies the near-threshold oscillations in A^{AC}_{5s1}.

Figure 4.331_Xe@C_{60}_n8 demonstrates the angular anisotropy parameter A^{AC}_{5s2} of knocked-out electrons from $5s$ subshell of Xe@C_{60} in fast projectile–atom collision, given by (3.124) in FRPAE, GFRPAE, and free Xe in RPAE at $q = 0.1$ as functions of ω. Reflection of the photoelectrons by the fullerenes shell in A^{AC}_{5s2} is almost entirely compensated in FRPAE but are considerably enhanced by polarization of the fullerenes shell taken into account by GFRPAE.

Figure 4.332_Xe@C_{60}_n9 gives the angular anisotropy parameter A^{AC}_{5s3} of knocked-out electrons from $5s$ subshell of Xe@C_{60} in fast projectile–atom collision, given by (3.124) in FRPAE and GFRPAE at $q = 0.1$ as functions of ω. Although the difference between results of RPAE and GRPAE is everywhere but close to ionization threshold is small, the oscillations.in A^{AC}_{5s3} are greatly enhanced by fullerenes polarization accounted for in the frame of GRPAE.

Figure 4.333_Xe@C_{60}_n10 shows the angular anisotropy parameter A^{AC}_{5s4} of knocked-out electrons from $5s$ subshell of Xe@C_{60} in fast projectile–atom collision, given by (3.124) in FRPAE, GFRPAE, and free Xe in RPAE at $q = 0.1$ as functions of ω. The angular anisotropy parameters A^{AC}_{5s1}, A^{AC}_{5s2}, A^{AC}_{5s3}, and A^{AC}_{5s4} are of the same order of magnitude. As to A^{AC}_{5s4}, it is considerably affected only by polarization of the fullerenes shell taken into account in GRPAE.

Figure 4.334_Xe@C_{60}_n11 represents the angular anisotropy nondipole parameters of knocked-out electrons in fast projectile–atom collision in the optical limit given by (3.125) at $q = 0.1$ for $5s$ subshell of Xe@C_{60}. The effects of fullerenes shell are not too big and concentrated close to ionization threshold.

Figure 4.335_Xe@C_{60}_n12 gives the angular anisotropy nondipole parameters of knocked-out electrons in fast projectile–atom collision in the absolute optical limit given by (3.125) at $q = 0$ for $5s$ subshell of Xe@C_{60} and free Xe in RPAE (see Fig. 4.177_Xe_m9). The GFRPAE values are bigger than FRPAE, which exceeds the nondipole parameters for free atoms.

4.8 Brief Discussion of Results

In this Chapter, we consider much less objects of research than in Chap. 2. Therefore, we find it necessary to add here a more detailed general discussion of the results obtained adding more details.

Cross-sections of elastic and inelastic scattering have been obtained in this chapter in HF and in RPAE (SRPAE) for a number of atoms and ions with filled and half-filled subshells.

As is seen, in all cases only inclusion of electronic correlations that is going beyond one-electronic HF approximation has allowed to reproduce Ramsauer minima [4.20], observed in cross-sections on electron-atom scattering.

Calculations of GOSes for many atoms are carried out in a very broad region of energies ω transferred during scattering (up to 100 Ry) and linear momentum q (up to 8 a.u.). Results are presented in one-electron HF approximation and with account of multielectronic correlations in RPAE. Four values of angular momentum L transferred to the atom during fast electron–atom collisions were considered. Thus, GOSes are found for dipole, monopole, and quadrupole and, in some cases, octupole transitions. Variations of the role of correlation effects with growth of ω and q have been demonstrated.

To check numerical accuracy of our calculations for GOSes, they have been carried out in two forms of the interaction operator between incoming particle and atomic electrons $\hat{A}(q)$, namely the *length form* $\hat{A}^r(q)$ and its modification—the *velocity* form $\hat{A}^v(q)$ [see (3.57)]. RPAE results in these two forms should coincide just as in calculations with exact wave functions. As acceptable accuracy, we consider the agreement between results in these two forms with an error of 1–2%.

Calculation data show an unexpected variety of mutual influences at growth of energy ω and linear moments q for all considered GOSes: monopole, dipole, quadrupole, and octupole in all atoms in ions. Multielectron effects in Kr and even more—in Xe are especially strong. With increase of q Giant and correlation resonances strongly vary (see, for example, [4.37]). In addition, with increase of q many new maxima appear for all GOSes, namely for dipole, monopole, and quadrupole transitions. Interelectron interaction dramatically influences GOSes of few-electron subvalent ns^2 subshells [4.38]. While at relatively small ω being strongly affected by neighbor valent multielectron subshells np^6, at high ω these subshells considerably influence GOSes of the next multielectronic shells.

It follows from calculations that with increase of q the relative role of correlations, particularly of intershell correlations, varies impressively. The qualitative reason of this effect is the fact that oscillations of operator $\exp(i\vec{q}\vec{r})$ [see (3.57)] as functions of r influence differently the matrix elements of transitions from outer, subvalent, and internal subshells of the considered atoms. As a result, the relative role of the second and first terms in (3.66) becomes different, thus leading to significant modifications of GOSes for given values ω and q.

Let us start with discussion of dipole GOSes. In Ne and Ar, the influence of external $2p^6$- and $3p^6$-subshells on $2s^2$ and $3s^2$, respectively, decreases with growth of q as it is visible from Figs. 4.26_Ne_e1–4.29_Ne_e4 and Figs. 4.57_Ar_e1–4.60_Ar_e4. It leads to results, which are closer to HF values than at small q. However, because of oscillations of $\exp(i\vec{q}\vec{r})$ with growth of q HF values of GOSes as functions of ω get an additional maximum in comparison with what takes place at small q. For Kr and Xe, the situation proved to be more complex. Indeed, as is seen from Figs. 4.106_Kr_e1–4.109_Kr_e4 and Figs. 4.136_Xe_e1–4.139_Xe_e4, the role of ten electrons of $3d$ shell in Kr and $4d$ shell in Xe, being important already at small q, with growth of q becomes absolutely dominating. GOSes for $4p$ and $4s$ shells in Kr and $5p$, $5s$ in Xe are determined almost completely by the influence of ten electrons $3d$ and $4d$ subshells in Kr and Xe, respectively. Entirely, GOSes in Ne, Ar, Kr, and Xe proved to be under strong influence of multielectronic correlations, and the relative role of the latter does not decrease, but even increases with growth of q.

Rather recently measurements were performed of GOSes not only dipole, but also for the first time nondipole, namely for the lowest discrete transitions in Ar [4.22]. The data have been received in inelastic scattering of electrons with energy 2.5 keV on Ar, covering the region of transferred energies up to 20 eV and linear momentum q till 2.5–3.0 a.u. Three clear maxima have been identified at 11.8, 13.4, and 14.2 eV. Having in mind the values of energy and dependence of GOSes from q, these levels were interpreted as $3p^6-3p^5(4s, 4s')$-, $3p^6-3p^5(4p, 4p')$-, and $3p^6-3p^5(5s, 5s', 3d, 3d')$ transitions, respectively. The resolution of experimental energy was insufficient to distinguish excitations with various total momentum, $j = 3/2$ and $j = 1/2$, from a core with $3p$-vacancy and to separate $3p$–$3d$ and $3p$–$5s$ levels.

GOSes for dipole and nondipole transitions are qualitatively others at small q, since dipole GOSes at $q \to 0$ are normally different from zero while all others tend to zero. The analysis of the situation with GOSes for $3p^6-3p^5(4p, 4p')$ transitions has resulted in conclusion [4.22] that these are quadrupole level.

To check interpretation of this level as quadrupole and to compare calculated and measured GOSes for dipole transitions, we have carried out calculations of GOSes in HF and RPAE [4.13]. Calculations have been performed also for outer electron excitation in Ne, Kr, and Xe.

As closely spaced in energy discrete levels cannot be distinguished in experiment, we present their sums: in Fig. 4.11_He_f4 the sum $(1s-3p) + (1s-3d)$ and in Fig. 4.12_He_f5—the sum of $(1s-4p) + (1s-4d)$ transitions in He alongside with experimental data from [4.8]. Similarly, Fig. 4.68_Ar_f8 shows the sum of dipole

and octupole $3p$–$3d$-contributions, while Fig. 4.69_Ar_f9 shows the same for $3p$–$4d$ transitions in Ar. Similar sums are given also for $4p$–$4d$, $4p$–$5d$ transitions in Kr and $5p$–$5d$, $5p$–$6d$ transitions in Xe. The region of the considered values of q is rather broad, up to $q \leq 4$ a.u.

Note that the energy of excitation ω, which is included in the formulas (3.58), (3.65), and (3.67) for discrete i–f transition, is designated as ω^{R}_{fi} in RPAE and differs from HF value $\omega^{\mathrm{HF}}_{fi} \equiv \varepsilon_f - \varepsilon_i$. Procedure of ω^{R}_{fi} calculation is described in [AC]. Energies in RPAE for above-mentioned transitions for Ne, Ar, Kr, and Xe are given in Table 4.1.

In our calculations, excitation energies with various total moment $j = 3/2$ and $j = 1/2$ from a core with $3p$-vacancy were considered as identical.

Let us discuss in more detail the results for Ar where comparison with experimental data [4.22] is possible [4.24]. RPAE energies of considered excitations are $\omega^{\mathrm{R}}_{3p-4s} = 12.01\,\mathrm{eV}$ of $3p$–$4s$ (dipole), $\omega^{\mathrm{R0}}_{3p-4p} = 13.45\,\mathrm{eV}$ (monopole), and $\omega^{\mathrm{R2}}_{3p-4p} = 13.70\,\mathrm{eV}$ (quadrupole) of $3p$–$4p$ levels. Energies of dipole $3p$–$5s$ and $3p$–$3d$ levels, are, respectively, $\omega^{\mathrm{R}}_{3p-5s} = 14.46\,\mathrm{eV}$ and $\omega^{\mathrm{R}}_{3p-3d} = 14.53\,\mathrm{eV}$. These values can be compared to experimental values: $\omega^{\mathrm{exp}}_{3p-4s} = 11.8\,\mathrm{eV}$, $\omega^{\mathrm{exp}}_{3p-4p} = 13.4\,\mathrm{eV}$, and $\omega^{\mathrm{exp}}_{3p-5s,3d} = 14.2\,\mathrm{eV}$. It is seen that the agreement is quite good.

Monopole and quadrupole levels differ only by 0.25 eV and consequently, as it is obvious from analysis of experimental data, their pure experimental separation is rather difficult. The same is true for $3p$–$5s$ and $3p$–$3d$ levels where separation is even less, only 0.07 eV. Calculated GOSes (in HF and RPAE) and the measured values [4.24] are presented together in Figs. 4.62_Ar_f2 and 4.70_Ar_f10. In Fig. 4.62_Ar_f2, the sum $G^0_{3p-4p}(q, \omega^{\mathrm{R0}}_{3p-4p})$ and $G^2_{3p-4p}(q, \omega^{\mathrm{R2}}_{3p-4p})$ [see definition (3.67)] is represented. It is compared with measured GOSes of $3p$–$4p$ level at 13.4 eV. Fig. 4.70_Ar_f10 shows the sum $G_{3p-5s}(q, \omega^{R1}_{3p-5s})$ and $G_{3p-3d}(q, \omega^{\mathrm{R1}}_{3p-3d})$ of GOSes of 14.2 eV level. It is seen that in both cases the agreement with experiment is satisfactory.

Figure 4.61_Ar_f1 shows the monopole $G^0_{3p-4p}(q, \omega^{\mathrm{R0}}_{3p-4p})$ and quadrupole $G^2_{3p-4p}(q, \omega^{\mathrm{R2}}_{3p-4p})$ GOSes. It is visible that the contribution of monopole GOSes is bigger, showing that in the sum of the calculated values shown in Fig. 4.62_Ar_f2, the main is the contribution of monopole transition. Hence, experimentally, the observed maximum at 13.4 eV is not a quadrupole level as is stated in [4.22], but instead a mixture of monopole and quadrupole ones, where the monopole contribution dominates [4.13]. We shall notice that at $q > 1.3$ a.u. quadrupole GOSes start to increase, while the monopole term decreases. Starting from $q > 2$ a.u. the quadrupole term dominates.

Recently, GOSes of several first levels for Ar have been measured [4.24] again. Dipole transition $3p$–$4s$ and a combination of monopole and quadrupole $3p$–$4p$ transitions have been considered. The contribution of monopole and quadrupole levels has been separated with the help of calculated multipliers. Received GOSes were compared to results of calculation. For monopole excitation it is done in

Fig. 4.72_Ar_f12, while for quadrupole—in Fig. 4.73_Ar_f13. There is a qualitative agreement and essential quantitative difference. However, there is no agreement of the total result presented in [4.22] with the sum of corresponding GOSes from [4.24]. Definitely higher accuracy of the experimental data is required.

Figure 4.71_Ar_f11 shows the reasonable accord with the available experimental data $G_{3p-4s}(q, \omega^{\mathrm{R}}_{3p-4s})$. This GOS as function of q reaches its minimum at $q \cong 1.25$ and then starts to increase. Let us note that the most affected by electron correlations is $3p$–$5s$ transition though its GOS is much less than that for $3p$–$3d$ transition.

The superposition of components representing various multipolarities is closely connected to the time of life of discrete excitations. For example, the monopole level can decay with emission of at least two photons while quadrupole level decays much faster, by emitting a single quadrupole photon. By changing q, it is possible to change the relative weight of various contributions to the total sum, thus increasing or reducing the rate of decay of the state excited in scattering with given q. In the mixture of components generated at a given value of q, short-lived component disappears faster, with growth of time increasing the relative weight of the other components.

The important problem is to improve the experimental resolution, which would help to distinguish closely located discrete levels. Other opportunity, as shown earlier, will be to study dependence of GOSes of discrete excitations and in such a way to distinguish very close located levels.

Calculations of cross-sections of Compton ionization and excitation have been carried out for external subshells and corresponding discrete transitions in atoms Ne, Ar, Kr, and Xe. Levels $np-(n+1)$, $(n+2)p$, $L = 0, 2$, $np-n$, $(n+1)d$ [$2p$–$3d$, $4d$ in Ne], $L = 1, 3$ and $np-(n+1)$, $(n+2)s$, $L = 1$ in Ne, Ar, Kr, and Xe for the transferred linear momentum $q < 8$ a.u. are chosen [4.16]. Difference in energy between considered monopole and quadrupole levels is small enough for all investigated atoms, so as the difference in energy between octupole and dipole levels. For example, below are presented energies for Ne: $\omega^{L=0}_{2p-3p} = 1.5023$, $\omega^{L=2}_{2p-3p} = 1.4379$, $\omega^{L=0}_{2p-4p} = 1.6074$, $\omega^{L=2}_{2p-5p} = 1.5981$, $\omega^{L=1}_{2p-3d} = 1.5886$, $\omega^{L=3}_{2p-3d} = 1.6379$, $\omega^{L=1}_{2p-3s} = 1.3481$, and $\omega^{L=1}_{2p-4s} = 1.5635$, all energies—in Ry.

Figure 4.42_Ne_h1 shows the results for $2p$–$3s$ transition, with the characteristic two-humped structure, even more expressed than for $2p$–$3p$ one at almost all q. Note that the cross-section for $2p$–$3s$ transition is approximately five times more than for $2p$–$4s$ one.

Because of proximity of considered levels' excitation energy, Fig. 4.44_Ne_h3 shows the relative cross-section for $2p$–$3p$ transition and their monopole and quadrupole component in RPAE at the same energy $\omega_{2p-3p} = 1.5$ Ry. Figure 4.43_Ne_h2 shows the much smaller contribution of dipole and octupole $2p$–$3d$ transitions. The energy $\omega_{2p-3d} \approx 1.589 \approx 1.6$ Ry almost coincides with $\omega_{2p-4p} \approx 1.607 \approx 1.6$ Ry and is close to $\omega_{2p-4d} \approx 1.64$ Ry, on the one hand and is rather close to $\omega_{2p-4s} \approx 1.564$ Ry on the other that makes them difficult to distinguish experimentally. That is why Fig. 4.45_Ne_h4 shows the sum of contributions, alongside with partial contributions of $2p$–$3d$, $2p$–$4p$, $2p$–$4s$,

and $2p$–$4d$ transitions. We see that for all q the contribution of $2p$–$4p$ transition dominates. The contribution of $2p$–$4s$ transition is almost of that size.

Figure 4.78_Ar_h1 shows the results for $3p$–$4s$ and $3p$–$5s$ transitions exited in Compton scattering, which again, as well as in Ne, has clear two-humps structure. Note that the ratio of $3p$–$4s$ to $3p$–$5s$ contributions in Ar is bigger than the similar ratio in Ne. In Ar, as well as in Ne, a number of levels are rather close to each other. For this reason in Fig. 4.82_Ar_h5, alongside with cross-sections of Compton excitation of $3p$–$5p$, $3p$–$3d$, $3p$–$5s$, and $3p$–$4d$-levels, their sum is also presented. The contribution of $3p$–$3d$ transition is dominating, since it proceeds between states with the same principal quantum number.

Monopole and quadrupole $3p$–$4p$ levels in Ar are very close in excitation energies that are $\omega^{L=0}_{3p-4p} = 1.0068\,\text{Ry}$ and $\omega^{L=2}_{3p-4p} = 1.0059\,\text{Ry}$, respectively. Therefore, in calculations their energy has been chosen as equal $\omega_{3p=4p} = 1\,\text{Ry}$. The received results are shown in Fig. 4.80_Ar_h3.

The situation in Kr and Xe is qualitatively similar with that taking place in Ne and Ar.

It is essential to notice that the role played by RPAE correlations in cross-sections of Compton scattering is not too big. The important exceptions are $np-(n+1)$, $(n+2)s$ transitions. All curves for $np-(n+1)$, $(n+2)p$ excitation have a common qualitative feature, namely, a strong maximum that shows up mainly at $q \approx 1$. In all curves additional interesting structure appears because of quadrupole contribution having two maxima: the first at $q \approx 1$ and the second that moves from $q \approx 4$ in Ne up to $q \approx 2$ in Xe. Curves for GOSes of $np-(n+1)$, $(n+2)s$ transitions have two-hump structure and $np-(n+1)s$-contribution is much bigger than that from $np-(n+2)s$ transition. However, curves for p–d transitions, both dipole and octupole, at least in considered q-region, have a single maximum which for dipole transition is located at smaller q than for the quadrupole one. Strength of the latter quickly increases on the way from Ne to Xe.

Calculation of GOSes in their optical limit permits to estimate or calculate in logarithmic approximation the total inelastic cross-section of fast electron on atoms, that was done for several atoms, mainly noble gases using formulas (3.70) and (3.71). Auxiliary curves were calculated that permit to improve the logarithmic accuracy.

Investigation of angular distribution of secondary electrons knocked-out off the target atom in fast projectile–atom collision permits to obtain information on dipole and nondipole atomic excitation matrix elements. The calculations employ formulas (3.72), (3.77), (3.79), and (3.82). By changing the linear momentum transferred to the target in collision, one can increase the role of nondipole parameters, making them much easier measurable than in photoionization (see Sect. 1.8). As examples, we performed calculations for He, Li^-, Ar, and Xe.

We give concrete examples for more general understanding of the role of fullerenes shell upon values of generalized oscillator strength differential in emission angle of the knocked-out electron for endohedrals $A@C_{60}$, determined by (3.123). Angular anisotropy parameters relative to the transferred to the atom in fast electron–atom collision linear momentum q are given by (3.124). As examples

of A we consider only noble gas atoms Ar and Xe, or, to be more precise, their valent and subvalent subshells $3p$, $3s$ and $5p$, $5s$, respectively. The limitation by only a few examples is determined by complexity of calculations, very approximate nature of model of the C_{60} shell employed and low probability that complicated experiments that are needed to determine these characteristics will be performed soon. So, what one needs is an illustration of the magnitude and specific features of these characteristics. This is given in figures of Sect. 4.7.

Let us discuss in more details the positron–atom scattering. Here we have represented results of our calculations of slow positron–atom elastic scattering cross-section [4.10]. We demonstrated efficiency of a very simple method (see Sect. 3.10), which allows taking into account formation of virtual positronium in this process.

Absence of decisive success after the polarization interaction in the second order in positron–electron interaction (3.144) is taken into account signals that qualitatively important omissions are present. We have assumed in [4.9] that the reason is in neglect of not simply the positron–atomic electron interaction, but of formation of virtual positronium in the intermediate state, which arises owing to temporary binding of the incoming positron and virtually or really excited atomic electron. This binding takes place far from the nuclei of the target atom.

We assume that being almost untouched by action of the atomic core, this electron and a positron can form a bound state almost identical to free positronium Ps. It changes the energy of an intermediate state, shifting it by I_{Ps}-positronium binding energy, and changes the wave function of an intermediate state, which is no more a product of HF wave functions of the positron, excited electron, and a vacancy created after virtual excitation of atomic electron. Instead of it, movement of a positron relative to electron is strongly changed due to their binding.

To include the mentioned above positronium virtual formation, it is necessary to take into account modification of corresponding wave functions instead of simple addition I_{Ps} to the denominator in (3.144). It means that it is necessary to replace product one-positron Hartree and one-electronic HF functions $\mid E_1 l_1, \varepsilon_2 l_2\rangle$ and energies E_1 and ε_2 with the wave functions and total energy of interacting, or bounded positron and electron, which move in the field of the target atom with a vacancy $\varepsilon_j l_j$. To find these functions and total energy, the three-body problem accounting for the interaction between incoming positron, atomic electron, and the vacancy created after virtual excitation of an atomic electron should be solved. This problem is very difficult. Therefore, we have presented here results of much more simple approach, which takes into account only the shift of energy caused by formation of virtual positronium and completely neglects changing of wave function of a positron and an electron [4.9].

To take into account shift of the excitation energy, I_{Ps} should be deducted from the sum of energies of a positron and electron $E_1 + \varepsilon_2$ in a denominator of polarization interaction of the second order, as it is made in (3.145). It is essential to have in mind that if the binding of positronium exceeds the binding energy of an electron in the target atom, $I_{\mathrm{Ps}} > I$, dipole polarizability of atom $\alpha(I_{\mathrm{Ps}})$ is a complex value, usually with a significant imaginary part.

It would be much easier to use (3.149) instead of (3.145), but asymptotic expression (3.149) is valid only at such big distances from atom, the contribution from which in total phase shift is small. This is why in our calculations formulas (3.145) and (3.147) were used.

Results of elastic scattering of positrons on He, obtained with the help of (3.145) and (3.147), are shown in Fig. 4.13_He_i1. It is visible that shift of energy because of positronium formation leads to appreciable reduction of cross-section at low energies. To receive our results, contributions of s-, p-, d-, f-phases of partial waves for an incoming positron have been taken into account. We shall notice that formation of virtual positronium leads to appreciable variations in all contributions of different partial waves.

The cross-section of elastic scattering for $(e^+ + \mathrm{He})$ at low energy is much less than for $(e^- + \mathrm{He})$. It is possible to explain it qualitatively as follows. The self-consistent field V^{sc} acting upon the incoming positron is repulsive, whereas polarization potential V^{pol}, which at big distances from atom r decreases as $[-\alpha(I_{\mathrm{Ps}})/2r^4]$ is attractive. It occurs because for He polarizability $\alpha(I_{\mathrm{Ps}})$ just as $\alpha(0)$, is positive. Note that for He V^{pol} and V^{sc} values are of the same order. Thus, contributions of V^{sc} and V^{pol} compensate each other, reducing the cross-section of elastic scattering. As to scattering of electrons, there V^{sc} is attractive as V^{pol}, and instead of compensation, corresponding rather big contributions are summed with each other, thus sharply increasing the electron–atom scattering cross-section.

In this sense, significant interest represents comparison of scattering $(e^+ + \mathrm{He})$ and $(e^+ + \mathrm{Li})$ because $\alpha_{\mathrm{Li}}(I_{\mathrm{Ps}})$ is negative, complex, and on absolute value it is much more than $\alpha_{\mathrm{He}}(I_{\mathrm{Ps}})$. The negative sign of $\alpha_{\mathrm{Li}}(I_{\mathrm{Ps}})$ means, according to (3.149), that the polarization potential instead of being always attractive can become also repulsive, as it has been already mentioned at the end of Sect. 3.8. This fact has a general meaning in physics. Indeed, if the projectile and an element of the target can form a bound system in an intermediate state, the polarization interaction can change its sign, becoming attractive.

It appears that a similar case can be found, for example, also in nuclear physics, namely in π-meson-nucleus scattering, where incoming π-meson and target's nucleon forms so-called Δ_{33}-resonance, thus leading to change of a sign in polarization interaction [3.33]. As to the potential imaginary part, from the point of view of elastic scattering it can be essential, being effectively both repulsive and attractive, depending on its value. Thus, it is possible to expect that due to the fact that V^{sc} and V^{pol} have the same sign, they make essential contribution, leading to very big cross-section, that is even more than $(e^- + \mathrm{Li})$ cross-section (see [3.32]).

Results for $(e^+ + \mathrm{Li})$ cross-section are shown in Fig. 4.192_Li_i1. It is seen that the inclusion of the energy shift by the value corresponding to formation of positronium in the intermediate state, considerably affects the cross-section at low energies.

The picture described earlier for scattering of a positron on He and Li is qualitatively correct also for pair Ne–Na. Indeed, $(e^+ + \mathrm{Ne})$ cross-section is unexpectedly small, much less than the geometrical and the cross-section of elastic scattering $(e^+ + \mathrm{Ne})$ is very big, much more than the geometrical.

For heavier noble gas atoms, namely Ar, Kr, Xe, polarization interaction increases considerably if the virtual formation of Ps is taken into account. The corresponding cross-section increases with growth of nuclear number. For the next alkaline atoms, similarly to the situation in Li–He pair, cross-sections of positron scattering on alkaline atoms are much bigger than on neighbor noble gases. Results for Kr and Xe are in qualitative agreement with those received in [4.28] using much more complex method.

Special attention deserves studying imaginary parts of scattering phases $\Delta\delta'_\ell(E)$. They describe corresponding contributions of partial waves to the inelastic scattering $e^+ + \mathrm{A} \to \mathrm{Ps} + \mathrm{A}^+$ cross-section. This cross-section $\sigma_{\mathrm{in}}(E)$ is expressed via imaginary part of phase shift $\mu_\ell(E)$ according to (3.14). Just as in calculations of elastic scattering cross-section $\sigma(E)$, we limit ourselves by taking the account first four partial waves, with $\ell = 0, 1, 2, 3$. Corresponding results for Li and Mg are shown in Figs. 4.192_Li_i1 and 4.258_Mg_i1, respectively.

It is interesting to learn whether it is possible within the framework of the simple approach, which is used here, to describe the bound states in $(e^+ + \mathrm{A})$-system. Indeed, it is not trivial at all, that with repulsive nature of V^{sc} and an opportunity of also repulsive V^{pol}, a bound state $(e^+ + \mathrm{A})$ can be formed. So, it would be reasonable to expect a bound state of positrons with those atoms, for which $\alpha_{\mathrm{A}}(I_{\mathrm{Ps}})$ is big (much more than in noble gases) and positive $\alpha_{\mathrm{A}}(I_{\mathrm{Ps}}) > 0$, so that potential V^{pol} would be strong enough and attractive. Interesting and exciting is the opportunity that $(e^+ + \mathrm{A})$ bound state would appear due to actions of imaginary part of polarization potential $\mathrm{Im}V^{\mathrm{pol}}$.

On the other hand, binding can occur owing to interaction of Ps and A^+ due to action of the Van der Vaals forces. Such interaction is particularly strong, if A^+ ion has the electronic structure similar to an atom of the first group of the periodic table of the elements, i.e., if A belongs to the second group of this table. To find out an opportunity of formation of the bound state, it is necessary to study the scattering phase shifts at zero energy: if at least one of them reaches π, the bound state in the respective channel is formed. However, it is necessary to check whether such a state is stable against decay in the channel $(\mathrm{Ps} + \mathrm{A}^+)$. It requires knowledge of energy of this bound state. To find this value is much more complicated than to calculate the phase shifts at zero energy of a positron e^+.

References

4.1. Amusia MYa, Cherepkov NA (1975) Many-electron correlations in the scattering processes. Case Stud At Phys 5:47–179
4.2. Amusia MYa, Tanchich A, Cherepkov NA, Chernysheva LV, Shapiro SG (1975) Slow electron-atom elastic scattering. Sov JETP 68(6):2023–2031
4.3. Andrick D (1973) The differential cross section of low energy electron–atom collisions. Adv At Mol Phys 9:207–242
4.4. Golden DE, Furst J, Mahgerefteh M (1988) Absolute elastic electron–helium scattering cross-section measurements from 2 to 19 eV. Phys Rev A 30(3):1247–1254

4.5. Ramsauer C, Kollath R (1932) (1932) Die Winkelverteilung der Streuulung langsamer Electronen an Gasmolekülen. Ann Phys (Leipzig) 404(5):529–561
4.6. Amusia MYa, Cherepkov NA, Sheftel SI (1970) Inelastic electron scattering on the noble-gas atoms. Sov Phys JETP 58(2):618–623
4.7. Amusia MYa, Chernysheva LV, Felfli Z, Msezane AZ (2001) Many-electron correlation effects in the generalized oscillator strengths of noble gas atoms. Phys Rev A 64:032711
4.8. Liu XJ, Zhu LF, Yuan ZS, Li WB, Cheng HD, Sun JM, Xu KZ (2004) The generalized oscillator strengths for the valence shell excitations in helium by fast electron impact. J Electron Spectrosc Relat Phenom 135:15–20
4.9. Amusia MYa, Cherepkov NA, Chernysheva LV, Shapiro SG (1976) The elastic scattering of slow positrons on He atom. J Phys B At Mol Phys 9(17): L531–L534
4.10. Amusia MYa, Cherepkov NA, Chernysheva LV (2003) Elastic scattering of slow positrons on atoms. JETP 124 1(7):1–9
4.11. Jaduszliwer E, Paul D (1973) Positron–helium scattering cross sections and phase shifts below 19 eV. Can J Phys 51:1565–1572
4.12. Linert I, Mielewska B, King GC, Zubek M (2006) Elastic electron scattering in neon in the 110°–180° scattering angle range. Phys Rev A 74:042701
4.13. Amusia MYa, Chernysheva LV, Felfli Z, Msezane AZ (2003) Determination of discrete transitions multipolarity using the generalized oscillator strength. Phys Rev A 67:022703 (1–8)
4.14. Amusia MYa, Chernysheva LV, Felfli Z, Msezane AZ (2007) Octupole contributions to the generalized oscillator strengths of discrete dipole transitions in noble gases. Phys Rev A 75:062703
4.15. Amusia MYa, Chernysheva LV, Felfli Z, Msezane AZ (2012) Cross sections of Compton scattering upon heavy atoms with account of many-electron correlations. J Phys B At Mol Opt Phys (submitted)
4.16. Amusia MYa, Chernysheva LV, Felfli Z, Msezane AZ (2002) Cross sections of discrete-level excitations of noble-gas atoms in Compton scattering. Phys Rev A 65(6):62705 (1–8)
4.17. Dababneh MS, Kauppila WE, Downing JB, Lapierre F, Pol V, Smart JH, Stein TS (1980) Measurements of total scattering cross sections for low-energy positrons and electrons colliding with krypton and xenon. Phys Rev A 22:1872–1877
4.18. Golden DE, Bandel HW (1965) Absolute total electron–helium–atom scattering cross sections for low electron energies. Phys Rev 138: A14–A21
4.19. Thomson DG (1966) The elastic scattering of slow electrons by neon and argon. Proc Royal Soc A 294:160
4.20. Ramsauer C (1921) Über den Wirkungsquerschnitt der Gasmolecüle gegenüber langsamen Elektronen. Ann Phys (Leipzig) 369(6):513–540
4.21. Panajotovic R, Filipovic D, Marinkovic B, Pejcev V, Kurepa M, Vuskovic L (1997) Critical minima in elastic electron scattering by argon. J Phys B At Mol Opt Phys 30:5877–5894
4.22. Fang XW, Leung KT (2000) Absolute generalized-oscillator-strength measurement of preionization-edge electronic excitations in the valence and $3p$ shells of argon. Phys Rev 62(062703):1–9
4.23. Chen Z, Amusia MYa, Msezane AZ (1999) Generalized oscillator strength for the argon $3p^6$–$3p^5 4s$ transition: correlation and exchange effects on characteristic minimum. Phys Rev A 60(6):5115–5117
4.24. Zhu LF, Cheng HD, Yuan ZC, Liu XJ, Sun JM, Xu KZ (2006) Generalized oscillator strengths for the valence-shell excitations of argon. Phys Rev A 73:042703
4.25. Amusia MYa, Chernysheva LV, Felfli Z, Msezane AZ (2002) Compton scattering upon heavy atoms with account of many-electron correlations. Surf Rev Lett 9(2):1155–1160
4.26. Stein TS, Kauppila WE (1982) Positron–gas scattering experiments. Adv At Mol Phys 18:53–96
4.27. Charlton M (1985) Experimental studies of positrons scattering in gases. Rep Prog Phys 48:737

4.28. Hewitt RN, Noble CJ, Bransden BH (1993) Positron collisions with alkali atoms at low and intermediate energies. J Phys B At Mol Opt Phys 26:3661
4.29. Johnson WR, Guet C (1994) Elastic scattering of electrons from Xe, Cs^+, and Ba^{2+}. Phys Rev A 49:1041
4.30. Amusia MYa, Chernysheva LV, Felfli Z, Msezane AZ (2006) Generalized oscillator strengths for the 3*d* electrons of Xe, Cs and Ba: effects of spin–orbit activated interchannel coupling. Phys Rev A 73:062716
4.31. Sinapius G, Raith W, Wilson WG (1980) Scattering of low-energy positrons from noble-gas atoms. J Phys At Mol Opt Phys B 13:4079
4.32. Amusia MYa, Zhivanovich Zh, Radojevich V, Cherepkov NA (1979) Generalized oscillator strength for beryllium atom in the random phase approximation with exchange. J Chem Phys 71(4):1761–1766
4.33. Amusia MYa, Sosnivker VA, Cherepkov NA, Chernysheva LV (1985) Elastic scattering of slow electrons on Ca atom. Sov JETP 55(12):2304–2311
4.34. Amusia MYa, Sosnivker VA (1989) ^{2}P-Resonance in the elastic scattering cross section of electrons upon calcium atom. Sov JETP 59(3):28–32
4.35. Ivanov VK (1999) Many-body effects in negative ion photodetachment. J Phys B At Mol Opt Phys 32(12): R67–R101
4.36. Ivanov VK (2004) Theoretical studies of photodetachment. Radiat Phys Chem 70:345–370
4.37. Amusia MYa, Ivanov VK, Sheinerman SA (1976) Intershell correlations in the inelastic scattering of fast electrons on the outer subshells in Ar and Xe. J Phys B At Mol Phys 9(9):1537–1553
4.38. Amusia MYa, Cherepkov NA, Chernysheva LV, Sheftel SI (1972) Densities of generalized oscillator strengths for Ar with the inclusion of correlations. Phys Lett A 40(1):5

Part III
Vacancies Decay

Chapter 5
Main Points on Vacancies Decay Theory

5.1 Most Important About Vacancies and Their Decay

A vacancy created in any atomic shell, except of the outermost one, can decay or undergo a transition into other states with one or more vacancies. Due to decay, the vacancy (the hole state) acquires a finite *width* Γ_k, where k denotes all quantum numbers of a subshell under consideration—principal quantum number n, angular momentum l, and total momentum j. The vacancy lifetime τ_k and its width Γ_k are connected by *the uncertainty principle* for the energy[1]:

$$\tau_k \Gamma_k \approx 1. \tag{5.1}$$

The decay of vacancies created in ionization or excitation of the target atom or ion results in emission of electrons and photons with given energies that are named spectral lines. These lines are usually characterized by their energies and widths. In the absence of vacancy decay width, atomic emission spectrum would be a set of zero width lines.

There are two main channels of vacancy decay: *radiative* and *nonradiative* or *Auger decay*. In radiative decay the hole undertakes a transition from the shell k to the shell i with smaller binding energy ε_i, the released energy $\omega_{ki} = \varepsilon_i - \varepsilon_k$ being emitted as a photon. In *a nonradiative* or *Auger decay*, the energy released in the transition of a hole from the shell k to the shell i is transferred to a third electron j, which undertakes a transition to the state q with positive energy, and leaves the atom.

To depict such processes, a diagrammatic technique developed in Sect. 1.3 will be used. The simplest diagrams for the radiative and nonradiative processes are depicted in (5.2a) and (5.2b), respectively:

[1]Note that in this book atomic system of units is used, in which charge and mass of an electron and Plank constant are equal to 1, $e = m = \hbar = 1$.

M. Amusia et al., *Handbook of Theoretical Atomic Physics*,
DOI 10.1007/978-3-642-24752-1_5, © Springer-Verlag Berlin Heidelberg 2012

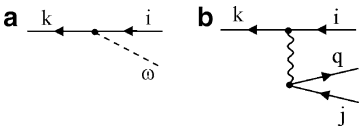

(5.2)

The width of radiative decay Γ_k^{γ}, whose amplitude is shown in (5.2a) is given by the following formula (see e.g., [BLP, AM, AICC]):

$$\Gamma_k^{\gamma} = \frac{1}{c^3} \sum_{i<F} \omega_{ki}^3 |\langle i|\vec{e}\vec{r}|k\rangle|^2, \tag{5.3}$$

where $\vec{e}$ is the emitted photon polarization vector. The sum runs over all occupied states $|\varepsilon_i| < |\varepsilon_k|$.

The Auger decay line width $\Gamma_k^{(\mathrm{A})}$, corresponding to the decay, whose amplitude is depicted by diagram (5.2b), is written as (see, e.g., [AM, AICC]):

$$\Gamma_k^{(\mathrm{A})} = 2\pi \sum_{i,j<F} \int_{q>F} |\langle kq|U|ij\rangle|^2 \delta(\varepsilon_j + \varepsilon_i - \varepsilon_q - \varepsilon_k). \tag{5.4}$$

For one-electron states, as in the previous chapters, the Hartree–Fock (HF) approximation is accepted. The many-electron correlations may be taken into account in the random phase approximation with exchange (RPAE), replacing the matrix element for radiative transition $\langle i|\vec{e}\vec{r}|k\rangle$ in (5.3) by the matrix element $\langle i|\vec{e}\vec{D}(\omega)|k\rangle$—solution of (1.37). For nonradiative transition, the account for correlation in RPAE means the replacement of $\langle kq|U|ij\rangle$ in (5.4) by $\langle kq|\Gamma(\omega)|ij\rangle$—the solution of (1.40) [5.1].

In addition to vacancy line broadening, the interaction of atomic electrons results in appearance of new lines. In particular, a single vacancy k can undertake a transition to final states, which are more complex than those represented by diagrams (5.2). As a result, the spectrum of final state becomes more complex and lines corresponding to two or more vacancies appear in addition to one-electron lines. The electrons originating in these processes can fill discrete state in the residual ion or go to continuum.

These lines are called *satellites*. They are primarily created due to the so-called shake process, i.e., sudden change of the field acting on the atomic electrons due to vacancy creation. This results in removal of outermost electrons. The shake process results in transition of one or more electrons to the excited levels of ionic core or to continuum. The first process is called *shake-up* and the second *shake-off*. The following diagram depicts the shake process:

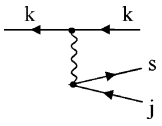

(5.5)

Note, that as distinct from (5.2b), the state of initial hole in (5.5) coincides with one of the holes in final state. The electron s is in discrete spectrum or in continuum. The total energies of atomic excited states of the type one electron–two holes $sk^{-1}j^{-1}$ are bigger than the energy of the state with one vacancy. Therefore, in photoelectron spectra they correspond to smaller kinetic energy of outgoing photoelectron and form the shake satellite photoelectron lines [5.2–5.6]. They form also a shake-off "tail" in the continuous spectrum. According to the Koopmans theorem [5.7], the first approximation to the ionization energy is the theoretical one-electron orbital energy. However, their calculations in the HF approximation are rather crude. Account for many-electron correlation by many-body perturbation theory (MBPT) [5.8] reduces the theoretical ionization energy of core subshells by up to 10–20 eV, and the results are usually in good agreement with experiment (up to 1–2 eV).

The Auger decay of the vacancy, the simplest version of which is shown by diagram (5.2), results in broadening of photoelectron line. In some cases the energy released in such a process is not enough for electron removal from the atom, but enough for its excitation to the empty bound state, which is denoted by double arrow:

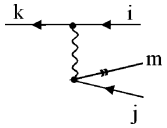

(5.6)

The matrix element of Auger transition becomes much larger, if principle quantum numbers of interacting vacancies $i^{-1}k^{-1}$ are the same, because of strong overlap of wave functions that constitute the corresponding to (5.6) integrand. These transitions are called Coster–Kronig transitions. If principle quantum numbers of all three vacancies are the same $n_i = n_j = n_k$, the matrix element is very large and such a transition is called super Coster–Kronig.

A *double Auger* transition, i.e., a decay of a vacancy into three holes and two electrons is also possible [5.9, 5.10] and exemplified by the following diagram:

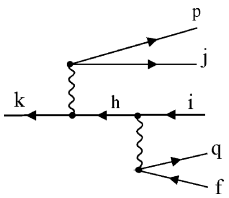

(5.7)

The diagrams with permutations of creation times for particle–hole pairs pj^{-1} and qf^{-1} and substitutions of a hole h by a particle in the intermediate state also contribute to the same line width. For more details, see the rules for diagram construction in Sect. 1.3.

In the present chapter, the processes mentioned above will be considered mainly in the frame of MBPT (see Sect. 1.4). The calculation techniques for filled and unfilled shells in ground states will be described.

In order to take into account RPAE corrections one has to substitute the dipole matrix element in (5.3) and Coulomb interaction matrix element in (5.6) by matrix elements from (1.37) and (1.40), respectively.

5.2 The Energies of Atomic Levels

In a single-electron picture of photoionization there are only one hole k in the final state and only one electron q in continuum, whose energies are connected by the energy conservation law:

$$\omega = \varepsilon_q - \varepsilon_k. \tag{5.8}$$

According to Koopmans theorem [5.7], the Hartree–Fock orbital energy ε_k equals to the ionization energy of subshell k. Comparison with experiment shows that one-electron approach (Koopmans theorem) significantly overestimates binding energies of core and intermediate levels. This difference is connected with the monopole relaxation of ionic core, i.e., change of radial parts of the wave functions after electron removal. Monopole relaxation results in a decrease of binding energies with respect to one-electron values and origin of shake-up and shake-off satellites.

The proper ionization energy is obtained as a difference of total energies of the initial neutral atom and the final ion, calculated self-consistently (ΔSCF-method):

$$E_b^{\Delta\mathrm{SCF}}(k) = E_{\mathrm{tot}}^{\mathrm{HF}}(k^{-1}) - E_{\mathrm{tot}}^{\mathrm{HF}}, \tag{5.9}$$

where k^{-1} denotes a state of the atom with a single vacancy in a k-subshell.

The ground state configuration is referred to as a *Fermi-vacuum*, which has no indexes and only excited relative to this state electron and hole states are indicated. Thus the satellite states, i.e., the double-hole–one-particle states are denoted as $i^{-1}j^{-1}s$. The Hartree–Fock ΔSCF-method is a good approximation for the ionization energy if initial and final states are well separated in energy from other atomic and ionic states and hence configuration interaction is small [5.11].

In some cases, it may happen that the energy difference between final one-hole state k^{-1} and some other two-hole–one-particle state $i^{-1}j^{-1}s$ is relatively small and the Coulomb interaction is large enough. For example, the energy of $4p^{-1}$ hole state in atoms surrounding Xe in the periodic table is close to the energy of double-hole–one-particle state $4d^{-2}4f$ and Coulomb interaction matrix element between these states is extremely large (since principal quantum numbers of the wave functions are the same). As a result, the $4p$ photoelectron spectra of these atoms show very strong line shifts, splitting and broadening [5.12], which are not described in the framework of HF method. As a result, the binding energies, calculated by ΔSCF-method do not agree well with the experiment. These effects may be accounted for in higher orders of perturbation theory by MBPT [5.13,5.14] or by configuration interaction method [5.15]. The relaxation of ionic core results in asymmetrical broadening of the main line and partial transfer of its intensity to additional (satellite) lines. In order to calculate line intensities the dynamic of relaxation process due to polarization of

atomic shell by core hole should be taken into account. This dynamic picture of relaxation process will be used in next sections of this chapter for the calculation of other line parameters: intensities, widths and asymmetry.

5.3 Polarization Interaction for Vacancies

The creation of inner vacancy k may be described as a sudden switching of a hole potential W_h. This potential polarises the electronic shells and leads to excitations of particle–hole pairs, which screen initial single-electron hole:

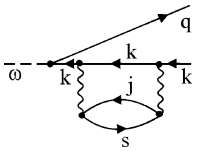

(5.10)

According to MBPT [5.16], the excitations of particle–hole pairs result in the evolution of the system under the action of polarization potential W_h. This polarization results in changes of the vacancy parameters (binding energy, width, and intensity) with respect to their one-electron values. Also, additional (satellite) lines corresponding to these complex states $k^{-1}j^{-1}s$ appear. The interaction of outgoing electron with the atom results in the same excited states. This process is depicted in the following diagram:

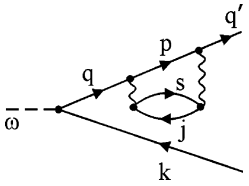

(5.11)

The influence of these processes on the intensity and angular distribution of photoelectrons is most important near the photoionization threshold.

In the present chapter we consider photoionization of core atomic levels, which are well separated in energy. In this case the probability of k-hole propagation to other hole states is small. This assumption corresponds to the *diagonal representation* [5.17]. This term is due to limitation by the diagrams with the same outer lines. In this approximation the lowest-order contribution to the hole state with respect to interelectron interaction is represented by the following diagram:

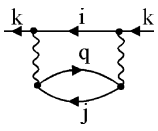

(5.12)

In the language of MBPT (see Sect. 1.3), this diagram in the above approximation represents the main contribution to a so-called *self-energy part of one-electron Green function*. Since the electron correlations resulting in satellite excitations very often are quite strong, the third-order diagrams, corresponding to the interaction between two-hole–one-particle states are important. The examples of such processes are as follows:

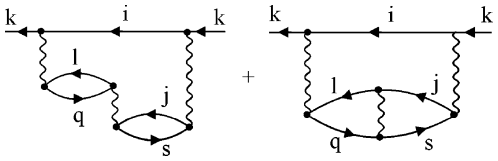

(5.13)

These processes define the width of resonant satellite state in the presence of underlying continuum. The influence of the polarization interaction and of other many-body processes upon the vacancy spectrum is considered in the present book in terms of spectral function technique, based on the Green's function approach.

5.4 Self-energy Part of Green's Function and Spectroscopic Parameters

The Green's function in one-electron approximation is presented as [5.11, 5.18]:

$$G^{\mathrm{HF}}(E) = \frac{1}{-E + \varepsilon_k - i\eta}, \tag{5.14}$$

where ε_k is the Hartree–Fock hole energy (corresponding to Koopman's theorem), E—energy parameter and η—infinitesimally small value. Spectral distribution or *spectral function* is defined by the following relation:

$$A(E) = \frac{\mathrm{Im}G(E)}{\pi}, \tag{5.15}$$

where $G(E)$ is the exact one-particle Green's function (see e.g., [5.19]).

Thus, in one-electron HF approximation the spectral function is the delta-function:

$$A^{\mathrm{HF}}(E) = \delta(E - \varepsilon_k). \tag{5.16}$$

The Green's function of a hole, suddenly created in a system of interacting Fermions, describes the system's evolution after removal of an electron. In the above-mentioned diagonal representation, the Green's function is written as:

$$G_k(E) = \frac{1}{-E + \varepsilon_k + \Sigma_k(E)}, \tag{5.17}$$

where $\Sigma_k(E)$ is the self-energy part of Green's function, which is defined by its real $\mathrm{Re}\Sigma_k(E)$ and imaginary $\mathrm{Im}\Sigma_k(E)$ parts.

Thus, the spectral function of a vacancy with account for many-electron correlations is written as [5.13, 5.19–5.21]:

$$A_k(E) = \frac{\mathrm{Im}G_k(E)}{\pi} = \frac{1}{\pi}\frac{\mathrm{Im}\Sigma_k(E)}{(-E+\varepsilon_k+\Sigma_k(E))^2+(\mathrm{Im}\Sigma_k(E))^2}. \tag{5.18}$$

In the lowest (second) order of MBPT, real and imaginary parts of the self-energy are given by the following two formulae [5.13, 5.17]:

$$\mathrm{Re}\Sigma_k(E) = \sum_{ijs}\left(\sum_{n_s}+\int_{\varepsilon_s}\mathrm{d}\varepsilon_s\right)\frac{(-1)^{l+h}|\langle kj|U|is\rangle|^2}{-E+\varepsilon_i+\varepsilon_j-\varepsilon_s}, \tag{5.19}$$

$$\mathrm{Im}\Sigma_k(E) = -\pi\sum_{ijs}(-1)^{l+h}|\langle kj|U|is\rangle|^2\delta(-E+\varepsilon_i+\varepsilon_j-\varepsilon_s), \tag{5.20}$$

here l is the number of Fermion loops and h is the number of hole lines in the Feynman diagram. Principal value integration is assumed in (5.19), $\langle kj|U|is\rangle$ are Coulomb matrix elements with exchange, which are represented in a following form:

$$\langle kj|U|is\rangle = \sum_{\lambda} f_\lambda\langle kj|V^\lambda|is\rangle + \sum_{\mu} g_\mu\langle ki|V^\mu|js\rangle, \tag{5.21}$$

where radial parts of Coulomb integrals V^λ_{kjis} are defined by formula (1.63), λ and μ are the transferred via Coulomb interaction angular moments, f_λ and g_μ are numeric coefficients, called weight factors.

Integration over angular variables and summing over spin variables is carried out analytically making use of graphical technique [5.22, 5.23]. The weight factors f_λ and g_μ are calculated for each vertex according to momentum diagram, which is topologically equivalent to Feynman diagram [5.24]. The applications of graphical technique to many-electron atoms are presented in [5.25].

The momentum diagram technique can be applied to Feynman diagrams according to following rules:

1. A fragment of a Feynman diagram with interaction line is replaced by topologically equivalent fragment of momentum diagram with arrows on the initial hole, final particle and interaction lines and a weight factor $(-1)^{\lambda+l_k+l_s}\langle kj|V^\lambda|is\rangle$ as follows:

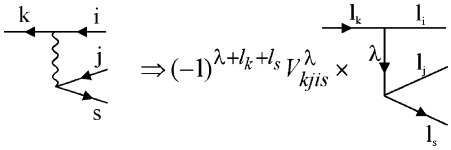

(5.22)

2. At this step, arrows on Feynman diagram, corresponding to lines and particles, are not taken into account. The directions of arrows in momentum diagrams are not essential for integer momentum values [5.25]. It should be also noted that since the Coulomb interaction is non-zero between configurations of the same parity only, the above phase factor may be also written as $(-1)^{\lambda+l_i+l_j}$ and the arrows are attached to the interaction line and two final hole lines i and j.
3. All angular momentum lines on each side of the vertex should be coupled into intermediate and total angular moments. In order to get correct weight factor for Feynman diagram, one should use graphical notation of [5.25] with heavy line that means multiplication by the factor $(2L+1)^{1/2}$ for all resultant moments.
4. When the hole state with angular momentum l and spin $s = 1/2$ $(l, 1/2, m_l, m_s)$ is coupled with some other state into total angular momentum and spin, magnetic quantum numbers and spin projection are reversed and additional phase multiplier $(-1)^{l+1/2+m_l+m_s}$ is taken into account [5.24]. In momentum graph it corresponds to adding of arrows toward the vertices in orbital and spin diagrams in all cases of hole states coupling.
5. Since we consider Coulomb interaction only, the spin diagram is obtained from orbital diagram by removing of interaction line and corresponding arrows.

Let us consider calculation of weight factor for the second-order diagram of satellite excitation and Auger decay accompanying photoionization. When the k-subshell of a closed shell atom is ionized, there is only one final ionic state with $L = l_k$ and $S = 1/2$. In LS coupling scheme two holes i^{-1} and $j^{-1}[j]$ are coupled into intermediate moments L_{ij} and S_{ij}. Since all states of different intermediate moments contribute to the hole screening, it is assumed that the sum over i and j in formulae of the self-energy (5.19) and (5.20) includes the sum over all possible values of L_{ij} and S_{ij}. The weight factors for Coulomb and exchange parts depend on L_{ij} and S_{ij} and are given by the following two formulae [5.26]:

$$f_\lambda = (-1)^{S_{ij}+1}\frac{[S_{ij}L_{ij}]^{1/2}}{2^{1/2}[l_k]^{1/2}}\begin{Bmatrix} L_{ij} & l_k & l_s \\ \lambda & l_j & l_i \end{Bmatrix}, \tag{5.23}$$

$$g_\mu = (-1)^{L_{ij}+l_k+l_s}\frac{[S_{ij}L_{ij}]^{1/2}}{2^{1/2}[l_k]^{1/2}}\begin{Bmatrix} L_{ij} & l_k & l_s \\ \mu & l_i & l_j \end{Bmatrix}, \tag{5.24}$$

where the following notations $[q] = 2q+1$ and $[S_{ij}L_{ij}] = (2S_{ij}+1)(2L_{ij}+1)$ are used in this chapter, and the expressions in curly brackets are the $6j$-symbols [IS].

This formula differs from formula of [5.27] by common phase factor only. Thus, we have presented the calculation technique for all quantities required for the calculation of the hole Green's function. We are in a position to consider the calculation of line parameters by the spectral function method.

The description of a system excitation in terms of quasi-particles is possible if the following relation between real and imaginary parts of the self-energy is fulfilled [5.18]:

$$\mathrm{Re}\Sigma_k(E) \gg \mathrm{Im}\Sigma_k(E). \tag{5.25}$$

The electron binding energy spectrum is defined by the solutions of Dyson equation [5.19]:

$$\tilde{E} = \varepsilon_k + \mathrm{Re}\Sigma_k(\tilde{E}). \tag{5.26}$$

Solutions of (5.26) correspond to the main line and all satellite photoelectron lines. Thus, the influence of relaxation on binding energy may be accounted for by two methods: solving the Dyson equation (5.26) or calculating the binding energy as the difference between total energies of ion and atom (ΔSCF-method).

Parameters of spectral lines may be obtained making use of Taylor expansion of the self-energy near the Green function pole.

When expanding the real part of the self-energy near the pole and neglecting the variation of imaginary part, one obtains the following formula for the spectral function:

$$A(E) = f\frac{1}{\pi}\frac{\Gamma/2}{(E-\tilde{E})^2 + (\Gamma/2)^2}, \tag{5.27}$$

where the line width is given by the following formula:

$$\Gamma = 2\pi f\,\mathrm{Im}\Sigma_k(\tilde{E}). \tag{5.28}$$

The *spectroscopic factor* f is defined by the following formula:

$$f = \frac{1}{1-\alpha}, \tag{5.29}$$

where

$$\alpha = \left.\frac{\partial \mathrm{Re}\Sigma_k(E)}{\partial E}\right|_{E=\tilde{E}}. \tag{5.30}$$

The spectroscopic factor is a part of total spectral distribution corresponding to a given line, representing a hole in the Fermion spectrum. Since a Fermion occupation number cannot be more than 1, it follows that $0 < f < 1$ and therefore the value α should be negative. It can be also shown [5.17, 5.20] that the following sum rules are fulfilled:

$$\sum f_n + \int_{-\infty}^{\varepsilon_i+\varepsilon_j-\varepsilon_s} \frac{1}{\pi}\frac{\mathrm{Im}\Sigma_k(E)\mathrm{d}E}{(\varepsilon_k - E + \Sigma_k(E))^2 + (\mathrm{Im}\Sigma_k(E))^2} = 1, \tag{5.31}$$

$$\sum_n f_n E_n + \int_{-\infty}^{\varepsilon_i+\varepsilon_j-\varepsilon_s} \frac{1}{\pi}\frac{E\mathrm{Im}\Sigma_k(E)\mathrm{d}E}{(\varepsilon_k - E + \Sigma_k(E))^2 + (\mathrm{Im}\Sigma_k(E))^2} = \varepsilon_k. \tag{5.32}$$

The first of the relations means that relaxation effects result in an appearance of discrete shake-up satellites and continuum spectrum of double ionization instead of a single line without change of total intensity. The second relation means that the center of gravity of the spectral distribution with account for relaxation coincides with one-electron energy of the vacancy. The same sum rule was obtained in the model in which the satellite intensity is proportional to the overlap between the initial state and relaxed final state [5.28].

In HF approximation all first-order diagrams with respect to interelectron interaction, i.e., diagrams corresponding to creation of single electron–hole pairs are taken into account in HF ground state (Brillouin theorem [5.7]). The next order of MBPT corresponds to admixture of two-hole–two-particle excitations $l^{-1}j^{-1}ps$ to the ground state—*ground state correlations*. In MBPT contributions of such correlations correspond to *time-reversal* diagrams [see discussion after (1.36)]. The interaction of ground state correlations with the hole k is shown in the following diagram:

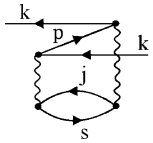

(5.33)

Contribution of this diagram to the hole self-energy is given by the following formula:

$$\mathrm{Re}\Sigma_k(E) = \sum_{ijsp}\left(\sum_{n_s,n_p} + \iint\limits_{\varepsilon_s,\varepsilon_p} \mathrm{d}\varepsilon_s \mathrm{d}\varepsilon_p\right)\frac{(-1)^{l+h}|\langle kj|U|ps\rangle|^2}{E+\varepsilon_j-\varepsilon_s-\varepsilon_p}. \tag{5.34}$$

Also, spontaneously created two-hole–two-electron $l^{-1}j^{-1}ps$ state (ground state correlation) is able to annihilate due to the action of the same interaction operator W_h as in the case of shake-up process, leading to the following diagram:

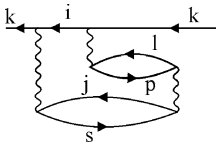

(5.35)

Contribution of this diagram to the real part of the self-energy is given by the following formula:

$$\mathrm{Re}\Sigma_k(E) = \sum_{jlsp}\left(\sum_{n_s,n_p} + \iint\limits_{\varepsilon_s,\varepsilon_p} \mathrm{d}\varepsilon_s \mathrm{d}\varepsilon_p\right)\frac{(-1)^{l+h}\langle lj|U|ps\rangle\langle kl|U|ip\rangle\langle ij|U|ks\rangle}{(\varepsilon_j+\varepsilon_l-\varepsilon_s-\varepsilon_p)(-E+\varepsilon_i+\varepsilon_j-\varepsilon_s)}. \tag{5.36}$$

Relaxation of suddenly created inner hole is a transition from the ground state wave functions to the relaxed wave functions and there is no unique choice for the calculation of the basis of wave functions. There are several approximations for the calculation of the wave functions, based on atomic Hartree–Fock method. In the frozen core approximation, the excited wave functions are calculated in the potential constructed from the radial parts of the ground state wave functions. The removal of electrons is accounted by changing the occupation numbers in two shells. In the relaxed approximation the wave functions of the ionic state $k^{-1}j^{-1}$ are

calculated self-consistently and the excited states are calculated in this field. In the intermediate relaxed-frozen core approximation the ionic state k^{-1} is calculated self-consistently and the removal of electron j is accounted for by changing the occupation number of the valence shell. The frozen core approximation corresponds to general many-body treatment of the system evolution under the action of W_h. The relaxed-frozen core approximation is usually used for the calculation of Auger rates, since its results for absolute values of Auger rates are superior [5.29]. The results of relaxed core approximation correspond more to the calculation of interactions in a final state and its results are in a good agreement with experiment for satellites line widths [5.30, 5.31].

Let us consider the vacancy relaxation in atom with unfilled shell $l_j^N L_j S_j$. Orbital and spin moments of the hole are coupled with those of the unfilled shell into several total resulting moments LS of ionic core. In $L-S$ coupling scheme these $L-S$ channels does not interact with each other. The MBPT method considered so far may be directly applied to each one of these $L-S$ channels, but the important point is the dependence of the relaxation on the atomic and ionic terms. This dependence will be investigated making use of graphical momentum technique.

We consider the contribution to vacancy relaxation due to satellite excitation from unfilled shell. In each one of these satellite $L-S$ channels the satellite state $l_i^{-1} l_j^{-1} l_s$ is defined by the term $\underline{L}_j \underline{S}_j$ of the shell l_j^{N-1} and intermediate moments and spin $L_{ij} S_{ij}$ corresponding to their coupling with l_i. Making use of graphical methods one easily obtains instead of (5.23) and (5.24), the following two formulae for weight factors:

$$
\begin{aligned}
f_{\lambda(L_j S_j L_{ij} S_{ij})} &= N_j^{1/2} G_{\underline{L}_j \underline{S}_j}^{L_j S_j} \sum_q (-1)^{L+L_j+\underline{L}_j+L_{ij}+l_i+l_k+S+3\underline{S}_j+2S_{ij}} \\
&\quad \times [q][L_j S_j L_{ij} S_{ij}]^{1/2} \times \begin{Bmatrix} \underline{L}_j & L & q \\ l_s & l_i & L_{ij} \end{Bmatrix} \begin{Bmatrix} l_k & l_j & q \\ l_s & l_i & \lambda \end{Bmatrix} \begin{Bmatrix} \underline{L}_j & L & q \\ l_k & l_j & L_j \end{Bmatrix} \\
&\quad \times \begin{Bmatrix} 1/2 & \underline{S}_j & S_{ij} \\ 1/2 & S & S_j \end{Bmatrix}, \qquad (5.37) \\
g_{\mu(L_j S_j L_{ij} S_{ij})} &= N_j^{1/2} G_{\underline{L}_j \underline{S}_j}^{L_j S_j} \left[L_j L_{ij} S_j S_{ij} \right]^{1/2} [S]^{-1} (-1)^{L+L_j+\underline{L}_j+L_{ij}+l_k+l_s+\mu} \\
&\quad \times \begin{Bmatrix} L & \underline{L}_j & \mu \\ l_i & l_s & L_{ij} \end{Bmatrix} \begin{Bmatrix} L & \underline{L}_j & \mu \\ l_j & l_k & L_j \end{Bmatrix} \delta(S, \underline{S}_j), \qquad (5.38)
\end{aligned}
$$

where $G_{\underline{L}_j \underline{S}_j}^{L_j S_j}$ are fractional parentage coefficients.

To obtain total contribution of satellite excitation from unfilled shell to the hole screening, the weight factors (5.37) and (5.38) should be summed over all terms $L_j S_j$ of configuration l_j^{N-1} and over all possible $L_{ij} S_{ij}$ values for each $L-S$ channel.

Excitations from inner closed shells $l_p^{4l_p+2}$ to unfilled shell l_j^N should also be taken into account. In this case angular momentum l_s is the same as l_j. When applying momentum diagram technique, one obtains the weight factors:

$$f_\lambda = (N+1)^{1/2} G^{\overline{L}_j \overline{S}_j}_{L_j S_j} [\overline{L}_j L_{ip} \overline{S}_j S_{ip}]^{1/2} (1)^{L+S+2S_j+3\overline{S}_J} \begin{Bmatrix} L_{ip} & l_k & l_j \\ \lambda & l_p & l_i \end{Bmatrix} \times \begin{Bmatrix} L & l_k & L_j \\ l_j & \overline{L}_j & L_{ip} \end{Bmatrix} \begin{Bmatrix} S & 1/2 & S_j \\ 1/2 & \overline{S}_j & S_{ip} \end{Bmatrix}, \tag{5.39}$$

$$g_\mu = (N+1)^{1/2} G^{\overline{L}_j \overline{S}_j}_{L_j S_j} [\overline{L}_j L_{ip} \overline{S}_j S_{ip}]^{1/2} (1)^{L+S+2S_j+3\overline{S}_j} \begin{Bmatrix} L_{ip} & l_k & l_j \\ \lambda & l_p & l_i \end{Bmatrix} \times \begin{Bmatrix} L & l_k & L_j \\ l_j & \overline{L}_j & L_{ip} \end{Bmatrix} \begin{Bmatrix} S & 1/2 & S_j \\ 1/2 & \overline{S}_j & S_{ip} \end{Bmatrix}, \tag{5.40}$$

where the terms $\bar{L}_j \bar{S}_j$ of configuration l_j^{N+1} are denoted by the line on the top.

It is seen from the above formulae that ionization of core shell in the presence of outer unfilled shell results in several independent $L-S$ channels. Each one of the satellite states is characterized by the parent term of unfilled shell in addition to angular and spin moments of two holes L_{ij} and S_{ij}. All these states contribute to the screening of core hole and we are in position to obtain the rules for carrying out the summing over these states.

The Dyson equation (5.26) has one solution corresponding to the main line and a group of solutions corresponding to satellite states. In this section we consider a solution corresponding to the main line and some simplifications will be done. In such a case the energy denominator equals to the excitation energy of particle–hole pair, which for outer shells is about 10–30 eV. If holes i and j belong to different atomic shells, the energy splitting between different $L_{ij} S_{ij}$ terms is about units of eV or less. Therefore, we neglect term splitting and perform the summing over L_{ij} and S_{ij} in formulae (5.23) and (5.24). Thus, for the term ($i = k$) we obtain:

$$|\langle kj|U|ks\rangle|^2 = \frac{2}{[\lambda l_k]} |\langle kj|V^\lambda|ks\rangle|^2 - \frac{4(-1)^{l_i+l_j}}{[l_k]} \begin{Bmatrix} l_k & l_k & \lambda \\ l_s & l_j & \mu \end{Bmatrix} \times \langle kj|V^\lambda|ks\rangle\langle kk|V^\mu|js\rangle + \frac{2}{[\mu l_k]} |\langle kk|V^\mu|js\rangle|^2. \tag{5.41}$$

In the case of unfilled shell the sum runs over all terms of configuration l_j^{N-1}, since all of the compatible angular momentum conservation terms contribute to the vacancy relaxation energy. Summing in formula (5.37) over q for the case of monopole satellite ($\lambda = 0$, $l_i = l_k$, and $l_j = l_s$), squaring and summing over intermediate moments L_{ij} and S_{ij}, we obtain:

$$f^2_{0(\underline{L}_j \underline{S}_j)} = \frac{N_j (G^{L_j S_j}_{\underline{L}_j \underline{S}_j})^2}{[l_k l_j]}. \tag{5.42}$$

Summing (5.42) over all terms of configuration l_j^{N-1} and making use of orthogonality relation of fractional parentage coefficients [IS], we obtain finally:

$$f^2_0 = \frac{N_j}{[l_k l_j]}. \tag{5.43}$$

Thus, we find that the contribution to monopole relaxation due to satellite excitation from unfilled shell is proportional to the number of electrons in this shell and is independent on the term of this shell $L_j S_j$, and on the term of ion core LS. Similar summation over the exchange term is not possible. However, for the core hole ionization the direct term is larger than the exchange, since in the former the square of core hole wave function is integrated over the same coordinate, but in the latter core hole wave function is integrated with the wave function of outer electron.

Carrying out similar summation in formula (5.39) for the satellite excitation to the partially filled shell, one obtains the following formula for direct monopole term:

$$f^2_0 = \frac{4l_j + 2 - N_j}{[l_k l_j]}. \tag{5.44}$$

Hence it follows that the direct term of the monopole hole screening due to the satellite excitation into unfilled shell is proportional to the number of empty places in the unfilled shell and does not depend neither on the term of unfilled shell nor on the term of ionic core.

The obtained formula for the leading weight factor for the monopole relaxation of open shell atoms makes possible an average estimation of monopole excitation accompanying photoionization in terms of the spectroscopic factor value.

Spectroscopic factors of inner shells vary from 0.91 for Li1s to 0.77 for Zn2p [5.26]. On the other hand, in most cases the spectroscopic factors are close to 0.8 and the account for spectroscopic factors in relative photoionization cross-sections is not essential, while they are always essential in calculation of absolute photoionization cross-sections. Theoretical value 0.8 of Ne1s spectroscopic factor is in good agreement with experiment [5.32].

When the solid samples are investigated using photoelectron spectroscopy the estimations of satellite intensities depend on the background subtraction method. The analysis for five elements Al, Cu, Mo, Sn, and Ta with Shirley-type background [5.33] resulted values 0.27, 0.24, 0.12, 0.20, and 0.28, respectively [5.34] (average value 0.22), what is in qualitative agreement with our results 0.11, 0.22, 0.18, 0.17, and 0.16 (average value 0.17).

Satellite structures of photoelectron spectra of noble gas atoms has been a subject of numerous experimental [5.2–5.6] and theoretical [5.21, 5.35] investigations. Satellites of photoionization of core and valence shells of noble gases arise from the interelectron correlations accompanying photoionization. In MBPT, satellites'

positions are calculated as solutions of Dyson equation. It can be easily shown that in the case of monopole shake-up satellites these solutions are shifted from Hartree–Fock energies of these two-hole–one particle states to higher binding energy side. The satellites' intensities are obtained as spectroscopic factors. This approximation is valid in far from threshold region where excitation of the same states by outgoing electron is negligible.

The formulae for the line shape (5.27), line width (5.28) and spectroscopic factor (5.29) were derived under condition (5.25) and the variation of imaginary part of self-energy was neglected. In the case of broad lines, the expansion of the imaginary part of the self-energy in powers of $(E - \tilde{E})$ should be taken into account and the following formulae are obtained [5.20] instead of (5.27) and (5.28):

$$A(E) = \frac{1}{\pi}\frac{1-\alpha}{(1-\alpha)^2+\beta^2}\frac{\tilde{\Gamma}/2+\beta(1-\alpha)(E-\tilde{E})}{(E-\tilde{E})^2+(\tilde{\Gamma}/2)^2}, \tag{5.45}$$

$$\tilde{\Gamma} = \frac{2(1-\alpha)\mathrm{Im}\Sigma_k(\tilde{E})}{(1-\alpha)^2+\beta^2}. \tag{5.46}$$

$$\tilde{f} = \frac{1-\alpha}{(1-\alpha)^2+\beta^2}, \tag{5.47}$$

where

$$\alpha = \frac{\partial \mathrm{Re}\Sigma_k(z)}{\partial x} = \frac{\partial \mathrm{Im}\Sigma_k(z)}{\partial y}, \tag{5.48}$$

$$\beta = \frac{\partial \mathrm{Im}\Sigma_k(z)}{\partial x} = -\frac{\partial \mathrm{Re}\Sigma_k(z)}{\partial y}. \tag{5.49}$$

It follows from formula (5.45) that the broadening of the main photoelectron lines due to the vacancy decay is always somewhat asymmetrical.

Asymmetrical broadening in photoelectron spectra may be also initiated by some other interactions. The lines in photoelectrons spectra of solid samples are always asymmetrical due to inelastic scattering of emitted electrons. The inelastic scattered electrons have smaller kinetic energies and that results in rising of the high binding energy side of the line in photoelectron spectrum [5.33, 5.34]. Hence it follows that experimentally observed asymmetry of broad lines is the result of two above-mentioned effects.

Another channel of core hole relaxation appears in conducting solids. This phenomenon, called Fermi surface relaxation [5.36, 5.37], results in asymmetry of the emitted electron spectrum in the same direction as inelastic scattering. This direction of asymmetry will be called the positive direction (positive slope in the photoelectron binding energy scale).

The preferential direction of line shape asymmetry due to Coster–Kronig decay in binding energy spectrum may be envisaged as follows. The increase of the binding energy of the initial hole state k^{-1} results in an increase of kinetic energy ε_s in final state $i^{-1}j^{-1}s$. The absolute value of the Coulomb matrix elements

$\langle kj|U|is\rangle$ that defines the width usually decrease with kinetic energy. Hence it follows that the "effective" line width decreases with the increase of binding energy and the direction of line asymmetry due to Coster–Kronig decay is negative (opposite to the direction of asymmetry due to inelastic electron scattering and Fermi surface relaxation). It should be also noted that the Fermi surface relaxation asymmetry is usually stronger than asymmetry due to Coster–Kronig decay and the latter is smeared by former in conducting solids.

Making use of formula (5.45), we can express asymmetrical Lorentzian line-shape as [5.38, 5.39]:

$$L_{\mathrm{a}}(x) = \frac{1 + \beta'(x - x_0)/\Gamma/2}{1 + (x - x_0)^2/(\Gamma/2)^2}. \tag{5.50}$$

In the case of asymmetrical broadening due to Auger and Coster–Kronig decay the line shape asymmetry parameter is connected with the derivatives of the self-energy α and β by the relation:

$$\beta' = \frac{\beta}{1 - \alpha}. \tag{5.51}$$

The total width Γ at the half height of asymmetrical line equals to the sum of the left halfwidth $\Gamma_l/2$ and the right $\Gamma_r/2$ halfwidth. It can be shown that these values in formula (5.50) are $\Gamma_l/2 = (\Gamma/2)/(1 - \beta')$ and $\Gamma_r/2 = (\Gamma/2)(1 + \beta')$ and the total width of the line up to higher-order correction is unchanged.

This property makes the asymmetrical profile (5.50) very convenient in spectral curve fitting by the least square method, since the width and the asymmetry of the line are independent parameters. The asymmetry index $\delta = \Gamma_r/\Gamma_l$ is connected with asymmetry parameter β' by the following formula:

$$\beta' = \frac{2(\delta - 1)}{(\delta + 1)}. \tag{5.52}$$

The fitting of photoelectron spectra by parameterized functions is routinely used for deconvolution of overlapping lines [5.40]. Usually three parameters representing Lorentzian width, Gaussian broadening, and asymmetry are sufficient to represent a line shape. Several parameters are also required to approximate the background. The instrumental line broadening is usually considered as a Gaussian and may be accounted for by convolution of asymmetrical line profile [e.g., defined by formula (5.50)] with Gaussian function or by the use of mixed Gaussian–Lorentzian functions [5.40]. The fitting of experimental spectrum by the line profile parameterized using theoretical parameters makes it possible to obtain experimental values of these parameters. Such parameterization is sufficient to fit lines, whose asymmetry is not very big (quasi-Lorentzian lines). In the case of strongly asymmetrical satellite line shapes, the Fano formula (1.50) is usually used for fitting of the line profile.

As an example of the above-described theory we consider the $2s$-line shapes of atoms from Si to Sc [5.39]. Several decay and satellite excitation channels accompanying removal of $2s$-electron were taken into account in calculations of $2s$-hole self-energy. The width and asymmetry of the line is defined mainly

by Coster–Kronig transitions, resulting in continuum electrons of relatively slow energies: $2s^{-1} \to 2p^{-1}3p^{-1}\varepsilon d(\varepsilon s)$ and $2s^{-1} \to 2p^{-1}3s^{-1}\varepsilon p$.

In agreement with the theory [5.39], the $2s$-asymmetry parameters obtained by fitting of experimental data for insulator solids samples are negative for atoms from Si to Sc. Theoretical width of Ar$2s$ line $\Gamma_{\text{th}} = 2.21\,\text{eV}$ [5.39] is in good agreement with experimental value $\Gamma_{\text{th}} = 2.25\,\text{eV}$ [5.41] and with other theoretical values [5.42] ($\Gamma = 2.27\,\text{eV}$). Experiment [5.41] also shows negative asymmetry of the Ar$2s$ line.

5.5 Satellite Lines Shapes in Photoelectron Spectra

In this section we consider relations between satellite line shape parameters: relaxation energy shift, intensity, and width. We consider satellites with unchanged vacancy state and introduce a small parameter Δ—satellite energy shift with respect to the one-electron value:

$$\Delta = \varepsilon_k + \varepsilon_j - \varepsilon_s - E. \tag{5.53}$$

In this notation the leading term of self-energy (5.19) in the vicinity of satellite $k^{-1}j^{-1}s$ is written as:

$$\text{Re}\Sigma^{(2)}_{k(js)k(js)}(\Delta) = -\frac{|\langle kj|U|ks\rangle|^2}{\Delta}. \tag{5.54}$$

In these notations the Dyson equation (5.26) is written as:

$$\varepsilon_k + \varepsilon_j - \varepsilon_s - \Delta = \varepsilon_k - \frac{|\langle kj|U|ks\rangle|^2}{\Delta}. \tag{5.55}$$

Taking into account the smallness of Δ, the solution of Dyson equation is written as:

$$\tilde{\Delta}_{k(js)} = \frac{|\langle kj|U|ks\rangle|^2}{\varepsilon_s - \varepsilon_j}. \tag{5.56}$$

In the above made assumption the spectroscopic factor coincides with the result of perturbation theory [LL]:

$$f_{k(js)} = \frac{1}{1 + |\langle kj|U|ks\rangle|^2/\tilde{\Delta}^2_{k(js)}} \approx \frac{\tilde{\Delta}^2}{|\langle kj|U|ks\rangle|^2} = \frac{|\langle kj|U|ks\rangle|^2}{(\varepsilon_s - \varepsilon_j)^2}. \tag{5.57}$$

Some of the photoelectron satellites corresponding to monopole excitations in the presence of a strong underlying continuum are strongly asymmetrical with raised high binding energy side [5.5, 5.6]. We will show that this preferential direction of

satellite asymmetry follows in the second order of perturbation theory and does not depend on the sign of matrix elements.

Let the imaginary part of the self-energy (5.20) be a constant value. In this approximation the behavior of spectral function (5.18) is defined by very sharp variations of $\mathrm{Re}\Sigma_k^{(2)}(E)$, which in the vicinity of the satellite is approximated by formula (5.54). This function diverges at $\Delta \to 0$ and the spectral function at this point tends to zero. Hence, it follows that the line is Lorentzian, if the shift of the line maximum from this point is larger than the line halfwidth:

$$\tilde{\Delta} \gg \frac{\Gamma}{2}. \tag{5.58}$$

Making use of (5.56) and (5.57), this inequality is transformed into:

$$\mathrm{Re}\Sigma_k(\tilde{\Delta}) \gg \mathrm{Im}\Sigma_k(\tilde{\Delta}). \tag{5.59}$$

Hence it follows that if the standard condition for the validity of quasiparticle approximation is fulfilled, the satellite line is Lorentzian and its profile may be described by the parameters calculated at one energy point. On the other hand, if real and imaginary parts of the self-energy are of the same order of magnitude the low binding energy side of the shake-up satellite line is effectively depressed. This corresponds to the preferential direction of asymmetry of satellite lines with rising of the high binding energy side.

The cases of violation of standard condition for quasi-particle picture may be found in experimental photoelectron spectra, estimating $\mathrm{Re}\Sigma_k$ as a satellite line shift from the center of gravity of the spectrum and $\mathrm{Im}\Sigma_k$ estimating by formula (5.28).

In order to envisage general trends of satellite broadening, we consider excitation of satellite $k^{-1} \to k^{-1}j^{-1}s$ in the presence of underlying continuum $k^{-1} \to k^{-1}l^{-1}q$. Final ionic states $k^{-1}l^{-1}$ and $k^{-1}j^{-1}$ may differ by one hole or correspond to identical two-hole states differing by coupling scheme. The lowest-order term is due to direct excitation of shake-off satellites:

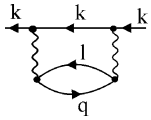

(5.60)

Contribution to the imaginary part of the self-energy and to the line width from the second-order diagrams are given by the following two formulae:

$$\mathrm{Im}\Sigma_k^{(2)}(E) = -\pi \sum_{l \le F; q > F} (-1)^{l+h} |\langle kl|U|kq\rangle|^2 \delta(\varepsilon_k + \varepsilon_l - \varepsilon_q - E). \tag{5.61}$$

$$\Gamma_0 = 2\pi f \sum_{l \le F; q > F} |\langle kl|U|kq\rangle|^2 \delta(\varepsilon_k + \varepsilon_l - \varepsilon_q - E), \tag{5.62}$$

On the other hand, the process of excitation of shake-up resonance and its decay into shake-off continuum is also possible [5.43–5.47]. Direct and exchange Feynman diagrams corresponding to this two-step process are as follows:

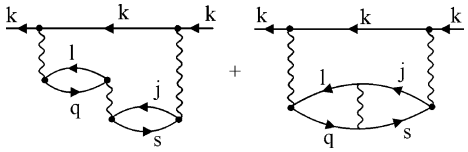

(5.63)

Corresponding third-order term of the imaginary part of the self-energy is represented as [5.43, 5.44]:

$$\mathrm{Im}\Sigma_k^{(3)}(E) = -2\pi \frac{\langle kj|U|ks\rangle}{\Delta} \sum_{l\le F;q>F} (-1)^{l+h} \langle kl|U|ks\rangle \langle jq|U|ls\rangle \times \delta(\varepsilon_k + \varepsilon_l + \varepsilon_q - E). \tag{5.64}$$

Angular parts for the external vertexes are the same as for the second-order diagram. The reduction of direct and exchange momentum graphs for the internal vertexes results in the following formulae for direct and exchange terms, respectively:

$$f_{jlsq}^{\lambda} = \frac{\left[L_{il}L_{ij}S_{il}S_{ij}\right]^{1/2}}{2} \begin{Bmatrix} L & l_i & \lambda \\ l_l & l_q & L_{il} \end{Bmatrix} \begin{Bmatrix} L & l_i & \lambda \\ l_j & l_s & L_{ij} \end{Bmatrix}, \tag{5.65}$$

$$g_{jslq}^{\mu} = \left[L_{il}L_{ij}S_{il}S_{ij}\right]^{1/2} \begin{Bmatrix} L_{ij} & L_{il} & \mu \\ l_l & l_j & l_i \end{Bmatrix} \begin{Bmatrix} L_{ij} & L_{il} & \mu \\ l_s & l_q & L \end{Bmatrix} \times (-1)^{L+L_{ij}+L_{il}+l_i+l_l+l_q+\mu} \delta(S_{ij}, S_{il}). \tag{5.66}$$

The contributions of the third-order diagrams are resonantly enhanced in the vicinity of a discrete satellite due to small value Δ in the denominator of (5.64). Hence it follows that contribution of the following fourth-order diagram should be included:

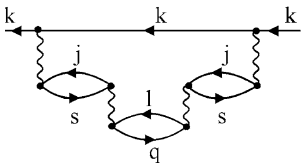

(5.67)

Corresponding fourth-order term of the imaginary part of the self-energy is written as:

$$\mathrm{Im}\Sigma_{k(js)}^{(4)}(E) = -\pi \frac{|\langle kj|U|ks\rangle|^2}{\Delta^2} \sum_{l\le F;q>F} (-1)^{l+h} |\langle jq|U|ls\rangle|^2 \delta(\varepsilon_k + \varepsilon_l - \varepsilon_q - E). \tag{5.68}$$

Substituting this expression into a general formula for the line width (5.28) and making use of approximate formula for the satellite spectroscopic factor (5.57), we obtain broadening of the line due interaction of resonance satellite state $k^{-1}j^{-1}s$ with continuum $k^{-1}l^{-1}q$:

$$\Gamma_r = 2\pi \sum_{l\le F, q>F} \langle jq|U|ls\rangle^2 \delta(\varepsilon_k + \varepsilon_l - \varepsilon_q - E). \tag{5.69}$$

Due to small variable Δ in the denominators in formulas for third- and fourth-order terms of $\mathrm{Im}\Sigma_k$, the requirement of slow variation of the self-energy is not fulfilled and the line profile is not defined by the set of parameters at one point on energy axis and calculation of spectral function is required. All three contributions to the imaginary part of the self-energy may be written by a single formula as:

$$\mathrm{Im}\Sigma_k^{(2,3,4)}(E) = -\pi \sum_{l\le F, q>F} (-1)^{l+h} \int \left(\langle kl|U|kq\rangle + \frac{\langle kj|U|ks\rangle\langle jq|U|ls\rangle}{\Delta} \right)^2 \times \delta(\varepsilon_k + \varepsilon_l - \varepsilon_q - E)\mathrm{d}\varepsilon_q, \tag{5.70}$$

where the phase multiplier $(-1)^{l+h}$ corresponds to the second-order diagram (5.60) and it is assumed that phase multipliers for internal loops are included in matrix elements.

This value is positively defined since the value $l + h$ is odd and we will call this approach as simplified fourth-order approach to the line width. Asymmetrical broadening of photoelectron shake-up satellites is a direct evidence of strongly correlated nature of these states.

5.6 Effects in Interaction Between Satellite States

In $4p$ photoelectron spectra of lanthanides and of some atoms before them instead of spin-doublet $4p_{1/2}$ and $4p_{3/2}$ a complex structure appears due to the super Coster–Kronig transitions to the states $4d^{-2}4f(\varepsilon f)$ [5.12–5.15, 5.48–5.50]. Similar effects appear in $5p$ spectra of actinide compounds [5.51]. This phenomenon called also as dynamic dipolar relaxation was investigated theoretically by MBPT [5.13, 5.14, 5.49] and configuration interaction (CI) method [5.15, 5.50, 5.51].

To obtain the satellite state parameters by CI method we consider the secular equation for two levels: initial hole state k^{-1} denoted as k and satellite state $i^{-1}j^{-1}m$, denoted as s:

$$\begin{vmatrix} \varepsilon_k - \lambda & H_{ks} \\ H_{ks} & E_s - \lambda \end{vmatrix} = 0, \tag{5.71}$$

where ε_k and E_s are the one-electron energies of initial vacancy state and satellite state and H_{ks} is the interaction matrix element corresponding to the diagram (5.6).

The weight factors for direct and exchange parts are given by formulae (5.23) and (5.24).

There are two essentially different cases. The case of $k = i$ describes the relaxation of core hole. According to the Brillouin theorem, the excitation of one-particle–one-hole pairs is accounted for in Hartree–Fock treatment of ground state. This term appears, since the relaxation is described by suddenly switched potential W_h of the core k-hole. The case $k \neq i$ corresponds to final state configuration interaction.

When solving (5.71) and making use of Taylor expansion in the small parameter $H_{ks}/(\varepsilon_k - E_s)$, we obtain the energies of the main line and satellite, respectively:

$$E'_k = \varepsilon_k + \frac{H_{ks}}{\varepsilon_k - E_s}, \quad E'_s = E_s - \frac{H_{ks}}{\varepsilon_k - E_s}. \tag{5.72}$$

The normalized eigenvector at the energy E'_k is written as:

$$\varphi(E'_k) = \frac{1}{\sqrt{1 + \frac{H_{ks}^2}{(\varepsilon_k - E_s)^2}}} \left(\varphi_k + \frac{H_{ks}}{\varepsilon_k - E_s} \varphi_s \right). \tag{5.73}$$

When comparing the result with approximate formula (5.57), we obtain that the satellite spectroscopic factor is presented in CI technique as a squared coefficient of φ_s in eigenstate at the energy of the main line. Thus, for small satellites CI and MBPT approaches are equivalent.

In the case of strongly interacting satellites one must include in secular equation also interaction between satellite states, which corresponds to the middle vertex in diagrams (5.63). Angular parts for direct and exchange terms of this interaction are given by formulae (5.65) and (5.66), respectively. The secular equation for two interacting satellites s and t is written as:

$$\begin{vmatrix} \varepsilon_k - \lambda & H_{ks} & H_{kt} \\ H_{ks} & E_s - \lambda & H_{st} \\ H_{kt} & H_{st} & E_t - \lambda \end{vmatrix}, \tag{5.74}$$

where H_{ks} and H_{kt} stand for the vacancy interaction with two-hole–one-particle states due to hole potential W_h and H_{st} stands for the configuration interaction between two-hole–one-particle states.

It follows from previous sections that MBPT is appropriate for the satellites if the interaction between two-hole–one-particle final states is significantly smaller than their interaction with the initial hole state and if the energy distance between final states is significantly larger than their energy shifts due to many-body effects. For the case under consideration this condition is fulfilled for Xe only, where the strongest is the interaction between the $4p_{1/2}$—vacancy and continuum states $4d^{-2}\varepsilon f$. This interaction results in almost complete disappearance of $4p_{1/2}$—line in spectra whereas the shape of $4p_{3/2}$ line remains unchanged.

In the next atoms Ba, Cs, and La the interaction between discrete states $4d^{-2}(^3F,^1D,^1G)4f(^2P)$ becomes significant and interaction of $4p_{1/2}^{-1}$ with continuum becomes small. Configuration interaction method should be used to calculate spectra of these atoms.

5.7 Radiative Decay

When electron is removed from any atomic shell except the outermost one two types of decay are possible: radiation decay and Auger decay. In the case of radiation decay the vacancy filling transition is accompanied by radiation of photon with energy ω. The probability of radiation transition of electron from a filled shell l_f^N to a vacancy state k^{-1} is given by the following relation [AM]:

$$W_{k\to f} = \frac{4\omega}{3c^3[l_k]}\langle l_k \| d^{V,R}(\omega) \| l_f \rangle^2, \tag{5.75}$$

where the dipole matrix elements $d^{V,R}(\omega)$ are defined in formulae (1.59a) and (1.59b).

In atomic units the probability of radiative decay coincides with a line halfwidth. In the lowest order of perturbation theory, i.e. neglecting the vacancy relaxation the total line width is the sum of radiative and Auger widths:

$$\Gamma_k = \sum_{ij} \Gamma^{\mathrm{A}}_{k-ij} + \sum_f \Gamma^{\gamma}_{k-f}. \tag{5.76}$$

In the first term the sum runs over all energetically allowed two-hole states $i^{-1}j^{-1}$, and in the second over all outer with respect to k shells. If the nondipolar transitions are neglected, the latter sum is limited by the subshells with $l_f = l_k \pm 1$.

In the calculations of line parameters by the spectral function method the radiative decay is accounted for in the self-energy part of a Green's function [5.11, 5.49]. The contribution to the self-energy part of Green's function of the vacancy k^{-1} filling by the electron from l_f^N subshell, accompanied by photon radiation, is represented by the following diagram:

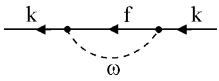

(5.77)

If the subshell l_f^N is initially completely filled, the topology of momentum diagram is the same as that of Feynman diagram (5.77), where the hole quantum numbers are replaced by their angular momentums and the ω line is replaced by momentum line with $l = 1$. It is clear that the resulting weight factor of this diagram equals to $1/[l_k]$. When comparing this result with formula (5.76) we obtain that in

calculations of radiation widths by graphical methods, each vertex containing dipole operator should be associated with the following weight factor:

$$w_{\text{rad}} = 2\sqrt{\frac{\omega}{3c^3}}\left\langle l_k \left\| d^{V,R}(\omega) \right\| l_f \right\rangle. \tag{5.78}$$

where $d^{V,R}(\omega)$ are defined in (1.2) and (1.3).

We consider a transition from a state $l_k^{-1} l_f^N (LS)(L'S')$ with a vacancy in a filled inner shell to a final state $l_f^{N-1}(L_1 S_1)$. Application of graphical methods results in the following formula for the radiation width of the state k^{-1}:

$$\Gamma^{\gamma}_{k\to f} = w^2_{\text{rad}}[LS]N \begin{Bmatrix} L' & L_1 & 1 \\ l_f & l_k & L \end{Bmatrix}^2 \left(G^{LS}_{L_1 S_1}\right)^2. \tag{5.79}$$

It is clear that the influence of monopole relaxation on the Auger and radiation line broadening is the same. Therefore, the following formula, differing by the spectroscopic factor f from the formula of [AICC], is valid for the radiation broadening:

$$\Gamma_{kf} = f\frac{4\omega}{3c^3[l_k]}|\langle l_k \| d^{V,R}(\omega) \| l_f \rangle|^2. \tag{5.80}$$

The RPAE correlations that are accounted for by substitution in (5.80) of the matrix elements of the operator $d^{V,R}(\omega)$ defined in (1.59a) and (1.59b) by the matrix elements of the operator $D^{V,R}(\omega)$ defined in (1.55). The influence of correlations upon Γ_{kf} may be essential and even lead to vanishing of Γ_{kf} due to destructive interference of the direct decay path and a path via virtual excitations of other electrons [5.1, 5.10, AICC].

Since the proper consideration in inner shell vacancy radiation decay requires account for relativistic effects, we consider briefly relativistic wave functions calculation [5.52–5.54]. In relativistic approximation the definition of atomic wave function is as follows:

$$\varphi_i(\vec{r}) = \varphi_{n\kappa m}(\vec{r}) = \frac{1}{r}\begin{pmatrix} F_{n\kappa}(r)\chi_{\kappa m}(\vec{r}) \\ iG_{nk}(r)\chi_{-\kappa m}(\vec{r}) \end{pmatrix}, \tag{5.81}$$

where $\chi_{\kappa m}$ are spin-angular function with relativistic quantum number κ. The latter is related to two quantum numbers l and j as follows:

$$\kappa = 2(l - j)(j + 1). \tag{5.82}$$

The equations of relativistic Hartree–Fock approximation (Hartree–Fock–Dirac approximation) are written as:

$$\left(\frac{\mathrm{d}}{\mathrm{d}r}-\frac{\kappa_i}{r}\right)G_i(r)-\left[\varepsilon_i-\tilde{U}_i(r)\right]F_i(r)=\frac{1}{r}\sum_{\substack{k\\ j\neq i}}D_k(i,j)\tilde{Y}^k_{ij}(r)F_j(r), \tag{5.83}$$

$$\left(\frac{\mathrm{d}}{\mathrm{d}r}+\frac{\kappa_i}{r}\right)F_i(r)-\left[2+\alpha^2\left(\varepsilon_i-\tilde{U}_i(r)\right)\right]G_i(r)$$
$$=-\frac{\alpha^2}{r}\sum_{k;j\neq i}D_k(i,j)\tilde{Y}^k_{ij}(r)G_j(r), \tag{5.84}$$

here α is the so-called fine structure constant $\alpha = 1/c \approx 1/137.04$.

The wave function is defined by its larger $F_i(r)$ and smaller $G_i(r)$ parts. The orthogonality relation (1.11) is replaced by the following one:

$$\int_0^\infty \left(F_i(r)F_j(r)+\alpha^2 G_i(r)G_j(r)\right)\mathrm{d}r = \delta_{ij}. \tag{5.85}$$

The self-consistent direct potential acting on electrons of i-shell is written as:

$$\tilde{U}_i(r)=\frac{1}{r}\left[\sum_{j,k}^{s}D_k(i,j)\tilde{Y}^k_{jj}(r)+\sum_{j,k}^{s}C_k(i,j)\tilde{Y}^k_{ii}(r)-Z\right], \tag{5.86}$$

where Z is the nuclear charge and

$$\tilde{Y}^k_{ij}(r)=r\int\frac{r^k_<}{r^{k+1}_>}\left[F_i(r')F_j(r)+\alpha^2G_i(r')G_j(r')\right]\mathrm{d}r'. \tag{5.87}$$

When neglecting exchange of small component and making use of substitution:

$$F_i(r)=\xi_i(r)P_i(r), \tag{5.88}$$

where

$$\xi_i(r)=\sqrt{1+\alpha^2/2\left[\varepsilon_i-U(r)\right]}, \tag{5.89}$$

one transforms a system of $2S$ (5.83) and (5.84) of the first order to the following system of S second-order equations:

$$\frac{\mathrm{d}^2}{\mathrm{d}r^2}P_i(r)+\left[2\varepsilon_i+\alpha^2\varepsilon_i^2-2U_i(r)-2\alpha^2\varepsilon_iU_i(r)-\frac{\kappa_i(\kappa_i+1)}{r^2}\right.$$
$$\left.+\alpha^2U_i^2(r)-\alpha^2W_i(r)\right]P_i(r)$$
$$=\xi_i(r)X_i(r), \tag{5.90}$$

where q_i is the number of electrons in a subshell and $\gamma_k(i,j)$ the weight factors, which are presented for the relativistic case in [5.53] and the potential $U_i(r)$ takes into account the finite size of the nucleus, its radius being R_{nucl}:

$$U_i(r) = \begin{cases} \frac{1}{r}\left\{ Y_i(r) - \frac{Z}{2}\left(\frac{r}{R_{\text{nucl}}}\right)\left[3 - \left(\frac{r}{R_{\text{nucl}}}\right)^2\right]\right\}, & r \le R_{\text{nucl}} \\ \frac{1}{r}[Y_i(r) - Z], & r > R_{\text{nucl}} \end{cases}, \tag{5.91}$$

$$Y_i(r) = \sum_{i=1}^{S}\left(q_i - \delta_{ij}\right) Y_{jj}^0(r) - \frac{2}{q_i}\sum_{j=1}^{S}\sum_{k>0}\gamma_k'(i,j) Y_{ij}^k(r), \tag{5.92}$$

$$Y_{ij}^k(r) = r\int_0^\infty \frac{r_<^k}{r_>^{k+1}}\left[\xi_i(r')P_i(r')\xi_j(r')P_j(r') + \alpha^2 G_i(r')G_j(r')\right], \tag{5.93}$$

$$G_i(r) = \frac{1}{2\xi_i^2(r)}\left[\frac{\mathrm{d}}{\mathrm{d}r}\left(\xi_i(r)P_i(r) + \frac{\kappa_i}{r}\xi_i(r)P_i(r)\right)\right], \tag{5.94}$$

$$W_i(r) = \frac{1}{4\xi_i^2(r)}\left[\frac{\mathrm{d}^2}{\mathrm{d}r^2}U_i(r) + \frac{3\alpha^2}{4\xi_i^2(r)}\left(\frac{\mathrm{d}}{\mathrm{d}r}U_i(r)\right)^2 - \frac{2\kappa_i}{r}U_i(r)\right], \tag{5.95}$$

$$X_i(r) = -\frac{2}{q_i r}\sum_{j\neq i}\sum_{k>0}\gamma_k(i,j)Y_{ij}^k(r)\xi_j(r)P_j(r). \tag{5.96}$$

Theoretical approaches for relativistic calculations of atomic radiative transitions were developed and calculations carried out in [5.55–5.61]. In relativistic approach the dipolar matrix element of electron transition from a filled shell (j_f, l_f, κ_f) to a single vacancy state (j_k, l_k, κ_k) is given by the following two formulae in length and velocity forms (or gauge), respectively:

$$\left\langle j_k \left| d^R(\omega) \right| j_f \right\rangle = \sqrt{2[j_k j_f]}\begin{pmatrix} j_k & j_f & 1 \\ 1/2 & -1/2 & 0 \end{pmatrix}\left[3J_1 + \frac{3}{2}\alpha(\kappa_f - \kappa_k)I_2^+ - 2\alpha I_2^-\right], \tag{5.97}$$

$$\left\langle j_k \left| d^V(\omega) \right| j_f \right\rangle = \sqrt{2[j_k j_f]}\begin{pmatrix} j_k & j_f & 1 \\ 1/2 & -1/2 & 0 \end{pmatrix}\left[\alpha(\kappa_k - \kappa_f)I_0^+ - \alpha I_0^- + \frac{1}{2}\alpha(\kappa_k - \kappa_f)I_2^+ + 2\alpha I_2^-\right]. \tag{5.98}$$

Radial integrals appearing in these formulae are written as:

$$J_1(\omega) = \int_0^\infty j_1(\alpha\omega r)\left[\xi_f(r)\xi_k(r)P_f(r)P_k(r) + \alpha^2 G_f(r)G_k(r)\right]\mathrm{d}r, \tag{5.99}$$

$$I_L^{\pm}(\omega) = \int_0^{\infty} j_L(\alpha\omega r)\left[\xi_f(r)P_f(r)G_k(r) \pm \xi_\kappa(r)P_k(r)G_f(r)\right]\mathrm{d}r. \quad (5.100)$$

In the above formulae, $j_L(\alpha\omega r)$ stands for the Bessel functions.

5.8 Nonradiative or Auger Decay

As it was mentioned at the very beginning of this chapter, due to interelectron interaction the inner shell vacancy in atom, molecule, or solid may be filled by an electron of outer shell that is accompanied by the ejection of one or more electrons into continuum. This type of transitions, as it was said above, is called Auger effect. The initial state in any Auger process is the ionized state, and final state involves doubly or triply ionized ionic state and electron (or electrons) in continuum. More complex processes, in which the initial state includes photoionization satellites, are also possible.

Consider a process of the filling of a vacancy k^{-1} by an electron from a shell i with simultaneous ejection of electron j to continuum q. These transitions correspond to diagram lines and are denoted as A-lines [5.62]. The contribution of this transition to the self-energy is represented by the following diagram:

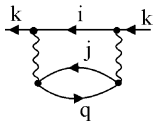

(5.101)

It is assumed that the diagrams with exchanged hole states in one or two vertexes are also included in this diagram. The representation of Auger process (5.101) is more convenient for spectral function technique and will be used throughout this section. In one-electron approximation Auger width of atomic vacancy k is given by formula (5.4). In this formula U denotes Coulomb interaction with holes exchange in final state taken into account. In relativistic case the interelectron interaction is more complex (see [BLP])

$$U_\omega = \frac{1}{r_{12}} - (\boldsymbol{\alpha}_1 \cdot \boldsymbol{\alpha}_2)\frac{\exp(i\omega r_{12})}{r_{12}} + (\boldsymbol{\alpha}_1 \cdot \nabla_1)(\boldsymbol{\alpha}_2 \cdot \nabla_2)\frac{\exp(i\omega r_{12}) - 1}{\omega^2 r_{12}}, \quad (5.102)$$

where r_{12} is the interelectron distance and $\omega = |\varepsilon_k - \varepsilon_i|/c \approx \omega' = |\varepsilon_j - \varepsilon_q|/c$ and $\boldsymbol{\alpha}_1, \boldsymbol{\alpha}_2$ are Dirac matrixes.

This general expression may be transformed to the form [5.63], in which the interaction is decomposed with respect to powers of fine structure constant α:

$$V_\omega = \frac{1}{r_{12}} - \frac{1}{r_{12}}\left[\frac{(\boldsymbol{\alpha}_1 \cdot \boldsymbol{\alpha}_2) + (\boldsymbol{\alpha}_1 \cdot r_1)(\boldsymbol{\alpha}_2 \cdot r_2)}{r_{12}^2}\right] - i\frac{2}{3}\omega(\boldsymbol{\alpha}_1 \cdot \boldsymbol{\alpha}_2) + O(\boldsymbol{\alpha}_1)(\boldsymbol{\alpha}_2)(\omega r_{12})^2, \quad (5.103)$$

where the second term represents the so-called Breit interaction [BLP], the contribution of which is of the order $(Z^*\alpha)^2$ relative to the Coulomb interaction. The third term is the leading imaginary term having the order $(Z^*\alpha)^3$ and the last term has the order $(Z^*\alpha)^4$. The value of Z^* stands for the effective atomic charge felt by the shell under consideration. It follows from an order of the magnitude estimations that for light atoms with $Z < 40$ a non-relativistic form including only Coulomb interaction is sufficient. For atoms $40 < Z < 70$ or for outer shells of heavy atoms relativistic formulation with the Breit interaction is adequate. For $70 < Z < 90$ the leading imaginary term should be also taken into account and for $Z > 90$ the complete interaction (5.103) should be used.

Non-relativistic Coulomb matrix elements of Auger transition (1.33) is replaced by relativistic one, corresponding to the first term in (5.103):

$$\langle \nu_1 \nu_3 \,|V|\, \nu_2 \nu_4 \rangle \equiv \int \mathrm{d}x \mathrm{d}x' \left[P_{\nu_1}(x) P_{\nu_2}(x) + \alpha^2 G_{\nu_1}(x) G_{\nu_2}(x) \right] \frac{1}{|\vec{r} - \vec{r}'|} \times \left[P_{\nu_3}(x) P_{\nu_4}(x) + \alpha^2 G_{\nu_3}(x) G_{\nu_4}(x) \right]. \tag{5.104}$$

In the present book we consider Auger process in light atoms and use Coulomb interaction as the transition matrix element in the form (1.33). In $L - S$ coupling scheme two vacancies in the final state are coupled into total momentum L_{ij} and spin S_{ij}, and then with electron q in continuum into total momentums L and S. It is clear that since the coupling scheme for Auger decay is the same as that for satellite excitation, one can use formulae (5.23) and (5.24).

The angular momentum graphical technique makes possible to generalize formulas for weight factors for the case of unfilled shells. We consider the case of ionization of filled inner shell $l_k^{4l_k+2}$ in the presence of an unfilled shell $l_j^{N_j}(L_j S_j)$. For each of the terms of unfilled shell $L_j S_j$ this process results in a number of initial LS terms, whose Auger decay processes are considered independently. The states after Auger decay are denoted as $l_i^{N_i'}(\underline{L}_i \underline{S}_i) l_j^{N_j'}(\underline{L}_j \underline{S}_j)(L_{ij} S_{ij}) l_q(LS)$. We underline the terms of configuration of $N_j - 1$ electrons by one line. The terms of configuration of $N_j - 2$ electrons will be underlined by two lines.

There are three cases depending on the final hole position which we consider separately. The reduction of momentum diagram for the case when two final state holes are created in a closed shell results in the following weight factor:

$$f^{\lambda}_{kiiq} = 2^{1/2} [L_{ij} S_{ij} \underline{\underline{L}}_i \underline{\underline{S}}_i]^{1/2} (-1)^{L_j + L_{ij} + \underline{\underline{S}}_i + S_j + S_{ij}} \times \begin{Bmatrix} S & S_j & 1/2 \\ \underline{\underline{S}}_i & 1/2 & S_{ij} \end{Bmatrix} \times \begin{Bmatrix} \underline{\underline{L}}_i & l_k & l_q \\ \lambda & l_i & l_j \end{Bmatrix} \begin{Bmatrix} L & l_k & L_j \\ \underline{\underline{L}}_i & L_{ij} & l_q \end{Bmatrix}. \tag{5.105}$$

In the case when one final vacancy is in initially filled shell and one vacancy in initially unfilled shell, the Coulomb interaction consists of direct and exchange parts, whose weight factors are as follows:

$$f^{\lambda}_{kjiq} = N_j^{1/2} G^{L_j S_j}_{\underline{L}_j \underline{S}_j} [L_{ij} S_{ij} L_j S_j]^{1/2} (-1)^{S+\underline{S}_j+1} \begin{Bmatrix} S & S_j & 1/2 \\ \underline{S}_j & S_{ij} & 1/2 \end{Bmatrix}$$
$$\times \sum_r [r] \begin{Bmatrix} \lambda & L_{ij} & r \\ \underline{L}_j & l_k & l_i \end{Bmatrix} \begin{Bmatrix} L & l_j & r \\ \underline{L}_j & l_k & L_j \end{Bmatrix} \begin{Bmatrix} L & l_j & r \\ \lambda & L_{ij} & l_q \end{Bmatrix}, \tag{5.106}$$

$$g^{\mu}_{kijq} = N_j^{1/2} G^{L_j S_j}_{\underline{L}_j \underline{S}_j} [L_{ij} S_{ij} L_j S_j]^{1/2} [S]^{-1} (-1)^{L+L_j+\underline{L}_j+l_k+l_q+\mu}$$
$$\times \begin{Bmatrix} L & \underline{L}_j & \mu \\ l_i & l_q & L_{ij} \end{Bmatrix} \begin{Bmatrix} L & \underline{L}_j & \mu \\ l_j & l_k & L_j \end{Bmatrix} \delta(S, \underline{S}_j). \tag{5.107}$$

In the case of two holes in initially unfilled shell there is a direct term only, and the corresponding formula is written as:

$$f^{\lambda}_{kjjq} = \left(N_j (N_j - 1)\right)^{1/2} \sum_{\underline{L}_j \underline{S}_j} G^{L_j S_j}_{\underline{L}_j \underline{S}_j} G^{\underline{L}_j \underline{S}_j}_{\underline{\underline{L}}_j \underline{\underline{S}}_j} \left[L_j \underline{L}_j S_j \underline{S}_j^{-1} \right]^{1/2}$$
$$\times (-1)^{L+L_j+\underline{L}_j+\underline{\underline{L}}_j+l_j+l_q} \times \begin{Bmatrix} L & \underline{L}_j & \lambda \\ l_j & l_k & L_j \end{Bmatrix} \begin{Bmatrix} L & \underline{L}_j & \lambda \\ l_j & l_q & \underline{\underline{L}}_j \end{Bmatrix} \delta(S, \underline{S}_j) \tag{5.108}$$

To envisage electron correlations, which are essential for calculation of Auger rates we consider as an example *KLL* Auger rates in Ne. It was shown [5.64] that the interaction of final state configurations $2s^{-2}(^1\mathrm{S})$ and $2p^{-2}(^1\mathrm{S})$ results in a significant decrease of the rate of the former transition and increase the rate of the latter one. Calculations by MBPT [5.65], by scattering theory [5.66] and multiconfiguration Dirac–Fock method [5.29] showed that the interactions involving a continuum electron also influence the Auger rates. It should be noted that in many cases the one-electron Auger matrix elements for atoms $6 < Z < 92$ [5.67] are sufficient to represent the experimental values.

The interaction between channels of Auger decay involving electron in continuum may be represented by the following diagrams (direct and exchange):

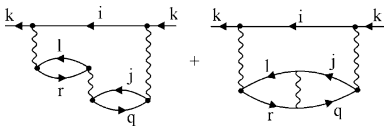

(5.109)

Contribution of these processes to the self-energy is written as:

$$\mathrm{Im}\Sigma_k(E) = -2\pi \sum_{i,j,l<F} (-1)^{l+h} \int \langle kj \,|U|\, iq \rangle \, \delta(E - \varepsilon_i - \varepsilon_j + \varepsilon_q)$$
$$\times \mathrm{d}\varepsilon_q \int \frac{\langle kl \,|U|\, iq \rangle \, \langle lr \,|U|\, jq \rangle \, \mathrm{d}\varepsilon_r}{\varepsilon_i + \varepsilon_l - \varepsilon_r - E}. \tag{5.110}$$

If two interacting final-state configurations differ by the states of two holes, the only possible coupling between them is the configuration interaction shown in the following diagram:

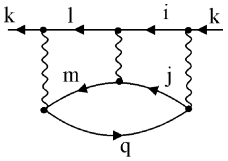

(5.111)

This interaction is non-zero if $L_{lm} = L_{ij}$ and $S_{lm} = S_{ij}$. Formula for the contribution of this diagram to the self-energy is written as:

$$\mathrm{Im}\Sigma_k(E) = -2\pi \sum_{i,j,l,m<F} (-1)^{l+h} \int \langle kj\,|U|\,iq\rangle\, \delta(E - \varepsilon_i - \varepsilon_j + \varepsilon_q) \times \mathrm{d}\varepsilon_q \frac{\langle km\,|U|\,lq\rangle\, \langle lm\,|U|\,ij\rangle}{\varepsilon_i + \varepsilon_m - \varepsilon_q - E}. \tag{5.112}$$

The wave functions in matrix element of Auger process may by calculated with different account for core relaxation. The approximation of relaxed vacancy assumes that relaxation process is faster than Auger decay and outgoing electron "feels" the relaxed field.

It is also possible to account for vacancy relaxation in a frozen core basis provided that the diagrams for interaction between satellite excitation and Auger decay are calculated directly:

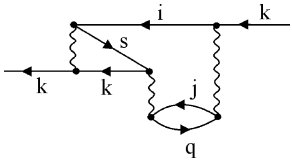

(5.113)

Contribution of this diagram to the self-energy is written as:

$$\mathrm{Im}\Sigma_a(E) = -2\pi(-1)^{l+h} \int \langle kj|U|iq\rangle \delta(E - \varepsilon_i - \varepsilon_j + \varepsilon_q)\mathrm{d}\varepsilon_q \left(\sum_s + \int_{\varepsilon_s} \mathrm{d}\varepsilon_s\right) \times \frac{\langle kl|U|iq\rangle\langle ki|U|ks\rangle}{\varepsilon_k + \varepsilon_i - \varepsilon_s - E} \tag{5.114}$$

The C_α satellites in Auger spectra [5.62] correspond to spectator satellite states of initial vacancy creation. The final states of these satellites differ from the final states of diagram Auger lines by the additional particle–hole pair $l^{-1}s$. Contribution of this process is represented by the following diagram:

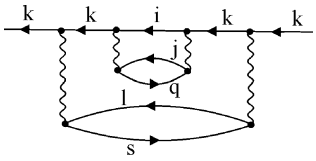

(5.115)

and is given by the formula:

$$\mathrm{Im}\Sigma_b(E) = 2\pi(-1)^{l+h} \int |\langle kj|U|iq\rangle|^2 \delta(E - \varepsilon_i - \varepsilon_j - \varepsilon_l + \varepsilon_s + \varepsilon_q) \mathrm{d}\varepsilon_q$$
$$\times \left(\sum_s + \int_{\varepsilon_s} \mathrm{d}\varepsilon_s \right) \frac{|\langle kl|U|ks\rangle|^2}{(\varepsilon_k + \varepsilon_l - \varepsilon_s - E)^2}. \tag{5.116}$$

There are two different possibilities to reach the Auger shake-up spectator satellite state—$i^{-1}j^{-1}l^{-1}sq$—resonant and non-resonant ones. In the resonant path, the excited photoelectron satellite state is decaying into the Auger satellite spectator state. These satellites are labeled as C_α [5.62].

In photoelectron spectra this path corresponds to a satellite with higher binding energy than—for the main line and in Auger spectrum—to a satellite with lower kinetic energy. The energy required to leave an ion in the excited state is taken partly from the photoelectron and partly from the Auger electron. On the other hand, the non-resonant path corresponding to the main photoelectron line binding energy is also possible [5.68, 5.69]. This is a path via virtual satellite states and the energy conservation is fulfilled in the final stage of Auger decay only. Hence all energy required to leave the doubly charged ion in excited state $i^{-1}j^{-1}l^{-1}s$ is taken from the Auger electron. We will call the Auger satellites, corresponding to the main photoelectron line binding energy as *the main line satellites*. The kinetic energies of the *main line satellites* are equal to the difference of the kinetic energies of the C_α satellites with the same final ionic state and corresponding shake-up satellite excitation energy. Since the main line satellites correspond to the main photoelectron line binding energy, they contribute to the main photoelectron line width.

The ground state correlations are also important in calculation of Auger rates. Since the creation of single particle–hole pairs are already included in the Hartree–Fock ground state we should take into account simultaneous creation of two particle–hole pairs $i^{-1}j^{-1}pr$, depicted by the following diagram:

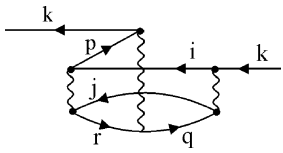

(5.117)

Contribution of this diagram to the self-energy of the state k^{-1} is given by the formula:

$$\mathrm{Im}\Sigma(E) = 2(-1)^{l+h} \int \langle kj\,|U|\,iq\rangle\,\delta(E-\varepsilon_i-\varepsilon_j+\varepsilon_q) \times \left(\sum_{p,r} + \int_{\varepsilon_p,\varepsilon_r} \mathrm{d}\varepsilon_p \mathrm{d}\varepsilon_r\right) \frac{\langle ij\,|U|\,pr\rangle\,\langle kr\,|U|\,pq\rangle}{\varepsilon_p+\varepsilon_r-\varepsilon_i-\varepsilon_j}. \quad (5.118)$$

5.9 Line Shapes of Low-Energy Auger Spectra

In order to calculated line shapes of Auger spectra we represent the imaginary part of the self-energy as a sum of contributions of different channels:

$$\mathrm{Im}\Sigma_k(E) = \sum_{ilq} \Omega_{kilq}(E)\delta(\varepsilon_i+\varepsilon_l-\varepsilon_q-E), \quad (5.119)$$

where $\Omega_{kilq}(E)$ denotes the contribution of transition $k^{-1} \to i^{-1}l^{-1}q$.

Therefore, the spectral function is a sum of functions of vacancy energy E and kinetic energies ε_q of Auger electrons:

$$A_k(E,\varepsilon_q) = \frac{\sum_{ilq}\Omega_{kilq}(E)\delta(\varepsilon_i+\varepsilon_l-\varepsilon_q-E)}{[\varepsilon_k+\mathrm{Re}\Sigma_k(E)-E]^2+[\mathrm{Im}\Sigma_k(E)]^2}. \quad (5.120)$$

Integration over all kinetic energies ε_q of Auger electrons results in the spectral function in the vacancy energy scale. In the Auger kinetic energy scale this function defines spectral densities of satellite decay into different Auger channels. If the requirement of slow variation of the self-energy is fulfilled, all Auger lines have the same Lorentzian widths and their intensities are proportional to partial widths $\Omega_{kilq}(E)$.

In the case of decay of shake-up satellites $i^{-1}j^{-1}s$ to continuum states $i^{-1}l^{-1}q$, the condition of slow variation of the self-energy usually is not fulfilled and distribution of the photoelectron line between low-energy Auger lines [5.70] becomes more complex [5.44–5.46, 5.71]. In this case the distribution of photoelectron line intensity between Auger channels is energy dependent:

$$\Omega_{klkq}(E) = \pi \left|\langle kl\,|U|\,kq\rangle + \frac{\langle kj\,|U|\,ks\rangle\,\langle jq\,|U|\,lr\rangle}{\varepsilon_k+\varepsilon_j-\varepsilon_s-E}\right|^2. \quad (5.121)$$

In the vicinity of resonance point at $E = \varepsilon_k+\varepsilon_j-\varepsilon_s$, $\Omega_{klkq}(E)$ is a very sharp function of energy. This function depends on the sign of the interference between two channels—resonant and non-resonant.

5.10 Two-Electron and Radiative Auger Decay

A double Auger decay, i.e., a transition from a one-hole state to a three-hole–two-particle state is depicted by a set Feynman diagrams; one of them may be plotted as follows [5.9, 5.72]:

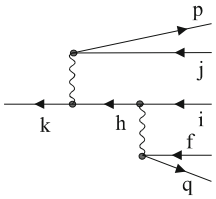

(5.122)

Diagrams corresponding to exchange of hole states at each vertex should be also taken into account. These diagrams are omitted for sake of brevity. The summation over intermediate states h is implied. Contributions of this process to two values are of interest: to the initial hole width and to the probability of the origin of the final states. The latter value strongly depends on the energy distribution between the electrons p and q.

In some cases the transition from the initial state k^{-1} to the final $i^{-1}j^{-1}f^{-1}pq$ state may be divided into two steps with energy conservation at each of them. This transition is called a cascade process. In the cascade process all the energy released in the transition of the initial hole k^{-1} to two-hole state $j^{-1}h^{-1}$ is transferred to the continuum electron p and the contribution of this process to the initial hole width is written as:

$$\Gamma_k = 2\pi \int |\langle kj\,|U|\,hp\rangle|^2\,\delta(\varepsilon_k - \varepsilon_h - \varepsilon_j + \varepsilon_p)\mathrm{d}\varepsilon_p. \tag{5.123}$$

The probability of forming of a given final state is written as:

$$\Gamma_{k,ijfpq} = 4\pi^2 \int |\langle kj\,|U|\,hp\rangle|^2\,\delta(\varepsilon_k - \varepsilon_h - \varepsilon_j + \varepsilon_p) \times \mathrm{d}\varepsilon_p \int \frac{1}{\Gamma_h} |\langle hf\,|U|\,iq\rangle|^2\,\delta(\varepsilon_h - \varepsilon_i - \varepsilon_f + \varepsilon_q)\mathrm{d}\varepsilon_q, \tag{5.124}$$

where Γ_h is the width of the intermediate hole h^{-1}.

The cascade process part of (5.122) results in two lines in Auger spectrum, whose energies correspond to the energy conservation in both steps.

The double Auger process results in continuous distribution of the released energy between electrons in the final state. New holes may also further decay resulting in a so-called tree of decay. This process starts from a hole in an inner shell and end up forming a highly charged ion. This complex process was considered within several simplifications in [5.72, 5.73].

Also a simultaneous decay of one-hole state into three-hole–two-particle state, in which the energy conservation is fulfilled between initial and final states is possible.

As the result of this process the released energy is continuously distributed between two electrons [5.72, 5.74, 5.75]. Contribution of this process to the initial vacancy width equals the probability of origin of final state regardless of energy distribution between particles p and q:

$$\Delta\Gamma_{k,ijfpq}=2\pi\left(\sum_{p}+\int_{\varepsilon_p}\mathrm{d}\varepsilon_p\right)\frac{|\langle kj\,|U|\,hp\rangle|^2\,|\langle hf\,|U|\,iq\rangle|^2\,\delta(\varepsilon_k-\varepsilon_i-\varepsilon_j-\varepsilon_f+\varepsilon_p+\varepsilon_q)}{(\varepsilon_k-\varepsilon_h-\varepsilon_j+\varepsilon_p)^2}. \tag{5.125}$$

The integrand in the above formula is the density of probability per unit energy range for the decay into definite energy of electron p.

Transition from initial two-hole state $i^{-1}j^{-1}$ to the other two-hole state $m^{-1}f^{-1}$ with simultaneous removal of electron from a shell h to continuum state q are also possible [5.72, 5.74, 5.75]. In this case the energy released in simultaneous filling of the vacancies i^{-1} and j^{-1} by the vacancies m and f is transferred to atomic electron h, which is ejected to continuum state q. Probability of this transition in a unit of time is written as:

$$\Gamma_{ijq,mfh}=2\pi\left|M_{ijq,mfh}\right|^2, \tag{5.126}$$

where $M_{ijq,mfh}$ is the matrix element of interaction between three electron states.

The MBPT is usually applicable to this process, since atomic subshells are quite well separated in energy and the Coulomb interaction between electrons of different subshells is relatively weak. It should be noted that the lowest-order diagrams of double Auger transition amplitude are of the second-order ones, whereas the diagrams of Auger decay of each one of the holes in the two-hole state are of the first order. Hence it follows that in a general case the contribution of double Auger decay to the probability of decay of two-hole state is rather small. However, it is far from being negligible, since it can relatively often reach 30% of the total decay probability [5.71].

But it can be of particular importance when the double Auger decay becomes the only possible non-radiative decay of two-hole state. It takes place, if the energy released in the transition of a single hole, say $i^{-1}\rightarrow m^{-1}$, is not sufficient for removal of electron from the h-subshell, but the energy released in double-hole process $i^{-1}j^{-1}\rightarrow m^{-1}f^{-1}$ is sufficient for this process.

The one-electron Auger decay of two-hole state [5.75–5.77], shown in the next diagram consists of a transition of a hole j^{-1} to a two-hole–one particle state $h^{-1}f^{-1}p$, i.e., virtual Auger process, and a subsequent transition of the state $i^{-1}p$ to a state $m^{-1}q$:

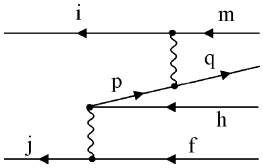

(5.127)

Amplitude of this process is written as:

$$M^{(1)}_{ij,mfhq}(E) = \left(\sum_p + \int_{\varepsilon_p} \mathrm{d}\varepsilon_p \right) \frac{\langle jp\,|U|\,fh\rangle\,\langle ip\,|U|\,mq\rangle}{E - \varepsilon_f - \varepsilon_h + \varepsilon_p} \delta(E - \varepsilon_f - \varepsilon_h - \varepsilon_m + \varepsilon_q), \tag{5.128}$$

where the sum runs over all discrete and continuum states p.

The process depicted in the following diagram is similar to the previous one, but the second interaction takes place between two-hole states and does not involve continuum transitions:

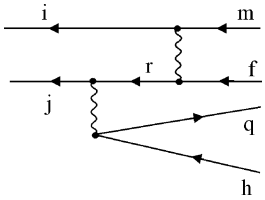

(5.129)

Formula for the amplitude of this process is written as:

$$M^{(2)}_{ij,mfhq}(E) = \sum_r \frac{\langle jh\,|U|\,rq\rangle\,\langle ip\,|U|\,mq\rangle}{E - \varepsilon_i - \varepsilon_r - \varepsilon_h + \varepsilon_q} \delta(E - \varepsilon_f - \varepsilon_h - \varepsilon_m + \varepsilon_q). \tag{5.130}$$

Sum runs over all possible hole states, but since atomic shells are well separated in energy it includes only few terms. In particular, if $r = j$, first vertex represents the excitation of shake-up satellite from the shell h.

Next diagram, differing from the previous one by the permutation of vertexes shows a transition of a deep two-hole state $i^{-1}j^{-1}$ to a two-hole state with smaller binding energy $r^{-1}m^{-1}$, with subsequent decay of one of them:

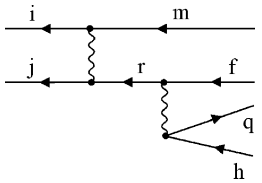

(5.131)

Contribution of this diagram to the amplitude of Auger decay of two-hole state is written as:

$$M^{(3)}_{ijq,mfh}(E) = \sum_r \frac{\langle ij\,|U|\,mr\rangle\,\langle rh\,|U|\,fq\rangle}{E - \varepsilon_m - \varepsilon_r} \delta(E - \varepsilon_f - \varepsilon_h - \varepsilon_m + \varepsilon_q) \tag{5.132}$$

In addition to above-considered diagrams, one should take into account diagrams differing by permutation of holes in initial and final states. Complete set of such states and formulas for angular parts is presented in [5.76–5.78].

One-electron Auger decay of two-hole state 1s-2 may result in the lines with kinetic energies larger than the binding energy of 1s-electron. If both initial vacancies are in the intermediate subshells, the Auger decay could result in that a deeper vacancy goes down and the shallow one floats up [5.76]. Also possible is the situation of counter movement, when the shallow vacancy goes down and the deeper one floats up [5.77]. Two-vacancy states may also have their own satellites [5.78, 5.79]. The diagram (5.131), in which $i^{-1}j^{-1} = m^{-1}f^{-1}$ is an example of such a process.

The vacancy decay due to interaction may not be pure Auger or pure radiative. The decay can take place with simultaneous ejection of electrons and radiation of photons and is called semi-Auger decay (see e.g., [5.10,5.80,5.81]). Such processes in the lowest order of inter-electron interaction are exemplified in

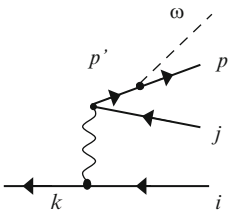

(5.133)

5.11 Single Photon Decay of Two-Hole States

Interactions between atomic electrons results also in simultaneous decay of two vacancies with ejection of one photon [5.82–5.85]. The energy of photon radiating in the decay of inner shell vacancies is large. Roughly speaking, for inner vacancies it is equal to the total energy of decaying vacancies. For such decay the transfer in the process energy is big so the interaction that leads to such a process is weak. Thus, in this section, just as in Sect. 5.10, we use perturbation expansion with respect to interelectron interaction. Simplest amplitude of this process $M_{j_1 j_2 i_1 i_2}$ is represented by the following diagram:

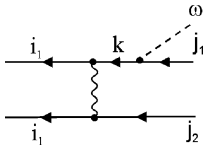

(5.134)

Also three other diagrams in which photon line is connected with other hole lines should be taken into account. The energy of radiated photon equals to $\omega_{j_1 j_2 i_1 i_2} = E_{j_1 j_2} - E_{i_1 i_2}$. The sum (and integration) in diagram (5.134) runs over all possible hole or particle states k. Probability (partial width) is given by the following formula:

$$\Gamma^{\gamma}_{j_1 j_2 i_1 i_2} = \frac{4}{3}\frac{\omega^3_{j_1 j_2 i_1 i_2}}{c^3}\left|M_{j_1 j_2 i_1 i_2}\right|^2. \tag{5.135}$$

Total width of single photon decay of two-hole state $\Gamma^{\gamma}_{i_1 i_2}$ is obtained from partial widths $\Gamma^{\gamma}_{j_1 j_2 i_1 i_2}$ by summing over $j_{1,2}$ with account for the energy conservation $\omega_{j_1 j_2 i_1 i_2} = E_{j_1 j_2} - E_{i_1 i_2}$.

The idea of this decay was pointed out in the 30s of the twentieth century by A. Sommerfeld while first real calculations were carried out much later [5.83]. It appeared that contributions from all four diagrams of type (5.134) should be taken into account and the sum should run over wide range of k. Significant role of large number k-states emphasize the many-electron character of single photon decay of two-vacancy states. Estimation demonstrates that the width $\Gamma^{\gamma}_{j_1 j_2 i_1 i_2}$, as a rule, is six orders of magnitude less than the Auger width of each of the levels i_1 and i_2. The ratio $\Gamma^{\gamma}_{j_1 j_2 i_1 i_2}$ to the doubled width of radiative decay is in the range from 0.002 to 0.47. We present as an example the results for the following decays:

Ne^{2+}: decay $1s^{-2} \to 2s^{-1}2p^{-1}$, width $\Gamma^{\gamma} = 1.3 \times 10^{-5}\,\mathrm{eV}$
Ar^{2+}: decay $2s^{-2} \to 3s^{-1}2p^{-1}$, width $\Gamma^{\gamma} = 4.06 \times 10^{-5}\,\mathrm{eV}$
Xe^{2+}: decay $4d^{-2} \to 5s^{-1}5p^{-1}$, width $\Gamma^{\gamma} = 0.43 \times 10^{-5}\,\mathrm{eV}$.

Experimental data for the decay in Ne—$1.4 \times 10^{-5}\,\mathrm{eV}$ are close to the above theoretical results.

The probability of single photon decay increases significantly for relatively small photon energy. That takes place, when the decaying vacancies are in the intermediate or even outer subshells. The decrease of $\omega_{j_1 j_2 i_1 i_2}$ in (5.135) is easily compensated by the growth of the amplitude, which includes wave functions with larger overlap. This may take place in the two-vacancy decay of intermediate shells. As this takes place, one of the final state vacancies may be deeper than one of the initial [5.77,5.86], i.e., deepening or oncoming movements are possible. Decay of double vacancy states in the intermediate shell leads to a wide variety of photon energies. In the considered case of noble gases—Ne, Ar, and Kr the photon energy $\omega_{j_1 j_2 i_1 i_2}$ varies in a wide range from 1 to 60 Ry, and radiation width varies from 0.06×10^{-7} to $227 \times 10^{-7}\,\mathrm{eV}$.

Single-photon and single-electron decay in ions with two or more vacancies is a purely correlation process. Its probability is determined by the electron–electron interaction, and this process gives rise to a significant number of new spectral lines of appreciable intensity [5.10].

5.12 Auger and Radiative Decay of Excited States

In this section we will describe the Auger decay of the excited state of an atom. Let us begin with the elementary exited state represented by an electron–hole pair ni. The amplitude of such decay in the lowest order of interelectron interaction causing transition with emission of an Auger electron q with energy E_q and creation of a hole k in any of the outer subshells, can be presented as (5.136):

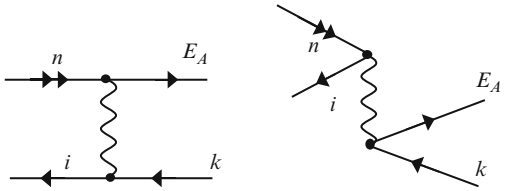

(5.136)

To the same class as the processes depicted by (5.136), belongs the decay of an electron-vacancy excitation in the presence of a vacancy [5.73]. Decay of such a state can proceed via a number of various channels, including that with emission of one electron [5.79] or a photon.

To the class of processes discussed in this section belongs the decay of excited states (5.137) and autoionization of double-excited states (5.138a) and *three-electron radiative decay* (5.138b). Autoionization processes, both single- and double, are possible if discrete resonance excitation is lying above the threshold of single-electron ionization. These processes are of interest in themselves, and also as a second or even a third–fourth "elementary" stage of multiple ionization of an atom or ionization into the excited state of an ion.

Double autoionization of resonantly excited states, exemplified by the diagram (5.137), as a matter of fact, is similar to the two-electronic Auger transitions, in which two electrons are emitted with any values of the orbital moments (l_1, l_2). The decay energy is distributed between outgoing electrons arbitrarily. Note that most probable is the situation when one electron is fast and the other is slow. The transition (5.137) also has features, characteristic for "contrary movement" of vacancies [5.77] in three-electronic Auger transitions if transition of an electron to a discrete level to treat as creation of a hole.

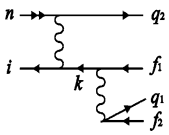

(5.137)

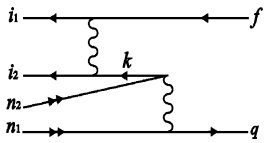

(5.138a)

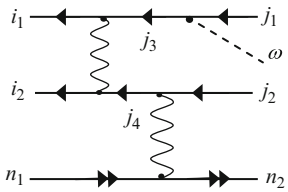

(5.138b)

As an example of (5.137) in [5.79] the following channels of double autoionization in Kr were considered: (a) $3d^{-1}5p\ [^1\mathrm{P}] \rightarrow 4s^{-2}\ [^1S] + (q_1q_2)$; (b) $3d^{-1}5p\ [^1\mathrm{P}] \rightarrow 4s^{-1}4p^{-1}\ [^1\mathrm{P}] + (q_1q_2)$; (c) $3d^{-1}5p[^1\mathrm{P}] \rightarrow 4s^{-1}4p^{-1}\ [^3\mathrm{P}] + (q_1q_2)$. It is shown that, the transition (a) can be only direct and therefore has only correlation nature. Channels (b) and (c) can proceed either directly, or in two sequential steps, via the intermediate state $4s^{-2}5p$.

The process (5.138b) gives new photon lines.

Autoionization of double excited states can lead to occurrence of structures in the cross-sections of single-electron ionization. The energy of these states is sufficient for ionization of a subvalent subshell, that at the resonant photon energy opens an additional (to traditionally considered $A+\omega \rightarrow A^+ + \mathrm{e}$) two-step channel $A+\omega \rightarrow A^* \rightarrow A^+ + \mathrm{e}$.

Application of the MBPT has allowed to consider and predict a number of other correlation effects [5.80], waiting for experimental verification yet.

To perform calculations with accuracy higher than achievable in frameworks of MBPT and its slightly improved versions, requires overcoming very significant computing difficulties and consequently, as a rule, is not carried out yet.

5.13 Angular Anisotropy and Spin Polarization of Auger Electrons

The difference in angular anisotropy and spin polarization of Auger electrons and photoelectrons is due to the difference in interaction operators. Coulomb operator of Auger transition is a scalar, unlike the dipole operator of the interaction of electromagnetic radiation with matter. Therefore, the angular distribution of photoelectrons is always asymmetrical, while the angular anisotropy of Auger electrons occurs only if the initial vacancy is anisotropic [5.87]. If the probability of finding a vacancy j_k in each of the states with magnetic quantum number m_k is the same, then the vacancy will be referred to as spherically symmetric.

If the flux of photons or charged particles produces in the target spherically symmetric vacancies, the angular distribution of Auger electrons will also be spherically symmetric. If the distribution of vacancies is asymmetrical, the angular distribution of Auger electrons will be asymmetrical.

There are two types of asymmetric distribution: *orientation* and *alignment*. Orientation one calls a distribution, in which the population of states with opposite sign of magnetic quantum numbers is different. Alignment is the distribution, symmetrical with respect to the sign of the magnetic quantum number. The difference of the population in the alignment is determined by the module of vacancy magnetic quantum number. From these definitions it follows that *orientation* is non-zero if the total momentum of a hole is non-zero if $j_i > 0$, and *alignment* is non-zero if $j_i > 1/2$.

Consider the case of ionization of the atom by unpolarized photon flux. In this case, the axis of quantization is the direction of photon flux, and the distribution of vacancies is symmetrical with respect to the plane perpendicular to this direction. Therefore, *orientation* is absent. However, alignment may be different from zero. This difference is connected with the fact that the probability of photoionization depends on the absolute value of the magnetic quantum number. In the case of K-shell ionization only one value of the modulus of the magnetic quantum number $|m| = 1/2$ is possible and the alignment does not exist also. Therefore, the angular distribution of K Auger spectra excited by unpolarized radiation is spherically symmetric.

If the initial state of Auger—spectrum is a vacancy in the p-shell, the alignment is different from zero at the $j = 3/2$ component of spin doublet. In this case, the angular anisotropy occurs when the spin–orbit splitting is larger than the width of the line. If the initial state in the Auger process will be a vacancy in the d—a shell, the two components of the spin doublet may be different from zero alignment. The theoretical description of the angular dependence and spin-polarization of the Auger spectra is given in a number of references [5.87–5.94]. For a quantitative description of anisotropic distributions of vacancies the technique of statistical tensors is usually used. The latter is defined as [5.90]:

$$\rho_{k\kappa} = \sum_{mm'} (-1)^{2j'-2m'} [k] \begin{pmatrix} j & k & j' \\ -m & \kappa & m' \end{pmatrix} \begin{pmatrix} j & j' & k \\ m & -m' & -\kappa \end{pmatrix} \left(j \,\|\rho_k\|\, j'\right). \tag{5.139}$$

In our case j coincides with j' and equals to the total vacancy momentum. The density matrix ρ is normalized to the cross-section of photoionization (or electron impact ionization):

$$Tr(\rho) = \sigma. \tag{5.140}$$

Thus, one obtains for zero-order statistical tensor:

$$\rho_{00}(jj) = \frac{\sigma}{[j]^{1/2}}. \tag{5.141}$$

It follows from the axial symmetry of the problem under consideration that only tensors of odd rank are non-zero and that the following relation is valid:

$$\rho_{k\kappa}(j, j) = \rho_{k0}(j, j)\delta_{k0}. \tag{5.142}$$

It is equivalent to the situation, when the atom is ionized by unpolarized radiation: the alignment may be obtained, but orientation not. The alignment degree is defined by the following parameters:

$$A_k = \frac{\rho_{k0}}{\rho_{00}} \quad k = 2, 4, \ldots \tag{5.143}$$

In the case of p-shell ionization the alignment is absent for the component $j_k = 1/2$, whereas for the $j_k = 3/2$ component the alignment is defined by the following formula [5.90, 5.91]:

$$A_2 = \frac{\sigma\left(\frac{3}{2}, \left|\frac{1}{2}\right|\right) - \sigma\left(\frac{3}{2}, \left|\frac{3}{2}\right|\right)}{\sigma\left(\frac{3}{2}, \left|\frac{1}{2}\right|\right) + \sigma\left(\frac{3}{2}, \left|\frac{3}{2}\right|\right)}. \tag{5.144}$$

where $\sigma(j, |m|)$ is the sum of photoionization cross-sections with total momentum of an ion with a hole, having momentum j and its projections $+m$ and $-m$.

In the case of d-shell photoionization both spin–orbit components can have non-zero alignment and the angular distribution of Auger L-spectra is not spherically symmetric. For the case of $l_k = 2$ and $j_k = 3/2$ the alignment is also given by formula (5.144). In the case of $l_k = 2$ and $j_k = 5/2$ A_2 is given by the formula:

$$A_2 = \frac{2}{7}\frac{4\sigma\left(\frac{5}{2}, \left|\frac{1}{2}\right|\right) + \sigma\left(\frac{5}{2}, \left|\frac{3}{2}\right|\right) - 5\sigma\left(\frac{5}{2}, \left|\frac{5}{2}\right|\right)}{\sigma\left(\frac{5}{2}, \left|\frac{1}{2}\right|\right) + \sigma\left(\frac{5}{2}, \left|\frac{3}{2}\right|\right) + \sigma\left(\frac{5}{2}, \left|\frac{5}{2}\right|\right)}. \tag{5.145}$$

In this case the fourth order term of alignment also appears [5.92]:

$$A_4 = \frac{3}{7}\frac{2\sigma\left(\frac{5}{2}, \left|\frac{1}{2}\right|\right) - 3\sigma\left(\frac{5}{2}, \left|\frac{3}{2}\right|\right) + \sigma\left(\frac{5}{2}, \left|\frac{5}{2}\right|\right)}{\sigma\left(\frac{5}{2}, \left|\frac{1}{2}\right|\right) + \sigma\left(\frac{5}{2}, \left|\frac{3}{2}\right|\right) + \sigma\left(\frac{5}{2}, \left|\frac{5}{2}\right|\right)}. \tag{5.146}$$

If the energy of photoelectrons substantially exceeds the energy of Auger electrons, we can consider that the Auger process occurs after the photoionization. Let J_i, J_f, and j be total moments of single ionized atom, double ionized atom, and Auger electron, respectively. From the conservation of angular momentum and parity in the Auger process, it follows that the total number of possible partial waves of the Auger electrons is limited by $2J_i + 1$ if $J_i \leq J_f$ and is limited by $2J_f + 1$ if $J_i > J_f$. To illustrate this statement we consider $N_4 \rightarrow O_{2,3}O_{2,3}$ Auger transition in the Xe ion:

$$Xe[4d]\, D_{3/2} \rightarrow Xe[5p^2]^3 P_1 + \begin{cases} \varepsilon s_{1/2}(V_1, \delta_1) \\ \varepsilon d_{3/2}(V_2, \delta_2) \\ \varepsilon d_{5/2}(V_3, \delta_3) \end{cases}, \tag{5.147}$$

where V_i is a Coulomb matrix element that causes the Auger decay in the considered channel and δ_i is electron phase in continuum.

If only relative intensities and angular distribution are measures the use of relative values makes possible to reduce the number of variables:

$$\begin{aligned} \nu_{1,3} &= \frac{V_1}{V_3}, \quad \delta_{1,3} = \delta_1 - \delta_3, \\ \nu_{2,3} &= \frac{V_2}{V_3}, \quad \delta_{2,3} = \delta_2 - \delta_3. \end{aligned} \tag{5.148}$$

In $L-S$ coupling there is only d-wave, $\delta_{2,3} = 0$ and the values $\nu_{2,3}$ are defined by the angular parts of wave functions only.

To consider the kinematics of the process in the case of unpolarized or circularly polarized radiation, the following coordinate system is used [5.93]:

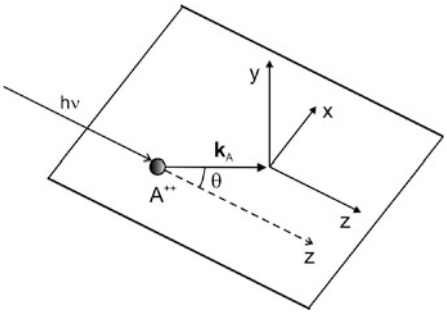

(5.149)

The basal plane passes through the photon and Auger electron directions. The coordinate system is chosen so that z direction coincides with photon direction and Y direction is perpendicular to the plane.

In the general case the angular anisotropy of Auger electrons is given by formula [5.92]:

$$W_e(\theta) = \frac{W_e}{4\pi}\left(1 + \sum_{k=2,4\ldots} \alpha_k A_{k0} P_k(\cos\theta)\right), \tag{5.150}$$

where $P_k(\cos\theta)$ are Legendre polynomials and factors α_k are given by the following formula [5.93]:

$$\begin{aligned} \alpha_k = \frac{1}{W}(-1)^{J+J_f-1/2}[J]^{1/2} \sum_{l,l',j,j'} [l\,l'\,j\,j'\,k]^{1/2}(-1)^{l'-l} \begin{pmatrix} l & l' & k \\ 0 & 0 & 0 \end{pmatrix} \begin{Bmatrix} J & J & k \\ j & j' & J_f \end{Bmatrix} \\ \times \begin{Bmatrix} j & j' & k \\ l' & l & \frac{1}{2} \end{Bmatrix} V_{lj} V^*_{l'j'}. \end{aligned} \tag{5.151}$$

Spin polarization of Auger electron in coordinate system of the direction of its movement is given by the following three formulae [5.92]:

$$P_z(\theta) = \frac{A_{10}\left(\beta_1 + \gamma_1 P_2(\cos\theta)\right)}{1 + \sum\limits_{k=2,4} A_{k0}\alpha_k P_k(\cos\theta)}, \tag{5.152}$$

$$P_y(\theta) = \frac{\sum\limits_{k=2,4} A_{k0}\xi_k \sin 2\theta}{1 + \sum\limits_{k=2,4} A_{k0}\alpha_k P_k(\cos\theta)}, \tag{5.153}$$

$$P_x(\theta) = \frac{\frac{3}{4}A_{10}\gamma_1 \sin 2\theta}{1 + \sum\limits_{k=2,4} A_{k0}\alpha_k P_k(\cos\theta)}. \tag{5.154}$$

Orientation A_{10} and alignment A_{20} are the parameters characterizing the ion. Orientation of ion is different from zero only in the case of polarized radiation that creates the primary vacancy, while the non-zero alignment is possible also when unpolarized radiation is used for ionization. Parameters α_k, β_1, γ_1, and ξ_k are called internal. The α_k parameter determines the angular distribution of Auger electrons, the ξ_k parameter characterizes the dynamical spin-polarization, i.e., polarization, which arises from the interference between two partial waves. The β_1 and γ_1 parameters characterize a so-called transferred spin polarization, i.e., transferred as a result of the interaction of the atom with polarized radiation. These parameters are given by the following three formulae [5.93, 5.94]:

$$\begin{aligned}\xi_k = {} & \frac{1}{W}(-1)^{J+J_f-1/2}4\sqrt{3}[J]^{1/2}\sum_{l,l',j,j'}[l\,l'\,j\,j'\,k]^{1/2}(-1)^{1/2+l'-j'} \\ & \times \begin{pmatrix} l & l' & k \\ 0 & 0 & 0 \end{pmatrix} \begin{Bmatrix} J & J & k \\ j & j' & J_f \end{Bmatrix} \times \begin{Bmatrix} l & l' & k \\ \frac{1}{2} & \frac{1}{2} & 1 \\ j & j' & k \end{Bmatrix} \mathrm{Im}\left(V_{lj}V^*_{l'j'}\right),\end{aligned} \tag{5.155}$$

$$\begin{aligned}\beta_1 = {} & \frac{1}{W}(-1)^{J+J_f+1/2}\sqrt{2}[J]^{1/2}\sum_{l,jj'}[jj']^{1/2} \\ & \begin{Bmatrix} J & J & 1 \\ j & j' & J_f \end{Bmatrix} \begin{Bmatrix} j & j' & 1 \\ \frac{1}{2} & \frac{1}{2} & l \end{Bmatrix} V_{lj}V^*_{lj'},\end{aligned} \tag{5.156}$$

$$\begin{aligned}\gamma_1 = {} & \frac{1}{W}(-1)^{J+J_f-1/2}[J]^{1/2} \times \sum_{ll',jj'}[jj']^{1/2} \\ & \times \frac{(l-j)[j]+(l'-j')[j']+2}{\sqrt{3}} \begin{Bmatrix} J & J & 1 \\ j & j' & J_f \end{Bmatrix} \begin{Bmatrix} j & j' & 1 \\ \frac{1}{2} & \frac{1}{2} & 0 \end{Bmatrix} V_{lj}V^*_{lj'},\end{aligned} \tag{5.157}$$

where J and J_f stand for total angular moments in intermediate and final ionic states, l and j are orbital and total moments of Auger electron V_{lj}—are reduced matrix elements with complex phase. In addition, the following notation is used:

$$W = \sum_{lj} V_{lj}^2. \tag{5.158}$$

5.14 Decay of Vacancies in Endohedral Atoms

As is was already mentioned in Sects. 1.13 and 1.14, recently much attention is paid to so-called endohedral atoms, i.e., atoms A encapsulated inside a fullerene shell F constructed mainly from carbon C atoms, and located on a surface with typical dimensions that are much larger than the atomic radius r_A. Most frequently discussed fullerene is almost perfectly spherically symmetric C_{60}.

In Sects. 1.13 and 1.14 we showed how the fullerene shell affecting the photoionization of the atom located inside can be taken into account. Here we will discuss the effect of F on the decay of vacancies in A. It is natural to distinguish decays of vacancies in endohedral atoms by the degree of participation of the fullerene electrons. Namely, the vacancy in the endohedral atom can be filled by an outer electron either of the same atom or by one the collectivized electrons of the fullerene, forming what could be called *atomic* and *fullerene* decays, respectively.

If atomic vacancy is deep enough, it can be filled by one of the non-collectivized inner electrons of carbon atoms that form the fullerene, presenting *molecular* decay.

If the atomic vacancy decays with emission of a photon, fullerene shell can absorb this photon radiating a photon of the same energy. Thus, the decay of a vacancy occurs via two channels. First,—recombination with photon emission by isolated atom. The second is a two-step process unfolding through electronic excitation of fullerene shell. The amplitudes of these channels interfere similar to what occurs for isolated atoms (see Sec. 1.5) where the decay probability can vary strongly from increase to almost complete suppression. The same thing can happen in Auger decay: the interaction between electrons, the internal and external, may change due to virtual excitations of electrons of C_{60}, which results in the replacement of pure Coulomb interaction V by the effective interaction $\Gamma(\omega)$ [see (1.40)], independent of the transmitted energy. The difference between V and $\Gamma(\omega)$ is determined by intra- and inter-shell effects.

The amplitude of the radiative decay may be represented by diagram similar to the diagrams for the radiative decay of an isolated atom [5.95]:

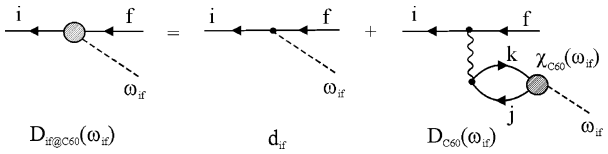

(5.159)

A substantial simplification of this expression, the same as in the case of photoionization, is possible. We assume that the radius of the fullerene is significantly larger than the thickness of its shell and the size of the atom. This leads to a ratio similar to (1.119) for the amplitude of radiative decay. As a result, the probability of this decay for the atomic transition $i \to f$ is expressed through the same parameters as in the case of photoabsorption endohedral atom (1.120):

$$\Gamma^{\mathrm{C}}_{\gamma,if} = \Gamma^{\mathrm{A}}_{\gamma,if} \left| 1 - \frac{\alpha_F(\omega_{if})}{R^3} \right|^2 \equiv |G_F(\omega)|^2 \Gamma^{\mathrm{A}}_{\gamma,if} \equiv \eta_{\mathrm{RR}}(\omega) \Gamma^{\mathrm{A}}_{\gamma,if}. \tag{5.160}$$

Notations here are the same as in (1.120).

For C_{60} the factor $G(\omega)$ is shown in Figs. 2.350_C60_g1 and 2.351_C60_g2. A decay of subvalent s-shell of endohedral noble gas atom is of special interest. Such vacancies decay in atoms only radiative, since the Auger decay is energetically forbidden. But the energy released in intra-atomic radiative decay is sufficient for removal of electron from the C_{60} shell. As a result the decay probability increases by 4–6 orders.

The Auger decay may be represented similar to (5.160), as a "photon" radiation with transition $i \to f$ with its subsequent absorption and ionization of C_{60} shell [5.95]:

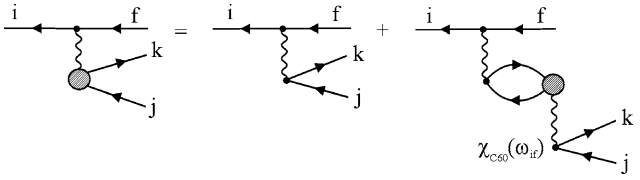

(5.161)

First, for subvalent vacancy decay we rightfully neglect the first term in right hand side of (5.161). Then the Auger decay probability $\Gamma^{\mathrm{C}}_{\mathrm{Au},if}$ defined by transition $i \to f$ is expressed through the atomic radiation width $\Gamma^{\mathrm{A}}_{\gamma,if}$ and atomic photoionization cross-section $\sigma_{\mathrm{c}}(\omega_{if})$ of the C_{60} electron shell by a photon of energy ω_{if} [5.95]:

$$\Gamma^{\mathrm{C}}_{\mathrm{Au},if} = \Gamma^{\mathrm{A}}_{\gamma,if} \frac{3}{8\pi} \left(\frac{c}{\omega_{if}} \right)^4 \frac{\sigma_{\mathrm{c}}(\omega_{if})}{R^6} \equiv \Gamma^{\mathrm{A}}_{\gamma,if} \eta_{\mathrm{AR}}(\omega). \tag{5.162}$$

The estimations show that all the values, except $\Gamma^{\mathrm{A}}_{\gamma,if}$, are very large—of the order about $10^4 - 10^6$. Making use of (5.160) and (5.162), one can easily calculate the so-called fluorescence yield $J_R(\omega_{if})$, i.e., the ratio of radiation probability to the total width:

$$J_R(\omega_{if}) = \frac{8\pi}{3} \left(\frac{\omega_{if}}{c} \right)^4 \frac{R^6}{\sigma_{\mathrm{c}}(\omega_{if})} \left| 1 - \frac{\alpha_{\mathrm{c}}(\omega_{if})}{R^3} \right|^2. \tag{5.163}$$

It is also of interest to estimate how the virtual excitations of the C_{60} electrons change the interactions between atomic electrons, participating in the transition

from level f to the level i, due to involvement of C_{60} electrons. It was shown in [5.95], that corresponding corrections are defined by the second term in square brackets of the following expression:

$$\Gamma^{\mathrm{C}}_{\mathrm{Au},i\to fkj} = \Gamma^{\mathrm{A}}_{\mathrm{Au},i\to fkj}\left|1-\frac{1}{2\pi}\sqrt{\frac{3}{2}}\frac{c^2}{\omega_{if}}\frac{\alpha_{\mathrm{c}}(\omega_{if})}{R^6}\left(\frac{\Gamma^{\mathrm{A}}_{\gamma,if}}{\Gamma^{\mathrm{A}}_{\mathrm{Au},i\to fkj}}\right)^{1/2}[\sigma^{\mathrm{A}}_j(\varepsilon_k)]^{1/2}\right|^2. \tag{5.164}$$

When estimating these corrections, it can be shown that they are much less than unity and therefore may be neglected.

The curve $\eta_{\mathrm{RR}}(\omega)$ was obtained in [5.95]. Making use of the energies considered as an example transitions, i.e., $2s \to 2p$ in Ne, $3s \to 3p$ in Ar, $4s \to 4p$ in Kr, and $5s \to 5p$ in Xe, one obtains corresponding values η_{RR}, which are large and change in the range from 3.5 to 6.2.

According to the formula (5.160) the ratio of Auger width to the radiation width is given by the value η_{AR} [5.95]. Owing to this factor the decay probability increases in $2\times10^4 - 4\times10^5$ times, approaching values, corresponding to the normal Auger decay, as if they are not forbidden by energy conservation.

It should be noted that in non-radiative transition in endohedral atom the electron with the energy $\varepsilon \le 70\,\mathrm{eV}$ is ejected and the probability of this process may change significantly due to reflection of photoelectron from the fullerene shell potential. As a result the probability of decay with ejection of electron with angular momentum l acquires the factor $F_l^2(k)$, where $F_l(k)$ is given by (1.106) and (1.107), where k is the linear momentum of outgoing electron.

We established strong changes of decay probabilities and investigated the influence of new channels opening. As in the case of photoionization, the results are expressed through experimentally observed characteristics of fullerene, its electron affinity and photoionization cross-section in the approximation that the fullerene radius is significantly larger than the atomic radius and the fullerene shell thickness.

References

5.1. Amusia MYa, Kazachkov MP, Cherepkov NA, Chernysheva LV (1972) Many-electron correlations in the processes of inner shell vacancies decay. Phys Lett A 39(2):93–94

5.2. Svensson S, Eriksson B, Martensson N, Wendin G, Gelius U (1988) Electron shake-up and correlation satellites and continuum shake-off distributions in X-ray photoelectron spectra of rare gas atoms. J Electron Spectrosc Relat Phenom 47:327–384

5.3. Svensson S, Mårtensson N, Gelius U (1987) Observation of autoionizing resonances in core-electron shakeup spectra. Phys Rev Lett 58:2639–2641

5.4. Krause MO, Whitfield SB, Caldwell CD, Wu JZ, Van der Meulen P, de Lange CA, Hansen RWC (1992) Outer ns, np correlation satellites in rare gases—a photoelectron spectroscopy study with an undulator photon source. J Electron Spectrosc Relat Phenom 58:79–104

5.5. Pahler M, Caldwell CD, Schaphorst SJ, Krause MO (1993) Intrinsic line widths of neon $2s2p(^{1,3}P)nl^2L$ correlation satellites. J Phys B At Mol Opt Phys 26:1617–1625

5.6. Kikas A, Osborne SJ, Ausmees A, Svensson S, Sairanen OP, Askela S (1996) High-resolution study of the correlation satellites in photoelectron spectra of rare gases. J Electron Spectrosc Relat Phenom 77:241–266
5.7. Cowan RD (1981) The theory of atomic structure and spectra. Los Alamos Series in Basic and Applied Sciences. University of California Press, Berkeley, p 650
5.8. Amusia MYa, Cherepkov NA, Chernysheva LV, Shapiro SG (1974) Elastic scattering of slow electrons and level shifts in Ar. Phys Lett A 46 (6):387–388
5.9. Amusia MYa, Kilin VA, Lee IS (1985) Three-electron auger-decay in atoms. Opt Spectrosc **59**(2):261–264 (in Russian)
5.10. Amusia MYa, Lee IS (1993) Decay of highly excited atomic states. In: Walters H, Hansch TW, Neizerk B (eds) Atomic physics 13, AIP Conference Proceedings, vol 275. New York, pp 375–387
5.11. Amusia MYa, Cherepkov NA (1975) Many-electron correlations in scattering processes. Case Stud Atom Phys 5(2):47–179
5.12. Kovalcyk SP, Ley L, Martin RL, Mcfeely FR, Shirley DA (1975) Relaxation and final-state structure in XPS of atoms molecules and metals. Faraday Discuss Chem Soc 60:7–17
5.13. Wendin G (1981) Breakdown of one-electron picture in photoelectron spectra. Structure and bonding, vol 45. Springer, Heidelberg, pp 1–123
5.14. Yarzhemsky VG, Teterin YuA, Sosulnikov MI (1992) Dynamic dipolar relaxation in X-ray photoelectron spectra of Ba4p subshell in barium compounds. J Electron Spectrosc Relat Phenom 59:211–222
5.15. Tagliaferri A, Braicovich L, van der Laan G, Ghiringhelli G, Brookes NB, Dallera C, Finazzi M, Weschke E, Hu Z, Kaindl G (1999) Many-body effects in non-resonant and resonant 4p spectroscopy of Gd meta. Phys Rev B 60:5728–5736
5.16. March NH, Young WH, Sampanthar S (1995) Many-body problem in quantum mechanics. Courier Dover Publ., New York, p 459
5.17. Amusia MYa, Kheifets AS (1984) The influence of many-electron effects on atomic photoelectron spectrum. JETP 86:1217–1226 (in Russian)
5.18. Galitsky VM, Migdal AB (1958) Application of quantum field theory to the many-body problem. JETP 34:139–150 (in Russian)
5.19. Abrikosov AA, Dzyaloshinski IE, Gorkov LP (1965) Methods of quantum field theory in statistical physics, 2nd edn. Prentice-Hall, NJ, p 365 (International series of monographs in natural philosophy, vol 4)
5.20. Kheifets AS, Amusia MYa, Yarzhemsky VG (1985) On the validity of the quasi-particle approximation in photoelectron spectroscopy. J Phys B At Mol Opt Phys 18:L343–L350
5.21. Yarzhemsky VG, Armen GB, Larkins FP (1993) Calculation of the shake-up satellites in the 1s and 2s X-ray photoelectron spectra on neon. J Phys B At Mol Opt Phys 26:2785–2794
5.22. Jucys AP, Levinsonas JB, Vanagas VV (1962) Mathematical apparatus of the theory of angular momentum. Olborne, London, p 158
5.23. Balcar E, Lovesey SW (2009) Introduction to the graphical theory of angular momentum. Springer, Heidelberg, p 227
5.24. Judd BR (1967) Second quantization and atomic spectroscopy. John Hopkins, Baltimore, p 62
5.25. Lindgren I, Morrison J (1982) Atomic many-body theory. Springer, Berlin, p 254
5.26. Yarzhemsky VG, Nefedov VI, Trzhaskovskaya MB, Band IM, Szargan R (2002) The influence core hole relaxation on the main line intensities in X-ray photoelectron spectra. J Electron Spectrosc Relat Phenom 123:1–10
5.27. Walters DL, Bhalla CP (1971) Nonrelativistic Auger rates, X-ray rates, and fluorescence yields for the K shell. Phys Rev A 3:1919–1927
5.28. Manne R, Åberg T (1970) Koopmans theorem for inner-shell photoionization. Chem Phys Lett 7:282–284
5.29. Tulkki J, Åberg T, Mäntykenttä A, Aksela H (1992) Relativistic multichannel calculation of the NeKLL and Ar $L_2M_{2,3}M_{2,3}$ Auger transition rates. Phys Rev A 43:1357–1366

5.30. Armen GB, Larkins FP (1991) Valence Auger and X-ray participator and spectator processes for neon and argon atoms. J Phys B At Mol Opt Phys 24:741–759
5.31. Armen GB, Larkins FP (1992) Valence-multiplet Auger decay of the doubly excited [νp2] states of neon and argon. J Phys B At Mol Opt Phys 25:931–947
5.32. Albiez A, Toma M, Weber W, Mehlhorn W (1990) $KL_{2,3}$ ionization in neon by electron impact in the range 1.5–50 keV: cross-section and alignment. Z Phys D 16:97–106
5.33. Shirley DA (1987) High-resolution X-ray photoemission spectra of the valence bands of gold. Phys Rev B 5:4709–4714
5.34. Seah MP, Gilmore IS (2006) Quantitative X-ray photoelectron spectroscopy: quadruple effects, shake-up, Shirley background, and relative sensitivity factors from a database of true X-ray photoelectron spectra. Phys Rev B 73:174113-1–10
5.35. Lagutin BM, Petrov ID, Sukhorukov VL, Whitfield SB, Langer B, Viefhaus J, Wehlitz R, Berrah N, Mahler W, Becker U (1996) Cross-sections and angular distributions of the photoelectron correlation satellites of the Xe atom. J Phys B At Mol Opt Phys 29:937–976
5.36. Doniah S, Sunjic M (1970) Many-electron singularity in X-ray photoemission and X-ray line spectra from metal. J Phys C 3:285–291
5.37. Hufner S, Wertheim GK (1975) Core-line asymmetries in X-ray photoemission spectra of metals. Phys Rev B 11:678–683
5.38. Yarzhemsky VG, Kolotyrkin IYa, Kaplan IG, Zhdan PA (1990) The use of asymmetric functions for the decomposition of X-ray spectra of the solid surface. Poverkhnost 2: 141–146 (in Russian)
5.39. Yarzhemsky VG, Reich T, Chernysheva LV, Streubel P, Szargan R (1996) Line shape asymmetry parameters in X-ray photoelectron spectra. J Electron Spectrosc Relat Phenom 77:15–24
5.40. Sherwood PMA (1996) Curve fitting in surface analysis and the effect of background inclusion in the fitting process. J Vac Sci Technol A 14:1424–1432
5.41. Glans P, LaVilla RE, Ohno M, Svennson S, Bray G, Wassdahl N, Nordgren J (1994) Determination of the lifetime width of the argon L_1-hole state. Phys Rev A 47:1539–1542
5.42. Karim KR, Chen MH, Craseman B (1984) Effect of exchange, electron correlation and relaxation on the $L_1 - L_{23}M_1$ Coster–Kronig spectrum of argon. Phys Rev A 29: 2605–2610
5.43. Yarzhemsky VG, Kheifets AS, Armen GB, Larkins FP (1995) Line widths and intensities of satellites in photoelectron spectra in the presence of underlying continuum. J Phys B At Mol Opt Phys 28:2105–2112
5.44. Yarzhemsky VG, Larkins FP (1998) Lineshapes of Auger decay of excited atomic states. J Electron Spectrosc Relat Phenom 96:149–156
5.45. Yarzhemsky VG, Larkins FP (1999) The shapes of Auger decay lines in photoelectron satellite spectra. Eur Phys J D 5:179–184
5.46. Yarzhemsky VG, Nefedov VI, Amusia MYa, Chernysheva LV (2002) The shapes of photoelectron satellite spectra. Surface Rev Lett 9:1209–1212
5.47. Svennson S, Martensson N, Basilier E, Malmquist PA, Gelius U, Siegbahn K (1976) Lifetime broadening and CI-resonances observed in ESCA. Phys Scripta 14:141–147
5.48. Ohno M, Wendin G (1987) Dynamic screening and interference effects in X-ray and Auger emission spectra. Z Phys D 5:233–240
5.49. Boring M, Cowan RD, Martin RL (1981) Satellite structure in the 5*p* and 5*s* X-ray-photoelectron spectra of the actinides. Phys Rev B 23:445–448
5.50. Yarzhemsky VG, Teterin YuA, Teterin AYu, Amusia MYa, Nefedov VI (2005) The structure of 4p X-ray photoelectron spectra of Xe and compounds of Cs, Ba, Ln. J Surface Invest X-ray Synchrotr Neutron Techn 6:3–8 (in Russian)
5.51. Grant IP (1970) Relativistic calculation of atomic structure. Adv Phys 19:747–811
5.52. Lindgren I, Rosen A (1974) Relativistic self-consistent field with application to hyperfine interactions. Part I: Relativistic self-consistent fields. Case Stud At Phys 4:97–149
5.53. Chernysheva LV, Yakhontov VL (1999) Two-program package to calculate the ground and excited state wave functions in the Hartree–Fock–Dirac approximation. Comp Phys Commun 119:232–255

5.54. Grant IP (1974) Gauge invariance of relativistic radiative transitions. Phys B At Mol Opt Phys 7:1458–1475
5.55. Scofield JH (1969) Radiative decay rates of vacancies in K and L shells. Phys Rev 179:9–16
5.56. Scofield JH (1974) Exchange corrections to K X-ray emission rates. Phys Rev A 9: 1041–1049
5.57. Scofield JH (1974) Relativistic Hartree–Slater values for K and L X-ray emission rates. At Data Nucl Data Tab 14:121–137
5.58. Chen MH, Craseman B (1981) Widths and fluorescence yields of atomic L-shell vacancy states. Phys Rev A 24:177–182
5.59. Chen MH, Craseman B (1983) Gauge dependence of atomic inner-shell transition rates from Dirac–Fock wave functions. Phys Rev A 28:2829–2837
5.60. Chen MH, Craseman B (1984) M X-ray emission rates in Dirac–Fock approximation. Phys Rev A 30:170–176
5.61. Trzhaskovskaya MB, Nikulin VK, Nefedov VI, Yarzhemsky VG (2001) Relativistic photoelectron angular distribution parameters in quadrupole approximation. J Phys B At Mol Opt Phys 34:3221–3237
5.62. Krause MO, Carlson TA, Moddeman WE (1971) Manifestation of atomic dynamics through the Auger effect. J de Phys 32:C4-139–C4-144
5.63. Huang KN (1978) Relativistic radiationless transitions in atoms. J Phys B At Mol Opt Phys 11:787–795
5.64. Bhalla CP (1973) Effect of configuration interaction of K-shell Auger spectrum of neon. Phys Lett A 44:103–104
5.65. Kelly HP (1975) K Auger rates calculated for Ne^+. Phys Rev A 11:556–565
5.66. Howat G, Åberg T, Goscinski O (1978) Relaxation and final-state channel mixing in the Auger effect. J Phys B At Mol Opt Phys 11:1575–1588
5.67. Chen MH, Larkins FP, Crasemann B (1990) Auger and Coster–Kronig radial matrix elements for atomic numbers $6 \leq Z \leq 92$. At Data Nucl Data Tab 45:1–205
5.68. Yarzhemsky VG, Sgamellotti A (2002) Auger rates of second row atoms calculated by many-body perturbation theory. J Electron Spectrosc Relat Phenom 125:13–24
5.69. Amusia MYa, Lee IS, Wehlitz R, Becker UJ (1993) Evidence for a new class of many-electron Auger-transitions in atoms. Phys B At Mol Opt Phys 26:41–46
5.70. Becker U, Wehlitz R (1994) Auger spectroscopy at low kinetic energies. J Electron Spectrosc Relat Phenom 67:341–361
5.71. Yarzhemsky VG, Amusia MYa, Chernysheva LV (2002) Lineshape of Ne1s photoionization satellite $[1s2s](^3S)$3s and its valence Auger decay spectrum. J Electron Spectrosc Relat Phenom 127:153–159
5.72. Amusia MYa, Lee IS, Kilin VA (1992) Double Auger decay of atoms: probability and angular distributions. Phys Rev A 45:4576–4587
5.73. Kochur AG, Sukhorukov VL (1996) Low-energy Auger spectra of xenon emitted by vacancy cascade following inner-shell ionization. J Phys B At Mol Opt Phys 29:3587–3598
5.74. Amusia MYa, Kilin VA, Lee IS (1984) Double Auger-decay of two K-vacancies in Ne. J Tech Phys 54(5):990–992
5.75. Amusia MYa, Lee IS (1991) Correlated decay of two vacancies in atoms. J Phys B At Mol Opt Phys 24:2617–2632
5.76. Amusia MYa (1979) Single-photon and single-electron decay of double vacancy states in atoms. Comm At Mol Phys **9**(1):23–34
5.77. Amusia MYa, Kilin VA, Kolesnikova AN, Lee IS (1984) Deepening of vacancies in correlation decays of two-hole atomic states. Lett J Tech Phys 10(17):1029–1033 (in Russian)
5.78. Amusia MYa, Kilin VA, Kolesnikova AN, Lee IS (1985) Contrary movement of vacancies in correlation decays of double hole states. Lett J Tech Phys 11(6):343–346 (in Russian)
5.79. Amusia MYa, Kilin VA, Kolesnikova AN, Lee IS (1987). Low-energy correlation satellites in two-vacancy atoms. Lett J Tech Phys 57(7):1246–1254 (in Russian)

5.80. Amusia MYa, Kilin VA, Lee IS (1992) The decay of an electron-vacancy excitation in the presence of another vacancy. J Phys B At Mol Opt Phys 25(3):657–666
5.81. Amusia MYa, Lee IS (1992) Radiative semi-Auger decay in atoms. Phys Scripta 41:23–27
5.82. Amusia MYa, Kolesnikova AN, Lee IS (1988) Radiative semi-auger satellites in the X-ray spectra. J Tech Phys (USSR Acad Sci) 58(3):442–451
5.83. Amusia MYa, Lee IS, Zinoviev AN (1977) Single photon decay of double hole states in atoms. Phys Lett A 60(4):300–302
5.84. Amusia MYa, Lee IS (1977) Single-photon decay of two-hole atomic states. JETP 73 2(8):430–437
5.85. Amusia MYa, Kolesnikova AN, Lee IS (1987) Cooperative decays of two-vacancy states. J Tech Phys (USSR Acad Sci) **57**(6):1228–1229
5.86. Amusia MYa, Kolesnikova AN, Lee IS (1986) Radiation of low-energy photons in combined decay of two vacancies. Izv USSR Acad Sci Ser Phys **50**(7):1279–1284
5.87. Flugge S, Mehlhorn W, Schmidt V (1972) Angular distribution of Auger electrons following photoionization. Phys Rev Lett 29:7–9
5.88. McFarlane SC (1972) The polarization of characteristic x-radiation excited be electron impact. J Phys B At Mol Opt Phys 5:1906–1915
5.89. Cleff B, Mehlhorn W (1974) On the angular distribution of Auger electrons following impact ionization. J Phys B At Mol Opt Phys 7:593–604
5.90. Berezhko EG, Kabachnik NM (1977) Theoretical study of inner-shell alignment of atoms in electron impact ionization: angular distribution and polarization of X-rays and Auger electrons. J Phys B At Mol Opt Phys 10:2467–2477
5.91. Kabachnik NM, Sazhina IP (2002) Spin polarization of Auger electrons from the decay of a $j = 3/2$ vacancy. J Phys B At Mol Opt Phys 35:3591–3598
5.92. Lohman B, Hergenhahn U, Kabachnik NM (1993) Spin polarization of Auger electrons from noble gases after photoionization with circularly polarized light. J Phys B At Mol Opt Phys 26:3327–3338
5.93. Kabachnik NM, Sazhina IP (1984) Angular distribution and spin polarization of Auger electrons. J Phys B At Mol Opt Phys 17:1335–1342
5.94. Balashov VV, Grum-Grzhimailo AN, Kabachnik NM (2000) Polarization and correlation phenomena in atomic collisions. A practical theory course. Plenum, New York, p 243
5.95. Amusia MYa, Baltenkov AS (2006) Vacancy decay in endohedral atoms. Phys Rev A 73:063206

Chapter 6
Vacancies Decay: Results of Calculations

6.1 Data Presentation and Used Formulas

In this chapter, we collect and comment figures and tables, which present data, obtained in calculations of photoelectron satellite intensities and line shapes, intensities of Auger spectra, some line shapes of low-energy Auger lines, and radiation widths.

The numbering of figures is organized similar to Chaps. 2 and 4, i.e., as follows: at first, goes the number of the respective chapter; the next letter denotes the considered atom as in the periodic table of chemical elements than goes the consecutive number of this figure in the chapter; the next small letter stands for the considered process. The following letters denote the process considered:

p—corresponds to photoelectron spectra

a—corresponds to Auger spectra

r—corresponds to radiative decay.

The last digit presents the number of the figure in the considered group.

The energies of decay are obtained using (5.8) and (5.9). Polarization corrections to the energy can be found using (5.12) and higher order corrections, exemplified by (5.13). Many-body corrections to the energy and width of a level are found using (5.19–5.21). The width of radiative decay Γ_k^{γ} is obtained using (5.3), whereas the Auger-decay line width $\Gamma_k^{(\mathrm{A})}$ is obtained using (5.4).

Spectral functions were calculated with account for fourth order corrections to imaginary part of the self-energy, using formulas (5.61), (5.64), and (5.68). The extension to Auger decay was achieved using (5.120). In calculations of satellite formations, one needs to have photoionization amplitudes in RPAE, for which the relation $\omega = \varepsilon - I_i$, where I_i is the i-vacancy ionization potential, is not valid. They amplitudes are called "off the energy shell" photoionization amplitudes. They are obtained by solving (1.37), where $\nu_1 = \varepsilon l \pm 1$ and $\nu_2 = nl$ with $\omega \neq \varepsilon + I_{nl}$. The action of the fullerenes shell upon the radiative and nonradiative decay is accounted for by using formulas (5.160) and (5.162). Off the shell photoionization cross-sections we present in Chapter 7

M. Amusia et al., *Handbook of Theoretical Atomic Physics*,
DOI 10.1007/978-3-642-24752-1_6, © Springer-Verlag Berlin Heidelberg 2012

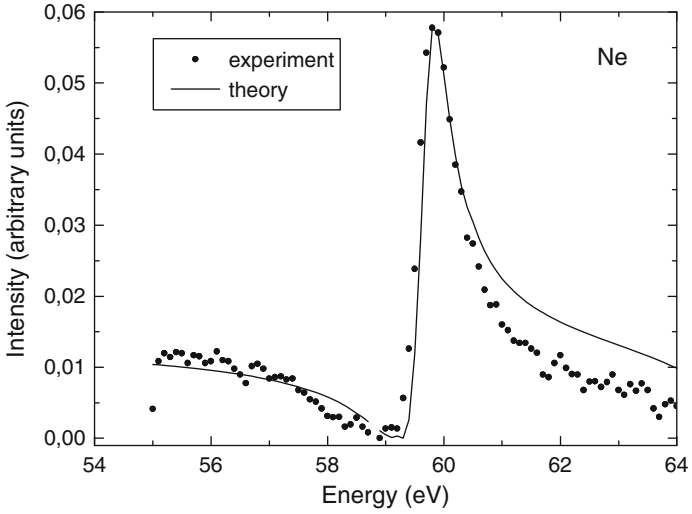

Fig. 6.1_Ne_p1 Line shape of satellite $1s2s^5(^3S)3s(^2S)$ in $1s$ photoionization spectrum of Ne. Experiment is from [6.1, 6.2]

6.2 Description of Figures

In this section, we present results of our calculations of the satellite line shapes, data on the RPAE photoionization amplitude "off the energy shell," and enhancement parameters that determine the effect of fullerenes shell upon radiative and non-radiative decay of s-vacancies in subvalent subshells of Ne, Ar, Kr, and Xe endohedral atoms.

Figures 6.1_Ne_p1–6.7_Ne_p7 (Ne) show results of calculations of satellites line-shapes in photoionization spectrum of Ne.

Figure 6.1_Ne_p1 presents the line-shape of satellite $1s2s(^3S)3s(^2S)$ in $1s$ photoionization spectrum of Ne. Experiment is from [6.1, 6.2]. Theoretical spectral function was calculated with account for fourth order corrections to imaginary part of the self-energy, using formulas (5.61), (5.64), and (5.68).

Figure 6.2_Ne_p2 contains the line-shape of satellite $2s2p^5(^3P)3s(^2P)$ in $2p$ photoionization spectrum of Ne. In this figure, 60 is the serial line number in experimental spectrum [6.3]. Solid line is the theoretical spectral function convoluted with Gaussian of halfwidth 0.17 eV. Points—fitting by the Fano profile with $q = -1.8$ and $\Gamma = 0.37$ eV. Experimental value: $q = -2.7$ [6.3]. Theoretical spectral function was calculated with account for fourth order corrections to imaginary part of the self-energy, using formulas (5.61), (5.64), and (5.68).

Figure 6.3_Ne_p3 gives the theoretical line shape of satellite $2s2p^5(^1P)3s(^2P)$ in $2p$ photoionization spectrum of Ne. In this figure, 67 is the serial line number in experimental spectrum [6.3]. Theoretical spectral function was calculated with

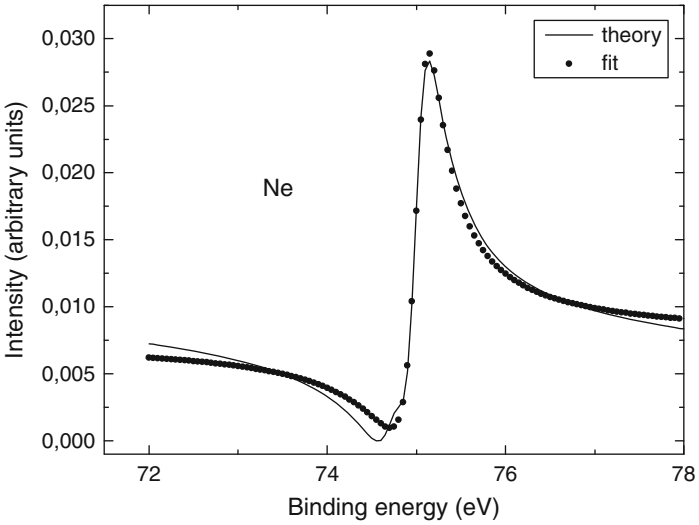

Fig. 6.2_Ne_p2 Line shape of satellite $2s2p^5(^3P)3s(^2P)$ in $2p$ photoionization spectrum of Ne (line 60) [6.3]. Solid line presents the theoretical spectral function convoluted with Gaussian of halfwidth 0.17 eV. Points—fitting by the Fano profile with $q = -1.8$ and $\Gamma = 0.37$ eV

account for fourth order corrections to imaginary part of the self-energy, using formulas (5.61), (5.64), and (5.68). Theoretical line shape reveals a deep minimum between two peaks, which is smeared by convolution with Gaussian corresponding to experimental resolution (see Fig. 6.4_Ne_p4).

Figure 6.4_Ne_p4 depicts theoretical shape of the satellite spectrum $2s2p^5$ $(^{2S+1}P)ns(^2P)$ of Ne$2p$ photoionization, convoluted with Gaussian of halfwidth 0.17 eV. Line numbers are given according to [6.3]. Theoretical spectral function was calculated with account for fourth order corrections to imaginary part of the self-energy, using formulas (5.61), (5.64), and (5.68). Note that the lines ^3Pns are strongly asymmetrical, while the lines ^1Pns are almost symmetrical.

Figure 6.5_Ne_p5 demonstrates the theoretical shape of the satellite spectrum $2s2p^5(^{2S+1}P)np(^2S)$ of Ne$2s$ photoionization, convoluted with Gaussian of halfwidth 0.17 eV. Line numbers are given according to [6.3].

Figure 6.6_Ne_p6 depicts the theoretical shape of photoionization satellite $2s2p^5(^3P)ns(^2P)$ (*solid line*), and shapes of its low-energy Auger decay into different channel (*dash–dotted lines*). Line number 60 is given according to [6.3]. Theoretical spectral function was calculated by spectral function approach with account for fourth order corrections extended to Auger decay with the help of (5.120). Predicted selectivity of decay into different low-energy Auger channels was confirmed experimentally [6.4].

Figure 6.7_Ne_p7 demonstrates the theoretical shape of Ne photoionization satellite $2s2p^5(^1P)3s(^2P)$ (*solid line*) and shapes of its low-energy Auger decay into different channel (*dash–dotted lines*). Line number 67 is given according

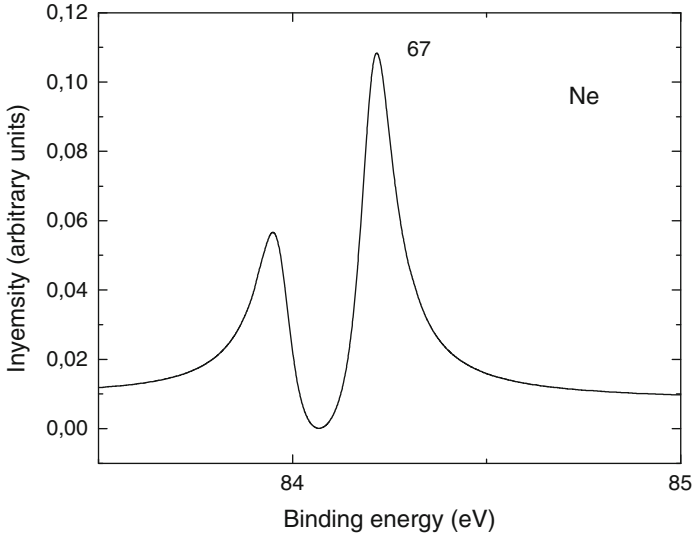

Fig. 6.3_Ne_p3 Theoretical line-shape of satellite $2s2p^5(^1P)3s(^2P)$ in $2p$ photoionization spectrum of Ne (line 67) [6.3]

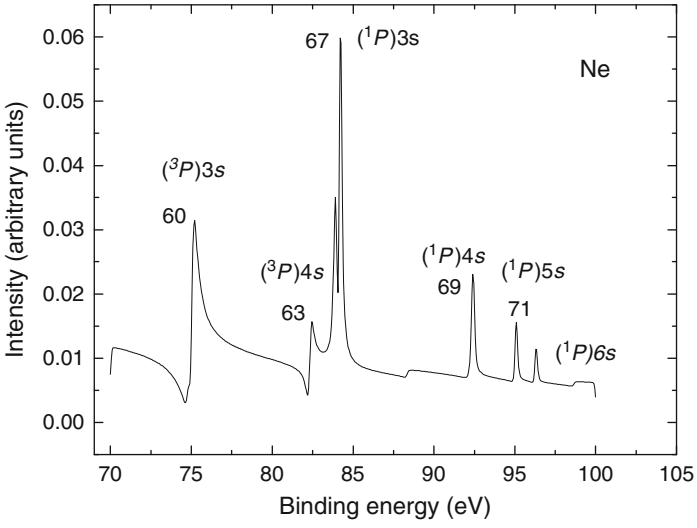

Fig. 6.4_Ne_p4 Theoretical shape of the satellite spectrum $2s2p^5(^{2S+1}P)ns(^2P)$ of Ne$2p$ photoionization, convoluted with Gaussian of halfwidth 0.17 eV. Line numbers according to [6.3]

to [6.3]. Theoretical spectral function was calculated with account for fourth order corrections extended to Auger decay with the help of (5.120).

Figure 6.8_Ne_a1 presents the theoretical shape of low-energy Auger decay of Ne photoionization satellite state $1s2s\ (^3S)3s(^2S)$. Theoretical spectral function

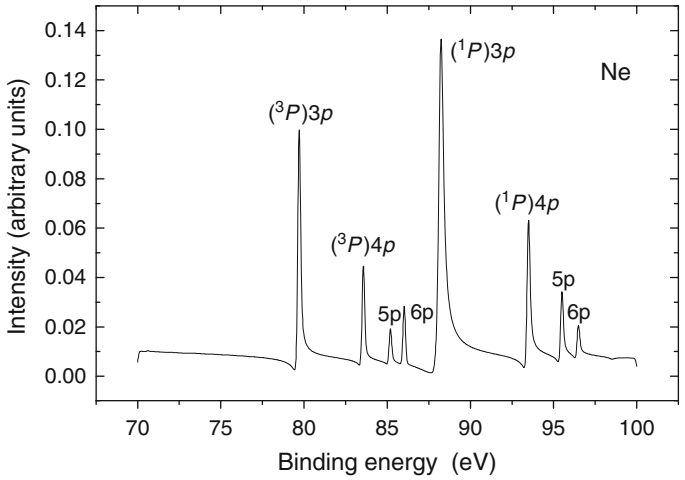

Fig. 6.5_Ne_p5 Theoretical shape of the satellite spectrum $2s2p^5(^{2S+1}P)np(^2S)$ of Ne2s photoionization, convoluted with Gaussian of halfwidth 0.17 eV

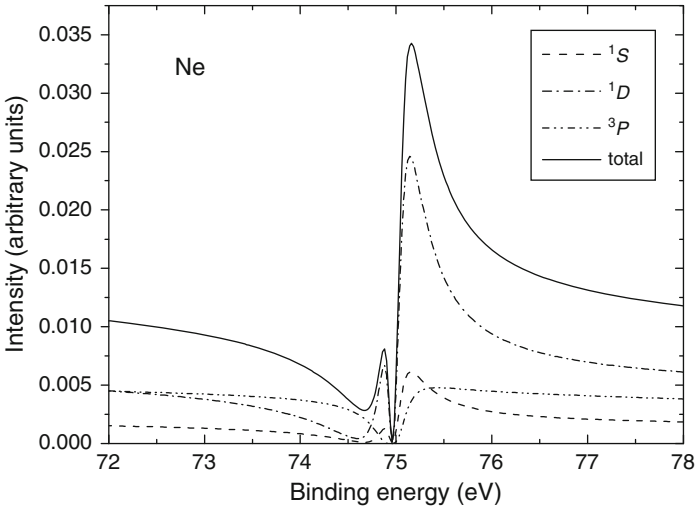

Fig. 6.6_Ne_p6 Theoretical shape of Ne photoionization satellite $2s2p^5(^3P)3s(^2P)$ (solid line), line 60 [6.3] and shapes of its low-energy Auger decay in different channels (dash–dotted lines)

was calculated with account of fourth order corrections extended to Auger decay using (5.120). Peaks with kinetic energies 8.3 and 12.9 eV correspond to decay into $1s2p^5(^1P)$ and $1s2p^5(^3P)$ ionic states, respectively. It is seen from this figure, that theoretical intensity ratio $^3P/^1P$ differs significantly from the statistical value 3. The experimental value 0.74 for this ratio [6.5] confirmed theoretical prediction.

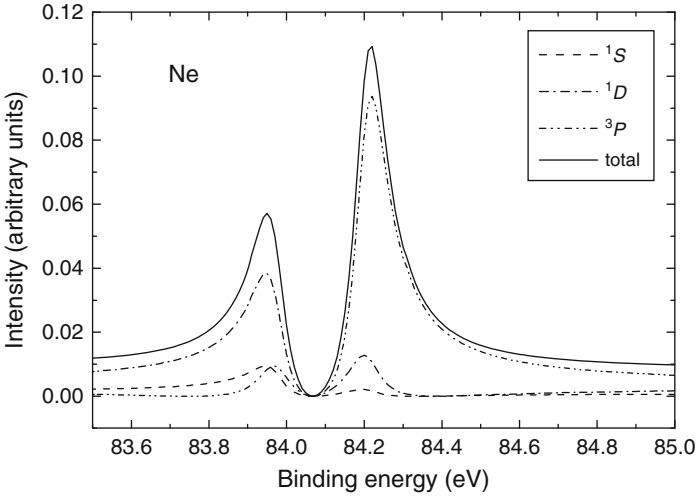

Fig. 6.7_Ne_p7 Theoretical shape of Ne photoionization satellite $2s2p^5(^1P)3s(^2P)$ (solid line) (line 67 [6.3]) and shapes of its low-energy Auger decay in different channels (dash–dotted lines)

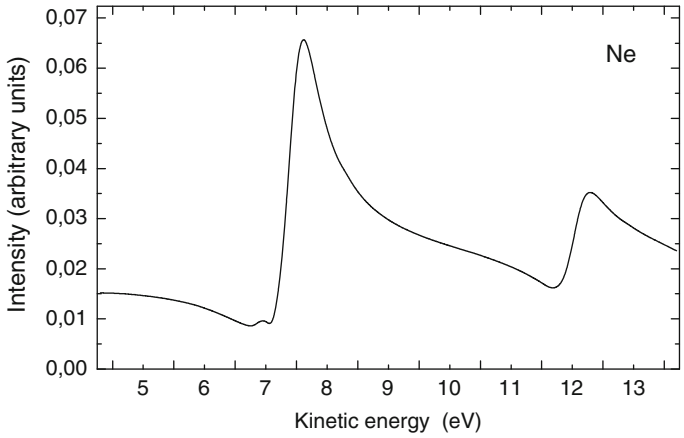

Fig. 6.8_Ne_a1 Theoretical shape of low-energy Auger decay of Ne photoionization satellite state $1s2s^5(^3S)3s(^2S)$. Peaks with kinetic energy 8.3 and 12.9 eV correspond to decay to $1s2p^5(^1P)$ and $1s2p^5(^3P)$ ionic states, respectively

Figures 6.9_Ar_p1 and 6.10_Ar_p2 (Ar) show the results of calculations of satellites line-shapes in photoionization spectrum.

Figure 6.9_Ar_p1 gives the theoretical shape of the satellite $3s3p^5(^3P)4s(^2P)$ in photoionization spectrum of Ar (line 68 [6.3]). In this figure, 68 is the serial line number in experimental spectrum [6.3].The line-shape is strongly asymmetrical in agreement with experiment [6.3]. Additional small peak at 47.6 eV is due to opening of continuum channel.

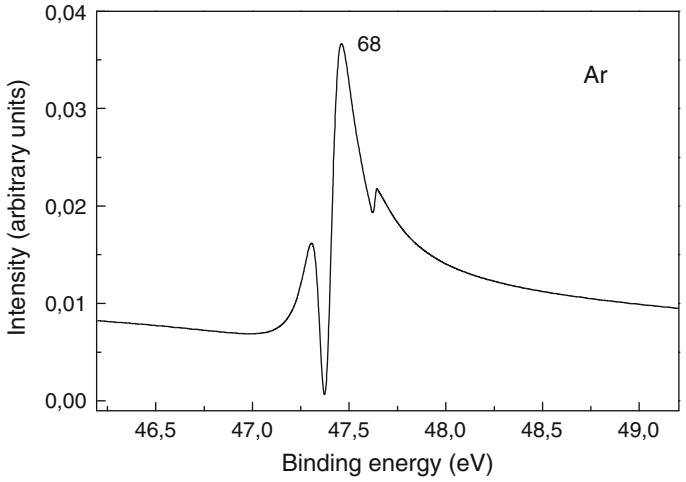

Fig. 6.9_Ar_p1 Theoretical shape of the satellite $3s3p^5(^3P)4s(^2P)$ in photoionization spectrum of Ar (line 68 [6.3])

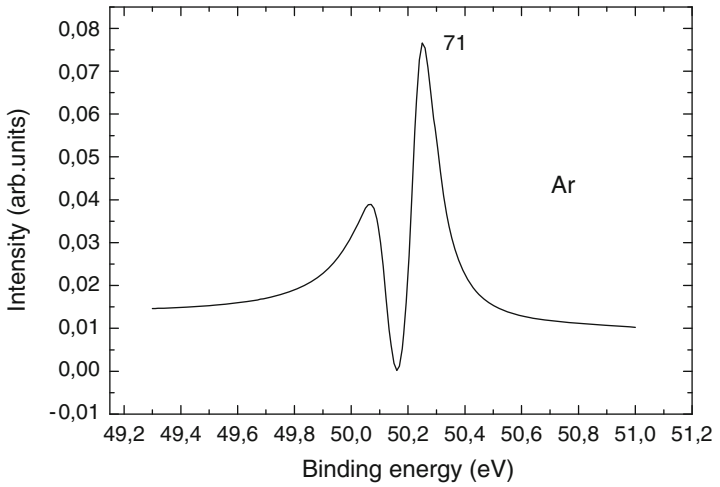

Fig. 6.10_Ar_p2 Theoretical shape of the satellite $3s3p^5(^1P)4s(^2P)$ of Ar photoionization (line 71 [6.3])

Figure 6.10_Ar_p2 depicts the theoretical shape of the satellite $3s3p^5(^1P)4s(^2P)$ of Ar photoionization (line 71 [6.3]). In this figure, 71 is the serial line number in experimental spectrum [6.3]. Theoretical spectral function was calculated with account for fourth order corrections to imaginary part of the self-energy, using formulas (5.61), (5.64), and (5.68). A significant minimum at 50.17 eV with full width at half minimum 0.1 is smeared by instrumental resolution resulting in an approximately symmetric line-shape [6.3].

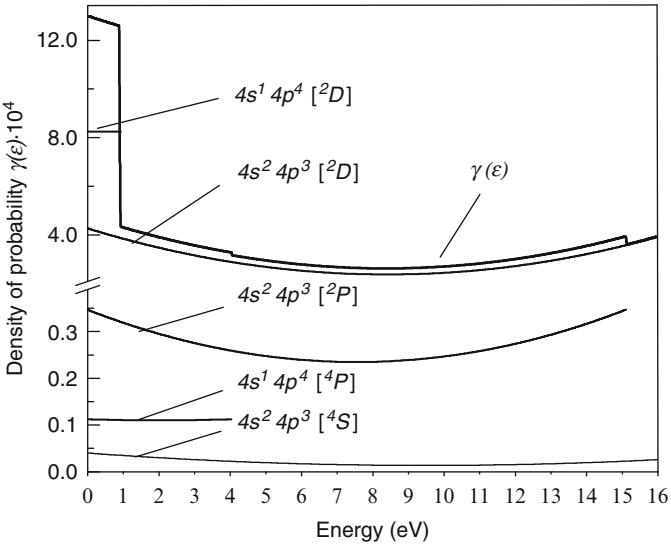

Fig. 6.11_Kr_a1 Probability density of double Auger decay as a function of kinetic energy of one of the Auger electrons for five double Auger decay channels of Kr$3d^{-1}$ state

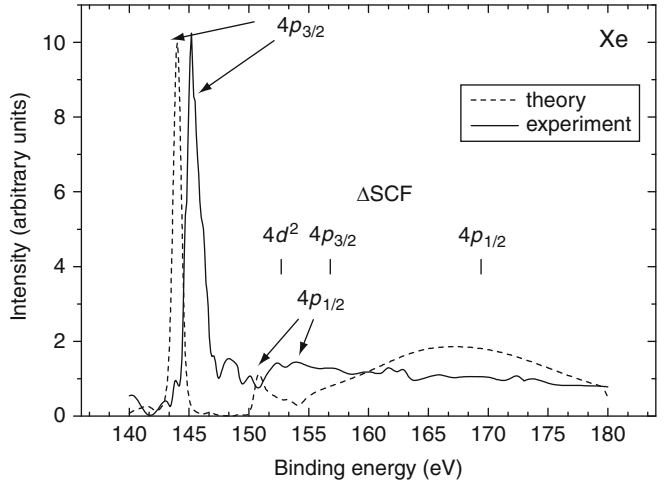

Fig. 6.12_Xe_p1 Theoretical Xe4p spectrum and experimental [6.6] photoelectron spectrum of Xe

Figure 6.11_Kr_a1 shows the probability density of double Auger decay as a function of kinetic energy of one of the Auger electrons for five double Auger decay channels of Kr$3d^{-1}$ state.

Figure 6.12_Xe_p1 demonstrates the theoretical Xe4p spectral function and experimental [6.6] photoelectron spectrum of Xe. Theoretical spectral function is

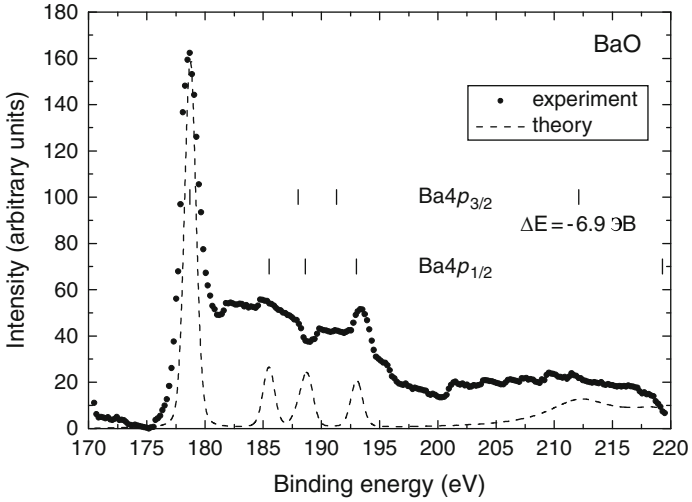

Fig. 6.13_Ba_p1 Theoretical Ba4p spectrum and experimental [6.7] photoelectron spectrum of BaO

calculated in the second order of MBPT. Theoretical thresholds for the states $4p_{1/2}^{-1}$, $4p_{3/2}^{-1}$, and $4d^{-2}$, obtained by relativistic ΔSCF method, are also shown. It follows from the figure, that dipole relaxation results in a significant decrease of binding energies of $4p_{1/2}$ and $4p_{3/2}$ energy levels, by 13 and 11 eV, respectively. The characteristic feature of Xe4p spectrum is almost complete absence of the $4p_{1/2}$ line due to very strong interaction of the initial state $4p_{1/2}^{-1}$ with continuum states $4d^{-2}\varepsilon f$.

Figure 6.13_Cs_p1 depicts the theoretical Cs4p-hole spectrum and experimental [6.7] photoelectron spectrum of CsCl. Configuration interaction method was used to calculate the spectrum.

Figure 6.14_Ba_p1 presents the theoretical Ba4p-hole spectrum and experimental [6.7] photoelectron spectrum of BaO. Configuration interaction method was used to calculate spectrum.

Figure 6.15_La_p1 shows the theoretical La4p-hole spectrum and experimental [6.7] photoelectron spectrum of LaF_3. Configuration interaction method was used to calculate the spectrum.

Figures 6.16_NeArKrXe_r1 and 6.17_NeArKrXe_a1 contain some data on radiation and Auger widths of noble gases Ne, Kr, Ar, and Xe endohedral atoms.

Figure 6.16_NeArKrXe_r1 presents the ratio $\eta_{RR}(\omega)$ of radiation widths of the same transitions in endohedral and isolated noble gases Ne, Kr, Ar, and Xe atoms as a function of photon energy. This ratio is determined by (5.160). As a fullerene C_{60} is considered. One can see, that the intensity of radiative transition is enhanced due to action of the fullerenes shell by a factor 3.5–6.

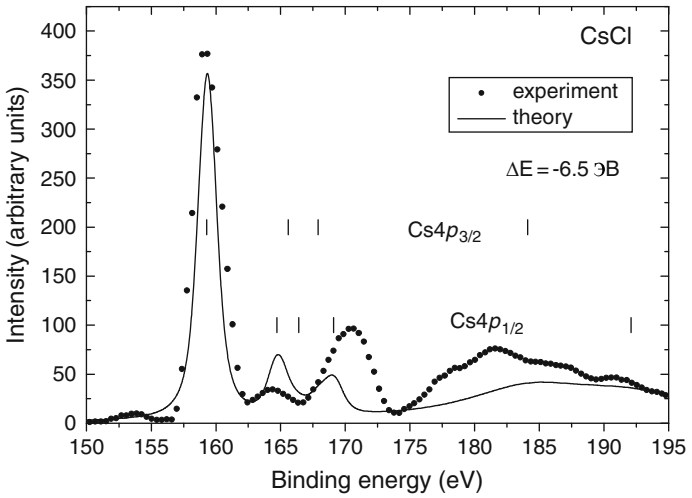

Fig. 6.14_Cs_p1 Theoretical Cs4p spectrum and experimental [6.7] photoelectron spectrum of CsCl

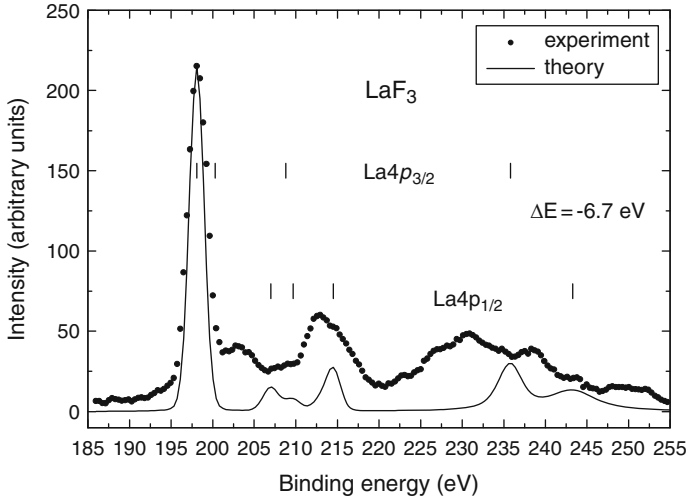

Fig. 6.15_La_p1 Theoretical La4p spectrum and experimental [6.7] photoelectron spectrum of LaF_3

Figure 6.17_NeArKrXe_a1 depicts the ratio $\eta_{AR}(\omega)$ of Auger and radiation width for endohedral noble gas Ne, Kr, Ar, and Xe atoms as a function of the transition energy. This ratio is determined by (5.162). As a fullerene C_{60} is considered. Due to opening of the Auger-decay channel, the probability of the decay of s-vacancy in the subvalent subshells is enhanced by four–five orders of magnitude.

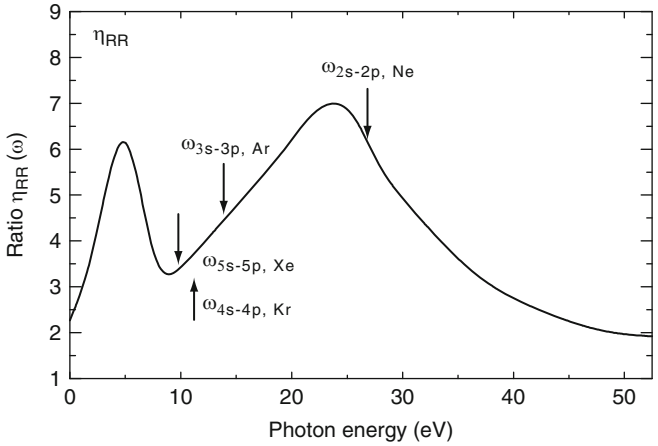

Fig. 6.16_NeArKrXe_r1 Ratio $\eta_{\mathrm{RR}}(\omega)$ of radiation widths of the same transitions in endohedral and isolated atoms as a function of photon energy. *Arrows* denote transitions $\omega_{2s-2p,\mathrm{Ne}} = 26.85\,\mathrm{eV}$—$2s$, $-2p$ in Ne; $\omega_{3s-3p,\mathrm{Ar}} = 13.50\,\mathrm{eV}$—$3s$, $-3p$ in Ar, $\omega_{4s-4p,\mathrm{Kr}} = 11.20\,\mathrm{eV}$—$4s$, $-4p$ in Kr; $\omega_{5s-5p,\mathrm{Xe}} = 9.90\,\mathrm{eV}$—$5s$, $-5p_{3/2}$ and $5s$, $-5p_{1/2}$ in Xe

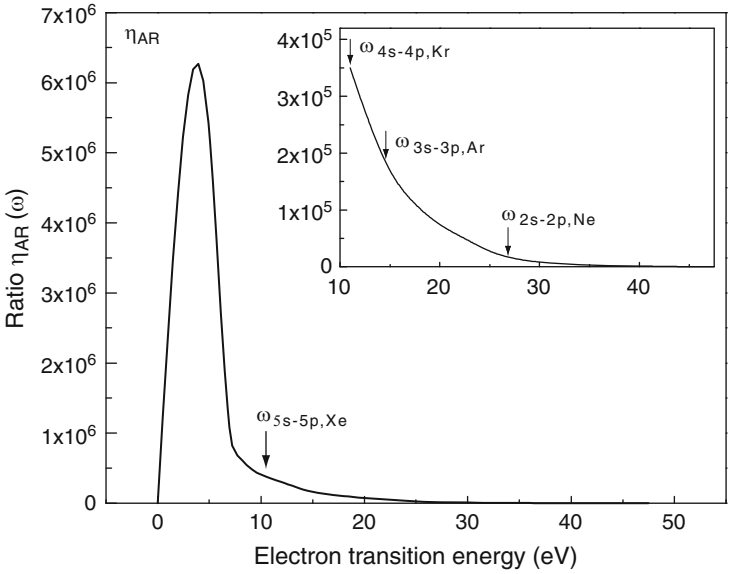

Fig. 6.17_NeArKrXe_a1 The ratio $\eta_{\mathrm{AR}}(\omega)$ of Auger and radiation widths for endohedral atoms as a function of the transition energy. *Arrows* denote transitions $\omega_{2s-2p,\mathrm{Ne}} = 26.85\,\mathrm{eV}$—$2s$, $-2p$ in Ne; $\omega_{3s-3p,\mathrm{Ar}} = 13.50\,\mathrm{eV}$—$3s$, $-3p$ in Ar; $\omega_{4s-4p,\mathrm{Kr}} = 11.20\,\mathrm{eV}$—$4s$, $-4p$ in Kr; $\omega_{5s-5p,\mathrm{Xe}} = 9.90\,\mathrm{eV}$—$5s$, $-5p_{3/2}$ and $5s$, $-5p_{1/2}$ in Xe

6.3 Description of Tables

In the tables, presented below, we collect data on radiative and non-radiative transitions, their energies, spectroscopic factors, and probabilities for main and satellite lines. We give some data on correlation decay that proceed due to account of interelectron interaction.

Table 6.1 compares ionization energies of atomic shells of noble gases calculated in different approximations [one-electron (5.8), ΔSCF (5.9), and MBPT (5.12) and (5.13)] with experimental data. Ionization energies calculated by relativistic ΔSCF method and by MBPT are in a good agreement with the experimental results, but the ionization energies based on Koopmans theorem (i.e., in one-electron approximation) are in all cases significantly bigger.

Table 6.2 displays spectroscopic factors of Ne1s photoelectron line (5.29), (5.30), and (5.57), the sum of all its shake-up satellites and shake-off continuum calculated in different approximations and experimental data [6.1, 6.8]. It is seen in the table that the intensities of shake-up and shake-off satellites depend strongly on the approximation used, but the spectroscopic factor of the main line is almost

Table 6.1 Theoretical and experimental ionization energies of atomic shells and levels (in eV)

Shell/level	Theory			Experiment
	One-electron	ΔSCF	MBPT	
Ne1s	893.03	869.58	868.8	869.0
Ar2$p_{1/2}$	262.14	250.36	248.8	251
Ar2$p_{3/2}$	259.79	247.27	246.5	248
Kr3$d_{3/2}$	102.84	92.79	91.10	92.6
Kr3$d_{5/2}$	101.43	91.46	89.72	91.8
Xe4$d_{3/2}$	73.81	67.975	67.4	69
Xe4$d_{5/2}$	71.68	65.92	65.3	67
Rn4$f_{5/2}$	250.15	236.01	234.27	242
Rn4$f_{7/2}$	242.92	229.02	227.01	235

Table 6.2 Theoretical (in different approximations of MBPT) and experimental spectroscopic factors f and binding energies E of Ne1s photoelectron line

Value	Theory			Experiment
	a	b	c	
f(shake-up)	0.106	0.079	0.048	0.126 [6.1]
f(shake-off)	0.194	0.171	0.217	
f(main line)	0.77	0.8	0.79	0.8 [6.8]
$E(1s)$[d](eV)	864.7	870.3	868.8	869.0

[a]"Frozen core" approximation in calculation of ReΣ

[b]"Frozen core" approximation in calculation of ReΣ. Ground state correlations are taken into account

[c]Relaxed-core approximation in calculation of ReΣ

[d]Ionization energy calculated as a sum of relativistic orbital energy $\varepsilon_{1s} = 893.0$ eV and ReΣ. Note that relativistic ionization energy, calculated by ΔSCF method equals to 869.6 eV

independent of the approximation and is in agreement with experiment [6.8]. The best results for the shake-up satellites are obtained in the "frozen core" approximation.

Table 6.3 presents radiation widths (in 10^{-5} eV) of some atomic shells calculated in Hartree–Fock approximation, using (5.3) for many atoms of the periodic table. For inner $1s^{-1}$ vacancies, the width rapidly increases from about 0.66×10^{-3} eV in Ne to almost 10 eV in Ba. For outer vacancies the variation is much smaller, from about 0.6×10^{-5} eV to 1×10^{-5} eV and is almost independent upon nuclear charge and principal quantum number of the vacancy.

Table 6.4 demonstrates the width of radiative transitions, with inclusion of electron correlations in RPAE. The correlations suppress the radiative decay probability by factors 4 and 6 for decay of vacancies in subvalent subshells $3s$ in Ar and $4s$ in Kr, respectively. The radiative decay for the $4p$ vacancy in Xe, the suppression factor is as big as 27.

Table 6.5 gives theoretical (in "frozen core" approximation) and experimental [6.1] shake-up satellite intensities of $2s$ photoionization spectrum of Ne atom. There is a good agreement of the theory with experiment for the far from threshold energy region ($h\nu = 1486.6$ eV).

Table 6.6 includes experimental [6.1, 6.3, 6.9] widths and shifts of several satellites in Ne photoionization spectrum and the values of $\mathrm{Re}\,\Sigma$ and $\mathrm{Im}\,\Sigma$ estimated on the basis of experimental data. $\mathrm{Re}\,\Sigma$ was estimated as satellite energy shift from the center of gravity of the spectrum. The estimation of $\mathrm{Im}\,\Sigma$ is based on the formula (5.28) and experimental values of satellite intensity and width. It follows from this data that condition of the validity of quasi-particle approximation (5.59) is violated in all cases.

Table 6.7 demonstrates spectroscopic factors for the $1s, 2p, 3d, 4f$, and $5f$ photoelectron lines used in photoelectron spectroscopy. It is for all atoms; from Li to Bk. The variation of the parameter is from 0.77 to 0.91. Note that measurements of the total intensity of shake-up for 46 elements in general agree with calculations, but not in details [6.10].

Table 6.8 presents theoretical widths and asymmetry parameters of $2s$—lines of some atoms. Asymmetry parameters were calculated by formula (5.51). The sign minus in this table denotes that this direction of asymmetry due to Auger decay of $2s$—line is opposite to the direction of asymmetry due to inelastic photoelectron scattering. This direction of asymmetry is in agreement with the results for Ar [6.11] and for insulating solids [6.12].

Table 6.9 presents theoretical (in different approximations [6.13–6.15]) and experimental Ne *KLL* Auger rates. The rates calculated in "the frozen core" approximation [6.15] with account for higher order diagrams are normalized for five diagram lines. Total Ne$1s$ width includes also Auger satellites, corresponding to main photoelectron line [see formulas (5.115) and (5.116) and Table 6.10]. Thus, Ne$1s$ width in this column is 110.9% of contributions of five diagram lines. Calculations in relaxed approximation have demonstrated that the strongest redistribution of intensities between channels is due to configuration interaction between core states $2s^{-2}(^1S)$ and $2p^{-2}(^1S)$ [6.16].

Table 6.3 Probabilities of radiation decay (radiation halfwidth at half height), in units of 10^{-5} eV

Transition	ω(Ry)	$\gamma^{(r)}$	$\gamma^{(v)}$	ω(Ry)	$\gamma^{(r)}$	$\gamma^{(v)}$
	Ne			Mg		
$1s^{-1} \to 2p^{-1}$	64.4	361.8	310.6	93.5	957.9	854.7
$2s^{-1} \to 2p^{-1}$	1.43	0.603	0.447	2.97	2.11	1.52
$2p^{-1} \to 3s^{-1}$				4.06	0.173	0.110
	Ar			Ca		
$1s^{-1} \to 2p^{-1}$	219.1	6090.8	5417.4	271.5	11,305	10621.6
$1s^{-1} \to 3p^{-1}$	239.0	659.4	611.6	296.1	1064.9	997.8
$2s^{-1} \to 2p^{-1}$	4.99	2.58	2.56	6.39	5.21	4.17
$2s^{-1} \to 3p^{-1}$	24.9	32.9	37.67	31.0	55.5	46.7
$2p^{-1} \to 3s^{-1}$	18.5	3.21	2.94	22.8	5.11	4.64
$3s^{-1} \to 3p^{-1}$	1.48	1.06	0.612	1.81	1.50	0.912
$4p^{-1} \to 4s^{-1}$				2.29	0.129	0.077
	Kr			Sr		
$1s^{-1} \to 2p^{-1}$	914.3	151.020	146.050	1021.4	190.270	184.460
$1s^{-1} \to 3p^{-1}$	1023.7	21,073	20,342	1146.0	27,730	26,844
$1s^{-1} \to 4p^{-1}$	1039.3	1525.14	1471.7	1165.2	2793.8	2703.5
$2s^{-1} \to 2p^{-1}$	13.8	13.09	11.60	14.79	14.30	12.60
$2s^{-1} \to 3p^{-1}$	123.1	1607.0	1472.7	139.38	2167.2	2003.0
$2s^{-1} \to 4p^{-1}$	138.8	126.4	115.77	158.59	237.81	219.7
$2p^{-1} \to 3s^{-1}$	104.3	92.39	82.36	119.04	120.03	108.00
$2p^{-1} \to 3d^{-1}$	118.4	2481.7	2259.7	134.60	3449.9	316.43
$2p^{-1} \to 4s^{-1}$	123.7	9.05	8.56	142.20	14.68	13.97
$2p^{-1} \to 5s^{-1}$				145.64	0.995	0.935
$3s^{-1} \to 3p^{-1}$	5.04	6.51	5.53	5.55	7.47	6.37
$3s^{-1} \to 4p^{-1}$	20.6	9.75	7.55	24.75	20.79	16.76
$3p^{-1} \to 3d^{-1}$	9.0	23.8	19.63	10.01	27.10	22.57
$3p^{-1} \to 4s^{-1}$	14.3	3.79	3.00	17.61	6.20	5.14
$3p^{-1} \to 5s^{-1}$				21.04	0.462	0.360
$3d^{-1} \to 4p^{-1}$	6.60	0.902	0.665	9.19	1.84	1.44
$4s^{-1} \to 4p^{-1}$	1.26	1.03	0.557	1.60	1.51	0.888
$4p^{-1} \to 5s^{-1}$				1.84	0.117	0.070
	Xe			Ba		
$1s^{-1} \to 2p^{-1}$	2093.2	840.974	822.968	2254.1	979.460	959.560
$1s^{-1} \to 3p^{-1}$	2378.4	150638.8	147227.8	2564.1	178.280	174.480
$1s^{-1} \to 4p^{-1}$	2436.8	28504.1	27849.5	2629.1	35.498	34.730
$1s^{-1} \to 5p^{-1}$	2447.9	2669.6	2608.1	2642.4	4506.9	4409.5
$2s^{-1} \to 2p^{-1}$	23.1	25.1	23.2	24.2	26.6	24.5
$2s^{-1} \to 3p^{-1}$	308.2	13532.9	12847.08	334.23	16,216	15,447
$2s^{-1} \to 4p^{-1}$	366.7	2789.8	2640.3	399.2	3516.2	3340.3
$2s^{-1} \to 5p^{-1}$	377.8	265.19	250.99	412.5	453.5	430.9
$2p^{-1} \to 3s^{-1}$	275.2	622.9	578.8	299.6	735.3	686.4
$2p^{-1} \to 3d^{-1}$	303.3	23271.8	22058.8	329.3	27,942	26,556
$2p^{-1} \to 4s^{-1}$	339.9	130.43	121.09	371.0	160.0	149.7

Table 6.3 Continued

Transition	ω(Ry)	$\gamma^{(r)}$	$\gamma^{(v)}$	ω(Ry)	$\gamma^{(r)}$	$\gamma^{(v)}$
	Ne			Mg		
$2p^{-1} \to 4d^{-1}$	350.0	3206.7	3028.9	382.1	4176.3	3956.6
$2p^{-1} \to 5s^{-1}$	353.7	15.77	15.02	387.09	23.95	22.87
$2p^{-1} \to 6s^{-1}$				389.8	1.83	1.74
$3s^{-1} \to 3p^{-1}$	9.9	16.69	14.88	10.48	18.02	16.07
$3s^{-1} \to 4p^{-1}$	68.3	387.4	346.66	75.46	504.7	455.4
$3s^{-1} \to 5p^{-1}$	79.4	41.25	36.74	88.75	73.07	65.63
$3p^{-1} \to 3d^{-1}$	18.2	55.07	48.12	19.28	58.97	51.61
$3p^{-1} \to 4s^{-1}$	54.7	61.19	55.79	60.97	76.23	69.95
$3p^{-1} \to 4d^{-1}$	64.9	300.21	264.54	72.08	419.24	372.72
$3p^{-1} \to 5s^{-1}$	68.5	7.78	7.17	77.05	11.89	11.03
$3p^{-1} \to 6s^{-1}$				79.76	0.927	0.845
$3d^{-1} \to 4p^{-1}$	40.2	23.74	22.55	45.71	29.95	28.66
$3d^{-1} \to 5p^{-1}$	51.3	2.37	2.12	59.00	4.00	3.62
$4s^{-1} \to 4p^{-1}$	3.7	5.11	4.13	4.01	5.77	4.72
$4s^{-1} \to 5p^{-1}$	14.80	4.15	3.10	17.30	8.34	6.50
$4p^{-1} \to 4d^{-1}$	6.46	20.35	15.53	7.10	23.34	18.07
$4p^{-1} \to 5s^{-1}$	10.13	3.00	2.27	12.07	4.66	3.70
$4p^{-1} \to 6s^{-1}$				14.78	0.399	0.297
$4d^{-1} \to 5p^{-1}$	4.64	0.939	0.695	6.20	1.81	1.41
$5s^{-1} \to 5p^{-1}$	0.97	0.7041	0.355	1.218	1.02	0.562
$5p^{-1} \to 6s^{-1}$				1.493	0.0916	0.0534

Calculations by the HF method

Table 6.4 Width of radiative transitions with inclusion of electron correlations in RPAE (in 10^{-5} eV)

Transition	HF-amplitude	Correlation transition	Amplitude with correlations	$\gamma^{(r)\mathrm{HF}}$	$\gamma^{(r)\mathrm{RPAE}}$
Ar $3s^{-1}$–$3p^{-1}$	1.02	$3p - \varepsilon d$, εs	−0.53	1.018	0.24
Kr $4s^{-1}$–$4p^{-1}$	1.02	$4p - \varepsilon d$, εs	−0.62	1.034	0.16
Xe $4p^{-1}$–$4d^{-1}$	−3.6	$4d - \varepsilon f$, εp	2.96	20.4	0.75

Table 6.10 gives the theoretical rates of Auger satellites corresponding to the main photoelectron line (Ne$1s$) binding energy. Calculations are performed according to formulas (5.115) and (5.116). Total intensity of the satellites is about 10% of the corresponding main line. Note that these Auger satellites contribute to broadening of the main photoelectron line.

Table 6.11 shows theoretical *KLL* Auger rates of C atom calculated in relaxed initial hole approximation. Initial states correspond to coupling of $1s$—hole with three terms on $2p^2$ configuration. The strongest redistribution of intensities between channels is due to configuration interaction between core states $2s^{-2}(^1S)$ and $2p^{-2}(^1S)$.

Table 6.5 Theoretical and experimental [6.1] shake-up satellite intensities of $2s$ photoionization spectrum of Ne atom (in % of the main line)

Satellite state	Binding energy (eV)	Intensity	
		Experiment	Theory
$2s2p^5(^3P)3p(^2S)$	78.90	1.10	1.27
$2s2p^5(^3P)4p(^2S)$	83.34	0.32	0.13
$2s2p^5(^3P)5p(^2S)^a$	84.70	0.14	0.05
$2s2p^5(^1P)3p(^2S)$	88.32	2.50	3.19
$2s2p^5(^1P)4p(^2S)$	93.61	0.64	0.50
$2s2p^5(^1P)5p(^2S)$	95.56	0.26	0.17

[a]With the state $2s2p^5(^1P)3s(^2P)$

Table 6.6 Experimental [6.1, 6.9] parameters of some satellite lines in photoelectron spectra of Ne atom

State	Γ (eV)[a]	f[b]	Im Σ (eV)[c]	Re Σ (eV)[d]
$[1s2s](^3S)3s(^2S)$	0.57	0.0062	46	55
$[2s2p](^3P)3s(^2P)$	0.42	0.0036	58	49
$[2s2p](^1P)3s(^2P)$	0.21	0.0022	48	59

[a]Full width at half height
[b]Satellite intensity relative to the main line and all other satellites
[c]Making use of formula (5.28)
[d]Satellite energy shift with respect to center of gravity of all discrete states

Table 6.12 depicts theoretical *KLL* Auger rates of N atom calculated in relaxed initial hole approximation. Initial states correspond to coupling of $1s$—hole with three terms of $2p^3$ configuration. The strongest redistribution of intensities between channels is due to configuration interaction between core states $2s^{-2}(^2P)$ and $2p^{-2}(^2P)$.

Table 6.13 gives theoretical *KLL* Auger rates of O atom calculated in relaxed initial hole approximation. Initial states correspond to coupling of $1s$—hole with three terms of $2p^4$ configuration. The strongest redistribution of intensities between channels is due to configuration interaction between core states $2s^{-2}(^{2S+1}L)$ and $2p^{-2}(^{2S+1}L)$.

Table 6.14 presents comparison of different theoretical Auger decay rates of two terms $1s^12p^4(^3P)^2P$ and $1s^12p^4(^3P)^4$P of O atom with experimental data. Best results are achieved in calculations performed in [6.18].

Table 6.15 demonstrates theoretical *KLL* Auger rates of F atom calculated in relaxed initial hole approximation. Initial states correspond to coupling of $1s$—hole with p^5 configuration. The strongest redistribution of intensities between channels is due to configuration interaction between core states $2s^{-2}(^2P)$ and $2p^{-2}(^2P)$.

Table 6.16 presents theoretical and experimental *LMM* Auger rates of Ar atom calculated in relaxed initial hole approximation. The agreement with experiment of our results is quite reasonable.

Table 6.7 Theoretical spectroscopic factors f for $1s$, $2p$, $3d$, $4f$, and $5f$ photoelectron lines

$1s$-line		$2p$-line		$3d$-line		$4f$-line		$5f$-line	
Atom	f	Atom	F	Atom	f	Atom	f	Atom	f
Li	0.91	Na	0.91	Ga	0.86	Hf	0.84	U	0.86
Be	0.88	Mg	0.88	Ge	0.87	Ta	0.84	Np	0.86
B	0.85	Al	0.89	As	0.87	W	0.84	Pu	0.86
C	0.84	Si	0.85	Se	0.86	Re	0.84	Am	0.85
N	0.82	P	0.85	Br	0.86	Os	0.84	Cm	0.85
O	0.81	S	0.84	Kr	0.86	Ir	0.84	Bk	0.86
F	0.81	Cl	0.83	Rb	0.86	Pt	0.84		
Ne	0.80	Ar	0.82	Sr	0.85	Au	0.84		
Na	0.82	K	0.87	Y	0.84	Hg	0.84		
		Ca	0.85	Zr	0.84	U	0.83		
		Sc	0.83	Nb	0.83	Np	0.83		
		Ti	0.82	Mo	0.82	Pu	0.83		
		V	0.81	Tc	0.82	Am	0.83		
		Cr	0.80	Ru	0.81	Cm	0.83		
		Mn	0.79	Rh	0.81	Bk	0.82		
		Fe	0.79	Pd	0.81				
		Co	0.78	Ag	0.81				
		Ni	0.78	Cd	0.80				
		Cu	0.78	In	0.82				
		Zn	0.77	Sn	0.83				
		Ga	0.79	Sb	0.85				
		Ge	0.80	Te	0.84				
		As	0.82	I	0.84				
		Se	0.83	Xe	0.84				
		Br	0.83						
		Kr	0.84						

Table 6.8 Theoretical widths (in eV) and asymmetry parameters (5.51) of $2s$-subshells of some atoms

Atoms	Si	Si^+	Si^{2+}	P^-	P	P^+	P^{2+}	S^-
Γ	1.00	1.09	1.11	1.14	1.25	1.31	1.37	1.41
β'	–0.011	–0.010	–0.006	–0.013	–0.013	–0.013	–0.012	–0.016
Atoms	S	S^+	S^{2+}	Cl	Ar	K	Ca	Sc
Γ	1.50	1.55	1.78	1.69	2.21	2.50	2.77	3.00
β'	−0.016	−0.015	−0.015	−0.017	−0.021	−0.022	−0.022	−0.022

Table 6.17 displays theoretical *LMM* Auger rates of S atom calculated in relaxed initial hole approximation. Initial states correspond to coupling of $2p$-hole with three terms of $3p^4$ configuration.

Table 6.18 contains theoretical *LMM* Auger rates of S atom (in %). The dominative transition contributes almost 40%, while the rest is distributed among many others.

Table 6.9 Theoretical (in different approximations) and experimental Ne *KLL* Auger rates (in %)

Lines	Final state	Theory					Experiment
		[6.13]	[6.14]		[6.15]		[6.8, 6.14]
		a,b	c	a	d	c	
A1	$2s^{-2}(^1S)$	6.1	6.31	6.03	7.8	5.3	6.2±0.3
A2	$2s^{-1}2p^{-1}(^1P)$	17.0	18.28	18.07	20.6	16.8	17.2±0.2
A3	$2s^{-1}2p^{-1}(^3P)$	6.1	9.46	6.82	6.2	8.9	6.3±0.2
A4	$2p^{-2}(^1S)$	9.6	8.76	8.79	8.1	10.1	9.5±0.4
A5	$2p^{-2}(^1D)$	61.2	57.12	60.27	57.3	58.9	60.9±0.2
Auger satellites					10.9		
Total, in m. at. un.		8.05	10.31	7.95	8.92	9.62	9.9±0.7

[a]Potential of relaxed final state
[b]Time-reversal diagrams (ground state correlations) are taken into account
[c]Potential of relaxed initial state
[d]Potential of "frozen" neutral atoms orbitals with a hole

Table 6.10 Auger rates of the main line satellites of Ne *KLL* spectrum (in % of line A5)

Final state	Rate	Final state	Rate
$2s^{-2}2p^{-1}(^2P)3s(^1P)$	0.11	$2s^{-1}2p^{-2}(^3P)(^2P)3p(^1P)$	0.48
$2s^{-2}2p^{-1}(^2P)3s(^3P)$	0.25	$2s^{-1}2p^{-2}(^3P)(^2P)3p(^3P)$	0.88
$2s^{-1}2p^{-2}(^1D)(^2D)3s(^1D)$	0.40	$2s^{-1}2p^{-2}(^3P)(^4P)3p(^3P)$	0.16
$2s^{-1}2p^{-2}(^1D)(^2D)3s(^3D)$	0.45	$2p^{-3}(^2P)3p(^1S)$	0.10
$2s^{-1}2p^{-2}(^1S)(^2S)3s(^1S)$	0.034	$2p^{-3}(^2P)3p(^3S)$	0.13
$2s^{-1}2p^{-2}(^1S)(^2S)3s(^3S)$	0.029	$2p^{-3}(^2P)3p(^1D)$	0.34
$2s^{-2}2p^{-1}(^2P)3p(^1S)$	0.47	$2p^{-3}(^2P)3p(^3D)$	0.43
$2s^{-2}2p^{-1}(^2P)3p(^3S)$	0.60	$2p^{-3}(^2D)3p(^1D)$	1.03
$2s^{-1}2p^{-2}(^1S)(^2S)3p(^1P)$	0.055	$2p^{-3}(^2D)3p(^3D)$	1.30
$2s^{-1}2p^{-2}(^1S)(^2S)3p(^3P)$	0.019	Total for $n = 3$	7.65
$2s^{-1}2p^{-2}(^1D)(^2D)3p(^1P)$	0.28	Total for $n = 4, 5$	1.89
$2s^{-1}2p^{-2}(^1D)(^2D)3p(^3P)$	0.09	Total continuum	8.90

Table 6.11 Theoretical *KLL* Auger rates of C atom (in %)

Final state	Initial state $1s^{-1}$			
	^2S	^2P	^4P	^2D
$2s^{-2}(^1S, ^3P, \text{or } ^1D)$	19.8	68.6	30.3	34.4
$2s^{-1}2p^{-1}(^1P)$	17.4	30.2		12.1
$2s^{-1}2p^{-1}(^3P)$	13.7	1.2	69.7	13.5
$2p^{-2}(^1S)$	49.1			40.0
Total m. at. un.	2.88	1.60	2.25	2.95

Table 6.19 shows characteristics of three-electron Auger transitions in Kr atom. There are transitions from singlet and triplet states $3s^{-1}4p^{-1}\,[^{1,3}P] \rightarrow 4s^{-2}[^1S]\,3d^{-1}[^2D]l_q[^{1,3}P](l_q = 1, 3)$ in Kr with energies $E_A = 7.801$ and $E_A = 7.764$ Ry,

Table 6.12 Theoretical *KLL* Auger rates of N atom (in %)

Final state	Initial state $1s^{-1}$					
	^3S	^5S	^1P	^3P	^1D	^3D
$2s^{-2}(^4S, ^2P, \text{or } ^2D)$	52.9	22.8	17.7	11.4	25.0	19.5
$2s^{-1}2p^{-1}(^2S)$			0.8	11.2		
$2s^{-1}2p^{-1}(^2P)$	40.2		28.2	7.7	22.1	6.2
$2s^{-1}2p^{-1}(^4P)$	6.9	77.2		8.3		8.0
$2s^{-1}2p^{-1}(^2D)$			0.001	16.6	1.5	26.0
$2p^{-2}(^2P)$			52.3	44.8	51.4	40.3
Total m. at. un.	1.81	2.93	3.25	3.91	3.80	4.12

Table 6.13 Theoretical *KLL* Auger rates of O atom (in %)

Final state	Initial state s^{-1}			
	^2S	^2P	^4P	^2D
$2s^{-2}(^1S, ^3P, \text{or } ^1D)$	6.6	17.0	11.2	10.7
$2s^{-1}2p^{-1}(^3S)$		16.3	3.4	
$2s^{-1}2p^{-1}(^5S)$			5.1	
$2s^{-1}2p^{-1}(^1P)$	20.0	3.2		3.9
$2s^{-1}2p^{-1}(^3P)$	11.8	0.3	12.5	2.7
$2s^{-1}2p^{-1}(^1D)$		7.3		12.8
$2s^{-1}2p^{-1}(^3D)$		0.6	22.0	7.9
$2p^{-2}(^1S)$	26.3			7.5
$2p^{-2}(^3P)$		55.3	45.8	
$2p^{-2}(^1D)$	35.3			54.5
Total m. at. un.	5.46	4.32	5.27	5.95

Table 6.14 Relative intensities of the *KLL* Auger spectrum, originating from ground ^3P term of O atom

Transition	Theory				Experiment
	[6.15]	[6.17]	[6.18]	[6.19]	[6.20]
$1s^{-1}(^2P) \rightarrow 2p^{-2}(^3P)$	1.26	1.17	1.29	1.74	1.4(2)
$1s^{-1}(^4P) \rightarrow 2p^{-2}(^3P)$	2.00	1.63	3.05	2.00	3.0(7)
$1s^{-1}(^4P) \rightarrow 2s^{-1}2p^{-1}(^5S)$	0.24	0.25	0.14	0.16	0.18(6)
$1s^{-1}(^4P) \rightarrow 2s^{-1}2p^{-1}(^3D)$	1.00	1.00	1.00	1.00	1.00
$1s^{-1}(^4P) \rightarrow 2s^{-1}2p^{-1}(^3P)$	0.57	0.60	0.49	0.55	0.44(4)
$1s^{-1}(^2P) \rightarrow 2s^{-1}2p^{-1}(^1D)$	0.18	0.17	0.13	0.21	0.16(3)
$1s^{-1}(^2P) \rightarrow 2s^{-1}2p^{-1}(^3S)$	0.40	0.53	0.51	0.81	0.58(5)
$1s^{-1}(^4P) \rightarrow 2s^{-1}2p^{-1}(^3S)$	0.14	0.25	0.17	0.22	0.20(2)
$1s^{-1}(^2P) \rightarrow 2s^{-2}(^3P)$	0.44	0.55	0.59	0.94	0.50(5)
$1s^{-1}(^4P) \rightarrow 2s^{-2}(^3P)$	0.53	0.83	0.64	0.68	0.64(1)

respectively. Note that $|E_{3s}|>|E_{4s}|$ and $|E_{4p}|<|E_{4s}|$, i.e., one vacancy goes up and the other vacancy goes down.

Table 6.20 demonstrates energies and partial widths of double Auger decay of Kr$3d^9$ state into five possible final states: $4s^14p^4(^4P)$, $4s^14p^4(^2D)$, $4s^24p^3(^4S)$,

Table 6.15 Theoretical *KLL* Auger rates of *F* atom (in %)

Final state	Initial state $1s^{-1}$	
	^1P	^3P
$2s^{-2}(^2P)$	9.7	8.5
$2s^{-1}2p^{-1}(^2S)$	0.8	1.7
$2s^{-1}2p^{-1}(^2P)$	24.2	6.1
$2s^{-1}2p^{-1}(^4P)$		7.9
$2s^{-1}2p^{-1}(^2D)$	0.4	13.4
$2p^{-2}(^2P)$	24.1	22.9
$2p^{-2}(^2D)$	40.8	39.5
Total m. at. un.	6.80	7.53

Table 6.16 The $L_2M_{23}M_{23}$ Auger rates of Ar (in %)

Final state	Present[a]	Present[b]	Theory [6.14]	Experiment [6.14]
$3p^{-2}(^1S)$	5.7	6.0	8.72	15.0 ± 2.0
$3p^{-2}(^1D)$	45.0	43.4	45.21	47.9 ± 0.4
$3p^{-2}(^3P)$	49.3	50.8	46.34	37.1 ± 0.4
Total $L_2M_{23}M_{23}$ (m. at. un.)	3.48	3.72	4.40	3.0 ± 0.7
Total L_2MM (m. at. un.)	4.72	4.96	5.80	4.4 ± 0.7

[a]Time-reversal diagrams are not taken into account
[b]Time-reversal diagrams are taken into account

Table 6.17 Theoretical *LMM* Auger rates of *S* atom (in %)

Final state	Initial state $2p^{-1}3p^4$				
	$^1S(^2P)$	$^3P(^2S)$	$^3P(^4S)$	$^3P(^2P)$	$^3P(^4P)$
$3s^{-2}3p^4(^1S, ^3P, \text{or } ^1D)$	3.49	11.34	0.81	0.001	37.17
$3s^{-1}3p^3(^4S)(^3S)$		60.38	14.55		
$3s^{-1}3p^3(^4S)(^5S)$			15.22		
$3s^{-1}3p^3(^2P)(^1P)$	14.65			5.74	
$3s^{-1}3p^3(^2P)(^3P)$	16.39	24.42		28.59	60.06
$3s^{-1}3p^3(^2D)(^1D)$		0.23		0.001	
$3s^{-1}3p^3(^2D)(^3D)$		3.62	0.12	0.06	2.77
$3p^2(^1S)$	17.65			14.97	
$3p^2(^3P)$	26.48		69.23	32.33	
$3p^2(^1D)$	21.35			18.31	
Total m. at. un.	2.189	0.231	9.356	4.174	0.0645

$4s^14p^4(^4P)$, and $4s^24p^3(^2D)$ [6.21], see also Fig. 6.11. Total contribution of this decay channel is 6.15×10^{-3} eV, see also Fig. 6.11.

Table 6.21 gives photon energies ω (eV) and partial widths W (10^{-7} eV) of the three-electron radiative transitions in Kr$4s^{-2}np \rightarrow 4p^{-2}n'l'$ [6.22]. The widths are small, no more than about 10^{-7} eV, but observable.

Table 6.22 collects energies (in eV) and rates (in 10^{-6} eV) of satellite Auger transitions $3d^{-1}[^2D] \rightarrow 4s^{-1}4p^{-2}[^2D]nl[LS] + \text{e}$ in Kr [6.23]. There are many

Table 6.18 Theoretical *LMM* Auger rates of *S* atom (in %)

Final state	Initial state $2p^{-1}3p^4$				
	$^3P(^2D)$	$^3P(^4D)$	$^1D(^2P)$	$^1D(^2D)$	$^1D(^2F)$
$3s^{-2}3p^4(^1S, ^3P, \text{or } ^1D)$	0.97	15.67	0.11	0.97	17.03
$3s^{-1}3p^3(^4S)(^3S)$	0.11	3.61			
$3s^{-1}3p^3(^4S)(^5S)$		0.25			
$3s^{-1}3p^3(^2P)(^1P)$	0.01		14.84	0.001	1.81
$3s^{-1}3p^3(^2P)(^3P)$	0.001	0.66	18.29	0.08	0.18
$3s^{-1}3p^3(^2D)(^1D)$	5.10		0.04	14.25	3.18
$3s^{-1}3p^3(^2D)(^3D)$	27.46	21.37	0.01	17.22	0.38
$3p^2(^1S)$			17.40	0	14.69
$3p^2(^3P)$	36.40	58.45	29.58	27.58	
$3p^2(^1D)$	29.94		19.64	39.91	62.91
Total m. at. un.	4.491	0.1795	2.459	4.754	0.180

Table 6.19 Characteristics of three-electron Auger decay in $\text{Kr}3s^{-1}4p^{-1}[^{1,3}P] \to 4s^{-2}[^1S]$ $3d^{-1}[^2D]l_q[^{1,3}P](l_q = 1, 3)$

M_α $(10^{-3}\ Ry^{1/2})$	$[^1P]$	$[^3P]$	$[^1P]$	$[^3P]$
	l_q=1	l_q=1	l_q=3	l_q=3
M_1	0.656	−3.956	−2.209	0.575
M_2	0.711	−4.014	−2.350	0.601
M_3	−0.237	−0.082	−0.030	0.041
M_4	−3.416 − i5.912	−1.718 − i3.100	1.838 + i6.155	−0.252 + i3.251
M_5	−3.555 − i6.153	−1.852 − i3.278	1.902 + i6.060	−0.336 + i3.221
M_6	0.075 − i0.121	0.312 − i0.008	0.843 − i0.236	−0.222 + i0.069
M_7	0.796	1.127	−0.831	0.140
M_8	0.845	1.168	−0.849	0.162
M_9	−1.720	−3.337	5.663	0.584
M_{tot}	−5.845 − i12.186	−12.321 − i6.386	−7.348 + i11.979	1.293 + i6.541
$\gamma^{(A)}(10^{-3}\,\text{Ry})$	1.148	1.210	1.245	0.279

The energies of Auger transitions in singlet and triplet channels are 7.801 and 7.764 Ry, respectively

Notations in Table 6.19

M_α is the partial amplitude, M_{tot} is the total amplitude, $\gamma^{(A)}$ is the probability, l_q - momentum of Auger-electron, and i corresponds to imaginary part of amplitude

Table 6.20 Energy E and width $\Gamma^{L_{\text{ic}}S_{\text{ic}}}$ of double Auger transitions $3d^9 \to 4s^14p^4[L_{\text{ic}}S_{\text{ic}}] + (e_1, e_2)$ and $3d^9 \to 4p^3[L_{\text{ic}}S_{\text{ic}}] + (e_1, e_2)$ in Kr [6.21]

Final ionic state	E(eV)	$\Gamma^{L_{\text{ic}}S_{\text{ic}}}$ (eV)	$\eta = \Gamma^{L_{\text{ic}}S_{\text{ic}}}/\Gamma \cdot 100\%$
$4s^14p^4(^2D)$	0.89	7.34×10^{-4}	12
$4s^14p^4(^4P)$	4.03	4.45×10^{-5}	< 1
$4s^24p^3(^2D)$	16.81	4.93×10^{-3}	80
$4s^24p^3(^2P)$	15.06	4.02×10^{-4}	7
$4s^24p^3(^4S)$	19.01	4.15×10^{-5}	< 1
$\Gamma = \sum_{L_{\text{ic}}S_{\text{ic}}} \Gamma^{L_{\text{ic}}S_{\text{ic}}}$		6.15×10^{-3}	100

Table 6.21 Photon energies ω (eV) and partial widths W (10^{-7} eV) of the three-electron radiative transitions in Kr $4s^{-2}np \rightarrow 4p^{-2}n'l'$ [6.22]

	$5p$		$6p$	
$4p^{-2}n'l'$	ω	W	ω	W
$^1S5s^2S$	30.07	0.57	37.72	0.07
$^1S6s^2S$	27.76	0.07	31.41	0.09
$^1S4d^2D$	26.83	0.49	30.48	0.06
$^1D5s^2D$	32.33	3.45	35.96	0.51
$^1D6s^2D$	27.00	0.37	30.65	0.71
$^1D4d^2P$	29.30	0.91	32.95	0.10
$^1D5d^2P$	26.05	0.24	29.70	0.07
$^1D4d^2D$	29.58	1.17	33.21	0.13
$^1D4d^2D$	26.15	0.33	29.85	0.09

Table 6.22 Energies (in eV) and rates (in 10^{-6} eV) of satellite Auger transitions $3d^{-1}[^2D] \rightarrow$ Kr$4s^{-1}4p^{-2}[^2D]nl[LS]$ + e in Kr [6.23]

State nl	Energy	Rate	States nl	Energy	Rate
$5s[^1D]$	16.944	3.656	$4d[^1D]$	16.594	21.678
$6s$	9.644	1.306	$5d$	9.427	12.171
$7s$	6.471	0.663	$6d$	6.349	7.009
$8s$	4.799	0.380	$7d$	4.731	4.417
$5s[^3D]$	18.067	12.105	$8d$	3.766	2.906
$6s$	9.989	5.336	$4d[^3D]$	17.999	5.698
$7s$	6.625	2.838	$5d$	9.746	7.404
$8s$	4.883	1.722	$6d$	6.498	4.581
$5p[^1P]$	13.838	16.897	$7d$	4.804	3.040
$6p$	8.392	11.273	$8d$	3.811	2.106
$7p$	5.839	6.889	$4d[^1S]$	16.677	462.430
$8p$	4.433	4.504	$5d$	9.544	95.087
$5p[^3P]$	14.598	7.442	$6d$	6.415	30.466
$6p$	8.633	7.742	$7d$	4.770	24.729
$7p$	5.949	5.555			
$8p$	4.496	4.043	$4d[^3S]$	17.956	32.755
$5p[^1D]$	13.963	5.838	$5d$	9.907	25.235
$6p$	8.373	2.215	$6d$	6.569	13.663
$7p$	5.821	1.137	$7d$	4.851	8.427
$8p$	4.422	0.683	$8d$	3.841	5.524
$5p[^1D]$	13.963	5.838			
$6p$	8.373	2.215	$4d[^1P]$	16.594	39.089
$7p$	5.821	1.137	$5d$	9.489	22.780
$8p$	4.422	0.683	$6d$	6.384	11.248
$5p[^3D]$	14.309	4.737	$7d$	4.751	6.557
$6p$	8.507	3.814	$8d$	3.781	4.138
$7p$	5.885	2.676			
$8p$	4.459	1.929	$4d[^3P]$	17.917	33.051

Table 6.22 Continued

State nl	Energy	Rate	States nl	Energy	Rate
$5p[^1F]$	14.471	13.805	$5d$	9.832	26.097
$6p$	8.567	4.912	$6d$	6.531	14.657
$7p$	5.915	2.376	$7d$	4.830	9.172
$8p$	4.475	1.352	$8d$	3.828	6.108
$5p[^3F]$	14.845	15.690			
$6p$	8.704	7.104	$4d[^1F]$	16.992	6.520
$7p$	5.980	3.999	$5d$	9.470	4.762
$8p$	4.512	2.528	$6d$	6.362	3.279
			$7d$	4.735	2.285
			$8d$	3.770	1.616
$4d[^3F]$	18.505	8.752	$4f[^1F]$	8.812	4.510
$5d$	9.768	7.880	$5f$	6.096	1.435
$6d$	6.500	5.346	$6f$	4.592	0.685
$7d$	4.804	3.725	$7f$	3.690	0.380
$8d$	3.813	2.653	$8f$	3.100	0.235
$4d[^1G]$	18.237	30.034	$4f[^3F]$	8.847	8.194
$5d$	9.795	18.033	$5f$	6.128	2.748
$6d$	6.505	11.273	$6f$	4.615	1.463
$7d$	4.813	7.491	$7f$	3.706	0.879
$8d$	3.815	5.168	$8f$	3.110	0.567
$4d[^3G]$	19.879	4.878	$4f[^1G]$	8.782	0.184
$5d$	10.091	4.305	$5f$	6.078	0.119
$6d$	6.630	3.177	$6f$	4.588	0.078
$7d$	4.879	2.284	$7f$	3.689	0.053
$8d$	3.856	1.662	$8f$	3.098	0.037
$4f[^1P]$	9.184	175.904	$4f[^3G]$	8.820	0.187
$5f$	6.271	62.843	$5f$	6.112	0.125
$6f$	4.689	24.895	$6f$	4.613	0.083
$7f$	3.738	10.535	$7f$	3.704	0.056
$8f$	3.139	4.075	$8f$	3.110	0.040
$4f[^3P]$	9.237	95.985	$4f[^1H]$	9.084	0.031
$5f$	6.313	32.421	$5f$	6.240	0.011
$6f$	4.716	15.626	$6f$	4.675	0.004
$7f$	3.760	7.204	$7f$	3.742	0.002
$8f$	3.151	4.784	$8f$	3.134	0.001
$4f[^1D]$	8.984	3.599	$4f[^3H]$	9.150	1.647
$5f$	6.177	1.750	$5f$	6.275	1.130
$6f$	4.638	1.010	$6f$	4.712	0.768
$7f$	3.706	0.637	$7f$	3.761	0.535
$8f$	3.119	0.431	$8f$	3.149	0.386
$4f[^3D]$	9.027	26.851	Total		1807.262
$5f$	6.215	8.265			
$6f$	4.663	4.559			
$7f$	3.735	2.762			
$8f$	3.129	1.823			

Table 6.23 Energies (in eV) and rates (in 10^{-6} eV) of satellite Auger transitions $3d^{-1}[^2D] \rightarrow 4s^{-1}4p^{-2}[^4P]\ nl[LS]$ + e in Kr [6.23]

State	Energy	Rate	State	Energy	Rate
$5s[^3P]$	19.860	3.877	$4d[^3F]$	20.134	0.695
$6s$	12.507	1.348	$5d$	12.431	0.424
$7s$	9.316	0.653	$6d$	9.262	0.279
$8s$	7.647	0.372	$7d$	7.603	0.186
$9s$	6.658	0.230	$8d$	6.633	0.130
$5p[^3P]$	13.287	14.785	$9d$	6.006	0.106
$6p$	10.108	2.370	$4f[^3D]$	11.612	111.864
$7p$	8.194	0.722	$5f$	8.910	22.497
$8p$	7.009	0.306	$6f$	7.418	9.894
$9p$	6.273	0.165	$7f$	6.515	4.156
$5p[^3D]$	17.112	0.823	$8f$	5.938	2.304
$6p$	11.338	0.390	$9f$	5.531	1.384
$7p$	8.715	0.263	$4f[^3F]$	3.675	4.598
$8p$	7.296	0.181	$5f$	9.025	1.104
$9p$	6.437	0.132	$6f$	7.479	0.344
$4d[^3D]$	13.545	3.582	$7f$	6.553	0.174
$5d$	11.892	1.287	$8f$	5.962	0.106
$6d$	9.037	0.761	$9f$	5.549	0.072
$7d$	7.489	0.501	$4f[^3G]$	11.729	0.127
$8d$	6.564	0.599	$5f$	8.980	0.084
$9d$	5.961	0.433	$6f$	7.462	0.056
$4d[^3P]$	18.332	16.352	$7f$	6.542	0.039
$5d$	11.991	5.362	$8f$	5.946	0.027
$6d$	9.077	2.577	$9f$	5.373	0.016
$7d$	7.508	1.489	Total		222.124
$8d$	6.573	.942			
$9d$	5.969	.958			

transitions with decay rates varying from 0.04×10^{-6} eV to about 460×10^{-6} eV. Some nl states contribute most prominently. These are $4d[^1S](462 \times 10^{-6}$ eV), $4f[^1P](176 \times 10^{-6}$ eV), $5d[^1S](90 \times 10^{-6}$ eV), and $5f[^1P](63 \times 10^{-6}$ eV), while the total rate of this channel is $1,807 \times 10^{-6}$ eV.

Table 6.23 present energies (in eV) and rates (in 10^{-6} eV) of satellite Auger transitions $3d^{-1}[^2D] \rightarrow 4s^{-1}4p^{-2}[^4P]\ nl[LS]$ + e in Kr [6.23]. There are many transitions with decay rates varying from 0.016×10^{-6} eV to about 112×10^{-6} eV. The total rate is eight times smaller than in Table 6.22. Slightly more than one half of the total rate, 111.9×10^{-6} eV, comes from $nl = 4f[^3D]$.

Table 6.24 demonstrates energies (in eV) and rates (in 10^{-6} eV) of satellite Auger transitions $3d^{-1}[^2D] \rightarrow 4p^{-3}[^2D]\ nl[LS]$ + e in Kr [6.23]. The total rate is almost the same as in Table 6.22. There are many transitions with decay rates varying from 0.001×10^{-6} eV to about 785.6×10^{-6} eV. Some nl states contribute most prominently. These are $4f[^1P](785.6 \times 10^{-6}$ eV), $4f[^3P](268.5 \times 10^{-6}$ eV), $5f[^1P](108.35 \times 10^{-6}$ eV) and $5p[^1P]$ $(726.7 \times 10^{-6}$ eV).

Table 6.24 Energies (in eV) and rates (in 10^{-6} eV) of satellite Auger transitions in $3d^{-1}[^2D] \rightarrow 4p^{-3}[^2D]\ nl[LS]$+e in Kr [6.23]

State	Energy	Rate	State	Energy	Rate
$5s[^1D]$	34.767	10.186	$6d$	21.576	0.522
$6s$	26.673	1.785	$7d$	19.904	0.377
$7s$	23.787	0.806	$8d$	18.916	0.277
$8s$	22.078	0.455	$9d$	18.282	0.207
$9s$	21.073	0.288	$4d[^3P]$	32.933	15.092
$5s[^3D]$	35.594	0.441	$5d$	26.451	1.343
$6s$	26.948	0.443	$6d$	23.336	0.571
$7s$	24.241	0.301	$8d$	20.717	0.285
$8s$	22.506	0.213	$9d$	20.094	0.213
$9s$	21.488	0.154	$4d[^1D]$	31.946	17.568
$5p[^1D]$	30.799	14.028	$5d$	27.024	6.766
$6p$	27.913	5.099	$6d$	24.140	4.405
$7p$	26.245	2.475	$7d$	22.580	3.119
$8p$	25.214	1.408	$8d$	21.644	2.193
$9p$	24.538	0.883	$9d$	21.039	1.614
$5p[^3D]$	31.904	16.953	$4d[^3D]$	32.748	1.206
$6p$	25.840	6.584	$5d$	26.372	0.637
$7p$	23.136	3.384	$6d$	23.098	0.386
$8p$	21.680	1.981	$7d$	21.401	0.252
$9p$	20.803	1.260	$8d$	20.403	0.174
$5p[^1P]$	31.888	71.090	$9d$	19.765	0.125
$6p$	25.861	13.506	$4d[^1F]$	31.619	3.105
$7p$	23.167	5.723	$5d$	25.850	1.457
$8p$	21.715	3.100	$6d$	23.078	0.851
$9p$	20.839	1.906	$7d$	21.561	0.541
$5p[^3P]$	31.354	18.370	$8d$	20.645	0.368
$6p$	25.789	7.935	$9d$	20.052	0.262
$7p$	23.223	4.163	$4d[^3F]$	36.735	4.011
$8p$	21.816	2.473	$5d$	27.315	2.316
$9p$	20.963	1.594	$6d$	23.925	1.411
$5p[^1F]$	31.783	11.870	$7d$	22.190	0.920
$6p$	25.844	5.055	$8d$	21.176	0.628
$7p$	23.176	2.661	$9d$	20.531	0.447
$8p$	21.735	1.579	$4d[^1G]$	35.766	3.415
$9p$	20.864	1.014	$5d$	24.543	2.801
$5p[^3F]$	31.859	0.889	$6d$	21.242	2.101
$6p$	25.850	0.443	$7d$	19.539	1.553
$7p$	23.163	0.251	$4d[^3G]$	32.564	0.531
$8p$	21.713	0.157	$5d$	27.024	0.436
$9p$	20.838	0.105	$6d$	23.677	0.349
$4d[^1P]$	32.618	0.841	$7d$	21.954	0.264
$5d$	24.782	0.710			
$5f$	20.026	5.287	$5f$	19.987	2.258
$6f$	18.508	2.515	$6f$	18.482	1.324
$7f$	17.589	1.408	$7f$	17.571	0.835
$8f$	16.993	0.877	$8f$	16.981	0.564

Table 6.24 Continued

State	Energy	Rate	State	Energy	Rate
$9f$	16.585	0.584	$9f$	16.577	0.398
$4f[^3D]$	22.979	8.510	$4f[^3F]$	23.025	1.847
$5f$	20.053	3.746	$5f$	20.085	1.030
$6f$	18.525	1.958	$6f$	18.544	0.615
$7f$	17.600	1.154	$7f$	17.614	0.396
$8f$	17.001	0.739	$8f$	17.009	0.271
$9f$	16.590	0.503	$9f$	16.597	0.192
$4f[^1P]$	23.139	785.580	$4f[^1G]$	22.736	0.124
$5f$	20.082	108.346	$5f$	19.985	0.010
$6f$	18.543	52.307	$6f$	18.480	0.003
$7f$	17.612	29.482	$7f$	17.571	0.001
$8f$	17.009	14.336	$8f$	16.981	0.001
$9f$	16.596	6.140	$9f$	16.577	0.000
$4f[^3P]$	22.796	268.525	$4f[^3G]$	21.989	6.124
$5f$	20.029	53.449	$5f$	20.104	1.713
$6f$	18.509	20.287	$6f$	18.555	0.999
$7f$	17.590	9.189	$7f$	17.620	0.628
$8f$	16.995	3.856	$8f$	17.015	0.422
$9f$	16.585	1.925	$9f$	16.995	0.284
			Total		1734.648

Table 6.25 Energies (in eV) and rates (in 10^{-6} eV) of satellite Auger transitions $3d^{-1}[^2D] \rightarrow 4p^{-3}[^2P]\ nl[LS]$ + e in Kr [6.23]

State	Energy	Rate	State	Energy	Rate
$5s[^1P]$	33.482	3.555	$9d$	18.739	1.306
$6s$	24.654	0.728	$4d[^3P]$	34.260	3.571
$7s$	22.492	0.370	$5d$	25.486	0.324
$8s$	20.778	0.219	$6d$	22.163	0.578
$9s$	19.769	0.143	$7d$	20.446	0.364
$5s[^3P]$	33.717	0.464	$8d$	19.442	0.241
$6s$	24.927	0.388	$9d$	18.805	0.170
$7s$	22.346	0.282	$5d$	25.486	0.324
$8s$	20.610	0.208	$6d$	22.163	0.578
$9s$	19.588	0.154	$7d$	20.446	0.364
$5p[^1D]$	29.655	13.608	$8d$	19.442	0.241
$6p$	23.984	5.800	$9d$	18.805	0.170
$7p$	21.384	3.244	$4d[^1D]$	35.441	24.914
$8p$	19.973	1.965	$5d$	26.852	1.141
$9p$	19.116	1.278	$6d$	23.554	0.578

Table 6.25 shows energies (in eV) and rates (in 10^{-6} eV) of satellite Auger transitions $3d^{-1}[^2D] \rightarrow 4p^{-3}[^2P]\ nl[LS]$ + e in Kr [6.23]. The total rate is 268.5×10^{-6} eV. The biggest rates are: 131.1×10^{-6} eV, 84.7×10^{-6} eV, and 79.26×10^{-6} eV for $4f[^1D]$, $4f[^3D]$, and $4f[^1F]\ nl$ states, respectively.

Table 6.25 Continued

State	Energy	Rate	State	Energy	Rate
$5p[^3D]$	30.056	13.760	$7d$	21.846	0.383
$6p$	24.024	6.332	$8d$	20.845	0.267
$7p$	21.328	3.712	$9d$	20.211	0.189
$8p$	19.870	2.271	$4d[^3D]$	34.492	8.692
$9p$	18.995	1.482	$5d$	26.620	0.695
$5p[^3S]$	30.402	1.279	$6d$	23.408	0.381
$6p$	24.315	0.578	$7d$	21.729	0.266
$7p$	21.602	0.316	$8d$	20.741	0.193
$8p$	20.139	0.255	$9d$	20.111	0.142
$9p$	19.260	0.164	$4d[^1F]$	33.270	8.438
$5p[^1P]$	29.638	0.417	$5d$	26.362	2.814
$6p$	23.640	0.212	$6d$	23.305	1.785
$7p$	20.953	0.273	$7d$	21.684	1.273
$8p$	19.501	0.157	$8d$	20.722	0.932
$9p$	18.628	0.099	$9d$	20.103	0.703
$5p[^3S]$	30.402	1.279	$4d[^3F]$	34.272	3.901
$5p[^3P]$	29.741	22.372	$5d$	24.993	0.422
$6p$	23.950	9.554	$6d$	21.621	0.293
$7p$	21.310	5.679	$7d$	19.889	0.221
$8p$	19.883	3.375	$8d$	18.878	0.168
$9p$	19.017	2.168	$9d$	18.238	0.131
$4d[^1P]$	30.147	20.831			
$5d$	24.486	8.000			
$6d$	21.746	4.603			
$7d$	20.240	2.848			
$8d$	19.329	1.878			
$4f[^1D]$	24.995	131.121	$4f[^3F]$	26.443	28.683
$5f$	21.745	33.072	$5f$	21.821	7.434
$6f$	20.237	14.424	$6f$	20.287	3.623
$7f$	19.329	5.621	$7f$	19.361	2.065
$8f$	18.735	2.505	$8f$	18.761	1.296
$9f$	18.331	0.318	$9f$	18.347	0.873
$4f[^3D]$	25.833	84.708	$4f[^1G]$	24.541	26.073
$5f$	21.847	14.628	$5f$	21.781	2.589
$8f$	18.767	2.518	$6f$	20.260	1.146
$9f$	18.354	1.704	$7f$	19.343	0.623
$4f[^1F]$	23.115	79.259	$8f$	18.746	0.379
$5f$	21.836	20.348	$9f$	18.339	0.251
			$4f[^3G]$	24.344	28.367
			$5f$	21.862	2.399
			$6f$	20.313	1.189
			$7f$	19.377	0.684
			$8f$	18.772	0.435
			$9f$	18.313	0.279
			Total		726.738

Table 6.26 Energies (in eV) and rates (in 10^{-6} eV) of satellite Auger transitions $3d^{-1}[^2D] \rightarrow 4p^{-3}[^4S]\ nl[LS] + \mathrm{e}$ in Kr [6.23]

State	Energy	Rate	State	Energy	Rate
$5p[^3P]$	33.645	11.428	$8d$	23.301	0.047
$6p$	28.167	4.504	$9d$	22.692	0.034
$7p$	25.628	2.262	$4f\ [^3F]$	25.317	3.534
$8p$	24.233	1.313	$5f$	23.939	0.772
$9p$	23.384	0.827	$6f$	22.438	0.415
$4d[^3D]$	37.545	22.760	$7f$	21.527	0.248
$5d$	28.761	1.027	$8f$	20.935	0.160
$6d$	25.825	0.194	$9f$	20.511	0.093
$7d$	24.248	0.077	Total		49.695

Table 6.27 Calculated widths for non-radiative transitions $b + \beta_1$ in Kr (see Graph 6.1)

Transition	Γ_{tot}	$\Gamma^{(\beta_1)}/\Gamma_{\mathrm{tot}}$	$\Gamma^{(b)}$	Γ
$3d^9 5p \rightarrow 4p^3 5s$	0.60	$\sim 1/3$	10^{-4}–10^{-5}	10^{-5}
$3d^9 6p \rightarrow 4p^3 5s$	0.44	$\sim 1/7$	10^{-4}–10^{-5}	10^{-5}
$3d^9 5p \rightarrow 4p^3 6s$	0.30	$\sim 2/3$	10^{-5}–10^{-6}	10^{-6}
$3d^9 6p \rightarrow 4p^3 6s$	0.19	$\sim 1/3$	10^{-5}–10^{-6}	10^{-6}
$3d^9 5p \rightarrow 4p^3 4d$	0.83	$\sim 1/6$	10^{-3}–10^{-4}	10^{-4}
$3d^9 6p \rightarrow 4p^3 4d$	0.86	$\sim 1/14$	10^{-3}–10^{-4}	10^{-4}
$3d^9 5p \rightarrow 4p^3 5d$	0.34	$\sim 3/5$	10^{-4}–10^{-5}	10^{-5}
$3d^9 6p \rightarrow 4p^3 5d$	0.18	$\sim 1/4$	10^{-4}–10^{-5}	10^{-5}

Γ_{tot} is the total width of the corresponding $4p^3 n'l'np$ state, $\Gamma^{(\beta)}{}_1/\Gamma_{\mathrm{tot}}$ is relative width of the second step transition β_1 $\Gamma^{(b)}$ is the partial width of the first-step transition, Γ is partial width of a corresponding two-step channel (in eV) [6.24]

Table 6.26 gives energies (in eV) and rates (in 10^{-6} eV) of satellite Auger transitions $3d^{-1}[^2D] \rightarrow 4p^{-3}[^2P]\ nl[LS]$ + e in Kr [6.23]. This is the weakest channel with the total rate 49.7×10^{-6} eV, of which almost one half, 22.76×10^{-6} eV comes from $nl = 4d[^3D]$.

Table 6.27 presents calculated widths for non-radiative transitions $b + \beta_1$ in Kr (see Graph 6.1). Γ_{tot} is the total width of the corresponding $4p^3 n'l'\ np$ state, $\Gamma^{(\beta)}{}_1/\Gamma_{\mathrm{tot}}$ is the relative width of the second step transition β_1, $\Gamma^{(b)}$ is the partial width of the first-step transition, Γ is partial width of a corresponding two-step channel (in eV) [6.24].

Table 6.28 presents integral contribution Γ_{e1e2} of different pairs $(l, l+1)$ to the total transition probability of transition $\mathrm{Kr}3d^{-1}5p[^1P] \rightarrow \mathrm{Kr}4s^{-2}[^1S]$ [6.24].

Table 6.29 presents partial amplitudes M_α, main contributions $M_\alpha(k)$ to the total amplitude M of the transition $3d^{-1}5p[^1P] \rightarrow 4s^{-2}[^1S] + \varepsilon p + \varepsilon d$ at different energies [6.25] (see Graph 6.2).

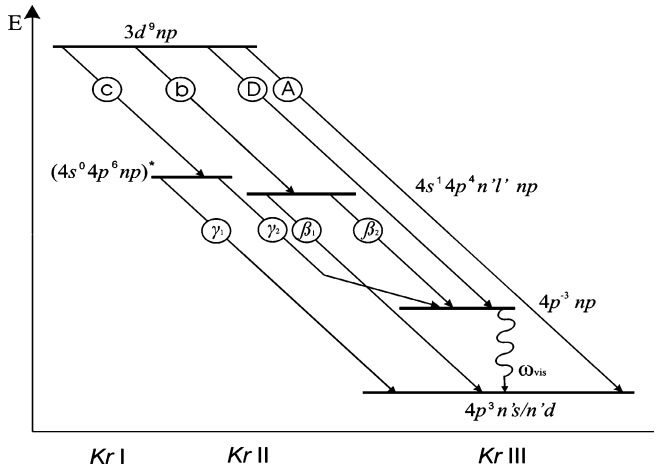

Graph 6.1 Transitions for Table 6.27

Table 6.28 Integral contribution Γ_{e1e2} of different pairs $(l, l+1)$ to the total transition probability of transition Kr$3d^{-1}5p[^1\mathrm{P}] \rightarrow$ Kr$4s^{-2}[^1S]$ [6.24]

(e_1, e_2)	$\Gamma_{e1e2}(10^{-4}\ \mathrm{eV})$	Fraction (%)
(s, p)	0.29	5
(p, d)	2.43	43
(d, f)	1.06	19
(f, g)	1.27	23
(g, h)	0.50	9
(h, i)	0.05	<1
Total	5.60	100

Table 6.29 Partial amplitudes M_α, main contributions $M_\alpha(k)$ total amplitude M of the transition $3d^{-1}5\mathrm{p}[^1P] \rightarrow 4s^{-2}[^1S] + \varepsilon p + \varepsilon d$ at different energies [6.25] (see Graph 6.2)

α	M_α	$M_\alpha(k)$	M_α	$M_\alpha(k)$	M_α	$M_\alpha(k)$
1	4.97	3.75(4p)	4.67	4.15(4p)	3.22	2.81(4p)
2	–16.06	–15.83(4s)	–12.24	–11.13(4s)	–8.33	–7.60(4s)
3	–16.06	–15.83(4s)	–12.24	–11.13(4s)	–8.33	–7.60(4s)
4	242.82	239.20(3d)	54.22	50.44(3d)	30.70	26.83(3d)
5	0.72	1.19(εf)	0.73	1.31(εf)	2.34	3.02(εf)
6	0.72	1.19(εf)	0.73	1.31(εf)	2.34	3.02(εf)
7	1.82–i95.68	–i95.68(εd)	7.48–i86.06	–i86.06(εd)	36.75–i100.06	i100.06(εd)
8	–4.40–i0.17	–3.05(4p)	–4.06–i0.18	–2.61(4p)	–3.64–i0.19	–2.27(4p)
9	–440–i0.17	–3.05(4p)	–4.06–i0.18	–2.61(4p)	–3.64–i0.19	–2.27(4p)
M	210.13–i96.02	(3d,4s,4p)	35.23–i86.42	(3d,4s,4p)	51.41–i100.44	(3d,4s,4p)

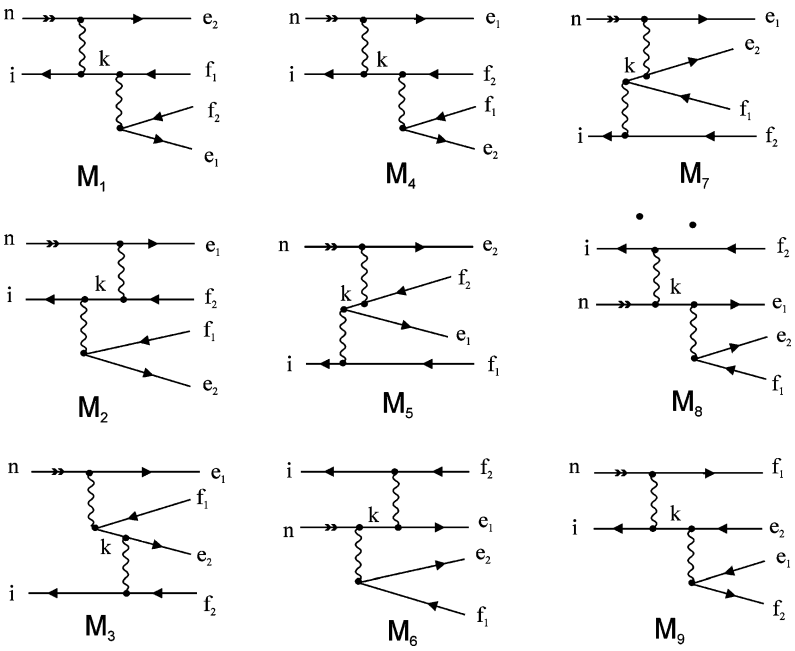

Graph 6.2 Diagrams for amplitudes presented in Table 6.29

References

6.1. Svensson S, Eriksson B, Martensson N, Wendin G, Gelius U (1988) Electron shake-up and correlation satellites and continuum shake-off distributions in X-ray photoelectron spectra of rare gas atoms. J Electron Spectrosc Relat Phenom 47:327–384

6.2. Svensson S, Martensson N, Gelius U (1987) Observation of autoionizing resonances in core-electron shakeup spectra. Phys Rev Lett 58:2639–2641

6.3. Kikas A, Osborne SJ, Ausmees A, Svensson S, Sairanen OP, Askela S (1996) High-resolution study of the correlation satellites in photoelectron spectra of rare gases. J Electron Spectrosc Relat Phenom 77:241–266

6.4. Kaneyasu T, Hikosaka Y, Shigemasa E, Penent F, Lablanquie P, Aoto T, Ito K (2007) Autoionization of the Ne^{+} Rydberg states formed viavalence photoemission. J Phys B At Mol Opt Phys 40:4047–4060

6.5. Hikosaka Y, Aoto T, Lablanquie P, Penent F, Shigemasa E, Ito K (2006) Experimental investigation of core—valence double photoionization PRL. Phys Rev Lett 97:053003

6.6. Svennson S, Martensson N, Basilier E, Malmquist PA, Gelius U, Siegbahn K (1976) Lifetime broadening and CI-resonances observed in ESCA. Phys Scripta 14:141–147

6.7. Yarzhemsky VG, Teterin YuA, Teterin AYu, Amusia MYa, Nefedov VI (2005) The structure of $4p$ X-ray photoelectron spectra of Xe and compounds of Cs, Ba, Ln. J Surface Invest X-ray Synchr Neutron Tech 6:3–8

6.8. Albiez A, Toma M, Weber W, Mehlhorn W (1990) $KL_{2,3}$ ionization in neon by electron impact in the range 1.5–50 keV: cross-section and alignment. Z Phys D 16:97–106

6.9. Pahler M, Caldwell CD, Schaphorst SJ, Krause MO (1993) Intrinsic line widths of neon $2s2p(^{1,3}P)nl^2L$ correlation satellites. J Phys B At Mol Opt Phys 26:1617–1625

6.10. Seah MP, Gilmore IS (2006) Quantitative X-ray photoelectron spectroscopy: quadrupole effects, shake-up, Shirley background and relative sensitivity factors from database of true X-ray photoelectron spectra. Phys Rev B 73:174113
6.11. Glans P, LaVilla RE, Ohno M, Svennson S, Bray G, Wassdahl N, Nordgren J (1994) Determination of the lifetime width of the argon L_1-hole state. Phys Rev A 47:1539–1542
6.12. Yarzhemsky VG, Reich T, Chernysheva LV, Streubel P, Szargan R (1996) Lineshape asymmetry parameters in X-ray photoelectron spectra J Electron Spectrosc Relat Phenom 77:15–24
6.13. Kelly HP (1975) K Auger rates calculated for Ne^+. Phys Rev A 11:556–565
6.14. Tulkki J, Åberg T, Mäntykenttä A, Aksela H (1992) Relativistic multichannel calculation of the Ne*KLL* and Ar $L_2M_{2,3}M_{2,3}$ Auger transition rates. Phys Rev A 43:1357–1366
6.15. Yarzhemsky VG, Sgamellotti A (2002) Auger rates of second row atoms calculated by many-body perturbation theory J Electron Spectrosc Relat Phenom 125:13–24
6.16. Bhalla CP (1973) Effect of configuration interaction of K-shell Auger spectrum of neon. Phys Lett A 44:103–104
6.17. Lohman B, Fritzsche S (1996) Intensities and angular distribution parameters for the KLL Auger transitions of atomic oxygen. J Phys B At Mol Opt Phys 29:5711–5723
6.18. Saha HP (1994) Theoretical studies of the K-shell Auger spectrum of atomic oxygen. Phys Rev A 49:894–898
6.19. Petrini D, de Araujo FX (1994) Auger process following 1s-photoionization: OIII lines. Astron Astrophys 282:315–317
6.20. Caldwell CD, Krause MO (1993) K-shell Auger spectrum of atomic oxygen. Phys Rev A 47:R759–R762
6.21. Kilin VA, Lazarev DA (1998) Double Auger decay of 3d vacancy in krypton. Russian Phys J 4(10):1001–1009
6.22. Ehresmann A, Kilin VA, Chernysheva LV, Schmoranzer H, Amusia MYa, Schartner K-H (1993) Three-electron radiative transitions. J Phys B At Mol Opt Phys 26:L97–L102
6.23. Kilin VA (2004) Correlation effects in multiple ionization processes. Dr. Sc.Thesis, Tomsk State University (in Russian)
6.24. Ehresmann A, Kilin VA, Schmoranzer H, Schartner K-H, Amusia MYa (1995) Assignment of new fluorescence lines from Kr III $4p^3 6s5d$ states observed after excitation of the Kr I $3d_{5/2}^9 5p$-resonance. J Phys B At Mol Opt Phys 28:965–977
6.25. Amusia MYa, Kilin VA, Ehresmann A, Schmoranzer H, Schartner K-H (1993) Double-autoionization decay of resonantly excited single-electron states. J Phys B At Mol Opt Phys 26:1281–1300

Chapter 7
Off-shell Photoionization Cross-sections: Results of Calculations

7.1 Data Presentation

In this chapter we present data for photoionization cross-sections beyond the energy conservation frame, or off-shell photoionization which are required for calculations of excited vacancy states. In Chaps. 5 and 6 we studied decay of not only simple HF vacancies but of more complex excited states that consist of several electrons and vacancies. The decay of these states generates new spectral lines, which are relatively intensive and noticeable in experimental spectra. Such effects were only briefly discussed in this book. But they are of interest and of some importance.

The first step to investigate the corresponding decay process is to consider the excitation of the above mentioned complex states. This is why we decided in this chapter to pay some attention to calculations of the cross-sections of creation of simplest among such states—satellites with higher excitation energy then that of corresponding HF vacancy. We consider these processes in two-step mechanism. At the first step the atom is singly ionized and in the second step another electron is excited to discrete state or to continuum. The energy conservation is fulfilled for the whole process. Hence the first step looks like creation of an intermediate state corresponding to one-electron photoionization beyond the energy conservation frame. In this chapter, we present photoionization cross-section beyond the energy conservation frame for Ne, Ar, Kr, and Xe. We believe that this mechanism is the most important for describing shake-up satellite intensity variation near threshold.

The numbering of figures is organized here similar to Chap. 5, i.e., as follows: at first, goes the number of the respective chapter, the next letters denotes the considered atom as in the Periodic Table of Chemical Elements, and then the small letter stands for the considered characteristic or property. The final number marks the considered figure among all others that illustrated the given characteristic or property for this atom. The following letter denotes the process considered:

p, that corresponds to photoelectron cross-section.

M. Amusia et al., *Handbook of Theoretical Atomic Physics*,
DOI 10.1007/978-3-642-24752-1_7, © Springer-Verlag Berlin Heidelberg 2012

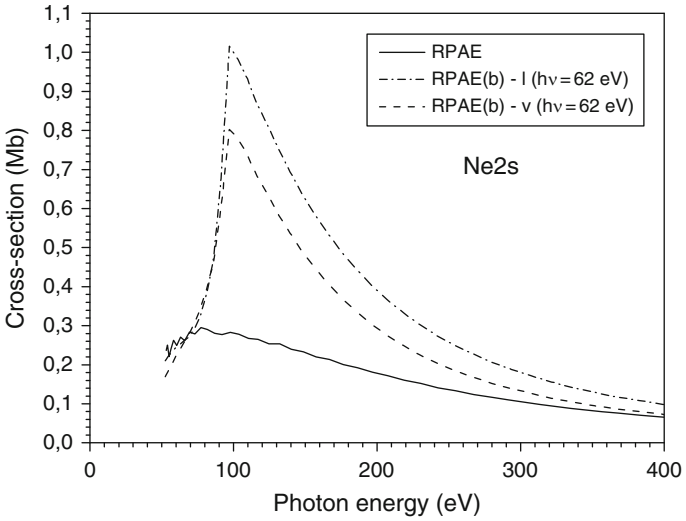

Fig. 7.1_Ne_p8 Ne2*s* photoionization cross-section in RPAE as a function of photon energy and Ne2*s* photoionization cross-section beyond the energy conservation for photon energy 62 eV RPAE(b) (*auxiliary curve*)

Complete consideration of Auger decay of excited states in addition to diagrams (5.137) with two Coulomb interaction lines includes also diagrams with three Coulomb interaction lines, shown in (7.1). The examples of such states are considered in the present chapter.

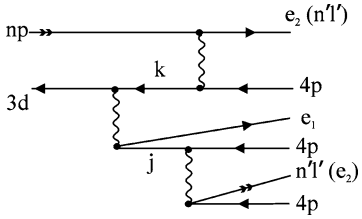

(7.1)

7.2 Description of Figures

We present here the results of one of the mechanisms that describe satellite excitation cross-section.

Figures 7.1_Ne_p8–7.13_Ne_p13 (Ne) show Ne2*s* photoionization cross-section in RPAE as a function of photon energy and Ne2*s* photoionization cross-section beyond the energy conservation frame or “off the energy shell”, denoted as RPAE(b).

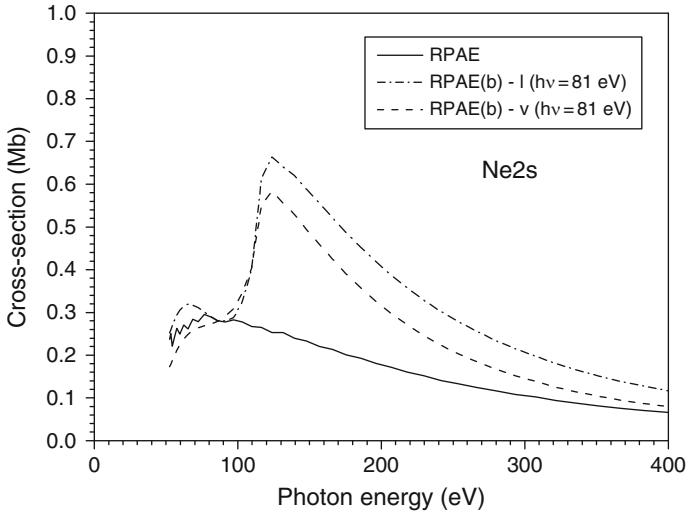

Fig. 7.2_Ne_p9 Ne2*s* photoionization cross-section in RPAE as a function of photon energy and Ne2*s* photoionization cross-section beyond the energy conservation for photon energy 81 eV RPAE(b) (*auxiliary curve*)

Figure 7.1_Ne_p1 presents Ne2*s* photoionization cross-section in RPAE as a function of photon energy and Ne2*s* photoionization cross-section beyond the energy conservation for photon energy 62 eV (*auxiliary curve*). These curves coincide at photon energy 62 eV. To obtain photoionization cross-section for photon energy 62 eV with the excitation of satellite shifted from the main line to larger binding energy by ΔE, one should use the value on auxiliary curve for the energy shifted to the left on ΔE from this point.

Figure 7.2_Ne_p2 depicts the Ne2*s* photoionization cross-section in RPAE as a function of photon energy and Ne2*s* photoionization cross-section beyond the energy conservation for photon energy 81 eV (*auxiliary curve*). These curves coincide at photon energy 81 eV. To obtain photoionization cross-section for photon energy 81 eV with the excitation of satellite shifted from the main line to larger binding energy by ΔE, one should use the value on auxiliary curve for the energy shifted to the left by ΔE from this point.

Figure 7.3_Ne_p3 shows the Ne2*s* photoionization cross-section in RPAE as a function of photon energy and Ne2*s* photoionization cross-section beyond the energy conservation for photon energy 103 eV (*auxiliary curve*). These curves coincide at photon energy 103 eV. To obtain photoionization cross-section for photon energy 103 eV with the excitation of satellite shifted from the main line to larger binding energy by ΔE, one should use the value on auxiliary curve for the energy shifted to the left by ΔE from this point.

Figure 7.4_Ne_p4 demonstrates the Ne2*s* photoionization cross-section in RPAE as a function of photon energy and Ne2*s* photoionization cross-section beyond the energy conservation for photon energy 131 eV (*auxiliary curve*). These curves

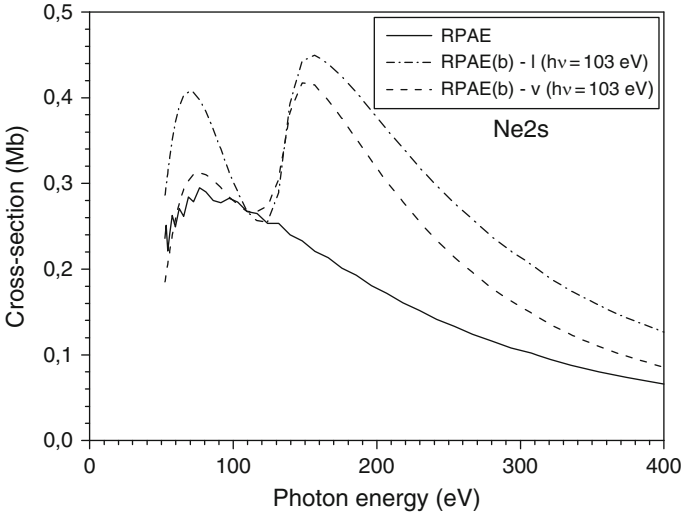

Fig. 7.3_Ne_p3 Ne2*s* photoionization cross-section in RPAE as a function of photon energy and Ne2*s* photoionization cross-section beyond the energy conservation for photon energy 103 eV RPAE(b) (*auxiliary curve*)

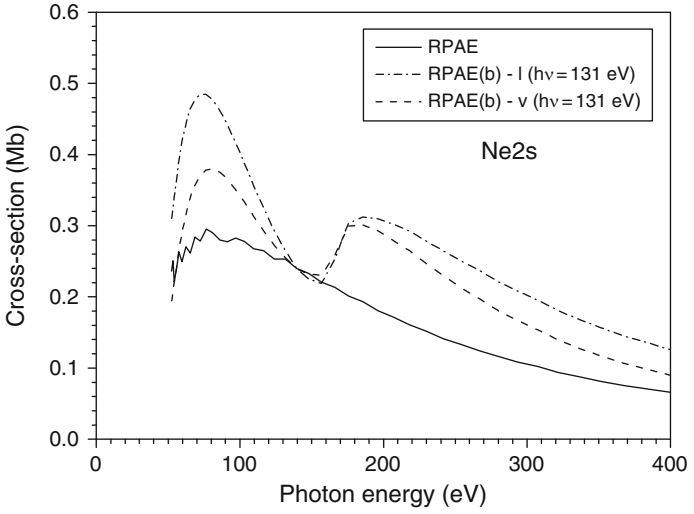

Fig. 7.4_Ne_p4 Ne2*s* photoionization cross-section in RPAE as a function of photon energy and Ne2*s* photoionization cross-section beyond the energy conservation for photon energy 131 eV RPAE(b) (*auxiliary curve*)

coincide at photon energy 131 eV. To obtain photoionization cross-section for photon energy 131 eV with the excitation of satellite shifted from the main line to larger binding energy by ΔE, one should use the value on auxiliary curve for the energy shifted to the left by ΔE from this point should be used.

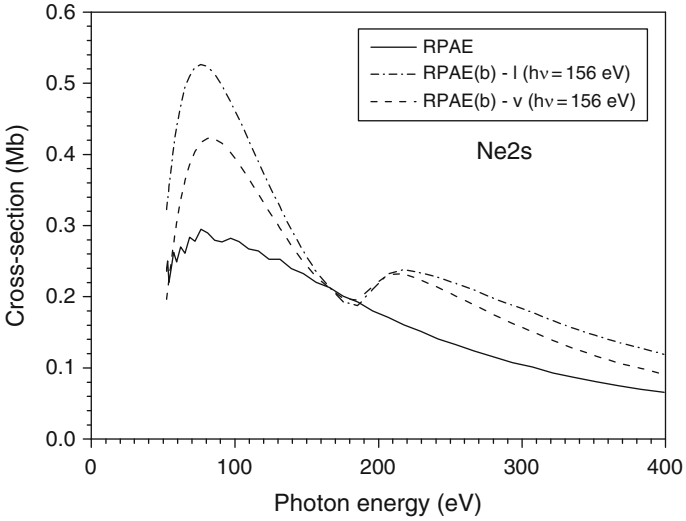

Fig. 7.5_Ne_p5 Ne2*s* photoionization cross-section in RPAE as a function of photon energy and Ne2*s* photoionization cross-section beyond the energy conservation for photon energy 156 eV RPAE(b) (*auxiliary curve*)

Figure 7.5_Ne_p5 gives the Ne2*s* photoionization cross-section in RPAE as a function of photon energy and Ne2*s* photoionization cross-section beyond the energy conservation for photon energy 156 eV (*auxiliary curve*). These curves coincide at photon energy 156 eV. To obtain photoionization cross-section for photon energy 156 eV with the excitation of satellite shifted from the main line to larger binding energy on ΔE, one should use the value on auxiliary curve for the energy shifted to the left by ΔE from this point.

Figure 7.6_Ne_p6 presents Ne2*s* photoionization cross-section in RPAE as a function of photon energy and Ne2*s* photoionization cross-section beyond the energy conservation for photon energy 185 eV (*auxiliary curve*). These curves coincide at photon energy 185 eV. To obtain photoionization cross-section for photon energy 185 eV with the excitation of satellite shifted from the main line to larger binding energy by ΔE, one should use the value on auxiliary curve for the energy shifted to the left by ΔE from this point.

Figures 7.7_Ne_p14–7.19_Ne_p19 contain the Ne2*p* photoionization cross-section in RPAE as a function of photon energy and Ne2*p* photoionization cross-section beyond the energy conservation frame, or "off the energy shell", denoted as RPAE(b).

Figure 7.7_Ne_p7 shows the Ne2*p* photoionization cross-section in RPAE as a function of photon energy and Ne2*p* photoionization cross-section beyond the energy conservation for photon energy 62 eV (*auxiliary curve*). These curves coincide at photon energy 62 eV. To obtain photoionization cross-section for photon energy 62 eV with the excitation of satellite shifted from the main line to larger

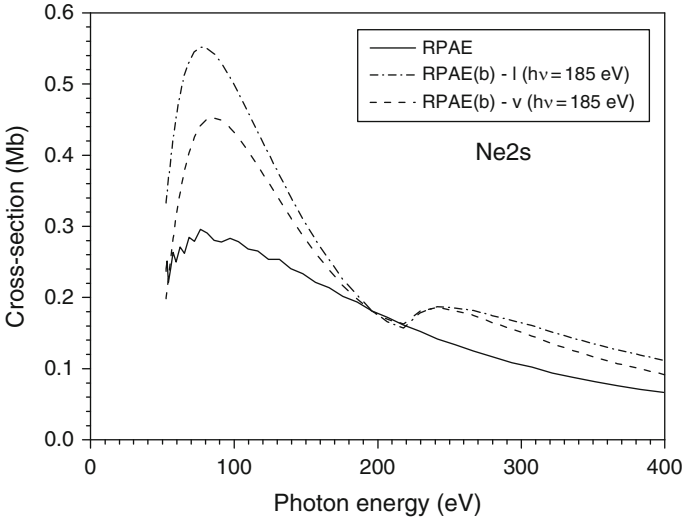

Fig. 7.6_Ne_p6 Ne2*s* photoionization cross-section in RPAE as a function of photon energy and Ne2*s* photoionization cross-section beyond the energy conservation for photon energy 185 eV RPAE(b) (*auxiliary curve*)

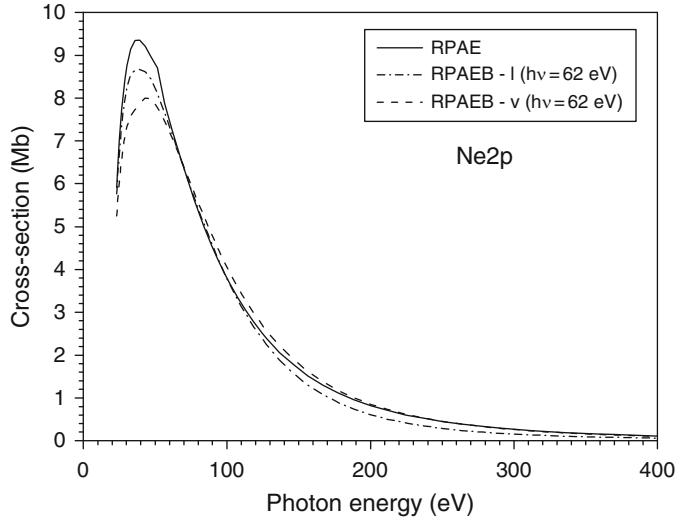

Fig. 7.7_Ne_p7 Ne2*p* photoionization cross-section in RPAE as a function of photon energy and Ne2*p* photoionization cross-section beyond the energy conservation for photon energy 62 eV RPAE(b) (*auxiliary curve*)

binding energy by ΔE, one should use the value on auxiliary curve for the energy shifted to the left by ΔE from this point.

Figure 7.8_Ne_p8 depicts the Ne2*p* photoionization cross-section in RPAE as a function of photon energy and Ne2*p* photoionization cross-section beyond the

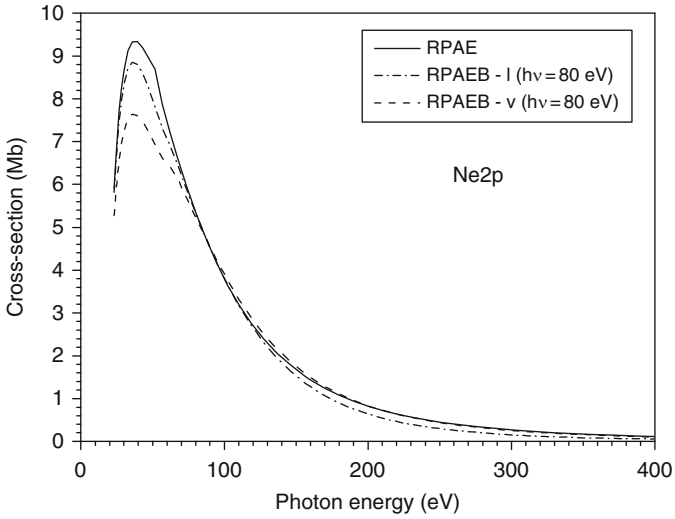

Fig. 7.8_Ne_p8 Ne2p photoionization cross-section in RPAE as a function of photon energy and Ne2p photoionization cross-section beyond the energy conservation for photon energy 80 eV RPAE(b) (*auxiliary curve*)

energy conservation for photon energy 80 eV (*auxiliary curve*). These curves coincide at photon energy 80 eV. To obtain photoionization cross-section for photon energy 80 eV with the excitation of satellite shifted from the main line to larger binding energy by ΔE, one should use the value on auxiliary curve for the energy shifted to the left by ΔE from this point.

Figure 7.9_Ne_p9 demonstrates the Ne2p photoionization cross-section in RPAE as a function of photon energy and Ne2p photoionization cross-section beyond the energy conservation for photon energy 102 eV (*auxiliary curve*). These curves coincide at photon energy 102 eV. To obtain photoionization cross-section for photon energy 102 eV with the excitation of satellite shifted from the main line to larger binding energy by ΔE, one should use the value on auxiliary curve for the energy shifted to the left by ΔE from this point should be used.

Figure 7.10_Ne_p10 represents the Ne2p photoionization cross-section in RPAE as a function of photon energy and Ne2p photoionization cross-section beyond the energy conservation for photon energy 127 eV (*auxiliary curve*). These curves coincide at photon energy 127 eV. To obtain photoionization cross-section for photon energy 127 eV with the excitation of satellite shifted from the main line to larger binding energy by ΔE, one should use the value on auxiliary curve for the energy shifted to the left on ΔE from this point.

Figure 7.11_Ne_p11 shows the Ne2p photoionization cross-section in RPAE as a function of photon energy and Ne2p photoionization cross-section beyond the energy conservation for photon energy 154 eV (*auxiliary curve*). These curves

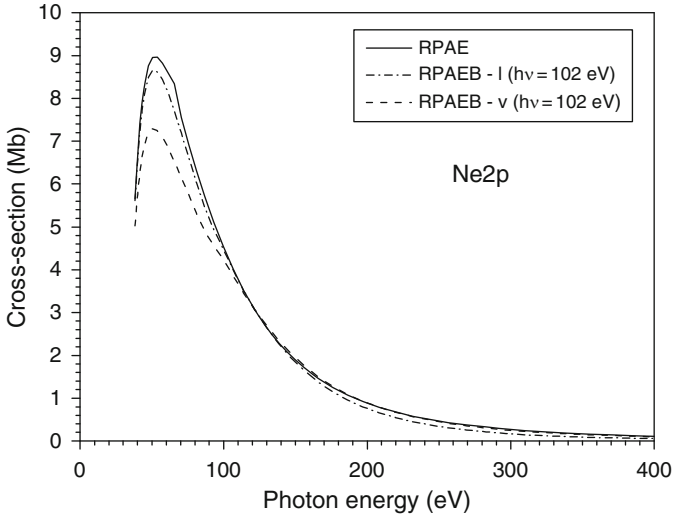

Fig. 7.9_Ne_p9 Ne2p photoionization cross-section in RPAE as a function of photon energy and Ne2p photoionization cross-section beyond the energy conservation for photon energy 102 eV RPAE(b) (*auxiliary curve*)

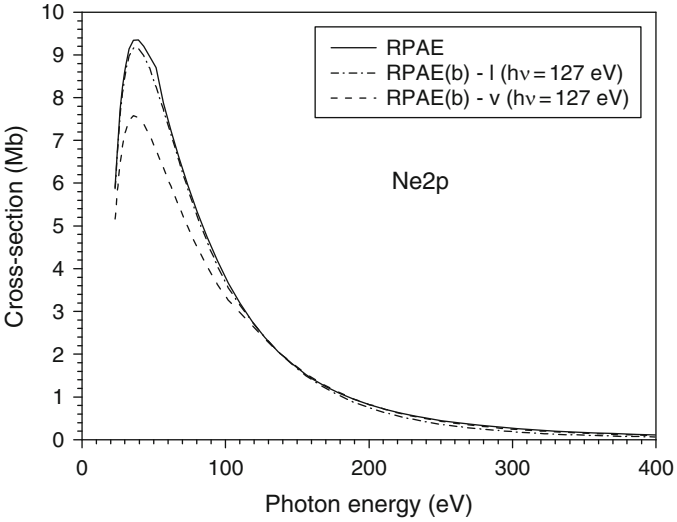

Fig. 7.10_Ne_p10 Ne2p photoionization cross-section in RPAE as a function of photon energy and Ne2p photoionization cross-section beyond the energy conservation for photon energy 127 eV RPAE(b) (*auxiliary curve*)

coincide at photon energy 154 eV. To obtain photoionization cross-section for photon energy 154 eV with the excitation of satellite shifted from the main line to larger binding energy on ΔE, the value on auxiliary curve for the energy shifted to the left on ΔE from this point should be used.

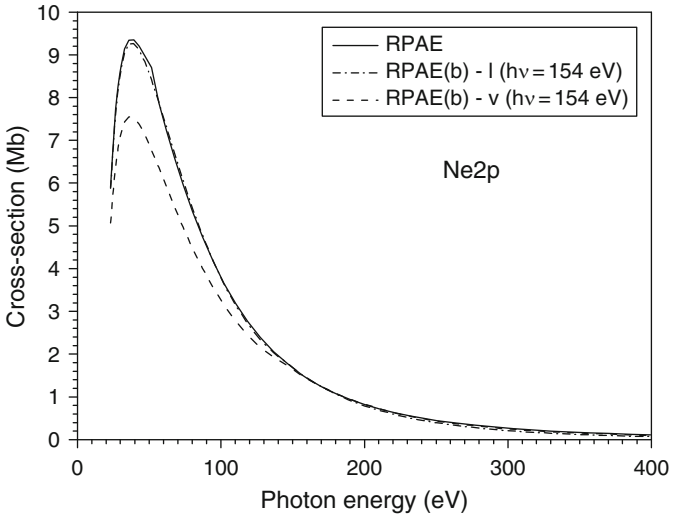

Fig. 7.11_Ne_p11 Ne2*p* photoionization cross-section in RPAE as a function of photon energy and Ne2*p* photoionization cross-section beyond the energy conservation for photon energy 154 eV RPAE(b) (*auxiliary curve*)

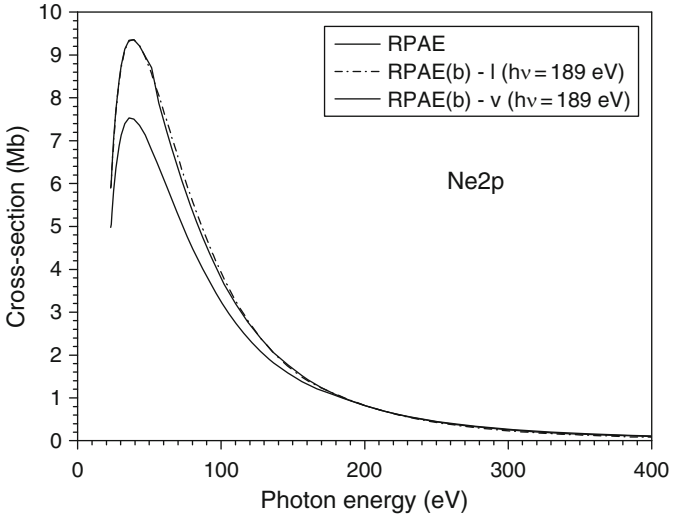

Fig. 7.12_Ne_p12 Ne2*p* photoionization cross-section in RPAE as a function of photon energy and Ne2*p* photoionization cross-section beyond the energy conservation for photon energy 189 eV RPAE(b) (*auxiliary curve*)

Figure 7.12_Ne_p12 gives the Ne2*p* photoionization cross-section in RPAE as a function of photon energy and Ne2*p* photoionization cross-section beyond the energy conservation for photon energy 189 eV (*auxiliary curve*). These curves coincide at photon energy 189 eV. To obtain photoionization cross-section for

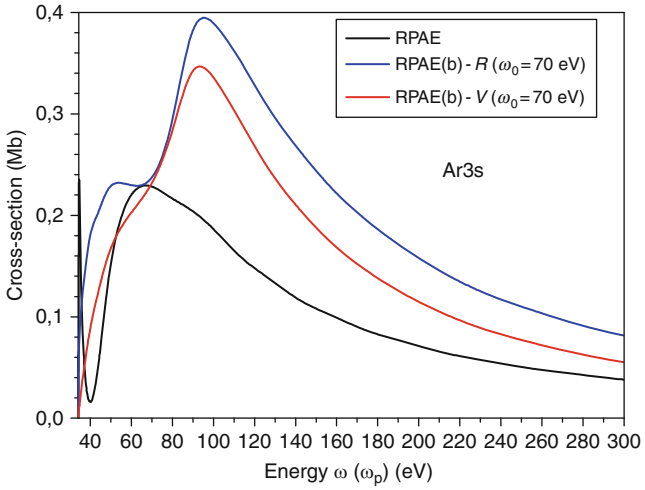

Fig. 7.13_Ar_p1 Ar3*s* photoionization cross-section beyond the energy conservation frame for photon energy $\omega_0 = 70$ eV RPAE(b) as a function of energy ω_p transferred to photoelectron. *Blue*—the length form, *red*—the velocity form, and *black*—Ar3*s* photoionization cross-section as a function of photon energy ω in RPAE. All curves coincide at 70 eV and at region to the left from this point (at the correlation minimum). The cross-section for satellite excitation is smaller than for the main line. Note essential alteration of the cross-section in length (R) and velocity (V) forms with deviation from on-shell RPAE

photon energy 189 eV with the excitation of satellite shifted from the main line to larger binding energy by ΔE, one should use the value on auxiliary curve for the energy shifted to the left on ΔE from this point.

Figures 7.13_Ar_p1–7.48_Xe_p12 present photoionization cross-sections of *ns* and *np* subshells of Ne, Ar, Kr, and Xe in RPAE beyond the energy conservation frame, or, as it is often called, "off the energy shell." It is denoted as RPAE(b). The photoionization cross-sections "off the energy shell" are required for calculation of photoionization cross-sections for excited vacancy states $i^{-1}j^{-1}s$ considered in Chap. 5. For the chosen mechanism the latter cross-section can be represented as:

$$\sigma_{ijs} = \sigma_{i,\omega_p}(\omega)\, f_{js}, \tag{7.2}$$

where f_{js} is the spectroscopic factor given by the formula (5.29), $\omega = \varepsilon_p + \varepsilon_s - \varepsilon_i - \varepsilon_j$ is the energy of a photon the absorption of which results in creation of two vacancies i and j, a photoelectron in continuum with kinetic energy ε_p and discrete or continuum satellite state with energy ε_s. In formula (7.2) $\omega_p = \varepsilon_p - \varepsilon_i$ is the energy transferred to photoelectron and $\sigma_{i,\omega_p}(\omega)$ is a cross-section out off energy shell. In this notations the energy transferred to satellite is $\Delta E_s = \varepsilon_s - \varepsilon_j$. Note that for single electron photoionization $\omega_p = \omega$ and subscript ω_p is omitted. In Figs. 7.13_Ar_p1–7.48_Xe_p12 we present also RPAE photoionization cross-sections with energy conservation. In figures the energy scale is the same for ω

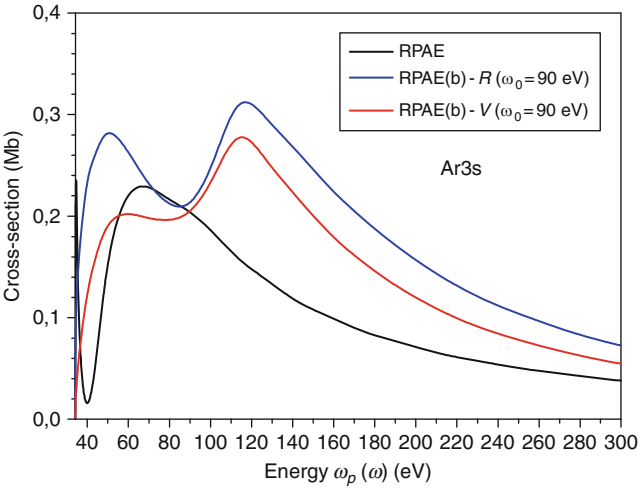

Fig. 7.14_Ar_p2 Ar3*s* photoionization cross-section beyond the energy conservation frame for photon energy $\omega_0 = 90$ eV RPAE(b) as a function of energy ω_p transferred to photoelectron. *Blue*—the length form, *red*—the velocity form and *black*—Ar3*s* photoionization cross-section as a function of photon energy ω in RPAE. All curves coincide at 90 eV. The cross-sections on auxiliary curve, corresponding to typical energy transfer to satellite (i.e., 30–40 eV) are approximately the same as at point 90 eV. The difference between the cross-sections in R and V forms beyond the energy conservation frame is significant. The RPAE(b) curve has two maxima

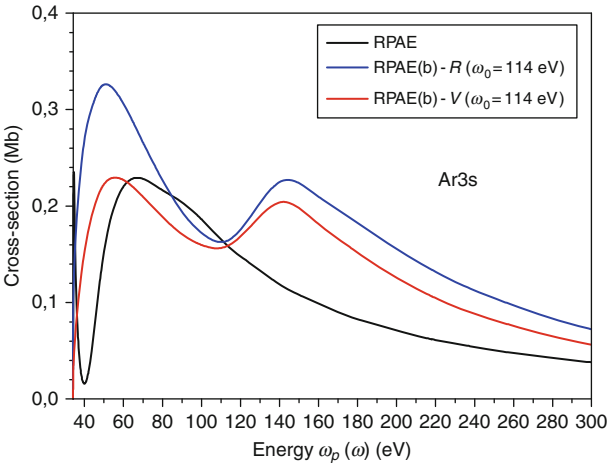

Fig. 7.15_Ar_p3 Ar3*s* photoionization cross-section beyond the energy conservation frame for photon energy $\omega_0 = 114$ eV RPAE(b) as a function of energy ω_p transferred to photoelectron. *Blue*—the length form, *red*—the velocity form, and *black*—Ar3*s* photoionization cross-section as a function of photon energy ω in RPAE. The RPAE(b) curve has two maxima. At the left maximum, which is similar to maximum on the main curve the difference between R and V forms is quite large, obviously due to electron correlations not fully accounted for. It is seen from this figure that the cross-section "off the energy shell," corresponding to satellite is about 20% larger than for the main line

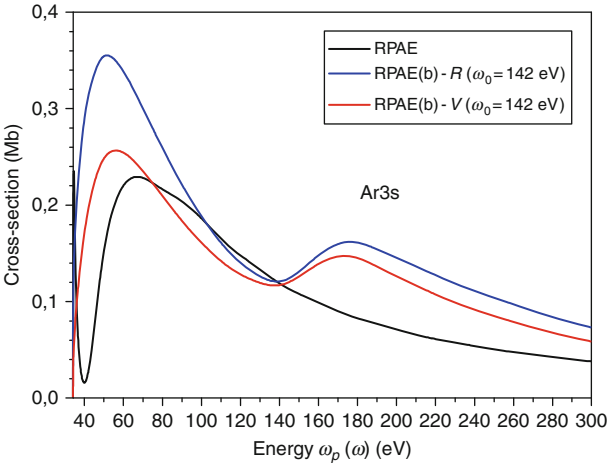

Fig. 7.16_Ar_p4 Ar3*s* photoionization cross-section beyond the energy conservation frame for photon energy $\omega_0 = 142\,\text{eV}$ RPAE(b) as a function of energy ω_p transferred to photoelectron. *Blue*—the length form, *red*—the velocity form, and *black*—Ar3*s* photoionization cross-section as a function of photon energy ω in RPAE. The RPAE(b) curve has two maxima. At the left maximum, which is similar to maximum on the main curve the difference between R and V forms is quite large due to electron correlations not fully accounted for. It is seen from this figure that the cross-section "off the energy shell," corresponding to satellite is about 30% larger than for the main line

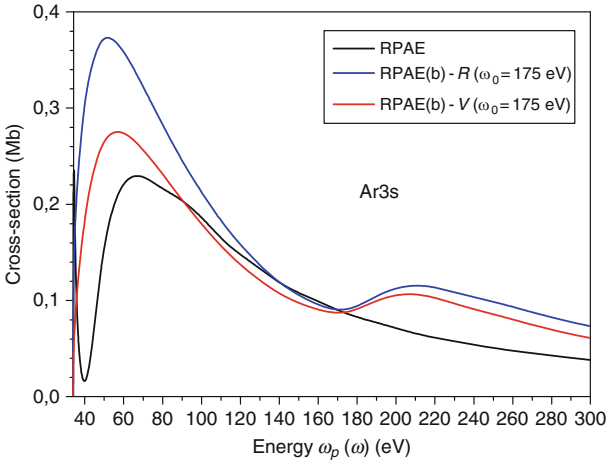

Fig. 7.17_Ar_p5 Ar3*s* photoionization cross-section beyond the energy conservation frame for photon energy $\omega_0 = 175\,\text{eV}$ RPAE(b) as a function of energy ω_p transferred to photoelectron. *Blue*—the length form, *red*—the velocity form, and *black*—Ar3*s* photoionization cross-section as a function of photon energy ω in RPAE. The RPAE(b) curve has two maxima, but the right one is not so significant as for smaller photon energies. At the left maximum, which is similar to the maximum on the main curve the difference between R and V forms is quite large due to electron correlations not fully accounted taken. It is seen from this figure that the cross-section "off the energy shell," corresponding to satellite is about 30% larger than for the main line

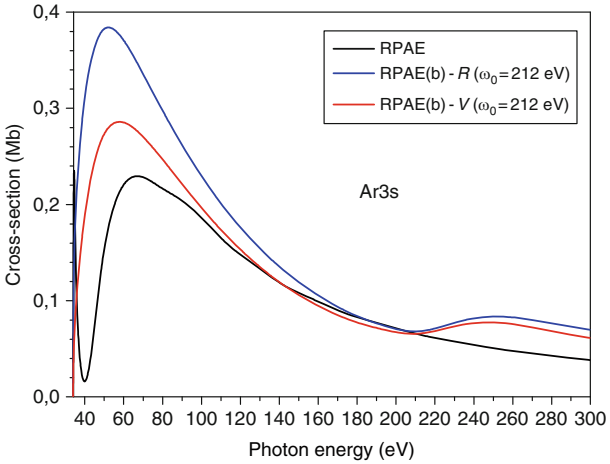

Fig. 7.18_Ar_p6 Ar3*s* photoionization cross-section beyond the energy conservation frame for photon energy $\omega_0 = 212\,\text{eV}$ RPAE(b) as a function of energy ω_p transferred to photoelectron. *Blue*—the length form, *red*—the velocity form, and *black*—Ar3*s* photoionization cross-section as a function of photon energy ω in RPAE. The RPAE(b) curve has two maxima, but the right one is not so significant as for small photon energies. At the left maximum, which is similar to maximum on the main curve the difference between R and V forms is quite large due to electron correlations not fully accounted for. It is seen from this figure that the cross-section "off the energy shell," corresponding to satellite is about 30% larger than for the main line

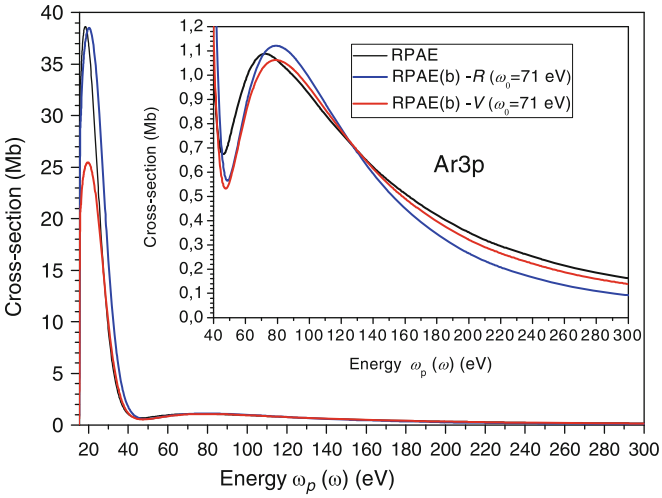

Fig. 7.19_Ar_p7 Ar3*p* photoionization cross-section beyond the energy conservation frame for photon energy $\omega_0 = 71\,\text{eV}$ RPAE(b) as a function of energy ω_p transferred to photoelectron. *Blue*—the length form, *red*—the velocity form, and *black*—Ar3*p* photoionization cross-section as a function of photon energy ω in RPAE. Two cross-sections are approximately the same at $\omega_p = \omega$ and cross-section for the satellite may be obtained making use of main photoionization curve and the same energy shift

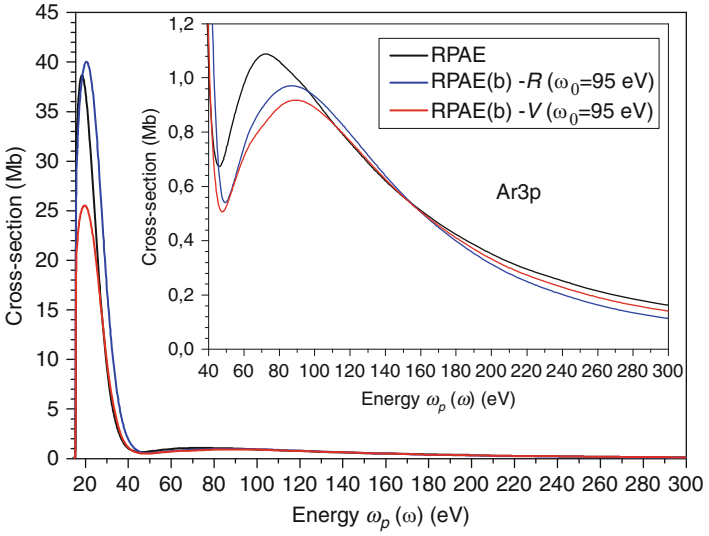

Fig. 7.20_Ar_p8 Ar3p photoionization cross-section beyond the energy conservation frame for photon energy $\omega_0 = 95$ eV RPAE(b) as a function of energy ω_p transferred to photoelectron. *Blue*—the length form, *red*—the velocity form, and *black*—Ar3p photoionization cross-section as a function of photon energy ω in RPAE. Two cross-sections are approximately the same at $\omega_p = \omega$ and cross-section for the satellite may be obtained making use of main photoionization curve and the same energy shift

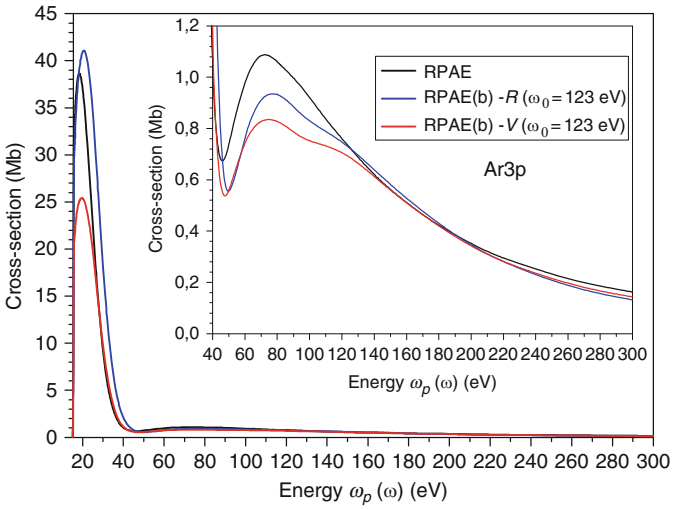

Fig. 7.21_Ar_p9 Ar3p photoionization cross-section beyond the energy conservation frame for photon energy $\omega_0 = 123$ eV RPAE(b) as a function of energy ω_p transferred to photoelectron. *Blue*—the length form, *red*—the velocity form, and *black*—Ar3p photoionization cross-section as a function of photon energy ω in RPAE. Two cross-sections are approximately the same at $\omega_p = \omega$ and cross-section for the satellite may be obtained making use of the main photoionization curve and the same energy shift

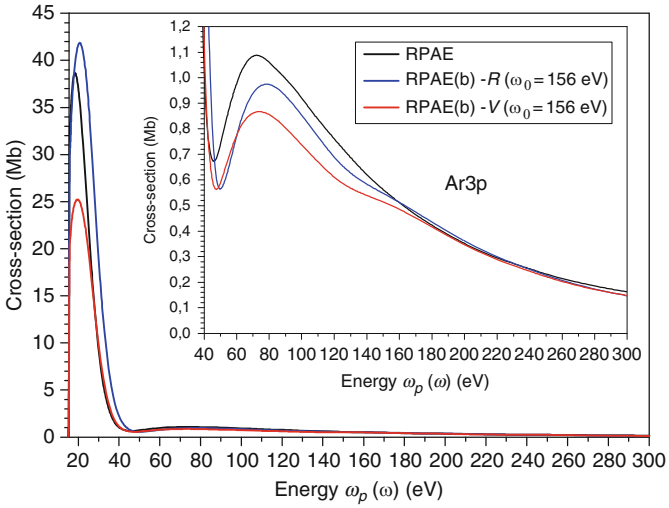

Fig. 7.22_Ar_p10 Ar3p photoionization cross-section beyond the energy conservation frame for photon energy $\omega_0 = 156$ eV RPAE(b) as a function of energy ω_p transferred to photoelectron. *Blue*—the length form, *red*—the velocity form, and *black*—Ar3p photoionization cross-section as a function of photon energy ω in RPAE. Two cross-sections are approximately the same at $\omega_p = \omega$ and cross-section for the satellite may be obtained making use of main photoionization curve and the same energy shift

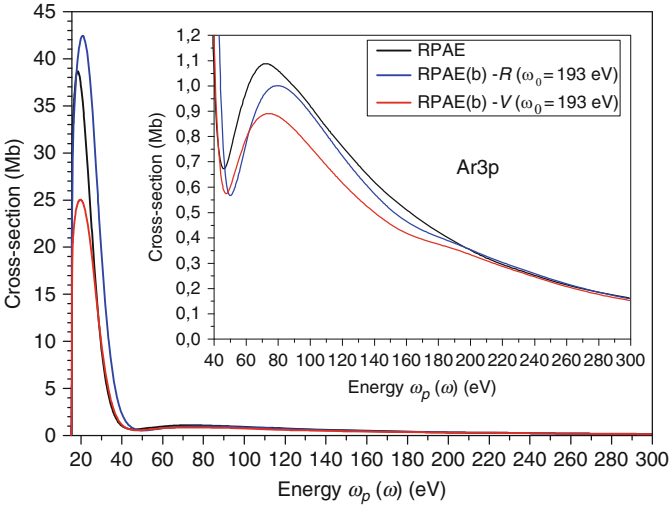

Fig. 7.23_Ar_p11 Ar3p photoionization cross-section beyond the energy conservation frame for photon energy $\omega_0 = 193$ eV RPAE(b) as a function of energy ω_p transferred to photoelectron. *Blue*—the length form, *red*—the velocity form, and *black*—Ar3p photoionization cross-section as a function of photon energy ω in RPAE. Two cross-sections are approximately the same at $\omega_p = \omega$ and cross-section for the satellite may be obtained making use of main photoionization curve and the same energy shift

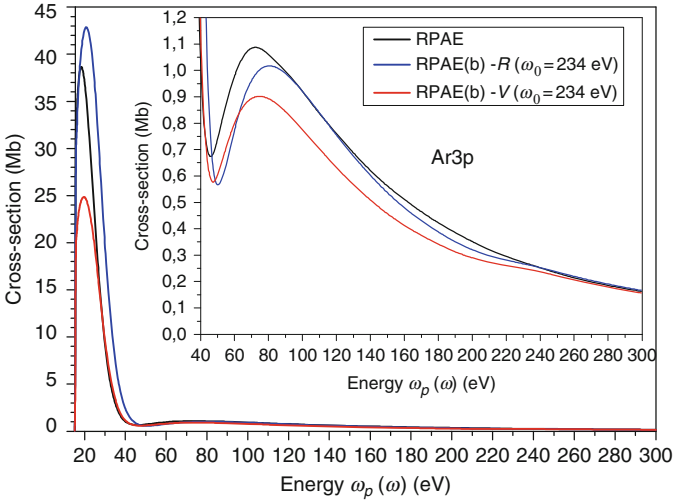

Fig. 7.24_Ar_p12 Ar3p photoionization cross-section beyond the energy conservation frame for photon energy $\omega_0 = 234$ eV RPAE(b) as a function of energy ω_p transferred to photoelectron. *Blue*—the length form, *red*—the velocity form and *black*—Ar3p photoionization cross-section as a function of photon energy ω in RPAE. Two cross-sections are approximately the same at $\omega_p = \omega$ and cross-section for the satellite may be obtained making use of main photoionization curve and the same energy shift

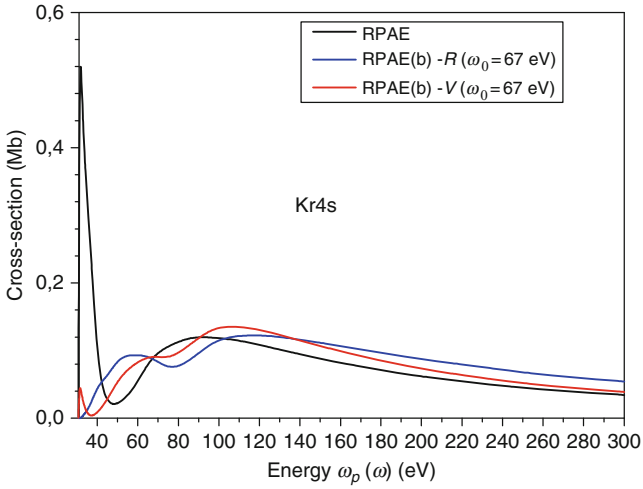

Fig. 7.25_Kr_p1 Kr4s photoionization cross-section beyond the energy conservation frame for photon energy $\omega_0 = 67$ eV RPAE(b) as a function of energy ω_p transferred to photoelectron. *Blue*—the length form, *red*—the velocity form, and *black*—Kr4s photoionization cross-section as a function of photon energy ω in RPAE. The RPAE(b) curve has two maxima, but differs significantly from RPAE curve only near threshold. Shift in energy by 30–40 eV to the left from the point 67 eV where the two curves intersect, corresponds to minimum and cross-section for satellite is significantly smaller then that for the main line

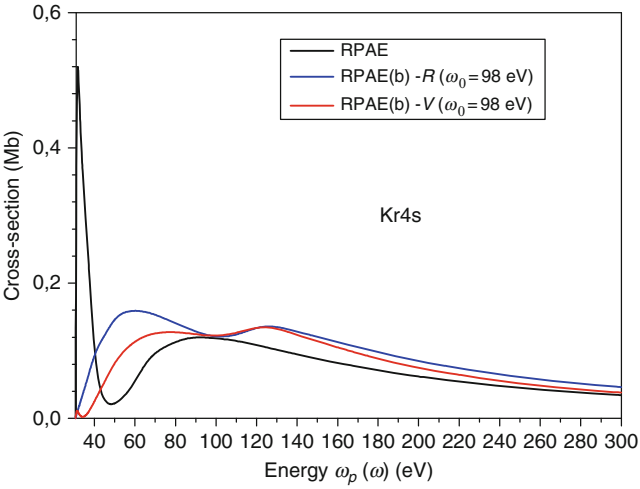

Fig. 7.26_Kr_p2 Kr4*s* photoionization cross-section beyond the energy conservation frame for photon energy $\omega_0 = 98$ eV RPAE(b) as a function of energy ω_p transferred to photoelectron. *Blue*—the length form, *red*—the velocity form, and *black*—Kr4*s* photoionization cross-section as a function of photon energy ω in RPAE. The RPAE(b) curve has two maxima, but differs significantly from RPAE curve only near threshold. The values on RPAE(b) curve at 98 eV and at energies shifted to the left by 30–40 eV are approximately the same as are the cross-sections for the satellite and for the main line

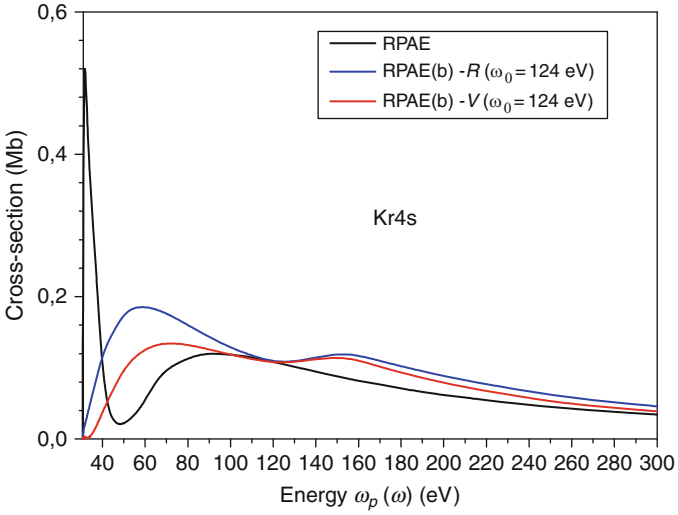

Fig. 7.27_Kr_p3 Kr4*s* photoionization cross-section beyond the energy conservation frame for photon energy $\omega_0 = 124$ eV RPAE(b) as a function of energy ω_p transferred to photoelectron. *Blue*—the length form, *red*—the velocity form, and *black*—Kr4*s* photoionization cross-section as a function of photon energy ω in RPAE. The RPAE(b) curve has two maxima, but differs significantly from RPAE curve only near threshold. The values on RPAE(b) curve at the energies shifted to the left by 30–40 eV are slightly larger than at the intersection point 124 eV

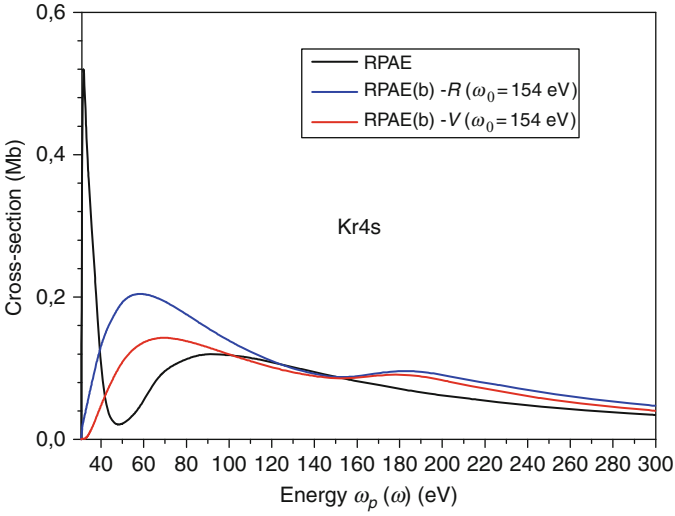

Fig. 7.28_Kr_p4 Kr4*s* photoionization cross-section beyond the energy conservation frame for photon energy $\omega_0 = 154$ eV RPAE(b) as a function of energy ω_p transferred to photoelectron. *Blue*—the length form, *red*—the velocity form, and *black*—Kr4*s* photoionization cross-section as a function of photon energy ω in RPAE. The RPAE(b) curve has two maxima, but differs significantly from RPAE curve only near threshold. When shifted by 30–40 eV to the left from the point 154 eV the cross-section "off the energy shell" increases by about 20–30%

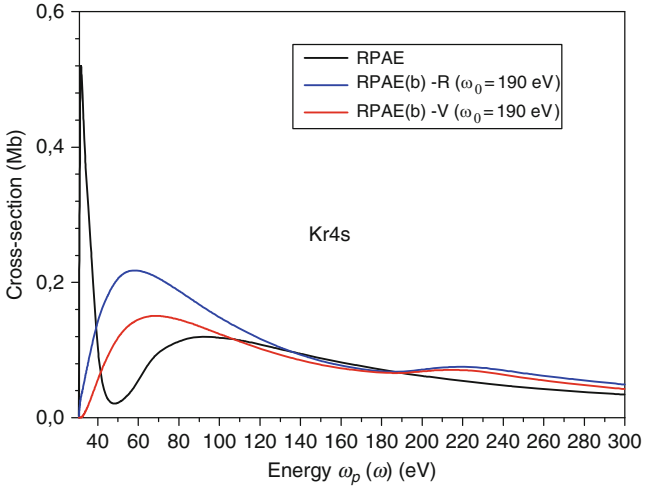

Fig. 7.29_Kr_p5 Kr4*s* photoionization cross-section beyond the energy conservation frame for photon energy $\omega_0 = 190$ eV RPAE(b) as a function of energy ω_p transferred to photoelectron. *Blue*—the length form and *red*—the velocity form, and *black*—Kr4*s* photoionization cross-section as a function of photon energy ω in RPAE. The maximum on RPAE(b) curve is in the region of correlation minimum on the main curve, but since it is far from energy conservation point, this feature is not essential for real cases. In a large energy interval both curves almost coincide and 20–30% increase of the cross-section for the satellite is predicted

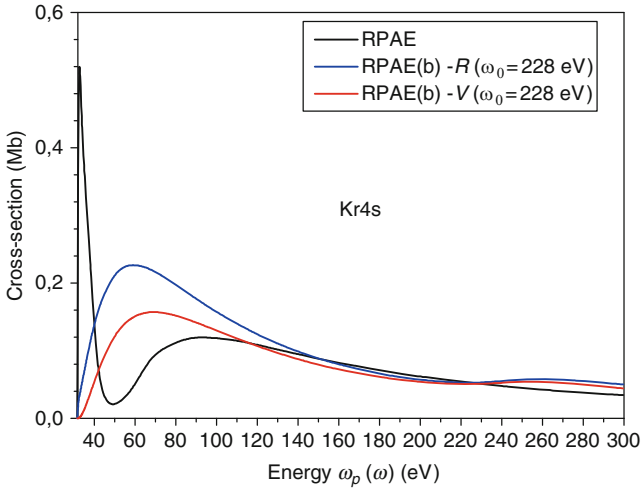

Fig. 7.30_Kr_p6 Kr4*s* photoionization cross-section beyond the energy conservation frame for photon energy $\omega_0 = 228$ eV RPAE(b) as a function of energy ω_p transferred to photoelectron. *Blue*—the length form, *red*—the velocity form, and *black*—Kr4*s* photoionization cross-section as a function of photon energy ω in RPAE. The maximum on RPAE(b) curve is in the region of correlation minimum on the main curve, but since it is far from energy conservation point, this feature is not essential for real cases. In a large energy interval both curves almost coincide and 20–30% increase of the cross-section for the satellite is predicted

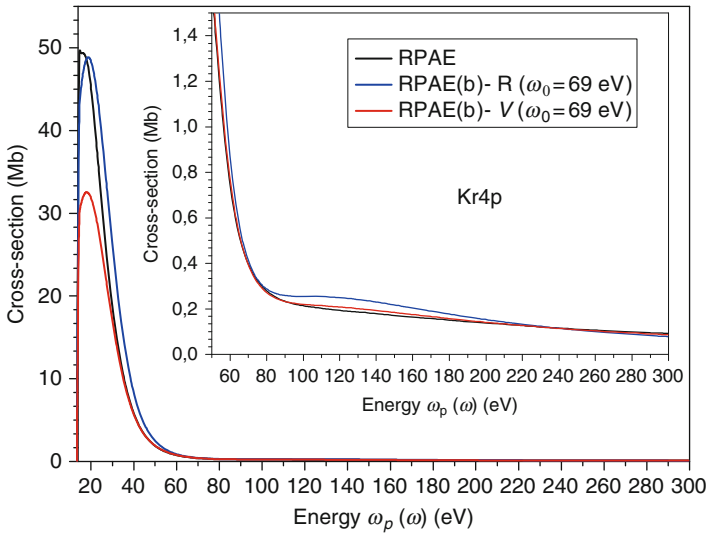

Fig. 7.31_Kr_p7 Kr4*p* photoionization cross-section beyond the energy conservation frame for photon energy $\omega_0 = 69$ eV RPAE(b) as a function of energy ω_p transferred to photoelectron. *Blue*—the length form, *red*—the velocity form, and *black*—Kr4*p* photoionization cross-section as a function of photon energy ω in RPAE. All curves are close to each other except region near threshold

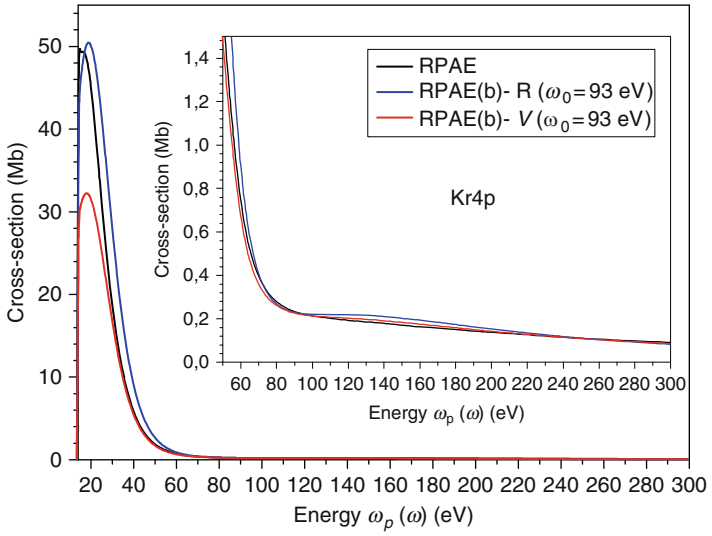

Fig. 7.32_Kr_p8 Kr4p photoionization cross-section beyond the energy conservation frame for photon energy $\omega_0 = 93$ eV RPAE(b) as a function of energy ω_p transferred to photoelectron. *Blue*—the length form, *red*—the velocity form, and *black*—Kr4p photoionization cross-section as a function of photon energy ω in RPAE. All curves are close to each other except region near threshold

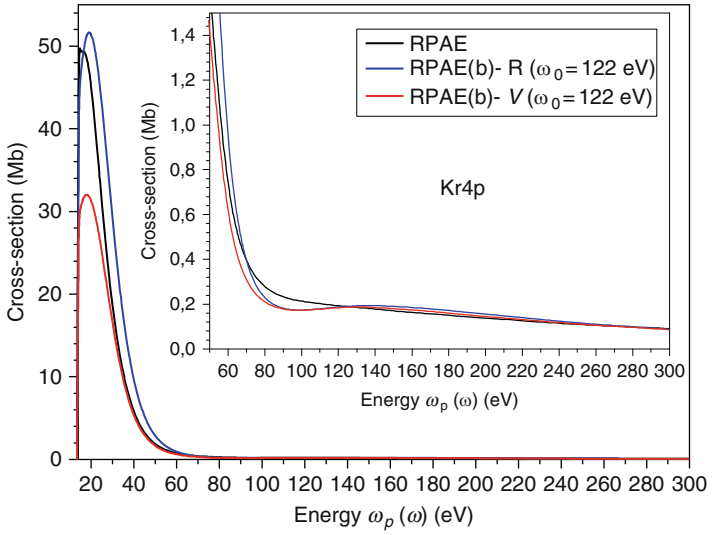

Fig. 7.33_Kr_p9 Kr4p photoionization cross-section beyond the energy conservation frame for photon energy $\omega_0 = 122$ eV RPAE(b) as a function of energy ω_p transferred to photoelectron. *Blue*—the length form, *red*—the velocity form, and *black*—Kr4p photoionization cross-section as a function of photon energy ω in RPAE. All curves are close to each other except region near threshold

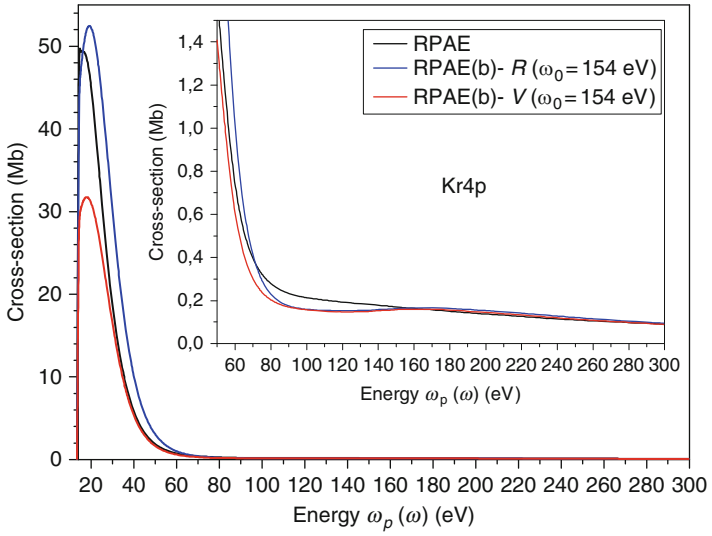

Fig. 7.34_Kr_p10 Kr4p photoionization cross-section beyond the energy conservation frame for photon energy $\omega_0 = 154$ eV RPAE(b) as a function of energy ω_p transferred to photoelectron. *Blue*—the length form, *red*—the velocity form, and *black*—Kr4p photoionization cross-section as a function of photon energy ω in RPAE. All curves are close to each other except region near threshold

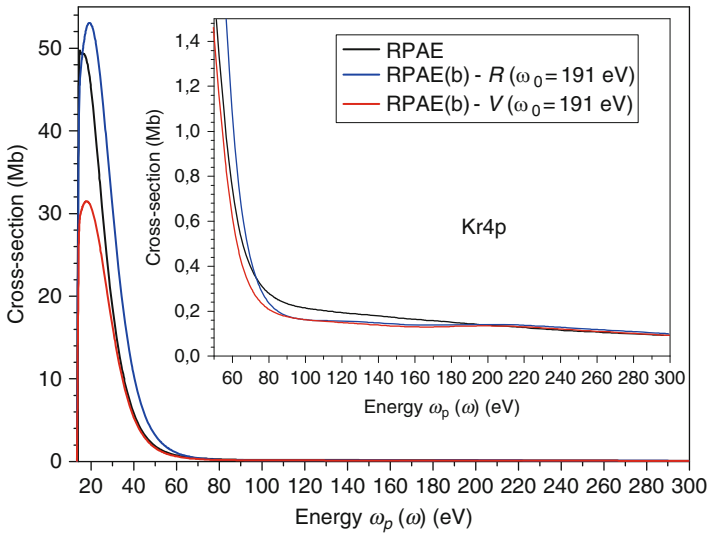

Fig. 7.35_Kr_p11 Kr4p photoionization cross-section beyond the energy conservation frame for photon energy $\omega_0 = 191$ eV RPAE(b) as a function of energy ω_p transferred to photoelectron. *Blue*—the length form, *red*—the velocity form, and *black*—Kr4p photoionization cross-section as a function of photon energy ω in RPAE. All curves are close to each other except region near threshold

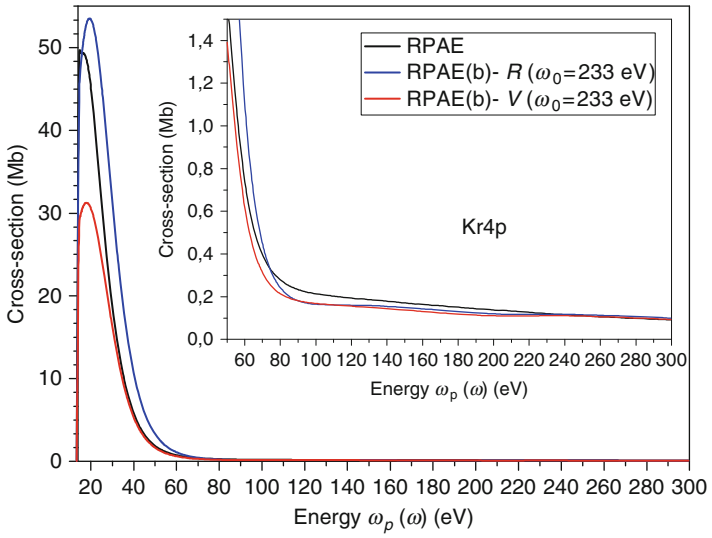

Fig. 7.36_Kr_p12 Kr4*p* photoionization cross-section beyond the energy conservation frame for photon energy $\omega_0 = 233$ eV RPAE(b) as a function of energy ω_p transferred to photoelectron. *Blue*—the length form, *red*—the velocity form, and *black*—Kr4*p* photoionization cross-section as a function of photon energy ω in RPAE. All curves are close to each other except region near threshold

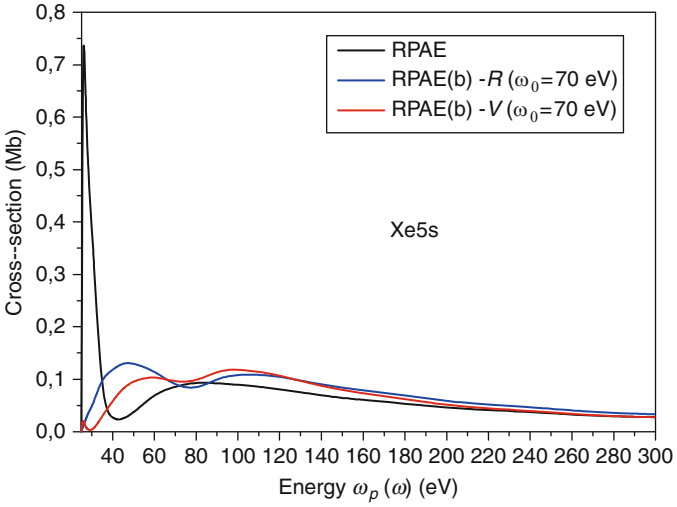

Fig. 7.37_Xe_p1 Xe5*s* photoionization cross-section beyond the energy conservation frame for photon energy $\omega_0 = 70$ eV RPAE(b) as a function of energy ω_p transferred to photoelectron. *Blue*—the length form, *red*—the velocity form, and *black*—Xe5*s* photoionization cross-section as a function of photon energy ω in RPAE. Two types of curves differ significantly near threshold and at the minimum. It is seen from the figure, that cross-section for the energy transfer to satellite 30–40 eV is approximately the same as for the main line

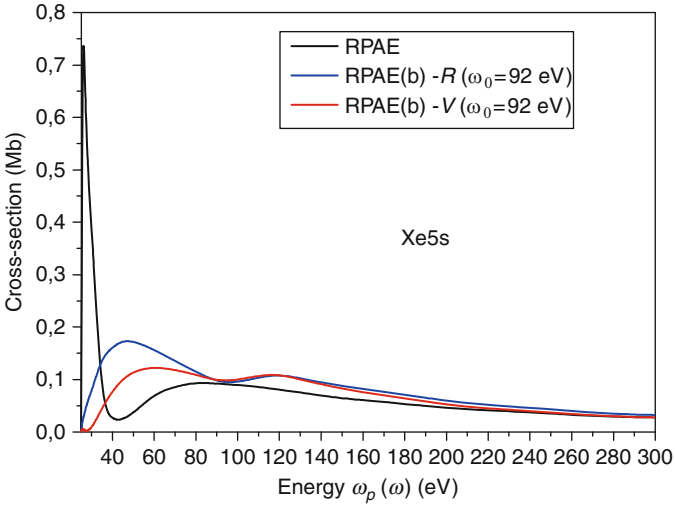

Fig. 7.38_Xe_p2 Xe5*s* photoionization cross-section beyond the energy conservation frame for photon energy $\omega_0 = 92$ eV RPAE(b) as a function of energy ω_p transferred to photoelectron. *Blue*—the length form, *red*—the velocity form, and *black*—Xe5*s* photoionization cross-section as a function of photon energy ω in RPAE. Two curves differ significantly near threshold and at the minimum. It is seen from the figure, that cross-section for the energy transfer to satellite 30–40 eV is about 20% larger than that for the main line

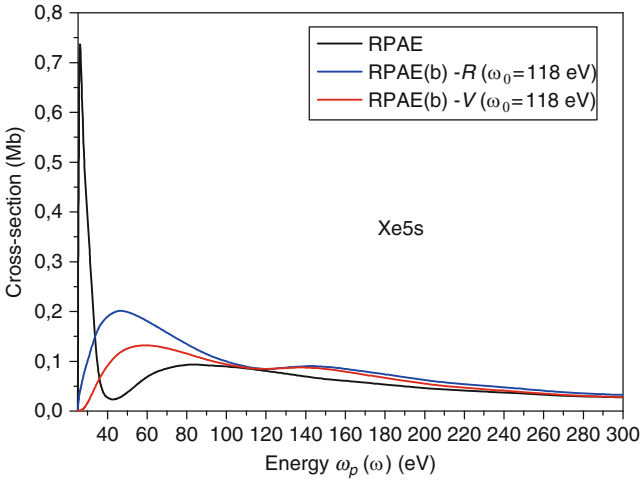

Fig. 7.39_Xe_p3 Xe5*s* photoionization cross-section beyond the energy conservation frame for photon energy $\omega_0 = 118$ eV RPAE(b) as a function of energy ω_p transferred to photoelectron. *Blue*—the length form, *red*—the velocity form, and *black*—Xe5*s* photoionization cross-section as a function of photon energy ω in RPAE. Two curves differ significantly near threshold and at the RPAE correlation minimum, where RPAE(b) curve has a maximum. It is seen from the figure, that cross-section for the energy transfer to satellite 30–40 eV is about 20–30% larger than that for the main line

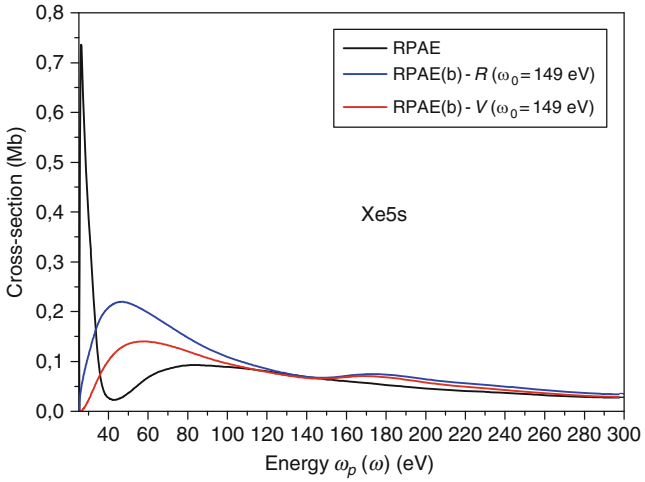

Fig. 7.40_Xe_p4 Xe5*s* photoionization cross-section beyond the energy conservation frame for photon energy $\omega_0 = 149$ eV RPAE(b) as a function of energy ω_p transferred to photoelectron. *Blue*—the length form, *red*—the velocity form, and *black*—Xe5*s* photoionization cross-section as a function of photon energy ω in RPAE. Two curves differ significantly near threshold and at the RPAE correlation minimum where RPAE(b) curve has a maximum. For the energy transfer to satellite 30–40 eV two curves almost coincide. The cross-section for the satellite is larger than that for the main line, but not very essential

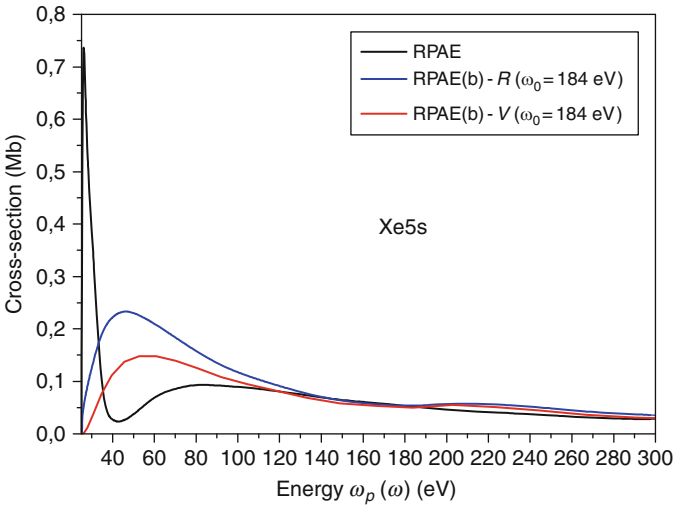

Fig. 7.41_Xe_p5 Xe5*s* photoionization cross-section beyond the energy conservation frame for photon energy $\omega_0 = 184$ eV RPAE(b) as a function of energy ω_p transferred to photoelectron. *Blue*—the length form, *red*—the velocity form, and *black*—Xe5*s* photoionization cross-section as a function of photon energy ω in RPAE. Two curves differ significantly near threshold and at the RPAE correlation minimum where RPAE(b) curve has a maximum. For the energy transfer to satellite 30–40 eV two curves almost coincide. The cross-section for the satellite is larger than that for the main line but not very essential

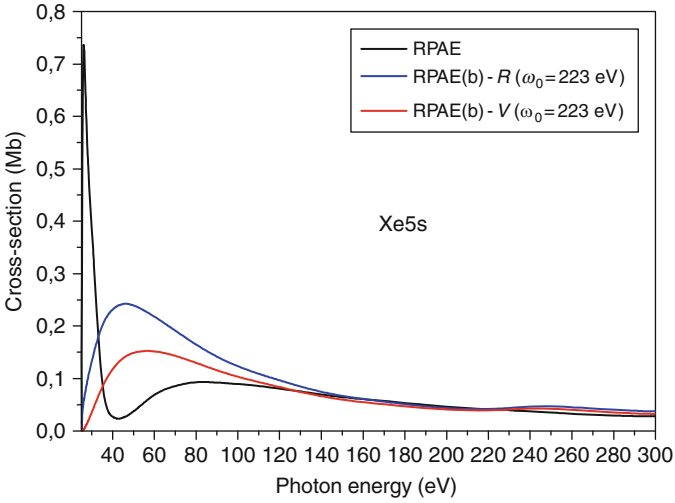

Fig. 7.42_Xe_p6 Xe5*s* photoionization cross-section beyond the energy conservation frame for photon energy $\omega_0 = 223$ eV RPAE(b) as a function of energy ω_p transferred to photoelectron. *Blue*—the length form, *red*—the velocity form, and *black*—Xe5*s* photoionization cross-section as a function of photon energy ω in RPAE. Two curves differ significantly near threshold and at the minimum, but for the energy transfer to satellite 30–40 eV two curves almost coincide. The cross-section for the satellite is larger than that for the main line, but not very essential

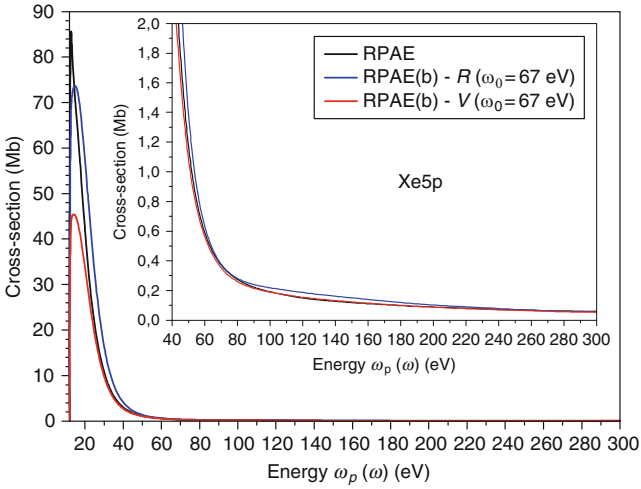

Fig. 7.43_Xe_p7 Xe5*p* photoionization cross-section beyond the energy conservation frame for photon energy $\omega_0 = 67$ eV RPAE(b) as a function of energy ω_p transferred to photoelectron. *Blue*—the length form, *red*—the velocity form, and *black*—Xe5*p* photoionization cross-section as a function of photon energy ω in RPAE. Two curves almost coincide and the cross-section for the satellite intensity calculation can be obtained making use of the main photoionization curve and the same energy shift. The cross-section for energy transfer to satellite 30–40 eV is significantly larger than that for the main line

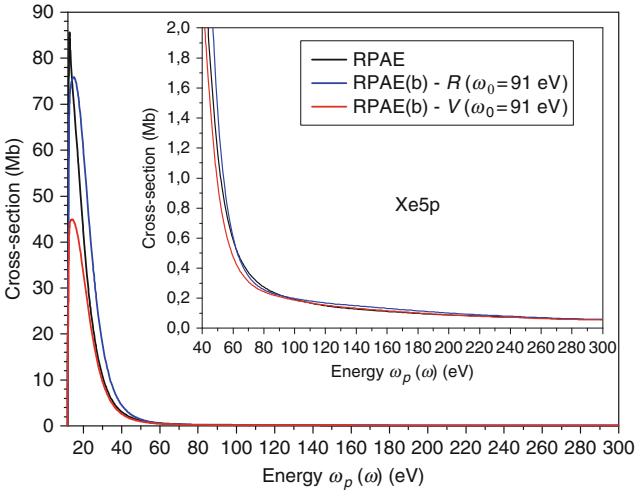

Fig. 7.44_Xe_p8 Xe5p photoionization cross-section beyond the energy conservation frame for photon energy $\omega_0 = 91$ eV RPAE(b) as a function of energy ω_p transferred to photoelectron. *Blue*—the length form, *red*—the velocity form, and *black*—Xe5p photoionization cross-section as a function of photon energy ω in RPAE. Two curves almost coincide and the cross-section for the satellite intensity calculation can be obtained making use of the main photoionization curve and the same energy shift. The cross-section for energy transfer to satellite 30–40 eV is significantly larger than that for the main line

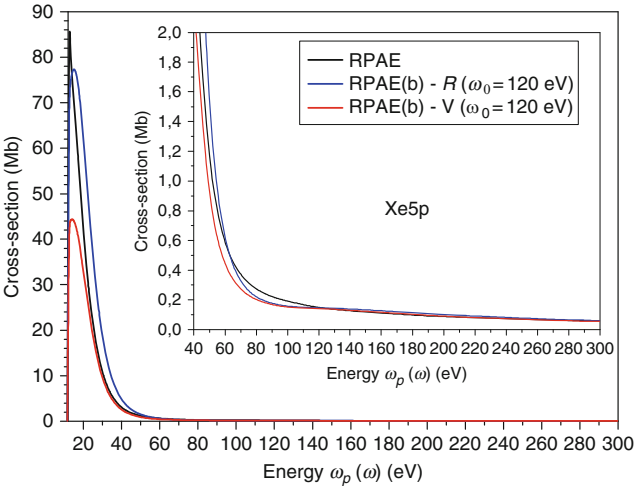

Fig. 7.45_Xe_p9 Xe5p photoionization cross-section beyond the energy conservation frame for photon energy $\omega_0 = 120$ eV RPAE(b) as a function of energy ω_p transferred to photoelectron. *Blue*—the length form, *red*—the velocity form, and *black*—Xe5p photoionization cross-section as a function of photon energy ω in RPAE. Two curves almost coincide and the cross-section for the satellite intensity calculation can be obtained making use of the main photoionization curve and the same energy shift. The cross-section for energy transfer to satellite 30–40 eV is larger than that for the main line

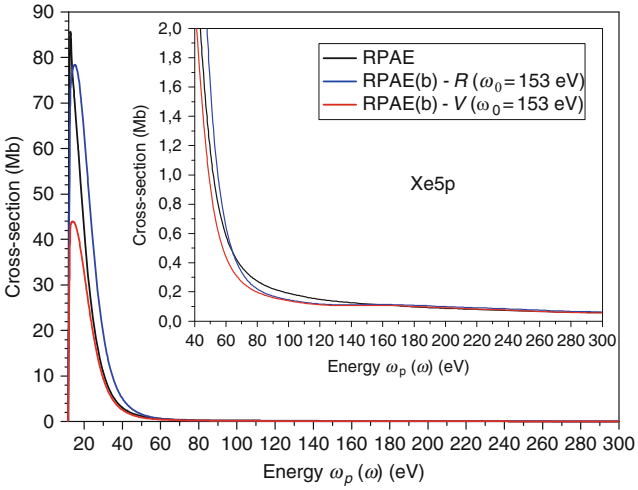

Fig. 7.46_Xe_p10 Xe5p photoionization cross-section beyond the energy conservation frame for photon energy $\omega_0 = 153$ eV RPAE(b) as a function of energy ω_p transferred to photoelectron. *Blue*—the length form, *red*—the velocity form, and *black*—Xe5p photoionization cross-section as a function of photon energy ω in RPAE. Two curves almost coincide and the cross-section for the satellite intensity calculation can be obtained making use of the main photoionization curve and the same energy shift. The cross-section for energy transfer to satellite 30–40 eV is larger than that for the main line

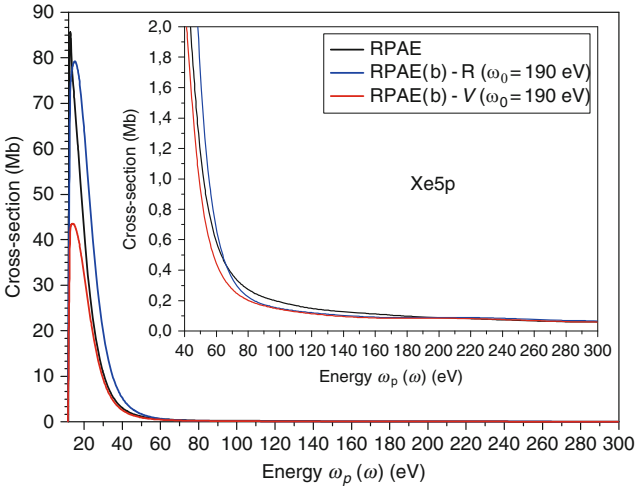

Fig. 7.47_Xe_p11 Xe5p photoionization cross-section beyond the energy conservation frame for photon energy $\omega_0 = 190$ eV RPAE(b) as a function of energy ω_p transferred to photoelectron. *Blue*—the length form, *red*—the velocity form, and *black*—Xe5p photoionization cross-section as a function of photon energy ω in RPAE. Two curves almost coincide and the cross-section for the satellite intensity calculation can be obtained making use of the main photoionization curve and the same energy shift. The cross-section for energy transfer to satellite 30–40 eV is larger than that for the main line

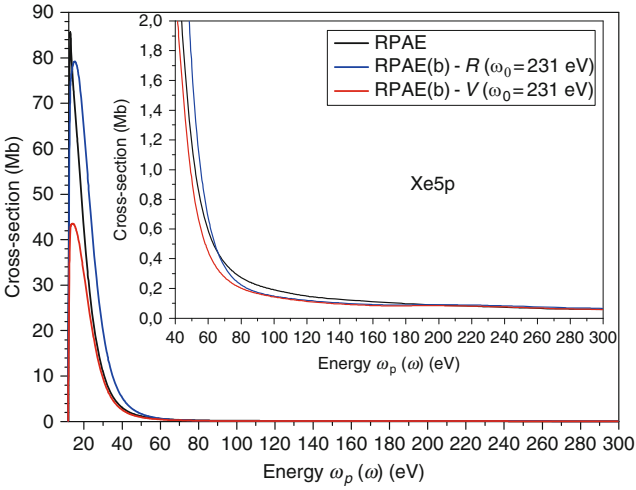

Fig. 7.48_Xe_p12 Xe5p photoionization cross-section beyond the energy conservation frame for photon energy $\omega_0 = 231$ eV RPAE(b) as a function of energy ω_p transferred to photoelectron. *Blue*—the length form, *red*—the velocity form, and *black*—Xe5p photoionization cross-section as a function of photon energy ω in RPAE. Two curves almost coincide and the cross-section for the satellite intensity calculation can be obtained making use of the main photoionization curve and the same energy shift. The cross-section for energy transfer to satellite 30–40 eV is larger than that for the main line

and ω_p. In this energy scale the kinetic energies ε_p of the photoelectron are the same for equals values of ω and ω_p, and shift to the left from the intersection point of both curves to the point under consideration equals to the energy transferred to satellite channel.

Formula (7.2) defines cross-section of shake-up satellite without taking into account for satellite excitation by the outgoing electron. For its calculation spectroscopic factor and photoionization cross-section beyond the energy conservation frame are required.

The dipole matrix elements $D_{ip}(\omega)$ off the energy shell are also required for the calculation of satellite excitation by outgoing electron [see formula (1.151)]. Note that in formula (1.151) additional subscript p, denoting kinetic energy ε_p of photoelectron is used, but in present chapter for the presentation in unified energy scale we use additional energy parameter ω_p.

In this chapter we call the value $\sigma_{i,\omega_p}(\omega)$ of the cross-section in formula (7.2) the *cross-section for satellite* (or the "off the energy shell") and compare it with $\sigma_i(\omega)$ for the main line. The value of spectroscopic factor f_{is}, which is usually about 0.01, is not included in this discussion. Thus, in order to calculate the satellite cross-section one should multiply satellite spectroscopic factor, considered in Chap. 5, by the photoionization cross-section "off the energy shell." The cross-sections "off the energy shell" photoionization are intermediate values of RPAE calculation program (see Chap. 1) and they are in output file of the program. Starting from any point

of photoionization curve $\sigma(\omega)$ and fixing ω_0 one can plot an auxiliary curve. Both curves coincide at $\omega = \omega_0$. Distance to the left from this point equals to the energy transfer to the satellite state. Shift to the right from this point corresponds to virtual continuum states. Integration over all supplementary curves for a given ω_0 is included in the direct knock formula (1.151).

General trends of cross-sections "off the energy shell" are similar for *np* subshells of all the atoms Ne, Ar, Kr, and Xe. For *np*-shells supplementary curves in all cases are close to RPAE photoionization curves. This means that in order to estimate photoionization cross-section of *np* subshell accompanied by energy transfer ΔE_s to satellite by photon of energy ω one can use RPAE photoionization cross-section for photon energy ω-ΔE_s. For the *ns* subshells, whose photoionization cross-section is strongly influenced by the *np* subshell, the trends for different atoms and photon energies are different and will be discussed in more details later.

It is interesting to note that usually photoionization cross-section with energy transfer to satellite is larger than the photoionization cross-section of single ionization. Recent experiments [7.1] show enhancement of satellite intensities relative to the main line near threshold. This enhancement is due to two effects: the increase of the channel of direct excitation of satellites by outgoing electron and the larger values of cross-section "off the energy shell" relative to single ionization cross-section. It should be also noted that some results on the vacancy decay of Chap. 5 [e.g., sum rules (5.31) and (5.32)] were obtained in the assumption of no changing vacancy photoionization cross-section on its energy. Hence it follows that in near threshold region these formulas should be corrected by account for variation of photoionization cross-section out "off the energy shell" value.

References

7.1. Yarzhemsky VG, Amusia MYa, Bolognesi P, Avaldi L (2010) A study of the Ne $2s2p^5(^3P)3s$ and $3p$ correlation satellites up to 75 eV above threshold. J Phys B At Mol Opt Phys 43: 185204

Chapter 8
Conclusion and Perspectives

This book contains the results of calculations of cross-sections and the probabilities of a wide range of atomic processes involving photons and electrons.

These are presented as follows:

(a) Total and partial photoabsorption cross-sections
(b) Dipole and nondipole anisotropy parameters of photoelectrons
(c) Cross-section for elastic scattering of slow electrons and positrons
(d) Generalized oscillator strengths (GOSs) of excitations of discrete and continuous spectrum
(e) Compton scattering cross-section with ionization or excitation
(f) Auger and radiative decays of created in these processes vacancies
(g) Satellite spectra, that accompany the decay of the main vacancy
(h) Multi-electron vacancy decay

As targets we considered atoms belonging to all groups of the periodic table. In some cases, ions are also considered, both positive and negative, of a number of atoms. We provide data for particular kind of endohedral atoms, namely atoms stuffed in the shell of the fullerene C_{60}. An example of a two-shell, or onion endohedral, is also considered.

For many of atoms the calculations of photoionization cross-sections were performed; for the smallest number of atoms: the data on the complex Auger decay of vacancies. The number of examples considered was defined by the labour consumption of the calculation process, reached a degree of its automation, and estimated by us, and therefore somewhat subjective, the need for appropriate mass data. The theoretical approaches used in the calculations were discussed with varying degrees of detail and highlighted, mainly depending on the extent and degree the respective methods were used to treat a given process or characteristics and discussed in the literature.

In the calculations, as the simplest was taken the one-electron Hartree–Fock (HF) approximation, and the interelectron correlations were accounted for mostly in the random-phase approximation with exchange (RPAE) and its various modifications. Some of the results were obtained with the help of the many-body perturbation

M. Amusia et al., *Handbook of Theoretical Atomic Physics*,
DOI 10.1007/978-3-642-24752-1_8, © Springer-Verlag Berlin Heidelberg 2012

theory (MBPT). Used computer programs are described and partly presented in [AC]. However, [AC] has been published a significant time ago, and therefore programs, used to obtain presented in this book results, were substantially modified and supplemented. These modifications take into account improvement of the computers, primarily personal, by increase in the operational speed and memory—both operational and on the hard disk. As a result, it became possible to take into account a much greater number of interacting electrons than before.

In carrying out mass calculations, the important factor is to control the accuracy of the obtained results. We have in mind the value of purely mathematical errors, inevitable in actual calculations in the framework of the chosen physical model or approach. The reliability of numerical results is controlled not only by the careful check of the input data, but also by increasing the number of points, at which are the wave functions obtained while solving the first step HF equations. We dramatically increased also the number of points of the energy in the finite sums, by which are replaced the corresponding integrals over energy with an infinite upper limit.

The convenient method for testing the numerical accuracy of calculation of photoionization cross-sections—full and partial, total or differential in angle of emission of a photoelectron—is the agreement of the results of calculations in the forms of "length" and "velocity" [(1.2), (1.3), and (1.60)]. Results in RPAE must be the same as with the exact wave functions in the initial and final states, [AM]. As to MBPT, HF, and various generalizations of RPAE, the results in the forms of "length" and "velocity" may be different. Note that the coincidence of results in the forms of "length" and "velocity" does not guarantee automatically the accuracy of the chosen approach in the sense of closeness to reliable, proven experimental data, as well as the distinction does not mean that the approximation is bad in describing experimental data. For example, giving a very low accuracy in the description of the experiment, the local one-electron potential, if it is the same for atomic and emitted electrons, leads to the coincidence of the calculation results in the forms of 'length" and "velocity," but with a strong deviation from the experiment.

What has been said in the previous paragraph is true for the GOS also, for which the operators in the forms of "length" and "velocity" presented are given in (3.57). We considered the difference of results in "length" and "velocity" forms within 2–3% as satisfactory, presenting in this case only the mean arithmetic value. The big difference usually indicates that not all electronic subshells and transitions that contribute essentially are taken into account. This is usually caused, in turn, by still existing limits of our computational capabilities.

An important test for the total cross-sections of photoabsorption and GOS obtained with the exact wave-functions is the dipole "sum rule" (see, for example, [AM]). For the photoionization cross-section it has the form (1.7). Note that it is valid not only for the exact wave functions, but also in RPAE. As part of MBPT, HF, and various generalizations of RPAE, the left-hand side in (1.7) does not coincide in general with the total number of electrons in an atom. To apply the sum rule to test the computational accuracy, it is necessary to calculate the cross-section up to very high energies. For an approximate estimate, however, this is not required: the sum rule is approximately satisfied for the majority of the atomic subshells, even if we

restrict the considered photon energy region by not going far beyond the position of the maximum in the photoabsorption cross-section of the considered subshell.

Sum rule analogous to (1.7), is valid for the GOS at any q (3.28):

$$\sum_{f,i} F_{fi}(\omega, q) \equiv Q(q) = N, \tag{8.1}$$

where the summation over f includes the discrete excitation and integration over the continuous spectrum, and on i—contains only a summation over occupied electron states.

Note that since, according to the definition of GOS, the expression $Q(0) = N$, zero is the sum of any GOS derivatives over $q$at zero: $\mathrm{d}^n Q(q)/\mathrm{d}q^n|_{q=0} \equiv Q^{(n)}(q)|_{q=0} = 0$. Until now such verification is not conducted, although the first derivative of the GOS has long been studied (see, for example, [8.1] where the He case is investigated).

The accuracy of calculations is also checked by closeness of their results to reliable established experimental results. Here, however, one should have in mind that in this book the results were obtained using the best suitable for mass calculations theoretical approaches. By themselves, these approaches do not guarantee the best agreement with experiment among some other approaches that could give better agreement for a particular atom or process in it. In contrast, well-established deviation between calculation data presented in this book and the experiment should attract the attention of both parties concerned—theorist and experimentalists. Such a difference can serve as a proof of how limited and not enough developed is the theoretical approach employed by us and whether are some shortcomings with the experiment, mainly the presence of systematic errors. As the side, interested in correctness of calculation data and responsible for it, we want to stress that the differences between theory—experiment is not so rarely helping us to find an error in the experiment. For example, recently calculated in the framework of used in this book approximation, the cross-section of iodine 4d-subshell photoionization [8.2] was three times greater than the value previously adopted in the literature. The subsequent verifying measurements [8.3] confirmed the correctness of the calculation, retaining, nevertheless, some differences between the results of calculation and experiment that will help, hopefully, to improve the methods of calculation. This is by no means an isolated or exceptional case.

Note that the aim of better agreement with experiment can often be achieved artificially, for example, by describing the atomic and departing in the absorption process electrons in two different fields, by the use of “fitting” or free parameters, etc. We are in most cases trying to obtain the theoretical data internally consistent, first in the HF, then RPAE, without caring too much directly about the agreement with experiment, but preferring it to theoretical consistency. Only in this case the discrepancy between the results of calculation and experiment will also indicate, in the general approach based on many-body theory (see [AM]), what should be additionally taken into account.

In the future, in the problem of collecting and storing data, we see, along with the creation of database of the results of calculations presented in this book, such a development of the technique of calculations, which will make it possible, when you specify the name of an atom and indicate a characteristic or cross-section of a process of interest, to calculate all necessary data in a predesigned and selected approach, for example, RPAE, presenting the results in the form of tables or figures, in seconds. Now such a program is still far from reality, but the rate of improvement of computers is extremely fast, so that this aim deserves attention. Note that the increase in speed and memory of personal computers make it possible to obtain data similar to those given in this book, not only for the atoms, but also for simple molecules.

As noted in the Preface, we hope that collected in this book data and methods used to obtain them may be helpful in the theoretical description of already performed experiments, and in the new proposals, for which theoretical estimates or calculations can be made in advance of performing measurements. All this, as stated in the Preface, will help the experimentalists to plan their activities more effectively, performing before real experiment a calculation experiment that is much more simple and less efforts consuming.

References

8.1. Amusia MYa, Zhivanovich Zh, Radojevich V, Cherepkov NA (1976) Photoabsorption for helium, lithium and beryllium atoms in the RPAE. Phys Rev A 13:1466–1474
8.2. Amusia MYa, Cherepkov NA, Chernysheva LV, Manson ST (2000) On the photoionization of the iodine atom and its ions. Phys Rev A 61:R020701–R020704
8.3. Kieldsen H, Andersen P, Folkmann F, Knudsen H, Kristensen B, West JB, Andersen T (2000) Absolute photoionization cross sections of I+ and I++ in the 4d ionization region. Phys Rev A 62:020702(R)

Index

Ag^+, 145
Al^+, 190
Alignment, 717, 718, 721
Amplitude, 10
  at high ω, 57
  of photoionization, 55
Angular anisotropy, 234, 717, 720
Angular anisotropy parameters, 23, 24, 41, 87, 97, 102, 128, 148, 308, 341, 352, 523, 569, 572, 573, 588, 653, 662, 668
Angular distributions, 22, 438, 443, 453
Angular momentum graphical technique, 706
Anisotropy parameter, 214
Annihilation, 8
Ar, 82, 87, 135, 192, 495, 498, 502, 512, 522, 523, 670, 673, 734, 738, 741, 744
$Ar@C_{60}$, 311, 651, 653
$Ar@C_{60}@C_{240}$, 392
As, 234
Asymmetrical broadening, 694
Asymmetry parameters, 17, 695, 741
Auger, 717, 721
  decay, 48, 682, 688, 705, 713, 720, 723, 731
  electrons, 710
  process, 706, 708, 719
  rates, 707, 741, 744
  satellite, 709
  spectra, 710
  width, 715
Autoionization, 717
Autoionization resonances, 24

B, 188
B^*, 188
Ba, 174, 633, 637, 737
Ba^*, 184
$Ba@C_{60}$, 333
Be, 166, 615
Beyond the energy conservation, 763, 767
B_k, 741
Born approximation, 425, 426, 432
Br^-, 279
$Br^-@C_{60}$, 381
Breit interaction, 706
Bremsstrahlung (BR), 456
Broadening, 697
Broad lines, 694

C, 743
C^*, 218
C^-, 218
C_{60}, 306, 348
Ca, 167, 621, 624
Ca^+, 170
Ca^{2+}, 168
$Ca^{2+}K$, 192
Cascade process, 711
$C_{60}@C_{240}$, 391
Cd, 173, 630, 631
Ce^+, 195
Ce^{3+}, 196
Ce^{4+}, 198
$Ce^+@C_{60}$, 360
$Ce^{3+}@C_{60}$, 364
$Ce^{4+}@C_{60}$, 365
Circularly polarized light one has, 28
Cl, 135, 270
Cl^-, 270
$Cl^-@C_{60}$, 375
Collision, 522, 523, 653, 662

M. Amusia et al., *Handbook of Theoretical Atomic Physics*,
DOI 10.1007/978-3-642-24752-1, © Springer-Verlag Berlin Heidelberg 2012

Compton excitation, 447, 507
Compton scattering, 444–446, 448, 485, 487, 506, 554, 673
Configuration interaction, 699, 700, 708, 737
Confinement resonances, 37, 306
Core hole relaxation, 694
Correlation corrections, 15
Correlation minima (CM), 435
Correlations, 3, 520
Coster–Kronig transitions, 683
Coulomb, 21
  interaction, 8
  matrix elements, 20, 687
  potential, 423
Cr, 248
Cr*, 250, 253
Cr^+, 255
Cr^-, 256
Creation, 8
Cross section, 59, 447, 762
Cs, 145, 148, 603, 738
Cs*, 150
Cs^+, 152
Cs^-, 155
$Cs^+@C_{60}$, 357
$Cs@C_{60}$, 332
Cu, 138

Density of quadrupole GOS, 526
Diagonal representation, 685
Diagrammatical technique, 7
Diagrams, 429, 457, 701
Dipolar polarizability, 42
Dipole, 20, 23, 442
  angular anisotropy, 273
  angular anisotropy parameters, 204, 409
  approximation, 4, 25
  Compton scattering, 507, 535
  GOS, 611, 623, 647
  GOSes, 498, 526, 544, 635
  polarizability, 28, 429
Direct knock out, 48
Direct knock satellites, 51
Discrete dipole, 502, 532
Discrete dipole excitations, 472
Discrete levels, 446
Discrete monopole, 483, 499
Discrete monopole excitations, 471
Discrete quadrupole, 501
Discrete quadrupole excitations, 473
Discrete transition, 446
Dispersion relation, 42
Distorted wave Born approximation (DWBA), 427
Double Auger, 711
  decay, 711
  transition, 711
Double autoionization, 716
Double excited states, 717
Double photoionization, 50
Double vacancy, 715
“Drag” current, 70, 77, 107
Dyson equation, 431, 689, 692, 696

Effective interaction, 15
Elastic scattering, 421, 424, 427
Elastic scattering phase, 36
Electron–atom scattering, 421
Electron correlations, 707
Electron–hole pair, 8, 10, 715
Electron scattering, 450, 468, 479, 495, 524, 541, 575, 585, 588, 594, 600, 608, 617, 622, 624, 631, 645
Electron–vacancy pairs, 12
Endohedral atoms, 35, 648, 722
Endohedrals, 35, 37, 39, 69, 306, 336, 450, 456, 738
Enhancement factor, 348
Eu, 203
Eu^+, 206
$Eu@C_{60}$, 336
Excitation, 17, 683
Excited atoms, 54
Excited states, 71, 716

F, 265, 744
F*, 265
F^-, 269, 645
F^{2+}, 267
Fast electron, 438
$F^-@C_{60}$, 370
Fe^+, 300
Fermi, 6
  level, 6
  step function, 14
  vacuum, 684
Feynman diagram, 687
Finite thickness potential, 39
For noble, 70
Frozen approximation, 690
FRPAE, 407
Fullerene decays, 722

Fullerenes, 35, 39, 40, 43–45, 69, 306, 334, 363, 450, 451, 456, 458, 656, 663, 673, 722–724

Ge^-, 228
Generalized oscillator strength (GOS), 427, 434, 437–439, 448, 450, 451, 453, 469, 471, 480, 483, 500, 518, 523, 526, 566, 573, 587, 601, 622, 637, 640, 643, 665, 669, 672, 673
GFRPAE, 407
Giant autoionization resonance, 68, 199
Giant endohedral resonances, 40, 313, 318
Giant resonance, 112
Golden sum rule, 5
GOS. *See* Generalized oscillator strength (GOS)
Graphical technique, 687
Green's function, 686
Ground state correlations, 690, 709
GRPAE, 19, 68
GWRPAE, 69

Half-filled level, 67
He, 70, 468, 470, 474, 477, 670, 675
HF angular, 19
HF approximation, 5
High ω limit, 55
High photon energies, 54, 58
Hund rule, 29

I, 284
I^+, 286
I^-, 292, 646
I^{2+}, 289
$I^-@C_{60}$, 385
Imaginary part of the self energy, 697
In, 193
Induced current, 46, 47
Inelastic and total scattering, 424
Inelastic processes, 422
Inelastic scattered, 47
Inelastic scattering, 433, 437, 450, 456, 523
Inelastic scattering cross section, 426
Interelectron interaction, 10
Interference confinement resonances, 39
Interference minima (IM), 16
Interference resonances (IR), 16, 435
Ionization energies, 684, 740

K, 133, 595
K^+, 133, 600
$K^+@C_{60}$, 353
Knock, 12
Knocked out, 443
Knocked-out electrons, 442
Koopman's theorem, 684, 686
Kr, 92, 96, 524, 526, 534, 669, 670, 737, 738, 741, 746
Kr^{5+}, 96
$Kr@C_{60}$, 316
$Kr@C_{60}@C_{240}$, 398

La, 194
$La@C_{60}$, 335
Length form, 4, 123
Li, 575, 676, 741
Li^+, 124, 579, 583
Li^-, 125, 585
Linear momentum, 38
Line shapes, 695, 710, 730, 734
Line width, 689, 699
L–S coupling, 720

Magic combination, 27, 330
Many-electron correlations, 436
Matrix elements, 7, 10
π-Meson-nucleus scattering, 675
Mg, 166, 616, 621, 676
Mn, 271
Mo, 258
Mo^*, 261
Momentum graphs, 688, 698
Monopole, 534, 536
  Compton scattering, 534, 536
  GOS, 543, 611, 635, 646
  relaxation, 693
Multi-electron correlations, 4, 422

N, 232, 641, 744
N^{3+}, 232
Na, 126, 588
Na^+, 594
Na^-, 130
$Na^+@C_{60}$, 351
Ne, 72, 76, 370, 479, 483, 484, 488, 494, 670, 673, 675, 730, 738, 740, 741, 763, 767
Ne^{3+}, 78
$Ne@C_{60}$, 306
$Ne@C_{60}@C_{240}$, 391

Negative ions, 34
Non-dipole, 26, 27, 41, 76, 96, 103, 123, 319, 442, 443, 523, 572
  angular anisotropy, 179, 275
  angular anisotropy parameters, 31, 70, 390
  parameters, 660

O, 744
O^+, 248
Octupole Compton scattering, 490, 536
Octupole GOSes, 498, 545
One-electron Auger decay of two-hole state, 712
Onion, 69
Onion-type endohedral atoms, 390
Open shell, 33
Open shell atoms, 32
Optical potential, 422
Orientation, 721
Oscillator strengths, 5, 28, 42, 67, 119, 157, 244, 262

P, 227, 232, 642, 643
Partial photoionization cross-section, 375
Partial wave phases, 468
Partial waves, 598
Pd^-, 283
Perturbation theory, 11, 13
Phases, 424, 425
Phase shifts, 424, 425, 429, 431
Photodetachment, 125, 155, 226, 284
Photodetachment cross-section, 269
Photoelectron, 325
  reflection, 325, 327
  scattering, 16, 38
Photoionization, 3, 9, 70, 731
  amplitudes, 40, 49
  cross section, 23, 31, 74, 83, 93, 96, 110, 150, 166, 173, 206, 218, 300, 322, 391, 408, 763, 766
Photon momentum, 46
Polarizability, 45, 70, 89, 423, 456, 458, 461
Polarization, 43, 364, 451, 459, 461
  amplitude factor, 44, 45
  factor, 306, 452
  interaction, 428–431, 433, 459, 685
  parameters, 28
Polarized light, 23
Polarized radiation, 27
Positive ions, 34
Positron, 459, 460
Positron scattering, 459, 474, 492, 511, 512, 539, 562, 578, 583, 589, 594, 602, 613, 615, 621, 624
Positron–atom scattering, 674
Positronium, 459–461, 674, 675
Post collision interaction (PCI), 49
Principal quantum number, 6
Propagation, 9
Pseudo potential, 36

Quadrupole, 27, 46, 47
  Compton scattering, 535
  excitations, 483
  GOS, 547, 613, 623, 636, 648
  polarizabilities, 41, 44
Quasi cross-section, 66
Quasi-free knock-out (QFK), 52
Quasiparticle approximation, 697

Radial integrals, 20, 21
Radiation decay, 715
Radiation probability, 723
Radiation width, 737, 741
Radiative, 748
  and Auger widths, 701
  decay, 682, 701, 722
Ramsauer minimum, 524, 541, 562
Rb, 140
Rb^+, 141
Rb^-, 143
$Rb^+@C_{60}$, 356
Recombination, 51
Reflection amplitude, 43
Reflection by two shells, 399
Reflection factors, 38
Reflection of photoelectrons, 381
Relativistic approach, 704
Relativistic quantum number, 702
Relativistic wave functions, 702
Relaxation, 700
Relaxed-frozen approximation, 691
Resonance, 710
RPAE, 13, 16, 17
RPAEO, 293
RPAEOS, 34

S, 745
Satellite excitation, 49, 50
Satellites, 682, 691, 693, 696, 730, 734, 741, 748, 763, 767

Sb, 236
Sc^{3+}, 190
Scattering, 431, 432, 461, 572
  of fast electrons, 540
  phases, 24, 48
  polarization interaction, 459
  shift, 457
Self-energy, 698, 699
Self-energy part, 701
Semi-Auger decay, 714
Semi-closed shell, 67
Semi-filled shells, 29, 448
Shake-off, 682
Shake-up, 682, 698, 699, 710
Shirley type background, 693
Short range potential, 423, 717
Si*, 220
Si^{+}, 222
Si^{-}, 226, 640
Si^{3+}, 224
Singularity, 22
Slow electron, 52
Small component, 703
Spectator satellite, 708
Spectral function, 686, 689, 730, 731, 736
Spectroscopic factors, 431, 689, 696, 740, 741
Spin–orbit potential, 427
Spin polarization, 106, 184, 721
Spin-polarized, 432
Spin-saturated states, 68
SPRPAE, 30, 31, 68
Sr, 172
Statistical tensors, 718
Sum rules, 689
Super-elastic scattering, 421
Supplementary curves, 50

Tc, 280
Thompson classical elastic scattering cross section, 445
Thompson cross section, 448
Thomson cross section, 491, 507, 537, 558
Thomson scattering, 444
Three-electron, 746
Three-electron radiative decay, 716
Time-forward, 14
Time-forward diagrams, 22
Time-reversal diagrams, 690
Time-reverse, 14
Total cross section, 5
Total photoionization cross-section, 381
Transition amplitude, 426
Transition operator, 434, 435
Two-electronic photoionization, 51
Two-electronic recombination, 51, 53
Two vacancies, 714

Unfilled shell, 692
“Up” and “down” electrons, 29
“Up” and “down” levels, 32
“Up”-electrons, 338

Vacancies, 7, 18
  “decay”, 10
  relaxation, 708
Virtual Auger, 712

Wavefunctions, 428
Weighted GOS, 651
Weight factors, 688, 691, 693, 701, 704, 706
Widths, 17, 682, 741, 747
Wigner law, 34

Xe, 97, 102, 541, 547, 554, 562, 572, 573, 669, 673, 736, 738
Xe^{+}, 110
Xe^{5+}, 116
Xe^{6+}, 118
$Xe@C_{60}$, 319, 662, 668
$Xe@C_{60}@C_{240}$, 406

Zn, 627